Carbon Nanotubes for Electronics and Energy

Habilitation

Dr. Benjamin S. Flavel
Department of Materials and Earth Sciences

TECHNISCHE
UNIVERSITÄT
DARMSTADT

Darmstadt 02/07/2018

Contents

Abstract i

Acknowledgement iii

Statement of Intent v

1. Introduction 1

1.1 Carbon Nanotubes 1

1.1.1 Structure and Property *1*

1.1.2 Suspension and Dispersion *4*

1.1.3 Separation *6*

1.1.4 Thin Films *9*

1.1.5 Energy Applications *11*

1.1.6 Silicon Solar Cells *11*

1.1.7 Fullerene Solar Cells *13*

1.1.8 Photosensitive Elements *15*

2. Publications 17

2.1 Separation of Carbon Nanotubes 17

2.1.1 Separation of Single-Walled Carbon Nanotubes by 1-Dodecanol-Mediated Size Exclusion Chromatography *17*

2.1.2 Separation of Single-Walled Carbon Nanotubes with a Gel Permeation Chromatography System *27*

2.1.3 Separation of Double-Walled Carbon Nanotubes by Size Exclusion Chromatography *39*

2.1.4 Sorting of Double-Walled Carbon Nanotubes According to Their Outer Wall Electronic Type via a Gel Permeation Method *51*

2.1.5 Double-Walled Carbon Nanotube Processing *63*

2.2 Carbon Nanotube Thin Films 99

2.2.1 Aligned Carbon Nanotube Thin Films from Liquid Crystal Polyelectrolyte Inks *99*

2.2.2 Dry Shear Aligning: A Simple and Versatile Method to Smooth and Align the Surfaces of Carbon Nanotubes *109*

2.3 Carbon Nanotube Silicon Solar Cells 117

2.3.1 Carbon Nanotube Silicon Solar Cells 117

2.3.2 Single-Walled Carbon Nanotube/Polyaniline/n-Silicon Solar Cells: Fabrication, Characterisation, and Performance Measurements 135

2.3.3 The Role of Nanotubes in Carbon Nanotube-Silicon Solar Cells 145

2.3.4 Nanotube Film Metallicity and its Effect on the Performance of Carbon Nanotube-Silicon Solar Cells 155

2.4 Carbon Nanotube Fullerene Solar Cells 169

2.4.1 Performance Enhancement of Polymer-Free Carbon Nanotube Solar Cells via Transfer Matrix Modeling 169

2.5 Carbon Nanotubes as Photosensitive Elements 181

2.5.1 Photocurrent Spectroscopy of (n,m) Sorted Solution-Processed Single-Walled Carbon Nanotubes 181

2.5.2 Photocurrent Imaging of Semiconducting Carbon Nanotube Devices with Local Mirrors 191

2.6 Additional Scientific Publications 197

2.6.1 Chemically Immobilised Carbon Nanotubes on Silicon: Stable Surfaces for Aqueous Electrochemistry 197

2.6.2 Nanoscale Structure of Lipid Domain Boundaries 207

2.6.3 Carbon Nanotube Network Electrodes for Dye Solar Cells 217

2.6.4 Patterning of Metal, Carbon and Semiconductor Substrates with Thin Organic Films by Microcontact Printing with Aryldiazonium Salt Inks 227

2.6.5 A Simple Approach to Patterned Protein Immobilization on Silicon via Electrografting from Diazonium Salt Solutions 237

2.6.6 Electrochemical Detection of Copper Using a Gly-Gly-His Modified Carbon Nanotube Biosensor 249

2.6.7 Comparison of Double-Walled with Single-Walled Carbon Nanotube Electrodes by Electrochemistry 261

2.6.8 Micropatterned Arrays of Porous Silicon: Towards Sensory Biointerfaces 273

2.6.9 Electrochemistry of Polystyrene Intercalated Vertically Aligned Single and Double-Walled Carbon Nanotubes on Gold Electrodes 285

2.6.10 Single- and Double-Sided Chemical Functionalization of Bilayer Graphene 291

2.6.11 Increased Redox-Active Peptide Loading on Carbon Nanotube Electrodes 303

2.6.12 *Patterned Forests of Vertically-Aligned Multiwalled Carbon Nanotubes Using Metal Salt Catalyst Solutions* 311

2.6.13 *Grafting of Poly(ethylene glycol) on Click Chemistry Modified Si(100) Surfaces* 317

2.6.14 *Waveguide-Integrated Electroluminescent Carbon Nanotubes* 327

2.6.15 *Fabrication of Carbon Nanotube Nanogap Electrodes by Helium Ion Sputtering for Molecular Contacts* 337

2.6.16 *Deposition of Semiconducting Single-Walled Carbon Nanotubes Using Light Assisted Dielectrophoresis* 343

2.6.17 *Light Emission, Light Detection and Strain Sensing with Nanocrystalline Graphene* 351

3. Supporting Information 363

3.1 Separation of Carbon Nanotubes 363

3.1.1 *Separation of Single-Walled Carbon Nanotubes by 1-Dodecanol-Mediated Size Exclusion Chromatography* 363

3.1.2 *Separation of Single-Walled Carbon Nanotubes with a Gel Permeation Chromatography System* 365

3.1.3 *Separation of Double-Walled Carbon Nanotubes by Size Exclusion Chromatography* 369

3.1.4 *Sorting of Double-Walled Carbon Nanotubes According to Their Outer Wall Electronic Type via a Gel Permeation Method* 383

3.2 Carbon Nanotube Thin Films 405

3.2.1 *Aligned Carbon Nanotube Thin Films from Liquid Crystal Polyelectrolyte Inks* 405

3.2.2 *Dry Shear Aligning: A Simple and Versatile Method to Smooth and Align the Surfaces of Carbon Nanotubes* 409

3.3 Carbon Nanotube Silicon Solar Cells 421

3.3.1 *The Role of Nanotubes in Carbon Nanotube-Silicon Solar Cells* 421

3.3.2 *Nanotube Film Metallicity and its Effect on the Performance of Carbon Nanotube-Silicon Solar Cells* 423

3.4 Carbon Nanotube Fullerene Solar Cells 431

3.4.1 *Performance Enhancement of Polymer-Free Carbon Nanotube Solar Cells via Transfer Matrix Modeling* 431

3.5 Carbon Nanotubes as Photosensitive Elements 445

3.5.1 Photocurrent Spectroscopy of (n,m) Sorted Solution-Processed Single-Walled Carbon Nanotubes 445

3.5.2 Photocurrent Imaging of Semiconducting Carbon Nanotube Devices with Local Mirrors 447

4. References 449

Abstract

Ever since their discovery, carbon nanotubes have been touted as a new material for the future and a correspondingly lengthy list of possible applications are often cited in the literature. This excitement for carbon nanotubes is a result of their richly varying physical, electronic and optical properties, where it is possible to have single, double and multiple carbon walls with each wall potentially being either semiconducting or metallic and possessing unique optical transitions covering the ultraviolet to infrared spectral range. However, to date the realization of many of the proposed applications has been hindered by exactly the characteristic that made carbon nanotubes so attractive in the first place, namely the inherent inhomogeneity and varying properties of as-prepared or grown material. In order to become a true advanced material of the future, methods to prepare carbon nanotubes with defined length, wall number, diameter, electronic and optical property are necessary. Additionally, such methods to sort carbon nanotubes must afford high purity levels, be amenable to large-scale preparation and be compatible with subsequent integration into device architectures.

In this work these issues are addressed with the use of gel based sorting techniques, which with the use of an automated gel permeation system allows for the routine preparation of milligram quantities of metallic and semiconducting carbon nanotubes, chirality pure single walled carbon nanotubes and even double walled carbon nanotubes sorted by their outer-wall electronic type. Having developed techniques to prepare large quantities, methodologies to control the order and orientation of this 1 D nanomaterial on the macro scale are developed. Inks of carbon nanotubes with liquid crystal concentrations and aligned films thereof are developed and this newfound control over the electronic and structural property opened the door for energy related applications. For example the use of thin films as the transparent electrodes in silicon:carbon nanotube solar cells or as the light harvesting layer in combination with fullerenes with the goal of creating an all carbon solar cell. Likewise on the few nanotube level the unique optical transitions of different nanotube chiralities are used in the fabrication of nanoscale photosensitive elements.

– This page intentionally left blank –

Acknowledgement

Fundamental to the scientific endeavour is the collaborative research effort of many and in this regard I have been particularly fortunate to work with many brilliant scientists. I am deeply grateful to my mentor Prof. Dr. Ralph Krupke who has not only provided me with many valuable scientific insights throughout the course of my research but also guided me in the intricacies of leading your own research group. I have also been fortunate to have many highly skilled doctoral students such as Dr. Katherine Moore, Dr. Moritz Pfohl and Mr. Asiful Alam who were willing to take a chance on a young and developing research group. It fills me with a great sense of pride to have been part of your academic development. Furthermore, I am indebted to Dr. Michael Engel and Dr. Daniel Tune who spent postdoctoral periods with my group. I wish you all the best in your own careers.

Science is also characterised by the never-ending pursuit of research funding and I am eternally grateful to a number of funding bodies. Firstly to the Australian Government for provision of an Endeavour Research Fellowship in 2009, the Alexander von Humboldt Fellowship for brining me to Germany as a Postdoctoral Fellow in 2011 – 2012 and most importantly the German Research Foundation (DFG) for admission into the Emmy Noether Program under grant number FL 834/1-1. The Emmy Noether Program from the DFG is a unique and fantastic opportunity for a young scientist and my scientific career to date would not have been possible without their trust and support.

Finally, on a personal level I wish to thank my friends and family and most importantly thank Sabrina for her love and support in my pursuit of an academic career.

– This page intentionally left blank –

Statement of Intent

This work is submitted in partial fulfilment of the requirements for Habilitation at the Technische Universität Darmstadt in the Department of Materials and Earth Science, where Habilitation is pursued in the field of Carbon Nanotubes under the mentorship of Prof. Dr. Ralph Krupke.

Submitted towards Habilitation are the scientific publications from my German Research Foundation (DFG) funded Emmy Noether research group from the period 2012 – 2015. Section 1 provides a brief overview to carbon nanotubes with the intent of allowing the reader to position the included publications in the research field along with their corresponding scientific significance. Section 2.1 – 2.5 then divides the publications into the subsections of ‘Separation of Carbon Nanotubes’, ‘Carbon Nanotube Thin Films’, ‘Carbon Nanotube Silicon Solar Cells’, ‘Carbon Nanotube Fullerene Solar Cells’ and ‘Carbon Nanotubes as Photosensitive Elements’. These publications are presented in chronological order and the corresponding supporting information can be found in section 3.

Additionally, scientific publications from my time as a Postdoctoral Researcher from 2009 – 2012 and those that have arisen through collaboration with other research groups are submitted in section 2.6 under ‘Additional Scientific Publications’ as non-assessment items. These items are provided to further verify the quality of my scientific research since completing my PhD in 2008.

Dr. Benjamin Scott Flavel

– This page intentionally left blank –

1.1 Carbon Nanotubes

1.1.1 Structure and Property

Carbon nanotubes are an allotrope of carbon having the form of hollow cylinders, often compared to rolled-up sheets of graphene, which is itself an extended hexagonal lattice of purely sp^2 bonded carbons. Strictly speaking, carbon nanotubes are either single-walled (SWCNTs) or multi-walled (MWCNTs), but the term double-walled carbon nanotubes (DWCNTs) is also often used in the literature in the case of two walls. A single carbon cylinder, be it a SWCNT or a component wall of a DWCNT or MWCNT, can be completely described, except for its length, by an intrinsic geometric property, $\mathbf{C_h}$, known as the chiral vector.[1-4] The chiral vector is defined by the equation $\mathbf{C_h} = n\mathbf{a_1} + m\mathbf{a_2}$ where the integers (n,m) are the number of steps along the zig-zag carbon bonds and $\mathbf{a_1}$, $\mathbf{a_2}$ are the graphene lattice basis vectors in real space (Figure 1 (a)). The chiral vector makes an angle, θ, known as the chiral angle, with the zig-zag or $\mathbf{a_1}$ direction. This angle determines the amount of 'twist' in the nanotube and two limiting cases exist where the chiral angle is at 0° and 30°. These are known as zig-zag (0°) and armchair (30°) based on the geometry of the carbon bonds around the circumference of the nanotube (Figure 1 (b) and Figure 1 (c)). All other conformations in which the C–C bonds lie at angles $0° < \theta < 30°$ are known as chiral (Figure 1 (d)).

Because the n,m integers completely describe nanotube chirality, they also determine the electronic band structure. Thus, it is the chirality that has the most impact on the optical and electronic properties of carbon nanotubes.[5] In particular, a slight change of the chiral angle yields nanotubes that are metallic conductors, low band gap or high band gap semiconductors. In the case of semiconductors, the band gap energy is inversely dependent on the nanotube diameter. The armchair nanotubes are the only type that are intrinsically metallic (zero band gap), although approximately a third of the zigzag nanotubes also exhibit metallic properties at room temperature because the band gap is smaller than the thermal energy, k_BT, allowing thermal excitation of carriers into the conduction band. All chiral nanotubes and the remaining two thirds of zigzag nanotubes are therefore semiconducting at room temperature. This leads to the observation that approximately 60 % of all nanotube chiralities are semiconducting with the remaining 40 % metallic.[6]

Carbon nanotubes are so small that they exhibit quasi-one dimensional properties, with the confinement of electrons into allowed momentum states giving rise to van Hove singularities in their electronic density of states (Figure 1(e) and Figure 1 (f)). In bulk semiconducting materials, the energy gap between the valance and conduction bands defines the absorption onset wavelength of the optical spectra, but in the case of carbon nanotubes the discrete electronic transitions in their DOS produce a series of characteristic peaks in the optical absorption spectra at correlated energies (Figure 1 (g)). In the case of bulk semiconducting materials the single particle model (an electron absorbs a photon and thus moves from a lower energy level to a higher one) provides a reasonably close approximation of empirical observations. However, the 1D confinement of electrons in carbon nanotubes causes a significantly higher electron-hole binding energy (eh) and electron-electron repulsion (ee), meaning that true consideration of the optical absorption spectra of nanotubes must be entirely excitonic in nature (light energy is absorbed by the material creating excited states a.k.a bound electron-hole pairs) with the many-body effects (eh and ee) included for an accurate description.[7] This means that the actual light energy required to produce a "v_i – c_i" transition is (Ec_i - Ev_i) + binding energy (eh) - self energy (ee), and leads to the experimental finding that E_{22}/E_{11} tends to a value of 1.8 with decreasing tube diameter, rather than the value of 2 as would be expected from density functional theory (DFT) calculations alone.[8] The excitonic nature of the optical properties is an important consideration for specialists however, in the interests of simplicity the single particle approximation is often sufficient to appreciate the concepts. There are two other important processes in nanotubes which, in addition to optical absorption spectroscopy, provide vital information regarding nanotube type and character. These are photoluminescence, in which semiconducting nanotubes are excited by an S_{22} photon which then decays emitting a detectable S_{11} photon and allowing chiral identification, and Raman spectroscopy, in which the magnitude of the shift in Raman scattered light, which is exquisitely sensitive to the strong vibrational phonon modes present in the lattice of carbon nanotubes, is plotted to yield a rich variety of structural information. Detailed treatments of these phenomena are readily available in the literature and the reader is referred to Pfeiffer et al.,[9] Shen et al.[10] and Kim et al.[11]

The simplest form of a MWCNT, the DWCNT, consists of two co-axially aligned SWCNTs and as such they share many of the same properties of SWCNTs,[12, 13] but owing to the presence of a second wall are more physically robust and electronically more complex.[14-16] Similarly to SWCNTs, DWCNTs are uniquely characterized by the chiral indices of the constituent inner and outer walls (n_i,m_i)@(n_o,m_o), where each wall can be either semiconducting (S) or metallic (M) depending on its chiral index (Figure 1 (h)).[17] This gives rise to four possible combinations of inner@outer wall, namely; M@M, M@S, S@M and S@S.[18] This is in contrast to MWCNTs, which display overall metallic behaviour due to the complex inter-wall coupling whereas in DWCNTs the inter-wall coupling is highly dependent on whether the lattice stacking of the two walls is commensurate or incommensurate.[13, 19-25] A DWCNT is commensurate if the ratio between the unit cell lengths of the two walls is a rational number and as a result, the DWCNT has a periodic lattice structure (Figure 1(i)). In an incommensurate DWCNT the ratio is an irrational number and the nanotube

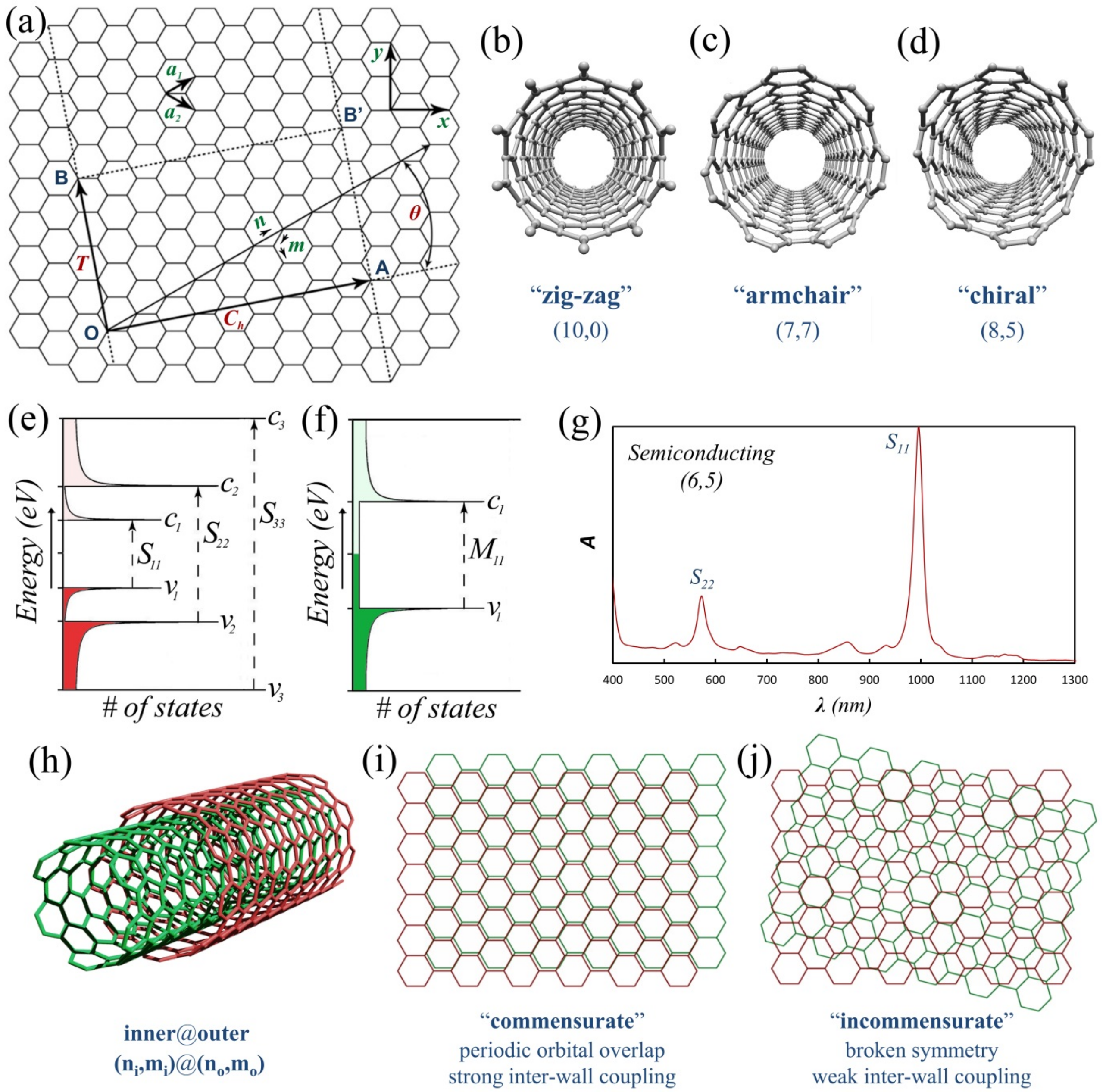

Figure 1 (a) A graphene sheet showing the geometry of a nanotube where the vectors OA and OB define the chiral and translational vectors $\mathbf{C_h}$ and $\mathbf{T}$, respectively, and the rectangle OAB'B defines the nanotube's unit cell. O, A, B and B' are reference atoms, $\mathbf{a_1}$ and $\mathbf{a_2}$ are the graphene lattice basis vectors and θ is the chiral angle. (b-d) Examples of the three classes of nanotube; zig-zag, armchair, and chiral. (e) and (f) Schematics of the electronic density of states of semiconducting and metallic (zigzag) nanotubes showing the valence and conduction bands, v_i and c_i, and optically active electronic transitions, S_{ii} and M_{ii}. (g) Optical absorption spectrum of the (6,5) semiconducting nanotube showing the S_{11} and S_{22} absorption features. (h) Schematic of a double walled nanotube. (i) and (j) Representations of commensurate and incommensurate lattice stacking.

experiences broken symmetry (Figure 1(j)). This causes reduced inter-wall coupling because the inter-wall transfer at each lattice site oscillates around zero in a quasiperiodic manner, resulting in a net interference that is destructive.[26] In general, the extra Coulomb interaction due to inter-wall coupling reduces the electron-hole binding energy and thus lowers the optical band gap (red shifting the absorption features) relative to the same (n,m) isolated tube however, there are some wall configurations in which inter-wall coupling interactions can increase the band gap (blue shifting the absorption features).

The richly varying optical and electronic properties of carbon nanotubes combined with their chemical reactivity provide great potential for both applications-based and fundamental research.[27-39] Indeed, the concentric structure of a MWCNT or DWCNT allows for the opportunity to simultaneously exploit the chemical reactivity of the outer wall whilst maintaining the pristine inner wall. During reactions, only the outer wall is exposed to the chemical environment and can be decorated with a high density of chemical moieties.[40-48] As a result of such shielding by outer wall, the inner wall does not suffer the drawbacks associated with functionalization, such as reduced conductivity due to degradation of the pristine sp^2 hybridized framework.[49, 50] However, to date the realisation of many of the literature proposed applications has been limited by the inability to synthesize pure, electronically well-defined raw material. While several synthesis methods can be optimized to produce high purity material each method inevitably produces a myriad of species including SWCNTs, MWCNTs, residual catalyst, amorphous carbon and fullerenes. This has spurred the development of a new research field investigating the sorting of carbon nanotubes by diameter, length and/or electronic character and is one of the focuses of this Habilitation.

1.1.2 Suspension and Dispersion

All sorting strategies share one commonality, namely the requirement for the production of suspensions of individualized carbon nanotubes in either water[51-54] or organic solvents.[55-60] This is achieved through either covalent,[40, 61, 62] or non-covalent methods.[51, 63-67] Covalent chemistry routes involve the introduction of functional groups to the nanotube ends and sidewalls, rendering them soluble.[61, 68-71] Such processes are extremely good at producing well dispersed, individualized nanotube suspensions, and often also exhibit some selectivity towards certain diameters[61, 72] or electronic types,[73, 74] which can provide useful routes toward separation based on these characteristics. However, covalent functionalization is often disadvantageous as it causes disruption of the conjugated π system of the nanotube by introducing sp^3 hybridization into the pristine sp^2 network.[49, 50] Non-covalent approaches include the use of surfactants such as sodium cholate (SC) or sodium dodecyl sulphate (SDS), [53, 54, 75-81] or dispersing agents such as DNA[52, 82-84] and organic polymers.[55-60, 85, 86] Dispersion of the nanotubes in these stabilizing agents is achieved via ultrasonication and often followed by centrifugation to remove remaining bundles and residual catalyst particles.[67]

For surfactant stabilized dispersions, the surface concentration and orientation of surfactant molecules on the nanotube sidewalls is highly dependent upon the type of surfactant, the concentration in solution and the diameter and electronic type of the nanotube.[75, 79, 80, 87-91] Generally, the surfactant first forms a random layer and, as more surfactant molecules bind to the surface, begins to form hemimicelles. Further addition of surfactant can cause the formation of a highly packed cylindrical micelle.[92] However, this varies for different diameters, with smaller nanotube diameters exhibiting less ordered surfactant structures.[87] For example, SDS wrapping of small diameter nanotubes (< 1 nm) tends to result in a highly disordered, random configurations at low SDS concentrations (packing densities of ~1.0 molecules nm^{-2})[93, 94] and more ordered, cylindrical wrapping at high SDS concentrations (2.8 molecules nm^{-2}).[93] The wrapping of large diameter nanotubes (> 1 nm) is also disordered at low concentration but forms hemi-micelles at high SDS concentration.[93, 94] Experiments suggest that the correlation between nanotube structure and wrapping is due to differences in the surface π-electron states of the various SWCNT curvatures, which affect the SDS/nanotube interaction.[79] When an SDS molecule wraps around a small diameter nanotube with a large bond curvature, it encounters a larger energetic barrier due to bending.[94] Therefore, it is energetically more favourable for the SDS to adsorb to larger diameter nanotubes with smaller curvatures, which is an underlying principle of several of the sorting methodologies described later.[75, 93, 95] The extent of SDS encapsulation is also dependent upon electronic character with metallic nanotubes having a higher degree of SDS wrapping than semiconducting nanotubes, owing to the increased polarizability.[53, 75, 90, 96]

Suspension of nanotubes with DNA[97-99] and proteins[100-106] relies primarily on strong π-stacking onto the nanotube sidewalls. This effectively individualizes the nanotubes and at the same time provides a negative surface charge density due to close proximity of the phosphate backbone to the nanotube.[97] As such, DNA wrapped SWCNTs have been sorted by electronic type[82, 97] and (n,m) species[83] through the use of ion-exchange gels. Likewise the dispersion and separation of SWCNTs with aromatic polymers in organic solvents relies upon π-stacking interactions and has the ability to prepare suspensions with a high semiconducting content (>99 %).[107-110] In this one-pot approach, raw carbon nanotube material is typically dispersed by ultrasonication in the presence of a chosen polymer followed by ultracentrifugation. Consequently, only those nanotubes with a preferential interaction with the polymer and those that have become individualized during ultrasonication remain suspended in the organic solvent. In pioneering works by Nish et al.,[85] Chen et al.,[86] and Hwang et al.,[57] organic polymers with the fluorene structure as part of their repeat unit were used, such as poly(9,9-dioctylfluorene-2,7-diyl) (PFO), poly[9,9-

dihexylfluorenyl-2,7-diyl)-co-(9,10-anthracene)] (PFH-A) and poly[(9,9-dioctylfluorenyl-2,7-diyl)-co-1,4-benzo-[2,1'-3]-thiadiazole)] (PFO-BT). After almost 10 years of development the polymer library has grown dramatically to now include polythiophenes, polycarbazoles and copolymers thereof,[111-121] alongside research to develop new polymers via click chemistry in an effort to avoid the strict synthetic conditions associated with Suzuki polycondensation or Yamamoto coupling.[122] Using the currently available polymer library, mixtures of semiconducting SWCNTs through to near-monochiral and monochiral suspensions and most recently even optical isomers thereof[123] have been demonstrated. For example, poly(9,9-dialkyl-2,7-fluorene) has been shown to be sensitive to large chiral angles (close to armchair: θ ≥ 25°)[57, 86, 124] and poly(N-decyl-2,7-carbazole) to lower chiral angles (typically 10° ≤ θ ≤ 20°).[118]

Despite the wide spread application of the polymer wrapping the exact mechanism responsible for separation remains poorly understood and is the subject of current discussion.[108, 109, 122, 125] Nevertheless, it is commonly agreed upon that the polymer interacts by aligning its aromatic backbone along the surface of a carbon nanotube so as to maximize π- π stacking.[108, 112, 114, 117, 126, 127] Peripheral groups are then believed to branch away from the nanotube into the solvent and facilitate solubility.[109, 125] Berton et al.[111] have developed a hybrid coarse grain model to describe this interaction by treating the nanotube and polymer as geometrical objects and assuming maximal (attractive) π- π interactions can be reached by maximizing the contact area. In this way a set of solutions for which the polymer lies flat on the surface of the nanotube were calculated. Intuitively, and also in agreement with Berton's model the number of favourable wrapping solutions increase with diameter, which may explain why certain polymers are highly (n,m) specific in the small diameter regime (i.e. due to other species having limited possible wrapping solutions).

1.1.3 Separation

Once a suspension of nanotubes has been obtained there are several techniques with varying degrees of complexity, specificity and success to separate carbon nanotubes by length, electronic type and chirality. A detailed review of these techniques can be found in section 2.1.5, where techniques traditionally developed for SWCNT separation are first explained followed by a discussion of how these techniques can be applied to more complicated systems such as DW- and MWCNTs.[128] However as the work presented in this Habilitation specifically pertains to aqueous gel based sorting an excerpt of this review is provided below.

The use of gel permeation chromatography was first demonstrated by Moshammer *et al.*,[129] and has since been shown to be extremely successful in the preparation of (n,m)-purified SWCNT suspensions. For SWCNTs, this technique has allowed for the high throughput separation of metallic from semiconducting species,[90, 91, 129] the isolation of specific (n,m) species[53, 79, 80] and most recently, the separation of optical isomers.[130] In general, the gel permeation method involves passing SDS suspended nanotubes through a stationary phase gel bed contained within a column, at which point semiconducting nanotubes with the highest affinity for the gel (an interaction determined by the SDS wrapping, and hence, the individual nanotube structure) are selectively removed from the bulk solution and retained on the gel matrix.[53] The metallic nanotubes, which exhibit no interaction with the gel, [53, 79, 90, 91] and other semiconducting nanotubes with no affinity to the gel (determined by surfactant concentration) continue to flow through the gel and can be collected. This observed sensitivity is driven by the SDS miscelle, which has been shown to be sensitive to electronic character and diameter. Metallic nanotubes are known to have a stronger interaction with SDS compared to semiconducting nanotubes[131] and become more fully wrapped and experience limited interaction with the gel as they traverse the column. The gel is then washed with SDS of either increased concentration[53, 79, 90] or lower pH[91, 132] or alternatively SC,[90, 129] which disrupts the interaction of the adsorbed semiconducting nanotubes with the gel and thus elutes them from the column for collection. This process can be repeated sequentially with the nanotubes that have the highest affinity for the gel becoming preferentially adsorbed each time.

While the exact mechanism of gel-based separation remains speculative owing to the difficulties associated with determining molecular dynamics on the nanoscale, evidence suggests that it is a kinetically driven selective adsorption process,[53] highly dependent on the SDS wrapping of the nanotubes.[89] This is evidenced by the clear relationship between SDS concentration and gel absorptivity,[53, 79, 89, 90] where an increase in SDS concentration allows additional SDS molecules onto the nanotube surface,[133] reducing its interaction with the gel. In addition to SDS concentration, pH[80, 91] and temperature[89] have also been shown to play important roles, giving rise to a number of separation strategies. While SDS-based separation is successful for small diameter SWCNTs (0.77 – 1 nm), adsorption of large diameter nanotubes (greater than ~1.2 nm) to the gel is quite limited.[134] Instead, a co-surfactant separation method can be used, where either the large diameter material is suspended in a co-surfactant solution and applied to a column, as demonstrated by Miyata *et al.*[135] and Wu *et al.,*[136] or where they are suspended in SC and applied to a column in SDS, as demonstrated by Zhang *et al.*[137]

In section 2.1.1 a one-column approach to separate small diameter monochiral and near monochiral SWCNTs using changes in pH is presented. This publication represented the first time that pH was shown to be important in nanotube separations and was the first time that (n,m) specific separation was shown on a single column. The ability to separate near monochiral suspensions was realized by slowly changing the pH from 4 to 1 in 12, 25 % reductive steps and 15 different (n,m) species with a purity of 16 – 93 % were obtained. Despite the mechanism for separation with changes in pH ultimately remaining unclear it is proposed that hydrolysis of the surfactant SDS led to the formation of 1-dodecanol, which is then incorporated into the micelle shell and changes the interaction with the gel medium. Section 2.1.2 details how this single column approach can then be applied to a commercially available gel permeation system (Figure 2 (a)) to routinely separate different (n,m) species with automated computer controlled pH gradients. Gradients of 10 – 90 % pH 3 were applied to the column and the eluent monitored with a diode array detector capable of measuring full spectra between 190 and 950 nm. Through measurement of elution profiles it was possible to develop routine time based separations of (n,m) species, where the user need only know in which region of the elution diagram they must collect pure samples. The use of an automated system also saw the (n,m) purity obtainable increase to 61 – 95 % (Figure 2 (b)).

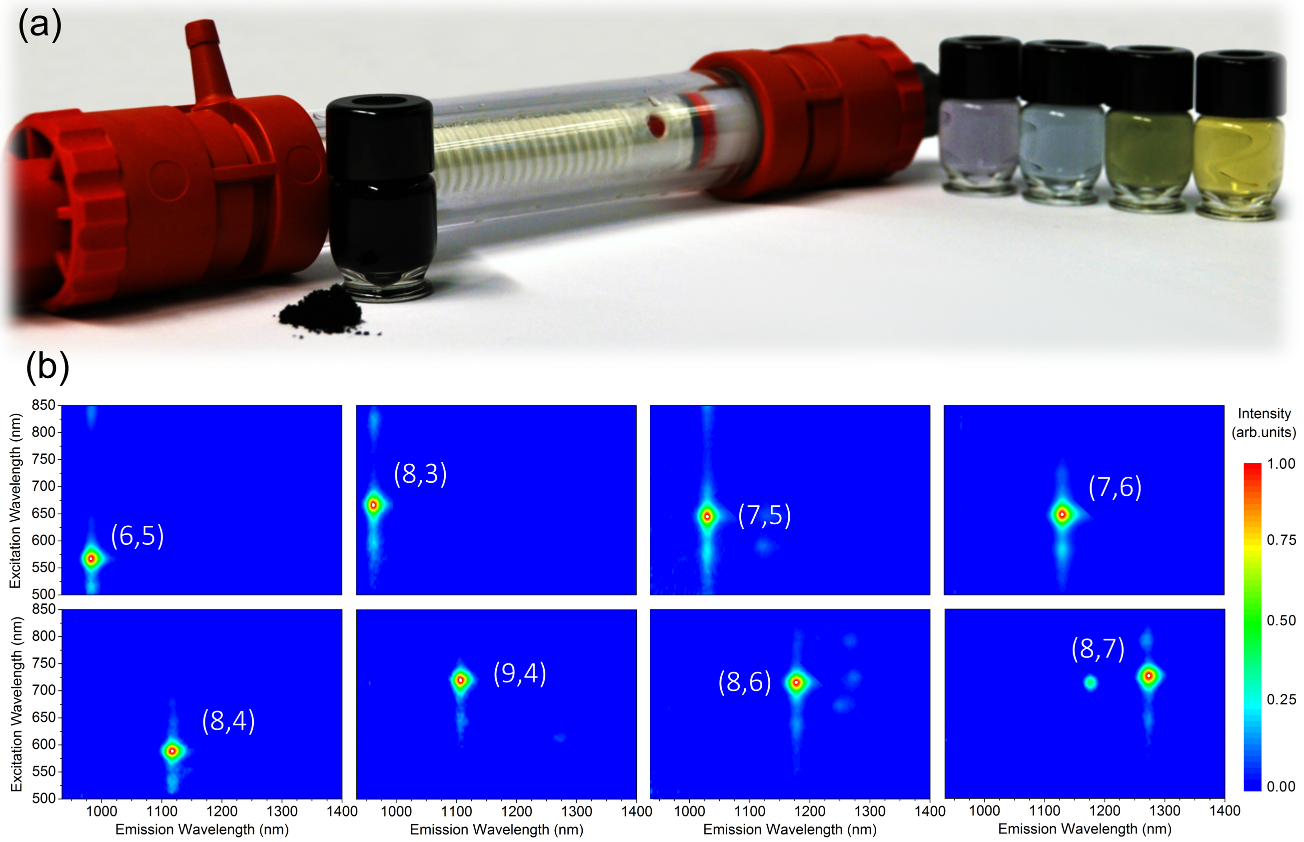

Figure 2 (a) The separation of SWCNTs begins with the suspension of raw HiPco material (black powder) in a 2 wt % sodium dodecyl sulfate in H_2O solution by sonication (black solution). This is then passed through a sephacryl gel column (center of image) with the use of an automated GPC system. Individual (n,m) species (coloured bottles) are then collected. (b) The high purity of the obtained (n,m) fractions can be verified with photoluminescence contour maps.

In section 2.1.3 the gel permeation technique is extended to large diameter CNTs (Figure 3 (a)) where it is shown that it is possible to separate DWCNTs from SWCNT impurities. It was determined from extensive AFM, TEM and Raman analysis that after sonication the DWCNT raw material contained two CNT populations of distinctly different length and diameter, namely DWCNTs and SWCNTs. The difference in length was assigned to an increased resistance to sonication-induced cutting upon inclusion of a second wall and consequently resulted in the DWCNTs being longer (725 ± 250 nm) than their SWCNT (310 ± 28 nm) counterparts. This large difference in length allowed for the use of size exclusion chromatography to separate the nanotube species and provided the starting point for an electronic type separation of the DWCNTs in section 2.1.4.[138] With the use of co-surfactant mixtures of SDS and SC the DWCNTs were further separated into fractions containing metallic and semiconducting outer walls with unknown inner walls. However upon integration into single nanotube field effect transistors the four unique inner@outer wall combinations of S@S, S@M, M@S and M@M were able to isolated. This work represented the second time that DWCNTs had been sorted by electronic type, however unlike previous work using density gradient ultracentrifugation, larger quantities could be prepared from the gel sorting technique and short channel FET devices were fabricated. The separation methods presented in section 2.1.1 – 2.1.4 form the basis for all subsequent work presented in this Habilitation using (n,m) or electronically pure nanotube material. Supporting information is provided in section 3.1.1, 3.1.2, 3.1.3 and 3.1.4.

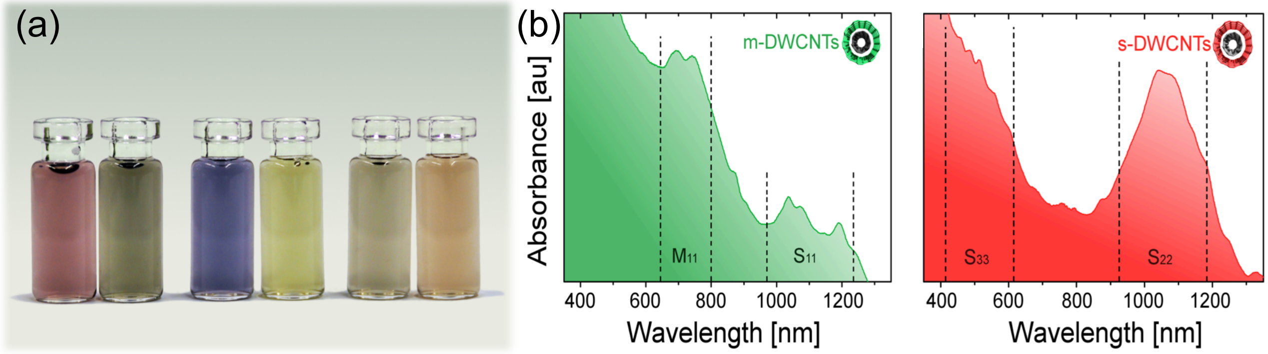

Figure 3 (a) metallic and semiconducting fractions of 1 nm diameter SWCNTs (metallic: red, semiconducting: green), 1.4 nm diameter SWCNTs (metallic: blue, semiconducting: yellow) and 1.6 – 2 nm DWCNTs (metallic outer-wall: light green, semiconducting outer-wall: bronze) and (b) absorption spectra of outer-wall sorted DWCNTs.

1.1.4 Thin Films

Many of the potential applications of carbon nanotubes require the fabrication of thin films and in the case of solution suspended material this can easily be achieved through techniques such as spray deposition or vacuum filtration. However, films from stabilized dispersions generally produce either sparse films with poor homogeneity and large void spaces on the nanoscale, or extremely rough and opaque films. Furthermore the extended ultrasonication required to coax the nanotubes into a metastable suspension invariably shortens them and introduces defects into the sidewalls which irreparably alter the electronic and optical properties of the pristine material. Additionally, the complete removal of surfactants, polymers or other wrapping agents from the films produced can be difficult. Due to the 1D property of carbon nanotubes an area of research that is also of great interest is in the production of thin films in which the nanotubes are highly aligned in one direction parallel to the surface. It is hoped that such an aligned films will enable replication of many of the 1D nanoscale properties of a nanotube on the macroscale.

Large area surface-aligned films have previously been generated from evaporation driven self-assembly of sidewall-functionalized[139] or surfactant-stabilized suspensions,[140, 141] from superacids with[142] or without[143] shear, from urea-water inks by Mayer rod coating,[144] from polymer/nanotube blends by Langmuir-Blodgett,[145] Langmuir-Schaeffer[146] or solution shearing onto pre-patterned substrates,[147] by shearing of solutions stabilized by DNA[148] or gellan gum,[149] as well as from the transfer of CVD grown stripes[150] or collapse of CVD grown forests.[151] This is in addition to a plethora of work regarding carbon nanotubes within different kinds of liquid crystals.[152-158] Despite their various advantages, many of the above methods of film formation still introduce damage due to extended ultrasonication, or are inherently limited to the small scale, require expensive or troublesome reagents (e.g. DNA, superacids) or extensive sidewall functionalization / wrapping agents / embedding matrix, or involve a high degree of manufacturing complexity.

For this reason thin films prepared from concentrated polyelectrolyte solutions of ‘nanotubide’ salts, which do not require any ultrasonication and leave no difficult-to-remove contaminants in the films are highly attractive. The ability to cause true dissolution of carbon nanotubes by electrostatic charging in polar media has been well known for the last decade[159] and such solutions are commonly exploited at low concentration in efficient sidewall functionalization schemes.[61, 160-164] However, carbon nanotubes can also be suspended in the very high concentration regime such that liquid crystal (LC) effects become important and allow for the alignment of nanotubes under shear force. The films produced by this method exhibit a very high degree of nanotube alignment, exceptional homogeneity of bundle widths throughout the film and remarkably low surface roughness.

In section 2.2.1 high concentrations of both as-grown and electronically sorted CNTs from the gel permeation method are used to prepare sodium nanotubide polyelectrolyte inks.[165] Using only sodium in dimethylacetamide, nanotube concentrations up to ~ 4 mg mL^{-1} are prepared and allows for the observation of liquid crystal domains of CNTs using cross polarized microscopy. These domains are then aligned by placing a 2 – 10 μL drop of polyelectrolyte between two glass slides, compression of the glass slides, and finally rapidly drawing the slides apart to create shear. Large area CNT films with a 2D nematic order parameter of ~ 0.7 were obtained, which compared to similar films from superacids contained smaller bundles and a smoother surface structure (RMS roughness, Rq ~ 2.2 nm). The improved alignment and surface structure is highlighted in Figure 4, where polyelectrolyte films are compared to films from superacids (chlorosulfonic acid) and traditional vacuum filtration. Additionally, a new method of nanotube film alignment known as dry-shear alignment is developed in section 2.2.2. Contrary to the polyelectrolyte method, where a shear force is applied in wet conditions, dry shear alignment can be performed to align virtually any nanotube film in the dry state, even those that were originally disordered. Although dry shear alignment is limited to the top layer of nanotubes this work challenged the assumption that carbon nanotube films are fixed structures, but rather they are dynamic and malleable systems containing mobile elements that are capable of significant restructuring and reordering with appropriate mechanical intervention.[166] Supporting information for these two publications is provided in section 3.2.1 and 3.2.2.

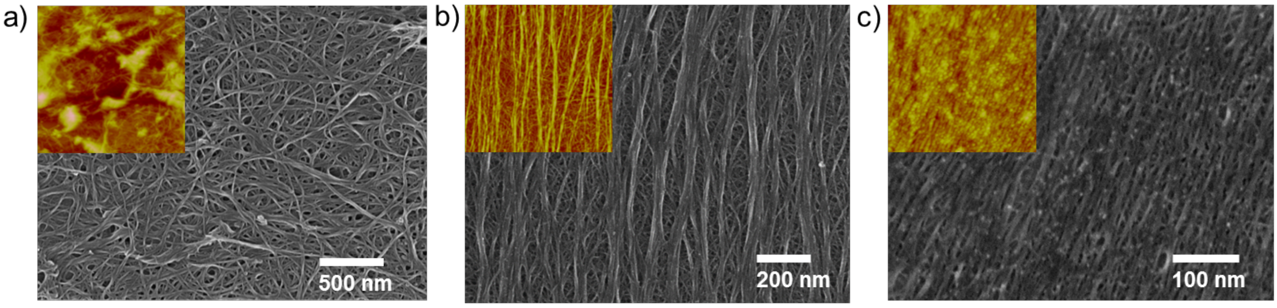

Figure 4 SEM images [inset AFM images] of (a) Vacuum filtered [6 µm x 6 µm x 280 nm], (b) Chlorosulfonic acid (CSA) [4 µm x 4 µm x 52 nm] and (c) Polyelectrolyte (PE) films [1 µm x 1 µm x 17 nm].

1.1.5 Energy Applications

Over the past five years, carbon nanotubes have attracted much attention in the organic solar cell community, from both a theoretical and practical point of view.[167-176] This is due to such desirable characteristics as their high charge carrier mobility along the nanotube axis and excellent stability towards degradation in ambient, humid, hot or high ultraviolet (UV) radiation conditions[177-179] and has lead to the development of two distinctly different types of devices, namely those that use carbon nanotubes as a light sensitize material (or in active layer composites) or as a transparent electrode material.

1.1.6 Silicon Solar Cells

As a transparent electrode material an architecture known as the nanotube:silicon heterojunction (NSH) has increasingly established itself in the field of solar cells. A typical device has architecture similar to that of a single junction crystalline silicon solar cell with the exception that a thin film of carbon nanotubes replaces the emitter layer. Despite ongoing discussions in the literature as to the exact mechanism of operation of such cells the nanotube films typically have 85+ % transmittance and it is widely accepted that they do contribute to photocurrent generation. Two proposed operation mechanisms are 1) The mechanism is that of an abrupt p-n junction solar cell with the nanotubes acting as the p-type emitter material. Photons are absorbed mainly in the n-type silicon base region with resulting excitons diffusing to the space-charge region where they are separated into free charge carriers under the action of the built in potential or 2) The mechanism is that of a Schottky junction solar cell, or the closely related metal insulator semiconductor (MIS) solar cell. In this configuration the nanotubes act as the metal, a thin SiO_x passivation layer on the silicon surface serves as the insulator (for MIS) and the n-type silicon is the semiconductor base region. Photons absorbed in the base region produce excitons which diffuse to an inversion layer created in the silicon adjacent to the Si/SiO_x or Si/metal junction. Charges are separated by the built in potential formed between the metal or SiO_x (which has a Fermi level pinned to that of the adjacent metal) and the silicon. Traditionally most NSH solar cells have employed inhomogeneous mixtures of metallic and semiconducting nanotubes with poorly defined electronic and optical properties, which has hindered an elucidation of the correct mechanism of operation.

In section 2.3.1 a literature review of the NSH field covering the period 2007 to 2012 is provided. This review has since been well cited and at the time appeared on the cover of the journal Advanced Energy Materials.[180, 181] In section 2.3.2 a hybrid NSH solar cell is prepared by combining the carbon nanotube layer with the conductive polymer polyaniline.[182] These devices benefited from the conformal interface coverage given by the polymer and the excellent electrical properties of the CNTs and outperformed either of their component counterparts. In section 2.3.3 and 2.3.4 the ability to prepare thin films of electronically sorted, small and large diameter SWCNTs is used to elucidate the mechanism of NSH solar cell operation.[183] In the literature carbon nanotubes had been reported to contribute to the measured photocurrent however these observations were complicated by spectral overlap of the silicon and often poorly defined nanotube absorption due to the use of unsorted nanotube films. By using sorted (n,m) species, so that the excitonic transition of the nanotubes is well defined and outside of the absorption range of silicon any contribution to the photocurrent from the nanotubes could easily be resolved. In Figure 5 external quantum efficiency measurements of NSH solar cells made from sorted carbon nanotubes can be seen, where it is definitively shown that the nanotubes do not contribute to the measured photocurrent. This was the first time that optically and electronically defined CNTs were used in a NSH solar cell and greatly enhanced the literature understanding of these devices. Supporting information can be found section 3.3.1 and 3.3.2.

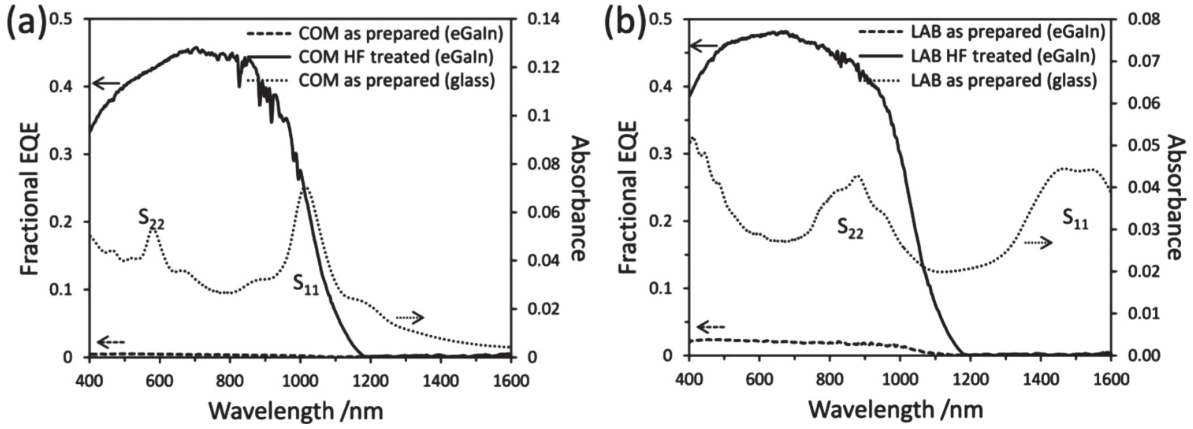

Figure 5 External quantum efficiency of as prepared and HF treated carbon nanotube:silicon solar cells fabricated with films of either (a) COM (small diameter) or (b) LAB (large diameter) semiconducting nanotubes. UV-Vis-NIR absorption spectra of corresponding films on glass are shown for comparison.

1.1.7 Fullerene Solar Cells

As an active material, the interest has been to absorb the infrared light excluded by traditional organic sensitizers. In addition, the presence of multiple excitonic transitions within SWCNTs may allow for solar cells built from carbon nanotubes to not only cover the infrared spectrum but also the visible and UV regimes. For example, small diameter (~0.8 – 1.2 nm) semiconducting nanotubes have their first excitonic transition (S_{11}) in the NIR (900 – 1250 nm), the second (S_{22}) in the visible (550 – 900 nm) and the third (S_{33}) in the UV.[184-186] This discussion can then of course be extended to consider other SWCNT synthetic routes such as arc discharge, laser ablation and the CoMoCAT process, which afford a completely different ensemble of (n,m) species and extend the accessible spectral regime. Due to the larger absorption cross-section of the S_{11} transition compared to S_{22}, S_{33}, etc. that most researchers have so far focused on the infrared regime. However, Arnold and co-workers have recently investigated quantum efficiency from S_{11}, S_{22} and even hot S_{11} + K transitions from (7,5) SWCNTs and found that the measured efficiency correlated well with the expected absorption cross section.[187]

The preparation of solar cells in which carbon nanotubes form the active material typically involves their combination with fullerene acceptor layers to form a Type II heterojunction and both polymer wrapped[56, 188] and aqueous surfactant based suspensions have been used.[79, 129, 132, 189] In terms of industrial applicability both methodologies have their advantages and disadvantages. In the case of solar cells from polymer wrapped carbon nanotubes the high semiconducting content (99+ %[107]) is important as the absence of metallic species reduces the potential for interlayer shorts or the introduction of trap states.[190] Additionally, the processing of SWCNTs in an organic medium is often more amenable to flat, thin film fabrication, whilst still being compatible with the surrounding layers in the device stack, and techniques such as doctorblading,[167] spincoating and spraycoating have been used in the past.[170, 172] It is likely for these reasons that most of the nanotube solar cell literature uses polymer wrapped SWCNTs as the donor material. However as outlined by Bindl et al.,[191] residual polymer in the film limits the intertube diffusion length to ~ 8 nm restricting the usage of thicker nanotube films and new strategies to remove the excess polymer are required. Although, the greatest limitation to polymer wrapping methodologies (at least for small diameters) is the low yield and expense of the polymer, which has likely contributed to the use of relatively small active areas of between 0.008 – 0.04 cm^2 until recently Guillot et al. fabricated solar cell devices with an active area of 0.101 cm^2 that were masked to 0.061 cm^2. [168, 170, 172, 188]

In contrast, the yield from surfactant based methods is significantly higher and the expense of the required chemicals lower; with gel permeation methods capable of routinely preparing milligram amounts of (n,m) sorted material, albeit with higher metallic nanotube content compared to polymer wrapping. Although, as shown in the work of Tulevski et al.,[192] surfactant based method can reach a semiconducting purity larger than 98 %. The use of aqueous suspensions also introduces new fabrication challenges due to the incompatibility of many common solar cells organic layers with water, and is probably a contributing factor to why the literature currently consists of limited examples of surfactant wrapped SWCNTs in these types of solar cells. [169] However, as techniques to routinely prepare large quantities of high purity polymer-free nanotubes and their subsequent integration into thin films develop it will become possible to produce active areas above a proof of principle scale, increase device efficiency, and at the same time reduce the overall device cost.

In section 2.4.1 films of polymer free (6,5) SWCNTs prepared using the gel permeation approach are integrated into SWCNT:C_{60} solar cells as depicted schematically in Figure 6.[193, 194] These solar cells displayed cutting edge internal quantum efficiency and possessed the current largest active area in the field of 0.105 cm^2. Additionally, transfer matrix calculations were used to predict the optimal exciton generation rate in the nanotubes based on the normal squared electric field intensity ($|E|^2$) for a combination of layers in the solar cell stack. Correlation of $|E|^2$ calculations to the SWCNT absorption profile then allowed for control over the ratio of external quantum efficiency (EQE) due to S_{11}, S_{22} and a combination thereof. This represents an important consideration for future light management in a SWCNT solar cell if the use multiple SWCNT optical transitions to cover a broad wavelength range is to be realised. Supporting information can be found in section 3.4.1.

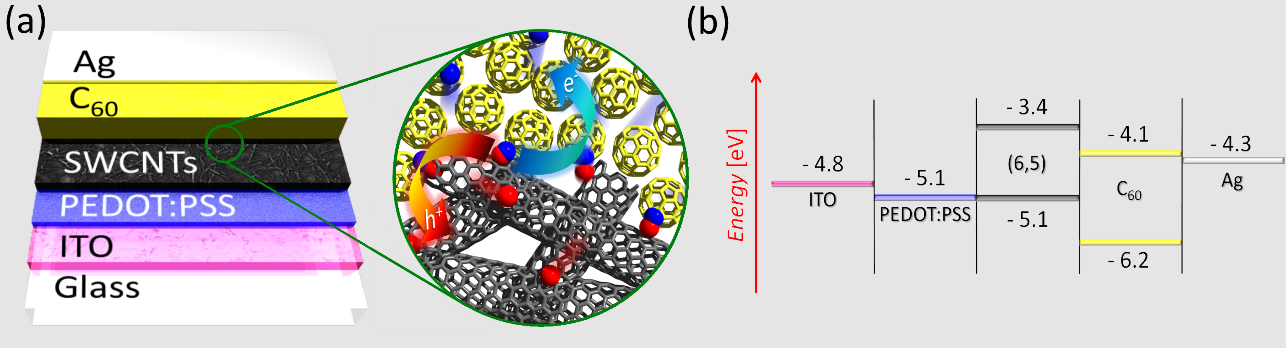

Figure 6 (a) Schematic of the solar cell architecture with a close up of the envisaged exciton dissociation at the SWCNT:C_{60} interface. Electrons (blue) migrate through C_{60} to the silver electrode while holes (red) are collected at the ITO in accordance with (b) the energy-level diagram of the device stack.

1.1.8 Photosensitive Elements

On the single or few nanotube level, fundamental investigations into photocurrent generation within a nanotube is an ongoing field of research. For these investigations, techniques such as dielectrophoretic deposition from solution[195-197] or chemical vapour deposition (CVD) growth of SWCNTs between a metalized source and drain contact in a CNT field-effect transistor (FET) is becoming standard. In this architecture photo-generated electrons and holes are typically separated by either an externally applied gate bias or by internal fields at the SWCNT-metal Schottky barrier.[198, 199] and photocurrent generation has therefore been studied in both substrate supported[200-204] and un-supported[205-207] nanotubes. However, unlike in the case of the SWCNT films discussed previously, a laser is typically used to address the CNTs due to the high power density required to measure photocurrent from only a few CNTs. Hence the laser source and CNT must be chosen carefully to ensure at least one of the CNT's optical transitions (usually S_{22}) matches the excitation source. The use of solution processed CNTs has the advantage of being able to prepare single chirality suspensions and thus prepare devices with pre-determined (n,m) indices and therefore absorption wavelength.

In section 2.5.1 and 2.5.2 (n,m) sorted SWCNTs from the gel permeation technique are integrated into field effect transistor devices (Figure 7 (a)) and photocurrent spectroscopy with the use of a super continuum light source attached to an acousto-optical tunable filter to provide the required wavelength selectivity is measured on arrays of photosensitive elements (Figure 7 (b)).[208] Additionally the entire setup was placed onto a x-y piezoelectric table, which allowed for not only spectrally resolved photocurrent measurements but also 2D surface mapping (Figure 7 (c)). This represented the first time that solution processed carbon nanotubes had been used for this kind of measurements and a good correlation between photocurrent generation and the optical property of the nanotubes was found. Furthermore the ability for photocurrent spectroscopy to be used as an analytical tool for the characterisation of carbon nanotube suspensions and FET devices is investigated. Due to the selectivity of the dielectrophoretic deposition[209] process used in device fabrication it is shown that whilst photocurrent measurements are able to provide qualitative information about a carbon nanotube suspension their ability to provide quantitative information appears to be limited. Supporting information can be found in section 3.5.1 and 3.5.2.

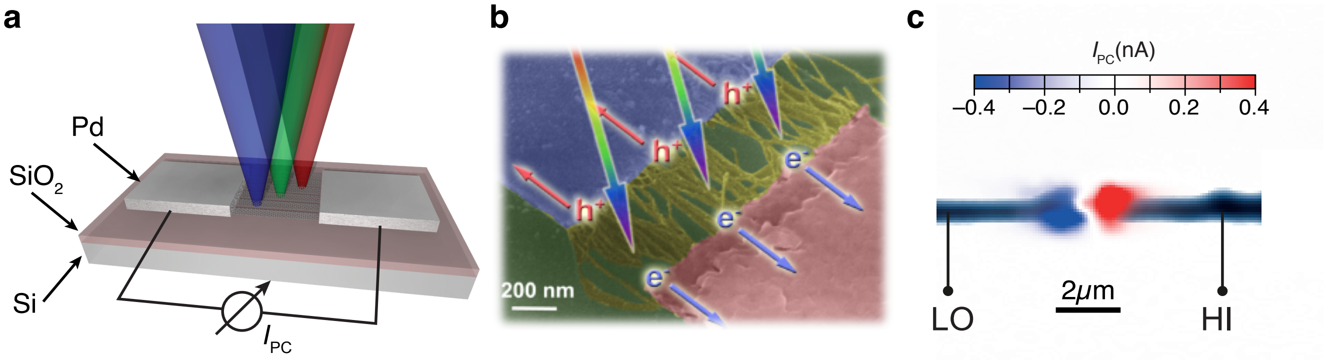

Figure 7 (a) 3D schematic of the measurement setup. A focussed light of variable wavelength is scanned across a carbon nanotube film with metallic contacts. (b) Scanning electron micrograph of a typical carbon nanotube device as shown schematically in (a), where the carbon nanotube density is approximately 10/µm. (c) Scanning photocurrent microscopy map (excited at 570 nm) overlaid on top of the simultaneously recorded elastically scattered signal from the sample.

2.1 Separation of Carbon Nanotubes

2.1.1 *Separation of Single-Walled Carbon Nanotubes by 1-Dodecanol-Mediated Size Exclusion Chromatography*

B. S. Flavel, M. Kappes, R. Krupke, F. Hennrich

ACS Nano 7 (2013) 3557–3564

DOI: 10.1021/nn4004956

Abstract

A simple, single column, high throughput, fractionation procedure based on size exclusion chromatography of aqueous/SDS (sodium dodecyl sulfate) suspensions of single-walled carbon nanotubes (SWCNTs) is presented. This procedure is found to yield monochiral or near monochiral SWCNT fractions of semiconducting-SWCNTs (s-SWCNTs). Unsorted and resulting monochiral suspensions are characterized using optical absorption and photoluminescence spectroscopy.

Contribution

B.S.F and R.K conceived and designed the project. B.S.F and F.H performed the experiments and wrote the paper. All authors contributed to the discussion and analysis of experimental results.

– This page intentionally left blank –

Separation of Single-Walled Carbon Nanotubes by 1-Dodecanol-Mediated Size-Exclusion Chromatography

Benjamin S. Flavel,[†,*] Manfred M. Kappes,[†,‡] Ralph Krupke,[†,§] and Frank Hennrich[†,*]

[†]Institute of Nanotechnology, Karlsruhe Institute of Technology, 76021 Karlsruhe, Germany, [‡]Institute of Physical Chemistry, Karlsruhe Institute of Technology, 76128 Karlsruhe, Germany, and [§]Institute of Materials Science, Technische Universität Darmstadt, 64287 Darmstadt, Germany

ABSTRACT A simple, single-column, high-throughput fractionation procedure based on size-exclusion chromatography of aqueous sodium dodecyl sulfate suspensions of single-walled carbon nanotubes (SWCNTs) is presented. This procedure is found to yield monochiral or near monochiral SWCNT fractions of semiconducting SWCNTs. Unsorted and resulting monochiral suspensions are characterized using optical absorption and photoluminescence spectroscopy.

KEYWORDS: carbon nanotubes · gel filtration · size-exclusion chromatography · separation · sorting · purification

Development and application of separation techniques for the fractionation of single-walled carbon nanotube (SWCNTs) is an active ongoing research field. Current research efforts are driven by the absence of a single synthesis method capable of affording carbon nanotube samples of preselected electronic type (metallic (m) or semiconducting (s)), diameter (d_t), chiral angle, or (n,m) index. Typically, SWCNTs are synthesized by techniques such as arc discharge, laser ablation, or the HiPco process, wherein a complex mixture of many different SWCNTs, described by a distribution of chiral indices (n,m), is obtained. Therefore, the separation of SWCNTs by fractionation of (n,m) species is an important, application-oriented goal. Previously, separation has been achieved by various groups utilizing such techniques as the wrapping of SWCNTs with short sequences of single-stranded DNA (ssDNA) and subsequent ion exchange chromatography (IEX),[1] the suspension of SWCNTs with surfactants followed by density gradient centrifugation[2−4] (DGC) or gel filtration.[5−7]

However, it is the Sephacryl gel filtration/size-exclusion chromatography (SEC) method developed by Moshammer *et al.*[4] that is the most straightforward and allows for high-throughput separation of m- from s-SWCNTs. This method relies upon the use of SWCNTs suspended in aqueous sodium dodecyl sulfate (SDS) and has also been shown to enrich zigzag and $(n,0)$ SWCNTs.[5] Recently Liu *et al.*[3] further improved the sorting of SWCNTs with SEC to include the addition of starting SDS-SWCNT suspensions to a series of gel columns and were capable of isolating 13 different (n,m) species.

Despite recent success, the mechanism of SWCNT separation by (n,m) species with gel filtration/SEC remains unclear. SEC is known to separate nanoscale objects passing through a column according to *differences in their size* and has been extensively used to *size-separate* SWCNTs. It was therefore proposed by Moshammer *et al.*[4] that the observed m/s-SWCNT separation is reliant upon appropriate initial dispersion of the raw SWCNT material by sonication, with the dispersion of SWCNTs in SDS shown to be selective to electronic structure. In fact, aqueous SDS starting suspensions obtained after sonication of SWCNT raw material were found to primarily contain s-SWCNTs in the form of bundles with m-SWCNTs predominantly suspended as individual tubes.[4] Upon introduction of the SWCNT-SDS suspension

* Address correspondence to
benjamin.flavel@partner.kit.edu,
frank.hennrich@kit.edu.

Received for review January 30, 2013
and accepted March 29, 2013.

10.1021/nn4004956

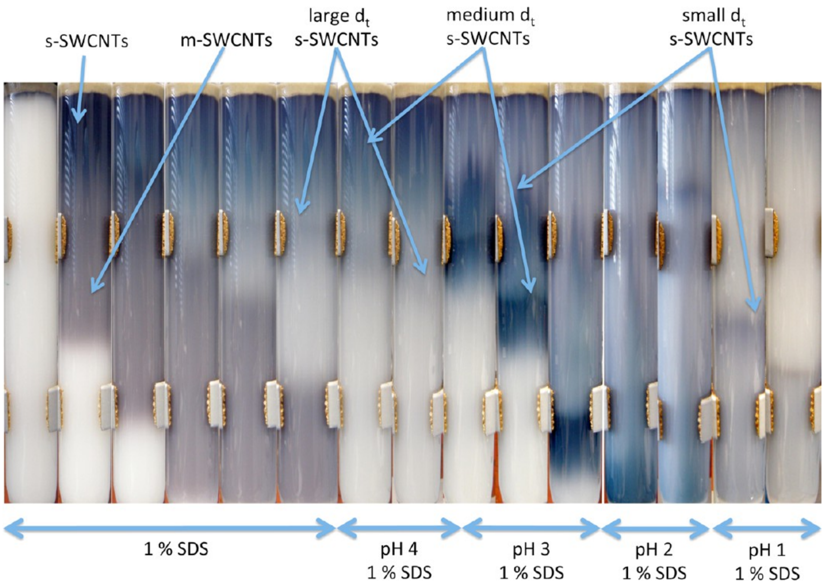

Figure 1. Time lapse photography of HiPCo SWCNTs suspended in 1 wt % SDS in H_2O on a Sephacryl S-200 size-exclusion gel, followed by subsequent reductions of pH.

to a size-exclusion gel medium, the bundles (s-SWCNTs) could therefore be easily separated from the individual (m-SWCNTs) tubes on the basis of their hydrodynamic size difference. By choosing an appropriate column medium, particle size, gel porosity, and eluent composition, it was therefore possible to run the SEC column as a "filter", with the longer, rigidly bundled s-SWCNTs becoming trapped on the gel and the smaller individualized m-SWCNTs being eluted in a 1 wt % SDS solution. Trapped s-SWCNTs were then removed from the gel by eluent exchange to 1 wt % SChol (sodium cholate). It is then the increased dispersibility of SWCNTs in SChol that allows for trapped s-SWCNTs to be further individualized and elute.

In the method of Liu *et al.*,[3] rather than changing the eluent medium, the wt % concentration of SDS was altered from 2 to 5%, allowing for the separation of 13 different (*n*,*m*) species. The authors explain their ability to then wash individual (*n*,*m*) s-SWCNT species from the gel by (*n*,*m*)-specific variations in the SDS coating of SWCNTs. These variations are proposed to be a result of differences in the surface π-electron states pertaining to individual (*n*,*m*) species (due to differing bond curvature), which alters the interaction between s-SWCNTs and SDS. Thereby, this results in a strongly curvature-dependent (*n*, *m*) separation method.

In this contribution, we demonstrate that Sephacryl S-200, an allyl dextran-based size-exclusion gel, can be used as a stationary phase such that monochiral or near monochiral SWCNTs can be simply produced on one column by altering the pH of the eluent. This, in turn, allows simple fractionation of (*n*,*m*)-pure or almost (*n*,*m*)-pure SWCNT suspensions from the total s-SWCNT population.

RESULTS AND DISCUSSION

As outlined in the Methods section, the high-throughput separation of (*n*,*m*)-pure s-SWCNTs with a single-column SEC approach involved the following steps: Initially, a 1 wt % SDS in H_2O suspension of raw HiPco-SWCNT material was added to a Sephacryl S-200 gel bed under 1 wt % SDS in H_2O. Upon addition of further 1 wt % SDS in H_2O, the m-SWCNTs were eluted from the column. This process can be seen in the time lapse photography in Figure 1, wherein the s-SWCNTs (blue-green color) can be seen clearly trapped on the top of the column in the gel while the m-SWCNTs (red-brown color) move through the gel.

This resulted in the establishment of essentially stationary colored bands on the Sephacryl gel, where the top to middle region of the gel is characterized by a color gradient of purple-blue to green-yellow. After complete separation of m- from s-SWCNTs, the pH of the 1 wt % SDS eluent solution was reduced from pH 7 to 1 in decrements of 1 pH level. Upon reaching pH 4, the trapped s-SWCNTs can be seen to separate into different colored moving eluent bands. The resolution of these bands was then improved upon further reduction of pH, with yellow, green, blue, and purple bands afforded for pH 4, 3, 2, and 1, respectively. Within the raw HiPco starting material, these bands corresponded to comparably large (yellow) to medium (green and blue) to small (purple) SWCNT diameters (d_t). This effect can be more precisely seen by absorption spectroscopy in Figure 2a, where the unsorted HiPco material is compared to fractions obtained at each pH level for the first optical transition (S_{11}) between 850 and 1350 nm. Complete absorbance spectra displaying both the first (S_{11}) and second (S_{22}) optical transitions between 500 and 1350 nm

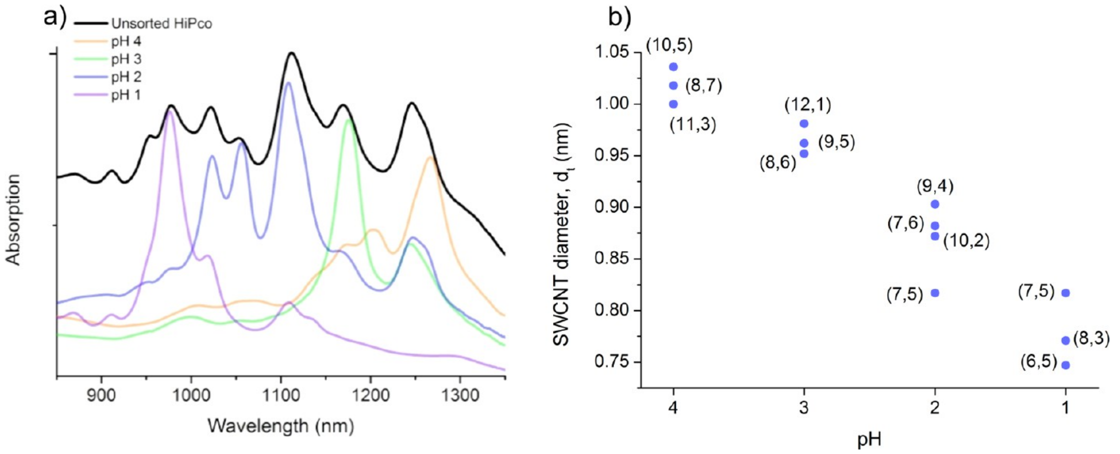

Figure 2. (a) Absorption spectra of unsorted HiPco material and fractions obtained at pH 4−1 in 1 wt % SDS and (b) SWCNT diameter dependence upon pH.

can also be found in Figure 1 of the Supporting Information. Due to the well-known doping effect[8] and subsequent quenching of the S_{11} optical transition, all fractions were neutralized to pH 7 in a 1 wt % SDS solution by dialysis prior to measurement.

Each fraction was found by photoluminescence spectroscopy to contain predominantly three individual (*n*,*m*) species; however, it is important to note that the displayed fractions only represent a "snapshot" of many fractions obtained at each pH level. Corresponding photoluminescence contour maps for each fraction can also be found in Figure 2 of the Supporting Information. The SWCNT diameter (d_t) of these species was then obtained by reference to the photoluminescence data of Weisman *et al.*[9] and is shown in Figure 2b, where it can be seen that d_t decreases with eluent pH. Upon summation of each (*n*,*m*) species diameter in a collected fraction, this trend is clearly seen with average d_t found to be 1.018, 0.957, 0.868, and 0.778 nm for pH 4, 3, 2, and 1, respectively.

The ability of this method to generate monochiral or near monochiral SWCNT suspensions was then realized by slowly changing the pH from 4 to pH 1 in 12, 25% reductive steps. In order to easily visualize the obtained fractions, photoluminescence spectroscopy was then used and is shown in Figure 3. Additionally, absorption spectra of each fraction are shown in Figure 4a. Furthermore, to allow comparison, a photoluminescence contour map of the unsorted HiPco SWCNT material is shown in Figure 3 of the Supporting Information, wherein 17 different (*n*,*m*) species are clearly visible. As found for coarse reductions in pH, the d_t of the collected SWCNT fractions were once again observed to decrease with pH, as shown in Figure 4b. However, in this instance, due to slight variations in the pH of the 1 wt % SDS eluent added to the top of the column and the establishment of a pH gradient across the column, it is more difficult to determine the true pH of each fraction. Therefore "elution order" is used, where fractions eluted later are obtained at relatively lower pH values compared to earlier fractions. To aid the eye, only the major (*n*,*m*) contribution is plotted in Figure 4b. Nanotube purity was then determined by the relative peak intensities of the contour map (uncorrected for the chiral-dependent quantum yield). Furthermore, the fitted peak area of absorption measurements was also used to calculate (*n*,*m*) purity, where the major (*n*,*m*) contribution was taken as a ratio of all other peaks.

As shown in Table 1, sorting of raw HiPco SWCNT material with pH variation resulted in the obtainment of 12 of the 17 (*n*,*m*) species with purities between 23 and 86%. The reduced purity level for absorption measurements is a result of the difficulty in accurately performing the peak fitting procedure in a region with many overlapping first interband transitions. The actual (*n*,*m*) purity is expected to lie between the value obtained from photoluminescence and that from absorption measurements. For an effective sorting method, it is also important to assess the yield of the various (*n*,*m*) species. While we did not measure this directly, it is noted that the starting solution has a dispersed SWCNT mass of approximately 1 mg and the final (*n*,*m*) fractions were in the microgram range. It should also be noted that between 450 and 550 nm, nanotube-related transitions are clearly seen in the absorption spectra. This absorption regime is typically associated with m-SWCNTs; however, due to an overlap of the third interband transition of HiPco s-SWCNTs and the first interband transition of HiPco m-SWCNTs, it is difficult to estimate the concentration of m-SWCNTs. However, preliminary electrical transport measurements indicate a metallic-/semiconducting-SWCNT ratio equivalent to standard Sephacryl S-200 separations. Despite being unable to achieve separations of the same purity as Liu *et al.*,[3] who were able to obtain 13 different (*n*,*m*) species with purities between 39 and 94%, the sorting of s-SWCNTs by pH variation presented in this work has the advantage of requiring a single SEC column, which significantly decreases the

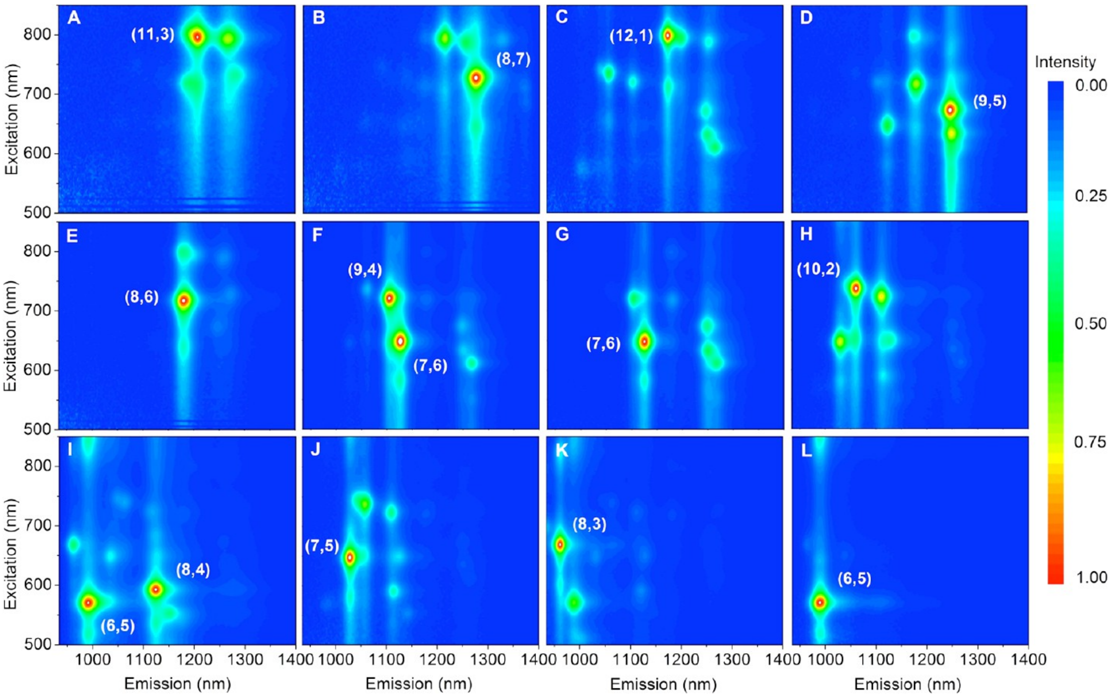

Figure 3. Photoluminescence contour maps of fractions (elution order A−L) obtained upon reducing the 1 wt % SDS eluent from pH 4 to pH 1 in 12 reductive steps.

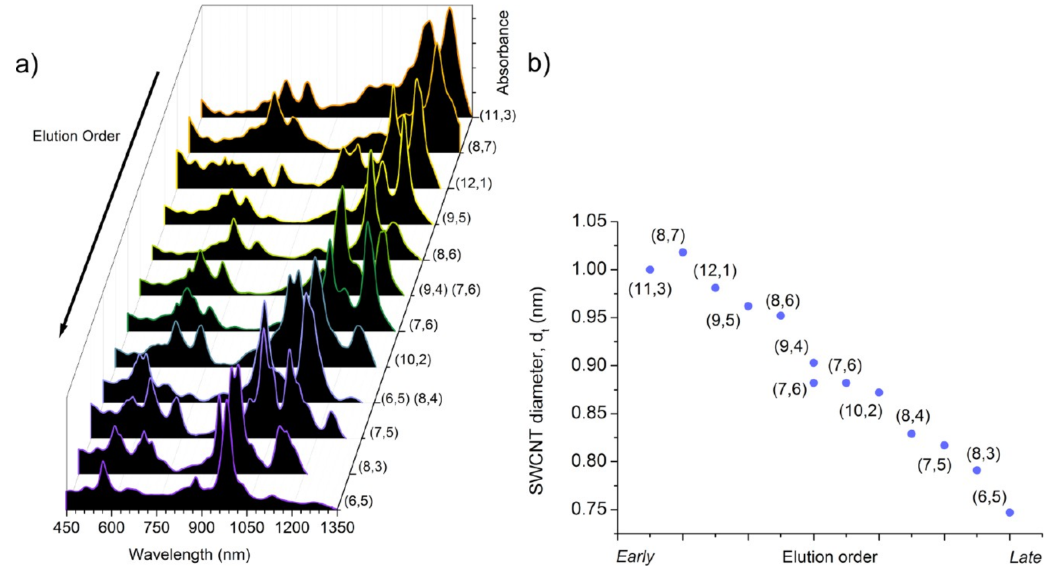

Figure 4. (a) Absorption spectra corresponding to fractions displayed in Figure 3 and (b) SWCNT diameter dependence upon elution order.

TABLE 1. Maximum Obtained Purity of Enriched (*n*,*m*) Species by Reducing the pH of the Eluent

(*n*,*m*) species	(6,5)	(7,5)	(7,6)	(8,3)	(8,4)	(8,6)	(8,7)	(9,4)	(9,5)	(10,2)	(11,3)	(12,1)
photoluminesence, purity (%)	86	40	38	46	30	57	44	32	35	30	41	28
absorption, purity (%)	72	27	27	19	25	64	37	19	32	17	19	23

complexity of the separation process. Additionally, the elution order of Liu *et al.*[3] (small to large diameter) appears to be opposite to the order observed in this work (large to small). However, it is important to remember that Liu *et al.* determined their elution order by considering the nanotube of strongest interaction with the gel (small diameter), which due to their multiple short-column approach results in it being the first collected species. In this work, we see the same trend, with strongly (small diameter) and weakly (large diameter) absorbed species located at the uppermost and midpoint of a single long column, respectively (Figure 1). Upon reduction of the pH, the established on-column nanotube ordering is maintained, and large to small diameter nanotube fractions are collected. Therefore, it is purely the experimental approach and definition of "first eluent" that results in a perceived difference.

Despite the mechanism responsible for the separation of (*n*,*m*) s-SWCNT species ultimately remaining unclear, we next provide an attempt to elucidate the most likely cause upon consideration of the SDS surfactant shell structure on nanotubes and similar carbon surfaces and the subsequent effect of pH. The morphology of SDS aggregates on graphite is well-known, with theoretical calculations and contact AFM measurements revealing the sp^2 carbon lattice to serve as a template for the organization of surfactant chains, which is responsible for defining the surfactant micelle morphology.[10−15] SDS micelles are found as ordered linear, parallel aggregates, which are oriented perpendicular to an underlying symmetry axis and spaced slightly more than twice the surfactant molecular length apart. These initially adsorbed molecules then act as nucleation sites for the growth of the hemispherical micelles, wherein adjacent molecules are oriented tail to tail, forming parallel semicylindrical rows, with tail groups oriented parallel to the symmetry axis.

On the other hand, the SDS micelle morphology for CNTs remains under debate with various theoretical groups proposing disordered[10] and ordered[16,17] structure. Experimentally, Yurekli *et al.*[18] also measured small-angle neutron scattering (SANS) of aqueous SDS-SWCNT suspensions and found SDS to form disordered aggregates. Alternatively, Richard *et al.*[19] with the use of cryo-TEM measurements found SDS to form hemispherical micelles on the sidewall of multiwalled nanotubes. However, common to all work is a strong dependence of the micelle structure on surfactant concentration and nanotube diameter. For partial SDS surfactant coverage (1.0 molecules/nm), Xu *et al.*[14] theoretically found SDS to be disordered for small (6,6) and large (18,18) or (30,30) d_t SWCNTs. Upon reaching full coverage (2.8 molecules/nm), they then found SDS to form stable hemispherical micelles for large (18,18) or (30,30) d_t SWCNTs, a result that is in agreement with the experimental work on graphite and multiwalled carbon nanotubes. For small (6,6) d_t SWCNTs and in agreement with the work of Wallace *et al.*,[20] SDS was found to form a cylinder-like monolayer micelle, in which the carbon nanotube forms the core with the surfactant extended radially from the center. It was therefore concluded that SDS hemispherical micelle ordering occurs on carbon nanotubes only in the case of high surfactant concentration and large diameter. Furthermore, Niyogi *et al.* have demonstrated m-SWCNTs to have a higher packing density (concentration) of SDS compared to s-SWCNTs,[21] which may therefore imply a higher degree of SDS ordering.

However, the morphology of the SDS micelle structure has also been shown to be susceptible to changes in the surrounding environment, with the addition of organic molecules or electrolyte tuning capable of surfactant shell modification.[19,22,23] Toward this end, upon reduction of pH, the presence of H^+ ions has been shown to lead to the hydrolysis of SDS between pH 2 and pH 3, which results in the formation of 1-dodecanol[24] as given by eq 1.

$$C_{12}H_{25}OSO_3{}^- + H_2O \rightarrow C_{12}H_{25}OH + HSO_4{}^- \qquad (1)$$

This hydrolysis mechanism is the cause of the well-known long-term instability of SDS and can also be initiated by heating.[22] Parachuri *et al.* have used AFM to show the addition of 5 mM 1-dodecanol to 100 mM SDS to cause significant structural changes in the continuous parallel semicylindrical surface micelle structure on graphite surfaces.[8,9] It is shown that the parallel semicylindrical structure is replaced by a herringbone pattern upon integration of 1-dodecanol into the micelle structure. If it is assumed (in agreement with Xu *et al.*[14]) that SDS forms semicylindrical micelles on the surface of carbon nanotubes, then a similar structural rearrangement can be expected for the SWCNT micelle upon addition of 1-dodecanol.

Such structural changes will then have a strong influence on the SWCNT's interaction with its surrounding environment. The total interaction of SWCNTs on the Sephacryl gel is strongly dependent upon van der Waals forces between the SWCNTs and the gel as well as steric and electrostatic interactions. Any differences in surfactant structure will therefore affect this interaction. For example, it is well-known that electrostatic interactions can occur between charged solutes and charged SEC packing materials. Sun *et al.*[25] conducted zeta-potential measurements of SDS-SWCNT suspensions and found the presence of SDS to lead to a net negative charge, which upon addition of neutral 1-dodecanol is likely reduced, which in turn would reduce the SWCNT interaction with the gel and cause nanotube elution. Alternatively, SEC is by definition a chromatographic process, which is capable of separating particles based on their hydrodynamic volume. The introduction of 1-dodecanol may either alter the hydrodynamic volume of individual tubes or have a debundling effect, likewise altering the hydrodynamic volume, as discussed in our previous work[4,5] where a surfactant change to sodium cholate is required for nanotube elution.

We therefore propose that during SWCNT starting suspension preparation with extended ultrasonication, a low concentration of 1-dodecanol is produced by microcavitation (heat), which is then integrated into

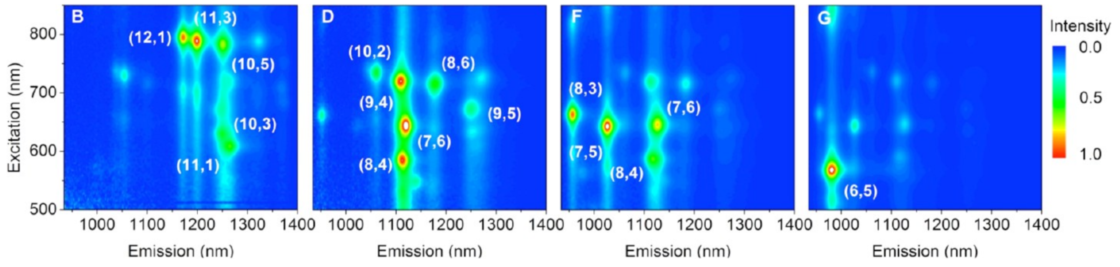

Figure 5. Photoluminescence contour maps of fractions (elution order A–G) upon addition of 5 μM 1-dodecanol to the starting HiPco raw material.

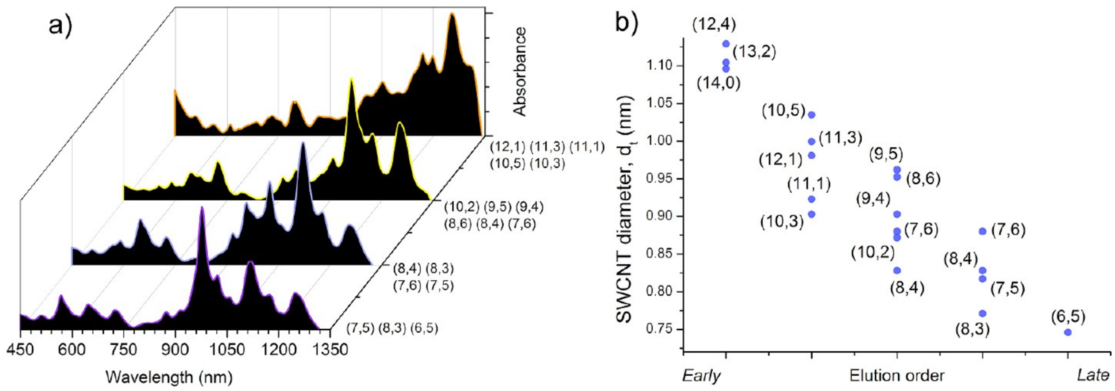

Figure 6. SWCNT diameter dependence upon elution order upon addition of 5 μM 1-dodecanol to the starting HiPco raw material.

the SDS-SWCNT hemimicellar structure. The resultant structural change alters the interaction of the SWCNTs, allowing them to move through the Sephacryl gel. As the sonicated SWCNTs are added to a freshly prepared 1 wt % SDS-filled gel column and further washed through with fresh 1 wt % SDS, the initial concentration of 1-dodecanol is quickly depleted and the nanotubes become trapped on the gel. It is also proposed, and in agreement with literature,[18] that metallic nanotubes have a higher SDS coverage compared to semiconducting nanotubes and hence have a higher degree of surfactant ordering and are therefore capable of integrating more 1-dodecanol and thereby move further and faster in the gel. This results in the observed metallic/semiconducting separation. The m-SWCNTs are either debundled[4,5] or have a significantly reduced electrostatic interaction with the gel as a result of the 1-dodecanol. A similar argument is also made for large and small diameter SWCNTs, where the increased integration of 1-dodecanol allows large diameter s-SWCNTs to move further in the column prior to stopping. Upon depletion of 1-dodecanol the s-SWCNTs either bundle together[4,5] or have an increased electrostatic interaction with the gel. Upon reducing the pH of the 1 wt % SDS solution, 1-dodecanol is then reintroduced by hydrolysis and allows the trapped s-SWCNTs to elute.

This model is supported by the following experiments. First, we repeated the separation of raw HiPco SWCNT material by adding increasing concentrations of 1-dodecanol to the pH-neutral, 1 wt % SDS eluent. Once again, the s-SWCNTs were trapped on the top half of the Sephacryl gel. Upon increasing the 1-dodecanol concentration in 1 μM steps to a final concentration of 5 μM, these SWCNTs could then be eluted in order of comparatively large to small d_t, as expected (data not shown). Second and alternatively, 5 μM 1-dodecanol was added to the raw starting material, which was then subsequently added to a Sephacryl gel column under 1 wt % SDS and further washed with fresh 1 wt % SDS. In this instance, the s-SWCNTs did not become trapped on the SEC gel (for a short column). However, the m-SWCNTs once again moved faster through the gel compared to large d_t s-SWCNTs, which in turn moved faster than small d_t s-SWCNTs. In this way, a metallic/semiconducting separation plus a s-SWCNT diameter separation was achieved in *one* step without changing surfactant, pH, or column. In addition to being extremely simple, this method also has the added benefit of not clogging the gel with trapped, unmoveable, s-SWCNTs, hence dramatically increasing column lifetime. Corresponding photoluminescence contour maps are shown in Figure 5 and Supporting Information Figure 4, with elution order A–G, and absorption spectra in Figure 6a. The diameter-dependent elution order is then more precisely seen in Figure 6b. Alternatively, the raw material was added to a column containing 5 μM 1-dodecanol in 1 wt % SDS; however, the excess of alcohol leads to all SWCNT species moving together without separation and highlights the importance of a 1-dodecanol gradient.

TABLE 2. Maximum Obtained Purity of Enriched (*n*,*m*) Species from the Addition of 5 μM 1-Dodecanol to the Raw HiPco SWCNT Material

(*n*,*m*) species	(6,5)	(7,5)	(7,6)	(8,3)	(8,4)	(9,4)	(10,2)	(10,5)	(11,3)	(12,1)	(12,4)	(13,2)
photoluminesence, purity (%)	50	26	22	22	20	18	28	16	25	21	16	32

Once again, aggregation of photoluminescence peak intensities allowed for the determination purity, as shown in Table 2. Furthermore, the additional photoluminescence contour maps found in Figure 4 of the Supporting Information allowed the concentration of the (13,2), (12,4), (10,2), and (9,4) s-SWCNTs to be determined. Additional to the (*n*,*m*) species obtained by pH sorting, the (10,5), (12,4), and (13,2) were also purified, resulting in a total of 15 out of the total 17 available (*n*,*m*) species being sorted in this work. Unfortunately, in comparison to fractions obtained from pH sorting, the purity of (*n*,*m*) species obtained from 1-dodecanol addition was found to be lower (between 16 and 50%). This is presumably due to the addition of 1-dodecanol resulting in a dynamic process without the static equilibration of SWCNT diameters across the gel prior to the beginning of the experiment. Furthermore, it should be noted that SWCNT separations from 1-dodecanol only serve as a proof of principle and provide insights into the mechanism responsible for SWCNT separation by pH variation. It is expected that after extensive optimization of the 1-dodecanol concentration s-SWCNT suspensions similar to those obtainable from pH variation will be achievable.

CONCLUSION

In conclusion, we have shown the (*n*,*m*) separation of 15 different nanotube species with a purity of 16–93%. Furthermore, sorting was achieved conveniently and simply in a single Sephacryl column without the need for a surfactant/eluent change. Upon tailoring the concentration of 1-dodecanol through reduction of pH or the direct addition of alcohol to the raw starting material, the originally strong interaction of s-SWCNT could be reduced and allowed for diameter-dependent fractionation.

METHODS

A brief description of the experimental methods is as follows. HiPco SWCNT raw material (NanoIntegris) was used in this work. In order to prepare starting suspensions, typically 10 mg of raw SWCNT material was suspended in 15 mL of H_2O with 1 wt % of SDS using a tip sonicator (Bandelin, 200 W maximum power, 20 kHz, in pulsed mode with 100 ms pulses) applied for 2 h at ~20% power. During sonication, the suspension was placed in a 500 mL water bath without additional cooling. The resulting dispersion was then centrifuged at ~100 000*g* for 1.5 h and carefully decanted from the pellet which was formed during centrifugation. The centrifuged SWCNT suspension was used as the "starting suspension" for gel filtration fractionation as described below.

A separate "reference suspension" of the raw HiPco SWCNTs was made by suspending 10 mg of raw SWCNTs in 15 mL of H_2O with 1 wt % of sodium cholate. After tip sonication, the suspensions were centrifuged at 100 000*g* for 1 h, and the suspension was carefully decanted of the supernatant.

Gel filtration was performed as described previously[4] using a Sephacryl S-200 (manufacturer stated stability to pH of between 2 and 13) gel filtration medium (Amersham Biosciences) in a glass column of 20 cm length and 2 cm inner diameter. After filling the glass column with the filtration medium, the gel was slightly compressed to yield a final height of ~14 cm. For the separation, ~10 mL of SWCNT starting suspension was applied to the top of the column, and subsequently, a solution of 1 wt % SDS in H_2O as eluent was pushed through the column by applying sufficient pressure with compressed air to ensure a flow of ~1 mL/min. After ~10 mL of 1 wt % eluent had been added to the column, most of the m-SWCNTs had moved through the column, whereas the s-SWCNTs remained trapped in the upper part of the gel. After applying a total of ~120 mL of SDS solution in this fashion, the metallic tubes were completely removed from the gel. The pH of the 1 wt % SDS in H_2O eluent was then changed from 4 to 1 upon addition of the appropriate concentration of HCl. The pH was reduced in 12 steps, whereby at each step 80 mL of eluent was applied to the gel. The s-SWCNTs subsequently eluted from the column were collected separately in 2 mL fractions.

For spectroscopic characterization, gel filtration fractions were subsequently dialyzed for 24 h to readjust the pH to 7 in 1 mL Float-A-Lyzer G2 dialysis devices (Spectra-Por) by using 500 mL of a 1 wt % SDS solution in water. UV–vis–NIR absorption spectra of the dialyzed fractions were recorded on a Varian Cary 500 spectrophotometer. Photoluminescence maps were measured in the emission range of ~900–1700 nm and excitation range of 500–950 nm (scanned in 3 nm steps) using a modified FTIR spectrometer (Bruker IFS66) equipped with a liquid-nitrogen-cooled Ge-photodiode and a monochromatized excitation light source as described elsewhere.[26]

Conflict of Interest: The authors declare no competing financial interest.

Acknowledgment. This research was supported by the Bundesministerium für Bildung und Forschung (BMBF) as administered by POF-NanoMicro. B.S.F. gratefully acknowledges the support of the Alexander von Humboldt Foundation.

Supporting Information Available: Absorption spectra of fractions obtained at pH 4–1 displaying the second interband transition (S_{22}), additional photoluminescence spectra of fractions obtained from variations in pH and the addition of 1-dodecanol, photoluminescence and absorption measurements of the raw/unsorted HiPco SWCNT material. This material is available free of charge *via* the Internet at http://pubs.acs.org.

REFERENCES AND NOTES

1. Tu, X.; Manohar, S.; Jagota, A.; Zheng, M. DNA Sequence Motifs for Structure-Specific Recognition and Separation of Carbon Nanotubes. *Nature* **2009**, *460*, 250–253.
2. Ghosh, S.; Bachilo, S. M.; Weisman, R. B. Advanced Sorting of Single-Walled Carbon Nanotubes by Nonlinear Density-Gradient Ultracentrifugation. *Nat. Nanotechnol.* **2010**, *5*, 443–450.
3. Arnold, M. S.; Green, A. A.; Hulvat, J. F.; Stupp, S. I.; Hersam, M. C. Sorting Carbon Nanotubes by Electronic Structure *via* Density Differentiation. *Nat. Nanotechnol.* **2006**, *1*, 60–65.

4. Arnold, M. S.; Stupp, S. I.; Hersam, M. C. Enrichment of Single-Walled Carbon Nanotubes by Diameter in Density Gradients. *Nano Lett.* **2005**, *5*, 713–718.
5. Liu, H.; Daisuke Nishide, D.; Tanaka, T.; Kataura, H. Large-Scale Single-Chirality Separation of Single-Wall Carbon Nanotubes by Simple Gel Chromatography. *Nat. Commun.* **2011**, *2*, 1–8.
6. Moshammer, K.; Hennrich, F.; Kappes, M. M. Selective Suspension in Aqueous Sodium Dodecyl Sulfate According to Electronic Structure Type Allows Simple Separation of Metallic from Semiconducting Single-Walled Carbon Nanotubes. *Nano Res.* **2009**, *2*, 599–606.
7. Blum, C.; Stürzl, N.; Hennrich, F.; Lebedkin, S.; Heeg, S.; Dumlich, H.; Reich, S.; Kappes, M. M. Selective Bundling of Zigzag Single-Walled Carbon Nanotubes. *ACS Nano* **2011**, *5*, 2847–2854.
8. Strano, M.; Huffman, C. B.; Moore, V. C.; O'Connell, M. J.; Haroz, E. H.; Hubbard, J.; Miller, M.; Rialon, K.; Kittrell, C.; Ramesh, S.; Hauge, R. H.; Smalley, R. E. Reversible, Band-Gap-Selective Protonation of Single-Walled Carbon Nanotubes in Solution. *J. Phys. Chem. B* **2003**, *107*, 6979–6985.
9. Weisman, R. B.; Bachilo, S. M. Dependence of Optical Transition Energies on Structure for Single-Walled Carbon Nanotubes in Aqueous Suspension: An Empirical Kataura Plot. *Nano Lett.* **2003**, *3*, 1235–1238.
10. Paruchuri, V. K.; Nalaskowski, J.; Shah, D. O.; Miller, J. D. The Effect of Co-surfactants on Sodium Dodecyl Sulfate Micellar Structures at a Graphite Surface. *Colloids Surf., A* **2006**, *272*, 157–163.
11. Paruchuri, V. K.; Nguyen, A. V.; Miller, J. D. Zeta-Potentials of Self-Assembled Surface Micelles of Ionic Surfactants Adsorbed at Hydrophobic Graphite Surfaces. *Colloids Surf., A* **2004**, *250*, 519–526.
12. Tummala, N. R.; Striolo, A. Role of Counterion Condensation in the Self-Assembly of SDS Surfactants at the Water Graphite Interface. *J. Phys. Chem. B* **2008**, *112*, 1987–2000.
13. Sammalkorpi, M.; Panagiotopoulos, A. Z.; Haataja, M. Structure and Dynamics of Surfactant and Hydrocarbon Aggregates on Graphite: A Molecular Dynamics Simulation Study. *J. Phys. Chem. B* **2008**, *112*, 2915–2921.
14. Dominguez, H. Self-Aggregation of the SDS Surfactant at a Solid−Liquid Interface. *J. Phys. Chem. B* **2007**, *111*, 4054–4059.
15. Wanless, E. J.; Ducker, W. A. Organization of Sodium Dodecyl Sulfate at the Graphite−Solution Interface. *J. Phys. Chem.* **1996**, *100*, 3207–3214.
16. Xu, Z.; Yang, X.; Yang, Z. A Molecular Simulation Probing of Structure and Interaction for Supramolecular Sodium Dodecyl Sulfate/Single-Wall Carbon Nanotube Assemblies. *Nano Lett.* **2010**, *10*, 985–991.
17. Islam, M. F.; Rojas, E.; Bergey, D. M.; Johnson, A. T.; Yodh, A. G. High Weight Fraction Surfactant Solubilization of Single-Wall Carbon Nanotubes in Water. *Nano Lett.* **2003**, *3*, 269–273.
18. Yurekli, K.; Mitchell, C. A.; Krishnamoorti, R. Small-Angle Neutron Scattering from Surfactant-Assisted Aqueous Dispersions of Carbon Nanotubes. *J. Am. Chem. Soc.* **2004**, *126*, 9902–9903.
19. Richard, C.; Balavoine, F.; Schultz, P.; Ebbesen, T. W.; Mioskowski, C. Supramolecular Self-Assembly of Lipid Derivatives on Carbon Nanotubes. *Science* **2003**, *300*, 775–778.
20. Wallace, E. J.; Sansom, M. S. P. Carbon Nanotube/Detergent Interactions *via* Coarse-Grained Molecular Dynamics. *Nano Lett.* **2007**, *7*, 1923–1928.
21. Niyogi, S.; Densmore, C. G.; Doorn, S. K. Electrolyte Tuning of Surfactant Interfacial Behavior for Enhanced Density-Based Separations of Single-Walled Carbon Nanotubes. *J. Am. Chem. Soc.* **2008**, *131*, 1144–1153.
22. Silvera-Batista, C. A.; Scott, D. C.; McLeod, S. M.; Ziegler, K. J. A Mechanistic Study of the Selective Retention of SDS-Suspended Single-Wall Carbon Nanotubes on Agarose Gels. *J. Phys. Chem. C* **2011**, *115*, 9361–9369.
23. Wang, R. K.; Chen, W.-C.; Campos, D. K.; Ziegler, K. J. Swelling the Micelle Core Surrounding Single-Walled Carbon Nanotubes with Water Immiscible Organic Solvents. *J. Am. Chem. Soc.* **2008**, *130*, 16330–16337.
24. Bethell, D.; Fessey, R. E.; Namwindwa, E.; Roberts, D. W. The Hydrolysis of C_{12} Primary Alkyl Sulfates in Concentrated Aqueous Solutions. Part 1. General Features, Kinetic Form and Mode of Catalysis in Sodium Dodecyl Sulfate Hydrolysis. *J. Chem. Soc., Perkin Trans. 2* **2001**, 1489.
25. Sun, Z.; Nicolosi, V.; Rickard, D.; Bergin, S. D.; Aherne, D.; Coleman, J. N. Quantitative Evaluation of Surfactant-Stabilized Single-Walled Carbon Nanotubes: Dispersion Quality and Its Correlation with Zeta Potential. *J. Phys. Chem. C* **2008**, *112*, 10692–10699.
26. Lebedkin, S.; Hennrich, F.; Kiowski, O.; Kappes, M. M. Photophysics of Carbon Nanotubes in Organic Polymer−Toluene Dispersions: Emission and Excitation Satellites and Relaxation Pathways. *Phys. Rev. B* **2008**, *77*, 165429-1-8.

2.1 Separation of Carbon Nanotubes

2.1.2 *Separation of Single-Walled Carbon Nanotubes with a Gel Permeation Chromatography System*

B. S. Flavel, K. E. Moore, M. Pfohl, M. M. Kappes, F. Hennrich

ACS Nano 8 (2014) 1817–1826

DOI: 10.1021/nn4062116

Abstract

A gel permeation chromatography system is used to separate aqueous sodium dodecyl sulfate suspensions of single-walled carbon nanotubes (SWCNTs). This automated procedure requires no pre-centrifugation, is scalable, and is found to yield monochiral SWCNT fractions of semiconducting SWCNTs with a purity of 61 – 95 %. Unsorted and resulting monochiral fractions are characterized using optical absorption and photoluminescence spectroscopy.

Contribution

B.S.F and F.H conceived the idea. B.S.F designed the experiments. B.S.F, K.E.M and M.P performed the experiments. B.S.F wrote the manuscript and all authors contributed to the discussion and analysis of experimental results.

– This page intentionally left blank –

Separation of Single-Walled Carbon Nanotubes with a Gel Permeation Chromatography System

Benjamin S. Flavel,[†,*] **Katherine E. Moore,**[†] **Moritz Pfohl,**[†] **Manfred M. Kappes,**[†,‡] **and Frank Hennrich**[†,*]

[†]Institute of Nanotechnology, Karlsruhe Institute of Technology, 76021 Karlsruhe, Germany, and [‡]Institute of Physical Chemistry, Karlsruhe Institute of Technology, 76128 Karlsruhe, Germany

ABSTRACT A gel permeation chromatography system is used to separate aqueous sodium dodecyl sulfate suspensions of single-walled carbon nanotubes (SWCNTs). This automated procedure requires no precentrifugation, is scalable, and is found to yield monochiral SWCNT fractions of semiconducting SWCNTs with a purity of 61–95%. Unsorted and resulting monochiral fractions are characterized using optical absorption and photoluminescence spectroscopy.

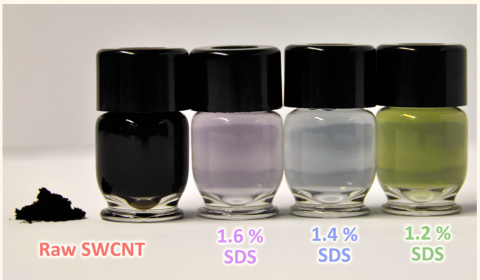

KEYWORDS: carbon nanotubes · gel filtration · size-exclusion chromatography · automated separation · sorting · purification

The development of new techniques for the preparation of monochiral single-walled carbon nanotube suspensions in a scalable, reproducible, and simple manner remains an ongoing challenge to the carbon nanotube community. Although chirality selective growth has been shown to be possible, direct synthesis methods remain limited to only a handful of different nanotube species such as (6,5), (7,6), or (9,8).[1−3] In order to gain access to the richly varying optical properties of SWCNTs, emphasis has therefore been placed upon the separation of raw carbon nanotube material. These raw materials are typically synthesized by techniques such as arc discharge, laser ablation, or the HiPco process and contain a complex mixture of metallic (m) and semiconducting (s) SWCNTs of varying diameter (D_t), chiral angle, or (*n*, *m*) index.

Previously separation of (*n*, *m*) pure SWCNTs has been achieved by various groups utilizing such techniques as the wrapping of SWCNTs with short sequences of single-stranded DNA (ssDNA) and subsequent ion exchange chromatography (IEX),[4] the suspension of SWCNTs with surfactants followed by density gradient ultracentrifugation (DGU),[5−7] or gel filtration.[8−11] Despite providing promising routes for the separation of SWCNTs, each of the above methods has drawbacks, be it the use of extended ultracentrifugation time, expensive density gradient medium and ssDNA, or the large amount of gel and gel columns required in the preparation of (*n*, *m*) pure SWCNT material. These factors combined with difficulty in often reproducing research results among groups have led to (*n*, *m*) pure SWCNT suspensions remaining on the small research scale and accessible to only a few groups. To this end, research has begun to develop new scalable methods for the preparation of SWCNT suspensions. For example Khripin *et al.*[12] have recently used immiscible polymer phases to spontaneously separate metallic and semiconducting SWCNTs on the liter scale. Likewise Tvrdy *et al.*[13] have also successfully separated liter volumes of mixtures of (7,5) and (8,3) and chirality pure (6,5), which was then used in the fabrication of a carbon nanotube based solar cell.[14] Liu *et al.*[15] achieved a single-chirality separation of seven (*n*, *m*) SWNT species using temperature-controlled gel chromatography. This method used temperature to selectively control the interaction between the SDS-wrapped SWCNTs and the allyl dextran-based Sephacryl gel. The control of the temperature enhanced the

* Address correspondence to
benjamin.flavel@kit.edu,
www.int.kit.edu/flavel,
frank.hennrich@kit.edu.

Received for review December 3, 2013
and accepted January 20, 2014.

10.1021/nn4062116

differences in the interactions of various (*n*, *m*) SWCNTs with the gel, enabling the separation of seven (*n*, *m*) species (purities between 56% and 93%). The authors speculate on the influence of temperature on the separation mechanism. They suggest that reducing the temperature may enhance the interactions between the adsorbed SDS molecules and nanotubes of certain specific chiralities (*e.g.*, near-armchair SWCNTs) and therefore that this may result in the reassembly of the SDS molecules on the nanotube surfaces, thus altering the dielectric constant around the SWCNTs and the absorbability of SWCNTs on the gel.

In our contribution to scale up, we have recently shown that the number of required Sephacryl gel columns can be reduced to one by altering the pH of the sodium dodecyl sulfate (SDS) eluent and demonstrated the separation of 15 different nanotube (*n*, *m*) species with a purity of 17−72%.[16] In that work we took a centrifuged 1 wt % SDS suspension of HiPco raw material and added it to a 14 cm high Sephacryl gel column. By changing the pH of the SDS eluent we showed that hydrolysis of SDS led to small quantities of 1-dodecanol being formed in solution. 1-Dodecanol is then incorporated into the SDS micelle of the SWCNTs. As it has been shown on graphite surfaces,[17,18] the integration of 1-dodecanol into the SDS micelle results in a structural conversion from a continuous parallel semicylindrical structure to a herringbone pattern. We expect a similar structural change for SWCNTs and attribute this structural change to a reduction in the SWCNT/gel interaction and the mechanism responsible for the elution of different SWCNT species. As discussed by Kataura and co-workers,[10] the initial SDS micelle of SWCNTs is strongly curvature-dependent[19] (hence also the nanotube gel/interaction strength) due to differences in the surface π-electron states. In other words, as the curvature of the SWCNT increases (smaller diameter), the SDS concentration/density decreases. Subsequently Duque *et al.*[20] have also experimentally confirmed the curvature-dependent wrapping of SDS. Hence our method was shown to have a strong dependence of elution order on nanotube diameter. In a recent paper, Kataura and co-workers follow on from our work varying the pH of SDS but provide an alternative explanation for the separation mechanism.[21] In their work they also observed the adsorbance of SWCNTs to the Sephacryl gel to be reduced under acidic pH conditions; however they describe the adsorbability as being related to a band structure dependent oxidation of SWCNTs, where oxidation confers positive charges onto the SWCNTs, and these charges enhance the electrostatic interactions of the SWCNTs with SDS, thereby leading to the condensation of SDS on the SWCNTs. This increase in SDS density around the SWCNT then reduces interaction between the SWCNTs and the gel. Despite the exact mechanism of separation with variations in pH remaining under debate, both explanations share one commonality, namely, changes in pH induce changes in the SDS micelle structure, which in turn reduces the SWCNT/gel interaction strength.

In this contribution we further build on our separation of SWCNTs by varying pH; however we apply our approach to a gel permeation chromatography (GPC) system. In doing so, we gain precise control over the pH of the SDS eluent and can utilize computer-controlled pH gradients in the separation of (*n*, *m*) SWCNT species. This allows us to reproducibly elute different (*n*, *m*) species with control over when (time-based) different fractions should be collected. This is a significant advantage over previous methods, where a vast number of fractions would need to be collected followed by absorption or photoluminescence spectroscopy to find the few (*n*, *m*) pure fractions. Our method also has the advantage of requiring no centrifugation; all raw materials are simply sonicated prior to use. This reduces the required infrastructure for (*n*, *m*) SWCNT sorting to a probe sonicator, a small amount of Sephacryl gel, and any pump system capable of dual solvent mixing.

RESULTS AND DISCUSSION

As outlined in our previous work,[16] the high-throughput separation of (*n*, *m*) pure s-SWCNTs with a single-column size exclusion chromatography (SEC) approach involved the use of a centrifuged 1 wt % SDS in H_2O suspension of raw HiPco-SWCNT material that was added to a Sephacryl S-200 gel bed under 1 wt % SDS in H_2O. This resulted in a starting material containing over 14 different (*n*, *m*) species, as shown by a photoluminescent contour map in Figure S1(a) of the Supporting Information. In this case centrifugation at ~100000*g* for 1.5 h was also necessary to remove any remaining catalyst particles and bundled carbon nanotubes and most importantly produce an SWCNT raw material with a reduced length distribution that is ideal for SEC sorting. Despite this preparatory centrifugation step, the resulting (*n*, *m*) suspensions afforded from our previous sorting effort were often intermixed with other (*n*, *m*) species and had a purity (by absorption spectroscopy) of 17−72%. In the current work we utilized the same raw HiPco material as before; however by tailoring the wt % of SDS we were able to limit the number of (*n*, *m*) SWCNT species absorbed on the gel for sorting to 1−6 species and this required no centrifugation. By dramatically reducing the number of species absorbed on the gel for a separation experiment, (*n*, *m*) species intermixing was therefore reduced and allowed for the preparation of much higher purity suspensions.

Preselection. As outlined in the Methods section, 80 mL of a 2 wt % SDS in H_2O suspension of raw HiPco-SWCNT material was prepared by 15 h sonication at constant temperature. Such a long sonication time is typical for the gel separation technique, where short nanotubes are required. In this work, no attempt was made to optimize the sonication time and thereby find the upper or lower bound length; however sonication represents an important third dimension to our separation process and will be investigated in the future. The raw material was then adjusted to 1.6 wt % SDS by the addition of H_2O, and 15 mL of the solution was added to the Sephacryl S-200 gel. The raw material was washed through the gel with a further 1.6 wt % SDS and collected. The diode array detector was used to monitor the washing process, and collection was stopped once a drop in intensity was observed. Although trace amounts of unbound SWCNTs are washed from the gel over the equilibrium time, collection of this entire volume would result in a weakly concentrated SWCNT suspension and make subsequent experiments difficult. The SWCNT material that remained absorbed to the gel is then the "starting material" for sorting with the GPC system. However, in order to initially understand which (*n*, *m*) species remained on the Sephacryl gel, 5 wt % SDS was added to the column to elute all adsorbed SWCNTs. An analogous process was then used to allow for preselection of adsorbed SWCNTs. Specifically, the SDS concentration of the SWCNTs initially washed through the gel (flow through) was adjusted in decrements of 0.2 wt % to cover the range 1.6−0.4 wt % SDS. As shown in the absorption spectroscopy in Figure 1, this resulted in a series of "starting materials" with increasing SWCNT diameter, where SWCNTs with a small, medium, and large D_t are designated to have a first optical transition (S11) in the regime 900−1050, 1050−1200, and 1200−1350 nm, respectively. Furthermore, it can be seen in Figure S2 of the Supporting Information that as the SDS concentration is reduced from 1.6 to 0.4 wt % SDS the relative concentration of small-diameter SWCNTs is reduced or completely removed. Interestingly, from the complex HiPco mixture, a suspension enriched in the (6,5) SWCNT, the species with the smallest diameter (D_t = 0.747 nm) can easily be prepared by adding the raw HiPco material to a column with 1.6 wt % SDS. From absorption measurements this material clearly also contains (7,5) and (7,6) species; however such a purity level may be useful to certain research groups.

The observation that changes in SDS concentration can control the adsorption of SWCNTs on the Sephacryl gel was also recently seen in work by Blanch *et al.*[11] In their work the SDS concentration of raw HiPco material was varied from 0.5 to 3.5 wt %, and it was found that for low SDS concentrations (0.5−1 wt % SDS) almost all SWCNT species in solution were absorbed on the gel and could be eluted with sodium deoxycholate. Alternatively for high SDS concentrations (2−3 wt % SDS) only small-diameter species such as (6,5), (8,3), and (7,6) were absorbed to the gel. For SDS concentrations below 0.5 wt % complete and irreversible adsorption to the gel was observed. However, in the work of Blanch *et al.*[11] they took "fresh" HiPco raw material and adjusted the SDS concentration sequentially instead of collecting the "flow-through" material and reducing the concentration. This is an important point differentiating our work from the work of Blanch *et al.* and is likely the reason for the missed potential to sequentially adsorb certain (*n, m*) species to the gel, as we have done. Likewise, Liu *et al.*[15] investigated the effect of SDS concentration on the adsorbance of SWCNTs to the Sephacryl gel. They described the decreased adsorbance at higher SDS concentrations as being related to a higher coverage and/or thickness of SDS around the SWCNT, which leads to a reduced interaction with the gel. With this in mind and the knowledge that the SDS micelle is strongly curvature-dependent,[19] it is therefore a logical conclusion that smaller diameter SWCNTs are less coated at relatively higher SDS concentrations and give rise to the sequential adsorption shown in our work. However, this is not forgetting one important requirement for the preparation of these "starting materials", namely, the sequential removal of smaller diameter SWCNT species. There exists a specific number of Sephacryl binding sites (secondary amide groups along the polymer backbone), which may bind to an s-SWCNT. This adsorption process has been shown to be a kinetically driven, competitive, process[13] with larger diameter SWCNTs passing through the gel if the adsorption sites are already taken by smaller diameter SWCNTs. Initially this would suggest that it is not necessary to adjust the SDS concentration and that the same result would be achieved through simply using multiple, sequential columns. Indeed we have tried this approach; however we note that this does not lead to complete removal of the smaller (*n*, *m*) species before proceeding to the subsequent column. Furthermore, and in agreement with the work of Tvrdy *et al.*, the concentration of

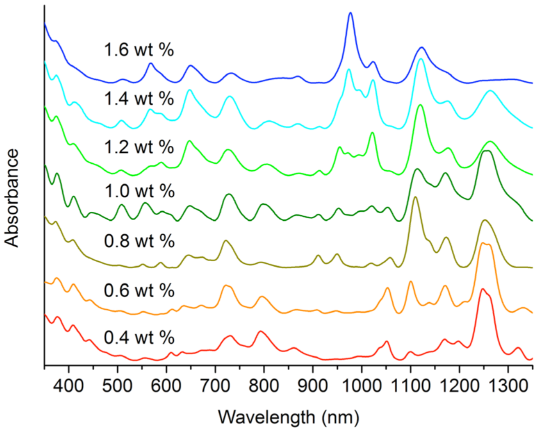

Figure 1. Absorption spectroscopy of "starting materials" (SWCNTs absorbed on the Sephacryl gel) obtained by sequentially reducing the SDS concentration from 1.6 to 0.4 wt %.

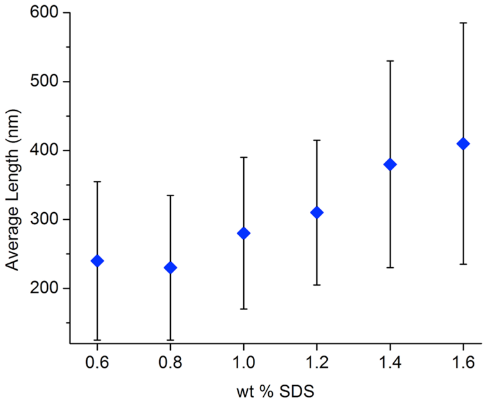

Figure 2. Average length of the SWCNT "starting material" as determined by AFM measurements.

SWCNTs absorbed on the gel dramatically decreases with sequential columns.[13] The SDS concentration must be reduced to ensure high concentration and (*n*, *m*) species removal. The importance of (*n*, *m*) species removal is also discussed by Liu *et al*., who use temperature control to sort SWCNTs and note that it is necessary to completely remove (6,4) (D_t = 0.683 nm) before proceeding to collect (6,5) (D_t = 0.747 nm).

In an attempt to further understand the observed selective adsorption we performed atomic force microscopy (AFM) measurements of the material absorbed to the gel for concentrations of 1.6−0.6 wt % SDS. These measurements are summarized in Figure 2, where the average length of the "starting material" is shown for each SDS concentration. The complete set of measurements for each SDS concentration can be found in the Supporting Information in Figure S3. For each "starting material" a Gaussian was fitted to the histogram to obtain the average length. It can be clearly seen that the relatively smaller diameter SWCNTs absorbed to the Sephacryl gel at higher SDS concentrations have relatively longer lengths compared to the SWCNTs absorbed at lower SDS concentrations. The implication of this observation for the adsorption of SWCNTs to the gel still requires investigation and remains speculative. However, this is an observation that is in agreement with the work of Clar *et al.*,[22] who discussed the SDS/SWCNT interface as being highly intricate. The surfactant shell around a SWCNT is dynamic, not well-defined and is expected to be heterogeneous, with some areas of the SWCNT completely exposed to the gel.[22] Therefore the strength of the SWCNT/gel interaction is likely controlled by not only nanotube diameter and SDS concentration but also length due to the interfacial area. This is also in agreement with Heller *et al.*,[23] who achieved simultaneous separation of SWCNT length and diameter by gel electrophoresis and column chromatography conducted on individually dispersed, ultrasonicated SWCNTs. They proposed a diameter-selective cutting mechanism with ultrasound treatment that was later confirmed by Hennrich *et al.*[24] In their mechanism the smaller diameter SWCNTs are cut to a lesser extent compared to the larger diameters due to the fact that strain forces associated with sonication induced cavitation scales with the square of the nanotube length and is also supposed to be diameter dependent. Scission of SWCNTs then stops when the strain force falls below a critical value for nanotube disruption.

Automated SWCNT Sorting. Upon having a defined "starting material" obtained from different SDS concentrations, we then used the GPC system to apply a pH gradient to the gel, which allowed us to separate the trapped SWCNTs (rather than simply washing all species off the column with 5 wt % SDS). At this point it important to note that the pH of the parent and daughter "starting materials" was between 7 and 8, and all experiments were performed at 23 °C. Figures 3 and 4 show photoluminescence (PL) contour maps corresponding to the "starting material" (1.6−0.6 wt % SDS) absorption spectra shown in Figure 1. A PL contour map of the 0.4 wt % SDS "starting material" can be found in Figure S1(b) of the Supporting Information. Upon looking at the PL contour maps the dependence of diameter adsorption of SWCNTs to the Sephacryl gel on changes in SDS concentration is further made clear. For example the "starting material" obtained at 1.4 wt % SDS (consisting primarily of (7,5), (6,5), (7,6), and (8,4) SWCNTs) has an average diameter of 0.818 nm compared to 0.6 wt % SDS (consisting primarily of (9,4), (9,5), (10,2), (10,3), (11,1), (8,6), and (8,7) SWCNTs), which has an average diameter of 0.933 nm. The SWCNT diameter values were taken from the data of Weisman *et al.*[25] Accompanying the PL contour map of each "starting material" the corresponding elution profile can also be found in Figures 3 and 4. In order to record these elution profiles, the GPC system was fitted with a diode array detector capable of measuring full spectra between 190 and 950 nm. Despite the ability to extract full spectral data at the completion of an experiment, during a run only two fixed wavelengths could be monitored. To ensure sensitivity to all (*n*, *m*) species in the second optical transition (S22) regime either 590, 650, or 720 nm was monitored with a resolution of ±10 nm.

Explanation of the elution diagrams and (*n*, m) separation is best served by beginning with the most simple situation of SWCNTs absorbed to the Sephacryl gel in 1.6 wt % SDS. In this instance the number of SWCNTs to be sorted is limited to essentially (6,5) with a small amount of (7,5) and (7,6) (as shown by absorbance measurements in Figure 1). In performing the separation the GPC system was operated isocratically in 1.6 wt % SDS with a quaternary pump mixing 1.6 wt % SDS (defined pump A) and 1.6 wt % SDS adjusted to pH 3 upon addition of HCl (defined pump B). The separation was then performed in the following manner: In preparation the Sephacryl gel was placed

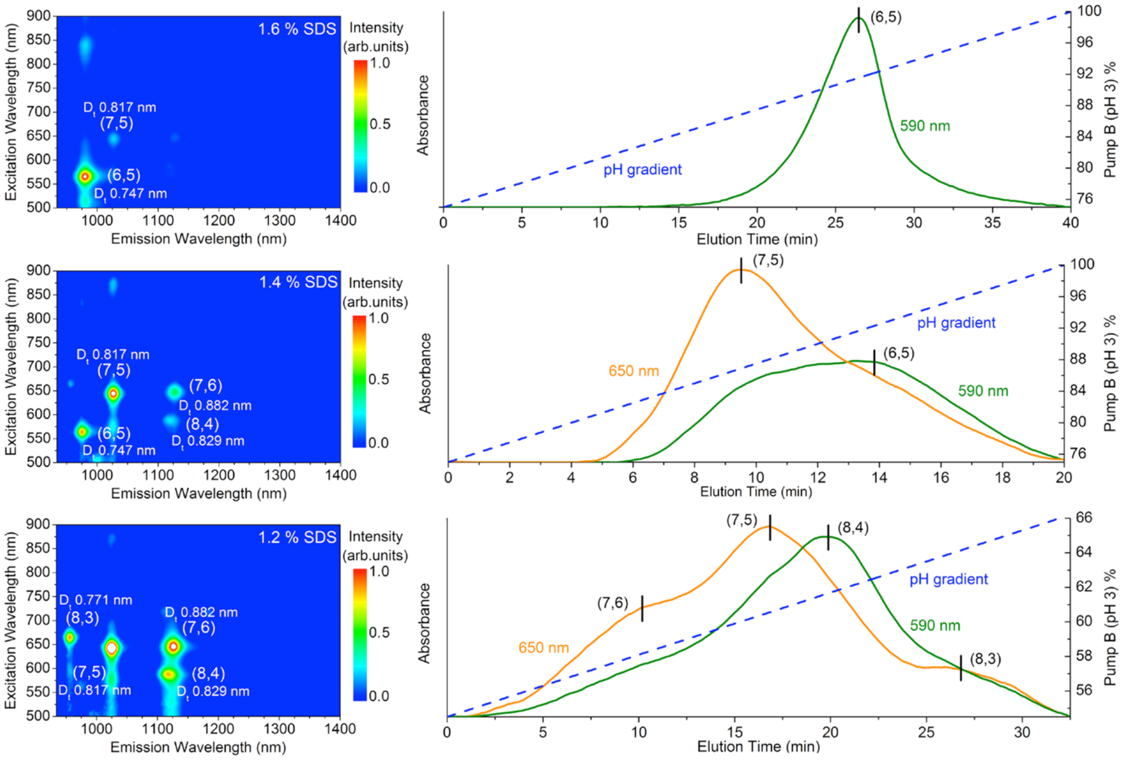

Figure 3. Photoluminescence contour maps of SWCNTs absorbed to the Sephacryl gel at 1.6, 1.4, and 1.2 wt % SDS ("starting materials") and the corresponding elution profile diagram.

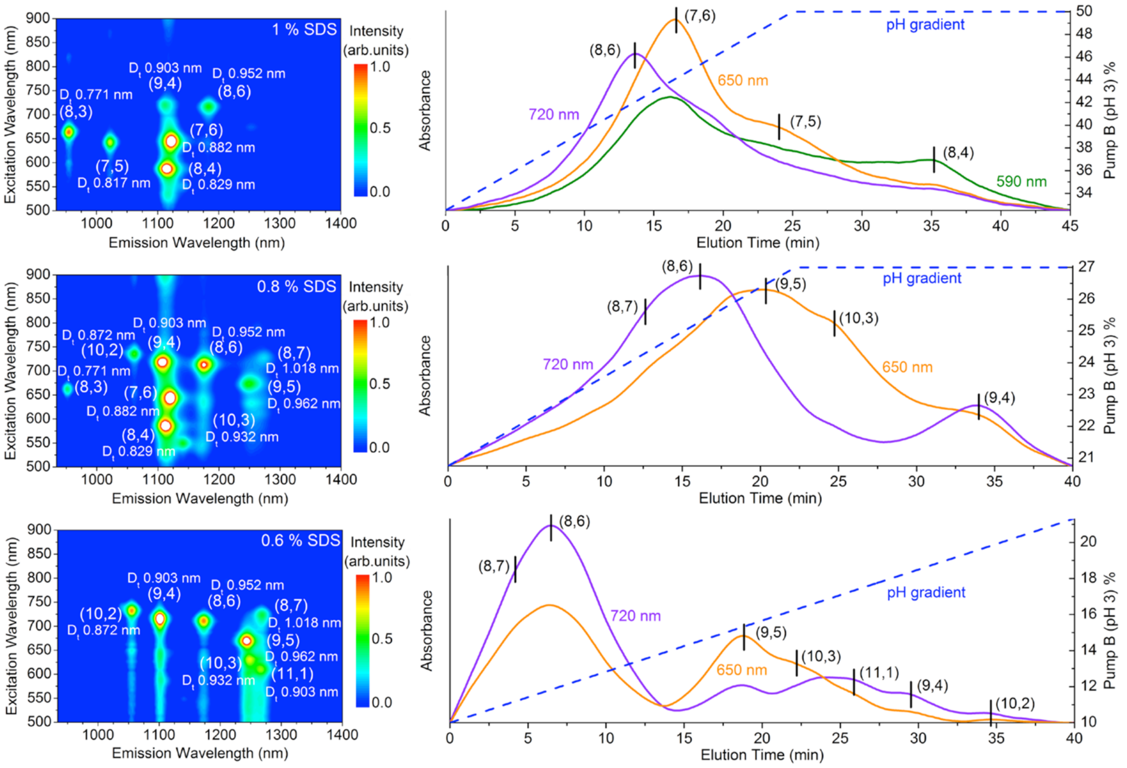

Figure 4. Photoluminescence contour maps of SWCNTs absorbed to the Sephacryl gel at 1, 0.8, and 0.6 wt % SDS ("starting materials") and the corresponding elution profile diagram.

under 1.6 wt % SDS by setting pump A to 100% at a pumping rate of 2 mL/min for 1.5 h. Fifteen milliliters of raw HiPco material (adjusted to 1.6 wt % SDS) was then pumped onto the Sephacryl gel and washed through with a further 1.6 wt % SDS. Importantly the "flow through" material was collected for subsequent separation steps. While maintaining a flow rate of 2 mL/min the quaternary pump was then used to bring the column under reduced pH conditions by setting pumps A and B in a ratio of 15:75% and holding there for 1.5 h. As depicted in Figure 3 the pumping ratio was then linearly varied to 100% pump B (pH 3, 1.6 wt % SDS) over a period of 40 min. By setting the diode array detector to 590 and 650 nm the elution of (6,5) SWCNTs can then be seen as a peak centered at 26 min (pH = 3.04) beginning at approximately 20 min (pH = 3.06) and ending at 35 min (pH = 3.01). Despite the presence of (7,5) and (7,6) in the "start material", these species were not observed to elute from the column in this region, a typical observation for (*n*, *m*) species in low concentration, such as (7,6) and (8,4) in the 1.4 wt % SDS separation. However, upon comparison of the absorption spectra for (6,5) presented in Figure 1 (1.6 wt % SDS) to that of Figure 7, it can be seen that the purity of (6,5) is dramatically improved due to the removal of (7,5) and (7,6). This procedure was then repeated for SDS concentrations of 1.4–0.6 wt % SDS upon sequentially adjusting the SDS concentration of the "flow through" material. In each case the SDS concentrations of pumps A and B were also adjusted. Upon looking at the 1.4 wt % SDS separation, a "start material" with now significantly more (7,5) and less (6,5) is obtained. This is reflected in the elution diagram with a larger peak of (7,5) eluting at 9.5 min (pH = 3.06) and a smaller peak for (6,5) at 14 min (pH = 3.03). In reading the elution diagrams in Figures 3 and 4, it is important to keep in mind that despite the pump ratio being varied linearly the real pH gradient is in fact asymptotic in nature. Furthermore time 0 is after the 1.5 h equilibrium time.

Despite 1.6 and 1.4 wt % SDS "start materials" being separated in the same pH window, *i.e.*, a linear gradient between 75% pump B (pH = 3.12) and 100% pump B (pH = 3), as the SDS concentration was further reduced from 1.2 to 0.6 wt % SDS the required pH window for elution was observed to shift. For example 1.2, 1, 0.8, and 0.6 wt % SDS "start materials" were separated in the linear pump regime of 55–66% (pH 3.25–3.18), 33–50% (pH 3.48–3.30), 20–27% (pH 3.69–3.56), and 10–21% (pH 4–3.67) pump B. This is in agreement with our previous work,[16] where we showed that the elution of relatively small diameter SWCNTs scaled relative to reductions in pH. However, in our previous work we varied the pH from 4 to 1 in order to elute the entire HiPco (*n*, *m*) ensemble, whereas in the current work we can work in the pH regime 4–3. This difference is attributed to previously working with a much larger Sephacryl gel column (14 cm instead of a 2 cm bed height) and an underestimation of the solvent volume required to equilibrate such a large gel to a set pH value and the speed at which SWCNTs transverse through the column. The use of the GPC system to apply a controlled gradient, a smaller column, and the ability to monitor UV *in situ* have allowed us to now be more precise with the required pH for (*n*, *m*) species elution. This is summarized in Figure 5, where the SWCNT diameter is plotted against (a) the required percentage of pump B (pH 3) and (b) the corresponding pH, where the peak position for each (*n*, *m*) species was taken from the elution diagram.

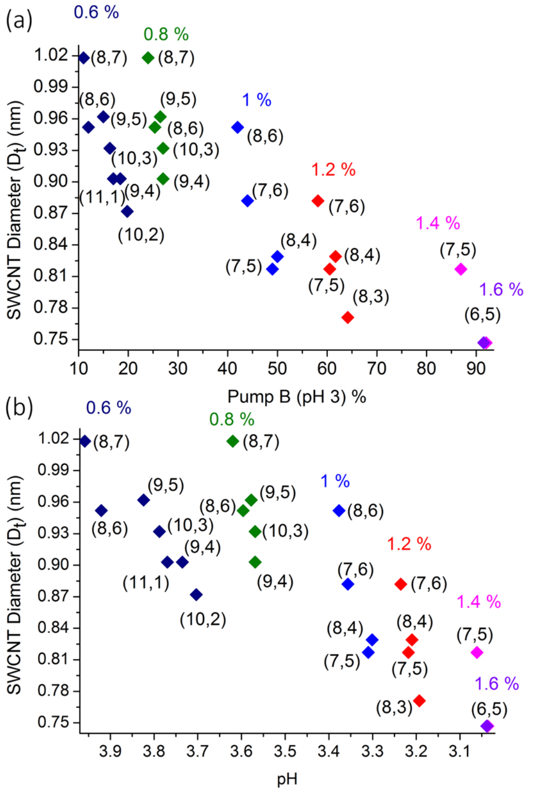

Figure 5. Single-walled carbon nanotube (SWCNT) diameter (D_t) dependence upon (a) the pumping rate of pump B and (b) the corresponding pH. The SDS concentration is color-coded.

Closer examination of the elution diagrams in Figures 3 and 4 reveals the presence of certain (*n*, *m*) species across multiple SDS concentration regimes. A good example is the (7,5) SWCNT, which is present in 1.4, 1.2, and 1 wt % SDS. Rather than having a fixed pH for elution, the position of (7,5) shifts from pH 3.06 to pH 3.22 to pH 3.30 for 1.4, 1.2, and 1 wt % SDS concentrations, respectively. This shift in position tends to rule out the possibility for SWCNT doping or band structure dependent oxidation[21] being responsible for (*n*, *m*) species elution. Rather we hypothesize in agreement with the AFM data presented in Figure 2 that there exists different types of (7,5) within the raw HiPco material following sonication. This (7,5) material has different lengths and more importantly different surfactant wrapping of the nanotube and consequently different overall interaction strength and (interfacial area per length) with the Sephacryl gel. With this in mind, it is therefore unsurprising that the elution point of (7,5) at different SDS concentrations can change. Of course, another possible explanation is

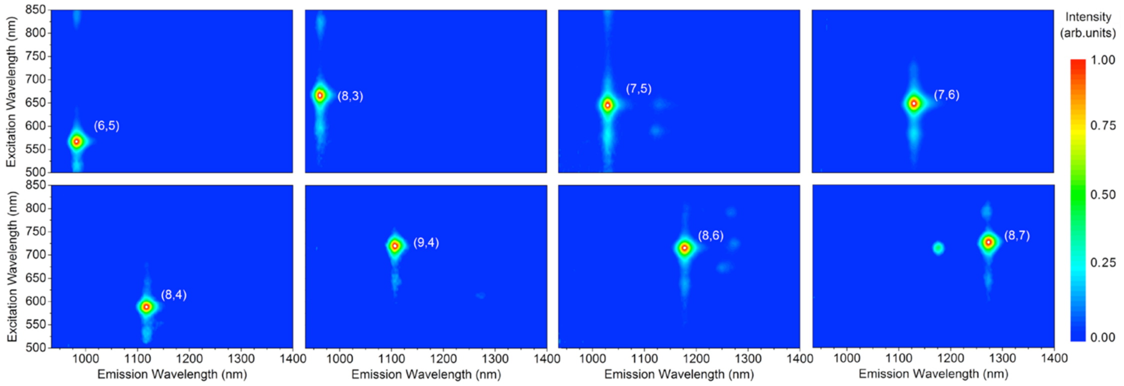

Figure 6. Photoluminescence contour maps of (*n*, *m*) fractions obtained from an automated gel permeation chromatography (GPC) system.

simply the differing size, shape, and or thickness of the SDS micelle around the SWCNT at different SDS concentrations. The interaction strength of the SWCNT will therefore also be different and may require reduced micelle modification, be it through band structure dependent oxidation or 1-dodecanol addition, for (*n*, *m*) species elution. However, we note that it is occasionally possible to elute the same (*n*, *m*) species at two different pH points in a fixed SDS concentration. For example (7,5) in 1 wt % SDS is often found to elute at pH 3.30 (23 min as shown in Figure 4) and also at pH 3.22, which would be the same pH point as required for 1.2 wt % SDS. Such an observation gives further weight to our speculation that the interfacial area and nonmonotonic length distribution of SWCNTs are also important. Another possible explanation is the potential for enantiomers; however we have made no attempt to verify this and believe it to be unlikely.

Contrary to typical elution diagrams from standard GPC separations the various peaks associated with different (*n*, *m*) species are seen to have a large degree of overlap, making it not immediately obvious how this method is conducive to the preparation of (*n*, *m*) pure samples. The trick lies in choosing the appropriate "starting material" for the (*n*, *m*) species desired. For example, it is always much easier to harvest an (*n*, *m*) species that has either the smallest or largest diameter in an ensemble under investigation. The largest diameter species always elutes first from the Sephacryl gel and the smallest last. These fractions are typically free of all other (*n*, *m*) species in the "starting material", and an automated collection of beginning or end conditions is easily achieved. For example if (7,5) was the desired SWCNT, this is better prepared from 1.4 wt % SDS, where it is the leading species compared to 1.2 and 1 wt % SDS, where (7,5) is surrounded by other (*n*, *m*) species. Likewise (8,6) is much better prepared from 1 wt % SDS compared to 0.8 or 0.6 wt % SDS. In the case of "starting materials" with many more (*n*, *m*) species present the separation can begin to break down due to the presence of multiple SWCNT with very similar or indeed the same diameter such as (9,4) and (11,1) as present in 0.6 wt % SDS. In this case we were unable to successfully separate these species, regardless of how finely the pH gradient was adjusted. Therefore when attempting to purify (9,4), it is better to choose a 0.8% SDS "starting solution" where it represents the smallest diameter SWCNT species. It should be noted that (7,6) and (8,4) were not found to elute in this pH regime. Furthermore, it should be noted that due to the decreased concentration of the "starting material" and the strong interaction of the SWCNTs, we were not able to perform a separation with 0.4 wt % SDS "starting material". Work to prepare the larger diameter SWCNTs is now under way; however it is expected that this goal is best achieved by choosing a different raw material such as that from laser ablation, where the larger diameter SWCNTs are in greater proportion.

Despite the inability to prepare pure suspensions of the larger diameter SWCNTs, we are now able to reproducibly sort eight different (*n*, *m*) species from the HiPco raw material as shown by photoluminescence contour maps in Figure 6 and the corresponding absorption measurements in Figure 7. Normalized raw absorbance data can also be found in Figure S4 of the Supporting Information. Furthermore, the fitted peak area from absorption measurements was used to calculate (*n*, *m*) purity, where the major (*n*, *m*) contribution was taken as a ratio of all other peaks. For this calculation only the first optical transition peak (S11) was taken and the absorbance cross section was assumed to be identical across all (*n*, *m*) species. Purity data can be found in Table 1. In this work we have managed to routinely prepare eight (*n*, *m*) species with a purity of 61–95%. This is an improvement compared to our previous work, where we isolated 10 (*n*, *m*) species with a purity of 19–30%, with only two species ((8,6) and (6,5)) on the level of 60–70%. This highlights the benefit of having a reduced (*n*, *m*) species "starting material" and also precise control over the pH. It should be noted that between 450 and 550 nm nanotube-related transitions are seen in the absorption spectra. This absorption regime is typically associated with

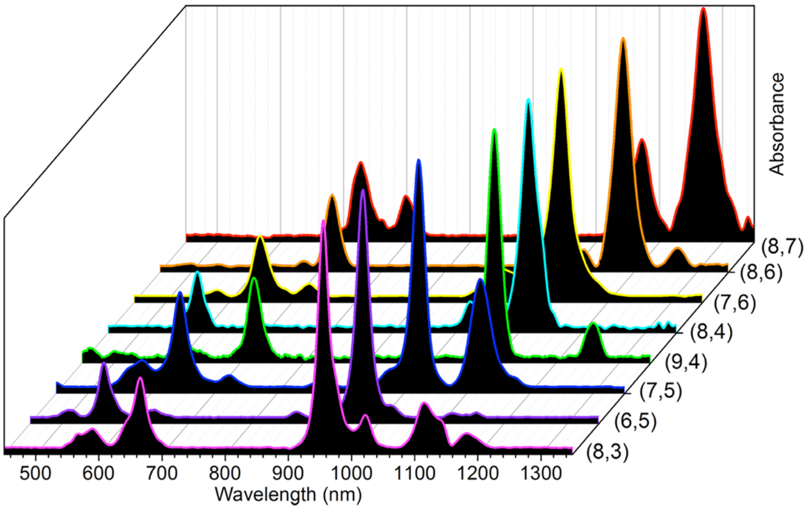

Figure 7. Absorption spectra corresponding to fractions displayed in Figure 6.

TABLE 1. Purity of (*n*, *m*) Species Obtained from the Gel Permeation Chromatography (GPC) System

	(*n*, *m*) species							
	(8,3)	(6,5)	(7,5)	(9,4)	(8,4)	(7,6)	(8,6)	(8,7)
purity (%)	64	92	61	76	76	95	88	77

m-SWCNTs; however, due to an overlap of the third interband transition (S33) of the HiPco s-SWCNTs, it is difficult to estimate the m-SWCNT concentration. Preliminary electrical transport measurements indicate a metallic/semiconducting-SWCNT ratio equivalent to standard Sephacryl S-200 separations. That is to say that 90% of all fabricated devices showed semiconducting behavior with an on/off ratio of at least 1 order of magnitude. Our fabricated devices had a gap width comparable to the average nanotube length and a 1 μm contact width with a nanotube density of 10−20 CNTs/μm. From this we estimate the degree of metallic/semiconducting-SWCNT separation to be >95%. In comparison to the initial work of Liu *et al.*,[10] who were able to obtain 13 different (*n*, *m*) species with purities of 39−94% our method is shown to afford superior purities. However, in comparison to the latest work in 2013 of Liu *et al.*,[15] who modified their initial approach to include temperature control and were able to prepare seven (*n*, *m*) species with a purity of 56−93%, our work is equivalent to the current state of the art. A trend also seen upon comparison to the work of Tvrdy *et al.*,[13] who prepared (6,5), (7,3), (7,5), and (7,6) with purities of 96, 87, 56, and 64%, respectively. For an effective sorting method it is also important to assess the yield of the various (*n*, *m*) species. While we did not measure this directly, it is noted that the starting solution has a mass on the milligram level and the final (*n*, *m*) fractions were below the μg level. This obvious problem in yield is due to only collecting beginning or end material, with a large portion of the eluent discarded. In the future we hope to be able to have less overlap of the individual (*n*, *m*) species and hence dramatically improve our yield. Upon eliminating the need for centrifugation in our method, a question is also raised as to the fate of impurity carbon and/or non-SWCNT material. This material is typically removed by centrifugation and must show up somewhere in our separation. We note that during the 1.5 h equilibration time (prior to the collection of (*n*, *m*) species) material is observed to elute from the column. Upon measuring absorbance spectra, this material is typically poorly defined or has no SWCNT absorption characteristics, and we have therefore attributed it to be such impurity carbon material.

Our method allows for routine time based separation (dependent on set pump conditions) of (*n*, *m*) species, where the users know in which region of the elution diagram they must collect pure (*n*, *m*) fractions. This is something that can easily become automated, as in our case where we plan to take an automated fraction collector and have a completely automated process from the injection of raw HiPco material through to the collection of (*n*, *m*) pure species. Upon maintaining the sonication conditions constant, the elution time and position of each (*n*, *m*) species at a set SDS concentration remained constant between experimental runs. Additionally, the gel column was found to be reusable with preliminary tests, showing the gel to be reusable up to 10 times. This is important if such a method is to become industrially applicable. As discussed by Strano *et al.*,[13] the (*n*, *m*) separation of SWCNTs is a process that is easily scalable to arbitrary large volumes of Sephacryl gel and raw material, and we believe our automated method will therefore form a crucial step toward the routine separation of SWCNTs. However, it is important to remember that upon increasing the separation volume (amount of gel and raw material) the elution timing will need to be adjusted/optimized to accommodate for the larger gel volume and the time required for the gel to reach pH equilibrium. In our initial experiments a 3-fold increase in gel volume has resulted in roughly a 3−4-fold increase in pH equilibrium time and therefore also the time required for a separation. Furthermore, factors such as flow rate and pressure applied to an increased gel bed volume will need to be optimized before a truly large-scale separation can be realized. Ideally one should keep the column length the same and scale the area with a fixed flow rate per area of gel. It is also likely that the next step in (*n*, *m*) purity will also come by combining the methodology of several groups into one process, for example, the use of a gel permeation chromatography system to vary not only pH and SDS concentration but also gel/eluent temperature.

CONCLUSION

In conclusion, we have shown the (*n*, *m*) separation of eight different SWCNT species with a purity of 61−95%. This separation was achieved without the use of centrifugation and with the use of a gel permeation system. The ability to achieve high-purity (*n*, *m*) suspensions routinely with use of a computer-controlled and automated system, without the need for specialist equipment, will hopefully allow many new research groups access to pure (*n*, *m*) suspensions and further foster development in the field of SWCNTs.

METHODS

HiPco SWCNT raw material (NanoIntegris) was used throughout this work. In order to prepare starting suspensions, 20 mg of raw SWCNT material was suspended in 80 mL of H_2O with 2 wt % sodium dodecyl sulfate using a tip sonicator (Weber Ultrasonics, 35 kHz, 500 W, in continuous mode) applied for 15 h at ~20% power. During sonication, the suspension was placed in a water-circulation bath to aid cooling.

Gel filtration was performed using 7 mL of the Sephacryl S-200 gel filtration medium (Amersham Biosciences) in a commercially available water-jacketed liquid chromatography column (XK 16/20, GE Healthcare) with 16 mm inner diameter and 20 cm length. After applying slight compression the gel yielded a final height of 2 cm. An Accel 250 LC water chiller (Thermoscientific) was then used to maintain the column temperature at 23 °C. Separation was performed with a SECcurity gel permeation chromatography 1260 Infinity system (Agilent Technologies). This consisted of a quaternary pump (G1311B), an autosampler (G2258A), a diode array detector (G1315D), and a fraction collector (CHF122SC, Advantec). The GPC system was controlled *via* the WinGPC UniChrom v.8.1 software (Polymer Standards Service GmbH). The diode array detector was used to monitor two fixed wavelengths at either 590, 650, or 720 nm during an experimental run with complete spectra measured from 190 to 950 nm with a bandwidth of 10 nm and a step width of 8 nm. Following sonication the SDS concentration of the raw material was adjusted to the appropriate concentration by the addition of H_2O. A 15 mL amount of SWCNT suspension was then pumped onto the gel column and washed through with further SDS. Importantly the “flow through” material was collected for subsequent dilution and separation steps. After loading the gel with SWCNTs the quaternary pump was used to mix SDS (pump A) with SDS at pH 3 (pump B) (prepared through the addition of the appropriate concentration of HCl). While maintaining a flow rate of 2 mL/min the quaternary pump was then used to bring the column under reduced pH conditions by setting pumps A and B to the appropriate ratio and holding there for 1.5 h. Once the gel reached equilibrium conditions, an appropriate pH gradient was applied to the gel over a period of 20−40 min, and 2 mL fractions were collected.

For spectroscopic characterization, the doping effect of reduced pH was removed by addition of 1 drop of 25% w/w tetramethylammonium hydroxide aqueous solution (Alfa Aesar) to each 2 mL fraction. This resulted in a SWCNT suspension that was slightly basic and ensured no spectroscopic features were missed. UV−vis−NIR absorption spectra were recorded on a Varian Cary 500 spectrophotometer. For ease of comparison, background subtraction of the UV−vis spectra was performed using the freeware fityk (http://fityk.nieto.pl/). Photoluminescence maps were measured in the emission range ~900−1700 nm and excitation range 500−950 nm (scanned in 3 nm steps) using a modified FTIR spectrometer (Bruker IFS66) equipped with a liquid nitrogen cooled Ge-photodiode and a monochromatized excitation light source as described elsewhere.[26]

Atomic force microscopy was performed in an air environment with a multimode head and Nanoscope III controller (Digital Instruments), operating in tapping mode. Commercially available silicon cantilevers with fundamental resonance frequency of 320 kHz were used. Images of 10 × 10 μm topographic (height) and amplitude were collected simultaneously at a scan rate of 0.5 Hz with the parameters' set point, amplitude, and feedback control optimized for each sample. A 0.7 μL sample of SWCNT solution was then dropped onto a 1 cm^2 silicon wafer and spin coated at 1500 rpm for 60 s.

Conflict of Interest: The authors declare no competing financial interest.

Acknowledgment. B.S.F. gratefully acknowledges support from the Deutsche Forschungsgemeinschaft's Emmy Noether Program under grant number FL 834/1-1. K.E.M. wishes to thank the Australian Nanotechnology Network (ANN), the Australian Microscopy and Microanalysis Research Facility (AMMRF), the Australian Government for an Australian Postgraduate Award, the Playford Memorial Trust, Flinders University, BankSA, the Amy Forwood Trust, and the Cathy Chandler Bursary. This research was also supported by the Bundesministerium für Bildung und Forschung (BMBF) as administered by the Helmholtz Program POF-NanoMicro.

Supporting Information Available: Photoluminescence contour maps of raw HiPco SWCNT material and SWCNTs absorbed to the Sephacryl gel at 0.4 wt % SDS. Absorption spectra of raw HiPco SWCNT material (flow through) following sequential reduction of the SDS concentration and separated (*n*, *m*) species. Histograms of the SWCNT length distribution for the various “starting materials”, as determined by AFM. This material is available free of charge *via* the Internet at http://pubs.acs.org.

REFERENCES AND NOTES

1. Wang, H.; Wang, B.; Quek, X. Y.; Wei, L.; Zhao, J. W.; Li, L. J.; Chan-Park, M. B.; Yang, Y. H.; Chen, Y. A. Selective Synthesis of (9,8) Single Walled Carbon Nanotubes on Cobalt Incorporated TUD-1 Catalysts. *J. Am. Chem. Soc.* **2010**, *132*, 16747–16749.
2. Liu, J.; Wang, C.; Tu, X. M.; Liu, B. L.; Chen, L.; Zheng, M.; Zhou, C. W. Chirality-Controlled Synthesis of Single-Wall Carbon Nanotubes Using Vapour-Phase Epitaxy. *Nat. Commun.* **2012**, *3*, 1199.
3. Bachilo, S. M.; Balzano, L.; Herrera, J. E.; Pompeo, F.; Resasco, D. E.; Weisman, R. B. Narrow (n,m)-Distribution of Single-Walled Carbon Nanotubes Grown Using a Solid

Supported Catalyst. *J. Am. Chem. Soc.* **2003**, *125*, 11186–11187.

4. Tu, X. M.; Manohar, S.; Jagota, A.; Zheng, M. DNA Sequence Motifs for Structure-Specific Recognition and Separation of Carbon Nanotubes. *Nature* **2009**, *460*, 250–253.
5. Arnold, M. S.; Stupp, S. I.; Hersam, M. C. Enrichment of Single-Walled Carbon Nanotubes by Diameter in Density Gradients. *Nano Lett.* **2005**, *5*, 713–718.
6. Arnold, M. S.; Green, A. A.; Hulvat, J. F.; Stupp, S. I.; Hersam, M. C. Sorting Carbon Nanotubes by Electronic Structure Using Density Differentiation. *Nat. Nanotechnol.* **2006**, *1*, 60–65.
7. Ghosh, S.; Bachilo, S. M.; Weisman, R. B. Advanced Sorting of Single-Walled Carbon Nanotubes by Nonlinear Density-Gradient Ultracentrifugation. *Nat. Nanotechnol.* **2010**, *5*, 443–450.
8. Moshammer, K.; Hennrich, F.; Kappes, M. M. Selective Suspension in Aqueous Sodium Dodecyl Sulfate According to Electronic Structure Type Allows Simple Separation of Metallic from Semiconducting Single-Walled Carbon Nanotubes. *Nano Res.* **2009**, *2*, 599–606.
9. Blum, C.; Sturzl, N.; Hennrich, F.; Lebedkin, S.; Heeg, S.; Dumlich, H.; Reich, S.; Kappes, M. M. Selective Bundling of Zigzag Single-Walled Carbon Nanotubes. *ACS Nano* **2011**, *5*, 2847–2854.
10. Liu, H. P.; Nishide, D.; Tanaka, T.; Kataura, H. Large-Scale Single-Chirality Separation of Single-Wall Carbon Nanotubes by Simple Gel Chromatography. *Nat. Commun.* **2011**, 2.
11. Blanch, A. J.; Quinton, J. S.; Shapter, J. G. The Role of Sodium Dodecyl Sulfate Concentration in the Separation of Carbon Nanotubes Using Gel Chromatography. *Carbon* **2013**, *60*, 471–480.
12. Khripin, C. Y.; Fagan, J. A.; Zheng, M. Spontaneous Partition of Carbon Nanotubes in Polymer-Modified Aqueous Phases. *J. Am. Chem. Soc.* **2013**, *135*, 6822–6825.
13. Tvrdy, K.; Jain, R. M.; Han, R.; Hilmer, A. J.; McNicholas, T. P.; Strano, M. S. A Kinetic Model for the Deterministic Prediction of Gel-Based Single-Chirality Single-Walled Carbon Nanotube Separation. *ACS Nano* **2013**, *7*, 1779–1789.
14. Jain, R. M.; Howden, R.; Tvrdy, K.; Shimizu, S.; Hilmer, A. J.; McNicholas, T. P.; Gleason, K. K.; Strano, M. S. Polymer-Free Near-Infrared Photovoltaics with Single Chirality (6,5) Semiconducting Carbon Nanotube Active Layers. *Adv. Mater.* **2012**, *24*, 4436–4439.
15. Liu, H. P.; Tanaka, T.; Urabe, Y.; Kataura, H. High-Efficiency Single-Chirality Separation of Carbon Nanotubes Using Temperature-Controlled Gel Chromatography. *Nano Lett.* **2013**, *13*, 1996–2003.
16. Flavel, B. S.; Kappes, M. M.; Krupke, R.; Hennrich, F. Separation of Single-Walled Carbon Nanotubes by 1-Dodecanol-Mediated Size-Exclusion Chromatography. *ACS Nano* **2013**, *7*, 3557–3564.
17. Paruchuri, V. K.; Nalaskowski, J.; Shah, D. O.; Miller, J. D. The Effect of Cosurfactants on Sodium Dodecyl Sulfate Micellar Structures at a Graphite Surface. *Colloid Surf. A* **2006**, *272*, 157–163.
18. Paruchuri, V. K.; Nguyen, A. V.; Miller, J. D. Zeta-Potentials of Self-Assembled Surface Micelles of Ionic Surfactants Adsorbed at Hydrophobic Graphite Surfaces. *Colloid Surf. A* **2004**, *250*, 519–526.
19. Tummala, N. R.; Striolo, A. Curvature Effects on the Adsorption of Aqueous Sodium-Dodecyl-Sulfate Surfactants on Carbonaceous Substrates: Structural Features and Counterion Dynamics. *Phys. Rev. E* **2009**, *80*, 021480.
20. Duque, J. G.; Densmore, C. G.; Doorn, S. K. Saturation of Surfactant Structure at the Single-Walled Carbon Nanotube Surface. *J. Am. Chem. Soc.* **2010**, *132*, 16165–16175.
21. Hirano, A.; Tanaka, T.; Urabe, Y.; Kataura, H. pH- and Solute-Dependent Adsorption of Single-Wall Carbon Nanotubes onto Hydrogels: Mechanistic Insights into the Metal/Semiconductor Separation. *ACS Nano* **2013**, *7*, 10285–10295.
22. Clar, J. G.; Silvera Batista, C. A.; Youn, S.; Bonzongo, J. C.; Ziegler, K. J. Interactive Forces between Sodium Dodecyl Sulfate-Suspended Single-Walled Carbon Nanotubes and Agarose Gels. *J. Am. Chem. Soc.* **2013**, *135*, 17758–17767.
23. Heller, D. A.; Mayrhofer, R. M.; Baik, S.; Grinkova, Y. V.; Usrey, M. L.; Strano, M. S. Concomitant Length and Diameter Separation of Single-Walled Carbon Nanotubes. *J. Am. Chem. Soc.* **2004**, *126*, 14567–14573.
24. Hennrich, F.; Krupke, R.; Arnold, K.; Stutz, J. A. R.; Lebedkin, S.; Koch, T.; Schimmel, T.; Kappes, M. M. The Mechanism of Cavitation-Induced Scission of Single-Walled Carbon Nanotubes. *J. Phys. Chem. B* **2007**, *111*, 1932–1937.
25. Weisman, R. B.; Bachilo, S. M. Dependence of Optical Transition Energies on Structure for Single-Walled Carbon Nanotubes in Aqueous Suspension: An Empirical Kataura Plot. *Nano Lett.* **2003**, *3*, 1235–1238.
26. Lebedkin, S.; Hennrich, F.; Kiowski, O.; Kappes, M. M. Photophysics of Carbon Nanotubes in Organic Polymer-Toluene Dispersions: Emission and Excitation Satellites and Relaxation Pathways. *Phys. Rev. B* **2008**, *77*, 165429.

2.1 Separation of Carbon Nanotubes

2.1.3 *Separation of Double-Walled Carbon Nanotubes by Size Exclusion Chromatography*

K. E. Moore, M. Pfohl, F. Hennrich, V. S. K. Chakradhanula, C. Kuebel, M. M. Kappes, J. G. Shapter, R. Krupke, **B. S. Flavel**

ACS Nano 8 (2014) 6756–6764

DOI: 10.1021/nn500756a

Abstract

In this report we demonstrate the separation of raw carbon nanotube material into fractions of double-walled (DWCNTs) and single-walled carbon nanotubes (SWCNTs). Our method utilizes the size exclusion chromatography Sephacryl gel S-200 and yielded two distinct fractions of single- and double- walled nanotubes with average diameters of 0.93 ± 0.03 nm and 1.64 ± 0.15 nm, respectively. The presented technique is easily scalable and offers an alternative to traditional density gradient ultracentrifugation methods. CNT fractions were characterized by atomic force microscopy, Raman and absorption spectroscopy as well as transmission electron microscopy.

Contribution

B.S.F conceived the idea and designed the project. B.S.F, K.E.M and M.P, V.S.K.C and F.H performed the experiments. B.S.F and K.E.M wrote the manuscript and all authors contributed to the discussion and analysis of experimental results.

– This page intentionally left blank –

Separation of Double-Walled Carbon Nanotubes by Size Exclusion Column Chromatography

Katherine E. Moore,[†,‡] Moritz Pfohl,[‡] Frank Hennrich,[‡] Venkata Sai K. Chakradhanula,[‡,⊥] Christian Kuebel,[‡,⊥,||] Manfred M. Kappes,[‡,§] Joe G. Shapter,[†] Ralph Krupke,[‡] and Benjamin S. Flavel[‡,*]

[†]Centre for Nanoscale Science and Technology, School of Chemical and Physical Sciences, Flinders University, 5000, Adelaide, Australia, [‡]Institute of Nanotechnology, Karlsruhe Institute of Technology, 76344, Eggenstein-Leopoldshafen, Germany, [§]Institute of Physical Chemistry, Karlsruhe Institute of Technology, 76128, Karlsruhe, Germany, [⊥]Helmholtz Institute Ulm Electrochemical Energy Storage, 89081 Ulm, Germany, and [||]Karlsruhe Nano Micro Facility, Karlsruhe Institute of Technology, 76344 Eggenstein-Leopoldshafen, Germany

ABSTRACT In this report we demonstrate the separation of raw carbon nanotube material into fractions of double-walled (DWCNTs) and single-walled carbon nanotubes (SWCNTs). Our method utilizes size exclusion chromatography with Sephacryl gel S-200 and yielded two distinct fractions of single- and double-walled nanotubes with average diameters of 0.93 ± 0.03 and 1.64 ± 0.15 nm, respectively. The presented technique is easily scalable and offers an alternative to traditional density gradient ultracentrifugation methods. CNT fractions were characterized by atomic force microscopy and Raman and absorption spectroscopy as well as transmission electron microscopy.

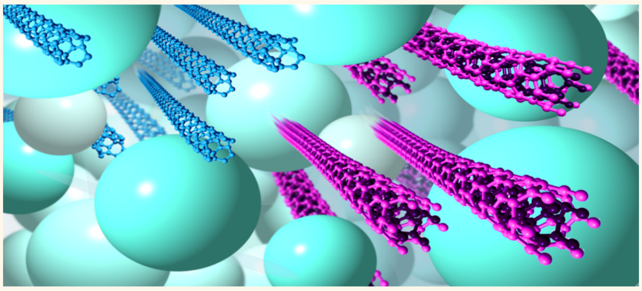

KEYWORDS: carbon nanotube · double · separation · sorting · purification · Sephacryl gel

Double-walled carbon nanotubes (DWCNTs) are a unique intermediate between single-walled carbon nanotubes (SWCNTs) and multiwalled carbon nanotubes (MWCNTs) and are therefore of fundamental interest to the carbon nanotube community. Due to the extraordinary electronic, physical, and optical properties of SWCNTs, a myriad of SWCNT integrated devices for sensing applications can be found in the literature.[1−3] However, for the development of advanced biosensors the integration of a biosensitive element is often necessary. Of course biomodification can be achieved through noncovalent functionalization, such as the wrapping of SWCNTs with DNA,[4,5] or the incorporation of molecules within the surfactant shell,[6] but sometimes it is also desirable to have covalent functionalization avenues available. In this regard, the use of SWCNTs becomes difficult due to degradation of their electronic properties from covalent modification, where disruption of the pristine sp^2-hybridized network is a requirement.[7] DWCNTs offer a unique solution to this problem, where covalent modification can be performed on an outer-wall nanotube only with the inner-wall nanotube remaining pristine and available for signal transduction.[8]

In order to realize this application or indeed alternatives such as field effect transistors[9,10] or atomic force microscopy (AFM) tips,[11] the ability to prepare highly pure DWCNTs is a requirement. Despite research efforts to develop growth processes that favor DWCNT formation, unwanted SWCNTs are still found to be present in the raw material.[12,13] Research efforts have therefore been directed toward methods to isolate and purify DWCNTs. One very successful method was pioneered by Hersam and co-workers in 2009.[14] Their process utilized density gradient ultracentrifugation (DGU) to separate surfactant-wrapped CNTs by their number of walls upon exploiting differences in the buoyant density. In 2010, Huh *et al.* utilized this method to not only separate DWCNTs but also isolate narrow length distributions.[15] This was done by altering both the density gradient and the vertical starting position of

* Address correspondence to benjamin.flavel@kit.edu, www.int.kit.edu/flavel.

Received for review February 7, 2014 and accepted June 4, 2014.

10.1021/nn500756a

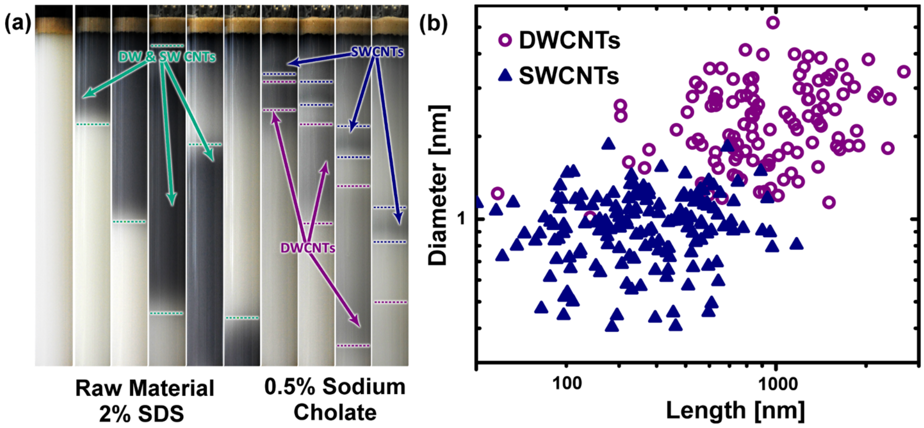

Figure 1. (a) Time-lapse photography (1 h) of the introduction of raw unsorted DWCNT material to the S-200 gel column for the separation of DWCNTs from SWCNTs and (b) diameter *vs* length of SWCNTs and DWCNTs as determined by AFM.

the unsorted material, creating a substantially greater than average density of the dispersed DWCNTs, thus exploiting the length-dependent translation of the nanotubes in response to applied centrifugation. They also reported the first hint of DWCNT separation according to the electronic character of the outer nanotube through the use of cosurfactants at different concentrations throughout the gradient medium. Hersam and co-workers later reported the preparation of high-quality semiconducting and metallic DWCNT fractions in 2011, by conducting sequential DGU, resulting in controlled separation of DWCNTs according to outer-shell electronic character.[16] They achieved very high outer-wall nanotube purity with reports of 96% and 98% for sorted semiconducting and metallic DWCNTs, respectively. While DGU has demonstrated very high quality separation, for many research groups without an ultracentrifuge or the technical expertise in the preparation of intricate density gradients, the preparation of high-purity DWCNT material remains unachievable. For this reason the development of alternative preparation methods is still of fundamental interest.

In this work we describe the use of Sephacryl gel column chromatography to separate SWCNTs from DWCNTs. The use of Sephacryl gel chromatography, developed by Moshammer *et al.* in 2009,[17] has already been shown to be extremely successful in the preparation of SWCNT suspensions. This method allows for the high-throughput separation of metallic (m-) from semiconducting (s-) SWCNTs and in some cases, even enriches zigzag and (n, 0) species.[18] The work of Liu *et al.*,[19] Tvrdy *et al.*,[20] and our group[21,22] has then further developed this technique to afford highly pure single-chirality suspensions. It is therefore a logical extension to apply Sephacryl gel techniques to DWCNTs.

RESULTS AND DISCUSSION

As outlined in the Methods section, 125 mL of a 2 wt % sodium dodecyl sulfate (SDS) in H_2O suspension of as-prepared DWCNT material was sonicated for 8 h at 15 °C to yield the raw DWCNT starting solution. This solution was then applied to an S-200 Sephacryl gel bed and washed through with further 2 wt % SDS with the "flow-through" material collected. Figure 1a shows time-lapse photographs of the Sephacryl gel column before addition of the starting material and at various times after addition. Despite a significant portion of the raw material passing through the column, a small fraction remained adsorbed to the gel at the top of the column (absorption spectra of raw and flow-through material can also be found in Figure S1 of the Supporting Information). This is consistent with the previous work of Blanch *et al.*[23] and Flavel *et al.*,[22] who have shown that for HiPco SWCNTs in relatively high SDS concentrations (1.6−2 wt %), only a small amount of the overall nanotube population is adsorbed to the gel, compared to relatively low SDS concentrations (0.4−0.8 wt %). This "flow-through" band is highlighted in green in Figure 1a. Upon addition of 0.5 wt % sodium cholate (SC), the adsorbed CNTs were then eluted from the gel column. This is consistent with previous work,[17] where surfactant exchange results in a reduced interaction of the nanotubes with the gel and subsequent elution. During elution the previously adsorbed DWCNTs and SWCNTs are observed to separate into two distinct bands that are highlighted purple and blue in Figure 1a, respectively. As can be seen in Figure 1a, the DWCNTs travel faster through the S-200 gel compared to the SWCNTs and therefore elute first from the column. Furthermore, the initially tight band of DWCNTs is found to spread out as it passes through the column, whereas the SWCNTs remain roughly confined in a band of the similar size. Despite the extensive use of Sephacryl S-200 size exclusion gel in the separation of SWCNTs,[19−22] the exact mechanism remains under discussion. This is highlighted in the recent work of Tvrdy *et al.*,[20] who identify the separation process of SWCNTs as a selective adsorption and not the expected size exclusion chromatographic (SEC) process, which would have retention time

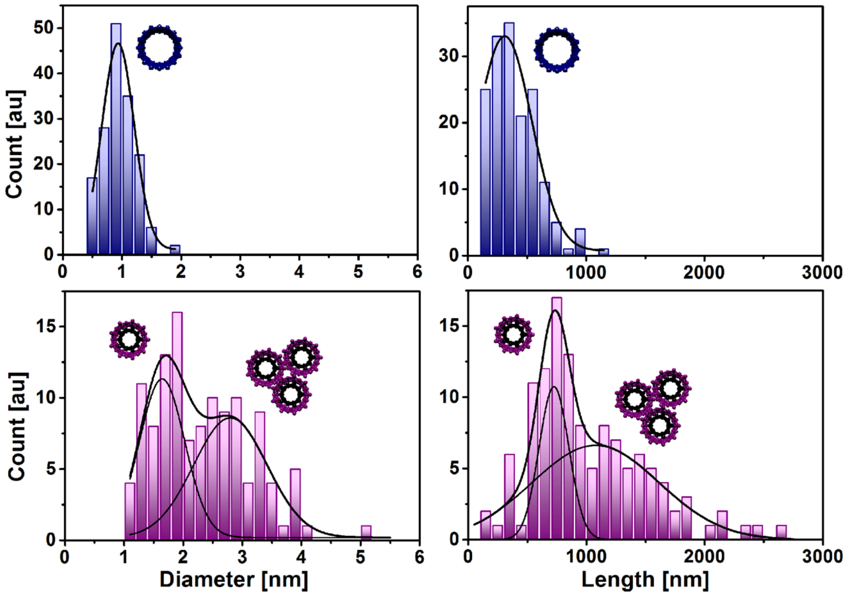

Figure 2. Diameter and length populations determined by AFM of sorted SWCNTs (top) and DWCNTs (bottom) with a Gaussian fit to indicate contribution from individually dispersed tubes and bundles.

dependence. We believe our work to be consistent with the adsorption mechanism proposed by Tvrdy *et al.*; however in the case of the DWCNTs it could be suggested that the spreading of the DWCNT band is due to a size-selective interaction on the gel. Absorption spectra of sequential fractions for the DWCNT and SWCNT material can be found in Figures S2 and S3. Upon inspection of Figure S2, it can be seen that only the leading edge of the "DWCNT band" contains a high content of DWCNTs, with a decrease in both the concentration and optical properites for later fractions. AFM investigation of the DWCNT sample for later fractions is shown in Figure S4 of the Supporting Information, in this case, the fraction labeled "Fraction 5" of the "DWCNTs band". It can be seen that there are indeed CNTs present with an average diameter of 1.05 ± 0.02 nm, which is therefore suggestive of SWCNTs. These SWCNTs have an average length of 910 ± 11 nm, similar to that of the DWCNT sample, which is discussed below. However, as there are no SWCNTs visible in the absorption measurement of "Fraction 5", we believe that they must be highly defected. In absorption measurements we see only a low concentration of DWCNTs, indicating that this nonedge band of DWCNTs is a combination of DWCNTs and defected SWCNTs. It is also important to note at this point that in the near-edge band of DWCNTs (used for all subsequent experiments) no SWCNT material was found by AFM or transmission electron microscopy (TEM). Hence in this case it is the separation of pristine DWCNTs from defected material with reduced adsorption properties that is observed, rather than size exclusion within the DWCNT population.

Likewise the clear separation of the SWCNT and DWCNT bands could also be due to size-dependent retention times on the gel. In Figure 2, AFM measurements comparing the SWCNT and DWCNT fractions are shown (representative AFM images can be seen in Figure S5 of the Supporting Information). In the case of the SWCNTs, a Gaussian can be fitted to the histograms of both the diameter and length with an average diameter of 0.93 ± 0.03 nm and average length of 310 ± 28 nm. It is apparent that the SWCNT sample consisted predominantly of individually dispersed nanotubes, without the presence of large bundles. In the case of DWCNTs, however, there are clearly two subpopulations for both diameter and length distributions, corresponding to individually dispersed DWCNTs and bundles. The increased affinity for DWCNTs to form bundles compared to SWCNTs is believed to be due to the significantly longer tube length and increased diameter, which would lead to increased van der Waals interactions.[24,25] The average diameter and length of the individually dispersed DWCNTs is 1.64 ± 0.15 nm and 725 ± 250 nm, respectively. A further observation from AFM is that the average diameter of the DWCNTs is larger than that of the SWCNTs by 0.71 nm, very close to twice the literature value of the intertube distance (3.44 Å),[26] indicating that the SWCNTs are approximately equivalent to the size of the inner tubes of DWCNTs. It is therefore possible that the presence of SWCNTs has origins in sonication-induced exfoliation of DWCNTs, as well as being present in the raw material.[12,13]

It is well known that raw DWCNT material contains not only small-diameter SWCNTs but also large-diameter SWCNTs and MWCNTs. Indeed it is therefore entirely possible that the additional peak that we have attributed to bundled DWCNT material could simply be attributed to MWCNTs or large-diameter SWCNTs. The only way to verify this is with TEM measurements. From TEM measurements we were unable to locate any MWCNTs in either the SWCNT or DWCNT fractions.

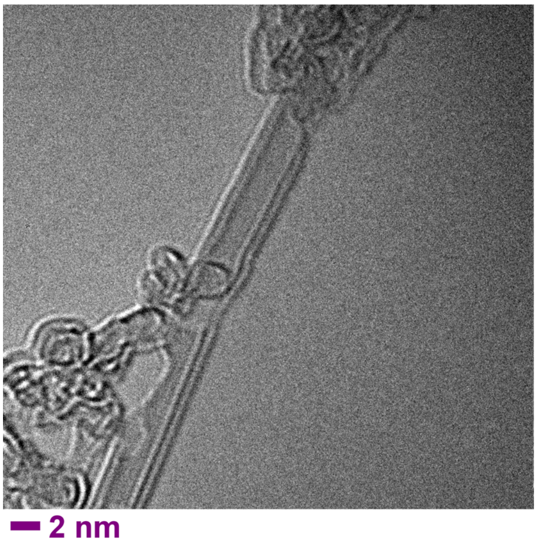

Figure 3. HRTEM micrograph of an individual DWCNT with an outer diameter of 1.7 nm.

Of course this does not rule out the possibility of their existence in either of the fractions due to TEM providing only a limited overview of the entire sample population. However, we note that as we did not see any MWCNTs in TEM, it is unlikely that MWCNTs are present in a high enough concentration to afford the second peak in the AFM diameter distribution of DWCNTs. It is therefore more likely bundling of DWCNTs. A representative TEM image of the DWCNT material can be found in Figure 3, where a free suspended DWCNT can clearly be seen. Furthermore, additional TEM of DWCNT films/bundles can also be found in Figure S5 of the Supporting Information. TEM has also allowed us to determine the location of any large-diameter SWCNTs after the separation process. Within the DWCNT material we were unable to locate any large-diameter SWCNTs; however they were found to be present in the small-diameter SWCNT fraction. This is shown in Figure S6 of the Supporting Information, where two SWCNTs with a diameter of ~2 nm can be seen.

The observation of DWCNTs being longer than the SWCNTs initially appears to be in disagreement with our recent work[22] and the proposed selective cutting mechanism of Hennrich *et al.*[27] and Heller *et al.*,[28] who suggested smaller diameter CNTs are cut to a lesser extent by sonication compared to those with larger diameters. The DWCNTs have a much longer tube length, over twice that of the SWCNTs. From a purely diameter-dependent perspective it would be expected that the DWCNTs (larger diameter) would be shorter than the SWCNTs (small diameter). However, we note that all previous work was performed purely on SWCNTs, and it is unclear what role an additional carbon inner core may play in aiding stability during sonication. Furthermore, in the work of Hersam *et al.*[14] DWCNTs were also found to be ~44% longer than their SWCNT counterparts.

Despite discussions on the cutting mechanism being dependent on wall number, the separation of these two species of CNTs by gel filtration is in agreement with Heller *et al.*,[28] who prepared length- and diameter-separated SWCNTs using both gel electrophoresis and column chromatography. They proposed the mobility of CNTs through the gel matrix to be largely length dependent, as it contributes to the majority of size differences in nanotubes. This is certainly true in this case and is highlighted in Figure 1b; it suggests that the sonication process is of vital importance to enable SEC of DWCNTs. In this work, the raw material contained both SWCNTs and DWCNTs produced in the same CVD synthesis, thus producing tubes of comparable defect contribution. If we make the assumption that the initial length of both tube types is the same, then the longer length of the DWCNTs can be attributed solely to the introduction of a secondary wall, which provides increased structural stability. If we do not assume that the initial length of both tube types is the same, then it may not necessarily be true that the DWCNTs are more stable and shortened at a slower rate. Unfortunately AFM of the raw material cannot be used to determine the initial tube lengths, as it contains a complex mixture of both SWCNTs and DWCNTs, as well as other carbonaceous material that is removed from the sample during separation. Thus, lengths determined from the raw material would not be an accurate representation of the enriched DWCNT and SWCNT samples collected. However, one must consider the mechanics of sonication-induced scission. Initially the nanotubes experience a certain strain force, which makes it unstable in the ultrasonic environment and scission occurs. This continues to occur until the strain force is below the critical value for nanotube disruption and the tube can no longer be shortened.[27] In this work the nanotubes were probe tip sonicated for 8 h, which is a considerable amount of time in such a disruptive environment. We speculate that after this time the CNTs are very close to reaching this critical value, essentially the minimum length, if they have not already. Thus, the rate of scission is unimportant, as given enough time, the nanotubes will reach their minimum length regardless. In this case, it is then only the value of the critical strain force that is relevant, which is determined by the initial size of the nanotubes, determined by tube diameter, initial length, or the number of tube walls. Irrespective of the initial size of the nanotube populations, after sonication there are two very distinct subpopulations, namely, DWCNTs and SWCNTs. If simply the difference in nanotube size was responsible for the separation observed in this work, one would also expect that the same result would be achievable for raw DWCNT material suspended in sodium cholate applied to an S-200 gel column. As a control we have performed this experiment and note that no separation of DWCNTs from SWCNTs is observed. This is summarized in

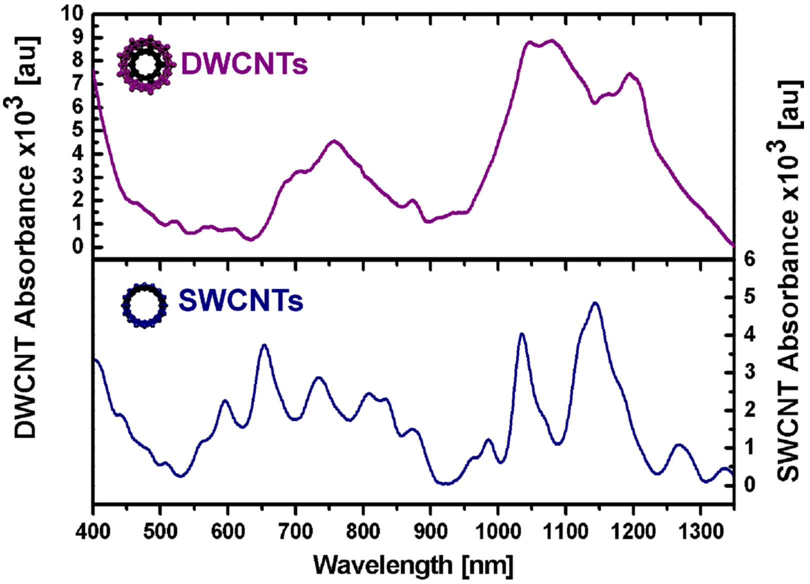

Figure 4. Absorption spectra of the resulting SWCNT and DWCNT fractions in 2 wt % sodium cholate solution. For ease of comparison, the DWCNT spectrum has been subtracted. Details of the background subtraction process can be found in Figure S8 of the Supporting Information.

Figure S7 of the Supporting Information. This tends to suggest that despite the DWCNT and SWCNT fractions having very different size distributions, the mechanism is not a simple size exclusion process. A likely explanation is that once CNTs become trapped on a Sephacryl gel column in SDS, it is the large-diameter CNTs that are first solubilized by sodium cholate with the small-diameter CNTs eluting last. In this case we certainly have two distinctly different diameter regimes, and the true mechanism is likely a combination of diameter-dependent solvation by sodium cholate and length-dependent size exclusion.

The collected SWCNT and DWCNT fractions were then analyzed by absorption spectroscopy. Figure 4 shows typical spectra of SWCNT and DWCNT suspensions in 0.5 wt % sodium cholate. The SWCNT spectra can be divided into two distinct regions, namely, 900–1250 nm and 550–900 nm, which correspond to the first (S_{11}) and second (S_{22}) optical transition of SWCNTs, respectively, and are in agreement with literature for small-diameter HiPco process prepared SWCNTs.[19−22] With the use of data from Weisman and co-workers,[29] this corresponds to CNT diameters of ~0.8–1.2 nm and is in agreement with our AFM measurements. Likewise the DWCNTs can also be divided into two regions; however, compared to SWCNTs, the peaks in the region of 950–1250 nm are distinctly broader. While this region most likely consists of some S_{11} transitions due to the presence of smaller diameter inner-wall nanotubes, this region is predominately dominated by the S_{22} optical transitions of large-diameter outer-wall nanotubes with ~1.5–2 nm diameter. The region 500–900 nm then consists of a mixture of S_{22} transitions of inner-wall nanotubes and S_{33} transitions of outer-wall nanotubes. Due to the strong absorption of water above 1400 nm, it was not possible to probe S_{11} transitions of the DWCNT fraction in solution (without the use of D_2O). Therefore, we prepared thin films of DWCNTs and SWCNTs on glass substrates *via* vacuum filtration.[30] These thin films in the dry state allowed us to perform absorption spectroscopy of the DWCNT and SWCNT fractions up to 2500 nm, as shown in Figure 5 (solid lines). Here it is important to remember that thin film measurements cannot be directly compared to solution measurements (highly dispersed CNTs) due to the excitonic properties of nanotubes being greatly affected by many-body interactions, Coulomb interaction, and charge transfer between adjacent nanotubes in bundles (thin CNT films). However, the presence of a clear S_{11} absorption (1600–2200 nm) can be seen for the DWCNTs that is not seen for SWCNTs. This large broad peak is a superposition of many carbon nanotube diameters ranging from 1.5 to 2 nm and is consistent with solution measurements.

The use of CNT thin films also allowed us to further verify the presence of DWCNT and SWCNT fractions *via* a method outlined by Hersam and co-workers[14,16] using thionyl chloride doping.

The treatment of CNT thin films with thionyl chloride has been shown to suppress small band gap optical transitions upon shifting the CNT Fermi level into the HOMO band.[14,16] In this way, the S_{11} and perhaps even some S_{22} transitions (for large-diameter CNTs) appear to be quenched in absorption spectroscopy measurements. Thionyl chloride doping experiments are represented by a dotted line in Figure 5. The broad S_{11} (1600–2200 nm) and S_{22} (900–1250 nm) regions and the S_{11} (900–1250 nm) region were suppressed for the DWCNTs and SWCNTs, respectively, upon thionyl chloride treatment. Interestingly, for the DWCNTs two peaks in the region 900–1250 nm remain after

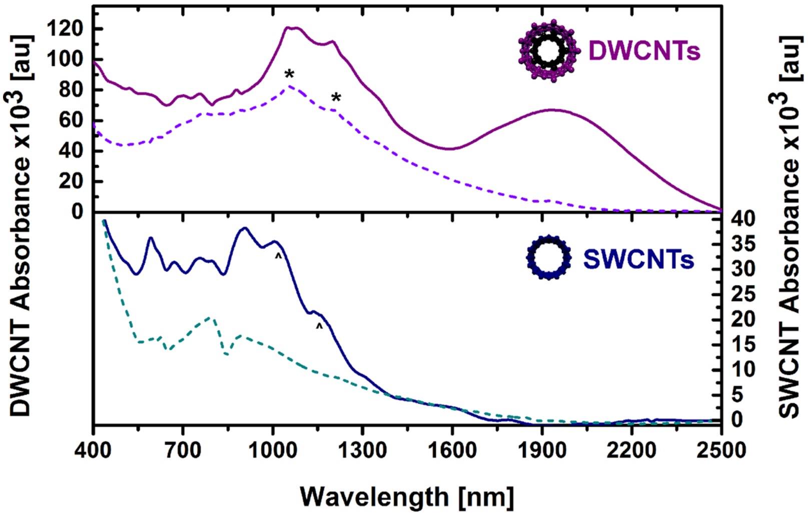

Figure 5. Absorption spectra of sorted DWCNT (top) and SWCNT (bottom) films, before and after treatment with thionyl chloride (solid and dashed line, respectively).

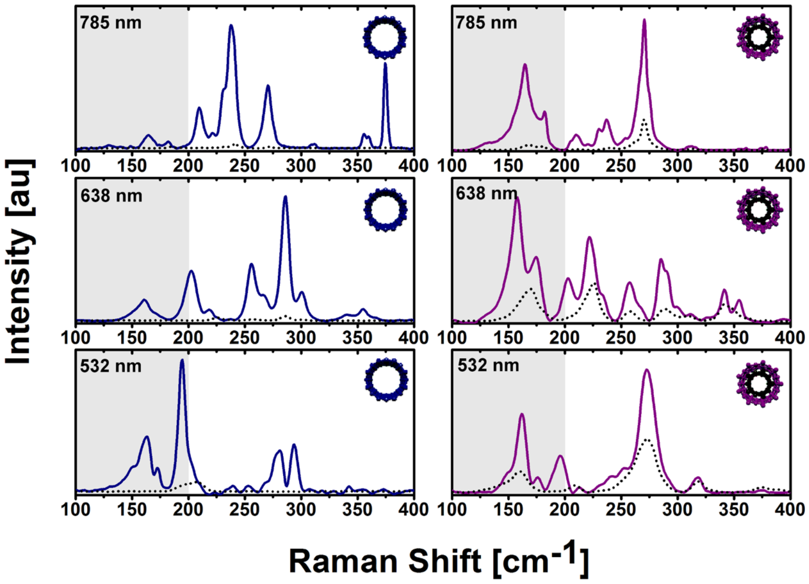

Figure 6. Raman spectra of the radial breathing modes of SWCNTs (left) and DWCNTs (right) with 785, 638, and 532 nm laser excitation before and after treatment with thionyl chloride (solid and dashed lines, respectively).

thionyl chloride doping, which are indicated by asterisks. These peaks are also seen in the SWCNT film (indicated by carats) before doping, and it can clearly be seen that these S_{11} transitions from nanotubes of this diameter are doped by thionyl chloride. The fact that peaks remain in this region for the DWCNT sample can only by explained by the presence of smaller diameter inner-wall SWCNTs. In this case the outer wall has shielded the inner wall from chemical doping by thionyl chloride.

Raman analysis was then further used to analyze the DWCNT and SWCNT thin films. In the work of Hersam and co-workers,[14,16] it was demonstrated that when the CNTs were treated with concentrated sulfuric acid, the exposed outer-wall nanotubes reacted at a significantly faster rate than the inner-wall nanotubes, where the outer wall acts as a protective shield for the inner wall. This was concluded from observing the CNT radial breathing modes (RBM) before and after acid treatment. This experiment has been reproduced in our work and can be seen in Figure S9 of the Supporting Information; however as it is unclear if one is only etching the outer wall, we have opted for a nondestructive approach to demonstrate the effect of inner-tube shielding. In this case, Raman spectra were recorded for each film before and after treatment with thionyl chloride. As mentioned previously, thionyl chloride quenches the small band gap energy transitions, resulting in significant changes in absorption. Figure 6 shows Raman spectra for SWCNTs (left) and DWCNTs (right) at the three different excitation wavelengths of 785, 638, and 532 nm. The use of different wavelengths allows for different diameter tubes to be probed and affords an accurate representation of the carbon nanotube population. The peak position of the RBM can be used in conjunction with the Kataura plot[31,32] and Weisman data[29] to determine the nanotube chiralities present in each sample and can be seen in the Supporting Information.

Peaks in the shaded region of Figure 6, below 200 cm^{-1}, are a result of excitation of tubes with diameters greater than ~1.2 nm, which in the case of DWNTs correspond to outer-wall tubes. Inversely, the region above 200 cm^{-1} corresponds to tubes with diameters between 0.50 and 1.2 nm. Before treatment, there are an abundance of peaks in each sample; however, there are slightly more peaks in the DWCNT case. This is expected, as the more complex structure of the DWCNTs gives rise to an increased number of nanotube types. Upon looking at the shaded regions of Figure 6, it is also evident that there are more peaks corresponding to large-diameter tubes present in the DWCNT sample. This is particularly apparent in the case of 785 and 638 nm laser excitation. As can be seen at 532 nm excitation, there are large-diameter SW tubes present in the SW fraction, which is confirmed by TEM (see Figure S6 of the Supporting Information). However, they are presumably very low in quantity, as there is not a significant S_{11} absorption visible in the absorption spectra of the film and AFM analysis shows minimal tubes with diameters above 1.4 nm. After thionyl chloride treatment there is a reduction in peak intensity for all SWCNTs peaks with only a few low-intensity peaks remaining at ~195, 290, and 240 cm^{-1} at 532, 638, and 785 nm laser excitation, respectively. However, it is noted that these peaks are reduced in intensity by ~91%, 97%, and 97%, respectively, with all remaining RBMs no longer present. This is expected in the SWCNT case, as all nanotubes are exposed to the thionyl choride chemical environment. A curious feature noted in the Raman measurement of undoped SWCNTs at 785 nm was a peak at 375 cm^{-1} corresponding to the (8,0) nanotube. This tube has a very small diameter of 0.626 nm and can be considered small enough to be contained within a DWCNT. However, after treatment this peak is completely removed, indicating it had been exposed to the thionyl chloride, and hence is a single small-diameter nanotube. Indeed the AFM histogram of SWCNT diameters in Figure 2 shows the presence of a small portion of individualized CNTs with diameters ranging between 0.4 and 0.6 nm. Whether this nanotube was initially present inside a DWCNT and removed *via* sonication remains speculative.

In the case of the DWCNT spectra, the effect of thionyl chloride is much more complex, with many peaks persistent after doping. From the 785 nm laser excitation spectrum, it is clear that the majority of the outer-wall nanotube RBMs, assigned as (15,6), (18,0), and (17,1) have been quenched (shaded region). Conversely, the peak at 270 cm^{-1} (11,0) retained 24% of its original intensity, an indication that this tube has been semiprotected from the doping agent. The 638 nm spectrum shows three clear outer-wall nanotube peaks at ~158 (16,6), 174 (18,0), and 200 cm^{-1} (9,9). These outer-wall nanotube peaks are then once again quenched upon exposure to thionyl chloride. The peaks above 200 cm^{-1} at ~220 (11,5), 258 (11,1), 290 (7,5), and 340 cm^{-1} (6,4) retain 46%, 27%, 24%, and 50% of their peak intensity, respectively, indicating that they are all inner-walled tubes, semiprotected from the thionyl chloride. Lastly, if one considers the spectra at 532 nm, there are two clear peaks associated with outer-wall nanotubes at ~162 (16,5) and 195 cm^{-1} (16,0), which after thionyl chloride treatment are reduced by ~73% and 100%. However, the inner-wall nanotube at ~273 cm^{-1} (12,0) is reduced in intensity by only ~57%. The observation of thionyl chloride to influence both the outer and inner wall (although to a significantly reduced extent) was unexpected by us but points out that the outer-wall shielding is not 100%. This has been observed previously by Kalbac *et al.*, who also observed that chemical doping of the inner tubes was strongly dependent on its electronic character, with metallic inner tubes doped more easily than semiconducting inner tubes.[33] The inner wall is obviously not completely isolated from the outer wall, and it is hence possible to see changes in the surrounding environment in the optical properties of both nanotubes.

CONCLUSION

In this work we have demonstrated the separation of DWCNTs from SWCNTs containing starting material using fast, easily scalable, and financially viable gel column chromatography. It was determined from extensive AFM analysis that the raw DWCNT material contained two CNT populations of distinctly different length and diameter, namely, DWCNTs and SWCNTs. This distinct difference in size may initially lead one to believe that a typical size exclusion process is responsible for the separation of DWCNTs from SWCNTs; however control experiments show that it is more likely a combination of diameter-dependent solvation by sodium cholate and length-dependent size exclusion. Regardless of the mechanism responsible for separation, this work provides a convenient avenue to prepare enriched DWCNTs in a straightforward and easily scalable manner.

METHODS

The DWCNT raw material (average diameter ~2 nm) used in this work was supplied by Unidym, lot no. OE-130807. Suspensions of raw material for size exclusion chromatography were prepared by suspending 50 mg of DWCNT powder in 125 mL of H_2O with 2 wt % of SDS (Sigma-Aldrich) using a tip sonicator (Bandelin, 200 W maximum power, 20 kHz, in pulsed mode with 100 ms pulses) applied for 8 h at ~20% power. During sonication, the suspension was placed in a 500 mL water bath to dissipate excess heat, without additional cooling. The CNT suspension was then ready to be introduced into the column.

Gel filtration was performed as previously[21] described with only a few changes using S-200 gel filtration medium (Amersham Biosciences) in a glass column 30 cm in length and 2 cm inner diameter. The column was filled with filtration medium and compacted slightly by applying pressure with compressed air to yield a final gel height of ~25 cm. For the separation, ~10 mL of as prepared DWCNT raw material solution was added to the top of the column, and subsequently, a solution of 2 wt % SDS in H_2O was washed through the column under applied pressure to ensure a flow rate of ~1 mL min^{-1}. During this step, single- and double-walled CNTs became trapped on the gel matrix. Once all starting material had been washed through, ~10 mL of 0.5 wt % sodium cholate was added to the column, which subsequently removed the DWCNTs followed by the SWCNTs from the gel medium. These two species were collected as 4 mL fractions for characterization.

Spectroscopic characterization of the sorted material was carried out by UV−vis−NIR spectroscopy and Raman spectroscopy. UV−vis−NIR absorption spectra of the sorted fractions were recorded on a Varian Cary 500 spectrophotometer. Raman absorption spectra were taken with an XploRA confocal microscope (Horiba) with laser energies of 1.58 eV (785 nm), 1.94 eV (638 nm), and 2.33 eV (532 nm) under a 50× objective. Power and gratings were optimized appropriately for each wavelength.

TEM samples were prepared by drop-casting suspensions containing the nanotubes in water onto lacey carbon coated copper grids (Quantifoil GmbH), dried using silica gel. Subsequently they were washed three times followed by drying under a silica gel environment.

SWCNT TEM investigations were performed in a ZEISS Libra 200FE transmission electron microscope operated at 200 kV and equipped with a field emission gun, an in-column filter (Omega-filter), a high-angle annular dark-field (HAADF) detector, and an energy-dispersive X-ray (EDX) spectrometer (SiLi detector, Noran). DWCNT TEM analysis was performed using an image-corrected FEI Titan 80-300 microscope operated at 300 kV and equipped with a Gatan US1000 CCD camera for TEM imaging and electron diffraction. All micrographs were taken with a 4K × 4K CCD camera and analyzed with the software package Digital Micrographs (version 1.71.38, Gatan Company).

Films of the sorted SWCNTs and DWCNTs were prepared by vacuum filtration[30] and then transferred onto clean glass substrates. Treatment of the films with 95−98% sulfuric acid (Sigma-Aldrich) was done by placing a few drops on the film and allowing 10 min for the reaction to occur. After exposure, the excess acid was removed with a pasteur pipet and the CNT sample allowed to dry in air for several days.

Films were doped with $SOCl_2$ (Sigma-Aldrich) by coating the surface with a few drops of $SOCl_2$ and allowing to air-dry for several minutes.

To prepare the AFM samples, 10 μL of CNT solution was spin coated onto 1 × 1 cm^2 clean silicon surfaces (ABC-Gmbh) at 1500 rpm for 1 min, then gently rinsed with H_2O. AFM tapping mode images were taken in ambient conditions with a multimode head and a NanoScope III controller (Digital Instruments) using silicon cantilevers (Mikromasch) with a fundamental resonance frequency between 250 and 400 kHz. Topographic height and phase images were obtained simultaneously with feedback controls optimized for each sample.

Conflict of Interest: The authors declare no competing financial interest.

Acknowledgment. The authors wish to acknowledge and thank Dr. Harald Roesner, of the University of Muenster, for assistance with TEM measrements. The authors also wish to acknowledge Unidym for a sample of their DWCNTs, lot no. OE-130807. K.E.M. appreciatively acknowledges the Australian Nanotechnology Network (ANN), The Playford Memorial Trust, and the Australian Microscopy and Microanalysis Research Facility (AMMRF). K.E.M. also wishes to thank the Cathy Chandler Bursary, the Amy Forwood Trust, BankSA, and Flinders University for overseas traveling scholarships. The authors are grateful to the Karlsruhe Nano Micro Facility (KNMF) for access to the TEM facilities. This research was also supported by the Bundesministerium fur Bildung und Forschung (BMBF) as administered by POF-NanoMicro. B.S.F. gratefully acknowledges support from the Deutsche Forschungsgemeinschaft's Emmy Noether Program under grant number FL 834/1-1.

Supporting Information Available: Extensive spectroscopic (absorption and Raman) and TEM data are available free of charge *via* the Internet at http://pubs.acs.org.

REFERENCES AND NOTES

1. Jin, H.; Heller, D. A.; Kalbacova, M.; Kim, J.-H.; Zhang, J.; Boghossian, A. A.; Maheshri, N.; Strano, M. S. Detection of Single-Molecule H_2O_2 Signalling from Epidermal Growth Factor Receptor Using Fluorescent Single-Walled Carbon Nanotubes. *Nat. Nanotechnol.* **2010**, *5*, 302–309.
2. Khalap, V. R.; Sheps, T.; Kane, A. A.; Collins, P. G. Hydrogen Sensing and Sensitivity of Palladium-Decorated Single-Walled Carbon Nanotubes with Defects. *Nano Lett.* **2010**, *10*, 896–901.
3. Cella, L. N.; Chen, W.; Myung, N. V.; Mulchandani, A. Single-Walled Carbon Nanotube-Based Chemiresistive Affinity Biosensors for Small Molecules: Ultrasensitive Glucose Detection. *J. Am. Chem. Soc.* **2010**, *132*, 5024–5026.
4. Zheng, M.; Jagota, A.; Strano, M. S.; Santos, A. P.; Barone, P.; Chou, S. G.; Diner, B. A.; Dresselhaus, M. S.; Mclean, R. S.; Onoa, G. B.; *et al*. Structure-Based Carbon Nanotube Sorting by Sequence-Dependent DNA Assembly. *Science* **2003**, *302*, 1545–1548.
5. Tu, X.; Manohar, S.; Jagota, A.; Zheng, M. DNA Sequence Motifs for Structure-Specific Recognition and Separation of Carbon Nanotubes. *Nature* **2009**, *460*, 250–253.
6. Roquelet, C.; Lauret, J.-S.; Alain-Rizzo, V.; Voisin, C.; Fleurier, R.; Delarue, M.; Garrot, D.; Loiseau, A.; Roussignol, P.; Delaire, J. A.; *et al*. Π-Stacking Functionalization of Carbon Nanotubes through Micelle Swelling. *ChemPhysChem* **2010**, *11*, 1667–1672.
7. Matsumura, H.; Ando, T. Conductance of Carbon Nanotubes with a Stone-Wales Defect. *J. Phys. Chem. Soc. Jpn.* **2001**, *70*, 2657–2665.
8. Huang, J.; Ng, A. L.; Piao, Y.; Chen, C.-F.; Green, A. A.; Sun, C.-F.; Hersam, M. C.; Lee, C. S.; Wang, Y. Covalently Functionalized Double-Walled Carbon Nanotubes Combine High Sensitivity and Selectivity in the Electrical Detection of Small Molecules. *J. Am. Chem. Soc.* **2013**, *135*, 2306–2312.
9. Ha, B.; Shin, D. H.; Park, J.; Lee, C. J. Electronic Structure and Field Emission Properties of Double-Walled Carbon Nanotubes Synthesized by Hydrogen Arc Discharge. *J. Phys. Chem. C* **2007**, *112*, 430–435.
10. Shimada, T.; Sugai, T.; Ohno, Y.; Kishimoto, S.; Mizutani, T.; Yoshida, H.; Okazaki, T.; Shinohara, H. Double-Wall Carbon Nanotube Field-Effect Transistors: Ambipolar Transport Characteristics. *Appl. Phys. Lett.* **2004**, *84*, 2412–2414.
11. Kuwahara, S.; Akita, S.; Shirakihara, M.; Sugai, T.; Nakayama, Y.; Shinohara, H. Fabrication and Characterization of High-Resolution AFM Tips with High-Quality Double-Wall Carbon Nanotubes. *Chem. Phys. Lett.* **2006**, *429*, 581–585.
12. Lyu, S. C.; Lee, T. J.; Yang, C. W.; Lee, C. J. Synthesis and Characterization of High-Quality Double-Walled Carbon Nanotubes by Catalytic Decomposition of Alcohol. *Chem. Commun.* **2003**, 1404–1405.
13. Yamada, T.; Namai, T.; Hata, K.; Futaba, D. N.; Mizuno, K.; Fan, J.; Yudasaka, M.; Yumura, M.; Iijima, S. Size-Selective Growth of Double-Walled Carbon Nanotube Forests from Engineered Iron Catalysts. *Nat. Nanotechnol.* **2006**, *1*, 131–136.
14. Green, A. A.; Hersam, M. C. Processing and Properties of Highly Enriched Double-Wall Carbon Nanotubes. *Nat. Nanotechnol.* **2009**, *4*, 64–70.
15. Huh, J. Y.; Walker, A. R. H.; Ro, H. W.; Obrzut, J.; Mansfield, E.; Geiss, R.; Fagan, J. A. Separation and Characterization of

Double-Wall Carbon Nanotube Subpopulations. *J. Phys. Chem. C* **2010**, *114*, 11343–11351.

16. Green, A. A.; Hersam, M. C. Properties and Application of Double-Walled Carbon Nanotubes Sorted by Outer-Wall Electronic Type. *ACS Nano* **2011**, *5*, 1459–1467.
17. Moshammer, K.; Hennrich, F.; Kappes, M. Selective Suspension in Aqueous Sodium Dodecyl Sulfate According to Electronic Structure Type Allows Simple Separation of Metallic from Semiconducting Single-Walled Carbon Nanotubes. *Nano Res.* **2009**, *2*, 599–606.
18. Blum, C.; Stürzl, N.; Hennrich, F.; Lebedkin, S.; Heeg, S.; Dumlich, H.; Reich, S.; Kappes, M. M. Selective Bundling of Zigzag Single-Walled Carbon Nanotubes. *ACS Nano* **2011**, *5*, 2847–2854.
19. Liu, H.; Nishide, D.; Tanaka, T.; Kataura, H. Large-Scale Single-Chirality Separation of Single-Wall Carbon Nanotubes by Simple Gel Chromatography. *Nat. Commun.* **2011**, *2*, 309.
20. Tvrdy, K.; Jain, R. M.; Han, R.; Hilmer, A. J.; McNicholas, T. P.; Strano, M. S. A Kinetic Model for the Deterministic Prediction of Gel-Based Single-Chirality Single-Walled Carbon Nanotube Separation. *ACS Nano* **2013**, *7*, 1779–1789.
21. Flavel, B. S.; Kappes, M. M.; Krupke, R.; Hennrich, F. Separation of Single-Walled Carbon Nanotubes by 1-Dodecanol-Mediated Size-Exclusion Chromatography. *ACS Nano* **2013**, *7*, 3557–3564.
22. Flavel, B. S.; Moore, K. E.; Pfohl, M.; Kappes, M. M.; Hennrich, F. Separation of Single-Walled Carbon Nanotubes with a Gel Permeation Chromatography System. *ACS Nano* **2014**, *8*, 1817–1826.
23. Blanch, A. J.; Quinton, J. S.; Shapter, J. G. The Role of Sodium Dodecyl Sulfate Concentration in the Separation of Carbon Nanotubes Using Gel Chromatography. *Carbon* **2013**, *60*, 471–480.
24. Clerk-Maxwell, J. O Ver De Continuiteit Van Den Gas- En Vloeistofiocstand Academisch Proefschrift. *Nature* **1874**, *10*, 477–480.
25. Hiemenz, P. C. *Principles of Colloid and Surface Chemistry*; Marcel Dekker: New York, 1977.
26. Saito, R.; Matsuo, R.; Kimura, T.; Dresselhaus, G.; Dresselhaus, M. S. Anomalous Potential Barrier of Double-Wall Carbon Nanotube. *Chem. Phys. Lett.* **2001**, *348*, 187–193.
27. Hennrich, F.; Krupke, R.; Arnold, K.; Rojas Stütz, J. A.; Lebedkin, S.; Koch, T.; Schimmel, T.; Kappes, M. M. The Mechanism of Cavitation-Induced Scission of Single-Walled Carbon Nanotubes. *J. Phys. Chem. B* **2007**, *111*, 1932–1937.
28. Heller, D. A.; Mayrhofer, R. M.; Baik, S.; Grinkova, Y. V.; Usrey, M. L.; Strano, M. S. Concomitant Length and Diameter Separation of Single-Walled Carbon Nanotubes. *J. Am. Chem. Soc.* **2004**, *126*, 14567–14573.
29. Bachilo, S. M.; Strano, M. S.; Kittrell, C.; Hauge, R. H.; Smalley, R. E.; Weisman, R. B. Structure-Assigned Optical Spectra of Single-Walled Carbon Nanotubes. *Science* **2002**, *298*, 2361–2366.
30. Wu, Z.; Chen, Z.; Du, X.; Logan, J. M.; Sippel, J.; Nikolou, M.; Kamaras, K.; Reynolds, J. R.; Tanner, D. B.; Hebard, A. F.; *et al.* Transparent, Conductive Carbon Nanotube Films. *Science* **2004**, *305*, 1273–1276.
31. Maruyama, S. *Kataura-Plot for Resonant Raman*. http://www.photon.t.u-tokyo.ac.jp/~maruyama/kataura/kataura.html (accessed 07/02/2014).
32. Araujo, P. T.; Doorn, S. K.; Kilina, S.; Tretiak, S.; Einarsson, E.; Maruyama, S.; Chacham, H.; Pimenta, M. A.; Jorio, A. Third and Fourth Optical Transitions in Semiconducting Carbon Nanotubes. *Phys. Rev. Lett.* **2007**, *98*, 067401(1−4).
33. Kalbac, M.; Green, A. A.; Hersam, M. C.; Kavan, L. Tuning of Sorted Double-Walled Carbon Nanotubes by Electrochemical Charging. *ACS Nano* **2010**, *4*, 459–469.

– This page intentionally left blank –

2.1 Separation of Carbon Nanotubes

2.1.4 *Sorting of Double-Walled Carbon Nanotubes According to Their Outer Wall Electronic Type via a Gel Permeation Method*

K. E. Moore, M. Pfohl, D. D. Tune, F. Hennrich, S. Dehm, V. S. K. Chakradhanula,
C. Kuebel, R. Krupke, **B. S. Flavel**

ACS Nano 9 (2015) 3849–3857

DOI: 10.1021/nn506869h

Abstract

The field of single-walled carbon nanotube (SWCNT) separation is broadly characterised by two techniques; density gradient ultracentrifugation (DGU), and the gel permeation method developed by us and others. DGU has since also been applied to the sorting of double-walled carbon nanotubes (DWCNTs), however the gel permeation method has remained underutilized for these more complex nanostructures. In this work, we demonstrate the application of the gel permeation technique to the sorting of DWCNTs according to their outer wall electronic type. Our method uses the Sephacryl S-200 gel and yields sorted fractions of DWCNTs with impurities removed and highly enriched in nanotubes with either metallic (M) or semiconducting (S) outer walls. The prepared fractions are fully characterized using optical absorption spectroscopy, transmission electron microscopy and atomic force microscopy, and the entire procedure is monitored in real time using process Raman analysis. The sorted DWCNTs are then integrated into single nanotube field effect transistors, allowing detailed electronic measurement of the transconductance properties of the four unique inner@outer wall combinations of S@S, S@M, M@S and M@M.

Contribution

B.S.F and K.E.M conceived the idea and designed the project. B.S.F, K.E.M, M.P, D.D.T, F.H, S.D and V.S.K.C performed the experiments. B.S.F and K.E.M wrote the manuscript and all authors contributed to the discussion and analysis of experimental results.

– This page intentionally left blank –

Sorting of Double-Walled Carbon Nanotubes According to Their Outer Wall Electronic Type *via* a Gel Permeation Method

Katherine E. Moore,[†,‡] Moritz Pfohl,[‡,§] Daniel D. Tune,[†,‡] Frank Hennrich,[‡] Simone Dehm,[‡] Venkata Sai K. Chakradhanula,[‡,⊥] Christian Kübel,[‡,⊥,‖] Ralph Krupke,[‡,§] and Benjamin S. Flavel*[,‡]

[†]Centre for Nanoscale Science and Technology, School of Chemical and Physical Sciences, Flinders University, Adelaide 5042, Australia, [‡]Institute of Nanotechnology, Karlsruhe Institute of Technology, 76021 Karlsruhe, Germany, [§]Institute for Materials Science, Technische Universität Darmstadt, 64287 Darmstadt, Germany, [⊥]Helmholtz Institute Ulm Electrochemical Energy Storage, 89081 Ulm, Germany, and [‖]Karlsruhe Nano Micro Facility, Karlsruhe Institute of Technology, 76021 Karlsruhe, Germany

ABSTRACT In this work, we demonstrate the application of the gel permeation technique to the sorting of double-walled carbon nanotubes (DWCNTs) according to their outer wall electronic type. Our method uses Sephacryl S-200 gel and yields sorted fractions of DWCNTs with impurities removed and highly enriched in nanotubes with either metallic (M) or semiconducting (S) outer walls. The prepared fractions are fully characterized using optical absorption spectroscopy, transmission electron microscopy, and atomic force microscopy, and the entire procedure is monitored in real time using process Raman analysis. The sorted DWCNTs are then integrated into single nanotube field effect transistors, allowing detailed electronic measurement of the transconductance properties of the four unique inner@outer wall combinations of S@S, S@M, M@S, and M@M.

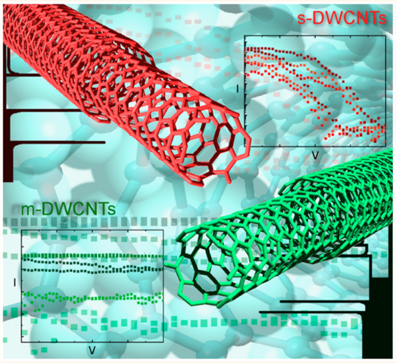

KEYWORDS: carbon nanotube · double · separation · electronic character · sorting · purification · Sephacryl gel

From an applications viewpoint, double-walled carbon nanotubes (DWCNTs) have long been idealized as candidates for use in nanotube-based sensor devices where it is proposed that the outer wall can be functionalized, leaving the inner wall pristine and available for signal transduction. For example, Wang *et al.* treated DWCNTs with concentrated acid mixtures, confirmed that functionalization was mostly limited to the outer wall,[1] then extended that work to show that diazonium-modified DWCNTs retained 33 times more current-carrying capacity than similarly functionalized SWCNTs when integrated into thin films.[2] Later, the same group used chemically modified DWCNT field effect transistors (FETs) for the detection of amines, observing 6000 times higher chemical selectivity for amine-containing analytes compared to other small molecules,[3] demonstrating that DWCNT FETs can achieve ultrahigh detection sensitivity (∼1 ppb) with the added advantages of increased selectivity and reduced occurrence of nonspecific binding.

From a fundamental viewpoint, DWCNTs represent the simplest form of a multi-walled carbon nanotube (MWCNT), which makes them ideal candidates for investigating the effects of the interwall coupling between component nanotubes, which can produce some remarkable and unexpected phenomena. For example, Okada and Oshiyama calculated that due to overlap of the electronic states of the constituent nanotubes, some S@S DWCNTs can behave entirely as metals,[4] while Moradian *et al.* calculated that in some mixed-wall DWCNTs the two walls can even exchange electronic type.[5] Such predictions have further drawn the attention of experimentalists to investigate the properties of DWCNTs through the use of FETs, notably Liu *et al.*[6] and Bouilly *et al.*,[7] who have provided unique insights into

* Address correspondence to benjamin.flavel@kit.edu.

Received for review December 2, 2014 and accepted March 10, 2015.

10.1021/nn506869h

the transconductance properties of the different inner@outer wall combinations of DWCNTs. Spectroelectrochemistry has also been employed by Kalbac *et al.* to investigate the effects of charge transfer between the four DWCNT combinations, where the required shift in Fermi level to achieve charge transfer from outer to inner wall was found to increase in the order of M@M < S@M < M@S < S@S.[8]

Notwithstanding the aforementioned studies, the use of DWCNTs has remained relatively limited despite their clear potential. This is in part due to DWCNTs suffering many of the same setbacks initially experienced by SWCNTs, in particular, the lack of a method to synthesize pure, electronically well-defined raw material. For this reason, several groups are focusing on the subsequent processing and sorting of DWCNT raw material. While sorting by inner wall type remains elusive, the relatively small field of DWCNT sorting has already seen density gradient ultracentrifugation (DGU) used in the removal of large and small diameter SWCNT contaminants[9] as well as DWCNT separation by length[10] and outer wall electronic type.[11] However, the use of Sephacryl gel chromatography has remained notably underutilized in the processing of DWCNTs. In the case of SWCNTs, the technique has allowed for the high-throughput separation of metallic from semiconducting species and in some cases can also enrich zigzag and (*n*, 0) species.[12] The works of Kataura and co-workers,[13,14] Strano and co-workers,[15,16] and our group[17,18] have further developed the technique to afford highly (n,m) pure SWCNT suspensions. In the field of DWCNT sorting, we recently demonstrated the use of Sephacryl gel to purify raw DWCNT material by removing SWCNT contaminants.[19] Based on the already proven success of Sephacryl gel for the separation of SWCNTs by electronic type, we anticipated that perhaps such an approach may also offer an avenue for the separation of DWCNTs. Although the ultimate goal remains the preparation of DWCNTs with both defined outer and inner walls, this current work makes a significant advance in that direction by providing a high-throughput method to prepare DWCNTs with defined outer wall electronic type.

The literature contains several examples of the electronic separation of large diameter arc-discharge (AD) SWCNTs by a cosurfactant gel separation. Miyata *et al.*,[20] Wu *et al.*[21] and Zhang *et al.*[22] have all demonstrated the use of cosurfactant separation for large diameter SWCNTs using sodium dodecyl sulfate (SDS) and sodium cholate (SC), and on the basis of these reports, a similar cosurfactant approach would intuitively appear to be applicable to DWCNTs with their relatively large outer walls. It is this method that we now describe.

RESULTS AND DISCUSSION

Raw DWCNTs suspended with SC were applied to a gel bed under SDS and washed through with further SDS solution, and the "flow-through" material was collected. Time-lapse photography (Figure S1 of the Supporting Information) shows that separation begins to occur rapidly with the formation of four bands of differing concentration and color. Over time, each band spreads out and is subsequently eluted at a different time. To follow this process, we monitored the composition of the eluted liquid using a process Raman analyzer, or "process Raman", where the integrated G-band intensity is plotted against time and is shown in Figure 1a. For comparison, the same process was repeated for large diameter AD SWCNTs and small diameter HiPco SWCNTs (see Figures S2 and S3, Supporting Information, for more information). For the DWCNT material, four bands were eluted at 7, 10, 18, and 20 min, respectively. The eluted material corresponding to each peak in the process Raman data was then measured using optical absorption spectroscopy (Figure S4, Supporting Information).

Bands 1 and 2 exhibit very similar optical properties, with two broad peaks at 695 and 750 nm and a series of peaks between 1030 and 1215 nm (the spectrum of band 2 can be seen in Figure 1b). These absorption regimes correspond to M_{11} transitions of large diameter (∼1.3−1.6 nm) metallic (m-) nanotube walls[23] and to the S_{11} transitions of smaller diameter (∼0.7−0.9 nm) semiconducting (s-) nanotube walls[24] or S_{22} transitions of large diameter s-nanotubes, respectively. Considering that the difference between these two diameter distributions is ∼0.6−0.8 nm, and knowing that the interwall spacing varies between 0.33 and 0.41 nm,[25] it is therefore likely that these peaks correspond to the inner- and outer-wall pairs of DWCNTs. In the case of band 1, there is additional broadness between 1030 and 1215 nm suggesting that there are other large-diameter s-nanotubes present. Furthermore, the large background and low peak intensity suggest that these nanotubes have poor optical properties and are most likely defected. The absorption spectrum of band 2 is, however, in good agreement with that previously reported by Green and Hersam for metallic outer-wall-enriched DWCNTs,[11] and it is this fraction that we assign to be metallic outer walled DWCNTs (m-DWCNTs) and these are used in further experiments.

The absorption measurement of band 3 (seen in Figure 1c) is significantly different from that of either band 1 or band 2. There is a large, broad feature centered at ∼1050 nm consisting of a multitude of peaks, with a series of smaller peaks between 400 and 600 nm. These peaks correspond to the S_{22} transitions of large diameter nanotubes (∼1.5−1.6 nm), S_{11} transitions of small diameter nanotubes (∼0.7−1 nm), and S_{33} transitions of large diameter semiconducting nanotubes, respectively. Importantly, there is a clear absence of peaks in the range of 600−800 nm; the region where large diameter M_{11} peaks were observed for bands 1 and 2. Again, this spectrum is in agreement

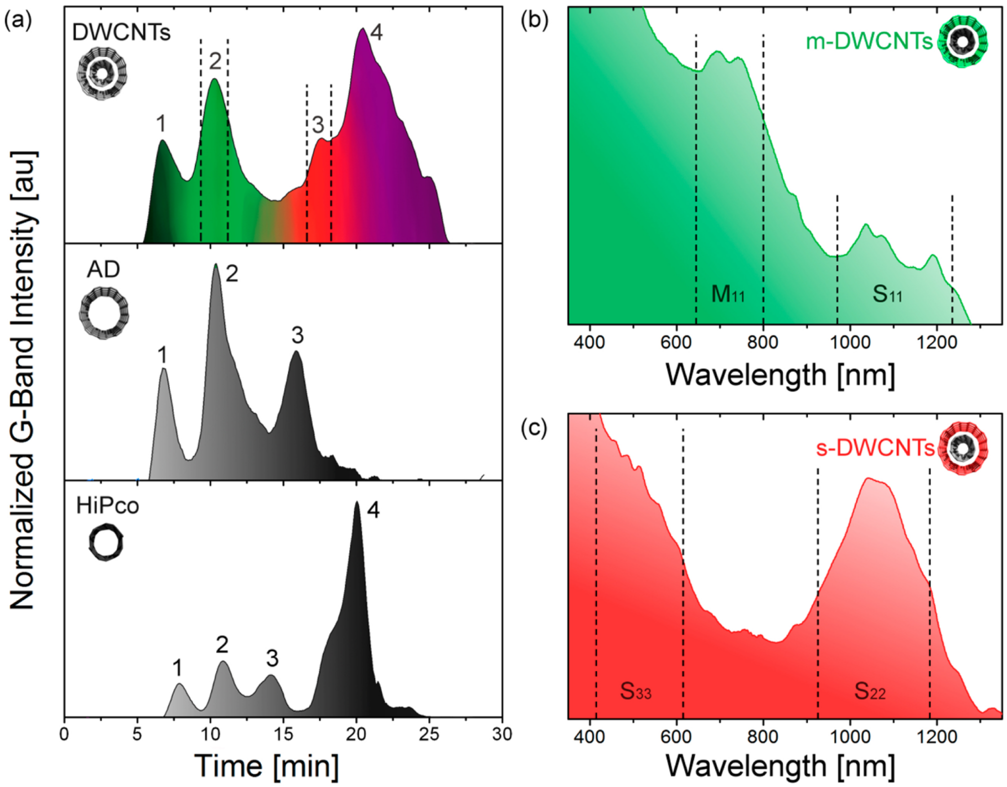

Figure 1. Cosurfactant separation of DWCNTs *via* gel permeation. (a) Elution profiles of the normalized G-band Raman mode intensity for DWCNTs, AD SWCNTs, and HiPco SWCNTs. The dashed lines in the DWCNT elution profile highlight bands 2 and 3, which from the absorption spectra, seen in (b) and (c), correspond to DWCNTs with metallic and semiconducting outer walls. Regions of S_{ii} and M_{ii} transitions are highlighted in each spectrum.

with the literature[11] and indicates that the vast majority of the large diameter nanotubes present are semiconducting in nature. Therefore, band 3 was assigned as semiconducting outer wall DWCNTs (s-DWCNTs) and this material was used for subsequent experiments.

Interestingly, the three bands observed in the AD SWCNT (1.3–1.7 nm) separation occur at approximately the same time as the first three bands of the DWCNT material (7, 10, and 16 min). Comparison of the absorption measurements of the three bands (Figure S2, Supporting Information) with those of the DWCNT material reveals that the AD SWCNTs undergo the same separation process, *i.e.*, defected material followed by metallic and then semiconducting nanotubes. However, despite the semiconducting fraction (band 3) exhibiting equally high purity as the s-DWCNTs, the metallic fraction (band 2) shows a large S_{22} feature, indicating the presence of many s-nanotubes. Thus, the cosurfactant gel separation is not as effective for metallic large diameter nanotubes as it is for DWCNTs, despite having the same mean diameter. While they are expected to be the same in terms of the surface properties, such as surfactant wrapping, it is important not to discount the presence of an inner wall, which will introduce an increased stiffness to the DWCNT and influence its permeation through the gel. Furthermore, the possibility for interwall coupling may provide an influence on the overall electronic properties of the DWCNT and its wrapping by SDS. These subtle differences may explain the difference between AD and DWCNT separation.

Lastly, band 4 (Figure S4, Supporting Information) shows peaks in the range of 1050–1250 nm and less intense, broader peaks between 600 and 800 nm. These are indicative of S_{11} and S_{22} transitions of small diameter SWCNTs, respectively, and are in agreement with our previous work, which also saw the SWCNTs eluted last from the column, despite the significantly different surfactant conditions used.[19] It can be seen that band 4 aligns well with the bulk of the HiPco “flow-through” material eluted at 20 min also. Interestingly, the HiPco SWCNTs also experience some degree of electronic sorting, with the first three peaks exhibiting M_{11} features (Figure S2, Supporting Information).

Comparing band 2 for all materials; it seems possible that the m-DWCNT fraction may contain large and small diameter m-SWCNTs. Likewise for band 3, the s-DWCNT fraction may contain large diameter s-SWCNTs and small diameter m-SWCNTs. However, as the concentration of these “contaminant” species is low in the raw material (<30%), their overall contribution to the m- and s-DWCNT fractions is likely to be similarly low and this is supported by TEM analysis, as discussed later. Additional characterization by Raman spectroscopy of nanotube films can be found in Figure S5 of the Supporting Information.

While Figure 1a shows well-isolated metallic and semiconducting bands, the route toward successful separation was not as straightforward as it at first appeared it might be. In light of previously reported diameter- and SDS concentration-dependent adsorption of small diameter SWCNTs[13,18,26] and our previous work on DWCNTs,[19] it was proposed that the preparation of m-DWCNTs may be as simple as sequentially reducing the SDS concentration until the flow-through material consisted only of m-DWCNTs. This approach was systematically investigated and was ultimately unsuccessful (see Figure S6 (a), Supporting Information). This suggests that SDS on its own does not exhibit any sensitivity toward electronic character for DWCNTs. Similarly, a separation in SC alone does not yield any enrichment by diameter or electronic type, as seen in our previous work.[19]

As previous reports in the literature for SWCNT sorting *via* gel permeation have demonstrated a high dependence upon surfactant encapsulation,[13,15] it therefore follows that the separation of DWCNTs is similar. The interaction between surfactant and nanotubes has been extensively investigated and reveals that different surfactant conformations (random, hemimicelle or cylindrical micelle) arise depending on nanotube diameter and the surfactant concentration of its environment.[27−29] For example, SDS wrapping of small diameter nanotubes (<1 nm) tends to result in a highly disordered random configuration at low SDS concentrations (packing densities of ~1.0 molecules nm^{-2})[28,30] and more ordered, cylindrical wrapping at high SDS concentrations (2.8 molecules nm^{-2}).[28] The wrapping of large diameters (>1 nm) is also disordered at low concentration but forms hemimicelles at high SDS concentration.[28,30] Furthermore, the extent of SDS encapsulation is also dependent upon electronic character with metallic nanotubes having a higher degree of SDS wrapping than semiconducting nanotubes, owing to the increased polarizability.[31] These different surfactant conformations are responsible for the nanotubes' interaction with the gel environment with lower wrapping densities causing a stronger interaction. Thus, in the low concentration regime, semiconducting nanotubes (with disordered surfactant encapsulation layers for both large and small diameters) are adsorbed to the gel, while metallic nanotubes experience no interaction.[13,15,26]

Although the correct mechanism of the cosurfactant separation remains speculative, we now present a possible mechanism based on the current understanding of SDS encapsulation mentioned above and reported SDS-based gel separations.[13,15,26]

Upon initial addition to a gel column under SDS, the nanotubes are entirely wrapped in SC and experience limited interaction with the gel. As they traverse the gel, a surfactant exchange process begins and an initial separation occurs. This separation is enhanced by washing with additional SDS, which results in nanotubes that are either partially or completely wrapped in SDS. As metallic nanotubes are known to have a stronger interaction with SDS compared to semiconducting nanotubes,[31] they may become more fully wrapped. In which case, the metallic nanotubes would continue to have a limited interaction with the gel as they traverse the column, as is commonly seen in SWCNT separations.[13,15,26] Consequently, the m-DWCNTs elute first from the gel.

From experiments with the raw material at 0.5 wt % SDS (see Figure S6 (a), Supporting Information), it is also clear that even at low SDS concentrations it is not possible to have a sufficiently low or disordered wrapping of SDS on the s-DWCNTs to facilitate a strong interaction with the gel. Nonetheless, due to the well-known electronic sensitivity of SDS,[11,13,31,32] it is expected that the interchange of SC with SDS occurs more readily on m-DWCNTs compared to s-DWCNTs. Likewise, the increased curvature of small diameter SWCNTs is expected to make it more difficult for SC to be exchanged with SDS. Consequently, as seen in the elution profile (Figure 1), bands of s-DWCNTs and SWCNTs form.

While Figure 1 demonstrates separation under optimized conditions (1 wt % SDS: 1 wt % SC), several other surfactant ratios and concentrations where also employed. In the case of a low SDS concentration on the column (0.5 wt %) and high relative SC concentration in solution (1 wt %), it is possible that the SDS concentration is too low to displace the SC from the nanotube sidewalls. Alternatively, for a high SDS concentration on the column (2 wt %) and a low relative SC concentration in solution (1 wt %), the SDS is quickly able to displace the SC and form stable hemispheres around the nanotube, limiting the interaction with the gel. In both cases the raw material remains together as one band, as seen in Figure S7 (b) and (c) (Supporting Information). When keeping the surfactant ratio the same (1:1), but increasing the concentration (2 wt %), the resolution of separation is also reduced, as seen in Figure S7 (d) (Supporting Information). This in line with previous computational work,[27,28] as well as experimental work of Kataura and co-workers,[13] Strano and co-workers,[15] Blanch *et al.*,[26] and our work,[17,18] where high concentrations of SDS in general reduce the interaction of nanotubes with the gel.

The proposed mechanism may also explain why taking enriched DWCNTs from our previous method,[19] which were separation from a mixture of SWCNTs and DWCNTs, is unsuccessful for subsequent separation according to outer wall electronic character (see Figure S6 (b) (Supporting Information) for more information). In our previous work, the DWCNTs were suspended in 2 wt % SDS and added to a gel column under 2 wt % SDS. Only a very small amount of the overall nanotube population became adsorbed to the gel, presumably

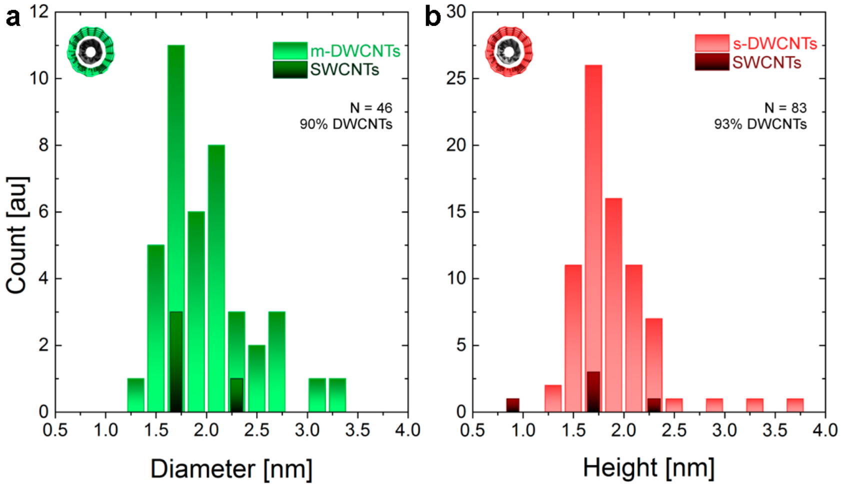

Figure 2. TEM analysis of the sorted DWCNTs with (a) metallic and (b) semiconducting outer walls, where diameter distributions can be seen for DWCNTs, SWCNTs, and MWCNTs. The sample number and resultant DWCNT purity are given in each case.

only those with a sufficiently low SDS coverage to facilitate an interaction with the gel. These adsorbed nanotubes were then washed off with 1 wt % SC, which is exactly the same surfactant and concentration used for starting material in the current work. Thus, it should follow that enriched DWCNTs obtained from the previous method can be further separated by electronic character using the method described in this work. However, no electronic separation of this material is observed. We attribute this to the fact that our proposed mechanism is reliant upon having DWCNTs with a strong tendency to be wrapped by both SDS and SC because our separation method is reliant on the intermixing of SC with SDS on the nanotube surface, but these nanotubes are not those that result from the previous method. In the previous method the use of a high SDS concentration yields only those nanotubes with a weak preference for SDS wrapping. Hence, the appropriate interchange/intermixing of surfactants exploited in the current work is simply overwhelmed by a stronger tendency to be wrapped with SC. Nevertheless, the current method also separates DWCNTs from SWCNTs (as seen in Figure 1 and Figure S4, Supporting Information), which makes a preliminary separation of DWCNTs from SWCNTs unnecessary.

To estimate the DWCNT purity as well as the electronic purity of m-DWCNT and s-DWCNT fractions, transmission electron microscopy (TEM), absorption spectroscopy, and atomic force microscopy (AFM) were employed. TEM histograms of diameter distributions of DWCNTs and SWCNTs are presented in Figure 2 with representative TEM micrographs for all separated fractions seen in Figures S8−S11 (Supporting Information). For the metallic enriched DWCNTs, it can be seen that the sample predominantly consists of DWCNTs with a purity of 90%, with very few SWCNTs present. This is in agreement with the absorption spectra, in which small diameter nanotubes in any significant amount cannot be identified. Furthermore, the TEM shows an average DWCNT diameter of ∼1.7 nm, in agreement with that obtained previously for metallic DWCNTs sorted form the same starting material.[11] TEM analysis of the semiconducting enriched fraction reveals a similar DWCNT purity of 93% and an average diameter of ∼1.6 nm. A negligible number of MWCNTs were observed (<2 in each sample) and TEM failed to reveal the presence of any other carbon structures such as nanoribbons. However, owing to the limitations associated with sample size in TEM analysis, we are unable to definitely discount the presence of either.

Despite AFM and TEM being established methods for nanotube characterization, it should be noted that a new approach has been recently reported by Kominkova *et al.*, which is capable of discerning the ratio of SWCNTs:DWCNTs, although it requires a spectroelectrochemical cell.[33] Due to the fact that TEM confirms that the samples contain predominantly DWCNTs, reasonable estimates of electronic purity can be obtained from the absorption spectroscopy measurements,[11] where the contributions from SWCNTs are thus assumed to be negligible. By measuring the absorption profile of nanotube films before and after treatment with thionyl chloride, which depletes S_{11} (and some S_{22}) transitions of the outer walls,[9,11,19] peak areas for metallic and semiconducting outer wall species can be calculated. These can then be compared to those of AD SWCNTs, which have a known composition of 1:2 metallic/semiconducting (see Figures S12 and S13, Supporting Information, for more information). This yields purities of ∼90% and ∼70% for semiconducting and metallic enriched DWCNTs, respectively, which is comparable to that achieved by Green and Hersam using DGU (96% and 98% respectively).[11] This compliments the existing literature on SWCNT sorting, where DGU[34−37] and gel-based sorting methods[12,13,15,18] have consistently proven to be the preferred techniques to achieve high purity carbon nanotube solutions.

While TEM and absorption spectroscopy are the accepted characterization methods for purity of enriched DWCNT material,[11] we have also included AFM measurements as it is a common method used to estimate diameter distributions. AFM samples were prepared by spin coating of nanotube suspensions onto silicon oxide surfaces. Representative AFM images can be seen in Figure S14 (Supporting Information) with diameter and length distributions seen in Figures S15−S17 (Supporting Information). While the measured average diameters of the m-DWCNT and s-DWCNT (1.61 ± 0.14 nm and 1.56 ± 0.04 nm, respectively) are in agreement with TEM there is a significant discrepancy regarding the number of small diameter nanotubes, which can only correspond to SWCNTs. This unexpectedly high proportion of small diameter nanotubes is also seen here in the case of large diameter AD SWCNTs. These have a diameter range of 1.3−1.7 nm, but the AFM shows that 25% of the AD nanotubes have diameters of 1 nm or less. This anomalous result raises questions about sample preparation; where the different surfactant wrapping of small and large diameter nanotubes may give rise to different degrees of bundling or adhesion during the spin-coating process. This could potentially generate a situation in which there is bias toward more of the small diameter nanotubes being individually present on the surface than in the real solution. Of course, this skews the statistical analysis toward smaller diameters because only those nanotubes that are individually dispersed on the surface are counted. This highlights the difficulty associated with correctly assessing the composition of carbon nanotube suspensions.

While AFM may suffer from problems associated with sample preparation, TEM and absorption spectroscopy also present challenges in characterization. TEM is the definitive tool for the conclusive identification of DWCNTs and provides quantitative characterization of the diameter distribution, yet it only samples a small proportion of the entire nanotube population. On the other hand, while absorption measurements probe the entire nanotube population, the interpretation of the resulting spectra is difficult due to convolution of the inner and outer wall optical transitions. This can be somewhat overcome by bleaching the optical transitions of the outer walls through doping, however in practice chemical shielding of the inner wall by its corresponding outer wall is not complete.[8] This also requires nanotubes to be in thin film form, which gives rise to large scattering backgrounds and red-shifting of the peak positions.[32,38−40] Although comparing M_{11} and S_{11} peak areas of sorted DWCNT material to those of the AD SWCNTs provides the best avenue for spectroscopic determination of purity at this time, it does not consider the differing absorption cross sections of the various nanotube species and is, thus, an estimate. In an attempt to improve the purity of the separated m- and s-DWCNT fractions, a subsequent separation step was also conducted. However, while it somewhat improved the purity of the s-DWCNT fraction, it made little overall difference to the purity of the m-DWCNT fraction (Figures S18 and S19, Supporting Information).

The fabrication of DWCNT FETs allows for a more thorough investigation of the electronic properties than can be obtained from a purely spectroscopic analysis. Previous work has employed top contact formation *via* metal deposition onto a substrate-bound nanotube, with the character of the contacting nanotube determined postfabrication.[6,7] However, in this work we use an already established technique for nanotube device fabrication−electrophoretic deposition,[41−43] which has been demonstrated on multiple occasions to afford highly aligned single nanotube contacts.[44,45] Owing to the greater polarizability of metallic SWCNTs they are preferentially deposited over their semiconducting counterparts during the electrophoretic deposition process, which makes it difficult to selectively deposit semiconducting nanotubes from a mixture of nanotube types.[41] With the addition of a second wall this becomes practically impossible, and thus high-purity s-DWCNTs suspensions are required.

DWCNT FETs were manufactured using electron-beam lithography, metal sputtering, and lift-off, followed by electrophoretic deposition from either a m- or s-DWCNT suspension. Both AFM and scanning electron microscopy (SEM) were then used to verify the presence of only a single nanotube per device as shown in Figure 3 as well as Figure S20 (Supporting Information). It should be noted that in order to definitively determine the inner@outer wall identity of each DWCNT either Raman or TEM would be required. However, as in the work of Liu *et al.*,[6] TEM measurements require a window in the substrate in order to free-suspend the nanotube and Raman would require a confocal microscope with a diffraction limited spot and enough available excitation wavelengths to excite all combinations of inner and outer wall. As neither of these approaches were available to us, our assignment of inner@outer wall is based on previous literature examples, in which this additional characterization was possible.[6,7] The first type of behavior seen for m-DWCNTs is shown in Figure 3a, where an entirely metallic behavior is seen, with no current modulation and an increasing current (I_s) with increasing source-drain voltage (V_s). The I_s, measured in the on state at $V_s = 1$ V, was ∼2.3×10^{-5} A with a calculated on/off ratio of 1.0. Although TEM of the DWCNT is the only way to conclusively confirm the identity of the inner and outer walls, as in Liu *et al.*,[6] this would require a specialized substrate and very long nanotubes. However, when

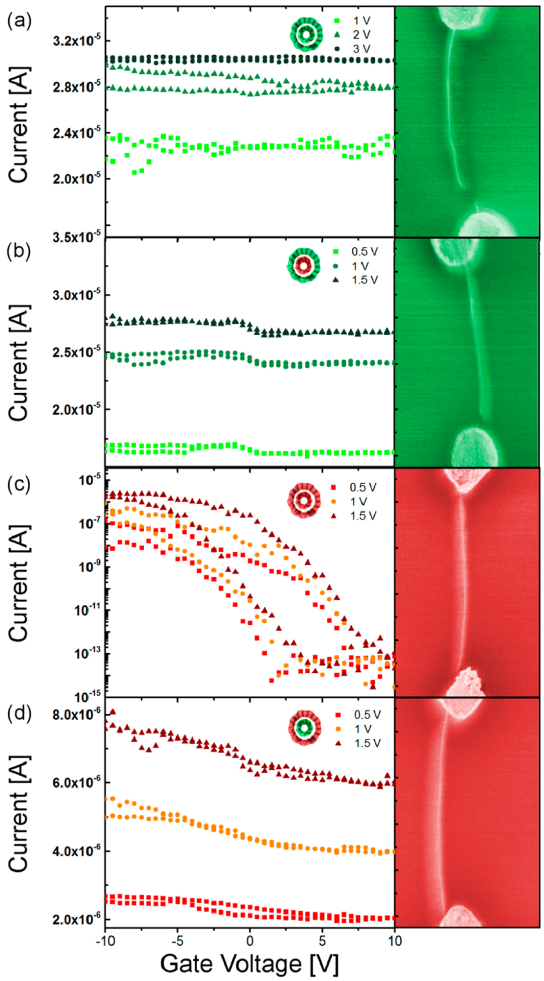

Figure 3. Transconductance measurements and corresponding false color SEM images of the four possible types of DWCNT FET: (a) M@M, (b) S@M, (c) S@S, and (d) M@S.

compared in conjunction with the spectroscopic analysis to accounts from the literature in which TEM was performed,[6,7] the transconductance measurements are a strong indicator of the presence of an M@M DWCNT.

The second type of behavior observed for metallic outer wall DWCNTs is shown in Figure 3b. Similarly to the M@M case in Figure 3a, a constant source−drain current is seen with varying gate voltage, with the exception of a slight modulation around $V_g = 0$ V. I_s in the "on-state" at $V_s = 1$ V was measured to be 2.5×10^{-5} A with an on/off ratio close to unity. This behavior is attributed to a S@M DWCNT and is in agreement with Bouilly *et al.*,[7] who also observed no modulation (on the logarithmic scale) for pristine S@M DWCNTs.

Parts c and d of Figure 3 display the two types of behavior found for devices fabricated using the s-DWCNT suspension. Figure 3c shows a very different behavior compared to that observed in the other three cases, with an on/off ratio of $\sim 10^8$ and an I_s in the on state of 3.8×10^{-7} A at $V_s = 1$ V. This strongly semiconducting behavior is assigned to an S@S DWCNT in agreement with the work of Liu *et al.*[6] and Bouilly *et al.*[7] According to the previously reported literature, the presence of a significant band gap may result from either a large interwall spacing, a lack of $\sigma-\pi$ rehybridization owing to large diameter inner walls, or curvature differences between the inner and outer walls.[4] Without TEM, the (*n*,*m*) indices of the inner and outer walls cannot be known precisely, and hence, any conclusions about the curvature difference and inner wall rehybridization could only be speculative. However, from the TEM and AFM data, the average interwall distance for s-DWCNTs was determined to be 0.38 ± 0.15 nm and the outer wall diameter of the measured DWCNT is 1.54 nm. TEM analysis of interwall distance for all DWCNT fractions can be found in Figure S21 (Supporting Information). Moradian *et al.*[5] modeled various commensurate DWCNTs (*i.e.*, where the ratio between the unit cell lengths of the two walls is a rational number) with the (20,0) outer wall, which has a diameter of 1.566 nm similar to that observed here. When an (8,0) nanotube was inserted as the inner wall (diameter = 0.626 nm), the DWCNT remained semiconducting with an interwall distance of 0.47 nm. If the inner wall is replaced by a (10,0) nanotube (diameter = 0.783 nm), the interwall distance is reduced to 0.3915 nm and the DWCNT becomes metallic in nature. Because the average interwall distance measured here is less than that presented by Moradian *et al.*, but the nanotube remains semiconducting, it is therefore likely that the observed semiconducting behavior is due to the S@S DWCNT being incommensurate.

The last remaining DWCNT combination is M@S, shown in Figure 3d. A slight current modulation is observed with an on/off ratio of 1.4 (marginally higher than M@M or S@M) and an on-state current of $I_s = 5.5 \times 10^{-6}$ A at $V_s = 1$ V. In this instance, the current is carried predominately by the inner metallic wall, with the large semiconducting outer wall being gateable. This behavior differs from that observed by Bouilly *et al.*,[7] who were unable to differentiate between M@M and M@S DWCNTs. The authors attributed this to the difficulty in determining the nature of the outer wall due to the constant current flowing thought the metallic inner wall. Of course, that problem is resolved in our work because the observation of current modulation can be coupled to the fact that the nanotube was deposited from a suspension of purified s-DWCNT material, clearly allowing the behavior to be attributed to an M@S device. This is also in agreement with the work of Liu *et al.*[6] who observed clear differences in behavior between the M@M and M@S DWCNT combinations.

CONCLUSION

In this work, we present a straightforward and scalable cosurfactant column chromatography technique to produce DWCNTs with defined outer wall electronic character. The enriched DWCNTs fractions were characterized with TEM, AFM, and absorption spectroscopy, and the time evolution of the sorting process was measured with process Raman analysis. Integration of the resultant sorted material into DWCNT field effect transistors *via* electrophoretic deposition has allowed detailed electronic measures of the nanotube characteristics to be made. In addition, correlation of the device's transconductance properties with precise knowledge of the composition of the starting solutions has allowed for accurate differentiation between the four unique inner@outer wall combinations of M@M, S@M, S@S, and M@S. We anticipate that the high throughput and relative simplicity of this approach will spur further interest into the investigation of the complex and intriguing interwall interactions of DWCNTs, as well as opening up the potential for exploiting such interactions in advanced sensor devices and other applications.

EXPERIMENTAL SECTION

The DWCNT raw material (average diameter ~2 nm) used in this work was supplied by Unidym (lot no. OE-130807). AD SWCNT raw material was obtained from Carbon Solutions (lot no. AP-387), and HiPco SWCNT raw material was obtained from NanoIntegris (lot no. R1-901). Raw nanotube starting material was prepared by suspending nanotube powder (50 mg) in aqueous SC (1 wt %, 125 mL, Sigma-Aldrich) using a tip sonicator (Weber Ultrasonics, 35 kHz, 500 W in continuous mode, 1 h, ~ 20% power). During sonication, the suspension was placed in a water bath (15 °C).

Gel filtration was performed as previously described[19] with only a few changes, using Sephacryl S-200 gel filtration medium (Amersham Biosciences) in a glass column (45 cm in length and 2 cm inner diameter). The column was filled with filtration medium (90 mL) and compacted slightly by applying pressure with compressed air to yield the desired gel height (~20 cm). The column was prepared for separation by washing with aqueous SDS (1 wt %, ~180 mL, Merk KGaA). For the separation, as-prepared nanotube suspension (~10 mL) was added to the top of the column. Once the nanotube material had completely entered the gel, the column was filled with a solution of aqueous SDS (1 wt %) under applied pressure to ensure a constant flow rate (~1 mL min^{-1}). The nanotubes were separated and the eluent was collected in fractions (~2 mL) for characterization.

Raman intensity was monitored in real-time with a Raman RXN Systems analyzer (Kaiser Optical Systems) fitted to the end of the column with an excitation wavelength of 785 nm.

Spectroscopic characterization of the sorted material was carried out by absorption spectroscopy. Absorption spectra of the sorted fractions were recorded on a Varian Cary 500 spectrophotometer.

Nanotube suspensions (10 μL) were spin-coated (1 min, 1500 rpm) onto clean silicon oxide surfaces (1 cm^2, ABC GmbH) and then gently rinsed with water. To measure nanotube lengths and heights, tapping mode AFM images were taken in ambient conditions with a multimode head and a NanoScope III controller (Digital Instruments) using silicon cantilevers (resonance frequency 250–400 kHz Mikromasch). Topographic height and phase images were obtained simultaneously with feedback controls optimized for each sample.

TEM samples were prepared by drop-casting aqueous suspensions of the nanotubes onto lacey carbon coated copper grids (Quantifoil GmbH) which were then placed in a drybox (silica gel). Subsequently, samples were washed four times with water and dried similarly. TEM analysis was performed using an aberration-corrected FEI Titan 80–300 microscope operated at 300 kV and equipped with a Gatan US1000 CCD camera for imaging and electron diffraction. All micrographs were obtained with a 2K × 2K CCD camera and analyzed using the Digital Micrographs software package (Version 1.71.38, Gatan Co.).

Boron-doped p-type silicon (0.005–0.001 Ω cm, 325 μm thickness, CZ, ⟨100⟩, ABC GmbH) with a thermally grown oxide (800 nm) was used in the fabrication of FETs for electronic characterization of the nanotubes. Pd source, drain, and gate electrodes, all with a Ti adhesion layer, were fabricated by electron-beam lithography, metal sputtering, and lift off. To deposit single nanotubes between source and drain contacts, a small volume (~7 μL) of nanotube suspension (diluted 1000× with water) was placed on top of the substrate and an RF signal (ω_d = 300 kHz, V_{pp} = 2 V) was applied between the source and gate electrodes. After a short period (~1 min) the substrate was rinsed five times each with water and methanol before drying with nitrogen, and then the generator was switched off. Electronic measurements were obtained using an Agilent 4155C semiconductor parameter analyzer.

Both SEM and AFM were employed to allow selection of only those devices that consisted of a single nanotube connection. A Zeiss Gemini with 1.00 kV EHT, 2.1 mm WD, aperture size of 20 μm, and magnification of 50K× was used for SEM imaging. AFM measurements were acquired using a Bruker Dimension FastScan AFM with NanoScope V controller, NanoScope control software (version 8.15) and ScanAsyst Air cantilevers. The peak-force tapping imaging mode was used with the scan rate and set point controlled manually, while the feedback gains and Z-limit were automatically adjusted to optimize image quality and the data was analyzed using the NanoScope Analysis software (version 1.4).

Conflict of Interest: The authors declare no competing financial interest.

Supporting Information Available: Supporting absorbance spectra, AFM statistics, Raman characterization, and TEM data. This material is available free of charge via the Internet at http://pubs.acs.org.

Acknowledgment. We thank Unidym for providing DWCNT material. K.E.M acknowledges the Karlsruhe House of Young Scientists, the Playford Memorial Trust, and the Australian Microscopy and Microanalysis Research Facility (AMMRF). We are grateful to the Karlsruhe Nano Micro Facility (KNMF) for access to the TEM facilities. This research was also supported by the Bundesministerium fur Bildung und Forschung (BMBF) as administered by POF-NanoMicro. B.S.F. gratefully acknowledges support from the Deutsche Forschungsgemeinschaft's Emmy Noether Program under Grant No. FL 834/1-1.

REFERENCES AND NOTES

1. Brozena, A. H.; Moskowitz, J.; Shao, B.; Deng, S.; Liao, H.; Gaskell, K. J.; Wang, Y. Outer Wall Selectively Oxidized, Water-Soluble Double-Walled Carbon Nanotubes. *J. Am. Chem. Soc.* **2010**, *132*, 3932–3938.
2. Piao, Y.; Chen, C.-F.; Green, A. A.; Kwon, H.; Hersam, M. C.; Lee, C. S.; Schatz, G. C.; Wang, Y. Optical and Electrical Properties of Inner Tubes in Outer Wall-Selectively Functionalized Double-Wall Carbon Nanotubes. *J. Phys. Chem. Lett.* **2011**, *2*, 1577–1582.
3. Huang, J.; Ng, A. L.; Piao, Y.; Chen, C.-F.; Green, A. A.; Sun, C.-F.; Hersam, M. C.; Lee, C. S.; Wang, Y. Covalently Functionalized Double-Walled Carbon Nanotubes Combine High Sensitivity and Selectivity in the Electrical Detection of Small Molecules. *J. Am. Chem. Soc.* **2013**, *135*, 2306–2312.
4. Okada, S.; Oshiyama, A. Curvature-Induced Metallization of Double-Walled Semiconducting Zigzag Carbon Nanotubes. *Phys. Rev. Lett.* **2003**, *91*, 216801.
5. Moradian, R.; Azadi, S.; Refii-tabar, H. When Double-Wall Carbon Nanotubes Can Become Metallic or Semiconducting. *J. Phys.: Condens. Matter* **2007**, *19*, 176209.

6. Liu, K.; Wang, W.; Xu, Z.; Bai, X.; Wang, E.; Yao, Y.; Zhang, J.; Liu, Z. Chirality-Dependent Transport Properties of Double-Walled Nanotubes Measured *in Situ* on Their Field-Effect Transistors. *J. Am. Chem. Soc.* **2008**, *131*, 62–63.
7. Bouilly, D.; Cabana, J.; Meunier, F.; Desjardins-Carrière, M.; Lapointe, F.; Gagnon, P.; Larouche, F. L.; Adam, E.; Paillet, M.; Martel, R. Wall-Selective Probing of Double-Walled Carbon Nanotubes Using Covalent Functionalization. *ACS Nano* **2011**, *5*, 4927–4934.
8. Kalbac, M.; Green, A. A.; Hersam, M. C.; Kavan, L. Tuning of Sorted Double-Walled Carbon Nanotubes by Electrochemical Charging. *ACS Nano* **2010**, *4*, 459–469.
9. Green, A. A.; Hersam, M. C. Processing and Properties of Highly Enriched Double-Wall Carbon Nanotubes. *Nat. Nanotechnol.* **2009**, *4*, 64–70.
10. Huh, J. Y.; Walker, A. R. H.; Ro, H. W.; Obrzut, J.; Mansfield, E.; Geiss, R.; Fagan, J. A. Separation and Characterization of Double-Wall Carbon Nanotube Subpopulations. *J. Phys. Chem. C* **2010**, *114*, 11343–11351.
11. Green, A. A.; Hersam, M. C. Properties and Application of Double-Walled Carbon Nanotubes Sorted by Outer-Wall Electronic Type. *ACS Nano* **2011**, *5*, 1459–1467.
12. Moshammer, K.; Hennrich, F.; Kappes, M. Selective Suspension in Aqueous Sodium Dodecyl Sulfate According to Electronic Structure Type Allows Simple Separation of Metallic from Semiconducting Single-Walled Carbon Nanotubes. *Nano Res.* **2009**, *2*, 599–606.
13. Liu, H.; Nishide, D.; Tanaka, T.; Kataura, H. Large-Scale Single-Chirality Separation of Single-Wall Carbon Nanotubes by Simple Gel Chromatography. *Nat. Commun.* **2011**, *2*, 309.
14. Liu, H.; Tanaka, T.; Urabe, Y.; Kataura, H. High-Efficiency Single-Chirality Separation of Carbon Nanotubes Using Temperature-Controlled Gel Chromatography. *Nano Lett.* **2013**, *13*, 1996–2003.
15. Tvrdy, K.; Jain, R. M.; Han, R.; Hilmer, A. J.; McNicholas, T. P.; Strano, M. S. A Kinetic Model for the Deterministic Prediction of Gel-Based Single-Chirality Single-Walled Carbon Nanotube Separation. *ACS Nano* **2013**, *7*, 1779–1789.
16. Jain, R. M.; Tvrdy, K.; Han, R.; Ulissi, Z.; Strano, M. S. Quantitative Theory of Adsorptive Separation for the Electronic Sorting of Single-Walled Carbon Nanotubes. *ACS Nano* **2014**, *8*, 3367–3379.
17. Flavel, B. S.; Kappes, M. M.; Krupke, R.; Hennrich, F. Separation of Single-Walled Carbon Nanotubes by 1-Dodecanol-Mediated Size-Exclusion Chromatography. *ACS Nano* **2013**, *7*, 3557–3564.
18. Flavel, B. S.; Moore, K. E.; Pfohl, M.; Kappes, M. M.; Hennrich, F. Separation of Single-Walled Carbon Nanotubes with a Gel Permeation Chromatography System. *ACS Nano* **2014**, *8*, 1817–1826.
19. Moore, K. E.; Pfohl, M.; Hennrich, F.; Chakradhanula, V. S.; Kuebel, C.; Kappes, M. M.; Shapter, J. G.; Krupke, R.; Flavel, B. S. Separation of Double-Walled Carbon Nanotubes by Size Exclusion Column Chromatography. *ACS Nano* **2014**, *8*, 6756–64.
20. Miyata, Y.; Shiozawa, K.; Asada, Y.; Ohno, Y.; Kitaura, R.; Mizutani, T.; Shinohara, H. Length-Sorted Semiconducting Carbon Nanotubes for High-Mobility Thin Film Transistors. *Nano Res.* **2011**, *4*, 963–970.
21. Wu, J.; Xie, L.; Hong, G.; Lim, H.; Thendie, B.; Miyata, Y.; Shinohara, H.; Dai, H. Short Channel Field-Effect Transistors from Highly Enriched Semiconducting Carbon Nanotubes. *Nano Res.* **2012**, *5*, 388–394.
22. Zhang, J.; Gui, H.; Liu, B.; Liu, J.; Zhou, C. Comparative Study of Gel-Based Separated Arcdischarge, Hipco, and Comocat Carbon Nanotubes for Macroelectronic Applications. *Nano Res.* **2013**, *6*, 906–920.
23. Araujo, P. T.; Doorn, S. K.; Kilina, S.; Tretiak, S.; Einarsson, E.; Maruyama, S.; Chacham, H.; Pimenta, M. A.; Jorio, A. Third and Fourth Optical Transitions in Semiconducting Carbon Nanotubes. *Phys. Rev. Lett.* **2007**, *98*, 067401.
24. Bachilo, S. M.; Strano, M. S.; Kittrell, C.; Hauge, R. H.; Smalley, R. E.; Weisman, R. B. Structure-Assigned Optical Spectra of Single-Walled Carbon Nanotubes. *Science* **2002**, *298*, 2361–2366.
25. Charlier, J. C.; Michenaud, J. P. Energetics of Multilayered Carbon Tubules. *Phys. Rev. Lett.* **1993**, *70*, 1858–1861.
26. Blanch, A. J.; Quinton, J. S.; Shapter, J. G. The Role of Sodium Dodecyl Sulfate Concentration in the Separation of Carbon Nanotubes Using Gel Chromatography. *Carbon* **2013**, *60*, 471–480.
27. Wallace, E. J.; Sansom, M. S. Carbon Nanotube Self-Assembly with Lipids and Detergent: A Molecular Dynamics Study. *Nanotechnology* **2009**, *20*, 045101.
28. Xu, Z.; Yang, X.; Yang, Z. A Molecular Simulation Probing of Structure and Interaction for Supramolecular Sodium Dodecyl Sulfate/Single-Wall Carbon Nanotube Assemblies. *Nano Lett.* **2010**, *10*, 985–991.
29. Duan, W. H.; Wang, Q.; Collins, F. Dispersion of Carbon Nanotubes with Sds Surfactants: A Study from a Binding Energy Perspective. *Chem. Sci.* **2011**, *2*, 1407–1413.
30. Tummala, N. R.; Striolo, A. Sds Surfactants on Carbon Nanotubes: Aggregate Morphology. *ACS Nano* **2009**, *3*, 595–602.
31. Niyogi, S.; Densmore, C. G.; Doorn, S. K. Electrolyte Tuning of Surfactant Interfacial Behavior for Enhanced Density-Based Separations of Single-Walled Carbon Nanotubes. *J. Am. Chem. Soc.* **2008**, *131*, 1144–1153.
32. Jain, R. M.; Howden, R.; Tvrdy, K.; Shimizu, S.; Hilmer, A. J.; McNicholas, T. P.; Gleason, K. K.; Strano, M. S. Polymer-Free Near-Infrared Photovoltaics with Single Chirality (6,5) Semiconducting Carbon Nanotube Active Layers. *Adv. Mater.* **2012**, *24*, 4436–4439.
33. Kominkova, Z.; Vales, V.; Hersam, M. C.; Kalbac, M. Towards Quantification of the Ratio of the Single and Double Wall Carbon Nanotubes in Their Mixtures: An *in Situ* Raman Spectroelectrochemical Study. *Carbon* **2014**, *78*, 366–373.
34. Arnold, M. S.; Stupp, S. I.; Hersam, M. C. Enrichment of Single-Walled Carbon Nanotubes by Diameter in Density Gradients. *Nano Lett.* **2005**, *5*, 713–718.
35. Arnold, M. S.; Green, A. A.; Hulvat, J. F.; Stupp, S. I.; Hersam, M. C. Sorting Carbon Nanotubes by Electronic Structure Using Density Differentiation. *Nat. Nanotechnol.* **2006**, *1*, 60–65.
36. Kim, W.-J.; Nair, N.; Lee, C. Y.; Strano, M. S. Covalent Functionalization of Single-Walled Carbon Nanotubes Alters Their Densities Allowing Electronic and Other Types of Separation. *J. Phys. Chem. C* **2008**, *112*, 7326–7331.
37. Ghosh, S.; Bachilo, S. M.; Weisman, R. B. Advanced Sorting of Single-Walled Carbon Nanotubes by Nonlinear Density-Gradient Ultracentrifugation. *Nat. Nanotechnol.* **2010**, *5*, 443–450.
38. Wang, F.; Dukovic, G.; Brus, L. E.; Heinz, T. F. The Optical Resonances in Carbon Nanotubes Arise from Excitons. *Science* **2005**, *308*, 838–841.
39. Ando, T. Excitons in Carbon Nanotubes. *J. Phys. Soc. Jpn.* **1997**, *66*, 1066–1073.
40. Ichida, M.; Mizuno, S.; Saito, Y.; Kataura, H.; Achiba, Y.; Nakamura, A. Coulomb Effects on the Fundamental Optical Transition in Semiconducting Single-Walled Carbon Nanotubes: Divergent Behavior in the Small-Diameter Limit. *Phys. Rev. B* **2002**, *65*, 241407.
41. Krupke, R.; Hennrich, F.; Weber, H. B.; Kappes, M. M. v. Löhneysen, H., Simultaneous Deposition of Metallic Bundles of Single-Walled Carbon Nanotubes Using Ac-Dielectrophoresis. *Nano Lett.* **2003**, *3*, 1019–1023.
42. Krupke, R.; Hennrich, F.; Weber, H. B.; Beckmann, D.; Hampe, O.; Malik, S.; Kappes, M. M.; v. Löhneysen, H. Contacting Single Bundles of Carbon Nanotubes with Alternating Electric Fields. *Appl. Phys. A: Mater. Sci. Process.* **2003**, *76*, 397–400.
43. Chung, J.; Lee, K.-H.; Lee, J.; Ruoff, R. S. Toward Large-Scale Integration of Carbon Nanotubes. *Langmuir* **2004**, *20*, 3011–3017.
44. Vijayaraghavan, A.; Marquardt, C. W.; Dehm, S.; Hennrich, F.; Krupke, R. Imaging Defects and Junctions in Single-Walled Carbon Nanotubes by Voltage-Contrast Scanning Electron Microscopy. *Carbon* **2010**, *48*, 494–500.
45. Steiner, M.; Engel, M.; Lin, Y.-M.; Wu, Y.; Jenkins, K.; Farmer, D. B.; Humes, J. J.; Yoder, N. L.; Seo, J.-W. T.; Green, A. A.; et al. High-Frequency Performance of Scaled Carbon Nanotube Array Field-Effect Transistors. *Appl. Phys. Lett.* **2012**, *101*, 053123.

– This page intentionally left blank –

2.1 Separation of Carbon Nanotubes

2.1.5 *Double-Walled Carbon Nanotube Processing*

K. E. Moore, D. D. Tune, **B. S. Flavel**

Advanced Materials 27 (2015) 3105–3137

DOI: 10.1002/adma.201405686

Abstract

Single-walled carbon nanotubes (SWCNTs) have been the focus of intense research and the body of literature continues to grow exponentially, despite more than two decades having passed since the first reports. As well as extensive studies of the fundamental properties, this has seen SWCNTs used in a plethora of applications as far ranging as microelectronics, energy storage, solar cells and sensors, to cancer treatment, drug delivery and neuronal interfaces. On the other hand, the properties and applications of double-walled carbon nanotubes (DWCNTs) have remained relatively under-explored. This is despite DWCNTs not only sharing many of the same unique characteristics of their single-walled counterparts, but also possessing an additional suite of potentially advantageous properties arising due to the presence of the second wall and the often complex inter-wall interactions that arise. For example, it is envisaged that the outer wall could be selectively functionalized whilst still leaving the inner wall in its pristine state and available for signal transduction. Likewise in DWCNT field effect transistors (FETs), where the outer wall can provide a convenient degree of chemical shielding of the inner wall from the external environment, allowing the excellent transconductance properties of pristine nanotubes to be more fully exploited. Additionally, DWCNTs should also offer unique opportunities to further our fundamental understanding of the inter-wall interactions within and between carbon nanotubes. However, the realization of these goals has so far been limited by the same challenge experienced by the SWCNT field until recent years, namely, the inherent heterogeneity of raw, as-produced DWCNT material. As such, there is now an emerging field of research regarding DWCNT processing which focuses on the preparation of material of defined length, diameter and electronic type, and which is rapidly building upon the experience gained by the broader SWCNT community. This review describes the background of the field, summarizing some relevant theory and the available synthesis and purification routes; then provides a thorough synopsis of the current state-of-the-art in DWCNT sorting methodologies, outlines contemporary challenges in the field, and discusses the outlook for various potential applications of the resulting material.

Contribution

B.S.F received an invitation to write a review on the field of double walled carbon nanotube sorting. B.S.F, K.E.M and D.D.T wrote the manuscript.

– This page intentionally left blank –

www.MaterialsViews.com

ADVANCED MATERIALS
www.advmat.de

Double-Walled Carbon Nanotube Processing

*Katherine E. Moore, Daniel D. Tune, and Benjamin S. Flavel**

Single-walled carbon nanotubes (SWCNTs) have been the focus of intense research, and the body of literature continues to grow exponentially, despite more than two decades having passed since the first reports. As well as extensive studies of the fundamental properties, this has seen SWCNTs used in a plethora of applications as far ranging as microelectronics, energy storage, solar cells, and sensors, to cancer treatment, drug delivery, and neuronal interfaces. On the other hand, the properties and applications of double-walled carbon nanotubes (DWCNTs) have remained relatively under-explored. This is despite DWCNTs not only sharing many of the same unique characteristics of their single-walled counterparts, but also possessing an additional suite of potentially advantageous properties arising due to the presence of the second wall and the often complex inter-wall interactions that arise. For example, it is envisaged that the outer wall can be selectively functionalized whilst still leaving the inner wall in its pristine state and available for signal transduction. A similar situation arises in DWCNT field effect transistors (FETs), where the outer wall can provide a convenient degree of chemical shielding of the inner wall from the external environment, allowing the excellent transconductance properties of the pristine nanotubes to be more fully exploited. Additionally, DWCNTs should also offer unique opportunities to further the fundamental understanding of the inter-wall interactions within and between carbon nanotubes. However, the realization of these goals has so far been limited by the same challenge experienced by the SWCNT field until recent years, namely, the inherent heterogeneity of raw, as-produced DWCNT material. As such, there is now an emerging field of research regarding DWCNT processing that focuses on the preparation of material of defined length, diameter and electronic type, and which is rapidly building upon the experience gained by the broader SWCNT community. This review describes the background of the field, summarizing some relevant theory and the available synthesis and purification routes; then provides a thorough synopsis of the current state-of-the-art in DWCNT sorting methodologies, outlines contemporary challenges in the field, and discusses the outlook for various potential applications of the resulting material.

1. Background

Carbon nanotubes are an allotrope of carbon having the form of hollow cylinders composed of rolled-up sheets of graphene, which is itself an extended hexagonal lattice of purely sp^2-bonded carbons. Strictly speaking, carbon nanotubes are either single-walled (SWCNTs) or multi-walled (MWCNTs), but for many reasons double-walled carbon nanotubes (DWCNTs) are prominent in the literature. A single carbon cylinder, be it an SWCNT or a component wall of a DWCNT or MWCNT, can be completely described, except for its length, by an intrinsic geometric property, $\mathbf{C}_h$, known as the chiral vector.[1,2] The chiral vector is defined by the equation $\mathbf{C}_h = n\mathbf{a}_1 + m\mathbf{a}_2$ where the integers (n,m) are the number of steps along the zig-zag carbon bonds and $\mathbf{a}_1$, $\mathbf{a}_2$ are the graphene lattice basis vectors in real space (**Figure 1**a). The chiral vector makes an angle, θ, known as the chiral angle, with the zig-zag or $\mathbf{a}_1$ direction. This angle determines the amount of "twist" in the nanotube and two limiting cases exist where the chiral angle is at 0° and 30°. These are known as zig-zag (0°) and armchair (30°) based on the geometry of the carbon bonds around the circumference of the nanotube (Figure 1b,c). All other conformations in which the C–C bonds lie at angles $0° < \theta < 30°$ are known as chiral (Figure 1d).

Because the n,m integers completely describe nanotube chirality, they also determine the electronic band structure. Thus, it is the chirality that has the most impact on the optical and electronic properties of carbon nanotubes. In particular, a slight change of the chiral angle yields nanotubes that are metallic conductors, low bandgap or high bandgap semiconductors. In the case of semiconductors, the bandgap energy is inversely dependent on the nanotube diameter. The armchair nanotubes are the only type that are intrinsically metallic (zero bandgap), although approximately a third of the zig-zag nanotubes also exhibit metallic properties at room temperature because the bandgap is smaller than the thermal energy, k_BT, allowing thermal excitation of carriers into

Dr. K. E. Moore, Dr. D. D. Tune
Centre for Nanoscale Science and Technology
School of Chemical and Physical Sciences
Flinders University
Adelaide 5042, Australia

Dr. K. E. Moore, Dr. D. D. Tune, Dr. B. S. Flavel
Institute of Nanotechnology
Karlsruhe Institute of Technology
76021 Karlsruhe, Germany
E-mail: benjamin.flavel@kit.edu

DOI: 10.1002/adma.201405686

the conduction band. All chiral nanotubes and the remaining two thirds of zig-zag nanotubes are therefore semiconducting at room temperature. This leads to the observation that approximately 60% of all nanotube chiralities are semiconducting with the remaining 40% metallic.[3]

Carbon nanotubes are so small that they exhibit quasi-1D properties, with the confinement of electrons into allowed momentum states giving rise to van Hove singularities in their electronic density of states (DOS) (Figure 1e,f). In bulk semiconducting materials, the energy gap between the valance and conduction bands defines the absorption onset wavelength of the optical spectra, but in the case of carbon nanotubes the discrete electronic transitions in their DOS produce a series of characteristic peaks in the optical absorption spectra at correlated energies (Figure 1g). In the case of bulk semiconducting materials, the single-particle model (an electron absorbs a photon and thus moves from a lower energy level to a higher one) provides a reasonably close approximation of empirical observations. However, the 1D confinement of electrons in carbon nanotubes causes a significantly higher electron–hole binding energy (*eh*) and electron–electron repulsion (*ee*), meaning that true consideration of the optical absorption spectra of nanotubes must be entirely excitonic in nature (light energy is absorbed by the material creating excited states a.k.a. bound electron–hole pairs) with the many-body effects (*eh* and *ee*) included for an accurate description.[4] This means that the actual light energy required to produce a "v_i–c_i" transition is ($Ec_i - Ev_i$) + binding energy (*eh*) − self energy (*ee*), and leads to the experimental finding that E_{22}/E_{11} tends to a value of 1.8 with decreasing tube diameter, rather than the value of 2 as would be expected from density functional theory (DFT) calculations alone.[5] The excitonic nature of the optical properties is an important consideration for specialists however, in the interests of simplicity, we present only the single-particle approximation throughout this review as this is sufficient to appreciate the concepts. There are two other important processes in nanotubes which, in addition to optical absorption spectroscopy, provide vital information regarding nanotube type and character. These are photoluminescence (PL), in which semiconducting nanotubes are excited by an S_{22} photon which then decays emitting a detectable S_{11} photon and allowing chiral identification, and Raman spectroscopy, in which the magnitude of the shift in Raman scattered light, which is exquisitely sensitive to the strong vibrational phonon modes present in the lattice of carbon nanotubes, is plotted to yield a rich variety of structural information. Detailed treatments of these phenomena are readily available in the literature and, in the case of DWCNTs, we refer the reader to Pfeiffer et al.,[6] Shen et al.[7] and Kim et al.[8]

DWCNTs consist of two coaxially aligned SWCNTs and, as such, they share many of the attractive properties of SWCNTs,[9,10] but, owing to the presence of a second wall, are more physically robust and electronically more complex.[11] Similar to SWCNTs, DWCNTs are uniquely characterized by the chiral indices of the constituent inner and outer walls (n_i,m_i)@(n_o,m_o), where each wall can be either semiconducting (S) or metallic (M) depending on its chiral index (Figure 1h).[12] This gives rise to four possible combinations of inner@outer wall; namely, M@M, M@S, S@M, and S@S. This is in contrast to MWCNTs, which are all metallic due to the complex inter-wall coupling. Because DWCNTs represent the simplest form of a MWCNT, they are interesting for investigation of inter-wall coupling, which has a significant influence on the electronic states of the nanotubes and is highly dependent on

Katherine E. Moore has a B.Sc. with First Class Honors and a Ph.D. in Nanotechnology from the Flinders University of South Australia. During her postgraduate degree she received many prestigious awards and grants and her work has been featured in several nanotechnology news platforms. Her research interests include the separation of carbon nanotubes, nanotube sensors, and single nanotube electronic devices.

Daniel D. Tune holds a B.Sc. and Ph.D. in Nanotechnology from the Flinders University of South Australia and is the 2014 recipient of the South Australian Science Excellence Award (PhD category). Daniel is currently working as a postdoctoral researcher in the Carbon Nanotube Solar Cells and Sensors group at the Institute of Nanotechnology, Karlsruhe Institute of Technology. His interests are in renewable energy, nanoelectronics, and composite nanostructures, with a focus on the understanding of carbon nanotubes, fullerenes and graphene, and the application of this in the development of new and improved devices and materials.

Benjamin S. Flavel obtained both a B.Sc. (Hons) and Ph.D. in Nanotechnology at the Flinders University of South Australia. He has since received research fellowships from the Australian Government's Endeavour Program, the Alexander von Humboldt Foundation and is currently a Junior Research Group Leader at the Institute of Nanotechnology, Karlsruhe Institute of Technology under the German Research Foundation's Emmy Noether Program. His research interests include the separation of carbon nanotubes and their integration into devices for optics, sensing, and energy.

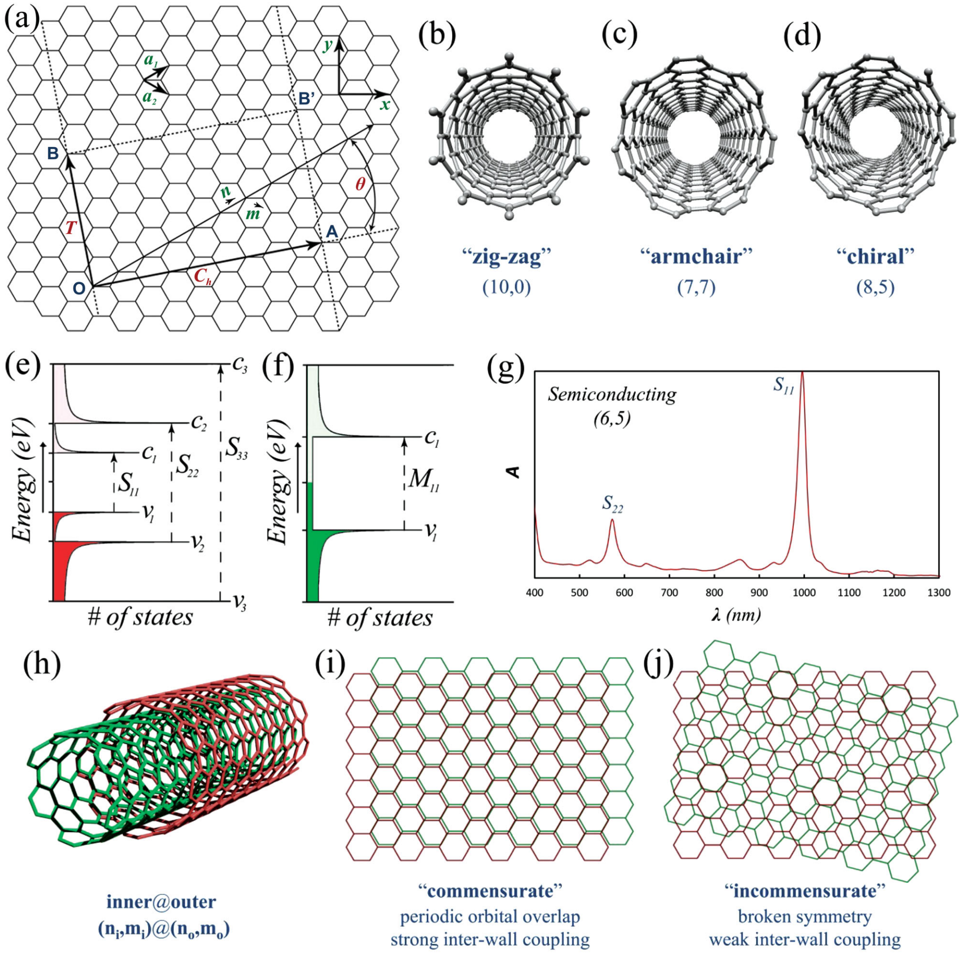

Figure 1. a) Unrolled graphene sheet showing the geometry of the (6,3) nanotube where the vectors OA and OB define the chiral and translational vectors C_h and T, respectively, and the rectangle OAB'B defines the nanotube's unit cell. O, A, B, and B' are reference atoms, a_1 and a_2 are the graphene lattice basis vectors and θ is the chiral angle. b–d) Examples of the three classes of nanotube sidewall; zig-zag, armchair, and chiral. e,f) Schematics of the electronic density of states of semiconducting and metallic (zig-zag) nanotubes showing the valence and conduction states, ν_i and c_i, and optically active electronic transitions, S_{ii} and M_{ii}. g) Optical absorption spectrum of the (6,5) semiconducting nanotube showing the S_{11} and S_{22} absorption features. h) Schematic of a double-walled carbon nanotube. i,j) Representations of commensurate and incommensurate lattice stacking.

whether the lattice stacking of the two walls is commensurate or incommensurate.[10,13–18] A DWCNT is commensurate if the ratio between the unit cell lengths of the two walls is a rational number and, as a result, the DWCNT has a periodic lattice structure (Figure 1i). In an incommensurate DWCNT, the ratio is an irrational number and the nanotube experiences broken symmetry (Figure 1j). This causes reduced inter-wall coupling because the inter-wall transfer at each lattice site oscillates around zero in a quasiperiodic manner, resulting in a net interference that is destructive.[19] In general, the extra Coulomb interaction due to inter-wall coupling reduces the electron–hole binding energy and thus lowers the optical bandgap (red shifting the absorption features) relative to the same (*n,m*) isolated tube; however, as discussed later, there are some wall configurations in which inter-wall coupling interactions increase the bandgap (blue shifting the absorption features).

An important characteristic of DWCNTs is that their concentric structure allows for the opportunity to simultaneously exploit the chemical reactivity of the outer wall as well as the excellent conductance of the unfunctionalized inner wall, making them ideal candidates for nanotube-based sensor devices. During reactions, only the outer wall is exposed to the chemical environment and can be decorated with a high density of chemical moieties.[20,21] As a result of such shielding by the outer wall, the inner wall does not suffer the drawbacks associated with functionalization, such as reduced conductivity due to degradation of the pristine sp^2 hybridized framework.[22]

DWCNTs exhibit great potential from both an applications-based and a fundamental viewpoint; however, their use has remained quite limited. This is in large part due to the lack of a method to synthesize pure, electronically well-defined raw material. While several synthesis methods, including arc discharge,[23–25] peapod growth[26,27] and catalytic chemical vapor deposition,[28] can be optimized to produce high-purity DWCNTs (up to 90%),[29] each method inevitably produces a myriad of contaminants including SWCNTs and MWCNTs, residual catalyst, amorphous carbon, and fullerenes. Purification methods exist to remove some of the unwanted contaminants and increase the DWCNT purity,[24,30] but they are unable to overcome the inherent dispersion of DWCNT lengths, diameters, and inner@outer wall electronic combinations. Like SWCNTs, such inhomogeneity imposes many limitations on potential applications and has spurred the development of new research focused on the preparation of DWCNT material sorted by diameter, length, and/or electronic character. This emerging field has seen the recent implementation of several strategies previously successful for SWCNT processing, such as reversible covalent modification,[31] biofunctionalization,[32] molecular nanocalipers,[33] density-gradient ultracentrifugation,[34,35] and gel permeation[36,37] with several other potential methods looking promising, such as polymer wrapping[38,39] and aqueous two-phase extraction.[40,41] As a result, well defined DWCNT material can now be used to further our fundamental knowledge of inter-wall interactions, to finally begin to realize their potential in advanced electronics and sensor applications, and to explore the rich new physics they possess.

In light of this, we present a review of DWCNT processing techniques and the significance they each pose in this developing field. This review complements others in the literature that are more focused on growth mechanisms, the origin of Raman modes, the effects of temperature, pressure, and doping, the thermal and mechanical properties, photoluminescence, and outer wall selective functionalization, for which we again refer the reader to Pfeiffer et al.,[6] Shen et al.[7] and Kim et al.[8]

2. DWCNTs: Metallic or Semiconducting?

Despite the ability to classify the individual electronic types of the inner and outer walls, identifying the overall electronic nature of a DWCNT is more complicated; being highly dependent on inter-wall interactions, which in turn depend on the inter-wall distance and whether the constituent nanotubes are commensurate or not.[17,42,43] Despite the fact that commensurate DWCNTs are rarely observed experimentally because it is unlikely to have two commensurate SWCNTs with the appropriate radius difference (ca. 0.33–0.41 nm[1,44] for the formation of a DWCNT,[10,13,45] they are commonly employed in theoretical studies. This is due to their defined unit cell lengths, which allow for the use of far simpler computational models and also result in very strong inter-wall coupling.[17,42,43] Indeed, theoretical calculations of commensurate DWCNTs have yielded some unexpected results, for example; a DWCNT in which both walls are semiconducting, but which exhibits overall metallic character.[17,42] Liang found that in the case of a commensurate S@S DWCNT, the energy gap scales inversely with the inter-wall coupling, which in turn is inversely proportional to the inter-wall distance.[14] Thus, as the inter-wall distance decreases, stronger inter-wall coupling causes the bandgap to vanish and the S@S DWCNT behaves as a metal.[14,17]

Okada and Oshiyama used DFT to further investigate the curious behavior of S@S DWCNTs.[42] For a (7,0)@(16,0) DWCNT, it was calculated that the conduction band of the inner wall and valance band of the outer wall merge, forming a finite density of states at the Fermi level. However, as the outer wall diameter is increased, and thereby also the inter-wall spacing, as seen in the case of (7,0)@(17,0) and (7,0)@(19,0), the electronic structure changes to yield semi-metallic behavior. DWCNTs of increasing inner wall diameter (with respect to a constant outer wall) were also investigated using the (8,0)@(19,0) and the (10,0)@(19,0), and both were determined to be semiconducting with finite bandgaps. Interestingly, the semiconducting (10,0)@(19,0) shares the same inter-wall spacing as the smaller (7,0)@(16,0); however, the latter is found to be metallic, highlighting the importance of the inner wall diameter and nanotube curvature on the overall electronic character of a DWCNT. Very small nanotube diameters (0.4–0.6 nm), with their greater curvature, exhibit increased σ–π rehybridization, leading to metallization.[42,46] From the work of Okada and Oshiyama,[42] it is therefore theorized that the metallization of S@S DWCNTs arises due to a combination of curvature differences between the inner and outer walls, rehybridization of the inner wall, and the inter-wall distance.[42]

Likewise, Moradian et al. used DFT calculations to investigate the cases of M@S and S@M DWCNTs and found equally surprising results.[17] For a (6,0)@(20,0) M@S DWCNT, the constituent nanotubes were found to maintain their individual electronic character; however, as a whole, and in agreement with Okada and Oshiyama,[42] the DWCNT behaves as a metal due to overlap of the valence and conduction states of the component walls. Decreasing the inter-wall distance was found to cause a semiconductor-to-metal phase transition in the outer wall. Thus, both constituent walls and the overall DWCNT exhibit metallic behavior. For S@M DWCNTs, all the nanotubes investigated were determined to be metallic and, once again, the inter-wall distance was found to have an effect on the electronic character of the constituent nanotubes. For example, in (10,0)@(21,0) and (14,0)@(21,0) DWCNTs, the semiconducting inner wall becomes metallic, but in the (8,0)@(21,0) DWCNT, where the inter-wall distance is larger, the two nanotubes exchange electronic type. Moradian et al. concluded that as the inter-wall distance is decreased, the semiconducting inner wall becomes metallic, whereas as the inter-wall distance is increased, an exchange of metallicity of the constituent nanotubes occurs.[17]

Despite the increased complexity, some theoretical studies have been performed on incommensurate DWCNTs.[15,19,47,48] These show that the type of conductance is dependent upon the position of the Fermi level and on the length of the nanotubes.[47,49,50] When the Fermi energy is close to the charge neutral point, the energy levels of the constituent nanotubes are uncorrelated and coupling is weak.[49] Thus, in this energy regime, conduction is confined to one nanotube and is expected to be ballistic, as seen in the work of Ahn et al.,[49] who observed that conductance was confined to the inner wall of the (9,1)@(17,2) DWCNT. As the Fermi energy was increased, conduction shifted from ballistic to diffusive and was distributed evenly among the inner and outer walls.

While the number of experimental investigations into the transfer of charge between the constituent walls of incommensurate DWCNTs has remained small, significant insights have been gained through the work of Kalbac et al.[51] and Liu et al.[18] In the work of Kalbac et al.,[51] in situ Raman spectroelectrochemical measurements were used to observe doping behavior and the effects of charge transfer between the inner and outer walls for different incommensurate M/S combinations. The results were obtained using DWCNTs with a defined outer wall electronic character, but with both metallic and semiconducting inner walls. By selecting appropriate laser excitation energies, Raman spectra of each of the four electronic combinations could be observed while the electrochemical potential (and thus Fermi level) was shifted in the positive or negative direction. When this change in Fermi level resulted in filling or depleting of an electronic state, bleaching of the Raman signal was observed.[52] As the inner wall is protected from the surrounding environment by the outer wall, it is neither in direct contact with a working electrode nor with compensating electrolyte counterions.[53] Thus, the origin of inner wall doping could only stem from transfer from its surrounding outer wall.[51] Through the use of this technique, Kalbac et al. determined that the potential required to observe charge transfer increased in the order of M@M < S@M < M@S < S@S. In each case, charge transfer was dependent upon the identity of both the outer and inner walls. For metallic outer walls, charge transfer to the inner wall could occur at small potentials close to the undoped state, whereas semiconducting outer walls required the first van Hove singularity to be filled. A similar observation was made for inner walls, with metallic nanotubes readily accepting charge from either outer wall type. Semiconducting inner walls accepted charge only when the filled states of the outer wall were higher than their first van Hove singularity. This means that for both the S@M and S@S DWCNTs, the inner wall only becomes doped when the electrochemical potential reaches that of the first van Hove singularity of the inner semiconducting wall. **Figure 2** shows a diagram of the respective DOS of each of the four electronic combinations of DWCNTs in the case of shifting the electrochemical potential in the negative direction. The position of the Fermi level required for electron transfer from the outer wall to the inner wall is indicated.

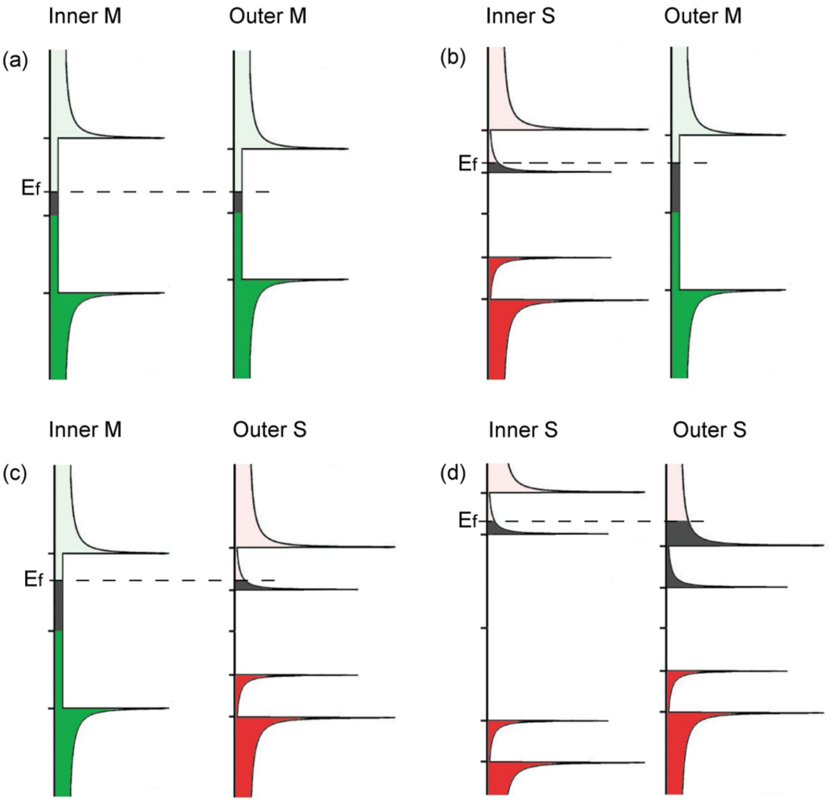

Figure 2. Schematic of the electronic structures of: a) M@M, b) S@M, c) M@S and d) S@S DWCNTs showing the Fermi level position at the point where electron transfer from the outer wall to the inner wall occurs, as described in ref. [51]. Adapted with permission.[51] Copyright 2011, Wiley-VCH.

Liu et al. also investigated incommensurate DWCNTs and have shown that under certain conditions coupling can be quite strong and can influence the electronic states of the nanotube.[18] In that work, optical transitions were observed between 480–750 nm (1.45–2.55 eV) for various suspended incommensurate $(n_i,m_i)@(n_o,m_o)$ combinations and the peak positions were compared to that of the individually suspended SWCNTs.[54] Significant shifts (–50 to 200 meV) were observed across 99 different $(n_i,m_i)@(n_o,m_o)$ combinations. While a redshift of ca. 50 meV can be attributed to the environmental effects seen previously for SWCNTs,[55] such effects cannot account for some of the very large and transition-dependent variations observed, especially the significant blue shifts for certain transitions. Therefore, such strong variations must be attributed to intrinsic effects, such as orbital hybridization between the inner and outer walls. Through the use of perturbation theory, the authors determined that any observed shift is reliant upon several factors including; the inner wall diameter and chiral angle, the outer wall diameter and chiral angle, and the energy level of the excitation. While these works provide insight into the complex and relatively unknown interactions between the constituent walls of incommensurate DWCNTs, there is still much that is yet to be understood.

3. The Characterization Problem

Absorption, PL, and Raman spectroscopy are the most commonly employed characterization techniques for SWCNTs and rely on an assumed relationship between structure and properties.[56] This relationship has afforded a well-documented library of nanotube optical and Raman transitions that allow for the easy identification of SWCNT species.[5,56–62] As DWCNTs are a coaxial arrangement of two SWCNTs, they exhibit similar optical and Raman features to the individual constituent nanotubes. The commonality of transitions often results in the application of the SWCNT library to DWCNTs; however, this can be problematic. One reason is that, in the case of DWCNTs, convolution of the inner and outer wall optical transitions occurs, which, in combination with the presence of additional SWCNTs, makes the identification of the constituent wall type difficult. Unfortunately there is no clear optical absorption feature exclusively indicative of DWCNTs. This problem can be demonstrated using material that consists of DWCNTs (1.5–2 nm) as well as small- (0.8–1 nm) and large-diameter (1.5–1.8 nm) SWCNTs as impurities.[21,34,35,63] In such material, the outer wall of a DWCNT has first-, second-, and third-order semiconducting transitions (S_{11}, S_{22} and S_{33}) at ca. 2000, ca. 1150, and ca. 600 nm and inner wall transitions at ca. 1050, ca. 650, and ca. 350 nm. It is clear that the S_{22} of the outer wall and S_{11} of the inner wall overlap, and likewise the S_{33} of the outer wall with the S_{22} of the inner wall. Further complicating the absorption measurements is the presence of the metallic M_{11} transitions of the inner and outer walls at ca. 550 and ca. 800 nm. The optical transitions of large-diameter SWCNT contaminants also share the same region as those of the DWCNT outer walls; whilst the optical transitions of the small-diameter SWCNTs share the same region as those of the DWCNT inner walls. **Figure 3** shows an example of the absorption spectra of small-diameter SWCNTs, large-diameter SWCNTs, sorted SWCNTs, and sorted DWCNTs, where the overlap of transitions between the small- and large-diameter nanotubes can be clearly seen.

Additionally, owing to strong absorption by water above 1400 nm, the S_{11} of the outer wall cannot be seen in a typical solution absorption measurement without the use of D_2O to extend the solvent window.[64] Consequently, without the corresponding S_{11} transition, interpretation of S_{22} and S_{33} transitions for (*n*,*m*) identification is difficult. This issue can be resolved with the use of thin films, as seen in Figure 3. However, the spectra can differ significantly from solution measurements, where the nanotubes are present in the isolated/individualized state. This is because the excitonic properties of the nanotubes are highly sensitive to many-body interactions, Coulomb interactions, and charge transfer between adjacent nanotubes in bundles.[65] Indeed there are many examples in the literature of discrepancies between solution and substrate-bound nanotube peak positions of up to ca. 50 meV.[55]

For DWCNTs, shifts in peak position are also seen on the individual nanotube level due to the effects of strong inter-wall coupling between the constituent walls.[19] Unlike SWCNTs, the optical spectra of DWCNTs are also affected by the relative

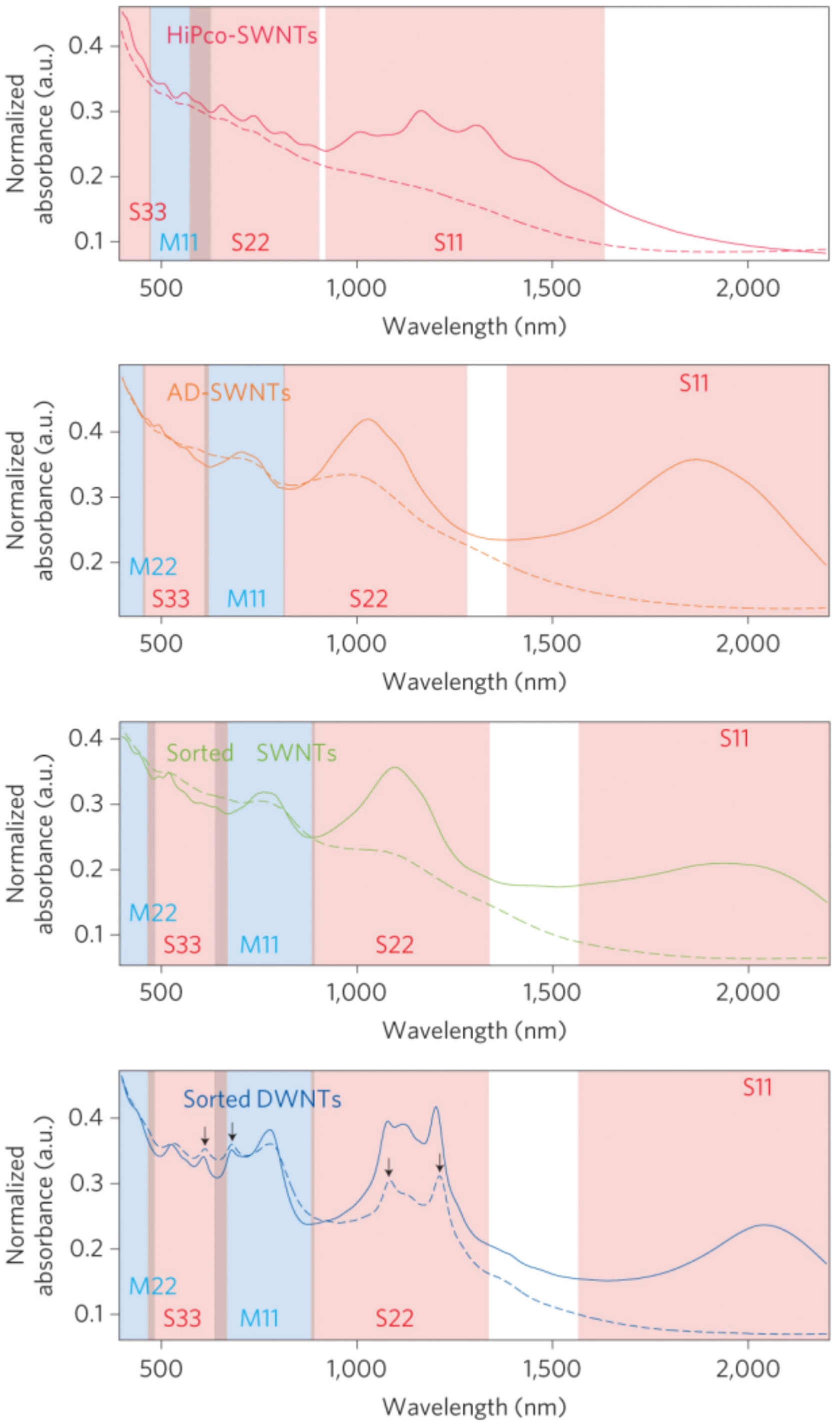

Figure 3. The absorbance spectra of films of HiPco SWCNTs (small diameter), arc-discharge (AD) SWCNTs (large diameter), sorted AD SWCNTs, and sorted DWCNTs before (solid curves) and after (dashed curves) doping with thionyl chloride. The first-, second- and third-order semiconducting optical transitions of the SWCNTs and the DWCNT outer wall (shaded red) are labelled S_{11}, S_{22}, and S_{33}, and the first- and second-order metallic transitions (shaded blue) are labeled M_{11} and M_{22}. For SWCNT materials, thionyl chloride doping completely suppresses the S_{11} transitions and significantly attenuates the S_{22} and M_{11} peaks. The sorted DWCNT film maintains several strong peaks (indicated by the arrows) in the S_{22}, S_{33}, and M_{11} regions that are attributed to inner walls of DWCNTs. Reproduced with permission.[34] Copyright 2009, Nature Publishing Group.

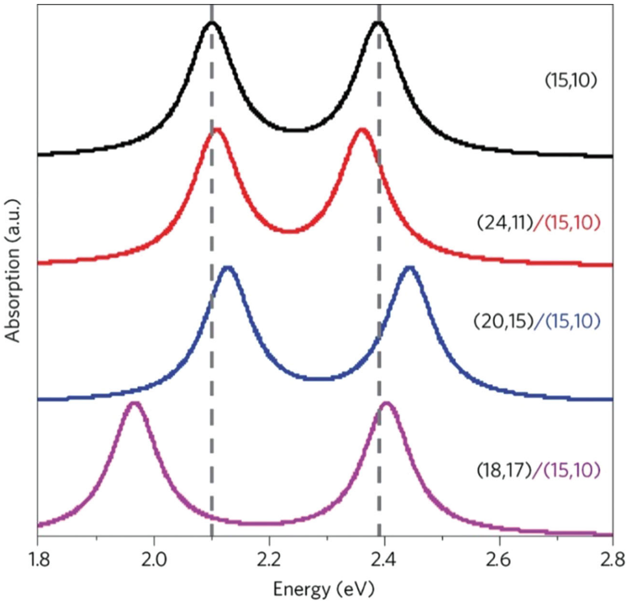

Figure 4. The effect of inter-wall coupling on the optical transitions of DWCNTs. Optical resonances (S_{33} and S_{44}) from the (15,10) nanotube show a significant energy shift. The amplitude of the energy shift depends sensitively on the specific optical transition and the outer nanotube species, and can be either positive or negative, with a magnitude as large as 150 meV. Reproduced with permission.[18] Copyright 2014, Nature Publishing Group.

handedness of the constituent walls i.e., the S- or R- stereoisomers.[18] This arises due to obvious differences in inter-wall coupling experienced by DWCNTs of different relative handedness. Overall, the effects of inter-wall coupling can produce unusual variations in the optical spectra, making chirality assignment based on the known optical properties of SWCNTs problematic. An example of this is given in **Figure 4**, which shows the third- and fourth-order optical transitions (S_{33} and S_{44}) of the (15,10) nanotube, both on its own (i.e., as an SWCNT) and when contained within the outer walls of various (*n,m*) indices. The different inter-wall coupling within the various (15,10)@(n_o,m_o) combinations significantly alters the peak position.

Notwithstanding the variance in peak position from the expected SWCNT transitions, it is possible to perform doping experiments wherein the origin of the transitions, whether from the inner or outer wall, can be elucidated by observing the effect of the doping on the optical transitions.[34–36] In theory, only the inner wall transitions should remain active due to shielding by the outer wall, and comparison between spectra before and after doping should allow for inner and outer wall identification. However, in practice such shielding is incomplete[66] and can often introduce a new level of uncertainty. The data in Figure 3 also show the optical absorption spectra of different DWCNTs before and after chemical doping with thionyl chloride. For each nanotube of different diameter, the S_{11} transition is completely depleted by the doping due to a shift of the nanotube Fermi level into the highest occupied molecular orbital (HOMO) as a result of the withdrawal of electrons by the powerful oxidizer.[34–36] In the case of the large-diameter nanotubes (denoted “AD” for the arc-discharge method of synthesis), significant attenuation of the S_{22} transition also occurs, and in the case of DWCNTs, this attenuation of S_{22} reveals the underlying S_{11} transitions corresponding to the inner walls. Whilst this cannot be used for chirality assignment, subtraction of the inner wall spectra obtained after doping from the convolution spectra of both inner and outer walls measured before doping has been used for determination of the electronic purity.[35] In a similar manner, doping/oxidation experiments can also be used in conjunction with Raman measurements.[34–36,67]

In Raman spectroscopy, the effect of inter-wall coupling can be clearly seen when comparing the SWCNT radial breathing modes (RBMs), which have a well-established relationship with the nanotube diameter, to those of DWCNTs. For a specific (n_i,m_i) inner wall nanotube, a cluster of RBMs with almost the same resonance energy is observed,[6] spanning an 18 cm^{-1} frequency range.[68] This cluster arises from the same (n_i,m_i) nanotube residing within multiple (n_o,m_o) outer walls, with the RBM shift dependent upon the strength of the inter-wall interaction.[69] This makes chirality assignment based on RBM frequency unreliable. Furthermore, the RBMs of DWCNT inner walls can have significantly narrower line widths than those usually observed for similar diameter SWCNTs (typically 12 cm^{-1}), with some DWCNT RBM line widths being as small as 0.4 cm^{-1}.[70] This is because the inner walls can be remarkably defect-free owing to the protective nature of the outer wall, and thus exhibit very long phonon lifetimes.[6]

Circumventing the aforementioned difficulties in exact chirality assignment using optical absorption or standard Raman spectroscopy, a new approach has been presented by Kalbac and co-workers to discern the ratio of single- to double-walled nanotubes using Raman spectro-electrochemistry.[71] This technique exploits the diameter dependence of the high frequency, two-phonon mode (G′), which is an overtone of the disorder-induced mode (D band).[72] While both modes demonstrate a dependence on diameter, the dependence is stronger for the G′, as is its intensity arises due to different selection rules.[73] This diameter dependence results in a DWCNT-specific doublet where the higher-frequency component corresponds to larger-diameter outer walls and the lower frequency component to smaller-diameter inner walls. Upon electrochemical doping, nanotubes in direct contact with a working electrode or with compensating electrolyte counterions (SWCNTs or DWCNT outer walls) experience an upshift in frequency as well as peak broadening. In the case of SWCNTs, all nanotubes are doped and the observed peaks are upshifted. In DWCNTs however, the inner walls are protected and only the outer-wall G’ peak is upshifted. Thus, the electrochemical doping accentuates the splitting and enables distinction of SWCNTs/outer walls from inner walls.[71] By comparing ratios of pure SWCNTs and DWCNTs and employing a model relating the peak area to the nominal composition, it is therefore possible to determine the contaminating SWCNT percentage. This technique offers the advantage of reproducible and precisely controlled doping compared with traditional chemical doping strategies[71] and, furthermore, results in a clear difference between the contribution of DWCNT inner walls and SWCNTs.

In terms of obtaining structural information, scanning tunneling microscopy (STM)[74] and transmission electron microscopy (TEM) are obvious choices as they can overcome the limitations of optical and Raman spectroscopy; however, TEM is considered the definitive tool for DWCNT measurement. TEM can achieve quantitative characterization of the real mean diameter of both the inner and outer walls, indications of the relative concentration of DWCNTs within a mixed sample containing single- and/or multi-walled contaminants, and the real diameter distribution and its standard deviation.[75] Additionally, by combining TEM with electron diffraction it is possible to determine the (*n,m*) type of the two constituent nanotubes in a DWCNT.[10] Unfortunately, TEM is time consuming and does not give a complete overview of the entire nanotube population under investigation nor does it provide any electronic information. The preparation of uniform samples that accurately represent the population can be difficult; surfactants are usually required to individualized nanotubes, but the presence of surfactant can introduce sample bias due to differences in surfactant wrapping of tubes and resultant interactions with the substrate during sample preparation. Therefore, unless the prepared DWCNT sample can be reliably assumed to be extremely uniform and fully representative, calculated (*n,m*) indices for individual nanotubes cannot be conclusively extrapolated to the entire ensemble. It is reasonable to assume that cryoTEM,[76] in which thin slices taken directly from the frozen nanotube suspension are analyzed, may circumvent this difficulty, but the technique has not yet been widely applied to DWCNTs. Thus, as a compromise, a combination of absorption techniques in conjunction with TEM is typically used to characterize DWCNT samples.

4. Synthesis Methods

4.1. Arc Discharge

The arc-discharge method was first used to prepare carbon nanotubes in 1991 by Iijima whilst attempting to synthesize C_{60}.[77] The synthesis technique involves applying a voltage and current between two closely spaced (typically 1–2 mm), highly pure graphite electrodes in an inert atmosphere. Typically, the anode is partially hollowed and filled with carbon feedstock (usually graphitic powder) and a catalyst/promoter, of which there are many combinations depending upon the desired product. Upon application of a current (steady state or pulsed), a plasma forms between the electrodes. Random collisions between the carbon atoms, catalyst particles, and gas then result in the formation of carbonaceous material as a macroscopic deposit on the cathode, as well as the reactor walls. Fullerenes and carbon nanotubes of varying types can be found within this carbonaceous soot.[78] The type of carbon nanotube produced can be tailored to be single-, double- or multi-walled through careful control of catalyst composition, atmosphere, current/voltage conditions, and carbon feedstock. This field is vast, but some significant reports on the optimization of these growth conditions to yield DWCNTs are now discussed.

Hutchison et al.[23] were the first to selectively synthesize DWCNTs with the steady-state arc-discharge method in 2001. They used a mixture of Ni, Co, and Fe catalyst within the graphite anode in an Ar/H_2 atmosphere with varying amounts of S included as a growth promoter. The resultant DWCNTs had a purity varying from ca. 10% to 70% and at the end of their study the authors concluded that the presence of S in the catalyst was not critical to the formation of DWCNTs. However, in later work by Saito et al., the presence of S as a growth promoter was concluded to be indispensable for the production of DWCNTs.[29] They also concluded that the catalyst must contain Fe and that H_2 was of vital importance for DWCNT production. Upon optimizing the catalyst (FeS:NiS:CoS = 1:1:1) and the atmosphere composition, the highest purity achieved was ca. 90% DWCNTs with the average outer diameter ranging from 2 to 5 nm. The presence of halides can also improve the yield of DWCNTs, as demonstrated by Qiu et al. using steady-state arc discharge in a hydrogen atmosphere.[25] Through the introduction of chloride (specifically KCl) to the catalyst mix, they achieved an increased yield of DWCNTs (10 wt% without KCl to 50 wt% with KCl) with a purity of 90%.

While an atmosphere containing H_2 is now commonly employed, it is possible to achieve DWCNT growth without the presence of reactive gases. Huang et al.[79] prepared DWCNTs without H_2 by customizing the shape of the cathode to a bowl-like structure. Using the now well-established catalysts of Ni, Co, Fe, and S, they demonstrated the growth of DWCNTs with a purity of ca. 80%. The DWCNTs possessed improved oxidation resistance compared to conventionally prepared arc-discharge- or catalytic chemical-vapor-deposition-produced DWCNTs, owing to the large hot region within the bowl-like cathode. This hot region allowed for in situ annealing or "defect-healing" of the DWCNTs. A report of DWCNT synthesis by Sugai et al. demonstrated the first use of high-temperature pulsed arc discharge without H_2.[24] Contrary to the steady-state methods, pulsed arc discharge also allows for DWCNT production without the presence of Fe and S. In this case, an Y/Ni catalyst commonly used in the formation of SWCNTs was used,[30,80] however a change from preferential formation of SWCNTs to DWCNTs occurred due to the increased temperature. It has been shown that the SWCNT diameter increases with increased temperature until 1200 °C, at which point the nanotube reaches a critical diameter and DWCNTs become the favored product. Owing to the highly controlled arc conditions (600 µs pulse at 50 Hz), small-diameter DWCNTs (1.6–2.0 nm) could be produced. Similarly, Zhao et al. also demonstrated the growth of DWCNTs without the presence of H_2 (or any expensive high-purity gases) with a steady-state arc-discharge approach.[81] In that work, Fe was used to catalyze the growth reaction with S present as a promoter, while dry air flowed throughout the reaction at reduced pressure. The authors showed that DWCNTs were the dominant product with diameters ranging between 3 and 7 nm, but that SWCNTs and triple-walled carbon nanotubes (TWCNTs) were also present, as well as a considerable amount of other carbonaceous material. Whilst the gross DWCNT purity is significantly reduced without the presence of H_2 (only 20% was reported by Sugai et al.[24] and no purity was estimated by Zhao et al.,[81] such a route offers the advantages of reduced cost and a simpler growth process, and minimizes the dangers associated with large-scale application of H_2 gas. In the future, the issue of low purity may be addressed through further optimization or post-growth purification strategies.

Although catalyst composition and reaction atmosphere are critically important for DWCNT growth and much work to date has been focused on these aspects, the literature also contains studies into the effect of the composition of the carbon feedstock. Li et al. demonstrated that MWCNTs/CNF (carbon nanofibers) can be successfully used to grow high-purity DWCNTs by steady-state arc discharge in a H_2 atmosphere.[82] The anodic carbon feedstock (usually high-purity graphite >99%) was substituted with the MWCNT/CNF mixture, which had a diameter range of 40–220 nm. The authors found that DWCNTs produced from MWCNTs/CNFs were of higher quality than those prepared by graphite powder using the same process and they determined the DWCNT purity to be 83% with the outer diameter ranging from 1.75 to 4.87 nm. Recently, Xu et al. demonstrated that asphalt[83] and petroleum coke[84] could also be used as the carbon feedstock in lieu of high-quality (and very expensive) graphitic powders. In both of those cases, Fe was used as the catalyst and, in the case of petroleum coke, an Ar atmosphere was shown to lead exclusively to the production of DWCNTs with diameters of 3–4.4 nm.

While arc-discharge methods can produce high-purity DWCNTs (up to 90%[29]) with few structural defects, it is limited to large diameters and provides low yield. For instance, arc-discharge methods generally produce nanotubes with diameters >2 nm. Although these may be desirable for some applications, large diameters are not easily characterized using Raman or absorption spectroscopy owing to limitations in the spectral windows, and very large diameters (>4 nm) can easily collapse.[85] Currently, the mean diameter distribution can be reduced through the use of pulsed arc-discharge methods to give nanotubes with diameters of 1.6–2 nm; however, this comes at great expense to the yield, which is significantly reduced to only 10%.[30] This is quite low compared to the yields of steady-state methods employing H_2, Fe, S, and halides, which produce large-diameter DWCNTs of up to 50%.[25] While the arc-discharge method may be limited to large diameters currently, future investigation into the thermodynamics and kinetics of growth, as well as the role of growth promoters, may lead to a higher level of control over the diameter.

4.2. Peapod Growth

DWCNTs can be grown by the so-called "peapod" method by first encapsulating a precursor material within an SWCNT and subsequently treating it to induce coalescence and thereby form an inner wall. The first report of this technique was by Smith et al.,[86] who observed that during the pulsed vaporization of graphite, a technique previously reported to synthesize SWCNTs and fullerenes,[87] C_{60} and C_{70} can become trapped inside appropriately sized SWCNTs. In situ TEM revealed that the fullerenes were deposited on the surfaces of the nanotubes from the gas phase and were seen to enter the nanotubes via the uncapped ends or through defect sites. Once inside the nanotubes, the fullerenes self-assembled into chains, called "bucky-peapods" with uniform center-to-center distances. After extended exposure to a 100 kV electron beam or, as later discovered, temperatures above 1100 °C,[26] the fullerenes coalesced to form the inner wall of a DWCNT with a nearly uniform inter-wall spacing of 0.3 nm. An in-depth investigation into the temperature dependence of the DWCNT formation conducted by Bandow et al. determined that the process of coalescence only occurs at temperatures above ca. 800 °C, becomes better with increasing temperature, and is complete at ca. 1200 °C.[88] The authors further report that other fullerenes, such as C_{76}, C_{78}, and C_{80}, can be used as a precursor material and that the diameter of the resultant inner tube is determined solely by the diameter of the parent wall, irrespective of the fullerene size. Thus, other carbon-containing aromatic precursor materials could very well be used for DWCNT formation, provided that they can be encapsulated by the parent nanotube. Indeed, there are several reports of SWCNT encapsulation of ferrocene[89] which further enables the introduction of a metal catalyst.[90]

Recently, peapod growth has been demonstrated by photon-induced decomposition of fullerenes.[27,91] With the use of a UV laser, Berd et al.[92] irradiated C_{60} peapods with photons of energy higher than that of the fullerene bandgap (1.7 eV for C_{60}) resulting in C_{60} fragmentation.[93] Berd et al.[92] determined the optimum laser excitation was 3.7 eV, which effectively achieved coalescence of the encapsulated C_{60} molecules while maintaining the structural integrity of the parent nanotube. This technique was claimed to be advantageous for nanoelectronic applications as it allows for in situ growth of DWCNTs at room temperature and in ambient conditions,[27,91] but, of course, most conceivable nanoelectronics applications will be exquisitely sensitive to the type of inner wall that is grown. This means that this technique has questionable real-world applicability unless the type of nanotube that is grown can be finely controlled.

The peapod growth method affords very high quality DWCNTs[70] that are clean of residual catalyst and enable the production of very thin DWCNTs (theory predicts diameters as small as 1.174 nm can be filled with C_{60}.[94] Purities of ca. 90% can be achieved, with the only source of contaminant being SWCNTs.[92] However, the method still requires small-diameter SWCNTs to first be synthesized, purified, and carefully processed to allow for the introduction of the precursor material.[95] There is also the issue of unfilled SWCNT contamination, which must currently be addressed post synthesis (although process refinements could likely address this issue in full). Such costly, time consuming, and inherently wasteful steps add significantly to manufacturing complexity, reducing the viability of commercial application and meaning that peapod growth will likely remain limited to small-scale research applications for the foreseeable future. Furthermore, poor filling of the parent outer wall with the coalesced inner wall remains an issue in that theoretical calculations predict that when the fully packed C_{60} molecules inside the parent nanotube have completely transformed, only ca. 2/3 of the parent nanotube has been filled, leaving empty space.[88] However, it is conceivable that this could be a distinct advantage in certain applications requiring non-standard on-tube changes in electronic properties, which could in theory be moved back and forth along the outer wall through control of the position of the inner wall, or similarly in nano-electromechanical systems (NEMS).

4.3. Catalytic Chemical Vapor Deposition

In catalytic chemical vapor deposition (CCVD) growth, a volatile gaseous carbon source (typically CH_4, CO, or C_2H_2) is decomposed at high temperature over metallic nanoparticles. The decomposed carbon atoms diffuse into the metal nanoparticles and, upon saturation, precipitate at the surface and initiate nanotube growth directly from the nanoparticle. Thus, the catalyst particles simultaneously act as nucleation points for nanotube growth and provide catalytic enhancement. The earliest report of CCVD growth was in 1976 by Oberlin et al., who decomposed benzene in a H_2 atmosphere at 1100 °C to produce nanotubes with diameters ranging from 2–50 nm, although these were not recognized as such at the time.[96] Later, Dai et al. used catalytic decomposition of CO over nanometer-sized Mo particles at 1200 °C to form individual SWCNTs with diameters ranging between 1 and 5 nm and realized that the diameter of the catalytic particles closely correlated to the diameter of the resultant nanotubes.[97] This correlation was further investigated by Cheung et al., who synthesized nanotubes using 3, 9, and 13 nm catalyst particles with C_2H_2 or CH_4 as the carbon source at a temperature of 800–1000 °C.[98] It was found that when the catalyst particles were small, the resultant nanotubes were primarily SWCNTs with ca. 30% DWCNTs. By increasing the size to 9 nm, SWCNTs, DWCNTs, and MWCNTs were produced. Finally when the catalyst particles were large (13 nm), only MWCNTs were produced. The shape of the catalyst is also important, as shown by Liu et al., who grew DWCNTs from CH_3 decomposition over porous Fe/MgO.[99] Through application of external pressure, the pore size was varied and the growth of the DWCNTs was found to be highly dependent on the pore size of the catalyst, with pores less than 30–50 nm producing only MWCNTs. It was proposed that the compression and small pore size resulted in deformation and agglomeration of the metal nanoparticles, yielding MWCNTs and carbon capsules. Furthermore, the pore size can physically hinder the growth of DWCNTs when the length of the DWCNTs reaches the depth of the pore. At this point growth can be terminated, extend into the catalyst structure, or buckle and change direction. Thus, large pore size or a loose stacked structure is best when using porous catalyst. However, the deliberate growth of high-purity DWCNTs is not as straightforward as simply controlling the catalyst size or shape and other factors such as catalyst composition,[100,101] temperature,[102,103] atmosphere,[104] and growth templates[105,106] also play pivotal roles.

The importance of catalyst composition was investigated by Hafner et al., who synthesized SWCNTs and DWCNTs from the catalytic decomposition of both CO and C_2H_4 using nanometer-sized alumina and Mo as the catalyst.[102] Only SWCNTs of monodisperse diameter were produced; however, when Fe was introduced into the catalyst mixture, the reaction also produced DWCNTs, highlighting the effectiveness of Fe for catalyzing DWCNT growth. Currently, Fe remains the most commonly used catalyst owing to its catalytic activity for the decomposition and formation of metastable carbides and because carbon is able to rapidly diffuse through and over the metal surface.[107] However, there are examples of other transition metal catalysts producing DWCNTs, such as by Flahaut et al. who used MgCoO catalyst.[108] They demonstrated gram-scale growth of DWCNTs (up to 1.3 g from 10 g of catalyst) using CH_4 as the feedstock by the inclusion of Mo in the catalyst mixture, which had already been shown to increase the yield of nanotube production.[109] It was later demonstrated that the preparation route for the catalyst was of equal importance as the catalyst composition itself.[101] By altering the synthesis route of MgCoMoO from urea-based combustion to citric-acid-based combustion (a milder combustion process) the catalyst had a higher specific surface area and improved homogeneity, resulting in almost 80% DWCNT growth. Similar to the arc-discharge method, the addition of S as a growth promoter can also change the reaction preference from SWCNTs to DWCNTs. This was investigated by Ci et al. for CCVD growth from C_2H_2 decomposition at 900–1100 °C.[110] It was reported that the growth of DWCNTs was strongly dependent on S addition and, without its inclusion in the catalyst material (ferrocene), only SWCNTs were produced. This was also the first report of CCVD synthesis of DWCNTs using a “floating catalyst”, a popular variation of CCVD used for SWCNT growth, which involves subliming the catalyst into the gas phase rather than using substrate-bound form and offers the advantage of producing very long nanotube ropes.[111] Further improvements in DWCNT purity can be achieved through temperature control.[102] It is found that by simply increasing the growth temperature from 700 °C to 850 °C, the production of DWCNTs increased from a composition of only 30% to 70%.

CCVD can be used as a means to grow DWCNTs in vertically aligned forests, which allows for their direct integration into applications such as sensors[112] and field emitters.[113–116] The first demonstration of vertically aligned DWCNTs grown on flat substrates was by Yamada et al. using water-assisted CCVD.[117] This was achieved using Fe-Al_2O_3 (30 nm)/SiO_2 (600nm)/Si, with C_2H_4 as the carbon feedstock, and a DWCNT purity of 85% was produced. The high purity was attributed to enacting precise control over the Fe catalyst film thickness, which largely determines the size of the catalyst particles formed upon heating. This was further investigated by Ci et al. who produced high-purity DWCNTs (88%) using Fe films on an Al support layer with C_2H_4 feedstock at 700–850 °C.[118] It was determined that an Fe film thickness of 1.5 nm deposited onto 10 nm of Al provided the greatest selectivity towards DWCNT growth. The optimized growth conditions resulted in ultra-low-density arrays due to the very large diameter of the resultant DWCNTs (7.9 nm) and the low catalyst particle density. Ultra-long, super-aligned DWCNT forests have been reported by Kim et al. with lengths of 9 mm in 10 h of growth time.[119] This was achieved by first reducing the catalyst (Fe film (1 nm)/Al_2O_3 (30 nm)) by exposure to a He/H_2 atmosphere at 750 °C. The reduction time had a significant effect on the density and size of the catalyst particles and ultimately changed the quality and alignment of the nanotubes forests, where, at 5 min of reduction time, the catalyst formed the smallest grain size, leading to the highest-quality growth.

Due to CCVD's compatibility with a wide variety of substrates, researchers are also focused on preparing aligned DWCNT arrays on substrates more easily integrated into electronics, such as silicon or gold. For instance, Chen et al. produced vertically aligned DWCNT arrays using point-arc microwave plasma CCVD to allow for direct measurement of field-emission properties.[114] In that work, a three-layered catalyst of Al_2O_3/Fe/Al_2O_3 (0.5 nm/0.8–1 nm/5 nm) was deposited onto both Cr (100 nm)/Si and SiO_2 (200 nm)/Si. The trilayer catalyst provides two functions: the thicker, bottom Al_2O_3 layer acts as a barrier, preventing the Fe catalyst from reacting with the underlying substrate; the thin, top Al_2O_3 layer serves to increase the surface diffusion barrier of the Fe atoms so as to suppress aggregation. Growth of the DWCNTs occurs via the decomposition of CH_4 in a hydrogen atmosphere at 600 °C, yielding outer diameters of 2.5–3.8 nm. It was determined that the Cr/Si substrate achieved a higher nanotube density, but had a lower growth rate than the SiO_2/Si substrate. This was attributed to the SiO_2 accumulating heat during the plasma radiation exposure. Importantly, when growing DWCNTs for direct integration into electronic applications, good contact between the DWCNTs and underlying substrate is essential. Chen et al. determined that the presence of Cr provided less resistance (compared to the SiO_2) and the DWCNT/Cr/Si surface demonstrated superior field emission. Liu et al. later showed that SiO_x (30 nm) deposited onto SiO_2 (100 nm)/Si surfaces could be directly used to catalyze DWCNT growth.[120] It was determined that the critical factors for growth were the thickness of the deposited SiO_2 layer and pre-growth heat treatment, which both affect the size of the resultant SiO_x catalyst particles and, in turn, the number of walls. Nanoparticles in the range of 3–5 nm (annealed for 10 min at 850 °C in Ar atmosphere) were found to be the most effective for DWCNT growth, achieving a purity of 70%. Growth directly on conducting metal foils has been reported by Iijima and co-workers, with Ni-based alloys containing Cr or Fe found to be best for DWCNT and SWCNT growth.[106] In that work, an Al_2O_3 (30 nm)/Fe (1 nm) catalyst layer was deposited onto various metal foils and then exposed to C_2H_4 in a H_2O/He atmosphere at 750 °C. By selectively tuning the catalyst thickness to 1.8 nm, DWCNTs were produced and measurement of the field-emission properties confirmed that good electrical contact had been established. As well, Fu et al. demonstrated that DWCNTs could be grown on catalyst (Fe/Al_2O_3)-coated Au films for use as field-effect emitters.[121] This was done by first reducing the catalyst in a H_2 atmosphere before introducing C_2H_4 at 700 °C.

CCVD is the most commonly used growth method to produce DWCNTs as it offers high yields, is cost effective and controllable, and is appropriate for industrial-scale production. Furthermore, the ability to grow nanotubes on a substrate enables direct integration into some applications, as well as ease of collection. However, despite considerable advances in favoring the growth of DWCNTs over other species, CCVD growth cannot yet be tuned to generate a specific DWCNT type and instead produces a heterogeneous mixture of DWCNTs with small- and large-diameter SWCNTs and even triple- and multi-walled contaminants, as well as amorphous carbon and remnants of metal catalyst. The slow development is in part due to the time-consuming nature of the experiments, where each CCVD run can take an entire day to complete and characterize, as well as the large parameter space of the CCVD process itself. Recently, Nikoleav et al. reported the use of automated experimentation as a means to overcome this cumbersome approach and conduct over 100 water-assisted CCVD growth cycles in a single day.[122] The adaptive and rapid experimentation system, equipped with in situ Raman spectroscopy, is capable of mapping regions of selectivity toward SWCNT and MWCNT nucleation and growth in a four-dimensional parameter space from only a limited number of input experiments. From this, the authors conclude that “perfect” selectivity does not exist because the probability of growing either SWCNTs or MWCNTs is never zero when the parameters are optimized to maximize growth of the other; therefore, the typical product is always a mixture of nanotube types.

5. Processing and Sorting

The field of DWCNT processing is still in relative infancy compared to the more extensively investigated field of SWCNTs. In some ways, the sorting of DWCNTs could be viewed as an extension of already-established SWCNT sorting techniques; however, even at this early stage of development, important differences are apparent and these will only become more prominent as researchers refine the specificity of their methodologies toward the ultimate goal of sorting by inner wall character. The discussion that follows is thus necessarily dominated in some parts by the descriptions of progress in SWCNT sorting. Where SWCNT sorting techniques have been utilized for DWCNTs, some notable results are presented, and in all cases the applicability and potential benefits in relation to DWCNT sorting are analyzed. Unless new techniques are developed that provide for targeted growth of highly pure DWCNTs of desired type, there is a clear need to improve the purity of as-produced DWCNT material in order to unlock their potential in useful applications. This can be achieved through several different approaches, where each approach targets certain contaminants. These approaches can be broadly grouped into two categories: purification, which involves the crude removal of amorphous carbon, fullerenes, SWCNTs, MWCNTs, and any remaining catalyst through chemical or thermal treatment; and sorting, where molecular control is enacted to finely refine the desired product according to requirements e.g., the preparation of material with exclusively semiconducting outer walls.

5.1. Purification

Several treatments can be applied post-synthesis to improve the purity of raw DWCNT material by selective removal of contaminants. For example, the pulsed arc-discharge method of Sugai et al. reported only 20% DWCNT purity due to the presence of fullerenes, SWCNTs, and amorphous carbon contamination.[24] Following purification, they were able to dramatically increase the DWCNT purity to ca. 90%. In their purification strategy, the as-prepared material is first washed with CS_2, a solvent known to selectively solubilize fullerenes, allowing their removal by standard laboratory separation techniques.[123] Residual catalyst particles are then dissolved via sonication in concentrated acid; in this case HCl. Treatment with various acids has been used extensively to purify SWCNTs and has been shown to effectively remove metal particles from as-grown nanotubes.[124] However, the process inevitably results in functionalization of the nanotubes to some degree, depending on the temperature and length of exposure. The amorphous carbon and SWCNT material were then removed via subsequent high temperature air oxidation at 500 °C for 1 h. As the SWCNTs have the same average diameter as the DWCNTs (ca. 2 nm), the authors conclude that the greater thermal stability of the DWCNTs originates from a higher degree of graphitization (with fewer defects) and from interactions between the inner and outer walls. The same group later quantified this effect by determining that under optimized conditions the oxidation rate of DWCNTs is half that of SWCNTs of the same diameter (1.6 nm); hence, SWCNTs are preferentially oxidized and removed.[30] Purities can be greatly improved (from 10% up to 90%) however some hollow and metal-filled carbon capsules remain even after HCl treatment and cannot be removed. Furthermore, it has been reported that hot air oxidation exhibits a selectivity toward metallic SWCNTs, with semiconducting species still remaining after 4 h at 420 °C, highlighting the need for the correct oxidation temperature in DWCNT purification.[125] However, no reports of air oxidation of DWCNTs specifically measure the electronic properties of the remaining SWCNTs; thus, it is unclear how the preference for metallic oxidation affects the remaining SWCNT population. While air oxidation can effectively remove amorphous carbon and SWCNTs in optimized conditions, and offers the advantage of oxidation without the introduction of sidewall defects, it can result in destruction of the nanotubes at temperatures above 750 °C.[126] Alternatively, refluxing in H_2O_2 for 12 h can also be used to oxidize unwanted SWCNTs, as demonstrated by Yoshida et al., who saw a dramatic improvement in DWCNT purity from only 10% initially to 95% after refluxing.[30] As with acid treatment, some oxygen-containing moieties are introduced at defect sites within the lattice,[127] but to a much lesser extent, and Raman studies show a dramatic decrease in the amount of amorphous carbon present.[128] Similar to hot air oxidation, the H_2O_2 also exhibits a preference to attack nanotubes of specific electronic character; however, in this case it is toward semiconducting character. This is evidenced by the H_2O_2 treatment of SWCNTs resulting in a population of ca. 80% metallic composition after ca. 1 h.[125] In the DWCNT case, refluxing in H_2O_2 is for a significantly increased duration and it is unclear whether or not metallic SWCNTs remain after such an extended time. However, one can conclude that, since air oxidation and H_2O_2 exhibit a preference toward metallic and semiconducting SWCNTs, respectively, a combination of the two may prove to be an efficient purification strategy.

5.2. Suspension

All sorting strategies share one commonality, namely the requirement for the production of suspensions of individualized carbon nanotubes in either water[58,61,129,130] or organic solvents.[131,132] This is achieved through either covalent[20,31,133] or non-covalent methods.[76,129,134–136] Covalent chemistry routes involve the introduction of functional groups to the nanotube ends and sidewalls, rendering them soluble.[31,137] Such processes are extremely good at producing well-dispersed, individualized nanotube suspensions, and often also exhibit some selectivity toward certain diameters[31,138] or electronic types,[139] which can provide useful routes toward separation based on these characteristics. However, covalent functionalization is often disadvantageous as it causes disruption of the conjugated π system of the nanotube by introducing sp^3 hybridization into the pristine sp^2 network.[22] Non-covalent approaches include the use of surfactants such as sodium cholate (SC) or sodium dodecyl sulphate (SDS),[60–62,130,140–143] or dispersing agents such as DNA[58,144–146] and organic polymers.[131,132,147,148] Dispersion of the nanotubes in these stabilizing agents is achieved via ultrasonication and often followed by centrifugation to remove remaining bundles and residual catalyst particles.[136]

For surfactant-stabilized dispersions, the surface concentration and orientation of surfactant molecules on the nanotube sidewalls is highly dependent upon the type of surfactant, the concentration in solution, and the diameter and electronic type of the nanotube.[60,62,140,149–153] Generally, the surfactant first forms a random layer and, as more surfactant molecules bind to the surface, begins to form hemimicelles. Further addition of surfactant can cause the formation of a highly packed cylindrical micelle.[154] However, this varies for different diameters, with smaller nanotube diameters exhibiting less-ordered surfactant structures.[149] For example, SDS wrapping of small-diameter nanotubes (<1 nm) tends to result in highly disordered, random configurations at low SDS concentrations (packing densities of ca. 1.0 molecules nm^{-2})[155,156] and more-ordered, cylindrical wrapping at high SDS concentrations (2.8 molecules nm^{-2}).[155] The wrapping of large-diameter nanotubes (>1 nm) is also disordered at low concentration but forms hemimicelles at high SDS concentration.[155,156] Experiments suggest that the correlation between nanotube structure and wrapping is due to differences in the surface π-electron states of the various SWCNT curvatures, which affect the SDS/nanotube interaction.[60] When an SDS molecule wraps around a small-diameter nanotube with a large bond curvature, it encounters a larger energetic barrier due to bending.[156] Therefore, it is energetically more favorable for the SDS to adsorb to larger-diameter nanotubes with smaller curvatures, which is an underlying principle of several of the sorting methodologies described later.[140,155,157] The extent of SDS encapsulation is also dependent upon the electronic character, with metallic nanotubes having a higher degree of SDS wrapping than semiconducting nanotubes, owing to their higher polarizability.[61,140,152,158] Co-surfactant wrapping, which relies upon competitive non-specific binding between different surfactants e.g., SC and SDS, provides a further parameter that can be exploited for nanotube separation according to electronic character.[58,130,142,143]

Suspension of nanotubes with DNA[159–161] and proteins[32,162–165] relies primarily on strong π-stacking onto the nanotube sidewalls. This effectively individualizes the nanotubes and at the same time provides a negative surface charge density due to close proximity of the phosphate backbone to the nanotube.[159] As such, DNA is particularly suitable for solubilization of DWCNTs, with several examples seen in the literature.[135,160,161,166] Using DNA, SWCNTs have been sorted by electronic type[144,159] and (n,m) species[145] through the use of ion-exchange gels. Because they contain biological elements, such suspensions are highly dependent on the pH of the solution, which must be optimized to achieve well-dispersed nanotube suspensions of high concentration. Suspension in organic solvents is used in polymer separation and will be discussed in Section 5.9. Once a good suspension of purified nanotubes has been obtained, there are several techniques that have been developed to sort them using a number of different strategies with varying degrees of complexity, specificity, and success.

5.3. Reversible Covalent Chemistry

Because various covalent modification schemes are selective to nanotube diameter, such inherently scalable approaches are highly attractive for the purification and separation of DWCNTs. One such approach demonstrated by Deng et al.[31] involves the Billups–Birch reductive alkylcarboxylation reaction. That work involved covalently functionalizing CNTs with alkylcarboxylic acids groups progressively from smaller-diameter nanotubes towards larger diameters. Addition of these groups rendered the nanotubes water soluble and the diameter-dependent nature of the reaction allowed for standard phase separation in water–hexane. This resulted in partitioning of functionalized samples into different aqueous extracts of decreasing functionalization and solubility, commensurate with increasing diameter. As well as providing such diameter-selective separation, a further advantage of this kind of approach is the reversible nature of the reactions. In the case of alkylcarboxylation, the sorted nanotubes can be returned to their pristine state through simple annealing. Because wall number is closely correlated with diameter, reductive alkylcarboxylation can also be used to selectively remove single- and multi-walled nanotubes, as well as carbonaceous by-products, from as-synthesized DWCNT material.[167]

In the reductive-alkylcarboxylation method, raw DWCNT material is added to liquid NH_3 containing Na to individualize the nanotubes and enable homogeneity of the subsequent reaction. When Na is added to NH_3, it dissolves completely, with nitrogen lone pairs coordinating to the metal, yielding an electronic liquid comprising $[Na(NH_3)_x]^+$ complexes and free electrons. When nanotubes are added to the solution, the solvated electrons are transferred to the various nanotubes and (aromatic) carbonaceous material, providing a negative surface charge and producing "nanotubide" radical anions. In this way, the van der Waals forces holding the nanotubes in bundles are gently overcome by strong Coulombic repulsion, thus individualizing them.[31] Upon addition of 6-bromohexanoic acid, as in the work of Deng et al.,[31] (or any molecule with a halogen-terminated alkyl chain) a reduction reaction occurs adding alkylcarboxylic acid groups to the nanotube sidewalls. The diameter selectivity arises due to the difference in the Fermi levels of the nanotubes, wherein smaller-diameter nanotubes (with higher Fermi levels)[168] exhibit a greater reduction potential than larger ones. Hence, the reduction by solvated electrons occurs preferentially on the smaller-diameter nanotubes and, with careful control of the reaction stoichiometry, this can then lead to preferential addition of alkylcarboxylic acid groups to the smaller nanotubes.

In the work of Deng et al.,[31] three reaction cycles were completed, each starting with further addition of Na and alkylcarboxylate source, before phase separation in a water/hexane mixture. The more easily functionalized SWCNTs and amorphous carbon were separated into the aqueous fraction, while the less-functionalized DWCNTs and MWCNTs were enriched in the insoluble solid. Deng et al. also demonstrated that the reduction occurs by defect activation and propagates exclusively from sp^3-hybridized sites, giving rise to clusters of functional groups, and thus explaining why the amorphous carbon, which primarily consists of sp^3-hybridized carbon atoms, can be eliminated so easily.[133] By further performing a subsequent 3-cycle alkylcarboxylation on the insoluble solid, the DWCNTs and MWCNTs were then selectively functionalized and water solubilized, leaving the remaining MWCNTs in the insoluble solid. A schematic illustration of the two-step diameter-dependent reaction can be seen in **Figure 5**. After the successful enrichment of DWCNTs, the alkyl functional groups were then removed by thermal annealing of the filtered and washed product in H_2/Ar. High-resolution TEM revealed that while the final sorted product did still contain some MWCNTs (likely resulting from their very high initial composition), the carbonaceous material and SWCNTs had been successfully removed, leading to DWCNT enrichment in the sample. This work not only demonstrates the applicability of covalent chemistry to enrich DWCNTs, but does so using a straightforward and highly scalable technique, which further allows the nanotubes to regain their pristine structure. Although no enrichment by electronic character was observed, the reduction potential of nanotubes does exhibit dependence on electronic character, and even on chirality. In theory it should therefore be possible to use a stoichiometric deficiency of Na to selectively functionalize only those nanotubes with the smallest reduction potential and thus facilitate some degree of sorting.

5.4. Biofunctionalization

An example of the use of biological elements to suspend and sort DWCNTs is seen in the 2011 work of Nie et al. in which DWCNTs were non-covalently biofunctionalized with the protein, lysozyme.[32] Lysozyme is particularly desirable for this purpose as it primarily consists of amine groups, which provide the nanotube with adequate water solubility,[165] and has hydrophobic residues within its core that readily interact with

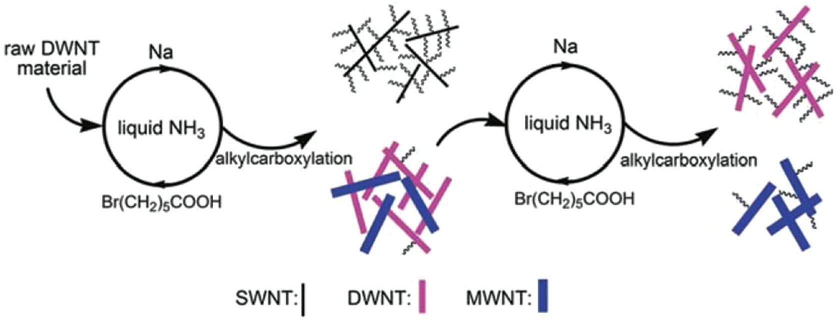

Figure 5. Schematic illustration of the two-stage enrichment of DWCNTs using diameter- and defect-selective alkylcarboxylation. By exploiting the diameter dependence of the reductive alkylcarboxylation of carbon nanotubes, the degree of functionalization and water solubility of the SWCNTs were selectively enhanced, allowing for their removal in aqueous extracts by water–hexane-phase extraction. Additional reaction cycles were performed on the insoluble solid, in which DWCNTs were enriched. Reproduced with permission.[167] Copyright 2011, Royal Society of Chemistry.

nanotubes through π–π stacking.[162] At low pH, protonated amines also interact with the defect sites of the nanotubes and at high pH, through amine adsorption.[162] It was observed that lysozyme selectively suspended large-diameter DWCNTs[32] and this is in agreement with computational studies where MWCNTs of larger diameter (40 nm) consistently showed stronger protein binding than those with a smaller diameter (10 nm).[164] This is also in agreement with studies of protein interactions with nanoparticles.[169] Nie et al. suggest that the stronger bundles formed by smaller-diameter nanotubes[32] may also contribute to their reduced solubilization via protein binding.[32] Because the large-diameter DWCNTs are selectively functionalized, centrifugation provides separation of the larger- and smaller-diameter DWCNTs into supernatant and pellet, respectively. TEM of the respective DWCNT samples reveals two distinct ranges of diameter, of 3–5 nm (Gaussian average of 4.0 nm) and 1–4 nm (Gaussian average of 2.7 nm). As diameter is strongly correlated with wall number, DWCNTs can also be separated from smaller-diameter SWCNTs, providing a convenient method for DWCNT enrichment of such samples. This was shown by adding a 4:1 mixture of pure DWCNTs and SWCNTs to a solution of lysozyme. The mixture was sonicated to aid solubilization and then centrifuged, yielding sediment and a lysozyme-biofunctionalized supernatant. Only large-diameter DWCNTs were found in the supernatant (as determined from TEM), highlighting the applicability of this approach to selectively produce fractions of large-diameter DWCNTs from such mixtures.

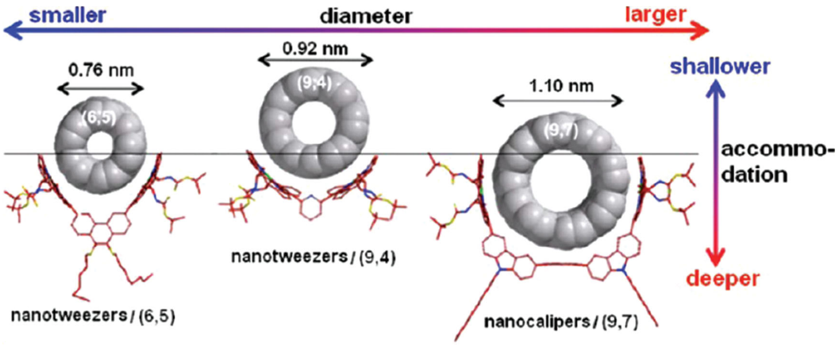

Figure 6. Computer-generated molecular modeling of the interactions between nanotweezers and nanocalipers and appropriately sized SWCNTs. By tailoring the chiral diporphyrin structure to a specific size and depth, the (6,5), (9,4) and (9,7) SWCNTs can be isolated. Reproduced with permission.[172] Copyright 2013, American Chemical Society.

In the work of Dresselhaus and co-workers, long and random single-stranded (ss-) DNA was employed to individualize DWCNTs, forming suspensions stable at high pH (>6.8–12.4).[160] As the pH becomes more acidic, the DNA begins to destabilize and then agglomerate due to protonation of the backbone phosphate groups. It is hypothesized that, as the larger-diameter nanotubes are more susceptible to bundling due to increased van der Waals forces, they agglomerate preferentially and can be separated through centrifugation from the suspended small-diameter DWCNTs. However, this is so far based solely on PL and optical absorption, which, as previously discussed, provide less certainty in the case of DWCNTs without corroboration from the more-conclusive TEM analysis.

5.5. Molecular Nanocalipers

The use of chiral diporphyrin nanotweezers and nanocalipers can achieve simultaneous discrimination of nanotube diameter, metallicity, and handedness in SWCNTs.[171,172] This technique involves tailoring of the diporphyrin structure to yield one that is sterically compatible with a nanotube of specific diameter and chiral angle. Such diporphyrins form stable host–guest complexes with the target nanotube through π–π and CH–π interactions, which can be separated from the remaining nanotubes via centrifugation. Specificity arises from careful selection of the spacing between the calipers, which affects the width of the host molecule and the depth at which the nanotube sits within the host.[171] These physical parameters become very important when targeting a specific nanotube, with larger nanotubes requiring a deeper position within the host.

Figure 6 shows an example of directly engineered diporphyrins and their complimentary nanotube types. For example, the (6,5) nanotube (diameter of 0.76 nm) can be accommodated by a nanotweezer structure. By altering the structure of the diporphyrin to have a slightly larger spacing, the (9,4) nanotube (diameter of 0.92 nm) can be accommodated. In order to accommodate nanotubes >1 nm, a nanocaliper structure can be used, which possesses arms that extend out to capture the target nanotube. Such tailored host structures not only allow for diameter sorting, but also for enantiomeric separation according to the handedness of the specific nanotube.[171,172] By inclusion of a chiral center within the diporphyrin, two mirror-image (*S*) and (*R*) hosts can be created for each target nanotube diameter, resulting in separation of left-handed (LH) and right-handed (RH) nanotube enantiomers. Initially, the enthalpies of association of the LH and RH nanotubes with an (*S*)-diporphyrin are approximately equal.[171] However, as the number of diporphyrin molecules bound to the nanotube surface increases, the formation of the RH:(*S*) complex becomes more energetically favorable than the LH:(*S*) complex. This means that RH:(*S*) becomes more stable and therefore, more soluble, than LH:(*S*). The opposite can be expected for the mirror-image host, with LH:(*R*) becoming more stable.

DWCNT sorting via the use of chiral diporphyrins was reported by Liu et al., wherein DWCNTs were successfully sorted from MWCNTs and, to a lesser extent, SWCNTs.[33] This was made possible by tailoring a chiral diporphyrin into a nanocaliper structure with a spacer of 1.9 nm between porphyrins. Extraction with the nanocaliper yielded significantly improved DWCNT purity (from 77% up to 90%) and narrower diameter distribution (from 1.23–3.23 nm to 1.25–2.75 nm). After removal of the nanocalipers via repeated washing of the centrifuged solid with tetrahydrofuran (THF) and pyridine, circular dichroism (CD) measurements were performed, where the presence of LH and RH DWCNTs species were confirmed. The authors thus concluded that the DWCNT enantiomers are most probably obtained through molecular recognition by the chiral diporphyrin nanocalipers.

5.6. Density-Gradient Ultracentrifugation

Density-gradient ultracentrifugation (DGU) is a technique originally designed for separating and isolating biological elements (such as macromolecules or viruses)[173] and was first used to separate SWCNTs by Hersam and co-workers in 2005.[58] This separation method involves taking individualized nanotubes suspended in surfactant and placing them into a graded fluid medium (usually iodixanol owing to its high viscosity and tunable density[142]) of varying density within a centrifuge tube.[58,130,140,143] The various nanotube species are then moved by centripetal forces until they reach their respective isopycnic points (the point where the nanotube's buoyant density matches that of the surrounding fluid medium). The key to the separation lies in the different buoyant densities of each nanotube species, which is a feature that is heavily reliant upon the physical structure of the nanotube itself, as well as the encapsulating surfactant and solvent molecules.

In the case of a binary surfactant, the structure of the surfactant shell is strongly influenced by the nanotube diameter.[140,157] Alternatively, in co-surfactant mixtures the polarizability of the SWCNT plays an important role and leads to non-equivalent wrapping of the two surfactants around different nanotubes.[158] This is especially true for surfactant mixtures with SDS, which is highly sensitive to electronic type[140,158] and results in the encapsulated nanotubes having a strong contrast in density. For example, the addition of SDS to SC-wrapped SWCNTs significantly increases the density of nanotubes with diameters of 0.83 nm and 0.98/1.03 nm, and facilitates their separation from smaller nanotubes (ca. 0.76 nm).[140] Therefore, by employing the appropriate conditions, SWCNT fractions with a narrow diameter distribution, or of defined semiconducting and metallic type, or even of enantiomerically pure single chirality can be produced by DGU.[130,140,143]

Due to the great success of DGU for SWCNTs, it was a natural step to extend the method to DWCNTs. In particular because the inclusion of an inner wall significantly alters the buoyant density and thus offers a convenient method to deal with unwanted SWCNT impurities. This was first achieved by Green and Hersam in 2009 using a two-step DGU process.[34] In the first step, raw material (DWCNT composition of 70%) is suspended in 1 wt% SC. The authors speculate that, due to the anionic planar structure of SC, its encapsulation layers are highly sensitive to nanotube diameter and therefore, its use affords fractions of SWCNTs, DWCNTs, and MWCNTs of very different densities.[34] Furthermore it is speculated that another advantage of SC is its limited sensitivity to the electronic character of the nanotubes, which means that any electronic perturbations of the outer wall by the inner wall will not have an impact on the surrounding surfactant layer. Therefore, for similar diameters, SC encapsulation does not vary between SWCNTs and DWCNTs, and the only difference is a much larger density for DWCNTs due to the inner wall. **Figure 7**a shows a schematic of the SC encapsulation of small- and large-diameter SWCNTs and DWCNTs, as well as its effect on their buoyant densities.

The density gradient consisted of 1.5 mL of 60 wt% iodixanol on the bottom, followed by 5 mL of a linear gradient varying from 32.5 to 17.5 wt% iodixanol with 1.5 mL of 15 wt% iodixanol on top, in which the DWCNTs initially resided. The remaining volume was filled with 0 wt% iodixanol and the linear density was then centrifuged at 41 000 rpm (207 570*g*) for 12 h. In this process the nanotubes are forced to sediment from their initial starting position of low density to a higher density. The advantage of top addition is that lower-density SWCNTS are prevented from reaching the isopycnic point of the much denser DWCNTs. As seen in Figure 7b, this results in 4 bands corresponding to small-diameter SWCNTs (ca. 0.7–1.1 nm),

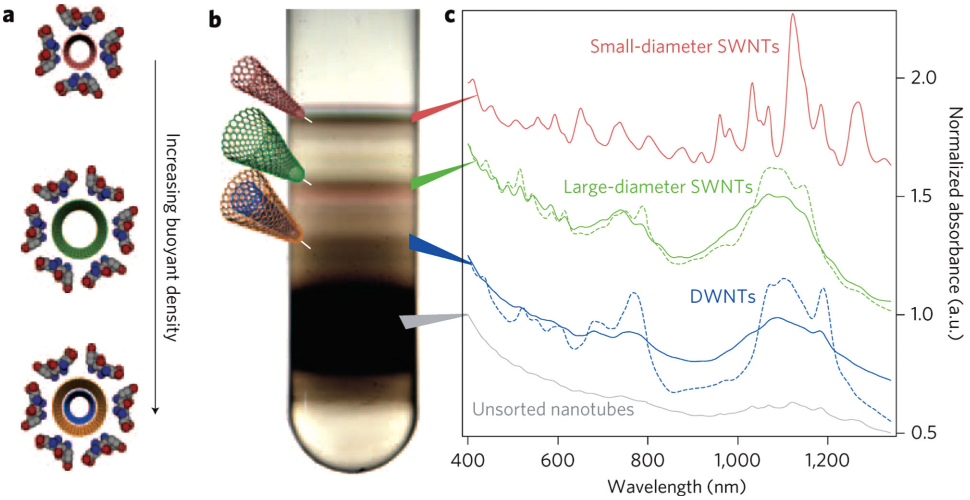

Figure 7. Separation of DWCNTs by the number of walls via DGU. a) Schematic illustration of nanotube encapsulation by SC and its effect on the resultant buoyant density. b) Photograph of a centrifuge tube following the first iteration of the separation showing four bands, corresponding to small-diameter SWCNTs, large-diameter SWCNTs, DWCNTs, and MWCNTs/carbonaceous impurities/bundles. c) Absorption spectra of each band following the initial separation and, in the case of large-diameter SWCNTs and DWCNTs, the first iteration. The absorbance is normalized and offset in each case. Reproduced with permission.[34] Copyright 2009, Nature Publishing Group.

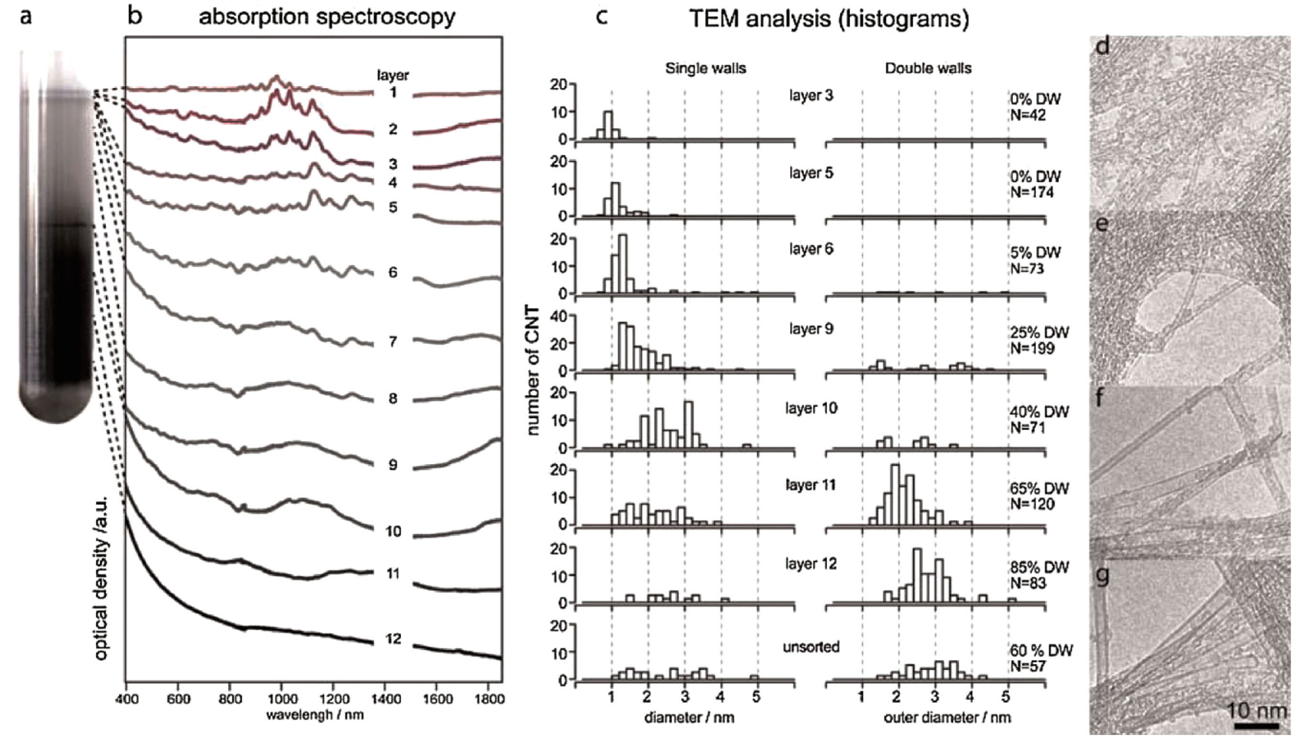

Figure 8. Analysis of the sorting efficiency of the DGU technique by TEM. a) Centrifuge tube of the DGU sorted DWCNT material showing several bands within the linear gradient. b) Absorption spectra of each layer. c) TEM analysis of the different bands showing an increase in mean diameter with increasing density, change in relative concentration of SWCNTs and DWCNTs and the change in distribution shape. d–g) TEM images of SWCNTs and DWCNTs from layers 3, 6, 10 and 12, respectively. Reproduced with permission.[174] Copyright 2008, Wiley-VCH.

large-diameter SWCNTs (ca. 1.6 nm), DWCNTs (ca. 1.6 nm), and MWCNTs, bundles, and carbonaceous impurities. The coarsely refined DWCNTs and large-diameter SWCNTs were then subjected to a second DGU step. In that step the material was now inserted into the bottom of the density gradient, which forced the nanotubes to move from high to low density with the goal of removing any slow-moving, dense species that did not reach their isopycnic points the first step. The second density gradient consisted of 1.5 mL of 60 wt% iodixanol on the bottom, 1 mL of coarsely refined DWCNTs in 33.5 wt% iodixanol, then 5 mL of density gradient ranging from 31 to 16 wt% iodixanol with the remaining space filled with 0 wt% iodixanol. The effect of a subsequent DGU step is clearly visible in the absorption spectra in Figure 7c (dashed lines), where a significant improvement in the purity of the large-diameter SWCNT and DWCNT fractions is seen, as evidenced by the sharper peaks and reduced scattering background.

In an investigation of the sorting efficiency of DGU, Loiseau and co-workers conducted a layer-by-layer analysis of nanotube content by TEM.[174] As seen in **Figure 8**a, twelve bands were taken from the centrifuge tube and characterized by TEM (over 100 nanotubes per band) and absorption spectroscopy (Figure 8b,c). As discussed,[34] the SWCNTs are found in the lower-density top half of the centrifuge tube with a trend of increasing diameter seen with increasing density (layers 1–5), whereas the highest-purity DWCNTs (85%) are found in layer 12. Between layers 6 and 12, a mixture of SWCNTs and DWCNTs were found with increasing DWCNT purity.

Extending the DGU method to sort DWCNTs according to electronic character was a seminal advancement toward the realization of high-technology DWCNT devices, and was achieved by Green and Hersam in 2011.[35] In that work, DWCNTs coarsely purified via their original method[34] were separated by outer wall electronic type using subsequent DGU iterations. However, in the subsequent DGU steps, co-surfactant mixtures of SC and SDS were used. Due to the very different surfactant wrapping of metallic and semiconducting nanotubes,[158] the difference in density between the two electronic types in co-surfactant mixtures is even greater than in the single surfactant case and this can be optimized for a particular metallic/semiconducting separation.[130,140,142] For instance, ratios of 1:4 SDS/SC and 3:2 SDS/SC have been found to be optimal for targeting large-diameter semiconducting and metallic SWCNTs, respectively.[140]

For semiconducting DWCNT enrichment, three iterations followed the initial coarse DGU step. In the first iteration, the DWCNTs were placed at the bottom of a 1 wt% 1:4 SDS/SC density gradient from 25 to 40 wt% iodixanol. The gradient was centrifuged (41 000 rpm or ca. 208 000g for 14 h) and resulted in further separation of DWCNTs and SWCNTs. However, separation according to electronic character was also seen owing to the introduction of SDS. The semiconducting outer wall enriched (s-) DWCNT layer was then isolated and used in the second iteration, which was a repetition of the first, but with the s-DWCNTs added to the top of the gradient. In the third iteration, a 3:2 SDS/SC ratio was used with the DWCNTs

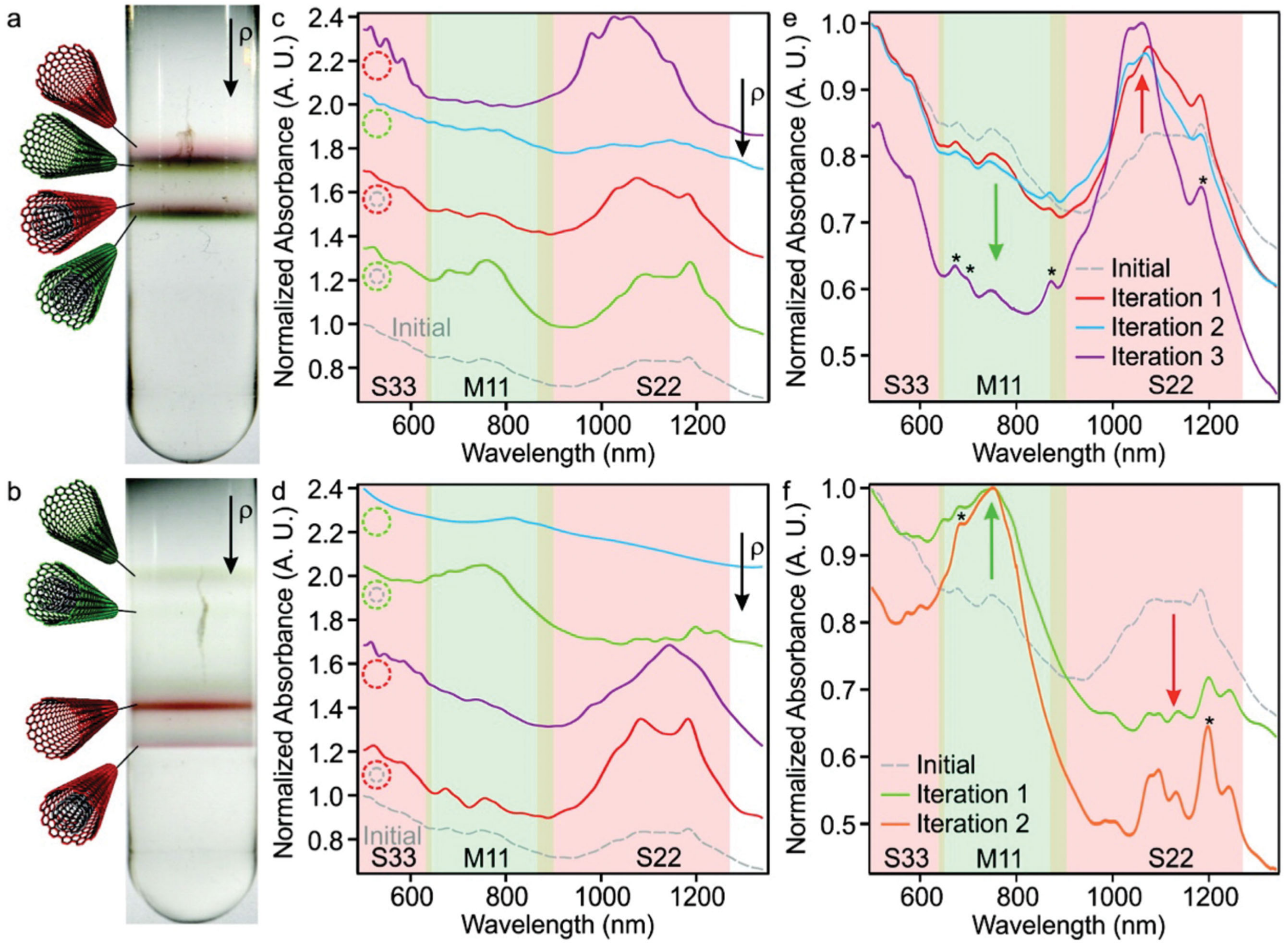

Figure 9. Separation of DWCNTs by outer wall electronic type. a–b) Photographs of centrifuge tubes following DGU separation of SWCNTs/DWCNTs targeted for semiconducting and metallic DWCNTs, respectively. c–d) Absorbance spectra of each band during the first-iteration separations targeting semiconducting and metallic DWCNTs, respectively. Metallic DWCNTs, semiconducting DWCNTs, metallic SWCNTs, semiconducting SWCNTs, and then coarsely enriched input DWCNT material are shown by the red, green, purple, blue, and dashed grey curves, respectively. The spectra are offset for clarity. e–f) Absorbance spectra obtained during successive DGU iterations to produce semiconducting and metallic DWCNTs, respectively. The asterisks mark the absorption peaks attributed to inner-DWCNT-wall transitions. S*ii* (M*ii*) label the *i*th order semiconducting (metallic) optical transitions of the SWCNTs and the outer walls of DWCNTs. Wavelength regions associated with semiconducting and metallic SWCNTs and outer wall DWCNTs transitions are shaded red and green, respectively. Reproduced with permission.[35] Copyright 2011, American Chemical Society.

moving from low to high density to remove any remaining metallic species. For metallic DWCNT enrichment, only two iterations followed the initial coarse DGU step and both used a 1 wt% 3:2 SDS/SC ratio, but differed in initial DWCNT placement.

Figure 9a shows the resultant layer structure for a co-surfactant ratio of 1:4 SDS/SC. Separation occurs primarily by diameter, however red and green fringes corresponding to metallic and semiconducting character, can also been seen. The absorption measurements of each fringe (seen in Figure 9c) also show signs of electronic sorting for both SWCNTs and DWCNTs, with enhanced S_{22} and M_{11} transitions. Alternatively, the separation with a co-surfactant mixture of 3:2 SDS/SC can be seen in Figure 9b, where the increased relative concentration of SDS has significantly changed the resultant band structure. Separation is now dominated by electronic character and occurs concomitantly with diameter, with the four bands visible corresponding to m-SWCNTs, m-DWCNTs, s-SWCNTs, and s-DWCNTs (absorption measurements shown in Figure 9d). As the m-CNTs are coated with an increased surface concentration of SDS compared to that of s-CNTs, their isopycnic points are at lower densities.[175,176] Figure 9e shows absorption spectra after the initial DGU step and the three subsequent iterations for s-DWCNT enrichment. While each DGU step yields enhancement of the S_{22} and reduction in M_{11} features, the most significant enrichment is seen in the final step, which employs the 3:2 SDS/SC co-surfactant mixture. Additionally, there is also a peak at ca. 1200 nm corresponding to the S_{11} transition of an inner wall. Figure 9f shows absorption spectra for each DGU step, targeting m-DWCNTs. Each separation sees the enhancement of the M_{11} transitions with S_{22} contributions from s-DWCNTs removed, revealing inner wall S_{11} peaks in the same region. In each case, very high purities were achieved with final fractions containing 96% and 98% semiconducting and metallic

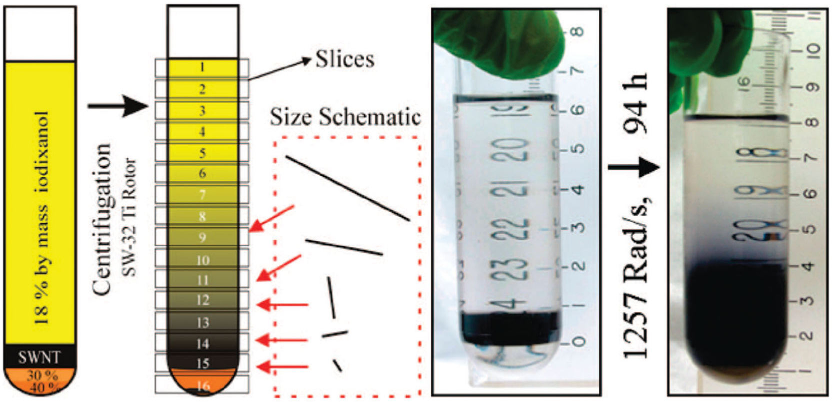

Figure 10. Schematic and photographs of the process of length separation by centrifugation for SWCNTs. An injection layer containing the SWCNTs, modified to the appropriate liquid density, is placed near the bottom of the tube to maximize the separation. Longer nanotubes move further in response to the applied centrifugation, and thus separate up the tube; any high-density impurities move in the opposite direction. Reproduced with permission.[141] Copyright 2008, American Chemical Society.

DWCNTs, respectively. This clearly demonstrates the effectiveness of the DGU technique.

5.7. Centrifugal Length Separation

In addition to the separation of carbon nanotubes by diameter and electronic type, centrifugation has also been used to prepare nanotubes with a narrow length distribution.[141,177] This length-dependent separation technique has previously been reported for the fractionation of SWCNTs with lengths in excess of 1 µm and is achieved by exploitation of the length-dependent friction coefficient through a dense liquid under centrifugation.[141,177] While this technique is very similar to DGU, it employs a fluid medium much denser than the nanotubes such that they can never reach their isopycnic points, and, rather, exploits transient motion, where longer nanotubes travel with greater velocity in opposition to the applied acceleration. This occurs because the rate of nanotube flow through the fluid has a non-linear dependence on length.[177] Separation occurs (with minimal chirality differentiation), provided that $\Delta\rho = \rho_S - \rho_{SWCNT} >> \Delta\rho_{SWCNT} = \rho_{SWCNT} - \rho_{SWCNT,i}$ where $\Delta\rho$ is the difference in density, ρ_S is the density of solution, ρ_{SWCNT} is the average density of all the SWCNT chiralities and $\rho_{SWCNT,i}$ is the density of an individual SWCNT chirality.[177] Thus, the key to length separation is to choose the linear density such that $\Delta\rho >> \Delta\rho_{SWCNT,}$ thus exploiting the transient motion regime and not the regime in which buoyancy equilibrium is reached. **Figure 10** shows a schematic representation and photographs of SWCNT length separation by centrifugation, where longer SWCNTs travel further from the injection layer.

In 2010, Fagan and co-workers separated DWCNTs according to length in a two-step method.[178] Firstly, the DWCNTs were coarsely enriched using the pre-established DGU method.[34] The enriched DWCNT material was then inserted into a centrifuge tube with a specially designed gradient derived from SWCNT length separations.[141,177] Then, 1 mL of high-density (40%, 1.21 g mL^{-1}) iodixanol was added, followed by 1 mL of slightly lower density (30%, 1.16 g mL^{-1}) containing the DWCNTs. Finally, 20 mL of 26% (1.14 g mL^{-1}) solution was added (the race layer in which fractionation occurs), with the concentration of surfactant remaining constant throughout, at 1 wt% deoxycholate (DOC). Importantly, the density of the surrounding medium is greater than the average density of the DWCNTs (ca. 1.11 g mL^{-1}), thus enabling transient motion and not buoyant density. The gradient was then centrifuged at 34 000g (16 640 rpm) for 49 h. The top-most layer (containing nanotubes that had travelled the furthest from the DWCNT injection layer), contained nanotubes with a length of 2.2 µm. As expected, the average length decreased for fractions closer to the injection layer, with the shortest average length reported as 0.6 µm, with each layer having a relatively narrow length distribution (distribution of layer 4 was ±0.18–0.3 µm).

Fagan and co-workers also report partial enrichment by electronic character using co-surfactants.[178] In that case, a slightly denser gradient was employed with an additional co-surfactant gradient; however, evidence of electronic enrichment was limited.

5.8. Gel Permeation

The use of Sephacryl gel permeation, first demonstrated by Moshammer et al.,[59] has been shown to be extremely successful in the preparation of (n,m)-purified SWCNT suspensions. For SWCNTs, this technique has allowed for the high-throughput separation of metallic species from semiconducting species,[59,152,153] the isolation of specific (n,m) species,[60–62] and, most recently, the separation of optical isomers.[179]

In general, the gel-permeation method involves passing SDS-suspended nanotubes through a stationary phase gel bed contained within a column, at which point semiconducting nanotubes with the highest affinity for the gel (an interaction determined by the SDS wrapping, and hence, the individual nanotube structure) are selectively removed from the bulk solution and retained on the gel matrix.[61] The metallic nanotubes, which exhibit no interaction with the gel,[60,61,152,153] as well as other semiconducting nanotubes with no affinity to the gel (determined by surfactant concentration), continue to flow through the gel and can be collected. The gel is then washed with SDS of either increased concentration[60,61,152] or lower pH,[153,180] or alternatively SC,[59,152] which disrupts the interaction between the adsorbed semiconducting nanotubes and the gel and thus elutes them from the column for collection. This process can be repeated sequentially with the nanotubes that have the highest affinity for the gel becoming preferentially adsorbed each time.

While the exact mechanism of gel-based separation remains speculative owing to the difficulties associated with determining the molecular dynamics on the nanoscale, evidence suggests that it is a kinetically driven selective adsorption process,[61] highly dependent on the SDS wrapping of the nanotubes.[151] This is evidenced by the clear relationship between SDS concentration and gel adsorptivity,[60,61,151,152] where an increase in the SDS concentration allows additional SDS molecules onto the nanotube surface,[176] reducing its interaction with the gel. In addition to the SDS concentration, pH[62,153] and temperature[151] have also been shown to play important roles, giving rise to a number of separation strategies. While SDS-based separation is successful for small-diameter SWCNTs (0.77–1 nm), adsorption of large-diameter nanotubes (greater than ca. 1.2 nm) to the gel is quite limited.[37] Instead, a co-surfactant separation method can be used, where either the large-diameter material is suspended in a co-surfactant solution and applied to a column, as demonstrated by Miyata et al.[181] and Wu et al.,[182] or where they are suspended in SC and applied to a column in SDS, as demonstrated by Zhang et al.[183] While all of these co-surfactant methods produced highly pure, semiconducting solutions (99%, 98%, and 98%, respectively), none report the purity of the metallic fraction, which is washed off of the gel in the flow-through.

Application of the gel-permeation technique to DWCNTs was first reported by Moore et al. in 2014,[36] wherein the separation of DWCNTs from SWCNTs was demonstrated, producing highly enriched fractions with mean diameters of 1.64 ± 0.15 and 0.93 ± 0.03 nm, respectively. In that work, DWCNT raw material was suspended in 2 wt% SDS by sonication for 8 h, and this was then added to a 25 cm Sephacryl S-200 gel column, also at 2 wt% SDS. While the bulk of the nanotubes passed through the gel, a small amount remained adsorbed to the top of the column. This is in agreement with previous work by Blanch et al.[152] and Flavel et al.[62] where it has been demonstrated that, at a relatively high SDS concentration (1.6–2 wt%), only a very small portion of the overall nanotube population is adsorbed in a competitive process, compared to that for low SDS concentrations (0.4–0.8 wt%).

Addition of 0.5 wt% SC resulted in the desorption of the nanotube material and two distinct bands formed in the column, the first of which was fast moving and dispersed while the second was slower moving and more tightly confined. This can be seen in **Figure 11**a, which shows time-lapse photographs of the initial adsorption and subsequent elution with SC. Extensive atomic force microscopy (AFM), absorption spectroscopy, TEM, and Raman spectroscopy revealed that those bands corresponded to DWCNTs and SWCNT, respectively. One explanation for the significant difference in elution rates is that the nanotubes undergo a size-exclusion process in which the retention time is dependent on the size. Indeed, extensive AFM revealed that there was a significant size difference between the two nanotubes types, which is summarized in Figure 11b. On average, the DWCNTs (ca. 700 nm) are twice as long as the SWCNTs (ca. 300 nm), which may be attributed to the increased structural stability of the DWCNTs during extensive sonication. This is in agreement with Green and Hersam who also observed that DWCNT lengths were ca. 40% longer than SWCNTs after 1.5 h of sonication.[34] However, a true size-exclusion process would also occur in SC, which the authors confirm is not the case. The mechanism is therefore likely a combination of two competing factors: diameter-dependent solvation by the surfactant and length-dependent size exclusion.

Analogous to the evolution of DWCNT sorting by the DGU method, the gel-permeation technique was then extended to the electronic sorting of DWCNTs.[37] In that work, a DWCNT suspension in 1 wt% SC was added to a 20 cm long gel column in 1 wt% SDS. Upon addition of the SC-encapsulated nanotubes to the column, they immediately underwent surfactant exchange, resulting in various ratios of SDS/SC wrapping, depending on the diameter and electronic character.[130,142,143] Owing to this difference in wrapping, nanotubes of different electronic types moved through the column at different rates, forming four bands, which were eluted from the column after different retention times. The four bands were shown to correspond to defected m-DWCNTs, m-DWCNTs, s-DWCNTs, and s-SWCNTs, respectively, with the elution order in excellent agreement with data from the separation of AD and HiPco SWCNTs of a similar electronic type. Thus, it is clear that the separation process is highly sensitive to the surface properties of each nanotube type, with the presence of the inner wall having little effect on the separation. The authors suggest that the mechanism is similar to that observed previously for SWCNT separation, where SDS is sensitive to electronic character and diameter.[60,61,152] Metallic nanotubes, which are known to have a stronger interaction with SDS compared to semiconducting nanotubes,[175] become more fully wrapped and experience limited interaction with the gel as they traverse the column. Thus, they elute first, followed by large- and small-diameter semiconducting nanotubes. **Figure 12**a shows the elution profile of DWCNTs, large-diameter AD SWCNTs and small-diameter HiPco SWCNTs. An excellent agreement between elution times is observed for metallic (Band 2) and semiconducting (Band 3) fractions of DWCNTs and AD SWCNTs, as well as between HiPco SWCNTs and SWCNTs within the DW sample. Absorption spectra of the enriched m- and s- DWCNT fractions are shown in Figure 12b,c, demonstrating clear enhancement of the M_{11} (600–800 nm) and S_{22}

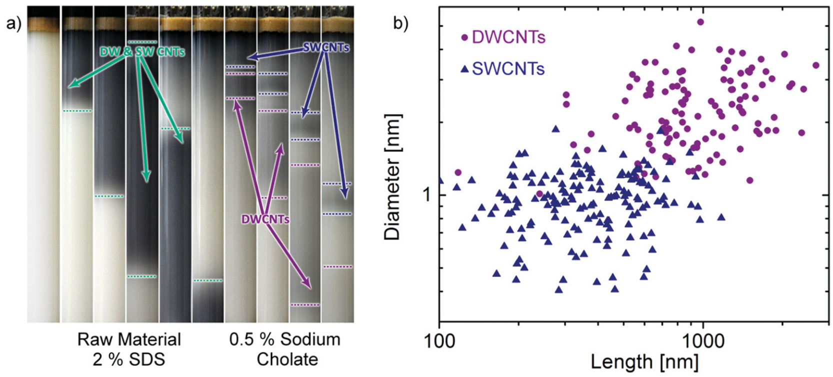

Figure 11. Separation of DWCNTs by gel permeation. a) Time-lapse photography (1 h) showing the introduction of raw, unsorted DWCNT material to the S-200 gel column for the separation of SWCNTs from DWCNTs and b) diameter vs length of SWCNTs and DWCNTs, as determined by AFM. Reproduced with permission.[36] Copyright 2013, American Chemical Society.

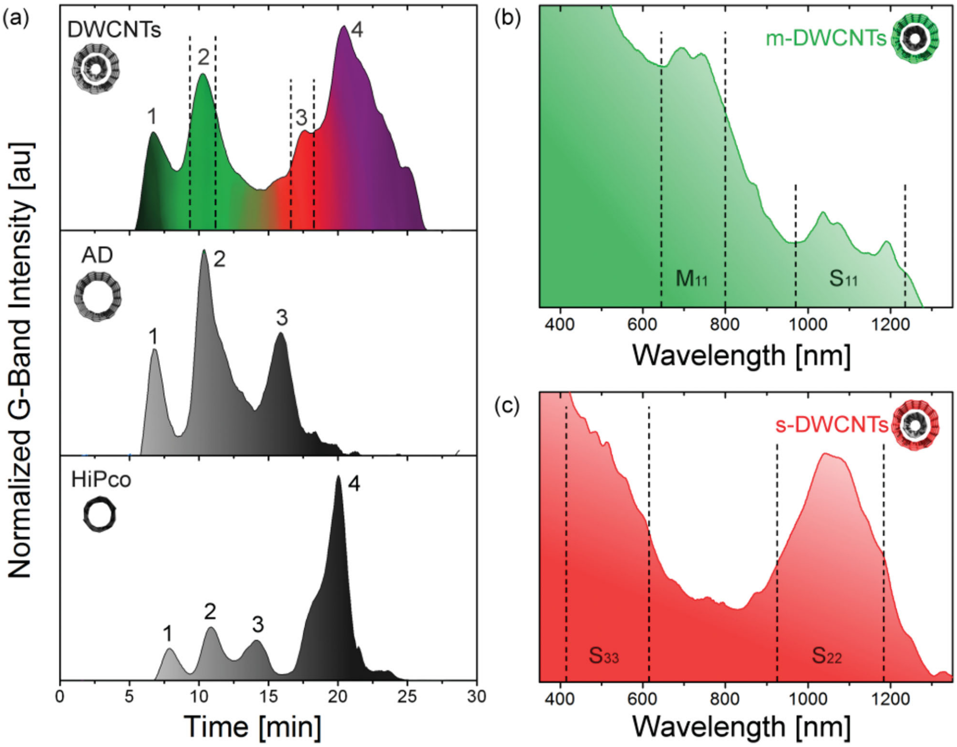

Figure 12. The co-surfactant separation of DWCNTs via gel permeation. a) Elution profiles of the normalized G-Band Raman mode intensity for DWCNTs, AD SWCNTs and HiPco SWCNTs. The dashed lines in the DWCNT elution profile highlight Band 2 and Band 3, which, from the absorption spectra seen in (b) and (c), correspond to DWCNTs with metallic and semiconducting outer walls. Regions of S_{ii} and M_{ii} transitions are highlighted in each spectrum. Reproduced with permission.[37] Copyright 2015, American Chemical Society.

(900–1200 nm) transitions with calculated purities of ca. 70% and ca. 90%, respectively.

5.9. Polymer Wrapping

The dispersion and separation of SWCNTs with aromatic polymers in organic solvents is receiving ever-increasing attention in the research community due to the ability of polymer wrapping to prepare suspensions with a highly pure semiconducting content (>99%).[184–186] In this one-pot approach, raw carbon nanotube material is typically dispersed by ultrasonication in the presence of a chosen polymer followed by ultracentrifugation. Consequently, only those nanotubes with a preferential interaction with the polymer and those that have become individualized during ultrasonication remain suspended in the organic solvent. In pioneering works by Nish et al.,[147] Chen et al.,[148] and Hwang et al.,[132] organic polymers with the fluorene structure as part of their repeat unit were used, such as poly(9,9-dioctylfluorene-2,7-diyl) (PFO), poly[9,9-dihexylfluorenyl-2,7-diyl)-*co*-(9,10-anthracene)] (PFH-A) and poly[(9,9-dioctylfluorenyl-2,7-diyl)-*co*-1,4-benzo-[2,1’-3]-thiadiazole)] (PFO-BT). After almost 10 years of development, the polymer library has grown dramatically to now include polythiophenes, polycarbazoles, and copolymers thereof,[39,187–192] alongside research to develop new polymers via click chemistry in an effort to avoid the strict synthetic conditions associated with Suzuki polycondensation or Yamamoto coupling.[193] Using the currently available polymer library, mixtures of semiconducting SWCNTs through to near-monochiral and monochiral suspensions and most recently even optical isomers thereof[194] have been demonstrated. For example, poly(9,9-dialkyl-2,7-fluorene) has been shown to be sensitive to large chiral angles (close to armchair: $\theta \geq 25°$)[132,148,195] and poly(*N*-decyl-2,7-carbazole) to lower chiral angles (typically $10° \leq \theta \leq 20°$).[191]

Despite the wide-spread application of polymer wrapping, the exact mechanism responsible for separation remains poorly understood and is the subject of current discussion.[185,186,193,196] Nevertheless, it is commonly agreed upon that the polymer interacts by aligning its aromatic backbone along the surface of a carbon nanotube so as to maximize π–π stacking.[38,39,185,188,190] Peripheral groups are then believed to branch away from the nanotube into the solvent and facilitate solubility.[186,196] Berton et al.[187] have developed a hybrid coarse-grain model to describe this interaction by treating the nanotube and polymer as geometrical objects and assuming maximal (attractive) π–π interactions can be reached by maximizing the contact area. In this way, a set of solutions for which the polymer lies flat on the surface of the nanotube were calculated as shown in **Figure 13** for poly(fluorene-*alt*-pyridine) around a 1.2 nm-diameter SWCNT. Intuitively, and also in agreement with Berton's model, the number of favorable wrapping solutions increase with diameter, which may explain why certain polymers are highly (n,m) specific in the small-diameter regime (i.e., due to other species having limited possible wrapping solutions).

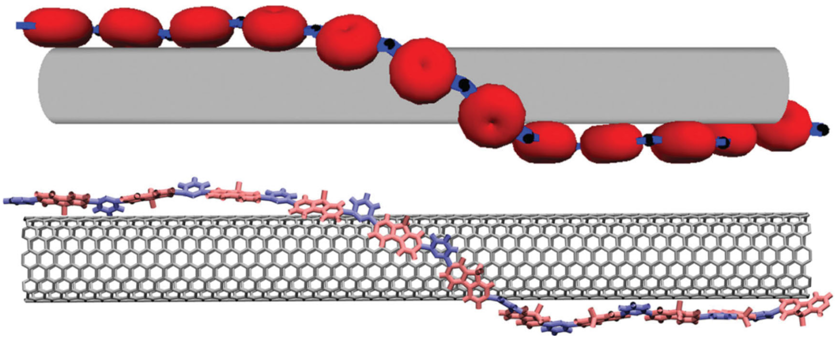

Figure 13. One of the geometric solutions for poly(fluorene-*alt*-pyridine) wrapped around a 1.2 nm-diameter SWCNT and the corresponding molecular model. Alkyl chains are simplified as methyl groups. The red discs and black dots represent the fluorene and pyridine moieties, and these two objects are connected by sticks whose lengths reflect the bonds between the fluorene moiety and the center of the pyridine ring. Adapted with permission.[187] Copyright 2014, Wiley-VCH.

The observed high selectivity of polymer systems to semiconducting SWCNTs is much less understood and experimental evidence suggests that it is dependent upon a number of factors, such as polymer concentration,[186] ultrasonication temperature,[185] and solvent choice.[132,147,185,196] Changes in any one of these parameters have been shown to influence not only the concentration of metallic SWCNTs in solution but also the polydispersity of the semiconducting species. For example Shea et al.[186] showed that for high starting concentrations of PFO in toluene (5 mg mL^{-1}) the polydispersity of s-SWCNT (n,m) species increased from 5 to 8 and m-SWCNTs became visible in optical absorption measurements. Conversely, at polymer concentrations below 1 mg mL^{-1}, no m-SWCNTs were suspended. As stated by the authors, the increased polydispersity and metallic content is likely to be a result of high PFO concentrations suspending not only individualized SWCNTs but also polydisperse bundles. Likewise, Han et al.[185] dispersed carbon nanotubes with PFO in cyclohexane at increasing temperature (5–55 °C) and found that increased ultrasonication temperature led to an overall higher concentration of s- and m- SWCNTs.

However, it is the choice of solvent that has captured the attention of many in the research community,[132,147,185,196] as it has dramatic effects on the semiconducting purity. As outlined by Wang et al.,[196] upon selecting a solvent, several rules are typically adhered to; namely, the solvent must solubilize the polymer, the SWCNTs must have a low intrinsic solubility in the solvent so that only polymer-wrapped nanotubes are dispersed, and the solvent must have a lower density than the SWCNTs so that the unwrapped SWCNT will sediment after centrifugation. Additionally, Wang et al.[196] go further to state that nonpolar solvents are necessary to prevent solvent interactions with polarized polymer-wrapped m-SWCNTs and allow for better selective sorting of s-SWCNTs. As an example, the use of conjugated polymers in polar solvents such as THF, typically have a higher dispersive yield (i.e., a higher final suspended mass of CNTs) but suspend both m- and s- SWCNT, whereas nonpolar solvents such as toluene, o-xylene, and m-xylene, whilst having a lower dispersive yield, have been shown to afford semiconducting purities of >99%.[184–186]

In the past, research efforts focused mainly on the dispersion of small-diameter (0.8–1.2 nm) carbon nanotubes from the CoMoCat or HiPco processes, and selectivity was shown to be poor for larger diameters.[38,187,197] As the research community now turns to larger-diameter nanotubes due to their potential application in telecommunications[198] and FETs,[199] new polymer systems are also beginning to appear in the literature. Initially it was believed that the poor selectivity to large diameters could be ascribed to the nature of the polymer backbone; however, recent studies point to side chains as playing an important role.[38,192,197,200] Gomulya and co-workers[38,39] investigated the effect of using polyfluorene derivatives with different-length alkyl side chains from C_6H_{13} up to $C_{18}H_{37}$, and found that an alkyl chain length of 8 carbons favored dispersion of diameters of 0.8–1.2 nm, whereas longer alkyls with 12–15 carbons can efficiently interact with nanotubes with diameters up to 1.5 nm. Unfortunately, in spite of improved sensitivity to large diameters, the longer alkyl chains also had the effect of increasing the interaction strength with the nanotubes, and thereby decreased the selectivity. In other work, Berton et al.[188] reported the dispersion of 1.3 nm-diameter SWCNTs using poly(9,9-didodecylfluorene-2,7-diyl-*alt*-anthracene-1,5-diyl); Tange et al.[201] dispersed 1.3 to 1.4 nm diameters with poly(9,9-dioctylfluorene-*alt*-benzothiadiazole) (F8BT), and Wang et al.[197] dispersed AD carbon nanotubes with poly(dithiafulvalene-fluorene-*co*-*m*-thiophene). To date, polymer wrapping has yet to be applied to DWCNTs, but, considering that the outer wall of a DWCNT has a diameter of greater than ca. 1.5 nm, these newly developed polymers look highly promising for the future of DWCNT processing. However, as several researchers point out, the polymer wrapping of a carbon nanotube is also associated with a charge transfer,[190,196,197] and what effect the presence of an electronically coupled inner wall may have on the sorting efficiency remains to be seen.

5.10. Aqueous Two-Phase Extraction

Another separation method that looks promising for the separation of DWCNTs is an adaptation of standard liquid-phase separation, recently applied to the separation of carbon nanotubes by Zheng and co-workers.[40] In this first report, SC-dispersed nanotubes (and an appropriate amount of SDS) were added to a mixture of two water-soluble polymers; polyethylene glycol (PEG) and dextran. Spontaneous and robust separation of the polymer phases occurred with the more-hydrophobic PEG-rich phase on top and the more-hydrophilic dextran-rich phase on the bottom. The nanotubes quickly and spontaneously separated into the two polymer phases with thermodynamic analysis revealing two distinct regimes. First, in the small-diameter regime (0.6–1.0 nm), curvature dominates the solvation free energy with smaller-diameter nanotubes such as (6,4) in the more-hydrophilic dextran-rich phase, and larger-diameter

Table 1. Comparison of the advantages and disadvantages of all current DWCNT-sorting methods with a focus toward commercial application.

Technique	Advantages	Disadvantages
Reversible covalent chemistry	✓ Diameter selective ✓ Easily scalable ✓ Pristine structure can be recovered ✓ Scalable	× Cannot distinguish between number of walls × Currently insensitive to electronic character × Multiple steps; time consuming
Biofunctionalization	✓ Diameter selective ✓ Easily scalable	× Cannot distinguish between SWCNTs/MWCNTs and DWCNTs × Not sensitive to electronic character
Molecular nanocalipers	✓ Diameter selective ✓ Sensitive to handedness ✓ Pristine nanotubes can be recovered ✓ Host can be reused	× Requires complex chemical engineering to make hosts × Requires expensive reagents × Limited evidence of electronic sensitivity
DGU	✓ Diameter selective ✓ Sensitive to electronic character ✓ Can distinguish between number of walls	× Requires expensive ultracentrifuge × Requires expensive density gradient medium × Requires technical expertise to make intricate density gradients × Multiple steps; time consuming
Centrifugal separation	✓ Length selective	× Requires pre-sorted DWCNT material × Limited evidence of electronic sensitivity × Requires expensive density gradient medium
Gel Permeation	✓ Diameter selective ✓ Sensitive to electronic character	× Requires expensive gel
Polymer wrapping	✓ Diameter selective ✓ Sensitive to electronic character ✓ Scalable	× Requires centrifuge × Requires expensive polymers
Aqueous two-phase extraction	✓ Diameter selective ✓ Sensitive to electronic character ✓ Easily scalable ✓ Inexpensive, readily available reagents ✓ True "one-pot" method	× Diameter selectivity currently limited to small diameter regime < 1.2 nm

nanotubes such as (7,5) and (8,4) in the more-hydrophobic PEG-rich phase. The second, larger-diameter regime (1.2–1.5 nm), is governed by the degree of nanotube polarizability, and a clean metallic/semiconductor separation can be achieved, with metallic nanotubes found in the more-hydrophilic dextran-rich phase and semiconducting nanotubes in the more-hydrophobic PEG-rich phase.[40] Investigation by Subbaiyan et al. determined that aqueous two-phase separation was driven by the hydrophobicity of the surfactant composition on the nanotube surface rather than the inherent hydrophobicity of the nanotube itself,[41] therefore allowing the surfactant identity and ratio to be tuned to target specific chiralities in a similar manner to gel permeation and DGU. By doing so, it is possible to enrich (6,5), (6,4)/(7,3) and (7,5) species. Since then, several advances have been made through variation of the surfactant concentration[202] and the type of polymer,[203] addition of salts[202] or DNA,[203] and the use of countercurrent chromatography.[204] Single-chirality nanotube suspensions can now be prepared for a number of species, and the use of countercurrent chromatography enables total fractionation with a recovery close to 90% of the starting material.[204] While this rapidly developing technique has made extraordinary advances for small-diameter (<1.2 nm) SWCNTs through elegant refinement, what is of most interest from the DWCNT perspective is the elementary separation of large-diameter nanotubes according to polarizability.[40] The ease with which clean metallic/semiconducting separation can be scaled up (Zheng and co-workers demonstrated separation on the liter scale) provides an obvious opportunity for DWCNT sorting and will most likely be capitalized upon in the near future.[40]

5.11. Analysis and Future Directions

While each of the previously discussed processing techniques led to enrichment of DWCNT material in some respect, each have their advantages and disadvantages, as summarized in **Table 1**. Some are inherent to the techniques themselves and others are simply a result of the current stage of development of the techniques, or of their application to DWCNTs.

As in the case of SWCNTs, an appropriate sorting method should be selected in accordance with the desired application. For instance, applications requiring DWCNTs to be free of SWCNT or MWCNT contaminants may find a number of techniques suitable, and the decision may ultimately depend on the availability of equipment, the cost, and the complexity. Where high-purity DWCNT enrichment is required, DGU and gel permeation may be more appropriate. However, both require specialist equipment and technical expertise, though gel permeation may be a more appropriate technique for those without an ultracentrifuge. While the purities achieved for DGU are currently higher than that achieved for gel permeation, future research may see the gel method further optimized, as has been demonstrated for SWCNTs.[59–61,151,179] Looking forward, it is inevitable that polymer wrapping and aqueous two-phase extraction will be successfully applied to DWCNTs; however, DGU is so far the only technique capable of distinguishing intrinsic differences between DWCNTs and SWCNTs, which are otherwise identical, except for the presence of the inner wall (with the added advantage of also offering sensitivity to electronic character).

Owing to the progress in DWCNT sorting, particularly for metallic/semiconducting separation, the sorted material can now be used to shed light on the intriguing properties of DWCNTs. For instance, Weisman and co-workers took DGU-purified fractions of DWCNTs to determine whether or not the inner walls of DWCNTs fluoresce.[205] Up until that point, there had been many reports of PL from the inner walls of DWCNTs.[160,206] However, considerable uncertainly surrounded the work due to the possibility of emission from SWCNT contamination.[205] High-resolution TEM was used to definitively characterize fractions of DWCNTs and SWCNTs, and to help identify the source of emission in each PL measurement. The results revealed that whilst PL was measurable from small- and **large-diameter** SWCNTs, it was not observed for fractions containing DWCNTs (10 000 times lower than for SWCNTs of similar diameter). The authors therefore suggest that, in previous reports, it was residual SWCNTs trapped within bundles or exposed inner walls, released during extensive chemical or physical treatment, that were responsible for the observed PL.

A similar investigation conducted by Yang et al. also used sorted, high-purity DWCNTs for PL measurements.[207] In that work, the authors showed that both sides of the debate are correct; the inner walls of DWCNTs do fluoresce for a narrow range of diameters (at a significantly reduced intensity than SWCNTs), but for all other diameters, complete quenching occurs. This was shown through extensive optical analyses that revealed that the only inner walls to exhibit PL were (9,4), (9,5), (8,6), (10,3), (7,6), and (10,2). The (9,4) nanotube showed significantly higher intensity than the other chiralities, but despite the DWCNTs being present in higher concentration, this intensity was still much less than that of the SWCNT sample, clearly indicating PL quenching of DWCNTs. The chiralities that were photoluminescent were found to share similar diameters with an average of ca. 0.929 nm, and they all had relatively large chiral angles. As a diameter of 0.930 nm is predicted to have the highest possible PL intensity,[5] this work suggests that only those with the highest theoretical PL intensity could overcome the quenching effect from the outer walls.

While these examples clearly demonstrate the benefits of an enriched DWCNT material, the ultimate goal in DWCNT processing is to obtain material sorted by inner wall character on a large scale, as this would unlock the potential of DWCNTs to be used in devices in ways that SWCNTs and MWCNTs cannot be. For example inner wall sorting would allow for large-scale fabrication of S@S FETs with on/off ratios of 10^8 or higher, or even the formation of M@M FETs, an idea contrary to our fundamental knowledge of modern electronics because their electrical resistance is insensitive to gate voltage,[10,208] but which has been nevertheless been proposed based on the results of theoretical calculations.[209] The motivation behind such a study is that we are rapidly approaching the limit for the improvement of Si-based electronics, with all-metallic DWCNT FETs offering the ability to be scaled down to make smaller-sized structures with less energy consumption and improved performance at higher frequencies.[210] An alternative is to use telescoping DWCNTs, where the interaction between the inner and outer wall in the overlapped region plays a crucial role in the electrical transport properties. By using computational methods for a (5,5)@(10,10) DWCNTs, it is predicted that the sensitivity of all-metallic DWCNTs to gate voltage can be tuned by varying the amount of overlap between the inner and outer wall.[209] Furthermore, it has been determined that, through optimization of this overlap, on/off current ratios as high as 10^4 could be achieved, which approaches that of many semiconducting nanotube devices (typically ca. 10^6).[211,212] Clearly, the ability to further sort DWCNTs according to inner wall electronic character would allow for the fabrication of electronic devices, not to mention many other applications outlined in the next section, that are currently not possible.

In this respect, even DGU so far provides no specificity because, for any given diameter, the buoyant density of the nanotubes has no dependence on electronic character, although differences in polarizability due to electronic character do have an influence on surfactant encapsulation, which indirectly affects the buoyant density. It has thus been suggested that sorting by inner wall character could be achieved by DGU by exploiting such minute differences in surfactant encapsulation, coupled with shallower density gradients and longer centrifugation time.[35] However, inner wall sorting by DGU remains elusive, confirming that the task is not at all trivial. In theory, it is possible that other techniques that are sensitive to the polarizability of the nanotubes, such as polymer, DNA, and co-surfactant wrapping, could be developed to a level of refinement whereby the subtle differences in polarizability arising from the character of the inner wall can be exploited to provide the desired separation. A careful evaluation of the magnitude of such differences in polarizability, arising due to the character of the inner wall, compared to the magnitude of the differences that arise due to the character of the outer wall and to the binding energy of the wrapping agent would be helpful in this regard. The perfect technique would be capable of sorting DWCNTs not just by inner wall electronic character, but by inner wall chirality. It is a somewhat remote possibility that one of the wrapping techniques could be refined to the necessary degree of sensitivity, especially considering the recent reports of sorting by outer wall stereoisomerism using polymers, but this would depend on subtle factors such as the orientation of the inner wall with respect to the outer wall. A more direct approach would be to use field effects to target specific chiralities. In this way, it could be possible to significantly alter the polarizability by, for example, irradiating the sample with light tuned to the S_{11} transition of an inner semiconducting nanotube. In conjunction with any of the techniques that are sensitive to polarizability, this could prove a powerful tool if the obvious practical challenges can be surmounted.

6. Devices and Applications

As processing techniques improve, DWCNTs are being employed in an increasing variety of devices and applications in which theory predicts they will offer benefits. These include FETs, which provide opportunities to investigate the intriguing effects of inter-wall coupling, and in various sensor and electronics applications. Such devices further demonstrate the need for DWCNT-sorting techniques, where DWCNTs of a specific type would provide ease of characterization and the ability to precisely tailor the electronic character for a specific function.

In many electronic applications it is desirable to use semiconducting nanotube species. While outer wall sorting greatly removes a large portion of metallic species, there are still come contaminant metallic inner walls present, which can result in electrical shorting. In such an instance, electrical breakdown can be used to remove any residual metallic species from a device in which nanotubes are integrated. The technique was first demonstrated by Collins et al., where application of a high bias voltage to an individual MWCNT resulted in wall-by-wall destruction.[154] The current distribution through a MWCNT favors the outermost wall, owing to its direct contact with the external electrode. Thus, upon application of a constant voltage across the nanotube, most of the current is carried through the outermost wall until enough power has been dissipated to induce Joule heating, resulting in the destruction of the individual nanotube. In the absence of significant defects or buckling, breaking normally occurs at the center[212] of the nanotube where the temperature is at a maximum,[213] resulting in a physical "cut" of the nanotube. The use of electrically induced breakdown for SWCNTs, enabling breakdown solely of the metallic elements, was also demonstrated.[154] This selectivity toward metallic nanotubes arises from the fact that gateable semiconducting nanotubes can be depleted of carriers so that the current is carried solely by the (non-gateable) metallic nanotube until enough power has been dissipated by them to cause significant heating and hence breakdown. Current-induced breakdown has since been used extensively for the removal of metallic nanotubes from FETs[214,215] and can produce highly purified networks of s-SWCNTs.[215]

Preserving all semiconducting walls is a much more difficult challenge for DWCNTs. In the case of DWCNTs, the situation is complicated by the possibility of either the inner or outer wall to be metallic, or both walls, or even special cases where two semiconducting walls become overall metallic in nature.[17,42] Thermal cross-talk between metallic and semiconducting walls is unavoidable, and heating of the metallic wall may lead to destruction of the semiconducting wall.[63] Hence, it is hard to design an experiment to selectively remove only metallic walls from an integrated film of mixed-wall DWCNTs. As an example, Wang and co-workers[63] deposited a film of semiconducting outer wall DWCNTs (purified using the DGU technique[35]) between two gold contacts, as shown in **Figure 14**b. Despite having 96% semiconducting outer wall purity, the presence of a small number of metallic outer walls and also metallic inner walls was evidenced in the transconductance measurements by a moderate on/off ratio of ca. 500 and on-state current of –700 nA. Electrical breakdown was performed by applying a source–drain bias of –100 V in cycles of 28 s, and three distinct regimes were identified with respect to the electronic properties of the devices. This process was followed by in situ monitoring of the off-state current during electrical breakdown as shown in Figure 14a. The first regime, after 1 cycle, corresponds to the removal of amorphous carbon and metallic percolation pathways, resulting in a 2-fold increase in on-state current (to –1.2 μA) and 4-fold increase in on/off current ratio (to 2×10^3). It is well known that the continued flow of current can result in annealing of carbon nanotubes, which may have also contributed to the observed improvement in on-state current.[216]

The second regime, consisting of two cycles, corresponds to the destruction of metallic nanotubes, and results in a decrease in both on- (–800 nA) and off-state current, with a significant increase in the on/off ratio (to 4.1×10^5). During the third regime, after a total of four cycles, no significant changes in the off-state current were seen, indicating the majority of metallic nanotubes have been removed. At this point the on-state current is reduced (–300 nA) due to destruction of some semiconducting pathways as a result of thermal cross-talk; however, the on/off ratio remains high at 1.4×10^4. Figure 14c shows a highlighted portion of the second regime wherein a stepwise decrease in the off-state current is observed, with each step corresponding to the destruction of a metallic pathway. Raman analysis was subsequently used in conjunction with diazonium chemistry to confirm that only DWCNTs with inner and outer semiconducting nanotubes were immune to electrical breakdown; however, whether the broken metallic outer walls remain around the semiconducting inner walls is not addressed.

In the case of few- or single-nanotube devices, more-controlled experiments are possible, and electrical breakdown has been used to selectively remove outer wall metallic nanotubes from DWCNTs. For example, Liu et al. demonstrated that the metallic outer wall of a (28,24)@(45,15) DWCNT can be "broken" by a high current.[10] While the device exhibited metallic behavior prior to electrical breakdown, afterwards, it became semiconducting with a low on/off current ratio of 20 – an order of magnitude lower that that observed for pure semiconducting SWCNTs of similar diameter. This suggests that the rest of the broken metallic outer wall remains in place, confounding the effect of the gate on the inner wall.[217] Wang et al. also demonstrated electrical breakdown of single-DWCNT devices, wherein the metallic inner wall of a M@S DWCNT was broken, significantly improving the on/off ratio.[217] Although such an approach essentially results in an SWCNT device, conflicting reports make it unclear if current-induced electrical breakdown leads to complete removal of the outer wall[154] or if the DWCNT remains mostly intact with only a small break in the outer wall.[217] The latter case would be of some interest to the carbon nanotube transistor community, as it could represent

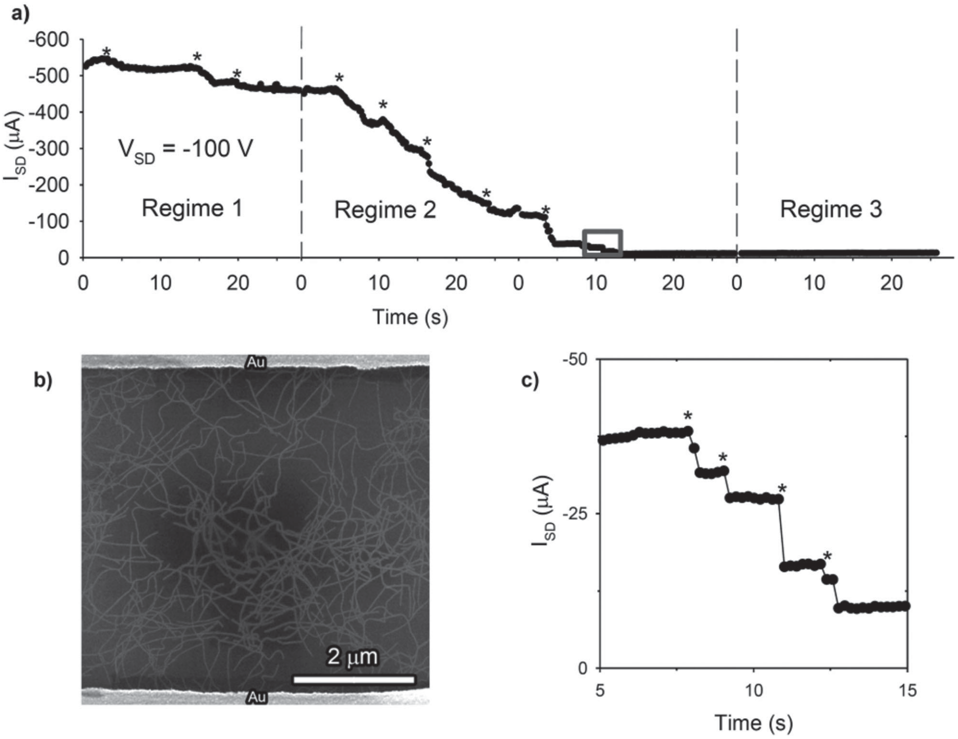

Figure 14. Enrichment of semiconducting DWCNTs by electrical breakdown of metallic percolation pathways. a) In situ current vs time measurement during electrical breakdown at a fixed source–drain bias (V_{SD} = –100 V) for the three regimes. Electrical breakdown events are characterized by sharp decreases in source–drain current (marked by the asterisks). b) Percolated DWCNT networks characterized by SEM before electrical breakdown. c) Enlargement of the boxed region in (a). Reproduced with permission.[63] Copyright 2014, Wiley-VCH.

a convenient method to provide a degree of shielding of an SWCNT from its surrounding environment.

In the work of Liu et al.,[10] DWCNTs were grown directly into an FET with narrow microfabricated slits for TEM analysis. This structure allowed the chirality of the inner and outer walls to be determined via electron diffraction and then directly correlated to in situ transconductance measurements. Although the inner@outer-wall combination was not controlled during growth, each of the four different types of DWCNTs could be located, and this allowed for comparison with theoretical calculations. As expected, the M@M (34,13)@(48,6) and S@M (19, 12)@(22,19) DWCNTs were found to be metallic in nature and showed no current modulation with varied gate voltages. However, the M@S and S@S DWCNTs were found to exhibit semiconducting character, albeit with very different on/off ratios. For the M@S (33,6)@(30,23) DWCNT, the on/off ratio was on the order of ca. 20. This is in stark contrast to the S@S (23,13)@(38,6) DWCNT with an on/off current ratio of ca. 10^4. Although metallic behavior was not observed for an S@S DWCNT in that study, Wang and co-workers[7] explain that this is still in accordance with the DFT predictions discussed previously in Section 2,[17,42] since the study employed large-diameter, incommensurate DWCNTs.

Similarly, Moore et al. characterized individual DWCNT FETs; however, in that case nanotube material of defined outer wall electronic type was used.[37] In that work, DWCNTs were gel-sorted by metallic or semiconducting outer wall and deposited onto lithographically-defined FET devices via dielectrophoretic deposition. Transconductance measurements revealed two sub-populations of behavior within each respective DWCNT outer wall type, which are shown in **Figure 15**. The first case corresponds to an M@M DWCNT with an on/off current ratio of unity at a source–drain voltage (V_{SD}) of 1 V, and no current modulation was observed with varying gate voltage. The second case, corresponding to S@M DWCNTs, exhibited an on/off ratio close to unity; however, a slight modulation with gate voltage was observed, revealing a semiconducting inner wall and differentiating it from the M@M case. The third case corresponds to S@S DWCNTs where typical p-type behavior was observed together with an on/off ratio of ca. 10^8. As the inter-wall distance is relatively low (0.380 ± 0.009 nm), the authors concluded that the behavior observed was from incommensurate DWCNTs. The last case corresponds to the M@S DWCNTs with a slight modulation observed and an on/off ratio of 1.4.

Bouilly et al. integrated DWCNTs of unknown chirality into FETs and used chemical functionalization to indirectly identify the four different DWCNT combinations.[218] This was done by assembling individual DWCNT FET devices (referred to as “pristine state”) and covalently functionalizing them using an outer-wall-selective, reversible aryldiazonium reaction (then referred to as “functionalized state”). This introduced phenyl groups onto the outer wall carbon lattice which inhibited current flow due to an increase in backscattering from defect-induced quasibound states.[219] The devices were then annealed at 500 °C, removing the phenyl groups and returning

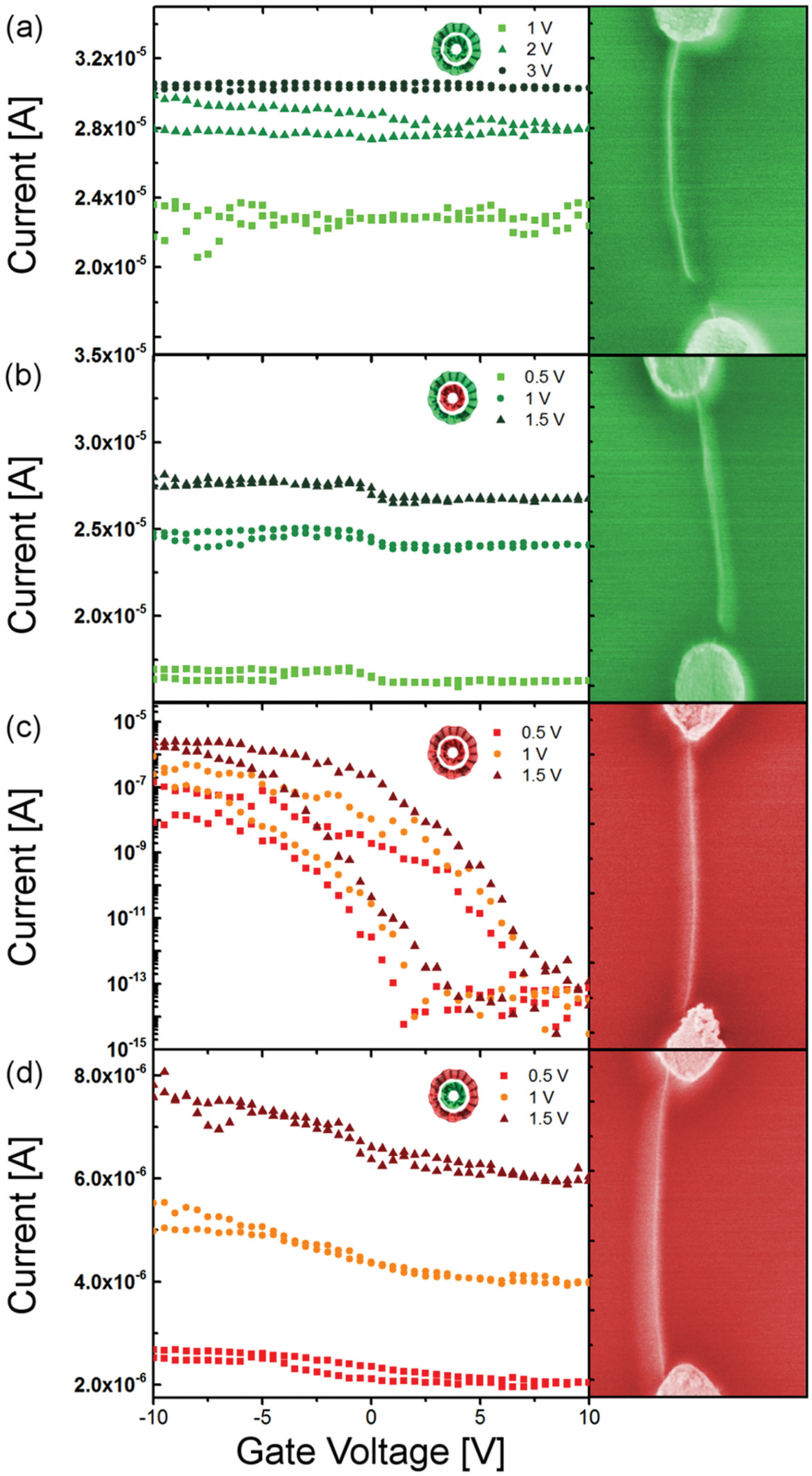

Figure 15. FETs comprising individual, electronically defined DWCNTs. Transconductance measurements at various source–drain voltages and corresponding false-color SEM images are shown and correspond to the four possible types of DWCNT FET: a) M@M, b) S@M, c) S@S, and d) M@S. Adapted with permission.[37] Copyright 2015, American Chemical Society.

the DWCNTs to their original ("defunctionalized") state. Transconductance measurements were made on DWCNTs in the pristine, functionalized, and defunctionalized states and they observed three distinct behaviors for the four inner@outer-wall combinations as shown in **Figure 16**.

The first was attributed to S@S DWCNTs, which, once again, were found not to be metallic, in contrast with the apparent predictions.[17,42] Indeed, this highlights the relative unlikelihood of inadvertently coming across an S@S DWCNT in the laboratory situation, which just happens to fit the strict requirements used in theoretical calculations, such that metallic behavior is observed. S@S DWCNTs were found to have an on/off ratio of ca. 10^4 in the pristine state, which remained high following functionalization. Consequently, the inner wall must also be semiconducting. The second behavior was attributed to S@M DWCNTs because an on/off ratio of ca. 10^2 was seen in the functionalized state, but in the pristine or defunctionalized states it was reduced to less than one order of magnitude. The authors attribute this lack of modulation in the pristine state to shorting of the device by the metallic outer wall. The third and last behavior was that attributable to either the M@S or M@M DWCNTs, in which no current modulation was observed in any of the pristine, functionalized or defunctionalized states. Owing to the constant current flowing through the metallic inner wall, the identity of the outer wall as being either metallic or semiconducting could not be determined.

The application of electronically defined DWCNTs in sensors for the detection of NH_3 was reported by Wang and co-workers.[220] In that work, DWCNTs with semiconducting outer walls[35] were first incorporated into thin-film FETs and then covalently functionalized using diazonium chemistry, resulting in the introduction of –COOH groups onto the outer wall. Upon exposure to NH_3, a change in transconductance behavior occurs and concentrations as low as 60×10^{-9} M (ca. 1 ppb) could be detected. Furthermore, the device exhibited 6000-times-higher sensitivity to amine-containing analytes (NH_3 and NH_2PhNH_2), compared with other small molecules. While this demonstrates a high sensitivity and selectivity, significant advances could stem from control over the inner wall. The high on-state current and on/off ratio of semiconducting nanotubes provide optimum performance in FETs and, coupled with the improved sensitivity of semiconducting nanotubes toward chemical or electrochemical changes in their environment,[221] this means that S@S DWCNTs would presumably provide both significantly higher on/off ratios and greatly improved sensitivity.[220]

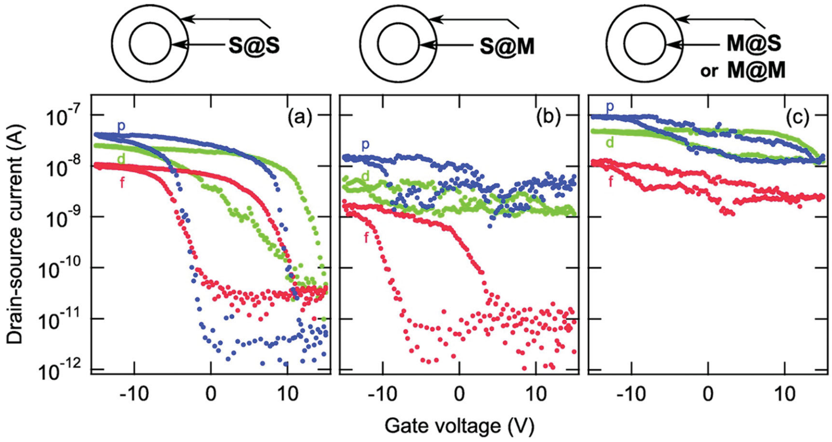

Figure 16. Transconductance measurements of individual DWCNT devices in the pristine (p – blue), functionalized (f – red), and defunctionalized (d – green) states as a function of gate voltage. The source-drain voltage is 10 mV. Three electrical signatures are distinguishable and assigned to the following electrical combinations: a) S@S, b) S@M, and c) M@S/M@M. Reproduced with permission.[218] Copyright 2011, American Chemical Society.

There is a variety of work directed to the implementation of DWCNTs in bioapplications (such as biosensors, drug carriers, or biocatalysts). An example is that conducted by Jung et al., who produced water-soluble, biologically and optically active protein-coated DWCNTs.[222] By employing a protein (specifically the mussel protein 3,4-dihydroxy-L-phenylalanin) as a biofunctionalization and individualization agent, the inherent insolubility in water and the low degree of biocompatibility of the DWCNTs was overcome. DWCNTs offer the most-appropriate material in such an instance because attachment of the protein requires covalent functionalization, which would render SWCNTs optically inactive.[223] Heavy covalent functionalization with carboxyl moieties, followed by attachment of the mussel protein through peptide bonds and subsequent ultracentrifugation yielded a uniform, transparent, protein-coated-DWCNT suspension. PL was used to characterize the suspension, and the authors concluded that several nanotube walls remained optically active, namely (6,4), (9,1), (8,3), (6,5), and (7,5), which the authors attribute to the inner walls. This is not in agreement with the work discussed previously by Yang et al.,[207] who determined that very few inner walls exhibit fluorescence, due to quenching. Jung et al. argue that the strongly oxidizing treatment of hydrogen peroxide would render the SWCNTs (which the authors estimate make up 5% of the pristine material) optically inactive; therefore, the PL could only originate from the inner walls.[222] Notwithstanding contemporary issues regarding the origin of the observed photoluminescence, it was determined that the protein-coated DWCNTs, when cast into thin films, remained conducting with an electrical conductivity of 5.31×10^3 S cm^{-1}.[222] Thus, protein coating may prove to be an effective means to realize the potential of DWCNTs in bioapplications because it can preserve the optical and Raman activity of the inner walls as well as the electronic functionality, providing two potential strategies for signaling.

The extra range of optical absorption provided by the inner wall of S@S DWCNTs could also be advantageous in respect to nanotube-based solar cells. Detailed modelling of the absorption properties of the first 70 semiconducting walls, spanning almost the entire useful region of the terrestrial solar spectrum, concluded that high-efficiency solar cells could only be obtained by using more than one type of nanotube absorber.[224] DWCNTs could thus provide the equivalent absorption range of a two-junction tandem nanotube solar cell in one single junction device. In several cases, DWCNTs have also been shown to be superior to their single- or multi-walled counterparts as transparent, conducting electrode materials in a variety of other photovoltaic architectures, including dye-sensitized[225] and carbon nanotube–silicon solar cells.[226]

The use of DWCNTs as electrochemical nanopores and nanochannels is currently being investigated, wherein they can mimic natural protein channels embedded within a biological system.[227] In this instance, nanotubes are incorporated into an epoxy membrane, resulting in a porous structure. By covalently functionalizing the protruding nanotube ends with chemical moieties, "gate molecules" capable of changing their physical orientation in response to external signals such as voltage, temperature, or light, can then be tethered to the nanotube, creating a gateable pore opening. Upon application of appropriate external stimuli, the gate molecules change their orientation, thus opening or closing the gate, and enabling or preventing ions and/or molecules to pass through the membrane. DWCNTs are an advantageous material for such a purpose because the smooth graphitic interior of the nanotubes provides faster fluid velocities than conventional membranes,[228] and because they provide adequate pore sizes and the outer wall enables a high density of functional groups at the nanotube ends. Zhan et al. recently used a one-step electro-oxidation process to attach an anodic dye (which acts as the gate molecule) to DWCNT/epoxy membranes.[227] The negative charge on the dye allows switching between an open and closed state through application of an external bias. When a negative bias is applied across the membrane, the anodic dye molecules are repelled away from the nanotube entrance and the pore is open. In this state, potassium ions are able to flow through the opening resulting in a measurable current. Conversely, when a positive bias is applied, the anionic dye molecules are dragged into the pore entrance, blocking or greatly reducing the flow of ionic current. While rectification of smaller molecules such as KCl was not observed due to the relatively large pore size (ca. 2 nm), a number of larger molecules, such as ferricyanide and sodium benzenesulphonate, were able to be rectified.

Field emission is another application where the properties of DWCNTs could be advantageous. In general, the geometry and chemical properties of nanotubes are ideal for field emission and owing to their low threshold voltage (the minimum gate-to-source voltage required to induce conduction between the source and the drain) and long lifetimes,[229] they could provide superior performance in applications such as field-emission displays[230] and miniature X-ray sources.[231] The high aspect ratios of the SWCNTs creates excellent point sources of field emission; however, molecules such as O_2 and H_2O affect the structure of the tip, leading to fluctuations in current[232] and the nanotubes are readily degraded at high emission currents.[233] MWCNTs offer increased stability; however, their smaller aspect ratios result in reduced emission performance compared with SWCNTs.[232] DWCNTs are an effective compromise, offering comparably high aspect ratios to SWCNTs with the added stability of an extra wall.[232,234] As such, there have been many reports on DWCNTs for field emission, with particular emphasis on enhancement through doping,[115,235] annealing,[116] growth,[114,236] and assembly[81,237] techniques.

DWCNTs present unique opportunities for nanoelectromechanical systems, in which wear and friction are the main causes of mechanical energy dissipation and component failure.[238] Cumings and Zettl observed ultra-low friction between sliding nanotube surfaces in experiments, leading to the suggestion that MWCNTs could be used as 0.1–1 GHz oscillators.[239] Rivera et al. investigated the oscillatory motion of DWCNTs resulting from displacing the inner wall by varying lengths and then releasing it.[240] Both commensurate and incommensurate DWCNTs were investigated, with the latter showing significantly lower frictional resistance. In each case, the oscillation was somewhat damped, suggesting that DWCNTs could potentially be harnessed as nanoscale shock-absorbers. Work by Ruoff and co-workers investigated the use of DWCNTs as rotational bearings.[241] Motivation for the investigation is that one of the major limitations of microbearings is that high friction-induced wear results in rapid disintegration. It was therefore hypothesized that atomically precise bearings, such as defect-free DWCNTs, could overcome this problem. Indeed, through molecular mechanical modeling, Ruoff and co-workers determined that the small interlayer friction between the inner and outer walls suggests that wear may not occur for typical rotational frequencies, leading to wearless rotational bearings. Recently, Zhang et al. demonstrated superlubricity on the macroscale and in ambient conditions using centimeters-long DWCNTs.[238] Superlubricity is a phenomenon where friction almost vanishes between two incommensurate surfaces, since the structural incompatibility between the concentric walls allows them to easily move relative to one another along their common axis.[242] This low friction arises because the lateral forces between the constituent walls are cancelled and this means that DWCNTs could be used as moving components in machines and electromechanical devices, with huge savings in energy, resource consumption, and maintenance.[243] Prior to this study, superlubricity had only been observed on the nanoscale, under high vacuum conditions;[242,244] thus, the work of Zhang et al.[238] poses a significant advance toward many practical applications, such as ultrasensitive sensors, fine-positioning devices, gyroscopes, and fast switches. By growing ultra-long, structurally perfect DWCNTs (important because the presence of any structural defects or adsorbed impurities on the surface would lead to an increase in friction), measurements of the length-independent inter-wall friction as low as 1 nN were obtained.

Lastly, DWCNTs have been employed as nanoscale mass sensors.[245] In this case, the DWCNT acts as a nanomechanical resonator and can be used for precision mass spectrometry because its resonant frequency, which is related to its mass and is exquisitely sensitive to the presence of any material on its surface. Carbon nanotubes are of great interest for such applications because of their low mass (typically four orders of magnitude lower than state-of-the-art micromachined resonators[246] and high elastic modulus,[247] which means that they can sustain high resonance frequencies. Despite SWCNTs possessing the smaller mass, DWCNTs provide a superior option for nanoscale mass spectrometers owing to their increased rigidity, which allows for even higher resonant frequencies, and their more-uniform electronic properties (ca. 5/9 of DWCNTs possess a metallic wall, whereas only ca. 1/3 of SWCNTs are metallic). Metallicity is important as it enables detection of the resonant frequency by broadcasting radio signals to the nanotube and listening for the vibrations. By using a single DWCNT attached to one electrode and in close proximity to a counter electrode, Jensen et al. were able to measure “mass noise” of just 0.4 Au atoms $Hz^{-1/2}$, which correlates to atomic sensitivity.[245] Besides the obvious advantages of sensitivity, the use of nanotubes as mass sensors does not require ionization of the test sample, and is therefore suitable for large biomolecules. A nanotube mass sensor is also sensitive at higher mass ranges and is vastly smaller than any current alternative, potentially allowing for lab-on-a-chip measurements.

7. Summary and Outlook

Whilst on the surface it may at first appear that the DWCNTs are merely an extension of the SWCNT field, it is now clear that pivotal, yet often subtle, differences exist in terms of their processing requirements, challenges, and outcomes, and in their potential for a host of useful applications and devices. The reports of DWCNT processing methods discussed in this review have made considerable progress toward the realization of high-purity DWCNT material for electronic, nanoelectromechanical, and sensor applications, and more, yet many avenues remain unexplored in this emerging field. Just as the more mature field of SWCNT separation has achieved chiral and isomeric specificity via a number of techniques in a relatively short period of time, it seems likely that significant advances will be made in the field of DWCNT processing through extension of established and evolving SWCNT sorting methodologies and continued research addressing the four fundamental challenges of targeted growth, controlled purification, sorting by outer wall electronic character and chirality, and the ultimate goal of sorting by inner wall electronic character and chirality. There are, of course, future issues of scale up that must be resolved to allow for production of far more than the spectroscopic quantities of material currently possible, yet overall, despite the significant difficulties involved in dealing with all of these challenges, they do not seem insurmountable and with the variety of potential applications continually growing, the outlook for the DWCNT field is indeed bright.

Acknowledgements

All the authors contributed equally to this work. K.E.M. appreciatively acknowledges and thanks the Karlsruhe House of Young Scientists, the

Playford Memorial Trust, and scholarship support from Professor Michael Brunger of the Flinders University of South Australia. B.S.F. gratefully acknowledges support from the Deutsche Forschungsgemeinschaft's Emmy Noether Program under grant number FL 834/1-1.

Note: In the originally published Review, the arrows relating to the "*m*" index in Figure 1a were misleading and the incorrect chirality was named in the caption. The Figure and caption were corrected herein on May 20, 2015.

Received: December 12, 2014
Revised: February 27, 2015

---

[1] M. S. Dresselhaus, G. Dresselhaus, R. Saito, *Carbon* **1995**, *33*, 883.
[2] a) T. W. Odom, J.-L. Huang, P. Kim, C. M. Lieber, *Nature* **1998**, *391*, 62; b) T. W. Odom, J.-L. Huang, P. Kim, C. M. Lieber, *J. Phys. Chem. B* **2000**, *104*, 2794; c) M. S. Dresselhaus, G. Dresselhaus, A. Jorio, *Annu. Rev. Mater. Res.* **2004**, *34*, 247.
[3] T. W. Ebbesen, P. M. Ajayan, *Nature* **1992**, *358*, 220.
[4] C. D. Spataru, S. Ismail-Beigi, L. X. Benedict, S. G. Louie, *Phys. Rev. Lett.* **2004**, *92*, 077402.
[5] S. M. Bachilo, M. S. Strano, C. Kittrell, R. H. Hauge, R. E. Smalley, R. B. Weisman, *Science* **2002**, *298*, 2361.
[6] R. Pfeiffer, T. Pichler, Y. A. Kim, H. Kuzmany, in *Carbon Nanotubes*, (Eds: A. Jorio, G. Dresselhaus, M. S. Dresselhaus), Springer, Berlin/Heidelberg, Germany **2008**, p. 495.
[7] C. Shen, A. H. Brozena, Y. Wang, *Nanoscale* **2011**, *3*, 503.
[8] Y. A. Kim, K.-S. Yang, H. Muramatsu, T. Hayashi, M. Endo, M. Terrones, M. S. Dresselhaus, *Carbon Lett.* **2014**, *15*, 77.
[9] T. Shimada, T. Sugai, Y. Ohno, S. Kishimoto, T. Mizutani, H. Yoshida, T. Okazaki, H. Shinohara, *Appl. Phys. Lett.* **2004**, *84*, 2412.
[10] K. Liu, W. Wang, Z. Xu, X. Bai, E. Wang, Y. Yao, J. Zhang, Z. Liu, *J. Am. Chem. Soc.* **2008**, *131*, 62.
[11] a) Y. A. Kim, H. Muramatsu, T. Hayashi, M. Endo, M. Terrones, M. S. Dresselhaus, *Chem. Phys. Lett.* **2004**, *398*, 87; b) Y. F. Li, R. Hatakeyama, T. Kaneko, T. Izumida, T. Okada, T. Kato, *Applied Physics Letters* **2006**, *89*, 093110; c) S. Kuwahara, S. Akita, M. Shirakihara, T. Sugai, Y. Nakayama, H. Shinohara, *Chem. Phys. Lett.* **2006**, *429*, 581.
[12] R. Saito, G. Dresselhaus, M. S. Dresselhaus, *Physical Properties of Carbon Nanotubes*, Vol. *4*, Imperial College Press, London **1998**.
[13] a) M. Kociak, K. Suenaga, K. Hirahara, Y. Saito, T. Nakahira, S. Iijima, *Phys. Rev. Lett.* **2002**, *89*, 155501; b) F. Villalpando-Paez, H. Son, D. Nezich, Y. P. Hsieh, J. Kong, Y. A. Kim, D. Shimamoto, H. Muramatsu, T. Hayashi, M. Endo, M. Terrones, M. S. Dresselhaus, *Nano Lett.* **2008**, *8*, 3879.
[14] S. D. Liang, *Phys. B (Amsterdam, Neth.)* **2004**, *352*, 305.
[15] S. Wang, M. Grifoni, *Phys. Rev. Lett.* **2005**, *95*, 266802.
[16] T. Okazaki, S. Bandow, G. Tamura, Y. Fujita, K. Iakoubovskii, S. Kazaoui, N. Minami, T. Saito, K. Suenaga, S. Iijima, *Phys. Rev. B: Condens. Matter Mater. Phys.* **2006**, *74*, 153404.
[17] R. Moradian, S. Azadi, H. Refii-tabar, *J. Phys.: Condens. Matter* **2007**, *19*, 176209.
[18] K. Liu, C. Jin, X. Hong, J. Kim, A. Zettl, E. Wang, F. Wang, *Nat. Phys.* **2014**, *10*, 737.
[19] S. Uryu, T. Ando, *Phys. Rev. B: Condens. Matter Mater. Phys.* **2005**, *72*, 245403.
[20] A. H. Brozena, J. Moskowitz, B. Shao, S. Deng, H. Liao, K. J. Gaskell, Y. Wang, *J. Am. Chem. Soc.* **2010**, *132*, 3932.
[21] Y. Piao, C.-F. Chen, A. A. Green, H. Kwon, M. C. Hersam, C. S. Lee, G. C. Schatz, Y. Wang, *J. Phys. Chem. Lett.* **2011**, *2*, 1577.
[22] a) E. T. Mickelson, C. B. Huffman, A. G. Rinzler, R. E. Smalley, R. H. Hauge, J. L. Margrave, *Chem. Phys. Lett.* **1998**, *296*, 188; b) J. Zhao, H. Park, J. Han, J. P. Lu, *J. Phys. Chem. B* **2004**, *108*, 4227.
[23] J. L. Hutchison, N. A. Kiselev, E. P. Krinichnaya, A. V. Krestinin, R. O. Loutfy, A. P. Morawsky, V. E. Muradyan, E. D. Obraztsova, J. Sloan, S. V. Terekhov, D. N. Zakharov, *Carbon* **2001**, *39*, 761.
[24] T. Sugai, H. Yoshida, T. Shimada, T. Okazaki, H. Shinohara, S. Bandow, *Nano Lett.* **2003**, *3*, 769.
[25] H. Qiu, Z. Shi, L. Guan, L. You, M. Gao, S. Zhang, J. Qiu, Z. Gu, *Carbon* **2006**, *44*, 516.
[26] B. W. Smith, D. E. Luzzi, *Chem. Phys. Lett.* **2000**, *321*, 169.
[27] M. Kalbáč, L. Kavan, L. Juha, S. Civiš, M. Zukalová, M. Bittner, P. Kubát, V. Vorlíček, L. Dunsch, *Carbon* **2005**, *43*, 1610.
[28] a) H. Dai, A. G. Rinzler, P. Nikolaev, A. Thess, D. T. Colbert, R. E. Smalley, *Chem. Phys. Lett.* **1996**, *260*, 471; b) J. Wei, L. Ci, B. Jiang, Y. Li, X. Zhang, H. Zhu, C. Xu, D. Wu, *J. Mater. Chem.* **2003**, *13*, 1340; c) A. Grüneis, M. H. Rümmeli, C. Kramberger, A. Barreiro, T. Pichler, R. Pfeiffer, H. Kuzmany, T. Gemming, B. Büchner, *Carbon* **2006**, *44*, 3177.
[29] Y. Saito, T. Nakahira, S. Uemura, *J. Phys. Chem. B* **2003**, *107*, 931.
[30] H. Yoshida, T. Sugai, H. Shinohara, *J. Phys. Chem. C* **2008**, *112*, 19908.
[31] S. Deng, A. H. Brozena, Y. Zhang, Y. Piao, Y. Wang, *Chem. Commun.* **2011**, *47*, 758.
[32] H. Nie, H. Wang, A. Cao, Z. Shi, S.-T. Yang, Y. Yuan, Y. Liu, *Nanoscale* **2011**, *3*, 970.
[33] G. Liu, Y. Saito, D. Nishio-Hamane, A. K. Bauri, E. Flahaut, T. Kimura, N. Komatsu, *J. Mater. Chem. A* **2014**, *2*, 19067.
[34] A. A. Green, M. C. Hersam, *Nat. Nanotechnol.* **2009**, *4*, 64.
[35] A. A. Green, M. C. Hersam, *ACS Nano* **2011**, *5*, 1459.
[36] K. E. Moore, M. Pfohl, F. Hennrich, V. S. Chakradhanula, C. Kuebel, M. M. Kappes, J. G. Shapter, R. Krupke, B. S. Flavel, *ACS Nano* **2014**, *8*, 6756.
[37] K. E. Moore, M. Pfohl, D. D. Tune, F. Hennrich, S. Dehm, V. S. K. Chakradhanula, C. Kuebel, R. Krupke, B. S. Flavel, *ACS Nano*; DOI: 10.1021/nn506869h.
[38] W. Gomulya, G. D. Costanzo, E. J. F. de Carvalho, S. Z. Bisri, V. Derenskyi, M. Fritsch, N. Frohlich, S. Allard, P. Gordiichuk, A. Herrmann, S. J. Marrink, M. C. dos Santos, U. Scherf, M. A. Loi, *Adv. Mater.* **2013**, *25*, 2948.
[39] S. K. Samanta, M. Fritsch, U. Scherf, W. Gomulya, S. Z. Bisri, M. A. Loi, *Acc. Chem. Res.* **2014**, *47*, 2446.
[40] C. Y. Khripin, J. A. Fagan, M. Zheng, *J. Am. Chem. Soc.* **2013**, *135*, 6822.
[41] N. K. Subbaiyan, S. Cambré, A. N. G. Parra-Vasquez, E. H. Hároz, S. K. Doorn, J. G. Duque, *ACS Nano* **2014**, *8*, 1619.
[42] S. Okada, A. Oshiyama, *Phys. Rev. Lett.* **2003**, *91*, 216801.
[43] V. Zólyomi, Á. Rusznyák, J. Kürti, Á. Gali, F. Simon, H. Kuzmany, Á. Szabados, P. Surján, *Phys. Status Solidi B* **2006**, *243*, 3476.
[44] W. Ren, F. Li, J. Chen, S. Bai, H.-M. Cheng, *Chem. Phys. Lett.* **2002**, *359*, 196.
[45] a) J. M. Zuo, I. Vartanyants, M. Gao, R. Zhang, L. A. Nagahara, *Science* **2003**, *300*, 1419; b) K. Hirahara, M. Kociak, S. Bandow, T. Nakahira, K. Itoh, Y. Saito, S. Iijima, *Phys. Rev. B: Condens. Matter Mater. Phys.* **2006**, *73*, 195420; c) K. Liu, Z. Xu, W. Wang, P. Gao, W. Fu, X. Bai, E. Wang, *J. Phys. D: Appl. Phys.* **2009**, *42*, 125412.
[46] Z. M. Li, Z. K. Tang, H. J. Liu, N. Wang, C. T. Chan, R. Saito, S. Okada, G. D. Li, J. S. Chen, N. Nagasawa, S. Tsuda, *Phys. Rev. Lett.* **2001**, *87*, 127401.
[47] a) K. H. Ahn, Y.-H. Kim, J. Wiersig, K. J. Chang, *Phys. Rev. Lett.* **2003**, *90*, 026601; b) J. Chen, L. Yang, H. Yang, J. Dong, *Chem. Phys. Lett.* **2004**, *400*, 384.
[48] S. Uryu, *Phys. Rev. B: Condens. Matter Mater. Phys.* **2004**, *69*, 075402.
[49] K.-H. Ahn, Y.-H. Kim, J. Wiersig, K. J. Chang, *Phys. E (Amsterdam, Neth.)* **2004**, *22*, 666.
[50] J. Chen, L. Yang, *J. Phys.: Condens. Matter* **2005**, *17*, 957.
[51] M. Kalbac, A. A. Green, M. C. Hersam, L. Kavan, *Chem. Eur. J.* **2011**, *17*, 9806.

[52] a) M. Kalbac, L. Kavan, L. Dunsch, *J. Phys. Chem. C* **2008**, *112*, 16759; b) M. Kalbac, H. Farhat, L. Kavan, J. Kong, K.-i. Sasaki, R. Saito, M. S. Dresselhaus, *ACS Nano* **2009**, *3*, 2320.

[53] J. Cambedouzou, J. L. Sauvajol, A. Rahmani, E. Flahaut, A. Peigney, C. Laurent, *Phys. Rev. B: Condens. Matter Mater. Phys.* **2004**, *69*, 235422.

[54] K. Liu, J. Deslippe, F. Xiao, R. B. Capaz, X. Hong, S. Aloni, A. Zettl, W. Wang, X. Bai, S. G. Louie, E. Wang, F. Wang, *Nat. Nanotechnol.* **2012**, *7*, 325.

[55] a) J. Lefebvre, J. M. Fraser, Y. Homma, P. Finnie, *Appl. Phys. A* **2004**, *78*, 1107; b) J. H. Choi, M. S. Strano, *Appl. Phys. Lett.* **2007**, *90*, 223114; c) M. Engel, K. E. Moore, A. Alam, S. Dehm, R. Krupke, B. S. Flavel, *ACS Nano* **2014**, *8*, 9324; d) K. Liu, X. Hong, Q. Zhou, C. Jin, J. Li, W. Zhou, J. Liu, E. Wang, A. Zettl, F. Wang, *Nat. Nanotechnol.* **2013**, *8*, 917; e) R. M. Jain, R. Howden, K. Tvrdy, S. Shimizu, A. J. Hilmer, T. P. McNicholas, K. K. Gleason, M. S. Strano, *Adv. Mater.* **2012**, *24*, 4436.

[56] A. M. Rao, E. Richter, S. Bandow, B. Chase, P. C. Eklund, K. A. Williams, S. Fang, K. R. Subbaswamy, M. Menon, A. Thess, R. E. Smalley, G. Dresselhaus, M. S. Dresselhaus, *Science* **1997**, *275*, 187.

[57] a) M. S. Dresselhaus, G. Dresselhaus, A. Jorio, A. G. Souza Filho, R. Saito, *Carbon* **2002**, *40*, 2043; b) P. T. Araujo, P. B. C. Pesce, M. S. Dresselhaus, K. Sato, R. Saito, A. Jorio, *Phys. E (Amsterdam, Neth.)* **2010**, *42*, 1251.

[58] M. S. Arnold, S. I. Stupp, M. C. Hersam, *Nano Lett.* **2005**, *5*, 713.

[59] K. Moshammer, F. Hennrich, M. Kappes, *Nano Res.* **2009**, *2*, 599.

[60] H. Liu, D. Nishide, T. Tanaka, H. Kataura, *Nat. Commun.* **2011**, *2*, 309.

[61] K. Tvrdy, R. M. Jain, R. Han, A. J. Hilmer, T. P. McNicholas, M. S. Strano, *ACS Nano* **2013**, *7*, 1779.

[62] B. S. Flavel, K. E. Moore, M. Pfohl, M. M. Kappes, F. Hennrich, *ACS Nano* **2014**, *82*, 1817.

[63] A. L. Ng, Y. Sun, L. Powell, C.-F. Sun, C.-F. Chen, C. S. Lee, Y. Wang, *Small* **2015**, *11*, 68.

[64] W. Wenseleers, I. I. Vlasov, E. Goovaerts, E. D. Obraztsova, A. S. Lobach, A. Bouwen, *Adv. Funct. Mater.* **2004**, *14*, 1105.

[65] a) T. Ando, *J. Phys.Soc. Jpn.* **1997**, *66*, 1066; b) M. Ichida, S. Mizuno, Y. Saito, H. Kataura, Y. Achiba, A. Nakamura, *Phys. Rev. B: Condens. Matter Mater. Phys.* **2002**, *65*, 241407; c) F. Wang, G. Dukovic, L. E. Brus, T. F. Heinz, *Science* **2005**, *308*, 838.

[66] M. Kalbac, A. A. Green, M. C. Hersam, L. Kavan, *ACS Nano* **2010**, *4*, 459.

[67] Y.-A. Kim, H. Muramatsu, M. Kojima, T. Hayashi, M. Endo, M. Terrones, M. S. Dresselhaus, *Chem. Phys. Lett.* **2006**, *420*, 377.

[68] A. Jorio, M. S. Dresselhaus, R. Saito, G. Dresselhaus, *Raman Spectroscopy in Graphene Related Systems*, John Wiley & Sons, New York **2010**.

[69] R. Pfeiffer, C. Kramberger, F. Simon, H. Kuzmany, V. N. Popov, H. Kataura, *Eur. Phys. J. B* **2004**, *42*, 345.

[70] R. Pfeiffer, H. Kuzmany, C. Kramberger, C. Schaman, T. Pichler, H. Kataura, Y. Achiba, J. Kürti, V. Zólyomi, *Phys. Rev. Lett.* **2003**, *90*, 225501.

[71] Z. Kominkova, V. Vales, M. C. Hersam, M. Kalbac, *Carbon* **2014**, *78*, 366.

[72] M. S. Dresselhaus, G. Dresselhaus, R. Saito, A. Jorio, *Phys. Rep.* **2005**, *409*, 47.

[73] M. A. Pimenta, A. Jorio, S. D. M. Brown, A. G. Souza Filho, G. Dresselhaus, J. H. Hafner, C. M. Lieber, R. Saito, M. S. Dresselhaus, *Phys. Rev. B: Condens. Matter Mater. Phys.* **2001**, *64*, 041401.

[74] M. H. Park, J. W. Jang, C. E. Lee, C. J. Lee, *Appl. Phys. Lett.* **2005**, *86*, 023110.

[75] Y. Sato, K. Yanagi, Y. Miyata, K. Suenaga, H. Kataura, S. Iijima, *Nano Lett.* **2008**, *8*, 3151.

[76] a) R. Bandyopadhyaya, E. Nativ-Roth, O. Regev, R. Yerushalmi-Rozen, *Nano Lett.* **2001**, *2*, 25; b) V. C. Moore, M. S. Strano, E. H. Haroz, R. H. Hauge, R. E. Smalley, J. Schmidt, Y. Talmon, *Nano Lett.* **2003**, *3*, 1379.

[77] S. Iijima, *Nature* **1991**, *354*, 56.

[78] E. G. Gamaly, T. W. Ebbessen, *Phys. Rev. B: Condens. Matter Mater. Phys.* **1995**, *52*, 2083.

[79] H. Huang, H. Kajiura, S. Tsutsui, Y. Murakami, M. Ata, *J. Phys. Chem. B* **2003**, *107*, 8794.

[80] T. Sugai, H. Omote, S. Bandow, N. Tanaka, H. Shinohara, *J. Chem. Phys.* **2000**, *112*, 6000.

[81] J. Zhao, Y. Su, Z. Yang, L. Wei, Y. Wang, Y. Zhang, *Carbon* **2013**, *58*, 92.

[82] L. Li, F. Li, C. Liu, H. M. Cheng, *Carbon* **2005**, *43*, 623.

[83] K. Xu, Y. Li, C. Xu, J. Gao, H. Liu, H. Yang, P. Richard, *Chem. Eng. J.* **2013**, *225*, 210.

[84] K. Xu, Y. Li, F. Yang, W. Yang, L. Zhang, C. Xu, T. Kaneko, R. Hatakeyama, *Carbon* **2014**, *68*, 511.

[85] R. H. Baughman, *Nat. Nanotechnol.* **2006**, *1*, 94.

[86] a) B. W. Smith, M. Monthioux, D. E. Luzzi, *Nature* **1998**, *396*, 323; B) B. W. Smith, M. Monthioux, D. E. Luzzi, *Chem. Phys. Lett.* **1999**, *315*, 31.

[87] T. Guo, P. Nikoleav, A. Thess, D. T. Colbert, R. E. Smalley, *Chem. Phys. Lett.* **1995**, *243*, 49.

[88] S. Bandow, M. Takizawa, K. Hirahara, M. Yudasaka, S. Iijima, *Chem. Phys. Lett.* **2001**, *337*, 48.

[89] a) L. Guan, Z. Shi, M. Li, Z. Gu, *Carbon* **2005**, *43*, 2780; b) L. Yongfeng, H. Rikizo, K. Toshiro, O. Takeru, *Jpn. J. Appl. Phys.* **2006**, *45*, L428; c) H. Shiozawa, T. Pichler, A. Grüneis, R. Pfeiffer, H. Kuzmany, Z. Liu, K. Suenaga, H. Kataura, *Adv. Mater.* **2008**, *20*, 1443.

[90] A. Barreiro, S. Hampel, M. H. Rümmeli, C. Kramberger, A. Grüneis, K. Biedermann, A. Leonhardt, T. Gemming, B. Büchner, A. Bachtold, T. Pichler, *J. Phys. Chem. B* **2006**, *110*, 20973.

[91] C. Kramberger, A. Waske, K. Biedermann, T. Pichler, T. Gemming, B. Büchner, H. Kataura, *Chem. Phys. Lett.* **2005**, *407*, 254.

[92] M. Berd, P. Puech, A. Righi, A. Benfdila, M. Monthioux, *Small* **2012**, *8*, 2045.

[93] M. Suzuki, T. Iida, K. Nasu, *Phys. Rev. B: Condens. Matter Mater. Phys.* **2000**, *61*, 2188.

[94] M. Melle-Franco, H. Kuzmany, F. Zerbetto, *J. Phys. Chem. B* **2003**, *107*, 6986.

[95] H. Kuzmany, W. Plank, R. Pfeiffer, F. Simon, *J. Raman Spectrosc.* **2008**, *39*, 134.

[96] A. Oberlin, M. Endo, T. Koyama, *J. Cryst. Growth* **1976**, *32*, 335.

[97] H. Dai, A. G. Rinzer, P. Nikolaev, A. Thess, D. T. Colbert, R. E. Smalley, *Chem. Phys. Lett.* **1996**, *260*, 471.

[98] C. L. Cheung, A. Kurtz, H. Park, C. M. Lieber, *J. Phys. Chem. B* **2002**, *106*, 2429.

[99] Y. Liu, W.-Z. Qian, Q. Zhang, G.-Q. Ning, Q. Wen, G.-H. Luo, F. Wei, *Carbon* **2008**, *46*, 1860.

[100] a) W. Z. Li, J. G. Wen, M. Sennett, Z. F. Ren, *Chem. Phys. Lett.* **2003**, *368*, 299; b) J. Wei, B. Jiang, D. Wu, B. Wei, *J. Phys. Chem. B* **2004**, *108*, 8844; c) G. Ning, F. Wei, Q. Wen, G. Luo, Y. Wang, Y. Jin, *J. Phys. Chem. B* **2005**, *110*, 1201; d) H. Qi, C. Qian, J. Liu, *Nano Lett.* **2007**, *7*, 2417; e) Q. Liu, W. Ren, F. Li, H. Cong, H.-M. Cheng, *J. Phys. Chem. C* **2007**, *111*, 5006.

[101] E. Flahaut, C. Laurent, A. Peigney, *Carbon* **2005**, *43*, 375.

[102] J. H. Hafner, M. J. Bronikowski, B. R. Azamian, P. Nikolaev, A. G. Rinzler, D. T. Colbert, K. A. Smith, R. E. Smalley, *Chem. Phys. Lett.* **1998**, *296*, 195.

[103] G. Xiong, Y. Suda, D. Wang, J. Huang, Z. Ren, *Nanotechnology* **2005**, *16*, 532.

[104] a) S. C. Lyu, B. C. Liu, C. J. Lee, H. K. Kang, C.-W. Yang, C. Y. Park, *Chem. Mater.* **2003**, *15*, 3951; b) S. C. Lyu, T. J. Lee, C. W. Yang, C. J. Lee, *Chem. Commun.* **2003**, *1404*; c) M. Hiramatsu, H. Nagao, M. Taniguchi, H. Amano, Y. Ando, M. Hori, *Jpn. J. Appl. Phys.* **2005**, *44*, L693; d) H. Ago, N. Uehara, N. Yoshihara, M. Tsuji, M. Yumura, N. Tomonaga, T. Setoguchi, *Carbon* **2006**, *44*, 2912; e) J. Huang, Q. Zhang, M. Zhao, F. Wei, *Nano Res.* **2009**, *2*, 872.

[105] a) J. Zhu, M. Yudasaka, S. Iijima, *Chem. Phys. Lett.* **2003**, *380*, 496; b) H. Ago, K. Nakamura, N. Uehara, M. Tsuji, *J. Phys. Chem. B* **2004**, *108*, 18908; c) G. Ning, Y. Liu, F. Wei, Q. Wen, G. Luo, *J. Phys. Chem. C* **2007**, *111*, 1969; d) Q. Zhang, M.-Q. Zhao, J.-Q. Huang, Y. Liu, Y. Wang, W.-Z. Qian, F. Wei, *Carbon* **2009**, *47*, 2600.

[106] T. Hiraoka, T. Yamada, K. Hata, D. N. Futaba, H. Kurachi, S. Uemura, M. Yumura, S. Iijima, *J. Am. Chem. Soc.* **2006**, *128*, 13338.

[107] S. B. Sinnott, R. Andrews, D. Qian, A. M. Rao, Z. Mao, E. C. Dickey, F. Derbyshire, *Chem. Phys. Lett.* **1999**, *315*, 25.

[108] E. Flahaut, R. Bacsa, A. Peigney, C. Laurent, *Chem. Commun.* **2003**, 1442.

[109] E. Flahaut, A. Peigney, C. Laurent, A. Rousset, *J. Mater. Chem.* **2000**, *10*, 249.

[110] L. Ci, Z. Rao, Z. Zhou, D. Tang, X. Yan, Y. Liang, D. Liu, H. Yuan, W. Zhou, G. Wang, W. Liu, S. Xie, *Chem. Phys. Lett.* **2002**, *359*, 63.

[111] a) H. M. Cheng, F. Li, G. Su, H. Y. Pan, L. L. He, X. Sun, M. S. Dresselhaus, *Appl. Phys. Lett.* **1998**, *72*, 3282; b) L. Ci, Y. Li, B. Wei, J. Liang, C. Xu, D. Wu, *Carbon* **2000**, *38*, 1933; c) Q. Liu, W. Ren, Z.-G. Chen, D.-W. Wang, B. Liu, B. Yu, F. Li, H. Cong, H.-M. Cheng, *ACS Nano* **2008**, *2*, 1722; d) H. M. Cheng, F. Li, X. Sun, S. D. M. Brown, M. A. Pimenta, A. Marucci, G. Dresselhaus, M. S. Dresselhaus, *Chem. Phys. Lett.* **1998**, *289*, 602; e) H. W. Zhu, C. L. Xu, D. H. Wu, B. Q. Wei, R. Vajtai, P. M. Ajayan, *Science* **2002**, *296*, 884.

[112] A. Modi, N. Koratkar, E. Lass, B. Wei, P. M. Ajayan, *Nature* **2003**, *424*, 171.

[113] S. C. Lim, Y. C. Choi, H. J. Jeong, Y. M. Shin, K. H. An, D. J. Bae, Y. H. Lee, N. S. Lee, J. M. Kim, *Adv. Mater.* **2001**, *13*, 1563.

[114] G. Chen, D. H. Shin, T. Iwasaki, H. Kawarada, C. J. Lee, *Nanotechnology* **2008**, *19*, 415703.

[115] K.-Y. Chun, H. S. Lee, C. J. Lee, *Carbon* **2009**, *47*, 169.

[116] S. I. Jung, S. H. Jo, H. S. Moon, J. M. Kim, D.-S. Zang, C. J. Lee, *J. Phys. Chem. C* **2007**, *111*, 4175.

[117] T. Yamada, T. Namai, K. Hata, D. N. Futaba, K. Mizuno, J. Fan, M. Yudasaka, M. Yumura, S. Iijima, *Nat. Nanotechnol.* **2006**, *1*, 131.

[118] L. Ci, R. Vajtai, P. M. Ajayan, *J. Phys. Chem. C* **2007**, *111*, 9077.

[119] H. Kim, J. Kang, Y. Kim, B. H. Hong, J. Choi, S. Iijima, *J. Nanosci. Nanotechnol.* **2011**, *11*, 470.

[120] T.-Y. Liu, L.-L. Zhang, W.-J. Yu, S.-S. Li, P.-X. Hou, H.-T. Cong, C. Liu, H.-M. Cheng, *Carbon* **2013**, *56*, 167.

[121] Y. Fu, S. Chen, J. Bielecki, A. Matic, T. Wang, L.-L. Ye, J. Liu, *Mater. Lett.* **2012**, *72*, 78.

[122] P. Nikolaev, D. Hooper, N. Perea-López, M. Terrones, B. Maruyama, *ACS Nano* **2014**, *8*, 10214.

[123] a) R. S. Ruoff, D. S. Tse, R. Malhotra, D. C. Lorents, *J. Phys. Chem.* **1993**, *97*, 3379; b) S. Bandow, S. Asaka, X. Zhao, Y. Ando, *Appl. Phys. A* **1998**, *67*, 23.

[124] a) J.-M. Moon, K. H. An, Y. H. Lee, Y. S. Park, D. J. Bae, G.-S. Park, *J. Phys. Chem. B* **2001**, *105*, 5677; b) M. T. Martinez, M. A. Callejas, A. M. Benito, M. Cochet, T. Seeger, A. Ansón, J. Schreiber, C. Gordon, C. Marhic, O. Chauvet, J. L. G. Fierro, W. K. Maser, *Carbon* **2003**, *41*, 2247; c) H. Hu, B. Zhao, M. E. Itkis, R. C. Haddon, *J. Phys. Chem. B* **2003**, *107*, 13838; d) J. Zhang, H. Zou, Q. Qing, Y. Yang, Q. Li, Z. Liu, X. Guo, Z. Du, *J. Phys. Chem. B* **2003**, *107*, 3712.

[125] Y. Miyata, Y. Maniwa, H. Kataura, *J. Phys. Chem. B* **2005**, *110*, 25.

[126] J. G. Wiltshire, A. N. Khlobystov, L. J. Li, S. G. Lyapin, G. A. D. Briggs, R. J. Nicholas, *Chem. Phys. Lett.* **2004**, *386*, 239.

[127] Y. Peng, H. Liu, *Ind. Eng. Chem. Res.* **2006**, *45*, 6483.

[128] Y. Feng, H. Zhang, Y. Hou, T. P. McNicholas, D. Yuan, S. Yang, L. Ding, W. Feng, J. Liu, *ACS Nano* **2008**, *2*, 1634.

[129] M. Zheng, A. Jagota, E. D. Semke, B. A. Diner, R. S. McLean, S. R. Lustig, R. E. Richardson, N. G. Tassi, *Nat. Mater.* **2003**, *2*, 338.

[130] S. Ghosh, S. M. Bachilo, R. B. Weisman, *Nat. Nanotechnol.* **2010**, *5*, 443.

[131] a) A. Nish, J.-Y. Hwang, J. Doig, R. J. Nicholas, *Nat. Nanotechnol.* **2007**, *2*, 640; b) F. Chen, B. Wang, Y. Chen, L.-J. Li, *Nano Lett.* **2007**, *7*, 3013; c) W. Gomulya, G. D. Costanzo, E. J. F. de Carvalho, S. Z. Bisri, V. Derenskyi, M. Fritsch, N. Fröhlich, S. Allard, P. Gordiichuk, A. Herrmann, S. J. Marrink, M. C. dos Santos, U. Scherf, M. A. Loi, *Adv. Mater.* **2013**, *25*, 2948; d) P. Gerstel, S. Klumpp, F. Hennrich, A. Poschlad, V. Meded, E. Blasco, W. Wenzel, M. M. Kappes, C. Barner-Kowollik, *ACS Macro Lett.* **2013**, *3*, 10; e) J. Ding, Z. Li, J. Lefebvre, F. Cheng, G. Dubey, S. Zou, P. Finnie, A. Hrdina, L. Scoles, G. P. Lopinski, *Nanoscale* **2014**, *6*, 2328.

[132] J. Y. Hwang, A. Nish, J. Doig, S. Douven, C. W. Chen, L. C. Chen, R. J. Nicholas, *J. Am. Chem. Soc.* **2008**, *130*, 3543.

[133] S. Deng, Y. Zhang, A. H. Brozena, M. L. Mayes, P. Banerjee, W.-A. Chiou, G. W. Rubloff, G. C. Schatz, Y. Wang, *Nat. Commun.* **2011**, *2*, 382.

[134] L. Vaisman, H. D. Wagner, G. Marom, *Adv. Colloid Interface Sci.* **2006**, *128–130*, 37.

[135] L. Cooper, H. Amano, M. Hiraide, S. Houkyou, I. Y. Jang, Y. J. Kim, H. Muramatsu, J. H. Kim, T. Hayashi, Y. A. Kim, M. Endo, M. S. Dresselhaus, *Appl. Phys. Lett.* **2009**, *95*, 233104.

[136] A. J. Blanch, C. E. Lenehan, J. S. Quinton, *J. Phys. Chem. B* **2010**, *114*, 9805.

[137] a) V. Georgakilas, N. Tagmatarchis, D. Pantarotto, A. Bianco, J.-P. Briand, M. Prato, *Chem. Commun.* **2002**, 3050; b) J. L. Hudson, M. J. Casavant, J. M. Tour, *J. Am. Chem. Soc.* **2004**, *126*, 11158; c) M. G. Ruther, F. Frehill, J. E. O'Brien, A. I. Minett, W. J. Blau, J. G. Vos, M. Panhuis, *J. Phys. Chem. B* **2004**, *108*, 9665; d) W.-J. Kim, N. Nair, C. Y. Lee, M. S. Strano, *J. Phys. Chem. C* **2008**, *112*, 7326.

[138] S. Banerjee, S. S. Wong, *Nano Lett.* **2004**, *4*, 1445.

[139] a) K. H. An, J. S. Park, C.-M. Yang, S. Y. Jeong, S. C. Lim, C. Kang, J.-H. Son, M. S. Jeong, Y. H. Lee, *J. Am. Chem. Soc.* **2005**, *127*, 5196; b) A. J. Blanch, C. E. Lenehan, J. S. Quinton, *J. Phys. Chem. C* **2011**, *116*, 1709.

[140] M. S. Arnold, A. A. Green, J. F. Hulvat, S. I. Stupp, M. C. Hersam, *Nat. Nanotechnol.* **2006**, *1*, 60.

[141] J. A. Fagan, M. L. Becker, J. Chun, P. Nie, B. J. Bauer, J. R. Simpson, A. Hight-Walker, E. K. Hobbie, *Langmuir* **2008**, *24*, 13880.

[142] F. Bonaccorso, T. Hasan, P. H. Tan, C. Sciascia, G. Privitera, G. Di Marco, P. G. Gucciardi, A. C. Ferrari, *J. Phys. Chem. C* **2010**, *114*, 17267.

[143] A. A. Green, M. C. Hersam, *Adv. Mater.* **2011**, *23*, 2185.

[144] M. Zheng, A. Jagota, M. S. Strano, A. P. Santos, P. Barone, S. G. Chou, B. A. Diner, M. S. Dresselhaus, R. S. Mclean, G. B. Onoa, G. G. Samsonidze, E. D. Semke, M. Usrey, D. J. Walls, *Science* **2003**, *302*, 1545.

[145] M. Zheng, E. D. Semke, *J. Am. Chem. Soc.* **2007**, *129*, 6084.

[146] X. Tu, S. Manohar, A. Jagota, M. Zheng, *Nature* **2009**, *460*, 250.

[147] A. Nish, J. Y. Hwang, J. Doig, R. J. Nicholas, *Nat. Nanotechnol.* **2007**, *2*, 640.
[148] F. M. Chen, B. Wang, Y. Chen, L. J. Li, *Nano Lett.* **2007**, *7*, 3013.
[149] M. F. Islam, E. Rojas, D. M. Bergey, A. T. Johnson, A. G. Yodh, *Nano Lett.* **2003**, *3*, 269.
[150] W. H. Duan, Q. Wang, F. Collins, *Chem. Sci.* **2011**, *2*, 1407.
[151] H. Liu, T. Tanaka, Y. Urabe, H. Kataura, *Nano Lett.* **2013**, *13*, 1996.
[152] A. J. Blanch, J. S. Quinton, J. G. Shapter, *Carbon* **2013**, *60*, 471.
[153] B. S. Flavel, M. M. Kappes, R. Krupke, F. Hennrich, *ACS Nano* **2013**, *7*, 3557.
[154] P. G. Collins, M. S. Arnold, P. Avouris, *Science* **2001**, *292*, 706.
[155] Z. Xu, X. Yang, Z. Yang, *Nano Lett.* **2010**, *10*, 985.
[156] N. R. Tummala, A. Striolo, *ACS Nano* **2009**, *3*, 595.
[157] T. J. McDonald, C. Engtrakul, M. Jones, G. Rumbles, M. J. Heben, *J. Phys. Chem. B* **2006**, *110*, 25339.
[158] M. C. Hersam, *Nat. Nanotechnol.* **2008**, *3*, 387.
[159] M. Zheng, A. Jagota, E. D. Semke, B. A. Diner, R. S. McLean, S. R. Lustig, R. E. Richardson, N. G. Tassi, *Nat. Mater.* **2003**, *2*, 338.
[160] J. H. Kim, M. Kataoka, Y. A. Kim, D. Shimamoto, H. Muramatsu, T. Hayashi, M. Endo, M. Terrones, M. S. Dresselhaus, *Appl. Phys. Lett.* **2008**, *93*, 223107.
[161] J. H. Kim, M. Kataoka, D. Shimamoto, H. Muramatsu, Y. C. Jung, T. Hayashi, Y. A. Kim, M. Endo, J. S. Park, R. Saito, M. Terrones, M. S. Dresselhaus, *ACS Nano* **2010**, *4*, 1060.
[162] D. Nepal, K. E. Geckeler, *Small* **2006**, *2*, 406.
[163] a) D. Nepal, K. E. Geckeler, *Small* **2007**, *3*, 1259; b) G. Raffaini, F. Ganazzoli, *J. Appl. Biomater. Biomech.* **2009**, *8*, 135.
[164] Q. Mu, W. Liu, Y. Xing, H. Zhou, Z. Li, Y. Zhang, L. Ji, F. Wang, Z. Si, B. Zhang, B. Yan, *J. Phys. Chem. C* **2008**, *112*, 3300.
[165] a) D. W. Horn, K. Tracy, C. J. Easley, V. A. Davis, *J. Phys. Chem. C* **2012**, *116*, 10341; b) M. Calvaresi, S. Hoefinger, F. Zerbetto, *Chem. Eur. J.* **2012**, *18*, 4308.
[166] a) Y. Li, T. Kaneko, R. Hatakeyama, *Small* **2010**, *6*, 729; b) C.-L. Cheng, G.-J. Zhao, *Nanoscale* **2012**, *4*, 2301.
[167] S. Deng, Y. Piao, A. H. Brozena, Y. Wang, *J. Mater. Chem.* **2011**, *21*, 18568.
[168] M. J. O'Connell, E. E. Eibergen, S. K. Doorn, *Nat. Mater.* **2005**, *4*, 412.
[169] a) M. Lundqvist, I. Sethson, B.-H. Jonsson, *Langmuir* **2004**, *20*, 10639; b) A. A. Vertegel, R. W. Siegel, J. S. Dordick, *Langmuir* **2004**, *20*, 6800.
[170] a) T. Dumitrică, C. M. Landis, B. I. Yakobson, *Chem. Phys. Lett.* **2002**, *360*, 182; b) H. G. Chae, T. V. Sreekumar, T. Uchida, S. Kumar, *Polymer* **2005**, *46*, 10925.
[171] X. Peng, N. Komatsu, S. Bhattacharya, T. Shimawaki, S. Aonuma, T. Kimura, A. Osuka, *Nat. Nanotechnol.* **2007**, *2*, 361.
[172] G. Liu, F. Wang, S. Chaunchaiyakul, Y. Saito, A. K. Bauri, T. Kimura, Y. Kuwahara, N. Komatsu, *J. Am. Chem. Soc.* **2013**, *135*, 4805.
[173] J. E. Hearst, J. Vinograd, *Proc. Natl. Acad. Sci. USA* **1961**, *47*, 999.
[174] R. Fleurier, J.-S. Lauret, E. Flahaut, A. Loiseau, *Phys. Status Solidi B* **2009**, *246*, 2675.
[175] S. Niyogi, C. G. Densmore, S. K. Doorn, *J. Am. Chem. Soc.* **2008**, *131*, 1144.
[176] J. G. Duque, C. G. Densmore, S. K. Doorn, *J. Am. Chem. Soc.* **2010**, *132*, 16165.
[177] J. A. Fagan, M. L. Becker, J. Chun, E. K. Hobbie, *Adv. Mater.* **2008**, *20*, 1609.
[178] J. Y. Huh, A. R. H. Walker, H. W. Ro, J. Obrzut, E. Mansfield, R. Geiss, J. A. Fagan, *J. Phys. Chem. C* **2010**, *114*, 11343.
[179] H. Liu, T. Tanaka, H. Kataura, *Nano Lett.* **2014**, *14*, 6237.
[180] B. S. Flavel, K. E. Moore, M. Pfohl, M. M. Kappes, F. Hennrich, *ACS Nano* **2014**, *8*, 1817.
[181] Y. Miyata, K. Shiozawa, Y. Asada, Y. Ohno, R. Kitaura, T. Mizutani, H. Shinohara, *Nano Res.* **2011**, *4*, 963.
[182] J. Wu, L. Xie, G. Hong, H. Lim, B. Thendie, Y. Miyata, H. Shinohara, H. Dai, *Nano Res.* **2012**, *5*, 388.
[183] J. Zhang, H. Gui, B. Liu, J. Liu, C. Zhou, *Nano Res.* **2013**, *6*, 906.
[184] K. S. Mistry, B. A. Larsen, J. L. Blackburn, *ACS Nano* **2013**, *7*, 2231.
[185] J. Han, Q. Ji, S. Qiu, H. Li, S. Zhang, H. Jin, Q. Li, *Chem. Commun.* **2015**, *51*, 4712.
[186] M. J. Shea, R. D. Mehlenbacher, M. T. Zanni, M. S. Arnold, *J. Phys. Chem. Lett.* **2014**, *5*, 3742.
[187] N. Berton, F. Lemasson, A. Poschlad, V. Meded, F. Tristram, W. Wenzel, F. Hennrich, M. M. Kappes, M. Mayor, *Small* **2014**, *10*, 360.
[188] N. Berton, F. Lemasson, J. Tittmann, N. Sturzl, F. Hennrich, M. M. Kappes, M. Mayor, *Chem. Mater.* **2011**, *23*, 2237.
[189] a) F. Lemasson, N. Berton, J. Tittmann, F. Hennrich, M. M. Kappes, M. Mayor, *Macromolecules* **2012**, *45*, 713; b) H. Wang, Y. Li, G. Jiménez-Osés, P. Liu, Y. Fang, J. Zhang, Y.-C. Lai, S. Park, L. Chen, K. N. Houk, Z. Bao, *Adv. Funct. Mater.* **2015**, *25*, 1837; c) H. L. Wang, G. I. Koleilat, P. Liu, G. Jimenez-Oses, Y. C. Lai, M. Vosgueritchian, Y. Fang, S. Park, K. N. Houk, Z. N. Bao, *ACS Nano* **2014**, *8*, 2609; d) H. Ozawa, T. Fujigaya, Y. Niidome, N. Hotta, M. Fujiki, N. Nakashima, *J. Am. Chem. Soc.* **2011**, *133*, 2651; e) H. Ozawa, T. Fujigaya, S. Song, H. Suh, N. Nakashima, *Chem. Lett.* **2011**, *40*, 470.
[190] K. Mulla, S. Liang, H. Shaik, E. A. Younes, A. Adronov, Y. Zhao, *Chem. Commun.* **2015**, *51*, 149.
[191] F. A. Lemasson, T. Strunk, P. Gerstel, F. Hennrich, S. Lebedkin, C. Barner-Kowollik, W. Wenzel, M. M. Kappes, M. Mayor, *J. Am. Chem. Soc.* **2011**, *133*, 652.
[192] H. W. Lee, Y. Yoon, S. Park, J. H. Oh, S. Hong, L. S. Liyanage, H. L. Wang, S. Morishita, N. Patil, Y. J. Park, J. J. Park, A. Spakowitz, G. Galli, F. Gygi, P. H. S. Wong, J. B. H. Tok, J. M. Kim, Z. A. Bao, *Nat. Commun.* **2011**, *2*, 541.
[193] P. Gerstel, S. Klumpp, F. Hennrich, O. Altintas, T. R. Eaton, M. Mayor, C. Barner-Kowollik, M. M. Kappes, *Polym. Chem.* **2012**, *3*, 1966.
[194] K. Akazaki, F. Toshimitsu, H. Ozawa, T. Fujigaya, N. Nakashima, *J. Am. Chem. Soc.* **2012**, *134*, 12700.
[195] N. Sturzl, F. Hennrich, S. Lebedkin, M. M. Kappes, *J. Phys. Chem. C* **2009**, *113*, 14628.
[196] H. L. Wang, B. Hsieh, G. Jimenez-Oses, P. Liu, C. J. Tassone, Y. Diao, T. Lei, K. N. Houk, Z. N. Bao, *Small* **2015**, *11*, 126.
[197] H. L. Wang, J. G. Mei, P. Liu, K. Schmidt, G. Jimenez-Oses, S. Osuna, L. Fang, C. J. Tassone, A. P. Zoombelt, A. N. Sokolov, K. N. Houk, M. F. Toney, Z. A. Bao, *ACS Nano* **2013**, *7*, 2659.
[198] a) S. Khasminskaya, F. Pyatkov, B. S. Flavel, W. H. Pernice, R. Krupke, *Adv. Mater.* **2014**, *26*, 3465; b) T. Hasan, Z. P. Sun, F. Q. Wang, F. Bonaccorso, P. H. Tan, A. G. Rozhin, A. C. Ferrari, *Adv. Mater.* **2009**, *21*, 3874.
[199] a) S. P. Schiessl, N. Fröhlich, M. Held, F. Gannott, M. Schweiger, M. Forster, U. Scherf, J. Zaumseil, *Appl. Mater. Interfaces* **2014**, *7*, 682; b) G. J. Brady, Y. Joo, M. Y. Wu, M. J. Shea, P. Gopalan, M. S. Arnold, *ACS Nano* **2014**, *8*, 11614; c) V. Derenskyi, W. Gomulya, J. M. S. Rios, M. Fritsch, N. Frohlich, S. Jung, S. Allard, S. Z. Bisri, P. Gordiichuk, A. Herrmann, U. Scherf, M. A. Loi, *Adv. Mater.* **2014**, *26*, 5969; d) S. Z. Bisri, J. Gao, V. Derenskyi, W. Gomulya, I. Iezhokin, P. Gordiichuk, A. Herrmann, M. A. Loi, *Adv. Mater.* **2012**, *24*, 6147.
[200] J. Gao, M. A. Loi, E. J. F. de Carvalho, M. C. dos Santos, *ACS Nano* **2011**, *5*, 3993.
[201] M. Tange, T. Okazaki, S. Iijima, *J. Am. Chem. Soc.* **2011**, *133*, 11908.
[202] J. A. Fagan, C. Y. Khripin, C. A. Silvera Batista, J. R. Simpson, E. H. Hároz, A. R. Hight Walker, M. Zheng, *Adv. Mater.* **2014**, *26*, 2800.

[203] G. Ao, C. Y. Khripin, M. Zheng, *J. Am. Chem. Soc.* **2014**, *136*, 10383.

[204] M. Zhang, C. Y. Khripin, J. A. Fagan, P. McPhie, Y. Ito, M. Zheng, *Anal. Chem.* **2014**, *86*, 3980.

[205] D. A. Tsyboulski, Y. Hou, N. Fakhri, S. Ghosh, R. Zhang, S. M. Bachilo, M. Pasquali, L. Chen, J. Liu, R. B. Weisman, *Nano Lett.* **2009**, *9*, 3282.

[206] a) T. Hertel, A. Hagen, V. Talalaev, K. Arnold, F. Hennrich, M. Kappes, S. Rosenthal, J. McBride, H. Ulbricht, E. Flahaut, *Nano Lett.* **2005**, *5*, 511; b) N. Kishi, S. Kikuchi, P. Ramesh, T. Sugai, Y. Watanabe, H. Shinohara, *J. Phys. Chem. B* **2006**, *110*, 24816; c) K. Iakoubovskii, N. Minami, S. Kazaoui, T. Ueno, Y. Miyata, K. Yanagi, H. Kataura, S. Ohshima, T. Saito, *J. Phys. Chem. B* **2006**, *110*, 17420; d) T. Hayashi, D. Shimamoto, Y. A. Kim, H. Muramatsu, F. Okino, H. Touhara, T. Shimada, Y. Miyauchi, S. Maruyama, M. Terrones, M. S. Dresselhaus, M. Endo, *ACS Nano* **2008**, *2*, 485.

[207] S. Yang, A. N. Parks, S. A. Saba, P. L. Ferguson, J. Liu, *Nano Lett.* **2011**, *11*, 4405.

[208] a) P. L. McEuen, M. Bockrath, D. H. Cobden, Y.-G. Yoon, S. G. Louie, *Phys. Rev. Lett.* **1999**, *83*, 5098; b) Y. Li, S. V. Rotkin, U. Ravaioli, *Nano Lett.* **2003**, *3*, 183.

[209] Q. Liu, L. Yu, H. Li, R. Qin, Z. Jing, J. Zheng, Z. Gao, J. Lu, *J. Phys. Chem. C* **2011**, *115*, 6933.

[210] S. V. Rotkin, K. Hess, *Appl. Phys. Lett.* **2004**, *84*, 3139.

[211] a) A. Bachtold, P. Hadley, T. Nakanishi, C. Dekker, *Science* **2001**, *294*, 1317; b) A. Javey, J. Guo, Q. Wang, M. Lundstrom, H. Dai, *Nature* **2003**, *424*, 654.

[212] A. Javey, J. Guo, M. Paulsson, Q. Wang, D. Mann, M. Lundstrom, H. Dai, *Phys. Rev. Lett.* **2004**, *92*, 106804.

[213] E. Pop, *Nanotechnology* **2008**, *19*, 295202.

[214] a) Y. Zhou, A. Gaur, S.-H. Hur, C. Kocabas, M. A. Meitl, M. Shim, J. A. Rogers, *Nano Lett.* **2004**, *4*, 2031; b) S. J. Kang, C. Kocabas, T. Ozel, M. Shim, N. Pimparkar, M. A. Alam, S. V. Rotkin, J. A. Rogers, *Nat. Nanotechnol.* **2007**, *2*, 230; c) S. Fujii, T. Tanaka, Y. Miyata, H. Suga, Y. Naitoh, T. Minari, T. Miyadera, K. Tsukagoshi, H. Kataura, *Appl. Phys. Express* **2009**, *2*, 071601.

[215] M. M. Shulaker, G. Hills, N. Patil, H. Wei, H.-Y. Chen, H. S. P. Wong, S. Mitra, *Nature* **2013**, *501*, 526.

[216] a) V. Derycke, R. Martel, J. Appenzeller, P. Avouris, *Appl. Phys. Lett.* **2002**, *80*, 2773; b) M. S. Wang, J. Y. Wang, Q. Chen, L. M. Peng, *Adv. Funct. Mater.* **2005**, *15*, 1825; c) Y. Woo, G. S. Duesberg, S. Roth, *Nanotechnology* **2007**, *18*, 095203; d) C. W. Marquardt, S. Dehm, A. Vijayaraghavan, S. Blatt, F. Hennrich, R. Krupke, *Nano Lett.* **2008**, *8*, 2767.

[217] S. Wang, X. L. Liang, Q. Chen, K. Yao, L. M. Peng, *Carbon* **2007**, *45*, 760.

[218] D. Bouilly, J. Cabana, F. Meunier, M. Desjardins-Carrière, F. Lapointe, P. Gagnon, F. L. Larouche, E. Adam, M. Paillet, R. Martel, *ACS Nano* **2011**, *5*, 4927.

[219] H. J. Choi, J. Ihm, S. G. Louie, M. L. Cohen, *Phys. Rev. Lett.* **2000**, *84*, 2917.

[220] J. Huang, A. L. Ng, Y. Piao, C.-F. Chen, A. A. Green, C.-F. Sun, M. C. Hersam, C. S. Lee, Y. Wang, *J. Am. Chem. Soc.* **2013**, *135*, 2306.

[221] M. E. Roberts, M. C. LeMieux, Z. Bao, *ACS Nano* **2009**, *3*, 3287.

[222] Y. C. Jung, H. Muramatsu, K. Fujisawa, J. H. Kim, T. Hayashi, Y. A. Kim, M. Endo, M. Terrones, M. S. Dresselhaus, *Small* **2011**, *7*, 3292.

[223] a) M. S. Strano, C. A. Dyke, M. L. Usrey, P. W. Barone, M. J. Allen, H. Shan, C. Kittrell, R. H. Hauge, J. M. Tour, R. E. Smalley, *Science* **2003**, *301*, 1519; b) H. Park, J. Zhao, J. P. Lu, *Nano Lett.* **2006**, *6*, 916.

[224] D. D. Tune, J. G. Shapter, *Energy Environ. Sci.* **2013**, *6*, 2572.

[225] a) S. Hwang, M. Batmunkh, M. J. Nine, H. Chung, H. Jeong, *ChemPhysChem* **2015**, *16*, 53; b) D. Zhang, X. Li, S. Chen, Z. Sun, X. Jiang Yin, S. Huang, *Microchim. Acta* **2011**, *174*, 73.

[226] a) D. D. Tune, B. S. Flavel, R. Krupke, J. G. Shapter, *Adv. Energy Mater.* **2012**, *2*, 1043; b) J. Wei, Y. Jia, Q. Shu, Z. Gu, K. Wang, D. Zhuang, G. Zhang, Z. Wang, J. Luo, A. Cao, D. Wu, *Nano Lett.* **2007**, *7*, 2317.

[227] X. Zhan, J. Wu, Z. Chen, B. J. Hinds, *Nanoscale Res. Lett.* **2013**, *8*, 1.

[228] M. Majumder, N. Chopra, R. Andrews, B. J. Hinds, *Nature* **2005**, *438*, 44.

[229] J.-M. Bonard, H. Kind, T. Stöckli, L.-O. Nilsson, *Solid-State Electron.* **2001**, *45*, 893.

[230] a) W. B. Choi, D. S. Chung, J. H. Kang, H. Y. Kim, Y. W. Jin, I. T. Han, Y. H. Lee, J. E. Jung, N. S. Lee, G. S. Park, J. M. Kim, *Appl. Phys. Lett.* **1999**, *75*, 3129; b) N. S. Lee, D. S. Chung, J. H. Kang, H. Y. Kim, S. H. Park, Y. W. Jin, Y. S. Choi, I. T. Han, N. S. Park, M. J. Yun, *Jpn. J. Appl. Phys.* **2000**, *39*, 7154.

[231] G. Z. Yue, Q. Qiu, B. Gao, Y. Cheng, J. Zhang, H. Shimoda, S. Chang, J. P. Lu, O. Zhou, *Appl. Phys. Lett.* **2002**, *81*, 355.

[232] Y.-W. Son, S. Oh, J. Ihm, S. Han, *Nanotechnology* **2005**, *16*, 125.

[233] J. M. Bonard, J.-P. Salvetat, T. Stockli, W. A. de Heer, L. Forró, A. Châtelain, *Appl. Phys. Lett.* **1998**, *73*, 918.

[234] K. Seko, J.-i. Kinoshita, Y. Saito, *Jpn. J. Appl. Phys.* **2005**, *44*, L743.

[235] C. Liu, K. S. Kim, J. Baek, Y. Cho, S. Han, S.-W. Kim, N.-K. Min, Y. Choi, J.-U. Kim, C. J. Lee, *Carbon* **2009**, *47*, 1158.

[236] T. Hiraoka, T. Yamada, K. Hata, D. N. Futaba, H. Kurachi, S. Uemura, M. Yumura, S. Iijima, *J. Am. Chem. Soc.* **2006**, *128*, 13338.

[237] J. Xu, T. Feng, Y. Chen, Z. Sun, *J. Nanomaterials* **2013**, *2013*, 1.

[238] R. Zhang, Z. Ning, Y. Zhang, Q. Zheng, Q. Chen, H. Xie, Q. Zhang, W. Qian, F. Wei, *Nat. Nanotechnol.* **2013**, *8*, 912.

[239] J. Cumings, A. Zettl, *Science* **2000**, *289*, 602.

[240] J. L. Rivera, C. McCabe, P. T. Cummings, *Nano Lett.* **2003**, *3*, 1001.

[241] S. Zhang, W. K. Liu, R. S. Ruoff, *Nano Lett.* **2004**, *4*, 293.

[242] M. Dienwiebel, G. S. Verhoeven, N. Pradeep, J. W. Frenken, J. A. Heimberg, H. W. Zandbergen, *Phys. Rev. Lett.* **2004**, *92*, 126101.

[243] M. Urbakh, *Nat. Nanotechnol.* **2013**, *8*, 893.

[244] a) J. M. Martin, C. Donnet, T. Le Mogne, T. Epicier, *Phys. Rev. B: Condens. Matter Mater. Phys.* **1993**, *48*, 10583; b) M. Hirano, K. Shinjo, *Phys. Rev. B: Condens. Matter Mater. Phys.* **1990**, *41*, 11837.

[245] K. Jensen, K. Kim, A. Zettl, *Nat. Nanotechnol.* **2008**, *3*, 533.

[246] Y. T. Yang, C. Callegari, X. L. Feng, K. L. Ekinci, M. L. Roukes, *Nano Lett.* **2006**, *6*, 583.

[247] M. M. J. Treacy, T. W. Ebbesen, J. M. Gibson, *Nature* **1996**, *381*, 678.

– This page intentionally left blank –

2.2 Carbon Nanotube Thin Films

2.2.1 *Aligned Carbon Nanotube Thin Films from Liquid Crystal Polyelectrolyte Inks*

D. D. Tune, A. J. Blanch, C. J. Shearer, K. E. Moore, M. Pfohl, J. G. Shapter,
B. S Flavel

Applied Materials & Interfaces (2015) 25857–25864

DOI: 10.1021/acsami.5b08212

Abstract

Single walled carbon nanotube thin films are fabricated by solution shearing from high concentration sodium nanotubide polyelectrolyte inks. The solutions are produced by simple stirring of the nanotubes with elemental sodium in dimethylacetamide and the nanotubes are thus not subject to any sonication-induced damage. At such elevated concentrations (~ 4 mg mL-1) the solutions exists in the liquid crystal phase and during deposition this order is transferred to the films, which are well aligned in the direction of shear with a 2D nematic order parameter of ~ 0.7 determined by polarized absorption measurements. Compared to similarly formed films made from superacids, the polyelectrolyte films contain smaller bundles and a much narrower distribution of bundle diameters. After p-doping with an organic oxidizer the films exhibit a very high DC to optical conductivity ratio of σDC/σOP ~ 35, corresponding to a calculated DC conductivity of over 7000 S cm-1. When very thin (T550 ~ 96 %), smooth (RMS roughness, Rq ~ 2.2 nm) and highly aligned films made via this new route are used as the front electrodes of carbon nanotube-silicon solar cells, the power conversion efficiency is almost an order of magnitude greater than that obtained when using the much rougher (Rq ~ 20 - 30 nm) and less conductive (peak σDC/σOP ~ 2.5) films formed by common vacuum filtration of the same starting material, and having the same transmittance.

Contribution

B.S.F, D.D.T and J.G.S conceived the idea for the project. D.D.T, A.J.B, C.J.S, K.E.M, and M.P performed the experiments. B.S.F and D.D.T wrote the manuscript and all authors analysed and discussed the results.

– This page intentionally left blank –

ACS APPLIED MATERIALS & INTERFACES

Research Article

www.acsami.org

Aligned Carbon Nanotube Thin Films from Liquid Crystal Polyelectrolyte Inks

Daniel D. Tune,[†,‡] Adam J. Blanch,[§] Cameron J. Shearer,[‡] Katherine E. Moore,[‡,∥] Moritz Pfohl,[†] Joseph G. Shapter,[*,‡] and Benjamin S. Flavel[*,†]

[†]Institute of Nanotechnology (INT), Karlsruhe Institute of Technology (KIT), 76021 Karlsruhe, Germany

[‡]Centre for Nanoscale Science and Technology (CNST), School of Chemical and Physical Sciences, Flinders University, Adelaide 5042, Australia

[§]Chair for Photonics and Optoelectronics, Department of Physics and Center for Nanoscience (CeNS), Ludwig-Maximilians-Universität München, D-80799 München, Germany

Supporting Information

ABSTRACT: Single walled carbon nanotube thin films are fabricated by solution shearing from high concentration sodium nanotubide polyelectrolyte inks. The solutions are produced by simple stirring of the nanotubes with elemental sodium in dimethylacetamide, and the nanotubes are thus not subject to any sonication-induced damage. At such elevated concentrations (~4 mg mL^{-1}), the solutions exist in the liquid crystal phase and during deposition this order is transferred to the films, which are well aligned in the direction of shear with a 2D nematic order parameter of ~0.7 determined by polarized absorption measurements. Compared to similarly formed films made from superacids, the polyelectrolyte films contain smaller bundles and a much narrower distribution of bundle diameters. After p-doping with an organic oxidizer, the films exhibit a very high DC electrical to optical conductivity ratio of σ_{DC}/σ_{OP} ~ 35, corresponding to a calculated DC conductivity of over 7000 S cm^{-1}. When very thin (T_{550} ~ 96%), smooth (RMS roughness, R_q ~ 2.2 nm), and highly aligned films made via this new route are used as the front electrodes of carbon nanotube-silicon solar cells, the power conversion efficiency is almost an order of magnitude greater than that obtained when using the much rougher (R_q ~ 20–30 nm) and less conductive (peak σ_{DC}/σ_{OP} ~ 2.5) films formed by common vacuum filtration of the same starting material, and having the same transmittance.

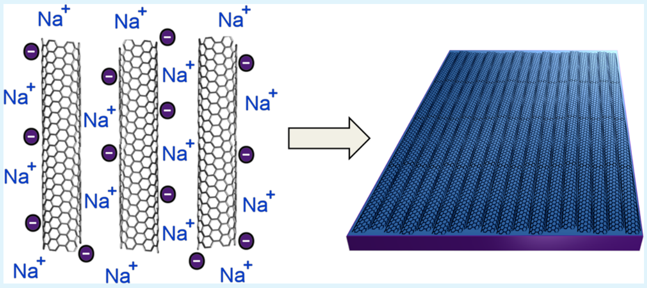

KEYWORDS: *alignment, nematic, sodium nanotubide, solar cells, thin films*

INTRODUCTION

The potential applications of carbon nanotube thin films are numerous and varied, but the commonly used preparation methods of spray deposition or vacuum filtration from stabilized dispersions generally produce either sparse films with poor homogeneity and large void spaces on the nanoscale, or extremely rough and opaque films. The extended ultrasonication often required to coax the nanotubes into a metastable suspension invariably shortens them and introduces defects into the sidewalls which irreparably alter the electronic and optical properties of the pristine material. Additionally, the complete removal of surfactants, polymers, or other wrapping agents from the films produced can be difficult. Despite these issues, important advances in applications that use nanotube thin films continue to be made. An area that is currently of great interest in the nanotube research community is in the production of thin films in which the nanotubes are highly aligned in one direction parallel to the surface because such films are expected to perform much better in a range of applications than their randomly oriented counterparts. Large area surface-aligned films have previously been generated from evaporation driven self-assembly of sidewall-functionalized[1] or surfactant-stabilized suspensions,[2,3] from superacids with[4] or without[5] shear, from urea-water inks by Mayer rod coating,[6] from polymer/nanotube blends by Langmuir–Blodgett,[7] Langmuir–Schaeffer,[8] or solution shearing onto prepatterned substrates,[9] by shearing of solutions stabilized by DNA[10] or gellan gum,[11] as well as from the transfer of CVD grown stripes[12] or collapse of CVD grown forests.[13] This is in addition to a plethora of work regarding carbon nanotubes within different kinds of liquid crystals.[14−20] Despite their various advantages, many of the aforementioned methods of film formation still introduce damage due to extended ultrasonication, or are inherently limited to the small scale, require expensive or troublesome reagents (e.g., DNA, superacids) or extensive sidewall functionalization/wrapping agents/embed-

Received: September 2, 2015
Accepted: October 29, 2015
Published: October 29, 2015

DOI: 10.1021/acsami.5b08212
ACS Appl. Mater. Interfaces 2015, 7, 25857−25864

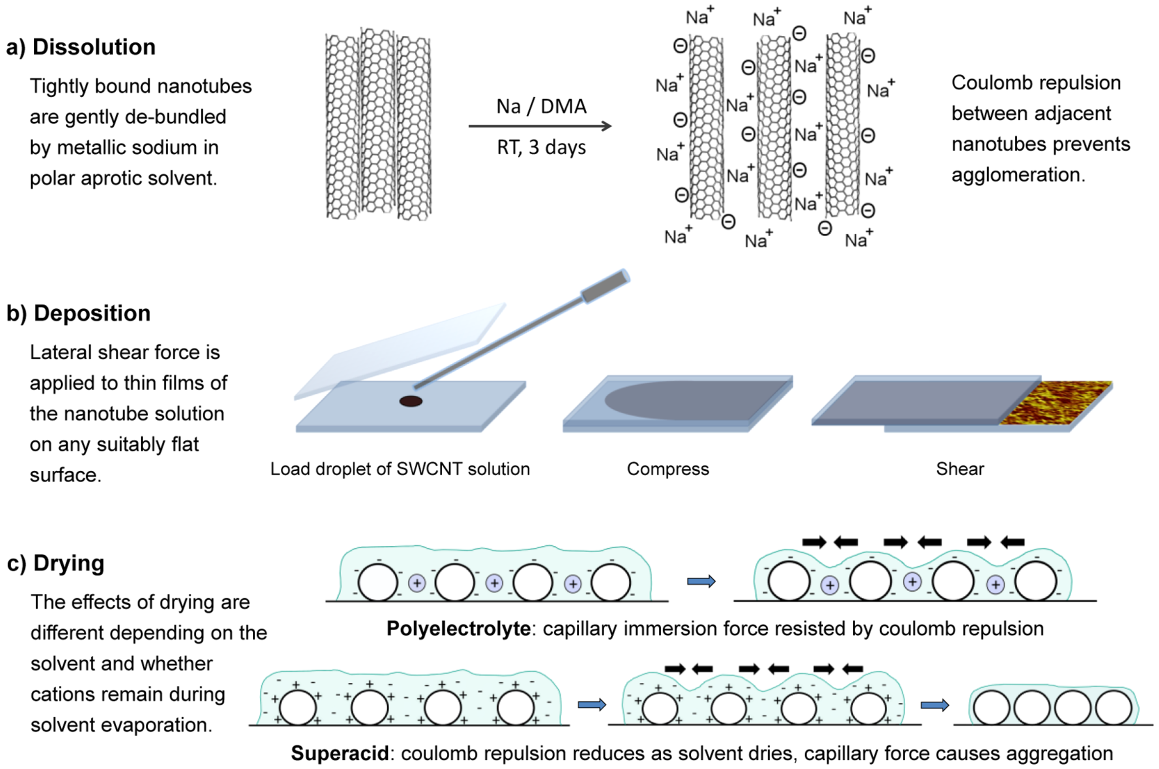

Figure 1. Diagrams showing the three important stages of nanotube film fabrication: (a) reductive dissolution with sodium in dimethylacetamide (DMA), (b) flattening and shear aligning of the solution, and (c) schematic illustrating factors influencing the film morphology during drying of either the polyelectrolyte or superacid nanotube solutions.

ding matrix, or involve a high degree of manufacturing complexity.

We report here a new method in which very thin carbon nanotube films are prepared from concentrated polyelectrolyte solutions of "nanotubide" salts, which do not require any ultrasonication to produce and leave no difficult-to-remove contaminants in the films. The ability to cause true dissolution of carbon nanotubes by electrostatic charging in polar media has been well-known for the past decade[21] and such solutions are commonly exploited at low concentration in efficient sidewall functionalization schemes.[22−27] However, the work reported herein comprises a new application of these polyelectrolyte salt solutions, exploiting the very high concentration regime in which liquid crystal (LC) effects become important. The films produced by this method exhibit a very high degree of nanotube alignment, exceptional homogeneity of bundle widths throughout the film and remarkably low surface roughness; a characteristic of great importance when considering their further incorporation into thin film electronics, organic photovoltaics, etc. Furthermore, the films have outstanding conductivity relative to optical transparency, display significant anisotropy in measurements of conductivity made perpendicular or parallel to the alignment axis and function as optical polarizers.

■ RESULTS AND DISCUSSION

HiPco single walled carbon nanotubes are fully dissolved in dimethylacetamide (DMA) by the addition of sodium metal and stirring at room temperature (Figure 1a) in a similar manner to Clancy et al.[28] The strongly electropositive sodium atoms donate their unpaired electrons to the nanotubes, generating negatively charged "nanotubide" anions and sodium cations in what is essentially the first half of the Billups−Birch reductive functionalization scheme.[22] The highly conjugated carbon framework is capable of stabilizing very high charge loads and the resulting Coulomb repulsion between adjacent nanotubes causes them to gently debundle without the need for ultrasonication.[29]

The resultant sodium nanotubide polyelectrolyte solution is stable for months (at least) when stored under inert atmosphere. A different method previously reported to produce nanotubide salts first requires dissolution of the sodium metal in liquid ammonia followed by addition of the nanotubes and subsequent evaporation of the ammonia to yield the dry salt,[30] which can then be dissolved in polar aprotic solvents such as dimethyl sulfoxide.[31] Another alternative method is to use room temperature tetrahydrofuran to produce the salt, employing intercalation compounds such as lithium naphthalenide[21] or crown ether complexes.[32] We find that although these serve to somewhat reduce the time taken to obtain a well individualized solution in DMA and increase the upper limit of concentration that can be sustained in a given solvent (by reducing metal precipitation onto the tube walls[32]), they must then also be removed from the produced films and are not required to obtain the LC phase necessary for the method described herein. The observation of LC phases in true solutions of carbon nanotubes was reported by Davis et al.[33] for nanotubes dissolved in chlorosulfonic acid (CSA) and later by Jiang et al.[32] in polyelectrolyte solutions. Unfortunately, CSA is hazardous, toxic, and somewhat difficult to handle, and although it has been used extensively in large scale industrial applications for many decades, less hazardous alternatives are desirable. Using only sodium in DMA, we have obtained solutions of nanotubide polyelectrolytes in concentrations up to

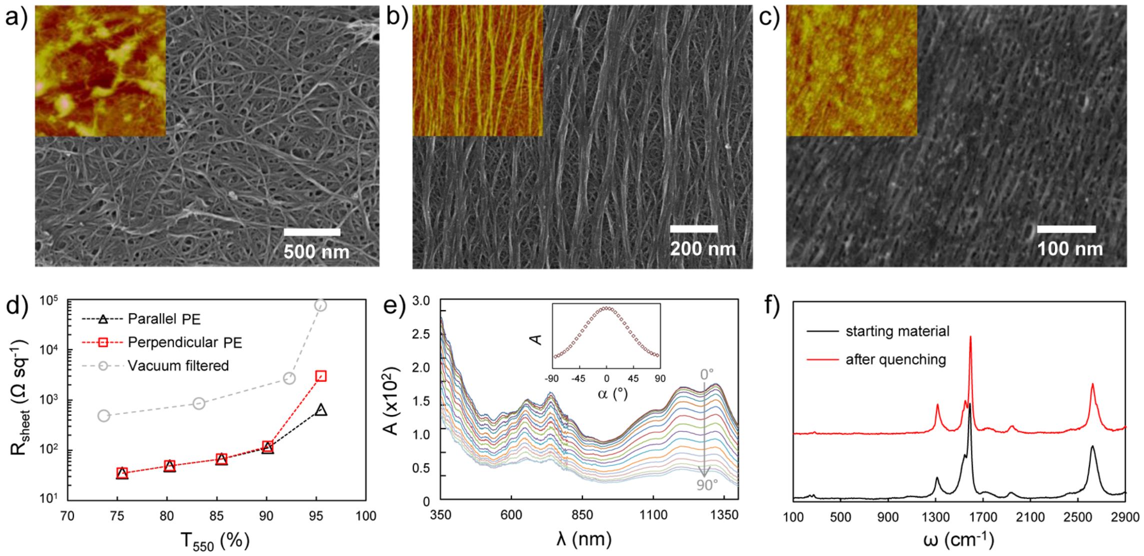

Figure 2. SEM images [inset AFM images] of (a) VF [4 μm × 4 μm × 280 nm], (b) CSA [4 μm × 4 μm × 52 nm], and (c) PE films [1 μm × 1 μm × 17 nm], where different scales are used to best show the surface features in each case. (d) Sheet resistance vs transmittance (taken with linear four-point probe oriented parallel or perpendicular to the alignment direction in the case of the aligned films). (e) Variation in absorbance with polarization angle [inset absorbance @ 1320 nm vs polarization angle]. (f) Examples of Raman spectra of the starting material vs films cast from PE solution (statistical analysis of the D- to G-band intensity ratio from 2000 individual spectra shown in Figure S6).

~4 mg mL^{-1}, as is required for the observation of LC domains as seen in cross polarized microscope images (Figure S1), and observed previously by Jiang et al.[32]

Typically, to produce the aligned films, a drop of nanotube solution (2−10 μL) is placed between two flat surfaces and compressed, then the two surfaces are rapidly drawn apart parallel to their contacting faces (Figure 1b). Li et al.[4] propose that the mechanism for the observed long-range ordering is through the shear-induced macroscale alignment of microscale LC domains pre-existing in the solution, and similar shear aligning has been observed by Zamora-Ledezma et al.[10] and modeled by Hobbie and Fry.[34] Films previously produced in a similar manner from CSA solutions were very smooth with excellent conductivity and a high degree of nanotube alignment over arbitrarily large areas.[4] However, the resultant films are observed to contain very large nanotube bundles up to a hundred nanometers across. This is despite the fact that the nanotubes as prepared herein are fully individualized when dissolved in the acid.[35] In fact, the CSA films (Figure 2) exhibit a bimodal bundle width distribution with very large, generally aligned bundles of 40.3 ± 19.2 nm overlaid on smaller, randomly ordered bundles of 4.8 ± 1.2 nm (Figure S2). This morphology is quite different to that of the films made from the polyelectrolyte (PE) solutions, which exhibit much smaller bundles and a narrower distribution of bundle widths of 10.7 ± 2.6 nm, despite it being unlikely that the nanotubes are completely individualized in such a high concentration nanotubide solution (particularly one that is free of coanions or cation chelating agents). Since the difference in morphology of the films does not reflect the difference in bundle size distributions in solution, some other mechanism(s) must be responsible. One possibility is directly related to the solvents; since DMA evaporates far quicker than CSA, which means that the capillary immersion force experienced by nanoparticles in thin liquid films[36] is exerted for a much shorter duration, and since the surface tension of CSA (72.3 mN m^{-1}) is much higher than that of DMA (36.7 mN m^{-1}), which means that the capillary force is also stronger, the net driving force for agglomeration is greater in the CSA films. As well, we note that the large bundles are observed only on the upper side of the film, that is, the one that faces the ambient environment during drying. Furthermore, as the acid solvent evaporates from the CSA films, the Coulomb repulsion between adjacent nanotubes, which is caused by reversible protonation of the sidewalls by the acid, must gradually decrease below the level required to resist the attraction due to the capillary immersion force and van der Waals interaction.

However, the the situation is likely to be quite different in the case of the PE solutions, in which the repulsion is due to the charging effect of the sodium which does not evaporate (as illustrated in Figure 1c). Rather, the concentration of sodium in the drying film rises until cation precipitation onto the nanotube sidewalls occurs,[25] and the presence of the salted out metal may confound the van der Waals attraction between sidewalls, further hampering the agglomeration process. In addition to the narrower and more homogeneous bundles, the RMS roughness, R_q, of the PE films is also somewhat better at 2.2 nm than the best CSA films produced in our laboratories, at around 3 nm, or the best in the literature, at 2.8 nm.[4] This makes them some of the smoothest solution deposited carbon nanotube thin films so far reported, and vastly smoother than vacuum filtered (VF) films of similar optical density, which can have $R_q \approx 20-30$ nm. The thickness of the three types of films shown in Figure 2, as extracted from AFM measurements, was 28, 9.2, and 6.5 nm for VF, CSA, and PE films, respectively (Figure S3).

The high order and dense packing of aligned nanotube films makes them substantially better conductors than the randomly aligned "spaghetti" films commonly produced by the usual vacuum filtration or spray deposition methods, in which the charge conduction mechanism is dominated by percolation.[37] This is especially apparent for very thin films which, when randomly oriented, are so sparse as to be at or below the percolation threshold, leading to very large sheet resistance, R_{sheet} (Figure 2d). In contrast, the PE films display a much more gradual increase in R_{sheet} with transparency and are at

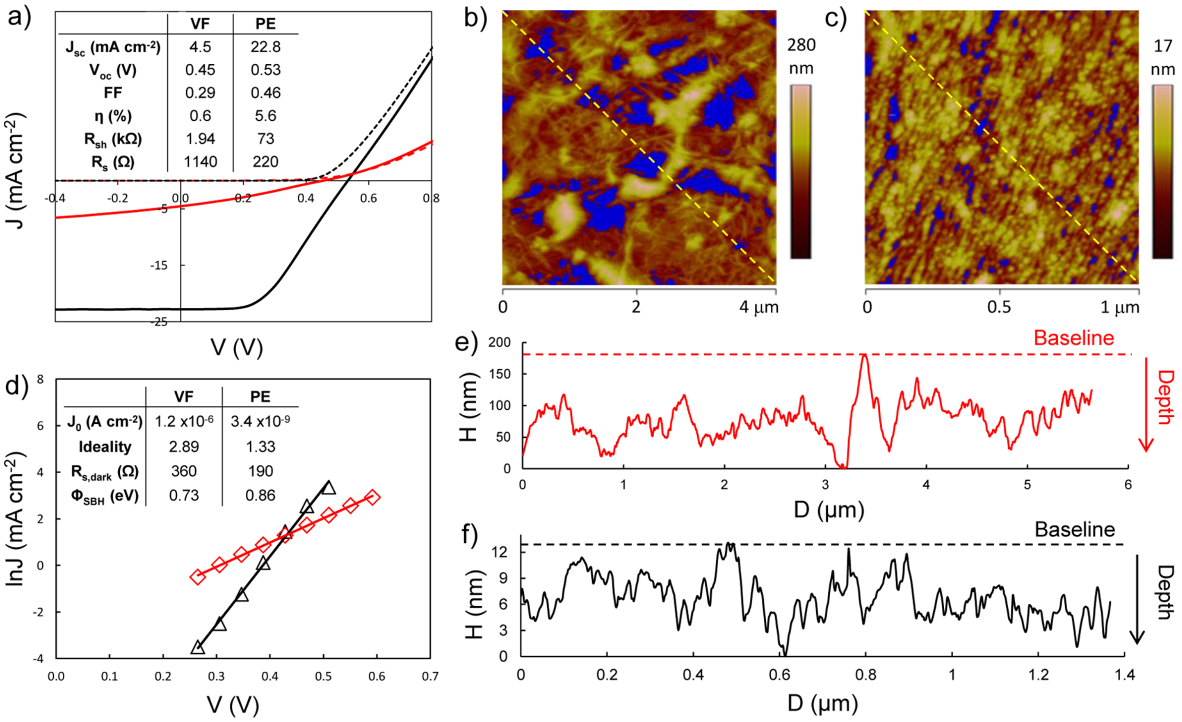

Figure 3. (a) Solar cell light (bold lines) and dark (dashed lines) characteristics of devices made with VF (red) and PE (black) films, both with T_{550} = 96%. (b) Visualization of the approximate proportion of nanotubes estimated to make contact with the silicon surface for VF films, where blue color indicates noncontacting regions and (c) corresponding image for PE films. (d) Semilog plots of current density vs voltage showing the straight line fits and corresponding diode characteristics calculated as described in the Supporting Information. (e, f) Height (H) vs lateral distance (D) cross sections taken from, and indicated by yellow dashed lines in, the AFM images shown in (b) and (c) and establish the baseline and depth whereby all nanotubes in the lower three-quarters of each film were considered to be able to make contact with the surface.

least an order of magnitude less resistive than corresponding randomly aligned films. It is only for the thinnest of the PE films that R_{sheet} increases considerably as those films also become sparse, but still with a degree of alignment. For the thickest PE films that we have produced, at T_{550} = 75%, R_{sheet} was only 35 Ω sq^{-1} after doping with $SOCl_2$, which is much less than the 480 Ω sq^{-1} measured for a VF film of similar transmittance and likewise doped. Even for a PE film of 95% transmittance, R_{sheet} was still only 650 Ω sq^{-1}, which is vastly better than the 76 kΩ sq^{-1} obtained from its VF counterpart. As well as these improvements, the very thin PE films exhibit anisotropy in the conductivity. This is observed when measurements of R_{sheet} are taken by linear four point probe oriented either parallel or perpendicular to the alignment axis, where the values obtained when parallel are up to ten times higher than when perpendicular, depending on thickness and degree of alignment. We attribute this to the fact that although the thicker PE films are so densely packed as to be considered closed, and thus not limited by percolation conductivity,[37] the thinner films are not closed, but are still generally aligned, which means that the number of percolation pathways parallel to the alignment direction is far greater than perpendicular to it. To compare the conductivity-transparency properties of these films to other thin nanotube films previously reported, the ratio of the electrical to optical conductivity, $\sigma_{\text{DC}}/\sigma_{\text{OP}}$, was calculated as per Hecht et al.[38] by substituting the measured R_{sheet} and T_{550} values (Figure S4) into:

$$T(\lambda) = \left(1 + \frac{1}{2R_S}\sqrt{\frac{\mu_0}{\varepsilon_0}}\,\frac{\sigma_{\text{OP}}(\lambda)}{\sigma_{\text{DC}}}\right)^{-2}$$
$$= \left(1 + \frac{188.5(\Omega)}{R_S}\,\frac{200(\text{S Cm}^{-1})}{\sigma_{\text{DC}}}\right)^{-2}$$

where $T(\lambda)$ is the wavelength-dependent transmittance, R_S is the sheet resistance, and μ_0 and ε_0 are the free space permeability and permittivity, respectively. To estimate the DC conductivity, σ_{DC}, a value of 200 S cm^{-1} has been used for the optical conductivity, σ_{OP}, as measured by Ruzicka et al.[39] For the PE films of 85% transparency this yields $\sigma_{\text{DC}}/\sigma_{\text{OP}}$ of ~1, which is comparable with others in the field.[40] However, after doping of the films with $SOCl_2$, $\sigma_{\text{DC}}/\sigma_{\text{OP}}$ was increased up to 35.7, corresponding to a DC conductivity of 7139 S cm^{-1}, which is one of the highest values ever reported for thin nanotube films formed by any method,[40] and ~16× higher than the similarly doped VF films of the same transmittance produced in this work.

As well as conductance anisotropy the PE films also function as good optical polarizers as shown in Figure 2e (with the absorbance of the CSA and VF shown for comparison in Figure S5). The 2D nematic order parameter is given by $S_{2D} = \langle 2\cos^2\theta - 1\rangle$ (where θ denotes the angle between an individual nanotube and the overall alignment director and the expression is averaged over all nanotubes in an ensemble).[41] The order parameter can be calculated from the polarized optical data via $S_{2D} = (A_{\parallel} - A_{\perp})/(A_{\parallel} + 2A_{\perp})$[42] yielding S_{2D} ~ 0.6 for the PE films, which is significantly better than the CSA films produced in our laboratories with S_{2D} ~ 0.2−0.4 or previously reported

DNA films[10] with $0.1 < S_{2D} < 0.15$. Similarly, the degree of absorbance polarization, $P = (A_{\parallel} - A_{\perp})/(A_{\parallel} + A_{\perp})$, can also be calculated, yielding $P \sim 0.7$ and $P \sim 0.3-0.5$ from the PE and CSA films, respectively and, of course, $P = 0$ for VF films. Although these values do not yet compete with the very best aligned CVD grown films,[12] they offer the twin advantages of low temperature fabrication and solution processing, as well as allowing for the ability to use virtually any kind of nanotube including, especially, those sorted by electronic type.[43−46] For that case in particular, the question of whether or not the polyelectrolyte method causes damage to the nanotubes is of great importance. Figure 2f shows the Raman spectra of small diameter semiconducting nanotube starting material and of the same material after casting into a PE film and quenching in air. The spectral shapes are almost identical, indicating that there is no significant change to the nanotubes, although a marginal increase in the D- to G-band intensity ratio from 0.25 ± 0.017 to 0.29 ± 0.012 (Figure S6, obtained by statistical analysis of 2000 individual Raman spectra over 2000 μm^2 areas of the films) indicates some slight increase in defect density, likely due to a small degree of hydrogenation[30] and/or hydroxylation[27] upon exposure of the dry film to atmosphere and subsequent rinsing steps, which were taken to remove the sodium and residual DMA from the films. EDX analysis of the PE films immediately after deposition (Figure S7) clearly shows the presence of sodium, as expected, as well as nitrogen, which we interpret as being due to residual dimethylacetamide. After rinsing thoroughly with water, the amount of both sodium and nitrogen were decreased to below 0.05 atom % within the excitation depth of the 5 kV electron beam.

To exemplify the performance gains that can be obtained by using these flat and aligned carbon nanotube films compared to the rough and randomly oriented ones produced by vacuum filtration, we fabricated carbon nanotube-silicon heterojunction solar cells,[47] which are often made with VF films. In this type of solar cell the nanotubes function as transparent, conducting frontside electrodes as well as setting up the built in potential near the silicon surface that is required to separate photoexcited electron−hole pairs.[48] As shown in Figure 3a, for thin nanotube films with T_{550} = 96%, dramatic differences in device performance are observed, with the PE devices typically producing over 9× more power than the VF type under AM1.5G conditions.

In addition to the large difference in film conductivity, other reasons for the performance improvement can be readily seen by analyses of the dark currents in forward bias, which yield ideality factors of around 2.9 and 1.3, and saturation current densities of around 1.2×10^{-6} and 3.4×10^{-9} A cm^{-2} for VF and PE devices, respectively. As illustrated in Figure 3b, where the proportion of nanotubes in contact with the silicon is estimated in the manner of Li et al.,[4] these differences are consistent with the fact that the VF films make poorer contact with the flat silicon surface than the PE films. This produces an inhomogeneous depletion region leading to inefficient electron−hole separation, as well as a high surface recombination velocity due to the large variety of surface states. In contrast, the smooth, dense and highly aligned PE films produce a more complete coverage of the silicon (Figure 3c), and it has been shown previously that such enhanced coverage leads to significant performance improvements.[49,50] This is likely due to a much higher quality depletion region in the underlying silicon as well as a reduction in the distance that must be traveled by excited carriers along the silicon surface to reach the nearest nanotube-silicon junction (maximum 20 nm for the PE films but up to 240 nm for the VF ones−taken as the shortest radius of the largest uncovered regions in Figure 3c). The Schottky barrier heights are given for comparison with previous and future work although whether or not such devices are in fact Schottky diodes[51,52] or not is still unclear with good evidence pointing instead to a pn junction mechanism,[49] and the possibility that they function in a new, hybrid fashion.[53]

CONCLUSION

For many devices in which carbon nanotube thin films are interfaced with other components, a method such as the one described herein that yields films which are exceptionally flat and ordered over large areas in such a way as to maximally exploit the very high aspect ratio of the material, is of great value. The issue of the true mechanism underlying the differences in morphology between polyelectrolyte and superacid films beyond the models proposed herein is an interesting question worthy of its own study. Although, irrespective of alignment within the film, the very high DC to optical conductivity ratio of the p-doped polyelectrolyte films is promising for a wide range of applications and despite the use of a short acting dopant in this work, there are others such as gold chloride which are known to have a more permanent effect. Alternatively, since the nanotubes in the as-deposited films are extremely electron-rich due to the sodium, this could provide a new route to the production of n-doped nanotube films, though isolation from the ambient atmosphere is an issue which will need to be addressed. Naturally, the use of exceptionally thin films which are surely much thinner than the optimum of the well-known film thickness−performance relationship for nanotube-silicon solar cells[54] means that it is not expected that the device efficiency in this work should rival that of the best reported elsewhere, which have been optimized for high performance. The power conversion efficiency of solar cells made with these new polyelectrolyte films can certainly be improved by using thicker films and optimized doping, and by adding antireflection layers such as TiO_2, and these are the subject of ongoing investigation. Nevertheless, the development of a versatile and relatively simple fabrication route that provides an alternative to the use of superacids while retaining the advantage of causing minimal disruption of the intrinsic properties of the nanotubes and yielding a final product with excellent thin film properties is a useful addition to the nanotube film fabrication toolset.

METHODS

Freshly cleaved sodium (50 mmol) (ACS reagent, Sigma) was added to a solution of oven-dried (150 °C, 3 h) single walled carbon nanotubes (SuperPurified HiPco, NanoIntegris, diameter 0.8−1.2 nm, length 100−1000 nm) in anhydrous DMA (5 mg mL^{-1}) (99.8%, Alfa-Aesar) in an argon glovebox and stirred vigorously for 3 days, over which time the solution developed from a very poor suspension of black solids in clear liquid to a smooth, high viscosity solution which was black in reflected light while transmitting a deep red/bronze color. This solution was centrifuged at 20 000g for 30 min and the supernatant was used in further processes. The sediment was quenched with DI water then captured on Teflon filter papers (0.5 μm, Phenomenex), rinsed first with methanol (EMSURE, Merck) then thoroughly with DI water, dried and then weighed, allowing the concentration of the supernatant to be calculated as approximately 4 mg mL^{-1}. Based on reports of nanotube dissolution in CSA[55,56] and in DMA,[28] it is clear that, to obtain the individualized LC state, both the stoichiometry and concentration of the solution must be carefully tuned, with C:M (where M is a Group I metal) ratios of <19 (corresponding to a fractional charge per carbon, $\delta > 0.053$) and volume fractions of 0.01−0.1 (corresponding to ∼1−10 mg mL^{-1} for HiPco nanotubes, assuming a bulk density of ∼0.1 g mL^{-1}). For CSA solutions, the acid (97%, Merck) was added to nanotubes at the same concentration (4 mg mL^{-1}) as in the polyelectrolyte solutions in order to provide a valid comparison, then stirred for 3 days and used directly. Centrifugation of this solution as per the sodium polyelectrolyte method did not result in any change to the morphology of the films that were prepared from the resultant supernatant.

VF films were captured on mixed cellulose ester (MCE) membranes (0.45 μm, HAWP, Merck Millipore) from surfactant-stabilized suspensions and rinsed thoroughly with copious DI water as per Wu et al.[57] and our previous work.[58] Films were deposited by placing them nanotube side down on the desired substrate, wetting with a drop of water, compressing with Teflon and baking at 110 °C for 15 min. To remove the MCE from the films, the substrates were placed in an acetone (EMSURE, Merck) bath for 30 min then transferred to two fresh acetone baths for a further 30 min each. Both CSA and PE films were produced by solution shearing by placing a small drop in between two glass slides, applying a compressive force of between 40−80 N (corresponding to an applied pressure of 27−43 kPa on the 7.5 × 2.5 cm^2 glass slides used) and then rapidly drawing the slides apart at a shear velocity of ∼0.01 m s^{-1}. Different thicknesses were prepared by varying the applied force and volume of liquid. After solvent evaporation, the slides were exposed to atmosphere then slowly immersed in water to float off the nanotube films, which were then captured from the water surface onto a desired substrate and dried in air at room temperature. To rinse the films without refloating them back off, the substrates were placed in a small volume of ethanol (EMSURE, Merck) and then approximately 10× that volume of water was added. After 30 min, the substrates were removed, the process was repeated, and they were then dried in air at 110 °C for 1 h.

Carbon nanotube-silicon solar cells were fabricated as described previously.[58] Briefly, Cr/Au front electrodes were patterned onto phosphorus doped n-type silicon substrates (1−5 Ω cm, ⟨100⟩, 100 nm thermal oxide) by photolithography and defined circular active areas (0.08 cm^2) in which the SiO_2 was removed by buffered oxide etch. Films were deposited as described above and the cells were completed with GaIn eutectic back electrodes and mounted on steel support plates. Before testing, all cells were treated sequentially with 2% HF, $SOCl_2$ and 2% HF again. This treatment sequence removes the thin oxide from the silicon surface as well as p-doping the nanotubes and dramatically increasing the conductivity of the nanotube films. Current−voltage data was taken from cells in the dark and under 100 mW cm^{-2} AM1.5G illumination (Class 2A, with irradiance measured by a silicon reference cell with NIST-traceable calibration). A circular aperture of 0.079 cm^2 was used to ensure that light could only impinge on the area of the cell in the region of interfacial contact between the nanotubes and the silicon. Diode characteristics were extracted in the usual manner from the semilog plots of the dark current data by fitting the linear regions found around V_{oc} (light) to the diode equation:

$$\ln J = \left(\frac{\beta}{n}\right)V + \ln J_0$$

where $\beta = q/kT$ and where J_0 is the reverse saturation current density, V is the applied potential, q is the elementary charge, k is the Boltzmann constant, T is the absolute temperature, and n is the ideality factor. The series resistance in the dark was extracted from the slope of the current−voltage data in the region $0.7 < V < 1$. Assuming that the devices are Schottky diodes, the barrier height was calculated from[59]

$$\sigma_{SBH} = -\frac{AT}{q}\ln\left(\frac{J_0}{kT^2}\right)$$

where A^* is the Richardson constant and a value of $A^* = 1.12$ A m^{-2} K^{-2} was used for moderately doped n-silicon.[53] Despite this the values are given for comparison with previous and future work.

The transmittance of films used in solar cells was measured with a spectrophotometer by placing identical films on glass. For VF films, the filtration membrane with captured nanotubes was cut in half and one-half was deposited onto the solar cells as described above. For PE films, the as deposited films were scored into two halves such that the two halves could be separately floated onto water and captured on either solar cell substrates or glass slides. The same films were used for Raman analysis as well as AFM and SEM imaging. SEM images were obtained with 5 kV accelerating voltage and a working distance of 2 mm. Raman maps were collected over 2000 μm^2 with an excitation wavelength of 532 nm. AFM imaging was performed in tapping mode at a tip velocity of 1 μm s^{-1} using Mikromasch probes (HQ:NSC15/Al BS, 40 N m^{-1} force constant), and roughness values were calculated from the raw images. Four-point probe measurements were taken using collinear Au-coated BeCu pins with a probe separation of 1 mm and contact area of 100 μm.

■ ASSOCIATED CONTENT

Ⓢ Supporting Information

The Supporting Information is available free of charge on the ACS Publications website at DOI: 10.1021/acsami.5b08212.

> Cross-polarized microscopy, bundle width histograms from SEM, conductivity−transparency relationships, and electrical to optical conductivity ratios, histograms of the D- to G- band intensity ratios from Raman maps, EDX spectra (PDF)

■ AUTHOR INFORMATION

Corresponding Authors

*E-mail: Benjamin.Flavel@kit.edu.
*E-mail: Joe.Shapter@flinders.edu.au.

Present Address

‖K.E.M.: International Center for Materials Nanoarchitectonics (MANA), National Institute for Materials Science (NIMS), Tsukuba, Ibaraki 305−0044, Japan.

Author Contributions

The manuscript was written through contributions of all authors. All authors have given approval to the final version of the manuscript.

Notes

The authors declare no competing financial interest.

■ ACKNOWLEDGMENTS

D.D.T., A.J.B., C.J.S., K.E.M., and J.G.S. acknowledge the South Australian node of the Australian Microscopy & Microanalysis Research Facility at Flinders University. K.E.M. thanks the Playford Memorial Trust. B.S.F. gratefully acknowledges support from the Deutsche Forschungsgemeinschaft's Emmy Noether Programm under Grant Number FL 834/1-1.

■ REFERENCES

(1) Shimoda, H.; Oh, S. J.; Geng, H. Z.; Walker, R. J.; Zhang, X. B.; McNeil, L. E.; Zhou, O. Self-Assembly of Carbon Nanotubes. *Adv. Mater.* **2002**, *14* (12), 899−901.

(2) Ko, H.; Tsukruk, V. V. Liquid-Crystalline Processing of Highly Oriented Carbon Nanotube Arrays for Thin-Film Transistors. *Nano Lett.* **2006**, *6* (7), 1443−1448.

(3) Engel, M.; Small, J. P.; Steiner, M.; Freitag, M.; Green, A. A.; Hersam, M. C.; Avouris, P. Thin Film Nanotube Transistors Based on Self-Assembled, Aligned, Semiconducting Carbon Nanotube Arrays. *ACS Nano* **2008**, *2* (12), 2445−2452.

(4) Li, X.; Jung, Y.; Sakimoto, K.; Goh, T.-H.; Reed, M. A.; Taylor, A. D. Improved Efficiency of Smooth and Aligned Single Walled Carbon

Nanotube/Silicon Hybrid Solar Cells. *Energy Environ. Sci.* **2013**, *6*, 879−887.

(5) Saha, A.; Ghosh, S.; Weisman, R. B.; Martí, A. A. Films of Bare Single-Walled Carbon Nanotubes from Superacids with Tailored Electronic and Photoluminescence Properties. *ACS Nano* **2012**, *6* (6), 5727−5734.

(6) Azoz, S.; Exarhos, A. L.; Marquez, A.; Gilbertson, L. M.; Nejati, S.; Cha, J. J.; Zimmerman, J. B.; Kikkawa, J. M.; Pfefferle, L. D. Highly Conductive Single-Walled Carbon Nanotube Thin Film Preparation by Direct Alignment on Substrates from Water Dispersions. *Langmuir* **2015**, *31* (3), 1155−1163.

(7) Giancane, G.; Ruland, A.; Sgobba, V.; Manno, D.; Serra, A.; Farinola, G. M.; Omar, O. H.; Guldi, D. M.; Valli, L. Aligning Single-Walled Carbon Nanotubes by Means of Langmuir−Blodgett Film Deposition: Optical, Morphological, and Photo-Electrochemical Studies. *Adv. Funct. Mater.* **2010**, *20* (15), 2481−2488.

(8) Cao, Q.; Han, S.-j.; Tulevski, G. S.; Zhu, Y.; Lu, D. D.; Haensch, W. Arrays of Single-Walled Carbon Nanotubes with Full Surface Coverage for High-Performance Electronics. *Nat. Nanotechnol.* **2013**, *8* (3), 180−186.

(9) Park, S.; Pitner, G.; Giri, G.; Koo, J. H.; Park, J.; Kim, K.; Wang, H.; Sinclair, R.; Wong, H. S.; Bao, Z. Large-Area Assembly of Densely Aligned Single-Walled Carbon Nanotubes Using Solution Shearing and Their Application to Field-Effect Transistors. *Adv. Mater.* **2015**, *27* (16), 2656−2662.

(10) Zamora-Ledezma, C.; Blanc, C.; Maugey, M.; Zakri, C.; Poulin, P.; Anglaret, E. Anisotropic Thin Films of Single-Wall Carbon Nanotubes from Aligned Lyotropic Nematic Suspensions. *Nano Lett.* **2008**, *8* (12), 4103−4107.

(11) Lu, L.; Chen, W. Large-Scale Aligned Carbon Nanotubes from Their Purified, Highly Concentrated Suspension. *ACS Nano* **2010**, *4* (2), 1042−1048.

(12) Ren, L.; Pint, C. L.; Booshehri, L. G.; Rice, W. D.; Wang, X.; Hilton, D. J.; Takeya, K.; Kawayama, I.; Tonouchi, M.; Hauge, R. H.; Kono, J. Carbon Nanotube Terahertz Polarizer. *Nano Lett.* **2009**, *9* (7), 2610−2613.

(13) deHeer, W. A.; Bacsa, W. S.; Châtelain, A.; Gerfin, T.; Humphrey-Baker, R.; Forro, L.; Ugarte, D. Aligned Carbon Nanotube Films: Production and Optical and Electronic Properties. *Science* **1995**, *268* (5212), 845−847.

(14) Song, W.; Kinloch, I. A.; Windle, A. H. Nematic Liquid Crystallinity of Multiwall Carbon Nanotubes. *Science* **2003**, *302* (5649), 1363.

(15) Islam, M. F.; Alsayed, A. M.; Dogic, Z.; Zhang, J.; Lubensky, T. C.; Yodh, A. G. Nematic Nanotube Gels. *Phys. Rev. Lett.* **2004**, *92* (8), 088303.

(16) Badaire, S.; Zakri, C.; Maugey, M.; Derré, A.; Barisci, J. N.; Wallace, G.; Poulin, P. Liquid Crystals of DNA-Stabilized Carbon Nanotubes. *Adv. Mater.* **2005**, *17* (13), 1673−1676.

(17) Zakri, C.; Poulin, P. Phase Behavior of Nanotube Suspensions: From Attraction Induced Percolation to Liquid Crystalline Phases. *J. Mater. Chem.* **2006**, *16* (42), 4095−4098.

(18) Davis, V. A. Liquid Crystalline Assembly of Nanocylinders. *J. Mater. Res.* **2011**, *26* (2), 140−153.

(19) Ould-Moussa, N.; Blanc, C.; Zamora-Ledezma, C.; Lavrentovich, O. D.; Smalyukh, I. I.; Islam, M. F.; Yodh, A. G.; Maugey, M.; Poulin, P.; Anglaret, E.; Nobili, M. Dispersion and Orientation of Single-Walled Carbon Nanotubes in a Chromonic Liquid Crystal. *Liq. Cryst.* **2013**, *40* (12), 1628−1635.

(20) Volpati, D.; Massey, M. K.; Johnson, D. W.; Kotsialos, A.; Qaiser, F.; Pearson, C.; Coleman, K. S.; Tiburzi, G.; Zeze, D. A.; Petty, M. C. Exploring the Alignment of Carbon Nanotubes Dispersed in a Liquid Crystal Matrix Using Coplanar Electrodes. *J. Appl. Phys.* **2015**, *117* (12), 125303.

(21) Penicaud, A.; Poulin, P.; Derre, A.; Anglaret, E.; Petit, P. Spontaneous Dissolution of a Single-Wall Carbon Nanotube Salt. *J. Am. Chem. Soc.* **2005**, *127* (1), 8−9.

(22) Liang, F.; Sadana, A. K.; Peera, A.; Chattopadhyay, J.; Gu, Z.; Hauge, R. H.; Billups, W. E. A Convenient Route to Functionalized Carbon Nanotubes. *Nano Lett.* **2004**, *4* (7), 1257−1260.

(23) Chattopadhyay, J.; Sadana, A. K.; Liang, F.; Beach, J. M.; Xiao, Y.; Hauge, R. H.; Billups, W. E. Carbon Nanotube Salts. Arylation of Single-Wall Carbon Nanotubes. *Org. Lett.* **2005**, *7* (19), 4067−4069.

(24) Liang, F.; Beach, J. M.; Kobashi, K.; Sadana, A. K.; Vega-Cantu, Y. I.; Tour, J. M.; Billups, W. E. In Situ Polymerization Initiated by Single-Walled Carbon Nanotube Salts. *Chem. Mater.* **2006**, *18* (20), 4764−4767.

(25) Voiry, D.; Roubeau, O.; Penicaud, A. Stoichiometric Control of Single Walled Carbon Nanotubes Functionalization. *J. Mater. Chem.* **2010**, *20* (21), 4385−4391.

(26) Deng, S.; Brozena, A. H.; Zhang, Y.; Piao, Y.; Wang, Y. Diameter-Dependent, Progressive Alkylcarboxylation of Single-Walled Carbon Nanotubes. *Chem. Commun.* **2011**, *47* (2), 758−760.

(27) Hof, F.; Bosch, S.; Eigler, S.; Hauke, F.; Hirsch, A. New Basic Insight into Reductive Functionalization Sequences of Single Walled Carbon Nanotubes (SWCNTs). *J. Am. Chem. Soc.* **2013**, *135* (49), 18385−18395.

(28) Clancy, A. J.; Melbourne, J.; Shaffer, M. S. P. A One-Step Route to Solubilised, Purified or Functionalised Single-Walled Carbon Nanotubes. *J. Mater. Chem. A* **2015**, *3* (32), 16708−16715.

(29) Pénicaud, A.; Poulin, P.; Anglaret, E.; Petit, P.; Roubeau, O.; Enouz, S.; Loiseau, A. Dissolution Douce of Single Walled Carbon Nanotubes. *AIP Conf. Proc.* **2005**, *786* (1), 266−270.

(30) Pekker, S.; Salvetat, J. P.; Jakab, E.; Bonard, J. M.; Forró, L. Hydrogenation of Carbon Nanotubes and Graphite in Liquid Ammonia. *J. Phys. Chem. B* **2001**, *105* (33), 7938−7943.

(31) Fogden, S.; Howard, C. A.; Heenan, R. K.; Skipper, N. T.; Shaffer, M. S. P. Scalable Method for the Reductive Dissolution, Purification, and Separation of Single-Walled Carbon Nanotubes. *ACS Nano* **2012**, *6* (1), 54−62.

(32) Jiang, C.; Saha, A.; Xiang, C.; Young, C. C.; Tour, J. M.; Pasquali, M.; Martí, A. A. Increased Solubility, Liquid-Crystalline Phase, and Selective Functionalization of Single-Walled Carbon Nanotube Polyelectrolyte Dispersions. *ACS Nano* **2013**, *7* (5), 4503−4510.

(33) Davis, V. A.; Ericson, L. M.; Parra-Vasquez, A. N. G.; Fan, H.; Wang, Y.; Prieto, V.; Longoria, J. A.; Ramesh, S.; Saini, R. K.; Kittrell, C.; Billups, W. E.; Adams, W. W.; Hauge, R. H.; Smalley, R. E.; Pasquali, M. Phase Behavior and Rheology of Swnts in Superacids. *Macromolecules* **2004**, *37* (1), 154−160.

(34) Hobbie, E. K.; Fry, D. J. Nonequilibrium Phase Diagram of Sticky Nanotube Suspensions. *Phys. Rev. Lett.* **2006**, *97* (3), 036101.

(35) Ramesh, S.; Ericson, L. M.; Davis, V. A.; Saini, R. K.; Kittrell, C.; Pasquali, M.; Billups, W. E.; Adams, W. W.; Hauge, R. H.; Smalley, R. E. Dissolution of Pristine Single Walled Carbon Nanotubes in Superacids by Direct Protonation. *J. Phys. Chem. B* **2004**, *108* (26), 8794−8798.

(36) Kralchevsky, P. A.; Nagayama, K. Lateral Capillary Forces between Partially Immersed Bodies. In *Studies in Interface Science*; Peter, A. K., Kuniaki, N., Eds.; Elsevier: Amsterdam, 2001; Vol. *10*, Chapter 7, pp 287−350.

(37) Hu, L.; Hecht, D. S.; Grüner, G. Percolation in Transparent and Conducting Carbon Nanotube Networks. *Nano Lett.* **2004**, *4* (12), 2513−2517.

(38) Hecht, D. S.; Heintz, A. M.; Lee, R.; Hu, L.; Moore, B.; Cucksey, C.; Risser, S. High Conductivity Transparent Carbon Nanotube Films Deposited from Superacid. *Nanotechnology* **2011**, *22* (16), 169501.

(39) Ruzicka, B.; Degiorgi, L.; Gaal, R.; Thien-Nga, L.; Bacsa, R.; Salvetat, J. P.; Forró, L. Optical and Dc Conductivity Study of Potassium-Doped Single-Walled Carbon Nanotube Films. *Phys. Rev. B: Condens. Matter Mater. Phys.* **2000**, *61* (4), R2468−R2471.

(40) Du, J.; Pei, S.; Ma, L.; Cheng, H.-M. 25th Anniversary Article: Carbon Nanotube- and Graphene-Based Transparent Conductive Films for Optoelectronic Devices. *Adv. Mater.* **2014**, *26* (13), 1958−1991.

(41) Mercurieva, A. A.; Birshtein, T. M. Liquid-Crystalline Ordering in Two-Dimensional Systems with Discrete Symmetry. *Makromol. Chem., Theory Simul.* **1992**, *1* (4), 205−214.

(42) White, D. L.; Taylor, G. N. New Absorptive Mode Reflective Liquid-Crystal Display Device. *J. Appl. Phys.* **1974**, *45* (11), 4718−4723.

(43) Arnold, M. S.; Stupp, S. I.; Hersam, M. C. Enrichment of Single-Walled Carbon Nanotubes by Diameter in Density Gradients. *Nano Lett.* **2005**, *5* (4), 713−718.

(44) Nish, A.; Hwang, J.-Y.; Doig, J.; Nicholas, R. J. Highly Selective Dispersion of Single-Walled Carbon Nanotubes Using Aromatic Polymers. *Nat. Nanotechnol.* **2007**, *2* (10), 640−646.

(45) Khripin, C. Y.; Fagan, J. A.; Zheng, M. Spontaneous Partition of Carbon Nanotubes in Polymer-Modified Aqueous Phases. *J. Am. Chem. Soc.* **2013**, *135* (18), 6822−6825.

(46) Flavel, B. S.; Moore, K. E.; Pfohl, M.; Kappes, M. M.; Hennrich, F. Separation of Single-Walled Carbon Nanotubes with a Gel Permeation Chromatography System. *ACS Nano* **2014**, *8* (2), 1817−1826.

(47) Wei, J.; Jia, Y.; Shu, Q.; Gu, Z.; Wang, K.; Zhuang, D.; Zhang, G.; Wang, Z.; Luo, J.; Cao, A.; Wu, D. Double-Walled Carbon Nanotube Solar Cells. *Nano Lett.* **2007**, *7* (8), 2317−2321.

(48) Tune, D. D.; Flavel, B. S.; Krupke, R.; Shapter, J. G. Carbon Nanotube-Silicon Solar Cells. *Adv. Ener. Mater.* **2012**, *2* (9), 1043−1055.

(49) Jung, Y.; Li, X.; Rajan, N. K.; Taylor, A. D.; Reed, M. A. Record High Efficiency Single-Walled Carbon Nanotube/Silicon P−N Junction Solar Cells. *Nano Lett.* **2013**, *13* (1), 95−99.

(50) Tune, D. D.; Flavel, B. S.; Quinton, J. S.; Ellis, A. V.; Shapter, J. G. Single-Walled Carbon Nanotube/Polyaniline/N-Silicon Solar Cells: Fabrication, Characterization, and Performance Measurements. *ChemSusChem* **2013**, *6* (2), 320−327.

(51) Jia, Y.; Cao, A.; Kang, F.; Li, P.; Gui, X.; Zhang, L.; Shi, E.; Wei, J.; Wang, K.; Zhu, H.; Wu, D. Strong and Reversible Modulation of Carbon Nanotube-Silicon Heterojunction Solar Cells by an Interfacial Oxide Layer. *Phys. Chem. Chem. Phys.* **2012**, *14* (23), 8391−8396.

(52) Tune, D. D.; Hennrich, F.; Dehm, S.; Klein, M. F. G.; Glaser, K.; Colsmann, A.; Shapter, J. G.; Lemmer, U.; Kappes, M. M.; Krupke, R.; Flavel, B. S. The Role of Nanotubes in Carbon Nanotube−Silicon Solar Cells. *Adv. Ener. Mater.* **2013**, *3* (8), 1091−1097.

(53) Harris, J. M.; Semler, M. R.; May, S.; Fagan, J. A.; Hobbie, E. K. Nature of Record Efficiency Fluid-Processed Nanotube−Silicon Heterojunctions. *J. Phys. Chem. C* **2015**, *119* (19), 10295−10303.

(54) Tune, D. D.; Shapter, J. G. Effect of Nanotube Film Thickness on the Performance of Nanotube-Silicon Hybrid Solar Cells. *Nanomaterials* **2013**, *3* (4), 655−673.

(55) Davis, V. A.; Parra-Vasquez, A. N. G.; Green, M. J.; Rai, P. K.; Behabtu, N.; Prieto, V.; Booker, R. D.; Schmidt, J.; Kesselman, E.; Zhou, W.; Fan, H.; Adams, W. W.; Hauge, R. H.; Fischer, J. E.; Cohen, Y.; Talmon, Y.; Smalley, R. E.; Pasquali, M. True Solutions of Single-Walled Carbon Nanotubes for Assembly into Macroscopic Materials. *Nat. Nanotechnol.* **2009**, *4* (12), 830−834.

(56) Green, M. J.; Parra-Vasquez, A. N. G.; Behabtu, N.; Pasquali, M. Modelling the Phase Behavior of Polydisperse Rigid Rods with Attractive Interactions with Applications to Single-Walled Carbon Nanotubes in Superacids. *J. Chem. Phys.* **2009**, *131* (8), 084901.

(57) Wu, Z.; Chen, Z.; Du, X.; Logan, J. M.; Sippel, J.; Nikolou, M.; Kamaras, K.; Reynolds, J. R.; Tanner, D. B.; Hebard, A. F.; Rinzler, A. G. Transparent, Conductive Carbon Nanotube Films. *Science* **2004**, *305* (5688), 1273−1276.

(58) Tune, D. D.; Blanch, A. J.; Krupke, R.; Flavel, B. S.; Shapter, J. G. Nanotube Film Metallicity and Its Effect on the Performance of Carbon Nanotube−Silicon Solar Cells. *Phys. Status Solidi A* **2014**, *211* (7), 1479−1487.

(59) Sze, S. M.; Ng, K. K. *Physics of Semiconductor Devices*, 3rd ed.; Wiley Interscience: New York, 2006.

2.2 Carbon Nanotube Thin Films

2.2.2 *Dry Shear Aligning: A Simple and Versatile Method to Smooth and Align the Surfaces of Carbon Nanotubes*

D. D. Tune, B. W. Stolz, M. Pfohl, **B. S Flavel**

Nanoscale 8 (2016) 3232 – 3236

DOI: 10.1039/C5NR08784H

Abstract

We show that the application of lateral shear force on a randomly oriented thin film of carbon nanotubes, in the dry state, causes significant reordering of the nanotubes at the film surface. This new technique of dry shear aligning is applicable to carbon nanotube thin films produced by many of the established methods.

Contribution

B.S.F, D.D.T conceived the idea for the project. D.D.T, B.W.S, and M.P performed the experiments. B.S.F and D.D.T wrote the manuscript and all authors analysed and discussed the results.

– This page intentionally left blank –

Nanoscale

COMMUNICATION

View Article Online
View Journal | View Issue

Cite this: *Nanoscale*, 2016, **8**, 3232

Received 10th December 2015,
Accepted 8th January 2016

DOI: 10.1039/c5nr08784h

www.rsc.org/nanoscale

Dry shear aligning: a simple and versatile method to smooth and align the surfaces of carbon nanotube thin films†

D. D. Tune,*[a,b] B. W. Stolz,[a] M. Pfohl[a] and B. S. Flavel*[a]

We show that the application of lateral shear force on a randomly oriented thin film of carbon nanotubes, in the dry state, causes significant reordering of the nanotubes at the film surface. This new technique of dry shear aligning is applicable to carbon nanotube thin films produced by many of the established methods.

The alignment of carbon nanotubes in thin films parallel to a surface is a topic of widespread research interest in the nanotube community. This is because, when carbon nanotubes are present as a randomly ordered bulk material, some of the often-touted electronic and optical properties of the individual nanotubes are suppressed, which confounds their full exploitation in a variety of devices and applications. We show here a new method of smoothing and aligning carbon nanotube thin films that is both inherently scalable and exceedingly simple. Depending on the type and purity of the nanotubes, the technique can also provide excellent surface alignment of the nanotubes in a dense and close packed array. A number of techniques of producing smooth and aligned carbon nanotube thin films over large areas have been reported with varying degrees of complexity, difficulty, and scalability, as well as resultant degree of nanotube alignment. These include the collapse of vertically aligned arrays[1–6] or exfoliation of CVD grown forests,[7,8] horizontal CVD growth,[9] use of Langmuir-Blodgett[10] or Langmuir-Schaeffer[11] deposition, solution shearing from superacids[12,13] or polyelectrolyte salt solutions[14] at liquid crystal concentrations of nanotubes, shear alignment in a liquid film followed by filtration,[15] evaporation-driven self-assembly of sidewall-functionalised[16] or surfactant-stabilised suspensions,[17,18] and floating evaporative self-assembly.[19] Whilst successful, many of these techniques require very specific preparation and some have limited applicability beyond the laboratory environment. In contrast, this Communication reports a simple method of smoothing and aligning the surfaces of carbon nanotube thin films on substrates by applying lateral shear force to the films in the dry state. The new technique is fundamentally different to other methods such as the collapse or 'pushing over' of dense and ordered arrays[1–6] which are already aligned in the vertical direction and are either reoriented by up to 90° to become horizontally aligned or are bent so that part of the length of each nanotube is more or less parallel to the surface. It is also different to the alignment of nanoparticles by drag forces in a thin liquid film followed by filtration,[15] or of nanotube liquid crystals.[12–14]

As illustrated in Fig. 1, the process of dry shear aligning (DSA) is straightforward; involving the application of compressive force between an aligner and a substrate holding a nanotube film and then shearing of the aligner relative to the substrate. As exemplified in the SEM images shown in Fig. 2, the effects on nanotube film morphology can be dramatic. Before DSA, the films are composed of dense mats of randomly oriented and interwoven nanotube bundles, with bundle diameters and film roughness varying depending on the technique used to form the film. After DSA, the nanotubes on the surface of the films are uniformly oriented in the direction of shear and have been densified. So far, in our labs, we have applied the DSA technique to small and large diameter single walled nanotubes, double walled nanotubes and multiwalled nano-

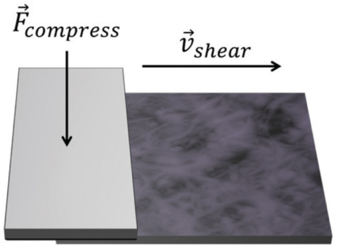

Fig. 1 Schematic of the dry shear aligning process.

---

[a] Institute of Nanotechnology, Karlsruhe Institute of Technology, 76021 Karlsruhe, Germany. E-mail: daniel.tune@kit.edu, benjamin.flavel@kit.edu
[b] Centre for Nanoscale Science and Technology, Flinders University, Adelaide 5042, Australia

† Electronic supplementary information (ESI) available: Detailed experimental methods, table of nanotube details, absorption spectra, further SEM data, plots of sheet resistance, DC to optical conductivity, and 2D order parameter as a function of transmittance. See DOI: 10.1039/c5nr08784h

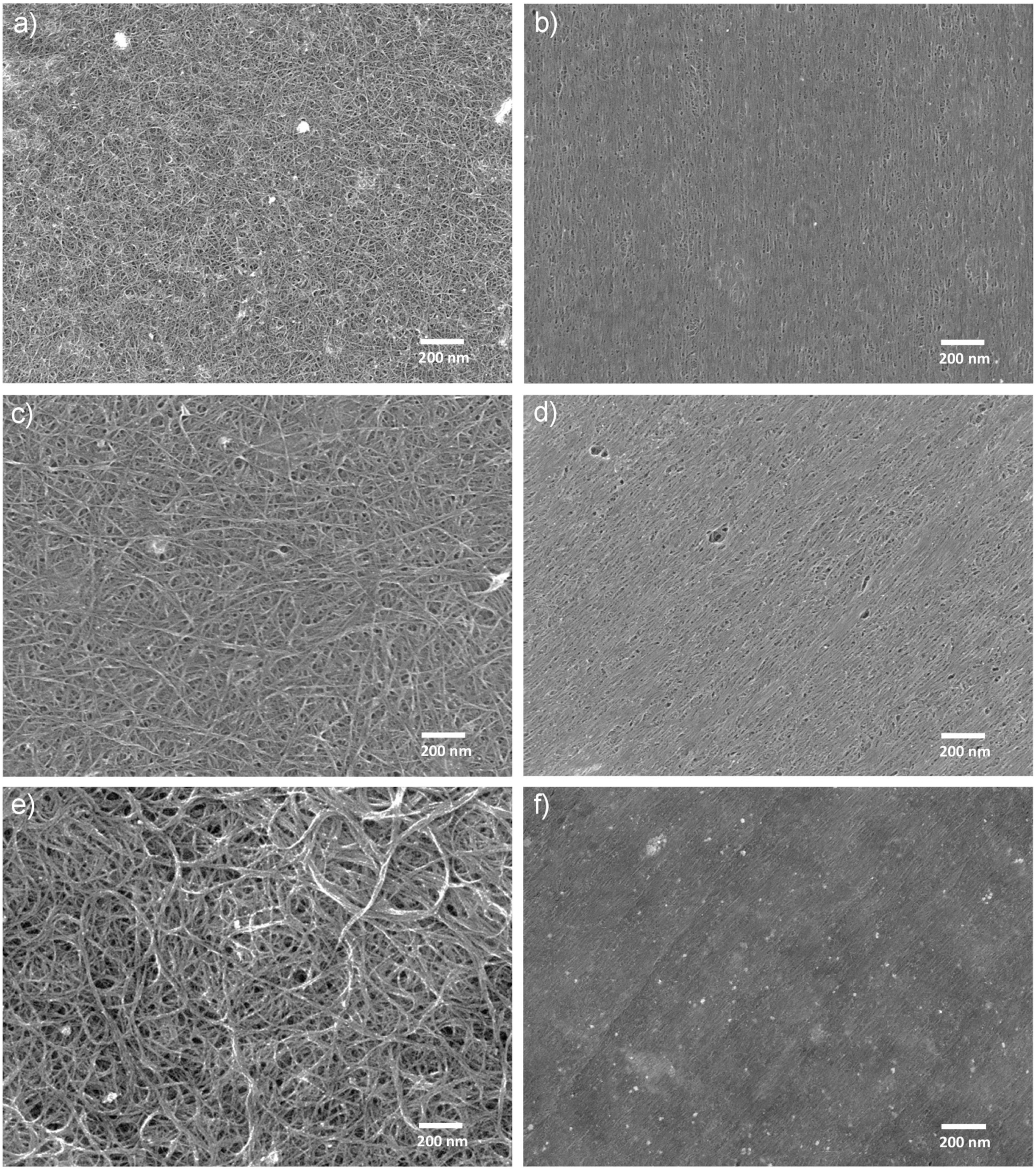

Fig. 2 SEM images of (a, c, e) as-prepared nanotube films and (b, d, f) the same films after dry shear aligning, where the film in (a) and (b) was produced by slide casting of HiPco nanotubes (SuperPureTubes, NanoIntegris) dissolved in sodium polyelectrolyte solution and had an order parameter after DSA of $S_{2D} = 0.41$, the film in (c) and (d) was produced by slide casting of gel sorted, small diameter metallic nanotubes made from raw HiPco material (NanoIntegris) and dissolved in sodium polyelectrolyte solution and had an order parameter after DSA of $S_{2D} = 0.28$, and the film in (e) and (f) was produced by vacuum filtration onto a mixed cellulose ester membrane (HAWP, Merck Millipore) of raw HiPco material suspended in 1 wt% SDS solution and had an order parameter after DSA of $S_{2D} = 0.22$. In all cases DSA was conducted on the films mounted on glass slides. Absorption spectra of the three kinds of nanotube film are shown in Fig. S1.†

tubes stabilised with surfactants, as well as those dissolved in chlorosulphonic acid or sodium polyelectrolyte solutions at concentrations below that required for liquid crystal ordering (if they were at liquid crystal concentration then the film formation process would already align the nanotubes, negating the need for DSA). The resultant level of order of the films follows the trend SW (small) > SW (large) > DW ≫ MW (Fig. S2†). We have observed no difference in the response of semiconducting, metallic or mixed nanotubes although the more pure and free of catalyst particulates and other contaminants the starting material is, the cleaner the final film is. This can be readily seen in Fig. 2(f) where many bright spots of high secondary electron emission are observed, corresponding to metal catalyst particles in the raw nanotube starting material, as well as some regions of blurriness which may correspond to amorphous carbon in the starting material, or perhaps to some residual surfactant. Also seen in Fig. 2(f) are some shallow striations due to the aligner surface (Teflon in this case) not being atomically flat. Better flattening and alignment is observed with higher purity material, whereas extensive damage occurs to the films when particulates are present during shearing (Fig. S3†). DSA can be applied to films created by vacuum filtration from aqueous or non-aqueous suspensions, or shearing/slide casting from isotropic solutions, with varying effects depending on the technique. In the case of vacuum filtration (Fig. S4†), the DSA technique can be applied directly on the film after it has been transferred to a surface (Fig. S4(e–h)†), or on the filtration membrane before transfer (Fig. S4(i–l)†). Or, DSA could be applied before transfer to flatten/align one side of the film and provide an improved junction with the substrate, then after transfer to flatten and align the other side to provide a better junction with any additional material layers in the respective device. Comparing DSA of films made by vacuum filtration of single, double and multiwalled nanotubes (Fig. S4, S5 and S6,† respectively) it is clear that the degree of reorganisation of the nanotubes is heavily dependent on their type and purity. The smaller the diameter of the nanotubes, the easier they are to rearrange and hence the better the flattening and alignment, with the best results obtained from material such as high purity, gel-sorted (6,5) nanotubes[20,21] (Fig. S7†). For the aligner, we use Teflon for films still attached to the filtration membrane, although polycarbonate, ceramic, glass and steel all yield positive results, and latex for films on glass or silicon, though nitrile and rubber are also effective.

Clearly, DSA is inherently scalable to nanotube films of arbitrary size and dimension without complication of the equipment setup since the essential elements are that pressure is applied to an aligner that is in contact with, and moving in relation to, a surface holding a nanotube thin film. In principle this could be applied in continuous roll-to-roll production processes. These characteristics are in stark contrast to some previous alternatives which could only be applied in batch production and which may require expensive tooling and/or add significantly to manufacturing complexity.[3–6,9–11,15] DSA does not require any specific preparation of the nanotubes over and above that required to form the film by a chosen method. Importantly, and in contrast to other potentially industrial-scale techniques such as the collapse or drawing of CVD grown forests, this means that DSA can be applied to the whole range of nanotubes from raw mixtures of type and chirality through to very highly purified, chirality sorted material.

In addition to the long range ordering apparent in Fig. 2, the other main effect of the DSA technique is to significantly reduce the film roughness. Fig. 3(a) and 3(b) show 3D AFM images of a vacuum filtered nanotube film before and after DSA. In this case the root mean squared roughness decreased substantially from 143 nm to just 3.3 nm, an outstanding improvement, and similar large decreases are observed for all the nanotube films we have studied, regardless of whether or not the nanotubes were aligned. The ability to create such smooth films is particularly advantageous in the context of using nanotube films in application where they are used in conjunction with thin layers of other materials. For example, where the nanotubes are used as electrodes or charge transport layers in organic photovoltaics, LEDs, capacitors, *etc.*, in which the thickness of the material layer on top of the nanotubes could be well below 100 nm. As one would predict, the anisotropy induced by DSA causes the nanotube films to have a different response to polarised light depending on orientation. Fig. 3(c) shows the optical spectrum of the film in Fig. 3(a) and is invariant under polarisation. Polarised optical absorption spectra from the same film (the other half of the filtration membrane) after the application of DSA are shown in Fig. 3(d) and yield a 2D order parameter of 0.16, where the order parameter was calculated as per White and Taylor[22] and where

$$S_{2D} = (A_{\parallel} - A_{\perp})/(A_{\parallel} + 2A_{\perp})$$

This value is somewhat less than might be expected based on the SEM images however it must be noted that the alignment occurs only on the surface of thicker films, leaving the inner regions in their randomly oriented state, and this is particularly true when the films are still bound to the filtration membrane; with a proportion of the material penetrating into the pores and less exposed to shear. A comprehensive study of the effect of DSA on varied thicknesses of vacuum filtered films of large diameter single walled nanotubes was conducted (Fig. S8, S9 and S10†). As well as the usual relationships between sheet resistance, thickness and doping which are well captured in the figure of merit ratio of DC electrical to optical conductivity (Fig. S10(a+c)†),[23] the data show both a small but distinct anisotropy in the conductance (Fig. S10(b+d)†) as well as a clear dependence of the extent of nanotube alignment on the film thickness, with a critical thickness corresponding to a transmittance of around T_{550} = 80% (Fig. S11†), above which the effects of DSA become more pronounced. This suggests that future fine tuning of the film thickness and DSA conditions may allow for the production of films composed only of the aligned surface region.

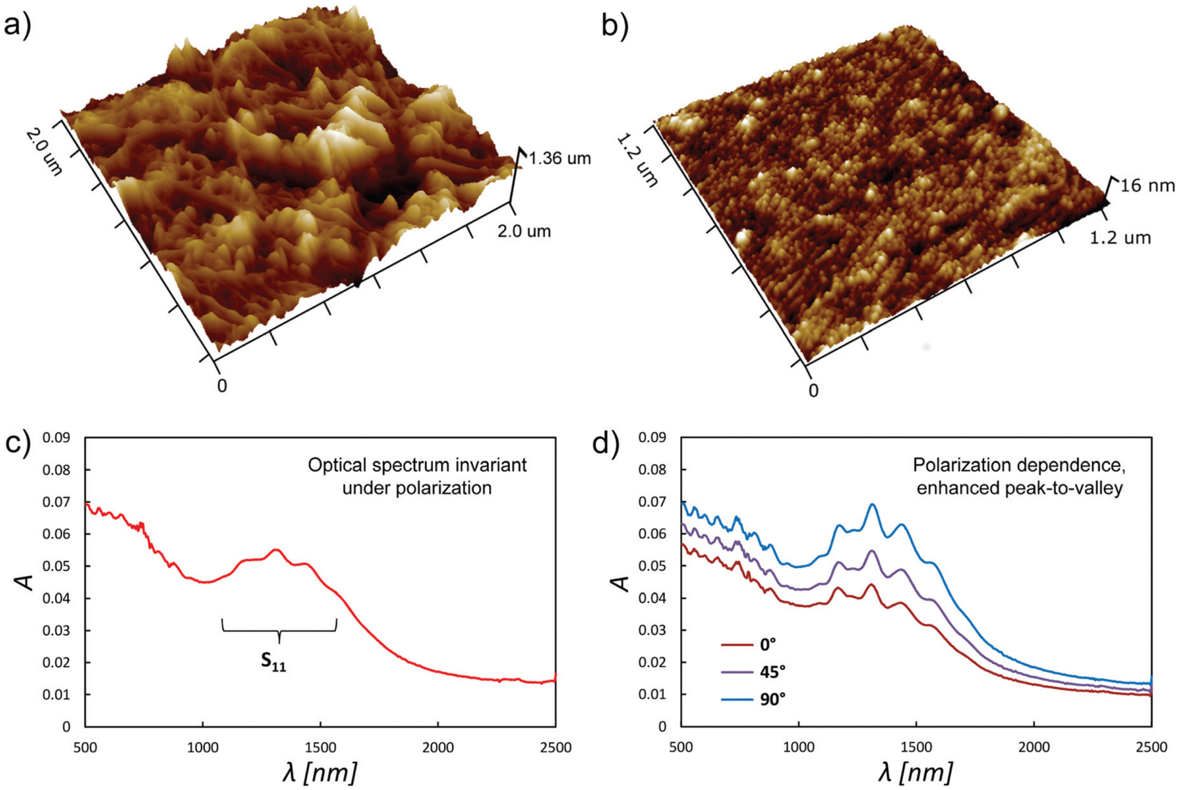

Fig. 3 (a) and (b) show 3D AFM images of a vacuum filtered nanotube film before and after DSA, respectively, while (c) and (d) show the corresponding polarised optical spectra.

Although the smoothing of the nanotube films is an intuitive process, the mechanism underlying alignment by DSA is not immediately clear. If the nanotubes were subjected to a flowing liquid, as in the case of nanotube fibre formation from chlorosulphonic acid in a faster flowing coagulant,[24] then the alignment could be explained as being due to the well-known effects of drag on the rotation/orientation of an anisotropic particle in a flow. Similarly for cellulose nanocrystals suspended in water, which can be aligned in thin liquid films subjected to doctor blading, as long as the volume concentration of the nanocrystals in the solvent is low enough to allow free movement,[25] and for nematic liquid crystals of carbon nanotubes dissolved by superacids[13] or *via* alkali metal reduction[14] and sheared in a thin liquid film. In such cases the alignment process can be understood in the context of well-known continuum theories modelling liquid crystal behaviour.[26] However, the situation is quite different in the case of a dry material. In determining the mechanism underlying DSA, considerable insight can be found in the work of Börzsönyi *et al.* who studied the shear induced alignment of various elongated particles and developed a numerical model of the experimental observations.[27] The process is shown to be very similar to that occurring in nematic liquid crystals, despite the completely different interparticle interactions involved. In Börzsönyi's model, the fundamental cause of the alignment is a reduction in friction between the material and the shearing plate by up to a third in the aligned state *vs.* the unaligned one. The degree of order scales with the aspect ratio of the individual particles up to 5 : 1 (the upper limit in the experiment). The fact that DSA appears so far to be a surface effect, unlike in the Börzsönyi *et al.* work, in which the degree of order was observed to be the same throughout the material, could be due to, (a) the much higher aspect ratio of the nanotubes (100 : 1 up to >1000 : 1) which, as discussed by Börzsönyi *et al.*, leads to much greater levels of entanglement between neighbours and thus hinders movement of the nanotubes, (b) the extremely low friction that exists between nanotube sidewalls,[28] reducing the penetration depth of the shear force (and perhaps explaining why the order parameter is lower for nanotube films deposited from surfactant-stabilised suspensions *vs.* those deposited from true solutions in superacid, *etc.* – the surface nanotubes are more free to slide past each other without the presence of residual surfactant) and, (c) the fact that in the Börzsönyi *et al.* experiments only one side of the bulk material was subject to a shearing surface whilst the other side was free to move, which is different to the situation in DSA where one side of the film is adhered to a stationary surface. Nevertheless, the model provides a strong foundation for understanding the current work.

In summary, dry shear aligning is a simple post-fabrication treatment that can yield dramatic improvements in film roughness and homogeneity, along with excellent alignment of the surface nanotubes. Apart from the presentation of a facile and scalable technique to generate outstandingly smooth films from much rougher starting material, the main conclusion of this work is that, perhaps contrary to assumption, carbon nanotube films like the ones used in this work are not fixed structures, but are dynamic and malleable systems containing mobile elements that are capable of significant restructuring and reordering with appropriate mechanical intervention. The observation of realignment of the nanotube bundles reveals the fluidity and plasticity of such films and is a practical insight that may inform future work in the field. Considering the widespread use of thin nanotube films across a broad swath of fundamental and applied nanoscience, we expect that the dry shear aligning technique may be of benefit to many in the nanotube research community.

Acknowledgements

B. S. Flavel gratefully acknowledges support from the Deutsche Forschungsgemeinschaft's Emmy Noether Programm under grant number FL 834/1-1.

References

1 B. Chen, G. Zhong, P. Goldberg Oppenheimer, C. Zhang, H. Tornatzky, S. Esconjauregui, S. Hofmann and J. Robertson, *ACS Appl. Mater. Interfaces*, 2015, **7**, 3626–3632.

2 S. Hu, Z. Xia and L. Dai, *Nanoscale*, 2013, **5**, 475–486.

3 M. Cole, P. Hiralal, K. Ying, C. Li, Y. Zhang, K. Teo, A. Ferrari and W. Milne, *J. Nanomater.*, 2012, **2012**, 8.

4 P. D. Bradford, X. Wang, H. Zhao, J.-P. Maria, Q. Jia and Y. T. Zhu, *Compos. Sci. Technol.*, 2010, **70**, 1980–1985.

5 W. Ding, S. Pengcheng, L. Changhong, W. Wei and F. Shoushan, *Nanotechnology*, 2008, **19**, 075609.

6 W. A. deHeer, W. S. Bacsa, A. Châtelain, T. Gerfin, R. Humphrey-Baker, L. Forro and D. Ugarte, *Science*, 1995, **268**, 845–847.

7 L. Zhang, X. Wang, W. Xu, Y. Zhang, Q. Li, P. D. Bradford and Y. Zhu, *Small*, 2015, **11**, 3830–3836.

8 K. Wang, S. Luo, Y. Wu, X. He, F. Zhao, J. Wang, K. Jiang and S. Fan, *Adv. Funct. Mater.*, 2013, **23**, 846–853.

9 L. Ren, C. L. Pint, L. G. Booshehri, W. D. Rice, X. Wang, D. J. Hilton, K. Takeya, I. Kawayama, M. Tonouchi, R. H. Hauge and J. Kono, *Nano Lett.*, 2009, **9**, 2610–2613.

10 G. Giancane, A. Ruland, V. Sgobba, D. Manno, A. Serra, G. M. Farinola, O. H. Omar, D. M. Guldi and L. Valli, *Adv. Funct. Mater.*, 2010, **20**, 2481–2488.

11 Q. Cao, S.-J. Han, G. S. Tulevski, Y. Zhu, D. D. Lu and W. Haensch, *Nat. Nanotechnol.*, 2013, **8**, 180–186.

12 S. Park, G. Pitner, G. Giri, J. H. Koo, J. Park, K. Kim, H. Wang, R. Sinclair, H. S. Wong and Z. Bao, *Adv. Mater.*, 2015, **27**, 2656–2662.

13 X. Li, Y. Jung, K. Sakimoto, T.-H. Goh, M. A. Reed and A. D. Taylor, *Energy Environ. Sci.*, 2013, **6**, 879.

14 D. D. Tune, A. J. Blanch, C. J. Shearer, K. E. Moore, M. Pfohl, J. G. Shapter and B. S. Flavel, *ACS Appl. Mater. Interfaces*, 2015, **7**(46), 25857–25864.

15 D. Vennerberg and M. R. Kessler, *Carbon*, 2014, **80**, 433–439.

16 H. Shimoda, S. J. Oh, H. Z. Geng, R. J. Walker, X. B. Zhang, L. E. McNeil and O. Zhou, *Adv. Mater.*, 2002, **14**, 899–901.

17 M. Engel, J. P. Small, M. Steiner, M. Freitag, A. A. Green, M. C. Hersam and P. Avouris, *ACS Nano*, 2008, **2**, 2445–2452.

18 H. Ko and V. V. Tsukruk, *Nano Lett.*, 2006, **6**, 1443–1448.

19 Y. Joo, G. J. Brady, M. S. Arnold and P. Gopalan, *Langmuir*, 2014, **30**, 3460–3466.

20 B. S. Flavel, K. E. Moore, M. Pfohl, M. M. Kappes and F. Hennrich, *ACS Nano*, 2014, **8**, 1817–1826.

21 B. S. Flavel, M. M. Kappes, R. Krupke and F. Hennrich, *ACS Nano*, 2013, **7**, 3557–3564.

22 D. L. White and G. N. Taylor, *J. Appl. Phys.*, 1974, **45**, 4718–4723.

23 D. S. Hecht, A. M. Heintz, R. Lee, L. Hu, B. Moore, C. Cucksey and S. Risser, *Nanotechnology*, 2011, **22**, 169501.

24 N. Behabtu, C. C. Young, D. E. Tsentalovich, O. Kleinerman, X. Wang, A. W. K. Ma, E. A. Bengio, R. F. ter Waarbeek, J. J. de Jong, R. E. Hoogerwerf, S. B. Fairchild, J. B. Ferguson, B. Maruyama, J. Kono, Y. Talmon, Y. Cohen, M. J. Otto and M. Pasquali, *Science*, 2013, **339**, 182–186.

25 A. B. Reising, R. J. Moon and J. P. Youngblood, *J. Sci. Technol. Forest Products Processes*, 2012, **2**, 32–41.

26 J. T. Jenkins, *Annu. Rev. Fluid Mech.*, 1978, **10**, 197–219.

27 T. Börzsönyi, B. Szabó, G. Törös, S. Wegner, J. Török, E. Somfai, T. Bien and R. Stannarius, *Phys. Rev. Lett.*, 2012, **108**, 228302.

28 R. Zhang, Z. Ning, Y. Zhang, Q. Zheng, Q. Chen, H. Xie, Q. Zhang, W. Qian and F. Wei, *Nat. Nanotechnol.*, 2013, **8**, 912–916.

– This page intentionally left blank –

2.3 Carbon Nanotube Silicon Solar Cells

2.3.1 *Carbon Nanotube Silicon Solar Cells*

D. D. Tune, **B. S. Flavel**, R. Krupke, J. G. Shapter

Advanced Energy Materials 2 (2012) 1043–1055

DOI: 10.1002/aenm.201200249

Abstract

Due to the high cost of silicon photovoltaics there is currently great interest in finding alternative semiconductor materials for light harvesting devices. Single-walled carbon nanotubes are an allotrope of carbon with unique electrical and optical properties and are promising as future photovoltaic materials. It is thus important to investigate the methods of exploiting their properties in photovoltaic devices. In addition to already extensive research using carbon nanotubes in organic photovoltaics and photoelectrochemical cells, another way to do this is to combine them with a relatively well understood model semiconductor such as silicon. Nanotube-silicon heterojunction solar cells are a recent photovoltaic architecture with demonstrated power conversion efficiencies of up to ~ 14% that may in part exploit the photoactivity of carbon nanotubes.

Contribution

An invited review appearing on the cover of the journal. B.S.F and D.D.T wrote the manuscript and all authors contributed their scientific input.

– This page intentionally left blank –

Vol. 2 • No. 9 • September • 2012

www.advenergymat.de

ADVANCED ENERGY MATERIALS

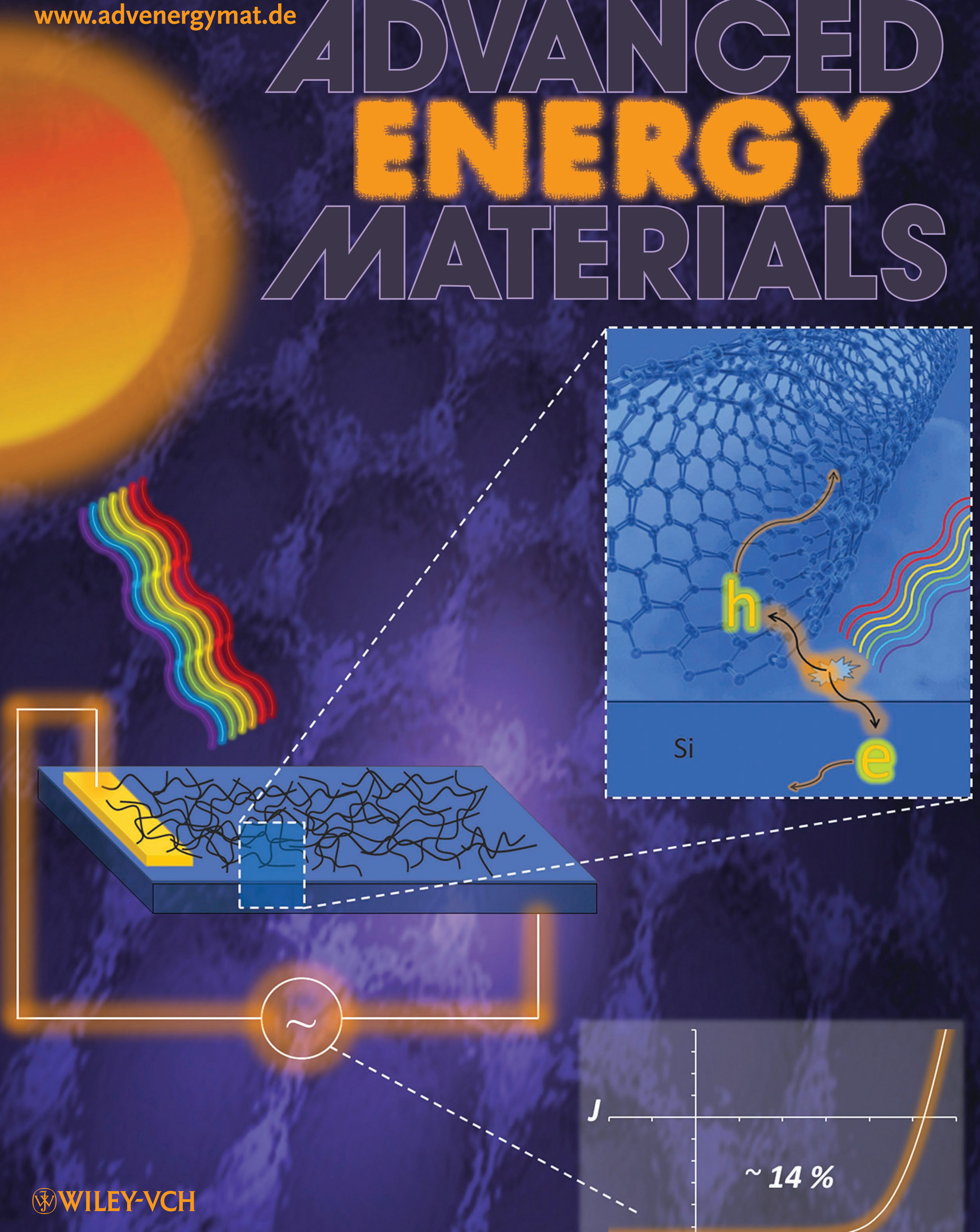

WILEY-VCH

– This page intentionally left blank –

Carbon Nanotube-Silicon Solar Cells

*Daniel D. Tune, Benjamin S. Flavel, Ralph Krupke, and Joseph G. Shapter**

Due to the high cost of silicon photovoltaics there is currently great interest in finding alternative semiconductor materials for light harvesting devices. Single-walled carbon nanotubes are an allotrope of carbon with unique electrical and optical properties and are promising as future photovoltaic materials. It is thus important to investigate the methods of exploiting their properties in photovoltaic devices. In addition to already extensive research using carbon nanotubes in organic photovoltaics and photoelectrochemical cells, another way to do this is to combine them with a relatively well understood model semiconductor such as silicon. Nanotube-silicon heterojunction solar cells are a recent photovoltaic architecture with demonstrated power conversion efficiencies of up to ~14% that may in part exploit the photoactivity of carbon nanotubes.

1. Carbon Nanotubes

In order to overcome the production costs associated with silicon solar cells and the toxicity and/or scarcity issues of other solid state semiconductors there is currently great interest in finding alternative semiconductor materials and/or alternative ways of fabricating current generation solar cells. One material with great potential in these areas is carbon, in the form of carbon nanotubes. Carbon is certainly not in limited supply and this material could be made very, very cheap with economies of scale in production. For reasons outlined later in this report carbon nanotubes show promise as photovoltaic elements. Since first reports of carbon nanotubes by Iijima,[1] and of single walled carbon nanotubes by Iijima and Ichihashi[2] and Bethune et al.[3] in the early 1990s, the explosion of research into carbon nanotubes has continued to expand exponentially largely due to their excellent and often unique electrical[4] and optical[5] properties. Carbon nanotubes are an allotrope of carbon having the form of hollow cylinders composed of rolled-up sheets of graphene. Carbon nanotubes can be single walled (SWNTs), double walled (DWNTs) or multi walled (MWNTs). A SWNT can be completely described, except for its length, by an intrinsic geometric property, $\mathbf{C}_h$, known as the chiral vector.[6] The chiral vector is defined by the equation $\mathbf{C}_h = n\mathbf{a}_1 + m\mathbf{a}_2$[7] where the integers ($n,m$) are the number of steps along the *zig-zag* carbon bonds and $\mathbf{a}_1$, $\mathbf{a}_2$ are the graphene lattice basis vectors in real space. As can be seen in **Figure 1**a the chiral vector makes an angle, θ, known as the chiral angle, with the *zig-zag* or $\mathbf{a}_1$ direction.[6b] The chiral angle determines the amount of 'twist' in the nanotube and two limiting cases exist where the chiral angle is at 0° and 30°.[6] These limiting cases are known as *zig-zag* (0°) and *armchair* (30°) based on the geometry of the carbon bonds around the circumference of the nanotube.[8] All other conformations in which the C–C bonds lie at angles $0° < \theta < 30°$ are known as *chiral*.[6b]

The n, m integers completely describe nanotube chirality and thus specify the electronic band structure. Therefore it is the chirality that has significant implications for the optical, mechanical and electronic properties of carbon nanotubes.[8] In particular by slightly changing the chiral angle it is possible to switch between metallic, low band gap and high band gap semiconducting carbon nanotubes.[6,8] When $n - m = 3p$ (p is an integer) the nanotube is metallic, when $n - m \neq 3p$ the nanotube is semiconducting[9] with band gap energy, E_g, dependent on the nanotube diameter, d_t, the C–C nearest neighbour potential overlap integral, $V_{pp}\pi$, and the C–C bond distance, a_{cc}, such that;

$$E_g = \frac{2V_{pp\pi}a_{cc}}{d_t} \tag{1}$$

Thus *armchair* nanotubes are the only intrinsically metallic type (no bandgap) although approximately one third of all *zigzag* nanotubes are also termed 'metallic' at room temperature since the energy gap is smaller than the thermal energy, k_BT, allowing thermal excitation of carriers into the conduction band. This use of the term metallic can lead to some confusion if it is assumed to have the same meaning as is the case for bulk metals. For example, whereas the colour of nanoparticulate metals is a result of plasmon resonance, the colour of metallic nanotubes arises from their excitonic properties.[10] All *chiral* nanotubes and the remaining two thirds of *zigzag* nanotubes are therefore semiconducting with band gaps defined by

---

D. D. Tune, Prof. J. G. Shapter
Centre for Nanoscale Science and Technology
Flinders University
Bedford Park, South Australia 5042, Australia
E-mail: Joe.Shapter@flinders.edu.au
Dr. B. S. Flavel, Prof. R. Krupke
Institute of Nanotechnology
Karlsruhe Institute of Technology
76021 Karlsruhe, Germany
Prof. R. Krupke
DFG Centre for Functional Nanostructures (CFN)
76131 Karlsruhe, Germany
Prof. R. Krupke
Department of Materials and Earth Sciences
Technische Universität Darmstadt
64287 Darmstadt, Germany

DOI: 10.1002/aenm.201200249

Equation 1. This leads to the observation that approximately 60% of all nanotube chiralities are semiconducting with the remaining 40% metallic.[11]

Carbon nanotubes are so small they exhibit quasi-one dimensional properties and the 1D confinement of electrons into allowed *k*-states gives rise to van Hove singularities in the electronic density of states (DOS) (Figure 1b,c). In bulk semiconducting materials the energy gap between the valance and conduction bands defines the absorption onset wavelength of the optical spectra. If nanotubes are considered similarly, in the manner of single particle excitations, then the discrete electronic transitions in the DOS should produce characteristic peaks in the UV-Vis-NIR absorption spectra of SWNTs at wavelengths corresponding to the transition energies of the respective nanotubes. However it is now known that the optical absorption spectra of nanotubes are entirely excitonic in nature and thus many-body effects must be considered for an accurate description of the optical properties of nanotubes.[12] This means that the actual light energy required to produce a "v_i–c_i" transition is ($Ec_i - Ev_i$) + binding energy (*eh*) - self energy (*ee*), and leads to the experimental finding that E_{22}/E_{11} tends to a value of 1.8 with decreasing tube diameter, rather than the value of 2 as would be expected from density functional theory calculations alone.[13]

Fundamental photovoltaic theory stipulates that one of the criteria for obtaining the highest efficiency devices is correct matching of the semiconductor's optical band gap to the solar spectrum.[14] The optimal band gap of ~1.1 eV is easily obtained with ~12–15 different semiconducting nanotube chiralities having a fundamental optical gap between 1.0–1.2 eV.[15] However calculations for the optimal band gap criterion apply to bulk semiconductors in which there is a smooth continuum of states above and below the gap but this is not the case for SWNTs with their discrete DOS features. Semiconducting nanotubes have a Fermi level in the middle of the band gap and could thus be termed 'intrinsic' similarly to undoped silicon. However when exposed to air they develop p-type characteristics due to the electron withdrawing nature of adsorbed oxygen molecules. Even in ultra-high vacuum this adsorbed oxygen is very difficult to remove and has likely skewed the results of much research carried out to date.[16] In addition, SWNTs can be chemically doped p-type by electron-withdrawing species such as strong oxidisers or oxidising acids,[17] or n-type by electron-donating species such as alkali metals,[18] hydrazine,[17b,19] nitrogen-rich polymers[20] and nitrogen-rich aromatic compounds.[21] Substitutional doping has also been demonstrated with boron (p-type)[22] and nitrogen (n-type).[23] This raises the exciting prospect of all-nanotube photovoltaics based on *p-n* or *p-i-n* heterojunctions, although such architectures are yet to be reported for other than single tube devices.

SWNTs were initially touted as the quintessential nanostructure and expectations of them were high. However the successful application of SWNTs into new and improved devices has been limited by the polychirality of as-produced and purified SWNTs. Electrical, optical and physical properties of SWNTs are highly dependent on nanotube chirality but although there are many reports of the sorting and characterisation of SWNTs in the literature these have often been in very small quantities unsuitable for further device fabrication. The performance of thin film and other solar cell devices does not scale up well from very small research cells due to the domination of edge effects thus appreciable quantities of sorted nanotubes are required for the fabrication of devices large enough to provide meaningful, scalable performance data. The sorting of nanotubes into populations of individual chirality in such quantities has until

Daniel Tune obtained a BSc in Nanotechnology from the Flinders University of South Australia in 2009 and is currently completing his PhD. His research interests are in the fields of renewable energy and nanoelectronics, with particular attention to the use of carbon nanotubes, fullerenes, and graphene. His present work involves the application of nanotechnology to improve current-generation solar cells and the investigation of new and emerging photovoltaics.

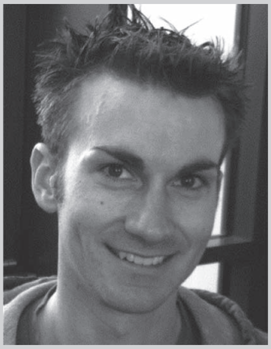

Benjamin Flavel is a physical chemist who completed both a BSc (Hons) in Nanotechnology and a PhD at the Flinders University of South Australia. He has since received the Australian Government's Endeavour Research Fellowship, completed at the University of Canterbury, New Zealand, and currently holds an Alexander von Humboldt Research Fellowship at the Karlsruhe Institute of Technology, Germany. His research interests include electrochemistry, carbon nanotube solar cells, and biosensors.

Joe Shapter obtained his PhD from the University of Toronto in 1990. In 1996 he moved to Flinders and is now Professor of Chemistry. He is currently the Director of the South Australian node of the Australian Microscopy and Microanalysis Research Facility (AMMRF). His group works with chemical attachment or deposition of carbon nanotubes to surfaces with both patterned and unpatterned approaches. These substrates have been used for applications including sensing and solar cells.

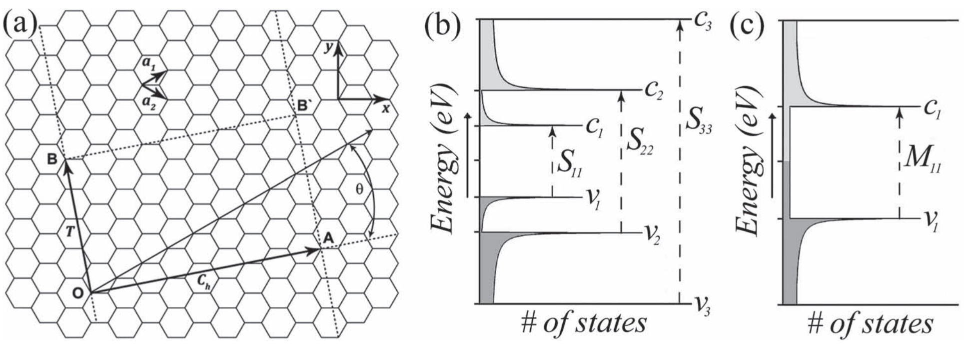

Figure 1. a) Unrolled graphene sheet showing the geometry of the (4,2) nanotube. The vectors OA and OB define the chiral and translational vectors $\mathbf{C}_h$ and **T**, respectively, and the rectangle OAB'B defines the unit cell; O, A, B and B' are reference atoms, $\mathbf{a}_1$, $\mathbf{a}_2$ are the graphene lattice real basis vectors and θ is the chiral angle.[9] Schematic of the electronic density of states (DOS) of (b) semiconducting and (c) metallic zigzag SWNTs showing valence and conduction bands, v_i and c_i, and optically active electronic transitions, S_{ii} and M_{ii}.

recently been unattainable. Today a number of methods for sorting of nanotubes are available such as dielectrophoresis,[24] density-gradient ultracentrifugation (DGU),[24b,25] selective polymer wrapping[26] or liquid-phase chromatography.[27] The choice of method depends on the targeted application and the subsequent need for sorting tubes by metallicity, diameter and/or chiral angle. For solar cells one would ideally like to use quantities of semiconducting nanotubes of a single chirality to have uniform electrical and optical properties. Selective polymer wrapping, DGU and liquid-phase chromatography can deliver single-chirality fractions for small-diameter nanotubes (<1.1 nm). However depending on the diameter and chirality distribution of the raw material the yield in obtaining a specific (n,m) fraction can be rather low. The strategy must therefore be to sort out (n,m)-tubes from raw material that already has a very narrow diameter distribution.

2. Carbon Nanotubes in Solar Cells

Shockley and Queisser used detailed balance calculations to derive a fundamental limit to the photovoltaic conversion efficiency (PCE) of a single junction solar cell.[28] Calculations have since been refined giving a limit of ~ 33%, however this is based on the assumption of one photon producing one exciton. SWNTs have been shown to exhibit multiple exciton generation (MEG) from a single photon.[29] In this process, a photon having energy equal to *n* multiples of the band gap is absorbed and produces *n* excitons. However, a complete solar cell device exploiting this property, and thus allowing violation of the Shockley Quiesser limit, is yet to be realised.

Currently the literature contains many cases of research utilising carbon nanotubes in solar cell devices. For example, nanotubes have been integrated into a variety of organic photovoltaics (OPVs).[30] However in these systems the carbon nanotubes are not so much responsible for exciton generation upon absorption of light but rather, by introducing carbon nanotubes into these polymeric systems, exciton dissociation or electron transport is enhanced within the material. There has also been much work in recent years incorporating carbon nanotubes into photoelectrochemical cells (PECs) either on their own[31] or as elements in donor-acceptor hybrids in conjunction with fullerenes,[32] fullerenes/P3HT,[33] fullerenes/porphyrin,[34] porphyrins,[35] pyrenes,[36] polythiophenes[37] and other photoactive polymers,[38] phthalocyanines,[35f,39] PAMAM dendrons,[40] quantum dots[41] and more. There is also a plethora of fundamental work looking at photoinduced charge transfer processes between carbon nanotubes and other species and it must be noted that the line between OPVs and PECs is blurred since photoelectrochemistry is also a method of characterising new OPV systems. Similarly, the implementation of carbon nanotubes in dye sensitised solar cells (DSCs) has included replacement for the platinum catalyst counter electrode,[42] improvement of the electrical properties of the titania[43] or replacement of the titania scaffold.[31c,44] For further information on the use of nanotubes in these types of light harvesting devices and structures we suggest excellent reviews by Imahori,[45] Sgobba,[46] Chitta,[47] Guldi,[48] and D'Souza.[49]

If carbon nanotubes are to offer a viable alternative to silicon in solar cells it is necessary to understand how photogeneration, transport and dissociation of excitons and charge carriers operates in large ensembles of them. One of the many paths to this goal is to combine them with a well understood, model semiconductor material such as silicon. Nanotube-silicon heterojunction (NSH) solar cells are a recent photovoltaic system which has been purported to utilise carbon nanotubes in photocurrent generation. A typical device has architecture similar to that of a single junction crystalline silicon solar cell with the exception that the emitter layer is replaced by a thin film of single, double or multi walled carbon nanotubes (SWNTs, DWNTs or MWNT's). The exact mechanism of operation of such cells is not well established however the operation mechanisms mentioned in the literature fall into two categories; 1) The mechanism is that of a *p-n* heterojunction solar cell (**Figure 2**a and Figure 2c), with the nanotubes acting as the p-type emitter material. Photons are absorbed mainly in the n-type silicon base region with resulting excitons diffusing to the space-charge region where they are separated into free charge carriers under the action of the built in potential formed by Fermi level equilibration at the junction. Photons can also be absorbed in the p-type nanotube region but since the nanotube films typically have 85+% transmittance this is not expected to be the dominant charge generation process.

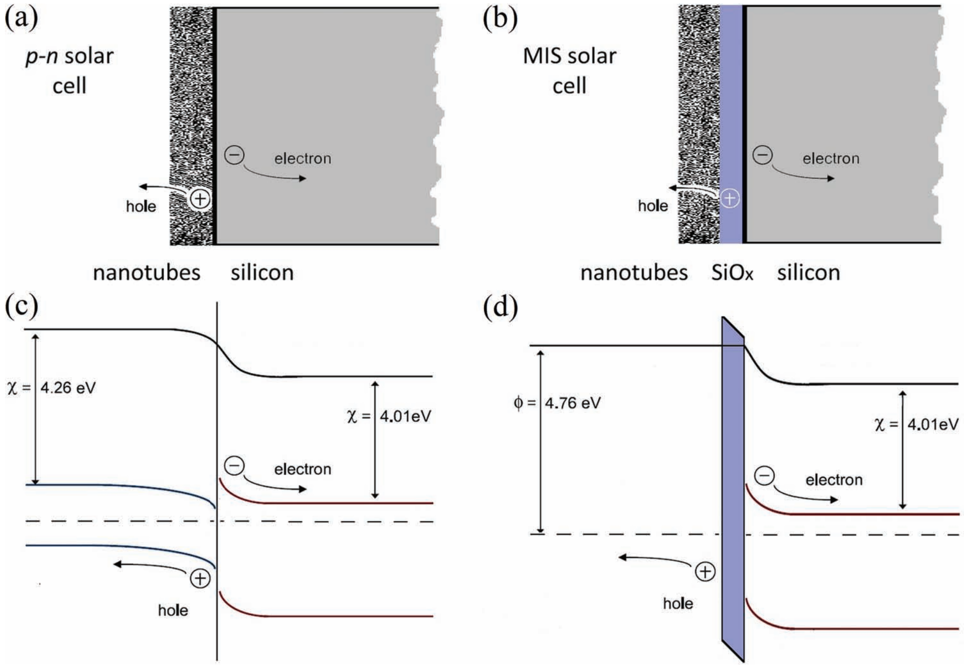

Figure 2. Device schematics and energy diagrams for *p-n* (a,c) and MIS (b,d) solar cells. The examples assume an electron affinity, work function and band gap for semiconducting carbon nanotubes of 4.26 eV, 4.76 eV, and 0.7 eV, respectively, a work function for metallic carbon nanotubes of 4.76 eV, and an electron affinity and band gap for silicon of 4.01 eV and 1.12 eV, respectively. The nanotube Fermi level is assumed to be ~0.1 eV below the middle of the bandgap due to oxygen adsorption and a dopant concentration of ~10^{15} cm^{-3} is assumed in silicon yielding a Fermi level ~0.25 eV below the conduction band edge. Adapted with permission.[53] Copyright 2011, American Institute of Physics.

2) The mechanism is that of a *Schottky* junction solar cell, or the closely related metal insulator semiconductor (MIS)[50] solar cell (Figure 2b,d). A *Schottky* junction is formed between a metal and a semiconductor[51] and can be employed as a solar cell device.[52] In this configuration the nanotubes act as the metal, a thin SiO_x passivation layer on the silicon surface serves as the insulator (for MIS) and the n-type silicon is the semiconductor base region. Photons absorbed in the base region produce excitons which diffuse to an inversion layer created in the silicon adjacent to the Si/SiO_x or Si/metal junction. Charges are separated by the built in potential formed between the metal or SiO_x (which has a Fermi level pinned to that of the adjacent metal) and the silicon. Once the charges are separated tunnelling is the mechanism of minority carrier transport through the thin insulating oxide layer of the MIS solar cell.

In fact, unlike in a bulk silicon *p-n* homojunction there are a great multitude of tiny nanotube-silicon heterojunctions, which are then further complicated by the presence of a distribution of nanotube chiralities. To date most NSH solar cells have employed inhomogeneous mixtures of metallic and semiconducting nanotubes and hence a combination of operation mechanisms is possible. It is tempting to presume that a device constructed with only semiconducting nanotubes would behave as a *p-n* junction solar cell whilst one with only metallic nanotubes would behave as a *Schottky* or MIS solar cell depending on the presence of an intermediate insulating layer.

3. Nanotube–Silicon Heterojunction Solar Cells

Although not an exhaustive list, the work detailed in the following covers some important and intriguing findings in the field and is summarised in **Table 1**, **2**, and **3**. The reporting of NSH solar cells began in 2007 with Wei et al.,[54] who demonstrated a 1.3% efficient device. In the design of Wei et al. DWNTs were deposited on n-silicon substrates via H_2O expansion and subsequent aqueous film transfer of an as-grown chemical vapour deposition (CVD) film as shown in **Figure 3**a. Wei et al. also demonstrated the importance of appropriate electrical contact to the bottom of n-Si substrate, an obvious contributing factor to series resistance. By depositing a Ti/Pd/Ag layer, which has good adhesion to, and forms good ohmic contacts with, silicon, the measured short circuit current density (J_{SC}) was enhanced by a factor of 10 compared with the use of silver paint as contact. However, overall PCE was low due to a poor fill factor (*FF*) of 0.19 as can be seen in Figure 3b. Benham et al.[55] probed the fundamental properties of nanotube-silicon junctions showing that tunnelling is the dominant mechanism of charge transport through untreated nanotube films at room temperature whilst, at temperatures above ~240 K, thermionic emission dominates.

Jia et al. reported a significant step forward from their 2007 work upon demonstrating a 7.4% efficient DWNT/n-Si device.[56] The DWNT film was prepared and deposited as in the earlier work. The higher efficiency relative to the earlier work can be attributed to a lowered series resistance. This was

Table 1. Summary of literature reports of NSH solar cells.

Publication details				Cell properties											
#	Year	Author	Journal	Subject	Active area [cm^2]	J$_{sc}$ [rnA.cm^{-2}]	V$_{oc}$ [V]	FF	η [%]	Rs [Ω]	R$_{SH}$ [Ω]	Rectification ratio	Ideality Factor		J$_{rev.sat}$ [mA.cm^{-2}]
													n_1	n_2	
1	2007	Wei	Nano. Lett.	DWNT solar ells	0.49	13.8	0.5	0.19	1.4	30 – 200	–	5×10^2	–	–	0.03
2	2008	Jia	Adv. Mat.	NSH solar cells	0.49	26	0.54	0.53	7.4	13	20	10^3	3.68	2.62	–
3	2008	Li	Appl. Phys. Lett.	SOCl$_2$ enhanced photo of NSH cells	0.25	21	0.48	0.28	1.3	–	–	10^2	–	–	0.05
4	2009	Li	ACS Nano	Light harvest high density NSH cells	0.25	26.5	0.49	0.35	4.5	16	–	4×10^2	–	–	0.03
5	2010	Jia	Mat. Res. Bull.	CNT films filtration NSH cells	0.49	18.6	0.53	0.42	4.1	–	–	–	–	–	–
6	2010	Ong	Nanotechnology	Hybrid NSH cells	0.25	14.6	0.37	0.3	1.7	150	7	–	3.75	–	–
7	2010	Wadhwa	Nano. Lett.	Electronic junction control NSH cells	0.08	25	0.55	0.79	10.9	–	–	–	–	–	–
8	2011	Jia	Nano. Lett.	High eff. NSH cells acid doping	0.09	36.3	0.53	0.72	13.8	25	–	–	1.4	–	–
9	2011	Jia	Appl. Phys. Lett.	Encapsulated NSH MIS cells 10%	0.09	29	0.56	0.68	10.9	65	–	1.2×10^5	1.44	–	–
10	2011	Wadhwa	Nano. Lett.	Electrolyte-induced inversion schottky	0.08	29.8	0.55	0.73	12.0	–	–	–	–	–	–

obtained in part by replacing the relatively thick isinglass (mica) front window with a thin SiO$_x$ window etched using photolithography. Reducing front window thickness has the effect of reducing bending/stretching of the nanotube film over the step that exists between the front window and the silicon active area. The lower series resistance gave a gain in J_{SC} from 13.8 to 26 mA cm^{-2} and an increase in FF from 0.29 to 0.53 compared to the earlier work.

Subsequently other groups have utilised alternative methods to deposit thin films of carbon nanotubes on n-type silicon. Li et al.[57] reported a NSH solar cell employing a SWNT film spray coated using an airbrushing technique from a dimethylformamide (DMF) suspension. Final devices were found to afford an efficiency of 1.3%. Li et al. investigated carbon nanotube film post-treatment methods in order to increase device efficiency. Hall Effect measurements showed that post-treatment of the SWNT films with SOCl$_2$ leads to increases in carrier density and effective mobility from 3.1×10^{15} to 4.6×10^{17} cm^{-2} and 0.23 to 1.02 cm^2 V^{-1} s^{-1}, respectively. Quoting the authors, "The major conduction mechanism of the SWNT coating

Table 2 Summary of literature reports of NSH solar cells.

Nanotubes										Front Content		Back Content	
#	Type	Source	Chirality (n,m)	Diameter [mn]	Thickness [nm]	R$_{sheet}$ [Ω.sq^{-1}]	Deposition Method	Treatment	T$_{550}$ [%]	Type	Thickness [nm]	Type	Thickness [μm]
1	DWNT	CVD	–	–	50	0.5 – 5	Aqueous film transfer	H$_2$O$_2$/HCl	>60	Ag	–	Ti/Pd/Ag	2
2	DWNT	CVD	–	2	20-50	–	Aqueous film transfer	H$_2$O$_2$/HCl	>60	Ag	–	Au/Ti	0.01
3	SWNT	HiPCO	–	0.6–1.1	–	170	Spray	SOCl$_2$	69	–	–	–	–
4	SWNT	–	(6,5) (7,5)	–	~250	~500	Spray	SOCl$_2$	57	Ag	–	Ag	–
5	DWNT	CVD	–	–	–	282	MCE	–	91	Ag	–	Ti/Au	50
6	SWNT	HiPCO	(7,6) (8,6)	0.9	20000–30000	1000	Spray	–	83	Ag	–	Cr/Au	0.02/0.15
7	SWNT	–	–		~45	–	MCE	–	–	Cr/Au	5/80	HF/Galn/Steel	–
8	SWNT	CVD	–	–	–	<200	Free transfer	HNO$_3$	>85	–	–	Ti/Au	–
9	SWNT	CVD	–	–	–	97	Free transfer	HNO$_3$	–	–	–	Ti/Au	–
10	SWNT	–	–	–	–45	–	Free transfer	–	–	Cr/Au	5/80	HF/Galn/Steel	–

Table 3. Summary of literature reports of NSH solar cells.

	Silicon						Notes
#	Plane	Dopant concentration [atoms cm^{-3}]	Resistivity [Ω cm]	Treatment	Thickness [μm]	Oxide [nm]	
1	–	–	–	HF	525	–	Series resistance reduced by deposited Ti/Pd/Ag on back contact instead of silver paint
2	–	10^{15}-10^{16}	2–3	HF	–	–	Improvement over #1 through replacing 2 μm Ti/Pd/Ag with 10 nm Au/Ti
3	–	–	–	–	–	–	Carrier density and effective mobility measurements (Hall Effect) before and after SOCF
4	–	–	–	–	–	–	Improvement over #3 through device optimisation
5	–	–	–	HF	–	–	Correlation of figure of merit (FM) for transparent, conductive thin films with PCE of NSH solar cells
6	<100>	–	0.01	HF	–	–	Photocurrent spectra - SWNT take part in photo-generation, compare centrifugation fractions
7	–	10^{14}–10^{15}	4-20	BOE	–	1000	Electronically gated with IL
8	–	10^{15}–10^{16}	2-4	HF	–	–	Nitric acid soaked nanotubes (0.1–0.5M)
9	–	10^{15}–10^{16}	2-5	HF	–	–	Oxide interlayer MIS design, PDMS encapsulation reduces reflection
10	<111>	10^{15}	–	BOE	–	4	Electronically gated with IL, line-etched CNT's

network shifted from variable range hopping toward tunnelling after the $SOCl_2$ treatment. The $SOCl_2$ treatment of SWNT films also leads to a slight increase in the open-circuit voltage and a significant increase in the short-circuit current through readjusting the Fermi level and enhancing the carrier density and mobility." Li et al. subsequently published a paper reporting a trebling of efficiency for similarly constructed, $SOCl_2$ post-treated devices[58] and further characterised the performance of devices fabricated by transferring an as-grown nanotube 'spider web' onto silicon.[59] The effect of $SOCl_2$ on SWNTs has been relatively well-studied and it has been shown to be a very good p-type dopant for SWNTs that increases conductivity in part by shifting the nanotube Fermi level into the valance band.[17b] However, $SOCl_2$ treatment bleaches the S_{11} transition in semiconducting nanotubes and it is unclear what effect this may have on the mechanism of action of NSH devices. It may well be that some devices function as *p-n* junctions before post treatment but then switch to (in this case much better performing) Schottky junction devices after the post treatment gives the nanotubes metallic characteristics.

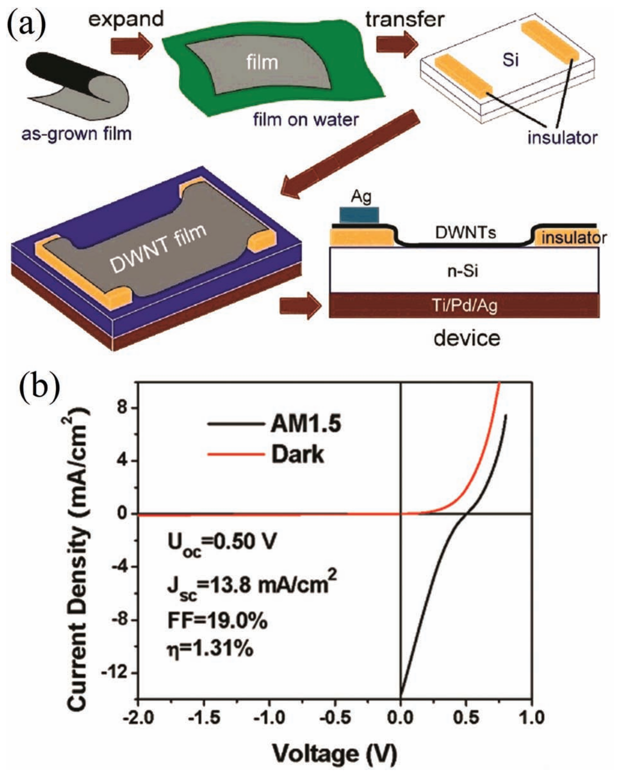

Figure 3. a) Schematic showing the fabrication process for DWNT/n-Si solar cell device and b) J-V data. Adapted with permission.[54] Copyright 2007, American Chemical Society.

Jia et al.[60] reported a nanotube deposition method employing vacuum filtration onto mixed cellulose ester (MCE) membranes with subsequent removal of the MCE by dissolving in acetone. The MCE deposition method was used for SWNTs and MWNTs but aqueous film transfer of a self-assembled film (as per their prior work[54,56]) was used for DWNTs. Considering the sensitivity of nanotube films' electrical characteristics to film morphology, this renders the comparison of these three films' performance in NSH solar cells less certain than would be the case if MCE deposition was also used for DWNTs. The report analyses the effect on performance of varying the area density of nanotubes. It was found that SWNT films outperform MWNTs only when the density is low, which is interpreted as indicating that optical transmittance is the most important variable in comparing SWNTs and MWNTs. The authors also correlate a figure of merit (FM) for transparent, conductive films with the PCE of NSH solar cells. The FM is defined in Equation 2 as;

$$F\,M = \frac{T_{550}(\%)}{R_s\left(\frac{\Omega}{sq}\right)} \tag{2}$$

where T_{550} is the optical transmittance for $\lambda = 550$ nm and R_S is the sheet resistance (not to be confused with the series resistance which shares the same nomenclature). It was found that the FM is proportional to PCE such that increasing film transparency or decreasing sheet resistance yields higher device efficiency. Optical transparency is increased for thinner films whereas the sheet resistance is decreased for thicker films. Thus at some point there must be a trade-off between these two variables with the optimal thickness likely constrained by the optimisation of other cell parameters. It is also interesting to note that $T \sim e^{-\alpha d}$, where α is the attenuation coefficient and d is the film thickness, and $R \sim 1/d$. Thus, the FM is apparently dominated by the exponential dependence of T on d and only for very thin films does R_s dominate. Even though the nanotube films are indeed very thin, this dependence of the PCE on the FM would seem to suggest that the role of the nanotubes is more that of a transparent, conducting film rather than as photoactive material. The effect of nanotube film thickness has also been investigated by Castrucci et al.[61] who similarly found that the density of the nanotube film (number of nanotube-silicon junctions) is a vital parameter in optimising performance.

In relation to the question of the mechanism of action of these devices, Ong et al.[62] made an important contribution, reporting that for their NSH cells “comparison of the photocurrent with the near infrared (NIR) absorption spectra clearly indicates an excellent matching of the S_{11} band (corresponding to the first interband transition for SWNTs with (7,6) and (8,6) chirality) with the photocurrent band located at ~ 1150 nm.” Thus, “the SWNT film contributes to the photoconversion process not only as a charge separator/transporter/collector but also as a light absorber. This is an important fact, distinguishing between a heterojunction solar cell with two active light absorbing components and a *Schottky* cell, where the metal component is not capable of absorbing photons”. The data in **Figure 4**b shows a small shoulder on the low energy side of the silicon photoresponse that is ~ 50 nm lower in wavelength than the relevant peak in the nanotube absorption spectrum (Figure 4a). The photocurrent due to silicon drops off sharply as the photon energy is increased. Le Borgne et al.[63] observe a similar, but smaller, drop in the high energy region of the photocurrent spectrum however, comparison with a silicon only cell shows a small improvement in the UV response corresponding with the π-π* transitions of the nanotubes. Nanotube films are known to produce photocurrents when deposited on semiconductor substrates (independent of any substrate photocurrent)[64] so, if there is a contribution from the nanotubes in Figure 4b then this seems to imply that the underlying mechanism of the nanotube-silicon architecture is that of a *p-n* junction not a *Schottky* junction. A rigorous study of the capacitance of nanotube-silicon junctions would likely shed more light on the issue.

In related work, Tsolov et al.[65] reported the mid-IR response of a silicon-carbon nanotube photodiode fabricated by CVD growth using an anodised aluminium oxide (AAO) template method on phosphorous doped n-type silicon (**Figure 5**a).

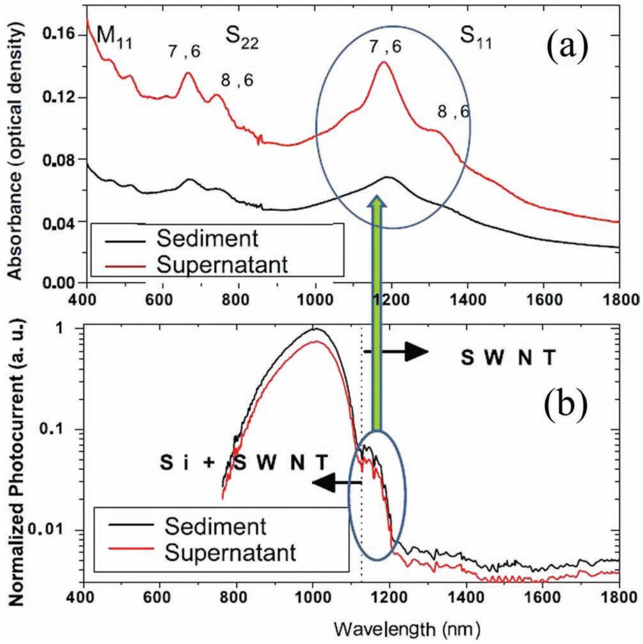

Figure 4. a) UV–vis–NIR spectra of SWNT films on glass, b) photocurrent spectra showing current peak corresponding to SWNT's S_{11} transition. Reproduced with permission.[62] Copyright 2010, IOP Publishing.

Whilst the use of a template is demonstrated as a facile method for producing aligned nanotube arrays on silicon it is claimed that the broad photocurrent response observed to span ~1.5–10 μm is due to the absorption of photons and generation of excitons by the nanotubes themselves. However this feature in the photocurrent spectrum could be due to free carrier absorption in the silicon as reported by Spitzer[66] (Figure 5b) and Schroder.[67]

Comparison of Figure 5a and b reveals the presence of three features at ~0.75 eV, 0.9 eV and 0.95 eV in (a) which are not represented in (b). These features are too far from the absorption band edge of silicon (1.12 eV) to be due to the silicon and might originate from the nanotubes. However MWNTs such as those used have not been shown to exhibit such well-defined absorption characteristics. On the contrary MWNTs are renowned for having rather broad featureless absorption spectra due to the complex mixing of states resulting from interactions between chirally dissimilar walls. It is also worth noting that a similar feature is observed on the low energy side of the silicon absorption as in the later work of Ong.[62] However the data of neither Tsolov nor Ong conclusively proves whether the nanotubes are contributing to the photocurrent of these devices. This question could likely be answered by an experiment similar to Ong's whereby cells are fabricated with larger diameter nanotubes where the energy of the first excitonic transition << absorption onset of silicon (e.g. 1400 nm) and the spectral response of such devices is measured. In this case any contribution from the nanotubes should be easily resolved.

Wadhwa et al.[68] report a novel method of improving NSH solar cells through electronic junction control of a SWNT/n-Si device by the use of a gate potential applied to the junction

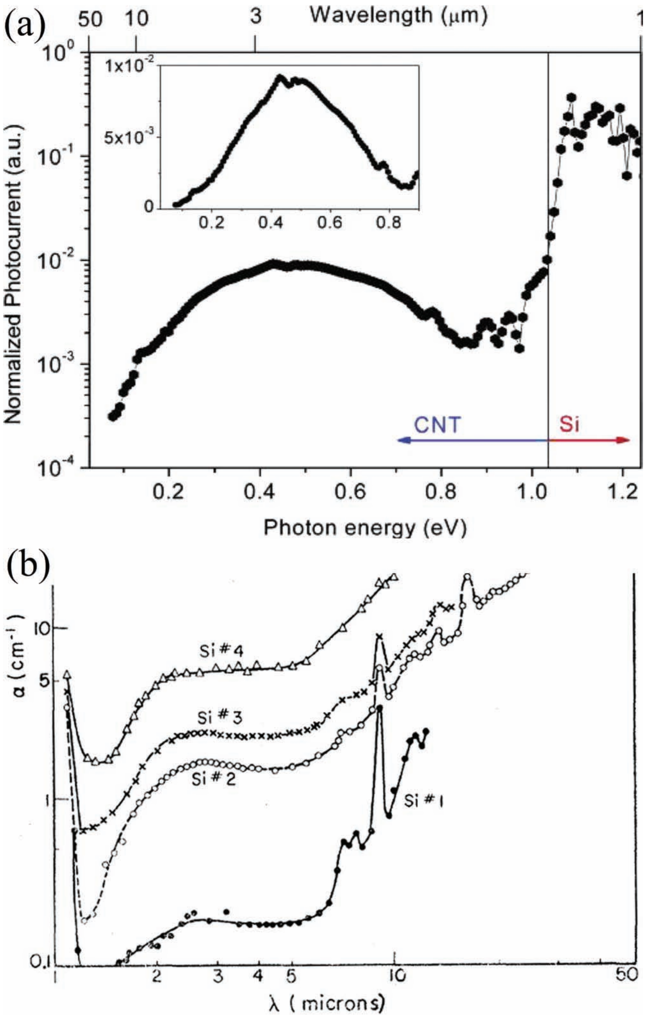

Figure 5. a) Mid-IR photocurrent response of AAO-templated aligned carbon nanotube array on silicon. Reproduced with permission.[65] Copyright 2007, American Chemical Society. b) IR absorption spectra of n-type silicon doped with: 1 arsenic ($N_d = 1.4 \times 10^{16}$ cm^{-3}), 2 antimony ($N_d = 8.0 \times 10^{16}$ cm^{-3}), 3 antimony ($N_d = 1.7 \times 10^{17}$ cm^{-3}), 4 phosphorous ($N_d = 3.2 \times 10^{17}$ cm^{-3}). Adapted with permission.[66] Copyright 1957, American Physical Society.

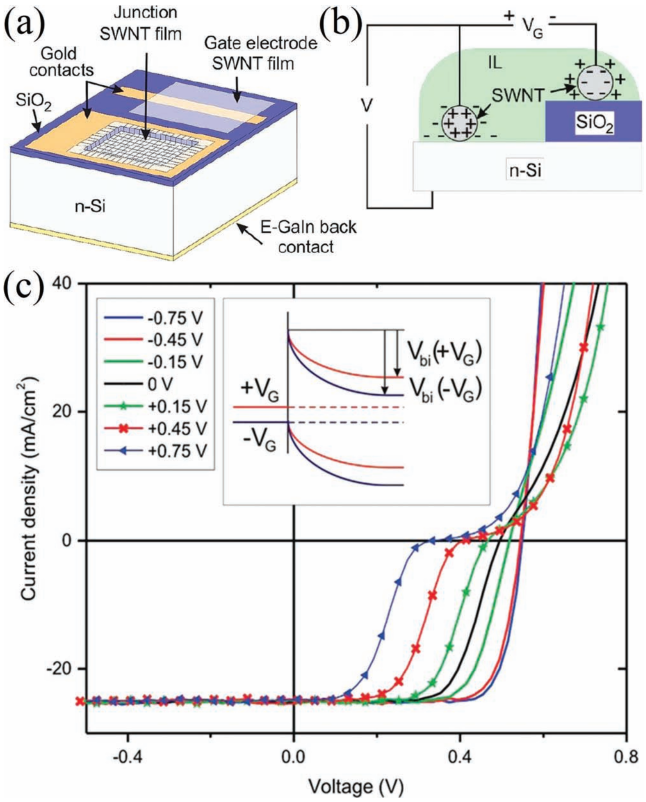

Figure 6. a) Schematic of electrically-gated NSH solar cell; b) schematic of charge distribution during gated operation; c) J-V characteristics of the device with varying gate voltage [Inset shows the change in built in potential V_{bi} due to more or less silicon band bending with gate voltage]. Adapted with permission.[68] Copyright 2010, American Chemical Society.

via the ionic liquid electrolyte 1-ethyl-3-methylimidazolium bis(trifluoromethylsulphonyl)imide (EMI-BTI) (**Figure 6**). The device exhibited a PCE of 8.5% which was dynamically and reversibly adjusted to between 4 and 11% by electronic gating. The mechanism of action of the electronic junction control is explained by considering the gate-induced modulation of the nanotube Fermi level and the gate-modulated enhancement or suppression of the interface dipole at the junction. Of course this argument would apply to both *Schottky* (metallic nanotubes) and *p-n* (semiconducting nanotubes) junction solar cells.

Jia et al.[69] has achieved the highest efficiency so far with a PCE of 13.8% by in situ doping of the nanotube film with 0.5 M HNO_3. The untreated device exhibited a PCE of 6.2% and the improvement was due to an increase in J_{SC} from 27 mA cm^{-2} to 36 mA cm^{-2} coupled with an increase in the *FF* from 0.47 to 0.72. Even after drying of the acid solution the cell maintained a higher efficiency than the original. Nitric acid doping of SWNT membranes has been shown to both decrease the tube-tube resistance and shift the Fermi level down towards the valance band (p-doping)[70] and these findings are used to explain to the observed increases in efficiency. Whilst decreasing the series resistance is necessary for a large *FF*, the observation of a slight decrease in V_{OC} is incongruent with p-doping. An increase in J_{SC} with nitric acid treatment is explained by considering the nanoscale structure of the junction, which is composed of many tiny junctions and leads to some nanotubes having no contact at all with the underlying silicon. It is proposed that the HNO_3 can play the part of an electrolyte, effectively bridging these 'unconnected' nanotubes to the silicon and allowing for the rapid shuttling of charge back and forth between tube and substrate. These Si-acid-SWNT units in the pores of the membrane form tiny photoelectrochemical cells where the silicon is the anode and the SWNTs are the cathode. This proposal is verified by showing that a similar (wet state) device in which the nanotubes and the silicon are separated by a distance of 300 nm also produces an appreciable photocurrent. Further support is given to the hypothesis by replacing the HNO_3 with an aqueous solution of NaCl. In this case a similar increase in the current density is also observed but, since the NaCl does

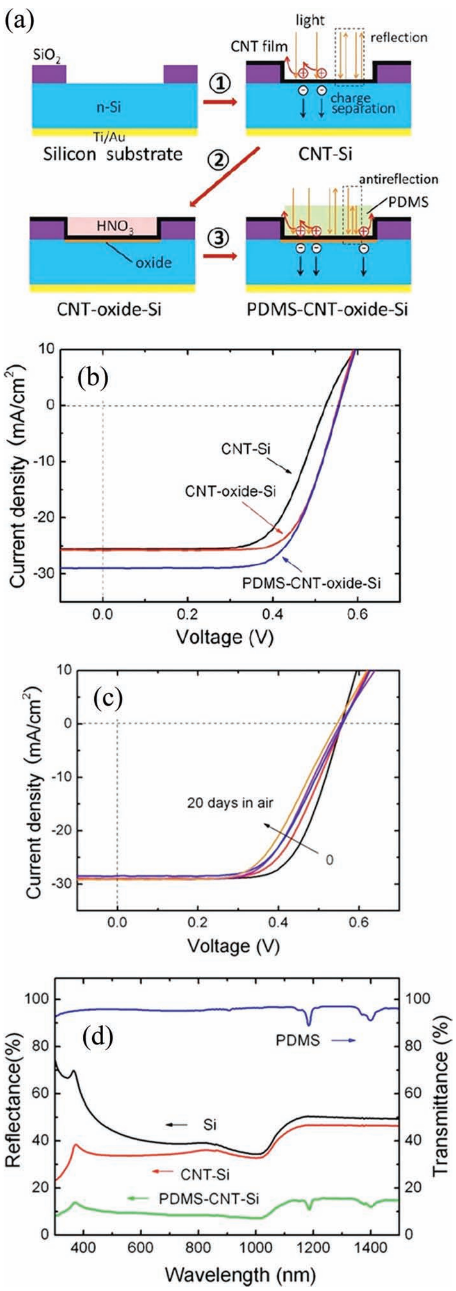

Figure 7. a) Schematic of device fabrication; b) J-V characteristics of the NSH cells before and after oxide formation and after encapsulation with PDMS; c) change in J-V characteristics of the PDMS encapsulated device over 20 days in air; d) reflectance data for the cells. Adapted with permission.[53] Copyright 2011, American Institute of Physics.

not have the ability to reduce the series resistance or dope the nanotubes, there is no corresponding increase in *FF*.

In another work by Jia et al.,[53] encapsulation of the active area by the insulating polymer polydimethylsiloxane (PDMS) is shown to increase efficiency whilst providing greatly improved device stability. Additionally, it is shown that the formation of a thin SiO_x layer inbetween the SWNTs and the underlying silicon leads to gains in V_{OC}. A schematic of the encapsulated device and fabrication steps is shown in **Figure 7**a. The gains in V_{OC} shown in Figure 7c are provided via the formation of the thin insulating oxide layer and can be understood by considering the effect the oxide has upon majority carrier transport across the junction. Majority carriers can surpass the potential barrier at the junction by thermionic emission but this process is suppressed in the presence of the oxide (while the minority carrier current across the junction via tunnelling would be largely unaffected). This reduces recombination between majority and minority carriers and hence the increased V_{OC}. Clear evidence for this is given by the reduction in dark current density at –1 V from 1.2×10^{-3} to 6.2×10^{-4} mA cm^{-2} after HNO_3 oxidation (Figure 7d). Additionally, minority carrier lifetime is increased from 14 μs to 19 μs after oxide formation whilst the bulk lifetime remains constant indicating that this is a surface effect. Presumably the increase in lifetime is due to the passivation of surface trap states and reduction in the frequency of recombination events. PDMS encapsulation is shown to improve the stability of the devices (Figure 7c) although a slight reduction in performance observed in the 20 day period which is attributed to the growth of an oxide layer that becomes too thick for tunnelling. Oxidation might be suppressed by hermetically sealing the device in an oxygen-free environment. PDMS encapsulation increases cell efficiency by reducing the reflectance from ~35–40% for silicon and silicon-SWNT to ~10% for the encapsulated device (**Figure 8**d).

It is suggested that the SWNT-oxide-Si resembles a traditional MIS structure and an energy band diagram is proposed, but this conflicts with the earlier work by Ong[62] where the SWNTs appear to display a photocurrent response. An analysis of the photocurrent spectra would perhaps shed light on this but such measurements can be problematic. This is due to two factors; 1) the SWNT film has very high transmittance and is thus expected to produce only a small fraction of the total photocurrent and 2) if the nanotube chirality is such that the position of the S_{11} transition overlaps the absorption range of the silicon such a small contribution may be difficult to elucidate. Nevertheless, if the nanotubes have been shown to produce a photocurrent when in the NSH architecture then this is incompatible with the proposed MIS mechanism.

Wadhwa et al.[71] extend previously reported work by engineering a grid pattern in the nanotube layer through oxygen plasma etching. A modest improvement in PCE from ~11% to ~12% is observed via this strategy. In this work the junction electrostatics are modelled showing that the mere presence of the ionic liquid EMI-BTI induces a depletion layer in the silicon without any applied gate voltage. This finding is commensurate with the observation of a prompt improvement in performance immediately upon introduction of the electrolyte. Although an electrolyte is used in the cell the authors are careful to distinguish between this architecture and that of a photoelectrochemical liquid junction cell (e.g., Grätzel cell[72]) in which the electrolyte plays the part of a redox shuffle between photoanode (silicon) and cathode (the nanotubes). This mechanism is precluded by the deliberately chosen large electrochemical window of the EMI-BTI electrolyte (–2.6 to 2.0 V vs. Fc/Fc$^+$). Thus the necessary depletion layer in the silicon is set up by the accumulation of negative ions at the surface. The cell is similar to the grating MIS cells reported by Godfrey and Green in 1978[73] and the mechanism of action

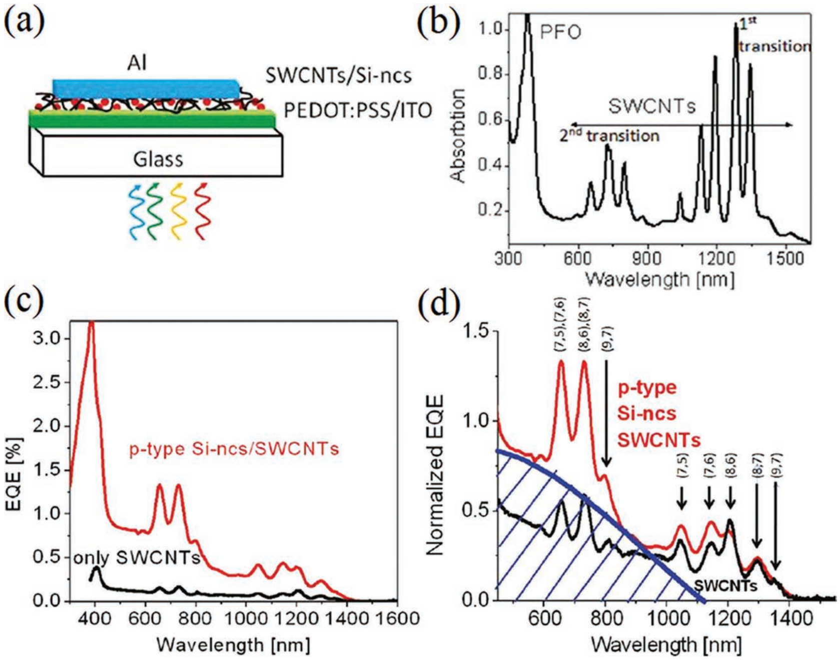

Figure 8. a) Device schematic; b) optical absorption spectrum of the PFO-wrapped SWNTs; c) spectrally resolved short circuit external quantum efficiency (EQE) of devices with (red/grey) and without (black) Si-ncs; d) normalised EQE showing peak assignments to first and second excitonic transitions in semiconducting SWNTs, the third line indicates overlap with the silicon absorption. Adapted with permission.[82] Copyright 2011, American Chemical Society.

of the grating is reasonably assumed to be as in those devices whereby there is photogeneration of excitons in the silicon which then travel along the surface until reaching a junction where the grid lines are. It is suggested that the increase in performance is due to the blocking of majority carrier current by the strong surface dipole setup by the accumulation of negative ions repelling electrons. This may also be relevant for the nitric acid doped work of Jia et al. whereby some of the performance gains in those works could be due in part to a similar build-up of NO_3^- ions at the junction providing majority carrier blocking in addition to that of the oxide layer. Chen, et al.[74] have continued this work, modelling of the effect of the ionic liquid on inversion layer properties and furthermore demonstrating significant improvements in device performance by the introduction of a highly doped back contact region. Such back contacts are shown to function as hole blocking layers, improving carrier separation and lowering surface recombination thus providing gains in both short circuit current density and fill factor.

It is clear that carbon nanotube films function, at least, as transparent conducting front electrodes. Carbon nanotube films have been used similarly in amorphous silicon solar cells,[75] heterojunction solar cells of quantum dots and silicon,[76] on silicon nanowires with[77] and without[78] photoactive polymers, as well as enhancing the performance of 'standard' *p-n* junction silicon solar cells.[79] Photovoltaic output from NSH cells can be improved by the addition of graphene 'patches' to the nanotube film[80] and by flowing gasses over the surface of the nanotube film, an effect that has been explored in the fabrication of gas sensors.[81]

Svrcek et al.[82] introduced a new branch in the NSH solar cell field by combining semiconducting SWNTs with silicon nanocrystals (Si-ncs) in a bulk heterojunction (BHJ) device (Figure 8a). This architecture differs from the nanotube-(planar) silicon case in that both the nanotubes and the silicon are of nanoscale dimension, with the Si-ncs having a diameter of ~3 nm. Another important difference is that, in contrast to nanotube-(planar) silicon devices which only generate power when the silicon is n-type, these BHJ devices only display a strong photocurrent when the Si-ncs are p-type (in n-type devices the short circuit current density is ~2 orders of magnitude smaller). The nanotubes were enriched in semiconducting chiralities by interaction with the p-type polymer poly-9,9-di-n-octyl-fluorenyl-2,7-diyl (PFO) followed by ultracentrifugation. Comparison of the absorption spectra of PFO-wrapped nanotubes in Figure 8b with the external quantum efficiency (EQE) data in Figure 8c shows unambiguously that the wrapped nanotubes contribute to the observed photocurrent, although contributions from both the Si-ncs and the PFO are also observable. In Figure 8d discrete photocurrent peaks are assigned to the individual nanotube chiralities present and show that the introduction of Si-ncs preferentially enhances the photocurrent due to smaller diameter, larger band gap nanotubes. The proposed mechanism of charge transfer from Si-ncs to SWNTs is supported by the observation of photoluminescence quenching (by a factor of >2) in Si-ncs upon addition of SWNTs.

In different but related work, Bindl et al.[83] combine semiconducting SWNTs with C_{60} in a device that builds on their prior carbon nanotube photodetector work.[84] This differs from other work involving nanotubes and fullerenes in that, in this work, it is the nanotubes that do the primary work of absorbing light energy rather than the fullerenes or other species complexed to them. As in the later work of Svrcek et al. both the nanotubes and semiconductor are of nanoscale dimension and the thermal deposition method employed for the C_{60} produces a conformal covering on the nanotube layer (**Figure 9**a). Importantly, the devices incorporate an exciton blocking layer of bathocuproine (BCP) between the C_{60} and the silver cathode. Comparison of the data in Figure 9b,c shows a clear correlation between the S_{11} absorption bands and the EQE of the devices, providing strong evidence of light harvesting by the nanotubes. The excitation of the smaller diameter nanotubes produces better device performance and there is a cut-off for the nanotube diameter above which excitation of these nanotubes yields significantly reduced performance. This is related to the band offset at the nanotube-C_{60} junction resulting in a positive driving force ΔE for C_{60} junctions with the smaller diameter, larger bandgap nanotubes and this effect has also been demonstrated elsewhere.[35f,85] It is shown that semiconducting-enriched nanotubes clearly outperform mixtures of

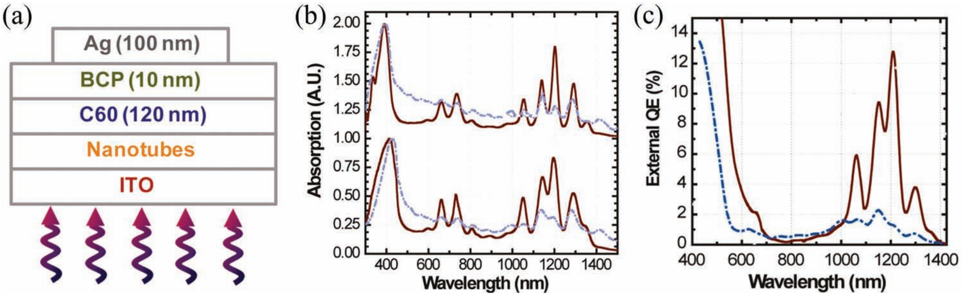

Figure 9. a) Device schematic; b) absorption spectra of mixed (dashed) and semiconducting-enriched (solid) nanotube solutions (top) and films (bottom); c) EQE of devices fabricated with mixed (dashed) and semiconducting-enriched (solid) nanotubes. Adapted with permission.[83] Copyright 2010, American Chemical Society.

semiconducting and metallic nanotubes (Figure 9d). It is found that efficiency is limited by the relatively short diffusion length which is estimated to be ~3 nm. This short diffusion length in the membrane may be due to the insulating effect of the PFO wrapping agent inhibiting tube-tube transfer. If so the devices may be improved by removing the PFO prior to deposition of the nanotubes, if possible. It would also be of interest to investigate the effect of post treatment of the nanotube films (prior to C_{60} deposition) with thionyl chloride or nitric acid. This would presumably increase the charge transport capability of the nanotubes although, since both treatments can bleach the optical absorption of nanotubes, they may be detrimental to performance. The fact that the nanotubes' discrete absorption ranges produce correspondingly discrete features in the spectrally resolved EQE is an inherent disadvantage in solar cell devices where it is desirable for the photoactive layer to absorb across the useful spectrum of solar radiation. However, a multijunction device comprising an appropriately engineered stack of nanotube chiralities can be envisioned whereby the individual absorption ranges of the component layers could be tailored such that the complete device exhibits a net absorption covering the desired spectral range.

4. Summary

Properties of carbon nanotubes make them promising candidates for incorporation into future low cost photovoltaic devices. From early reports of ~1% power conversion efficiency, the field of nanotube-silicon heterojunction solar cells has rapidly seen performance gains up to ~11% for 'dry' cells and cells employing electrolyte assisted junction control, and up to ~14% for cells doped in situ with nitric acid. However the mechanism of action is still unclear, with findings such as the figure of merit established by Jia et al. suggesting *Schottky/MIS* whilst the photocurrent spectra of Ong et al. may suggest *p-n* characteristics. The polychirality of nanotubes employed in many of the devices reported so far certainly confounds this issue and thus as chirality sorted material becomes more available to the nanotube research community we anticipate measurements on devices employing purely metallic or semiconducting nanotubes. Post treatment of nanotube films with strong oxidisers and oxidising acids has been shown to markedly improve device performance through reduction in film resistivity and adjustment of the nanotube Fermi level. The use of ionic liquid electrolytes to provide electronic junction control has been demonstrated to be an effective method of significantly improving the performance of nanotube-silicon heterojunction solar cells although it is unlikely this could see practical application in commercial devices. Furthermore, one may argue that the addition of nanotubes to silicon solar cells that already exhibit efficiencies in excess of ~24% is unhelpful. However it must be noted that, compared to several decades of very extensive research into silicon solar cells, this is still quite a new, and relatively small, research area and as such it is worthwhile to investigate these devices further. Considering the apparent ease with which good efficiencies have been achieved in a short time by a limited number of researchers it is likely that significant potential exists in the field. As clearly demonstrated, carbon nanotube films function well as transparent, conducting front electrodes and as such could at least offer improved performance of silicon solar cells through reduced optical shading. The ability of carbon nanotubes to harvest light when combined with silicon nanocrystals or C_{60} in solid state devices has been unequivocally demonstrated but it remains to be seen whether or not this is ever true in the case of nanotubes combined with planar monocrystalline silicon.

Acknowledgements

Ben Flavel gratefully acknowledges the support of the Alexander von Humboldt Foundation.

Received: April 2, 2012

---

[1] S. Iijima, *Nature* **1991**, *354*, 56.
[2] S. Iijima, T. Ichihashi, *Nature* **1993**, *363*, 603.
[3] D. S. Bethune, C. H. Kiang, M. S. d. Vries, G. Gorman, R. Savoy, J. Vazquez, R. Beyers, *Nature* **1993**, *363*, 605.
[4] a) J. W. Mintmire, C. T. White, *Carbon* **1995**, *33*, 893; b) Y. Ouyang, Y. Yoon, J. Guo, *J. Computer-Aided Mater. Design* **2007**, *14*, 73.
[5] a) Z. Wu, Z. Chen, X. Du, J. M. Logan, J. Sippel, M. Nikolou, K. Kamaras, J. R. Reynolds, D. B. Tanner, A. F. Hebard, A. G. Rinzler, *Science* **2004**, *305*, 1273; b) A. Ugawa, J. Hwang, H. H. Gommans, H. Tashiro, A. G. Rinzler, D. B. Tanner, *Curr. Appl. Phys.* **2001**, *1*, 45.

[6] a) E. T. Thostenson, Z. Ren, T.-W. Chou, *Composites Sci. Technol.* **2001**, *61*, 1899; b) M. S. Dresselhaus, G. Dresselhaus, A. Jorio, *Annu. Rev. Mater. Res.* **2004**, *34*, 247; c) T. W. Odom, J.-L. Huang, P. Kim, C. M. Lieber, *J. Phys. Chem. B* **2000**, *104*, 2794.

[7] a) T. W. Odom, J.-L. Huang, P. Kim, C. M. Lieber, *Nature* **1998**, *391*, 62; b) M. S. Dresselhaus, G. Dresselhaus, R. Saito, *Carbon* **1995**, *33*, 883.

[8] a) T. Belin, F. Epron, *Mater. Sci. Engin. B* **2005**, *119*, 105; b) M. Terrones, *Annu. Rev. Mater. Res.* **2003**, *33*, 419.

[9] S. Reich, C. Thomsen, J. Maultzsch, *Carbon Nanotubes: Basic Concepts and Physical Properties*, Wiley-VCH Verlag GmbH & Co. KGaA, Weinheim, Germany **2004**.

[10] E. H. Hároz, B. Y. Lu, P. Nikolaev, S. Arepalli, R. H. Hauge, J. Kono, *J. Am. Chem. Soc.* 2011, 134, 4461.

[11] T. W. Ebbesen, P. M. Ajayan, *Nature* **1992**, *358*, 220.

[12] C. D. Spataru, S. Ismail-Beigi, L. X. Benedict, S. G. Louie, *Phys. Rev. Lett.* **2004**, *92*, 077402.

[13] S. M. Bachilo, M. S. Strano, C. Kittrell, R. H. Hauge, R. E. Smalley, R. B. Weisman, *Science* **2002**, *298*, 2361.

[14] *Handbook of Photovoltaic Science and Engineering* (Eds: A. Luque, S. Hegedus), John Wiley & Sons, Chichester, England **2010**.

[15] R. B. Weisman, S. M. Bachilo, *Nano Lett.* **2003**, *3*, 1235.

[16] P. G. Collins, K. Bradley, M. Ishigami, A. Zettl, *Science* **2000**, *287*, 1801.

[17] a) H. Tantang, J. Y. Ong, C. L. Loh, X. Dong, P. Chen, Y. Chen, X. Hu, L. P. Tan, L.-J. Li, *Carbon* **2009**, *47*, 1867; b) T. M. Barnes, J. L. Blackburn, J. van de Lagemaat, T. J. Coutts, M. J. Heben, *ACS Nano* **2008**, *2*, 1968.

[18] C. Zhou, J. Kong, E. Yenilmez, H. Dai, *Science* **2000**, *290*, 1552.

[19] C. Klinke, J. Chen, A. Afzali, P. Avouris, *Nano Lett.* **2005**, *5*, 555.

[20] Z. Li, V. Saini, E. Dervishi, V. P. Kunets, J. Zhang, Y. Xu, A. R. Biris, G. J. Salamo, A. S. Biris, *Applied Physics Letters* **2010**, *96*, 033110.

[21] C. Biswas, S. Y. Lee, T. H. Ly, A. Ghosh, Q. N. Dang, Y. H. Lee, *ACS Nano* **2011**, *5*, 9817.

[22] P. Redlich, J. Loeffler, P. M. Ajayan, J. Bill, F. Aldinger, M. Rühle, *Chem. Phys. Lett.* **1996**, *260*, 465.

[23] a) P. Ayala, R. Arenal, M. Rümmeli, A. Rubio, T. Pichler, *Carbon* **2010**, *48*, 575; b) C. L. Pint, Z. Sun, S. Moghazy, Y.-Q. Xu, J. M. Tour, R. H. Hauge, *ACS Nano* **2011**, *5*, 6925.

[24] a) R. Krupke, S. Linden, M. Rapp, F. Hennrich, *Adv. Mater.* **2006**, *18*, 1468; b) K. Arnold, F. Hennrich, R. Krupke, S. Lebedkin, M. M. Kappes, *Phys. Status Solidi* **2006**, *243*, 3073.

[25] M. C. Hersam, *Nat. Nanotechnol.* **2008**, *3*, 387.

[26] a) J.-Y. Hwang, A. Nish, J. Doig, S. Douven, C.-W. Chen, L.-C. Chen, R. J. Nicholas, *J. Am. Chem. Soc.* **2008**, *130*, 3543; b) F. Hennrich, S. Lebedkin, M. M. Kappes, *Phys. Status Solidi* **2008**, *245*, 1951.

[27] a) N. Stürzl, F. Hennrich, S. Lebedkin, M. M. Kappes, *J. Phys. Chem. C* **2009**, *113*, 14628; b) K. Moshammer, F. Hennrich, M. M. Kappes, *Nano Res.* **2009**, *2*, 599; c) X. Tu, S. Manohar, A. Jagota, M. Zheng, *Nature* **2009**, *460*, 250; d) H. Liu, D. Nishide, T. Tanaka, H. Kataura, *Nat. Commun.* **2011**, *2*, 309.

[28] W. Shockley, H. J. Queisser, *J. Appl. Phys.* **1961**, *32*, 510.

[29] a) S. Wang, M. Khafizov, X. Tu, M. Zheng, T. D. Krauss, *Nano Lett.*2010, 10, 2381; b) N. M. Gabor, Z. Zhong, K. Bosnick, J. Park, P. L. McEuen, *Science* **2009**, *325*, 1367.

[30] a) B. J. Landi, R. P. Raffaelle, S. L. Castro, S. G. Bailey, *Prog. Photovoltaics: Res. Appl.* **2005**, *13*, 165; b) E. Kymakis, G. A. J. Amaratunga, *Appl. Phys. Lett.* **2002**, *80*, 112; c) E. Kymakis, I. Alexandrou, G. A. J. Amaratunga, *J. Appl. Phys.* **2003**, *93*, 1764; d) A. D. Pasquier, H. E. Unalan, A. Kanwal, S. Miller, M. Chhowalla, *Appl. Phys. Lett.* **2005**, *87*, 203511; e) V. Sgobba, D. M. Guldi, *J. Mater. Chem.* **2008**, *18*, 153; f) A. Kongkanand, R. Martinez Dominguez, P. V. Kamat, *Nano Lett.* **2007**, *7*, 676; g) C. Li, Y. Chen, Y. Wang, Z. Iqbal, M. Chhowalla, S. Mitra, *J. Mater. Chem.* **2007**, *17*, 2406.

[31] a) L. Wei, N. Tezuka, T. Umeyama, H. Imahori, Y. Chen, *Nanoscale* **2011**, *3*, 1845; b) M. A. Bissett, J. G. Shapter, *J. Phys. Chem. C* **2010**, *114*, 6778; c) D. D. Tune, B. S. Flavel, J. S. Quinton, A. V. Ellis, J. G. Shapter, *Sol. Energy Mater. Sol. Cells* **2010**, *94*, 1665; d) S. Barazzouk, S. Hotchandani, K. Vinodgopal, P. V. Kamat, *J. Phys. Chem. B* **2004**, *108*, 17015.

[32] a) T. Umeyama, N. Tezuka, M. Fujita, S. Hayashi, N. Kadota, Y. Matano, H. Imahori, *Chem. Eur. J.* **2008**, *14*, 4875; b) T. Umeyama, N. Tezuka, S. Seki, Y. Matano, M. Nishi, K. Hirao, H. Lehtivuori, N. V. Tkachenko, H. Lemmetyinen, Y. Nakao, S. Sakaki, H. Imahori, *Adv. Mater.* **2010**, *22*, 1767; c) N. Tezuka, T. Umeyama, S. Seki, Y. Matano, M. Nishi, K. Hirao, H. Imahori, *J. Phys. Chem. C* **2010**, *114*, 3235.

[33] N. Tezuka, T. Umeyama, Y. Matano, T. Shishido, K. Yoshida, T. Ogawa, S. Isoda, K. Stranius, V. Chukharev, N. V. Tkachenko, H. Lemmetyinen, H. Imahori, *Energy Env. Sci.* **2011**, *4*, 741.

[34] F. D'Souza, S. K. Das, A. S. D. Sandanayaka, N. K. Subbaiyan, D. R. Gollapalli, M. E. Zandler, T. Wakahara, O. Ito, *Phys. Chem. Chem. Phys.* **2012**, *14*, 2940.

[35] a) T. Umeyama, N. Tezuka, F. Kawashima, S. Seki, Y. Matano, Y. Nakao, T. Shishido, M. Nishi, K. Hirao, H. Lehtivuori, N. V. Tkachenko, H. Lemmetyinen, H. Imahori, *Angew. Chem. Int. Ed.* **2011**, *50*, 4615; b) T. Umeyama, M. Fujita, N. Tezuka, N. Kadota, Y. Matano, K. Yoshida, S. Isoda, H. Imahori, *J. Phys. Chem. C* **2007**, *111*, 11484; c) M. A. Bissett, J. G. Shapter, *J. Electrochem. Soc.* **2011**, *158*, K53; d) T. Hasobe, S. Fukuzumi, P. V. Kamat, *J. Phys. Chem. B* **2006**, *110*, 25477; e) G. M. A. Rahman, A. Troeger, V. Sgobba, D. M. Guldi, N. Jux, D. Balbino, M. N. Tchoul, W. T. Ford, A. Mateo-Alonso, M. Prato, *Chem. Eur. J.* **2008**, *14*, 8837; f) A. S. Sandanayaka, N. K. Subbaiyan, S. K. Das, R. Chitta, E. Maligaspe, T. Hasobe, O. Ito, F. D'Souza, *ChemPhysChem* 2011, 12, 2266.

[36] a) D. M. Guldi, G. M. A. Rahman, M. Prato, N. Jux, S. Qin, W. Ford, *Angew. Chem. Int. Ed.* **2005**, *44*, 2015; b) V. Sgobba, G. M. A. Rahman, D. M. Guldi, N. Jux, S. Campidelli, M. Prato, *Adv. Mater.* **2006**, *18*, 2264.

[37] a) G. M. A. Rahman, D. M. Guldi, R. Cagnoli, A. Mucci, L. Schenetti, L. Vaccari, M. Prato, *J. Am. Chem. Soc.* **2005**, *127*, 10051; b) V. Sgobba, A. Troeger, R. Cagnoli, A. Mateo-Alonso, M. Prato, F. Parenti, A. Mucci, L. Schenetti, D. M. Guldi, *J. Mater. Chem.* **2009**, *19*, 4319; c) G. Giancane, A. Ruland, V. Sgobba, D. Manno, A. Serra, G. M. Farinola, O. H. Omar, D. M. Guldi, L. Valli, *Adv. Funct. Mater.* **2010**, *20*, 2481.

[38] T. Umeyama, N. Kadota, N. Tezuka, Y. Matano, H. Imahori, *Chem. Phys. Lett.* **2007**, *444*, 263.

[39] S. P. Campidelli, B. Ballesteros, A. Filoramo, D. D. a. Díaz, G. de la Torre, T. s. Torres, G. M. A. Rahman, C. Ehli, D. Kiessling, F. Werner, V. Sgobba, D. M. Guldi, C. Cioffi, M. Prato, J.-P. Bourgoin, *J. Am. Chem. Soc.* **2008**, *130*, 11503.

[40] M. A. Bissett, I. Koper, J. S. Quinton, J. G. Shapter, *Phys. Chem. Chem. Phys.* **2011**, *13*, 6059.

[41] a) D. M. Guldi, G. M. A. Rahman, V. Sgobba, N. A. Kotov, D. Bonifazi, M. Prato, *J. Am. Chem. Soc.* **2006**, *128*, 2315; b) G. Mountrichas, A. S. D. Sandanayaka, S. P. Economopoulos, S. Pispas, O. Ito, T. Hasobe, N. Tagmatarchis, *J. Mater. Chem.* **2009**, *19*, 8990.

[42] a) K. Suzuki, M. Yamaguchi, M. Kumagai, S. Yanagida, *Chem. Lett.* **2003**, *32*, 28; b) T. N. Murakami, M. Gratzel, *Inorg. Chim. Acta* **2008**, *361*, 572; c) H. Zhu, H. Zeng, V. Subramanian, C. Masarapu, K.-H. Hung, B. Wei, *Nanotechnology* **2008**, *19*, 465204.

[43] a) W. Lee, J. Lee, S. H. Lee, J. Chang, W. Yi, S. H. Han, *J. Phys. Chem. C* **2007**, *111*, 9110; b) T. Y. Lee, P. S. Alegaonkar, J.-B. Yoo, *Thin Solid Films* **2007**, *515*, 5131.

[44] a) T. Chen, S. Wang, Z. Yang, Q. Feng, X. Sun, L. Li, Z.-S. Wang, H. Peng, *Angew. Chem. Int. Ed:* **2011**, *50*, 1815; b) P. Brown, K. Takechi, P. V. Kamat, *J. Phys. Chem. C* **2008**, *112*, 4776.

[45] H. Imahori, T. Umeyama, *J. Phys. Chem. C* **2009**, *113*, 9029.

[46] V. Sgobba, D. M. Guldi, *Chem. Soc. Rev.* **2009**, *38*, 165.

[47] R. Chitta, F. D'Souza, *J. Mater. Chem.* **2008**, *18*, 1440.

[48] a) D. M. Guldi, G. M. A. Rahman, F. Zerbetto, M. Prato, *Acc. Chem. Res.* **2005**, *38*, 871; b) D. M. Guldi, *J. Phys. Chem. B* **2005**, *109*, 11432; c) D. M. Guldi, *Phys. Chem. Chem: Phys.* **2007**, *9*, 1400.

[49] a) F. D'Souza, A. S. D. Sandanayaka, O. Ito, *J. Phys. Chem. Lett.* **2010**, *1*, 2586; b) F. D'Souza, O. Ito, *Chem. Soc. Rev.* **2012**, *41*, 86.

[50] a) M. A. Green, R. B. Godfrey, L. W. Davies, *The Australian Physicist* **1976**, *13*, 177; b) J. Shewchun, R. Singh, M. A. Green, *J. Appl. Phys.* **1977**, *48*, 765.

[51] W. Schottky, *Z. Phys.* **1939**, *113*, 367.

[52] W. A. Anderson, A. E. Delahoy, R. A. Milano, *J. Appl. Phys.* **1974**, *45*, 3913.

[53] Y. Jia, P. Li, X. Gui, J. Wei, K. Wang, H. Zhu, D. Wu, L. Zhang, A. Cao, Y. Xu, *Appl. Phys. Lett.* **2011**, *98*, 133115.

[54] J. Wei, Y. Jia, Q. Shu, Z. Gu, K. Wang, D. Zhuang, G. Zhang, Z. Wang, J. Luo, A. Cao, D. Wu, *Nano Lett.* **2007**, *7*, 2317.

[55] A. Behnam, J. L. Johnson, Y. Choi, M. G. Ertosun, A. K. Okyay, P. Kapur, K. C. Saraswat, A. Ural, *Appl. Phys. Lett.* **2008**, *92*.

[56] Y. Jia, J. Wei, K. Wang, A. Cao, Q. Shu, X. Gui, Y. Zhu, D. Zhuang, G. Zhang, B. Ma, L. Wang, W. Liu, Z. Wang, J. Luo, D. Wu, *Adv. Mater.* **2008**, *20*, 4594.

[57] Z. Li, V. P. Kunets, V. Saini, Y. Xu, E. Dervishi, G. J. Salamo, A. R. Biris, A. S. Biris, *Appl. Phys. Lett.* **2008**, *93*, 243117.

[58] Z. Li, V. P. Kunets, V. Saini, Y. Xu, E. Dervishi, G. J. Salamo, A. R. Biris, A. S. Biris, *ACS Nano* **2009**, *3*, 1407.

[59] Z. Li, Y. Jia, J. Wei, K. Wang, Q. Shu, X. Gui, H. Zhu, A. Cao, D. Wu, *J. Mater. Chem.* **2010**, *20*, 7236.

[60] Y. Jia, P. Li, J. Wei, A. Cao, K. Wang, C. Li, D. Zhuang, H. Zhu, D. Wu, *Mater. Res. Bull.* **2010**, *45*, 1401.

[61] P. Castrucci, S. Del Gobbo, L. Camilli, M. Scarselli, S. Casciardi, F. Tombolini, A. Convertino, G. Fortunato, M. De Crescenzi, *J. Nanosci. Nanotechnol.* **2011**, *11*, 9202.

[62] P.-L. Ong, W. B. Euler, I. A. Levitsky, *Nanotechnology* **2010**, *21*, 105203.

[63] V. L. Borgne, P. Castrucci, S. D. Gobbo, M. Scarselli, M. D. Crescenzi, M. Mohamedi, M. A. E. Khakani, *Appl. Phys. Lett.* **2010**, *97*, 193105.

[64] a) P. Castrucci, C. Scilletta, S. Del Gobbo, M. Scarselli, L. Camilli, M. Simeoni, B. Delley, A. Continenza, M. De Crescenzi, *Nanotechnol.* **2011**, *22*, 115701; b) M. A. El Khakani, V. L. Borgne, B. Aissa, F. Rosei, C. Scilletta, E. Speiser, M. Scarselli, P. Castrucci, M. D. Crescenzi, *Appl. Phys. Lett.* **2009**, *95*, 083114.

[65] M. B. Tzolov, T.-F. Kuo, D. A. Straus, A. Yin, Xu, *J. Phys. Chem. C* **2007**, *111*, 5800.

[66] W. Spitzer, H. Y. Fan, *Phys. Rev.* **1957**, *108*, 268.

[67] D. K. Schroder, R. N. Thomas, J. C. Swartz, *IEEE Solid-State Circuits* **1978**, *13*, 180.

[68] P. Wadhwa, B. Liu, M. A. McCarthy, Z. Wu, A. G. Rinzler, *Nano Lett.* **2010**, *10*, 5001.

[69] Y. Jia, A. Cao, X. Bai, Z. Li, L. Zhang, N. Guo, J. Wei, K. Wang, H. Zhu, D. Wu, P. M. Ajayan, *Nano Lett.* **2011**, *11*, 1901.

[70] J. L. Blackburn, T. M. Barnes, M. C. Beard, Y.-H. Kim, R. C. Tenent, T. J. McDonald, B. To, T. J. Coutts, M. J. Heben, *ACS Nano* **2008**, *2*, 1266.

[71] P. Wadhwa, G. Seol, M. K. Petterson, J. Guo, A. G. Rinzler, *Nano Lett.* **2011**, *11*, 2419.

[72] B. O'Regan, M. Gratzel, *Nature* **1991**, *353*, 737.

[73] R. B. Godfrey, M. A. Green, *Appl. Phys. Lett.* **1978**, *33*, 637.

[74] W. Chen, G. Seol, A. G. Rinzler, J. Guo, *Appl. Phys. Lett.* **2012**, *100*, 103503.

[75] a) S. Del Gobbo, P. Castrucci, M. Scarselli, L. Camilli, M. De Crescenzi, L. Mariucci, A. Valletta, A. Minotti, G. Fortunato, *Appl. Phys. Lett.* **2011**, *98*, 183113; b) M. Schriver, W. Regan, M. Loster, A. Zettl, *Solid State Commun.* **2010**, *150*, 561.

[76] a) X. Li, Y. Jia, J. Wei, H. Zhu, K. Wang, D. Wu, A. Cao, *ACS Nano* **2010**, *4*, 2142; b) P. Li, S. Wang, Y. Jia, Z. Li, C. Ji, L. Zhang, H. Li, E. Shi, Z. Bian, C. Huang, J. Wei, K. Wang, H. Zhu, D. Wu, A. Cao, *Nano Res.* **2011**, *4*, 979.

[77] K. Golap, A. Sudip, H. R. Aryal, R. Afre, T. Soga, M. Sharon, W. Koichi, M. Umeno, *J. Phys. D: Appl. Phys.* **2009**, *42*, 115104.

[78] a) Q. Shu, J. Wei, K. Wang, S. Song, N. Guo, Y. Jia, Z. Li, Y. Xu, A. Cao, H. Zhu, D. Wu, *Chem. Commun.* **2010**, *46*, 5533; b) Q. Shu, J. Wei, K. Wang, H. Zhu, Z. Li, Y. Jia, X. Gui, N. Guo, X. Li, C. Ma, D. Wu, *Nano Lett.* **2009**, *9*, 4338.

[79] Y. F. Zhang, Y. F. Wang, N. Chen, Y. Y. Wang, Y. Z. Zhang, Z. H Zhou, L. M. Wei, *Nano-Micro Lett.* **2010**, *2*, 22.

[80] C. Li, Z. Li, H. Zhu, K. Wang, J. Wei, X. Li, P. Sun, H. Zhang, D. Wu, *J. Phys. Chem. C* **2010**, *114*, 14008.

[81] G. Fan, L. Fan, Z. Li, X. Bai, S. Mulligan, Y. Jia, K. Wang, J. Wei, A. Cao, D. Wu, B. Wei, H. Zhu, *J. Mate. Chem.* **2012**, *22*, 3330.

[82] V. Švrček, S. Cook, S. Kazaoui, M. Kondo, *J. Phys. Chem. Lett.* **2011**, *2*, 1646.

[83] D. J. Bindl, M.-Y. Wu, F. C. Prehn, M. S. Arnold, *Nano Lett.* **2010**, *11*, 455.

[84] D. J. Bindl, N. S. Safron, M. S. Arnold, *ACS Nano* **2010**, *4*, 5657.

[85] A. S. D. Sandanayaka, E. Maligaspe, T. Hasobe, O. Ito, F. D'Souza, *Chem. Commun.* **2010**, *46*, 8749.

– This page intentionally left blank –

2.3 Carbon Nanotube Silicon Solar Cells

2.3.2 *Single-Walled Carbon Nanotube/Polyaniline/n-Silicon Solar Cells: Fabrication, Characterisation, and Performance Measurements*

D. D. Tune, **B. S. Flavel**, J. S. Quinton, A. V. Ellis, J. G. Shapter

Chemistry & Sustainability Energy & Materials 6 (2013) 320–327

DOI: 10.1002/cssc.201200600

Abstract

Carbon nanotube–silicon solar cells are a recently investigated photovoltaic architecture with demonstrated high efficiencies. Silicon solar-cell devices fabricated with a thin film of conductive polymer (polyaniline) have been reported, but these devices can suffer from poor performance due to the limited lateral current-carrying capacity of thin polymer films. Herein, hybrid solar-cell devices of a thin film of polyaniline deposited on silicon and covered by a single-walled carbon nanotube film are fabricated and characterized. These hybrid devices combine the conformal coverage given by the polymer and the excellent electrical properties of single-walled carbon nanotube films and significantly outperform either of their component counterparts. Treatment of the silicon base and carbon nanotubes with hydrofluoric acid and a strong oxidizer (thionyl chloride) leads to a significant improvement in performance.

Contribution

B.S.F and D.D.T designed and performed the experiments. All authors were involved in the preparation of the manuscript and analysis of results.

– This page intentionally left blank –

DOI: 10.1002/cssc.201200600

Single-Walled Carbon Nanotube/Polyaniline/n-Silicon Solar Cells: Fabrication, Characterization, and Performance Measurements

Daniel D. Tune,[a] Benjamin S. Flavel,[b] Jamie S. Quinton,[a] Amanda V. Ellis,[a] and Joseph G. Shapter*[a]

Carbon nanotube–silicon solar cells are a recently investigated photovoltaic architecture with demonstrated high efficiencies. Silicon solar-cell devices fabricated with a thin film of conductive polymer (polyaniline) have been reported, but these devices can suffer from poor performance due to the limited lateral current-carrying capacity of thin polymer films. Herein, hybrid solar-cell devices of a thin film of polyaniline deposited on silicon and covered by a single-walled carbon nanotube film are fabricated and characterized. These hybrid devices combine the conformal coverage given by the polymer and the excellent electrical properties of single-walled carbon nanotube films and significantly outperform either of their component counterparts. Treatment of the silicon base and carbon nanotubes with hydrofluoric acid and a strong oxidizer (thionyl chloride) leads to a significant improvement in performance.

Introduction

In recent years it has become clear that carbon nanotubes (CNTs) show great promise as elements of photovoltaic systems. The huge diversity of CNTs means that their excellent, and often unique, electrical and optical properties can be finely tuned to suit specific application requirements. CNTs can be both covalently and noncovalently functionalized allowing the production of an almost limitless variety of macromolecules and supramolecular species. Coupled with the ability to easily process them by using a variety of methods, these characteristics have resulted in a plethora of research involving their incorporation into light-harvesting structures and devices. For example, CNTs have been employed in a range of organic photovoltaics,[1] as elements of donor–acceptor hybrids in photoelectrochemical cells with porphyrins,[2] phthalocyanines,[3] quantum dots,[4] polyamidoamine dendrons,[5] fullerenes,[6] and more, and in various roles in dye-sensitized solar cells.[7] CNTs are known to exhibit many properties attractive in photovoltaics including direct band gaps, ballistic conduction,[8] moderate and tunable binding energies,[9] and multiple electron–hole pair generation from single photons.[10]

A widely researched application of CNTs in light-harvesting devices is that in which randomly aligned films are employed as transparent conducting electrodes. Recently, such films have been applied to silicon-based photovoltaics in CNT–silicon solar cells.[11] In these devices, a thin film of CNTs is deposited on the surface of a moderately doped n-type silicon substrate. At the points where the nanotubes contact the substrate, a localized depletion region is set up in the silicon substrate due to Fermi level equilibration between the (moderately p-type) CNTs and the silicon substrate. Under illumination, electron–hole pairs photogenerated in the silicon base diffuse to these regions, in which they are separated by the built-in potential, with resultant holes transported through the CNT film to be extracted into an external circuit. In the short time since initial reports, the field of CNT–silicon solar cells has seen power-conversion efficiencies of up to 14% for small-area research cells.[12] Similar efficiencies have been achieved with novel strategies involving ionic-liquid-mediated gating of the CNT–silicon junction electrostatics.[13] In addition to process improvements, the considerably improved performance of the most recent devices relative to earlier reports is a result of either the buildup of negative ions adjacent to the silicon surface[13] or the presence of a thin oxide layer.[12] Both of these have the effect of creating a more complete depletion region in the silicon layer compared to the relatively inhomogeneous region that exists when no ionic liquid/oxide is present. The effect of the oxide on device performance has been further studied[14] and shown to improve the shunt resistance, yielding a reduced reverse bias saturation current, as well as shifting charge transport across the interface from purely thermionic emission to a mixture of thermionic emission and tunneling. Recently, hybrid silicon–organic heterojunction solar cells of poly(3,4-ethylenedioxythiophene) poly(styrenesulphonate) (PEDOT:PSS) on n-type silicon surfaces modified with a regular nanocone structure have been demonstrated with efficiencies of about 11%.[15] Herein, we examine high-efficiency hetero-

---

[a] *D. D. Tune, Prof. J. S. Quinton, Prof. A. V. Ellis, Prof. J. G. Shapter*
Flinders Center for Nanoscale Science and Technology
Flinders University
SA 5042 (Australia)
Fax: (+61) 8-8201-2905
E-mail: Joe.Shapter@flinders.edu.au

[b] *Dr. B. S. Flavel*
Institute of Nanotechnology
Karlsruhe Institute of Technology
76021 Karlsruhe (Germany)

junction solar cells, in which a thin layer of a conducting polymer, polyaniline (PANI), is placed between the silicon base and the CNTs. PANI–silicon heterojunction solar cells have been reported previously,[16] but such devices can suffer from relatively poor performance for silicon-based photovoltaics largely due to the limited lateral conductivity of thin PANI films. This poor conductivity is overcome in our devices by the presence of the highly conductive transparent CNT film.

Results and Discussion

Figure 1 a shows an SEM image of the edge of the active area after deposition of the CNT film (gold on the right). The film contains wrinkles, which could be an imprint from the filter paper or contraction due to the evaporation of water during the film immobilization step. The film morphology on this scale is that of a relatively isotropic randomly aligned CNT network containing CNT bundles of about 15 nm in diameter (Figure 1 c). AFM measurements of the CNT films reveal an average film thickness of about 35 nm (Figure 1 b).

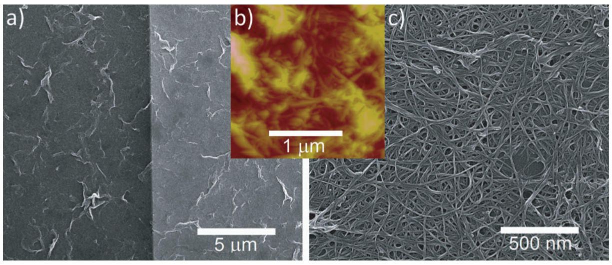

Figure 1. a) SEM image of the SWNT-coated silicon surface showing the edge of the active area (silicon on the left, gold on the right); b) AFM image of the SWNT membrane, from which thickness measurements were obtained; c) magnified SEM image of the SWNT membrane shown in (a).

Raman spectra of single-walled carbon nanotube (SWNT) films on glass (Figure 2) show the characteristic modes. The radial breathing mode (RBM) is located at a Raman shift of 167.6 cm^{-1}. By the method of Alvarez et al.,[17] which takes into account tube–tube interactions when CNTs are present in the bundled state, RBM was used to calculate the CNT diameter to be about 1.4 nm, which is in good agreement with supplier specifications. Of note is the small D-band at 1336 cm^{-1}, giving a D/G ratio of 0.023 and indicating that the CNTs used in this study are relatively defect-free. This is in stark contrast to the usual spectra obtained from HNO_3-treated CNTs, which show a much higher level of disordered carbon atoms (larger D/G ratio). The low level of defects in these CNT films is likely due to a reduced affinity of the TritonX100 surfactant for defective CNT sidewalls, which means that centrifugation of the aqueous SWNT/TritonX100 suspension removes all but the most defect-free tubes.

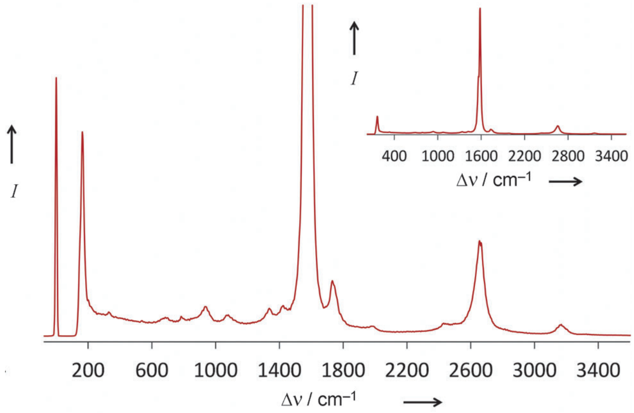

Figure 2. Raman spectrum of the SWNTs used, magnified to show all features. Inset: full spectrum showing the intensity of the dominant G-band relative to other features.

Subsequently, the UV/Vis–near IR (NIR) absorption properties of PANI and SWNTs were investigated (Figure 3). HF was used to remove silicon oxide from the active area of the solar cell devices. However, to obtain comparable UV/Vis–NIR measurements from the films on glass, HCl was used in lieu of HF to prevent damage to the surface of the glass substrate and/or peeling of the CNT film. The presence of broad yet reduced signals in the spectra of SWNTs (Figure 3 a) indicated that they were not highly dispersed, which was in agreement with the bundle sizes observed in SEM micrographs. Absorption signals in UV/Vis–NIR spectra corresponded to SWNT excitonic transitions for semiconducting and metallic CNTs with the absorption regions S_{11} and S_{22} located at about 1870 and 1040 nm, respectively, and the region M_{11} at about 700 nm. Average CNT diameter was again confirmed through the position of S_{11}, which is characteristic of CNTs of about 1.4 nm in diameter.[18] A common method to improve the electrical properties of CNT films is to expose them to $SOCl_2$ (organic oxidizer). This has the effect of hole-doping the CNTs [Eq. (1)]:

$$2\,SOCl_2 + 4e^- \rightarrow S + SO_2 + 4\,Cl^- \qquad (1)$$

Following treatment with $SOCl_2$, there is complete bleaching of the S_{11} absorption region and a substantial decrease in the intensity of region S_{22}. Such bleaching of region S_{11} is consistent with electron transfer from the top of the CNT valence band to the organic oxidizer as previously observed.[19]

PANI films (Figure 3 b) show the expected π–π* absorption in the UV region and the emeraldine base (EB) single peak at 550 nm, corresponding to a molecular exciton associated with the quinone diimine structure of partially protonated polymer in the compact coil conformation.[20] The compact coil conformation is expected because PANI is spin-coated from dimethylformamide (DMF) onto the highly hydrophobic silicon hydride surface.[21] The dip below zero in absorbance is a minor background subtraction issue, but this does not qualitatively affect spectra. After $SOCl_2$ treatment the well-resolved signal at 550 nm is replaced by a broad absorption tail corresponding to a Peierl's gap in the expanded coil conformation of the pernigraniline base (PB), beginning at about 500 nm, with a signal at about 800 nm and extending well into the IR region.[22] The spectra of PANI–SWNT hybrid films (Figure 3 c) are a summation of the individual component spectra as expected.

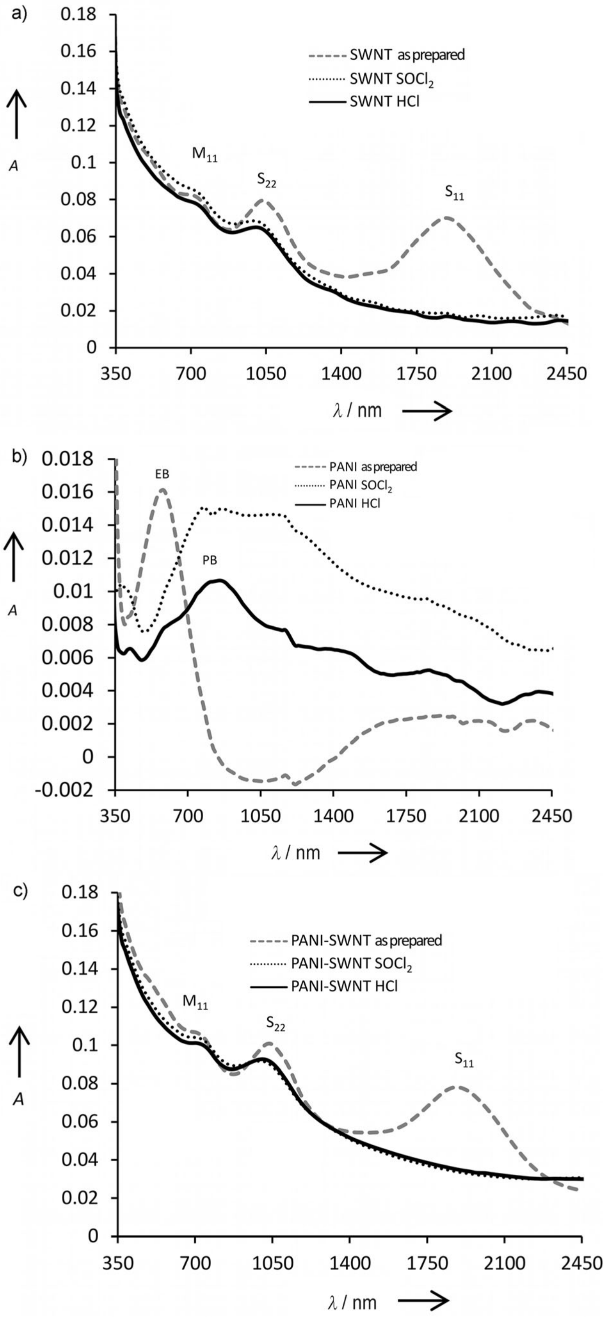

Figure 3. UV/Vis–NIR absorption spectra of a) SWNT membranes, b) PANI films, and c) SWNT membranes on PANI films. Note the different scale in (b).

Regardless of post-treatment, PANI films all exhibit sheet-resistance (R_{sheet}) values on the order of $M\Omega\,sq^{-1}$ (Table 1), confirming the poor conductivity of the films herein. In contrast, untreated CNT films have R_{sheet} values that are lower by a factor of about 10^4 and these are reduced further following treatment with $SOCl_2$ and acid. The hybrid films of PANI and CNTs begin with R_{sheet} values that are almost double that of films containing only CNTs (1300 and 850 $\Omega\,sq^{-1}$, respectively), but after treatment these films exhibit relatively similar values to the pure CNT films (310 and 270 $\Omega\,sq^{-1}$, respectively).

The light current-density–voltage (*J–V*) characteristics of cells fabricated solely with PANI (Figure 4 a) show poor performance with a power-conversion efficiency of about 0.005 %. This is probably due to the aforementioned poor conductivity of PANI films used herein, the effect of which is evident by the fact that series-resistance (R_S) values are on the order of kΩ. However, PANI films on a silicon base do exhibit the diode-like behavior expected for semiconductor–synthetic-metal systems. After treatment with $SOCl_2$ this behavior tends more towards ohmic, whereas after HF treatment the device returns to a more diode-like behavior, albeit with a reduced open-circuit voltage.

The *J–V* characteristics of cells fabricated solely with CNTs (Figure 4 b) initially show a conversion efficiency of about 0.13 %, which is higher than that of PANI cells by a factor of about 10^2. However, the poor fill factor (*FF*) indicates that the cells are substantially underperforming: the sigmoidal nature of *J–V* curves has been shown to be a result of limited interfacial electron transfer,[23] which could be due to the formation of an oxide layer. After treatment of CNT films with $SOCl_2$ the efficiency is increased to about 0.9 %, predominantly through an increase in the short-circuit current density (J_{SC}), but with a small increase in open-circuit voltage (V_{OC}). Performance gains through $SOCl_2$ treatment of CNT–silicon heterojunction solar cells have been reported previously.[24] The effect of $SOCl_2$ on SWNTs has been relatively well-studied and it has been shown to be a very good p-type dopant for SWNTs that increases conductivity in part by shifting the CNT Fermi level into the valence band (as evidenced in this study by the bleaching of S_{11} absorption), and increases film conductivity by reducing barriers at the tube–tube junctions.[25] After $SOCl_2$ treatment, the conduction mechanism of the CNT films switches from variable range hopping/thermionic emission over tube–tube barriers to tunneling through them.[26] A further brief treatment with dilute HF is sufficient to remove the electron-transfer-limiting surface oxide and yields a doubling of both J_{SC} and *FF* which results in a substantial increase in device performance up to about 3.4 %. The S-bend kink feature is now absent in accordance with the improved interfacial electron transfer rate, however the *FF* is still rather low.

The *J–V* characteristics of hybrid devices using both PANI and SWNTs are shown in Figure 4 c. Immediately apparent is the improved *FF* and increased V_{OC} values in all devices regardless of treatment. However, *FF* values of the devices before treatment are still low. Because *FF* can be regarded as a measure of the ability of the cells to maintain charge separation, this indicates a greater level of recombination occurring in the untreated devices. Specifically, in the fresh devices under illumination, R_S is high (2.46 kΩ) and the shunt resistance (R_{SH}) is low (176 Ω). Neglecting the small contribution of the thin PANI film in the vertical plane, R_S can be attributed to the poor electrical properties of the CNT film before $SOCl_2$ treatment. As shown in Table 1, R_{sheet} decreases substantially from 1300 to 310 $\Omega\,sq^{-1}$ and transmittance (T_{550}) increases marginally from 75.2 to 76.8 % with $SOCl_2$ treatment. The S-bend kink feature is present in the fresh hybrid devices and after $SOCl_2$ treatment, but, as with the SWNT devices, disappears after the second

Table 1. Measurements for the three films/membranes/device types. R_{SH} and R_S values are estimated from the axis intercepts of the light *J–V* curves.

Device type	Treatment	V_{OC} [V]	J_{SC} [mA cm^{-2}]	*FF*	Efficiency [%]	R_{sheet} [Ω sq^{-1}]	T_{550} [%]	R_{SH} [Ω]	R_S [Ω]
	fresh	0.26	0.087	0.22	0.005	1.9×10^6	96.4	32845	35169
PANI	$SOCl_2$	0.13	0.17	0.22	0.005	1.7×10^6	98	9792	11590
	HF/HCl	0.17	0.11	0.22	0.004	2.5×10^6	98.4	18235	20777
	fresh	0.25	2.76	0.19	0.13	8.5×10^2	79.8	748	1873
SWNT	$SOCl_2$	0.35	11.41	0.22	0.89	1.8×10^2	79.7	370	764
	HF/HCl	0.39	21.71	0.4	3.36	2.7×10^2	81.3	680	93
	fresh	0.4	19.54	0.14	1.11	1.3×10^3	75.2	176	2460
PANI–SWNT	$SOCl_2$	0.53	27.1	0.37	5.25	3.1×10^2	76.8	10291	468
	HF/HCl	0.52	27.38	0.68	9.66	3.1×10^2	77.5	6077	37

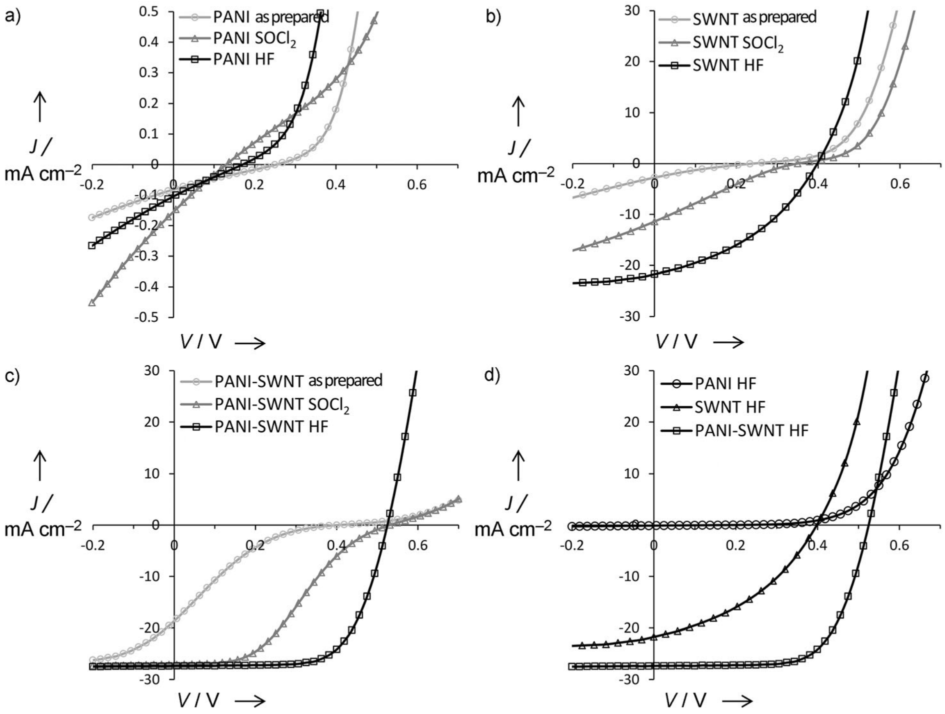

Figure 4. Light *J–V* characteristics of solar cell devices with a) purely PANI (note the different scale), b) purely SWNTs, c) hybrid devices of PANI and SWNTs, and d) comparison of all three devices after $SOCl_2$ doping and HF oxide removal.

acid treatment. If we assume that polyaniline protects the silicon substrate from oxidation, then the origin must result from some change to polyaniline, the CNT film, or the CNT–polyaniline junction. It is known that protonation of polyaniline–graphene junctions improves interfacial charge transfer[27] and this is likely also the case for CNT–polyaniline junctions. Although the growth of an atmospheric oxide on the silicon caused performance degradation in a matter of hours, the beneficial effect of $SOCl_2$ treatment was long lasting: a brief exposure of the active area to dilute HF was enough to "refresh" device performance, even after several days (although after several weeks this was no longer the case). Repeated exposure to HF would eventually cause undercutting and collapse of the Ti/Au electrode around the active area, as indicated by a large abrupt change in *J–V* characteristics. Thus, for long term stability the devices would require protection from the atmosphere.

Relative to solar cells without PANI, the use of PANI may have an effect on the silicon depletion region similar to that in the ionic-liquid-modified devices of Wadhwa et al.[13a,b] In that model SWNT devices suffer from the CNT film, being a porous network, not forming a complete conformal covering on the silicon surface. This produces an incomplete and nonhomogeneous depletion region in the silicon base and results in reduced performance. However, PANI does form a complete conformal covering, producing a much better depletion region and serving the additional function of maintaining a physical separation between photogenerated holes travelling through the CNT film and electrons in the underlying silicon layer.

To obtain the Schottky diode parameters, dark *J–V* characteristics were analyzed by using the thermionic emission model [Eq. (2)]:[28]

$$J = J_S\left[e^{\frac{q(V-JAR)}{nkT}} - 1\right] \tag{2}$$

where J_S is the reverse saturation current density, V the applied potential, q the elementary charge, k the Boltzmann constant, A the interfacial area, R the series resistance, T the absolute temperature, and n the ideality factor. For $V - JAR \gg 3kT/q$ (≈ 20 mV), the -1 term can be dropped because the exponential term dominates. Taking the logarithm, differentiating with respect to J and rearranging affords Equation (3):[29]

$$\frac{\mathrm{d}V}{\mathrm{d}(\ln J)} = RAJ + \frac{n}{\beta} \tag{3}$$

where $\beta = q/kT$. A plot of $\mathrm{d}V/\mathrm{d}(lnJ)$ versus J yields the series-resistance and n values from the intercept and slope, respectively (Figure 5 a).

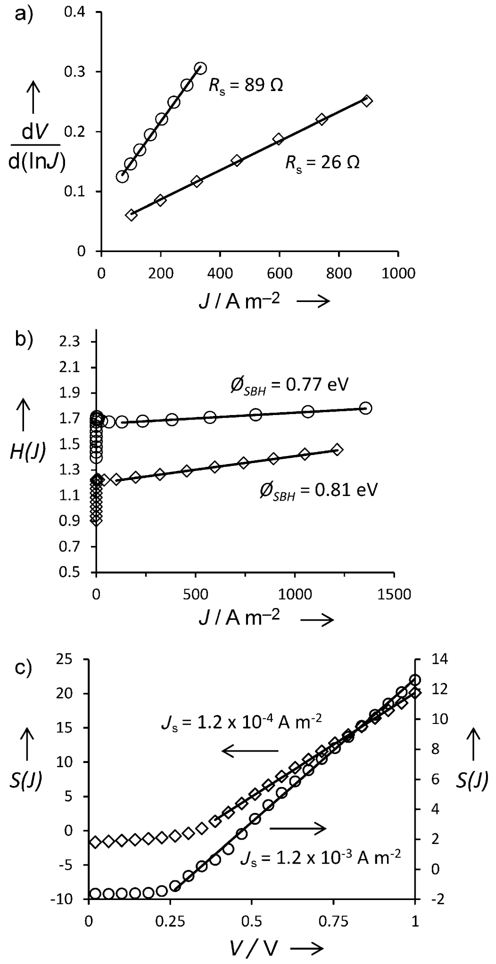

Figure 5. Dark current analysis of SWNT (○) and SWNT–PANI (◇) devices; a) $\mathrm{d}V/\mathrm{d}(lnJ)$ versus J; b) $H(J)$ versus J; c) $S(J)$ versus V.

We additionally define parameter $H(J)$[Eq.(4)], such that:[29]

$$H(J) = V - \left(\frac{n}{\beta}\right) \ln\left(\frac{J}{A^{*}T^{2}}\right) = RAJ + n\,\varnothing_{\mathrm{SBH}} \tag{4}$$

where A^{*} is the Richardson constant. Subsequently, a plot of $H(J)$ versus J yields the Schottky barrier height ($\varnothing_{\mathrm{SBH}}$), and a self-consistency check against Equation (3) through a second measure of the series resistance (Figure 5 b). A new parameter, $S(J)$, can be defined by taking the logarithm of Equation (2) and rearranging to obtain Equation (5):

$$S(J) = \ln J + \frac{\beta JAR}{n} = \left(\frac{\beta}{n}\right)V + \ln J_{\mathrm{S}} \tag{5}$$

A plot of $S(J)$ versus V, using n and R from Equation (3), yields a straight line and extrapolation to zero bias yields J_S (Figure 5 c), which can then be used as an additional estimation of $\varnothing_{\mathrm{SBH}}$ because J_{S} [Eq. (2)] is defined as:[28]

$$J_{\mathrm{S}} = A^{*}T^{2}e^{-\frac{q\varnothing_{\mathrm{SBH}}}{kT}} \tag{6}$$

The results of the dark current analysis are shown in Table 2 together with efficiency and FF values calculated from light measurements.

The hole-doping effect of $SOCl_2$ can be seen in the increased $\varnothing_{\mathrm{SBH}}$ values and a decrease by two orders of magnitude the in reverse saturation current density for the SWNT and SWNT–PANI devices after treatment. The ability of $SOCl_2$ to also improve film conductivity can be seen in the reduced series resistance and concurrent decrease in ideality factor towards unity. The modeled increases in $\varnothing_{\mathrm{SBH}}$ values are consistent with the measured increases in V_{OC} values; for SWNT devices $\varnothing_{\mathrm{SBH}}$ increases by 0.13 eV, whereas V_{OC} increases by 0.14 V, and for PANI–SWNT devices $\varnothing_{\mathrm{SBH}}$ increases by 0.13 eV, whereas V_{OC} increases by 0.12 V. Comparison of $\varnothing_{\mathrm{SBH}}$ values in PANI and PANI–SWNT devices seems to suggest that the maximum effective barrier height of these devices is limited by the PANI–Si interface to 0.81 eV. This is consistent with a model, in which the PANI–Si interface is the photoactive junction and the CNTs function as efficient transporters of holes to the external circuit. The superior depletion region of PANI–SWNT devices relative to SWNT devices is also evidenced in the order of magnitude decrease in the reverse saturation current density when PANI is present. This is also seen in the increased shunt resistance of PANI–SWNT devices relative to those containing SWNTs only.

Relative to the highly developed regime of front-side metallization currently employed in commercial silicon solar cells, the devices described herein are not optimized. For example, relative to state-of-the-art literature examples, the electrical characteristics of PANI films used herein were poor and there is much that could be done to improve these in future investigations. Also, although the CNTs used in these devices had been purified to remove any residual catalyst or amorphous carbon and were highly defect-free, as evidenced in the Raman measurements, the UV/Vis–NIR spectra show that the films

Table 2. Change in device characteristics before and after ($SOCl_2$/HF) film treatment.

Device type	$\varnothing_{\mathrm{SBH}}$ [eV]	n	R [Ω]	J_{s} [A m^{-2}]	Efficiency [%]	FF
PANI	0.81–0.81	2.16–2.05	33–33	3.4×10^{-4}–2.8×10^{-4}	0.005–0.004	0.22–0.22
SWNT	0.64–0.77	3.68–2.02	242–89	1.3×10^{-1}–1.2×10^{-3}	0.13–3.36	0.19–0.40
PANI–SWNT	0.68–0.81	3.30–1.38	112–26	7.5×10^{-2}–1.2×10^{-4}	1.11–9.66	0.14–0.68

comprise a range of CNT chiralities, including both metallic and semiconducting varieties. In another study[30] we will show that, contrary to the assumption of some authors, nanotube–silicon heterojunction solar cells do not operate as p–n junction solar cells, with the nanotubes contributing to the observed photocurrent. Taking this into account, it can be reasonably assumed that such devices will perform better as the metallicity of the CNT film is increased, which is exactly the effect of the $SOCl_2$ treatment. Thus, presumably devices fabricated using chirality-sorted metallic CNTs will outperform those fabricated with mixed CNTs, and devices fabricated with doped chirality-sorted semiconducting CNTs will outperform either the mixed or metallic CNT devices whether they are doped or not. This is due to the fact that conductivity scales with carrier density and a semiconducting CNT with a Fermi level doped up to the conduction band has a much higher electron density at that point than at any point accessible in a metallic CNT.[25,31] In the ideal case of CNT–polyaniline–silicon hybrid devices fabricated with state-of-the-art polyaniline films and highly doped single-chirality semiconducting CNT membranes, considerable gains in performance over that reported herein are likely. The CNT films could be significantly thinner and more transparent and these CNT films are also intrinsically antireflective. Such hybrid films as those reported herein could provide improved front-contact performance over current metallization strategies through reduced optical shading and enhanced carrier collection over the entire front solar-cell surface and, considering the rapidly dropping cost of CNTs and their relative ease of processing, potentially reduced production costs.

Conclusions

Hybrid carbon CNT–PANI–silicon heterojunction solar cells were fabricated and shown to clearly outperform their CNT–silicon and polyaniline–silicon counterparts. Other reports of CNT–silicon solar cells used controlled oxide growth or the introduction of an ionic liquid to improve the performance; however, the use of an intermediate layer of conductive polymer is a new step with a demonstrated positive effect. Furthermore, the use of a layer of CNTs to improve the electrical properties of an underlying conductive polymer film clearly has broad applications, ranging from solar cells and organic light-emitting diodes to touch-sensitive interfaces and more. The increased performance in the hybrid devices reported herein is attributed to the synergistic combination of an improved silicon depletion region due to conformal surface covering by the polymer and the high conductivity and current-carrying capacity of the CNT film. These devices show good photovoltaic performance, and optimization of device components could lead to significant performance gains. The hybrid PANI–CNT films thus show potential as improved front-side electrodes for current and future generations of commercial silicon solar cells and photodetectors.

Experimental Section

SWNTs (P3, Carbon Solutions) were heated at reflux in 5 M nitric acid (0.2 mg mL^{-1}) for 24 h to dissolve any residual catalyst particles, then passed through Teflon filters (0.45 μm, FHLP, Millipore, USA), and rinsed with copious amounts of deionized water until the filtrate pH stabilized at near neutral. The filtrate was sonicated at 50 W_{RMS} in an aqueous solution of TritonX100 (1 %, Sigma–Aldrich, Australia) at a concentration of 0.2 mg mL^{-1} for 2 h. The resulting black suspension was then centrifuged at 20 000 g for 30 min, and the sediment was discarded. To form SWNT membranes, the supernatant was filtered through mixed cellulose ester (MCE) membranes (0.45 μm, HSWP, Millipore, USA) at 210 μL cm^{-2} and rinsed thoroughly with deionized water. Circular regions of SWNT–MCE with areas of 0.18 cm^2 were taken for device fabrication. PANI (emeraldine base, $M_w = 10\,000$, Sigma–Aldrich, Australia) was sonicated in DMF (Sigma–Aldrich, Australia) at a concentration of 1 mg mL^{-1} for 30 min and then centrifuged at 20 000 g for 30 min. The supernatant was passed through Teflon filters (1 μm, Millipore, USA) and then, for the devices with PANI, three drops of the filtrate were spin-coated onto substrates at a spin speed of 3000 rpm, and the resulting films were baked in air at 130 °C for 2 h.

For device fabrication, phosphorous-doped n-type silicon wafers (CZ, 1–20 Ω cm, <100>, ABC GmbH, Germany), polished on one side, and with a thermal oxide layer (100 nm) were diced into pieces (1 cm^2). UV photolithography was used to define circular holes (0.08 cm^2) in the sputtered front metal contacts (Ti/Au, 5:95 nm) of each device and then, following lift-off, the oxide in this region was etched with buffered oxide etchant (BOE). For PANI devices (Figure 6 a) spin-coating was performed immediately after etching. For SWNT (Figure 6 b), and SWNT-PANI devices (Figure 6 c), films were deposited onto

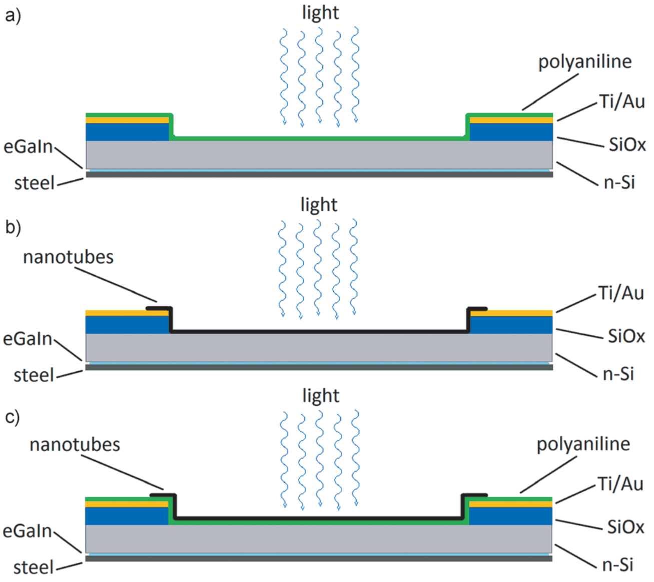

Figure 6. Silicon solar-cell devices with a) only PANI, b) only SWNTs and c) hybrid device of SWNTs and PANI.

the substrate surfaces by placing the circular SWNT–MCE membranes, CNT side down, concentrically over the front side holes. The membranes were wetted with deionized water, then compressed with Teflon, and baked at 130 °C for 15 min. Upon cooling, the substrates were immersed in acetone to dissolve the MCE, leaving the CNT membranes tightly adsorbed onto the substrate surfaces providing circular active areas (0.08 cm^2) surrounded by toroidal regions (0.1 cm^2), in which the CNT membranes overlap the front metal contacts. After BOE etching of the rear oxide, the devices were completed with a eutectic back contact (eGaIn, Sigma–Aldrich, Australia) and mounted on steel plates.

SEM images of the SWNT electrodes were obtained using a FEI Helios Nanolab 600. Prior to imaging, all samples were sputter-coated with platinum (5 nm). AFM images were taken in air by means of a multimode head and Nanoscope V controller (Digital Instruments, Veeco, USA), operating in tapping mode using commercially available silicon cantilevers (FESP-ESP, Veeco, USA) with nominal fundamental resonance frequencies of 70–85 kHz. UV/Vis–NIR spectra were obtained by means of a Varian Cary 5G spectrophotometer with a resolution of 1 nm by passing the beam through glass slides, upon which PANI, SWNT, or PANI–SWNT films were deposited as previously described. Raman spectra were collected by means of a WiTEC alpha300R microscope using a 100× objective (NA 0.9) and a laser (532 nm) operating at constant power for each experiment up to a possible maximum of about 60 mW. Sheet-resistance measurements were taken using a four-point probe in linear conformation from films (2×2 cm^2) on glass. Current–voltage data were collected by means of a Keithley 2400 SMU instrument and recorded using a custom LabView Virtual Instrument program. For light experiments cells were illuminated by collimated 100 $mW\,cm^{-2}$ light (100 $mW\,cm^{-2}$) from a xenon-arc source passed through an AM1.5G filter. The irradiance at the sample plane was measured with a silicon reference cell (PV Measurements, NIST-traceable calibration). Data were obtained by scanning from 1 to -1 V and several curves were recorded to verify the stability of output characteristics. Before measurements, cells without PANI were briefly exposed to HF (2%) and then rinsed with ethanol and dried with N_2. This removed the native oxide layer, leaving a hydride-terminated silicon surface. Power-conversion efficiencies were calculated assuming an active area of 0.08 cm^2, corresponding to the circular-etched area, within which silicon was in contact with the CNTs. To verify the validity of this assumption (i.e., to preclude the possibility of photocurrent from either PANI covering the front metal contact or the overlapping region of CNTs), a circular aperture (0.08 cm^2) was placed over the cells close to the surface so that light could only impinge upon the device in the assumed circular active area. For cells with CNTs there was no difference between the photovoltaic output thus obtained and that obtained when there was no aperture present.

Acknowledgements

This work is supported by the Australian Microscopy and Microanalysis Research Facility (AMMRF). B.F. gratefully acknowledges the support of the Alexander von Humboldt Foundation.

Keywords: materials science · nanotubes · nanotechnology · polymers · raman spectroscopy

[1] a) E. Kymakis, G. A. J. Amaratunga, *Appl. Phys. Lett.* **2002**, *80*, 112; b) A. D. Pasquier, H. E. Unalan, A. Kanwal, S. Miller, M. Chhowalla, *Appl. Phys. Lett.* **2005**, *87*, 203511; c) B. J. Landi, R. P. Raffaelle, S. L. Castro, S. G. Bailey, *Prog. Photovoltaics* **2005**, *13*, 165–172; d) V. Sgobba, A. Troeger, R. Cagnoli, A. Mateo-Alonso, M. Prato, F. Parenti, A. Mucci, L. Schenetti, D. M. Guldi, *J. Mater. Chem.* **2009**, *19*, 4319–4324; e) C. Li, Y. Chen, Y. Wang, Z. Iqbal, M. Chhowalla, S. Mitra, *J. Mater. Chem.* **2007**, *17*, 2406–2411.

[2] a) T. Hasobe, S. Fukuzumi, P. V. Kamat, *J. Phys. Chem. B* **2006**, *110*, 25477–25484; b) T. Umeyama, M. Fujita, N. Tezuka, N. Kadota, Y. Matano, K. Yoshida, S. Isoda, H. Imahori, *J. Phys. Chem. C* **2007**, *111*, 11484–11493; c) G. M. A. Rahman, A. Troeger, V. Sgobba, D. M. Guldi, N. Jux, D. Balbino, M. N. Tchoul, W. T. Ford, A. Mateo-Alonso, M. Prato, *Chem. Eur. J.* **2008**, *14*, 8837–8846; d) M. A. Bissett, J. G. Shapter, *J. Electrochem. Soc.* **2011**, *158*, K53–K57.

[3] A. S. D. Sandanayaka, E. Maligaspe, T. Hasobe, O. Ito, F. D'Souza, *Chem. Commun.* **2010**, *46*, 8749–8751.

[4] a) D. M. Guldi, G. M. A. Rahman, V. Sgobba, N. A. Kotov, D. Bonifazi, M. Prato, *J. Am. Chem. Soc.* **2006**, *128*, 2315–2323; b) G. Mountrichas, A. S. D. Sandanayaka, S. P. Economopoulos, S. Pispas, O. Ito, T. Hasobe, N. Tagmatarchis, *J. Mater. Chem.* **2009**, *19*, 8990–8998.

[5] M. A. Bissett, I. Koper, J. S. Quinton, J. G. Shapter, *Phys. Chem. Chem. Phys.* **2011**, *13*, 6059–6064.

[6] a) T. Umeyama, N. Tezuka, M. Fujita, S. Hayashi, N. Kadota, Y. Matano, H. Imahori, *Chem. Eur. J.* **2008**, *14*, 4875–4885; b) N. Tezuka, T. Umeyama, S. Seki, Y. Matano, M. Nishi, K. Hirao, H. Imahori, *J. Phys. Chem. C* **2010**, *114*, 3235–3247.

[7] a) K. Suzuki, M. Yamaguchi, M. Kumagai, S. Yanagida, *Chem. Lett.* **2003**, *32*, 28–29; b) T. Y. Lee, P. S. Alegaonkar, J.-B. Yoo, *Thin Solid Films* **2007**, *515*, 5131–5135; c) P. Brown, K. Takechi, P. V. Kamat, *J. Phys. Chem. C* **2008**, *112*, 4776–4782; d) D. D. Tune, B. S. Flavel, J. S. Quinton, A. V. Ellis, J. G. Shapter, *Solar Energy Mater. Solar Cells* **2010**, *94*, 1665–1672; e) T. Chen, S. Wang, Z. Yang, Q. Feng, X. Sun, L. Li, Z.-S. Wang, H. Peng, *Angew. Chem.* **2011**, *123*, 1855–1859; *Angew. Chem. Int. Ed.* **2011**, *50*, 1815–1819; f) L. J. Larsen, D. D. Tune, P. Kemppinen, K. N. Winzenberg, S. E. Watkins, J. G. Shapter, *J. Photochem. Photobiol. A* **2012**, *235*, 72–76; g) M. A. Bissett, J. G. Shapter, *J. Phys. Chem. C* **2010**, *114*, 6778–6783.

[8] C. T. White, T. N. Todorov, *Nature* **1998**, *393*, 240–242.

[9] a) J. Maultzsch, R. Pomraenke, S. Reich, E. Chang, D. Prezzi, A. Ruini, E. Molinari, M. S. Strano, C. Thomsen, C. Lienau, *Phys. Rev. B* **2005**, *72*, 241402; b) C. D. Spataru, F. Léonard, *Phys. Rev. Lett.* **2010**, *104*, 177402.

[10] a) N. M. Gabor, Z. Zhong, K. Bosnick, J. Park, P. L. McEuen, *Science* **2009**, *325*, 1367–1371; b) S. Wang, M. Khafizov, X. Tu, M. Zheng, T. D. Krauss, *Nano Lett.* **2010**, *10*, 2381–2386.

[11] D. D. Tune, B. S. Flavel, R. Krupke, J. G. Shapter, *Adv. Energy Mater.* **2012**, *2*, 1043–1055.

[12] a) Y. Jia, P. Li, X. Gui, J. Wei, K. Wang, H. Zhu, D. Wu, L. Zhang, A. Cao, Y. Xu, *Appl. Phys. Lett.* **2011**, *98*, 133115; b) Y. Jia, A. Cao, X. Bai, Z. Li, L. Zhang, N. Guo, J. Wei, K. Wang, H. Zhu, D. Wu, P. M. Ajayan, *Nano Lett.* **2011**, *11*, 1901–1905.

[13] a) P. Wadhwa, B. Liu, M. A. McCarthy, Z. Wu, A. G. Rinzler, *Nano Lett.* **2010**, *10*, 5001–5005; b) P. Wadhwa, G. Seol, M. K. Petterson, J. Guo, A. G. Rinzler, *Nano Lett.* **2011**, *11*, 2419–2423; c) W. Chen, G. Seol, A. G. Rinzler, J. Guo, *Appl. Phys. Lett.* **2012**, *100*, 103503.

[14] Y. Jia, A. Cao, F. Kang, P. Li, X. Gui, L. Zhang, E. Shi, J. Wei, K. Wang, H. Zhu, D. Wu, *Phys. Chem. Chem. Phys.* **2012**, *14*, 8391–8396.

[15] S. Jeong, E. C. Garnett, S. Wang, Z. Yu, S. Fan, M. L. Brongersma, M. D. McGehee, Y. Cui, *Nano Lett.* **2012**, *12*, 2971–2976.

[16] a) W. Wang, E. A. Schiff, *Appl. Phys. Lett.* **2007**, *91*, 133504; b) J. R. Cárdenas, E. A. de Vasconcelos, W. M. de Azevedo, E. F. da Silva, I. Pepe, A. F. da Silva, S. S. Ribeiro, K. A. Silva, *Appl. Surf. Sci.* **2008**, *255*, 688 – 690.
[17] L. Alvarez, A. Righi, T. Guillard, S. Rols, E. Anglaret, D. Laplaze, J.-L. Sauvajol, *Chem. Phys. Lett.* **2000**, *316*, 186 – 190.
[18] R. B. Weisman, S. M. Bachilo, *Nano Lett.* **2003**, *3*, 1235 – 1238.
[19] M. J. O'Connell, E. E. Eibergen, S. K. Doorn, *Nat. Mater.* **2005**, *4*, 412 – 418.
[20] a) J. E. de Albuquerque, L. H. C. Mattoso, D. T. Balogh, R. M. Faria, J. G. Masters, A. G. MacDiarmid, *Synth. Met.* **2000**, *113*, 19 – 22; b) A. G. MacDiarmid, *Synth. Met.* **1997**, *84*, 27 – 34.
[21] J. K. Avlyanov, Y. Min, A. G. MacDiarmid, A. J. Epstein, *Synth. Met.* **1995**, *72*, 65 – 71.
[22] J. E. de Albuquerque, L. H. C. Mattoso, R. M. Faria, J. G. Masters, A. G. MacDiarmid, *Synth. Met.* **2004**, *146*, 1 – 10.
[23] J. Nelson, J. Kirkpatrick, P. Ravirajan, *Phys. Rev. B* **2004**, *69*, 035337.
[24] Z. Li, V. P. Kunets, V. Saini, Y. Xu, E. Dervishi, G. J. Salamo, A. R. Biris, A. S. Biris, *Appl. Phys. Lett.* **2008**, *93*, 243117.
[25] T. M. Barnes, J. L. Blackburn, J. van de Lagemaat, T. J. Coutts, M. J. Heben, *ACS Nano* **2008**, *2*, 1968 – 1976.
[26] Z. Li, V. P. Kunets, V. Saini, Y. Xu, E. Dervishi, G. J. Salamo, A. R. Biris, A. S. Biris, *ACS Nano* **2009**, *3*, 1407 – 1414.
[27] R.-X. Wang, L.-F. Huang, X.-Y. Tian, *J. Phys. Chem. C* **2012**, *116*, 13120 – 13126.
[28] S. M. Sze, K. K. Ng, *Physics of Semiconductor Devices, 3rd ed.*, Wiley Interscience, **2006**.
[29] S. K. Cheung, N. W. Cheung, *Appl. Phys. Lett.* **1986**, *49*, 85 – 87.
[30] D. D. Tune, F. Hennrich, S. Dehm, M. F. G. Klein, A. Colsmann, J. G. Shapter, U. Lemmer, M. Kappes, R. Krupke, B. S. Flavel, **2012**, unpublished results.
[31] J. L. Blackburn, T. M. Barnes, M. C. Beard, Y.-H. Kim, R. C. Tenent, T. J. McDonald, B. To, T. J. Coutts, M. J. Heben, *ACS Nano* **2008**, *2*, 1266 – 1274.

Received: August 14, 2012

2.3 Carbon Nanotube Silicon Solar Cells

2.3.3 *The Role of Nanotubes in Carbon Nanotube-Silicon Solar Cells*

D. D. Tune, F. Hennrich, S. Dehm, M. F. G. Klein, K. Glaser, A. Colsmann,
J. G. Shapter, U. Lemmer, M. M. Kappes, R. Krupke, **B. S. Flavel**

Advanced Energy Materials 3 (2013) 1091–1097

DOI: 10.1002/aenm.201200949

Abstract

The mechanism of action of nanotube-silicon heterojunction solar cells is under discussion with literature reports suggesting either p-n or Schottky junction characteristics. The crux of the issue is whether the nanotubes contribute to the observed photocurrent or not. In order to further understand the mechanism of action of these solar cells, devices were fabricated using nanotubes sorted by (n,m) species, so that the excitonic transition is well defined and is outside the range of absorption of silicon and such that any contribution to the photocurrent from the nanotubes should be easily resolved from that of the silicon by analysis of the photocurrent spectrum. The devices exhibited the photocurrent spectra of silicon only, indicating that the nanotubes do not contribute to the photocurrent. However, by changing the back contact electrode material, results were obtained that appear to show such a contribution.

Contribution

B.S.F, D.D.T and R.K conceived the idea for the project. B.S.F, D.D.T, M.F.G.K, K.G and S.D performed the experiments. B.S.F and D.D.T wrote the manuscript and all authors were involved in the scientific discussion and analysis of results.

– This page intentionally left blank –

ADVANCED ENERGY MATERIALS
www.advenergymat.de

The Role of Nanotubes in Carbon Nanotube–Silicon Solar Cells

*Daniel D. Tune, Frank Hennrich, Simone Dehm, Michael F. G. Klein, Konstantin Glaser, Alexander Colsmann, Joseph G. Shapter, Uli Lemmer, Manfred M. Kappes, Ralph Krupke, and Benjamin S. Flavel**

The mechanism of action of nanotube-silicon heterojunction solar cells is under discussion with literature reports suggesting either p-n or Schottky junction characteristics. The crux of the issue is whether the nanotubes contribute to the observed photocurrent or not. In order to further understand the mechanism of action of these solar cells, devices were fabricated using nanotubes sorted by (n,m) species, so that the excitonic transition is well defined and is outside the range of absorption of silicon and such that any contribution to the photocurrent from the nanotubes should be easily resolved from that of the silicon by analysis of the photocurrent spectrum. The devices exhibited the photocurrent spectra of silicon only, indicating that the nanotubes do not contribute to the photocurrent. However, by changing the back contact electrode material, results were obtained that appear to show such a contribution.

1. Introduction

Carbon nanotube-silicon solar cells have seen rapidly increasing research interest in recent years[1] with advances made in just the last year bringing the current maximum power conversion efficiency to 11.5% in the dry state,[1b] 15% with a TiO_2 antireflective layer[1d] and >18% in the wet state.[2] In this architecture, a thin film of carbon nanotubes is placed in contact with the surface of a silicon wafer to produce a photoactive junction. Such nanotube-semiconductor junctions have wide application in a range of advanced materials fields including electronics, catalysis, sensing and more. In the literature, there are two main mechanisms suggested for how these devices convert light to electrical power; the devices work in the manner of 1) a p-n heterojunction solar cell, with the nanotubes contributing as photoactive material[3] or, 2) a metal-semiconductor (MS) Schottky junction solar cell or the closely related metal-insulator-semiconductor (MIS) solar cell, where the nanotubes operate as transparent conducting electrodes.[4] Carbon nanotubes have been shown to a) produce a photocurrent when exposed to light,[5] b) be capable of forming photoactive p-n junctions[6] and c) be capable of contributing to photocurrent generation in photoactive donor-acceptor pairs.[7] Additionally, it is known that air-exposed semiconducting single walled carbon nanotubes are p-type due to oxygen adsorption.[8] Considering this, it is not unreasonable to assume that nanotube-silicon solar cells could function in the manner of p-n junctions. Indeed, the literature contains reports that suggest exactly that; recent measurements on nanotube-silicon devices by Jung preclude the MIS or MS mechanism.[1b] However, other measurements on similar nanotube-silicon devices show greatly enhanced (500x) performance with an interfacial oxide layer, suggesting an MIS-type mechanism.[1e]

A more direct probe of the mechanism of action is to use photocurrent spectroscopy to measure the external quantum efficiency (EQE) of the devices. Contribution from the nanotubes to the photocurrent would convincingly rule out an MS or MIS mechanism. In the work of Tzolov,[3a] photocurrent spectroscopy of nanotube-silicon devices shows a broad feature in the IR that is attributed to the nanotubes. However this feature is very similar to the free carrier absorption profile of the silicon substrate,[9] confounding the issue. Also, in the EQE data of Ong[3g] there is a feature that is attributed to photocurrent generation by the nanotubes. However this small feature in the

---

D. D. Tune, Prof. J. G. Shapter
Centre for Nanoscale Science and Technology
Flinders University
Bedford Park, SA 5042, Australia

Dr. F. Hennrich, S. Dehm, Prof. M. M. Kappes,
Prof. R. Krupke, Dr. B. S. Flavel
Institute of Nanotechnology (INT)
Karlsruhe Institute of Technology (KIT)
76021 Karlsruhe, Germany
E-mail: benjamin.flavel@partner.kit.edu

M. F. G. Klein, K. Glaser, Dr. A. Colsmann, Prof. U. Lemmer
Light Technology Institute (LTI)
Karlsruhe Institute of Technology (KIT)
76131 Karlsruhe, Germany

Dr. A. Colsmann, Prof. U. Lemmer, Prof. R. Krupke
DFG Centre for Functional Nanostructures (CFN)
Karlsruhe Institute of Technology (KIT)
76131 Karlsruhe, Germany

Prof. R. Krupke
Institute of Materials Science
Technische Universität Darmstadt
64287 Darmstadt, Germany

DOI: 10.1002/aenm.201200949

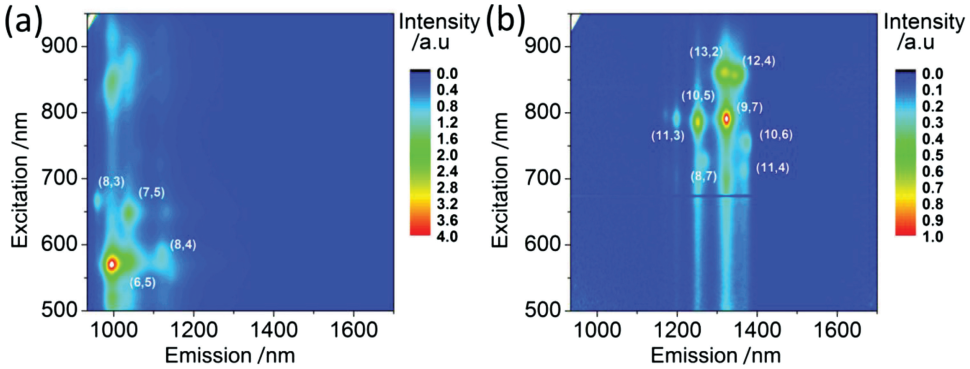

Figure 1. Photoluminescence spectra of sorted nanotube material (see text): (a) CoMoCat and (b) laser ablation. Spectra were taken in aqueous solution where photoluminescence of $\lambda > 1400$ nm is not observable due to absorption by water.

EQE, which roughly corresponds to the optical gap of the (7,6) nanotubes used in the study (~1150 nm), sits right on the edge of the silicon absorption spectrum (~1200 nm) thus the conclusion of device p-n junction characteristics based solely on this feature is uncertain.

To determine more conclusively whether or not nanotubes contribute to photocurrent generation in carbon nanotube-silicon solar cells, devices were fabricated using two different semiconducting nanotube samples enriched in either small or large diameter nanotubes. These were chosen since the first excitonic transition (S_{11}) of the major (6,5) chirality in the small diameter nanotubes lies at ~980 nm and overlaps the silicon spectrum similarly to the (7,6) nanotubes used by Ong,[3g] whereas in the larger diameter nanotubes the gap is ~1320 nm, well above the absorption onset wavelength of silicon. Any contribution to the photocurrent from the larger diameter nanotubes should thus be easily resolved by analysis of the photocurrent spectrum.

2. Results

Figure 1 shows photoluminescence (PL) measurements of the semiconducting fractions of nanotubes produced by the a) CoMoCat and b) laser ablation methods (hereafter referred to as COM and LAB), where the excitation and emission energies correspond to the second (S_{22}) and first (S_{11}) excitonic transitions, respectively. It can be clearly seen that the two samples are composed of markedly different populations of nanotube chiralities. The smaller diameter COM sample contains a very high proportion of the (6,5) nanotube species whilst the larger diameter LAB material has the (9,7) species and smaller quantities of (10,5), (13,2) and (12,4). Absorption of emitted photons by the inner filter effect of water for $\lambda >$ 1400 nm prevents any larger diameter nanotube species from being observed. Although the LAB material contains a larger number of nanotube species it is clear that the LAB material will still have its first excitonic transitions, S_{11}, corresponding to wavelengths >1250 nm, well outside that of any of the COM material (~950–1150 nm) and, importantly for this study, well outside the range of silicon absorption.

UV-Vis-NIR absorption spectra of nanotube films on glass (**Figure 2**, dash-dotted lines) support the PL measurements, with the COM material displaying a dominant S_{11} absorption peak at ~1030 nm and the LAB material showing a broad absorption band spanning ~1300–1800 nm. The sharp Gaussian present in the absorption spectrum of the COM material is indicative of the (n,m) purity of the nanotube sample as also measured by photoluminescence, whereas the broad band present in the spectrum of the LAB material is a convolution of several peaks relating to the four major (n,m) species shown in the PL measurements. Closer inspection reveals a substantial difference between the positions of the S_{11} transitions as measured by PL and UV-Vis-NIR. The PL yields an S_{11} of ~ 980nm for the (6,5)

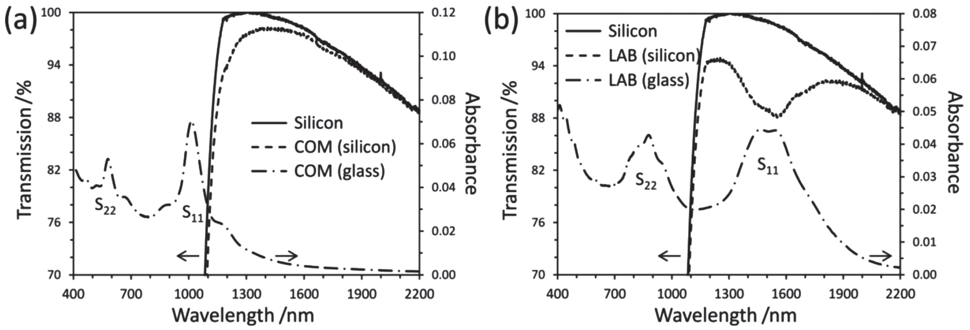

Figure 2. UV-Vis-NIR spectra of films prepared from the semiconducting fractions of (a) COM and (b) LAB nanotubes. Transmission spectra are shown for films on silicon and absorption spectra are shown for films on glass.

species and ~1320 nm for the (9,7) species whereas the absorption spectra yield ~1030 nm for the (6,5) and at least ~1490 nm for the (9,7). This apparent shift in the energy of S_{11} has been reported in the literature and, in the case of the (6,5) nanotube, exactly matches that observed elsewhere.[10]

Here it is important to note that the PL measurements are performed on highly disperse, aqueous solutions of surfactant-wrapped semiconducting nanotube material immediately following the sorting process. However, the transmission spectra are obtained from dry nanotube films on glass substrates, prepared from the sorted fractions, wherein the relatively surfactant-free nanotubes are present as bundles. Since the excitonic properties of carbon nanotubes are greatly affected by many body interactions, Coulomb interaction and charge transfer between adjacent nanotubes in bundles significantly distorts the thin film transmission measurements. Additionally, in the dry transmission measurements, the filter effect of water is not an issue thus the contribution of the larger diameter nanotubes is observable, yielding a much larger apparent shift in S_{11} of the more polychiral LAB material than for the purer COM material. Therefore, if there is a contribution from the nanotubes then the S_{11} features in the transmission measurement of the dry films (not those in the PL of the aqueous suspensions) should be represented in the EQE of solar cell devices that employ the same dry films.

The UV-Vis-NIR transmission properties of nanotube films on silicon (Figure 2, dotted lines) are dominated by silicon absorption due to a) the fundamental bandgap (<1200 nm, steep onset) and b) free carrier absorption (>1400 nm, slow onset). Since the wavelength of light corresponding to the first excitonic transition, S_{11}, of the major (6,5) nanotube species in the COM material is well below that corresponding to silicon's fundamental bandgap, the major absorption features due to (6,5) material are not discernible. Still, a small contribution to the absorption can be seen in the region 1000–1400 nm (Figure 2(a), dotted lines) arising from the shoulder on the higher wavelength side of the main (6,5) peak. In the case of the LAB material, the S_{11} absorption energies of the major chiralities are well below silicon's bandgap. Consequently, the S_{11} absorption features of this material are clearly visible in the range 1300–1800 nm (Figure 2(b), dotted lines) and exactly match the corresponding features in the absorbance spectra of LAB films on glass (Figure 2(b), dash-dotted lines).

Carbon nanotube-silicon solar cells were fabricated with semiconducting COM and LAB nanotube material (the same thickness films as those used for the optical measurements), with eGaIn back contact electrodes, and the EQE of as prepared and HF treated devices was measured (**Figure 3**). Immediately apparent is the poor response of the as prepared devices due to a thick oxide formed on the silicon during the nanotube film deposition. On the other hand, the HF treated device shows a significant improvement in EQE. The high porosity of the nanotube film means that hydrofluoric acid can penetrate through to the underlying silicon allowing the oxide to be removed without harm to the nanotubes.[11] Indeed, the presence of an S_{11} absorption feature in the UV-Vis-NIR spectra of the LAB nanotube films on silicon show that they are still present and their electronic properties unchanged after the HF treatment although adsorbed oxygen will have been largely replaced with fluorine.[11]

Comparison of the EQE of COM solar cell devices with the UV-Vis-NIR absorption spectra of COM films on glass shows no correlation between the position of S_{11} and any features in the EQE. Importantly, a similar comparison of the EQE of LAB solar cell devices with the UV-Vis-NIR absorption spectra of LAB films on silicon also shows no such correlation. Any contribution to photocurrent generation resulting from photons absorbed via the S_{11} transition of the nanotubes should be clearly visible in the EQE in the range corresponding to the observed peak in the UV-Vis-NIR. Even though the photocurrent response of the COM nanotubes would be obscured by the silicon response, we note that (a) EQE measurements are extremely sensitive by design, (b) the peak S_{11} absorption of the (thin) (6,5) films was ~10% and, (c) the EQE of none of the devices approached 100%, leaving plenty of room for the nanotube response to be observed over that of the silicon base. In fact, the EQE of both COM and LAB devices are very similar to each and show no significant deviation from what would be expected from a silicon Schottky junction solar cell, which is in apparent disagreement with.[3g] It is possible that different mechanisms apply to devices made with different nanotube species due to variations in band alignment with the silicon substrate thus the lack of a response from the LAB devices

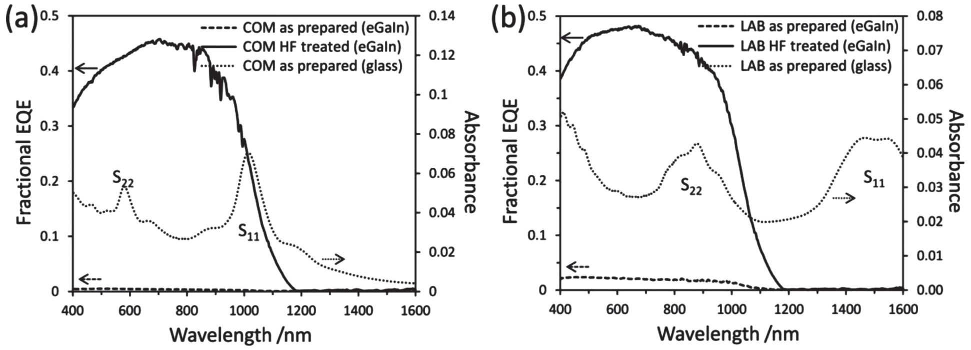

Figure 3. External quantum efficiency of as prepared and HF treated carbon nanotube-silicon solar cells fabricated with films of either (a) COM or (b) LAB semiconducting nanotubes with eGaIn back contact electrodes. UV-Vis-NIR absorption spectra of corresponding films on glass are shown for comparison.

cannot be interpreted to mean that there can be no response from devices using larger bandgap material such as COM (6,5) and the (7,6)-enriched material used in.[3g] However we observe no response from either the smaller bandgap LAB or the larger bandgap COM devices used in this study and we note that the LUMO of the (7,6) nanotube is only ~80 meV below (6,5). The light (AM1.5G) and dark IV measurements for the devices shown in the EQE measurements yielded V_{OC} = 410 mV, J_{SC} = 9.4 mA/cm^2, FF = 0.35, R_{series} = 95 Ω, n = 1.46 and efficiency = 1.4% for LAB and V_{OC} = 395 mV, J_{SC} = 17.4 mA/cm^2, FF = 0.35, R_{series} = 150 Ω, n = 1.26 and efficiency = 2.4% for COM and these are comparable with the V_{OC} = 370 mV, J_{SC} = 14.6 mA/cm^2, FF = 0.3, R_{series} = 150 Ω, n = 3.75 and efficiency = 1.7% in[3g].

It was demonstrated that the nanotubes do not contribute to the photocurrent in these devices but then the influence of the back contact was studied by fabricating otherwise identical solar cell devices using silver paste as the back contact electrode instead of eGaIn, and measuring the EQE (**Figure 4**). The work function of eGaIn is φ ~ 4.16 eV whereas for silver paste φ ~ 4.5–4.8 eV and eGaIn makes a good ohmic contact to n-type silicon (φ ~ 4.26 eV) whereas silver paste does not. In the spectra of as prepared COM (silver) devices (Figure 4(a), dotted line) there is a prominent feature in the range ~ 900–1200 nm that is not present in devices where eGaIn is used as the back contact (Figure 4(a), dashed line). A similar feature is also present in the EQE of the as prepared, silver-backed LAB devices (Figure 4(b), dotted line) and even after HF treatment this feature remains clearly apparent as a shoulder in Figure 4(a), solid line. Importantly, the features in the EQE, before and after HF treatment of the silicon, appear to be independent of any of the nanotube absorption characteristics shown for comparison in Figure 4(a) and Figure 4(b), dash-dotted lines.

The decrease in the EQE towards shorter wavelengths (1000–900 nm) is typical of a back-illuminated Schottky junction solar cell.[12] Here it is important to note that the terms 'front-illuminated' and 'back-illuminated' refer to whether the rectifying contact is illuminated directly, or indirectly through the device substrate, respectively. To determine whether or not this is the origin of the 900–1200 nm feature in Figure 4, the internal quantum efficiency (IQE) of a back-illuminated solar cell with an ohmic contact and a rectifying contact, as shown in **Figure 5**(a), has been calculated using the analytical model of Basu and Saha.[12] Equation (9) in that work uses as fitting parameters the thickness of the semiconducting layer t, the width of the depletion layer d, the minority carrier diffusion length L, the minority carrier diffusion coefficient D, the surface recombination velocity s, and the wavelength-dependent absorption coefficient α (λ). This work used t = 525 µm, L = 500 µm, $D = 10^{-3}$ m^2.s^{-1}, for 525 µm thick n-Si with a donor density of 10^{14} cm^{-3},[13] used α (λ) from Green[14] and $d \leq 10^{-6}$ m and s = 1 m.s^{-1} were set as best fit to the photocurrent spectra of our as-prepared cells with silver back contacts. The IQE of a front-illuminated solar cell with a rectifying contact and an ohmic contact, as shown in Figure 5(b), has also been calculated, based on the analytical model of Soukoup and Akers[15] requiring only L and α (λ) as parameters, which was chosen identical to the back-illuminated case. Figure 5(c) shows the IQE modeling results for front- and back--illuminated solar cells. The non-monotonic behavior for the back-illuminated cell is due to the enhanced absorption of shorter wavelength light by the substrate and the limited diffusion of the minority carrier towards the charge separating back contact. Hence a back-illuminated device can generate photocurrent only in the long wavelength range.

Comparing the IQE spectrum of the modelled back-illuminated silicon Schottky junction solar cell, Figure 5(a), with the feature observed in the EQE of the silver-backed carbon nanotube-silicon solar cell, Figure 4(a), solid line and dotted line, it seems likely that the enhanced EQE in the wavelength range close to the absorption edge of silicon arises due to the contribution of a rectifying back contact rather than as a result of contribution to the photocurrent from the nanotubes. The presence of this contact leads to predictably poor solar IV parameters of V_{OC} = 180 mV, J_{SC} = 0.5 mA/cm^2, FF = 0.14, R_{series} = 24 kΩ, n = 1.97 and efficiency = 0.01% for LAB and V_{OC} = 226 mV, J_{SC} = 3.1 mA/cm^2, FF = 0.17, R_{series} = 53 kΩ, n = 2.06 and efficiency = 0.12% for COM. This is despite the fact that the silver backed devices were otherwise identical to the eGaIn devices and the silver paste itself is highly conductive.

The nanotube films used in this study and others are, by design, very thin and it may be that the contribution of such

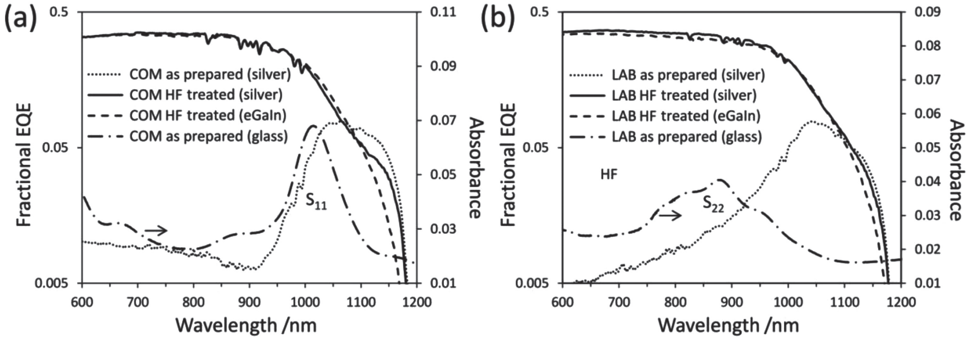

Figure 4. External quantum efficiency of as prepared and HF treated carbon nanotube-silicon solar cells fabricated with films of either (a) COM or (b) LAB semiconducting nanotubes with silver paint or eGaIn back contact electrodes. Note, a log EQE scale has been used to allow visual comparison between the shape of the small "as prepared" EQE profile and the much larger "HF treated" profile. UV-Vis-NIR absorption spectra of the corresponding nanotube films on glass are shown for comparison. There was no photocurrent response from any device for $\lambda > 1200$ nm.

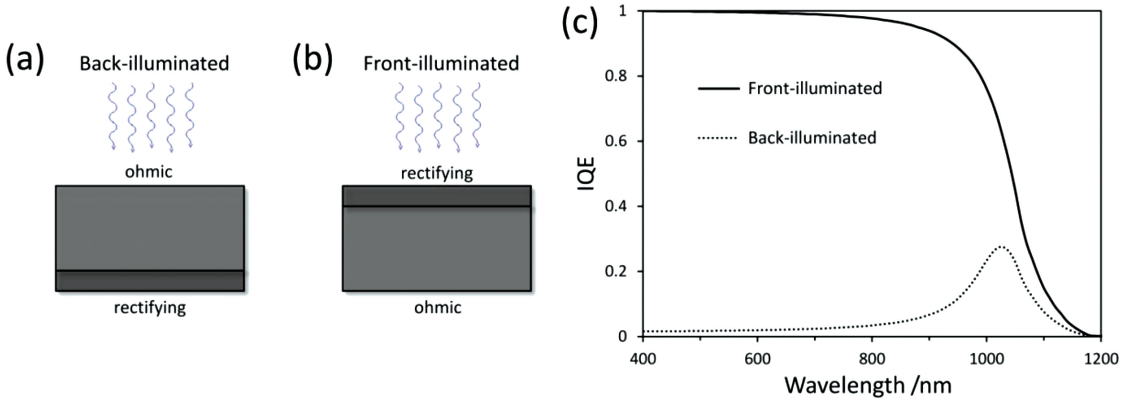

Figure 5. The schematics in (a) and (b) show the two solar cells modelled with back- and front-illuminated rectifying contacts, respectively, and their calculated IQE is shown in (c).

a film is so small that it could not be observed. However, a device made with a much thicker nanotube film not only does not show a contribution from the nanotubes but, rather, shows distinct reductions in efficiency in the regions of the nanotubes' S_{11}, S_{22} and π–π* absorptions (Figure S1). This is expected though since any exciton produced in the nanotube film away from a nanotube-silicon junction would have no driving force for separation and cannot percolate far through the nanotube network in the manner of free charges. Any contribution could only come from the nanotubes in a thin region close to the silicon surface and so a thicker film effectively just gets in the way.

If the nanotubes do not contribute to the photocurrent then it may be that they function primarily as transparent front electrodes. This is possible even for a device made with high purity semiconducting nanotube material as, even without the presence of fluorine resulting from intentional acid treatment, adsorbed oxygen molecules act as p-type dopants. Indeed, for electrode purposes, one would ideally like to use highly doped semiconducting nanotubes (with a Fermi level pushed into the valence or conduction band) in preference to metallic nanotubes.[16] Even if the nanotubes do not contribute to the photocurrent, this would not necessarily mean that the mechanism of action of the devices is not that of a p-n junction. Measurements by Jung[1b] on their carbon nanotube-silicon solar cells indicate that the mechanism is similar to that of a single crystal silicon p-n homojunction. In those devices, removal of the native oxide significantly improved device performance. However, measurements by Jia[1e] on similar devices showed the opposite; that the presence of an interfacial oxide layer improved device performance, indicating an MIS mechanism. These differing results may be related to the structure of the nanotube films in the different devices. In Jia's devices the nanotube bundles were present as a porous, randomly aligned membrane but in Jung's the bundles were very highly aligned by design. The difference could also be due to the different types of nanotube material, their (n,m) species purity or the effects of treatments they received during fabrication. Such apparently conflicting data further illustrates the complexity and diversity of carbon nanotube films and their properties and underscores the need for more work to determine the effect of various films' nanostructure and component nanotube type/species.

3. Conclusion

The photocurrent spectra of carbon nanotube-silicon solar cells fabricated with small and large diameter semiconducting nanotubes do not show any features that could be attributed to photocurrent generation by the nanotubes. This is despite the fact that the nanotubes used in this work were deliberately chosen so that any such contribution should be clearly discernible. Thus the nanotubes in the devices reported herein are not contributing elements of a p-n junction-type solar cell. Photocurrent spectra of carbon nanotube-silicon solar cells fabricated with non-ohmic back contact electrodes do show a similar feature to that which has been elsewhere attributed to photocurrent generation by the nanotubes. However the data herein suggests that this feature arises due to the choice of back contact electrode material. With these understandings in mind, future research endeavours in this field should be largely directed towards exploiting and optimising the application of carbon nanotubes as front contact electrodes. With very high transparency and excellent conductivity, carbon nanotubes are well suited to this purpose and could have the potential to surpass the performance of the current generation of front metallisation strategies via reduced optical shading and enhanced carrier collection over the full solar cell surface.

4. Experimental Section

Two types of SWNT raw materials were used for this study: (i) CoMoCat SWNTs (Sigma-Aldrich) and (ii) SWNTs prepared in-house by pulsed laser vaporisation in an argon atmosphere using carbon targets doped with 1 atom% Ni and Co catalyst and an oven operated at 1000 °C.[17] For the starting suspensions each of the SWNT material (typically 10 mg) was suspended with sodium dodecyl sulphate (SDS) (1 wt.%) in H_2O (15 ml) using a tip sonicator (Bandelin, 200 W maximum power, 20 kHz, in pulsed mode with 100 ms pulses) applied for 2 hr at 20% power. The resulting dispersion was then centrifuged at 100,000 g for 1 hr (Beckmann Coulter) to remove larger agglomerates.

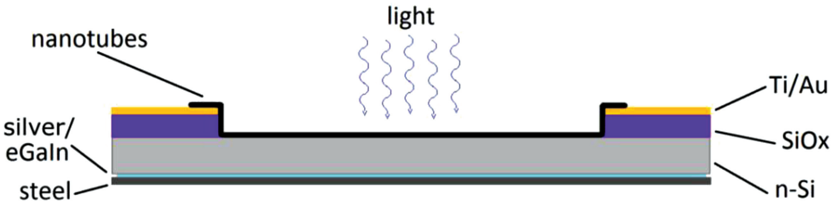

Figure 6. Schematic showing solar cell device structure.

Gel filtration was performed as described by Moshammer[18] using Sephacryl S-200 gel filtration medium (Amersham Biosciences) in a glass column of 20 cm length and 2 cm inner diameter. After filling the glass column with the filtration medium, the gel was slightly compressed to yield a final height of approximately 14 cm. For the separation, SWNT starting suspension (10 ml) was applied to the top of the column and subsequently a solution of SDS (1 wt.%) in H_2O as eluent was pushed through the column by applying sufficient pressure with compressed air to ensure a flow of ~1 ml/min. After ~10 ml of this eluent had been added most of the metallic SWNTs had moved through the column whereas the semiconducting SWNTs remained trapped in the upper part of the gel. After applying a total of 20 ml of SDS solution in this fashion, the metallic nanotubes were completely removed from the gel. By then changing the eluent from SDS (1 wt.%) in H_2O to sodium cholate (2 wt.%) in H_2O the semiconducting SWNTs also subsequently eluted completely from the column and were collected separately in fractions of approximately 1 ml.

Randomly aligned nanotube membranes were prepared similarly to Wu.[19] Briefly, the nanotubes were filtered through mixed cellulose ester (MCE) membranes (0.45 μm, HAWP, Millipore) and rinsed thoroughly with deionised water. Circular regions (0.32 cm^2) of the resulting SWNT-MCE membrane were taken for device fabrication. Phosphorous doped n-type silicon wafers (CZ, 5–25 Ω.cm, <100>, ABC GmbH), polished on one side and with a thermal oxide (100 nm) were diced into pieces (2 cm^2). E-beam lithography (Raith) was used to define square regions (0.09 cm^2) in the negative resist (maN-2403, micro resist technology GmbH, Germany), which was developed and then the front metal contact (Ti/Au, 5/50 nm) was sputtered. Following lift off the oxide in these regions was etched with a reactive ion etcher (50 sccm CHF_3, 5 sccm O_2, 140 W) (Plasmalab 80 Plus, Oxord). The SWNT films were deposited onto the substrate surfaces by placing the circular SWNT-MCE membranes, nanotube side down, centred over the etched holes. The membranes were wetted with deionised water then compressed and baked (80 °C, 15 min). Upon cooling, the substrates were immersed in acetone to dissolve the MCE leaving nanotube membranes of approximately 35 nm in thickness[20] tightly adsorbed onto the substrate surfaces providing 0.09 cm^2 square active areas surrounded by 0.23 cm^2 regions where the nanotube membranes overlap the front metal contacts. After etching of the rear oxide with HF (2%) the devices were completed with silver paste or gallium indium eutectic (eGaIn) back contacts and mounted on steel plates (**Figure 6**).

UV-Vis-NIR spectra of films of sorted nanotube material were recorded with a Varian Cary 500 spectrophotometer. In the transmission measurements of films on silicon, the maximum transmission was 111–116% at 1300 nm due to the uncoated silicon used as a baseline having a greater absorbance than the nanotube coated sample thus the spectra were normalized to 100% at 1300 nm. A similar process was applied to the absorption spectra of films on glass, for the same reason. Photoluminescence excitation (PL) maps of sorted nanotube material in solution were measured in the emission range of 900–1700 nm and excitation range of 500–950 nm (scanned in 3 nm steps) using a modified FTIR spectrometer (Bruker IFS66) equipped with a liquid nitrogen cooled Ge photodiode and a monochromatised excitation light source as described elsewhere.[21] The EQE was measured using a setup consisting of a 450W xenon light source, an optical chopper (47.7 Hz), a 300 mm monochromator (LOT-Oriel), a custom designed current amplifier (DLPCA-S, Femto Messtechnik) and a digital lock-in amplifier (eLockin 203, Anfatec). A modified photoreceiver (OE-200-S, Femto Messtechnik) with a Si/InGaAs sandwich diode was used to monitor the stability of the monochromatic light beam. Initial calibration was carried out with reference silicon and germanium diodes (Thorlabs, NIST traceable calibration).

Supporting Information

Supporting Information is available from the Wiley Online Library or from the author.

Acknowledgements

B.S. Flavel gratefully acknowledges the support of the Alexander von Humboldt Foundation. M.F.G. Klein is further supported by the Karlsruhe School of Optics & Photonics (KSOP).

Received: November 17, 2012
Revised: March 7, 2013

---

[1] a) X. Li, Y. Jung, K. Sakimoto, T.-H. Goh, M. A. Reed, A. D. Taylor, *Energy & Env. Sc.* **2013**; b) Y. Jung, X. Li, N. K. Rajan, A. D. Taylor, M. A. Reed, *Nano Lett.* **2012**, *13*, 95; c) D. D. Tune, B. S. Flavel, R. Krupke, J. G. Shapter, *Adv. Energy Mat.* **2012**, *2*, 1043; d) E. Shi, L. Zhang, Z. Li, P. Li, Y. Shang, Y. Jia, J. Wei, K. Wang, H. Zhu, D. Wu, S. Zhang, A. Cao, *Sci. Rep.* **2012**, *2*, 884; e) Y. Jia, A. Cao, F. Kang, P. Li, X. Gui, L. Zhang, E. Shi, J. Wei, K. Wang, H. Zhu, D. Wu, *PCCP* **2012**, *14*, 8391; f) D. Kozawa, K. Hiraoka, Y. Miyauchi, S. Mouri, K. Matsuda, *Appl. Phys. Express* **2012**, *5*, 042304.

[2] *See reference 10 in [1b].*

[3] a) M. B. Tzolov, T.-F. Kuo, D. A. Straus, A. Yin, J. Xu, *J. Phys. Chem. C* **2007**, *111*, 5800; b) J. Wei, Y. Jia, Q. Shu, Z. Gu, K. Wang, D. Zhuang, G. Zhang, Z. Wang, J. Luo, A. Cao, D. Wu, *Nano Lett.* **2007**, *7*, 2317; c) A. Arena, N. Donato, G. Saitta, S. Galvagno, C. Milone, A. Pistone, *Microelectron. J.* **2008**, *39*, 1659; d) Z. Li, V. P. Kunets, V. Saini, Y. Xu, E. Dervishi, G. J. Salamo, A. R. Biris, A. S. Biris, *Appl. Phys. Lett.* **2008**, *93*, 243117; e) Z. Li, V. P. Kunets, V. Saini, Y. Xu, E. Dervishi, G. J. Salamo, A. R. Biris, A. S. Biris, *ACS Nano* **2009**, *3*, 1407; f) Z. Li, V. Saini, E. Dervishi, V. P. Kunets, J. Zhang, Y. Xu, A. R. Biris, G. J. Salamo, A. S. Biris, *Appl. Phys. Lett.* **2010**, *96*, 033110; g) P. L. Ong, W. B. Euler, I. A. Levitsky, *Nanotechnology* **2010**, *21*, 105203.

[4] a) A. Behnam, J. L. Johnson, Y. Choi, M. G. Ertosun, A. K. Okyay, P. Kapur, K. C. Saraswat, A. Ural, *Appl. Phys. Lett.* **2008**, 92; b) Y. Jia, J. Wei, K. Wang, A. Cao, Q. Shu, X. Gui, Y. Zhu, D. Zhuang, G. Zhang, B. Ma, L. Wang, W. Liu, Z. Wang, J. Luo, D. Wu, *Adv. Mater.* **2008**, *20*, 4594; c) Y. Jia, P. Li, J. Wei, A. Cao, K. Wang, C. Li, D. Zhuang, H. Zhu, D. Wu, *Mater. Res. Bull.* **2010**, *45*, 1401; d) Z. Li, Y. Jia, J. Wei, K. Wang, Q. Shu, X. Gui, H. Zhu, A. Cao, D. Wu, *J. Mater. Chem.* **2010**, *20*, 7236; e) P. Wadhwa, B. Liu, M. A. McCarthy, Z. Wu, A. G. Rinzler, *Nano Lett.* **2010**, *10*, 5001; f) Y. Jia, P. Li, X. Gui, J. Wei, K. Wang, H. Zhu, D. Wu, L. Zhang, A. Cao, Y. Xu, *Appl. Phys. Lett.* **2011**, *98*, 133115; g) P. Wadhwa, G. Seol, M. K. Petterson, J. Guo, A. G. Rinzler, *Nano Lett.* **2011**, *11*, 2419.

[5] a) A. Fujiwara, Y. Matsuoka, H. Suematsu, N. Ogawa, K. Miyano, H. Kataura, Y. Maniwa, S. Suzuki, Y. Achiba, *Jpn. J. Appl. Phys., Part 2* **2001**, *40*, L1229; b) M. Freitag, Y. Martin, J. A. Misewich, R. Martel, P. Avouris, *Nano Lett.* **2003**, *3*, 1067.
[6] J. U. Lee, *Appl. Phys. Lett.* **2005**, *87*, 073101.
[7] a) D. J. Bindl, M.-Y. Wu, F. C. Prehn, M. S. Arnold, *Nano Lett.* **2010**, *11*, 455; b) V. Švrček, S. Cook, S. Kazaoui, M. Kondo, *J. Phys. Chem. Lett.* **2011**, *2*, 1646.
[8] P. G. Collins, K. Bradley, M. Ishigami, A. Zettl, *Science* **2000**, *287*, 1801.
[9] W. Spitzer, H. Y. Fan, *Physical Review* **1957**, *108*, 268.
[10] R. M. Jain, R. Howden, K. Tvrdy, S. Shimizu, A. J. Hilmer, T. P. McNicholas, K. K. Gleason, M. S. Strano, *Adv. Mater.* **2012**, *24*, 4436.
[11] K. Kim, J. Ryu, C. Lee, J. Jang, K. Park, *J Mater Sci: Mater Electron* **2009**, *20*, 120.
[12] P. Basu, H. Saha, *Phys. Status Solidi A* **1976**, *37*, 625.
[13] J. A. del Alamo, R. M. Swanson, *Solid-State Electron.* **1987**, *30*, 1127.
[14] M. A. Green, M. J. Keevers, *Prog. Photovoltaics* **1995**, *3*, 189.
[15] R. J. Soukup, L. A. Akers, *J. Appl. Phys.* **1978**, *49*, 4031.
[16] A. G. Rinzler, E. P. Donoghue, *ACS Nano* **2011**, *5*, 3425.
[17] S. Lebedkin, P. Schweiss, B. Renker, S. Malik, F. Hennrich, M. Neumaier, C. Stoermer, M. M. Kappes, *Carbon* **2002**, *40*, 417.
[18] K. Moshammer, F. Hennrich, M. M. Kappes, *Nano Res.* **2009**, *2*, 599.
[19] Z. Wu, Z. Chen, X. Du, J. M. Logan, J. Sippel, M. Nikolou, K. Kamaras, J. R. Reynolds, D. B. Tanner, A. F. Hebard, A. G. Rinzler, *Science* **2004**, *305*, 1273.
[20] D. D. Tune, B. S. Flavel, J. S. Quinton, A. V. Ellis, J. G. Shapter, *ChemSusChem* **2013**, 10.1002/cssc.201200600.
[21] S. Lebedkin, F. Hennrich, O. Kiowski, M. M. Kappes, *Phys. Rev. B: Condens. Matter Mater. Phys.* **2008**, *77*, 165429.

– This page intentionally left blank –

2.3 Carbon Nanotube Silicon Solar Cells

2.3.4 *Nanotube Film Metallicity and its Effect on the Performance of Carbon Nanotube-Silicon Solar Cells*

D. D. Tune, A. J. Blanch, R. Krupke, **B. S. Flavel**, J. G. Shapter

Phys. Status Solidi A (2014) 1479–1487

DOI: 10.1002/pssa.201431043

Abstract

Research into silicon solar cells that use a thin film of single walled carbon nanotubes as the front electrode is an important area of increasing research activity. This paper provides the first ever direct performance comparison between devices fabricated with either semiconducting, metallic or mixed nanotubes to probe the effect of the semiconducting/metallic nature, or 'metallicity', of the nanotube film on solar cell performance and properties. HiPco nanotube material sorted using the gel chromatography technique is highly purified in either metallic or semiconducting nanotube species. The solar cells fabricated with the metallic nanotubes greatly outperform their semiconducting or mixed counterparts. The operating mechanisms underlying this observation and its implications in regards to current understanding are discussed in light of recent literature. Dramatic increases in performance as well as substantial changes in the effect of metallicity due to subsequent hole doping of the sorted nanotube films are also demonstrated. Using highly pure semiconducting and metallic carbon nanotubes, film metallicity is shown to be a vital factor in the performance of carbon nanotube–silicon solar cells.

Contribution

B.S.F, D.D.T and J.G.S conceived the idea for the project. B.S.F, D.D.T and A.J.B performed the experiments and all authors were involved in the preparation of the manuscript.

– This page intentionally left blank –

ISSN 1862-6300
Phys. Status Solidi A
211 · No. 7 July
1473–1680 (2014)

physica status solidi a

www.pss-a.com

applications and materials science

7
2014

Advanced Materials Physics

Nanotube film metallicity and its effect on the performance of carbon nanotube–silicon solar cells

Daniel D. Tune, Adam J. Blanch, Ralph Krupke, Benjamin S. Flavel, and Joseph G. Shapter

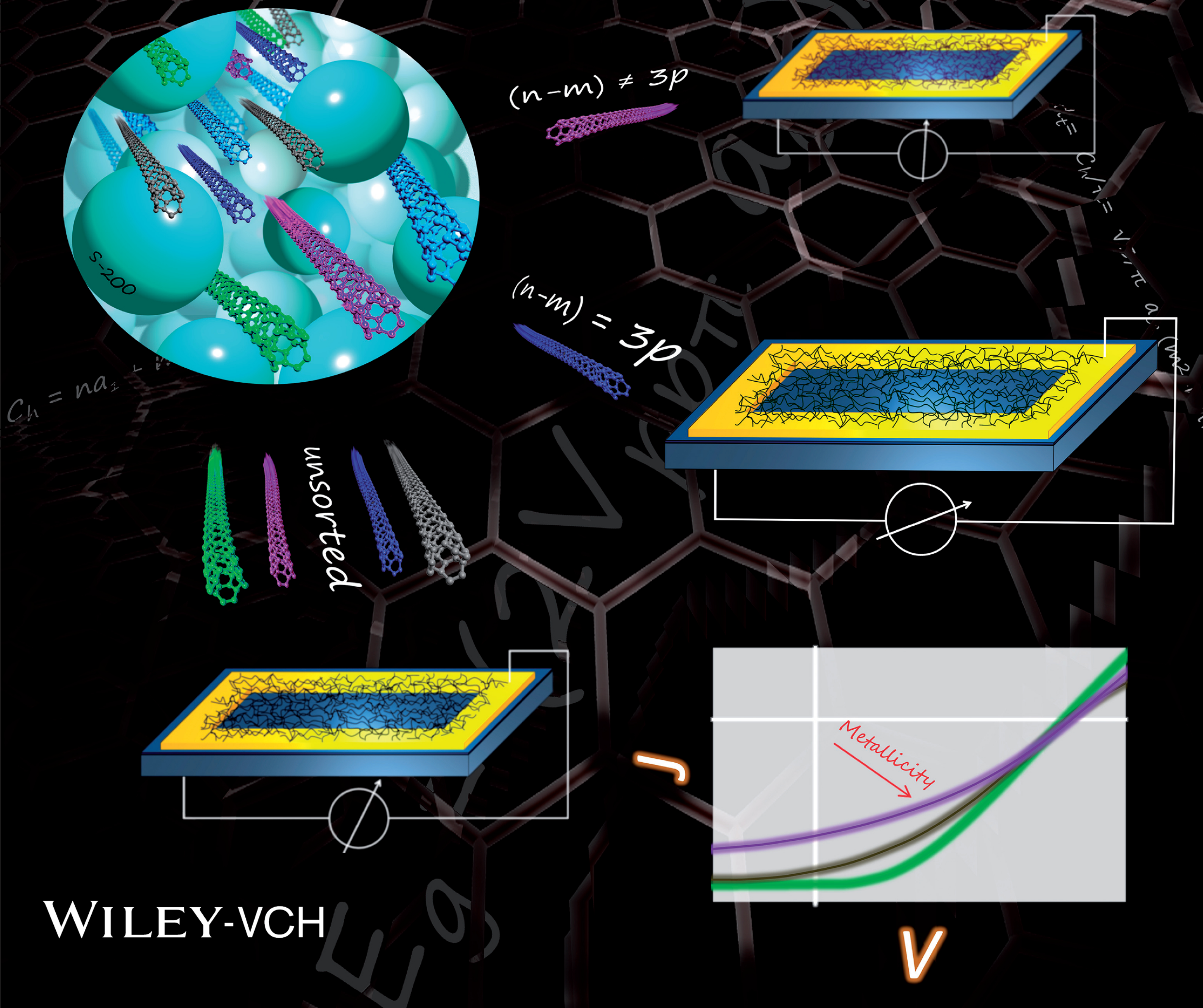

WILEY-VCH

– This page intentionally left blank –

Phys. Status Solidi A **211,** No. 7, 1479–1487 (2014) / **DOI** 10.1002/pssa.201431043

physica status solidi a
www.pss-a.com
applications and materials science
Advanced Materials Physics

Nanotube film metallicity and its effect on the performance of carbon nanotube–silicon solar cells

Daniel D. Tune[1], Adam J. Blanch[2], Ralph Krupke[3,4,5], Benjamin S. Flavel[,3], and Joseph G. Shapter*[,1]**

[1] Centre for Nanoscale Science and Technology (CNST), The Flinders University of South Australia, SA 5042, Australia
[2] Department für Physik und Center for Nanoscience (CeNS), Lehrstuhl für Photonik und Optoelektronik, Ludwig-Maximilians-Universität München, Amalienstr. 54 (2nd Floor), 80799 München, Germany
[3] Institute of Nanotechnology (INT), Karlsruhe Institute of Technology (KIT), 76021 Karlsruhe, Germany
[4] DFG Centre for Functional Nanostructures (CFN), Karlsruhe Institute of Technology (KIT), 76131 Karlsruhe, Germany
[5] Institute of Materials Science, Technische Universität Darmstadt, 64287 Darmstadt, Germany

Received 22 January 2014, revised 21 March 2014, accepted 25 March 2014

Keywords carbon nanotubes, doping, photovoltaic devices, solar cells, thin films

---

* Corresponding author: e-mail joe.shapter@flinders.edu.au, Phone: +61 8 8201 2005, Fax: +61 8 8201 2905
** e-mail benjamin.flavel@kit.edu, Phone: +49 721 608 26977

Research into silicon solar cells that use a thin film of single walled carbon nanotubes as the front electrode is an important area of increasing research activity. This paper provides the first ever direct performance comparison between devices fabricated with either semiconducting, metallic or mixed nanotubes to probe the effect of the semiconducting/metallic nature, or 'metallicity', of the nanotube film on solar cell performance and properties. HiPCO nanotube material sorted using the gel chromatography technique is highly purified in either metallic or semiconducting nanotube species. The solar cells fabricated with the metallic nanotubes greatly outperform their semiconducting or mixed counterparts. The operating mechanisms underlying this observation and its implications in regards to current understanding are discussed in light of recent literature. Dramatic increases in performance as well as substantial changes in the effect of metallicity due to subsequent hole doping of the sorted nanotube films are also demonstrated.

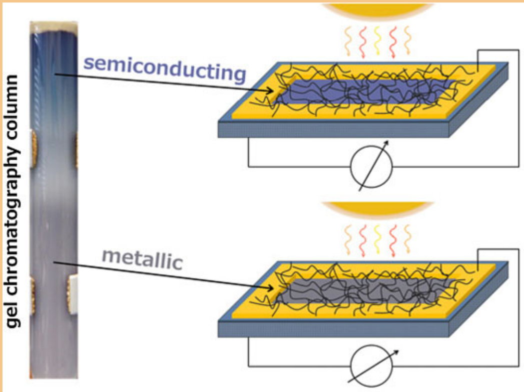

Using highly pure semiconducting and metallic carbon nanotubes, film metallicity is shown to be a vital factor in the performance of carbon nanotube–silicon solar cells.

1 Introduction Reliance on silicon is ubiquitous in the modern world however material limitations require the incorporation of a range of other materials with desirable properties that can be exploited at the nanoscale where several size-related drawbacks of bulk silicon begin to dominate the usefulness of the material, particularly the well-known heat production and dissipation issues affecting microelectronics. Heterojunctions between single walled carbon nanotubes (SWCNTs) and silicon are predicted to be technologically important, having broad application in a variety of fields and receiving increasing attention [1]. Although there have been major fundamental advances there there is still much to be understood to enable the promise of a fruitful marriage between established silicon technology and the carbon newcomer. For many years, a major factor limiting progress in the understanding and application of SWCNT–silicon heterojunctions has been the polydispersity of as-produced SWCNT material. Whilst technological routes to the separation or sorting of SWCNTs by (n,m) species have been known for some time [2], production has predominantly been in small research quantities and there has been slow progress in scale-up, although several recent refinements to chromatographic separation methods may offer practical solutions. These include tailoring the tube–gel interaction through temperature control [3], pH variation [4] and surfactant concentration [5], as well as advances in fundamental understanding of the interactions [6].

A promising application of SWCNT–silicon heterojunctions is in photovoltaic devices [7]. Interest in this field has been growing rapidly in the last few years and SWCNT–silicon solar cells have seen very significant performance gains, with recent reports of dry-state, small area efficiencies from Jia et al. [8] (2011, 10.9%), Jung et al. [9] (2012, 11.2%) and Shi et al. [10] (2012, 15%). There has been work towards revealing the mechanism of action of these devices [11–15], numerous papers involving performance improvement through optimisation of device structure parameters [16, 17] and the effect of doping the nanotube films [18, 19], as well as other reports of novel ways to improve upon the basic SWCNT–silicon design [20, 21]. However, in some respects the data is apparently conflicting; with reports suggesting that the mechanism is either that of a p–n, Schottky or metal–insulator–semiconductor (MIS) junction. Confusion may be arising as a result of the complexity and diversity of SWCNT films, their metallicity, various nano- and microstructures, component species and the effect of any treatments they receive during device fabrication. Also, the literature reveals that the particular physical structures of the SWCNT–silicon junctions present in a device are vital characteristics in terms of performance, and perhaps operating mechanism. For example, devices that use vacuum filtration and spray deposited films are inevitably quite porous, containing holes that generate a range of junction types depending on fabrication conditions and treatment methods. These include SWCNT–Si, SWCNT–SiO_2–Si and SWCNT–SiO_x–Si, as well as the SiO_2–Si and/or SiO_x–Si junctions present on the surface regions where none of the SWCNTs make contact with the underlying silicon. Pintossi et al. [22] recently showed that while the presence of SiO_2 between the SWCNTs and the silicon is beneficial, the presence of SiO_x is certainly not. Much of the data derived from such ‘patchy’ films supports a Schottky operating mechanism. On the other hand, the use of highly aligned SWCNT films [9, 15, 23] produces a more conformal coverage of the silicon which enhances the quality of the diode [21], narrows the polydispersity of junction types and greatly increases the number of SWCNT–Si junctions, not to mention significantly increasing the conductivity of the film and reducing the recombination current through minimisation of charge traps and intertube barriers. Of these, the reports by Li et al. [15], and Jung et al. [9], which use very highly aligned films produced by the ‘sliding-coating’ method derived from Saha et al. [24], strongly support a p–n mechanism.

Most of the literature so far has used mixtures of nanotube types. As a step towards more fully understanding the role of SWCNT film metallicity in these devices, this report details the first direct performance comparison between SWCNT–silicon heterojunction solar cells fabricated with unsorted (u-SWCNTs) and sorted metallic (m-SWCNT) and semiconducting (s-SWCNT) material. Additionally, a remarkably different effect is observed between the three systems upon p-type doping of the SWCNT films using an electron withdrawing chemical treatment ($SOCl_2$).

2 Experimental Vacuum filtration films of mixed and type-sorted SWCNTs with significantly different optical spectra (Fig. S1, see Supporting Information, online at www.pss-a.com) were used to fabricate solar cells and also deposited on glass and silicon to allow optical, Raman and AFM characterisation as well as measurement of the sheet resistance. For each material type, three different optical densities were used; roughly corresponding to average transmittances in the visible/NIR of $T_{av} = 96\%$, 90% and 84% (see Fig. S2, Supporting Information). Each solar cell was made in duplicate and solar cell parameters are averaged from both devices with the standard deviation most often contained within the extent of the data point markers.

SWCNT dispersions were generated from solutions (25 ml) of SDS (either 2% or 0.5% w/v as indicated) containing HiPCO SWCNTs ($1\,mg\,ml^{-1}$) via tip ultrasonication (Sonics VCX 750 W) for 45 min. Sonication (20 kHz) was performed with a Ti microtip (6.5 mm) operating at 22% of the maximum amplitude (corresponding to a power input of approximately $0.4\,W\,ml^{-1}$) [25]. Samples were cooled with ice water during exposure to ultrasound and were ultracentrifuged directly after sonication. Ultracentrifugation was carried out at fixed angle (90 min, 40500 rpm, approx. 120×10^3 g) in an ultracentrifuge (Optima L-100XP, Beckman–Coulter), with the upper 75–85% of the supernatant collected via pipette. U-SWCNT films were prepared from this supernatant after dilution.

For metal–semiconductor separation, the gel chromatography technique was used [36]. SWCNTs dispersed in aqueous SDS (0.5% w/v) were used as a starting solution. This concentration was selected as it has been found to provide the best metal–semiconductor separation for the HiPCO distribution [5]. A glass column with a fritted disc was filled with Sephacryl S-200 HR (*N*,*N*′-methylenebisacrylamide cross linked allyl-dextran; 25–75 μm diameter) gel bead solution (30 ml) to give a bed height of approximately 22 cm. The gel was first washed with DI water (30 ml) followed by aqueous SDS (30 ml, 0.5% w/v) before addition of the SWCNT solution (10 ml). Elution was facilitated by application of unregulated nitrogen flow to the top of the column, giving a variable flow rate (0.5–0.8 $ml\,min^{-1}$). The flow through eluate was collected with the addition of SDS solution (15 ml, 0.5% w/v) to the column until the coloured mobile band was observed to be completely eluted. This flow through solution is very highly enriched in metallic species and was therefore used to prepare m-SWCNT films.

Although it is possible to collect the s-SWCNT fraction in this process by further eluting the SWCNT material that is adsorbed to the gel, this would provide a large number of different SWCNT species with varied optical properties. To obtain a semiconducting fraction of significantly reduced chirality distribution, the gel separation process was performed again in a manner similar to that in reference [26]. In this case, SWCNTs dispersed in aqueous SDS (2% w/v) were used as the starting suspension with less of the gel beads (0.6 ml), providing a thin gel bed. The gel was washed with DI water and SDS solution (2% w/v) prior to addition of SWCNT solution (10 ml), which was passed through the gel bed and collected. The gel was then washed with DI water and SDS solution (6 ml, 2% w/v) before changing the eluent to aqueous sodium deoxycholate (DOC) (0.5% w/v). The s-SWCNTs are desorbed from the gel in this surfactant and were collected (3 ml aliquot). The gel bed was then flushed by DI water and SDS solution (2% w/v) before repeating this procedure, re-using the same original SWCNT dispersion to generate a second semiconducting fraction. Three such fractions were collected before replacing the gel and collecting additional fractions. Suspensions of the unsorted material and the enriched fractions were diluted in DI water (150 ml) and this was used to prepare films.

Randomly aligned SWCNT films were prepared similarly to Wu [27] and Hu [28]. The required volume of SWCNT suspension (see Fig. S3, Supporting Information) was diluted with DI water and then filtered onto large pore mixed cellulose ester (MCE) 'target' membranes (0.45 μm, HAWP, Millipore) over a smaller pored 'stencil' membrane (25 nm, VSWP, Millipore). The large difference in flow rates between target and stencil allows the fabrication of well-defined film shapes on the target membrane. The films made this way are highly reproducible and the thickness/optical density are precisely controllable by varying the concentration and/or volume of SWCNT suspension, with the additional benefit of minimising wastage of SWCNT material. The SWCNT films were rinsed thoroughly with DI water (3 × 50 ml, then 250 ml). Circular regions (0.32 cm^2) of the resulting SWCNT-MCE membrane were taken for device fabrication.

Phosphorous doped n-type silicon wafers (CZ, 5–25 Ω cm, ⟨100⟩, SSP, ABC GmbH) with a thermal oxide (100 nm) were diced into rectangular pieces (1 × 1.5 cm^2). UV photolithography was used to define circular regions (0.08 cm^2) in a positive resist (AZ1518, micro resist technology GmbH), which was developed and then the front metal contact (Ti/Au, 5/145 nm) was sputtered (Fig. 1). Following lift off the oxide in these regions was removed with buffered oxide etch. The SWCNT films were deposited onto the substrate surfaces by placing the circular SWCNT-MCE membranes, SWCNT side down, centred over the etched holes. The membranes were wetted with DI water then compressed and baked (80 °C, 15 min). Following cooling, the substrates were immersed in acetone (1 h) to dissolve the MCE. After removal from this first acetone bath and drying with N_2, the devices were washed in a further three baths of fresh acetone (1 h each) and with mild stirring of the solvent. After the final drying with N_2, substrates were obtained with SWCNT membranes tightly adsorbed onto their surfaces providing circular active areas (0.08 cm^2) surrounded by toroidal regions (0.24 cm^2) where the SWCNT membranes overlap the front metal contacts. After etching of the rear oxide the devices were completed with gallium indium eutectic (eGaIn) back contacts and mounted on steel plates (2 cm^2). The solar cells thus produced are called 'as-prepared'.

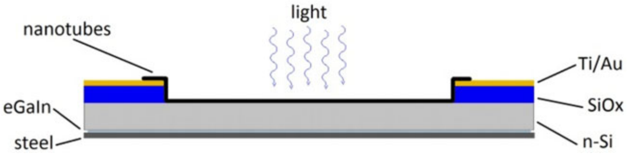

Figure 1 Solar cell device structure.

UV–Visible–NIR absorbance spectra of the SWCNT films were measured using a spectrophotometer (Cary50, Varian) by passing the beam through films mounted on glass. Simple background subtraction was performed using the absorbance spectra of the glass substrates. Transmittance spectra were calculated post-measurement from the absorbance data. Sheet resistance measurements were taken from the same films using a four point probe (KeithLink) in linear geometry and a multimeter (GDM-8261, GW Instek). Photoluminescence (PL) excitation maps of sorted nanotube material in solution were measured (emission range of 900–1700 nm, excitation range of 500–950 nm, scanned in 3 nm steps) using a modified FTIR spectrometer (Bruker IFS66) equipped with a liquid nitrogen cooled Ge photodiode and a monochromatised excitation light source.

3 Results and discussion

Photoluminescence (PL) measurements taken of aqueous suspensions of the three types of SWCNT material (Fig. 2) show that they are composed of distinctly different populations. The unsorted material contains the expected large range of chiralities with $S_{11} < 1400$ nm (the measurement cut-off due to water absorption). The PL process involves absorption of a high energy photon through S_{22}, followed by decay of the excited state to S_{11} and then radiative relaxation down to the ground state. Naturally, m-SWCNTs cannot be observed by this technique because (a) there is no M_{22} in the practical range of measurement and (b) even if there were, non-radiative recombination is by far the dominant mechanism. However, the m-SWCNT PL data are still important in that it indicates the metallic purity of the m-SWCNT fraction or, more correctly, the lack of semiconducting species. The s-SWCNT fraction is dominated by the (6,5) nanotube, but also with significant amounts of (6,4), (7,5), (7,6) and traces of others.

Current–voltage measurements obtained from solar cells fabricated with the three different kinds of SWCNT starting material (Fig. 3a–c) show remarkably different output characteristics (summarised in Table S1, Supporting Information). The devices made with m-SWCNTs clearly

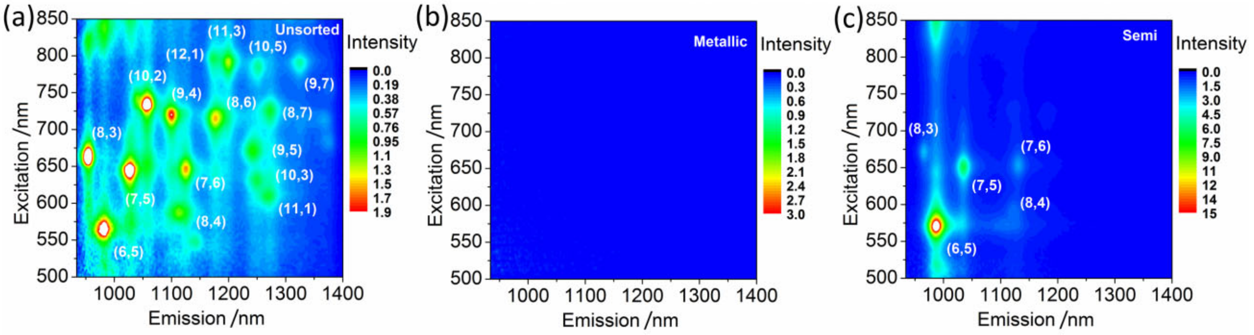

Figure 2 Photoluminescence maps of (a) unsorted, (b) metallic and (c) semiconducting SWCNT material. Note that m-SWCNTs cannot be observed by this measurement, see text.

outperform their semiconducting and unsorted counterparts. This is despite great care being taken to ensure that the amount of material (optical density) in the different films is comparable (Fig. 3d–f). The reasons for these differences in performance are quite complex. In the case of the semiconducting material and the devices with the thinnest of the unsorted films it can easily be argued that the poor performance is due to the very high sheet resistance (R_{sheet}) of those films, in the MΩ range (Fig. 3g–i), which causes a high series resistance (R_{s}) in the resulting devices – a dependence that has been observed previously [17]. However, this reasoning fails when trying to rationalise the approximately 20× greater power conversion efficiency (PCE) when using metallic versus unsorted SWCNTs in the thicker film devices (which have comparable R_{sheet}). Furthermore, the fact that R_{sheet} is relatively the same for the unsorted and metallic devices with the thicker films (U-84 and M-84), yet R_{s} is around 3× larger in the unsorted devices, means that other factors must be involved.

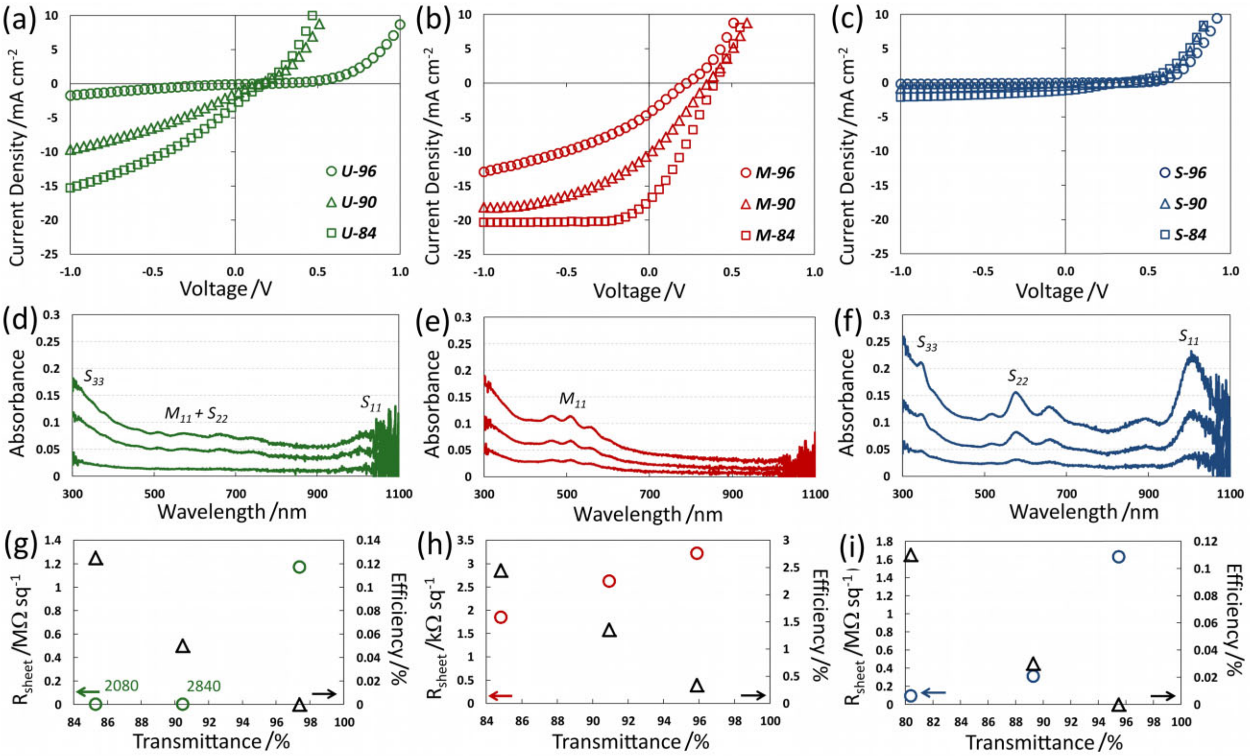

Figure 3 Current–voltage characteristics of as-prepared solar cell devices made with either (a) unsorted (denoted 'U'), (b) metallic (M) or (c) semiconducting (S) SWCNT material at three different optical densities (approximately 96%, 90% and 84% transmittance). (d–f) Show the corresponding UV–Vis–NIR absorption spectra (obtained from SWCNT films on glass) and (g–i) show the variation of R_{sheet} and PCE as a function of SWCNT film transmittance. Noise in the longer wavelength region of the optical spectra is simply an artefact of the instrument near its upper limit.

Comparison of the first transition peak positions shown in the UV–Vis–NIR measurements (Fig. 3e and f) with the data from Hároz et al. [29] and Weisman et al. [30] indicates that the species in the m-SWCNT HiPCO material could be the (7,7), (8,8) and (9,9), and correlates well with PL measurements for the s-SWCNTs. Thus, although the u-SWCNT material contains a distribution of SWCNT diameters, the m-SWCNT and s-SWCNT diameters are relatively similar and so the performance differences are not due to diameter. Also, AFM measurements show that the morphology of the films, including thickness, bundle size, level of connectivity and degree of alignment (none), is comparable for similar optical densities (Figs. S5–S8, Supporting Information). So, if not due to simple morphological differences in the films, the substantial difference in output characteristics must arise as a result of some other differences between the SWCNT films used.

The unsorted material was suspended with sodium dodecyl sulphate (SDS) and the m-SWCNT material was suspended and eluted with SDS, however, the s-SWCNT material was suspended in SDS but eluted by the addition of sodium deoxycholate (DOC) and it is conceivable that this may in some way give rise to the observed performance differences. However, it must be noted that, (a) the films were thoroughly rinsed with a very large volume of DI water and this is expected to remove much surfactant, (b) films produced with DOC have been shown to outperform, in terms of electrical characteristics, those made with SDS due to improved fine structure (smaller bundles, better connectivity) [31], although this was not observed for these filtered films where the inherent effect of aggregation due to filtering through defined pores dominates the effect of different surfactants on the film structure and, (c) the brief acid treatment and ethanol rinse applied to the films/devices prior to measurement is expected to also desorb surfactant molecules.

It seems likely then that the differences in output characteristics are caused by inherent differences in the SWCNTs. Considering the density of states (DOS) of s-SWCNTs, silicon and m-SWCNTs shown in Fig. 4, it is clear that an energy diagram for these devices is not a trivial matter. One may (boldly) draw up the (S_{11}) band alignment of the s-SWCNT/silicon interface as a classical p–n junction but in the case of m-SWCNTs, the M_{11} transition shown in Fig. 4(c) is an optical transition only – despite the existence of the Van Hove singularities (VHSs) this is not a semiconducting material and should thus never form a semiconductor–semiconductor p–n junction. Furthermore, the single particle model shown in Fig. 4(a) and Fig. 4(c) is a simplification; the SWCNT's absorption properties are in fact entirely excitonic in nature [32]. It may be that in such a simplified model the junction-defining characteristics are not retained.

If unavoidable p-type doping of the SWCNTs by adsorbed oxygen molecules is assumed to shift the SWCNT Fermi energy down by a modest 100 meV (a reasonable figure for large bandgap SWCNTs) [33] then the difference in Fermi energies between the moderately doped n-type silicon and the (6,5) s-SWCNTs is approximately $4.6 - 4.26\,\text{eV} = 0.34\,\text{eV}$. This difference presumably causes the formation of a built-in potential, V_{bi}, upon contact between the two materials, which in turn sets an approximate limit on the open circuit voltage, V_{OC}, and this correlates well with that measured from devices (0.33 V for S-84 devices). The V_{OC} of the metallic devices tended towards a higher value of 0.45 V with increasing film thickness. The distribution of species in the unsorted material, and thus conduction/valance state and first excitonic transition energies, will surely give rise to the formation of intertube energy barriers and localised charge traps in the film. This will contribute to an enhanced recombination current that will reduce the device potential under illumination. This is both the likely cause of the lower V_{OC} of 0.19 V and a likely contributor to the approximately 3× greater R_{s} in the thicker unsorted (U-84) versus metallic (M-84) devices, which have very similar R_{sheet} of 2.08×10^3 and $1.85 \times 10^3\,\Omega\,\text{sq}^{-1}$,

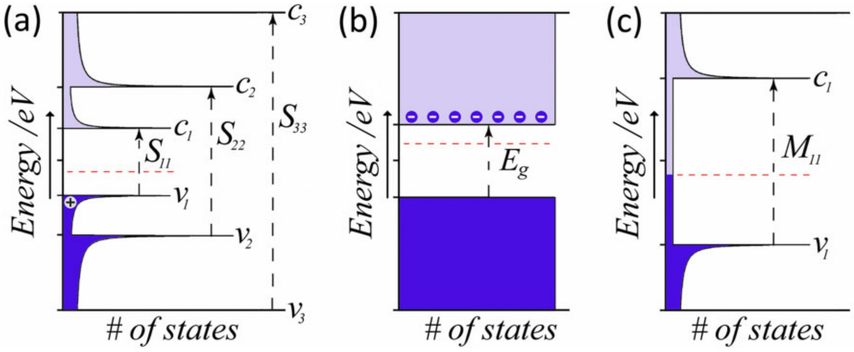

Figure 4 Density of states of the (a) s-SWCNTs, (b) bulk silicon and (c) m-SWCNTs used in devices. The valance (v_i) and conduction (c_i) states (or HOMO and LUMO levels) are indicated in the SWCNTs, as are the optical transitions giving rise to the S_{ii} and M_{11} excitons. The bandgap energy (E_g) of silicon is 1.12 eV and the Fermi energy is indicated by dashed lines. The Fermi energy in the silicon is shifted up by around 0.25 eV due to the moderate n-doping whilst that of the SWCNTs is shifted down slightly to account for p-type doping by adsorbed oxygen molecules [33].

respectively. The fill factor (FF) is roughly the same for all three kinds of SWCNTs (likely limited by the high R_s). However, the reverse saturation current density, J_0, through the metallic devices, which depends on the quality of the diode, is over an order of magnitude lower than through the unsorted, and over two orders lower than through the semiconducting devices. That is, it follows the trend m-SWCNT < u-SWCNT < s-SWCNT (where a lower J_0 entails better performance). This is consistent with the observation that, whatever the operating mechanism, the width and homogeneity of the space charge region set up in the silicon, and thus the quality of the diode, will depend heavily on the initial carrier concentration at the Fermi level of the SWCNT, which follows the trend m-SWCNT > u-SWCNT > s-SWCNT. As well, a visual inspection of the current–voltage curves in the reverse bias regime suggests that, at least in the thicker film devices, the m-SWCNT devices are better at maintaining charge separation (slope around 0). In short, the performance of the solar cells follows the trend in SWCNT film metallicity with the m-SWCNT solar cells significantly outperforming the unsorted devices, which in turn outperform the semiconducting devices.

The situation becomes remarkably different after the application of the powerful organic oxidiser, $SOCl_2$, to the SWCNT films (Fig. 5). Following treatment with $SOCl_2$ there is almost complete bleaching of the S_{11} absorption and a substantial decrease in the intensity of S_{22} and this is consistent with electron transfer from the top of the SWCNT valance states to the organic oxidiser [34]. The electron withdrawing nature of this treatment has a strong p-type doping effect on the SWCNTs and has been repeatedly shown to greatly improve SWCNT film conductivity [35, 36], and the performance of similar solar cells made with them [17, 18]. This is clearly in evidence here; the s-SWCNT and u-SWCNT films underwent decreases in R_{sheet} of 2–3 orders of magnitude, depending on film thickness. Concurrently, around a 20× improvement in s-SWCNT device efficiency (0.11–2.01% for S-84) was observed, and around 35× improvement in u-SWCNT device efficiency (0.13–4.51% for U-84), accompanied by relatively similar increases for the thinner film devices. It should not be possible to p-dope the m-SWCNTs down into the VHS by chemical doping alone (an increase in the work function of about 1.2 eV!) and this is confirmed in this case by the lack of observation of M_{11} bleaching seen in the UV–Vis–NIR (Fig. 5e). Therefore, unlike in the case of u-SWCNT and s-SWCNTs, the p-doping should not significantly alter the density of states at the Fermi level (see Fig. 4c). The $SOCl_2$ lowers the contact resistance at the tube–tube junctions, tightening the bundles as observed by M_{11} peak broadening in Fig. 5e. These two effects should improve the conductivity of the film, but not nearly to the same degree as shifting the Fermi energy fully into a VHS. This is commensurate with the observation of only relatively minor improvements in R_{sheet} (around 10–70%, depending on thickness) and PCE (2.45–4.51% for M-84) for the m-SWCNT films/devices. The improvements in PCE are

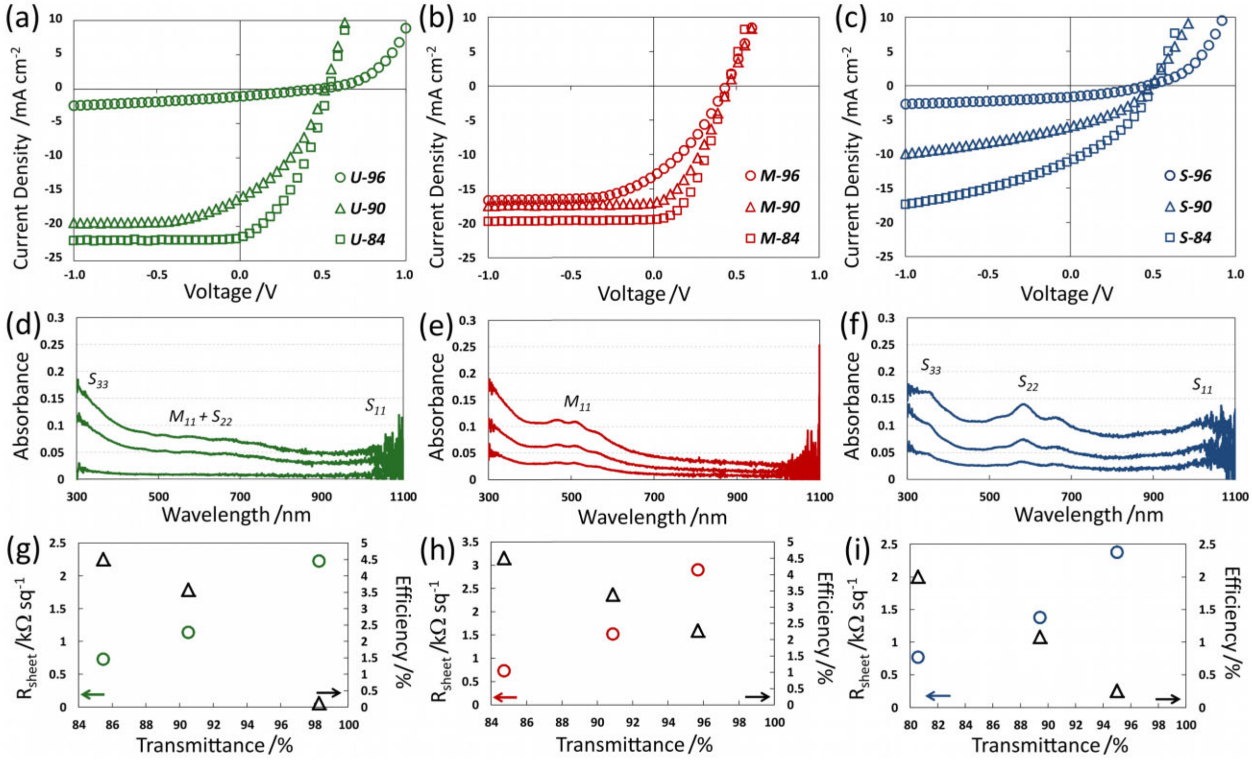

Figure 5 Current–voltage output of solar cells, optical absorption and R_{sheet} of SWCNT films, after doping with $SOCl_2$.

well correlated with measured improvements in R_{sheet} of the SWCNT films while changes in the trends in efficiency with film transmittance (comparing Fig. 3g–i and Fig. 5g–i) exactly match changes in the corresponding trends in R_{sheet}, i.e. the very noticeable change for the unsorted and semiconducting films from nonlinear before treatment to distinctly linear after (the trend in the m-SWCNT film R_{sheet} with transmittance remained linear).

The $SOCl_2$ treatment greatly increases carrier (hole) density, reducing energy barriers at tube-tube junctions [36] and switching the conduction mechanism from thermionic emission over tube-tube barriers to tunnelling through them [37]. The fact that R_{sheet} of the thinner m-SWCNT films remained relatively unaffected after treatment compared to the other films is consistent with the fact that the metallic film conductivity was not initially limited to any great degree by low carrier density at the Fermi level, unlike the semiconducting and unsorted films. It is more likely that the metallic films were already limited instead by their density, degree of (mis)alignment and level of connectivity, which then also become the limiting factors in the semiconducting and unsorted SWCNT films after the $SOCl_2$ treatment. However, despite the obvious huge changes in SWCNT film conductivity, R_{sheet} of the three thickest films is, conveniently, almost identical (726, 727 and 768 $\Omega\,\text{sq}^{-1}$ for unsorted, metallic and semiconducting, respectively). This precludes the improved conductivity due to the $SOCl_2$ treatment as the only contributor to the observed differences between device types.

One striking difference after treatment is that both J_{SC} and V_{OC} of the unsorted SWCNT solar cells are now higher than their metallic counterparts, although the FF values are lower in the unsorted, which results in solar cells of both types being equally efficient (at 4.5%). This may be because the complex mixing of states in the films' DOS means that the average carrier density in the unsorted films is now higher at the new Fermi energy since these films contain a proportion of s-SWCNTs doped into their VHS, providing a higher carrier density than is attainable in the m-SWCNTs [38]. Considering the nanoscale dimension of the basic material elements and their presumably homogeneous physical mixing in the film as well as their high conductivity, particularly after doping, it is not unreasonable that the bulk material properties may be an average of those of the individual SWCNT species. Thus, in some respects, the SWCNT films behave like an alloy – where the electrical properties of the composite can exhibit features not found in any single component. In this case, it may be possible to fabricate SWCNT films with specifically tailored properties provided by defined compositional ratios of two or more SWCNT species. With a plethora of SWCNT species, each with their own peculiar electronic structure and resulting varieties of SWCNT–silicon heterojunction properties, there is great opportunity for exploration and leverage of such characteristics in future solar cells and electronic devices.

As mentioned, there is some disagreement as to the underlying photovoltaic mechanism of action of SWCNT–silicon junctions, be it p–n, Schottky or MIS, and this must be addressed in light of the results of the mixed/metallic/semiconducting comparison described herein. A small increase in the quantum efficiency at wavelengths corresponding to the SWCNTs has been reported by Del Gobbo et al. [13] and by Ong et al. [11] This could be due to a p–n mechanism, or possibly a photoconductive effect improving performance (an hypothesis supported by the fact that the contribution in Ref. [13] was only observed to correspond to metallic nanotubes). An absence of SWCNT contribution to photocurrent, despite careful attempts to reveal it, has also been reported [14], but this does not necessarily preclude a p–n mechanism as a p–n junction may exist (with the SWCNTs taking the role of the p-type material) even without observing a photocurrent response from the SWCNTs if the conduction band energy offset at the SWCNT-Si heterojunction is large enough to allow for rectification, but not large enough to overcome the exciton binding energy. In other words if the change in electron affinity between the SWCNT and Si does not exceed the SWCNT exciton binding energy then there should be no driving force for splitting the exciton into separable charge, but the change in electron affinity may be sufficient to establish a p–n diode. Nonetheless, it is unclear how the function of the m-SWCNT devices could be explained in this context, or indeed the $SOCl_2$ treated s-SWCNT devices, in which the doping has produced significant metallic character. In the work of Jung et al. [9], the activation energy, E_a, of the SWCNT–silicon solar cells was determined to be 1.12 eV, the same as the silicon bandgap. In the conventional understanding this indicates that it is the silicon that produces the photocurrent and therefore a p–n junction mechanism applies. Of course, this also indicates that it is not the s-SWCNTs that take the role of the p side of the active junction because $E_a = E_g$ should only occur for a silicon p–n homojunction [39] (or if the bandgap of the nanotubes just happens to be exactly the same as silicon, which is unlikely in general and certainly not the case in the Jung et al. work, which used mixed SWCNTs). Additionally, even if the SWCNTs do not act as the p-type material in a p–n junction, this does not necessarily preclude an underlying p–n mechanism for the devices because this mechanism also underlies the MIS system [40], where the active junction exists between the silicon bulk and the inversion layer created adjacent to the oxide.

However, our understanding of the underlying physics of Schottky barriers shifted around the turn of the century, as summarised by Tung.[41]. In light of this, the question of how large a Schottky barrier can actually be may be revisited. Sze [39] and Tung [41] make it clear that the height of the activation barrier is not a good criteria for differentiating between a Schottky and p–n junction. It turns out that if the Fermi level pinning between the silicon and the 'metal' is absent then the Schottky barrier can become as large or even larger than the band gap of silicon. Often this is not observed with elemental metals and alloys because of interface dipoles pinning the Fermi level, but if those dipoles are not there then the Schottky barrier height simply scales with the work function of the metal. Interestingly, from SWCNT/metal junctions we know that Fermi level pinning is absent and Barone et al. [42] showed that the work function of SWCNTs can vary at least from 3.9 to 5.2 eV depending on doping. Also, Tongay et al. [43] confirms the absence of Fermi level pinning in HOPG-nSi junctions and it is pointed out that the Mott model works well. Hence increasing the 'metal' nanotube work function by p-doping with $SOCl_2$ (or gold chloride [9, 44]), in combination with the absence of Fermi level pinning, might easily explain large Schottky barriers that are on the order of the band gap of silicon. A Schottky model would also explain the positive influence of a thin oxide layer as explained by Card and Yang [45] and Doghish and Ho [46]. Nevertheless, Jung et al. [9] also measured a very long minority carrier lifetime, which is difficult to explain with reference to the Schottky mechanism. In short, there is a strong case for an underlying p–n mechanism, but also an alternate line of reasoning which poses that the devices are Schottky junctions just as with graphene-silicon [47] and graphene-germanium [48] devices, where the existence of a s-SWCNT bandgap just confuses the issue and where the important characteristics are the Fermi energy relative to silicon for the establishment of a built-in potential, the SWCNT carrier density and mobility, and the film density and degree of alignment which give rise to the conductivity and ampacity of the film. Whilst the results of the current study do not resolve this issue, they do provide clear guidance in the design of future experiments that may, as well as raising the possibility that the operating mechanism may depend on the metallicity of SWCNT film used.

4 Conclusions In summary, the first ever direct performance comparison between SWCNT–silicon heterojunction solar cells fabricated with unsorted, metallic, or semiconducting SWCNTs is presented. Whilst the conductivity and ampacity of the SWCNT film are always primary factors determining the performance of these solar cells, it is also evident that the metallicity of the SWCNT film also plays a very significant role. This result may call into question some earlier reported conclusions regarding the role of the SWCNTs in devices which used mixed SWCNTs and the underlying operating mechanism of these photovoltaic systems. Armed with this new understanding, future investigations should be better able to resolve some of the outstanding questions regarding SWCNT–silicon solar cells.

Acknowledgements The authors wish to thank The Australian Microscopy and Microanalysis Research Facility. B. Flavel gratefully acknowledges support from the Deutsche Forschungsgemeinschaft's Emmy Noether Program under grant number FL 834/1-1.

References

[1] M. F. L. De Volder, S. H. Tawfick, R. H. Baughman, and A. J. Hart, Science **339**, 535 (2013).

[2] M. S. Arnold, S. I. Stupp, and M. C. Hersam, Nano Lett. **5**, 713 (2005);
M. S. Arnold, A. A. Green, J. F. Hulvat, S. I. Stupp, and M. C. Hersam, Nature Nano **1**, 60 (2006);
X. Tu, S. Manohar, A. Jagota, and M. Zheng, Nature **460**, 250 (2009);
K. Moshammer, F. Hennrich, and M. Kappes, Nano Res. **2**, 599 (2009);
S. Ghosh, S. M. Bachilo, and R. B. Weisman, Nature Nano **5**, 443 (2010);
C. Blum, N. Stürzl, F. Hennrich, S. Lebedkin, S. Heeg, H. Dumlich, S. Reich, and M. M. Kappes, ACS Nano **5**, 2847 (2011).

[3] H. Liu, T. Tanaka, Y. Urabe, and H. Kataura, Nano Lett. **13**, 1996 (2013).

[4] B. S. Flavel, M. M. Kappes, R. Krupke, and F. Hennrich, ACS Nano **7**, 3557 (2013).

[5] A. J. Blanch, J. S. Quinton, and J. G. Shapter, Carbon **60**, 471 (2013).

[6] K. Tvrdy, R. M. Jain, R. Han, A. J. Hilmer, T. P. McNicholas, and M. S. Strano, ACS Nano **7**, 1779 (2013).

[7] D. D. Tune, B. S. Flavel, R. Krupke, and J. G. Shapter, Adv. Energy Mater. **2**, 1043; (2012).
W. B. Euler, and V. A. Karachevtsev, Photophysics of Carbon Nanotubes Interfaced with Organic and Inorganic Materials (Springer, London 2012);
D. Jariwala, V. K. Sangwan, L. J. Lauhon, T. J. Marks, and M. C. Hersam, Chem. Soc. Rev. **42**, 2824 (2013);
L. Yang, S. Wang, Q. Zeng, Z. Zhang, and L.-M. Peng, Small, **9**, 1225 (2013).

[8] Y. Jia, P. Li, X. Gui, J. Wei, K. Wang, H. Zhu, D. Wu, L. Zhang, A. Cao, and Y. Xu, Appl. Phys. Lett. **98**, 133115 (2011).

[9] Y. Jung, X. Li, N. K. Rajan, A. D. Taylor, and M. A. Reed, Nano Lett. **13**, 95 (2012).

[10] E. Shi, L. Zhang, Z. Li, P. Li, Y. Shang, Y. Jia, J. Wei, K. Wang, H. Zhu, D. Wu, S. Zhang, and A. Cao, Sci. Rep. **2**, 884 (2012).

[11] P. L. Ong, W. B. Euler, and I. A. Levitsky, Nanotechnology **21**, 105203 (2010).

[12] Y. Jia, A. Cao, F. Kang, P. Li, X. Gui, L. Zhang, E. Shi, J. Wei, K. Wang, H. Zhu, and D. Wu, Phys. Chem. Chem. Phys. **14**, 8391 (2012).

[13] S. Del Gobbo, P. Castrucci, S. Fedele, L. Riele, A. Convertino, M. Morbidoni, F. De Nicola, M. Scarselli, L. Camilli, and M. De Crescenzi, J. Mater. Chem. C **1**, 6752 (2013).

[14] D. D. Tune, F. Hennrich, S. Dehm, M. F. G. Klein, K. Glaser, A. Colsmann, J. G. Shapter, U. Lemmer, M. M. Kappes, R. Krupke, and B. S. Flavel, Adv. Energy Mater. **3**, 1091 (2013).

[15] X. Li, Y. Jung, K. Sakimoto, T.-H. Goh, M. A. Reed, and A. D. Taylor, Energy Environ. Sci. **6**, 879 (2013).

[16] P. Castrucci, S. Del Gobbo, L. Camilli, M. Scarselli, S. Casciardi, F. Tombolini, A. Convertino, G. Fortunato, and M. De Crescenzi, J. Nanosci. Nanotechnol. **11**, 9202 (2011);
D. Kozawa, K. Hiraoka, Y. Miyauchi, S. Mouri, and K. Matsuda, Appl. Phys. Express **5**, 042304 (2012);
A. Znidarsic, A. Kaskela, P. Laiho, M. Gaberscek, Y. Ohno, A. G. Nasibulin, E. I. Kauppinen, and A. Hassanien, J. Phys. Chem. C **117**, 13324 (2013);
V. Le Borgne, L. A. Gautier, and M. A. El Khakani, Appl. Phys. Lett. **103**, 073103 (2013).

[17] D. Tune and J. Shapter, Nanomaterials **3**, 655 (2013).

[18] Z. Li, V. P. Kunets, V. Saini, Y. Xu, E. Dervishi, G. J. Salamo, A. R. Biris, and A. S. Biris, Appl. Phys. Lett. **93**, 243117 (2008).

[19] Y. Jia, A. Cao, X. Bai, Z. Li, L. Zhang, N. Guo, J. Wei, K. Wang, H. Zhu, D. Wu, and P. M. Ajayan, Nano Lett. **11**, 1901 (2011);
W. Feijiu, K. Daichi, M. Yuhei, H. Kazushi, M. Shinichiro, and M. Kazunari, Appl. Phys. Express **6**, 102301 (2013).

[20] P. Wadhwa, B. Liu, M. A. McCarthy, Z. Wu, and A. G. Rinzler, Nano Lett. **10**, 5001 (2010);
P. Wadhwa, G. Seol, M. K. Petterson, J. Guo, and A. G. Rinzler, Nano Lett. **11**, 2419 (2011);
K. Cui, T. Chiba, S. Omiya, T. Thurakitseree, P. Zhao, S. Fujii, H. Kataura, E. Einarsson, S. Chiashi, and S. Maruyama, J. Phys. Chem. Lett. **4**, 2571 (2013).

[21] D. D. Tune, B. S. Flavel, J. S. Quinton, A. V. Ellis, and J. G. Shapter, ChemSusChem **6**, 320 (2013).

[22] C. Pintossi, G. Salvinelli, G. Drera, S. Pagliara, L. Sangaletti, S. D. Gobbo, M. Morbidoni, M. Scarselli, M. De Crescenzi, and P. Castrucci, J. Phys. Chem. C **117**, 18688 (2013).

[23] J. Di, Z. Yong, X. Zheng, B. Sun, and Q. Li, Small **9**, 1367 (2013).

[24] A. Saha, S. Ghosh, R. B. Weisman, and A. A. Martí, ACS Nano **6**, 5727 (2012).

[25] A. J. Blanch, C. E. Lenehan, and J. S. Quinton, Carbon **49**, 5213 (2011).

[26] H. Liu, D. Nishide, T. Tanaka, and H. Kataura, Nature Commun. **2**, 309 (2011).

[27] Z. Wu, Z. Chen, X. Du, J. M. Logan, J. Sippel, M. Nikolou, K. Kamaras, J. R. Reynolds, D. B. Tanner, A. F. Hebard, and A. G. Rinzler, Science **305**, 1273 (2004).

[28] L. Hu, D. S. Hecht, and G. Grüner, Nano Lett. **4**, 2513 (2004).

[29] E. H. Hároz, B. Y. Lu, P. Nikolaev, S. Arepalli, R. H. Hauge, and J. Kono, J. Am. Chem. Soc. **134**, 3 (2012).

[30] R. B. Weisman and S. M. Bachilo, Nano Lett. **3**, 1235 (2003).

[31] M. Shimizu, S. Fujii, T. Tanaka, and H. Kataura, J. Phys. Chem. C **117**, 5 (2013).

[32] C. D. Spataru, S. Ismail-Beigi, L. X. Benedict, and S. G. Louie, Phys. Rev. Lett. **92**, 077402 (2004).

[33] P. G. Collins, K. Bradley, M. Ishigami, and A. Zettl, Science **287**, 1801 (2000).

[34] M. J. O'Connell, E. E. Eibergen, and S. K. Doorn, Nature Mater. **4**, 412 (2005).

[35] U. Dettlaff-Weglikowska, V. Skákalová, R. Graupner, S. H. Jhang, B. H. Kim, H. J. Lee, L. Ley, Y. W. Park, S. Berber, D. Tománek, and S. Roth, J. Am. Chem. Soc. **127**, 5125 (2005);
H. Tantang, J. Y. Ong, C. L. Loh, X. Dong, P. Chen, Y. Chen, X. Hu, L. P. Tan, and L.-J. Li, Carbon **47**, 1867 (2009).

[36] T. M. Barnes, J. L. Blackburn, J. van de Lagemaat, T. J. Coutts, and M. J. Heben, ACS Nano **2**, 1968 (2008).

[37] Z. Li, V. P. Kunets, V. Saini, Y. Xu, E. Dervishi, G. J. Salamo, A. R. Biris, and A. S. Biris, ACS Nano **3**, 1407 (2009).

[38] A. G. Rinzler and E. P. Donoghue, ACS Nano **5**, 3425 (2011).

[39] S. M. Sze and K. K. Ng, Physics of Semiconductor Devices (Wiley Interscience, USA, 2006).

[40] J. Shewchun, R. Singh, and M. A. Green, J. Appl. Phys. **48**, 765 (1977).

[41] R. T. Tung, Mater. Sci. Eng. R **35**, 1 (2001).

[42] V. Barone, J. E. Peralta, J. Uddin, and G. E. Scuseria, J. Chem. Phys. **124**, 024709 (2006).

[43] S. Tongay, T. Schumann, and A. F. Hebard, Appl. Phys. Lett. **95**, 222103 (2009).

[44] K. K. Kim, J. J. Bae, H. K. Park, S. M. Kim, H.-Z. Geng, K. A. Park, H.-J. Shin, S.-M. Yoon, A. Benayad, J.-Y. Choi, and Y. H. Lee, J. Am. Chem. Soc. **130**, 12757 (2008).

[45] H. C. Card and E. S. Yang, Appl. Phys. Lett. **29**, 51 (1976).

[46] M. Y. Doghish and F. D. Ho, IEEE Trans. Electron. Devices **40**, 1446 (1993).

[47] X. Li, H. Zhu, K. Wang, A. Cao, J. Wei, C. Li, Y. Jia, Z. Li, X. Li, and D. Wu, Adv. Mater. **22**, 2743 (2010);
E. Shi, H. Li, L. Yang, L. Zhang, Z. Li, P. Li, Y. Shang, S. Wu, X. Li, J. Wei, K. Wang, H. Zhu, D. Wu, Y. Fang, and A. Cao, Nano Lett. **13**, 1776 (2013);
C. Xie, J. Jie, B. Nie, T. Yan, Q. Li, P. Lv, F. Li, M. Wang, C. Wu, L. Wang, and L. Luo, Appl. Phys. Lett. **100**, (2012).

[48] L.-H. Zeng, M.-Z. Wang, H. Hu, B. Nie, Y.-Q. Yu, C.-Y. Wu, L. Wang, J.-G. Hu, C. Xie, F.-X. Liang, and L.-B. Luo, ACS Appl. Mater. Interf. **5**, 9362 (2013).

– This page intentionally left blank –

2.4 Carbon Nanotube Fullerene Solar Cells

2.4.1 *Performance Enhancement of Polymer-Free Carbon Nanotube Solar Cells via Transfer Matrix Modeling*

M. Pfohl, K. Glaser, J. Ludwig, D. D. Tune, S. Dehm, C. Kayser, A. Colsmann,
R. Krupke, **B. S. Flavel**

Advanced Energy Materials 6 (2016) 1501345

DOI: 10.1002/aenm.201501345

Abstract

In this work, polymer-free (6,5) single walled carbon nanotubes (SWCNTs) prepared using the gel permeation approach are integrated into SWCNT:C_{60} solar cells. Evaporation driven self-assembly is used to form large-area SWCNT thin films from the surfactant-stabilized aqueous suspensions. The thicknesses of various layers within the solar cell are optimized by theoretical modeling using transfer matrix calculations; where the distribution of the electric field within the stack is matched to light absorption by the SWCNTs through either their primary (S_{11}) or secondary (S_{22}) absorption peak, or a combination thereof. The validity of the model is verified experimentally through a detailed parameter study and then used to develop SWCNT:C_{60} solar cells with high open circuit voltage (0.44 V) as well as a cutting edge internal quantum efficiency of up to 86 % through the nanotube S_{11} transition, over an active area of 0.105 cm^2.

Contribution

B.S.F conceived the idea for the project. B.S.F, M.P, D.D.T and R.K designed the experiments. B.S.F, M.P, K. G, D.D.T, S.D, C.K performed the experiments. B.S.F, M.P and D.D.T wrote the manuscript and all authors contributed to the scientific interpretation of the results.

– This page intentionally left blank –

Performance Enhancement of Polymer-Free Carbon Nanotube Solar Cells via Transfer Matrix Modeling

*Moritz Pfohl, Konstantin Glaser, Jens Ludwig, Daniel D. Tune, Simone Dehm, Christian Kayser, Alexander Colsmann, Ralph Krupke, and Benjamin S. Flavel**

Polymer-free (6,5) single-walled carbon nanotubes (SWCNTs) prepared using the gel permeation approach are integrated into SWCNT:C_{60} solar cells. Evaporation-driven self-assembly is used to form large-area SWCNT thin films from the surfactant-stabilized aqueous suspensions. The thicknesses of various layers within the solar cell are optimized by theoretical modeling using transfer matrix calculations, where the distribution of the electric field within the stack is matched to light absorption by the SWCNTs through either their primary (S_{11}) or secondary (S_{22}) absorption peaks, or a combination thereof. The validity of the model is verified experimentally through a detailed parameter study and then used to develop SWCNT:C_{60} solar cells with high open-circuit voltage (0.44 V) as well as a cutting-edge internal quantum efficiency of up to 86% through the nanotube S_{11} transition, over an active area of 0.105 cm^2.

1. Introduction

Over the past 5 years, single-walled carbon nanotubes (SWCNTs) have attracted much attention in the organic solar cell community, from both a theoretical and practical point of view, as either a light sensitizing material, or in active layer composites.[1–7] This is due to such desirable characteristics as their high charge carrier mobility along the nanotube axis and excellent stability toward degradation in ambient, humid, hot or high UV radiation conditions.[8] As an active material, a key driver of this interest has been the desire to absorb the infrared light excluded by traditional organic sensitizers. In addition, the presence of multiple excitonic transitions within SWCNTs may allow for solar cells built from them to not only cover the infrared spectrum but also the visible and UV regimes. For example, small diameter (≈0.8–1.2 nm) semiconducting nanotubes have their first excitonic transition (S_{11}) in the NIR (900–1250 nm), the second (S_{22}) in the visible (550–900 nm), and the third (S_{33}) in the UV.[9] Due to the larger absorption cross section of the S_{11} transition compared to S_{22}, S_{33}, etc. most researchers have so far focused on the infrared regime. However, Bindl and Arnold have recently investigated the quantum efficiency from S_{11}, S_{22}, and even hot S_{11} + K transitions from (7,5) SWCNTs and found that the measured efficiencies correlated well with the expected absorption cross sections.[10]

The development of SWCNT solar cells capable of harvesting light across such a broad wavelength range introduces new questions regarding the ideal design of the layer stack such that there is adequate electric field intensity from the incoming light at the positions where the nanotubes absorb. To this end, transfer matrix calculations (TMCs) are particularly useful because it is possible to predict the optimal exciton generation rate in the nanotubes based on the normal squared electric field intensity ($|E|^2$) for any combination of layers in a solar cell stack.[11] By correlating $|E|^2$ calculations to the SWCNT absorption profile, we demonstrate control of the ratio of external quantum efficiency (EQE) due to S_{11}, S_{22}, and a combination thereof through variation of the stack design. This complements the work of Bindl and Arnold and Guillot et al. who used solar cell stack designs which resulted in electric fields distributed across either S_{22} and S_{11} or specifically across S_{11}.[1,2,6,10]

The preparation of semiconducting pure SWCNTs suitable for use in SWCNT:C_{60} solar cells can broadly be divided into two categories; first, via selective polymer wrapping in an organic medium,[12,13] or second, through aqueous surfactant-based methods such as gel permeation chromatography (GPC),[14,15] density gradient ultracentrifugation (DGU), or the newly developed phase transfer method.[16,17] In terms of industrial applicability, both methodologies have their advantages and disadvantages. For example polymer wrapping with poly(9,9-dioctylfluorenyl-2,7-diyl) (PFO) or regioregular poly(3-alkylthiophene)s (rr-P3ATs) has been shown to be highly

M. Pfohl, Dr. D. D. Tune, S. Dehm,
Prof. R. Krupke, Dr. B. S. Flavel
Institute of Nanotechnology
Karlsruhe Institute of Technology (KIT)
76021 Karlsruhe, Germany
E-mail: benjamin.flavel@kit.edu

M. Pfohl, Prof. R. Krupke
Institute of Materials Science
Technische Universität Darmstadt
64287 Darmstadt, Germany

K. Glaser, J. Ludwig, C. Kayser, Dr. A. Colsmann
Light Technology Institute
Karlsruhe Institute of Technology (KIT)
76131 Karlsruhe, Germany

Dr. D. D. Tune
Centre for Nanoscale Science and Technology
Flinders University
Adelaide 5042, Australia

DOI: 10.1002/aenm.201501345

selective to small diameter SWCNTs and capable of yielding extremely high semiconducting contents of >99%.[18] In the case of SWCNT solar cells this observed high selectivity is important as the absence of metallic species reduces the potential for interlayer shorts or the introduction of trap states.[19] Additionally, the processing of SWCNTs in an organic medium is often more amenable to flat, thin film fabrication, while still being compatible with the surrounding layers in the device stack, and techniques such as doctorblading,[1] spin-coating, and spray-coating have been used in the past.[4,6] It is likely for these reasons that most of the nanotube solar cell literature uses polymer-wrapped SWCNTs as the donor material. Pioneering the field in 2010, Bindl et al., used PFO-wrapped SWCNTs in combination with different electron and hole acceptor materials such as fullerene C_{60}, [6,6]-phenyl C_{61} butyric acid methyl ester ($PC_{61}BM$) or poly(3-hexylthiophene) (P3HT), respectively, and showed that the SWCNTs form a Type-II heterojunction with sufficient energetic offset to drive exciton dissociation and the generation of photocurrent.[1] Power conversion efficiencies of 1% with C_{60} and 3.1% with $PC_{71}BM$ were obtained using planar junctions and bulk heterojunction (BHJ) solar cells, respectively.[2,5] In the planar architecture, an EQE and internal quantum efficiency (IQE) of 40% and more than 85% were obtained at S_{11}.[2,10] Despite these remarkable results, new strategies to remove the excess polymer are required. As was later outlined by Bindl et al.,[20] residual PFO limits the intertube diffusion length to ≈8 nm and therefore restricts the usage of thicker nanotube films. However, the greatest limitation to polymer wrapping methodologies (at least for small diameters) is the low yield and expense of the polymer, which has likely contributed to the use of relatively small active areas of between 0.008 and 0.04 cm^2 until, recently, Guillot et al. fabricated solar cell devices with an active area of 0.101 cm^2 that were masked to 0.061 cm^2.[2,4,6,12] Although the use of small areas is convenient in the obtainment of statistics, increasing the active area is an important issue to address if carbon nanotube solar cells are to develop as a technology. Toward this end, Bao and co-workers have looked at the role of the polymer's alkyl side chains in increasing the yield of sorting small diameter nanotubes for solar cell applications.[4] Likewise, Blackburn and co-workers have demonstrated a spray-coating technique that is compatible with large area film fabrication.[21]

In contrast, the yield from surfactant-based methods is significantly higher; with our recently developed automated gel permeation system capable of routinely preparing mg amounts of (n,m) sorted material, albeit with higher metallic nanotube content compared to polymer wrapping. Although, as shown in the work of Tulevski et al.,[22] surfactant-based method can reach a semiconducting purity larger than 98%. The use of an aqueous suspension introduces new fabrication challenges due to the incompatibility of many common solar cells organic layers with water, which is probably a contributing factor in why the literature currently only provides one example of the use of surfactant-wrapped SWCNTs in these types of solar cells. In that work, Jain et al. prepared a SWCNT film via vacuum filtration of surfactant-stabilized (6,5) nanotubes and placed this in contact with C_{60} as an electron acceptor.[3] Despite having a 100 nm thick nanotube film, the current contribution from the nanotubes was only 0.5% in the EQE, with an overall power conversion efficiency of 0.1% and, although not reported, an evidently low IQE.

In our work, we have also investigated surfactant-wrapped (6,5) SWCNTs however, instead of vacuum filtration, we have used evaporation-driven self-assembly (EDSA) to form our nanotube films. In previous reports, this approach has yielded closed films and stripes of horizontally aligned nanotubes on silicon dioxide from surfactant wrapped, enriched (6,5) nanotube solutions in 0.1 and 1 wt% sodium dodecyl sulfate (SDS).[23,24] Recently, Li et al. published videos of SWCNT stripe formation via a "slip-stick" mechanism, demonstrating that the dynamic contact line pinning and SDS concentration are responsible for the horizontal alignment of nanotubes.[23] In this report, the stripe formation was suppressed by adjusting the evaporation speed of the nanotube solution and surfactant concentration to create thin (≈2 nm), homogenously closed films over large areas (≈2 cm^2). Similarly to the work of Wang et al., our design consists of the nanotube film sandwiched between a poly(3,4-ethylenedioxythiophene) polystyrene sulfonate (PEDOT:PSS) hole transport layer and a C_{60} electron acceptor and transport layer in a planar organic heterojunction solar cell.[4]

2. Results and Discussion

The solar cell architecture is shown in **Figure 1**a and a solution optical density spectrum and photoluminescence contour map of the (6,5) SWCNTs used in this work are shown in **Figure 2**a,b, respectively. Additional information regarding the peak fitting procedure used to determine (n,m) purity can be found in Figure S1 in the Supporting Information. Following the method of Ghosh et al.,[25] the purity of (6,5) was determined to be 93% with minor (6,4), (7,5), and (7,6)

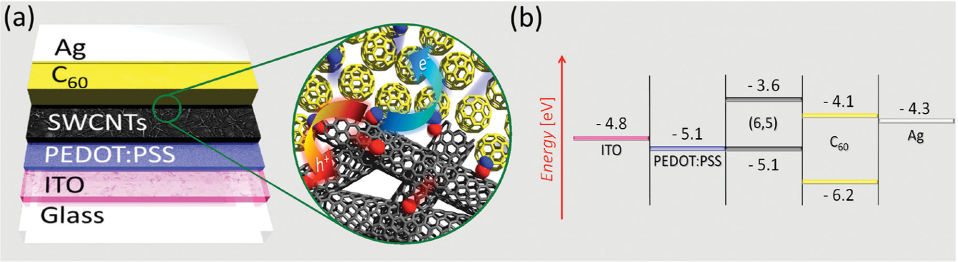

Figure 1. a) Schematic of the solar cell architecture with a close-up of the envisaged exciton dissociation at the SWCNT:C_{60} interface. Electrons (blue) migrate through C_{60} to the silver electrode while holes (red) are collected at the ITO in accordance with b) the energy-level diagram of the device stack.

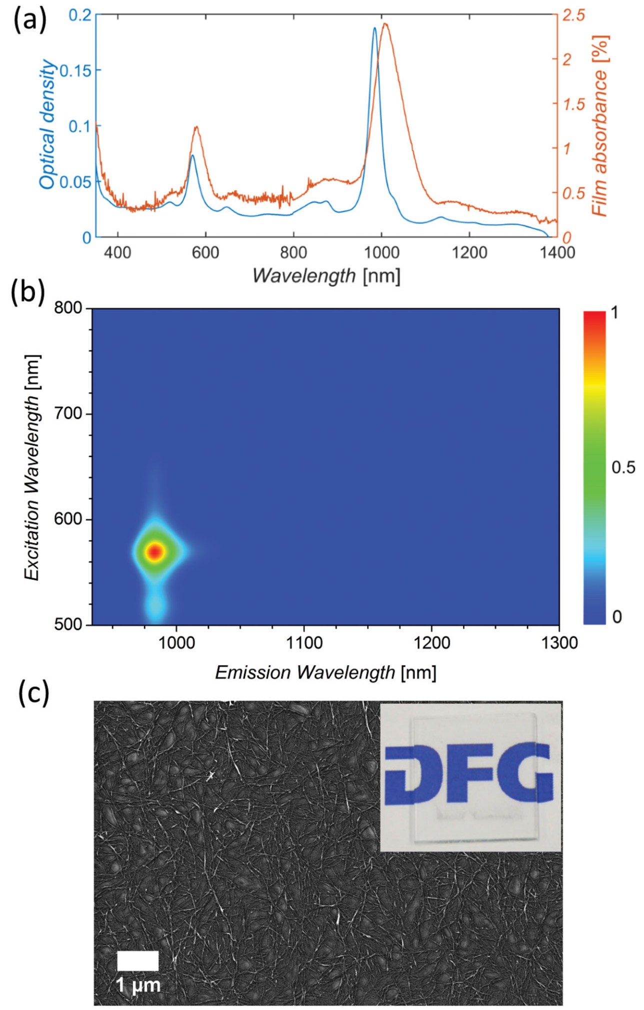

Figure 2. a) Optical density of the suspension measured with a 2 mm path length and film absorbance of (6,5) SWCNTs on glass, scaled by a factor of 3.1 to the mean absorbance determined from reflectance measurements in Figure S11 (Supporting Information), b) a normalized photoluminescence contour map of the SWCNTs in aqueous suspension, c) SEM image of the porous (6,5) nanotube film produced by evaporation-driven self-assembly. Inset shows a comparable film on glass to demonstrate the optical transparency.

impurities also present. The films made from this material are highly transparent, as seen in Figure 2a and the inset of Figure 2c. The nanotube films used in this work absorb ≈1.1% in the region of their S_{22} transition and ≈2.5% at S_{11}. As has been well documented in the literature, the absorption features of the nanotube films are red-shifted and broadened compared to those from the solution measurements, due to differences in the surrounding environment and to bundling of nanotubes.[26] This equates to a 10 nm shift for S_{22} (from 570 to 580 nm) and 24 nm for S_{11} (from 984 to 1008 nm). The morphology of a typical 2 cm^2 (6,5) film obtained by EDSA was also investigated and a representative scanning electron microscopy (SEM) image is shown in Figure 2c. The films are porous and disordered, consisting of bundles of nanotubes. As outlined in Figure S2, Supporting Information, the bundle height (SWCNT film thickness) is determined from atomic force microscopy (AFM) measurements to be a log normal distribution with an average of 2.1 ± 0.7 nm, and with a surface coverage of 60 ± 8%. Nevertheless, as will be shown later, these sub-monolayer thin films significantly outperform similar devices made from much thicker films (100 nm).[3]

The highest occupied molecular orbital (HOMO) energy of the nanotube films was determined by photo-electron yield spectroscopy in air (PESA) to be 5.10 ± 0.02 eV (Figure S3, Supporting Information), which was used to draw the energy band diagram shown in Figure 1b. The lowest unoccupied molecular orbital (LUMO) was calculated based on the work by Bindl et al. by adding the optical bandgap and exciton binding energy, determined by the works of Dukovic et al. and Perebeinos et al., to the HOMO.[27,28] In the work of Dukovic et al., a dielectric constant of 3 was used however in our work the dielectric environment is mostly determined by C_{60} with a dielectric constant of 4.4 and we have consequently scaled the exciton binding energy in accordance with Perebeinos et al.[29] The work functions and the energies of the HOMO and LUMO of all other materials were taken from literature or, in the case of C_{60}, from the works of Bindl et al.[27,30] The LUMOs of the nanotubes (−3.6 eV) and C_{60} (−4.05 eV) exhibit an energetic offset of 0.45 eV, which is more than the expected 0.25 eV exciton binding energy, that was previously reported by Wu et al.[19] After dissociation, the holes are collected through the nanotubes, PEDOT:PSS and indium tin oxide (ITO) electrode while electrons are collected by C_{60}/Ag.

Assuming that the thickness of the (6,5) SWCNT film, along with the glass, ITO and silver electrodes remain constant, varying the thickness of PEDOT:PSS (0 to 100 nm) and C_{60} (1 to 200 nm) in steps of 1 nm leads to more than 20 000 different possible combinations of layers in the solar cell design depicted in Figure 1a. Although it is not expected that 1 nm changes in thickness result in major differences in solar cell performance, such large data sets can easily be calculated with the aid of TMCs and are a helpful tool to optimize the layer thicknesses within the device such that absorption by the SWCNTs is maximized.

In the numerical modeling used in TMCs, it is important to precisely know the optical parameters of all layers. The complex refractive indices (n and k) of all materials in our devices except for the (6,5) SWCNTs are readily available in the literature (see Experimental Section and Supporting Information). The literature values of n and k are compared to the measured absorption profiles for C_{60} and PEDOT:PSS in Figure S4a,b (Supporting Information). Fagan et al. and Battie et al. have provided values of the complex refractive index of (6,5) films, which are plotted in Figure S4c, although they used different methods to obtain the film.[31] In Fagan's approach, DNA-wrapped (6,5) nanotubes were investigated based on their horizontal alignment in films whereas in Battie's approach, DGU was used to sort highly enriched (6,5) solutions. Unfortunately, not only do the two approaches yield different values, but neither of the absorption profiles calculated (Equation S2 to Equation S4, Supporting Information) using these different complex refractive indices, shown in Figure S4d, are in good agreement with that measured from the (6,5) nanotube films used in this study. Because of this lack of reliable values of the complex refractive index, and in light of the very high (>97%) transmittance of the films

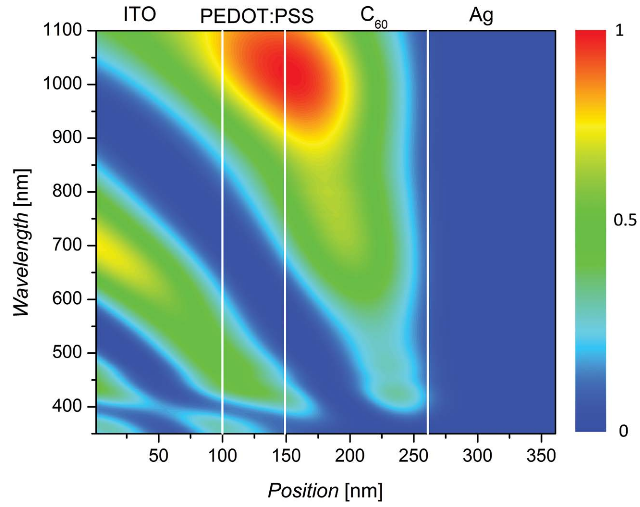

Figure 3. Normalized spatial distribution of the normalized squared electric field intensity, $|E|^2$, as a function of wavelength and position within the solar cell stack. Light is incident from the left, i.e., through the opaque ITO electrode. A layer stack consisting of 49 nm of PEDOT:PSS and 112 nm of C_{60} is shown and was calculated to maximize exciton generation rate through the S_{11} transition of the SWCNTs.

used herein, the influence of the SWCNT film on the position of the electric field intensity has been neglected. A similar approach of neglecting the nanotubes has previously shown qualitative agreement between $|E|^2$ and EQE for thin (<5 nm) PFO-wrapped (7,5) nanotube films, even with a light absorption at the nanotube's S_{11} transition of more than 50%.[2] In this way, the solar cells in the present study were optimized by maximizing $|E|^2$ where the (6,5) film is located at the interface of PEDOT:PSS and C_{60}. Rather than using TMCs to predict current densities or estimate EQE, they were employed in this study to estimate the exciton generation rate for all layer combinations and wavelength ranges. The exciton generation rate was calculated based on a (6,5) SWCNT film absorbance measurement, which was used instead of the product of absorption coefficient α and the real part of the complex refractive index n in Equation S3 (Supporting Information) and then employed in Equations S5,S7 (Supporting Information). A detailed approach and the formulas used are described in the Supporting Information. From these calculations, the optimum thickness combination for a maximized exciton generation rate from the SWCNTs through S_{11} was found to be at 49 nm of PEDOT:PSS and 112 nm of C_{60}. The corresponding normalized (to the incoming electric field $|E_0^+|$) $|E|^2$ can be visualized in a 2D plot as shown in **Figure 3**, where blue areas indicate low light intensity, and red areas represent high light intensity that holds the potential to be absorbed by the material.

The validity of the theoretical model was then tested experimentally in a parametric study varying the PEDOT:PSS and C_{60} layer thicknesses. For PEDOT:PSS, thicknesses of 11, 30, 41, 61, and 86 nm with an error of ±5 nm were used with a constant C_{60} thickness of 110 ± 5 nm and all combinations were made in triplicate (i.e., three substrates, each holding four separate solar-cell-active areas). The mean short-circuit current densities (J_{SC}, mA cm^{-2}), open-circuit voltages (V_{OC}, V), power conversion efficiencies (η, %) and fill factors (FF) of the corresponding devices are summarized in **Figure 4**a and depicted in

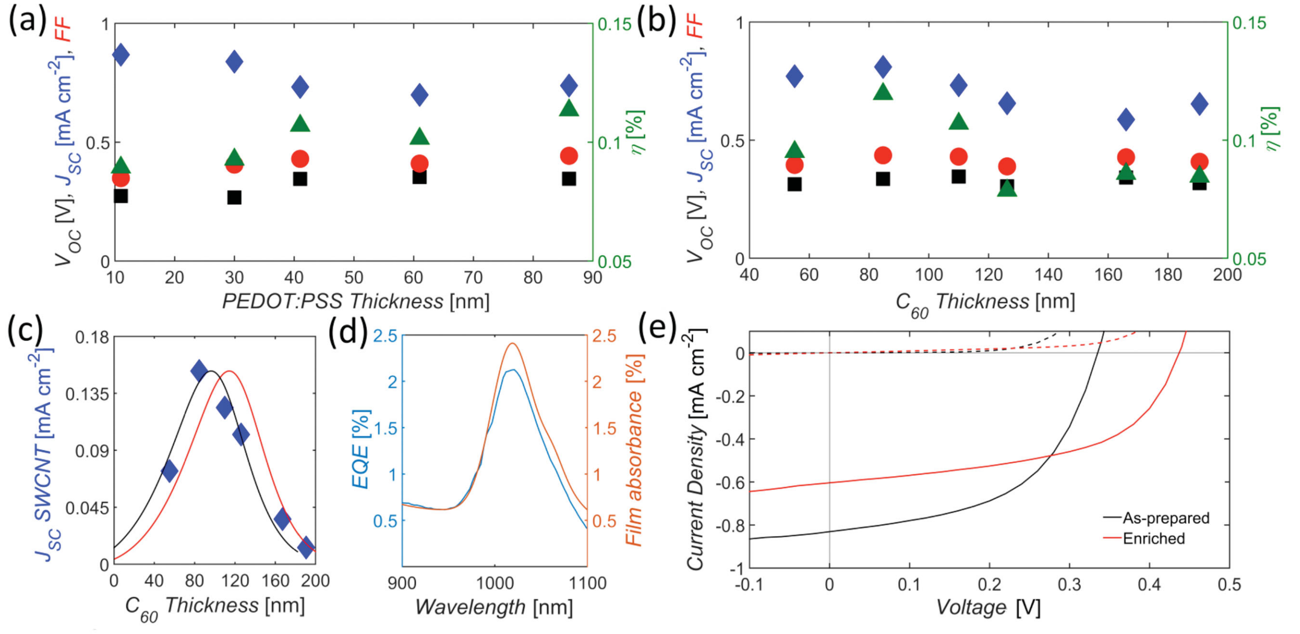

Figure 4. V_{oc}, J_{sc}, FF, and η values from parametric investigations of: a) PEDOT:PSS and b) C_{60} layer thicknesses. c) Correlation between the short circuit current density calculated to be due to the nanotube's S_{11} transition from 800 to 1100 nm (blue diamonds, Equation (1) and the theoretically predicted exciton generation rate-based on Equation S7 (Supporting Information) (red curve) normalized to the maximum current from the nanotubes for the same wavelength range. The black curve is the best fit of the exciton generation rate to the calculated current from the SWCNTs. d) Comparison between solar cell EQE and mean (6,5) nanotube film absorbance in the region of the nanotube's S_{11} transition. e) Light (solid line) and dark (dotted line) J–V measurements from solar cells made with as-prepared and (6,5) enriched SWCNTs.

more detail in Figures S5,S6 (Supporting Information). All cells without PEDOT:PSS failed (see Figure S7, Supporting Information), as well as some of the 11 nm ones. We attribute this to the porous nature of the SWCNT film that allows for direct contact of C_{60} with ITO in the absence of PEDOT:PSS or through pin holes in the case of thin films. Once the layer is sufficiently thick, the influence of PEDOT:PSS on the device current density is minor. Therefore, no immediate trend is clearly visible across all thicknesses. The FF and V_{OC} are approximately the same for all thicknesses and η is found to be largest for 41 and 86 nm. Having comparable J_{SC}, V_{OC}, and FF for these two thicknesses, 41 nm was chosen for the following C_{60} thickness study due to it being closer to the optimum of 49 nm predicted from the TMC model.

Solar cells with six different C_{60} layer thicknesses were tested: 55 ± 2, 85 ± 4, 110 ± 5, 126 ± 2, 167 ± 2, and 191 ± 2 nm and the results are plotted in Figure 4b. Once again, many devices from thin films failed (only two out of 12 possible devices worked for 55 nm of C_{60}), which in this case we attribute to electrical shorts between isolated rough regions of the nanotube film and the silver top electrode (one such isolated region has been highlighted in Figure S2d, Supporting Information). These regions in the SWCNT film likely consist of agglomerated bundles, impurities in the surfactant or catalytic particles from the nanotube growth process. For this reason, an additional physical buffer layer between C_{60} and silver can be beneficial.[2,6] Solar cells with 85 nm of C_{60} performed best with the highest J_{SC}, FF, and η. Any further increase of the C_{60} layer thickness resulted in a slight decrease of all parameters, as depicted in Figure 4b. However, the difference across devices with different C_{60} layer thicknesses is only small, likely due to C_{60} being significantly thicker compared to the SWCNTs, which means that its contribution is much larger, as visible in the EQE measurements from 300 to 800 nm shown in Figure S8 (Supporting Information). The relative contributions of C_{60} and SWCNTs to the photocurrent generation are also indicated in Figure S8 (Supporting Information) and calculated to be 82.9% for C_{60} and 17.1% for the S_{11} regime of (6,5) nanotubes (for 85 nm of C_{60}). For all different thicknesses of C_{60}, the interface with the nanotubes remains basically the same and with exciton diffusion lengths in C_{60} ranging from 6 to 35 nm, any increase in thickness beyond this value does not necessarily generate more current.[32] Hence, the lack of any significant variation in Figure 4b for increasing C_{60} layer thickness.

A much closer correlation between experiment and theoretical TMC calculations becomes obvious when comparing the photocurrent contribution from the (6,5) SWCNTs to the predicted exciton generation rate, as shown in Figure 4c for 41 nm of PEDOT:PSS. The current contribution from the nanotube film in the S_{11} region (800–1100 nm) was calculated from EQE using Equation (1):

$$J_{sc} = \frac{e}{hc} \int \lambda \cdot \mathrm{EQE}(\lambda) \cdot \phi(\lambda)\, \mathrm{d}\lambda \tag{1}$$

where e is the elementary charge, h is the Planck's constant, c is the speed of light, λ is the wavelength, and ϕ is the photon flux. In this calculation, only the S_{11} transition was considered due to an overlap of C_{60} with S_{22}, as seen in Figure S8 (Supporting Information). The optimum exciton generation rate for 41 nm of PEDOT:PSS was calculated to be at 114 nm of C_{60}. However, upon experimentally comparing the calculated exciton generation rate to the integrated photocurrent, a maximum of 96 nm of C_{60} was found. Qualitatively, this is in good agreement when considering that no nanotubes were assumed in the TMC model. Taking the nanotube contribution into account in future models will likely provide a closer agreement with experimental data.

Calculating the $|E|^2$ distribution throughout the solar cell and correlating this with the efficiency through the S_{11} transition of (6,5), we looked into tailoring the $|E|^2$ distribution such as to maximize photocurrent from S_{11}, S_{22}, or a combination of both. This approach is attractive in terms of light management in solar cells or toward transparent solar cells in which the nanotubes absorb only in the infrared. As shown in **Figure 5**a, comparing the calculated $|E|^2$ at the position of the nanotubes (interface of PEDOT:PSS and C_{60}) for different C_{60} thicknesses and a constant 41 nm thickness of PEDOT:PSS reveals the opportunity to maximize electric field intensity almost equally at both nanotube transitions (62 nm C_{60}), or primarily at S_{22} (200 nm of C_{60}), or almost exclusively at S_{11} (118 nm of C_{60}). In Figure 5b–d, these theoretical predictions are correlated with experimental EQE measurements, where the typical absorbance spectrum of a (6,5) film is also shown for reference. The EQE peak corresponding to the nanotube's S_{11} follows the electric field intensity well however, for S_{22}, the correlation is less clear due to the overlap of a peak centered at 620 nm, which has its origins in C_{60} being interfaced with other materials.[33] Nevertheless, a shoulder at 590 nm can still be clearly seen in the EQE spectrum and this we attribute to photocurrent generated through S_{22}. For 126 nm of C_{60}, a minimum in $|E|^2$ is predicted and neither the S_{22} feature at 590 nm nor the 620 nm peak associated with C_{60} is observed experimentally while, for 191 nm of C_{60}, the S_{22} region is obviously enhanced in line with the predictions. A comparison of $|E|^2$ throughout the solar cell stacks for calculated optima and experimentally prepared solar cells is shown in Figure S9 (Supporting Information). The exciton generation rate is shown as a function of C_{60} thickness and wavelength in Figure S10 (Supporting Information). The ability to predict and move the electric field intensity in SWCNT:C_{60} solar cells in this way is especially interesting in regard to designing future tandem solar cells or the use of large diameter nanotubes that absorb even further in the infrared than the (6,5) nanotubes used herein.

To gain an understanding of the scale and origin of internal losses, the IQE was also calculated for the optimal combination of PEDOT:PSS and C_{60}, as shown in Figure 4d. To eliminate the potential for artefacts and discrepancies due to inhomogeneity of the films, the absorbance of the active area was measured in situ at seven different locations. Further details, along with the raw and fitted data, are provided in Figure S11 of the Supporting Information. Based on an EQE at S_{11} of 2.1% and an average absorbance of ≈2.5% at the same wavelength, an overall IQE of 86 ± 12% at the S_{11} transition was calculated, which outperforms earlier work with an EQE at the S_{11} transition of 0.5% and corresponding absorbance of the film of 35%.[3] This is quite remarkable considering the large difference in nanotube film thickness of ≈2 nm (this work) and 100 nm (the earlier work). Exploiting the photocurrent generation efficiency from the nanotubes to a degree of 86% is comparable to the best IQE values for polymer-wrapped nanotube solar cells that also used very thin nanotube films (≈7 nm) albeit with much higher absorption due to the use of denser films.[10,27] In the current polymer-free work, the limiting factor in terms of photocurrent generation and therefore power conversion efficiency is the high transmittance of the film. On the other hand, the porous nature of the films, which causes the high transmittance, has the advantage of preventing exciton quenching by metallic nanotubes, as would occur in denser and thicker films.[5] Having isolated bundles of SWCNTs also reduces the charge trapping influence of large diameter, smaller bandgap nanotubes.[3] It is for this reason that despite having equivalent IQE in our work the EQE remains low compared to the work of Guillot et al. and Bindl and Arnold who achieved values above 20% with much denser, polymer-wrapped films.[2,6,10]

With the goal of investigating possible improvements to device performance by increasing the semiconducting purity of the (6,5) suspension, we performed DGU, which is known to enrich the semiconducting purity and remove catalyst particles and bundles.[16] Absorption spectra of the enriched material obtained from DGU is shown in Figure S12 (Supporting Information) where a clear difference in the background, which is associated with metallic nanotubes, catalytic particles, and carbon residues, can be seen. In order to reduce the content of the DGU medium (iodixanol), the collected fraction was dialyzed, which resulted in a reduction in the nanotube concentration as measured by optical density (OD). Consequently, thin films formed from DGU enriched (6,5), henceforth referred to as "enriched (6,5)," were typically sparser than from the as-prepared material. The *J*–*V* curves of solar cells comprising as-prepared and enriched (6,5) nanotube films are shown in Figure 4e. The photocurrent is less from the enriched (6,5) films due to their lower density and there is only a slight increase in FF from 53% to 54% however, a significant improvement in V_{OC} was observed from 0.36 to 0.44 V. Important parameters are compared in **Table 1**. The shunt resistance (R_{sh}) was extracted from the slope of the *J*–*V* curve at V_{OC} and is 14% larger for solar cells comprising enriched (6,5) material than for as-prepared nanotubes, indicating a substantial decrease in alternative current paths, e.g., by the reduction of metallic tubes or trap states compared to the as-prepared solution. The series resistance (R_s) was extracted for as-prepared and enriched (6,5) from the illuminated *J*–*V* curve between 0.52 and 0.66 V and 0.54 to 0.66 V, respectively (see Figure S13, Supporting Information). The series resistance for the enriched (6,5) material is smaller but results only in a small increase in fill factor. The ideality factor was extracted from the slope of the dark current measurement $(\mathrm{d}V\,\mathrm{d}ln(J)^{-1})$ in the linear region of 0.28 to 0.38 V and 0.4 to 0.5 V, for the as-prepared and enriched

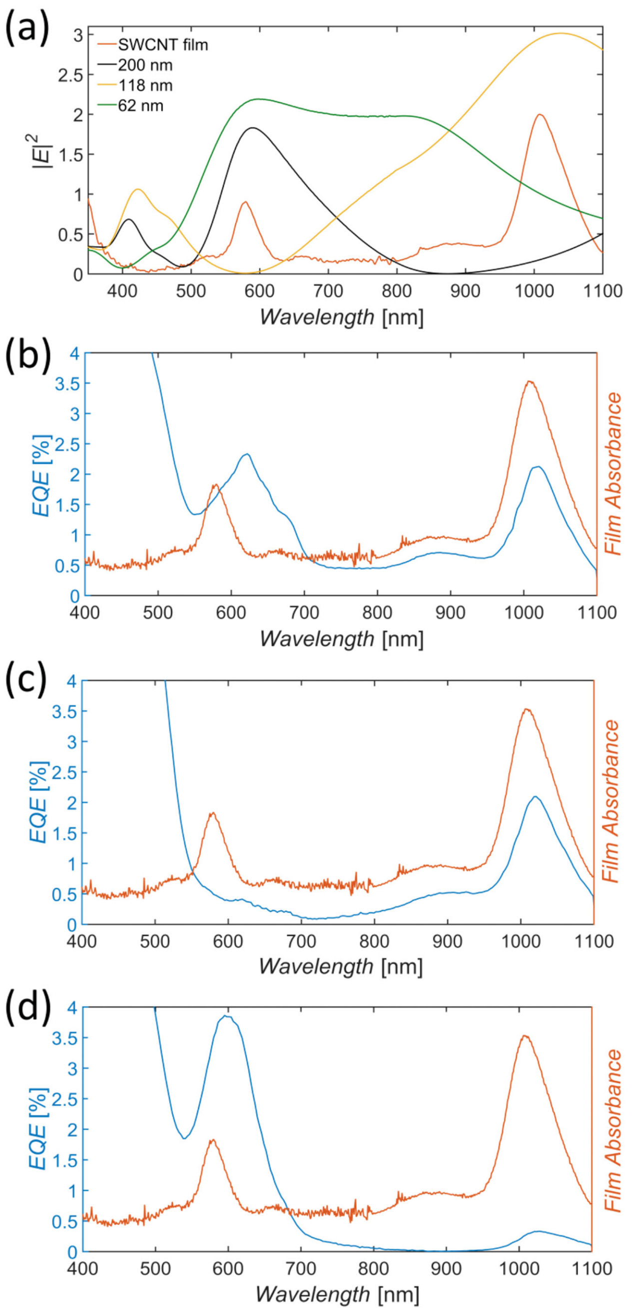

Figure 5. a) Variation in the electric field intensity, $|E|^2$, for different C_{60} layer thicknesses at a constant PEDOT:PSS thickness of 41 nm, b–d) show EQE spectra of solar cells with C_{60} thicknesses of 85, 126, and 191 nm, respectively. All plots show the normalized absorbance of a (6,5) nanotube film to guide the eye as to the positions of the S_{11} and S_{22} transitions of the nanotubes.

Table 1. Key performance parameters for solar cells made from as-prepared and enriched (6,5) SWCNT films. Resistances were calculated from the *J*–*V* curves recorded under illumination.

	V_{OC} [V]	J_{SC} [mA cm^{-2}]	FF [%]	η [%]	J_0 [mA cm^{-2}]	R_{SH} [Ω cm^2]	R_S [Ω cm^2]	Ideality
As-prepared	0.34	0.83	52	0.15	7.6×10^{-4}	2112	28	1.6
Enriched	0.44	0.60	54	0.14	3.5×10^{-4}	2946	22	1.8

(6,5) material, respectively.[34] Reverse saturation current densities (J_0) are on the same order for both materials. Having an ideality factor between 1 and 2 indicates recombination losses due to Shockley-Read-Hall (SRH) recombination, also called "trap charges," at or near the interface of the SWCNTs and C_{60}.[34] Trap charges, or monomolecular recombination, occur if the electron hole pair is not dissociated fast enough upon being created.[35] Crucial for fast dissociation is a sufficient LUMO level offset between donor and acceptor material. Organic solar cells with energy offsets between 0.2 and 0.3 eV often suffer from suppressed quantum efficiencies and fill factors.[35] Similar effects can also be attributed to bimolecular recombination, which occurs when successfully dissociated electrons and holes collide at the diffusive interface of the two semiconductors. A clear differentiation between mono- and bimolecular recombination can be obtained by light intensity (I)-dependent V_{OC} measurements.[36] Based on the works of Cowan et al.,[37] the slope of the fitted V_{OC} to $ln(I)$ curve for BHJ solar cells should be equal to $k_B T\ e^{-1}$ (25.5 mV at room temperature, bimolecular recombination), whereas $2k_B T\ e^{-1}$ is expected for silicon solar cells (51 mV at room temperature, SRH/monomolecular recombination). Having slopes of $2.3k_B T\ e^{-1}$ (58 mV) for enriched material and $4.3k_B T\ e^{-1}$ (109 mV) for as-prepared (6,5) nanotubes (Figure S14a,b, Supporting Information, respectively) puts them in the regime of monomolecular recombination due to interface traps.[38] The increased slope for solar cells from as-prepared material is correlated with a reduction in V_{OC}.[38] Combining the increase in R_{SH} and the significantly smaller slope in the light-intensity-dependent V_{OC} measurements indicates a marked reduction in trap-assisted recombination in solar cells made from the enriched (6,5) material, likely due to a reduction of the content of metallic SWCNTs. The influence of metallic tubes on the J–V characteristics was additionally verified by comparing a solar cell with SWCNTs to a "C_{60}-only" solar cell without nanotubes in Figure S15 (Supporting Information). The absence of as-prepared SWCNTs in the solar cell stack resulted in a V_{OC} of 0.44 V, which is comparable to the V_{OC} obtained for enriched (6,5) solar cells. The negative impact of metallic SWCNTs on the quantum efficiency and exciton diffusion length was also verified in recent works by Gong et al.,[5] who similarly showed a dramatic increase in device efficiency upon increasing the semiconducting purity of their SWCNT films from 95% to 98%.

3. Conclusion

To conclude, SWCNT:C_{60} solar cells have been prepared using large area, highly transparent films of polymer-free (6,5)-enriched SWCNTs formed from aqueous solution with the aid of a novel evaporation-driven self-assembly. By theoretical modeling of the electric field intensity within the layer stack using extensive TMCs, light in the solar cells was effectively managed so as to maximize photocurrent output from the different optical transitions of the nanotubes. These results confirm the validity of this powerful modeling tool for predicting and tailoring light absorption in carbon nanotube solar cells, even when the contribution of the nanotube film is neglected in the model. With optimal layer thicknesses, SWCNT:C_{60} solar cells were constructed that showed V_{OC} of 0.44 V and IQE of 86%, which are the highest values so far reported for polymer-free variants of this design. This is despite the fact that, in contrast with earlier work, the nanotube films used were exceptionally thin, being sub-monolayer in terms of nanotube bundles, which provides a strong indication that very large improvements in overall power conversion efficiency could be obtained with appropriate multilayer and/or multijunction cell designs.

4. Experimental Section

ITO glass substrates (PGO, 20 ± 6 Ω □$^{-1}$, 1.0 ± 0.1 mm) were covered with a structured foil, etched with HCl (fuming 37%; Merck), rinsed with water and dried to form the bottom contact and afford an active area of 0.105 cm^2 together with a silver top contact. PEDOT:PSS (Al 4083, 500 to 5000 Ω cm; Ossila) was filtered (Millex-HV, 0.45 µm; Merck), mixed with ethanol (VWR) in ratios of 1:1 or 1:3 for thicknesses starting at 30 nm and below, respectively, and then sonicated (10 min). This was then spin coated (1000–5000 rpm for 60 s, to yield a series of different layer thicknesses) and baked in an inert atmosphere (250 °C, 10 min) before being covered with poly(methyl methacrylate) (40 nm, PMMA 950K 0.25 µm/4000 rpm; Allresist). The desired thickness of PMMA was achieved by mixing with anisole (Merck) in a 1:4 ratio and subsequent spin coating (5000 rpm, 60 s) followed by a baking step (160 °C, 10 min). The PMMA layer served to protect PEDOT:PSS from degradation during deposition of the SWCNT film and was removed prior to the evaporation of C_{60} and silver. (6,5) SWCNTs were prepared from HiPco raw material (NanoIntegris) as outlined previously using a GPC system.[14] Due to the high affinity of (6,5) to the Sephacryl-S200 gel (Amersham Biosciences) and their ability to displace other (n,m) species at 1.6 wt% SDS (Merck), 1 wt% sodium cholate (SC ≥ 99%; Sigma–Aldrich) was used as an eluent in a one-column approach without the use of a pH gradient. The simplicity of this approach allowed us to prepare large quantities of (6,5) and avoid device variations due to differences between suspensions. Films of (6,5) SWCNTs were first prepared on a "dummy" substrate before being transferred onto the solar cell. SiO_2 substrates were oxygen plasma treated (3 min, 200 W, 100 mTorr, 20 sccm) to increase the hydrophilicity of the surface prior to being covered with PMMA (200 nm). The hydrophilic surface activation of SiO_2 allowed for water to later penetrate between the SiO_2 and PMMA and thus assist transfer of the SWCNT film.[39] SWCNT films were prepared by evaporation driven self-assembly in an oven (60 °C, 6 h) by immersing the PMMA-coated SiO_2 substrate vertically in a 1 wt% SC suspension adjusted to an OD of 0.025 at S_{11}. Films were 2 cm^2 in size after evaporation. The SWCNT film was then scored into a rectangle ≈1.3 cm^2 in size and slowly immersed into water to detach the SWCNT-coated PMMA from the SiO_2. Prior to the final detachment of the film, the substrate was withdrawn from the water and re-immersed in glycerol (99.5%; VWR). The advantage of using glycerol is twofold: the PMMA/SWCNT film is less mobile on the glycerol surface, resulting in greater control over film alignment onto the active areas of the solar cell, and glycerol does not dissolve PEDOT:PSS. Following film transfer, the solar cell substrates were heated (120 °C, 15 min) in air to promote contact between nanotubes and the substrate. Remaining glycerol residues were then dissolved in ethanol. Finally, the PMMA was dissolved overnight in chloroform (≥99.8%; Sigma–Aldrich). Various thicknesses of C_{60} (99.9+%; Sigma–Aldrich) from 55 to 190 nm were then evaporated through a shadow mask with a Lesker SPECTROS (temperature range from 380 °C to 450 °C and pressure of $7–9 \times 10^{-7}$ Pa) with the layer thickness monitored by quartz crystals. In the final step, a 100 nm silver top electrode was evaporated.

Solution absorption measurements were carried out on a Varian Cary 500 spectrophotometer, whereas films were measured on a Bruker microscope (Vertex 80/Hyperion 2000 FTIR)). Film thicknesses were measured with a DektakXT profiler (Bruker) and an ICON AFM

(Bruker) using silicon cantilevers from Mikromasch (Mikromasch, USA, 325 kHz, 40 N m^{-1}). Nanotube films were additionally characterized using SEM (Zeiss Ultra Plus). The HOMO of (6,5) films, shown in Figure 1b, was measured on an ITO substrate by PESA (AC-2E, Riken Keiki) as shown in Figure S3 of the Supporting Information.[40] The solar cells were characterized with a Keithley 238 source meter under AM1.5G illumination from a Newport 300 W solar simulator. Following *J–V* characterization, EQE was measured with a 450 W Xenon light source, an optical chopper (84.7 Hz), a 300 mm monochromator (LOT-Oriel), a custom-designed current amplifier (DLPCA-S, Femto Messtechnik), and a digital lock-in amplifier (eLockin 203 Anfatec). Initial calibration was carried out with a calibrated UV-enhanced silicon diode (SM1PD2A, Thorlabs).

TMCs were performed using the MATLAB code available from the McGehee group at Stanford and as outlined by Burkhard et al. and Pettersson et al.[11,41] The complex refractive indices of glass, ITO, PEDOT:PSS, and C_{60} were included in the code and the electric field intensity and exciton generation rate were calculated for all layer combinations presented in this study.[11,41,42] Further information can also be found in the Supporting Information.

Supporting Information

Supporting Information is available from the Wiley Online Library or from the author.

Acknowledgements

B.S.F. gratefully acknowledges support from the Deutsche Forschungsgemeinschafts (DFG) Emmy Noether Program under grant number FL 834/1-1. R.K. acknowledges funding by the German Science Foundation INST 163/354-1 FUGG. K.G., C.K., and A.C. acknowledge funding by the German Federal Ministry for Education and Research (BMBF) under contract 03EK3504 (project TAURUS) and support by the DFG Center for Functional Nanostructures (CFN). M.P. acknowledges Tanja Puerckhauer for PESA measurements.

Received: July 6, 2015
Revised: September 25, 2015
Published online: October 30, 2015

[1] D. J. Bindl, N. S. Safron, M. S. Arnold, *ACS Nano* **2010**, *4*, 5657.
[2] M. J. Shea, M. S. Arnold, *Appl. Phys. Lett.* **2013**, *102*, 243101.
[3] R. M. Jain, R. Howden, K. Tvrdy, S. Shimizu, A. J. Hilmer, T. P. McNicholas, K. K. Gleason, M. S. Strano, *Adv. Mater.* **2012**, *24*, 4436.
[4] H. Wang, G. I. Koleilat, P. Liu, G. Jiménez-Osés, Y.-C. Lai, M. Vosgueritchian, Y. Fang, S. Park, K. N. Houk, Z. Bao, *ACS Nano* **2014**, *8*, 2609.
[5] M. Gong, T. A. Shastry, Y. Xie, M. Bernardi, D. Jasion, K. A. Luck, T. J. Marks, J. C. Grossman, S. Ren, M. C. Hersam, *Nano Lett.* **2014**, *14*, 5308.
[6] S. L. Guillot, K. S. Mistry, A. D. Avery, J. Richard, A.-M. Dowgiallo, P. F. Ndione, J. van de Lagemaat, M. O. Reese, J. L. Blackburn, *Nanoscale* **2015**, *7*, 6556.
[7] a) D. D. Tune, J. G. Shapter, *Energy Environ. Sci.* **2013**, *6*, 2572; b) D. O. Bellisario, R. M. Jain, Z. Ulissi, M. S. Strano, *Energy Environ. Sci.* **2014**, *7*, 3769; c) D. D. Tune, F. Hennrich, S. Dehm, M. F. G. Klein, K. Glaser, A. Colsmann, J. G. Shapter, U. Lemmer, M. M. Kappes, R. Krupke, B. S. Flavel, *Adv. Energy Mater.* **2013**, *3*, 1091; d) M. Engel, K. E. Moore, A. Alam, S. Dehm, R. Krupke, B. S. Flavel, *ACS Nano* **2014**, *8*, 9324.
[8] a) L. Yang, P. Kim, H. M. Meyer, S. Agnihotri, *J. Colloid Interface Sci.* **2009**, *338*, 128; b) G. Chen, T. M. Paronyan, E. M. Pigos, A. R. Harutyunyan, *Sci. Rep.* **2012**, *2*, 343; c) T. Dürkop, S. A. Getty, E. Cobas, M. S. Fuhrer, *Nano Lett.* **2003**, *4*, 35.
[9] a) H. Kataura, Y. Kumazawa, Y. Maniwa, I. Umezu, S. Suzuki, Y. Ohtsuka, Y. Achiba, *Synth. Met.* **1999**, *103*, 2555; b) R. B. Weisman, S. M. Bachilo, *Nano Lett.* **2003**, *3*, 1235; c) E. H. Haroz, S. M. Bachilo, R. B. Weisman, S. K. Doorn, *Phys. Rev. B* **2008**, *77*, 125405.
[10] D. J. Bindl, M. S. Arnold, *J. Phys. Chem. C* **2013**, *117*, 2390.
[11] L. A. A. Pettersson, L. S. Roman, O. Inganäs, *J. Appl. Phys.* **1999**, *86*, 487.
[12] A. Nish, J.-Y. Hwang, J. Doig, R. J. Nicholas, *Nat. Nano* **2007**, *2*, 640.
[13] F. Chen, B. Wang, Y. Chen, L.-J. Li, *Nano Lett.* **2007**, *7*, 3013.
[14] a) B. S. Flavel, M. M. Kappes, R. Krupke, F. Hennrich, *ACS Nano* **2013**, *7*, 3557; b) B. S. Flavel, K. E. Moore, M. Pfohl, M. M. Kappes, F. Hennrich, *ACS Nano* **2014**, *8*, 1817.
[15] a) K. Moshammer, F. Hennrich, M. Kappes, *Nano Res.* **2009**, *2*, 599; b) H. Liu, D. Nishide, T. Tanaka, H. Kataura, *Nat. Commun.* **2011**, *2*, 309.
[16] M. S. Arnold, A. A. Green, J. F. Hulvat, S. I. Stupp, M. C. Hersam, *Nat. Nano* **2006**, *1*, 60.
[17] C. Y. Khripin, J. A. Fagan, M. Zheng, *J. Am. Chem. Soc.* **2013**, *135*, 6822.
[18] K. S. Mistry, B. A. Larsen, J. L. Blackburn, *ACS Nano* **2013**, *7*, 2231.
[19] M.-Y. Wu, R. M. Jacobberger, M. S. Arnold, *J. Appl. Phys.* **2013**, *113*, 204504.
[20] D. J. Bindl, M. J. Shea, M. S. Arnold, *Chem. Phys.* **2013**, *413*, 29.
[21] R. C. Tenent, T. M. Barnes, J. D. Bergeson, A. J. Ferguson, B. To, L. M. Gedvilas, M. J. Heben, J. L. Blackburn, *Adv. Mater.* **2009**, *21*, 3210.
[22] G. S. Tulevski, A. D. Franklin, A. Afzali, *ACS Nano* **2013**, *7*, 2971.
[23] H. Li, T. C. Hain, A. Muzha, F. Schöppler, T. Hertel, *ACS Nano* **2014**, *8*, 6417.
[24] M. Engel, J. P. Small, M. Steiner, M. Freitag, A. A. Green, M. C. Hersam, P. Avouris, *ACS Nano* **2008**, *2*, 2445.
[25] S. Ghosh, S. M. Bachilo, R. B. Weisman, *Nat. Nano* **2010**, *5*, 443.
[26] a) M. J. O'Connell, S. M. Bachilo, C. B. Huffman, V. C. Moore, M. S. Strano, E. H. Haroz, K. L. Rialon, P. J. Boul, W. H. Noon, C. Kittrell, J. Ma, R. H. Hauge, R. B. Weisman, R. E. Smalley, *Science* **2002**, *297*, 593; b) S. Reich, C. Thomsen, P. Ordejón, *Phys. Rev. B* **2002**, *65*, 155411.
[27] D. J. Bindl, M. Y. Wu, F. C. Prehn, M. S. Arnold, *Nano Lett.* **2011**, *11*, 455.
[28] a) G. Dukovic, F. Wang, D. Song, M. Y. Sfeir, T. F. Heinz, L. E. Brus, *Nano Lett.* **2005**, *5*, 2314; b) V. Perebeinos, J. Tersoff, P. Avouris, *Phys. Rev. Lett.* **2004**, *92*, 257402.
[29] a) R. B. Capaz, C. D. Spataru, S. Ismail-Beigi, S. G. Louie, *Phys. Rev. B* **2006**, *74*, 121401; b) A. F. Hebard, R. C. Haddon, R. M. Fleming, A. R. Kortan, *Appl. Phys. Lett.* **1991**, *59*, 2109.
[30] a) J. Huang, P. F. Miller, J. S. Wilson, A. J. de Mello, J. C. de Mello, D. D. C. Bradley, *Adv. Funct. Mater.* **2005**, *15*, 290; b) S. Sapp, S. Luebben, Y. B. Losovyj, P. Jeppson, D. L. Schulz, A. N. Caruso, *Appl. Phys. Lett.* **2006**, *88*, 152107; c) A. W. Dweydari, C. H. B. Mee, *Phys. Status Solidi A* **1975**, *27*, 223.
[31] a) J. A. Fagan, J. R. Simpson, B. J. Landi, L. J. Richter, I. Mandelbaum, V. Bajpai, D. L. Ho, R. Raffaelle, A. R. H. Walker, B. J. Bauer, E. K. Hobbie, *Phys. Rev. Lett.* **2007**, *98*, 147402; b) Y. Battie, D. Jamon, A. En Naciri, J.-S. Lauret, A. Loiseau, *Appl. Phys. Lett.* **2013**, *102*, 091909.
[32] a) J. J. M. Halls, K. Pichler, R. H. Friend, S. C. Moratti, A. B. Holmes, *Appl. Phys. Lett.* **1996**, *68*, 3120; b) D. Qin, P. Gu, R. S. Dhar, S. G. Razavipour, D. Ban, *Phys. Status Solidi A* **2011**, *208*, 1967.
[33] F. Yan, X. M. Bao, X. W. Wu, H. L. Chen, *Appl. Phys. Lett.* **1995**, *67*, 3471.
[34] J. L. Gray, in *Handbook of Photovoltaic Science and Engineering*, John Wiley & Sons, Ltd., West Sussex, UK **2011**, p. 82.
[35] J. D. Servaites, M. A. Ratner, T. J. Marks, *Energy Environ. Sci.* **2011**, *4*, 4410.
[36] G. A. H. Wetzelaer, M. Kuik, M. Lenes, P. W. M. Blom, *Appl. Phys. Lett.* **2011**, *99*, 153506.

[37] S. R. Cowan, A. Roy, A. J. Heeger, *Phys. Rev. B* **2010**, *82*, 245207.

[38] M. Gong, T. A. Shastry, Q. Cui, R. R. Kohlmeyer, K. A. Luck, A. Rowberg, T. J. Marks, M. F. Durstock, H. Zhao, M. C. Hersam, S. Ren, *ACS Appl. Mater. Interfaces* **2015**, *7*, 7428.

[39] T. Suni, K. Henttinen, I. Suni, J. Mäkinen, *J. Electrochem. Soc.* **2002**, *149*, G348.

[40] M. Uda, *Jpn. J. Appl. Phys.* **1985**, *24*, 284.

[41] G. F. Burkhard, E. T. Hoke, M. D. McGehee, *Adv. Mater.* **2010**, *22*, 3293.

[42] a) S. L. Ren, Y. Wang, A. M. Rao, E. McRae, J. M. Holden, T. Hager, K. Wang, W. T. Lee, H. F. Ni, J. Selegue, P. C. Eklund, *Appl. Phys. Lett.* **1991**, *59*, 2678; b) E. D. Palik, *Handbook of Optical Constants of Solids*, Vol. *3*, Academic Press, Massachusetts, USA **1998**.

– This page intentionally left blank –

2.5 Carbon Nanotubes as Photosensitive Elements

2.5.1 *Photocurrent Spectroscopy of (n,m) Sorted Solution-Processed Single-Walled Carbon Nanotubes*

M. Engel, K. E. Moore, A. Alam, S. Dehm, R. Krupke, **B. S. Flavel**

ACS Nano 8 (2014) 9324–9331

DOI: 10.1021/nn503278d

Abstract

Variable-wavelength photocurrent microscopy and photocurrent spectroscopy are used to study the photoresponse of (n, m) sorted single-walled carbon nanotube (SWNT) devices. The measurements of (n, m) pure SWCNT devices demonstrate the ability to study the wavelength-dependent photoresponse in situ in a device configuration and deliver photocurrent spectra that reflect the population of the source material. Furthermore, we show that it is possible to map and determine the chirality population within a working optoelectronic SWCNT device.

Contribution

B.S.F and R.K conceived the idea for the project. B.S.F, M.E, K.E. A.A, S.D and R.K performed the experiments. B.S.F and M.E wrote the manuscript and all authors participated in the scientific evaluation of the results.

– This page intentionally left blank –

Photocurrent Spectroscopy of (*n*, *m*) Sorted Solution-Processed Single-Walled Carbon Nanotubes

Michael Engel,[†,#] **Katherine E. Moore,**[†,‡] **Asiful Alam,**[†] **Simone Dehm,**[†] **Ralph Krupke,**[†,§,*] **and Benjamin S. Flavel**[†,*]

[†]Institute of Nanotechnology, Karlsruhe Institute of Technology, 76021, Karlsruhe, Germany, [‡]Centre for Nanoscale Science and Technology, School of Chemical and Physical Sciences, Flinders University, 5000, Adelaide, Australia, and [§]Institute for Materials Science, Technische Universität Darmstadt, 64287, Darmstadt, Germany. [#]Present address: IBM Thomas J. Watson Research Center, Yorktown Heights, New York 10598, United States.

ABSTRACT Variable-wavelength photocurrent microscopy and photocurrent spectroscopy are used to study the photoresponse of (*n*, *m*) sorted single-walled carbon nanotube (SWNT) devices. The measurements of (*n*, *m*) pure SWCNT devices demonstrate the ability to study the wavelength-dependent photoresponse *in situ* in a device configuration and deliver photocurrent spectra that reflect the population of the source material. Furthermore, we show that it is possible to map and determine the chirality population within a working optoelectronic SWCNT device.

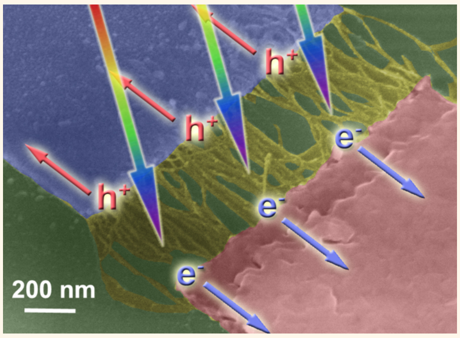

KEYWORDS: spectrally resolved photocurrent · carbon nanotube · chirality sorted · supercontinuum light source

Recently the use of single-walled carbon nanotubes (SWCNTs) for next-generation all-carbon solar cells and light-sensitive devices has gained increasing attention in the literature.[1] While SWCNTs have traditionally been integrated into a variety of organic photovoltaic systems, the role of carbon nanotubes in these systems was strictly limited to their use as an efficient electron transport medium. The latest focus is aimed at capitalizing on the unique and richly varying optical properties of SWCNTs. In order to appreciate this point, it is only necessary to consider the SWCNTs produced by the HiPco process and the possible applications they may have for photovoltaics. The HiPco raw material consists of a multitude of semiconducting (s-SWCNT) species of varying diameter (D_t), chiral angle, or (*n*, *m*) index, and each of these species has unique first (S_{11}) and second (S_{22}) optical transitions in the region ~900−1350 nm and ~500−850 nm, respectively.[2,3] Therefore, upon selecting the appropriate (*n*, *m*) combination of SWCNTs, it is theoretically possible to fabricate a solar cell capable of harvesting light in not only the visible but also the infrared,[4] a spectral region excluded by traditional silicon solar cells. Alternatively, it is envisaged that upon selecting highly pure (*n*, *m*) material, it would be possible to create a device that is sensitive to the discrete optical transitions of the SWCNTs, hence paving the way for optical sensors.[5] This discussion can then of course be extended to consider other SWCNT synthetic routes such as arc discharge, laser ablation, and the CoMoCAT process, which afford a completely different ensemble of (*n*, *m*) species and extend the accessible spectral regime, not to mention the possibility of probing higher order optical transitions (S_{33}, S_{44}, *etc.*), multiple exciton generation,[6] and the potential for metallic SWCNTs (m-SWCNTs) to be used as metallic contacts.

The realization of these goals has led to the development of several different approaches. Toward the fabrication of solar cells from thin films of SWCNTs, Svreck *et al.*[7] have combined poly-9,9-di-*n*-octylfluorenyl-2,7-diyl (PFO)-wrapped SWCNTs with silicon nanocrystals and shown that the photocurrent is unambiguously correlated to the optical properties of the nanotubes. Likewise, Bindl *et al.*[8,9] integrated PFO-wrapped SWCNTs

* Address correspondence to
benjamin.flavel@kit.edu,
ralph.krupke@kit.edu.

Received for review June 17, 2014
and accepted August 12, 2014.

10.1021/nn503278d

into bilayered heterojunctions with C_{60} as an acceptor. Jain *et al.*[10] then demonstrated the viability of this bilayered heterojunction approach with polymer-unwrapped, surfactant-stabilized, (6,5) SWCNTs. Despite initial SWCNT/C_{60} solar cells boasting relatively low efficiencies, Shea *et al.*[11] have recently reported efficiencies of up to 1%. Nevertheless, it remains clear that further work is required in order to achieve devices comparable to other well-established organic photovoltaic systems. Perhaps this is indeed achieved through using multiple nanotube layers as suggested by Shea *et al.*,[11] but the field also benefits from photocurrent studies on the single- or few-nanotube level, where a more fundamental investigation of the generation of photocurrent is possible.

From a technological standpoint the fabrication of single- or few-nanotube devices is not new. Techniques such as dielectrophoretic deposition from solution[12,13] or chemical vapor deposition (CVD) growth of SWCNTs between metalized source and drain contacts in CNT field-effect transistors are becoming standard. In this architecture photogenerated electrons and holes are typically separated by either an externally applied gate bias or internal fields at the SWCNT–metal Schottky barrier.[14,15,39,40] Photocurrent generation has therefore been studied in both substrate-supported[6,16–19] and unsupported[20–22] CNTs. However, unlike in the case of the SWCNT films discussed previously, a laser is typically used to address the CNTs due to the high power density required to measure photocurrent from only a few CNTs. Hence the laser source and CNT must be chosen carefully to ensure at least one of the CNT's optical transitions (usually S_{22}) matches the excitation source. From this point of view one could call such systems "nanoscale solar cells"; however, as the ability to produce power under illumination on the single-nanotube level is yet to be shown, it is more realistic to refer to them as "nanoscale photodetectors" or simply appreciate the fundamental spectroscopic investigation that is possible on this scale. The literature contains many such examples. For example the early work of Chen *et al.*[16] and further work by Engel *et al.*[17] using SWCNTs placed between asymmetric metal contacts (with high and low work function) to achieve a strong built-in electric field allowed for the efficient separation of electron–hole pairs. Alternatively, Lee *et al.*[19,22] formed a p–n junction along the length of a single carbon nanotube by electrostatic doping using a pair of split gate electrodes. Electron–hole pairs were then separated in the middle of the device where the electric field was the greatest.

Most recently, Barkelid *et al.*[20,21] used a similar split gate design and provided a comparison of the photocurrent generated in semiconducting and metallic carbon nanotubes. In their work they suggest that the photocurrent generated from semiconducting nanotubes had photovoltaic origins, whereas in the case of metallic nanotubes it was photothermoelectric. In other words the photocurrent in s-SWCNTs arises from an electric field (built-in or applied), and the photocurrent in m-SWCNTs is mediated by a difference in Seebeck coefficients. In performing their study Barkelid *et al.*[20,21] addressed a problem in the literature, namely, seemingly conflicting results with some reports stating the photocurrent to be photothermoelectric[23–26] in origin while others showed a photovoltaic behavior.[16,17,22] Reflecting on the device design of many groups reporting photothermoelectric origins, either unsorted metallic CNTs[24] or a film of CNTs was used.[23,27] Hence discrimination between these two effects was understandably difficult. However, in the work of Amer *et al.*,[28] who exclusively worked on split gate devices from metallic CNTs, it is important to note that the photocurrent signal was clearly seen to originate from the center of the nanotube (position of split gates), which would suggest that the photocurrent originated from the p–n junction rather than the contacts. Moreover, in 2014, DeBorde *et al.*[29] found evidence of both photovoltaic and photothermoelectric mechanisms, where the type of mechanism responsible was found to depend on the gate voltage, *i.e.*, if the carbon nanotube was in the off- or on-state, respectively. Indeed the discussion of photocurrent generation in CNTs appears to be far from resolved. More important at this point is the conclusion that if such fundamental studies are to be performed, the suspension of CNTs used, or growth mechanism applied, must be limited to CNTs of well-defined and controlled electronic and optical property.

Toward this end DeBorde *et al.*[30] have used chemical vapor deposition to integrate single-chirality carbon nanotubes into field-effect transistor devices. In their work, due to each device consisting of only one CNT, each device was by definition single chirality and correspondingly had well-defined optical properties. This allowed DeBorde *et al.*[30] to measure photoconductivity spectra for each device and identify the chiral indices upon comparison to a catalogue of known CNT exciton resonances. Consequently the use of photocurrent measurements may prove to be a useful characterization technique for device-integrated CNTs. Such a characterization tool would also be advantageous compared to traditional techniques involving the scattering of polarized light by CNTs,[31] where the point of measurement must be sufficiently far away from any metal contact to avoid Rayleigh scattering from the electrodes, therefore limiting the technique to long channel devices with long CNTs ($\sim$20 μm[31]). Although long channel devices are easily achieved with CVD growth, solution-processed CNTs typically have lengths on the order of a few micrometers and make such devices impractical. This is where photocurrent characterization may play an important role.

The use of solution-processed CNTs has the added advantage of being able to prepare single-chirality suspensions and thus prepare CNT devices with predetermined (n, m) indices. This is different from CVD growth, where the type of CNT grown is unknown and varies between devices. For this reason many groups focus their efforts on solution processing of (n, m) pure SWCNTs. This has been achieved *via* techniques such as the wrapping of SWCNTs with single-stranded DNA (ssDNA),[32] density gradient ultracentrifugation,[33−35] and Sephacryl gel filtration.[36−38] In our contribution to this field we have recently shown that 15 different (n, m) semiconducting species can be prepared from the HiPco raw material using the Sephacryl gel filtration method upon changing the pH of the eluent.[2] Most recently we have then applied our technique to an automated gel permeation chromatography (GPC) system. This system is capable of applying controlled pH gradients to a gel column and allowed us to demonstrate the scalable preparation of semiconducting (n, m) species with a purity of 61−95%.[3] In the present work we now integrate the prepared (n, m) SWCNT species into two terminal electronic devices to allow the measurement of spectrally resolved photocurrent. Furthermore, to our knowledge this is the first example of photocurrent spectroscopy being used to characterize solution-processed SWCNTs.

RESULTS AND DISCUSSION

With the use of dielectrophoresis, single-chirality SWCNTs were deposited into devices for the measurement of photocurrent. Each device consisted of two palladium contacts with a width of 1 μm and a gap-size (channel width) of 600 nm on a Si/SiO_2 substrate. To any set of palladium contacts either the (6, 5), (7, 6), (7, 5), (8, 3), or (9, 4) SWCNT species were deposited to yield a single-chirality SWCNT device. For each of the SWCNT species a corresponding solution absorption measurement is shown in Figure 1. As our measurement setup is currently capable of measurement only in the visible regime, only the S_{22} region for each (n, m) species is shown. Complete spectra from 500−1300 nm for each (n, m) species, where both S_{22} and S_{11} are visible, along with the normalization factors used are available in Figure S1 of the Supporting Information. As expected for pure (n, m) SWCNT suspensions, every species has only one major S_{22} resonance with no or minor additional resonances. We attribute minor resonances to the impurity of additional (n, m) SWNT species. This issue of impurities will be revisited later. Moreover, with the exception of (7, 5) and (7, 6), it can also be seen that all S_{22} optical resonances are well separated. The position of each transition is further listed in Table 1. Each chirality therefore possesses a "fingerprint" that should be possible to resolve in a photocurrent spectroscopy experiment.

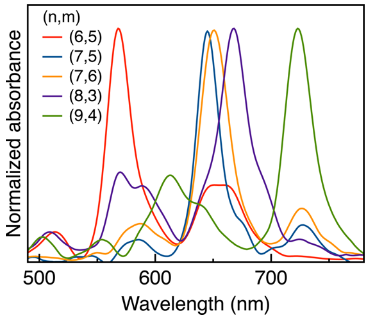

Figure 1. Solution absorption spectra of the five different (n, m) SWNT species used in this work: (6, 5), (7, 5), (7, 6), (8, 3), and (9, 4).

A typical device can be seen both schematically (a) and *via* SEM (b) in Figure 2, where in this case (6, 5) SWCNTs have been deposited between the contacts. It can also be clearly seen that the SWCNTs are predominantly aligned in the direction of the electric field during deposition and that they directly bridge the 600 nm gap. Consequently, the SWCNTs used in this work do not form a percolative current path. Instead each CNT individually contributes to the overall photocurrent measured. On average approximately 10−20 SWCNTs were deposited after dielectrophoresis.

Single-chirality devices were then placed into our custom-built setup for the measurement of photocurrent. In this setup the excitation source was a commercial supercontinuum light source with an attached acousto-optical tunable filter (AOTF) to provide the required wavelength selectivity. The light output was then fiber coupled into a microscope and focused onto the SWCNT device with an objective as seen in Figure 2a. Additionally the entire setup was placed onto an x−y piezoelectric table, which allowed for not only spectrally resolved photocurrent measurements but also 2D surface mapping.

A 2D photocurrent map is shown in Figure 2c, where the short-circuit photocurrent has been overlaid onto

TABLE 1. Responsivity of Each (n, m) SWCNT Device and a Comparison of the S_{22} Optical Transition Obtained from Solution Absorption and Photocurrent Spectroscopy

SWCNT (n, m)	super continuum light source power (mW)	peak photocurrent (pA)	responsivity (pA/mW)	photocurrent maxima (nm)	photocurrent fwhm (nm)	absorption maxima (nm)	absorption fwhm (nm)
(6, 5)	0.24	52.00	216.67	557	47.7	569	23.8
(7, 5)	0.66	28.60	43.33	648	48.8	645	21.1
(7, 6)	0.66	31.00	46.97	644	46.1	651	26.8
(8, 3)	0.94	8.53	9.07	666	59.8	667	35.7
(9, 4)	2.38	6.28	2.64	706	52.9	723	27.1

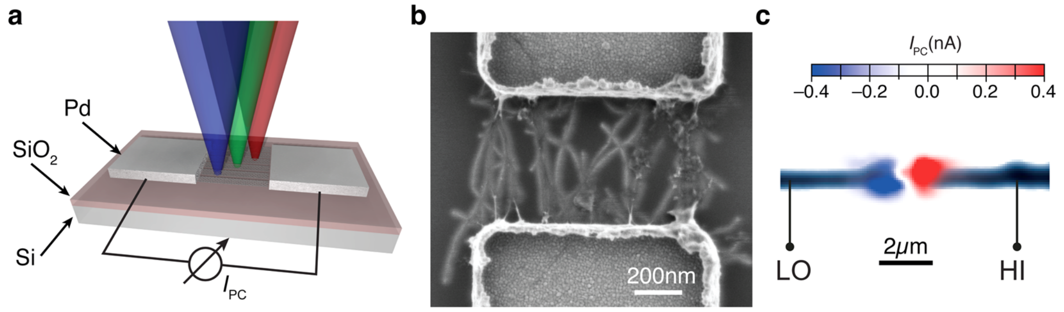

Figure 2. **(a) 3D schematic of the measurement setup. A focused light beam of variable wavelength is scanned across a carbon nanotube film interfaced with metallic contacts. (b) Scanning electron micrograph of a typical carbon nanotube device as schematically shown in (a), where the nanotube density is approximately 10/μm. (c) Scanning photocurrent microscopy map (excited at 570 nm) overlaid on top of the simultaneously recorded elastically scattered signal from the sample.**

the corresponding 2D map of elastically scattered light. In this example a device with (6, 5) SWCNT species was excited at 570 nm, corresponding to the S_{22} optical transition for the (6, 5) SWCNT. As a comparison we also measure at off-resonant wavelengths and consistently observe a drop in the maximum photocurrent amplitude. The two metal contacts can clearly be seen on either side of the 2D map with two photocurrent lobes (blue minima and red maxima) located in the middle of the device. Hence we are able to spatially correlate the photocurrent with respect to the metallic contacts. It is noted that the photocurrent lobes are located close to the SWCNT−metal contact. This is to be expected due to the built-in electric field at the SWCNT−metal Schottky barrier being responsible for electron−hole separation. The presence of positive and negative photocurrent maxima is due to the use of symmetric palladium contacts. Therefore, the band bending due to dissimilar work functions of the metal and SWCNT are symmetric on either end of the SWCNT. Intuitively, when both SWCNT−metal contacts are equally illuminated by the light source (in the center of the device), an equal and opposite photocurrent will therefore be observed on either side of the SWCNT. This would consequently lead to a vanishing net overall photocurrent, a feature that is seen in the middle of our device in the 2D photocurrent map. The two photocurrent lobes therefore correspond to off-center excitation of the SWCNTs, where the photocurrent contribution from one end of the SWCNT outweighs that of the other end. In this work it is the translation of the light source across the device that ensures that such off-center excitation occurs.

For reference, representative transconductance curves for SWCNT devices can be found in Figure S2 of the Supporting Information. It can be seen that we observe p-type transfer characteristics for our devices. Upon noting which of the two palladium electrodes is placed on the high or low connection to the source meter, it is possible to determine the flow direction of carriers across the nanotube channel. In the setup the source meter is measuring the flow direction of electrons and not the technical current. From this standpoint we were able to determine that excitation of an SWCNT in our device through the S_{22} transition leads to a flow of holes onto the palladium contact. This observation is then in agreement with the hole conductance seen in Figure S2.

With the ability to measure photocurrent from single-chirality nanotube devices we are therefore able to perform the main objective of this work, namely, the measurement of spectrally resolved photocurrent, where we would like to show a one-to-one correlation between optical absorption data and photocurrent. For these measurements the device was positioned under the beam *via* the $x-y$ table so as to maximize the photocurrent signal (*i.e.*, off-center photoexcitation of the device to maximize one of the photocurrent lobes). The sample position was then fixed and the wavelength swept between 500 and 750 nm in 5 nm steps. The reason for this is the finite spectral resolution of the AOTF, which outputs a single wavelength with a full-width at half-maximum (fwhm) of 5 nm. For each wavelength step we let the beam and photocurrent settle for three seconds. This proved to be a good compromise between signal-to-noise ratio and measurement speed with regard to position stability of the device.

In Figure 3 the photocurrent for the five different (*n*, *m*) SWNT devices can then be seen as a function of excitation wavelength. For each SWCNT species a clear peak in the photocurrent can be seen. This is attributed once again to electron−hole pairs formed through S_{22} irradiation that get separated and subsequently collected at the contact. With the use of a calibrated silicon diode we then calculate the responsivity of each device, as can be found in Table 1. Furthermore, we make a comparison between the photocurrent peak position and that of the absorption measurement in solution. In general, good agreement between the peak position in the photocurrent and absorption data is seen. However, we do note that a slight blue-shift is seen for (7,5), (7,6), and (8,3) of 1−7 nm and a larger blue-shift for (6, 5) and (9, 4) of 12−17 nm. The exact

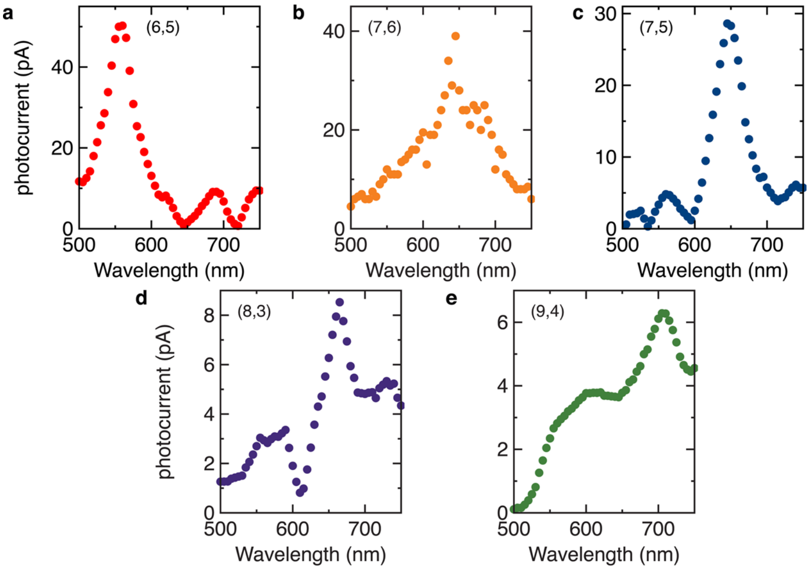

Figure 3. Normalized photocurrent as a function of wavelength for carbon nanotube devices comprising (a) (6, 5), (b) (7, 5), (c) (7, 6), (d) (8, 3), and (e) (9, 4) SWNT species.

origin of the observed blue-shift seen in our work remains speculative. As outlined in the Supporting Information from Liu *et al.*[31] it is well known that the optical resonances of carbon nanotubes are highly sensitive to the surrounding dielectric environment.[41−43] For example, the optical resonances of SWCNTs in micelle suspensions (as in our case for the absorption measurement) are typically red-shifted by 16 meV (S_{22}) and 28 meV (S_{11}) compared to free-suspended SWCNTs.[42] Likewise, Liu *et al.*[31] showed a 30 meV red-shift for SWCNTs on a Si/SiO$_2$ surface (the substrate used in our work) compared to free suspended SWCNTs. Furthermore, Fantini *et al.*[44] showed that bundling of carbon nanotubes leads to on average a 70 meV red-shift compared to suspended micelle-wrapped nanotubes. In our case the final dielectric environment for the SWCNTs in a device is complicated by the presence of different regions along the nanotube, all of which likely contribute to the final peak position that we see in the photocurrent. In our device we have a region of nanotube in contact with metal, a small region of free suspended nanotube (from the top of the metal contact to the substrate), and a region that is in contact with the silicon substrate. Additionally, there is the possibility for residual surfactants to be present and the formation of carbon nanotube bundles on the surface. All of these factors will give rise to a different dielectric environment for the nanotube, and how that will impact the peak position in photocurrent measurements remains unclear. Indeed we expected a red-shift as in the work of Liu *et al.*;[31] however other than to speculate that the observed blue-shift may be a result of the small free suspended region of nanotubes in close proximity to the metallic contact, this issue currently remains unclear to us. However, it can be seen that the population of (*n*, *m*) SWNT species in solution is reflected in a device configuration.

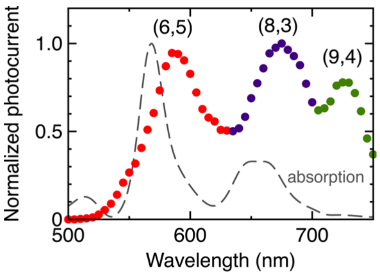

Figure 4. Normalized photocurrent as a function of wavelength for a "high-density" carbon nanotube device. The photocurrent peaks are chirality assigned based on the absorption spectrum (gray).

The question now arises of whether photocurrent measurements can be used as a routine technique for the determination of (*n*, *m*) species in solution or on a surface. In this case the issue of impurity levels becomes important. This is an issue that is best addressed from a larger ensemble of SWCNTs so as to better replicate the entire population of SWCNTs. Due to the obvious presence of additional (*n*, *m*) species, the (6, 5) suspension used in this work was chosen as the ideal test solution. Once again dielectrophoresis was used to deposit the suspension; however an increased alternating voltage was used so as to afford a 10-fold increase in the number SWCNTs in the device. Figure 4 shows a plot of the measured photocurrent spectrum of such a device. As expected, instead of a single photocurrent peak at approximately 557 nm as in Figure 3, multiple photocurrent peaks became visible at 650 and 730 nm. Unexpected is the relative intensity of the additional photocurrent peaks. For comparison, the solution absorption spectrum of the (6, 5) SWCNT suspension is shown. Initially obvious is a red-shift of the photocurrent peak, which as previously discussed is to be expected for a device containing a film of carbon nanotubes where bundling becomes a likely result. Additionally, minor peaks at 650 and 730 nm can also be seen in the absorption spectrum, but their intensity is significantly lower compared to the S_{22} transition of (6, 5) at 557 nm. Here we attribute these peaks to (8, 3), (7, 5), or (9, 4) impurities. Benedict *et al.*[45] and Kozinsky *et al.*[46] help to provide an explanation of this result, by showing that the polarizability of semiconducting carbon nanotubes scales inversely proportional to the band gap. Therefore, nanotubes with a smaller band gap (larger diameter) are more easily deposited by dielectrophoresis. Here we argue that under the present assembly conditions that the larger diameter species such as (9, 4) and (7, 5) are deposited in preference to the smaller diameter (6, 5) SWCNT. This is despite the total contribution of (9, 4), (7, 5), and (8, 3) to the overall SWCNT population in solution being lower. From this point of view, SWCNT photocurrent measurements appear to be capable of providing qualitative information about a nanotube suspension, but their use in a quantitative analysis may be limited. Additionally, for any routine analysis of SWCNTs, the ability to probe not only S_{22} but also S_{11} optical transitions is necessary. This point is made especially clear upon examining the absorption data for the (7, 5), (7, 6), and (8, 3) SWCNTs. All of these species have an S_{22} transition within the region of 640−660 nm (Figure 1). Consequently, upon consideration of only S_{22}, it would be difficult to determine the (*n*, *m*) species from truly unknown SWCNT suspensions. It is only in combination with the complementary S_{11} data (Figure S1) that one obtains a reliable "fingerprint" for each (*n*, *m*) species. For this reason we plan to extend our measurement system with an additional AOTF capable of infrared selectivity.

SUMMARY

In this work we have demonstrated photocurrent spectroscopy of single-chirality carbon nanotube optoelectronic devices and found that our results show good correlation with optical spectroscopy techniques. This technique may offer an *in situ* analytic tool for the characterization of future carbon nanotube devices. Alternatively, the ability to measure single-chirality photocurrent spectra paves the way for increased understanding of the mechanism of photocurrent generation in carbon nanotubes and/or energy transfer processes from photoactive molecules. This understanding will help to develop future applications of carbon nanotubes in solar cells and light-sensitive devices.

METHODS

HiPco SWCNT raw material (NanoIntegris) was used throughout this work. In order to prepare suspensions for (*n*, *m*) purification, 20 mg of raw SWCNT material was suspended in 80 mL of H_2O with 2 wt % sodium dodecyl sulfate (SDS) using a tip sonicator (Weber Ultrasonics, 35 kHz, 500 W, in continuous mode) applied for 15 h at ∼20% power. During sonication, the suspension was placed in a water-circulation bath at 15 °C to aid cooling. As described in detail previously,[3] a SECcurity gel permeation chromatography 1260 Infinity system (Agilent Technologies) was then used to separate this raw SWCNT suspension into (*n*, *m*) pure fractions with the use of sequential 0.2 wt % reductions in SDS concentration and a pH gradient of pH 3−4. Seven milliliters of the Sephacryl S-200 gel medium (Amersham Biosciences) was placed into a commercially available water-jacketed liquid chromatography column (XK 16/20, GE Healthcare) with 16 mm inner diameter and 20 cm length. After applying slight compression the gel yielded a final height of 2 cm. An Accel 250 LC water chiller (Thermoscientific) was used to maintain the column temperature at 23 °C. Absorption spectra of the sorted fractions were recorded on a Varian Cary 500 spectrophotometer.

Dielectrophoresis was then used to deposit the prepared (*n*, *m*) SWCNT suspensions into devices for photocurrent measurements. An array of metallic contacts (where each contact constitutes a device) was patterned on a degenerately doped silicon substrate with an 800 nm layer of silicon dioxide using standard electron beam lithography and a PMMA resist. Following lithography 5 nm of titanium and 50 nm of palladium were deposited by sputtering before a final lift-off process was performed in acetone. The resultant metallic contacts had a width of 1 μm and a gap-size of 600 nm. A 30 μL amount of diluted SWCNT suspension was then dropped onto the array of metallic contacts, and an alternating voltage was applied to the silicon substrate and one common metallic electrode. In this way, SWCNTs were deposited simultaneously into multiple devices.[13] Typical deposition parameters were frequency f = 1 MHz, peak-to-peak voltage V_{pp} = 6 V, and time t = 15 min. The nanotube suspension was used without dilution and resulted in a CNT density of approximately 10/μm except for the device shown in Figure 4, where we had approximately 10 times the surface density. Scanning electron microscopy of resultant devices was taken with a Zeiss Ultra Plus.

Photocurrent measurements were taken with a SuperK Extreme EXW-6 broadband supercontinuum light source (NKT Photonics), where the excitation wavelength was tuned between 500 and 825 nm with the use of the SuperK Select acousto-optic tunable filter (NKT Photonics). The resultant light was linearly polarized and had a bandwidth of 5 nm. A microscope objective of numerical aperture 0.5 was then used to focus the quasi-monochromatic light onto an SWCNT device with an intensity of a few hundred microwatts. This corresponds to a diffraction-limited laser spot of diameter less than 1 μm, which is comparable to the channel length (metallic contact gap-size) of the device. With the help of a motorized x−y stage the fabricated devices were also scanned with a spatial resolution of 375 nm to produce a "photocurrent map". Furthermore, the elastically scattered light was measured with a silicon photodiode and overlaid on the photocurrent map to allow for the position of the photocurrent relative to the SWCNT device to be determined. The resolution is consequently determined by the laser spot diameter and the step size of the motorized stage. The generated zero-bias photocurrent signal was measured with a Keithley 6430 source meter.

Conflict of Interest: The authors declare no competing financial interest.

Acknowledgment. The authors gratefully acknowledge Martin Pfeiffer for assistance with LabVIEW. B.S.F. gratefully acknowledges support from the Deutsche Forschungsgemeinschaft's Emmy Noether Program under grant number FL 834/1-1.

R.K. acknowledges support by the Deutsche Forschungsgemeinschaft (INTST 163/354-1 FUGG). This research was also supported by the Bundesministerium fur Bildung und Forschung (BMBF) as administered by POF-NanoMicro.

Supporting Information Available: Complete absorption spectra of the SWCNT material used in this work and representative transconductance curves are provided. This material is available free of charge *via* the Internet at http://pubs.acs.org.

REFERENCES AND NOTES

1. Tune, D. D.; Flavel, B. S.; Krupke, R.; Shapter, J. G. Carbon Nanotube-Silicon Solar Cells. *Adv. Energy Mater.* **2012**, *2*, 1043–1055.
2. Flavel, B. S.; Kappes, M. M.; Krupke, R.; Hennrich, F. Separation of Single-Walled Carbon Nanotubes by 1-Dodecanol-Mediated Size-Exclusion Chromatography. *ACS Nano* **2013**, *7*, 3557–3564.
3. Flavel, B. S.; Moore, K. E.; Pfohl, M.; Kappes, M. M.; Hennrich, F. Separation of Single-Walled Carbon Nanotubes with a Gel Permeation Chromatography System. *ACS Nano* **2014**, *8*, 1817–1826.
4. Tune, D. D.; Shapter, J. G. The Potential Sunlight Harvesting Efficiency of Carbon Nanotube Solar Cells. *Energ. Environ. Sci.* **2013**, *6*, 2572–2577.
5. Barone, P. W.; Baik, S.; Heller, D. A.; Strano, M. S. Near-Infrared Optical Sensors Based on Single-Walled Carbon Nanotubes. *Nat. Mater.* **2005**, *4*, 86–U16.
6. Gabor, N. M.; Zhong, Z. H.; Bosnick, K.; Park, J.; McEuen, P. L. Extremely Efficient Multiple Electron-Hole Pair Generation in Carbon Nanotube Photodiodes. *Science* **2009**, *325*, 1367–1371.
7. Svrcek, V.; Cook, S.; Kazaoui, S.; Kondo, M. Silicon Nanocrystals and Semiconducting Single-Walled Carbon Nanotubes Applied to Photovoltaic Cells. *J. Phys. Chem. Lett.* **2011**, *2*, 1646–1650.
8. Bindl, D. J.; Safron, N. S.; Arnold, M. S. Dissociating Excitons Photogenerated in Semiconducting Carbon Nanotubes at Polymeric Photovoltaic Heterojunction Interfaces. *ACS Nano* **2010**, *4*, 5657–5664.
9. Bindl, D. J.; Wu, M. Y.; Prehn, F. C.; Arnold, M. S. Efficiently Harvesting Excitons from Electronic Type-Controlled Semiconducting Carbon Nanotube Films. *Nano Lett.* **2011**, *11*, 455–460.
10. Jain, R. M.; Howden, R.; Tvrdy, K.; Shimizu, S.; Hilmer, A. J.; McNicholas, T. P.; Gleason, K. K.; Strano, M. S. Polymer-Free Near-Infrared Photovoltaics with Single Chirality (6,5) Semiconducting Carbon Nanotube Active Layers. *Adv. Mater.* **2012**, *24*, 4436–4439.
11. Shea, M. J.; Arnold, M. S. 1% Solar Cells Derived from Ultrathin Carbon Nanotube Photoabsorbing Films. *Appl. Phys. Lett.* **2013**, *102*, 243101.
12. Krupke, R.; Hennrich, F.; Weber, H. B.; Beckmann, D.; Hampe, O.; Malik, S.; Kappes, M. M.; Lohneysen, H. V. Contacting Single Bundles of Carbon Nanotubes with Alternating Electric Fields. *Appl. Phys. A: Mater. Sci. Process.* **2003**, *76*, 397–400.
13. Vijayaraghavan, A.; Blatt, S.; Weissenberger, D.; Oron-Carl, M.; Hennrich, F.; Gerthsen, D.; Hahn, H.; Krupke, R. Ultra-Large-Scale Directed Assembly of Single-Walled Carbon Nanotube Devices. *Nano Lett.* **2007**, *7*, 1556–1560.
14. Avouris, P.; Freitag, M.; Perebeinos, V. Carbon-Nanotube Photonics and Optoelectronics. *Nat. Photonics* **2008**, *2*, 341–350.
15. Balasubramanian, K.; Burghard, M.; Kern, K.; Scolari, M.; Mews, A. Photocurrent Imaging of Charge Transport Barriers in Carbon Nanotube Devices. *Nano Lett.* **2005**, *5*, 507–510.
16. Chen, C. X.; Lu, Y.; Kong, E. S.; Zhang, Y. F.; Lee, S. T. Nanowelded Carbon-Nanotube-Based Solar Microcells. *Small* **2008**, *4*, 1313–1318.
17. Engel, M.; Steiner, M.; Sundaram, R. S.; Krupke, R.; Green, A. A.; Hersam, M. C.; Avouris, P. Spatially Resolved Electrostatic Potential and Photocurrent Generation in Carbon Nanotube Array Devices. *ACS Nano* **2012**, *6*, 7303–7310.
18. Freitag, M.; Martin, Y.; Misewich, J. A.; Martel, R.; Avouris, P. H. Photoconductivity of Single Carbon Nanotubes. *Nano Lett.* **2003**, *3*, 1067–1071.
19. Lee, J. U.; Gipp, P. P.; Heller, C. M. Carbon Nanotube p-n Junction Diodes. *Appl. Phys. Lett.* **2004**, *85*, 145–147.
20. Barkelid, M.; Zwiller, V. Single Carbon Nanotube Photovoltaic Device. *J. Appl. Phys.* **2013**, *114*, 154320.
21. Barkelid, M.; Zwiller, V. Photocurrent Generation in Semiconducting and Metallic Carbon Nanotubes. *Nat. Photonics* **2014**, *8*, 48–52.
22. Lee, J. U. Photovoltaic Effect in Ideal Carbon Nanotube Diodes. *Appl. Phys. Lett.* **2005**, *87*, 073101.
23. St-Antoine, B. C.; Menard, D.; Martel, R. Position Sensitive Photothermoelectric Effect in Suspended Single-Walled Carbon Nanotube Films. *Nano Lett.* **2009**, *9*, 3503–3508.
24. Tsen, A. W.; Donev, L. A. K.; Kurt, H.; Herman, L. H.; Park, J. Imaging the Electrical Conductance of Individual Carbon Nanotubes with Photothermal Current Microscopy. *Nat. Nanotechnol.* **2009**, *4*, 108–113.
25. Zhang, Y.; Iijima, S. Elastic Response of Carbon Nanotube Bundles to Visible Light. *Phys. Rev. Lett.* **1999**, *82*, 3472–3475.
26. St-Antoine, B. C.; Menard, D.; Martel, R. Photothermoelectric Effects in Single-Walled Carbon Nanotube Films: Reinterpreting Scanning Photocurrent Experiments. *Nano Res.* **2012**, *5*, 73–81.
27. Sczygelski, E.; Sangwan, V. K.; Wu, C. C.; Arnold, H. N.; Everaerts, K.; Marks, T. J.; Hersam, M. C.; Lauhon, L. J. Extrinsic and Intrinsic Photoresponse in Monodisperse Carbon Nanotube Thin Film Transistors. *Appl. Phys. Lett.* **2013**, 102.
28. Amer, M. R.; Chang, S. W.; Dhall, R.; Qiu, J.; Cronin, S. B. Zener Tunneling and Photocurrent Generation in Quasi-Metallic Carbon Nanotube pn-Devices. *Nano Lett.* **2013**, *13*, 5129–5134.
29. DeBorde, T.; Aspitarte, L.; Sharf, T.; Kevek, J. W.; Minot, E. D. Photothermoelectric Effect in Suspended Semiconducting Carbon Nanotubes. *ACS Nano* **2014**, *8*, 216–221.
30. DeBorde, T.; Aspitarte, L.; Sharf, T.; Kevek, J. W.; Minot, E. D. Determining the Chiral Index of Semiconducting Carbon Nanotubes Using Photoconductivity Resonances. *J. Phys. Chem. C* **2014**, *118*, 9946–9950.
31. Liu, K. H.; Hong, X. P.; Zhou, Q.; Jin, C. H.; Li, J. H.; Zhou, W. W.; Liu, J.; Wang, E. G.; Zettl, A.; Wang, F. High-Throughput Optical Imaging and Spectroscopy of Individual Carbon Nanotubes in Devices. *Nat. Nanotechnol.* **2013**, *8*, 917–922.
32. Tu, X. M.; Manohar, S.; Jagota, A.; Zheng, M. DNA Sequence Motifs for Structure-Specific Recognition and Separation of Carbon Nanotubes. *Nature* **2009**, *460*, 250–253.
33. Arnold, M. S.; Green, A. A.; Hulvat, J. F.; Stupp, S. I.; Hersam, M. C. Sorting Carbon Nanotubes by Electronic Structure Using Density Differentiation. *Nat. Nanotechnol.* **2006**, *1*, 60–65.
34. Arnold, M. S.; Stupp, S. I.; Hersam, M. C. Enrichment of Single-Walled Carbon Nanotubes by Diameter in Density Gradients. *Nano Lett.* **2005**, *5*, 713–718.
35. Ghosh, S.; Bachilo, S. M.; Weisman, R. B. Advanced Sorting of Single-Walled Carbon Nanotubes by Nonlinear Density-Gradient Ultracentrifugation. *Nat. Nanotechnol.* **2010**, *5*, 443–450.
36. Liu, H. P.; Tanaka, T.; Urabe, Y.; Kataura, H. High-Efficiency Single-Chirality Separation of Carbon Nanotubes Using Temperature-Controlled Gel Chromatography. *Nano Lett.* **2013**, *13*, 1996–2003.
37. Moshammer, K.; Hennrich, F.; Kappes, M. M. Selective Suspension in Aqueous Sodium Dodecyl Sulfate According to Electronic Structure Type Allows Simple Separation of Metallic from Semiconducting Single-Walled Carbon Nanotubes. *Nano Res.* **2009**, *2*, 599–606.
38. Tvrdy, K.; Jain, R. M.; Han, R.; Hilmer, A. J.; McNicholas, T. P.; Strano, M. S. A Kinetic Model for the Deterministic Prediction of Gel-Based Single-Chirality Single-Walled Carbon Nanotube Separation. *ACS Nano* **2013**, *7*, 1779–1789.

39. Sfeir, M. Y.; Misewich, J. A.; Rosenblatt, S.; Wu, Y.; Voisin, C.; Yan, H.; Berciaud, S.; Heinz, T. F.; Chandra, B.; Caldwell, R.; *et al.* Infrared Spectra of Individual Semiconducting Single-Walled Carbon Nanotubes: Testing the Scaling of Transition Energies for Large Diameter Nanotubes. *Phys. Rev. B* **2010**, 195424.
40. Mohite, A.; Lin, J.; Sumanasekera, G. U.; Alphenaar, B. W. Field-Enhanced Photocurrent Spectroscopy of Excitonic States in Single-Wall Carbon Nanotubes. *Nano Lett.* **2006**, 1369–1373.
41. Okazaki, T.; Saito, T.; Matsuura, K.; Ohshima, S.; Yumura, M.; Iijima, S. Photoluminescence Mapping of "As-Grown" Single-Walled Carbon Nanotubes: A Comparison with Micelle-Encapsulated Nanotube Solutions. *Nano Lett.* **2005**, *5*, 2618–2623.
42. Lefebvre, J.; Fraser, J. M.; Homma, Y.; Finnie, P. Photoluminescence from Single-Walled Carbon Nanotubes: A Comparison Between Suspended and Micelle-Encapsulated Nanotubes. *Appl. Phys. A: Mater. Sci. Process.* **2004**, *78*, 1107–1110.
43. Choi, J. H.; Strano, M. S. Solvatochromism in Single-Walled Carbon Nanotubes. *Appl. Phys. Lett.* **2007**, *90*, 223114.
44. Fantini, C.; Jorio, A.; Souza, M.; Strano, M. S.; Dresselhaus, M. S.; Pimenta, M. A. Optical Transition Energies for Carbon Nanotubes from Resonant Raman Spectroscopy: Environment and Temperature Effects. *Phys. Rev. Lett.* **2004**, *93*, 147406.
45. Benedict, L. X.; Louie, S. G.; Cohen, M. L. Static Polarizabilities of Single-Wall Carbon Nanotubes. *Phys. Rev. B* **1995**, *52*, 8541–8549.
46. Kozinsky, B.; Marzari, N. Static Dielectric Properties of Carbon Nanotubes from First Principles. *Phys. Rev. Lett.* **2006**, *96*, 166801.

2.5 Carbon Nanotubes as Photosensitive Elements

2.5.2 *Photocurrent Imaging of Semiconducting Carbon Nanotube Devices with Local Mirrors*

A. Alam, **B. S. Flavel**, S. Dehm, U. Lemmer, R. Krupke

Physica Status Solidi B 251 (2014) 2471–2474

DOI: 10.1002/pssb.201451272

Abstract

Photocurrent spectroscopy has recently been used by several research groups to study the light–matter interaction in carbon nanotubes. To achieve this, long-channel devices with symmetric metallic contacts are typically used, where photocurrent of opposite sign is generated at the two contacts. However, in short-channel devices (<1 mm) the diffraction limited laser spot results in simultaneous excitation of both metal–nanotube contacts and leads to partial cancellation of the photocurrent. In this work, we avoid simultaneous excitation of both metal–nanotube contacts by fabricating an isolated metallic mirror over one of the contacts. With the use of (6,5) carbon nanotubes we demonstrate a unipolar photocurrent signal, that is consistent with the second order interband absorption of a (6,5) nanotube.

Contribution

B.S.F and R.K conceived the idea for the project. A.A, B.S.F, S.D and R.K performed the experiments. R.K and A.A wrote the manuscript and all authors contributed to the scientific evaluation of the results.

– This page intentionally left blank –

Phys. Status Solidi B **251**, No. 12, 2471–2474 (2014) / **DOI** 10.1002/pssb.201451272

physica status solidi b
www.pss-b.com
basic solid state physics

Photocurrent imaging of semiconducting carbon nanotube devices with local mirrors

Asiful Alam[*,1,2], **Benjamin S. Flavel**[2], **Simone Dehm**[2], **Uli Lemmer**[3,4], **and Ralph Krupke**[**,1,2,4]

[1] Institute of Material Science, Technical University of Darmstadt, Darmstadt 64287, Germany
[2] Institute of Nanotechnology, Karlsruhe Institute of Technology, Karlsruhe 76021, Germany
[3] Light Technology Institute, Karlsruhe Institute of Technology, Karlsruhe 76131, Germany
[4] DFG Center for Functional Nanostructures, Karlsruhe 76028, Germany

Received 2 June 2014, revised 19 August 2014, accepted 21 August 2014

Keywords carbon nanotubes, photocurrent spectroscopy, supercontinuum scanning microscopy

---

[*] Corresponding author: e-mail asiful.alam@kit.edu, Phone: +49 721 608-28988
[**] e-mail ralph.krupke@kit.edu, Phone +49 721 608-26417, Fax: +49 721 608-26268

Photocurrent spectroscopy has recently been used by several research groups to study the light–matter interaction in carbon nanotubes. To achieve this, long-channel devices with symmetric metallic contacts are typically used, where photocurrent of opposite sign is generated at the two contacts. However, in short-channel devices (<1 μm) the diffraction-limited laser spot results in simultaneous excitation of both metal–nanotube contacts and leads to partial cancellation of the photocurrent. In this work, we avoid simultaneous excitation of both metal–nanotube contacts by fabricating an isolated metallic mirror over one of the contacts. With the use of (6,5) carbon nanotubes we demonstrate a unipolar photocurrent signal, that is consistent with the second order interband absorption of a (6,5) nanotube.

1 Introduction Semiconducting single-walled carbon nanotubes (s-SWCNTs) are considered to have great potential in optoelectronic applications [1]. Both light emission as well as absorption has been studied extensively using s-SWCNT devices [2–6]. Such devices are typically fabricated with a field-effect transistor geometry consisting of either a single nanotube or a film of nanotubes as the carrier transport channel. While, the absorption of light by s-SWCNTs is attributed to its chirality (n,m) [7, 8], carrier transport across a nanotube in such an architecture is primarily determined by the presence of an electric field at the metal–nanotube contacts [9, 10]. The position and direction of the electric field is then often elucidated with the use of a photocurrent or photovoltage map, where a laser is scanned across the device allowing for the spatially defined current or voltage to be measured [11–15]. These maps show that in devices with symmetric work function metal contacts, the strongest photocurrent signals originate near the metal–nanotube contacts due to the presence of a high electrostatic potential gradient. However, recent progress shows that charge-carrier separation in devices with asymmetric metal contacts can occur away from the metal contacts with the maximum photocurrent generated at the center of the channel [11].

Typically, CNT devices for photocurrent measurements have sufficiently long channels to avoid the diffraction limitations of the laser spot. As a result, the signal generated at both ends of the nanotube is independent from each other. However, this is not the case for short-channel devices (<1 μm). When the diffraction-limited laser spot has a diameter comparable to the CNT channel length, photo-excited carriers are generated simultaneously at both ends of the nanotube. For symmetric work function metal contacts, this results in a reduction in the measureable photocurrent signal due to opposing internal electric fields at the metal–nanotube contact. Several groups have overcome this problem by reducing the spot size with immersion objectives [11] or tip-enhanced microscopy, where a 30 nm diameter spot size can be achieved [12].

In this article, we provide an alternative approach to investigate short channel s-SWCNT devices by using local mirrors and a supercontinuum-excited scanning microscope. The devices under test were fabricated with isolated metallic pads over one of the metal–nanotube contacts. These pads (or mirrors) reflect light and are therefore expected to suppress carrier generation at one end of the nanotube. Hence, we are able to demonstrate that such devices generate unipolar photocurrent signals as opposed to the typical ambipolar behavior in long channel devices [13–15]. This new device concept paves the way for photocurrent generation from s-SWCNT devices under non-local illumination.

2 Experiment details

The nanotubes chosen for this study were (6,5) s-SWNTs in a 1 wt. % sodium cholate stabilized aqueous dispersion, sorted by size exclusion chromatography [16–18] and density gradient ultracentrifugation [19]. A complete absorption spectrum of the material ranging from 450 to 1100 nm can be found in the Supporting Information. The (6,5) nanotubes have a diameter (d_t) and bandgap (ΔE) of approximately 0.8 nm and 1.270 eV, respectively [7]. For technical reasons, the study was carried out in the visible part of the spectrum, which includes the second order interband transition of (6,5) nanotubes at ~570 nm. Hence, devices consisting of a majority of (6,5) nanotubes are likewise expected to generate a maximum photoresponse in this region.

Figure 1a shows the device architecture along with the experimental setup. In order to avoid bending of the nanotubes, 50 nm palladium electrodes were embedded into the 800 nm thick SiO_2/p-doped Si substrate. This was achieved by etching away the oxidized silicon with the help of a chromium mask fabricated lithographically using negative resist (maN-2403). Once the oxide had been etched away the mask was then removed by adding perchloric acid in ceric ammonium nitrate and palladium was subsequently sputtered on the sample to yield an array of palladium contacts with a channel length of 600 nm. Nanotubes were then deposited from suspension via dielectrophoresis [20, 21] resulting in short channel s-SWCNT field-effect transistor arrays [22]. Such devices were observed to be p-type due to the well-known doping effects induced by oxygen molecules adsorbed on the nanotube surface [23] (see Fig. 1c).

Before fabricating the chromium mirrors a 30 nm film of aluminum oxide was grown via atomic layer deposition (ALD) for isolation purposes. Part of the oxide was also etched away using potassium hydroxide in order to expose the Pd electrodes for electrical connections via probe needles. The electron transport was observed to change after the growth of the aluminum oxide and exhibited n-type behavior as shown in Fig. 1c. This change is likely induced during the ALD process as reported by Grigoras et al. [24].

Finally, 50 nm thick chromium mirrors were fabricated over one of the contacts with PMMA and e-beam lithography. These mirrors reflect light away from one of the contacts and serve to avoid destructive interference of the otherwise opposite photocurrents. From the scanning electron micrograph of the device, it is possible to determine the open channel length of the fabricated device. For instance, the device shown in Fig. 1b has an open channel close to 400 nm.

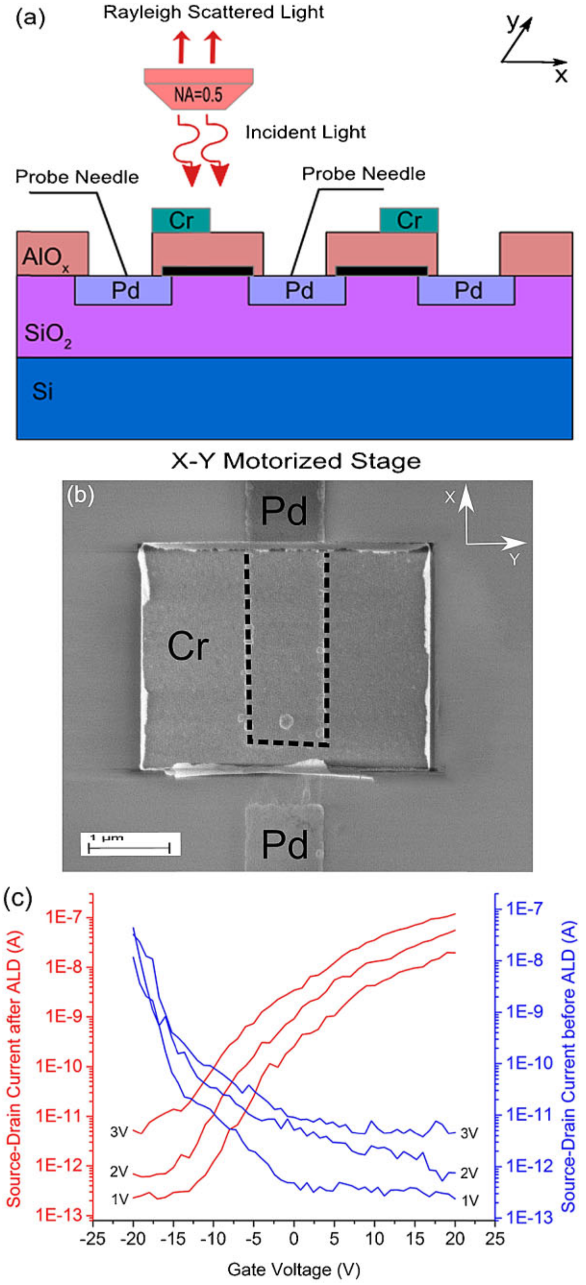

Figure 1 (a) Schematic of the experimental setup and the device architecture. The s-SWCNTs are represented by thick black lines. (b) Scanning electron micrograph of a device. The barely visible (6,5) s-SWNTs connect the Pd electrodes. They are coated by an AlO_x layer and partially covered by a Cr mirror. The outline of the electrode underneath the mirror is also shown as dashed lines. (c) Source–drain current versus gate voltage of a device before (blue) and after (red) growing the aluminum oxide layer for source–drain voltages of 1, 2, and 3 V.

We used a NKT SuperK Extreme EXW-6 broadband supercontinuum light source to excite the nanotubes. The wavelength was tuned between 500 and 825 nm with the use of a NKT SuperK Select acousto-optic tunable filter. The light was linearly polarized with a bandwidth of 5 nm. The polarization axis of the light was measured to be 12° with respect to the x-axis shown in the figures. A microscope objective of numerical aperture 0.5 was used to focus the quasi-monochromatic light onto the device with intensity of a few hundred microwatts. This corresponds to a diffraction-limited laser spot of diameter less than 1 μm, which is comparable to the channel length of the device. With the help of a motorized x–y stage, the fabricated devices were scanned with a spatial resolution of 375 nm. For each scan, a photocurrent map and a Rayleigh-scattering map was recorded, the resolution being determined by the laser spot diameter and the step size of the motorized stage.

Light reflected from the sample was focused onto a Silicon Sensor PC-50-6 silicon PIN photodiode in order to measure the intensity of light reflected from the sample. The photodiode produced a short-circuit current, which was directly related to the photon count and measured by a Keithley 2400 sourcemeter.

The photocurrent generated by the s-SWNT device was measured using a Keithley 6430 sourcemeter, which detects the flow of electrons in zero-voltage source mode. It reads a positive current when electrons flow into the source end (high terminal) and vice versa, which is opposite to the usual reading of the conventional current direction. Using this configuration, it is possible to determine the direction of flow of carriers across the nanotube channel.

3 Results Figure 2a shows the spatial distribution of Rayleigh-scattered or backscattered light of such a device measured using a photodiode sensor. The incident light was set to 570 nm, the nominal position of the second order interband transition wavelength of the (6,5) nanotubes, in order to maximize the photon absorption by the CNT channel. In Fig. 2a, the electrodes and mirrors are clearly distinguishable from the oxidized silicon because they have a higher reflectance. The gap between the mirror and the "mirror-free" electrode is shown as dashed lines on both the Rayleigh-scattering map as well as the photocurrent map.

From the photocurrent map, it can be seen that a signal is generated at only one contact (see Fig. 2b). Overall, the photocurrent signal is unipolar with its polarity defined by the electrical connections. In Fig. 2b, a positive current is generated at the drain end, indicating the flow of electrons across the nanotube channel from drain to source.

In Fig. 2c, a cross-section through the maximum photocurrent along the x-axis is shown together with the variation of the electrostatic potential across the device (Fig. 2c). Since the photocurrent I_{pc} denotes here the flow of electrons and not holes, the relationship with the electrostatic potential ϕ is given by $I_{\mathrm{pc}} \propto + \mathrm{d}/\mathrm{d}x[\phi(x)]$. The derived electrostatic potential profile is in agreement with the

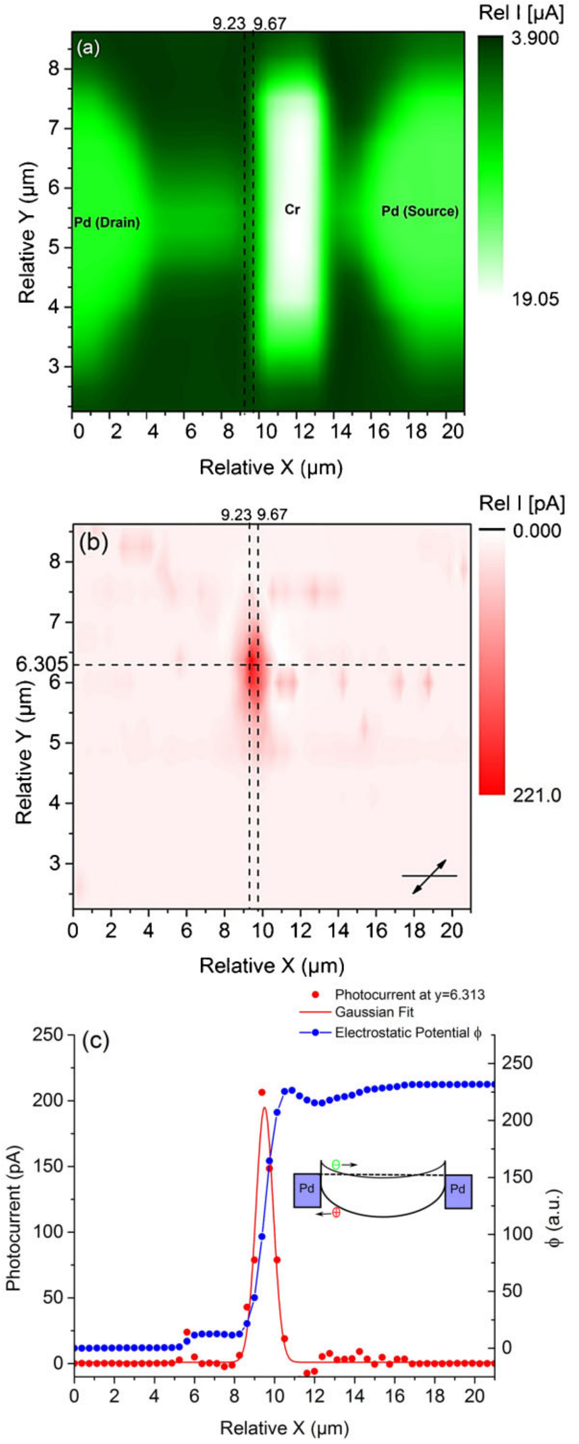

Figure 2 (a) Rayleigh-scattering spatial map of a (6,5) s-SWCNT device irradiated at 570 nm. The open nanotube channel is illustrated by vertical dash lines. (b) Corresponding photocurrent map of the device measured simultaneously. The polarization direction of the incident light is indicated by an inset. (c) Cross-section through the center of the photocurrent spot along the x-axis. The full-width at half-maximum is ~1 μm. Plotted is also the variation of the electrostatic potential across the device, and as an inset the corresponding exciton dissociation at the irradiated contact together with the band profile of the n-type s-SWCNT device.

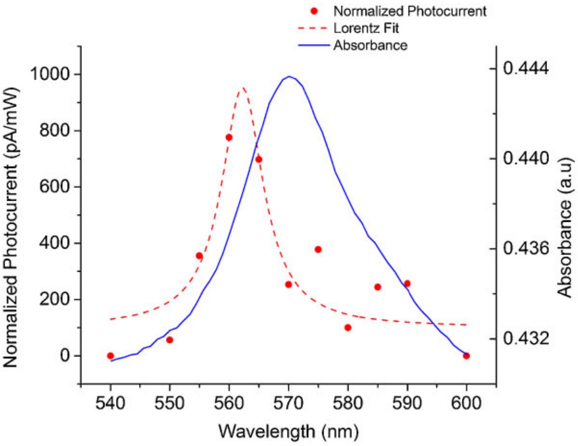

Figure 3 Photocurrent spectrum in comparison to the absorption spectrum of the (6,5) dispersion. The photocurrent signal PC has been normalized to the incident light power.

expected band bending of an n-type CNT transistor and the corresponding transport data, respectively. As sketched in the inset of Fig. 2c, the exciton at the drain contact is dissociated by the local electric field and causes an electron to flow to the source.

Finally, a photocurrent spectrum was generated by recording the maximum photocurrent at different incident wavelengths. The current was then also normalized to the intensity of the incident light. Figure 3 shows the wavelength-dependent photoresponse with a peak near 570 nm. A Lorentzian was fitted to the data. The photocurrent spectrum shows good correlation with the absorption spectrum of the (6,5) dispersion that has been used for the device fabrication and indicates photocurrent generation via excitonic absorption at the second order interband transition.

4 Conclusions In summary, short channel s-SWCNT devices with metallic mirrors were investigated using supercontinuum-excited scanning microscopy. Such devices generate interference-free photocurrent signals as only one of the contacts was illuminated. Photocurrent maps of such devices showed a unipolar signal and the photocurrent spectrum, generated from photocurrent maps, showed good correlation with the absorption spectrum of the nanotube dispersion. We believe this device schematic could be useful for photocurrent measurements under non-local illumination, which remains to be investigated in the future.

Acknowledgements B. S. F. gratefully acknowledges support from the Deutsche Forschungsgemeinschaft's Emmy Noether Program under grant number FL834/1-1. R. K. acknowledges support by the Deutsche Forschungsgemeinschaft (INTST 163/354-1 FUGG). A.A. acknowledges support by the Deutsche Forschungsgemeinschaft under grant number OR262/1-2.

References

[1] P. Avouris, M. Freitag, and V. Perebeinos, Nature Photon. **2**, 341 (2008).
[2] J. A. Misewich, R. Martel, P. Avouris, J. C. Tsang, S. Heinze, and J. Tersoff, Science **300**, 783 (2003).
[3] K. Balasubramanian, Y. Fan, M. Burghard, K. Kern, M. Friedrich, U. Wannek, and A. Mews, Appl. Phys. Lett. **84**, 2400 (2004).
[4] M. Freitag, Y. Martin, and J. Misewich, Nano Lett. **24**, 1087 (2003).
[5] M. H. P. Pfeiffer, N. Stürzl, C. W. Marquardt, M. Engel, S. Dehm, F. Hennrich, M. M. Kappes, and U. Lemmer, Opt. Express **19**, 1184 (2011).
[6] M. Kinoshita, M. Steiner, M. Engel, J. P. Small, A. A. Green, M. C. Hersam, R. Krupke, E. E. Mendez, and P. Avouris, Opt. Express **18**, 25738 (2010).
[7] R. Weisman and S. Bachilo, Nano Lett. **100**, 1235 (2003).
[8] S. M. Bachilo, M. S. Strano, C. Kittrell, R. H. Hauge, R. E. Smalley, and R. B. Weisman, Science **298**, 2361 (2002).
[9] J. Svensson and E. E. B. Campbell, J. Appl. Phys. **110**, 111101 (2011).
[10] Z. Chen, J. Appenzeller, J. Knoch, Y. Lin, and P. Avouris, Nano Lett. **5**, 1497 (2005).
[11] M. Engel, M. Steiner, and R. Sundaram, ACS Nano **6**, 7303 (2012).
[12] N. Rauhut, M. Engel, M. Steiner, R. Krupke, P. Avouris, and A. Hartschuh, ACS Nano **6**, 6416 (2012).
[13] K. Balasubramanian, M. Burghard, K. Kern, M. Scolari, and A. Mews, Nano Lett. **5**, 507 (2005).
[14] Y. Ahn, W. Tsen, Y. Park, and J. Park, Nano Lett. **14**, 3320 (2007).
[15] M. Freitag, J. C. Tsang, A. Bol, D. Yuan, J. Liu, and P. Avouris, Nano Lett. **7**, 2037 (2007).
[16] K. Moshammer, F. Hennrich, and M. M. Kappes, Nano Res. **2**, 599 (2009).
[17] B. S. Flavel, M. M. Kappes, R. Krupke, and F. Hennrich, ACS Nano **7**, 3557 (2013).
[18] B. S. Flavel, K. E. Moore, M. Pfohl, M. M. Kappes, and F. Hennrich, ACS Nano **8**, 1817 (2014).
[19] M. S. Arnold, A. A. Green, J. F. Hulvat, S. I. Stupp, and M. C. Hersam, Nature Nanotechnol. **1**, 60 (2006).
[20] R. Krupke, F. Hennrich, H. B. Weber, D. Beckmann, O. Hampe, S. Malik, M. M. Kappes, and H. V. Löhneysen, Appl. Phys. A, Mater. Sci. Process. **76**, 397 (2003).
[21] M. Ganzhorn, A. Vijayaraghavan, A. A. Green, S. Dehm, A. Voigt, M. Rapp, M. C. Hersam, and R. Krupke, Adv. Mater. **23**, 1734 (2011).
[22] A. Vijayaraghavan, S. Blatt, D. Weissenberger, M. Oron-Carl, F. Hennrich, D. Gerthsen, H. Hahn, and R. Krupke, Nano Lett. **7**, 1556 (2007).
[23] S. Heinze, J. Tersoff, R. Martel, V. Derycke, J. Appenzeller, and P. Avouris, Phys. Rev. Lett. **89**, 106801 (2002).
[24] K. Grigoras, M. Y. Zavodchikova, A. G. Nasibulin, E. I. Kauppinen, V. Ermolov, and S. Franssila, J. Nanosci. Nanotechnol. **11**, 8818 (2011).

Supporting Information

Additional supporting information may be found in the online version of this article at the publisher's website.

2.6 Additional Scientific Publications

2.6.1 *Chemically Immobilised Carbon Nanotubes on Silicon: Stable Surfaces for Aqueous Electrochemistry*

B. S. Flavel, D. J. Garrett, J. Lehr, J. G. Shapter, A. J. Downard

Electrochimica Acta 55 (2010) 3995–4001

DOI: 10.1016/j.electacta.2010.02.046

Abstract

Diazonium ion chemistry has been used to electrochemically graft aminophenyl layers onto p-type silicon (100) substrates. A condensation reaction was used to immobilise single-walled carbon nanotubes with high carboxylic acid functionality directly to this layer. Electrochemical monitoring of the aminophenyl groups confirmed the formation of an amide linkage between the single-walled carbon nanotubes and the aminophenyl layer. The carbon nanotube electrode showed high stability and good electrochemical performance in aqueous solution. At moderate scan rates the $Ru(NH3)_6^{+3/+2}$ couple exhibited quasi-reversible electron transfer kinetics with a standard heterogenous rate constant of 1.2×10^{-3} cm s^{-1} at the covalently-linked carbon nanotube surface. The electrode thus combines the advantages of a silicon substrate for easy integration into sophisticated electrical and electronic devices, carbon nanotubes for desirable electrochemical properties, and stability in aqueous medium for future applications in environmental sensing.

Contribution

B.S.F and A.J.D designed the project. B.S.F, D.J.G and J.L performed the experiments, B.S.F wrote the paper and all authors contributed to the scientific interpretation of the results.

– This page intentionally left blank –

Electrochimica Acta 55 (2010) 3995–4001

Contents lists available at ScienceDirect

Electrochimica Acta

journal homepage: www.elsevier.com/locate/electacta

Chemically immobilised carbon nanotubes on silicon: Stable surfaces for aqueous electrochemistry

Benjamin S. Flavel[a,c,*], David J. Garrett[a,b], Joshua Lehr[a,b], Joseph G. Shapter[c], Alison J. Downard[a,b,**]

[a] *Department of Chemistry, University of Canterbury, Private Bag 4800, Christchurch 8140, New Zealand*
[b] *MacDiarmid Institute for Advanced Materials and Nanotechnology, Private Bag 4800, Christchurch 8140, New Zealand*
[c] *School of Chemistry, Physics & Earth Sciences, Flinders University, Sturt Road, Bedford Park, Adelaide, South Australia 5001, Australia*

ARTICLE INFO

Article history:
Received 17 December 2009
Received in revised form 8 February 2010
Accepted 13 February 2010
Available online 20 February 2010

Keywords:
Silicon
Cyclic voltammetry
p-Phenylenediamine
Diazonium
Electrochemical grafting

ABSTRACT

Diazonium ion chemistry has been used to electrochemically graft aminophenyl layers onto p-type silicon (1 0 0) substrates. A condensation reaction was used to immobilise single-walled carbon nanotubes with high carboxylic acid functionality directly to this layer. Electrochemical monitoring of the aminophenyl groups confirmed the formation of an amide linkage between the single-walled carbon nanotubes and the aminophenyl layer. The carbon nanotube electrode showed high stability and good electrochemical performance in aqueous solution. At moderate scan rates the $Ru(NH_3)_6{}^{+3/+2}$ couple exhibited quasi-reversible electron transfer kinetics with a standard heterogenous rate constant of $1.2 \times 10^{-3}\ cm\ s^{-1}$ at the covalently-linked carbon nanotube surface. The electrode thus combines the advantages of a silicon substrate for easy integration into sophisticated electrical and electronic devices, carbon nanotubes for desirable electrochemical properties, and stability in aqueous medium for future applications in environmental sensing.

1. Introduction

The construction of sensors using carbon nanotubes is a very active area of research. There has been a strong emphasis on the development of gas sensors [1,2], and on biosensors [3,4] aimed at medical applications. In contrast, the design of carbon-nanotube-based sensors for use in the aquatic environment is a relatively recent effort [5–11]. The ability to test water quality is vital to maintain potable supplies and the need for water monitoring will only grow as increasing populations require increasing volumes of drinking water. One of the difficulties in testing water is that pollutants range in size from large particulates to simple ions (heavy metal ions) [12]. Additionally contaminates can be biological or chemical in nature. This diversity of pollutants makes the testing of water a very challenging exercise.

Much of the recent research towards the development of carbon-nanotube-based sensors for analytes of environmental importance has involved preparation of complex composite materials. Such composites typically incorporate a catalyst (nanoparticle, molecular or biological species), nanotubes (which enhance the response of the sensor), and a component to aid immobilisation of the composite on an electrode surface. For example, carbon nanotube/copper powder/mineral oil composites have been used to detect dissolved ammonia [10], a carbon nanotube paste electrode fabricated from fluorine doped carbon nanotubes and mineral oil allowed analysis of copper ion content in various aqueous media [6] and poly(allylamine hydrochloride)-wrapped carbon nanotubes combined with horseradish peroxidise gave a sensor for phenolics [5]. In other examples ferrocene-modified chitosan combined with carbon nanotubes could be used to detect sulphites [7] and porphyrin combined with carbon nanotubes in an ionic liquid paste gave an electrode sensitive to trichloroacetic acid [8], an organohalide pollutant. In a different approach, gold nanoparticles electrodeposited on carbon nanotubes drop coated on a glassy carbon electrode have been used to detect organophosphate pesticides [11]. These examples illustrate that while nanotube-based sensors can detect various analytes of concern in the aquatic environment, many different sensor architecture have been utilised. A generic sensor platform that can be adapted to multiple species of interest would have obvious advantages in terms of fabrication of devices for monitoring water quality.

Silicon is an attractive substrate for design of a generic sensor platform incorporating carbon nanotubes. Use of silicon allows highly developed micro- and nanofabrication procedures to be used in sensor fabrication and facilitates the incorporation of the sens-

---

* Corresponding author at: School of Chemistry, Physics & Earth Sciences, Flinders University, Sturt Road, Bedford Park, Adelaide 5001, South Australia, Australia. Tel.: +61 8 82013038.

** Corresponding author at: Department of Chemistry, University of Canterbury, Private Bag 4800, Christchurch 8140, New Zealand.

E-mail addresses: ben.flavel@flinders.edu.au (B.S. Flavel), alison.downard@canterbury.ac.nz (A.J. Downard).

0013-4686/$ – see front matter © 2010 Elsevier Ltd. All rights reserved.
doi:10.1016/j.electacta.2010.02.046

ing surface into devices. Recent work in our group has focussed on the covalent attachment of single-walled carbon nanotubes to silicon substrates [13–20]. This work has demonstrated the stability of these constructs in organic solvents under continuous potential scans [21] as well as during field emission experiments where the electrodes were stable for days even while producing currents of 100 μA [20]. The electrodes have a high surface area and the nanotubes provide a low resistivity pathway to the substrate; both these properties can be exploited to make highly efficient sensors. However, these electrodes are not suitable for fabrication of sensors for use in environmental monitoring because the ester bond linking the carbon nanotubes to the silicon substrate can be easily hydrolysed in aqueous media.

Very recently we have demonstrated the chemical assembly of vertically aligned carbon nanotubes on carbon electrodes [22]. The carbon nanotubes were attached to a tether layer through amide bonds and the tether layer was covalently attached to the substrate via C–C bonds. The tether layer was prepared by electrochemical reduction of 4-aminobenzene diazonium salt solution which results in grafting of aminophenyl groups to the carbon surface. Recent work in this group and others has shown the formation of a C–C bond on carbon substrates gives very stable surface layers [22,23]. The electrode assembly was shown to be stable in aqueous solution over a wide potential range and was resistant to degradation from sonication in acid, base and organic solvent. An interesting feature of the chemically assembled carbon nanotube electrodes is that the aminophenyl groups form a passivating layer on the carbon surface which blocks electron transfer between solution species and the underlying electrode. However, after assembly of carbon nanotubes, the rate of electron transfer is accelerated, to an extent dependent on the coverage of the carbon nanotubes on the surface. At relatively high surface coverages of carbon nanotubes, the rate of electron transfer between solution species and the electrode is the same as at a bare electrode and the carbon nanotube assemblies can be used to monitor solution species. A high rate of electron transfer for redox species immobilised on the carbon nanotubes is also observed and this behaviour has been exploited in a recently reported electrochemical biosensor [24]. Although the accelerating effect of chemically assembled carbon nanotubes on electron transfer rates has also been observed at other

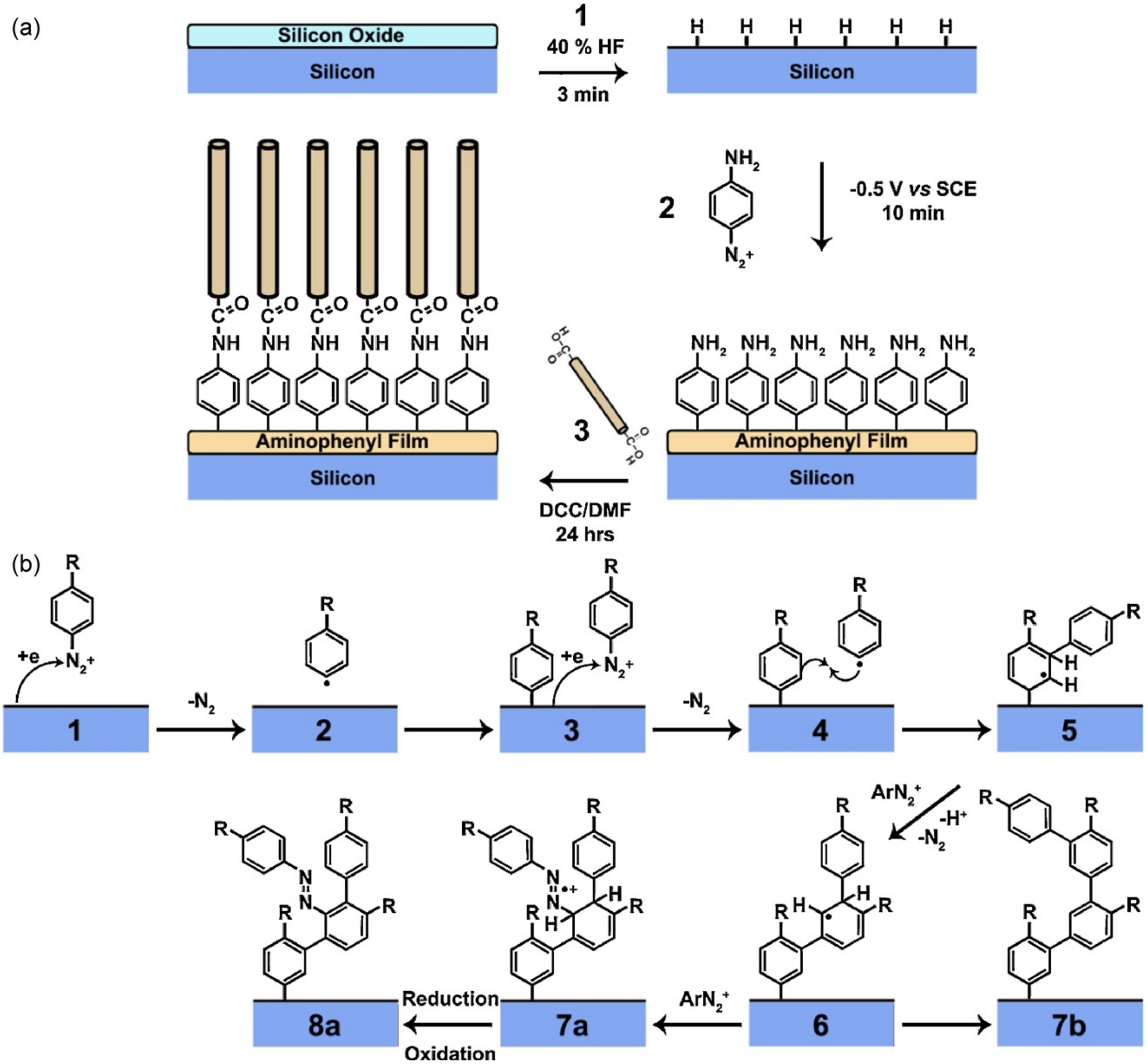

Fig. 1. Schematic of (a) carbon nanotube electrode fabrication in the presence of DCC and (b) multilayer film formation from reduction of a diazonium cation. R = NH_2 in this work.

electrode materials functionalised with tether layers through different routes [19,22,25–27], the origin of the behaviour is not well understood.

Covalent grafting of nanoscale organic layers through the reduction of aryldiazonium salts proceeds at many materials including hydrogen-terminated silicon surfaces [22,23,28–36]. Attachment through Si–C bonds is expected to give relatively high mechanical, thermal and hydrolytic stability to the layers on silicon. These factors, along with the behaviour observed at the carbon electrodes described above, has prompted this work in which we immobilise carbon nanotubes on diazonium-derived tether layers on silicon. There are previous reports of the use of diazonium cation chemistry to link carbon nanotubes to silicon substrates by Joyeux et al. [37] and Chen et al. [38], but this earlier work does not investigate the use of surfaces as electrodes for measurements in aqueous media. We demonstrate here that modification of silicon with a passivating tether layer via reduction of 4-aminobenzene diazonium salt, followed by assembly of carbon nanotubes which ‘restore’ the good electrochemical properties, and provides a surface which can be used for electrochemical measurements in aqueous media.

2. Experimental

2.1. Preparation of chemically immobilised carbon nanotube electrodes

The preparation of carboxylated single-walled carbon nanotubes (SWCNTs) has been described in detail previously [16]. In brief, single-walled carbon nanotubes from Carbon Solutions Inc., USA, P2-SWNT, were refluxed in 3 M nitric acid for 24 h. The dilute nitric acid solution was then decanted off and the nanotubes were placed into a more aggressive oxidiser, namely a 3:1 (v/v) solution of concentrated sulphuric acid (98%) and concentrated nitric acid (70%) and ultrasonicated for 8 h at 0 °C [39,40]. The shortened nanotubes were then diluted in 500 mL of MilliQ water and filtered through a 0.45 μm polytetrafluoroethylene (PTFE) membrane. The nanotubes were further washed with MilliQ water to bring the pH to 5–7 and dried under vacuum [39].

The strategy for fabrication of silicon surfaces with covalently attached carbon nanotubes is shown schematically in Fig. 1(a). Firstly, highly boron doped p-type silicon (1 0 0) (Virginia Semiconductor Inc. USA) was cut into 2 cm × 2 cm sized wafers and (step 1) placed into 40% hydrofluoric acid (Sigma–Aldrich) for a period of 3 min to remove the native silicon oxide and hydrogenate the underlying surface [41,42]. The silicon wafer was then washed with methanol and dried thoroughly under nitrogen. The *p*-aminobenzenediazonium cation was prepared by the method of Lyskawa and Belanger [43]. In brief, 3 mL of 20 mM *p*-phenylenediamine (Sigma–Aldrich) in 1 M hydrochloric acid (Sigma–Aldrich) was added to an equal volume of 20 mM 99% sodium nitrite (Sharlau Chemie, Spain) at room temperature. This solution was used to graft aminophenyl films to the H-terminated silicon substrate (step 2) by applying a potential of −0.5 V *vs* SCE (saturated calomel electrode) for 10 min. Immediately after grafting the silicon substrate was ultra sonicated in MilliQ water for 5 min then dried with nitrogen. The modified silicon sample was then immersed for 24 h in a 5 mL 99.9% *N*,*N*-dimethyl formamide (DMF) (Southern Cross Scientific Pty. Ltd.) solution containing both 2.5 mg of 99.0% *N*,*N*′-dicyclohexylcarbodiimide (DCC) (Fluka Production GmbH) and 1 mg of carboxyl functionalised carbon nanotubes (step 3). Prior to introducing the substrate, the carbon nanotube/DCC/DMF solution was ultrasonicated for 5 h to evenly disperse the carbon nanotubes. Finally the modified silicon wafer was rinsed in acetone and air dried.

2.2. Electrochemistry

Electrochemical experiments were performed with an Autolab PGSTAT3C2 Potentiostat/Glavanostat (Eco Chimie B.V., The Netherlands). Silicon substrates were mounted in a glass electrochemical cell that exposed a circular area of surface to the cell solution as described previously [44]. The underside of the silicon substrate was adhered to copper foil to form the working electrode

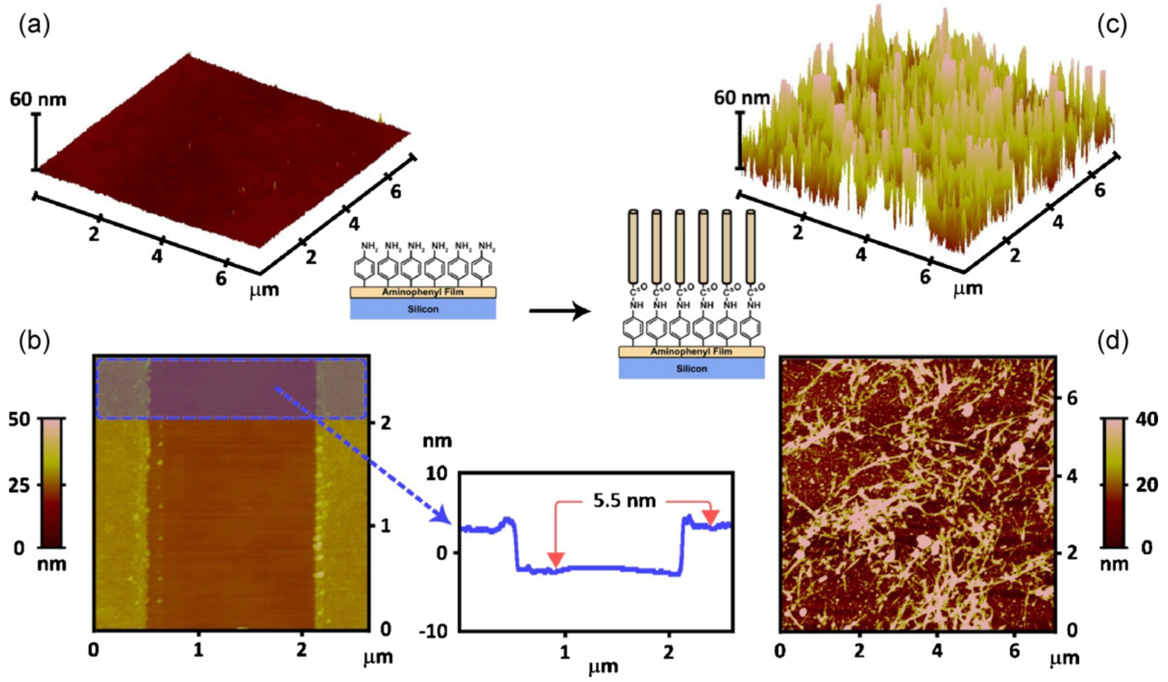

Fig. 2. Atomic force microscopy images of (a) an unmodified aminophenyl layer followed by (b) a scratch in an aminophenyl layer and the corresponding line profile and (c), (d) an aminophenyl layer modified with single-walled carbon nanotubes in the presence of DCC.

with a platinum wire and saturated calomel electrode (SCE) used as the counter and reference electrodes, respectively. A Viton o-ring defined the geometric area of the working electrode. For the electrochemical grafting of aminophenyl films the working area was 0.26 cm^2; subsequent analysis was based on a smaller area (0.13 cm^2) of the grafted surface. Voltammetry of aminophenyl films was performed in 0.1 M sulphuric acid (Labscan Asia Co. Ltd., Thailand) using an initial potential of 0 V, a switching potential of 1.2 V and a scan rate of 0.1 V s^{-1}. Cyclic voltammograms of 1 mM ruthenium (III) hexaamine chloride (Sigma–Aldrich) in pH 7.5 potassium phosphate buffer solution were obtained by sweeping the potential, initially in the negative direction, between 0.2 and −0.6 V at scan rates of 0.025–0.75 V s^{-1}.

2.3. Atomic force microscopy (AFM)

Atomic force microscope images were taken in air with a Dimension 3100 and Nanoscope IIIa controller (Digital Instruments, Veeco, USA) operating in tapping mode. Silicon cantilevers (TAP300Al-G series, Budget Sensors, Innovative Solutions Bulgaria Ltd.) with a fundamental resonance frequency between 200 and 400 kHz were used. Topographic (height) images were obtained at a scan rate of 0.5 Hz with the parameters set point, amplitude, scan size, and feedback control optimised for each sample. All images show background subtracted data using the flatten feature in the Digital Instruments software. Depth profiling of aminophenyl films was performed with a 3 lever cantilever chip configuration (NSC 12, MikroMash, Estonia). These levers have lengths (D) 300, (E) 350, and (F) 250 µm with corresponding resonant frequencies of 28, 21 and 41 kHz, respectively. The method of depth profiling by "scratching" the film has been described in detail previously [44]. In brief the atomic force microscope, operating in tapping mode, was aligned using one of the shorter cantilevers (D or F). When this cantilever engaged the surface and was raster scanned, cantilever E (not in resonance) imbedded into the aminophenyl layer and effectively scratched away the film. Four complete scans over a 10 × 1.25 µm area were used to remove sections of the aminophenyl layer. After layer removal, the shorter cantilever was withdrawn from the surface and offset to the location of the scratch for imaging. To establish whether the scratching technique removed underlying substrate in addition to the surface film, the procedure was also carried out with bare H-terminated silicon samples. There was no evidence of damage to the silicon surface indicating that substrate is not removed during these measurements.

3. Results and discussion

Fig. 2(a) shows an atomic force microscope image of an electrografted aminophenyl film on silicon, which can be seen to be relatively smooth and homogenous with an image root mean square roughness of 1.05 nm. Film thickness information was obtained by selectively scratching away the aminophenyl film with the use of an atomic force microscope cantilever. The results of this experiment are shown in Fig. 2(b) where a darker bare underlying silicon 'trench' can be seen surrounded by the lighter aminophenyl layer. Upon taking the average cross section over a 0.58 × 2.58 µm area as depicted by the shaded rectangle and the corresponding line profile, the film thickness was found to be 5.5 nm. The value is in agreement with previous work on carbon substrates with films electrografted from diazonium salt solutions under similar conditions. In those studies maximum film thicknesses were in the range of 4–6 nm and it was concluded that the films were multilayered [44,45].

Fig. 1(b) shows the mechanism proposed by Pinson and coworkers [46] for the formation of multilayer films from diazonium salts. The diazonium cation is reduced at the electrode surface and eliminates N_2, forming the aryl radical. It appears that the radical attacks the substrate forming a covalent bond between the surface and the aryl group [23]. As further radicals are produced, they either graft directly to the substrate or attack already-grafted aryl groups, building up a disordered multilayer film structure [47]. There is strong spectroscopic evidence for the presence of azo groups in multilayer films [46,48,49]; these may result from reaction of diazonium cations with radical centres in the growing film and it is believed the resulting layer is a combination of structure 8a and 7b.

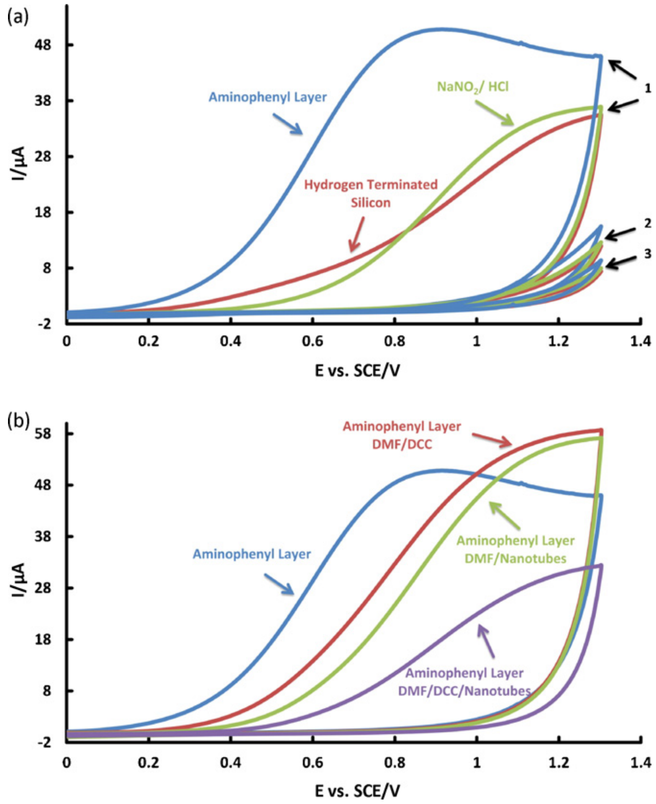

Fig. 3. Cyclic voltammograms, recorded at a scan rate of 0.1 V s^{-1} in 0.1 M H_2SO_4 of (a) H-terminated silicon, H-terminated silicon after immersion in a HCl solution containing $NaNO_2$ and H-terminated silicon modified with an aminophenyl layer (numbers indicate the scan number). (b) Aminophenyl layers after immersion in the solutions indicated.

Several studies have demonstrated that at a given grafting potential, growth of diazonium-derived films are self-limiting, with respect to surface concentration and thickness [44,45]. This can be explained by considering that as the film grows, electron transfer to aryldiazonium cations occurs over an increasing distance and hence the rate of electron transfer progressively decreases. Eventually the film becomes so thick that reduction essentially stops and the film reaches its maximum thickness. Electrografted films typically reach limiting thickness within a few minutes and hence it is assumed that the 5.5 nm film formed here after 10 min grafting represents the maximum thickness achievable under these conditions.

Further insight into the structure of the aminophenyl tether layer was gained from cyclic voltammetric experiments in 0.1 M H_2SO_4. To verify the presence of amine, three scans from 0 to 1.2 V at 0.1 V s^{-1} were performed on the modified silicon surface. On the first scan, Fig. 3(a), there is a single broad irreversible wave centred at 0.9 V; this can be assigned to the aminophenyl groups. For comparison, cyclic voltammetry was repeated on hydrogen-terminated silicon prior to electrografting and on a surface immersed in a solution containing only sodium nitrite and hydrochloric acid (no *p*-phenylenediamine was present). In both cases it can be seen that the oxidation current is significantly smaller than that recorded for an aminophenyl film. This current is assigned to oxidation of the silicon surface. For all surfaces, the second and subsequent scans gave very low currents. Complete oxidation of the aminophenyl layer is assumed to occur in the first scan of the modified surface, while passivation of the unmodified surfaces during the first scan leads to the low currents observed in the second and third scans for these samples. The response obtained at the aminophenyl grafted surface is in agreement with our previous measurements on carbon [49], work by Lyskawa and Belanger [43] on gold and values obtained for the oxidation of aniline to its radical cation during polymerization of polyaniline in acidic media [50].

Fig. 2(c) and (d) show atomic force microscope images, 3-dimensionally and in top view, respectively, of an aminophenyl layer after reaction with single-walled carbon nanotubes under conditions which promote amide bond formation. Immediately it can be seen in (c) that the surface has become rougher, and this is reflected by an increase of image root mean square roughness to 20.2 nm. The ‘saw tooth’ like surface topography observed is characteristic of vertical alignment [15–17,19,21,51] and carbon nanotube bundle heights of between 10 and 150 nm were found. This is in agreement with previous work [15–17,19,21,51,52] attaching carbon nanotubes to silicon with the use of condensation reactions. However, unlike previous work a large number of carbon nanotubes are also observed, as shown in (d), to be horizontally aligned on the surface to form a dense ‘mat’. Disordered arrangements of carbon nanotubes have previously been observed by our group in the case of carbon nanotubes immobilised on poorly aligned tether layers [14,19]. Poor alignment of the tether layer leads to regions of exposed hydrocarbon chains, which through van der Waal’s interactions with the hydrophobic sidewalls of the single-walled carbon nanotubes, promotes disordered assembly. The similar result obtained in this work can be explained by consideration of the multilayer film structure shown in Fig. 1(b). Hydrophobic interactions between carbon nanotubes and the exposed aryl rings within the disordered aminophenyl film may result in a disordered carbon nanotube layer. It is interesting to note that in our earlier work, single-walled carbon nanotubes assembled on carbon surfaces by the same route were shown to be vertically aligned with a very low incidence of horizontally positioned carbon nanotubes. The different results obtained at the silicon and carbon substrates [22] could be due to factors such as the relative smoothness of the substrates, the thickness or density of the aminophenyl film on each substrate or a different degree of carboxylation of single-walled carbon nanotubes used for each electrode preparation.

The role of the tether layer in carbon nanotube immobilisation was further investigated by comparing the aminophenyl oxidation peak before and after reaction of the tether layer with carbon nanotubes. Fig. 3(b) shows the first scan of cyclic voltammograms obtained in 0.1 M H_2SO_4 (0.1 V s^{-1}) at aminophenyl layers exposed to different carbon nanotube solutions. For each surface, the charge associated with the oxidation peak is directly related to the number of aminophenyl groups undergoing oxidation. However, the absolute surface concentration cannot be calculated because the number of electrons involved in the irreversible oxidation of the aminophenyl groups in the film environment is unknown. Table 1 lists the calculated charges associated with oxidation of the various surfaces. The approximate charge for oxidation of an aminophenyl layer prior to further reaction (2.0×10^{-4} C) was calculated by subtracting the charge for oxidation of an unmodified surface (hydrogen-terminated silicon). Upon immersion of an aminophenyl layer in a DMF/DCC/nanotube solution for 24 h, the charge decreases to 1.0×10^{-5} C. Hence a significant number of amine sites have been utilised in binding carbon nanotubes, presumably by formation of amide linkages. It is assumed that the remaining charge is associated with bare regions of film (where no carbon nanotubes were bound) and aminophenyl functionalities buried within the film. For comparison, aminophenyl films were immersed for 24 h in DMF/DCC (no carbon nanotubes) and DMF/nanotube (no DCC) solutions. In both cases the charge due to oxidation of aminophenyl groups was found to be somewhat less than that of a freshly prepared surface (1.3×10^{-4} and 9.7×10^{-5} C, respectively) but significantly greater than that of the surface reacted in DMF/DCC/nanotube solution. This is strong evidence that no amide bonds are formed in the absence of DCC and nanotubes. Interestingly, using atomic force microscopy, an assembly of carbon nanotubes was also observed on an aminophenyl layer after immersion in the DMF/nanotube solution. It is clear from the results described above that in this case, carbon nanotubes are not covalently bound to the tether layer and hence are most likely immobilised through electrostatic interactions [22]. The possibility that electrostatic interactions may play a role in single-walled carbon nanotube assembly on amine terminated tether layers has previously been highlighted by Tour and co-workers [53]. The voltammograms of Fig. 3(b) also show that all layers exposed to DMF exhibit a distinct change in shape of the oxidation peak wave and a positive shift in peak potential compared with that obtained prior to exposure to DMF solution. These effects are attributed to solvent and ion ingress and egress, along with associated film rearrangements as has previously been observed for nitroazobenzene [45], carboxyphenyl and methylphenyl films alternately immersed in organic solvents and aqueous media [54]. Further, the similarity of the responses after immersion in the two different DMF solutions supports the proposal that the changes are due to the solvent.

Table 1
Charges associated with the irreversible oxidation of modified silicon surfaces.

Substrate	Charge (C)
Hydrogen-terminated silicon	1.29×10^{-4}
$NaNO_2$/HCl	2.00×10^{-6}
Aminophenyl layer	1.98×10^{-4}
Aminophenyl layer DMF/DCC	1.34×10^{-4}
Aminophenyl layer DMF/nanotubes	9.70×10^{-5}
Aminophenyl layer DMF/DCC/nanotubes	1.00×10^{-5}

The electrochemical performance of silicon surfaces, unmodified and modified with carbon nanotubes, was assessed in an aqueous medium by cyclic voltammetry of the $Ru(NH_3)_6^{+3/+2}$ redox couple in pH 7.5 potassium phosphate buffer solution. Fig. 4(a) shows the first scan from 0.2 to −0.6 V at a scan rate of 0.1 V s^{-1}, obtained at various surfaces. For an unmodified, hydrogen-terminated silicon substrate the response is quasi-reversible with $\Delta E_p = 80$ mV. After an aminophenyl layer was grafted no peaks appear at the potentials seen on the unmodified surface or within the scan limits, indicating that $\Delta E_p > 800$ mV. A similar response was observed for an aminophenyl layer immersed for 24 h in a DMF/DCC solution in the absence of carbon nanotubes. Evidently, the multilayer aminophenyl film blocks electron transfer between the substrate and the redox probe, an effect frequently observed for multilayer films grafted by aryldiazonium salt solutions [43,55–57]. It should be noted that the blocking behaviour observed is not a result of electrostatic repulsion of the ruthenium cation from the aminophenyl film. The pK_a of aniline is 4.6 and although the pKa of the aminophenyl film is not expected to be precisely this, it should be similar thus resulting in negligible protonation at pH 7.5. When the scans were repeated after incubation for 24 h in a DMF solution containing nanotubes a significant increase in current and decrease in ΔE_p can be seen. Electrodes soaked in the presence and absence of DCC gave similar responses with $\Delta E_p = 183$ and 170 mV, respectively. Clearly, as observed previously on carbon surfaces [22], the addition of carbon nanotubes has decreased

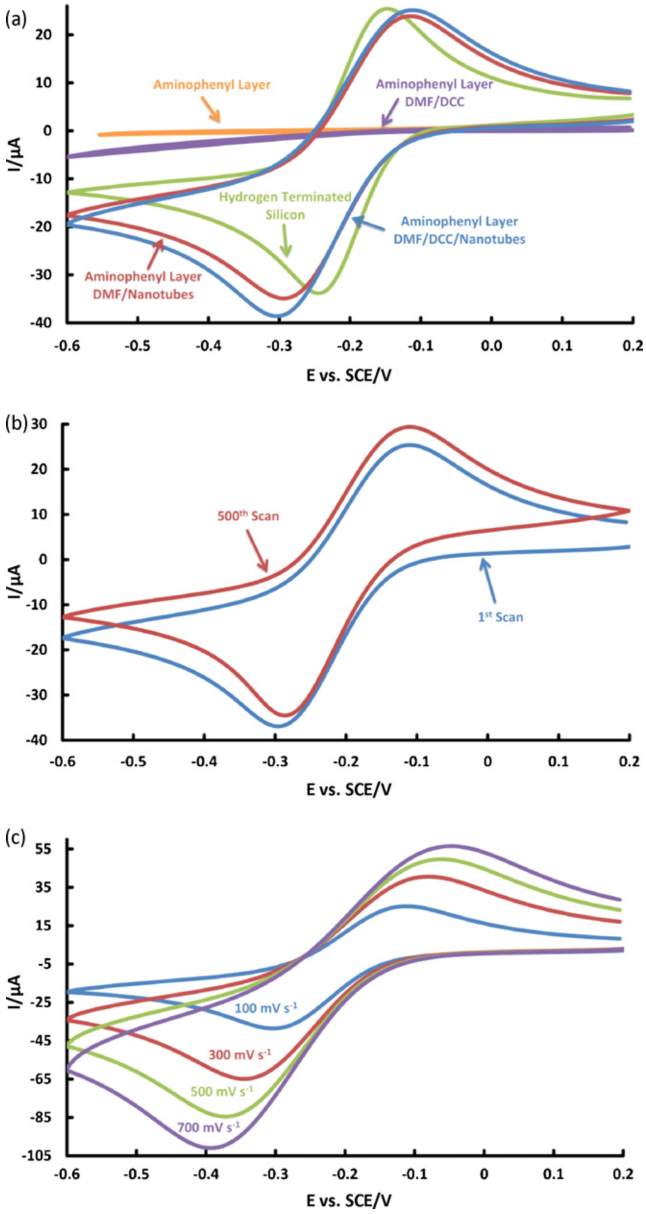

Fig. 4. Cyclic voltammograms of 1 mM $Ru(NH_3)_6{}^{+3/+2}$ in pH 7.5 potassium phosphate buffer. (a) Scans (0.1 V s^{-1}) obtained at silicon surfaces modified as indicated; (b) 1st and 500th scans (0.1 V s^{-1}) at an aminophenyl layer reacted with DMF/DCC/nanotubes and (c) scans obtained at an aminophenyl layer reacted with DMF/DCC/nanotubes using the scan rates indicated.

the blocking properties of the film, almost restoring the electron transfer rate to that observed prior to film grafting.

The stability to repeated potential scanning between 0.2 and −0.6 V in aqueous medium was tested for the covalently assembled carbon nanotube electrode (scan rate of 0.1 V s^{-1}) by repeated cycling of the electrode. Fig. 4(b) shows the 1st and 500th scan, where it can be seen that after 500 repeat scans the response to $Ru(NH_3)_6{}^{+3/+2}$ showed no change in peak current or ΔE_p. The stability of these aminophenyl-based surfaces is in dramatic contrast to those in which carbon nanotubes are assembled on silicon surfaces via an ester linkage [15–17,19,21,51,52]. Those electrodes could only be used for a single voltammetric measurement in aqueous conditions because of the hydrolytic instability of the ester bond.

The electron transfer rate of the $Ru(NH_3)_6{}^{+3/+2}$ couple at the covalently immobilised carbon nanotube surface was examined using cyclic voltammetry at scan rates from 0.025 to 0.75 V s^{-1}.

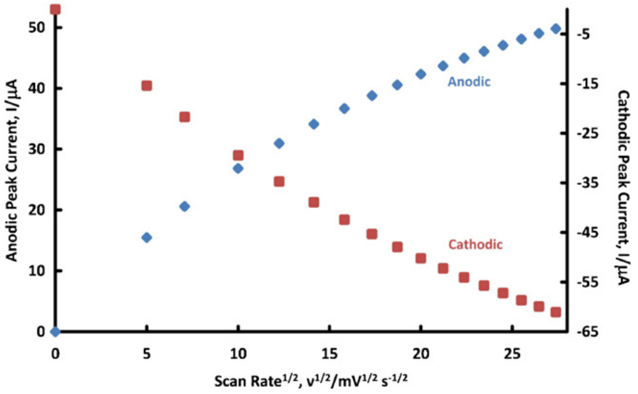

Fig. 5. Dependence of peak current on the square root of scan rate for the $Ru(NH_3)_6{}^{+3/+2}$ redox couple pH 7.5 potassium phosphate for of an aminophenyl layer reacted with DMF/DCC/nanotubes.

Fig. 4(c) shows scan rates of 0.1, 0.3, 0.5 and 0.7 V s^{-1}. There is a non-linear relationship between peak current and the square root of the scan rate, Fig. 5, consistent with a quasi-reversible redox system. The standard heterogenous rate constant for a quasi-reversible system can then be calculated from ΔE_p values using the method of Nicholson [58,59] which introduces the dimensionless kinetic parameter, Ψ. By interpolating/extrapolating the values of Ψ from the data provided by Nicholson [58], the corresponding rate constant can be determined from the following equation:

$$\psi = \frac{\gamma^{\alpha} k^{\circ}}{\sqrt{\pi a D_O}} \quad \text{where} \quad \gamma = \left(\frac{D_O}{D_R}\right)^{1/2} \text{ and } a = \frac{nF\upsilon}{RT}$$

where k° is the standard heterogenous rate constant (cm s^{-1}), D_O and D_R are the diffusion coefficients of the oxidised and reduced states (cm^2 s^{-1}), α is the transfer coefficient and the remaining terms have their usual significance. To determine the rate constant, it is assumed that the diffusion coefficient of both redox states of ruthenium hexaamine are equivalent to $D = 3.89 \times 10^{-6}$ cm^2 s^{-1} and that $\alpha = 0.5$ [60]. The standard heterogenous rate constants values shown in Table 2 were calculated from the voltammograms at each scan rate, giving an average value of 1.2×10^{-3} cm s^{-1}. From the voltammograms shown in Fig. 4(a), this value is clearly lower than that at H-terminated silicon, where a rate constant of 3.86×10^{-3} cm s^{-1} was obtained. The slower electron transfer rate observed at the aminophenyl-carbon nanotube assembly is most likely due to charge transfer resistance arising from the aminophenyl layer. Nevertheless, the electron transfer rate is unlikely to limit the use of the electrodes for electroanalysis and in any case, the rate may be increased by use of a thinner tether layer. In this work the aminophenyl layer was relatively thick and previous work [44] has shown that in general, thinner layers, grafted with the use of a shorter grafting time or a more positive potential, decrease the charge transfer resistance.

Table 2
Standard heterogenous rate constants for the $Ru(NH_3)_6{}^{+3/+2}$ redox couple, pH 7.5 potassium phosphate buffer, at a silicon surface modified with an aminophenyl tether layer and reacted with DMF/DCC/nanotubes.

Scan rate, ν (mV s^{-1})	ΔE_p (mV)	K° (cm s^{-1})
25	120	1.23×10^{-3}
50	146	1.16×10^{-3}
100	171	1.29×10^{-3}
150	191	1.22×10^{-3}
200	205	1.12×10^{-3}
Average		1.2×10^{-3}

4. Conclusions

This work has provided a new method for fabricating single-walled carbon nanotube electrodes on silicon through the use of an electrografted aminophenyl layer. Unlike previous silicon carbon nanotube assemblies, these electrodes showed excellent stability to repeated electrochemical cycling in an aqueous environment. The immobilisation method is compatible with incorporation of other sensing components and hence can form the basis of a range of sensors. Work is now underway to tether the free end of the carbon nanotubes to a selective biomolecule, allowing for the electrochemical detection of water born species of importance to water quality monitoring.

Acknowledgments

This work was funded by the MacDiarmid Institute for Advanced Materials and Nanotechnology. B.S. Flavel wishes to thank the Australian Government's Endeavour Research Fellowship program, and D.J. Garrett and J. Lehr thank the Tertiary Education Commission for Top Achiever Doctoral Scholarships.

References

[1] J.R. Stetter, G.J. Maclay, Enabling Technology for MEMS and Nanodevices, Wiley-VCH Verlag GmbH & Co. KGaA, 2008.
[2] J. Li, Y. Lu, Q. Ye, M. Cinke, J. Han, M. Meyyappan, Nano Lett. 3 (2003) 929.
[3] Y. Zhou, H. Yang, H.-Y. Chen, Talanta 76 (2008) 419.
[4] J. Wang, Electroanalysis 17 (2005) 7.
[5] L. Liu, F. Zhang, F. Xi, X. Lin, Biosens. Bioelectron. 24 (2008) 306.
[6] S.Y. Ly, Talanta 74 (2008) 1635.
[7] H. Zhou, W. Yang, C. Sun, Talanta 77 (2008) 366.
[8] W. Tu, J. Lei, H. Ju, Chem. Eur. J. 15 (2009) 779.
[9] V.K.K. Upadhyayula, S. Ghoshroy, V.S. Nair, G.B. Smith, M.C. Mitchell, S. Deng, Res. Lett. Nanotechnol. 2008 (2008) 156358.
[10] F. Valentini, V. Biagiotti, C. Lete, G. Palleschi, J. Wang, Sens. Actuators B 128 (2007) 326.
[11] Y. Zhang, T.-F. Kang, Y.-W. Wan, S.Y. Chen, Microchim. Acta 165 (2009) 307.
[12] United States Environmental Protection Agency, Environmental Protection Agency National Primary Drinking Water Regulations, 816-F-09-004 (2009).
[13] K.T. Constantopoulos, C.J. Shearer, A.V. Ellis, N.H. Voelcker, J.G. Shapter, Adv. Mater. 21 (2009) 1.
[14] B.S. Flavel, J. Yu, A.V. Ellis, J.S. Quinton, J.G. Shapter, Nanotechnology 19 (2008) 445301.
[15] B.S. Flavel, J. Yu, J.G. Shapter, J.S. Quinton, J. Mater. Chem. 17 (2007) 4757.
[16] B.S. Flavel, J. Yu, J.G. Shapter, J.S. Quinton, Carbon 45 (2007) 2551.
[17] J. Yu, D. Losic, M. Marshall, T. Bocking, J.J. Gooding, J.G. Shapter, Soft Matter 2 (2006) 1081.
[18] J. Yu, S. Mathew, B.S. Flavel, M.R. Johnston, J.G. Shapter, J. Am. Chem. Soc. 130 (2008) 8788.
[19] J. Yu, J.G. Shapter, J.S. Quinton, M.R. Johnston, D.A. Beattie, Phys. Chem. Chem. Phys. 9 (2007) 510.
[20] C.J. Shearer, J. Yu, K.M. O'Donnell, L. Thomsen, P.C. Dastoor, J.G. Shapter, J. Mater. Chem. 18 (2008) 5753.
[21] J. Yu, J.G. Shapter, M.R. Johnston, J.S. Quinton, J.J. Gooding, Electrochim. Acta 52 (2007) 6206.
[22] D.J. Garrett, B.S. Flavel, J.G. Shapter, K.H.R. Baronian, A.J. Downard, Langmuir 26 (2010) 1848.
[23] P. Allongue, M. Delamar, B. Desbat, O. Fagebaume, R. Hitmi, J. Pinson, J.M. Saveant, J. Am. Chem. Soc. 119 (1997) 201.
[24] G. Liu, J.J. Gooding, Electrochem. Commun. 11 (2009) 1982.
[25] P. Diao, Z. Liu, J. Phys. Chem. B 109 (2005) 20906.
[26] J. Liu, A. Chou, R. Wibowo, M.N. Paddon-Row, J.J. Gooding, Electroanalysis 17 (2005) 38.
[27] F. Hauquier, G. Pastorin, P. Hapiot, M. Prato, A. Bianco, B. Fabre, Chem. Commun. (2006) 4536.
[28] V. Mevellec, S. Roussel, L. Tessier, J. Chancolon, M. Mayne-L'Hermite, G. Deniau, P. Viel, S. Palacin, Chem. Mater. 19 (2007) 6323.
[29] A. Adenier, N. Barre, E. Cabert-Deliry, A. Chausse, S. Griveau, F. Mercier, J. Pinson, C. Vautrin-Ui, Surf. Sci. 600 (2006) 4801.
[30] F. Barriere, A.J. Downard, J. Solid State Chem. 10 (2008) 1231.
[31] M. Delamar, R. Hitmi, J. Pinson, J.M. Saveant, J. Am. Chem. Soc. 114 (1992) 5883.
[32] M. Pandurangappa, N.S. Lawrence, R.G. Compton, Analyst 127 (2002) 1568.
[33] M.P. Stewart, F. Maya, D.V. Kosynkin, S.M. Dirk, J.J. Stapleton, C.L. McGuiness, D.L. Allara, J.M. Tour, J. Am. Chem. Soc. 126 (2003) 370.
[34] J. Pinson, F. Podvorica, Chem. Soc. Rev. 34 (2005) 429.
[35] C. Bourdillon, M. Delamar, C. Demaille, R. Hitmi, J. Moiroux, J. Pinson, J. Electroanal. Chem. 336 (1992) 113.
[36] A.J. Downard, Electroanalysis 12 (2000) 1085.
[37] X. Joyeux, P. Mangiagalli, J. Pinson, Adv. Mater. 21 (2009) 4404.
[38] B. Chen, A.K. Flatt, H. Jian, J.L. Hudson, J.M. Tour, Chem. Mater. 17 (2005) 4832.
[39] J. Gooding, R. Wibowo, J. Lie, W. Yang, D. Losic, S. Orbons, F.J. Mearns, J.G. Shapter, D.B. Hibbert, J. Am. Chem. Soc. 125 (2003) 9006.
[40] X. Nan, Z. Gu, Z. Liu, J. Colloid Interface Sci. 245 (2002) 311.
[41] P. Allongue, C. Henry de Villeneuve, J. Pinson, F. Ozanam, J.N. Chazalviel, X. Wallart, Electrochim. Acta 43 (1998) 2791.
[42] D.K. Aswal, S.P. Koiry, B. Jousselme, S.K. Gupta, S. Palacin, J.V. Yakhmi, Physica E 41 (2009) 325.
[43] J. Lyskawa, D. Belanger, Chem. Mater. 18 (2006) 4755.
[44] P.A. Brooksby, A.J. Downard, Langmuir 20 (2004) 5038.
[45] P.A. Brooksby, A.J. Downard, J. Phys. Chem. B 109 (2005) 8791.
[46] P. Doppelt, G. Hallais, J. Pinson, F. Podvorica, S. Verneyre, Chem. Mater. 19 (2007) 4570.
[47] J.K. Kariuki, M.T. McDermott, Langmuir 17 (2001) 5947.
[48] M. Toupin, D. Belanger, Langmuir 24 (2008) 1910.
[49] S.S.C. Yu, E.S.Q. Tan, R.T. Jane, A.J. Downard, Langmuir 23 (2007) 11074.
[50] Y. Wei, G.W. Jang, C.C. Chan, K.F. Hsueh, R. Hariharan, S.A. Patel, C.K. Whitecar, J. Phys. Chem. B 94 (1990) 7711.
[51] J. Yu, B.S. Flavel, J.G. Shapter, Fullerenes Nanotubes Carbon Nanostruct. 16 (2008) 18.
[52] B.S. Flavel, J. Yu, J.G. Shapter, J.S. Quinton, Soft Matter 5 (2009) 164.
[53] L. Cai, J.L. Bahr, Y. Yao, J.M. Tour, Chem. Mater. 14 (2002) 4235.
[54] M.G. Paulik, P.A. Brooksby, A.D. Abell, A.J. Downard, J. Phys. Chem. C 111 (2007) 7808.
[55] M. D'Amours, D. Belanger, J. Phys. Chem. B 107 (2003) 4811.
[56] A.J. Downard, M.J. Prince, Langmuir 17 (2001) 5581.
[57] B. Ortiz, C. Saby, G.Y. Champagne, D. Belanger, J. Electroanal. Chem. 455 (1998) 75.
[58] R.S. Nicholson, Anal. Chem. 37 (1965) 1351.
[59] A.J. Bard, L.R. Faulkner, Electrochemical Methods: Fundamentals and Applications, John Wiley & Sons, New York, 2000 (Chapter 6).
[60] A.T. Beisler, K.E. Schaefer, S.G. Weber, J. Chromatogr. A 986 (2003) 247.

– This page intentionally left blank –

2.6 Additional Scientific Publications

2.6.2 *Nanoscale Structure of Lipid Domain Boundaries*

M. R. Nussio, R. D. Lowe, N. H. Voelcker, **B. S. Flavel**, C. T. Gibson, M. J. Sykes, J. O. Miners, J. G. Shapter

Soft Matter 6 (2010) 2193–2199

DOI: 10.1039/B923719D

Abstract

Analysis of membrane domain segregation and phase separation is important for the understanding of cell membrane structure and function. In this paper, we report an atomic force microscopy approach using both derivatised tip functionalities and force–volume imaging for the analysis of membrane phase separation. Simultaneous topology and mapping of interaction forces of binary component phospholipid bilayer membranes were performed. Measurements enabled the lateral mapping of bilayer lipid composition at a resolution of 10–20 nm, providing insights into dynamic membrane structure and behaviour. Very sharp boundaries between the two domains are observed in addition to domain boundaries that are quite diffuse with both lipids intermixing. Additionally, some nanoscale domains of one lipid within the domain of the second lipid are observed. The sharp boundaries of the large domains are observed in regions close to these nanodomains.

Contribution

M.R.N, J.O.M, J.G.S and N.H.V conceived and designed the project. M.R.N, R.D.L, B.S.F, C.T.G and M.J.S performed the experiments. M.R.N wrote the paper and all authors contributed to the experimental discussion and interpretation of results.

– This page intentionally left blank –

Nanoscale structure of lipid domain boundaries†

Matthew R. Nussio,[a] Rachel D. Lowe,[a] Nicolas H. Voelcker,*[a] Benjamin S. Flavel,[a] Christopher T. Gibson,[a] Matthew J. Sykes,[b] John O. Miners[b] and Joseph G. Shapter*[a]

Received 12th November 2009, Accepted 10th March 2010
First published as an Advance Article on the web 1st April 2010
DOI: 10.1039/b923719d

Analysis of membrane domain segregation and phase separation is important for the understanding of cell membrane structure and function. In this paper, we report an atomic force microscopy approach using both derivatised tip functionalities and force–volume imaging for the analysis of membrane phase separation. Simultaneous topology and mapping of interaction forces of binary component phospholipid bilayer membranes were performed. Measurements enabled the lateral mapping of bilayer lipid composition at a resolution of 10–20 nm, providing insights into dynamic membrane structure and behaviour. Very sharp boundaries between the two domains are observed in addition to domain boundaries that are quite diffuse with both lipids intermixing. Additionally, some nanoscale domains of one lipid within the domain of the second lipid are observed. The sharp boundaries of the large domains are observed in regions close to these nanodomains.

Introduction

Soft lipid bilayer membranes essentially 'define' cells and organelles. Membranes are of vital importance as they serve as the interface between the cell and extracellular environment.[1] Moreover, they participate in and regulate a host of cellular activities (*e.g.* biosynthesis, detoxification, metabolism, signalling, sorting, cell–cell interactions, motility *etc.*), in addition to separating the sites where these occur.[2] The involvement of membranes in diverse, critical cellular functions justifies the existence of a spectrum of constituent phospholipids while their relative abundance in the cell's bilayer membrane influences cellular functions. Membranes comprise phospholipid bilayers into which proteins are integrated.[3] For example, it is recognised that the activities of integral transmembrane proteins are sensitive to changes in the lipid environment.[4] Moreover, it is believed that the lateral organisation of membrane components defying the fluid nature of the membrane plays a key role in cell physiology and pathology. Therefore, in addressing the current lack of understanding of membrane organisation and its function, the characterisation of the spatial organisation of membrane lipids with nanoscale feature resolution has attracted major interest.[5–7]

Membrane interactions can be studied and simulated *in vitro* by the use of artificial membranes.[8–10] Although cell membranes comprise a range of phospholipid classes, each with a great variation in acyl chain composition, artificial membranes generated from binary and ternary phospholipid mixtures are emerging as attractive reductive models for studying membrane physiological processes. The most widely used models utilise lipid membranes of planar and spherical configuration, and are complementary to one another as both types are derived from amphipathic phospholipids.[11] Possessing a lipid bilayer structure, both systems are attractive models for investigations into a variety of physical, chemical and biological phenomena. The ability of phospholipids to form bilayers stems from their amphipathic molecular structure given that they consist of both hydrophilic and hydrophobic regions. The polar groups of the phospholipids face outward towards the cytoplasm and extracellular environment, and their hydrocarbon chains are oriented away from these interfaces, forming the hydrophobic interior of the membrane.

Supported phospholipid bilayers (SPB) are one such artificial membrane and have become a popular model system for the characterisation of membrane structure,[12–14] drug interactions[15–18] and transmembrane protein structure.[19,20] SPB are planar, extended bilayers adsorbed onto suitable flat substrates only separated from the surface by a thin layer of water or a polymer cushion layer.[21,22] These systems constitute an attractive model for studying membrane physiological processes in a biomimetic environment for proteins and other biomolecules held in a defined orientation.

Several techniques have been developed to image and quantify the lateral composition of membranes. A form of high-resolution secondary ion mass spectrometry (NanoSIMS) has recently revealed lipid distribution within a phase-separated membrane with a lateral resolution of ~100 nm.[5] NanoSIMS relies on the incorporation of stable isotope labels into each membrane component. However, since secondary ion mass spectrometry is performed in vacuum, supported bilayer samples require freeze-drying before analysis making connection to physiological systems difficult.

Confocal laser scanning fluorescence microscopy is a second technique that has been widely employed to investigate biological processes including those on cell surfaces and model bilayers. Visualisation of lipid membranes using fluorescence

---

[a] *School of Chemistry, Physics and Earth Sciences, Flinders University, Sturt Road, Bedford Park, Adelaide, SA, 5001, Australia. E-mail: nico.voelcker@flinders.edu.au; Fax: +61-8-8201-2905; Tel: +61-8-8201-5338; joe.shapter@flinders.edu.au; +61-8-8201-2905; +61-8-8201-2005*

[b] *Department of Clinical Pharmacology, Flinders University, Sturt Road, Bedford Park, Adelaide, SA, 5001, Australia*

† Electronic supplementary information (ESI) available: Some basic insights into force measurements with AFM are provided to help the reader understand the measurements discussed in the manuscript. See DOI: 10.1039/b923719d

microscopy[23–28] permits the distinction of lipid phases within the membrane by means of dye-labelled lipids or polarity-sensitive probes. More recently, by virtue of fluorescence correlation spectroscopy (FCS) analysis[6,29,30] phospholipid bilayer heterogeneities in binary mixtures have been observed.[6] However, the lateral resolution of such fluorescence-based techniques is diffraction-limited and the required fluorescently labeled lipids have been reported to perturb membrane organisation.[31–33] Recent approaches to circumvent diffraction limits in far field optical microscopy have also been developed,[34] affording a focal plane resolution of 20 to 30 nm. These new approaches are still far from routine and hence their application to examine membranes on the nanoscale remains challenging.

The majority of work to characterise nanoscale properties of membranes has been done using scanning probe microscopy. In particular, atomic force microscopy (AFM) has been applied to obtain high resolution surface topology of biological membranes and has the resolution to study bilayer domains and phases.[7,13,18] Utilising lateral force microscopy, frictional properties of phospholipid bilayers have been investigated.[35] Using chemically tailored AFM tip functionalities, the chemical composition of self-assembled monolayer mixtures has been elucidated.[36] However, employing lateral force microscopy to measure chemical variation in phospholipid bilayers is challenging since measurements can cause surface defects due to the tip puncturing of the soft membrane surface.[35]

Recent advances in force imaging have seen the development of approaches that can map recognition forces with the same resolution of the simultaneously collected topographic images.[37–41] These approaches, which are detailed in the ESI†, include pulsed force mode scanning force microscopy (PFM-SFM),[37] Topography and Recognition (TREC) imaging,[39–42] and Digital Pulsed Force Mode (DPFM).[43] For various reasons, all these approaches are difficult to use for soft samples such as lipid bilayers.

The shortcomings of some of these scanning probe approaches can be overcome by a specialised imaging technique known as force–volume (FV), which can measure high resolution force curves such that the topology and interaction forces are measured simultaneously. However, FV imaging has been limited to producing elasticity maps of heterogeneous materials including biominerals,[44] carbon nanotubes,[45] polymer composites,[46–48] bacterial surface[49] and living cells.[50–52] FV imaging, where the topology and interaction forces are measured simultaneously, has been available for some time[53] and applied in the early experiments to polymer surfaces.[48,54,55] This approach rasters the AFM tip over the surface to measure the forces as a function of x and y, thereby creating a force density map. The tip-sample forces are directly correlated to sample topography. This approach is slower than some more recent techniques but has the two-fold advantage of allowing very fine tuning of the maximum (or threshold) force applied and generally measures more precise force curves.[40] These advantages ensure that on soft samples such as SLBs proper topography of undisturbed layers can be measured with force curves corresponding to interactions between the tip and intact bilayer.

Recently, the interaction forces between functionalised AFM tips and surface charges from phospholipid headgroups of a bilayer have been measured by force spectroscopy.[56] Previous efforts have also reconstructed a sequence of force–distance curves to create a 2D adhesion map for bilayer domains.[57,58] Other FV work created charge density maps of biological surfaces[59] but these measurements only characterised the contrast between the substrate and the SPB. Very recent work has highlighted the possibility of nanoscale mapping of the biological samples.[52]

In summary, the lack of reliable nanoscale chemical analysis on cell membranes is a significant problem in membrane research. Probing the chemical composition of phospholipid bilayers on the nanometre scale is an inherently difficult task, mainly due to the dynamics and variation of phase and chemical composition, which demand fast and high resolution techniques. The problem is acerbated by the fact that each leaflet of the cell's bilayer comprises a different lipid composition and hence, analytical techniques to chemically identify the membrane components in both leaflets are unavailable.[60] In-fluid atomic force microscopy combined with spectroscopy (so called force–volume (FV) imaging) can deliver the required resolution and chemical insights.

In the work presented in this paper, model membranes have been examined using FV imaging with functionalised AFM tips to provide new insights into lipid dynamics at levels not previously possible. With aid of the detailed force curves obtained *via* this technique and defined surface modification of Si_3N_4 cantilevers, we have imaged the topology and mapped the interaction forces of binary component phospholipid bilayer membranes at a lateral resolution of 20 nm, allowing insights into bilayer membrane organisation and composition and a detailed examination of domain boundary composition. A binary mixture of phosphatidylcholine and phosphatidylserine was utilised in these experiments, but the continued development of this technique has the potential to examine multiple head-group functionalities, lending itself to the compositional analysis of physiologically relevant biological membranes. The resolution reached during the current study surpasses that achieved previously on lipid bilayers.

Materials and methods

Vesicle preparation

Multilamellar vesicles (MLVs) were prepared by first dissolving aliquots of dipalmitoyl phosphatidylcholine (DPPC, transition temperature, $T_M = 41$ °C) and/or dioleoyl phosphatidylserine (DOPS, transition temperature, $T_M = -11$ °C) (Avanti Polar Lipids, Birmingham, AL, USA) in chloroform, followed by evaporation of the solvent under nitrogen. Lipid samples were further dried under vacuum for 3 h prior to being suspended in 10 mM HEPES buffer, 150 mM NaCl and 4 mM $CaCl_2$. The final concentration of lipids was 0.5 mM. Samples were left to hydrate overnight, followed by sonication for 30 min. During sonication, periodic vortex mixing was carried out prior to vesicle extrusion (Avanti Mini-Extruder, Avanti Polar Lipids, Birmingham, AL, USA) 21 times through a polycarbonate membrane filter of defined pore diameter, typically 100 nm. Extrusion was performed at temperatures above the transition temperature (T_M) of the component phospholipids, since gel-state lipids are difficult to extrude at lower temperatures.[61] Resultant small unilamellar vesicles (SUVs) have a monodisperse size distribution as measured by dynamic light scattering (HPPS, Malvern Instruments) and were used for all further experiments.

AFM imaging

The visualization of SPBs was performed using a commercial AFM (Nanoscope IV, Digital Instruments, Santa Barbara, CA) operating at room temperature. All images were obtained by means of *in situ* tapping mode using triangular Si_3N_4 cantilevers (Digital Instruments) with a spring constant of 0.12 N m^{-1} operating at the cantilever resonance frequency. Formation of SPBs was achieved by depositing 100 μL of 100 nm SUV solution (10 mM HEPES, 150 mM NaCl and 4 mM $CaCl_2$, pH 7) on a freshly cleaved mica surface. Prepared surfaces were then incubated for 4 h at 4 °C.[7] Prior to imaging, surfaces were rinsed with 10 mM HEPES and 150 mM NaCl at pH 7 to remove any unbound calcium ions. Both high resolution (512 × 512 points) and low resolution (64 × 64 points) topographical images were collected. The low resolution images were collected in concert with the FV images.

Chemical modification of AFM probes

Commercial triangular Si_3N_4 cantilevers were cleaned in a water plasma prior to further modification. Following plasma cleaning, tips were modified using silane deposition from solution.[62] Modification of plasma treated tips with 3-aminopropyltriethoxysilane (APTES) (0.5% v/v in hexadecane) was performed by deposition overnight (16 h) at room temperature followed by rinsing in chloroform and drying under a gentle stream of N_2.

Force spectroscopy and force–volume imaging

Force plots were acquired using either triangular Si_3N_4 cantilevers or APTES modified Si_3N_4 cantilevers with a nominal spring constant of 0.15 N m^{-1}. As the dimensions of cantilevers can vary significantly, spring constants were calculated for unmodified and modified probes by the method developed by Sader *et al.*[63] The measured force constants agreed with the manufacturer's nominal value for both the unmodified and the modified probes. The quality factor (*Q*-factor) of the cantilever for unmodified and modified probes yielded $Q \approx 61$ and 58, respectively. As the spring constant remained unchanged and as cantilevers were modified with only a thin layer of silane, it can be assumed that the tip radius (15–20 nm) was not dramatically altered. Unless otherwise stated, 200 force curves over more than five positions were obtained for each surface analysed using force spectroscopy. All force curve measurements acquired 256 sample data points.

FV imaging collects force curves at each x, y pixel of the image by measuring cantilever deflection. Whilst a height image is also produced by this technique, the strength of this technique is that the information contained in the 3D data set can be decoupled from the topographic information. FV images (32 × 32 force curves) were collected at a scan rate of 0.0723 Hz, in relative trigger mode. The trigger mechanism was set to 3 nm of cantilever deflection.

All AFM experiments were performed in 10 mM HEPES, 1 mM NaCl at pH 7 at room temperature. In this work, we focus on the force data obtained for the retract cycle. The force measurements presented are given with ± one standard deviation. For the measurement of adhesion as function of pH, the buffer used for pH samples 5.5–10.5 was 10 mM HEPES, 1 mM NaCl adjusted with NaOH and for the pH 3 samples 10 mM sodium acetate, 1 mM NaCl was used and pH adjusted with acetic acid.

Results and discussion

The initial experiments examined the nanomechanical properties of each single component lipid layer using an unmodified AFM tip. Force extension curves can provide useful information regarding the maximum force that a membrane can withstand before breaking.[56,64,65] The breakthrough force measured for DPPC and DOPS bilayers was 1.68 ± 0.31 nN and 0.66 ± 0.11 nN, respectively ($n = 100$). This difference in breakthrough force is expected as DPPC is in the gel state while DOPC is in the liquid state at room temperature. For all further experiments, this information was used to apply an appropriate trigger threshold below the breakthrough force of each single component lipid layer. Subsequent experiments examined the force retraction curves for single component lipid layers using both an unmodified and an APTES-modified AFM tip at pH 7. Experiments also measured the adhesion of the modified aminosilane AFM tip to the mica substrate at pH 7, which yielded adhesive force of 0.33 ± 0.09 nN. In the case of DPPC, there is a shift to lower forces of adhesion from the unmodified to the amine functionalized tip. The adhesion force drops from an average of 0.51 ± 0.14 nN to almost zero (Fig. 1a). In contrast, for DOPS the modified tip increases the observed adhesion forces dramatically by almost an order of magnitude, from an average of 0.43 ± 0.07 nN to 3.45 ± 0.51 nN (Fig. 1b).

In order to explain the observed results, changes in adhesion after chemical modification of the AFM tip were probed by measuring the adhesion for the substrate and each of the constituent lipids as a function of pH. These data are presented in Fig. 2. Different tips were used for the experiments presented in Fig. 1 and 2. Different tips often give different absolute values of adhesion forces but all the trends observed are consistent with each tip. The adhesion observed is likely due to a combination of hydrogen bonding and charge effects. For mica, the initial high adhesion is due to electrostatic interactions between a positively charged tip interacting and the negatively charged surface. The isoelectric point for mica is in the range of pH 3–3.5[66] whilst the isoelectric point of APTES on silica is around 6.5.[67] With increasing pH the mica surface should become more negatively charged and by pH 5 the charge difference between the tip and the surface will have reached its maximum value. The charge on the tip likely starts to drop around pH 5.5 and this will see a decrease in adhesion, which is what we observe experimentally. Above pH 9, the amines on the tip are not protonated, which explains why the observed adhesion forces are low.

The isoelectric point for DPPC is pH 4.[68] Given the similarity of the isoelectric points for mica and DPPC one would expect the adhesion curves as a function of pH to be very similar. This is consistent with our experimental observations. The higher

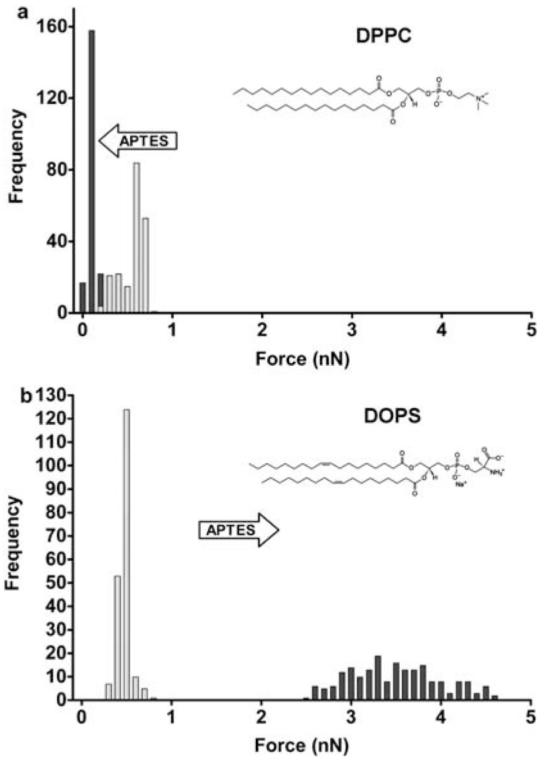

Fig. 1 Histograms corresponding to the adhesion force obtained with both an unmodified (□) and an APTES-modified (■) tip on single component (a) DPPC and (b) DOPS supported phospholipid bilayers. Modification of Si_3N_4 tips with APTES gave an enhanced adhesion contrast between DPPC (average adhesion 0 nN with modified tip) and DOPS (average adhesion 3.45 ± 0.51 nN with modified tip) bilayers. Measurements were performed in 10 mM HEPES and 1 mM NaCl at pH 7. Insets: molecular structures of (a) DPPC, and (b) DOPS.

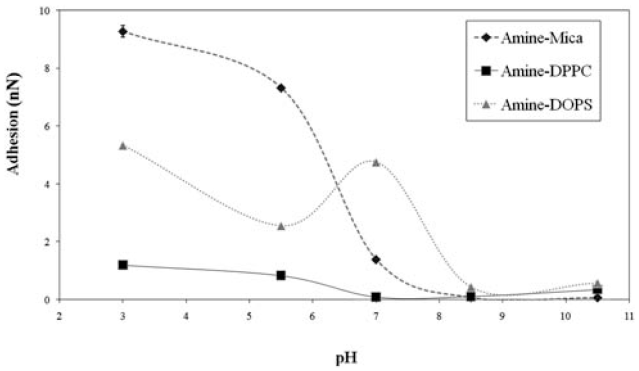

Fig. 2 Adhesion forces observed as a function of pH for interactions of an AFM tip modified with ATPES (hence amine terminated) with mica, DPPC and DOPS.

adhesion for mica is likely a reflection of a higher density of negative charges at the same pH.

Increasing pH will reduce the charge on the tip reducing the adhesion. For the lipids, the difference in response towards tip surface chemical structure can be attributed to the difference in functionality of the head groups in the two lipids (see inset Fig. 1). The isoelectric point for DOPS is at pH 1.2.[69] At low pH, the interactions are dominated by the oppositely charged tip and the lipid bilayer surface. With increasing pH, the charge of the tip decreases leading to a weaker adhesion. In the region of pH 7, however, a peak in the adhesion is observed. We attribute this peak to the fact that at this pH, the partly protonated APTES functionalised tip is able to electrostatically interact with the rather exposed serine's carboxylate, effectively competing with the serine's amine group. Such bonds can form when the solvent is expelled from the interaction volume when tip and bilayer are brought in contact.[56] From this pH value on, the adhesion decreases dramatically as the tip loses its positive charge. Similar effects have been described before[56] for adhesion measurements between functionalised AFM tips and lipid bilayers. The APTES functionalised tip is unable to interact electrostatically with the less exposed phosphate group of DOPS or DPPC. This explains why in the case of DPPC, no peak is observed in the adhesion at pH 7.

In contrast, the small adhesion of the unmodified tip is due to attractive interactions of oxygen containing species on the tip (*e.g.* silanols) and with lipid head groups, which only allows poor discrimination between DPPC and DOPS (by an adhesion force difference of 0.1 nN). Our simple tip modification thus affords the opportunity to reliably discriminate between the lipid head groups.

A binary mixture of DPPC and DOPS was prepared at a molar ratio of 50 : 50. This composition was chosen to yield the largest number of domain boundaries possible making the study of these regions as straightforward as possible. SPBs from this lipid mixture exhibited phase separation such that the DPPC gel domains were typically ~1 nm higher than the neighbouring DOPS liquid phase domains (Fig. 3) in accordance with literature results.[7] Zooming in to image a smaller region of the bilayer, Fig. 4a shows a topographic image acquired with 64 × 64 pixel resolution as opposed to the 512 × 512 pixel resolution used in our normal topographical imaging (see Fig. 3). Fig. 4b represents the corresponding FV image obtained using an amine functionalised AFM tip where the adhesion force is mapped as a function of lateral position. As the tip modification affords two very different adhesion forces for each component phospholipid, the position of the lipids can be readily observed on the force adhesion map.

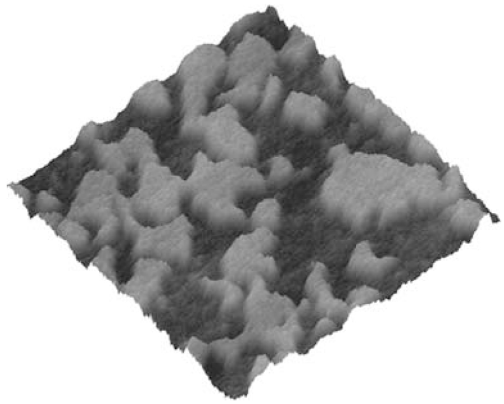

Fig. 3 AFM topographic image (1.5 × 1.5 μm^2; *Z*-scale: 5 nm, 512 lines × 512 lines) of a 50 : 50 DPPC : DOPS supported phospholipid bilayer. DPPC domains extend 1.18 ± 0.09 nm above surrounding DOPS domains.

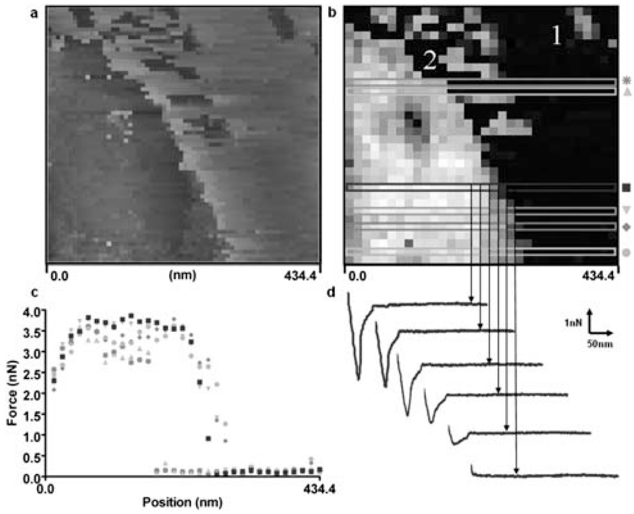

Fig. 4 (a) Topographic height image (64 lines × 64 lines) and (b) FV adhesion map (32^2 forces curves) of a 50 : 50 DPPC : DOPS supported phospholipid bilayer. Lighter regions in the FV adhesion map correspond to greater force associated with DOPS phospholipids. FV images were recorded at a relative trigger threshold of 3.0 nm to prevent bilayer rupturing. The numbers 1 and 2 label DOPS nanodomains within the DPPC domain. (c) Adhesion force as a function of position for several lines in FV adhesion map. Several lines demonstrate a gradual decline in adhesion at the interface, implying that intermixing between DOPS and DPPC bilayer domains take place. (d) Associated retraction force curves for a sample line. A gradual change in adhesion is observed between DOPS and DPPC bilayer domains.

In the FV image, the adhesion forces can be mapped along a line moving horizontally from left to right. Some representative force curves from a representative line are shown in Fig. 4d. The change of adhesion force when moving the tip across the interface from one lipid domain to the other is conspicuous. Considering the results from single component bilayers (see Fig. 1), DOPS domains are associated with high adhesion whilst DPPC domains display essentially no adhesion. In the upper part of the FV image (Fig. 4b), nanoscale DOPS-rich domains within a larger DPPC domain are apparent. These nanodomains are on the order of 100 nm in lateral dimensions and cannot be resolved at this level of detail by any other technique. These nanodomains are almost certainly mixtures of the two lipids with one lipid present in significantly higher concentrations. It may also be the case that the domains arise due to different amounts of each lipid in the upper and lower leaflets in a given region.

Fig. 5a shows a histogram representative of the adhesion forces obtained for the entire FV image of the two component system. If there was no intermixing of the two lipids, this histogram would be expected to be simply the sum of the histograms for modified tips shown in Fig. 1a and b. Indeed, as expected, the histogram for the two component system resembles the overlay of the histograms for each single component system. However, closer examination reveals that for the binary system, adhesion forces between 1.0 nN and 2.5 nN were measured that are not observed for the single component systems (Fig. 5b). These are from regions where an intermixing of the two lipids has occurred.

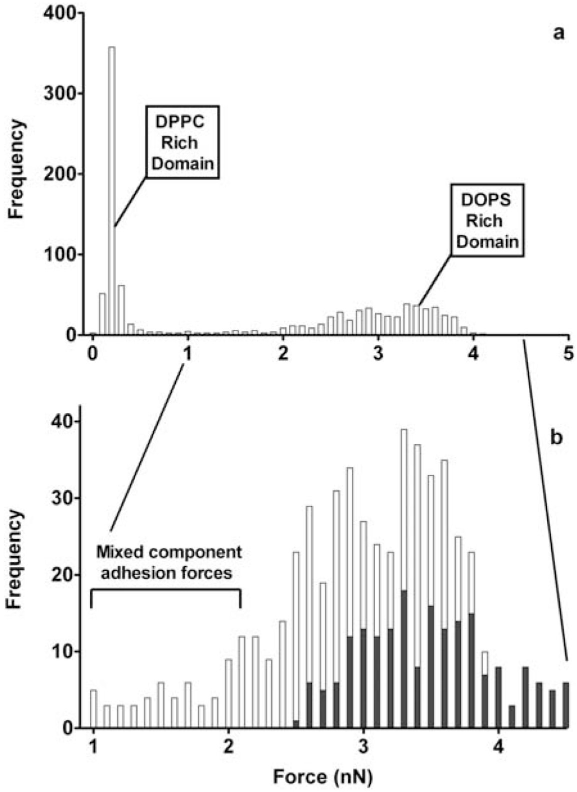

Fig. 5 (a) Histogram of adhesion forces measured over the entire FV image for the two component system in Fig. 4. Two distinct regions of adhesion are observed which are comparable to those obtained for single component DPPC and DOPS bilayers (Fig. 1). (b) Histograms of adhesion forces for DOPS rich domains from Fig. 4 (□) between 1 and 4.5 nN and from pure DOPS bilayers (■) (from Fig. 1). The overlay reveals a region of adhesion forces for the two component system which are smaller than those observed for pure DOPS bilayers. This implies the intermixing of DPPC and DOPS domains for the two component system.

The adhesion forces for several lines in the FV image are summarised in Fig. 4c. For lines in the upper part of the image, there is a pronounced step in adhesion from one region of lipid to the other. However, in the lower part of the image, the change in adhesion across the step is gradual and several values between the two extremes of the two pure lipids are observed. This result indicates that in fact the lipid domain boundary in this region is not as well defined, consistent with significant intermixing of the two lipids. This intermixing occurs over a region of about 40 nm and may influence bilayer properties significantly. This indicates that our technique is sensitive to lateral lipid composition on the scale of 10–20 nm. To the best of our knowledge, this resolution is superior to the resolution obtained by optical microscopy or mass spectrometric techniques.

Studies utilising FCS have hinted at heterogeneities of lipid packing at the domain boundary of binary mixtures of DOPC and DPPC.[6] The previously unknown lipid intermixing phenomenon described here may also play an important role in the formation and movement of lipid rafts or in the formation and functional behaviour of protein assemblies in the complex and phase separated structures of physiological membranes. Association of proteins into distinct lipid microdomains is governed by either chemical or physical properties of the lipid microdomain environment. For example, it is understood that glycosylphosphatidyl (GPI)-anchored proteins partition to enrich lipid rafts, while many transmembrane proteins are located in nonraft phases.[70] Proteins can also be confined to the area of the microdomain if the activation energy of passing the domain barrier is larger than the kinetic energy of the protein itself.[71] Hypothetically, the intermixing boundary observed in the current study could potentially provide a mechanism for proteins in different lipid environments to interact.

As previously discussed, there exists a sharp boundary in the upper part of the images of Fig. 4 where there is a pronounced step in adhesion from one region of lipid to the other. These sharp boundary regions only occur where nanodomains are observed. We propose that one possible explanation is that the sharp edge exists after the intermixed region has separated from the DOPS/DPPC domain boundary, hence generating the observed DOPS-rich nanodomains that exist in the DPPC membrane component. The presence of the sharp boundary suggests that the dynamic movement in a lipid membrane is driven by the diffusion of one component into another at the boundary such that initially an intermixed region is formed. Near the middle of the image, a DPPC-rich nanodomain can also be seen in the DOPS membrane component further suggesting the movement of one lipid in another domain. This diffusion will lead to the formation of an intermixed "bulge" along the boundary resulting in the formation of an attached nanodomain of intermixed components which eventually separates from the boundary leaving behind a sharp boundary and creating a new nanodomain of one lipid within a large domain of the other. A similar lipid-driven effect may be involved in and add to protein-controlled cell membrane deformations including *endo-* and *exo*cytosis, budding and membrane traffic between organelles. It is well conceivable that this process also drives the movement of membrane bound proteins through a lipid region, contributing to membrane signalling or other biological functions.

In an FCS study which measured the mobility of dye-labelled lipid molecules, DPPC domains within a DOPC matrix have previously identified locations where the mobility of the lipid probes was almost the same as the liquid phase DOPC regions.[6] It was inferred that the biphasic mobility of the observed nanoscale DPPC-rich domains may have been due to DPPC packing heterogeneities or DOPC clusters surrounding lipid fluorescent probes. The results reported in this paper suggest that this measured change may have been due to nanodomains absorbed into larger microdomains. A recent study utilising NanoSIMS has also revealed the existence of a fluid phase subdomain within a gel phase domain, which was assumed to represent trapping of the fluid-phase subdomain upon expansion of the gel-phase domain.[5] Results from the current study infer the observed nanodomains are not trapped, but actually move through the gel-phase microdomain. The variation in distance from the lipid boundary to the observed nanodomains suggests diffusion must be occurring. Additionally, it appears that nanodomains further from the boundary (see domain 1 in Fig. 4b) are much more intermixed than those closer to the boundary (see domain 2 in Fig. 4b) showing that the diffusion of one component into the other continues after the initial formation of the nanodomain. As SIMS requires the sample to be freeze-dried, it would be challenging to infer dynamic processes using this technique.

A theoretical model for the process of phase separation in multicomponent membranes has previously been proposed[72] whereby the distribution of domain sizes and the ability of nanodomains to merge forming micrometre-scale domains were strongly dependent on the line tension, a derived energy per unit length, of the bilayer membrane. Several possibilities were apparent, one of which described nanodomains coexisting within large domains. However, at higher line tensions, nanodomains would merge into microdomains. The FV images cannot follow the nanodomains to observe their combination into microdomains or determine other possible roles, but our work does provide substantial evidence of the existence of the nanodomains.

Elucidating the role of the fine structure and composition of cellular membranes has been of significant interest in the past few decades. Exactly how membrane domains influence the transduction of cellular signals is under constant investigation. Unpublished studies from this laboratory have further characterised the headgroup interaction as a function of pH with modified probes, in addition to a range of other lipid headgroups. The development of this technique to monitor physiological relevant membranes will have potential applications in defining the role of cellular membranes, in particular their domains, and how their dynamic structure and molecular associations affect cell membrane signalling or biological functions.

Conclusion

With the aid of FV imaging, we have demonstrated the ability to sense lateral lipid composition on the scale of 10–20 nm. Insights into the dynamic structure of phase separated regions have also been obtained. The formation of nanodomains of lipids leaves a sharp domain boundary while diffuse boundaries with extensive lipid intermixing are observed in regions far from the observed nanodomains.

Acknowledgements

This work is supported by the Australian Microscopy and Microanalysis Research Facility (AMMRF). The authors wish to thank Dr Mickey Huson and co-workers from CSIRO (Textile and Fibre Technology) for providing and offering assistance with the software "Force Volume".

References

1 K. J. Van Vliet and P. Hinterdorfer, *Nano Today*, 2006, **1**, 18–25.
2 P. V. Escriba, *Trends Mol. Med.*, 2006, **12**, 34–42.
3 J. K. Seydel and M. Wiese, *Drug-membrane Interactions: Analysis, Drug Distribution and Modeling*, Wiley-VCH, Weinheim, 2002.
4 A. G. Lee, *Biochim. Biophys. Acta, Biomembr.*, 2004, **1666**, 62–87.
5 M. L. Kraft, P. K. Weber, M. L. Longo, I. D. Hutcheon and S. G. Boxer, *Science*, 2006, **313**, 1948–1951.
6 A. R. Burns, D. J. Frankel and T. Buranda, *Biophys. J.*, 2005, **89**, 1081–1093.
7 I. Reviakine, A. Simon and A. Brisson, *Langmuir*, 2000, **16**, 1473–1477.
8 E. Kalb, S. Frey and L. K. Tamm, *Biochim. Biophys. Acta, Biomembr.*, 1992, **1103**, 307–316.
9 H. M. McConnell, T. H. Watts, R. M. Weis and A. A. Brian, *Biochim. Biophys. Acta*, 1986, **864**, 95–106.
10 L. K. Tamm and H. M. McConnell, *Biophys. J.*, 1985, **47**, 105–113.
11 H. T. Tien and A. Ottova, *J. Membr. Sci.*, 2001, **189**, 83–117.

12 O. Domenech, A. Morros, M. E. Cabanas, M. T. Montero and J. Hernandez-Borrell, *Biochim. Biophys. Acta, Biomembr.*, 2007, **1768**, 100–106.

13 O. Domenech, F. Sanz, M. T. Montero and J. Hernandez-Borrell, *Biochim. Biophys. Acta, Biomembr.*, 2006, **1758**, 213–221.

14 S. Chiantia, J. Ries, N. Kahya and P. Schwille, *ChemPhysChem*, 2006, **7**, 2409–2418.

15 Z. Leonenko, E. Finot and D. Cramb, *Biochim. Biophys. Acta, Biomembr.*, 2006, **1758**, 487–492.

16 M. T. Montero, M. Pijoan, S. Merino-Montero, T. Vinuesa and J. Hernandez-Borrell, *Langmuir*, 2006, **22**, 7574–7578.

17 A. Berquand, M. P. Mingeot-Leclerq and Y. F. Dufrene, *Biochim. Biophys. Acta, Biomembr.*, 2004, **1664**, 198–205.

18 M. R. Nussio, M. Liddell, M. J. Sykes, J. O. Miners and J. G. Shapter, *J. Scanning Probe Microsc.*, 2007, **2**, 42–46.

19 S. Merino-Montero, O. Domenech, M. T. Montero and J. Hernandez-Borrell, *Biophys. Chem.*, 2006, **119**, 78–83.

20 H. Mueller, H. Butt and E. Bamberg, *J. Phys. Chem. B*, 2000, **104**, 4552–4559.

21 E. H. Reimhult, F. Höök and B. Kasemo, *Langmuir*, 2003, **19**, 1681–1691.

22 E. Sackmann, *Science*, 1996, **271**, 43–48.

23 T. Baumgart, S. T. Hess and W. W. Webb, *Nature*, 2003, **425**, 821–824.

24 S. L. Veatch and S. L. Keller, *Phys. Rev. Lett.*, 2005, **94**, 148101.

25 K. Gaus, T. Zech and T. Harder, *Mol. Membr. Biol.*, 2006, **23**, 41–48.

26 T. Parasassi and E. Gratton, *J. Fluoresc.*, 1995, **5**, 59–69.

27 F. M. Harris, K. B. Best and J. D. Bell, *Biochim. Biophys. Acta, Biomembr.*, 2002, **1565**, 123–128.

28 M. Kusube, N. Tamai, H. Matsuki and S. Kaneshima, *Biophys. Chem.*, 2005, **117**, 199–206.

29 M. Eigen and R. Rigler, *Proc. Natl. Acad. Sci. U. S. A.*, 1994, **91**, 5740–5747.

30 N. O. Peterson, P. L. Hoddelius, P. W. Wiseman, O. Seger and K.-E. Magnusson, *Biophys. J.*, 1993, **65**, 1135–1146.

31 B. R. Lentz, *Chem. Phys. Lipids*, 1989, **50**, 171–190.

32 B. R. Lentz, *Chem. Phys. Lipids*, 1993, **64**, 99–116.

33 J. Repakova, J. M. Holopainen, M. R. Morrow, M. C. McDonald, P. Capkova and I. Vattulainen, *Biophys. J.*, 2005, **88**, 3398–3410.

34 S. H. Hell, *Science*, 2007, **316**, 1153–1158.

35 G. Oncins, S. Garcia-Manyes and F. Sanz, *Langmuir*, 2005, **21**, 7373–7379.

36 A. Noy, C. D. Frisbie, L. F. Rozsnyai, M. S. Wrighton and C. M. Lieber, *J. Am. Chem. Soc.*, 1995, **117**, 7943–7951.

37 S. Kruger, D. Kruger and A. Janshoff, *ChemPhysChem*, 2004, **5**, 989–997.

38 J. Legleiter, M. Park, B. Cusick and T. Kowalewski, *Proc. Natl. Acad. Sci. U. S. A.*, 2006, **103**, 4813–4818.

39 L. A. Chtcheglova, J. Waschke, L. Wilding, D. Drenckhahn and P. Hinterdorfer, *Biophys. J.*, 2007, **93**, L11–L13.

40 P. Hinterdorfer and Y. F. Dufrene, *Nat. Methods*, 2006, **3**, 347–355.

41 A. Ebner, D. Nikova, T. Lange, J. Häberle, S. Falk, A. Dübbers, R. Bruns, P. Hinterdorfer, H. Oberleithner and H. Schillers, *Nanotechnology*, 2008, **19**, 384017.

42 S. Lee, J. Mandic and K. J. V. Vliet, *Proc. Natl. Acad. Sci. U. S. A.*, 2007, **104**, 9609–9614.

43 A. Gigler, C. Gnahm, O. Marti, T. Schimmel and S. Walheim, *J. Phys. Conf. Ser.*, 2007, **61**, 346–351.

44 A. N. Parbhu, W. G. Bryson and R. Lal, *Biochemistry*, 1999, **38**, 11755–11761.

45 M. A. Poggi, P. T. Lillehei and L. A. Bottomley, *Chem. Mater.*, 2005, **17**, 4289–4295.

46 S. Tan, R. L. Sherman Jr and W. T. Ford, *Langmuir*, 2004, **20**, 7015–7020.

47 J. Song, J. F. L. Duval, M. A. Cohen Stuart, H. Hillborg, U. Gunst, H. F. Arlinghaus and G. J. Vancso, *Langmuir*, 2007, **23**, 5430–5438.

48 P. Eaton, J. R. Smith, P. Graham, J. D. Smart, T. G. Nevell and J. Tsibouklis, *Langmuir*, 2002, **18**, 3387–3389.

49 F. Gaboriaud, B. S. Parcha, M. L. Gee, J. A. Holden and R. A. Strugnell, *Colloids Surf., B: Biointerfaces*, 2008, **62**, 206–213.

50 A. P. Quist, S. K. Rhee, H. Lin and R. Lal, *J. Cell Biol.*, 2000, **148**, 1063–1074.

51 C. V. G. Reddy, K. Malinowska, N. Menhart and R. Wang, *Biochim. Biophys. Acta, Biomembr.*, 2004, **1667**, 15–25.

52 E. Dague, D. Alsteens, J.-P. Latge, C. Verbelen, D. Raze, A. R. Baulard and Y. F. Dufrene, *Nano Lett.*, 2007, **7**, 3026–3030.

53 M. Radmacher, M. Fritz, J. P. Cleveland, D. A. Walters and P. K. Hansma, *Langmuir*, 1994, **10**, 3809–3814.

54 H. A. Mizes, K.-G. Loh, R. J. D. Miller, S. K. Ahuja and E. F. Grabowski, *Appl. Phys. Lett.*, 1991, **59**, 2901–2903.

55 A. Valsesia, M. M. Silvan, G. Ceccone, D. Gilliland, P. Colpo and F. Rossi, *Plasma Processes Polym.*, 2005, **2**, 334–339.

56 S. Garcia-Manyes, P. Gorostiza and F. Sanz, *Anal. Chem.*, 2006, **78**, 61–70.

57 Y. F. Dufrêne, W. R. Barger, J. D. Green and G. U. Lee, *Langmuir*, 1997, **13**, 4779–4784.

58 Y. F. Dufrêne, T. Boland, J. W. Schneider, W. R. Barger and G. U. Lee, *Faraday Discuss.*, 1999, **111**, 79–94.

59 W. F. Heinz and J. H. Hoh, *Biophys. J.*, 1999, **76**, 528–538.

60 G. W. Feigenson, *Nat. Chem. Biol.*, 2006, **2**, 560–563.

61 R. C. MacDonald, R. I. MacDonald, B. P. Menco, K. Takeshita, N. K. Subbarao and L. R. Hu, *Biochim. Biophys. Acta, Biomembr.*, 1991, **1061**, 297–303.

62 D. Losic, K. Short, J. G. Shapter and J. J. Gooding, *Aust. J. Chem.*, 2003, **56**, 1039–1043.

63 J. E. Sader, I. Larson, P. Mulvaney and L. R. White, *Rev. Sci. Instrum.*, 1995, **66**, 3789–3798.

64 S. Garcia-Manyes, G. Oncins and F. Sanz, *Biophys. J.*, 2005, **89**, 1812–1826.

65 S. Garcia-Manyes, G. Oncins and F. Sanz, *Biophys. J.*, 2005, **89**, 4261–4274.

66 T. S. Tsapikouni and Y. F. Missirlis, *Colloids Surf., B: Biointerfaces*, 2007, **57**, 89–96.

67 M. I. Goller, C. Barthet, G. P. McCarthy, R. Corradi, B. P. Newby, S. A. Wilson, S. P. Armes and S. Y. Luk, *Colloid Polym. Sci.*, 1998, **276**, 1010–1018.

68 R. Zimmermann, D. Küttner, L. Renner, M. Kaufmann, J. Zitzmann, M. Müller and C. Werner, *Biointerphases*, 2009, **4**, 1–6.

69 M. B. Abramson, R. Katzman and H. P. Gregor, *J. Biol. Chem.*, 1964, **239**, 70–76.

70 J. J. Sieber, K. I. Willig, C. Kutzner, C. Gerding-Reimers, B. Harke, G. Donnert, B. Rammner, C. Eggeling, S. H. Hell, H. Grubmuller and T. Lang, *Science*, 2007, **317**, 1072–1076.

71 G. Vereb, J. Szollosi, J. Matko, P. Nagy, T. Farkas, L. Vigh, L. Matyus and T. A. Waldmann, *Proc. Natl. Acad. Sci. U. S. A.*, 2003, **100**, 8053–8058.

72 V. A. J. Frolov, Y. A. Chizmadzhev, F. S. Cohen and J. Zimmerberg, *Biophys. J.*, 2006, **91**, 189–205.

– This page intentionally left blank –

2.6 Additional Scientific Publications

2.6.3 *Carbon Nanotube Network Electrodes for Dye Solar Cells*

D. D. Tune, **B. S. Flavel**, J. S. Quinton, A. V. Ellis, J. G. Shapter

Solar Energy Materials 94 (2010) 1665–1672

DOI: 10.1016/j.solmat.2010.05.026

Abstract

The photovoltaic properties of a new working electrode for dye sensitised solar cells, consisting of networks of covalently bound single walled carbon nanotubes on indium tin oxide, have been investigated. Following covalent sensitisation of the carbon nanotube networks with a ruthenium dye an appreciable cathodic photocurrent is measured upon illumination with simulated sunlight. Significant increases in photocurrent density are observed by building up sequential layers of carbon nanotube cross-linked with ethylenediamine to form a three-dimensional dye sensitised single walled carbon nanotube network. Such electrodes are promising for the future fabrication of low cost, minimal material use solar cells.

Contribution

D.D.T and J.G.S conceived the idea for the project. D.D.T and B.S.F performed the experiments and wrote the paper. All authors contributed to the scientific discussion and analysis of results.

– This page intentionally left blank –

Solar Energy Materials & Solar Cells 94 (2010) 1665–1672

Contents lists available at ScienceDirect

Solar Energy Materials & Solar Cells

journal homepage: www.elsevier.com/locate/solmat

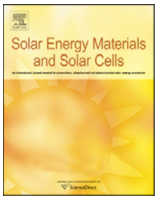

Single walled carbon nanotube network electrodes for dye solar cells

Daniel D. Tune, Benjamin S. Flavel, Jamie S. Quinton, Amanda V. Ellis, Joseph G. Shapter*

Centre for Nanoscale Science and Technology, School of Chemical and Physical Sciences, Flinders University, Bedford Park, GPO Box 2100, Adelaide SA 5001, Australia

ARTICLE INFO

Article history:
Received 10 March 2010
Received in revised form
3 May 2010
Accepted 9 May 2010
Available online 2 June 2010

Keywords:
Single walled carbon nanotubes (SWCNT)
Indium tin oxide (ITO)
N3 dye
Atomic force microscopy (AFM)
Scanning electron microscopy (SEM)
UV–visible spectroscopy

ABSTRACT

The photovoltaic properties of a new working electrode for dye sensitised solar cells, consisting of networks of covalently bound single walled carbon nanotubes on indium tin oxide, have been investigated. Following covalent sensitisation of the carbon nanotube networks with a ruthenium dye an appreciable cathodic photocurrent is measured upon illumination with simulated sunlight. Significant increases in photocurrent density are observed by building up sequential layers of carbon nanotube cross-linked with ethylenediamine to form a three-dimensional dye sensitised single walled carbon nanotube network. Such electrodes are promising for the future fabrication of low cost, minimal material use solar cells.

1. Introduction

Since they were first reported by Iijima in 1991 [1] single walled carbon nanotubes (SWCNTs) have attracted great interest across a diverse range of fields including microelectronics [2–4], medicine [5–8], energetic materials [9,10], polymers [11–13], energy storage [14,15] and more recently, light harvesting [16–23]. The use of SWCNTs in light harvesting devices has evolved primarily due to their unique electrical and optical properties arising as a result of one-dimensional (1D) confinement of electron and phonon states in the highly ordered SWCNT structure. Depending on the orientation of the sidewall lattice some SWCNTs may be considered metallic or semiconducting with bandgaps up to 1.1 eV depending on their diameter, level of defects or functionalisation, and degree of aggregation or bundling. Furthermore, SWCNTs have been shown to have excellent electrical conductivity in the longitudinal direction but to conduct poorly through their sidewalls unless functionalised [24].

The electrical conductivity of SWCNTs, combined with their very large surface area to volume ratio, makes them an ideal alternative scaffold material for the photoactive sensitiser in photoelectrochemical dye sensitised solar cells (DSCs) based on the O'Regan/Grätzel architecture [25]. Replacement of the titania in these cells with SWCNTs is expected to increase the surface area per volume for dye attachment and provide an improved electrical pathway. The potential benefits of SWCNT-based architectures for this application have been previously reported. For example, it has recently been shown that photoactive porphyrins coordinated to SWCNT arrays increase absorption of visible light and provide excellent electron transport [17]. Lee et al. [21,22] have used multi-walled carbon nanotubes (MWCNTs) similarly as scaffold for covalently bound Ru(II) dye molecules and have additionally shown significant increases in the conversion efficiencies of TiO_2 solar cells by incorporating MWCNTs. Lee et al. [18,20,26] have repeatedly shown increases in charge collection efficiencies of photoelectrochemical cells following incorporation of SWCNTs. The increase was shown to occur via suppression of electron–hole recombination and is largely independent of both the sensitiser used and the structure of the electrode surface. In other work, the semiconducting nature of SWCNTs has been used by Li et al. [16] on n-doped silicon surfaces to produce a simple p-n heterojunction solar cell with remarkable efficiency.

In previous work, we have demonstrated that covalent attachment of SWCNTs to fluorine tin oxide (FTO) coated glass yields electrodes, which produce photocurrent when incorporated into a photoelectrochemical cell [27]. However, the energy output of such a device is quite low due to the small amount of active material on the substrate. In this work we have increased the amount of active material on the surface via sequential addition of SWCNTs to form a randomly dispersed network. SWCNTs previously functionalised with carboxyl groups using a well established technique [28] were covalently bound to hydroxylated indium tin oxide (ITO) by a condensation reaction. Subsequent treatments with SWCNT were facilitated via an

---

* Corresponding author. Tel.: +61 8 8201 2005; fax: +61 8 8201 2905.
E-mail address: joe.shapter@flinders.edu.au (J.G. Shapter).

0927-0248/$ - see front matter © 2010 Elsevier B.V. All rights reserved.
doi:10.1016/j.solmat.2010.05.026

ethylenediamine linker, forming a three-dimensional randomly dispersed network. We have also fabricated hybrid solar cell electrodes utilising dye sensitised SWCNTs. Networks of SWCNTs were used as a scaffold for ruthenium dye molecules, which were covalently bound to the free end and sidewalls of the SWCNTs via the ethylenediamine linker. Both the unsensitised and dye sensitised architectures were then used as the working electrode in a solar cell.

2. Experimental details

2.1. Preparation of functionalised SWCNT solution

SWCNTs (Carbon Solutions Inc., CA, USA, P2-SWNT) were refluxed for 24 h in 3 M HNO_3 at 1 mg mL^{-1} to remove remaining catalyst and carbonaceous impurities and to increase the number of defect sites on the SWCNT sidewalls. The acid was then decanted and the SWCNTs were functionalised with carboxyl groups by ultrasonication at 50 W_{RMS} for 8 h in a 3:1 v/v solution of 98% H_2SO_4 and 70% HNO_3 at a concentration of 1 mg mL^{-1}—a process also known as 'cutting'. The temperature was maintained at ~5 °C throughout the reaction. The acid/SWCNT mixture was poured into 1 L of deionised (DI) water (pH 5.5, ~5 °C), filtered through 0.45 μm polycarbonate membrane filters (MilliPore) and washed with DI water until the pH of the filtrate stabilised at 5.5. The filtered SWCNTs were dried in air at 80 °C for 24 h then added at a concentration of 0.2 mg mL^{-1} to a solution of dimethylsulphoxide (DMSO) (99.9%, Sigma-Aldrich) containing *N*,*N*′-dicyclohexylcarbodiimide (DCC) (0.2 mg mL^{-1}, 99% Fluka Production GmbH) and 4-dimethylaminopyridine (DMAP) (0.05 mg mL^{-1}, Sigma-Aldrich). A suspension of SWCNTs was affected by ultrasonication of this solution at 50 W_{RMS} for 1 h under nitrogen and this resulting suspension was then used immediately.

2.2. SWCNT attachment to ITO

The preparation of SWCNT on ITO is shown schematically in Fig. 1(a–c). ITO coated glass slides (Sigma-Aldrich) with a sheet resistance of 8–12 $\Omega\,\square^{-1}$ and film thickness of 120–160 nm were cut into 2 × 1.5 cm samples. All samples were ultrasonically cleaned for a period of 10 min each in DI water, ethanol and acetone. The ITO surfaces were then hydroxylated by ultrasonication for 10 min in a solution of 1:1 v/v ethanol and DI water saturated with sodium hydroxide [29]. The hydroxylated ITO surfaces were rinsed with a copious amount of DI water and dried under a stream of nitrogen. The samples were then immersed in the freshly prepared functionalised SWCNT suspension and maintained at 80 °C under nitrogen for 1 h to produce ITO-SWCNT. Upon removal the samples were rinsed with DMSO followed by acetone and dried under a stream of nitrogen.

The ITO-SWCNT samples were immersed in ethylenediamine (EDA) (Sigma-Aldrich) containing DCC (0.2 mg mL^{-1}) and DMAP (0.05 mg mL^{-1}) at 50 °C for 30 min to produce ITO-SWCNT-EDA (Fig. 1(d)). After rinsing with DI water and drying under a stream of nitrogen the samples were returned to the SWCNT solution and maintained at 80 °C under nitrogen for 1 h to produce ITO-SWCNT-EDA-SWCNT (i.e. 2 treatments of SWCNT hereafter referred to as ITO-2-SWCNT). Rinsing followed by re-immersion in the above EDA solution at 50 °C for 30 min produced ITO-SWCNT-EDA-SWCNT-EDA (i.e. 2 treatments of SWCNT terminating in EDA, hereafter referred to as ITO-2-EDA) and the process was repeated for subsequent treatments.

EDA terminated samples were immersed for 24 h at 50 °C in a DMSO solution containing DCC (0.2 mg mL^{-1}), DMAP (0.05 mg mL^{-1}) and a ruthenium dye (0.2 mg mL^{-1}) to produce ITO-*x*-SWCNT-N3 (Fig. 1(e) and (f)). The ruthenium dye used was (cis-bis(4,4-dicarboxy-2,2-bipyridine) dithiocyanato ruthenium(II)) (Solaronix SA, Ru535) first reported by Nazeeruddin et al. [30] and otherwise known as 'N3'. Upon removal the samples were rinsed with DMSO and acetone then dried with a stream of nitrogen.

2.3. Raman spectroscopy

Raman spectra were collected with a WiTEC *alpha300R* Microscope in Raman mode using a 100 × objective (Numerical Aperture 0.9) and 532 nm laser (E_{laser}=2.33 eV) operating at constant power for each experiment up to a possible maximum of ~60 mW. Raman data was collected by the WiTEC Control software and analysed in the WiTEC Project software with the surface perpendicular to the excitation source. Spectra were collected over an integration time of 1 s.

2.4. Atomic force microscopy

Atomic force microscope (AFM) images were taken in air with a multimode head and Nanoscope IV controller (Digital Instruments, Veeco, CA, USA) operating in tapping mode using commercially available silicon cantilevers (FESP-ESP series, Veeco, CA, USA) with nominal fundamental resonance frequencies between 70 and 85 kHz. Topographic (height) images were obtained at a scan rate of 0.5 μm s^{-1} with the parameters set point, amplitude and feedback control optimised for each sample. All images were background subtracted to a 3rd order polynomial using the flatten feature of the Digital Instruments' Nanoscope software version 6.14. Analysis of surface properties such as roughness was conducted using the same software.

2.5. Scanning electron microscopy

Scanning electron microscope (SEM) images of the SWCNT electrodes were obtained on a CamScan MX2500 scanning electron microscope (CamScan Electron Optics Limited, Cambridgeshire, UK) with a tungsten hairpin filament within an hour of preparation. Prior to imaging all samples were sputter coated with a 5 nm platinum coating (determined by an in situ quartz crystal microbalance (QCM)) using an Emitech K575X sputter coater (Quorum Technologies, UK) with 75 mA deposition current. During imaging the sample was held at an angle of 20° with respect to the electron beam.

2.6. UV–visible spectroscopy

Spectra were obtained on a Varian Cary 50 with a resolution of 2 nm. In all experiments the spectrum of the quartz cuvette was used as the baseline although additional subtraction of solvent spectra was performed where indicated.

2.7. Fabrication of DSC

The counter electrode used was fluorine tin oxide (FTO) coated glass. Platinum (5 nm) was deposited on the counter electrode surface using the method described in Section 2.5. A thermoset plastic gasket (Surlyn^{TM}–Solaronix SA) was placed between each ITO sample (24 × 18 mm^2) and a similarly sized FTO counter electrode (Fig. 2). The resulting device was maintained at 100 °C for 10 min to set the gasket. The active area was 150 ± 10 mm^2 with a rectangular geometry (15 mm × 10 mm). The electrolyte used was a solution of 1-propyl 3-methylimidazolium iodide

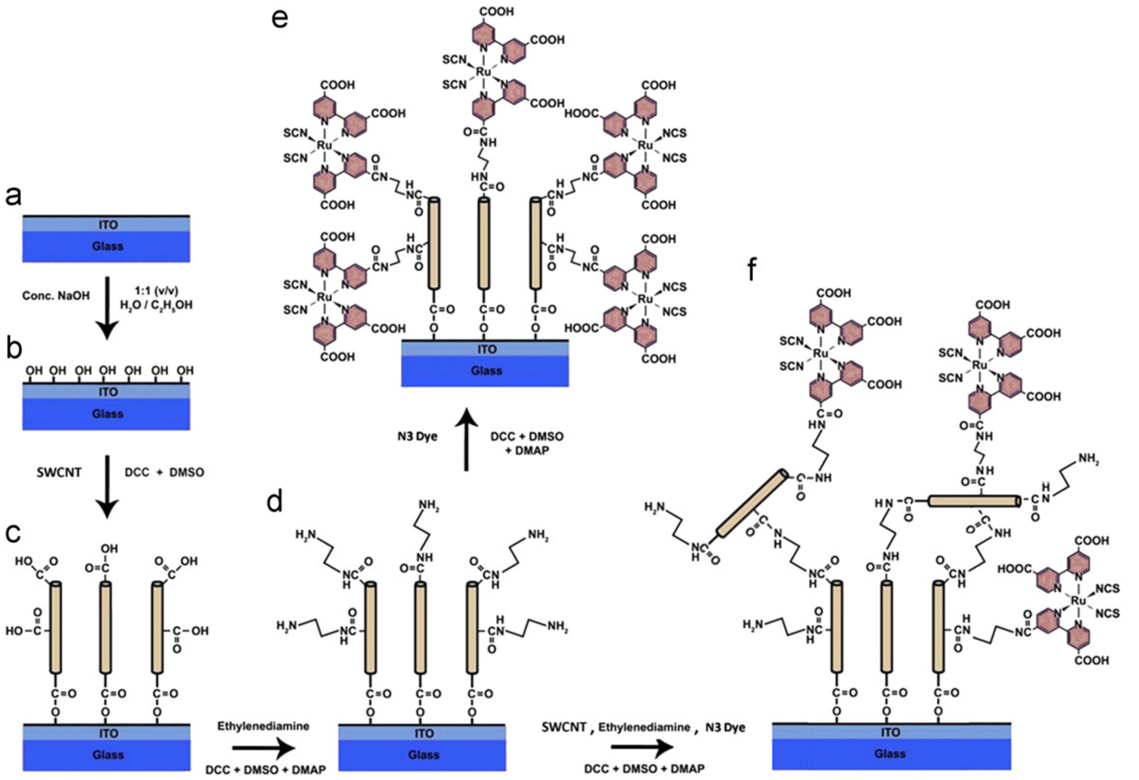

Fig. 1. Reaction pathway beginning with ITO coated glass (a) which is hydroxylated (b) and SWCNTs are added (c). To these are attached diamine linker molecules (d), which facilitate addition of either the dye sensitiser (e) or further layers and then dye (f). Not shown to scale.

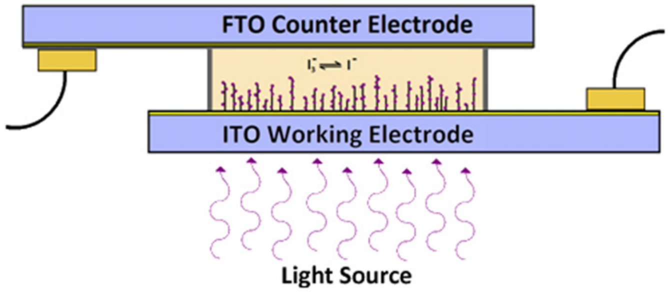

Fig. 2. Schematic of a complete cell incorporating ITO-SWCNT-EDA-N3 (ITO-1-SWCNT-N3) as the working electrode.

(0.8 M), iodine (0.1 M) and benzimidazole (0.3 M) in 3-methoxypropionitrile (MPN), otherwise known as 'Robust' electrolyte, and the cell was hermetically sealed. Note that no reflective material was used to seal the fill hole in the counter electrode as this yields erroneous results due to double passing of incident light through the active layer of the cell.

2.8. *Photovoltaic performance measurements*

All cells tested were illuminated with a quartz arc lamp producing 25 mW cm^{-2} at the sample surface and all tests were conducted at 25 °C. Light was channelled to the cell through an optical fibre with 2 cm between fibre output and the cell which was aligned perpendicularly to the source. Light entered the cell through the ITO working electrode. Current–voltage data was collected on a Keithley 236 Source Measure Unit with firmware revision A10. Data was recorded using a custom Digital Instruments' LabView^{TM} Virtual Instrument. The irradiance of the light source was measured using a NIST-calibrated photodiode (818-SL, Newport Corporation) with OD3 filter (883-SL, Newport Corporation) both with serial number 11177. Irradiance measurements were conducted at 25 °C with a distance of 2 cm between fibre output and the OD filter.

3. Results and discussion

The morphology of the electrode surfaces was investigated with AFM and SEM. Images showing electrodes with one to five treatments of SWCNTs are presented in Fig. 3. There was no discernable difference between surfaces before or after treatment with EDA or dye. SWCNT bundle widths, obtained by measuring 25 bundles from each of four separate AFM images (100 bundles in total), were found to be 24 ± 7 nm. The AFM images and their 3D representations show a mixture of horizontally and vertically oriented SWCNT bundles. In Fig. 3 the ITO substrate is visible in both AFM and SEM images of surfaces after one or two SWCNT treatments due to incomplete coverage but cannot be seen after the third treatment as the cross-linked SWCNT network becomes denser. Correspondingly, the surface area as calculated by the AFM software increases for the first three SWCNT treatments but then plateaus (Fig. 4). We interpret this to mean that full coverage of the surface is achieved with three treatments, after which the network increases in thickness. Of course, the total surface area of the SWCNT network is increasing but the AFM tip can only penetrate so far into it, hence the plateau. Amorphous carbonaceous impurities remaining from the cutting process, observed as bright globules, are also present in the images. Centrifugation of SWCNT suspensions is a commonly employed method of purification [31]. The removal of amorphous carbonaceous impurities prior to surface deposition of the SWCNTs and the effect on DSC performance of such treatment will be a focus of future investigation.

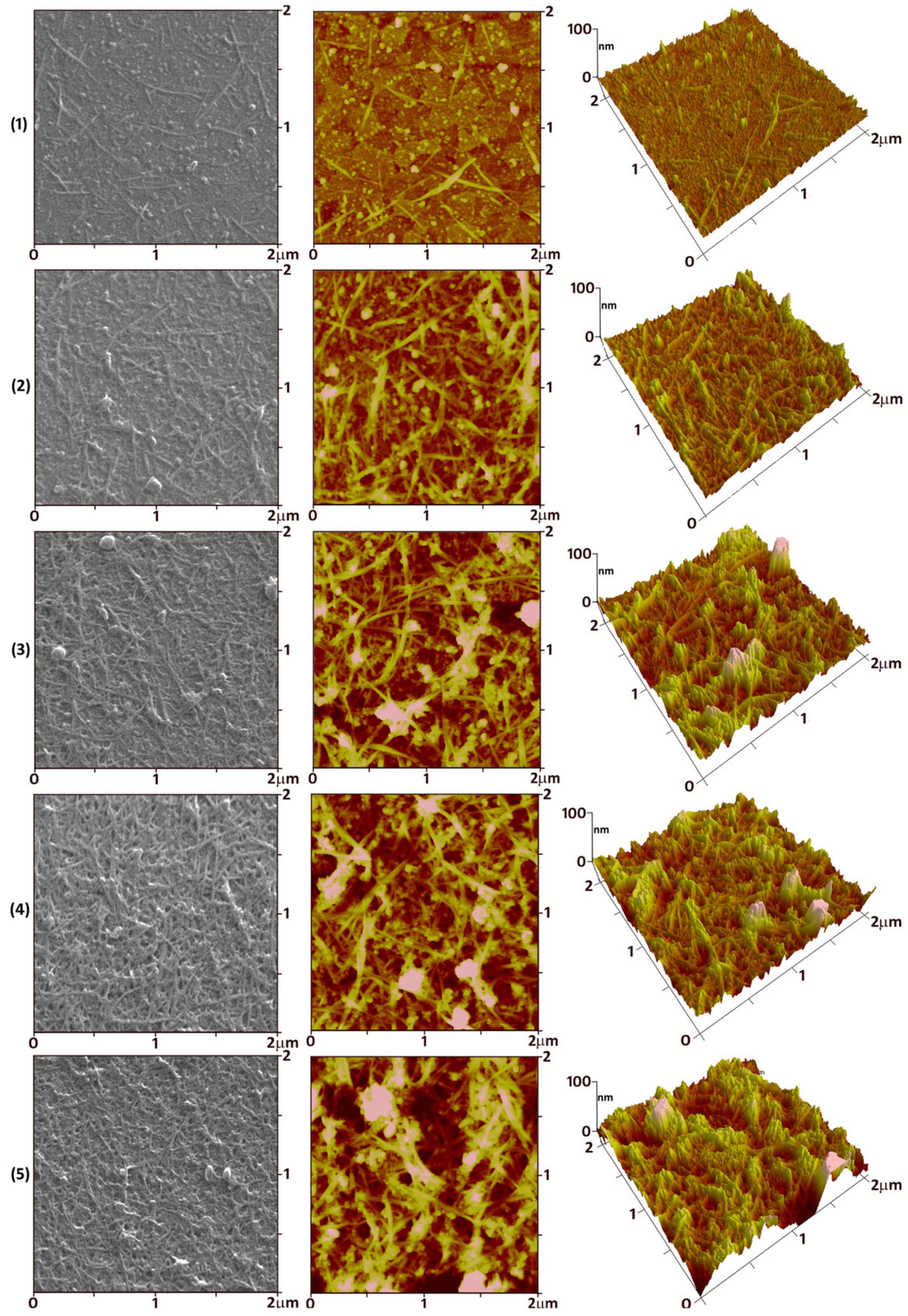

Fig. 3. The SWCNT electrodes from 1 treatment (top) to 5 treatments (bottom). SEM images are shown in the left column; tapping mode AFM images are shown in the centre column and 3D representations of the AFM images are shown in the right column. The SEM and AFM images are not of the same location on the surface.

Raman spectra of both sensitised and unsensitised SWCNT electrode surfaces were recorded; however, there was no discernible difference before or after EDA functionalisation or subsequent dye sensitisation. Analysis of the peak position of the SWCNT-specific radial breathing mode (RBM) gives a diameter of the individual SWCNT between 1.3 and 1.7 nm, calculated by the method of Alvarez et al. [32], which is in good agreement with supplier specifications of approximately 1.4 nm.

The sheet resistance of the ITO glass used in this work was measured with a two point probe to be $11\,\Omega\,\square^{-1}$, which is in accordance with the manufacturer specifications of $8\text{–}12\,\Omega\,\square^{-1}$. The same measurement protocol was used to measure the sheet resistance of each unsensitised SWCNT electrode giving values of 21, 23, 24, 26 and $28\,\Omega\,\square^{-1}$ for electrodes with 1–5 treatments of SWCNTs, respectively. This increase is consistent with a model in which sheet resistance is controlled by the number and type of junctions between SWCNTs and agrees well with the findings of Nirmalraj et al. [33] for acid treated SWCNT films. The sheet resistances of the dye sensitised SWCNT electrodes were 28, 29, 31, 33 and $35\,\Omega\,\square^{-1}$ for 1–5 treatments, respectively. The marginally higher values for the dye sensitised electrodes are anticipated due to the slightly insulating effect of the EDA functionalisation.

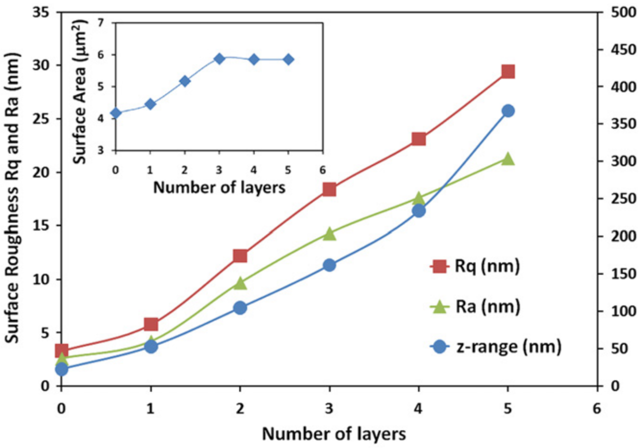

Fig. 4. Surface analysis of the layered SWCNT electrodes taken from AFM images shown in Fig. 3. Plots show the variation in *z*-range, RMS roughness (R_q) and mean roughness (R_a) with increasing treatments of SWCNTs (inset: variation in surface area with subsequent SWCNT treatments).

UV–visible spectra were recorded for the SWCNT electrodes prior to dye sensitisation, as shown in Fig. 5(A–E). A broad increase in absorbance with additional treatments of SWCNTs can be clearly seen. A plot of absorbance vs. the number of treatments yields a linear relationship at all wavelengths. However, the slope of this relationship is greater at the positions of the absorbance maxima. The height of these maxima, taken as a percentage of the background, decreases with each successive treatment of SWCNTs. This indicates that with each additional treatment the scattering process (the background) becomes increasingly dominant with respect to the electronic excitation processes (the maxima).

The unsensitised SWCNT electrodes show a broad absorbance centred at ~460 nm, a much smaller one at ~750 nm and another broad absorbance centred at ~1050 nm. The positions of these absorption maxima agree very well with the work of Fluerier et al. [34] using the same arc-discharge P2-SWCNT from Carbon Solutions, Inc. The absorbance at 1050 nm is attributed to ν_2–c_2 interband transitions in the electronic density of states (DOS) of semiconducting SWCNT and is denoted S_{22} (Fig. 6). The low energy ν_1–c_1 (S_{11}) transitions near 1800 nm were not probed in this work. The presence of the absorbance at ~750 nm is characteristic of the primary electronic transition within metallic SWCNTs (denoted M_{11}) and was unexpected in this work since the oxidative treatment of SWCNTs in concentrated mixed acid under ultrasonication is generally thought to remove metallic characteristics from mixtures of metallic and semiconducting SWCNTs [35,36]. Evidently, the cutting process employed in this work did not completely remove all metallic SWCNTs.

The absorbance maximum ~460 nm is not present in UV–vis spectra of the functionalised SWCNTs in DMSO (Fig. 5(F)), the ITO

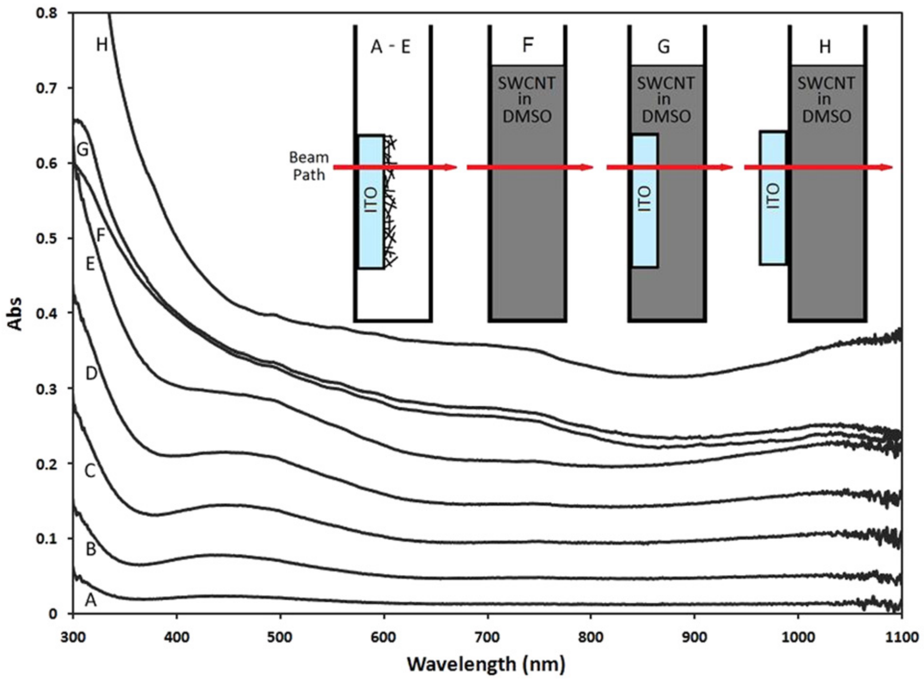

Fig. 5. UV–vis spectra of the layered SWCNT electrodes and control experiments: (A) ITO-1-SWCNT, (B) ITO-2-SWCNT, (C) ITO-3-SWCNT, (D) ITO-4-SWCNT, (E) ITO-5-SWCNT, (F) SWCNT in DMSO, (G) clean ITO internal, (H) clean ITO external. For (A-E) the beam passed through the quartz cuvette and the functionalised ITO sample; the quartz spectrum was removed as background. For (F) the beam passed through a quartz cuvette containing SWCNT in DMSO; the quartz+DMSO spectrum was removed as background. For (G) and (H) the beam passed through a quartz cuvette containing SWCNT in DMSO with a clean ITO sample either in contact with the solution (G) or external to the cuvette (H) and the quartz+DMSO spectrum was removed as background. Of note is the broad absorbance from ~350 to ~600 nm present only in (A–E). The greater absorbance displayed in (F), (G) and (H) is attributed to the larger number of SWCNTs sampled in solution than on the ITO surfaces in (A–E). The even higher absorbance displayed in (H) is due to additional scattering at the air-filled ITO/quartz interface.

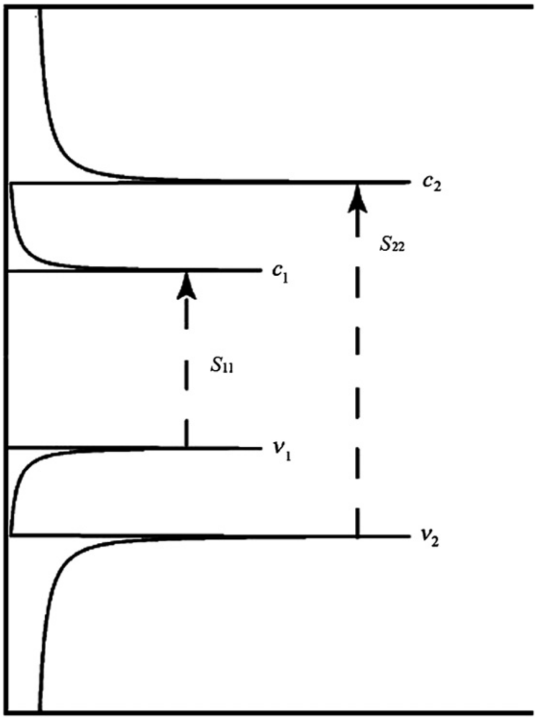

Fig. 6. The electronic density of states (DOS) of semiconducting SWCNTs showing transitions between the 1st, 2nd and 3rd valence and conduction bands.

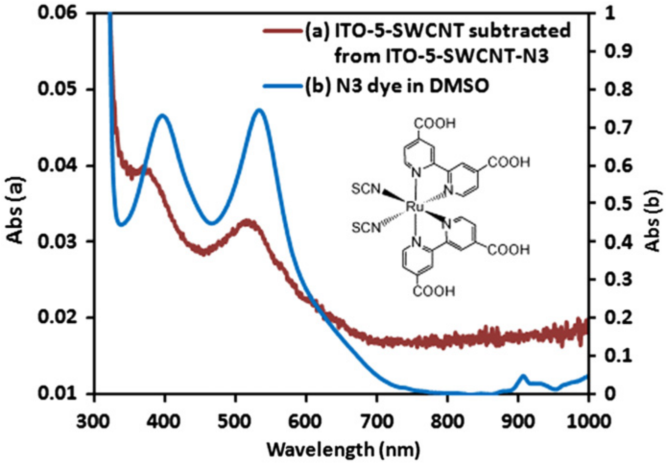

Fig. 7. (a) The difference spectrum produced by subtracting ITO-3-SWCNT from ITO-3-SWCNT-N3 and (b) UV–vis spectrum of the N3 ruthenium dye in DMSO (inset: N3 molecular structure).

glass (Fig. 5(H)) or when the hydroxylated ITO is immersed in SWCNT solution without coupling agent (Fig. 5(G)) and is therefore a property of the interface between the SWCNTs and ITO. Evidently the covalent bonding between these two different semiconducting materials leads to the formation of a newly accessible electronic transition in the region where the DOS of the two materials combine. The presence of this absorption peak extending broadly through the visible region of ~350–600 nm helps to explain why the SWCNT-only cells are photoactive without any dye sensitisation and is a promising result for an unoptimised device. It is anticipated that future optimisation of the architecture to exploit this property may lead to significant performance gains.

UV–visible spectra were also recorded for the SWCNT electrodes after dye sensitisation. Compared to the spectra of the unsensitised SWCNT electrodes, they show a broad increase of ~3–5% absorbance across all wavelengths with full retention of all the features. Difference spectra produced by subtracting ITO-*x*-SWCNT from ITO-*x*-SWCNT-N3 (where *x* is the number of SWCNT treatments) display two distinct peaks at ~525 and ~380 nm as shown in Fig. 7(a). This correlates very well with the UV–vis spectrum of the N3 ruthenium dye shown in Fig. 7(b), which displays two characteristic absorbance maxima at ~540 and ~405 nm corresponding to the two separate metal-to-ligand charge transfer (MLCT) pathways between the ruthenium centre and its dual bipyridine and thiocyanate ligands [30,37]. There is a shift of the MLCT bands, which can be attributed to the effect of the DMSO solvent used to obtain the absorption spectrum of the dye compared to that of the SWCNT electrode which was obtained in air. SWCNTs display a strong absorbance near 260 nm due to π–π^* transitions characteristic of extended aromatic systems [38] hence the high energy intraligand (π–π^*) charge-transfer transitions of the dye near 300 nm were not measurable.

The photovoltaic performance of solar cells fabricated using both sensitised and unsensitised SWCNT electrodes is presented in Fig. 8(a and b) and Table 1. Importantly, in contrast to DCSs using a titania scaffold for dye adsorption, the observed photocurrent of the SWCNT-based DSC flows in the reverse direction, i.e. they display a cathodic photocurrent. In titania-based cells the excited dye injects photo-generated electrons into the conduction band of the titania with the resultant holes in the dye being filled by oxidation of triiodide to iodide. In these SWCNT-based cells, photo-generated electrons must reduce the iodide to triiodide with resultant holes being refilled by electrons returning from the external circuit via the ITO and SWCNTs. This reversal of the direction of photocurrent is certainly a result of a substantial difference in the potential of SWCNTs conduction band(s) compared to that of titania and suggests a markedly different mechanism of electron transfer within and between the components of the DSC. This effect and the electronic basis for it are currently being investigated.

The dye sensitised electrodes (ITO-*x*-SWCNT-N3) also display a cathodic photocurrent indicating that electrons flow both directly from SWCNT to electrolyte (as before) and additionally now via the dye. However, dye sensitisation of the SWCNT electrodes after any number of treatments examined in this work does increase the magnitude of the observed photocurrent density (Fig. 8(b)). For a single treatment of SWCNTs the observed photocurrent density is 2.0 μA cm^{-2} which is increased to 2.8 μA cm^{-2} by dye sensitisation—a gain of 40% (Table 1). Upon further treatment with SWCNTs and EDA without dye sensitisation, additional increases in photocurrent density are observed up to a maximum of 4.9 μA cm^{-2} for five treatments. For the dye sensitised electrodes the increase is approximately linear with additional SWCNT treatments up to a maximum of 6.2 μA cm^{-2} for five treatments. For the SWCNT-only electrodes the increase is linear up to three treatments but then appears to approach a saturation level. This is likely due to an increased occurrence of electron–hole recombination in the denser networks due to (a) the increased distance between the point of photo-generation of charge carriers and the ITO electrode and/or (b) the greater number of (insulating) EDA links that must be traversed by the carriers or (c) scattering from the SWCNTs near the surface means excitation of the SWCNTs further from the surfaces is limited.

Addition of the dye opens up a second mechanism for the generation of charge carriers, namely excitation of the dye. After dye excitation the two possible routes for the charge carriers are through the SWCNTs or direct transfer to the electrolyte. In all cases introduction of the dye increase the photocurrent observed. However, the magnitude of the increase in photocurrent density

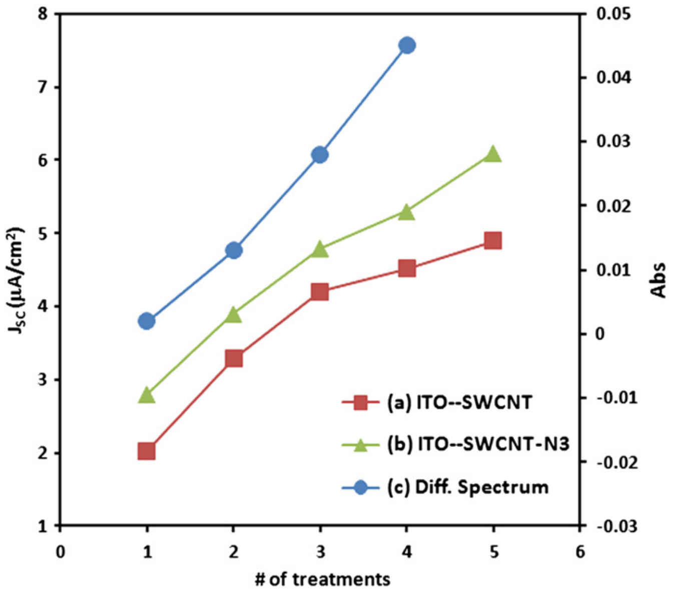

Fig. 8. (a) Increase in J_{SC} with increase in number of SWCNT treatments without dye sensitisation. (b) Increase in J_{SC} with increase in number of SWCNT treatments with dye sensitisation. (c) Increase in the UV–visible absorbance (at 450 nm) of difference spectra produced by subtracting the spectrum of ITO-*x*-SWCNT from the spectrum of ITO-*x*-SWCNT-N3. The standard deviation in each measurement is contained within the data points.

Table 1
Photovoltaic properties of the SWCNT network electrodes showing the open circuit voltage (V_{OC}), the short circuit current density (J_{SC}) and the cell fill factor (FF).

Cell	V_{OC} (mV)	J_{SC} (μA/cm^2)	FF
ITO-1-SWCNT	47	2.0	0.28
ITO-2-SWCNT	46	3.3	0.30
ITO-3-SWCNT	44	4.2	0.32
ITO-4-SWCNT	43	4.5	0.31
ITO-5-SWCNT	43	4.9	0.31
ITO-1-SWCNT-N3	43	2.8	0.28
ITO-2-SWCNT-N3	41	3.9	0.27
ITO-3-SWCNT-N3	41	4.8	0.29
ITO-4-SWCNT-N3	39	5.3	0.32
ITO-5-SWCNT-N3	36	6.2	0.29

upon dye sensitisation is a constant for the first three treatments of SWCNTs but begins to increase for the fourth and fifth. This would seem to suggest that for the first three treatments the total number of dye molecules attached does not increase. However the difference in UV–vis absorbance between the dye sensitised and SWCNT-only electrodes (Fig. 8(c)), taken as a direct measure of the amount of dye on the surface, increased approximately linearly from ~0.2 absorbance units for one treatment up to ~4.5 absorbance units for four treatments (at 450 nm). Therefore, subsequent treatments to the first increases the number of available sites for dye attachment and hence the amount of dye on the surface.

This increasing amount of dye is not reflected in the observed photocurrent for the first three treatments. This may be due to the position of the dye in the networks. The ends of SWCNT are more reactive and hence the location where one would expect the dye to attach first. When there are few SWCNTs present as is the case for few treatments, one would expect a large fraction of the dye to be on the ends of SWCNTs. Charge carriers are transported down the length of SWCNT much more efficiently than through the sidewalls [39]. Thus, for a few treatments, charge carriers generated by excitation of the dye will be very likely to transfer to the SWCNT where the electron–hole recombination within the cross-linked networks discussed earlier will play an important role and limit the photocurrent produced. With four and five treatments it is likely that some of the ends of the SWCNTs will be unavailable for reaction and the increased surface area will mean more side wall defect sites will be available as points of attachment for dye molecules. Thus, now a large fraction of the dye molecules will be on the sidewalls of SWCNTs where transfer of the charge carriers to SWCNTs will be much harder. This will mean an increased rate of carriers transferred directly to the electrolyte increasing the photocurrent observed. This indicates that charge separation due to the dye is beginning to dominate that occurring within the SWCNTs.

The voltages produced by the cells are of the order of mV. This small value is likely due to a combination of factors: incomplete coverage of the electrode surface, a significant back reaction caused by low shunt resistance at the ITO and/or SWCNT surfaces, electron–hole recombination within the network, poor matching of SWCNT and dye—effectively a high series resistance, and poor matching of SWCNT and electrolyte potentials limiting the maximum obtainable voltage. The nanotubes used are a combination of metallic and semiconducting tubes and the metallic tubes would be expected to lower the potential of system by providing sites for exciton recombination. All these factors also contribute to the modest fill factors of ~0.3 for all the electrodes produced in this work. Investigation into the relative contributions of these various factors and strategies for mitigation will be the subject of future work. Of course, the quantity of photoactive material on the surface is miniscule compared to that in conventional DSCs so it was not expected that the power generated would be comparable.

The low photocurrent densities in the μA range can be explained in part by the small quantities of material on the surface (the networks are only a few microns thick) and also by charge recombination occurring either within the network or within the SWCNTs themselves. On comparison of J_{SC} and UV–vis absorption variations between cells with a single treatment of unsensitised SWCNTs and two treatments, it is seen that while J_{SC} increased from 2.0 to 3.3 $\mu A\,cm^{-2}$, a gain of 65%, UV–vis absorption (at 500 nm) increased from 0.021–0.069, a gain of 228 %. In a simple model UV–vis absorption is taken as a measure of the amount of SWCNT on the surface, including both absorption and scattering. The disparity between the increases in J_{SC} and UV–vis absorption with additional SWCNT treatments indicates a substantial drop in conversion efficiency going from one treatment of SWCNTs to two, and the trend is continued with subsequent treatments. Furthermore, it also suggests that charge recombination is more prevalent in the networks than in the individual SWCNTs.

4. Conclusion

Photoelectrochemical cells fabricated from SWCNTs covalently bound to ITO and sensitised with a Ru(II) dye have been produced and characterised. Randomly dispersed networks created by sequential treatments with SWCNTs and ethylenediamine were shown to increase the quantity of dye attached thus improving photocurrent density. Results for the unsensitised SWCNT electrodes confirm that SWCNT networks on ITO are themselves photoactive with spectral evidence showing a broad absorbance spanning the visible region. The photovoltaic performance of cells containing both dye sensitised SWCNT and SWCNT-only electrodes was measured showing an appreciable, though modest, photoresponse. The source of the low power generated compared to conventional titania-based DSCs is largely due to far less photoactive material being present on the electrode surface, although a significant mismatch of potential energy levels between the different components of the cells is also implicated. Additionally, a markedly reduced fill factor indicates substantial electron–hole recombination within the cells. The performance of both the dye sensitised and SWCNT-only network based cells reported in this work is promising for future low cost, minimal material use solar cell applications if the underlying mechanism of action is further understood.

Acknowledgements

This work is supported by the Australian Microscopy and Microanalysis Research Facility (AMMRF).

References

[1] S. Iijima, Helical microtubules of graphitic carbon, Nature 354 (1991) 56–58.

[2] K. Ryu, A. Badmaev, C. Wang, A. Lin, N. Patil, L. Gomez, A. Kumar, S. Mitra, H.S.P. Wong, C. Zhou, CMOS-analogous wafer-scale nanotube-on-insulator approach for submicrometer devices and integrated circuits using aligned nanotubes, Nano Letters 9 (2008) 189–197.

[3] J. Yu, J.G. Shapter, J.S. Quinton, M.R. Johnston, D.A. Beattie, Direct attachment of well-aligned single-walled carbon nanotube architectures to silicon (1 0 0) surfaces: a simple approach for device assembly, Physical Chemistry Chemical Physics 9 (2007) 510–520.

[4] B.S. Flavel, J. Yu, J.G. Shapter, J.S. Quinton, Electrochemical characterisation of patterned carbon nanotube electrodes on silane modified silicon, Electrochimica Acta 53 (2008) 5653–5659.

[5] K. Bin, Y. Decai, D. Yaodong, C. Shuquan, C. Da, D. Yitao, Cancer-cell targeting and photoacoustic therapy using carbon nanotubes as ′Bomb′ agents, Small 5 (2009) 1292–1301.

[6] A.M. Yusof, N.A. Buang, L.S. Yean, M.L. Ibrahim, The use of multi-walled carbon nanotubes as possible carrier in drug delivery system for aspirin, in: Nanoscience & Nanotechnology: International Conference on Nanoscience and Nanotechnology, Shah Alam, Selandor, Malaysia, pp. 390–394.

[7] C. Lynam, N. Gilmartin, A.I. Minett, R. O'Kennedy, G. Wallace, Carbon nanotube-based transducers for immunoassays, Carbon 47 (2009) 2337–2343.

[8] J. Wang, X. Deng, S. Yang, H. Wang, Y. Zhao, Y. Liu, Rapid translocation and pharmacokinetics of hydroxylated single-walled carbon nanotubes in mice, Nanotoxicology 2 (2008) 28–32.

[9] S.H. Tseng, N.H. Tai, W.K. Hsu, L.J. Chen, J.H. Wang, C.C. Chiu, C.Y. Lee, L.J. Chou, K.C. Leou, Ignition of carbon nanotubes using a photoflash, Carbon 45 (2007) 958–964.

[10] B. Kang, Y. Dai, S. Chang, D. Chen, Explosion of single-walled carbon nanotubes in suspension induced by a large photoacoustic effect, Carbon 46 (2008) 978–981.

[11] L. Liu, A.H. Barber, S. Nuriel, H.D. Wagner, Mechanical properties of functionalized single-walled carbon-nanotube/poly(vinyl alcohol) nanocomposites, Advanced Functional Materials 15 (2005) 975–980.

[12] F. Cordella, M. De Nardi, E. Menna, C. Hébert, M.A. Loi, Tuning the photophysical properties of soluble single-wall carbon nanotube derivatives by co-functionalization with organic molecules, Carbon 47 (2009) 1264–1269.

[13] J. Zhang, H. Han, S. Wu, S. Xu, Y. Yang, C. Zhou, X. Zhao, Conductive carbon nanoparticles hybrid PEO/P(VDF-HFP)/SiO_2 nanocomposite polymer electrolyte type dye sensitized solar cells, Solid State Ionics 178 (2007) 1595–1601.

[14] M. Hirscher, K.H.J. Buschow, W.C. Robert, C.F. Merton, I. Bernard, J.K. Edward, M. Subhash, V. Patrick, Hydrogen absorption in carbon nanotubes: a critical review, Encyclopedia of Materials: Science and Technology Elsevier, Oxford, 2006, pp. 1–4.

[15] Y. Chen, P. Wang, C. Liu, H.-M. Cheng, Improved hydrogen storage performance of Li–Mg–N–H materials by optimizing composition and adding single-walled carbon nanotubes, International Journal of Hydrogen Energy 32 (2007) 1262–1268.

[16] Z. Li, V.P. Kunets, V. Saini, Y. Xu, E. Dervishi, G.J. Salamo, A.R. Biris, A.S. Biris, Light-harvesting using high density p-type single wall carbon nanotube/n-type silicon heterojunctions, ACS Nano 3 (2009) 1407–1414.

[17] J. Yu, S. Mathew, B.S. Flavel, M.R. Johnston, J.G. Shapter, Ruthenium porphyrin functionalized single-walled carbon nanotube arrays—a step toward light harvesting antenna and multibit information storage, Journal of the American Chemical Society 130 (2008) 8788–8796.

[18] W. Lee, L. Jungwoo, L. Sangjin, Y. Whikun, H. Sung-Hwan, C. Byung Won, Enhanced charge collection and reduced recombination of CdS/TiO_2 quantum-dots sensitized solar cells in the presence of single-walled carbon nanotubes, Applied Physics Letters 92 (2008) 153510–153513.

[19] R. Ulbricht, S.B. Lee, X. Jiang, K. Inoue, M. Zhang, S. Fang, R.H. Baughman, A.A. Zakhidov, Transparent carbon nanotube sheets as 3-D charge collectors in organic solar cells, Solar Energy Materials and Solar Cells 91 (2007) 416–419.

[20] W. Lee, J. Lee, S.H. Lee, J. Chang, W. Yi, S.H. Han, Improved photocurrent in Ru(2,2′-bipyridine-4,4′-dicarboxylic acid)$_2$(NCS)$_2$/Di(3-aminopropyl)viologen/single-walled carbon nanotubes/indium tin oxide system: suppression of recombination reaction by use of single-walled carbon nanotubes, Journal of Physical Chemistry C 111 (2007) 9110–9115.

[21] T.Y. Lee, P.S. Alegaonkar, J.-B. Yoo, Fabrication of dye sensitized solar cell using TiO_2 coated carbon nanotubes, Thin Solid Films 515 (2007) 5131–5135.

[22] T.Y. Lee, J.-B. Yoo, Adsorption characteristics of Ru(II) dye on carbon nanotubes for organic solar cell, Diamond and Related Materials 14 (2005) 1888–1890.

[23] R.E. Camacho, A.R. Morgan, M.C. Flores, T.A. McLeod, Carbon nanotube arrays for photovoltaic applications, JOM 59 (2007) 39–42.

[24] J. Li, A. Cassell, L. Delzeit, J. Han, M. Meyyappan, Novel three-dimensional electrodes: electrochemical properties of carbon nanotube ensembles, The Journal of Physical Chemistry B 106 (2002) 9299–9305.

[25] B. O'Regan, M. Gratzel, A low-cost, high-efficiency solar cell based on dye-sensitized colloidal TiO_2 films, Nature 353 (1991) 737–740.

[26] W. Lee, L. Jungwoo, L. Haiwon, Y. Whikun, H. Sung-Hwan, Enhanced charge-collection efficiency of In_2S_3/In_2O_3 photoelectrochemical cells in the presence of single-walled carbon nanotubes, Applied Physics Letters 91 (2007) 043515–043518.

[27] M.A. Bissett, J.G. Shapter, Photocurrent response from vertically aligned single walled carbon nanotube arrays, Journal of Physical Chemistry C 114 (2010) 6778–6783.

[28] M.W. Marshall, S. Popa-Nita, J.G. Shapter, Measurement of functionalised carbon nanotube carboxylic acid groups using a simple chemical process, Carbon 44 (2006) 1137–1141.

[29] Mea Huang, Small molecules as cross-linkers: fabrication of carbon nanotubes/thionine self-assembled multilayers on amino functionalized surfaces, Chemical Communications 44 (2005) 5560–5562.

[30] M.K. Nazeeruddin, A. Kay, I. Rodicio, R. Humphry-Baker, E. Mueller, P. Liska, N. Vlachopoulos, M. Graetzel, Conversion of light to electricity by *cis-bis* (2,2′-bipyridyl-4,4′-dicarboxylate)ruthenium(II) charge-transfer sensitizers ($X = Cl-$, $Br-$, $I-$, $CN-$, and $SCN-$) on nanocrystalline titanium dioxide electrodes, Journal of the American Chemical Society 115 (1993) 6382–6390.

[31] D. Yoon, J.-B. Choi, C.-S. Han, Y.-J. Kim, S. Baik, The quantitative characterization of the dispersion state of single-walled carbon nanotubes using Raman spectroscopy and atomic force microscopy, Carbon 46 (2008) 1530–1534.

[32] L. Alvarez, A. Righi, T. Guillard, S. Rols, E. Anglaret, D. Laplaze, J.-L. Sauvajol, Resonant Raman study of the structure and electronic properties of single-wall carbon nanotubes, Chemical Physics Letters 316 (2000) 186–190.

[33] P.N. Nirmalraj, P.E. Lyons, S. De, J.N. Coleman, J.J. Boland, Electrical connectivity in single-walled carbon nanotube networks, Nano Letters 9 (2009) 3890–3895.

[34] R. Fleurier, J.-S. Lauret, U. Lopez, A. Loiseau, Transmission electron microscopy and UV–vis–IR spectroscopy analysis of the diameter sorting of carbon nanotubes by gradient density ultracentrifugation, Advanced Functional Materials 19 (2009) 2219–2223.

[35] Z.-B. Zhang, J. Li, A.L. Cabezas, S.-L. Zhang, Characterization of acid-treated carbon nanotube thin films by means of Raman spectroscopy and field-effect response, Chemical Physics Letters 476 (2009) 258–261.

[36] C.-M. Yang, J.S. Park, K.H. An, S.C. Lim, K. Seo, B. Kim, K.A. Park, S. Han, C.Y. Park, Y.H. Lee, Selective removal of metallic single-walled carbon nanotubes with small diameters by using nitric and sulfuric acids, The Journal of Physical Chemistry B 109 (2005) 19242–19248.

[37] M.K. Nazeeruddin, S.M. Zakeeruddin, R. Humphry-Baker, M. Jirousek, P. Liska, N. Vlachopoulos, V. Shklover, C.-H. Fischer, M. Gratzel, Acid base equilibria of (2,2-bipyridyl-4,4-dicarboxylic acid)ruthenium(II) complexes and the effect of protonation on charge-transfer sensitization of nanocrystalline titania, Inorganic Chemistry 38 (1999) 6298–6305.

[38] R. Saito, G. Dresselhaus, M.S. Dresselhaus, in: Physical Properties of Carbon Nanotubes, Electronic Structure of Single-walled Nanotubes, Imperial College press, 1998, pp. 59–70.

[39] J. Yu, J.G. Shapter, M.R. Johnston, J.S. Quinton, J.J. Gooding, Electron-transfer characteristics of ferrocene attached to single-walled carbon nanotubes (SWCNT) arrays directly anchored to silicon (1 0 0), Electrochimica Acta 52 (2007) 6206–6211.

2.6 Additional Scientific Publications

2.6.4 *Patterning of Metal, Carbon and Semiconductor Substrates with Thin Organic Films by Microcontact Printing with Aryldiazonium Salt Inks*

J. Lehr, D. J. Garrett, M. G. Paulik, **B. S. Flavel**, P. A. Brooksby, B. E. Williamson,
A. J. Downard

Analytical Chemistry 82 (2010) 7027–7034

DOI: 10.1021/ac101785c

Abstract

Surface modification through reduction of aryldiazonium salts to give covalently attached layers is a widely investigated procedure. However, realization of potential applications of the layers requires development of patterning methods. Here, we demonstrate that microcontact printing with poly(dimethylsiloxane) stamps inked with aqueous acid solutions of aryldiazonium salts gives stable organic layers on gold, copper, silicon, and graphitic carbon surfaces. Depending on the substrate-diazonium salt combination, the layers range from relatively irregular multilayers to smooth films with close to monolayer thickness. After printing, surface attached aminophenyl and carboxyphenyl groups retain their usual reactivity toward amide bond formation with solution species, and hence, the method is a simple route to patterned, covalently attached, reactive tether layers. Multicomponent patterned films can be prepared by printing a second modifier onto a film-coated surface. Microcontact printing using aryldiazonium salt inks is experimentally very simple and is applicable to the broad range of substrates capable of spontaneously reducing aryldiazonium salts.

Contribution

J.L and A.J.D conceived the idea for the project. J.L, D.J.G, M.G.P, B.S.F and P.A.B performed the experiments. J.L and A.J.D wrote the paper and all authors contributed scientifically to the interpretation of the results.

– This page intentionally left blank –

Anal. Chem. **2010**, *82*, 7027–7034

Patterning of Metal, Carbon, and Semiconductor Substrates with Thin Organic Films by Microcontact Printing with Aryldiazonium Salt Inks

Joshua Lehr,[†,‡] David J. Garrett,[†,‡] Matthew G. Paulik,[‡,§] Benjamin S. Flavel,[‡,¶] Paula A. Brooksby,[‡] Bryce E. Williamson,[‡] and Alison J. Downard*[,†,‡]

MacDiarmid Institute for Advanced Materials and Nanotechnology, Private Bag 4800, Christchurch, 8140, New Zealand, and Department of Chemistry, University of Canterbury, Private Bag 4800, Christchurch, 8140, New Zealand

Surface modification through reduction of aryldiazonium salts to give covalently attached layers is a widely investigated procedure. However, realization of potential applications of the layers requires development of patterning methods. Here, we demonstrate that microcontact printing with poly(dimethylsiloxane) stamps inked with aqueous acid solutions of aryldiazonium salts gives stable organic layers on gold, copper, silicon, and graphitic carbon surfaces. Depending on the substrate−diazonium salt combination, the layers range from relatively irregular multilayers to smooth films with close to monolayer thickness. After printing, surface attached aminophenyl and carboxyphenyl groups retain their usual reactivity toward amide bond formation with solution species, and hence, the method is a simple route to patterned, covalently attached, reactive tether layers. Multicomponent patterned films can be prepared by printing a second modifier onto a film-coated surface. Microcontact printing using aryldiazonium salt inks is experimentally very simple and is applicable to the broad range of substrates capable of spontaneously reducing aryldiazonium salts.

Localized immobilization of molecular species is an important step in the fabrication of surfaces for applications that include chemical and biological sensors, biochips, molecular electronics, and tissue engineering. A large research effort over many years has established a suite of patterning methods, compatible with the best-known surface modification strategies, particularly those based on assembly of alkanethiols at noble metal surfaces, and reactions of silanes at oxide surfaces and alkenes at silicon. A relatively recently developed surface modification method is grafting from aryldiazonium salts solutions.[1,2] The mechanism, scope, and applications of this method have been widely investigated;[3−9] however, patterning techniques appropriate for use with this approach have received little attention.

Surface grafting from aryldiazonium salt solutions proceeds via reduction of the aryldiazonium cation and elimination of dinitrogen to yield an aryl radical capable of reaction with the surface.[2] For some substrates, a covalent linkage between the modifier and the surface has been directly demonstrated;[10−12] for others, covalent attachment has been inferred on the basis of the orientation of surface groups[13,14] or the stability of the layer.[2,15,16] Under commonly used grafting conditions, attack by aryl radicals on pregrafted groups gives a multilayered, covalently coupled film structure.[17,18] The stability of the grafted layers is a key advantage of this modification method; other attractive features are its wide substrate compatibility (from noble and industrial metals to semiconductors[9−11,19−22]) and the opportunity for further chemistry involving the grafted groups. Electrografting at an externally

---

* To whom correspondence should be addressed. E-mail: alison.downard@canterbury.ac.nz. Fax: +64-3-3642110.

[†] MacDiarmid Institute for Advanced Materials and Nanotechnology.

[‡] University of Canterbury.

[§] Present address: AgResearch Ltd, Private Bag 4749, Christchurch, 8140, New Zealand.

[¶] Present address: School of Chemistry, Physics and Earth Sciences, Flinders University, Bedford Park, SA 5042, Australia.

(1) Delamar, M.; Hitmi, R.; Pinson, J.; Saveant, J. M. *J. Am. Chem. Soc.* **1992**, *114*, 5883–5884.
(2) Allongue, P.; Delamar, M.; Desbat, B.; Fagebaume, O.; Hitmi, R.; Pinson, J.; Saveant, J.-M. *J. Am. Chem. Soc.* **1997**, *119*, 201–207.
(3) Adenier, A.; Bernard, M.-C.; Chehimi, M. M.; Cabet-Deliry, E.; Desbat, B.; Fagebaume, O.; Pinson, J.; Podvorica, F. *J. Am. Chem. Soc.* **2001**, *123*, 4541–4549.
(4) Barriere, F.; Downard, A. J. *J. Solid State Electrochem.* **2008**, *12*, 1231–1244.
(5) Downard, A. J. *Electroanalysis* **2000**, *12*, 1085–1096.
(6) Fave, C.; Leroux, Y.; Trippe, G.; Randriamahazaka, H.; Noel, V.; Lacroix, J. C. *J. Am. Chem. Soc.* **2007**, *129*, 1890–1891.
(7) Pinson, J.; Podvorica, F. *Chem. Soc. Rev.* **2005**, *34*, 429–439.
(8) Ranganathan, S.; Steidel, I.; Anariba, F.; McCreery, R. L. *Nano Lett.* **2001**, *1*, 491–494.
(9) Stewart, M. P.; Maya, F.; Kosynkin, D. V.; Dirk, S. M.; Stapleton, J. J.; McGuiness, C. L.; Allara, D. L.; Tour, J. M. *J. Am. Chem. Soc.* **2004**, *126*, 370–378.
(10) Bernard, M. C.; Chausse, A.; Cabet-Deliry, E.; Chehimi, M. M.; Pinson, J.; Podvorica, F.; Vautrin-Ul, C. *Chem. Mater.* **2003**, *15*, 3450–3462.
(11) Boukerma, K.; Chehimi, M. M.; Pinson, J.; Blomfield, C. *Langmuir* **2003**, *19*, 6333–6335.
(12) Combellas, C.; Kanoufi, F.; Pinson, J.; Podvorica, F. I. *Langmuir* **2005**, *21*, 280–286.
(13) Anariba, F.; Viswanathan, U.; Bocian, D. F.; McCreery, R. L. *Anal. Chem.* **2006**, *78*, 3104–3112.
(14) Ricci, A.; Bonazzola, C.; Calvo, E. J. *Phys. Chem. Chem. Phys.* **2006**, *8*, 4297–4299.
(15) D'Amours, M.; Belanger, D. *J. Phys. Chem. B* **2003**, *107*, 4811–4817.
(16) Shewchuk, D. M.; McDermott, M. T. *Langmuir* **2009**, *25*, 4556–4563.
(17) Doppelt, P.; Hallais, G.; Pinson, J.; Podvorica, F.; Verneyre, S. *Chem. Mater.* **2007**, *19*, 4570–4575.
(18) Kariuki, J. K.; McDermott, M. T. *Langmuir* **2001**, *17*, 5947–5951.
(19) Delamar, M.; Desarmot, G.; Fagebaume, O.; Hitmi, R.; Pinson, J.; Saveant, J. M. *Carbon* **1997**, *35*, 801–807.
(20) Liang, H. H.; Tian, H.; McCreery, R. L. *Appl. Spectrosc.* **2007**, *61*, 613–620.
(21) Mahmoud, A. M.; Bergren, A. J.; McCreery, R. L. *Anal. Chem.* **2009**, *81*, 6972–6980.

10.1021/ac101785c

applied potential is the most widely used strategy for the reduction step, but simple immersion of the substrate in a solution of an aryldiazonium salt can also lead to formation of surface layers. This spontaneous, or open-circuit potential (OCP), reaction has been reported for a range of metals, semiconductors, and carbon materials[4] and appears to involve electron transfer from the substrate to the aryldiazonium cation in solution.

Currently, there are few examples of patterned organic layers prepared by reduction of aryldiazonium salts. In the earliest report, we used mechanical scribing with an atomic force microscope (AFM) tip to remove regions of electrografted film from a carbon substrate.[23] A second aryldiazonium salt was then electrografted to the bare regions, creating a surface with dual chemical functionality. In a soft lithographic approach, we patterned a carbon substrate by adhering a poly(dimethylsiloxane) (PDMS) mold to the surface (either bare or film-coated) to form microchannels.[24] The channels were subsequently filled, either with aryldiazonium salt solution for site-specific electrografting or with reagents used for electrochemical or chemical conversion of the pre-existing surface film. Most recently, we demonstrated that conventional photolithography can be coupled with electrografting to give large areas of micrometer-sized patterns of modifiers on highly doped silicon.[22] Charlier, Palacin, and co-workers,[25] and Cougnon, Bélanger, and co-workers[26] have established that the scanning electrochemical microscope is a useful tool for localized surface grafting from aryldiazonium salts, while the former research group has also reported elegant patterning methods specific to silicon substrates. In one example, they used ionic implantation to create locally doped areas of silicon and, thus, achieved site-specific electrografting of an aryldiazonium salt.[27] In another example, they illuminated p-type silicon through a mask to locally increase the substrate conductivity and allow electrografting to proceed.[28] Palacin and co-workers have also explored the use of a patterned agarose hydrogel containing an aryldiazonium salt solution sandwiched between two electrodes as an electrochemical "printing" method.[29] Finally, Corgier and Bélanger have adapted the methods of colloidal nanolithography to electrograft organic groups to the nanoscale spaces between polystyrene beads assembled on carbon and gold surfaces.[30]

All of the patterning methods described above involve electrochemical generation of aryl radicals at an externally applied potential. In an earlier communication, we established that spontaneous, OCP reduction of aryldiazonium salts by carbon substrates can also be used.[31] We showed that microcontact printing (MCP) using PDMS stamps and aryldiazonium salt inks gave micrometer-scale patterns of modifiers on glassy-carbon-like thin films (pyrolyzed photoresist film; PPF). MCP is a very simple and relatively fast patterning method and, in these respects, has obvious advantages over the electrochemical methods outlined above.[32]

In this paper, we investigate the characteristics (surface concentration, thickness, homogeneity, and chemical reactivity) of layers prepared using MCP and OCP reduction of aryldiazonium salts on PPF. We demonstrate that the method can be extended to metal (Au and Cu) and semiconductor (Si) substrates and provide guidelines concerning its general applicability in terms of substrate/diazonium cation combinations and the characteristics of the resultant films. We also demonstrate a unique feature of MCP of aryldiazonium salts: covalently coupled two-component surfaces can be prepared simply by printing a second layer onto a previously modified surface.

EXPERIMENTAL SECTION

Materials. Aqueous solutions were prepared using Millipore Milli-Q water (>18 MΩ cm). Tetrafluoroborate salts of 4-nitrobenzenediazonium (NBD) and 4-carboxybenzenediazonium (CBD) were synthesized using standard procedures.[33] 4-Aminobenzenediazonium salt (ABD) was synthesized as a 20 mM solution in 0.5 M HCl.[34] Procedures for preparing citrate-capped Au nanoparticles (~13 nm diameter),[35] PPF,[36] and planar Au films (Au/NiCr/Si),[37] and drying acetonitrile (ACN) have been described previously.

Uncut single walled carbon nanotubes (SWCNTs) (Carbon Nanotechnologies Incorporated) were acid-treated by adding 25 mg to 27 mL of 3:1 concentrated H_2SO_4 and HNO_3 and sonicating for 10 h while adding ice to the ultrasonicator bath to maintain a temperature close to 20 °C. Following sonication, the solution was poured into 500 mL of distilled water. After standing overnight, the solution was filtered under suction through Millipore 0.22 μm hydrophilic polyvinylidene fluoride filter membranes and then washed with copious amounts of water. The dried SWCNT cakes were peeled from the filters and resuspended in DMSO to give a 1 mg mL^{-1} stock solution.

Si(100) wafers (1−20 Ω cm, Silicon Quest and Micro Materials) were cut into ~15 × 15 mm^2 tiles, immersed in 40% HF (Sigma-Aldrich) for 3 min (*Caution*: HF is hazardous; handle with care and appropriate personal protective clothing), washed with methanol, dried in a stream of N_2 gas, and used within 10 min of HF treatment. Small pieces of Cu plate were immersed in 16 M HNO_3 for 10 s, washed with water, immersed in 17 M acetic acid for 30 s, and dried in a stream of N_2 gas.[38] Fabrication and solvent extraction of PDMS stamps followed previously described procedures.[24] The stamps were either nonpatterned or had a test pattern with micrometer-sized features.

---

(22) Flavel, B. S.; Garrett, D. J.; Lehr, J.; Shapter, J. G.; Downard, A. J. *Electrochim. Acta* **2010**, *55*, 3995–4001.

(23) Brooksby, P. A.; Downard, A. J. *Langmuir* **2005**, *21*, 1672–1675.

(24) Downard, A. J.; Garrett, D. J.; Tan, E. S. Q. *Langmuir* **2006**, *22*, 10739–10746.

(25) Ghorbal, A.; Grisotto, F.; Charlier, J.; Palacin, S.; Goyer, C.; Demaille, C. *ChemPhysChem* **2009**, *10*, 1053–1057.

(26) Cougnon, C.; Gohier, F.; Belanger, D.; Mauzeroll, J. *Angew. Chem., Int. Ed.* **2009**, *48*, 4006–4008.

(27) Charlier, J.; Palacin, S.; Leroy, J.; Del Frari, D.; Zagonel, L.; Barrett, N.; Renault, O.; Bailly, A.; Mariolle, D. *J. Mater. Chem.* **2008**, *18*, 3136–3142.

(28) Charlier, J.; Clolus, E.; Bureau, C.; Palacin, S. *J. Electroanal. Chem.* **2008**, *622*, 238–241.

(29) Mouanda, B.; Eyeffa, V.; Palacin, S. *J. Appl. Electrochem.* **2009**, *39*, 313–320.

(30) Corgier, B. P.; Belanger, D. *Langmuir* **2010**, *26*, 5991–5997.

(31) Garrett, D. J.; Lehr, J.; Miskelly, G. M.; Downard, A. J. *J. Am. Chem. Soc.* **2007**, *129*, 15456–15457.

(32) Xia, Y. N.; Whitesides, G. M. *Angew. Chem., Int. Ed.* **1998**, *37*, 551–575.

(33) Saunders, K. H.; Allen, R. L. M. *Aromatic Diazo Compounds*, 3rd ed.; Edward Arnold: London, 1985.

(34) Lyskawa, J.; Belanger, D. *Chem. Mater.* **2006**, *18*, 4755–4763.

(35) Grabar, K. C.; Freeman, R. G.; Hommer, M. B.; Natan, M. J. *Anal. Chem.* **1995**, *67*, 735–743.

(36) Brooksby, P. A.; Downard, A. J. *Langmuir* **2004**, *20*, 5038–5045.

(37) Lehr, J.; Williamson, B. E.; Flavel, B. S.; Downard, A. J. *Langmuir* **2009**, *25*, 13503–13509.

(38) Chamoulaud, G.; Belanger, D. *J. Phys. Chem. C* **2007**, *111*, 7501–7507.

Electrochemistry. Electrochemical measurements were made at room temperature in an N_2 atmosphere. The electrochemical cell exposed a circular area (0.18 cm^2 for PPF or 0.79 cm^2 for Au) of substrate to the cell solution, as described previously.[36] The auxiliary and reference electrodes were Pt and SCE, respectively. Cyclic voltammograms were recorded with a scan rate of 100 mV s^{-1}.

Surface concentrations of grafted nitrophenyl (NP) groups were estimated from cyclic voltammograms of modified surfaces in 0.10 M H_2SO_4. The area under the irreversible reduction peak at $E_{p,c} \approx -0.6$ V and the area under the oxidation peak at $E_{p,a} \approx 0.3$ V was determined by fitting the data with polynomial baselines and mixed Lorentzian−Gaussian curves, using the Levenberg−Marquardt algorithm implemented via *Linkfit* software.[36] The surface concentration was then calculated using Faraday's law, as previously described,[36] with an estimated ±20% uncertainty in the absolute surface concentration.

Microcontact Printing. Within 2 h of use, PDMS stamps were treated with O_2 plasma (100 W at 0.1 Torr for 5 min). Stamps were immersed in 20 mM aryldiazonium cation ink for 2 min, dried to tackiness in a stream of N_2 gas, and placed on the substrate for 30 min. Unless stated otherwise, all printed samples were ultrasonicated for 5 min in Milli-Q water and dried in a stream of N_2 prior to analysis or further treatment. Each stamp was used with only one type of ink. The compositions of printing inks are denoted "diazonium cation/solvent". Control samples were prepared in the same way but using a solution from which the aryldiazonium salt had been omitted ("blank" ink).

Characterization of Films and Patterns. AFM (Digital Instruments Dimension 3100) depth-profiling measurements were performed on modified PPF samples by scratching with the AFM tip to remove a section of film, as described previously.[36] Three average line profiles were obtained from each of two 10 × 1.25 μm^2 scratches per sample. Each line profile gave two thickness values: one from the step down into the scratch and the other from the step out of the scratch. Thus, the reported thickness for each sample is a mean of 12 values, and the uncertainties are two standard deviations of the mean. Condensation figures were obtained by allowing water vapor to condense on surfaces and imaging using an Olympus BX60 inverted light microscope equipped with a polarizer and an Olympus DP10 camera. Scanning electron microscopy (SEM) images were obtained using a JEOL 7000 high-resolution instrument with an accelerating voltage of 15 kV.

The procedure for measuring water contact angles has been described previously.[31] Measurements were made using two 1 μL drops of Milli Q water placed on each duplicate sample or control. The stated values are the means of the four measurements, and the uncertainties are two standard deviations of the mean.

RESULTS AND DISCUSSION

This section is divided into four parts. The first describes printing with aryldiazonium salt inks on PPF, Au, and Si substrates using nonpatterned PDMS stamps. The second part demonstrates that printing with patterned PDMS stamps gives micrometer-scale patterned layers on Au, PPF, Si, and Cu. The reactivity of the printed layers is described in the third part, and finally, we show that a second modifier can be printed onto an already modified surface to create patterned, covalently coupled, two-component surfaces.

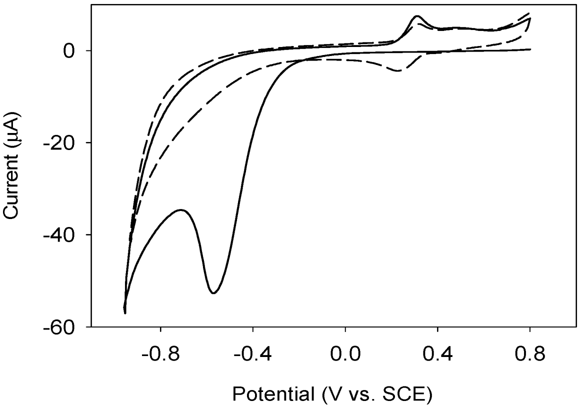

Figure 1. First (—) and second scan (---) cyclic voltammograms in 0.1 M H_2SO_4 of a PPF surface printed with NBD/1 M H_2SO_4 ink for 30 min.

Nonpatterned Printing on PPF, Gold, and Silicon. Preliminary results establishing successful MCP of PPF using DMF- and 1 M H_2SO_4-based aryldiazonium salt inks have been reported earlier.[31] In both that work and the present study, PPF was used as the carbon substrate because aryldiazonium salts spontaneously graft to its surface at OCP from acidic aqueous solution[31] and its low surface roughness facilitates measurement of film thickness.[39] Here, two aryldiazonium cations were chosen for detailed examination of the printing process. The NBD derivative was selected as a relatively easily reduced species (in cyclic voltammograms, $E_{p,c} \approx 0$ V vs SCE in 0.1 M H_2SO_4 at a scan rate of 100 mV s^{-1}) that is additionally convenient because the resultant grafted NP moieties can be readily detected and quantified by electroreduction. The CBD cation was selected as a more difficult to reduce species ($E_{p,c} \approx -0.3$ V vs SCE in 0.1 M H_2SO_4 at a scan rate of 100 mV s^{-1}), but which gives grafted carboxyphenyl (CP) films whose chemical reactivity makes them useful as tether layers for subsequent coupling reagents. CP groups are not electroactive in the potential range accessible in 0.1 M H_2SO_4, but their presence can be detected by water contact angle measurements.

Figure 1 shows consecutive cyclic voltammograms of a PPF surface printed with NBD/1 M H_2SO_4 ink using a nonpatterned stamp. The first scan, from 0.8 to −0.9 V, shows the characteristic, irreversible reduction ($E_{p,c} \approx -0.60$ V) of surface-attached NP groups to aminophenyl (eq 1) and hydroxyaminophenyl groups (eq 2) but no evidence for physisorbed aryldiazonium cations, which, if present, would be reduced at $E_{p,c} \approx 0$ V. The return scan shows the reversible oxidation ($E_{p,a} = 0.35$ V) of hydroxyaminophenyl to nitrosophenyl groups (eq 3),[40] with the nitrosophenyl/hydroxyaminophenyl redox couple appearing as the only significant feature in subsequent cycles. These results are consistent with immobilized NP groups, spontaneously grafted to the surface during printing. Table 1 lists electroactive-NP surface concentrations, Γ_{NP}, determined for three nonpatterned NBD/1 M H_2SO_4 samples from the

---

(39) Ranganathan, S.; McCreery, R. L. *Anal. Chem.* **2001**, *73*, 893–900.

(40) Ortiz, B.; Saby, C.; Champagne, G. Y.; Belanger, D. *J. Electroanal. Chem.* **1998**, *455*, 75–81.

Table 1. Surface Concentration and Film Thickness Data for NP Films Printed on PPF

sample	Γ_{NP} /mol cm^{-2}	film thickness/nm
1	$(5 \pm 1) \times 10^{-10}$	1.5 ± 0.4
2	$(6 \pm 1) \times 10^{-10}$	2.4 ± 0.6
3	$(16 \pm 3) \times 10^{-10}$	1.7 ± 0.4

first-scan, along with the corresponding film thicknesses obtained by AFM depth profiling.

$$\text{Surface}\text{—}C_6H_4\text{—}NO_2 + 6H^+ + 6e^- \rightarrow \text{Surface}\text{—}C_6H_4\text{—}NH_2 + 2H_2O \quad (1)$$

$$\text{Surface}\text{—}C_6H_4\text{—}NO_2 + 4H^+ + 4e^- \rightarrow \text{Surface}\text{—}C_6H_4\text{—}NHOH + H_2O \quad (2)$$

$$\text{Surface}\text{—}C_6H_4\text{—}NHOH \rightleftharpoons \text{Surface}\text{—}C_6H_4\text{—}NO + 2H^+ + 2e^- \quad (3)$$

Previously, we have found that single layers of NP groups electrografted to PPF have $\Gamma_{NP} = (2.5 \pm 0.5) \times 10^{-10}$ mol cm^{-2},[36] and similar values were obtained for methylphenyl and CP groups electrografted to flat Au substrates.[41] A monolayer of vertically oriented NP groups has a calculated thickness of 0.8 nm;[36] hence, both the concentration and thickness data in Table 1 indicate the formation of multilayer domains with an average thickness of 2 to 3 layers.[18] Table 1 also shows significant variations between films prepared under the same conditions and no systematic relationship between Γ_{NP} and average AFM-determined film thickness. The initial OCPs differ significantly between PPF samples, particularly from different preparation batches, and we attribute the sample-to-sample variations in Table 1 to this variability of “activity”. We,[37] and others,[37,42,43] have observed that the substrate potential increases as the spontaneous reduction of aryldiazonium cations proceeds and that film growth stops when the potential becomes too positive to sustain reduction. The initial OCP, therefore, influences the amount of charge that can be transferred before the “cutoff” potential is reached, and consequently, it helps to determine the amount of material that can be attached to the surface in the absence of an externally applied potential.

The lack of a clear relationship between Γ_{NP} and the “average” film thickness is attributed to differences in the measurement scales of the associated methods. The surface concentration data are averages over a large area (0.18 cm^2), whereas the AFM film thicknesses are derived from three depth profiles across two 10×1.25 μm^2 scratches per sample. For films of highly variable thickness, the average results of a few measurements performed over a small area may not yield results that are representative of the whole-sample average. The possibility of multilayer grafting, coupled with an inhomogeneous distribution of aryldiazonium cations on the inked stamp, is likely to lead to films of variable thickness, and the large uncertainties for the AFM thickness values are consistent with this. Clearly, such variability will be a limitation when highly reproducible and homogeneous films are required.

Successful modification of PPF after printing with CBD/1 M H_2SO_4 ink was confirmed by a decrease of the water contact angles from 68 ± 2° to 31 ± 2°, consistent with the attachment of hydrophilic CP groups. In contrast, control surfaces gave an unchanged postprinting contact angle of 68 ± 11°. Cyclic voltammograms (not shown) revealed no signals between 0.8 and −0.5 V, confirming the absence of physisorbed CBD (expected reduction peak at −0.3 V). AFM depth-profiling measurements on two films gave an average film thickness of 1.0 ± 0.2 nm, close to that expected for a monolayer. Printed CP films are, thus, on average, thinner and significantly more uniform than printed NP films. The different morphology can be attributed to the lower reduction potential for CBD. Because CBD is more difficult to reduce than NBD, its reduction ceases at a lower substrate OCP and a correspondingly smaller amount of CP is grafted to the surface. The more limited degree of spontaneous reduction diminishes the prevalence of significant multilayer “outgrowths”, and a more uniform film thickness results. Vautrin-Ul and co-workers have reported results consistent with this interpretation,[44] finding that spontaneous reduction of NBD rapidly gave thick, nonuniform films on zinc but formed thin homogeneous layers more slowly on a less-reducing nickel surface. Hence, for substrates that act as the reducing agent for aryldiazonium cation-based grafting, when the potential driving force for reduction is large (the aryldiazonium derivatives are easily reduced in comparison with the reducing power of the substrate), thicker and more irregular films will be formed than when the driving force is lower.

The feasibility of printing using other aryldiazonium salt/substrate combinations was also examined in experiments described in the Supporting Information. Electrochemical (Figures S-1, S-2) or AFM depth-profiling measurements confirmed that printing of ABD on PPF, NBD on Au, and NBD on Si gave the expected modified surfaces. For Si samples, the oxide layer was removed or significantly thinned by HF treatment prior to printing. Samples with an intact native oxide layer could not be modified.

To summarize, we expect printing to be successful for all aryldiazonium salt−substrate combinations for which the grafting reaction proceeds spontaneously at OCP in solution. As is found for layers grafted from solution, the stability of attachment will depend mainly on the substrate; for example, very stable layers are formed by grafting onto graphitic carbon,[2,15] but the stability of the layers on Au is significantly less.[16]

Patterned Microcontact Printing of Gold, PPF, Silicon, and Cu. Having successfully demonstrated that printing with aqueous aryldiazonium salt inks leads to surface modification, we next investigated patterning of surfaces. Figures 2−4 show images of Au, PPF, Si, and Cu substrates printed with aryldiazonium salt inks and with blank inks.

In Figure 2, SEM images of Au substrates patterned with NP, aminophenyl (AP), and CP groups are compared with images from

---

(41) Paulik, M. G.; Brooksby, P. A.; Abell, A. D.; Downard, A. J. *J. Phys. Chem. C* **2007**, *111*, 7808–7815.

(42) Le Floch, F.; Simonato, J.-P.; Bidan, G. *Electrochim. Acta* **2009**, *54*, 3078–3085.

(43) Smith, R. D. L.; Pickup, P. G. *Electrochim. Acta* **2009**, *54*, 2305–2311.

(44) Adenier, A.; Cabet-Deliry, E.; Chausse, A.; Griveau, S.; Mercier, F.; Pinson, J.; Vautrin-Ul, C. *Chem. Mater.* **2005**, *17*, 491–501.

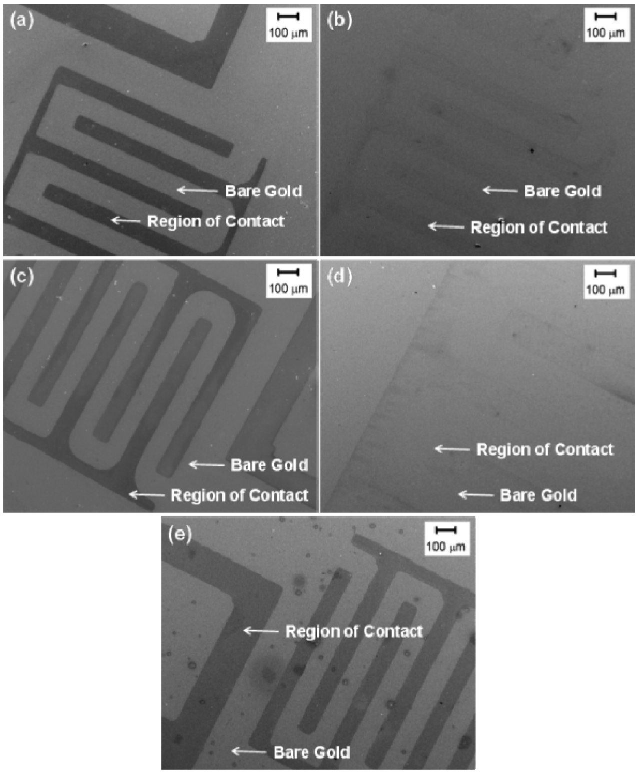

Figure 2. SEM images of Au substrates patterned by printing with (a) NBD/1 M H_2SO_4, (b)1 M H_2SO_4, (c) ABD/0.5 M HCl, (d) 0.5 M HCl, and (e) CBD/1 M H_2SO_4 inks.

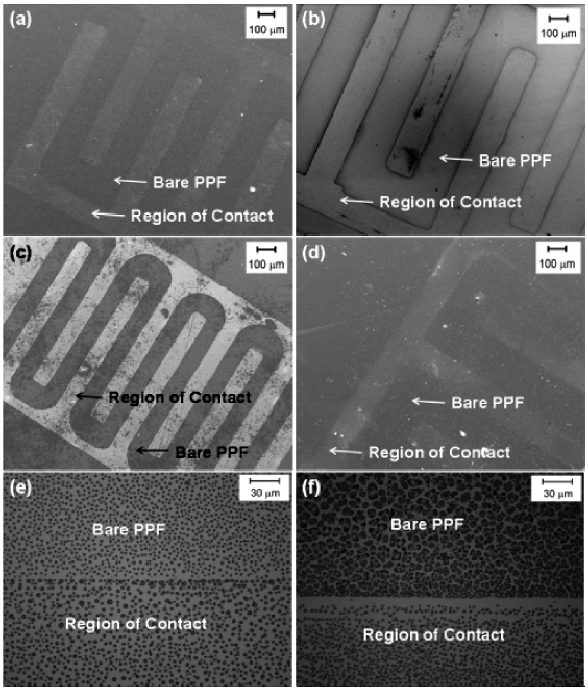

Figure 3. SEM images (a−d) and optical micrographs (e, f) of PPF surfaces printed with (a) NBD/1 M H_2SO_4, (b, f) 1 M H_2SO_4, (c) 20 mM ABD/0.5 M HCl, (d) 0.5 M HCl, and (e) CBD/1 M H_2SO_4 inks. The surfaces shown in (c) and (d) were immersed in Au nanoparticle solution for 40 min before imaging; surfaces shown in (e) and (f) were treated with water vapor before imaging.

the corresponding controls. The aryldiazonium salt inks give clearly defined patterns with feature sizes down to 20 μm, whereas the blank inks give faint patterns, which are attributed to PDMS residues.

SEM is not a good technique for imaging organic films on carbon substrates. Consequently, the image contrast for PPF patterned with NP (Figure 3a) is just marginally better than that for the control sample (Figure 3b). To overcome this inherent limitation, alternative methods were used to image surfaces patterned with AP and CP groups. For the former, after printing with ABD/0.5 M HCl (or blank 0.5 M HCl), the surfaces were immersed for 40 min, at pH $\sim$ 5, in a solution of citrate-capped Au nanoparticles. Preferential assembly of nanoparticles (via electrostatic interactions) on the AP-modified areas clearly revealed the patterns (compare Figure 3c,d). For surfaces patterned with CP groups (by printing with CBD/1 M H_2SO_4 ink) and the corresponding blanks, condensation figures were imaged by optical microscopy (Figures 3e,f). Although the pattern is well-defined in both the CP-printed sample and the blank, the relative sizes of water droplets in the stamped and "bare" areas are the opposite in the sample and blank. Water droplets are larger in the CP areas than on bare PPF, consistent with addition of hydrophilic CP groups to the surface; in contrast, areas contacted by the stamp inked with 1 M H_2SO_4 only are smaller than on bare PPF, suggesting hydrophobic contaminants have been transferred to the surface by the stamp. (Note that the sizes of water droplets on bare PPF in Figures 3e,f are not the same because the size depends on the extent of evaporation prior to image capture.)

Patterning of NP and AP groups on Si was also successful as revealed by the SEM images of Figure 4a−d. There is strong contrast between the grafted and bare areas in Figure 4a,c, in comparison with the faint patterns of the controls (Figure 4b,d).

As a final example to demonstrate the wider applicability of MCP with aqueous aryldiazonium salt inks, a Cu surface was patterned with NP groups. Copper is known to react spontaneously with NBD at OCP in both aqueous and nonaqueous conditions.[38,45] The SEM image in Figure 4e shows strong contrast between NP-printed areas and bare Cu, whereas only a very faint pattern is seen on the control (Figure 4f). The roughness of the Cu surface, evident in both images, leads to incomplete contact with the stamp and accounts for the "patchy" appearance of the pattern in Figure 4e.

These examples confirm that MCP is a very simple route to patterning conducting surfaces. The scope of the method and the characteristics of the patterned layers will be determined by the substrate−diazonium salt combination as described in the previous section.

Printed Tether Layers for Further Immobilization Chemistry. The utility of MCP can be enhanced by printing layers that act as tethers for further immobilization reactions. Two examples are demonstrated here, on the basis of coupling of secondary reagents (4-nitroaniline (NA) and SWCNTs) to primary layers of CP or AP printed on PPF. The selection of these reagents was based on their ease of detection: NA by its redox chemistry and SWCNTs by AFM imaging.

---

(45) Hurley, B. L.; McCreery, R. L. *J. Electrochem. Soc.* **2004**, *151*, B252–B259.

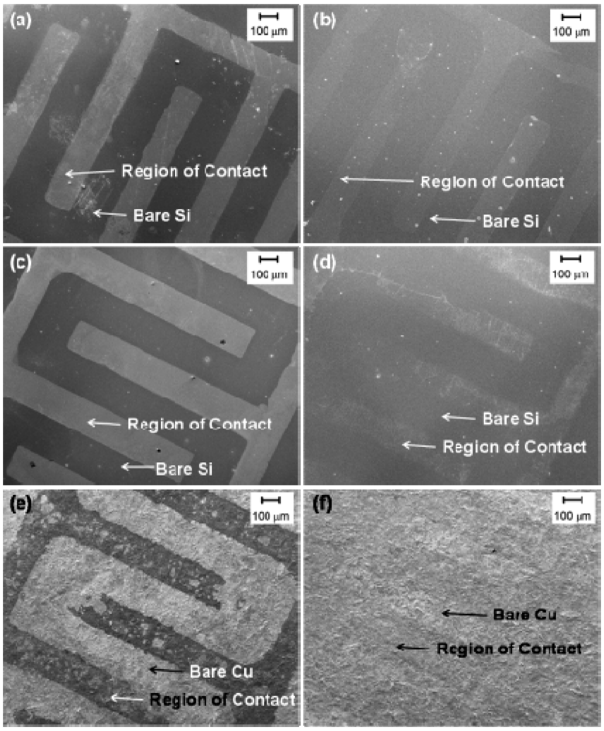

Figure 4. SEM images of (a−d) Si samples patterned by printing with (a) NBD/1 M H_2SO_4, (b) 1 M H_2SO_4, (c) ABD/0.5 M HCl, and (d) 0.5 M HCl inks; (e, f) Cu samples patterned by printing with (e) NBD/1 M H_2SO_4 and (f) 1 M H_2SO_4 inks.

Table 2. Film Thicknesses for NA Layer Coupled to CP Film and Associated Controls

surface	film thickness/nm[a]
PPF-CP	1.0 ± 0.3
PPF-CP/$SOCl_2$/NA	2.0 ± 0.5
PPF-CP/NA	1.0 ± 0.4
PPF-H_2SO_4/$SOCl_2$/NA	0.4 ± 0.2

[a] AFM line profiles are shown in Figure S-4 (Supporting Information).

NA + CP on PPF. CP groups were printed on PPF using nonpatterned stamps and CBD/1 M H_2SO_4 ink. The films were activated by immersion in $SOCl_2$ for 30 min and then transferred to a 20 mM NA/ACN solution at room temperature for 24 h to promote coupling of NA groups to the CP layer via the formation of amide bonds. These samples are denoted PPF−CP/$SOCl_2$/NA. Controls were also prepared: PPF−CP blanks were obtained by printing CP films onto PPF without subsequent activation or immersion in NA/ACN; for PPF−CP/NA blanks, only the activation step was omitted; and for PPF−H_2SO_4/$SOCl_2$/NA, blanks were prepared by printing PPF with blank 1 M H_2SO_4, followed by "activation" and immersion in NA/ACN. Prior to their analysis, all samples and controls were sonicated for 5 min in ACN.

AFM depth profiling results are shown in Table 2, and cyclic voltammograms of the modified surfaces and typical AFM line profiles are shown in Figures S-3 and S-4 (Supporting Information). Activation of the CP film and reaction with NA increased the film thickness from 1.0 ± 0.3 to 2.0 ± 0.5 nm, consistent with the coupling of NA groups to the CP layer. When the activation step was omitted, there was no change in film thickness, confirming that NA does not physisorb to the CP film. Interestingly, a thin surface layer of NA was detected electrochemically (Figure S-3, Supporting Information) and by AFM measurements on the PPF−H_2SO_4/$SOCl_2$/NA controls. The measured thickness (0.4 ± 0.2 nm) of this film is less than expected for a monolayer of NA groups (0.8 nm), indicating a submonolayer coverage. We assume that NA couples directly to a low concentration of carboxylate functionalities on the (otherwise) bare PPF surface.

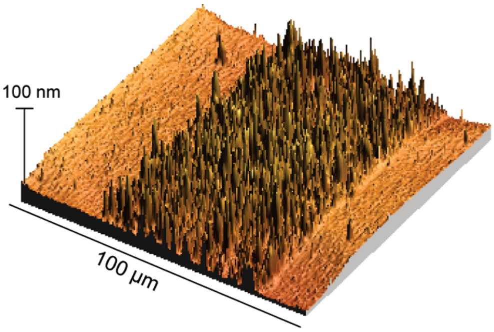

Figure 5. AFM image of VACNTs tethered to a patterned AP layer on PPF.

SWCNT + AP on PPF. This second example of the utility of printed films as tethers is based on recent work in which we assembled and characterized vertically aligned carbon nanotube (VACNT) forests on AP films electrografted to PPF.[46] To test whether printed AP films could be used similarly, PPF surfaces were patterned using ABD/0.5 M HCl ink and then immersed in a DMSO solution (2 mL) of cut SWCNTs (0.2 mg mL^{-1}) and *N*,*N*′-dicyclohexylcarbodiimide (1 mg mL^{-1}) for 24 h at 65 °C. These conditions promote formation of amide bonds between surface-immobilized AP groups and carboxylate groups at the cut ends of the SWCNTs. The resultant surfaces were sonicated in acetone for 10 s and then in isopropyl alcohol for 10 s prior to imaging by AFM. The image shown in Figure 5 (and the SEM image in Figure S-5, Supporting Information) is similar to those previously obtained for VACNTs on electrografted AP tether layers.[46]

These examples demonstrate that MCP yields tether layers with their usual reactivity, and hence, the method can be used to prepare patterned substrates which form the basis of more complex structures.

Buildup MCP Patterning of Two-Component Surfaces. Two- or multicomponent films in which secondary modifiers are patterned on top of a continuous base film have potential applications in sensing, where (for example) the base film is tailored to reduce nonspecific interactions with the analyte while the patterned secondary modifiers act either as tethers for attachment of recognition species or as the recognition elements themselves. This "buildup" method relies on the ability of the substrate to reduce the secondary modifiers by electron transfer across the base film. Reduction of the printed secondary modifier generates radicals which couple to the base film. Hence, a covalently coupled structure spontaneously forms in a single, simple step requiring no additional reagents. The buildup method

---

(46) Garrett, D. J.; Flavel, B. S.; Shapter, J. G.; Baronian, K. H. R.; Downard, A. J. *Langmuir* **2010**, *26*, 1848–1854.

Table 3. Film Thickness Measurements on PPF Substrates Modified with CP Films with and without Overprinting of a NP Layer[a]

	film thickness/nm[b]	
sonication solvent and time	CP region	CP/NP region
H_2O (5 min)	1.6 ± 0.3	2.2 ± 0.3
H_2O (5 min)	1.4 ± 0.3	2.1 ± 0.2
H_2O (5 min) + ACN (30 min)	1.7 ± 0.6	2.1 ± 0.3
H_2O (5 min) + ACN (30 min)	1.5 ± 0.4	2.0 ± 0.2

[a] Samples were prepared in duplicate. [b] AFM line profiles are shown in Figure S-7 (Supporting Information).

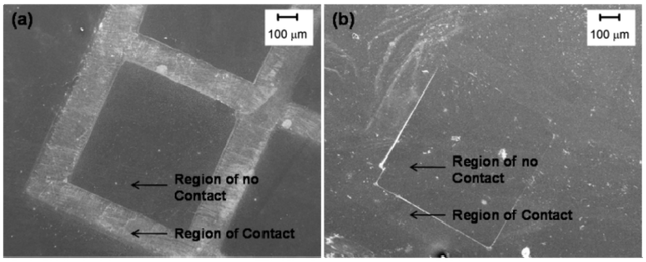

Figure 6. SEM images of surfaces that were immersed in 10 mM CBD/0.1 H_2SO_4 for 30 min and subsequently printed with (a) ABD/0.5 M HCl and (b) 0.5 M HCl inks. After printing, the surfaces were immersed in Au nanoparticle solution for 40 min.

was demonstrated by printing the secondary modifiers NP and AP.

CP + NP on PPF. NP groups were printed onto a base CP film grafted spontaneously to PPF at OCP. Two ~3.0 × 1.5 mm^2 PPF samples were immersed in 10 mM CBD/0.1 M H_2SO_4 solution for 30 min to form the base films. One half of each sample was then printed with a nonpatterned stamp using NBD/1 M H_2SO_4 ink. Cyclic voltammetry (Figure S-6, Supporting Information) confirmed that NBD had reacted in the expected manner giving an NP layer.

AFM depth profiling measurements of printed and unprinted sections (Table 3) show that printing increases the film thickness, consistent with attachment of NP to the CP layer. The magnitude of the increase (~0.4−0.7 nm) corresponds to the addition of a submonolayer of NP groups on top of the CP film. However, NP is also expected to couple within the CP film, and hence, the concentration of printed NP groups may be higher than indicated by film thickness data.

To test the stability of the printed layers, the samples were sonicated in ACN for 30 min and the AFM measurements were repeated. The data in the lower part of Table 3 indicate that the film thicknesses did not change significantly, consistent with covalent attachment both to the substrate surface and between the base and printed layers.

CP + AP on PPF. In the second example of the buildup printing approach, AP groups were patterned onto a spontaneously grafted layer of CP groups using a patterned stamp with ABD/0.5 M HCl ink. A blank was also prepared on a CP layer by printing with blank 0.5 M HCl ink. The printed surfaces were immersed for 40 min in a solution of Au nanoparticles and then sonicated in H_2O for 30 s prior to analysis by SEM. Figure 6 shows the SEM images where the assembled Au nanoparticles clearly reveal the patterned immobilization of AP (Figure 6a) in comparison with the control (Figure 6b).

The buildup approach for preparing patterned two- or multicomponent surfaces should be applicable to all substrates at which grafting from aryldiazonium salt solutions proceeds spontaneously at OCP. However, the requirement that the second aryldiazonium cation be reduced by the substrate places some limitations on the nature and thickness of the base film and also on the aryldiazonium cation derivative. For strongly reducing substrates (such as zinc), it should be possible to print even relatively difficult-to-reduce aryldiazonium cations onto thick base films. On the other hand, printing on less-reducing substrates (such as Au) is likely to be successful only with easily reduced aryldiazonium salt derivatives on thin base films. In the examples above, the base films were formed by spontaneous grafting from a aryldiazonium salt solution. There is no reason why MCP, electrografting, and/or other classes of modifiers cannot be used. Methods such as electro-oxidation of primary amines[47] or arylhydrazines;[48] electroreduction of iodonium,[49,50] sulfonium[51] salts, or vinylic compounds;[52] photolytic or thermal grafting of alkenes and alkynes;[53−56] or photografting of arylazides[57] would greatly widen the range of functionalities that could be added to the surface.

CONCLUSION

Microcontact printing using aryldiazonium salt inks has been applied to carbon, metal, and semiconductor substrates to give stable, covalently attached, thin films. The thickness and the morphology of the printed film appear to depend on the potential driving force for reduction of the aryldiazonium cation by the substrate. Aminophenyl and carboxyphenyl groups in printed layers retain the ability to form amide bonds with solution species and, consequently, provide useful tethers for more complex surface structures.

Microcontact printing using aryldiazonium salts is applicable to all substrate−diazonium salt combinations for which surface modification proceeds spontaneously at open circuit potential in solution. The variable film thickness and roughness, which is substrate- and film-dependent, may be a limitation for some potential applications; however, compared with other methods for patterning layers using aryldiazonium salts, microcontact is low cost and simple to implement with no requirement for electrochemical capability. Tightly defined patterns with feature sizes tens of micrometers upward can be routinely prepared, and

---

(47) Barbier, B.; Pinson, J.; Desarmot, G.; Sanchez, M. *J. Electrochem. Soc.* **1990**, *137*, 1757–1764.
(48) Malmos, K.; Iruthayaraj, J.; Pedersen, S. U.; Daasbjerg, K. *J. Am. Chem. Soc.* **2009**, *131*, 13926–13927.
(49) Vase, K. H.; Holm, A. H.; Norrman, K.; Pedersen, S. U.; Daasbjerg, K. *Langmuir* **2007**, *23*, 3786–3793.
(50) Vase, K. H. j.; Holm, A. H. k.; Pedersen, S. U.; Daasbjerg, K. *Langmuir* **2005**, *21*, 8085–8089.
(51) Vase, K. H.; Holm, A. H.; Norrman, K.; Pedersen, S. U.; Daasbjerg, K. *Langmuir* **2008**, *24*, 182–188.
(52) Palacin, S.; Bureau, C.; Charlier, J.; Deniau, G.; Mouanda, B.; Viel, P. *ChemPhysChem* **2004**, *5*, 1469–1481.
(53) Lasseter, T. L.; Cai, W.; Hamers, R. J. *Analyst* **2004**, *129*, 3–8.
(54) Ssenyange, S.; Anariba, F.; Bocian, D. F.; McCreery, R. L. *Langmuir* **2005**, *21*, 11105–11112.
(55) Sun, B.; Colavita, P. E.; Kim, H.; Lockett, M.; Marcus, M. S.; Smith, L. M.; Hamers, R. J. *Langmuir* **2006**, *22*, 9598–9605.
(56) Yu, S. S. C.; Downard, A. J. *Langmuir* **2007**, *23*, 4662–4668.
(57) Gross, A. J.; Yu, S. S. C.; Downard, A. J. *Langmuir* **2010**, *26*, 7285–7292.

multicomponent patterned surfaces can be fabricated simply by printing on top of a base film. The two-component structures were shown to be stable to prolonged sonication, indicating covalent coupling of the second modifier to the base layer. The availability of such a method will facilitate application of the aryldiazonium salt surface modification approach in areas such as the fabrication of bio- and chemical sensors.

ACKNOWLEDGMENT

This work was supported by the MacDiarmid Institute for Advanced Materials and Nanotechnology. J.L. and D.J.G thank the New Zealand Tertiary Education Commission for doctoral scholarships and B.S.F. thanks the Australian Government's Endeavour Research Fellowship program. We thank Dr. John Loring for use of the *Linkfit* curve fitting software.

SUPPORTING INFORMATION AVAILABLE

Characterizations of the following modified surfaces prepared by printing using nonpatterned stamps: AP on PPF, NP on Au, and NP on HF-treated Si; cyclic voltammograms of CP layers and bare PPF after activation with $SOCl_2$ and reaction with 4-nitroaniline; repeat cyclic voltammograms of a PPF surface bearing a CP film, overprinted with an NP layer; figures of AFM line profiles of data presented in Tables 2 and 3; SEM image of the surface shown in Figure 5. This material is available free of charge via the Internet at http://pubs.acs.org.

Received for review July 6, 2010. Accepted July 10, 2010.

AC101785C

2.6 Additional Scientific Publications

2.6.5 *A Simple Approach to Patterned Protein Immobilization on Silicon via Electrografting from Diazonium Salt Solutions*

B. S. Flavel, A. J. Gross, D. J. Garrett, V. M. Nock, A. J. Downard

Applied Materials & Interfaces 2 (2010) 1184–1190

DOI: 10.1021/am100020a

Abstract

A highly versatile method utilizing diazonium salt chemistry has been developed for the fabrication of protein arrays. Conventional ultraviolet mask lithography was used to pattern micrometer sized regions into a commercial photoresist on a highly doped p-type silicon (100) substrate. These patterned regions were used as a template for the electrochemical grafting of the in situ generated p-aminobenzenediazonium cation to form patterns of aminophenyl film on silicon. Immobilization of biomolecules was demonstrated by coupling biotin to the aminophenyl regions followed by reaction with fluorescently labeled avidin and visualization with fluorescence microscopy. This simple patterning strategy is promising for future application in biosensor devices.

Contribution

B.S.F conceived the idea for the project. B.S.F, A.J.G, D.J.G, V.M.N performed the experiments, B.S.F wrote the paper and all authors contributed to the scientific discussion and evaluation of the manuscript.

– This page intentionally left blank –

ACS APPLIED MATERIALS & INTERFACES

April 2010
Volume 2
Number 4
www.acsami.org

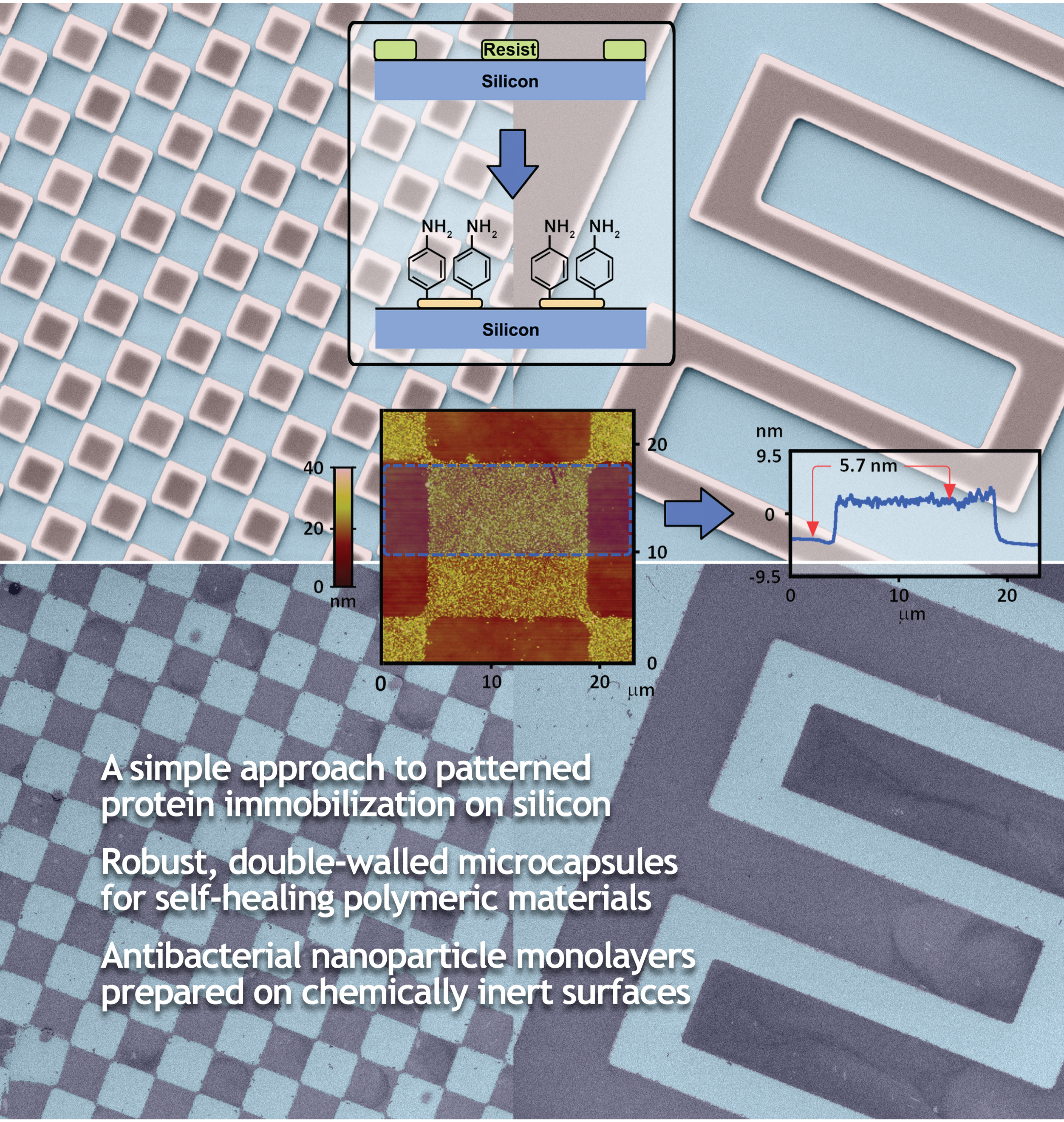

A simple approach to patterned protein immobilization on silicon

Robust, double-walled microcapsules for self-healing polymeric materials

Antibacterial nanoparticle monolayers prepared on chemically inert surfaces

ACS Publications
High quality. High impact.

www.acs.org

– This page intentionally left blank –

A Simple Approach to Patterned Protein Immobilization on Silicon via Electrografting from Diazonium Salt Solutions

Benjamin S. Flavel,*,†,‡ Andrew J. Gross,†,§ David J. Garrett,†,§ Volker Nock,§,|| and Alison J. Downard*,†,§

Department of Chemistry and Department of Electrical & Computer Engineering, University of Canterbury, Private Bag 4800, Christchurch 8140, New Zealand, and MacDiarmid Institute for Advanced Materials and Nanotechnology, Private Bag 4800, Christchurch 8140, New Zealand

ABSTRACT A highly versatile method utilizing diazonium salt chemistry has been developed for the fabrication of protein arrays. Conventional ultraviolet mask lithography was used to pattern micrometer sized regions into a commercial photoresist on a highly doped p-type silicon (100) substrate. These patterned regions were used as a template for the electrochemical grafting of the in situ generated *p*-aminobenzenediazonium cation to form patterns of aminophenyl film on silicon. Immobilization of biomolecules was demonstrated by coupling biotin to the aminophenyl regions followed by reaction with fluorescently labeled avidin and visualization with fluorescence microscopy. This simple patterning strategy is promising for future application in biosensor devices.

KEYWORDS: *p*-phenylenediamine • electrochemical • biotin • avidin • pattern

INTRODUCTION

In recent years, there has been considerable interest in the fabrication of patterned arrays of biological species such as cells (1, 2), proteins (3, 4), and DNA (5, 6) on solid surfaces (4, 7). These arrays have potential applications in molecular electronics (7, 8), biofuel cells (1), tissue engineering (9), and biosensors and biochips (10). Such future devices will exploit the ability of surface bound receptors to selectively bind target analytes from a complex mixture of other species (4, 9). Preparation of patterned surfaces for these purposes typically involves the use of a self-assembled monolayer and conventional lithographic techniques such as microcontact printing (2, 11), selective photochemical activation (7, 8, 12), and photo and electron beam lithography with resists (10, 13−16). The goal is usually to fabricate areas of defined shape and size that support or resist immobilization of biological species (17).

A variety of different substrates including silicon (1, 4, 8, 12, 15, 17), carbon (18, 19), glass (7), quartz (20), gallium nitride (21), gold (2, 6, 17, 22, 23), and polymers such as poly(dimethylsiloxane) (24−26), polyimide (14), poly(methyl methacrylate) (11, 27, 28), and polycarbonate (20, 29) have been functionalized for biomolecule and cell immobilization. However, for device fabrication, silicon is most attractive because an active surface constructed on silicon has the potential to be combined with integrated circuit technology.

The most straightforward approaches to modification of silicon surfaces are those that do not require the removal of the native surface oxide and do not require use of rigorously dry and air-free conditions. Silane chemistry is most commonly used to modify silicon bearing its native oxide layer (8, 9, 12, 13, 15, 28, 30) because of the simplicity of homogeneous layer formation and well-established patterning protocols (31−34). Recently, diazonium cation chemistry has also been shown to offer a route to modification of silicon surfaces, without the need to first remove the native oxide layer (35). Electroreduction of aryldiazonium cations generates, after elimination of dinitrogen, aryl radicals capable of covalent grafting at the electrode surface. Charlier et al. (35) demonstrated that at n-type silicon (100), electroreduction of 4-nitrobenzene-diazonium cation gave strongly adherent films. Under the conditions used in their study, the films were more than 15 nm thick, consistent with a multilayer structure. The utility of these surfaces for applications in biological media have not yet been investigated.

Currently, there are a limited number of examples of patterned organic layers prepared by the electrochemical reduction of diazonium salts and to our knowledge only two examples on a silicon substrate. In one example, Charlier et al. (35) used ionic implantation to create locally doped silicon surfaces to selectively control the electrografting of 4-nitrobenzenediazonium tetrafluoroborate. In the second example, the same researchers (36) illuminated p-type silicon through a mask, to locally increase the substrate conductivity and allow electrografting of 4-nitrophenyl films. On other surfaces, Ghorbal et al. (37) have used scanning

---

* Corresponding author. E-mail: ben.flavel@flinders.edu.au (B.F.); alison.downard@canterbury.ac.nz (A.J.D.).

Received for review January 10, 2010 and accepted March 04, 2010

† Department of Chemistry, University of Canterbury.

‡ Present address: School of Chemistry, Physics & Earth Sciences Flinders University, Sturt Road, Bedford Park, Adelaide, South Australia 5001.

§ MacDiarmid Institute for Advanced Materials and Nanotechnology.

|| Department of Electrical & Computer Engineering, University of Canterbury.

DOI: 10.1021/am100020a

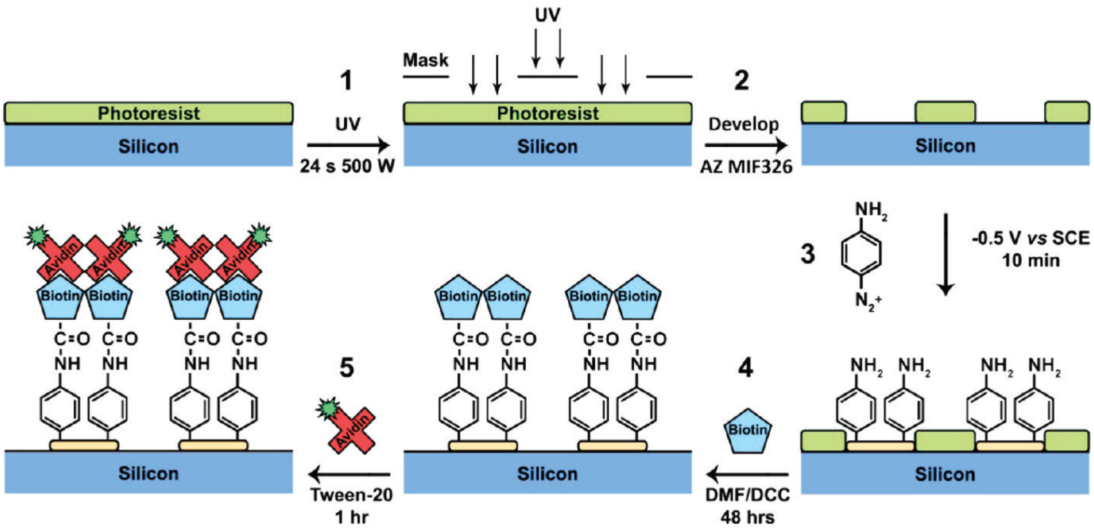

FIGURE 1. Schematic for fabrication of patterned aminophenyl layers on silicon and attachment of biotin and avidin.

electrochemical microscopy to electrograft nanometre wide lines of vinylic monomers onto a gold substrate. In earlier work, we used mechanical scribing with an atomic force microscope probe to remove regions of electrografted film on a carbon substrate. A second aryldiazonium salt was then electrochemically grafted to the bare regions creating a surface with dual chemical functionality (38). In a different, soft lithographic approach, we patterned a carbon substrate by adhering a poly(dimethylsiloxane) mold to the surface to form micro fluidic channels. The channels were subsequently filled with diazonium salt solution for site specific electrochemical grafting (39). Finally, despite not being an electrochemical method, it is worth mentioning that we have also utilized the spontaneous reduction of aryldiazonium salts on carbon to pattern via microcontact printing with poly(dimethylsiloxane) stamps (40).

The patterning techniques described above all have specific advantages and limitations and there remains a need for additional methods that can quickly and reproducibly fabricate large areas of micrometer-sized patterns of covalently attached films, without restriction on the pattern design. Here we describe the use of conventional photolithography to pattern commercial photoresist onto a silicon surface followed by electrochemical grafting of *p*-aminobenzenediazonium cations to the exposed silicon affording, after removal of the photoresist, a patterned aminophenyl film. To demonstrate the potential application of these patterned surfaces for biomolecule immobilization, we used a condensation reaction to immobilize biotin. This allowed for the subsequent biomolecular recognition reaction with the fluorescently labeled protein avidin, which was imaged with fluorescence microscopy.

EXPERIMENTAL SECTION

Milli-Q water (MillQ Plus, Millipore, USA) with resistivity ≥18 MΩ cm, was used for aqueous solutions and cleaning. Citrate capped colloidal gold nanoparticles were prepared using the method outlined by Chen et al. (41) and Dong et al. (42).

The procedure for fabrication of patterned aminophenyl layers on silicon and subsequent attachment of biotin and avidin is shown schematically in figure 1. First, highly boron doped p-type silicon (100) with resistivity <0.001 Ω cm (Virginia Semiconductor, Inc.) was cut into 2 cm × 2 cm sized wafers and cleaned by ultrasonication (Elmasonic S 30H, Elma Hans Schmidbauer GmbH & Co KG, Germany) in 99.5% acetone (Mallinckrodt Chemicals) for 5 min followed by 5 min in 99.5% isopropyl alcohol (Sigma-Aldrich) with thorough drying with nitrogen between each solvent. Any remaining surface contamination was removed using an Emitech K1050X plasma asher (Emitech, UK) operating at 100 W RF power in high purity oxygen (BOC Limited, Australia) for a period of 10 min. Immediately after cleaning, positive tone photoresist AZ1518 (Microchemicals, Germany) was spin-coated to a thickness of ~2 μm at 3000 rpm for 30 s on a PWM32-PS-R790 spinner system (Headway Research Inc., USA) and soft baked for 60 s at 100 °C on a standard hot plate. A MA6 mask aligner (Suess Microtec, Germany) operating in vacuum-mode was used to pattern the photoresist by a 24 s exposure to a 350 W ultraviolet lamp through chrome on glass masks. After exposure, the photoresist was developed by immersion in AZ MIF326 developer (Microchemicals, Germany) for 25 s, rinsed with water, and dried with nitrogen.

Patterned silicon substrates were used for the electrochemical grafting of aminophenyl films from the corresponding diazonium salt, prepared in situ as described by Lyskawa et al. (43) In brief, 3 mL of 20 mM *p*-phenylenediamine (Sigma-Aldrich) in 1 M hydrochloric acid (Sigma-Aldrich) was added to an equal volume of 20 mM 99% sodium nitrite (Sharlau Chemie, Spain) at room temperature to yield the *p*-aminobenzenediazonium cation. Aminophenyl films were grafted to the silicon substrate by applying a potential of −0.5 V vs SCE for 10 min. Immediately after grafting, the silicon substrate was ultrasonicated in Milli-Q water, acetone and isopropyl alcohol for 5, 15, and 5 min respectively. This treatment removed any loosely bound film material and also the surrounding photoresist layer leaving the silicon substrate patterned with aminophenyl groups.

To couple biotin to the patterned aminophenyl film, the substrate was immersed in 10 mL of degassed 99.9% *N*,*N*-dimethylformamide (DMF) (Southern Cross Scientific Pty. Ltd.) containing 0.01 M D-biotin and 5 mg of 99.0% *N*,*N'*-dicyclohexylcarbodiimide (DCC) (Merck, Germany). After incubation for 24 h under nitrogen, the substrate was rinsed with copious amounts of N,N-dimethylformamide and water before being ultrasonicated for 5 min in 0.5% Tween-20 (Sigma-Aldrich), rinsed with water and dried with nitrogen. This procedure was repeated twice, giving a total incubation time of 48 h. Following immobilization of biotin, the samples were incubated in 0.25

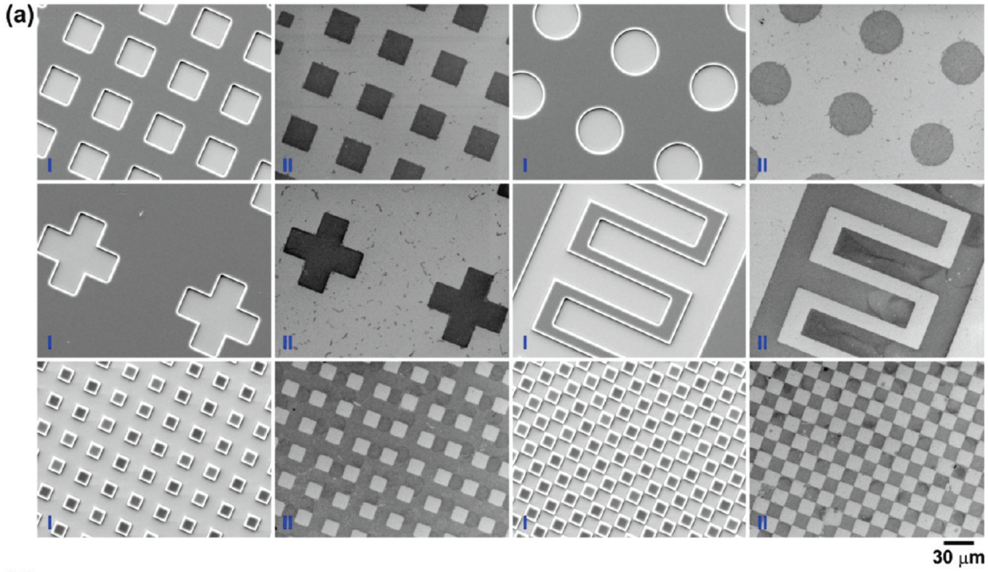

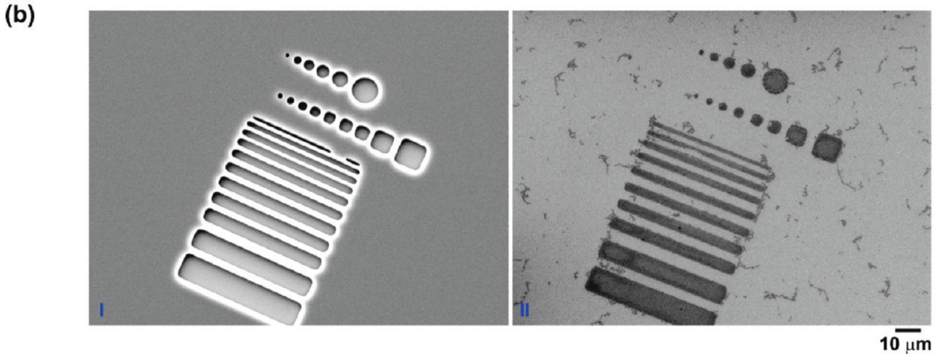

FIGURE 2. SEM images of (I) patterned photoresist and (II) aminophenyl films after electrografting and removal of photoresist for (a) various geometric shapes and (b) a resolution test pattern.

mg mL^{-1} of 80% lyophilized avidin fluorescein isothiocyanate (Sigma-Aldrich) in 0.5% Tween-20 for 1 h, at room temperature in the dark. Samples were rinsed with 0.5% Tween-20, dried with nitrogen, and stored in the dark for no longer than 1 h prior to microscopic analysis.

Electrochemistry. Electrochemical grafting and analyses were performed with an Autolab PGSTAT3C2 Potentiostat/Galvanostat (Eco Chemie B.V., The Netherlands). Silicon substrates were mounted in a glass electrochemical cell that exposed a circular area of surface to the cell solution as described previously (44). A Viton O-ring defined the geometric area of the working electrode (0.94 cm^2). A copper foil on the underside of the silicon substrate provided electrical connection to the working electrode; a platinum wire and saturated calomel electrode (SCE) were used as counter and reference electrodes, respectively.

Microscopy. Atomic force microscope (AFM) images were taken in air with a Dimension 3100 and Nanoscope IIIa controller (Digital Instruments, Veeco, USA). Silicon cantilevers (TAP300Al-G series, Budget Sensors, Innovative Solutions Bulgaria Ltd.) with a fundamental resonance frequency of 200−400 kHz were used in tapping mode. Topographic (height) images were obtained at a scan rate of 0.5 Hz with the parameters set point, amplitude, scan size, and feedback control optimized for each sample. All images presented are background subtracted data using the flatten feature in the Digital Instruments software.

Fluorescence microscopy was undertaken using an Eclipse 80*i* microscope equipped with a D-FL universal epi-fluorescence attachment and a 100 W mercury lamp (Nikon Instruments, Japan). Samples were focused using LU Plan Fluor BD objectives (50x, 20x and 10x) (Nikon Instruments, Japan) and passed through an FITC filter block (465 − 495 nm excitation filter, 505 nm dichroic, 515−555 BA emission filter). Fluorescence images were captured under darkened conditions by a DS-5Mc-U1 cooled CCD camera and recorded with the NIS-elements v3.07 (Nikon Instruments, Japan) software.

Scanning electron microscope (SEM) images were obtained using a 7000 HRSEM (JEOL, Japan) with an accelerating voltage of 15 kV. For the patterned photoresist films on silicon a thin layer of gold and palladium was sputter deposited onto the substrate with an E5000 SEM coating unit (Quorum Technologies, Ringmer, UK).

RESULTS & DISCUSSION

Figure 2a, I shows SEM images of the AZ1518 photoresist on silicon after patterning by ultraviolet light exposure for 24 s through fabricated chrome on glass masks. A series of simple geometric shapes with dimensions as low as 15 μm were patterned into the photoresist. Each shape was patterned multiple times with increasing dimensions up to a maximum of 120 μm. For each pattern the corresponding image after electrografting of an aminophenyl film and removal of photoresist is shown in Figure 2a, II. In these SEM images, regions patterned by aminophenyl film appear dark compared to the surrounding silicon. This is most likely due to the long electrografting time producing a relatively insulating film (43, 45−48). To determine the maximum attainable resolution with this technique, we patterned a resolution test into the photoresist as shown in Figure 2b, I. A series of

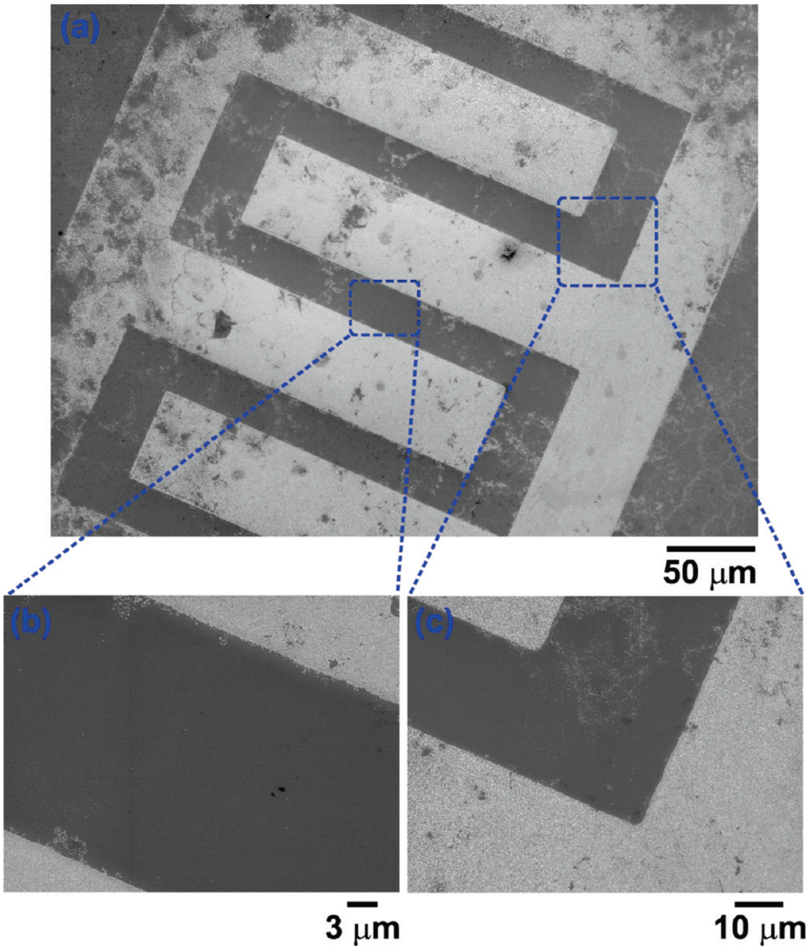

FIGURE 3. SEM images of citrate-capped gold nanoparticles immobilized on (a) a patterned aminophenyl film with (b, c) magnified regions to highlight the highly defined nature of the pattern.

lines, squares, and circles from 10 to 1 μm were patterned. Increments of 1 μm in width were used for the lines and squares, and circle diameters of 1, 2, 4, 8, and 10 μm were used. For each shape, a 500 nm feature was also fabricated; however, photoresist exposure and development issues led to poorly defined features, which is particularly evident in the case of the 500 nm line in Figure 2b, I.

Upon aminophenyl film deposition and photoresist removal, Figure 2 b, II, it can be seen that all structures from 10 to 1 μm can be resolved; however, none of the 500 nm structures are evident. This is assumed to be due to incomplete removal of the photoresist during patterning, which would prevent contact between the solution and the underlying silicon substrate during electrografting. It can also be seen in Figure 2b, II that in the case of sub-4 μm squares and circles, the dimensions of the aminophenyl features appear smaller than the corresponding photoresist feature. Tapering of the edges of the photoresist that define the feature during photoresist development is the likely origin of this effect.

The maximum lateral resolution, which is easily reproducible with this technique using the equipment in our laboratory is between 1 and 4 μm. This is comparable to the 1 μm line widths achieved by Charlier et al. (35) utilizing local silicon doping as a promoter of patterned electrografting of diazonium salts. However, unlike that work, the technique presented here is applicable to a wide range of surfaces, not solely materials suitable for patterned doping. It is anticipated that this approach can be applied to graphitic carbons, metals, semiconductors, and even insulating materials (such as Teflon and glass) (49, 50). Although aryldiazonium salt-derived films have been patterned to significantly higher lateral resolutions, utilizing an atomic force microscope cantilever tip (37, 38) that approach is limited by the slow serial nature of atomic force microscope lithography (15, 33).

To verify the presence of amine functionality on the modified surface, the patterned electrografted films were immersed in gold nanoparticle solution (pH ~5) for 40 min. The SEM image in Figure 3a shows gold nanoparticles (lighter regions) self-assembled onto the aminophenyl film modified areas. The self-assembly of gold nanoparticles onto amine terminated layers has been observed many times in the past and is driven by the electrostatic attraction between the negatively charged, citrate-capped, gold nanoparticles and the partially protonated amine layer (p*K*a ~7.5) (51−54). These results thus confirm the presence of the amine functionality. It can also be seen in the enlarged images b and c that the edges of the aminophenyl pattern are well-defined.

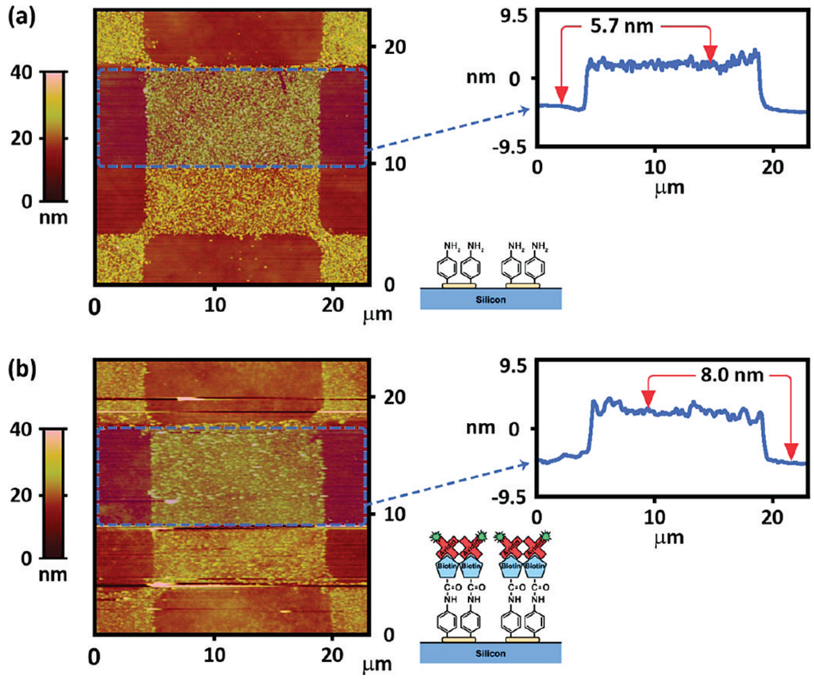

FIGURE 4. AFM image of a 15 µm "checkerboard" pattern (a) before and (b) after coupling with biotin and avidin fluorescein isothiocyanate and corresponding average line profiles.

Further investigation of the patterned surface by atomic force microscopy, as shown in figure 4 (a), reveals the unmodified silicon surface is clean, indicating complete removal of the photoresist material. The electrografted film is "grainy" in appearance, consistent with the branching growth (55) of multilayer films that results in a loosely packed structure (44, 56, 57). Upon taking the average cross section over a 7.5 × 23 µm, area as defined by the dashed lines in Figure 4a, the corresponding line profile gives a film thickness of 5.7 ± 0.2 nm. This is in strong agreement with previous film thickness measurements made using an atomic force microscope tip to remove a section of the film followed by scanning across the film and the scratch to obtain the film thickness. By this method an aminophenyl film, electrografted to silicon under identical conditions to those used here (−0.5 V vs SCE for 10 min) was shown to have a thickness of ~5.5 nm (48). (We note that the result obtained here also provides further validitation to the atomic force microscope scratching method as used in many previous experiments for the determination of film thickness (44).)

The same surface shown in Figure 4a was also imaged with atomic force microscopy after coupling the aminophenyl film with biotin followed by incubation with avidin fluorescein isothiocyanate (Figure 4b). As can be seen by comparison of the line profile graphs, the height of the modified area has now increased by 2.3 nm. This increase confirms the immobilization of biotin and avidin on the aminophenyl film. The egg white avidin molecule has a size of 5 nm as determined by X-ray diffraction (58−60); however, in air, the size of the molecule is typically smaller than in an aqueous environment due to denaturation (58). Furthermore, in addition to denaturation, it is well-known that because of their softness, most biological samples can easily be deformed or damaged by an atomic force microscope cantilever (61) and this effect may contribute to the measured height of the biotin−avidin layer. Values of between 1.7 and 3 nm have previously been determined by atomic force microscopy (58, 60) and are in agreement with our work.

Fluorescence microscopy was also used to visualize avidin fluorescein isothiocyanate immobilized on the patterned aminophenyl layers. Figure 5 shows the characteristic green fluorescence on a (a) 15 µm "checkerboard" pattern (b) 100 µm wide cross, and (c) 60 µm diameter circle. Traces of nonspecific binding of avidin were observed on the unmodified silicon areas; however, increased protection against nonspecific adsorption can be afforded by passivating the background silicon with a protein resistant poly(ethylene glycol) silane (27, 62), or using a blocking agent such as bovine serum album (BSA). Control samples patterned with aminophenyl film were incubated in avidin fluorescein isothiocyanate without first immobilizing biotin, and as expected, only trace levels of fluorescence was observed within the patterns or the background. Furthermore, an aminophenyl film placed in a biotin/DMF solution in the absence of DCC prior to incubation in avidin fluorescein isothiocyanate showed little fluorescence, demonstrating that covalent attachment is a prerequisite for biotin immobilization. These observations, consistent with selective interaction of avidin and, by inference, biotin, at the modified silicon surface confirm that biotin can be covalently coupled to the aminophenyl film and subsequently form a complex with avidin. This provides a simple and straightforward method for patterned immobilization of proteins via complexation of biotin-labeled proteins with immobilized avidin.

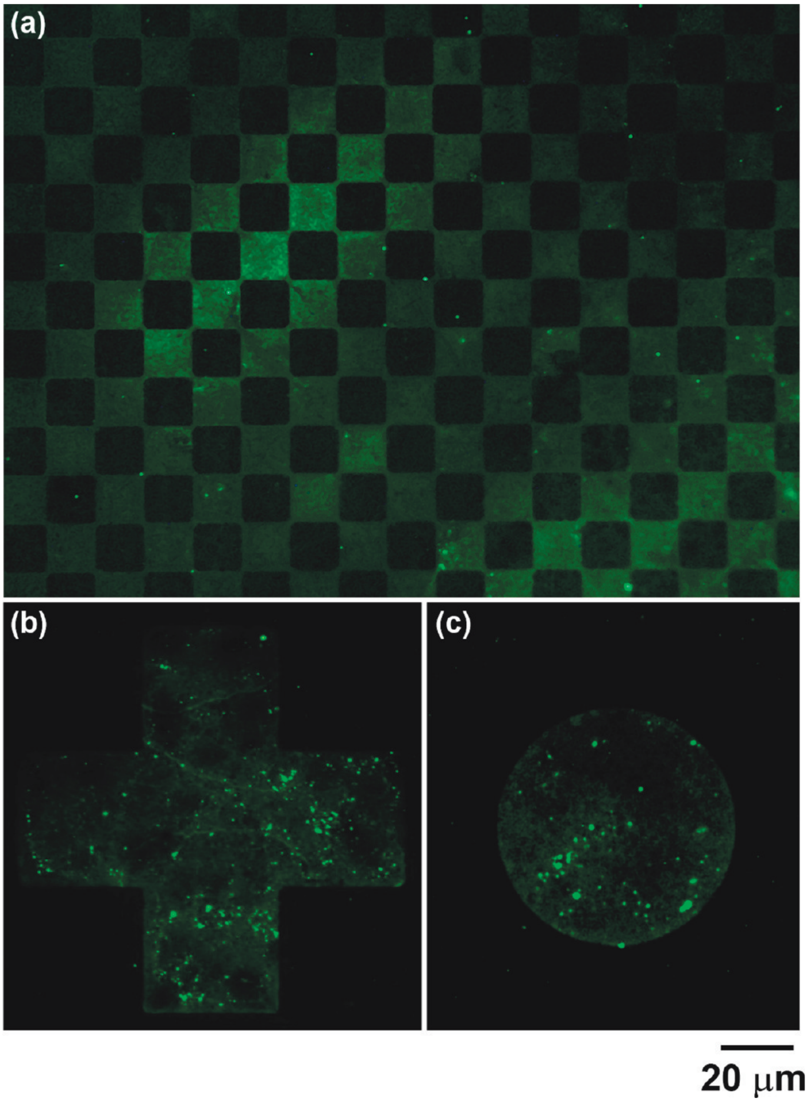

FIGURE 5. Fluorescence microscopy image of avidin fluorescein isothiocyanate immobilized on (a) 15 μm "checkerboard" pattern, (b) 100 μm wide cross, and (c) 60 μm diameter circle.

CONCLUSION

This work has demonstrated a simple, convenient photolithographic method for patterning silicon with electrografted aminophenyl films. Attractive features of the method are that removal of the native oxide layer is not necessary prior to grafting and the method is suitable for rapid patterning of large surface areas. Use of diazonium salts for grafting gives films that are sufficiently stable to withstand the cleaning steps necessary for removal of photoresist. It is anticipated that this method can be extended to many different substrates and a variety of aryldiazonium salts. Patterns with lateral features down to 1 μm were achieved, however, with the use of electron beam lithographic techniques, lower dimensions should be possible. To demonstrate the potential application of patterned substrates in biosensing devices, biotin was covalently coupled to the patterned aminophenyl film to facilitate the immobilization of the protein avidin. Atomic force and fluorescence microscopy confirmed the selective immobilization of avidin on the aminophenyl film. In work currently under way, we are investigating preparation of patterned aminophenyl films that are amenable to electrochemical as well as fluorescence detection methods.

Acknowledgment. This work was funded by the MacDiarmid Institute for Advanced Materials and Nanotechnology. B.S.F. thanks the Australian Government's Endeavour Research Fellowship program; A.J.G. thanks the MacDiarmid Institute for a Doctoral Scholarship, and D.J.G. thanks the Tertiary Education Commission for a Bright Futures Top Achiever Doctoral Scholarship. We thank Helen Devereux for technical assistance.

REFERENCES AND NOTES

(1) Bearinger, J. P.; Dugan, L. C.; Wu, L.; Hill, H. A.; Christian, T.; Hubbell, J. A. *BioTechniques* **2009**, *46*, 209.
(2) Mrksich, M.; Dike, L. E.; Tien, J.; Ingber, D. E.; Whitesides, G. M. *Exp. Cell Res.* **1997**, *235*, 305.
(3) Blawas, A. S.; Reichert, W. M. *Biomaterials* **1998**, *19*, 595.
(4) Lee, C.-S.; Lee, S.-H.; Park, S.-S.; Kim, Y.-K.; Kim, B.-G *Biosens. Bioelectron.* **2003**, *18*, 437.
(5) Demers, L. M.; Ginger, D. S.; Park, S.-J.; Li, Z.; Chung, S.-W.; Mirkin, C. A *Science* **2002**, *296*, 1836.

(6) Smith, E. A.; Wanat, M. J.; Cheng, Y.; Barreira, S. V. P.; Frutos, A. G.; Corn, R. M. *Langmuir* **2001**, *17*, 2502.
(7) Choi, H. J.; Kim, N. H.; Chung, B. H.; Seong, G. H. *Anal. Biochem.* **2005**, *347*, 60.
(8) Koyano, T.; Saito, M.; Miyamoto, Y.; Kaifu, K.; Kato, M. *Biotechnol. Prog.* **1996**, *12*, 141.
(9) Christman, K. L.; Enriquez-Rios, V. D.; Maynard, H. D. *Soft Matter* **2006**, *2*, 928.
(10) Bashir, R.; Gomez, R.; Sarikaya, A.; Ladisch, M. R.; Sturgis, J.; Robinson, J. P. *Biotechnol. Bioeng.* **2001**, *73*, 324.
(11) Schmalenberg, K. E.; Buettner, H. M.; Uhrich, K. E. *Biomaterials* **2004**, *25*, 1851.
(12) Orth, R. N.; Clark, T. G.; Craighead, H. G. *Biomed. Microdev.* **2003**, *5*, 29.
(13) Harnett, C. K.; Satyalakshmi, K. M.; Craighead, H. G. *Langmuir* **2001**, *17*, 178.
(14) Schwarz, A.; Rossier, J. S.; Roulet, E.; Mermod, N.; Roberts, M. A.; Girault, H. H. *Langmuir* **1998**, *14*, 5526.
(15) Zhang, G.-J.; Tanii, T.; Zako, T.; Hosaka, T.; Miyake, T.; Kanari, Y.; Funatsu, T.; Ohdomari, I *Small* **2005**, *1*, 833.
(16) Mooney, J. F.; Hunt, A. J.; McIntosh, J. R.; Liberko, C. A.; Walba, D. M.; Rogers, C. T *Proc. Natl. Acad. Sci. U.S.A.* **1996**, *93*, 12287.
(17) Veiseh, M.; Zareie, M. H.; Zhang, M. *Langmuir* **2002**, *18*, 6671.
(18) Chenghong, L.; Jiaqi, D. *Anal. Chem.* **1996**, *68*, 3344.
(19) Kong, Y.-T.; Boopathi, M.; Shim, Y.-B *Biosens. Bioelectron.* **2003**, *19*, 227.
(20) Brooks, S. A.; Dontha, N.; Brandon Davis, C.; Stuart, J. K.; O'Neill, G.; Kuhr, W. G. *Anal. Chem.* **2000**, *72*, 3253.
(21) Baur, B.; Steinhoff, G.; Hernando, J.; Purrucker, O.; Tanaka, M.; Nickel, B.; Stutzmann, M.; Eickhoff, M. *Appl. Phys. Lett.* **2005**, *87*, 263901.
(22) Ignatov, S.; Shishniashvili, D.; Ge, B.; Scheller, F. W.; Lisdat, F. *Biosens. Bioelectron.* **2002**, *17*, 191.
(23) Brockman, J. M.; Frutos, A. G.; Corn, R. M. *J. Am. Chem. Soc.* **1999**, *121*, 8044.
(24) De Silva, M. N.; Desali, R.; Odde, D. J. *Biomed. Microdev.* **2004**, *6*, 219.
(25) Nishikawa, M.; Yamamoto, T.; Kojima, N.; Kikuo, K.; Fujii, T.; Sakai, Y. *Biotechnol. Bioeng.* **2007**, *99*, 1472.
(26) Shamansky, L. M.; Davis, C. B.; Stuart, J. K.; Kuhr, W. G. *Talanta* **2001**, *55*, 909.
(27) Christman, K. L.; Requa, M. V.; Enriquez-Rios, V. D.; Ward, S.; Bradley, K. A.; Turner, K. L.; Maynard, H. D. *Langmuir* **2006**, *22*, 7444.
(28) Jonkheijm, P.; Weinrich, D.; Schröder, H.; Niemeyer, C. M.; Waldmann, H. *Angew. Chem., Int. Ed.* **2008**, *47*, 9618.
(29) Bora, U.; Sharma, P.; Kumar, S.; Kannan, K.; Nahar, P. *Talanta* **2006**, *70*, 624.
(30) Arakaki, A.; Hideshima, S.; Nakagawa, T.; Niwa, D.; Tanaka, T.; Matsunga, T.; Osaka, T. *Biotechnol. Bioeng.* **2004**, *88*, 543.
(31) Aswal, D. K.; Lenfant, S.; Guerin, D.; Yakhmi, J. V.; Vuillaume, D. *Anal. Chim. Acta* , *568*, 84.
(32) Flavel, B. S.; Yu, J.; Ellis, A. V.; Quinton, J. S.; Shapter, J. G. *Nanotechnol.* **2008**, *19*, 445301.
(33) Flavel, B. S.; Yu, J.; Shapter, J. G.; Quinton, J. S. *Carbon* **2007**, *45*, 2551.
(34) St. John, P. M.; Craighead, H. G. *Appl. Phys. Lett.* **1996**, *68*, 1022.
(35) Charlier, J.; Palacin, S.; Leroy, J.; Del Frari, D.; Zagonel, L.; Barrett, N.; Renault, O.; Bailly, A.; Mariolle, D. *J. Mater. Chem.* **2008**, *18*, 3136.
(36) Charlier, J.; Clolus, E.; Bureau, C.; Palacin, S. *J. Electroanal. Chem.* **2009**, *625*, 97.
(37) Ghorbal, A.; Grisotto, F.; Charlier, J.; Palacin, S.; Goyer, C.; Demaille, C. *Chem. Phys. Chem* **2009**, *10*, 1053.
(38) Brooksby, P. A.; Downard, A. J. *Langmuir* **2005**, *21*, 1672.
(39) Downard, A. J.; Garrett, D. J.; Tan, E. S. Q. *Langmuir* **2006**, *22*, 10739.
(40) Garrett, D. J.; Lehr, J.; Miskelly, G. M.; Downard, A. J. *J. Am. Chem. Soc.* **2007**, *129*, 15456.
(41) Guan, F.; Chen, M.; Yang, W.; Wang, J.; Yong, S.; Xue, Q. *Appl. Surf. Sci.* **2005**, *240*, 24.
(42) Jin, Y.; Kang, X.; Song, Y.; Zhang, B.; Cheng, G.; Dong, S. *Anal. Chem.* **2001**, *73*, 2843.
(43) Lyskawa, J.; Belanger, D. *Chem. Mater.* **2006**, *18*, 4755.
(44) Brooksby, P. A.; Downard, A. J. *Langmuir* **2004**, *20*, 5038.
(45) D'Amours, M.; Belanger, D. *J. Phys. Chem., B* **2003**, *107*, 4811.
(46) Downard, A. J.; Prince, M. J. *Langmuir* **2001**, *17*, 5581.
(47) Ortiz, B.; Saby, C.; Champagne, G. Y.; Belanger, D. *J. Electroanal. Chem.* , *455*, 75.
(48) Flavel, B. S.; Garrett, D. J.; Lehr, J.; Shapter, J. G.; Downard, A. J. *Electrochim. Acta* **2010**, in press.
(49) Pinson, J.; Podvorica, F. *Chem. Soc. Rev.* **2005**, *34*, 429.
(50) Mevellec, V.; Roussel, S.; Tessier, L.; Chancolon, J.; Mayne-L'Hermite, M.; Deniau, G.; Viel, P.; Palacin, S. *Chem. Mater.* **2007**, *19*, 6323.
(51) Shipway, A. N.; Katz, E.; Willner, I. *Chem. Phys. Chem.* **2000**, *1*, 18.
(52) Park, J.; Lee, H. *Colloids Surf., A* **2005**, *275*, 133.
(53) Shipway, A. N.; Lahav, M.; Willner, I. *Adv. Mater.* **2000**, *12*, 993.
(54) Li, Q.; Zheng, J.; Liu, Z. *Langmuir* **2003**, *19*, 166.
(55) Yu, S. S. C.; Tan, E. S. Q.; Jane, R. T.; Downard, A. J. *Langmuir* **2007**, *23*, 11074.
(56) Brooksby, P. A.; Downard, A. J. *J. Phys. Chem., B* **2005**, *109*, 8791.
(57) Paulik, M. G.; Brooksby, P. A.; Abell, A. D.; Downard, A. J. *J. Phys. Chem., C* **2007**, *111*, 7808.
(58) Misawa, N.; Yamamura, S.; Yong-Hoon, K.; Tero, R.; Nonogaki, Y.; Urisu, T. *Chem. Phys. Lett.* **2006**, *419*, 86.
(59) Aoki, R.; Arakawa, T.; Misawa, N.; Tero, R.; Urisu, T.; Tekeuchi, A.; Ogino, T. *Surf. Sci.* **2007**, *601*, 4915.
(60) Ebner, A.; Hinterdorfer, P.; Gruber, H. J. *Ultramicroscopy* **2007**, *107*, 922.
(61) Zhang, Y.; Sheng, S.; Shao, Z *Biophys. J.* **199671**, 2168.
(62) Papra, A.; Bernard, A.; Juncker, D.; Larsen, N. B.; Michel, B.; Delamarche, E. *Langmuir* **2001**, *17*, 4090.

AM100020A

– This page intentionally left blank –

2.6 Additional Scientific Publications

2.6.6 *Electrochemical Detection of Copper Using a Gly-Gly-His Modified Carbon Nanotube Biosensor*

B. S. Flavel, M. Nambiar, J. G. Shapter

Silicon 3 (2011) 163–171

DOI: 10.1007/s12633-011-9080-0

Abstract

Diazonium ion chemistry has been used to electrochemically graft aminophenyl layers onto p-type silicon (100) substrates. A condensation reaction was used to immobilise single-walled carbon nanotubes with high carboxylic acid functionality directly to this layer. The surface immobilised carbon nanotubes were then modified with the tripeptide Gly-Gly-His for the selective detection of copper ions in aqueous environments. The stepwise assembly and sensitivity of this biosensor to copper was characterised by X-ray photoelectron spectroscopy and differential pulse voltammetry, respectively. The ability to detect copper ion concentrations down to 1 μM was demonstrated. As this biosensor combines the advantages of a silicon substrate for easy integration into sophisticated electrical and electronic devices, diazonium salt derived films for stability in aqueous environments and carbon nanotubes for desirable electrochemical properties, it is expected to have important future applications in environmental sensing.

Contribution

J.G.S conceived and designed the project. B.S.F and M.N performed the experiments, B.S.F wrote the paper and all authors contributed to the scientific interpretation of the results.

– This page intentionally left blank –

Silicon (2011) 3:163–171
DOI 10.1007/s12633-011-9080-0

ORIGINAL PAPER

Electrochemical Detection of Copper Using a Gly-Gly-His Modified Carbon Nanotube Biosensor

Benjamin S. Flavel · Monessha Nambiar · Joseph G. Shapter

Received: 18 November 2010 / Accepted: 2 March 2011 / Published online: 12 April 2011

Abstract Diazonium ion chemistry has been used to electrochemically graft aminophenyl layers onto p-type silicon (100) substrates. A condensation reaction was used to immobilise single-walled carbon nanotubes with high carboxylic acid functionality directly to this layer. The surface immobilised carbon nanotubes were then modified with the tripeptide Gly-Gly-His for the selective detection of copper ions in aqueous environments. The stepwise assembly and sensitivity of this biosensor to copper was characterised by X-ray photoelectron spectroscopy and differential pulse voltammetry, respectively. The ability to detect copper ion concentrations down to 1 μM was demonstrated. As this biosensor combines the advantages of a silicon substrate for easy integration into sophisticated electrical and electronic devices, diazonium salt derived films for stability in aqueous environments and carbon nanotubes for desirable electrochemical properties, it is expected to have important future applications in environmental sensing.

Keywords Silicon · p-phenylenediamine · Peptide · Electrochemical grafting · Heavy metal sensing

B. S. Flavel (✉) · M. Nambiar · J. G. Shapter (✉)
School of Chemical and Physical Sciences, Flinders University,
Sturt Road, Bedford Park,
Adelaide, South Australia 5001
e-mail: ben.flavel@flinders.edu.au

J. G. Shapter
e-mail: joe.shapter@flinders.edu.au

1 Introduction

The ability to maintain quality potable water supplies and the need for water monitoring continues to grow as larger populations require increasing volumes of water [1]. One aspect of water quality with particular importance is the determination of heavy metal ion concentrations. In high doses, heavy metals are toxic and can cause damage to the central nervous system resulting in various neuropsychiatric disorders [2, 3]. For this reason government organisations typically enforce strict regulations over the allowed concentration of heavy metal ions in potable water supplies. For example, Australian and World Health Organisation guidelines currently stipulate a maximum copper (Cu^{2+}) and cadmium (Cd^{2+}) concentration of 30 μM and 27 nM, respectively [4–6]. A variety of techniques such as atomic absorption spectroscopy [7], inductively coupled plasma mass spectroscopy [8], X-ray fluorescence spectroscopy [9] and surface plasmon resonance [10] already exist for heavy metal ion detection. Whilst these techniques are highly accurate, they typically require expensive instrumentation, pre-concentration steps, trained personnel and are not compatible with in field sampling and analysis [11, 12]. However, electrochemical based sensors utilising voltametric methods fulfil the criteria for an inexpensive, easy and rapid detection system. Furthermore, electrochemical sensors are compatible with flow through analysis and are capable of miniaturization to allow for multi-analyte detection [12].

In order to develop a voltametric metal ion sensor a highly specific recognition element must be immobilised to an electrode which is capable of converting the specific metal ion recognition event into an electrical signal [10, 12]. For metal ion detection, peptides and oligopeptides are the ideal candidates with many examples of highly selective metal binding in the protein literature [13, 14]. Peptides represent the simplest biological recognition elements for binding metals [14] and ability to alter the amino acid sequence within an oligopeptide provides control over tuning the affinities of the ligands to different metal ions [12]. Furthermore, peptides maintain their metal selectivity in aqueous environments [15] and it is envisaged that upon designing an appropriate generic electrode platform any metal ion could be detected in water [13]. Several examples of peptide based electrochemical metal ion sensors currently exist in the literature and it is work by Gooding and co-workers that constitutes a significant amount of this research [11]. In these examples a monolayer of 3-mercaptopropionic acid was self-assembled on a gold electrode followed by the covalent tethering of either the copper selective tripeptide Gly-Gly-His [3, 12, 13] or the cadmium selective peptides γ-Glu-Cys-Gly [16] or His-Ser-Gln-Lys-Val-Phe [6]. With the use of Osteryoung square wave voltammetry concentrations as low as 3 and 0.9 nM were detected for copper and cadmium, respectively. More recently, Lin et al. [14] have developed a different sensor architecture utilising the conducting polymer poly(3-thiopheneacetic acid) functionalised with Gly-Gly-His on a gold electrode capable of copper ion detection in the range 0.02–20 μM.

Whilst detection limits in the nM regime compare favourably with atomic spectroscopy techniques, [12] electrode systems utilising an alkanethiol tether layer are well known to be limited by thermal instability [17, 18], UV photoxidation [19] and adsorbate solution interchange leading to poor long term stability [20]. For this reason Liu et al. [11] investigated the use of aryldiazonium chemistry to electrochemically graft carboxyphenyl moieties onto a glassy carbon electrode followed by further modification with Gly-Gly-His. Surface layers generated from aryldiazonium salts are known to be highly stable, forming a covalent bond with the electrode substrate and have been shown to be resistant to degradation from acid, base and organic solvent [1, 21, 22]. However, clearly the use of glassy carbon as a substrate is not ideal for integration into current electronic devices and there exists a need for new forms of electrode architectures.

One form of electrode interface gaining considerable interest in the field of electro-analysis is that with carbon nanotubes [1, 22–24]. Carbon nanotubes have been shown to exhibit very stable electrochemical behaviour with a wide potential window and high chemical inertness at low cost [25], hence making them the ideal electrode platform. Within this field there has been significant emphasis on the development of gas sensors [26, 27] or biosensors [28, 29] aimed at medical applications. However, the design of carbon nanotube based sensors for aqueous detection is a relatively recent effort [30–36]. Much of this recent research has involved the preparation of complex composite materials. Such composites typically incorporate a catalyst (nanoparticle, molecular or biological species), nanotubes (which enhance the response of the sensor), and a component to aid immobilisation of the composite on an electrode surface. For example Ly et al. [31] developed a carbon nanotube paste electrode fabricated from fluorine doped carbon nanotubes and mineral oil for the detection copper ion content in various aqueous media. However, such complicated architectures are far from a generic platform suitable for the attachment of a variety of metal ion sensitive peptides.

Very recently we have demonstrated a simple approach to chemically assemble vertically aligned carbon nanotubes on silicon electrodes [1]. Silicon is an attractive substrate for the design of a generic sensor platform as it allows highly developed microfabrication and nanofabrication procedures to be used in sensor fabrication and facilitates the incorporation into future devices. Carboxyl functionalised single-walled carbon nanotubes were attached through an amide bond to a tether layer formed from the electrochemical reduction of a 4-aminobenzene diazonium salt solution. This carbon nanotube electrode showed high stability and good electrochemical performance in aqueous solution [1]. Furthermore, due to the high surface area and abundance of carboxyl functionalities on a vertically aligned carbon nanotube electrode [1, 22] this system offers the ideal scaffold for further modification with peptides for metal ion sensing. In this work we demonstrate a new form of electrode utilising vertically aligned carbon nanotubes and the tripeptide Gly-Gly-His to develop a copper ion sensor on silicon.

2 Experimental

The preparation of carboxylated single-walled carbon nanotubes (SWCNTs) has been described in detail previously [37]. In brief, single-walled carbon nanotubes (SWCNTs) from Carbon Solutions Inc, USA, P2-SWNT, were refluxed in 3 M nitric acid for 24 h. The dilute nitric acid solution was then decanted off and the nanotubes were placed into a more aggressive oxidiser, namely a 3:1 v/v solution of concentrated sulphuric acid (98%) and concentrated nitric acid (70%) and ultrasonicated for 8 h at 0 °C [38, 39]. The shortened nanotubes were then diluted in 500 mL of MilliQ water and filtered through a 0.45 μm polytetrafluoroethylene (PTFE) membrane. The nanotubes were further washed with MilliQ water to bring the pH to 5–7 and then dried under vacuum [38].

The strategy for fabrication of Gly-Gly-His modified carbon nanotubes electrodes on silicon is shown schematically in Fig. 1. Highly boron doped p-type silicon (100) (Virginia Semiconductor, Inc., USA) was cut into 2 cm×2 cm sized wafers and (step 1) placed into 40% hydrofluoric acid (Sigma-Aldrich) for a period of 3 min to remove the native silicon oxide and hydrogenate the underlying surface [40, 41]. The silicon wafer was then washed with methanol and dried thoroughly under nitrogen. The p-aminobenzenediazonium cation was prepared by the method of Lyskawa et al. [42]. In brief, 3 mL of 20 mM *p*-phenylenediamine (Sigma-Aldrich) in 1 M hydrochloric acid (Sigma-Aldrich) was added to an equal volume of 20 mM 99% sodium nitrite (Sharlau Chemie, Spain) at room temperature. This solution was used to graft aminophenyl films to the H-terminated silicon substrate (step 2) by applying a potential of −0.5 V vs Ag/AgCl for 10 min. Immediately after grafting the silicon substrate was ultrasonicated in MilliQ water for 5 min then dried with nitrogen. The modified silicon sample was then immersed for 24 h in a 5 mL 99.9% N,N-dimethyl formamide (DMF) (Southern Cross Scientific Pty. Ltd.) solution containing both 2.5 mg of 99.0% N,N'-diyclohexylcarbodiimide (DCC) (Fluka Production GmbH) and 1 mg of carboxyl functionalised carbon nanotubes (step 3). Prior to introducing the substrate, the carbon nanotube/DCC/DMF solution was ultrasonicated for 5 h to evenly disperse the carbon nanotubes. After attachment the electrode was rinsed with acetone and dried with nitrogen. The tripeptide Gly-Gly-His was then covalently attached through reaction of the amino group of the first glycine with the carboxylic acid group of the immobilised carbon nanotubes. The carbon nanotube immobilised substrate was immersed for 24 h in a 30 mg mL^{-1} Gly-Gly-His (Sigma-Aldrich) pH 7.0 solution consisting of 50 mM ammonium acetate (Koch-Light Laboratories) in 0.1 M potassium chloride (Chem-Supply) to afford the final Gly-Gly-His modified carbon nanotube biosensor (step 4). Cu^{2+} ions were then accumulated at the electrode surface in a stirred solution of copper acetate at open circuit potential for 10 min (step 5). A stock solution of 1 mM copper acetate (Ajax Finechem) was prepared in 0.1 M potassium chloride and 50 mM ammonium acetate solution, which was then further diluted to obtain desired concentrations. Following copper ion incubation the substrate was rinsed with copper free ammonium acetate/potassium chloride solution, dried with nitrogen and used immediately for electrochemical measurement. After measurement copper could be removed from the Gly-Gly-His to regenerate the electrode by immersion in 0.1 M $HClO_4$ (Sigma-Aldrich) at open circuit potential for 30 s.

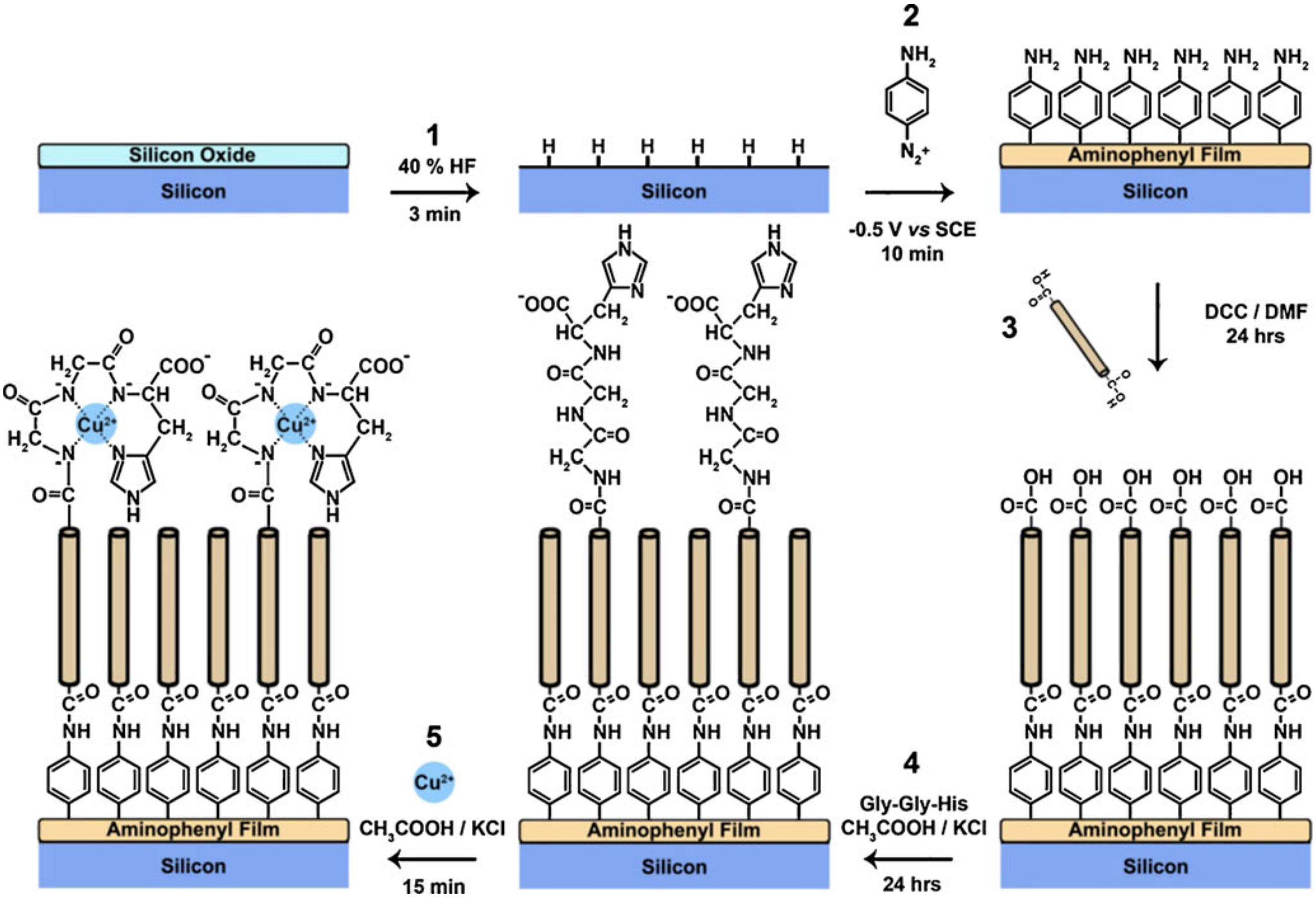

Fig. 1 Fabrication a Gly-Gly-His modified carbon nanotube electrode for detection of Cu^{2+}

Electrochemical experiments were performed with a BAS100B Electrochemical Analyser (Bioanalytical Systems Inc., USA), operating in differential pulse voltammetry (DPV) mode. Silicon substrates were mounted in a glass electrochemical cell that exposed a circular area of surface to the cell solution as described previously [43]. The underside of the silicon substrate was adhered to copper foil to form the working electrode with a platinum wire and Ag/AgCl used as the counter and reference electrodes, respectively. A Viton o-ring defined the geometric area of the working electrode. For the electrochemical grafting of aminophenyl films the working area was 0.26 cm^2; subsequent analysis was based on a smaller area (0.13 cm^2) of the grafted surface. Voltammetry was performed in a solution of 50 mM ammonium acetate in 0.1 M potassium chloride by sweeping the potential in the negative direction between 0.1 and −0.6 V. Analysis of voltammograms to determine peak current and area were performed with the Peakfit software (SigmaPlot, Cranes Software International Pty., Ltd.).

X-ray photoelectron spectroscopy was performed with a Kratos Axis Ultra X-ray photoelectron spectrometer (Kratos Analytical, Shimadzu). Survey spectra (0–1,100 eV) were obtained followed by high resolution spectra of the C 1s, N 1s and Cu 2p regions. Spectra were referenced to the Au $4f_{7/2}$ peak and analysed using the CasaXPS (Casa Software Ltd.) software.

3 Results & Discussion

In a previous publication the development of single walled carbon nanotube electrodes with high aqueous stability, based on electrochemically grafted aminophenyl tether layers on silicon was described [1]. Atomic force microscopy and electrochemical analysis techniques were used to provide characterisation of the electrode system to step 3 of Fig. 1. In this publication additional characterisation of electrode fabrication is provided by X-ray photoelectron spectroscopy along with stepwise analysis of covalent attachment of the peptide Gly-Gly-His for copper detection. Further electrochemical analysis was then performed to determine electrode sensitivity and lifetime.

Figure 2 shows stepwise X-ray photoelectron survey spectra from the electrochemical grafting of an aminophenyl tether layer (step 2, Fig. 1) to the final complexation of copper ions (Cu^{2+}) with Gly-Gly-His (step 5, Fig. 1). Different electrode substrates representing each step towards final electrode fabrication were used for analysis. Spectrum (a) shows an electrochemically grafted aminophenyl layer where peaks associated with 2s and 2p transitions from the underlying silicon substrate can be seen centred at 99 and 151 eV respectively, a 1s peak from nitrogen associated with aminophenyl groups at 400 eV and intense 1s peaks associated with oxygen and carbon at 531 and 285 eV, respectively [44]. The peak at 200 eV is associated with chlorine which is a result of the grafting solution used for the aminophenyl film. Following the covalent attachment of single walled carbon nanotubes (b) an increase in oxygen intensity can be seen and is attributed to the presence of a variety of oxygen containing functional groups, in particular carboxylic acids from acid treatment [20]. Interestingly, an increase in the intensity of silicon peaks at 99 and 151 eV is also observed. Presently the origin of this increase is unclear, however an increase in electron transport through surface layers following attachment of carbon nanotubes has previously been observed [1, 45] and would explain the increased intensity of the substrate peaks. The emergent peak at 685 eV is associated with a 1s transition of fluorine [44] and is a result of substrate treatment with hydrofluoric acid during electrode fabrication. The inherently random and highly disordered structure of aryldiazonium derived films [1, 46] coupled with the fact that each sample for X-ray photoelectron spectroscopy was created separately may lead to the observation of this peak. Between samples there are differences in the structure or porosity of an aminophenyl layer possibly allowing greater access to the underlying surface. Similarly, this effect may also be the cause of the increased silicon peak intensity. Coupling of the Gly-Gly-His peptide to the immobilised carbon nanotubes via an amide bond (c), as expected [3, 11, 14], resulted in an increase in the nitrogen content at 400 eV. Following 10 min incubation of a Gly-Gly-His modified carbon nanotube electrode in 1 mM copper acetate in 0.1 M potassium chloride and 50 mM ammonium acetate solution (d), a new peak centred at 933 eV associated with a $2p_{3/2}$ transition from co-ordinated copper ions can be seen. In both spectra (c) and (d) a peak centred at 378 eV can also be seen and is associated with potassium [44] from the 0.1 M potassium chloride used.

To provide a more detailed analysis of the attachment of Gly-Gly-His to immobilised carbon nanotubes on an aminophenyl layer high resolution scans of the C 1s, N 1s and Cu 2p regions are shown in Fig. 3. In the case of a single walled carbon nanotube electrode (step 3, Fig. 1) or a Gly-Gly-His modified electrode (step 4, Fig. 1) no copper was observed in the high resolution scans and hence are not included. Figure 3 (a) shows the deconvoluted C 1s and N 1s spectra for single walled carbon nanotube immobilised on an aminophenyl tether layer. The C 1s spectrum was deconvoluted into five components with the main peak at 284.87 eV associated with alkyl carbons. Components at 285.77 and 285.67 eV are associated with the aminophenyl tether layer and are assigned to C=C and C-N, respectively. The amide bond (N-C=O) formed between the amino-

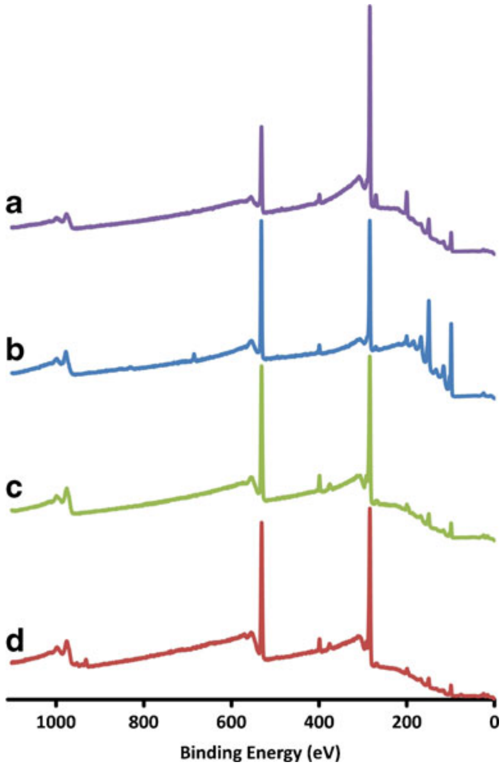

Fig. 2 X-ray photoelectron spectra of the sequential steps in electrode fabrication. **a** An aminophenyl film, **b** modified with carbon nanotubes, **c** modified with Gly-Gly-His and **d** after incubation in Cu^{2+} solution

phenyl tether layer and single walled carbon nanotubes was then seen at 287.17 eV along with remaining carboxylic acid groups (HO-C=O) at 287.47 eV [20, 44]. The N 1s spectrum was deconvoluted into 2 components. A component at 399.82 eV was consistent with the presence of amino groups (N-H_2) at the electrode surface. The second smaller component at 400.72 eV is in agreement with work by Lyskawa et al. [42] and was assigned to azo bridges (N=N-C) within the aminophenyl film. It is well known that diazonium is prone to coupling resulting in the formation of an azobenzene derivative that may be involved in film growth [1, 42].

After covalent attachment of Gly-Gly-His to the immobilised carbon nanotube surface, Fig. 3 (b), the C 1s spectrum was deconvoluted into 6 components with the main component centred at 284.87 eV. The component at 283.08 eV is attributed to the formation of a carbide bond (C-Si) between the aminophenyl tether layer and the underlying silicon surface [44, 47]. The formation of a covalent bond between carbon substrates and aryldiazonium is well established and is expected to proceed at other substrates such as silicon [1, 21, 22]. However, the intensity of this peak is low and is not observed for every sample analysed which may again be a result of the random and highly disordered structure of aryldiazonium derived films [1, 46]. In comparison to the C 1s spectra shown in Fig. 3 (a) an increase in the peaks centred at 286.58 and 287.38 eV can be seen which was attributed to the C=N and C-N of the imidazolyl group of the histidine and amide bond (N-C=O) between glycines and histidine, respectively. The presence of a peak at 288.58 eV associated with carboxylic acids is believed to be a combination of both the un-reacted groups on the carbon nanotube and the addition of Gly-Gly-His. Upon examination of the N 1s spectrum for Gly-Gly-His modified carbon nanotubes the presence of C=N and C-N from the imidazolyl group is also reflected by the emergence of a third peak centred at 398.68 eV [3, 11, 14].

As seen in Fig. 2 (c) and (d) the C 1s and N 1s regions remained the same following incubation of a Gly-Gly-His modified carbon nanotube electrode in 1 mM copper acetate, however peaks associated with copper appeared and are shown in high resolution in Fig. 3 (c). The complexation of copper ions (Cu^{2+}) by Gly-Gly-His are confirmed by the two peaks at 931.60 and 951.95 eV, associated with $Cu_{2p3/2}$ and $Cu_{2p1/2}$, respectively [14, 48].

To demonstrate the potential of Gly-Gly-His modified carbon nanotubes to measure the concentration of copper ions in solution differential pulse voltammetry was performed. After incubation in 1 mM copper acetate solution for 10 min and rinsing with copper free 0.1 M potassium chloride and 50 mM ammonium acetate solution a modified electrode was placed into pH 7.0 ammonium acetate buffer and scanned between 100 and −600 mV. A redox peak centred at −176 mV can clearly be seen in Fig. 4 (a). This redox process is attributed to the Cu^{2+}/Cu^0 process and was found to be 20 mV more negative than 1 mM copper acetate in pH 7.0 ammonium acetate buffer at hydrogen terminated silicon as seen in Fig. 4 (b). This negative shift has been observed previously by Liu et al. [11] who immobilised Gly-Gly-His to a glassy carbon electrode with the use of a 4-carboxyphenyl diazonium salt derived tether layer and is attributed to the stepwise coating of an electrode with layers [49]. A variety of control experiments were also performed in pH 7.0 ammonium acetate buffer in order to ensure that the measured redox peak was indeed associated with copper ions complexed by Gly-Gly-His and can be found in Fig. 4 (a). An aminophenyl layer (Fig. 1, step 2), an aminophenyl layer modified with carbon nanotubes (Fig. 1, step 3) and Gly-Gly-His modified carbon nanotubes (Fig. 1, step 4) all displayed no electrochemistry between 100 and −600 mV. Furthermore, carbon nanotubes immobilised on an aminophenyl layer without Gly-Gly-His modification were placed into 1 mM copper acetate for 10 min also exhibited no electrochemical behaviour. This is an interesting result because upon X-ray photoelectron spectroscopy analysis of this control sample it only exhibited 37% less copper on the surface compared to a substrate modified with Gly-Gly-His. This result suggests that

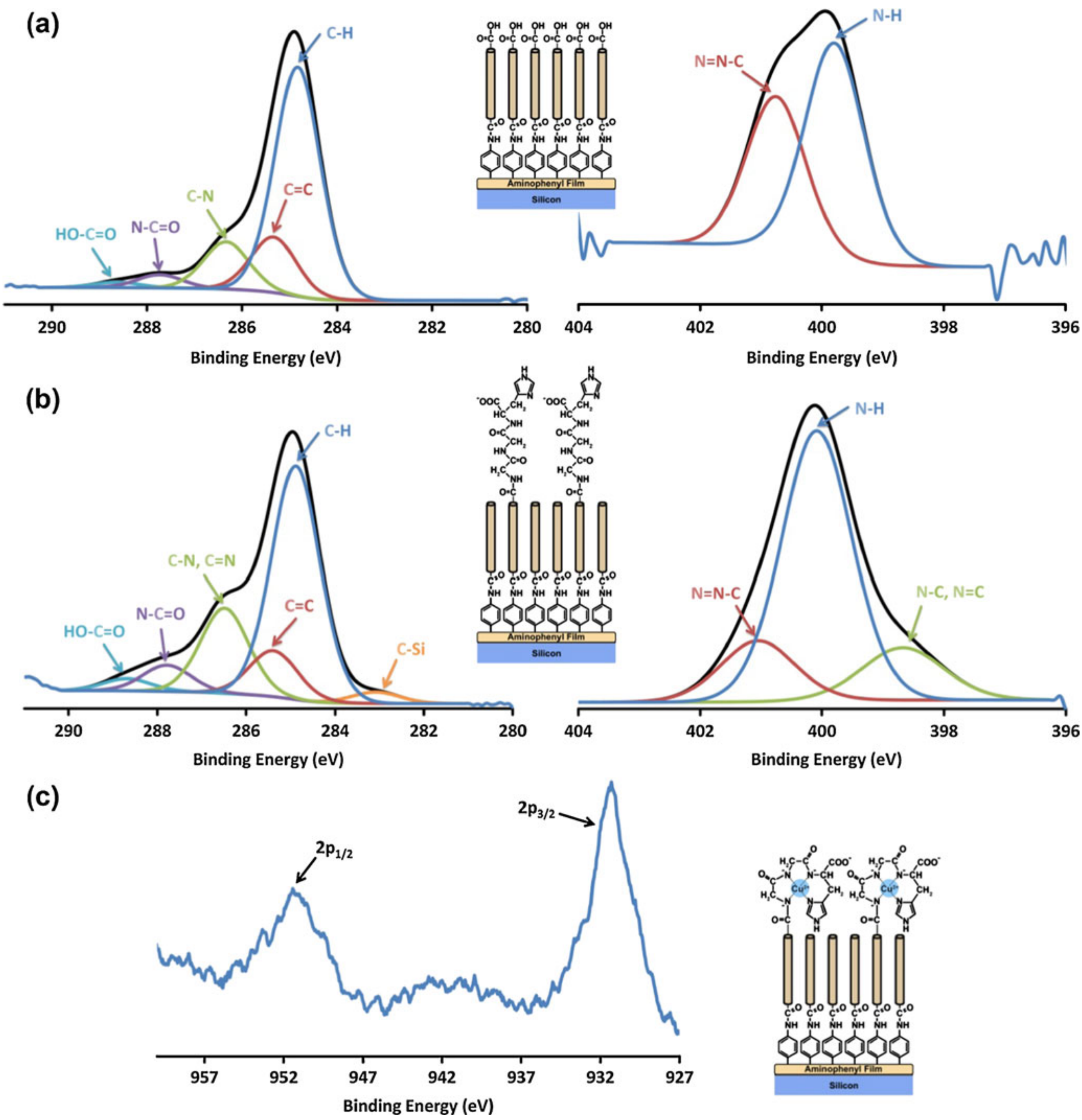

Fig. 3 High resolution X-ray photoelectron spectra and peak fit of the C 1s and N 1s region for **a** carbon nanotubes immobilised on an aminophenyl layer and **b** after modification with Gly-Gly-His. **c** X-ray photoelectron spectrum of the Cu 2p region for an electrode incubated in Cu^{2+} solution

complexation with Gly-Gly-His and hence a chemical connection to the carbon nanotube electrode as opposed to a physisorbed species is a requirement for the observation of electrochemical behaviour in this system.

For quantification purposes a series of different copper acetate concentrations from 1 to 50 μM were prepared by dilution from a 1 mM stock solution and the peak current measured by differential pulse voltammetry as shown in Fig. 5. A second order polynomial was fitted to the data with the error bars representing standard error of multiple measurements. For each concentration the data point shown is taken from the peak current of the first sweep. Due to electrochemical peak currents below the sensitivity of the potentiostat, copper concentrations below 1 μM could not be measured. A minimum concentration detection of 1± 6 μM does not compare favourably with previous reports

Fig. 4 Differential pulse voltammograms in pH 7.0 ammonium acetate buffer of **a** various control experiments in the fabrication of a Gly-Gly-His modified carbon nanotube electrode and **b** 1 mM Cu^{2+} at hydrogen terminated silicon

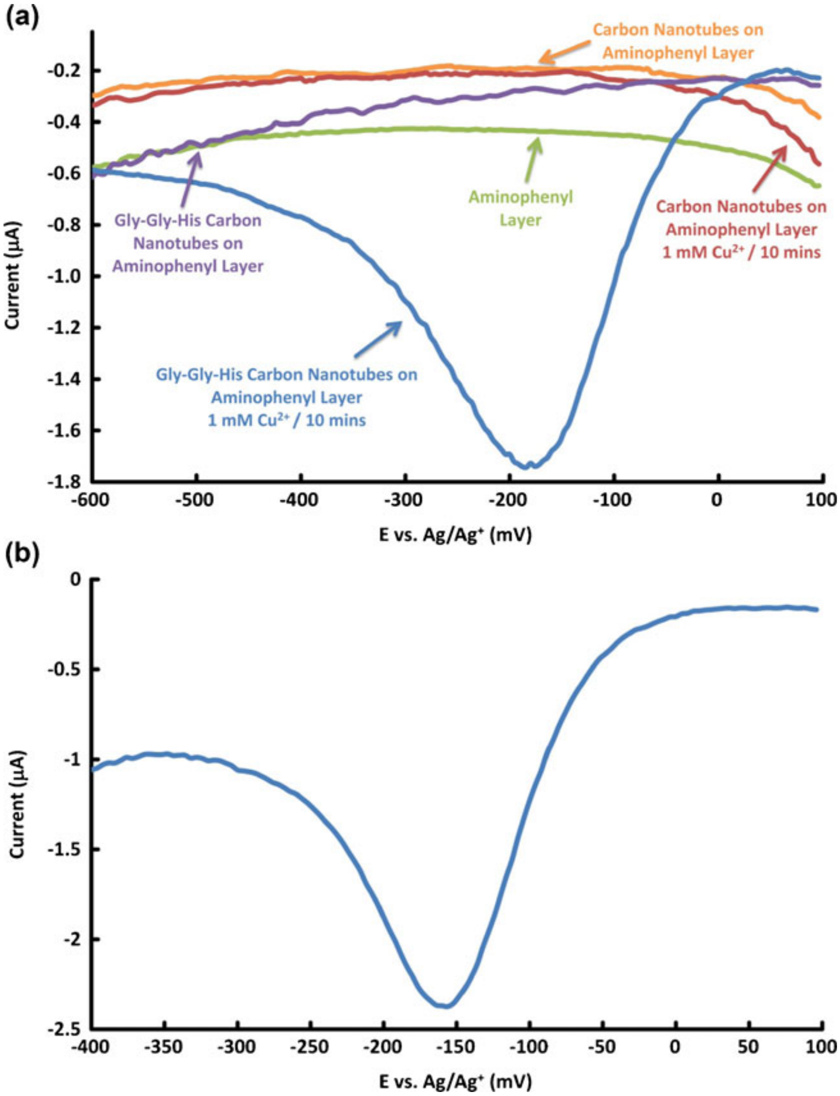

Fig. 5 Calibration curve of the differential pulse voltammetry peak current density of Cu^{2+} at a Gly-Gly-His modified carbon nanotube electrode

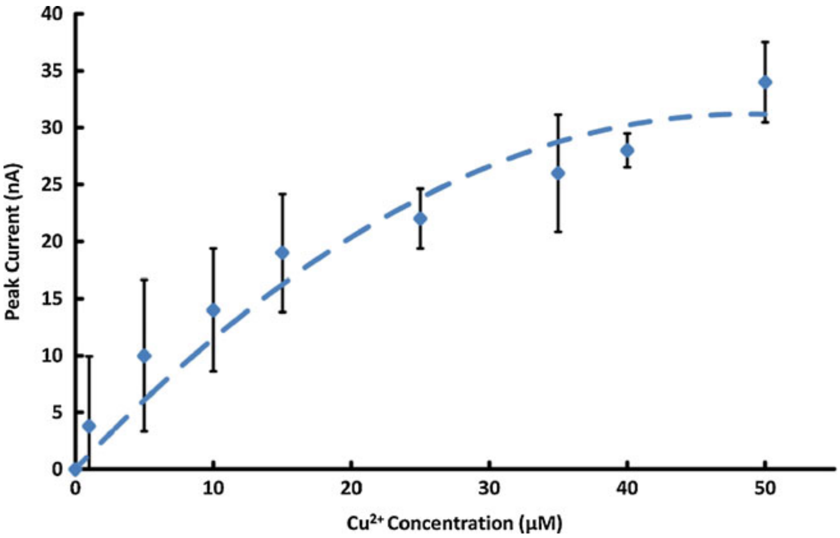

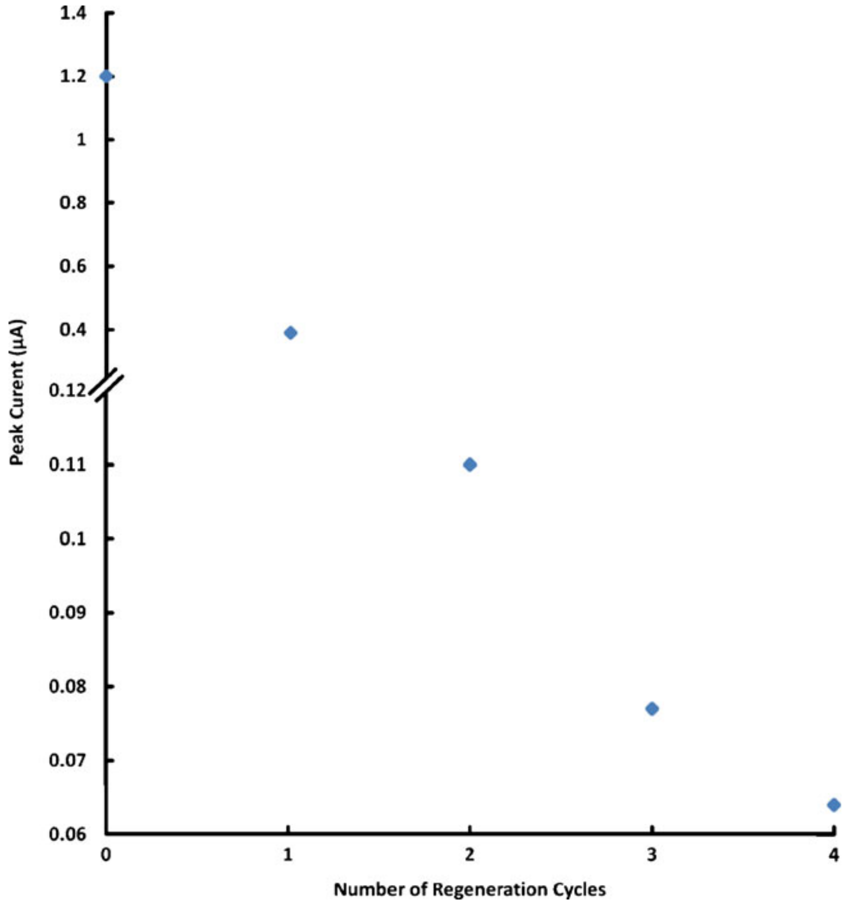

Fig. 6 Plot of the differential pulse voltammatry peak current versus the number of times that an electrode was regenerated in 0.1 M $HClO_4$ after exposure to 1 mM Cu^{2+}

[3, 11–14, 50] where copper detection down to 3 nM was achieved. However, it should be noted that in each of those examples a gold base electrode, capable of delivering significantly greater currents compared to semiconducting silicon were used. Furthermore, the detection limit in this work is sensitive in the range outlined by Australian health guidelines [4–6] and is hence still of relevance for analysis of potable supplies and further opens avenues for simple sampling techniques.

Ideally for field analysis the sensor system could be used for repeated measurements of the copper ion concentration in a series of water samples. Due to the sensor's requirement for copper complexation, the electrode must be regenerated and captured copper ions released from the Gly-Gly-His. This is typically achieved by treatment with 0.1 M $HClO_4$ [3, 12, 13]. To determine the potential for regeneration of the electrode copper ions were accumulated in a 1 mM solution for a period of 10 min and a differential pulse measurement taken. The electrode was then placed in 0.1 M $HClO_4$ for 30 s at open circuit potential. After exposure to the 0.1 M $HClO_4$ no electrochemical behaviour was observed between 100 and −600 mV indicating removal of the accumulated copper ions. This process was repeated and the peak current for successive regenerations measured and plotted in Fig. 6. It can be seen that the peak current significantly decreased for successive regeneration and that after 4 regenerations no redox behaviour was observed. The reduction in current is believed to be due to the harsh acid cleaving the bond between Gly-Gly-His and the carbon nanotube. This is in stark contrast to previous results by Yang et al. [13] who reported regeneration up to 20 times before current degradation. Perchloric acid is an oxidising agent and has been shown to be capable of oxidising nanotubes at room temperature [51]. The oxidation due to perchlorate ions is generally thought to be slow but we speculate that the application of a potential to the substrate may increase the rate of oxidation. This oxidation will occur at the reactive sites in the nanotubes. These sites are at the end of the nanotube where the peptides are also attached. The further oxidisation of the nanotube with the introduction of the perchloric acid will likely see the disruption of the bonding between the nanotube and peptide hence reducing the sensor's capability to detect copper.

This approach to the detection of heavy metal ions is completely generic requiring only a species capable of capturing a metal ion and the attachment of that species to the nanotube. There are many chemistries available to attach moieties to functionalised nanotubes [24, 52, 53]. Once attached, if the species can selectively extract the metal of interest from the matrix being analysed then assuming the metal has multiple oxidation states, the proximity of the electrode facilitates oxidation and/or reduction providing quantitative detection of metal.

4 Conclusion

This work has provided a new method for fabricating a copper ion sensor consisting of a Gly-Gly-His modified single walled carbon nanotube electrode on silicon through the use of an electrografted aminophenyl layer. This new sensor system demonstrated copper ion sensitivity down to 1±6 μM, which is of relevance under current water regulations within Australia. This sensor system is compatible with incorporation of other metal sensitive peptides and work is now underway to detect further metal species in water.

Acknowledgements The authors gratefully acknowledge the support of the South Australian node of the Australian Microscopy & Microanalysis Research Facility (AMMRF) for access to the Kratos Axis Ultra X-ray photoelectron spectrometer.

References

1. Flavel BS, Garrett DJ, Lehr J, Shapter JG, Downard AJ (2010) Electrochim Acta 55:3995–4001
2. Malcik N, Oktar O, Ozser ME, Caglar P, Bushby L, Vaughan A, Kuswandi B, Narayanaswamy R (1998) Sens Actuators B 53:211–221
3. Chow E, Wong ELS, Böcking T, Nguyen QT, Hibbert DB, Gooding JJ (2005) Sens Actuators B 111–112:540–548
4. NHMRC and Agriculture and Resource Management Council of Australia and New Zealand, Australian Water Drinking Guidelines (1996) Inorganic Chemicals: Copper, Fact Sheet No. 49
5. NHMRC and Agriculture and Resource Management Council of Australia and New Zealand, Australian Water Drinking Guidelines (1996) Inorganic Chemicals: Cadmium, Fact Sheet No. 44.
6. Chow E, Hibbert DB, Gooding JJ (2005) Electrochem Commun 7:101–106
7. Bannon DI, Chisolm JJ (2001) Clin Chem 47:1703–1704
8. Liu HW, Jiang SJ, Liu SH (1999) Spectrochim Acta B 54:1367–1375
9. Eksperiandova LP, Blank AB, Makarovskaya YN (2002) X-ray Spectrom 31:259–263
10. Foranzi ES, Zhang H, Chen W, Tao N (2005) Environ Sci Technol 39:1257–1262
11. Liu G, Nguyen QT, Chow E, Böcking T, Hibbert DB, Gooding JJ (2006) Electroanalysis 18:1141–1151
12. Yang W, Gooding JJ, Hibbert DB (2001) Analyst 126:1573–1577
13. Yang W, Chow E, Willet GD, Hibbert DB, Gooding JJ (2003) Analyst 128:712–718
14. Lin M, Cho MS, Choe WS, Lee Y (2009) Biosens Bioelectron 25:28–33
15. White BR, Holcombe JA (2007) Talanta 71:2015–2020
16. Chow E, Hibbert DB, Gooding JJ (2005) Analyst 130:831–837
17. Delamarche E, Michel B, Kang H, Gerber Ch (1994) Langmuir 10:4103–4108
18. Horn AB, Russell DA, Shorthouse LJ, Simpson TRE (1996) J Chem Soc Faraday Trans 92:4759–4762
19. Schoenfisch MH, Pemberton JE (1998) J Am Chem Soc 120:4502–4513
20. Yu J, Shapter JG, Quinton JS, Johnston MR, Beattie DA (2007) Phys Chem Chem Phys 9:510–520
21. Allongue P, Delamar M, Desbat B, Fagebaume O, Hitmi R, Pinson J, Saveant J–M (1997) J Am Chem Soc 119:201–207
22. Garrett DJ, Flavel BS, Shapter JG, Baronian KHR, Downard AJ (2010) Langmuir 26:1848–1854
23. Flavel BS, Yu J, Shapter JG, Quinton JS (2008) Electrochim Acta 53:5653–5659
24. Flavel BS, Yu J, Shapter JG, Quinton JS (2007) J Mater Chem 17:4757–4761
25. Valentini F, Amine A, Orlanducci S, Terranova ML, Palleschi G (2003) Anal Chem 75:5413–5421
26. Stetter JR, Maclay GJ (2008) Adv Micro Nanosys 357.
27. Li J, Lu Y, Ye Q, Cinke M, Han J, Meyyappan M (2003) Nano Lett 3:929–938
28. Zhou Y, Yang H, Chen H-Y (2008) Talanta 76:419–423
29. Wang J (2005) Electroanalysis 17:7–14
30. Liu L, Zhang F, Xi F, Lin X (2008) Biosens Bioelectron 24:306–312
31. Ly SY (2008) Talanta 74:1635–1641
32. Zhou H, Yang W, Sun C (2008) Talanta 77:366–371
33. Tu W, Lei J, Ju H (2009) J Euro Chem A 15:779–784
34. Upadhyayula VKK, Ghoshroy S, Nair VS, Smith GB, Mitchell MC, Deng S (2008) Res Lett Nanotech 156358
35. Valentini F, Biagiotti V, Lete C, Palleschi G, Wang J (2007) Sens Actuators B 128:326–333
36. Zhang Y, Kang T-F, Wan Y-W, Chen SY (2009) Microchim Acta 165:307–311
37. Flavel BS, Yu J, Shapter JG, Quinton JS (2007) Carbon 45:2551–2558
38. Gooding JJ, Wibowo R, Lie J, Yang W, Losic D, Orbons S, Mearns FJ, Shapter JG, Hibbert DB (2003) J Am Chem Soc 125:9006–9007
39. Nan X, Gu Z, Liu Z (2002) J Colloid Interface Sci 245:311–318
40. Allongue P, Henry de Villeneuve C, Pinson J, Ozanam F, Chazalviel JN, Wallart X (1998) Electrochim Acta 43:2791–2798
41. Aswal DK, Koiry SP, Jousselme B, Gupta SK, Palacin S, Yakhmi JV (2009) Phys E 41:325–344
42. Lyskawa J, Belanger D (2006) Chem Mater 18:4755–4763
43. Brooksby PA, Downard AJ (2004) Langmuir 20:5038–5045
44. Moulder JF, Stickle WF, Sobol PE, Bomben KD, Handbook of X-ray Photoelectron Spectroscopy, Perkin Elmer Corporation.
45. Yu J, Losic D, Marshall M, Böcking T, Gooding JJ, Shapter JG (2006) Soft Matter 2:1081–1088
46. Kariuki JK, McDermott MT (2001) Langmuir 17:5947–5951
47. Binner J, Zhang Y (2001) J Mater Sci Lett 20:123–126
48. Bi X, Yang K-L (2007) Langmuir 23:11067–11073
49. Nishizawa M, Sunagawa T, Yoneyama H (1997) Langmuir 13:5215–5217
50. Yang W, Jaramillo D, Gooding JJ, Hibbert DB, Zhang R, Willet GD, Fisher KJ (2001) Chem Commun 1982–1983.
51. Hernadi K, Siska A, Thien-Nga L, Forro L, Kiricsi I (2001) Solid State Ionics 141–142:203–209
52. Yu J, Matthew S, Flavel BS, Johnston MR, Shapter JG (2008) J Am Chem Soc 130:8788–8796
53. Tune DD, Flavel BS, Quinton JS, Ellis AV, Shapter JG (2010) Sol Mat 94:1665–1672

– This page intentionally left blank –

2.6 Additional Scientific Publications

2.6.7 *Comparison of Double-Walled with Single-Walled Carbon Nanotube Electrodes by Electrochemistry*

K. E. Moore, **B. S. Flavel**, A. V. Ellis, J. G. Shapter

Carbon 49 (2011) 2639–2647

DOI: 10.1016/j.carbon.2011.02.048

Abstract

Double-walled carbon nanotubes (DWCNTs) were selectively functionalised by treatment with concentrated nitric and sulphuric acid, resulting in carboxylated outer and pristine inner tube constituents. The functionalised DWCNTs were then incorporated into two types of pre-existing carbon nanotube (CNT) electrode platforms, and the performance of each was compared to single-walled carbon nanotubes (SWCNTs). To make the CNT electrode platforms DWCNTs were covalently bound to fluorinated tin oxide glass (FTO) or electrografted aminophenyl tether layers on silicon. The performance of single- compared to double-walled CNTs on FTO or silicon supported electrodes was then determined through electrochemical methods, using the redox probes, ferrocene and ruthenium hexaamine, respectively. The DWCNTs showed an improved heterogeneous rate constant. This improvement was attributed to the protection of the electronic properties of the inner wall of the DWCNT during the chemical modification and suggests that DWCNTs may offer a useful alternative to SWCNTs in future electronic devices.

Contribution

K.E.M and J.G.S conceived the idea for the project. K.E.M performed the experiments and wrote the paper. All authors contributed to the scientific interpretation and evaluation of the manuscript.

– This page intentionally left blank –

CARBON 49 (2011) 2639–2647

available at www.sciencedirect.com

journal homepage: www.elsevier.com/locate/carbon

Comparison of double-walled with single-walled carbon nanotube electrodes by electrochemistry

Katherine E. Moore, Benjamin S. Flavel, Amanda V. Ellis, Joseph G. Shapter *

Flinders Centre for Nanoscale Science and Technology, School of Chemical and Physical Sciences, Flinders University, Sturt Road, Bedford Park, Adelaide, SA 5001, Australia

ARTICLE INFO

Article history:
Received 21 January 2011
Accepted 17 February 2011
Available online 22 February 2011

ABSTRACT

Double-walled carbon nanotubes (DWCNTs) were selectively functionalised by treatment with concentrated nitric and sulphuric acid, resulting in carboxylated outer and pristine inner tube constituents. The functionalised DWCNTs were then incorporated into two types of pre-existing carbon nanotube (CNT) electrode platforms, and the performance of each was compared to single-walled carbon nanotubes (SWCNTs). To make the CNT electrode platforms DWCNTs were covalently bound to fluorinated tin oxide glass (FTO) or electrografted aminophenyl tether layers on silicon. The performance of single- compared to double-walled CNTs on FTO or silicon supported electrodes was then determined through electrochemical methods, using the redox probes, ferrocene and ruthenium hexaamine, respectively. The DWCNTs showed an improved heterogeneous rate constant. This improvement was attributed to the protection of the electronic properties of the inner wall of the DWCNT during the chemical modification and suggests that DWCNTs may offer a useful alternative to SWCNTs in future electronic devices.

1. Introduction

Carbon nanotubes (CNTs) have emerged as a promising new class of electronic materials due to their nanoscale dimensions and outstanding properties, which include the ability to conduct a current density three orders of magnitude higher than typical conductors, such as copper and aluminium [1], and the ability to conduct electrons ballistically [2–4]. Such unique properties are already seeing CNTs incorporated into many nanoscale electronic devices such as transistors [5,6], logic gates [7,8] and electrodes [9–11]. Their incorporation into these devices relies upon a high degree of control and manipulation, a process which is currently achieved through methods such as functionalisation [12,13], polymer wrapping [14,15] or the use of surfactants [16,17]. Whilst these methods are effective at attaining control over the nanotubes, modification of the unique physical properties occurs in each case, leading to an undesirable loss of conductivity [18].

Traditionally, single-walled carbon nanotubes (SWCNTs) have been used for device fabrication. However it has recently been suggested that double-walled carbon nanotubes (DWCNTs) may offer a superior alternative [19,20]. It has been proposed that upon chemical modification, the outer tube will act as a protective sheath, hence preserving the electronic properties of the inner tube. Selective functionalisation has been observed experimentally by Ellis and Bubendorfer [21] and also by Brozena et al. [22] who confirmed selective outer-wall functionalisation of DWCNTs with Raman spectroscopy. Several groups are now taking advantage of this approach. For example, Hayashi and co-workers [19,23] have utilised selectively functionalised DWCNTs for the purpose of self-assembling CdSe quantum dots onto the nanotubes for use in electronic and biomedical applications.

---

* *Corresponding author*: Fax: +61 8 8201 2905.
E-mail address: joe.shapter@flinders.edu.au (J.G. Shapter).

0008-6223/$ - see front matter © 2011 Elsevier Ltd. All rights reserved.
doi:10.1016/j.carbon.2011.02.048

The two concentric graphene-like tubes making up the coaxial arrangement of DWCNTs are each capable of exhibiting metallic or semi-conducting character and have been found to possess a range of interesting electrical [24], thermal [25] and mechanical [26] properties. For example, Saito et al. [27] have suggested that upon arrangement of a semi-conducting and metallic nanotube, it would be possible to create molecular wires covered by an insulator or molecular capacitors for use in memory devices.

Furthermore, the high electrochemically accessible surface area of CNT arrays, combined with their high electronic conductivity and useful mechanical properties, make CNTs an attractive material for use in electrochemical sensors [28]. Recently, there have been many examples of new electrode platforms, which take advantage of the superior electrical properties of CNTs compared to typical macroscale materials. For example, Gooding et al. [29] have developed a CNT-based enzymatic electrochemical biosensor by covalently attaching protein decorated SWCNTs to a cysteamine modified gold electrode. Bissett and Shapter [10] have reported the production of vertically aligned SWCNT arrays covalently bonded to FTO glass for use in solar cells.

While CNTs can be attached to many surfaces [29–31], attachment to silicon based electrode devices has attracted much attention as it facilitates incorporation into current silicon-based technology. Pioneering this field was Yu et al. [9] who developed a silicon based electrode surface consisting of SWCNTs covalently bonded to silicon via an ester linkage. The electron transfer rate for a ferrocene redox solution was determined to be 4.54×10^{-3} cm s^{-1} [32], which is comparable to platinum, glassy carbon and polypropylene composite graphite (CPP) [9], indicating that such a surface would further applications in nano-electronic, opto-electronic and biosensor devices. Yu et al. [33] then went onto develop light harvesting antenna and multi-bit information storage by chemically modifying the immobilised CNTs with ruthenium porphyrin and ferrocene methanol.

While the electrodes of Yu et al. [9,33] show great potential in the field of nanoscale electronic devices, their long term stability and application to 'real world' conditions is limited by the attachment chemistry. Ester linkages are easily made and reasonably stable for a short period of time, however the bond can easily be cleaved in water. Therefore, only electrode platforms with applications in organic solvents are possible. Clearly this means that many desirable applications such as biosensor systems and water quality sensing are not feasible. To solve this problem Flavel et al. [11] have utilised aryl-diazonium chemistry to fabricate an aminophenyl tether layer on a silicon substrate which is capable of forming a stable bond with CNTs and allows for use in aqueous environments.

In this work we demonstrate that DWCNTs are a superior choice of material for incorporation into electronic devices, compared to their single-walled counterparts. Using the previously reported oxidative acid method for functionalising SWCNTs [12], DWCNTs were functionalised and incorporated into two types of CNT-based electrochemical electrodes; a fluorinated tin oxide glass (FTO)- and a silicon–aminophenyl-CNT electrode previously reported for SWCNTs by Bissett and Shapter [10] and Flavel et al. [11], respectively. Electrochemical kinetic measurements were performed to obtain the electron transfer rate, which allowed a comparison with electrodes fabricated with SWCNTs.

2. Experimental

2.1. CNT functionalisation

Y–Ni catalyst assisted DC arc discharge synthesised SWCNTs (Carbon Solutions Inc., CA, USA, P2-SWCNT) and CVD produced DWCNTs (ShenZhen Nanotech Port Co., Shenzhen, China) were purchased. The CNTs were then functionalised with carboxylic acid groups by ultrasonication (Elma S30 H Ultrasonic) in a 3:1 v/v solution of 98% H_2SO_4 and 70% HNO_3 (Sigma–Aldrich) at a nanotube concentration of 1 mg mL^{-1} for 8 h and 2.5 h at 0 °C for SWCNTs and DWCNTs, respectively. Acid oxidation was then quenched by addition of 1 L of MilliQ water, filtration through a 0.4 μm HTTP polycarbonate filter (Adelab Scientific, Thebaton, SA) and further washing with MilliQ water until a filtrate of pH 5 was achieved. The filtered nanotubes were then dried in air for 24 h in an 80 °C oven. Once dry, the nanotubes were suspended in a solution of dimethylsulphoxide (DMSO) (99.9%, ACS Spectroscopic Grade, Sigma–Aldrich) containing 0.2 mg mL^{-1} CNTs, 0.25 mg mL^{-1} *N*,*N*′-dicyclohexylcarbodiimide (DCC) (99% Fluka Production GmbH) and 0.14 mg mL^{-1} dimethylaminopyridine (DMAP) (99% Sigma–Aldrich). The nanotubes were dispersed by sonication for 1 h and then stored under nitrogen.

2.2. Preparation of FTO–CNT electrodes

Prior to use, fluorinated tin oxide glass (TCO22-15, Solaronix SA, 15 Ω/square) was ultrasonically cleaned in acetone (99.5%, Merck) for 30 s, thoroughly rinsed with MilliQ water and dried under nitrogen gas. The surfaces were then hydroxylated by treatment with 5:1:1 v/v NH_4OH:H_2O_2:MilliQ water (AR Grade, Sigma–Aldrich) followed by 5:1:1 v/v HCl:H_2O_2:MilliQ water (AR Grade, Sigma–Aldrich), with each step performed for 20 min at 80 °C, as shown in Fig. 1(a) – step 1. The hydroxylated FTO glass substrates were then incubated in the prepared CNT solution for 24 h at 80 °C to afford a vertically aligned CNT-FTO surface (step 2). Following attachment, the FTO-CNT surface was thoroughly rinsed with propan-2-ol and dried under nitrogen gas.

2.3. Preparation of silicon-aminophenyl-CNT electrodes

Prior to use, highly boron doped, p-type silicon (1 0 0) (Siltronix France, $\Omega = 0.001$–$0.003\ \Omega$) was ultrasonically cleaned in acetone, thoroughly rinsed with MilliQ water and dried under nitrogen gas. The silicon was then treated with hydrofluoric acid (40%, Sigma–Aldrich) to remove the native oxide layer and hydrogenate the underlying surface, as shown in Fig. 1(b) – step 1. The silicon wafer was then washed with MilliQ water and dried under nitrogen gas. The *p*-aminobenzene diazonium cation was prepared by adding 5 mL of 20 mmol L^{-1} *p*-phenylenediamine (Sigma–Aldrich) in 1 mol L^{-1} hydrochloric acid to an equal volume of 20 mmol L^{-1} sodium nitrite (99%,

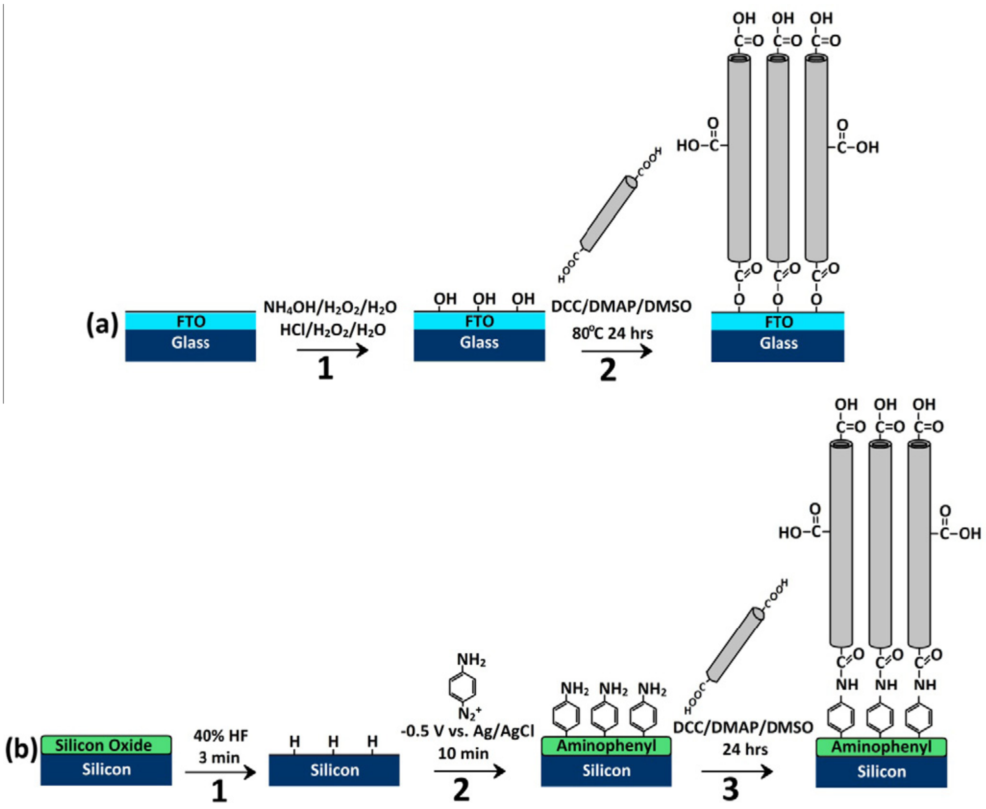

Fig. 1 – Schematic of (a) FTO-CNT and (b) Si-aminophenyl-CNT electrode fabrication.

Sharlau Chemie) at room temperature. This solution was then used to graft aminophenyl films to the H-terminated silicon substrate by applying a potential of −0.5 V vs. Ag/AgCl for 10 min (step 2). The substrate was then thoroughly washed with MilliQ water and dried under nitrogen gas. The modified silicon surface was then immersed in CNT solution for 24 h, after which, it was rinsed with propan-2-ol (95%, AR Grade, Merck) and dried under nitrogen (step 3).

2.4. *Atomic force microscopy*

AFM tapping mode images were taken in ambient conditions with a multimode head and a NanoScope V controller (Digital Instruments, Veeco, Santa Barbara, USA) using silicon cantilevers (Mikromasch, USA) with a fundamental resonance frequency between 250 and 400 kHz. Topographic height and phase images were obtained simultaneously with feedback controls optimised for each sample. All images represent flattened data using the NanoScope version 8.0 (Digital Instruments, USA) software package. Samples for length determination were prepared by spin coating acetone dispersed DWCNTs at a concentration of 0.05 mg mL^{-1} onto freshly cleaved mica surfaces at 2000 rpm. Length determination of the DWCNTs was carried out using the NanoScope software.

2.5. *Confocal Raman spectroscopy*

Raman spectra and spectral images were taken using an *alpha300R* (WiTEC, Germany) microscope operating in Raman mode, equipped with a 532 nm laser ($E_{laser} = 2.33$ eV) and a 40× objective (Numerical Aperture 0.6). Broad spectra (0–3200 cm^{-1}) and high resolution (0–500 cm^{-1}) spectra were obtained with an integration time of 5 and 15 s, respectively. In both cases, the reported measurement represents the average of 10 different locations.

Three 10 × 10 μm confocal images were obtained from each surface at an integration time of 0.2 s and the reported data is indicative over the whole surface. The spectral images were analysed using the WiTEC Project software version 2.04.

2.6. *Electrochemistry*

All electrochemistry measurements were taken using a BAS100B Electrochemical Analyser (Bioanalytical Systems Inc., USA), operating in cyclic voltammetry mode. The SWCNT- and DWCNT-based electrodes were mounted in the electrochemical cell exposing a 0.26 cm^2 circular area of surface to the cell solution. The CNT modified surface formed the working electrode, with platinum mesh and silver/silver chloride used as the counter and reference electrodes, respectively.

Two electrolyte solutions were used throughout the experiments, a ferrocene solution containing 0.1 mol L^{-1} tetrabutylammonium perchlorate (TBAP) (Fluka, electrochemical grade) and 1 mmol L^{-1} ferrocene (98%, Sigma–Aldrich) in acetonitrile, and a ruthenium hexaamine solution containing 1 mmol L^{-1} ruthenium (III) hexaamine chloride (Sigma–Aldrich) in pH 7.5 potassium phosphate buffer. All data was collected using BAS100W software version 2.3 (Bioanalytical

Systems Inc., USA) with data presented representing a Fourier transform of the raw signal. Two electrochemical experiments were carried out, one with the Si-aminophenyl-CNT electrodes using ruthenium hexaamine solution and one using the FTO-CNT electrodes using ferrocene solution. For the ruthenium hexaamine redox probe, the potential was swept from 200 to −600 mV vs. Ag/AgCl at scan rates of 20–1000 mV s^{-1}. For the ferrocene redox probe, the potential was swept from 0 to 1000 mV vs. Ag/AgCl at scan rates of 20–1000 mV s^{-1}.

3. Results and discussion

Valuable insights into the physical and electronic properties of SWCNTs and DWCNTs can be obtained by measurement of their radial breathing modes (RBMs) with Raman spectroscopy. In the case of multi-walled or large diameter CNTs, the Raman cross section is small and the detection of RBMs is quite difficult [34]. However due to the relatively small diameter (<2 nm) of the DWCNTs used here, resonance RBM vibrations can be observed. Fig. 2(a) shows the Raman spectrum between 100 and 500 cm^{-1} of DWCNTs functionalised in concentrated acid for varying amounts of time where the RBM vibrations can clearly be seen. For comparison, the inset of Fig. 2(b) shows the RBM spectrum of SWCNTs functionalised for 8 h in concentrated acid. While the spectra look similar, there are clear differences between the spectrum of single- and double-walled CNTs. It can be seen that the RBM frequencies of DWCNTs occur over a much wider Raman frequency range (120–400 cm^{-1}) and display many more peaks than that of SWCNTs. This can be explained by considering that each RBM peak corresponds to a tube of different diameter and as such, DWCNTs, which have a larger diameter distribution, will have more RBM constituent peaks. It can also be observed that the DWCNT RBM spectrum consists of two main components corresponding to the outer (120–220 cm^{-1}) and inner (230–400 cm^{-1}) tube pairs, respectively. After acid oxidation, the intensity of the peaks centred around 150 cm^{-1}, which correspond to the outer walls of the DWCNT, were observed to decrease. However, the peaks corresponding to inner wall nanotubes around 260 cm^{-1} were found to persist after 1.5 and 2.5 h of acid treatment. It should be noted that the peak at 300 cm^{-1} in the pristine sample disappears after 1.5 h of acid treatment. This peak is believed to correspond to impurity small diameter, highly reactive SWCNTs present in the CVD produced sample. The retention of the inner tubes' RBMs and the simultaneous disappearance of those corresponding to the outer walls, strongly suggests that outer wall selectivity of functionalisation has occurred. This has been observed previously [21,22,35] and is attributed to the acid being unable to attack the intensely hydrophobic interior of the tubes.

It has previously been observed that CNT functionalisation by concentrated acid treatment results in a reduction of average tube length [12]. This is due to the combination of concentrated acid and localised surface sonication at defects sites along the CNTs' side walls, which are opened up and cleaved over treatment time. Marshall et al. [12] have previously used atomic force microscopy (AFM) to investigate the relationship between functionalisation time and SWCNT length, where a linear relationship was found. However, to our knowledge the average length of DWCNTs with varying functionalisation has not previously been reported, and so was investigated in this work.

The average length of pristine and functionalised DWCNTs was determined using atomic force microscopy. Several images were obtained for each sample, some of which are shown in Fig. 3. Immediately it can be seen that the sample functionalised for 1.5 h (a) shows less dispersed, longer tubes

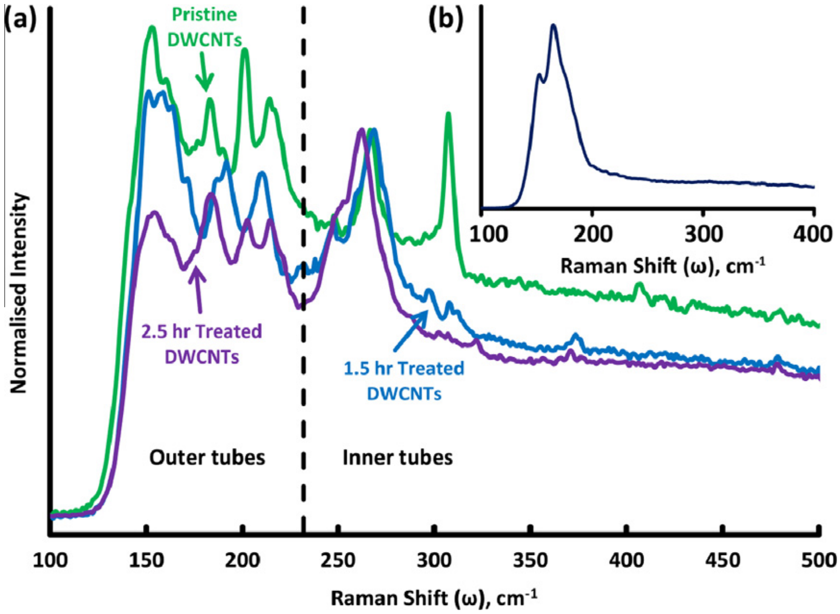

Fig. 2 – Raman spectra showing the low frequency RBM vibrations of (a) pristine DWCNTs and DWCNTs after 1.5 and 2.5 h of functionalisation time and (b) SWCNTs functionalised for 8 h. The DWCNT spectrum has been normalised to the peak at 260 cm^{-1}.

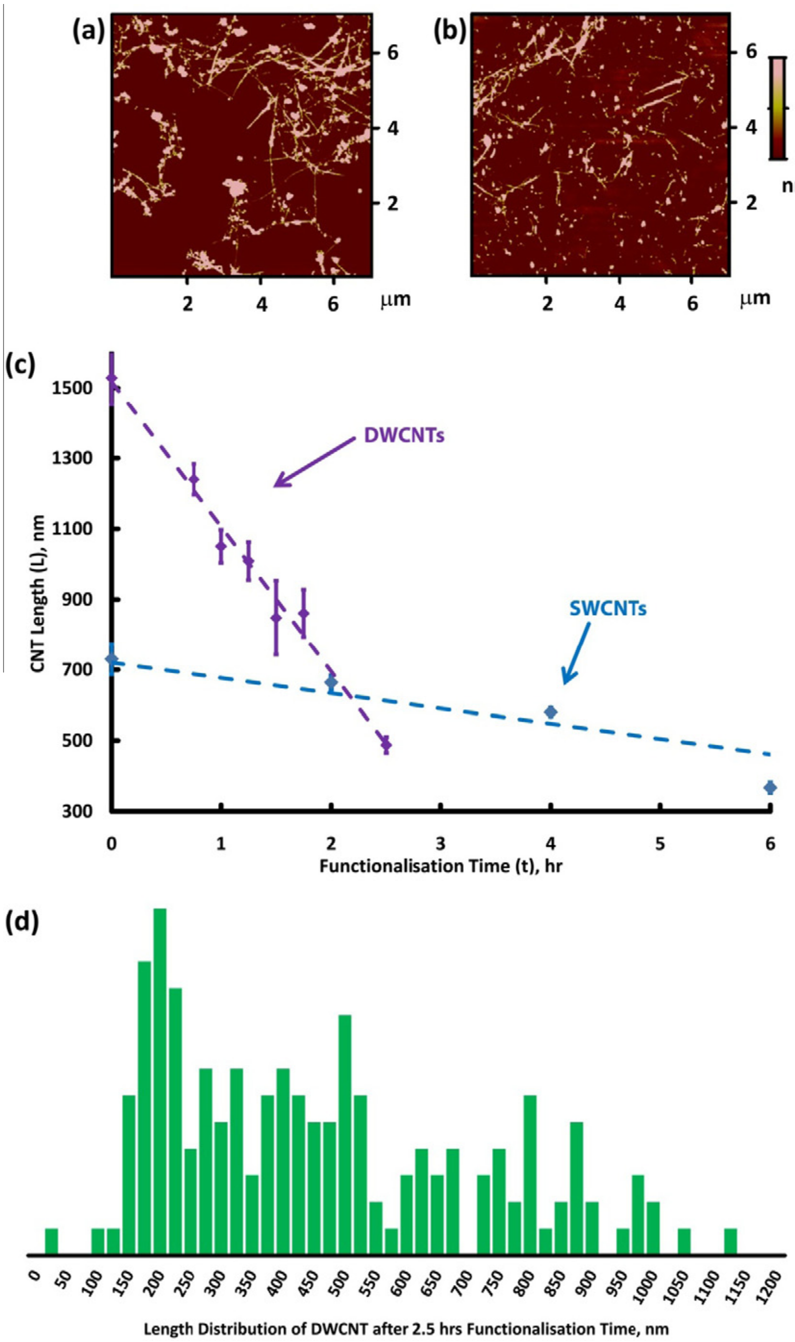

Fig. 3 – AFM images of DWCNTs functionalised for (a) 1.5 h and (b) 2.5 h. (c) Mean CNT length as a function of acid treatment time for DWCNTs, as determined in this work, and for SWCNTs, as determined in [12] and (d) length distribution of DWCNTs after 2.5 h of functionalisation time.

than the sample exposed for 2.5 h (b). Fig. 3(c) shows the measured length of DWCNTs with functionalisation time compared to that of SWCNTs determined by Marshall et al. [12]. The average length of the DWCNTs before treatment was determined to be 1.53 µm, which after acid treatment for 2.5 h reduced to 480 nm. A clear linear trend between the length of the CNTs and functionalisation time can also be seen, a trend which has also been observed for SWCNTs. However, the linear trend observed by Marshall et al. [12] had a considerably different slope to that observed in this study. From the data it can be concluded that DWCNTs are much more reactive than their single-walled counterparts. This may be due to the large number of defects within the DWCNT lattice, which occur commonly for chemical vapour deposition (CVD) grown MWCNTs [36,37]. The SWCNTs measured by Marshall et al. [12] were produced using the arc discharge method, which is known to produce high quality SWCNTs with few defects [38].

It can be observed in Fig. 3(d) that a distribution of nanotube lengths exists for 2.5 h functionalised DWCNTs, with

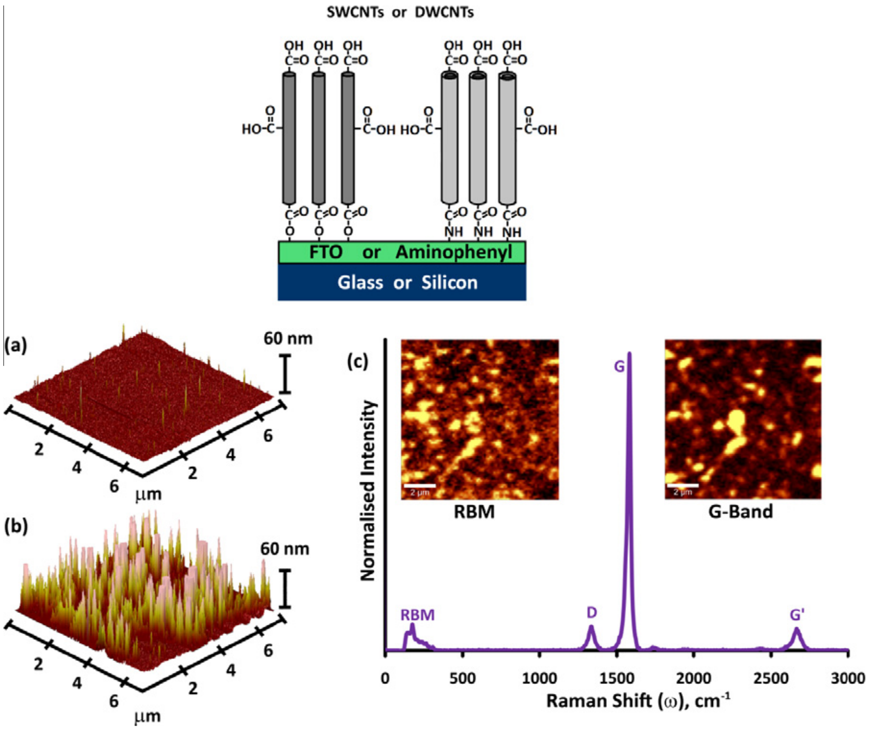

Fig. 4 – Summary of CNT substrate characterisation (a) 3D AFM image of an unmodified aminophenyl substrate, (b) 3D AFM image after modification with SWCNT and (c) Raman spectrum of FTO surfaces reacted with DWCNTs. The inset shows the RBM and G-band intensity maps of each respective surface.

an average length of 480 nm and a maximum length of 1.15 µm. The distribution of lengths has a log–normal relationship, which is in agreement with previous work introducing carboxyl functionality into SWCNTs [29,39].

Two different types of samples were prepared to assess the electrochemical performance of SWCNT compared to DWCNT. One sample (on FTO) was prepared to confirm that both types of the nanotubes can act as electrochemical electrodes, while the second sample (on Si) was used to isolate the observed electron transport in the nanotubes only. Both samples were characterised using AFM and Raman spectroscopy to demonstrate that nanotubes were present on the substrates. Fig. 4 shows a summary of the sample characterisations with the full set of data for both substrates and both types of nanotubes provided in Supplementary material. Fig. 4(a) shows an atomic force microscopy image of an electrodeposited aminophenyl layer film on silicon. The layer is relatively smooth and homogenous, and should have a thickness of 4–6 nm, as determined previously by Flavel et al. [11]. Fig. 4(b) shows a 3D AFM image of an aminophenyl layer after reaction with SWCNTs. It can be seen in that the surface has become considerably rougher, due to the presence of CNTs. The ‘saw tooth’ like topography is characteristic of vertical alignment of CNTs and has been observed previously for a range of different surfaces [11,31,33,40,41].

Fig. 4(c) shows the hydroxylated FTO surface after incubation in solution containing DWCNTs and coupling promoters (DCC and DMAP). From the spectra, it is clear that the nanotubes have been successfully attached to the surface, as signature nanotube peaks are present, such as the radial breathing modes (RBMs) (centred around 200 cm^{-1}) and G (Graphitic) (1600 cm^{-1}) vibrational modes. The confocal images (inset of Fig. 4(c)) correspond to the RBM and G-band intensity maps, where bright and dark regions correspond to high and low Raman intensity, respectively. From these images it is therefore possible to determine where CNTs reside on the surface [10,42–44] and it is clear that a high coverage has been obtained.

The electrochemical performance of the FTO and silicon electrodes with and without the addition of CNTs was tested using cyclic voltammetry. For the hydroxylated FTO surfaces, ferrocene solution containing 0.1 mol L^{-1} tetrabutylammonium perchlorate (TBAP) and 1 mmol L^{-1} ferrocene in acetonitrile was used for all measurements. Fig. 5(a) shows cyclic voltammograms at 0.1 V s^{-1} for hydroxylated FTO glass before and after incubation in CNT solutions. For the unmodified hydroxylated FTO surface, oxidation and reduction peaks can be observed, with a peak-to-peak separation (ΔE_p) of 517 mV indicating that electron transfer is occurring between the redox probe and electrode surface. Upon covalent attachment of both SWCNTs and DWCNTs, ΔE_p decreased to 391 and 366 mV, respectively. As the peak-to-peak separation is a sign of how quickly the redox probe is exchanging electrons with the working electrode surface, with a smaller ΔE_p indicating faster redox, it can be seen that the addition of both single- and double-walled CNTs has improved the electrode. Furthermore, this improvement is slightly greater in the case of DWCNTs.

In Fig. 5(b) the electrochemical performance of the silicon surfaces, unmodified and modified with aminophenyl and CNTs, was assessed in an aqueous medium with the $Ru(NH_3)_6^{+3/+2}$ redox couple in pH 7.5 potassium phosphate

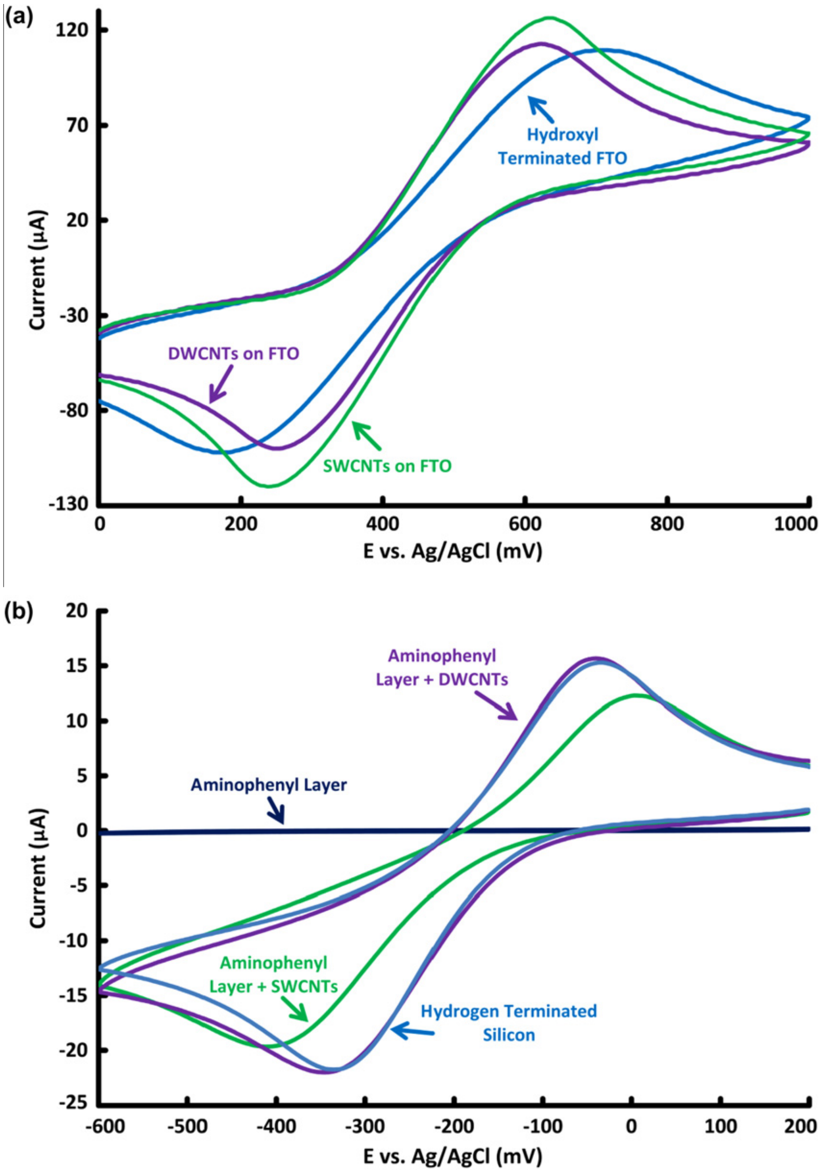

Fig. 5 – Cyclic voltammograms of (a) FTO surfaces modified as indicated in a solution of 1 mmol L^{-1} $Fe(C_5H_5)_2$ in 0.1 mol L^{-1} TBAP–CH_3CN and (b) silicon surfaces modified as indicated in a solution of 1 mmol L^{-1} $Ru(NH_3)_6^{+3/+2}$ in pH 7.5 potassium phosphate buffer at a scan rate of 100 mV s^{-1}.

buffer solution. For the unmodified hydrogen terminated silicon surface the response is quasi-reversible with $\Delta E_p = 290$ mV. The aminophenyl layer was then electrografted and the surface was passivated with no observable oxidation or reduction peaks, indicating that $\Delta E_p > 800$ mV. This was expected as it has been previously shown that the multilayer aminophenyl film blocks electron transport between the surface and the redox probe [11,45,46].

Upon incubation of the surfaces with single- and double-walled CNT solutions the electron transfer capabilities of the substrates were restored and redox current was again observed. The Si-aminophenyl-CNT surfaces gave ΔE_p values of 448 and 306 mV for single- and double-walled tubes, respectively. From the peak-to-peak separations, the addition of DWCNTs fully restored the electron transport capabilities of the surface. However in the case of the SWCNT electrode, ΔE_p is larger than that of the hydroxylated silicon, indicating that while the electron transfer capabilities are restored, they are not restored to the original value of the silicon surface.

The standard heterogeneous rate constant for a quasi-reversible system can be calculated for each scan rate using the measured ΔE_p values and the method developed by Nicholson [47,48]. This method involves determining the dimensionless kinetic parameter, ψ, which can be determined by interpolating/extrapolating the values of ΔE_p from the data provided by Nicholson [47]. The corresponding rate constant can be calculated from the following equation:

$$\psi = \frac{\gamma^{\alpha} k^{o}}{\sqrt{\pi a D_o}} \text{ where } \gamma = \left(\frac{D_o}{D_R}\right)^{1/2} \text{ and } a = \frac{nFv}{RT}$$

where k^o is the standard heterogeneous rate constant (cm s^{-1}), D_o and D_R are the diffusion coefficients of the oxidised and reduced states ($cm^2 s^{-1}$), α is the transfer coefficient and the remaining terms have their usual significance. In order to determine the standard heterogeneous rate constants for the FTO-based electrodes, the diffusion coefficient for both redox states of ferrocene are assumed to be equivalent at $D = 2.5 \times 10^{-5}$ $cm^2 s^{-1}$ [39] and the electron transfer coefficient $\alpha = 0.5$ [47]. Similarly, the diffusion coefficient for both redox states of $Ru(NH_3)_6^{+3/+2}$ are assumed to be equivalent at $D = 3.89 \times 10^{-6}$ $cm^2 s^{-1}$ [11].

Table 1 shows the calculated standard heterogeneous rate constants for hydroxylated FTO and hydrogenated silicon surfaces before and after modification. The rate constants were averaged over the 20, 50 and 100 $mV s^{-1}$ voltammograms in each case. The rate constant of hydroxylated FTO glass was determined to be 4.64×10^{-4} $cm s^{-1}$. After the surface was incubated in CNT solutions, the rate constants were 5.76×10^{-4} and 6.03×10^{-4} $cm s^{-1}$ for single- and double-walled CNTs, respectively. While the rate for the covalently bound DWCNTs is slightly faster than that of the SWCNTs, the difference between the two values is negligible.

The rate constant of hydrogenated silicon was determined to be 3.48×10^{-4} $cm s^{-1}$. After electrografting of the surface with aminophenyl and incubation in CNT solution, the rate constants were 1.99×10^{-4} and 3.76×10^{-4} $cm s^{-1}$ for single- and double-walled CNTs, respectively. This result is evidence that the DWCNT electrode is superior with a rate constant almost twice that of the SWCNT electrode. The slower electron transfer rate of the SWCNT electrode with respect to the hydrogen terminated silicon, has previously been attributed to charge transfer resistance arising from the aminophenyl layer [11]. However in the case of the DWCNT electrode, no resistance was observed.

While the FTO electrodes showed no difference in the performance of the single- and double-walled CNTs as seen in Table 1, a significant difference was observed for the electrodeposited aminophenyl silicon electrodes. In the case of the FTO-CNT electrodes, redox reactions can still occur at areas of exposed SnO and so the observed current is not limited to electron transfer with just the CNTs. The silicon-aminophenyl electrodes however, have electron blocking properties at the surface and so redox only occurs at areas where there are CNTs, which restore the electron transfer properties. This means that the observed current must be transported through the attached CNTs and so provides a direct comparison of the performance of single- and double-walled CNTs without other competing transport processes. Clearly, as seen in Table 1, the electron transport rates for the DWCNTs are close to double those of SWCNT demonstrating that double wall tubes do provide a more effective electron transport medium compared to single-walled tubes. This result shows the incorporation of DWCNTs into existing CNT technologies can improve performance, due to superior electron transport through the inner tube constituent.

Table 1 – Standard heterogeneous rate constants for the Fc or $Ru(NH_3)_6^{+3/+2}$ redox couple at FTO and silicon surfaces, respectively, unmodified and modified with SWCNTs and DWCNTs.

Sample	k^o ($cm s^{-1}$)	Error ($cm s^{-1}$)
FTO	4.64×10^{-4}	$\pm 6.09 \times 10^{-5}$
FTO-SWCNT	5.76×10^{-4}	$\pm 5.61 \times 10^{-5}$
FTO-DWCNT	6.03×10^{-4}	$\pm 5.89 \times 10^{-5}$
Si	3.48×10^{-4}	$\pm 1.76 \times 10^{-5}$
Si-aminophenyl-SWCNT	1.99×10^{-4}	$\pm 2.81 \times 10^{-5}$
Si-aminophenyl-DWCNT	3.76×10^{-4}	$\pm 1.32 \times 10^{-5}$

4. Conclusion

This work has demonstrated that DWCNTs are a superior conducting material for use in electrochemical electrodes. DWCNTs were selectively functionalised and incorporated into two types of pre-existing CNT electrodes. Using electrochemical methods the DWCNT electrodes were found to exhibit superior electron transfer kinetics compared to that of SWCNTs. Due to their more complex structure, they provide an improved electron pathway after chemical modification, enabling faster electron kinetics with a solution redox probe.

Acknowledgements

K.M. wishes to thank the Sir Ross and Keith Smith Honours Scholarship Fund. This work is supported by the Australian Microscopy and Microanalysis Research Facility (AMMRF).

Appendix A. Supplementary data

Supplementary data associated with this article can be found, in the online version, at doi:10.1016/j.carbon.2011.02.048.

REFERENCES

[1] Hong S, Myung S. Nanotube electronics: a flexible approach to mobility. Nat Nanotechnol 2007;2(4):207–8.

[2] Kong J, Yenilmez E, Tombler TW, Kim W, Dai H, Laughlin RB, et al. Quantum interference and ballistic transmission in nanotube electron waveguides. Phys Rev Lett 2001;87:106801-1–4.

[3] White CT, Todorov TN. Quantum electronics: nanotubes go ballistic. Nature 2001;411(6838):649–51.

[4] Liang W, Bockrath M, Bozovic D, Hafner JH, Tinkham M, Park H. Fabry–Perot interference in a nanotube electron waveguide. Nature 2001;411(6838):665–9.

[5] Tans SJ, Verschueren ARM, Dekker C. Room-temperature transistor based on a single carbon nanotube. Nature 1998;393(6680):49–52.

[6] Martel R, Shmidt T, Shea HR, Hertel T, Avouris P. Single- and multi-walled carbon nanotube field-effect transistors. Appl Phys Lett 1998;73:2447–9.

[7] Javey A, Kim H, Brink M, Wang Q, Ural A, Guo J, et al. High-[kappa] dielectrics for advanced carbon-nanotube transistors and logic gates. Nat Mater 2002;1(4):241–6.

[8] Derucke V, Martel R, Appenzeller J. Carbon nanotube inter- and intramolecular logic gates. Nano Lett 2001;1(9):453–6.

[9] Yu J, Shapter JG, Quinton JS, Johnston MR, Beattie DA. Direct attachment of well-aligned single-walled carbon nanotube architectures to silicon (1 0 0) surfaces: a simple approach for device assembly. Phys Chem Chem Phys 2006;9:510–20.

[10] Bissett MA, Shapter JG. Photocurrent response from vertically aligned single-walled carbon nanotube arrays. J Phys Chem C 2010;114(14):6778–83.

[11] Flavel BS, Garrett DJ, Lehr J, Shapter JG, Downard AJ. Chemically immobilised carbon nanotubes on silicon: stable surfaces for aqueous electrochemistry. Electrochim Acta 2010;55(12):3995–4001.

[12] Marshall MW, Popa-Nita S, Shapter JG. Measurement of functionalised carbon nanotube carboxylic acid groups using a simple chemical process. Carbon 2006;44(7):1137–41.

[13] Strano MS, Dyke CA, Usrey ML, Barone PW, Allen MJ, Shan H, et al. Electronic structure control of single-walled carbon nanotube functionalization. Science 2003;301(5639):1519–22.

[14] Zheng M, Jagota A, Semke ED, Diner BA, McLean RS, Lustig SR, et al. DNA-assisted dispersion and separation of carbon nanotubes. Nat Mater 2003;2(5):338–42.

[15] Nish A, Hwang J-Y, Doig J, Nicholas RJ. Highly selective dispersion of single-walled carbon nanotubes using aromatic polymers. Nat Nanotechnol 2007;2(10):640–6.

[16] Moore VC, Strano MS, Haroz EH, Hauge RH, Smalley RE, Schmidt J, et al. Individually suspended single-walled carbon nanotubes in various surfactants. Nano Lett 2003;3(10):1379–82.

[17] Islam MF, Rojas E, Bergey DM, Johnson AT, Yodh AG. High weight fraction surfactant solubilization of single-wall carbon nanotubes in water. Nano Lett 2003;3(2):269–73.

[18] Matsumura H, Ando T. Conductance of carbon nanotubes with a Stone–Wales defect. J Phys Soc Jpn 2001;70(9):2657–65.

[19] Hayashi T, Shimamoto D, Kim YA, Muramatsu H, Okino F, Touhara H, et al. Selective optical property modification of double-walled carbon nanotubes by fluorination. ACS Nano 2008;2(3):485–8.

[20] Kim YA, Muramatsu H, Park KC, Shimamoto D, Jung YC, Kim JH, et al. CdSe quantum dot-decorated double walled carbon nanotubes: the effect of chemical moieties. Appl Phys Lett 2008;93(5):051901–3.

[21] Ellis AV, Bubendorfer A. Raman scattering analysis of changes induced by chemical treatment of double-walled carbon nanotubes. Chem Phys Lett 2005;412:449–53.

[22] Brozena AH, Moskowitz J, Shao B, Deng S, Liao H, Gaskell KJ, et al. Outer wall selectively oxidized, water-soluble double-walled carbon nanotubes. J Am Chem Soc 2010;132(11):3932–8.

[23] Muramatsu H, Kim YA, Hayashi T, Endo M, Yonemoto A, Arikai H, et al. Fluorination of double-walled carbon nanotubes. Chem Commun 2005;15:2002–4.

[24] Liu K, Wang W, Xu Z, Bai X, Wang E, Yao Y, et al. Chirality-dependent transport properties of double-walled nanotubes measured in situ on their field-effect transistors. J Am Chem Soc 2008;131(1):62–3.

[25] Kim YA, Muramatsu H, Hayashi T, Endo M, Terrones M, Dresselhaus MS. Thermal stability and structural changes of double-walled carbon nanotubes by heat treatment. Chem Phys Lett 2004;398(1–3):87–92.

[26] Peng B, Locascio M, Zapol P, Li S, Mielke SL, Schatz GC, et al. Measurements of near-ultimate strength for multiwalled carbon nanotubes and irradiation-induced crosslinking improvements. Nat Nano 2008;3(10):626–31.

[27] Saito R, Matsuo R, Kimura T, Dresselhaus G, Dresselhaus MS. Anomalous potential barrier of double-wall carbon nanotube. Chem Phys Lett 2001;348(3–4):187–93.

[28] Baughman RH, Zakhidov AA, de Heer WA. Carbon nanotubes – the route toward applications. Science 2002;297(5582):787–92.

[29] Gooding JJ, Wibowo R, Liu J, Yand W, Orbons S, Mearns FJ, et al. Protein electrochemistry using aligned carbon nanotube arrays. J Am Chem Soc 2003;125(30):9006–7.

[30] Tune DD, Flavel BS, Quinton JS, Ellis AV, Shapter JG. Single walled carbon nanotube network electrodes for dye solar cells. Sol Energy Mater Sol Cells 2010;94(10):1665–72.

[31] Garrett DJ, Flavel BS, Shapter JG, Baronian KHR, Downard AJ. Robust forests of vertically aligned carbon nanotubes chemically assembled on carbon substrates. Langmuir 2009;26(3):1848–54.

[32] Yu J, Shapter JG, Quinton JS, Johnston MR, Beattie DA. Direct attachment of well-aligned single-walled carbon nanotube architectures to silicon (1 0 0) surfaces: a simple approach for device assembly. Phys Chem Chem Phys 2007;9(4):510–20.

[33] Yu J, Mathew S, Flavel BS, Johnston MR, Shapter JG. Ruthenium porphyrin functionalized single-walled carbon nanotube arrays – a step toward light harvesting antenna and multibit information storage. J Am Chem Soc 2008;130(27):8788–96.

[34] Ren W, Li F, Chen J, Bai S, Cheng H-M. Morphology, diameter distribution and Raman scattering measurements of double-walled carbon nanotubes synthesized by catalytic decomposition of methane. Chem Phys Lett 2002;359(3–4):196–202.

[35] Pehrsson PE, Zhao W, Baldwin JW, Song C, Liu J, Kooi S, et al. Thermal fluorination and annealing of single-wall carbon nanotubes. J Phys Chem B 2003;107(24):5690–5.

[36] Barber AH, Andrews R, Schadler LS, Wagner HD. On the tensile strength distribution of multiwalled carbon nanotubes. Appl Phys Lett 2005;87(20):203106-1–3.

[37] Grobert N. Carbon nanotubes – becoming clean. Mater Today 2007;10(1–2):28–35.

[38] Keidar M, Levchenko I, Arbel T, Alexander M, Waas AM, Ostrikov K. Increasing the length of single-wall carbon nanotubes in a magnetically enhanced arc discharge. Appl Phys Lett 2008;92(4):043129-1–3.

[39] Yu J, Losic D, Marshall M, Bocking T, Gooding JJ, Shapter JG. Preparation and characterisation of an aligned carbon nanotube array on the silicon (1 0 0) surface. Soft Matter 2006;2(12):1081–8.

[40] Flavel BS, Yu J, Shapter JG, Quinton JS. Patterned attachment of carbon nanotubes to silane modified silicon. Carbon 2007;45:2551–8.

[41] Flavel BS, Yu J, Shapter JG, Quinton JS. Patterned polyaniline and carbon nanotube–polyaniline composites on silicon. Soft Matter 2008;5:164–72.

[42] Ko H, Pikus Y, Jiang C, Jauss A, Hollricher O, Tsukruk VV. High-resolution Raman microscopy of curled carbon nanotubes. Appl Phys Lett 2004;85(13):2598–600.

[43] Mews A, Koberling F, Basché T, Philipp G, Duesberg GS, Roth S, et al. Raman imaging of single carbon nanotubes. Adv Mater 2000;12(16):1210–4.

[44] Jiang C, Zhao J, Therese HA, Friedrich M, Mews A. Raman imaging and spectroscopy of heterogeneous individual carbon nanotubes. J Phys Chem B 2003;107(34):8742–5.

[45] Downard AJ, Prince MJ. Barrier properties of organic monolayers on glassy carbon electrodes. Langmuir 2001;17(18):5581–6.

[46] Lyskawa J, Bélanger D. Direct modification of a gold electrode with aminophenyl groups by electrochemical reduction of in situ generated aminophenyl monodiazonium cations. Chem Mater 2006;18(20):4755–63.

[47] Nicholson RS. Theory and application of cyclic voltammetry for measurement of electrode reaction kinetics. Anal Chem 1965;37(11):1351–5.

[48] Bard AJ, Faulkner LR. Electrochemical methods: fundamentals and applications. 2nd ed. New York: John Wiley and Sons Inc.; 2001.

– This page intentionally left blank –

2.6 Additional Scientific Publications

2.6.8 *Micropatterned Arrays of Porous Silicon: Towards Sensory Biointerfaces*

B. S. Flavel, M. J. Sweetman, C. J. Shearer, J. G. Shapter, N. H. Voelcker

Applied Materials & Interfaces 3 (2011) 2463–2471

DOI: 10.1021/am2003526

Abstract

We describe the fabrication of arrays of porous silicon spots by means of photolithography where a positive photoresist serves as a mask during the anodization process. In particular, photoluminescent arrays and porous silicon spots suitable for further chemical modification and the attachment of human cells were created. The produced arrays of porous silicon were chemically modified by means of a thermal hydrosilylation reaction that facilitated immobilization of the fluorescent dye lissamine, and alternatively, the cell adhesion peptide arginine-glycine-aspartic acid-serine. The latter modification enabled the selective attachment of human lens epithelial cells on the peptide functionalized regions of the patterns. This type of surface patterning, using etched porous silicon arrays functionalized with biological recognition elements, presents a new format of interfacing porous silicon with mammalian cells. Porous silicon arrays with photoluminescent properties produced by this patterning strategy also have potential applications as platforms for in situ monitoring of cell behaviour.

Contribution

B.S.F conceived the idea for the project and designed the experiments. B.S.F, M.J.S, and C.J.S performed the experiments. B.S.F wrote the paper and all authors contributed in its critical scientific evaluation.

– This page intentionally left blank –

ACS APPLIED MATERIALS & INTERFACES

RESEARCH ARTICLE

www.acsami.org

Micropatterned Arrays of Porous Silicon: Toward Sensory Biointerfaces

Benjamin S. Flavel,* Martin J. Sweetman, Cameron J. Shearer, Joseph G. Shapter, and Nicolas H. Voelcker*

Centre for Nanoscale Science and Technology, School of Chemical and Physical Sciences, Flinders University,
Sturt Road, Bedford Park, Adelaide, South Australia, 5001

ABSTRACT:

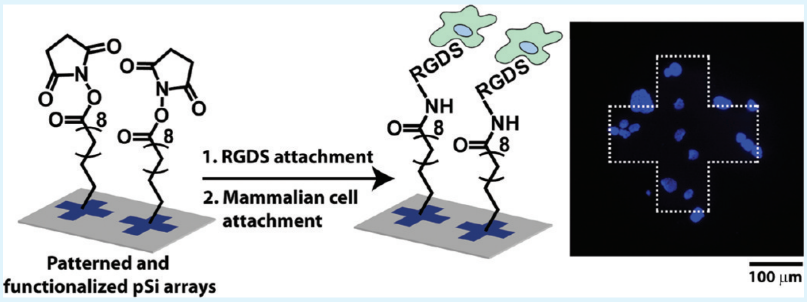

We describe the fabrication of arrays of porous silicon spots by means of photolithography where a positive photoresist serves as a mask during the anodization process. In particular, photoluminescent arrays and porous silicon spots suitable for further chemical modification and the attachment of human cells were created. The produced arrays of porous silicon were chemically modified by means of a thermal hydrosilylation reaction that facilitated immobilization of the fluorescent dye lissamine, and alternatively, the cell adhesion peptide arginine-glycine-aspartic acid-serine. The latter modification enabled the selective attachment of human lens epithelial cells on the peptide functionalized regions of the patterns. This type of surface patterning, using etched porous silicon arrays functionalized with biological recognition elements, presents a new format of interfacing porous silicon with mammalian cells. Porous silicon arrays with photoluminescent properties produced by this patterning strategy also have potential applications as platforms for in situ monitoring of cell behavior.

KEYWORDS: porous silicon, photoluminescence, biointerface, cell adhesion, photolithography

INTRODUCTION

Porous silicon, a material initially reported by Uhlir et al. in 1956[1] as a product of an accidental discovery during silicon wafer machining, and then mostly ignored until a revival of the material by Canham et al. in 1990[2] has since been the subject of a flurry of intense research activity. This is due to potential applications in optoelectronics,[3,4] chemical and biochemical sensing,[5−9] new material supports,[10,11] drug delivery,[12,13] in vivo electronics,[14,15] molecular separation,[16] and surface-enhanced mass spectroscopy.[17−19] Porous silicon is an inorganic material typically produced from crystalline silicon wafers by electrochemical anodization in an electrolyte mixture of hydrofluoric acid (HF), water and ethanol, with (*n*-type) or without (*p*-type) above band gap illumination.[9,20,21] The resulting nanostucture consists of unidirectional aligned pores running perpendicular to the surface.[9] By controlling the current density, crystalline orientation of the wafer, type and concentration of dopant, and electrolyte composition, we can fabricate a variety of different pore morphologies, porosities, and pore sizes.[12,22] The process of pore formation is reproducible, fast, inexpensive, and compatible with standard integrated circuit processes, and leads to a surface with many interesting properties.[22,23] For example, porous silicon exhibits strong Fabry-Pérot fringes[24,25] and has a surface area in the order of 200−500 m^2 cm^{-3}.[23,26] However, two of the most exciting features are its high biocompatibility[9,11−13,25,27−29] and intrinsic photoluminescence.[22,30−33]

A visible red photoluminescence is observed from porous silicon consisting of an ensemble of interconnected nanometre sized silicon crystallites, which have diameters small enough to exhibit quantum confinement.[22] Numerous examples of porous silicon-based optical sensors can be found in the literature utilizing changes in photoluminescence[22,32−34] or reflectivity[7,23,24,35−37] when exposed to target analytes. For example, aromatics such as benzene and anthracene,[38] and nitro-aromatics such as trinitrotoluene and 2,4-dinitrotoluene[39] have been reported to quench the photoluminescence of porous silicon. This principle has been used by Létant et al.[22] who have developed an electronic artificial nose based on porous silicon capable of discriminating between a series of solvent vapors, ethyl esters, and perfumes. In a further example by Létant et al.,[34] the enzyme β-glucuronidase was immobilized to photoluminescent silicon, which demonstrated concentration dependent, reversible

Received: March 21, 2011
Accepted: June 9, 2011
Published: June 09, 2011

quenching of photoluminescence capable of detecting 25 μM p-nitrophenyl-β-D-glucuronide. In contrast, Di Francia et al.[33] have linked single-strand DNA to photoluminescent porous silicon and observed an enhancement in light emission upon complementary strand interaction allowing for detection without labeling steps.

Similarly, porous silicon is finding its niche in cell biology as a biodegradeable support for mammalian cells and tissues.[27,28,40−42] It has long been established that surface topographical cues play an important role in mediating cell orientation and biocompatibility of surfaces[43] with the unique structure of porous silicon proving to be an ideal candidate for the provision of such cues. In fact, Bayliss et al.[40] have shown that porous silicon has a higher viability for various mammalian cell lines compared to glass, polycrystalline silicon or bulk silicon. Furthermore, Low et al.[28] and Khung et al.[44] have demonstrated that surface chemistry and morphological structure of porous silicon play an important role in the adhesion of mammalian cells. Khung et al.[44] have shown that pore size can have a dramatic effect on the ability of cells to adhere to the surface, and that cells prefer large (1−3 μm) to small (100 and 300 nm) pores by comparison. Low et al.[28] showed that for some cell lines amine-functionalization or collagen-coating were required in order to facilitate cell adhesion to porous silicon.

Furthermore it has been shown that porous silicon facilitates close contact with living cells allowing for the direct measurement of cellular signals.[27,45] Predicated on these findings, potential applications such as interfacing of electronics with human neural circuitry, for example enabling reconnection of severed nerve endings[46] are well in sight. At the same time, sensor platforms integrated into cell culture ware will significantly spur discoveries in areas including high-throughput drug testing and stem cell technologies. Schwartz et al.[47] have pioneered the idea of a so-called 'Smart Petridish' where the changes in the optical properties of a porous silicon report on a physiological change occurring in primary rat hepatocytes and *Pseudomonas syringae* bacteria[48] in real time, without interfering with the cells to be studied and with sensitivity exceeding that of traditional cell-based assays.

All of these applications would be considerably enhanced by access to techniques allowing the facile generation of porous silicon patterns.[9] Unfortunately, few examples currently exist in the literature[49−55] of a generic method to reproducibly fabricate porous silicon patterns. Sirbuly et al.[49] have reported a dry removal soft lithography approach where a poly(dimethysiloxane) stamp is adhered to a porous silicon wafer, which upon removal leaves microstructures of porous silicon in the uncontacted regions. In addition, Chattopadhyay et al.[53] and Bao et al.[54] utilized ion beam techniques to create photoluminescent arrays of porous silicon. In turn, Khung et al.[56] used direct ultraviolet laser writing to generate patterned porous silicon. However, the arguably most obvious method to fabricate patterned surfaces is with conventional photolithography. In this area Wang et al.[50] have utilized masks of silicon nitride and silicon carbide. The ceramic coating in these examples was used to ensure substrate pattern retention upon anodization in hydrofluoric acid. More recently, Li et al.[55] have employed a conventional photoresist combined with platinum metal-assisted chemical etching to create a porous silicon based protein microarray. Chen et al.[57] have also used photolithography to create gel pad microarrays templated by patterned porous silicon. Patterned, nanoporous alumina arrays have previously been fabricated through photolithographic techniques and used for mammalian cell culture.[58] The cell adhesion peptide arginine-glycine-aspartic acid (RGD) has been grafted to porous alumina surfaces to enhance cell attachment.[59,60] We perceive two major advantages of using porous silicon over porous alumina in the context of biomaterial and biointerface applications. First, porous silicon is well-known as a biocompatible and biodegradable material and has been investigated as a platform for mammalian cell culture for over a decade.[28,61−65] In contrast to porous alumina, porous silicon completely degrades in aqueous media, with the only product of degradation the nontoxic silicic acid.[66] Second, porous silicon exhibits photoluminescence properties that can be used as a means for noninvasive monitoring of binding events within the pores.[67,68]

In this work, we describe for the first time the use of conventional photolithographic techniques to create arrays of porous silicon by electrochemical anodization without the use of ceramic or metal assistive layers, thereby dramatically reducing the complexity of the fabrication process. The ability to fabricate photoluminescent and nonphotoluminescent porous silicon suitable for further chemical modification by hydrosilylation is demonstrated. Furthermore, immobilization of the dye lissamine, and the cell adhesion peptide arginine-glycine-aspartic acid-serine (RGDS) shows that functionalization of porous silicon arrays with bioactive compounds is feasible. The RGDS-functionalized surface facilitated attachment of human lens epithelial cells. This demonstration of porous silicon patterning and selective cell attachment opens new vistas toward the development of optical sensory components of cell culture systems, which may become viable alternatives to conventional intrusive cell-based assays.

■ EXPERIMENTAL SECTION

Fabrication of Patterned Porous Silicon Arrays. The procedure for fabrication of patterned porous silicon substrates by the electrochemical etching of silicon in a solution of ethanolic HF is shown schematically in figure 1. First, silicon was cut into 1.5 × 1.5 cm^2 sized wafers and cleaned by ultrasonication (Elmasonic S 30H, Elma Hans Schmidbauer GmbH & Co KG, Germany) in 99.5% acetone (Mallinckrodt Chemicals) for 5 min followed by 5 min in 99.5% isopropyl alcohol (Sigma-Aldrich) with thorough drying with nitrogen gas between each solvent. Immediately after cleaning, positive tone photoresist AZ1518 (Microchemicals, Germany) was spin-coated to a thickness of ~2 μm at 3000 rpm for 30 s on a WS-400B-6NPP/Lite spinner system (Laurell Technologies Corporation, USA) and soft baked for 60 s at 100 °C on a standard hot plate. An Omnicure S1000 ultraviolet lamp (EXFO Life Sciences and Industrial Division, Canada) was used to pattern the photoresist by a 10 s exposure to 100 W ultraviolet light through a chrome on glass mask (step 1). After exposure, the photoresist was developed by immersion in AZMIF326 developer (Microchemicals, Germany) for 25 s, rinsed with water, dried with dry air (step 2) and immediately transferred to a custom built Teflon etching cell (approximately 1.8 cm^2 working area) and covered with an ethanolic solution of HF. Two etching conditions were followed, one to produce photoluminescent porous silicon and the other for surfaces suitable for dye immobilization or mammalian cell attachment (step 3). Photoluminescent porous silicon surfaces were fabricated from boron doped *p*-type silicon (100) with resistivity 3−6 Ω cm (Silicon Quest International, USA) with an etching solution of 1:4 aqueous HF (48% (w/w), Merck, Germany) to ethanol (100% undenatured, Chem-Supply, Australia). A current of 4 mA was applied for 10 min using a Keithley 2425 source meter (Keithley, USA). Patterned porous silicon for dye immobilization and cell attachment was prepared from boron doped *p*-type silicon (100) with resistivity 0.00055−0.001 Ω cm (Virginia

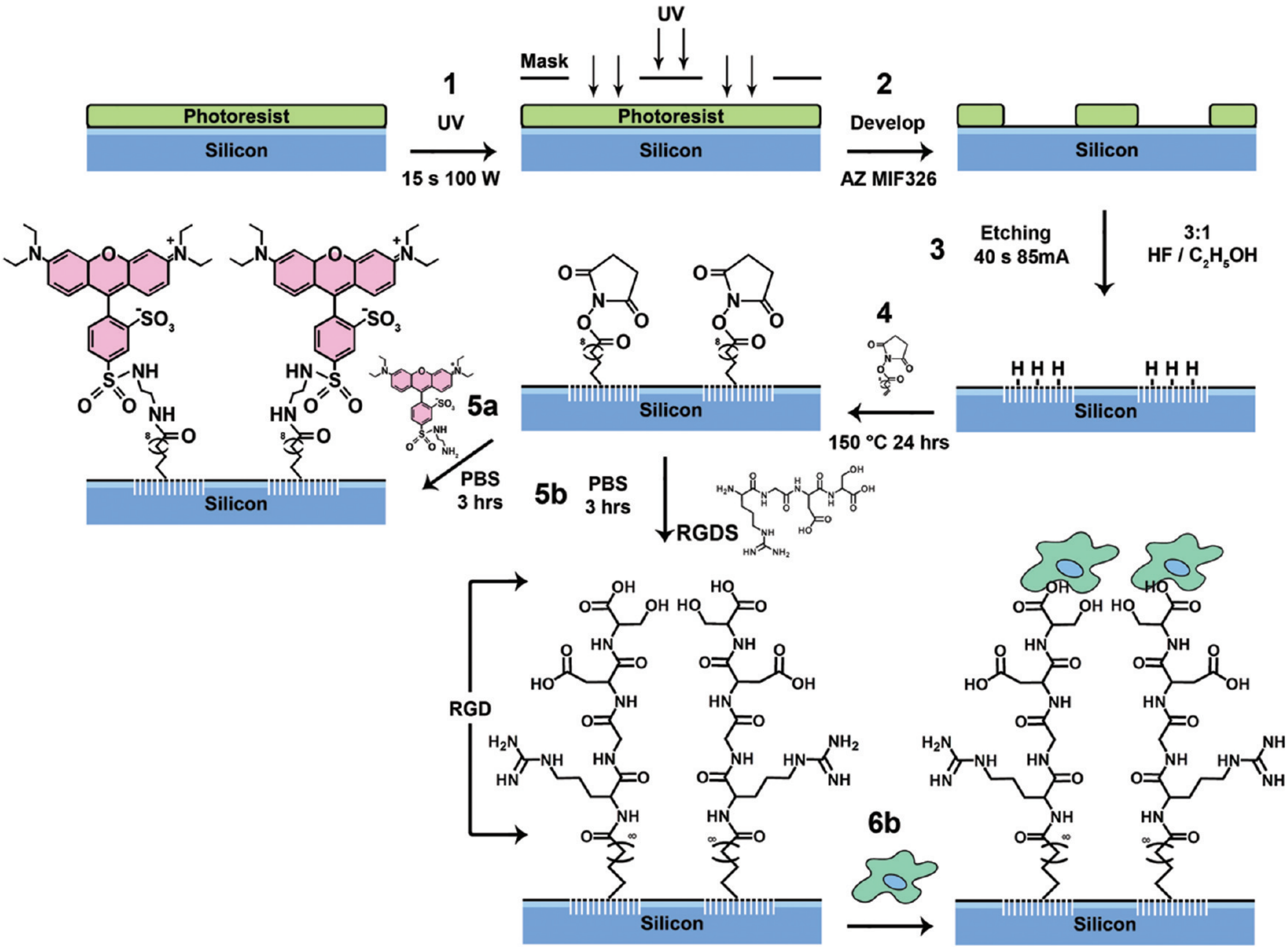

Figure 1. Schematic of porous silicon microarray fabrication and the subsequent immobilization of lissamine dye (5a) and selective attachment of human lens epithelial cells (6b) mediated by an immobilized cell adhesion peptide.

Semiconductor, USA) with an etching solution of 3:1 aqueous HF: ethanol. A current of 85 mA was applied for 40 s. After anodization, the porous silicon was washed sequentially with methanol (Chem-Supply, Australia), acetone and dichloromethane (Chem-Supply, Australia) before being dried under a stream of nitrogen gas.

Surface Modification. For lissamine dye immobilization and cell attachment, patterned porous silicon was further modified by means of thermal hydrosilylation (step 4), where a freshly etched porous silicon surface was immersed in a degassed (three freeze−pump−thaw cycles) 100 mM solution of synthesized N-hydroxysuccinimide alkene (NHS) in mesitylene,[69] under positive argon pressure. The reaction vessel was then sealed, flooded with argon and immersed in an oil bath. The reaction was allowed to proceed at 150 °C for 24 h. After completion of the reaction, the vessel was allowed to cool, before the porous silicon surface was removed and rinsed with copious amounts of dichloromethane and dried under a stream of nitrogen gas. To this surface, either lissamine (step 5a) or arginine-RGDS (step 5b) was covalently attached. The porous silicon surface was allowed to react with either 0.1 mg/mL lissamine (Invitrogen, USA) or 0.1 mg/mL RGDS (Peptides International, USA) in pH 7.4 phosphate buffer saline solution (PBS) for 3 h. After reaction, the surface was washed with PBS solution and Milli-Q water and dried under a stream of nitrogen gas.

Cell Culture. SRA human lens epithelial cells were cultured on the RGDS functionalized surface (step 6b). SRA cells were cultured in Dulbecco's Modified Eagle Medium containing 5 mM L-glutamine, 100 IU/mL penicillin, 100 μg/mL streptomycin sulfate (Invitrogen, USA) and 10% v/v fetal bovine serum (Bovogen Biologicals, Australia) and maintained at 37 °C in 5% CO_2. To investigate cell attachment to the RGDS functionalized surfaces, cells were incubated on the surface at a density of 1×10^5 cells/mL in pH 7.4 PBS solution for 4 h. After this time, the surfaces were rinsed with PBS solution and PBS-Tween (0.05%) to remove any nonspecifically or weakly attached cells. During the final 30 min of incubation, 10 μL of a 200 μg/mL stock solution of Hoechst 33342 (Invitrogen, USA) fluorescent stain was added to the culture medium of each surface.

Microscopy. Scanning electron microscope (SEM) images were obtained using a Helios Nanolab 650 Dual Beam (FEI, USA) with an accelerating voltage of 10 kV. Fluorescence microscopy images were captured with an Eclipse 50*i* microscope equipped with a D-FL universal epi-fluorescence attachment and a 100 W mercury lamp (Nikon Instruments, Japan). Fluorescence images were recorded by a cooled CCD camera (Nikon Instruments, Japan) in darkened conditions with the NIS-elements v3.07 (Nikon Instruments, Japan) software. Patterned arrays of porous silicon and cells were visualized with the use of a 540/25 nm excitation filter and a 605/55 nm emission filter, with patterned cells visualized with a 340−380 nm excitation filter and a 435−485 nm emission filter.

Spectroscopy. Fluorescence spectroscopy measurements were performed with a Cary Eclipse fluorescence spectrometer (Varian Inc., USA). Operating in fluorescence/emission mode with emission and

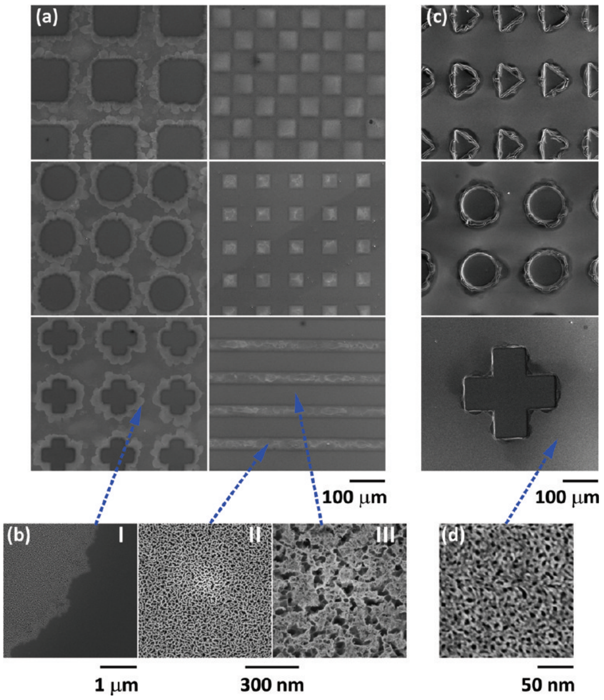

Figure 2. (a, b) Scanning electron microscopy images of patterned nonphotoluminescent porous silicon, and (c, d) photoluminescent porous silicon patterns; b-III corresponds to the patterned porous silicon area.

excitation slit widths of 5 nm, a patterned photoluminescent porous silicon substrate was mounted inside a quartz cuvette and excited with 312 nm light. Infrared spectroscopy measurements were performed on a Nicolet Avatar 370MCT spectrometer (Thermo Electron Corporation, USA). The spectrometer was fitted with a transmission accessory and all spectra were recorded and analyzed using OMNIC version 7 software. Spectra were recorded over a range of 650−4000 cm^{-1}, at a resolution of 2 cm^{-1} and taken as an average of 64 scans. All samples were blanked to a clean unetched and non- functionalized silicon wafer.

■ RESULTS AND DISCUSSION

The conventional photoresist AZ1518 was spin coated onto *p*-type silicon (100). Patterns with simple geometric shapes (squares, circles, crosses and lines) of dimensions as low as 15 μm were transferred into the resist layer by exposure to ultraviolet light through chrome-on-glass masks. These patterned shapes allowed for selective exposure of the silicon substrate to an ethanolic HF solution during electrochemical etching to afford patterned porous silicon. By changing the resistivity of the silicon substrate, HF concentration, etching time and current density it was possible to fabricate not only patterned arrays of nonphotoluminescent, but also photoluminescent porous silicon. By etching 0.00055−0.001 Ω cm silicon for 45 s with a current of 85 mA in a 3:1 aqueous HF/ethanol solution, patterns of nonphotoluminescent porous silicon were formed. Figure 2a shows scanning electron microscopy images of the resulting structures where a silicon surface consisting of three distinctly different morphologies can be seen. These different morphologies are enlarged in Figure 2b. Surrounding each patterned porous silicon shape is flat crystalline silicon, and the interface between these two regions can clearly be seen, Figure 2b-I. However each shape consisted of two different types of porous silicon, a central region with pores of approximately 35 − 105 nm in diameter, Figure 2b-III, surrounded by an area consisting of smaller pores of approximately 12 − 38 nm in diameter, Figure 2b-II. The region of smaller pores is attributed to dissolution of the photoresist around the edges of the patterns by the ethanolic HF solution during anodization. This diffuse region typically extends 20−40 μm outside the central porous silicon area. For photoresist patterns below this length scale such as the 15 μm "checker board" and line pattern, Figure 2a, this resulted in a surface of alternating large and small pore size porous silicon.

To gain a more complete understanding of the surface structure, we fractured the silicon substrate along the edge of a porous silicon feature allowing for cross-sectional images to be obtained. Figure 3a shows a scanning electron microscope image of a nonphotoluminescent cross-shaped porous silicon feature where the central porous area was 2.74 μm thick and tapered out over 16.6 μm toward the edge of the pattern. Within this tapered region, the porous silicon retained the structure and pore size of the central area. Surrounding the tapered region, porous silicon with pore size as shown in Figure 2b-II was formed with a depth of approximately 14 nm before terminating in flat silicon. This tapering effect can be attributed to the combined effect of undercut etching, experienced when performing masked etching on semiconductor silicon surfaces[70] and the photoresist dissolution. In the case of insulating etching masks (such as the photoresist mask used here), undercut etching occurs as the electric field is forced to pass through the patterned gaps in the mask.[71] This leads to the etching of the silicon in the areas underneath the mask at the edges of the patterned areas.[72] This undercut etching can be clearly seen in Figure 3a, where the undercut etching extends out 16.6 μm from the patterned feature. The thin, small pore region Figure 2b-II and Figure 3a is attributed to the photoresist dissolution around the edges of the patterned features.

Upon etching 3−6 Ω cm silicon for 10 min with a current of 4 mA in a 1:4 aqueous HF/ethanol solution patterns of photoluminescent silicon were produced as shown in Figure 2c and Figure 3b. In this instance, because of the small pore size of the central photoluminescent region, it was not possible to measure pore diameter accurately with the scanning electron microscope. Such small pore sizes are to be expected due to the very low etching current, with these pores exhibiting quantum confinement effects necessary for the porous silicon to be photoluminescent.[2] Because of etching time required to fabricate photoluminescent porous silicon, complete dissolution of the photoresist was observed, and the underlying surface was therefore also etched and showed pores with a diameter of approximately 4 nm, as shown in Figure 2d. These areas did not photoluminesce. Although this pore size here was small compared to the nonphotoluminescent porous silicon described earlier, it was still too large to exhibit quantum confinement.

Upon examination of cross sections of the photoluminescent porous silicon, tapering effects were also observed (Figure 3b). As previously shown in images c and d in Figure 2, nonphotoluminescent porous silicon surrounded the patterned photoluminescent region and was found to exist with a depth of 1.2 μm. However, in this instance, the patterned photoluminescent region was found to be recessed 4.45 μm below the initial height of the silicon substrate. Figure 3b reveals that the patterned porous silicon region is 440 nm thick. Our explanation for the recessed porous silicon regions is as follows: during the initial stages of anodization, a layer of photoluminescent porous silicon is fabricated within the regions not covered by photoresist,

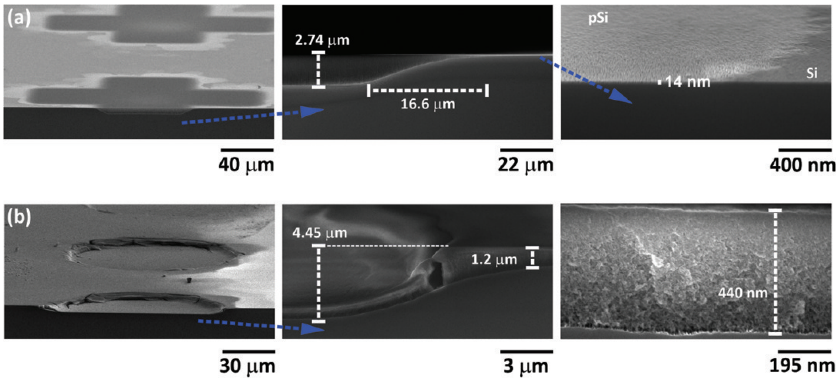

Figure 3. Cross-sectional scanning electron microscopy images of patterned (a) nonphotoluminescent and (b) photoluminescent porous silicon.

whereas the resist-covered silicon is protected. However, over time, the photoresist dissolves and the etching conditions change. First, the total surface area of exposed silicon increases upon photoresist dissolution, which causes a drop in the overall current density at the silicon surface due to the use of a constant current power supply. Second, the already low HF concentration at the pore etching front decreases further as it is consumed in the formation of new pores. Both of these changed parameters result in the dissolution (electropolishing) of the patterned photoluminescent silicon. Furthermore, the changed parameters result in a shift to a new etching regime causing larger pores to be formed around the photoluminescent patterns. Upon comparison of photoluminescent patterns etched for different times it was observed that increasing the etching time resulted in patterns recessed deeper into the silicon substrate. For photoluminescent patterns etched at similar times to nonphotoluminescent patterns it was possible to avoid any recession. However, the photoluminescent intensity was very low. Solid state fluorescence spectroscopy was performed on the photoluminescent patterns and showed an emission peak of 625 nm upon irradiation with 312 nm light as shown in Figure 4a. This peak is in agreement with literature values for photoluminescent porous silicon.[73] Fluorescence microscopy images of the photoluminescent patterns were also found to be well-defined as shown in Figure 5a. As previously discussed, the porous regions surrounding the patterned shapes did not luminesce. We believe that these photoluminescent arrays of porous silicon spots may find applications as biocompatible optical sensor arrays.[74,75]

To demonstrate the feasibility of functionalizing patterned porous silicon regions, the fluorescent dye lissamine and the cell adhesion peptide RGDS were immobilized in separate experiments by means of hydrosilylation chemistry. By performing a hydrosilylation reaction on the freshly etched porous silicon patterns, a functionalized alkene compound only conjugates to the porous surface of the etched areas that have Si—H functionality. This means that the porous silicon surface is selectively functionalized over the surrounding flat silicon surface that has not come into contact with HF and retains its native silicon oxide functionality. Hydrosilylation reactions and further functionalizations were only carried out on the nonphotoluminescent porous silicon surfaces. This type of surface functionalization reaction has been demonstrated to produce stable porous silicon surfaces, able to last for extended time in aqueous media.[61,76] The surface modifications were followed by transmission infrared spectroscopy as shown in Figure 4. Figure 4b shows a series of infrared spectra corresponding to each step in the surface modification for producing the RGDS functionalized surfaces. The spectra correspond to freshly etched porous silicon, N-hydroxysuccinimide (NHS) ester functionalized porous silicon, and RGDS-functionalized porous silicon before and after quenching of the NHS residues that had not reacted with the peptide using ethanolamine. Methylene stretching vibrations around 2900 cm^{-1} confirm the successful attachment of the alkene species to the porous silicon surface using thermal hydrosilylation.[77] A large reduction in the intensity of Si—H stretching vibrations at 2100 cm^{-1} also confirms successful reaction of the initial hydride terminated porous silicon surface.[78] The peaks at 2230 and 1100 cm^{-1} correspond to oxygen backbonded Si—H and Si—O, respectively.[79] These peaks are representative of surface oxidation, which commonly occurs as a side reaction during thermal hydrosilylation.[80] Figure 4c displays an enlarged section of the infrared spectra that allows for changes in the carbonyl stretching vibrations to be easily visualized. The spectra corresponding to the NHS ester functionalized porous silicon surface shows a set of three peaks between 1850 and 1700 cm^{-1} that correspond to the carbonyl stretching vibration of the ester (1810 cm^{-1}) and the symmetric and asymmetric stretching of the NHS ester carbonyls (1780 and 1730 cm^{-1}, respectively).[79,81] We observed that after the RGDS is immobilized on the surface the intensity of these carbonyl peaks (especially the peaks at 1780 and 1810 cm^{-1} associated with the symmetric and ester carbonyl stretching of the NHS) is reduced. Following RGDS immobilization, the peak around 1730 cm^{-1} has broadened, consistent with the presence of carbonyl stretching bands of the peptide, and there is a small peak present at 1530 cm^{-1} which corresponds to N—H bending modes of amide II vibrations.[82] The reduction of the NHS carbonyl peak intensity and the presence of the amide bond indicate the successful attachment of the RGDS to the NHS ester. After the surface was reacted with ethanolamine, it was observed that the NHS ester carbonyl peak had almost disappeared, indicating successful quenching of the remaining NHS ester functionalities on the functionalized porous silicon surface. Figure 4d,e show the infrared spectra series for lissamine dye immobilization on the porous silicon surface. The spectra in panels d and e in Figure 4 are almost identical to those in b and c in Figure 4. After reaction with lissamine, a conspicuous amide I peak at 1650 cm^{-1} appeared, indicating the successful attachment of the amino functional dye to the surface. The expanded spectral window in Figure 4e shows further vibrational peaks, which we attributed to other functional groups of the lissamine dye (such as sulphones and sulphonamides).[83]

Fluorescence microscopy was used to visualize the porous silicon patterns after lissamine functionalization. In Figure 5b,

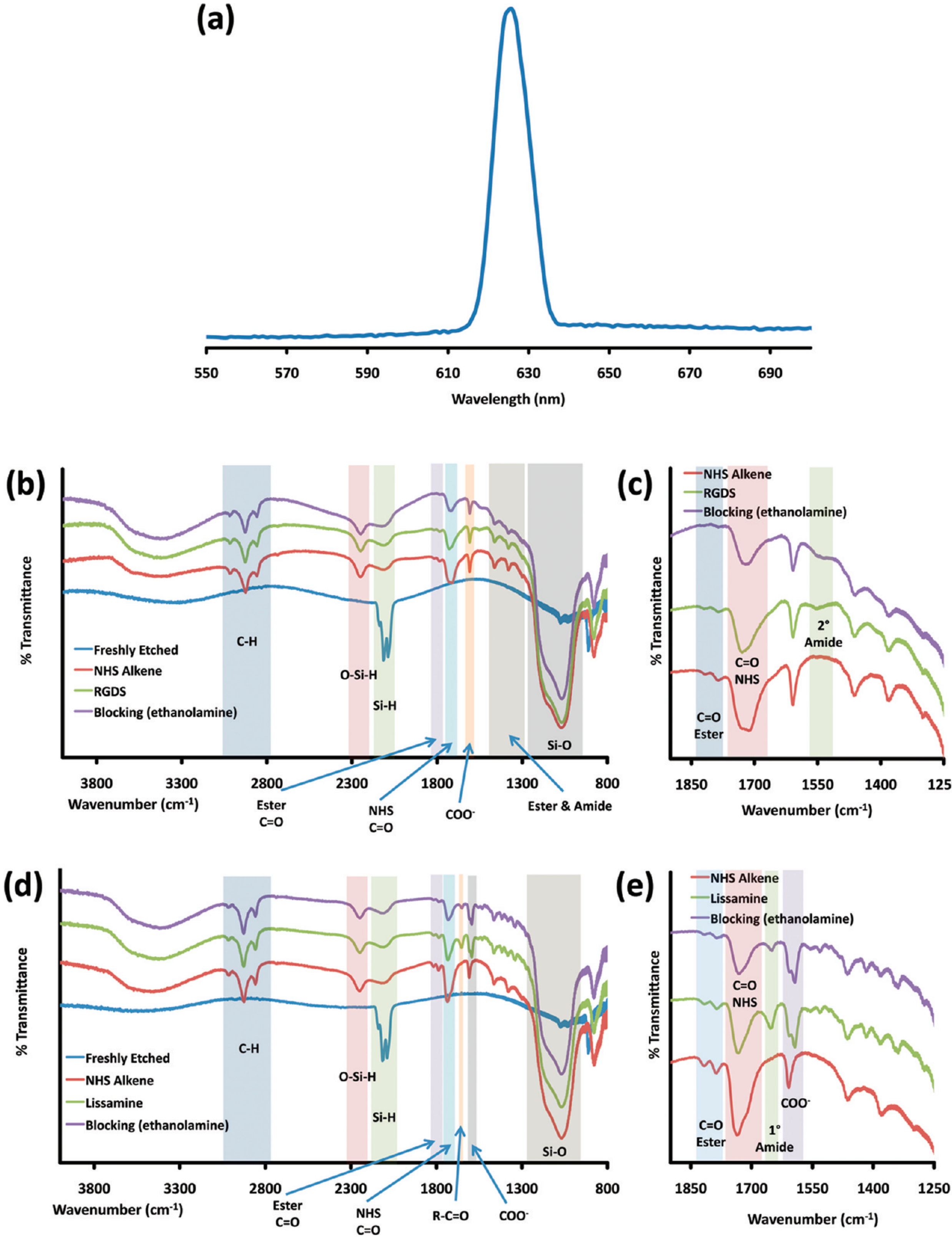

Figure 4. (a) Fluorescence spectrum of photoluminescent porous silicon. Transmission infrared spectra of various porous silicon surface modifications resulting in the immobilization of (b, c) RGDS and (d, e) lissamine.

highly defined arrays of lissamine functionalized porous silicon were observed. This is in contrast to the poorly defined patterns due to electric field decay and photoresist removal seen by scanning electron microscope in images a and b in Figure 2. The observed difference can be simply explained by considering the available surface area for lissamine modification. The high

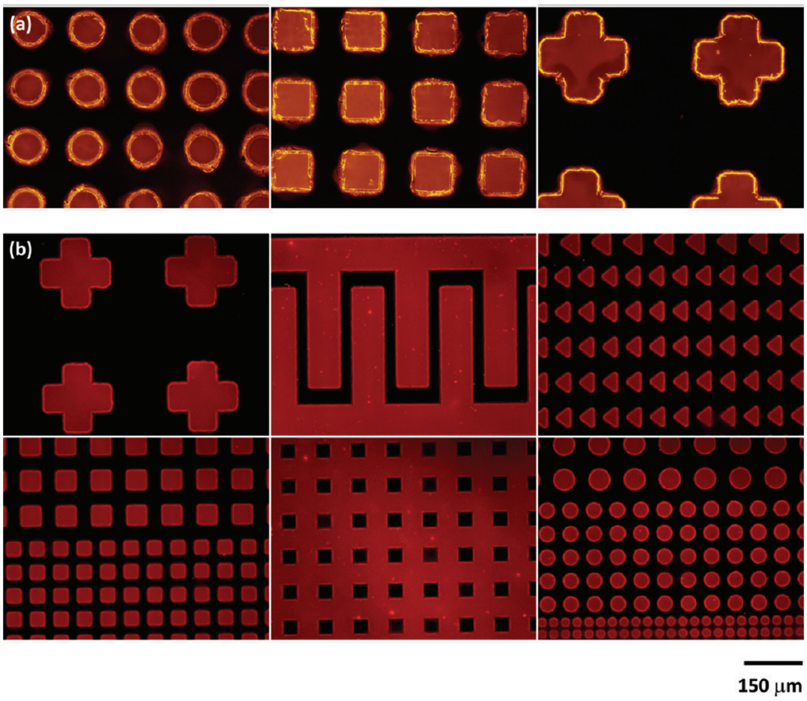

Figure 5. (a) Fluorescence microscopy images of patterned photoluminescent porous silicon and (b) nonphotoluminescent patterned porous silicon after lissamine immobilization.

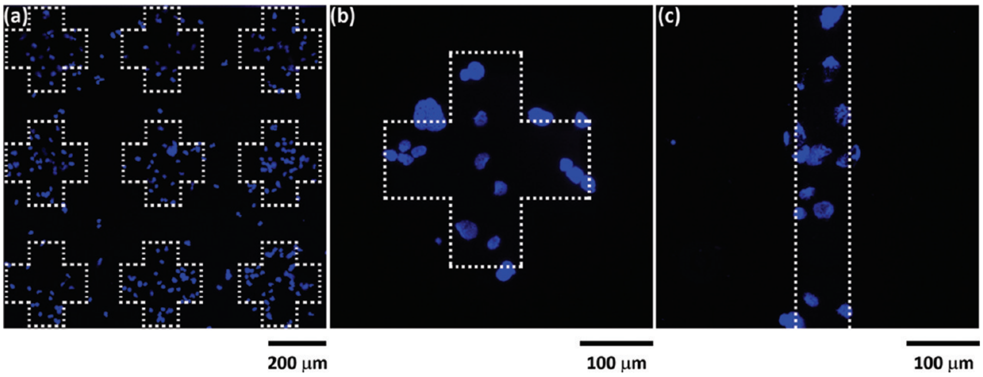

Figure 6. Fluorescence microscopy images of Hoechst 33342 stained human lens epithelial cells on patterned porous silicon arrays (patterns are highlighted by dotted lines, which serve as a guide to the eye).

etch depth of the central region (2.74 μm) as compared to the thin surrounding areas (14 nm) allow for significantly more lissamine loading in the central regions as opposed to the periphery. This results in a strong fluorescence contrast between the central and the surrounding regions.

To demonstrate the response of mammalian cells to the generated RGDS functionalized porous silicon, we incubated surfaces with human lens epithelial cells at a cell seeding density of 1×10^5 cells/mL. This particular cell line was chosen because of our interest in developing cell-based assays on primary ocular cells in culture.[42] To visualize cell attachment to the patterned porous silicon arrays, the cell nuclei were stained with Hoechst 33342. Cell attachment was visualized using fluorescence microscopy as shown in Figure 6. The characteristic blue fluorescence of the Hoechst 33342 stained cell nucleus can clearly be seen. To aid the eye, patterned porous silicon regions are highlighted in the figure with a dotted line. By counting the number of cells immobilized within a patterned region and comparing it to the number of cells nonspecifically bound to the flat silicon it was found that 90% of all cells were bound within the porous silicon regions. A higher density of cells within the patterned region is expected, since the RGDS sequence is known to interact with the extracellular regions of integrins in the cell membrane and helps to anchor the cells to the surface.[84] Washing of the incubated surface with PBS and PBS-Tween (0.05%) removed most of the nonspecifically or weakly bound cells, leaving behind only cells that were strongly attached to the surfaces. It should be noted that no attempt had been made to incorporate low-fouling coatings on the flat silicon surface, for example using silanization with polyethylene glycol silanes.[85] For this reason, cell adhesion to the functionalized surfaces was carried out in PBS in the absence of serum proteins, to negate the effects of proteins nonspecifically adsorbing to the silicon surface and influencing cell attachment. Only a short (4 h) incubation time was used to investigate cell attachment to the functionalized porous silicon arrays. Cell morphology and proliferation on these arrays were not investigated as part of this study.

CONCLUSION

This work has demonstrated a simple, photolithographic method for the fabrication of patterns of porous silicon. Attractive features of this method include that the use of ceramic coatings such as silicon carbide or the use of additional metal layers for metal-assisted etching are not necessary. Furthermore, the method is suitable for rapid patterning of large surface areas. Arrays of photoluminescent and nonphotoluminescent porous silicon have been demonstrated. Photoluminescent arrays of porous silicon are expected to have applications in the fabrication of optical sensing systems where changes in photoluminescence will be used to detect target analyte molecules. On nonphotoluminescent porous silicon, selective chemical functionalization was demonstrated by the immobilization of lissamine and RGDS after thermal hydrosilylation with an NHS ester-terminal alkene on the porous regions. We demonstrate that human lens epithelial cells selectively attach to the RGDS functionalized patterned porous silicon. Taken together, our results constitute a significant advance in our efforts of developing optical sensor arrays interfaced with mammalian cells in culture for nonintrusive detection of cellular processes.

AUTHOR INFORMATION

Corresponding Author

*E-mail: ben.flavel@flinders.edu.au (B.S.F.); nico.voelcker@flinders.edu.au (N.H.V.).

ACKNOWLEDGMENT

Authors gratefully acknowledge the support of the South Australian node of the Australian Microscopy & Microanalysis Research Facility (AMMRF) for access to the Helios Nanolab scanning electron microscope. Authors thank Mr. Yazad Irani for preparation of the epithelial cell line, supplied by and used with permission from Professor Venkat Reddy from the Kellogg Eye Centre, University of Michigan, Ann Arbor, MI, USA. This work was supported by the Australian Research Council.

REFERENCES

(1) Uhlir, A. *Bell Syst. Technol. J.* **1956**, *35*, 333.

(2) Canham, L. T. *Appl. Phys. Lett.* **1990**, *57*, 1046–1048.

(3) Cullis, A. G.; Canham, L. T.; Calcott, P. D. J. *J. Appl. Phys.* **1997**, *82*, 909–965.

(4) Brus, L. *J. Phys. Chem.* **1994**, *98*, 3575–3581.

(5) Létant, S. E.; Sailor, M. J. *Adv. Mater.* **2000**, *12*, 355.

(6) Zangooie, S.; Bjorklund, R.; Arwin, H. *Sens. Actuators, B* **1997**, *43*, 168.

(7) Dancil, K. P. S.; Greiner, D. P.; Sailor, M. J. *J. Am. Chem. Soc.* **1999**, *121*, 7925–7930.

(8) Starodub, V. M.; Fedorenko, L. L.; Sisetskiy, A. P.; Starodub, N. F. *Sens. Actuators B* **1999**, *58*, 409.

(9) Jane, A.; Dronov, R.; Hodges, A.; Voelcker, N. H. *Trends Biotechnol.* **2009**, *27*, 230–238.

(10) Fan, S.; Chapline, M. G.; Franklin, N. R.; Tombler, T. W.; Cassell, A. M.; Dai, H. *Science* **1999**, *283*, 512.

(11) Nussio, M.; Oncins, G.; Ridelis, I.; Szili, E.; Shapter, J.; Sanz, F.; Voelcker, N. H. *J. Phys. Chem.* **2009**, *113*, 10339–10347.

(12) Anglin, E. J.; Cheng, L.; Freeman, W. R.; Sailor, M. J. *Adv. Drug Delivery Rev.* **2008**, *60*, 1266–1277.

(13) McInnes, S.; Voelcker, N. H. *Future Med. Chem.* **2009**, *1*, 1051–1074.

(14) Canham, L. T. *Adv. Mater.* **1995**, *7*, 1033.

(15) Li, X.; Coffer, J. L.; Chen, Y. D.; Pinizzotto, R. F.; Newey, J.; Canham, L. T. *J. Am. Chem. Soc.* **1998**, *120*, 11706.

(16) Velleman, L.; Shearer, C.; Voelcker, N. H.; Shapter, J. G. *Nanoscale* **2010**, *2*, 1756–1761.

(17) Wei, J.; Buriak, J. M.; Siuzdak, G. *Nature* **1999**, *399*, 243.

(18) Lowe, R. D.; Guild, G.; Harpas, P.; Kirkbride, P.; Hoffmann, P.; Voelcker, N. H.; Kobus, H. *Rapid Commun. Mass Spectrom.* **2009**, *23*, 3543–3548.

(19) Lowe, R. D.; Szili, E. J.; Kirkbride, P.; Thissen, H.; Siuzdak, G.; Voelcker, N. H. *Anal. Chem.* **2010**, *82*, 4201–4208.

(20) Lau, H. W.; Parker, G. J.; Greef, R.; Hölling, M. *Appl. Phys. Lett.* **1995**, *67*, 1877–1879.

(21) Li, X.; Bohn, P. W. *Appl. Phys. Lett.* **2000**, *77*, 2572–2574.

(22) Létant, S. E.; Content, S.; Tan, T. T.; Zenhausern, F.; Sailor, M. J. *Sens. Actuators B* **2000**, *69*, 193–198.

(23) Stefano, L. D.; Rotiroti, L.; Rendina, I.; Moretti, L.; Scognamiglio, V.; Rossi, M.; Auria, S. D. *Biosens. Bioelectron.* **2006**, *21*, 1664–1667.

(24) Lin, V. S.-Y.; Motesharei, K.; Dancil, K.-P. S.; Sailor, M. J.; Ghadiri, M. *Science* **1997**, *278*, 840–843.

(25) Stewart, M. P.; Buriak, J. M. *Adv. Mater.* **2000**, *12*, 859–869.

(26) Singh, S.; Sharma, S. N.; Govind; Shivaprasad, S. M.; Lal, M.; Khan, M. A. *J. Mater. Sci. Mater. Med.* **2009**, *20*, S181–S187.

(27) Sapelkin, A. V.; Bayliss, S. C.; Unal, B.; Charalambou, A. *Biomaterials* **2006**, *27*, 842–846.

(28) Low, S. P.; Williams, K. A.; Canham, L. T.; Voelcker, N. H. *Biomaterials* **2006**, *27*, 4538–4546.

(29) Salonen, J.; Lehto, V.-P. *Chem. Eng. J.* **2008**, *137*, 162–172.

(30) Bisi, O.; Ossicini, S.; Pavesi, L. *Surf. Sci. Rep.* **2000**, *38*, 1–126.

(31) Föll, H.; Christophersen, M.; Carstensen, J.; Hasse, G. *Mater. Sci. Eng., R* **2002**, *39*, 93–141.

(32) Seals, L.; Gole, J. L.; Tse, L. A.; Hesketh, P. J. *J. Appl. Phys.* **2002**, *91*, 2519–2523.

(33) Francia, G. D.; Ferrara, V. L.; Manzo, S.; Chiavarini, S. *Biosens. Bioelectron.* **2005**, *21*, 661–665.

(34) Létant, S. E.; Hart, B. R.; Kane, S. R.; Hadi, M. Z.; Sheilds, S. J.; Reynolds, J. G. *Adv. Mater.* **2004**, *16*, 689–693.

(35) Worsfold, O.; Voelcker, N. H.; Nishiya, T. *Langmuir* **2006**, *22*, 7078–7083.

(36) Voelcker, N. H.; Alfonso, I.; Ghadiri, M. R. *ChemBioChem* **2008**, *9*, 1176–1786.

(37) Lin, V. S.-Y.; Janshoff, A.; Steinem, C.; Voelcker, N. H.; Ghadiri, M. R. *Tetrahedron* **2004**, *60*, 11259–11267.

(38) Song, J. H.; Sailor, M. J. *J. Am. Chem. Soc.* **1997**, *119*, 7381.

(39) Content, S.; Trogler, W. C.; Sailor, M. J. *Chem.—Eur. J.* **2000**, *6*, 2205.

(40) Bayliss, S. C.; Heald, R.; Fletcher, I.; Buckberry, L. D. *Adv. Mater.* **1999**, *11*, 318.

(41) Bayliss, S. C.; Buckberry, L. D.; Harris, P. J.; Rousseau, C. *Thin Solid Films* **1997**, *297*, 308.

(42) Low, S. P.; Voelcker, N. H.; Canham, L. T.; Williams, K. A. *Biomaterials* **2009**, *30*, 2873–2880.

(43) Craighead, H. G.; James, C. D.; Turner, A. M. P. *Curr. Opin. Solid State Mater. Sci.* **2001**, *5*, 117–184.

(44) Khung, Y. L.; Barritt, G.; Voelcker, N. H. *Exp. Cell Res.* **2008**, *314*, 789–800.

(45) Mayne, A. H.; Bayliss, S. C.; Barr, P.; Tobin, M.; Buckberry, L. D. *Phys. Status Solidi A* **2000**, *182*, 505–513.

(46) Heiduschka, P.; Thanos, S. *Prog. Neurobiol.* **1998**, *55*, 433.

(47) Schwartz, M. P.; Derfus, A. M.; Alvarez, S. D.; Bhatia, S. N.; Sailor, M. J. *Langmuir* **2006**, *22*, 7084–7090.

(48) Alvarez, S. D.; Schwartz, M. P.; Migliori, B.; Rang, C. U.; Chao, L.; Sailor, M. J. *Phys. Status Solidi A* **2007**, *204*, 1439–1443.

(49) Sirbuly, D. J.; Lowman, G. M.; Scott, B.; Stucky, G. D.; Buratto, S. K. *Adv. Mater.* **2003**, *15*, 149–152.

(50) Wang, H.; Welker, B.; Gao, Y.; Federici, J. F.; Levy, R. A. *Mater. Lett.* **1995**, *23*, 209–214.

(51) Ohmukai, M.; Okada, K.; Tstusumi, Y. *J. Mater. Sci.: Mater. Electron.* **2005**, *16*, 119–121.

(52) Nassiopoulos, A. G.; Grigoropoulos, S.; Canham, L.; Halimaoui, A.; Berbezier, I.; Gogolides, E.; Papadimitriou, D. *Thin Solid Films* **1995**, *255*, 329–333.

(53) Chattopadhyay, S.; Bohn, P. W. *J. Appl. Phys.* **2004**, *96*, 6888–6894.

(54) Bao, X.-M.; Yang, H.-Q. *Appl. Phys. Lett.* **1993**, *63*, 2246–2247.

(55) Li, H.-F.; Han, H.-M.; Wu, Y.-G.; Xiao, S.-J. *Appl. Surf. Sci.* **2010**, *256*, 4048–4051.

(56) Khung, Y. L.; Graney, S.; Voelcker, N. H. *Biotechnol. Prog.* **2006**, *22*, 1388–1393.

(57) Chen, L.; Chen, Z.-T.; Wang, J.; Xiao, S.-J.; Lu, Z.-H.; Gu, Z.-Z.; Kang, L.; Chen, J.; Wu, P.-H.; Tang, Y.-C.; Liu, J.-N. *Lab Chip* **2009**, *9*, 756–760.

(58) Swan, E. E. L.; Popat, K. C.; Grimes, C. A.; Desai, T. A. *J. Biomed. Mater. Res. Part A* **2005**, *72A*, 288–295.

(59) Lee, H. J.; Kim, D. N.; Park, S.; Lee, Y.; Koh, W.-G. *Acta Biomater.* **2011**, *7*, 1281–1289.

(60) Leary Swan, E. E.; Popat, K. C.; Desai, T. A. *Biomaterials* **2005**, *26*, 1969–1976.

(61) Sweetman, M. J.; Harding, F. J.; Graney, S. D.; Voelcker, N. H. *Appl. Surf. Sci.* **2011**, *257*, 6768–6774.

(62) Low, S. P.; Voelcker, N. H.; Canham, L. T.; Williams, K. A. *Biomaterials* **2009**, *30*, 2873–2880.

(63) de-Leon, S. B.-T.; Oren, R.; Spira, M. E.; Korbakov, N.; Yitzchaik, S.; Sa'ar, A. *Phys. Status Solidi A* **2005**, *202*, 1456–1461.

(64) Chin, V.; Collins, B. E.; Sailor, M. J.; Bhatia, S. N. *Adv. Mater.* **2001**, *13*, 1877–1880.

(65) Bayliss, S. C.; Heald, R.; Fletcher, D. I.; Buckberry, L. D. *Adv. Mater.* **1999**, *11*, 318–321.

(66) Mayne, A. H.; Bayliss, S. C.; Barr, P.; Tobin, M.; Buckberry, L. D. *Phys. Stat. Sol. A* **2000**, *182*, 505–515.

(67) Rea, I.; Lamberti, A.; Rendina, I.; Coppola, G.; Gioffrè, M.; Iodice, M.; Casalino, M.; De Tommasi, E.; De Stefano, L. *J. Appl. Phys.* **2010**, *107*, 014513–1 - 014513—4.

(68) Kilian, K. A.; Lai, L. M. H.; Magenau, A.; Cartland, S.; Bocking, T.; Di Girolamo, N.; Gal, M.; Gaus, K.; Gooding, J. J. *Nano Lett.* **2009**, *9*, 2021–2025.

(69) Yin, H. B.; Brown, T.; Greef, R.; Wilkinson, J. S.; Melvin, T. *Microelectron. Eng.* **2004**, *73—74*, 830–836.

(70) Kruger, M.; Arens-Fischer, R.; Thonissen, M.; Munder, H.; Berger, M. G.; Luth, H.; Hilbrich, S.; Theiss, W. *Thin Solid Films* **1996**, *276*, 257–260.

(71) Steiner, P.; Lang, W. *Thin Solid Films* **1995**, *255*, 52–58.

(72) Lammel, G.; Renaud, P. *Sens. Actuators, A* **2000**, *85*, 356–360.

(73) Song, J. H.; Sailor, M. J. *J. Am. Chem. Soc.* **1997**, *119*, 7381–7385.

(74) Starodub, V. M.; Fedorenko, L. L.; Sisetskiy, A. P.; Starodub, N. F. *Sens. Actuators, B* **1999**, *58*, 409–414.

(75) Jane, A.; Dronov, R.; Hodges, A.; Voelcker, N. H. *Trends Biotechnol.* **2009**, *27*, 230–239.

(76) Buriak, J. M. *Chem. Commun.* **1999**, 1051–1060.

(77) Stewart, M. P.; Buriak, J. M. *J. Am. Chem. Soc.* **2001**, *123*, 7821–7830.

(78) Lees, I. N.; Lin, H.; Canaria, C. A.; Gurtner, C.; Sailor, M. J.; Miskelly, G. M. *Langmuir* **2003**, *19*, 9812–9817.

(79) Guo, D. J.; Xiao, S. J.; Xia, B.; Wei, S.; Pei, J.; Pan, Y.; You, X. Z.; Gu, Z. Z.; Lu, Z. *J. Phys. Chem. B* **2005**, *109*, 20620–8.

(80) Giovannozzi, A. M.; Rocchia, M. *Sens. Actuators, B* **2008**, *130*, 795–801.

(81) Yang, M.; Teeuwen, R. L. M.; Giesbers, M.; Baggerman, J.; Arafat, A.; Wolf, F. A. d.; Hest, J. C. M. v.; Zuilhof, H. *Langmuir* **2008**, *24*, 7931–7938.

(82) Bocking, T.; Kilian, K. A.; Gaus, K.; Gooding, J. J. *Adv. Funct. Mater.* **2008**, *18*, 3827–3833.

(83) Innocenti, A.; Casini, A.; Alcaro, M. C.; Papini, A. M.; Scozzafava, A.; Supuran, C. T. *J. Med. Chem.* **2004**, *47*, 5224–5229.

(84) Koepsel, J. T.; Murphy, W. L. *Langmuir* **2009**, *25*, 12825–12834.

(85) Andruzzi, L.; Senaratne, W.; Hexemer, A.; Sheets, E. D.; Ilic, B.; Kramer, E. J.; Baird, B.; Ober, C. K. *Langmuir* **2005**, *21*, 2495–2504.

– This page intentionally left blank –

2.6 Additional Scientific Publications

2.6.9 *Electrochemistry of Polystyrene Intercalated Vertically Aligned Single and Double-Walled Carbon Nanotubes on Gold Electrodes*

K. E. Moore, **B. S. Flavel**, C. J. Shearer, A. V. Ellis, J. G. Shapter

Electrochemistry Communications 13 (2011) 1190–1193

DOI: 10.1016/j.elecom.2011.08.047

Abstract

Electrochemical electrodes incorporating double- and single-walled carbon nanotubes (CNTs) were fabricated on cysteamine modified flat gold substrates. Through covalent coupling of the amine end groups with carboxyl functionalized CNTs, a dense forest of vertically aligned CNTs was produced. To these a 30 nm thick insulating polystyrene layer was spin coated, resulting in exposure of the uppermost carbon nanotube ends. The electrochemical performance of each electrode was then determined using the redox probe ruthenium hexaamine. Once surrounded by polymer, the double-walled CNTs (DWCNTs) showed an improved electron transfer rate, compared to the single-walled electrode. This improvement was attributed to the protection of the electronic properties of the inner wall of the DWCNT during the chemical modification and suggests that DWCNTs may offer a useful alternative to SWCNTs in future electrochemical sensors and biosensors.

Contribution

K.E.M, A.V.E and J.G.S conceived the idea for the project. K.E.M, B.S.F and C.J.S performed the experiments. K.E.M wrote the paper and all authors contributed to the scientific evaluation of the results.

– This page intentionally left blank –

Electrochemistry Communications 13 (2011) 1190–1193

Contents lists available at SciVerse ScienceDirect

Electrochemistry Communications

journal homepage: www.elsevier.com/locate/elecom

Electrochemistry of polystyrene intercalated vertically aligned single- and double-walled carbon nanotubes on gold electrodes

Katherine E. Moore [a], Benjamin S. Flavel [b], Cameron J. Shearer [a], Amanda V. Ellis [a], Joseph G. Shapter [a,*]

[a] *Flinders Centre for Nanoscale Science and Technology, Flinders University, Sturt Road, Bedford Park, Adelaide 5001, South Australia*
[b] *Institute of Nanotechnology, Karlsruhe Institute of Technology, D-76021 Karlsruhe, Germany*

ARTICLE INFO

Article history:
Received 6 June 2011
Received in revised form 10 August 2011
Accepted 30 August 2011
Available online 10 September 2011

Keywords:
Double-walled carbon nanotubes
Cyclic volammetry
Gold electrode

ABSTRACT

Electrochemical electrodes incorporating double- and single-walled carbon nanotubes (CNTs) were fabricated on cysteamine modified flat gold substrates. Through covalent coupling of the amine end groups with carboxyl functionalized CNTs, a dense forest of vertically aligned CNTs was produced. To these a 30 nm thick insulating polystyrene layer was spin coated, resulting in exposure of the uppermost carbon nanotube ends. The electrochemical performance of each electrode was then determined using the redox probe ruthenium hexaamine. Once surrounded by polymer, the double-walled CNTs (DWCNTs) showed an improved electron transfer rate, compared to the single-walled electrode. This improvement was attributed to the protection of the electronic properties of the inner wall of the DWCNT during the chemical modification and suggests that DWCNTs may offer a useful alternative to SWCNTs in future electrochemical sensors and biosensors.

1. Introduction

In recent years there has been considerable interest in utilizing SWCNTs for electrochemical sensors [1] and biosensing devices [2]. Whilst SWCNTs are an extremely desirable material for incorporation into the aforementioned devices, achieving the level of manipulation required without adversely affecting the physical properties of the SWCNTs is difficult.

There are several methods to chemically assemble CNTs onto various types of substrates, which are detailed in the recent review by Diao and Liu [3]. These methods involve chemically functionalizing the nanotubes, most commonly with carboxylic acid groups [4] and covalently linking them to the surface via ester [5–6] or amide linkages [7]. Other methods involve electrochemical reduction of a diazonium to form a tether layer to which CNTs can be covalently attached [8–9]. A major issue with covalent attachment is that the CNTs require covalent functionalization, a process with introduces defects into the hexagonally bonded sp^2 carbon network [10], disrupting many of the attractive properties of the CNTs, particularly the conductivity [11].

Typically SWCNTs are used for device fabrication, however it has been suggested that DWCNTs may offer a superior alternative [12]. It has been proposed that upon chemical modification, the outer tube will act as a protective sheath, hence preserving the electronic properties of the inner tube. This selective functionalization has been demonstrated previously using Raman spectroscopy, which confirmed selective outer-wall functionalization of DWCNTs [13].

Recently, electrodes consisting of DWCNTs covalently bound to aminophenyl tether layers on silicon have been shown to have a superior heterogeneous electron transfer rate compared to those comprised of SWCNTs [13]. While these silicon based electrodes confirmed that DWCNTs are advantageous for use in electrochemical devices, very low electron transfer rates were reported and the surface structure resembled that of a dense conducting mat. It has been previously shown that vertically aligned SWCNTs electrodes have a faster charge transfer rate compared to randomly dispersed SWCNTs, indicating that for electrochemical studies, aligned CNTs are superior [14] and a more desirable surface structure for the further attachment of redox active species.

In this work, highly ordered vertically aligned CNT electrodes were fabricated by depositing cysteamine onto a flat gold surface and coupling the amine terminal groups with carboxyl functionalized SWCNTs and DWCNTs. In order to isolate electron transport to the CNTs only, insulating polystyrene (PS) was spin coated onto the surfaces to fill the voids between CNT bundles. PS was used as it has been shown [15] that its aromatic rings have an affinity for CNTs, due to π-π stacking.

2. Experimental

2.1. Preparation of polymer coated Au/cysteamine/CNT electrodes

DC arc discharge synthesized SWCNTs (Carbon Solutions Inc., P2-SWCNT, bundle diameter 4–5 nm, length 0.5–1.5 μm) and CVD produced DWCNTs (Nanolab, diameter 3–5 nm, length 1–5 μm) were purchased then functionalized and filtered using the previously reported method

---

* Corresponding author. Tel.: +61 8 8201 2005; fax: +61 8 8201 2905 1692 678161.
E-mail address: joe.shapter@flinders.edu.au (J.G. Shapter).

1388-2481/$ – see front matter © 2011 Elsevier B.V. All rights reserved.
doi:10.1016/j.elecom.2011.08.047

[13]. This process removes catalyst present in the CNT samples. CNTs were suspended in a solution of dimethylsulfoxide (Sigma-Aldrich) containing 0.2 mg mL^{-1} CNTs, 0.25 mg mL^{-1} *N,N′*-dicyclohexylcarbodiimide (DCC) (Fluka) and 0.14 mg mL^{-1} dimethylaminopyridine (DMAP) (Sigma-Aldrich). It is critical to keep moisture out of the suspension to prevent CNTs from crashing out of solution. Cysteamine modified gold surfaces were produced using the method of Losic et al. [16]. This substrate was then exposed to CNT solution for 24 h, after which it was rinsed with propan-2-ol (Merck) and dried under nitrogen.

Polymer solution containing 0.5% w/w PS ($M_w \approx 154000$ g mol^{-1}, Sigma Aldrich) in toluene (Sigma Aldrich) was added drop-wise to the Au/cyst/CNT electrodes until the whole surface was covered. The surfaces were then spun using a 150 mm Spin Coater (Laurell Technologies Corporation) at 3000 rpm for 1 min. The PS concentration and spin rates are critical to obtain appropriate polymer thicknesses.

2.2. Atomic Force Microscopy (AFM)

AFM tapping mode images were taken in ambient conditions with a multimode head and NanoScope V controller (Bruker) using silicon cantilevers (Mikromasch) with a fundamental resonance frequency between 250 and 400 kHz. All images represent flattened data using the NanoScope v8.0 (Digital Instruments) software package.

2.3. Electrochemistry

All electrochemistry measurements were taken using a BAS100B Electrochemical Analyser (Bioanalytical Systems Inc.). The CNT-based electrodes were mounted in the electrochemical cell exposing a 0.26 cm^2 circular area of surface to the cell solution. The CNT modified surface formed the working electrode, with platinum mesh and Ag/AgCl used as the counter and reference electrodes, respectively.

Cyclic voltammograms of 1 mmol L^{-1} Ru(NH$_3$)$_6$Cl$_3$ (Sigma-Aldrich) in pH 7.5 potassium phosphate buffer solution were obtained at scan rates of 20–1000 mV s^{-1}.

3. Results and discussion

Fig. 1(a) shows an AFM image of gold after exposure to cysteamine solution, which is observed to be relatively smooth and homogeneous with a root mean square roughness of 0.54 nm. Once the cysteamine covered gold was immersed in the CNT solution (Fig. 1(b)), the surface is dramatically rougher, with a root mean square roughness of 15.5 nm. This 'saw tooth' like surface topography has been observed previously for a range of different surfaces [8,17] and is characteristic of vertical alignment. The CNT bundles have an apparent height of ~45 nm for both single and double-walled CNTs. This observed height is shorter than the suspended nanotube length of ~450 nm [13]. This decrease has been observed previously [18] and is believed to occur because a) assembly of shorter CNTs occurs preferentially to their slower moving, longer counterparts [19]; b) in AFM imaging there is an interaction between the cantilever tip and the vertically aligned CNTs whereby the nanotubes slightly buckle or are pushed sideways, decreasing the observed length [5,20]; and c) due to AFM tip curvature, it cannot reach the substrate when imaging the closely packed needle-like structures [3]. Previous work by Gooding et al. has shown the rate constant for heterogeneous electron transfer is essentially independent of the length of the nanotubes [7] so the actual length will not affect the observations reported here. Bundle size was similar for both CNT samples (147 ± 6 nm for SWCNTs; 158 ± 11 nm for DWCNTs).

To determine polymer thickness needed on the CNT electrodes, different thicknesses of PS were spin coated onto the gold/cysteamine surfaces and electrochemically analyzed. The polymer thickness required to block electron transport to the electrode surface was found by replicating polymer spin conditions on flat silicon and was determined to be 30 nm by AFM, as shown in Fig. 1(c). Spin coating conditions remained constant for both single and double-walled CNTs, and the AFM image of DWCNT/PS surfaces is shown in Fig. 1(d). After polymer deposition similar 'saw tooth' topography is observed however the short nanotubes are no longer visible. The polymer interactions with both types of nanotubes can be expected to be the same leading to similar depositions on both CNT surfaces. To further verify the presence of attached CNTs on the surface, confocal Raman images and spectra were taken.

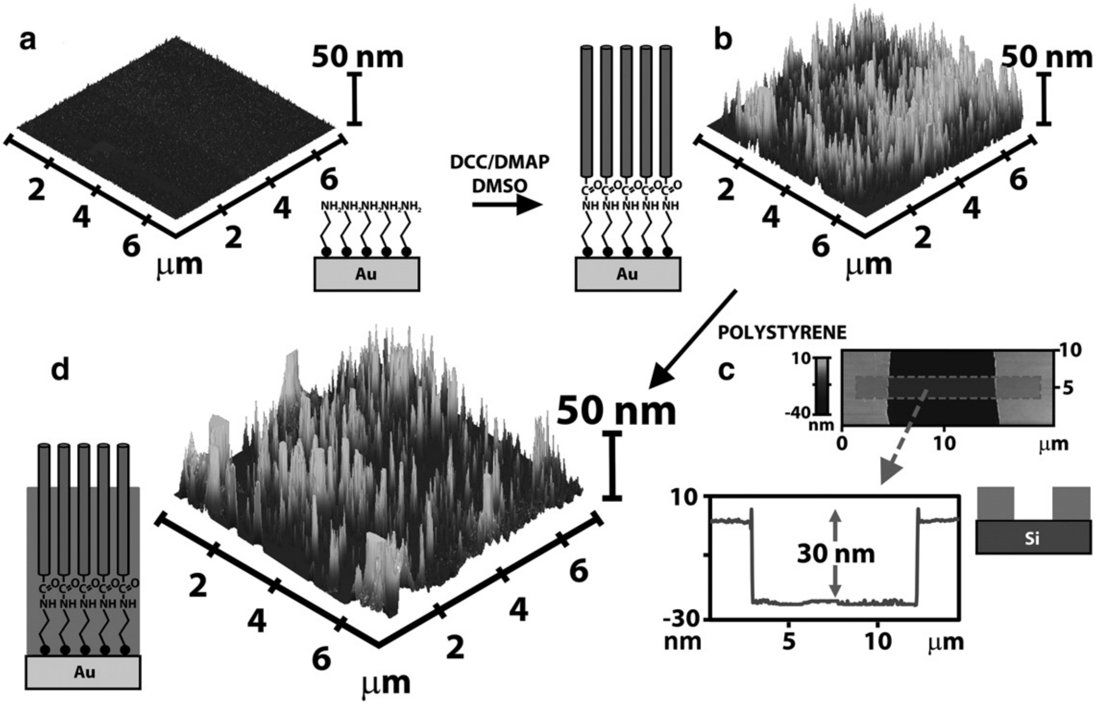

Fig. 1. AFM images of (a) a cysteamine modified gold surface, (b) subsequent covalent attachment of DWCNTs in the presence of DCC and DMAP, (c) PS spin coated onto flat silicon showing the film thickness and (d) DWCNT/cysteamine/gold electrode coated with PS.

The electrochemical performance of the gold/cysteamine electrodes with and without the addition of CNTs and PS was tested using aqueous cyclic voltammetry of the $Ru(NH_3)_6^{+3/2}$ redox couple in pH 7.5 potassium phosphate buffer solution. Fig. 2(a) shows scans for cysteamine modified gold surfaces with and without CNTs. From the insert, the peak-to-peak separation (ΔE_p) for the bare gold surface is 141 mV. Previous work has shown ΔE_p ranging between 60 and 70 mV [21–22] indicating there is a small amount of contamination on the gold surface despite electrochemical cleaning in H_2SO_4 with cycling until consistent CV curves were obtained. The surfaces are internally consistent and so the comparisons made are valid. For the cysteamine/gold surface, oxidation and reduction peaks can be observed, with ΔE_p of 151 mV indicating that the short chain alkane thiol has not blocked electron transfer between the redox probe and electrode surface in agreement with previous observations that the addition of cysteamine to gold only slightly increased ΔE_p and did not significantly change the electron transport properties of the electrode [7]. Upon covalent attachment of both SWCNTs and DWCNTs, ΔE_p was 150 mV and 137 mV, respectively. The addition of DWCNTs has improved the electrode, whilst the performance after addition of SWCNTs remains unchanged.

Fig. 2(b) shows CVs of various cysteamine modified gold substrates spin coated with PS. The polymer coated cysteamine/gold surface behaves as expected with no redox peaks due to the polymer's insulating nature. This indicates that addition of PS to the electrochemical surfaces completely blocks electron transport. In contrast, the CNT electrodes still maintain oxidation and reduction peaks after the addition of PS. For DWCNTs, clear reduction and oxidation peaks can be observed with ΔE_p of 182 mV. This separation is greater than that observed for DWCNT electrodes without polymer and indicates that redox to the gold surface has been nullified and can now only occur through the nanotubes. For the polymer coated SWCNT electrode, the redox current has been greatly suppressed but redox peaks are visible. The significantly lower current compared to the DWCNT surface can be attributed to disruption of the π orbitals caused by *sp*^{3} hybridisation due to chemical attack. The ΔE_p was 190 mV, slightly greater than that of the DWCNT electrode.

Table 1
Apparent electron transfer rates and the associated errors for the $Ru(NH_3)_6^{+3/+2}$ redox couple at gold surfaces reacted with SWCNTs and DWCNTs. Values were calculated from background subtracted data.

Sample	k_{app} (cm s^{-1})	Uncertainty (cm s^{-1})
Gold	1.70×10^{-3}	$\pm3.59\times10^{-5}$
Gold/Cysteamine	1.25×10^{-3}	$\pm6.86\times10^{-5}$
Gold/Cysteamine/SWCNTs	1.63×10^{-3}	$\pm7.25\times10^{-5}$
Gold/Cysteamine/DWCNTs	1.79×10^{-3}	$\pm4.13\times10^{-5}$
Gold/Cysteamine/SWCNTs/PS	7.82×10^{-4}	$\pm7.38\times10^{-5}$
Gold/Cysteamine/DWCNTs/PS	1.18×10^{-3}	$\pm5.65\times10^{-5}$

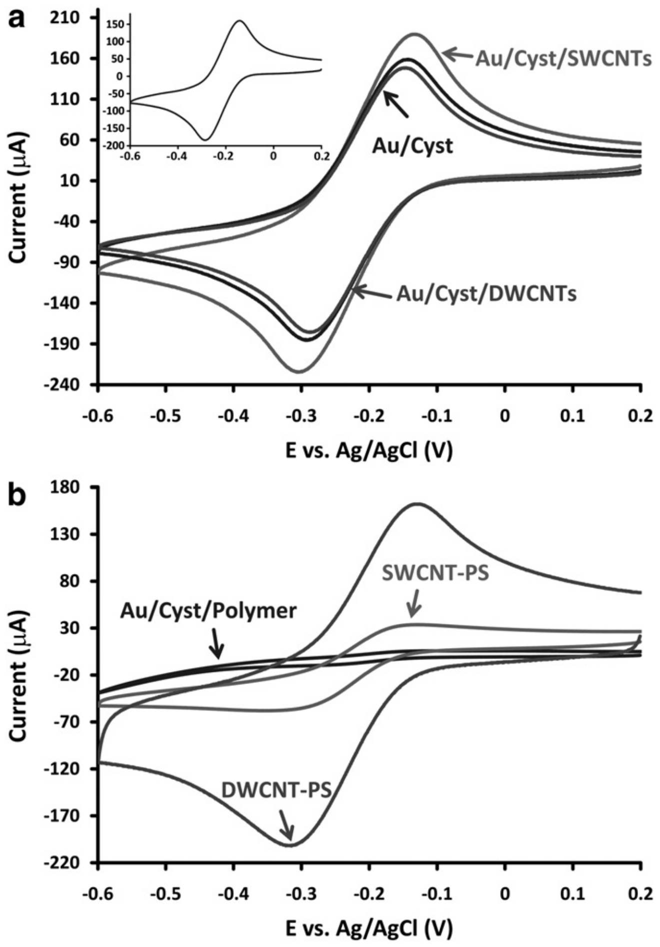

Fig. 2. Cyclic voltammograms of 1 mmol L^{-1} $Ru(NH_3)_6^{+3/+2}$ in pH 7.5 phosphate buffer for scans (0.1 V s^{-1}) obtained at gold surfaces modified with (a) cysteamine and with CNT solutions and (b) subsequently with PS.

The apparent electron transfer rate constant for a quasi-reversible system can be calculated using the method developed by Nicholson [23]. The diffusion coefficient for both redox states of $Ru(NH_3)_6^{+3/+2}$ are assumed to be equivalent at $D = 3.89\times10^{-6}$ cm^2 s^{-1}[8] and the electron transfer coefficient $\alpha = 0.5$ [23].

The rate constants for electrochemically cleaned gold and the surface with cysteamine layer confirm that the alkane thiol did not drastically alter the electron transfer properties of the surface (see Table 1). The rate constants also demonstrate that there is no significant difference between the electrochemical performances of the CNT electrodes. After addition of PS to fill the voids, the rates for the SWCNT and DWCNT electrodes show an increased difference between the performances of the CNTs which can be attributed to the polymer blocking electron transfer to the cysteamine/gold surface and limiting electron transport to the CNTs only. The DWCNT electrode showed a greater apparent electron transfer rate than its single-walled counterpart, confirming DWCNTs better protect the nanotube conduction pathway after chemical modification. While DWCNTs are expected to have more defects due to the CVD production process [24], the number of defects within a nanotube type is consistent for each electrode. As this experiment is focussed on comparing how each type of nanotube electrode is affected by polymer treatment, rather than a comparison of the absolute behaviour of each system, the different number of defects in the two systems is not critical for the final result of the experiment.

4. Conclusion

Electrochemical electrodes were synthesized by covalently attaching two types of carboxyl functionalized CNTs, double and single walled, to cysteamine modified flat gold surfaces. The apparent electron transfer rate constants were determined before and after intercalation with insulating PS. DWCNTs demonstrated superior electrochemical performance compared to their single-walled counterparts, due to their unique structure which allows chemical modification on the outer tube while maintaining the intrinsic electronic properties of the inner tube.

Acknowledgements

KM wishes to thank the Australian Government for an APA scholarship as well as the Playford Memorial Trust for a top up scholarship. This work is supported by the Australian Microscopy and Microanalysis Research Facility (AMMRF).

References

[1] M. Yang, Y. Yang, Y. Liu, G. Shen, R. Yu, Biosensors and Bioelectronics 21 (2006) 1125–1131.

[2] M. Delvaux, S. Demoustier-Champagne, Biosensors and Bioelectronics 18 (2003) 943–951.

[3] P. Diao, Z. Liu, Advanced Materials 22 (2010) 1430–1449.

[4] M.W. Marshall, S. Popa-Nita, J.G. Shapter, Carbon 44 (2006) 1137–1141.

[5] J. Yu, J.G. Shapter, J.S. Quinton, M.R. Johnston, D.A. Beattie, Physical Chemistry Chemical Physics 9 (2006) 510–520.

[6] S. Banerjee, T. Hemraj-Benny, S.S. Wong, Advanced Materials 17 (2005) 17–29.

[7] J.J. Gooding, R. Wibowo, J. Liu, W. Yand, S. Orbons, F.J. Mearns, J.G. Shapter, D.B. Hibbert, Journal of American Chemical Society 125 (2003) 9006–9007.

[8] B.S. Flavel, D.J. Garrett, J. Lehr, J.G. Shapter, A.J. Downard, Electrochimica Acta 55 (2010) 3995–4001.

[9] O. Arias de Fuentes, T. Ferri, M. Frasconi, V. Paolini, R. Santucci, Angewandte Chemie 123 (2011) 3519–3523.

[10] J. Zhao, H. Park, J. Han, J.P. Lu, The Journal of Physical Chemistry B 108 (2004) 4227–4230.

[11] H. Matsumura, T. Ando, Journal of the Physical Society of Japan 70 (2001) 2657–2665.

[12] T. Hayashi, D. Shimamoto, Y.A. Kim, H. Muramatsu, F. Okino, H. Touhara, T. Shimada, Y. Miyauchi, S. Maruyama, M. Terrones, M.S. Dresselhaus, M. Endo, ACS Nano 2 (2008) 485–488.

[13] K.E. Moore, B.S. Flavel, A.V. Ellis, J.G. Shapter, Carbon 49 (2011) 2639–2647.

[14] J.J. Gooding, A. Chou, J. Liu, D. Losic, J.G. Shapter, D.B. Hibbert, Electrochemistry Communications 9 (2007) 1677–1683.

[15] M.F. Islam, E. Rojas, D.M. Bergey, A.T. Johnson, A.G. Yodh, Nano Letters 3 (2003) 269–273.

[16] D. Losic, J.G. Shapter, J.J. Gooding, Australian Journal of Chemistry 54 (2001) 643–648.

[17] D.J. Garrett, B.S. Flavel, J.G. Shapter, K.H.R. Baronian, A.J. Downard, Langmuir 26 (2009) 1848–1854.

[18] J. Yu, D. Losic, M. Marshall, T. Bocking, J.J. Gooding, J.G. Shapter, Soft Matter 2 (2006) 1081–1088.

[19] Z. Liu, Z. Shen, T. Zhu, S. Hou, L. Ying, Z. Shi, Z. Gu, Langmuir 16 (2000) 3569–3573.

[20] B.S. Flavel, J. Yu, J.G. Shapter, J.S. Quinton, Carbon 45 (2007) 2551–2558.

[21] P. Krysinski, M. Brzostowska-Smolska, Journal of Electroanalytical Chemistry 424 (1997) 61–67.

[22] S.E. Creager, D.M. Collard, M.A. Fox, Langmuir 6 (1990) 1617–1620.

[23] R.S. Nicholson, Analytical Chemistry 37 (1965) 1351–1355.

[24] A.H. Barber, R. Andrews, L.S. Schadler, H.D. Wagner, Applied Physics Letters 87 (2005) 203106(1–3).

2.6 Additional Scientific Publications

2.6.10 *Single- and Double-Sided Chemical Functionalization of Bilayer Graphene*

A. Felten, **B. S. Flavel**, L. Britnell, A. Eckmann, P. Louette, J.-J. Pireaux, M. Hirtz,
R. Krupke, C. Casiraghi

Small 9 (2013) 631–639

DOI: 10.1002/smll.201202214

Abstract

An experimental study on the interaction between the top and bottom layer of a chemically functionalized graphene bilayer by mild oxygen plasma is reported. Structural, chemical, and electrical properties are monitored using Raman spectroscopy, transport measurements, conductive atomic force microscopy and X-ray photoelectron spectroscopy. Single- and double-sided chemical functionalization are found to give very different results: single-sided modified bilayers show relatively high mobility (200–600 $cm^2 V^{-1} s^{-1}$ at room temperature) and a stable structure with a limited amount of defects, even after long plasma treatment (>60 s). This is attributed to preferential modification and limited coverage of the top layer during plasma exposure, while the bottom layer remains almost unperturbed. This could eventually lead to decoupling between top and bottom layers. Double-sided chemical functionalization leads to a structure containing a high concentration of defects, very similar to graphene oxide. This opens the possibility to use plasma treatment not only for etching and patterning of graphene, but also to make heterostructures (through single-sided modification of bilayers) for sensors and transistors and new graphene derivatives materials (through double-sided modification).

Contribution

A.F, R.K, and C.C conceived the idea for the project. A.F, B.S.F, L.B, A.E, P.L, J.J.P and M.H performed the experiments. A.F wrote the paper and all authors were involved in the scientific evaluation and analysis of results.

– This page intentionally left blank –

NANO MICRO
small

Single- and Double-Sided Chemical Functionalization of Bilayer Graphene

Alexandre Felten, Benjamin S. Flavel, Liam Britnell, Axel Eckmann, Pierre Louette, Jean-Jacques Pireaux, Michael Hirtz, Ralph Krupke, and Cinzia Casiraghi*

An experimental study on the interaction between the top and bottom layer of a chemically functionalized graphene bilayer by mild oxygen plasma is reported. Structural, chemical, and electrical properties are monitored using Raman spectroscopy, transport measurements, conductive atomic force microscopy and X-ray photoelectron spectroscopy. Single- and double-sided chemical functionalization are found to give very different results: single-sided modified bilayers show relatively high mobility (200–600 cm^2 V^{-1} s^{-1} at room temperature) and a stable structure with a limited amount of defects, even after long plasma treatment (>60 s). This is attributed to preferential modification and limited coverage of the top layer during plasma exposure, while the bottom layer remains almost unperturbed. This could eventually lead to decoupling between top and bottom layers. Double-sided chemical functionalization leads to a structure containing a high concentration of defects, very similar to graphene oxide. This opens the possibility to use plasma treatment not only for etching and patterning of graphene, but also to make heterostructures (through single-sided modification of bilayers) for sensors and transistors and new graphene-derivatives materials (through double-sided modification).

1. Introduction

Graphene and few-layer graphene have recently been proposed as one of the basic building blocks for future nano-electronics.[1] The ultimate 2-dimensional character and the sp^2 configuration of the carbon network indeed leads to exceptional electronic, mechanical, and optical properties.[2–5]

Dr. A. Felten, Dr. C. Casiraghi
Physics Department
Free University Berlin
Arnimallee 14, 14195 Berlin, Germany
E-mail: alexandre.felten@fu-berlin.de

Dr. A. Felten, Dr. B. S. Flavel, Dr. M. Hirtz, Prof. R. Krupke
Institute of Nanotechnology
Karlsruhe Institute of Technology
76021 Karlsruhe, Germany

L. Britnell
School of Physics and Astronomy
Manchester University
M13 9PL Manchester, UK

A. Eckmann, Dr. C. Casiraghi
School of Chemistry and Photon Science Institute
Manchester University
M13 9PL Manchester, UK

Dr. P. Louette, Prof. J.-J. Pireaux
Research Center for the Physics of Matter
and Radiation (PMR)
University of Namur (FUNDP)
rue de Bruxelles 61, 5000 Namur, Belgium

Dr. M. Hirtz
Karlsruhe Nano Micro Facilitiy (KNMF)
76344 Eggestein-Leopoldshafen, Germany

Prof. R. Krupke
DFG Center for Functional Nanostructures (CFN)
76128 Karlsruhe, Germany
Institute für Materialwissenschaft
Technische Universität Darmstadt
64287 Darmstadt, Germany

DOI: 10.1002/smll.201202214

In order to develop graphene-based electronics, various approaches have been used to carefully tune and control the properties of graphene. In particular, chemical functionalization has been shown to be a facile and effective way for the modification of graphene. For example, chemisorption of hydrogen and fluorine has been reported:[6,7] Depending on the amount of bonded hydrogen or fluorine, it is possible to carefully tune the electronic properties of graphene from metallic to insulating. Furthermore, by exposing both surfaces of a suspended graphene, it is possible to achieve full hydrogenation or fluorination, leading to the creation of stoichiometric graphene-based derivatives, called graphane and fluoro-graphene, respectively.[6,7] Similarly to hydrogenation and fluorination, it has been shown that the covalent bonding with oxygen can induce a conversion of the carbon atoms from sp^2 to sp^3 hybridization, which produces changes in the optical and electronic properties of graphene.[8,9] The opening of a band gap, which should increase for increasing oxygen functionalization, has been predicted in such material.[10] Chemical modification of graphene can be easily obtained by exposing the material to a plasma. This method is very attractive for industrial applications because it is a simple, fast and scalable process. Depending on the plasma gas used, various species such as oxygen, fluorine, nitrogen and chlorine can be grafted to the graphene surface.[9,11–13] In addition, plasma methods are already used for patterning and etching of graphene.[14]

Whereas covalently modified monolayer graphene has been extensively studied in the literature, little is known about the possible tunability of the properties of bilayer graphene by chemical modification.[9,11,15,16] Usually, bilayer graphene is shown to be less reactive than a single layer graphene sheet, i.e. its optical and electronic properties change slower than the ones of graphene exposed to the same conditions.[15,16] For example, Dong et al.[17] have modified bilayer graphene using bromophenyl groups derived from diazonium salts. They showed that bilayer has smaller reactivity compared to monolayer. However, they also evidenced that the modification was occurring only at defects sites. Because of it they were able to observe only slight p-doping and no change in the resistance. Plasma treatment, in contrast, is a very different process which allows fast and large modification of graphene and does not depend on the defect concentration. Nourbakhsh et al.[9] compared experimentally and theoretically the plasma modification of mono and bilayer graphene. Their calculations showed that oxidized bilayer graphene, unlike monolayer, retains its semimetallicity even at oxygen densities as high as 50%.

In the case of plasma treatment, modification strongly depends on the ion energy involved in the process.[18] Nevertheless, under mild energetic conditions, it is normally assumed that chemical functionalization of graphite and few-layer graphene by oxygen plasma exposure happens layer by layer.[9,18,19] In the case of a bilayer graphene, it is normally assumed that only the top layer would be chemically functionalized, while the bottom layer is unperturbed. This opens the possibility to use plasma treatment to protect graphene from the environment by passivating the top layer of a bilayer. This is particularly important in sensing devices, where the sensitivity of graphene to environmental conditions, such as doping and charge transfer, strongly affect the reliability of the device. In addition, chemical functionalization by oxygen plasma allows having epoxy and hydroxyl groups on the surface,[9] which can be used to anchor chemical and biological objects to graphene.[20] The possibility to produce an insulating layer on top of graphene could be further used to develop in-situ gate dielectrics in field-effect transistors[21] and hetero-structures based transistors.[22]

In this work we aim at studying the interaction between the top and bottom layer of a chemically functionalized bilayer graphene by mild oxygen plasma. We are challenging the suggestion that chemical functionalization by plasma happens layer-by-layer: in contrast to previous studies,[9,11,16] where a lack of data and statistics did not allow to give a clear picture of the evolution of the bi-layer under plasma treatment, structural, chemical and electronic properties are here monitored at different stages of the plasma exposure by Raman spectroscopy, transport measurements, conductive AFM and X-ray photoelectron spectroscopy. For a better understanding, comparison between mono- and bilayer graphene is also shown. Our study reveals a peculiar behavior for one-sided chemically functionalized bilayer: while the monolayer becomes insulating upon increasing oxygen plasma exposure, the bilayer retains its ambipolar behavior with carrier mobility between 200–600 $cm^2\ V^{-1}\ s^{-1}$, even after long plasma treatment. We attribute this to the chemically functionalized graphene top-layer. In order to further confirm this result, double-sided chemical functionalization of bilayer has been performed: in the framework of the layer-by-layer functionalization, this process should allow chemisorption to take place on both layers. This material is very attractive because it is expected to have a four-layer structure such as dopant/carbon/carbon/dopant and an optical gap of 2.12 eV, in case of hydroxyl groups.[23] Raman spectroscopy clearly shows that double-sided chemical functionalization leads to a strongly distorted structure, compared to single-sided functionalized bilayer, in agreement with the theoretical predictions of ref. [23].

2. Results and Discussion

Figure 1a,b shows optical micro-graphs of a mono- and a bilayer graphene flakes in a 2-probe device configuration with source-drain electrodes separated by 4 μm. The number of layers has been determined by optical contrast and Raman spectroscopy. Both flakes were mechanically exfoliated on the same SiO_2 substrate and are separated by less than 1 mm ensuring identical plasma treatment conditions. The devices were exposed to repeated oxygen plasma treatments followed each time by Raman and electrical characterization. The plasma experiments were carried out at very low power (5 W) and short treatment exposure (5–120 s). Figure 1c,d shows the optical micro-graphs of the mono- and bilayer graphene corresponding to Figure 1a,b after 80 s exposure to oxygen plasma. We observe that the monolayer disappeared

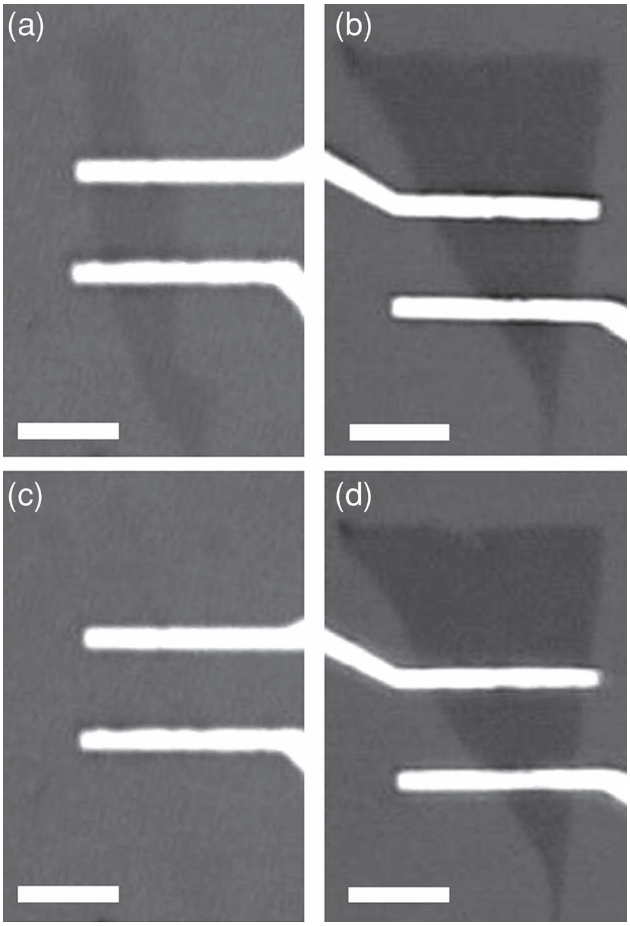

Figure 1. (a,b) Optical micrographs of pristine mono- and bilayer graphene devices, respectively. (c,d) Optical images of the same devices after 80 s oxygen plasma treatment. The scale bar (bottom left) is 5 µm and it is the same in all the figures.

while the bilayer is still optically visible. Raman spectroscopy is a fast, non destructive and powerful technique for the characterization of graphene:[24] it allows to unambiguously identify graphene,[25] probe doping and charged impurities,[26,27] as well as characterize disorder and defects.[28–30] The evolution of the Raman spectra of mono- and bilayer graphene measured for increasing exposure time to oxygen plasma is shown in **Figures 2**a and b, respectively. The pristine spectrum shows the two main Raman peaks of graphene: the G band around 1580 cm^{-1} and the 2D band around 2700 cm^{-1}. The 2D band acts as a fingerprint to assign the number of layers in graphene; a monolayer can be fitted with one Lorentzian exhibiting a full width at half maximum (FWHM) between 20–30 cm^{-1}, while a bilayer is composed by four components.[24]

Figure 2 shows that after oxygen plasma exposure, new features corresponding to defect activated bands appear in the Raman spectra. The most prominent ones are the so called D and D' band at ~1340 cm^{-1} and ~1620 cm^{-1}, respectively.[31] The Raman spectrum of the monolayer graphene shows drastic changes upon increasing oxygen plasma exposure. After 5 s of exposure, an intense D peak is already observed. Its intensity first increases and then rapidly decreases for increasing plasma exposure. After 10 s, a broadening of all peaks is observed (see Figure S1 in SI for quantitative data), followed by the suppression of the 2D band intensity, and a merging of the G and D' bands into one single peak. At 80 s the Raman signal is largely attenuated and finally disappears after longer treatment time, suggesting complete etching of the monolayer. This is confirmed by the optical image in Figure 1c where no optical contrast is seen at the supposed flake position. The changes in the Raman spectra of modified bilayer graphene are less drastic. From 5 to 60 s, the D and D' bands intensities increase slowly while the 2D band decreases. From 60 to 120 s, very little variation is observed

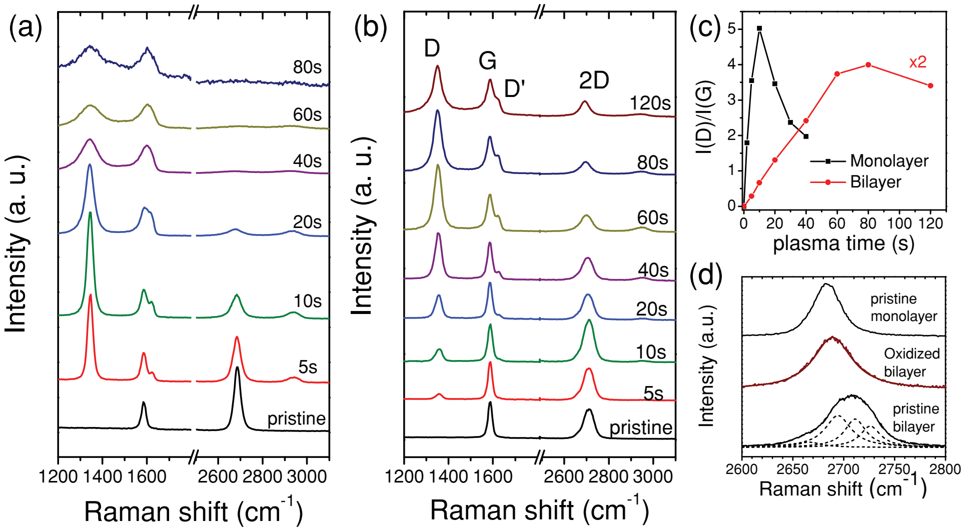

Figure 2. Raman spectra evolution of (a) monolayer and (b) bilayer graphene for increasing exposure to oxygen plasma. (c) D and G band integrated intensity ratio, I(D)/I(G), of mono- and bilayer graphene for increasing exposure time to oxygen plasma. (d) 2D Raman spectra of a pristine monolayer, pristine bilayer and oxygen plasma treated bilayer graphene (5 W, 120 s). The excitation wavelength is 514 nm.

in the spectra. As shown in Figure 1d, bilayer graphene is still optically visible after 80 s of treatment and the optical contrast slightly decreases from 23% for the pristine flake to 21% after 80 s plasma exposure. These results point out that the bilayer is less affected by the plasma treatment than the monolayer and that a stable configuration is reached after 40s. The higher resistance of the bilayer towards oxygen plasma could be attributed to its smaller intrinsic roughness (ripples)[32] and/or its better screening of the substrate charge puddles.[33,34]

The difference between the Raman spectral evolution of monolayer and bilayer graphene is quantified in Figure 2c by plotting the integrated height ratio of D and G band intensities, I(D)/I(G) as a function of the plasma exposure. I(D)/I(G) has been widely used in the literature to quantify the defect density in sp^2-bonded carbons: it is well known that at low defect concentrations I(D)/I(G) increases for increasing amount of disorder, while I(D)/I(G) decreases with disorder for high defect concentrations.[30,31,35] In the case of monolayer graphene, I(D)/I(G) clearly increases at short plasma-exposure time. This likely corresponds to the introduction of defects into the sp^2 lattice. The intensity ratio then decreases at high plasma-exposure time which is attributed to amorphisation of graphene due to the high density of defects. Amorphisation also becomes evident by the massive increase in the FWHM of all peaks and the disappearance of the 2D band.[36]

A similar qualitative evolution of the I(D)/I(G) ratio is observed for the bilayer (Figure 2c). However the bilayer has a much slower linear increase and reaches a maximum I(D)/I(G) of ~4 after 60 s, whereas the monolayer reaches a maximum ratio of ~5 after only 10 s, i.e. the bilayer does not achieve high defect concentration. In Figure 2c, we multiplied the calculated I(D)/I(G) of the bilayer by 2 since its G peak intensity is twice the one of graphene. Note that in the case of bilayer I(D)/I(G) does not strongly change after 60 s plasma exposure. In the initial regime, differences between monolayer and bilayer graphene are very pronounced with an intensity ratio up to 12 times higher for the monolayer. This suggests that the top layer reactivity in bilayer graphene is indeed much smaller compared to a single sheet. This is in agreement with previous results[11,37] and theoretical calculations, which predicts a maximum coverage of 25% in the case of bilayer.[23]

Figure 2d compares the 2D Raman spectra of pristine monolayer, pristine bilayer and oxidized bilayer graphene. The 2D peak of the monolayer graphene is fitted using one Lorentzian component of FWHM ~30 cm^{-1} centered at 2684 cm^{-1}. Due to its two pairs of conduction and valence bands allowing four double-resonance processes,[24] the bilayer graphene 2D band is best fitted using four Lorentzian components. The oxygen plasma treatment progressively transforms the 2D band of the bilayer into the one of a monolayer. After 120 s it can be fitted with one Lorentzian of FWHM ~46 cm^{-1} centered at 2689 cm^{-1}. The larger FWHM is attributed to the lose of the AB-stacking configuration after introduction of defects.

Tapping-mode and conductive AFM was performed on pristine and modified bilayer graphene in order to investigate the nature of defects after plasma treatment.[22,29] **Figure 3** shows topographic (a, c) and current images (b,d) of pristine and modified bilayer. The topographic images show the typical roughness of graphene on silicon oxide substrates.[38] A more detailed study of the surface topography and thickness of the modified bilayer can be found in Figure S2 and S3. It can be seen that bilayer graphene shows very little structural changes upon increasing plasma exposure as compared to the monolayer. The current measured on pristine bilayer (Figure 3b) shows a uniform distribution with a calculated local resistance of 12 kΩ, mostly coming from the contact resistance at the AFM tip. The variations seen in the image are coming from the electrical noise in the instrument (on the order of 2% of the signal). After oxygen plasma treatment (5 W, 100 s), the surface of the bilayer shows large inhomogeneities in the local resistance varying from 30 kΩ to almost insulating behaviour. These insulating regions can be associated with sp^3 carbon-oxygen clusters. The fact that oxygen atoms tend to cluster instead of being homogeneously distributed at the surface could be due to a preferential binding to local distortion in the graphene lattice (ripples).[6] In addition, the first adatom could also produce a defected region which favors the anchorage of further atoms in its surroundings. The AFM measurements thus reveal that the local surface resistance of the plasma modified bilayer is high and inhomogeneous. This result confirms chemisorptions on the top layer.

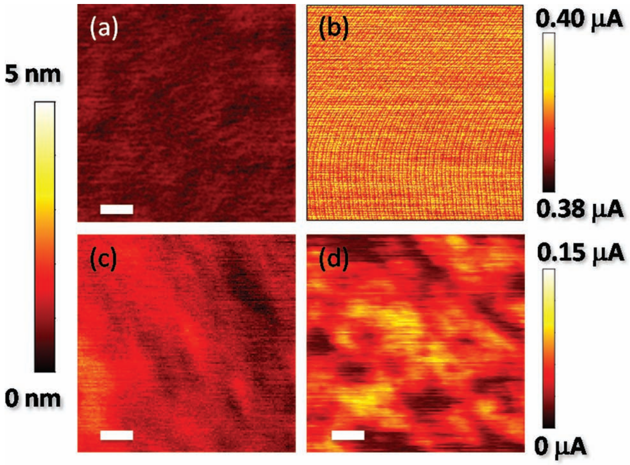

Figure 3. (a,c) Contact mode topographic AFM image of pristine and oxygen plasma treated bilayer graphene. (b,d) current map obtained with bias of 5 mV. Scale bar = 60 nm. Regular pattern in (b) is a measurement artifact.

X-ray photoelectron spectroscopy (XPS) was performed on the modified bilayer graphene in order to investigate the surface chemistry of the functionalized top layer. We used a micro-XPS equipment which allowed measurement on exfoliated flakes with 30 µm lateral resolution. **Figure 4**a shows the optical image of the bilayer graphene flake. The circle indicates the region where the XPS spectrum was measured. Figure 4b shows the comparison between the C1s peak of modified bilayer (5 W, 100 s; red curve) and pristine bilayer (black dotted curve). Functionalized bilayer shows a shoulder at high binding energy (286–289 eV) corresponding to carbon-oxygen bonds. The intensity of carbon-oxygen bonds is much

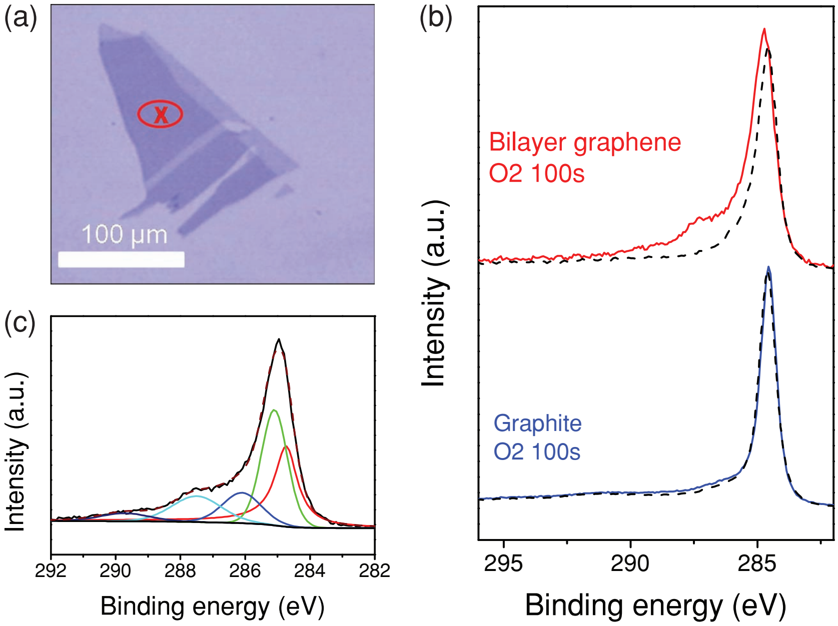

Figure 4. (a) Optical image of the bilayer graphene. The cross indicates the regions where the bilayer C1s spectrum is extracted. (b) XPS C1s spectra of bilayer (red curve) and graphite (blue curve), both treated in oxygen plasma for 100s. The upper and lower dotted black curve corresponds to the C1s of pristine bilayer and pristine graphite respectively. (c) Curve fitting of the oxidized bilayer graphene with components attributed as follow: red–sp^2 carbons, green–sp^3 carbons, blue $-$C$-$OH, cyan $-$C=O or C$-$O$-$C, and navy blue $-$COOH.

less pronounced in the case of oxidized graphite (blue curve) due to the penetration depth of electrons which probes around 20 graphitic layers while only the first layer is functionalized by the plasma. The C1s spectrum of the oxidized bilayer is then fitted using five components corresponding to sp^2 C–C, sp^3 C–C, hydroxyl C–OH, carbonyl C=O or epoxy C–O–C, and carboxyl COOH groups (Figure 4c).[39] The relative amount of these components corresponds respectively to 36.4%, 32.3%, 12.7%, 13.9% and 4.3%. These numbers should be treated with care because of the uncertainty inherent to the peak fitting. However, they show the complexity of the surface chemistry of the bilayer. Presence of carboxyl groups is of particular interest since they are commonly used as attachment points for molecules and biological objects. As an example, covalent attachment of DNA on plasma modified bilayer graphene is shown later in the discussion.

Transport measurements were carried out to study the electronic properties of oxidized graphene. The graphene transistors were fabricated on Si/SiO$_2$ substrate using conventional electron beam lithography followed by metal sputtering (1 nm Ti and 50 nm Pd). The measurements were performed in air and at room temperature. **Figure 5**a,b plots the resistance of the mono- and bilayer graphene devices as a function of the back gate voltage for increasing plasma duration. The source-drain voltage was set to 10 mV. The pristine sheets are slightly p-doped with hole mobilities of ~6700 and ~2300 cm^2 V^{-1} s^{-1} for graphene and bilayer graphene, respectively.

The electronic properties of plasma treated monolayer graphene are drastically degraded even after short oxygen plasma exposure. The film resistance increases by 1 order of magnitude after 10 s and additional 4 orders of magnitude after 20 s. For longer treatment time, the device resistance increases beyond the measurement range of the semiconductor parametric analyzer. These results are consistent with Raman measurements where an exposure of 20 s corresponds to the beginning of the high defect density regime. Rapid degradation of the structural and electrical

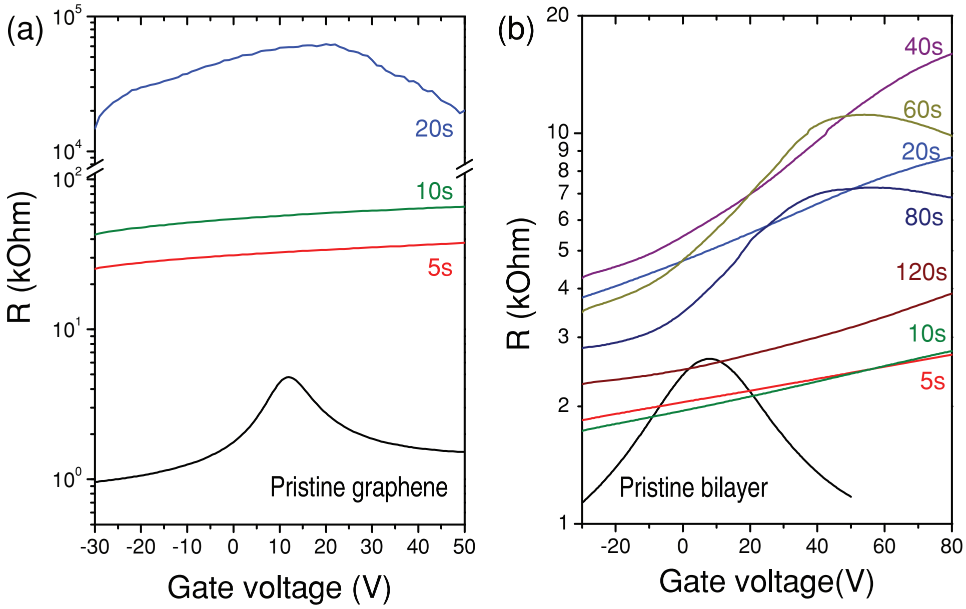

Figure 5. Resistance of graphene (a) and bilayer (b) devices as a function of the back gate voltage for increasing plasma exposure.

properties shows that, even at very low power and short time processes, oxygen plasma is very aggressive toward single graphene sheets, in agreement with previous results.[10,19,40]

Bilayer graphene, on the contrary, shows a very peculiar behavior upon plasma oxidation (Figure 5b). For short plasma exposure, the device resistance slightly increases with a very large shift of the Dirac point to a positive gate voltage beyond 80 V. A positive shift of the Dirac point can be explained by hole doping from oxygen species.[41] From 5 to 40 s, electron conduction cannot be induced. At 60 s we observe a slight decrease in the resistance which surprisingly is accompanied by a downshift of the Dirac point to ~50 V. After 120 s, the resistance further decreases while the Dirac point has been shifted up again to >80 V. It is worth noting that the total resistance of the bilayer device at zero gate voltage never exceeds 6 kΩ. We analyzed four devices and observed similar behavior (Figure S5 in SI). A possible explanation for this intriguing electrical behavior is that the oxygen plasma induces a mechanical deformation of the top layer. After 60 s of treatment the oxygen coverage may be high enough to induce a relatively strong wrinkling of the top layer, which may lead to decoupling of the two layers. In this situation, the decoupled bottom layer will mainly contribute to the current transport which may explain why the total resistance of the device is decreasing and the Dirac point is downshifting.

These results can be compared with recent works on modified bilayer. Dong et al.[17] have shown that modification of the bilayer using bromophenyl groups leads only to a p-doping of the bilayer with no changes in the resistance and mobility of the device. This different behavior compared to our results could be attributed to the different modification process with diazonium salts, which involves grafting only at pre-existing defect sites. In their study, Nourbakhsh et al.[9] have shown that the electrical properties of the bilayer after one short exposure to an O_2 plasma stay constant. Since no evolution of the electrical properties was presented, this result may correspond to our samples modified with 60–80 s plasma, where the resistance of the bilayer is decreased and the Dirac point is down-shifted.

To determine the mobility of the bilayer graphene, the $R(V_G)$ curves were fitted using the formula:[42]

$$R = R_c + \frac{L/W}{\mu e\sqrt{\left(\frac{C_g(V_G - V_D)}{e}\right)^2 + n_0^2}}$$

where R_c is the contact resistance, V_G the back gate voltage, V_D the Dirac point, μ the mobility, C_g is the back gate capacitance and n_0 represents the density of carriers at the minimum conductivity. We only fitted the hole-conduction branch of the curves since the data covers a wider range for gate voltages below the Dirac point. **Figure 6** shows the mobility of mono- and bilayer for increasing plasma duration. The mobility of the bilayer quickly decreases from ~2300 $cm^2 V^{-1} s^{-1}$ for pristine device to ~200 $cm^2 V^{-1} s^{-1}$ after 20 s of treatment. After 40 s this trend is reversed and μ_h increases to ~600 $cm^2 V^{-1} s^{-1}$. This observation is surprising since an increase in defect density should induce a rapid and irreversible drop of the mobility as observed for graphene. However, bilayer graphene does not follow the same trend presumably due to preferential chemisorption on the top layer. Once the maximum coverage is achieved on the top layer, then the material will be stable even under long plasma exposure preventing amorphization and decrease of mobility. A further explanation could be related to distortion induced by the chemisorption: the conversion of the bond from sp^2 to sp^3 induces strong distortion of the top layer. We speculate that at high coverage the top layer could "shrink" and decouple from the bottom layer. In this case, the relatively high mobility observed, should be attributed entirely to the bottom layer. Note that the calculated hole mobility of plasma oxidized bilayer graphene is 4–10 times lower than that of the pristine bilayer sample, it is comparable to the mobility of bilayer graphene grown by chemical vapor deposition (350–580 $cm^2 V^{-1} s^{-1}$), and it is higher than the mobility of reduced monolayer graphene oxide (0.5–200 $cm^2 V^{-1} s^{-1}$).[43–45]

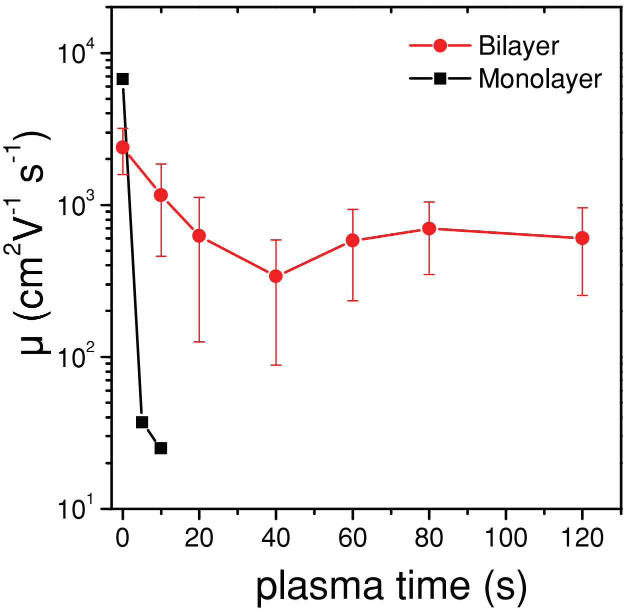

Figure 6. Hole mobility of the mono- and bilayer graphene sheet for increasing oxygen plasma exposure time.

We now move to double-sided oxygen plasma functionalization. In this case, the plasma treatment was performed on a suspended bilayer by exposing each side one after the other to the plasma under exactly the same conditions (**Figure 7**a). The non-exposed side is directly facing the surface of the electrode which therefore prevents its modification by the plasma gas. The bilayer membrane broke down after 120s exposure (60 s on each side), while measuring the Raman spectrum. Figure 7b compares the Raman G, D and D' peaks of suspended and supported bilayers after 120 s of oxygen plasma treatment. The spectrum of the supported bilayer after 60 s and monolayer after 40 s are also shown for comparison. The two spectra of suspended and supported bilayer exposed for 120 s are clearly different with the suspended one presenting a spectrum very similar to graphene oxide,[38,39] i.e. merging of G and D' peaks and much broader FWHM of the D peak (79.3 cm^{-1} compared to 40.3 cm^{-1} in the supported bilayer). Figure 7c shows the evolution of the D band FWHM

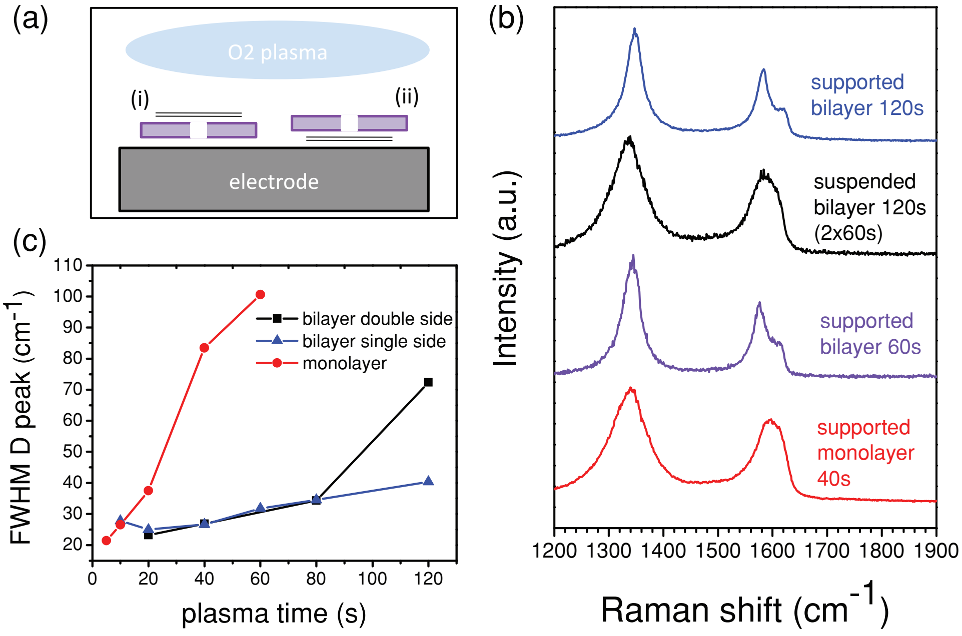

Figure 7. (a) Schematic representation of the double-side functionalization. The bilayer is sitting on a hole. First the top layer is exposed (i), then the sample is turned around and the bottom layer is exposed through the hole under otherwise identical conditions (ii). (b) Comparison of the G, D and D' Raman bands of supported and suspended bilayer graphene after 120 s exposure to oxygen plasma. The spectrum of the supported bilayer after 60 s and monolayer after 40 s are also shown for comparison. (c) Evolution of the D band FWHM for the monolayer, and single-side and double-side functionalized bilayers.

for monolayer, and single- and double-sided functionalized bilayer. Similar FWHM are first observed for single- and double-sided treated bilayer graphene which suggests that, for short treatment time, the introduction of defects by the oxygen plasma is similar in both type of functionalization. It is only after 80 s of treatment (40 s on each side) that the D band width strongly increases, reaching values observed in the monolayer. The double-sided chemical functionalization thus results in a new material which becomes highly disordered, in agreement with the theoretical predictions of ref. [23]. The oxygen treatment strongly changes the interaction between the two layers[9] and it is likely that the pristine layered structure is lost in double-sided bonding because of the formation of interlayer bonds.[46]

Finally, we show that covalent attachment of DNA to the single-sided functionalized bilayer is possible, leading the way to the fabrication of new graphene-based chemical and biological sensors. The DNA experiment was performed in 2 steps. First, the plasma treated bilayer was exposed to an amino- and FAM (carboxy fluorescein)-modified single strand DNA (NH_2-CAGAACCATAGACCCATAATTACT-FAM). In presence of carboxyl groups, the amino-terminated end of the DNA will react to form a covalent amide bond. The attachment of the DNA to the graphene could then in principle be visualized by fluorescence microscopy. Unfortunately, successful bonding of the DNA cannot be immediately confirmed due to drastic fluorescence quenching induced by the graphene.[47,48] In order to restore the fluorescence, a second step consisting in the hybridization with the complementary strand DNA was needed. Indeed, it has been shown that upon formation of the duplex, (i) physisorbed DNA strands are removed from the surface[49,50] and (ii) the fluorescein dye to graphene distance is increased for covalently attached DNA, hence restoring fluorescence.[47] **Figure 8** shows the fluorescent microscopy image of a plasma treated bilayer graphene after exposure to the amino- and FAM-modified DNA and its complementary strand. The fluorescence observed on the graphene confirms successful covalent attachment. In addition, a control experiment using non plasma functionalized graphene bilayer showed no fluorescence (see Supporting Information) which corroborates our results. These findings validate single-sided functionalized bilayer as a new building block in the fabrication of biosensors. Furthermore, the

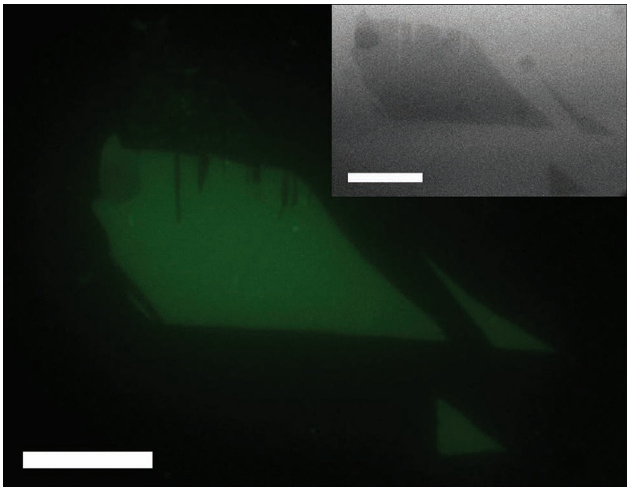

Figure 8. Fluorescent micrograph of a single-sided plasma-functionalized bilayer after covalent attachment with an amino- and FAM-modified single strand DNA and hybridization with its complementary strand. The inset shows a corresponding bright field image. The scale bars equal 20 µm.

simplicity of the functionalization procedure and the relatively high mobilities of the material provide two advantages over conventional graphene oxide.

3. Conclusion

In conclusion, we have studied the interaction between the top and bottom layer of a chemically functionalized bilayer by mild oxygen plasma. We aim to challenge the usual assumption of layer-by-layer chemical functionalization by plasma exposure. We have shown that plasma treatment is a simple method to tune the coupling between the layers: single-side treatment of bilayer led to the formation of a stable structure with relatively high charge mobility, which could be related to decoupling between the top and bottom layer. In contrast, exposure of both sides of the bilayer leads to a highly disordered structure similar to graphene oxide. This opens the possibility to use plasma treatment not only for etching and patterning of graphene, but also to make heterostructures (through single-sided modification of bilayer) for sensors and transistors and new graphene-derivatives materials (through double-sided modification).

4. Experimental Section

Graphene was produced by mechanical exfoliation of graphite (National de Graphite) onto 300 nm grown silicon oxide on doped silicon substrate (Active Business Company GmbH). Graphene sheets were identified by optical microscopy and the number of layers was confirmed using Raman spectroscopy. The graphene transistors were fabricated using conventional electron beam lithography followed by metal sputtering (1 nm Ti and 50 nm Pd). The source and drain electrodes were separated by 4 µm in order to avoid Raman measurements on the contacts (the laser spot size is ~500 nm). The silicon substrate was used as back gate. Before the measurements, the samples were annealed at 300 °C under vacuum for 4 hours in order to remove residue of PMMA left on graphene after the lithography process.

The graphene samples were modified in oxygen plasma at 100 mTorr, 5 W and with different duration. The experiments were carried out in a Plasmalab 80Plus from Oxford Instruments (capacitively coupled RF at 13.56 MHz). Each oxygen plasma treatment was immediately followed by Raman and electrical characterization. Raman spectra were measured using a 100x objective at 514 nm on a WITec spectrometer. The laser power was adjusted to 1 mW. All peaks were fitted using Lorentzian lines except for the D' band where a Fano line shape was used. Electrical measurements were performed in air at room temperature with an Agilent 4155C semiconductor parametric analyzer. XPS measurements were performed on a Thermo Scientific K-alpha. The spot size and pass energy were set to 30 µm and 50 eV respectively. A monochromatized Al Kα line hν = 1486.6 eV was used as the photon source, and photoelectrons were collected at an angle of 0° relative to the sample surface normal. Topography and current AFM images in Figure 3 were obtained with Atomic Force Microscope Nanoscope Dimension V (Bruker) in contact mode with conductive Pt/Ir coated cantilevers PPP-CONTPt (Nanosensors). This technique provides information on local conductivity, and can be used to distinguish the patches of sp^3 carbon (typically insulating) within perfect graphene matrix.[22,30] Current was measured at fixed bias of 5 mV applied to the tip via Keithley 2400 SourceMeter. Images were obtained in ambient conditions with scan rate 0.2 Hz and applied force of about 5 nN. Topography AFM images in the supporting information were obtained using a Dimension Icon (Bruker) AFM in tapping mode with Tap300Al-G cantilevers (BudgetSensors). Annealing of the oxidized bilayer was performed at 200 °C in high vacuum (10^{-6} mbar) for 2 h.

All DNA samples were purchased from Integrated DNA Technologies. The covalent attachment was performed by exposing the sample to a solution of 2.5 µM of the amino- and FAM-modified for 2 h. The fluorescent DNA was then hybridized by adding the sample in a PBS buffer solution (BupH, Thermo Scientific, pH 7.2) containing 3 µM of the complementary DNA. The sample was left in solution overnight and then carefully washed with PBS. The same procedure was repeated twice. Fluorescence images of the fluorescently labeled DNA on graphene were taken on an upright Eclipse 80i fluorescence microscope (Nikon) equipped with an Intensilight (Nikon) and a CoolSNAP HQ2 camera (Photometrics). After putting a cover slip onto the sample still wet with PBS, images were obtained with a 50x objective and 15 s exposure time. Images were contrast enhanced for reproduction only, all intensity measurements and comparisons for control experiments were done on raw and unaltered data from original images.

Supporting Information

Supporting Information is available from the Wiley Online Library or from the author.

Acknowledgements

A.F., B.F., and C.C. acknowledge the Alexander von Humboldt Foundation for financial support. The authors acknowledge S. Dehm for assistance with electron beam lithography and K. S. Novoselov for useful discussions. This work was partly carried out with the support of the Karlsruhe Nano Micro Facility (KNMF, www.kmf.kit.edu), a Helmholtz Research Infrastructure at Karlsruhe Institute of Technology (KIT, www.kit.edu).

---

[1] K. S. Novoselov, A. K. Geim, S. V. Morozov, D. Jiang, Y. Zhang, S. V. Dubonos, I. V. Grigorieva, A. A. Firsov, *Science* **2004**, *306*, 666.
[2] A. K. Geim, K. S Novoselov, *Nat. Mater.* **2007**, *6*, 183.
[3] C. Lee, X. Wei, J. W Kysar, J. Hone, *Science* **2008**, *8*, 902.
[4] P. Avouris, *Nano Lett.* **2010**, *10*, 4285.
[5] A. K. Geim, *Science* **2009**, *324*, 1530.
[6] D. C. Elias, R. R. Nair, T. M. Mohiuddin, S. V. Morozov, P. Blake, M. P. Halsall, A. C. Ferrari, D. W. Boukhvalov, M. I. Katsnelson, A. K. Geim, K. S Novoselov, *Science* **2009**, *323*, 610.
[7] R. Nair, W. Ren, R. Jalil, I. Riaz, V. G. Kravetz, L. Britnell, P. Blake, F. Schedin, A. S. Mayorov, S. Yuan, M. I. Katsnelson, H.-M. Cheng,

W. Strupinski, L. G. Bulusheva,, A. V. Okotrub, I. V. Grigorieva, A. N. Grigorenko, K. S Novoselov, A. K. Geim, *Small* **2010**, *24*, 2877.
[8] T. Gokus, R. R. Nair, A. Bonetti, M. Böhmler, A. Lombardo, K. S. Novoselov, A. K. Geim, A. C. Ferrari, A. Hartschuh, *ACS Nano* **2009**, *3*, 3963.
[9] A. Nourbakhsh, M. Cantoro, A. V. Klekachev, G. Pourtois, T. Vosch, J. Hofkens, M. H. van der Veen, M. M. Heyns, S. De Gendt, B. F. Sels, *J. Phys. Chem. C* **2011**, *115*, 16619.
[10] A. Nourbakhsh, M. Cantoro, T. Vosch, G. Pourtois, F. Clemente, M. H. van der Veen, J. Hofkens, M. M. Heyns, S. De Gendt, B. F. Sels, *Nanotechnology* **2010**, *21*, 435203.
[11] M. Jaiswal, C. H. Y. X. Lim, Q. Bao, C. T. Toh, K. P. Loh, B. Ozyilmaz, *ACS Nano* **2011**, *5*, 888.
[12] Y.-C. Lin, C.-Y. Lin, P.-W. Chiu, *Appl. Phys. Lett.* **2010**, *96*, 133110.
[13] J. Wu, L. Xie, Y. Li, H. Wang, Y. Ouyang, J. Guo, H. Dai, *J. Am. Chem. Soc.* **2011**, *133*, 19668.
[14] L. Liu, S. Ryu, M. R. Tomasik, E. Stolyarova, N. Jung, M. S. Hybertsen, M. L. Steigerwald, L. E. Brus, G. W. Flynn, *Nano Lett.* **2008**, *8*, 1965.
[15] F. M. Koehler, A. Jacobsen, K. Ensslin, C. Stampfer, W. J. Stark, *Small* **2010**, *6*, 1125.
[16] M. Wojtaszek, N. Tombros, A. Caretta, P. H. M. van Loosdrecht, B. J. van Wees, *J. Appl. Phys.* **2011**, *110*, 063715.
[17] X. Dong, Q. Long, A. Wei, W. Zhang, L.-J. Li, P. Chen, W. Huang, *Carbon* **2012**, *50*, 1517.
[18] Z. Luo, T. Yu, K.-J. Kim, Z. Ni, Y. You, S. Lim, Z. Shen, S. Wang, J. Lin, *ACS Nano* **2009**, *3*, 1781.
[19] T. Gokus, R. R. Nair, A. Bonetti, M. Böhmler, A. Lombardo, K. S. Novoselov, A. K. Geim, A. C. Ferrari, A. Hartschuh, *ACS Nano* **2009**, *3*, 3963.
[20] D. R. Dreyer, S. Park, C. W. Bielawski, R. S. Ruoff, *Chem. Soc. Rev.* **2010**, *39*, 228.
[21] B. Standley, A. Mendez, E. Schmidgall, M. Bockrath, *Nano Lett.* **2012**, *12*, 1165.
[22] L. Britnell, R. V. Gorbatchev, R. Jalil, B. D. Belle, F. Schedin, M. I. Katsnelson, L. Eaves, S. V. Morozov, A. S. Mayorov, N. M. R. Peres, A. H. Castro Neto, J. Leist, A. K. Geim, L. A. Ponomarenko, K. S. Novoselov, *Nano Lett.* **2012**, *12*, 1707.
[23] D. W. Boukhvalov, M. I. Katsnelson, *Phys. Rev. B* **2008**, *78*, 085413.
[24] A. C. Ferrari, *Sol. State Comm.* **2007**, *143*, 47.
[25] Y. K. Koh, M.-H. Bae, D. G. Cahill, E. Pop, *ACS Nano* **2011**, *5*, 269.
[26] C. Casiraghi, S. Pisana, K. S. Novoselov, A. K. Geim, A. C. Ferrari, *Appl. Phys. Lett.* **2007**, *91*, 233108.
[27] C. Casiraghi, *Phys. Status Solidi RRL* **2009**, *3*, 175.
[28] E. H. M. Ferreira, M. V. O. Moutinho, F. Stavale, M. M. Lucchese, R. B. Capaz, C. A. Achete, A. Jorio, *Phys. Rev. B* **2010**, *82*, 125429.
[29] P. Venezuela, M. Lazzeri, F. Mauri, *Phys. Rev. B.* **2011**, *80*, 241413.
[30] A. Eckmann, A. Felten, A. Mishchenko, L. Britnell, R. Krupke, K. S. Novoselov, C. Casiraghi, *Nano Lett.* **2012**, *12*, 3925.
[31] L. G. Cancado, A. Jorio, E. H. Martins Ferreira, F. Stavale, C. A. Achete, R. B. Capaz, M. V. O. Moutinho, A. Lombardo, T. S.Kulmala, A. C. Ferrari, *Nano Lett.* **2011**, *11*, 3190.
[32] J. C. Meyer, A. K. Geim, M. I. Katselnov, K. S. Novoselov, T. J. Booth, S. Roth, *Nature* **2007**, *446*, 60.
[33] R. Sharma, J. H. Baik, C. J. Perera, M. S. Strano, *Nano Lett.* **2010**, *10*, 398.
[34] X. Fan, R. Nouchi, K. Tanigaki, *J. Phys. Chem. C* **2011**, *115*, 12960.
[35] M. M. Lucchese, F. Stavale, E. H. Martins Ferreira, C. Vilani, M. V. O. Moutinho, R. B. Capaz, C. A. Achete, A. Jorio, *Carbon* **2010**, *48*, 1592.
[36] E. H. M. Ferreira, M. V. O. Moutinho, F. Stavale, M. M. Lucchese, R. B. Capaz, C. A. Achete, A. Jorio, *Phys. Rev. B* **2010**, *82*, 125429.
[37] S. Ryu, J. Maultzsch, M. Y. Han, P. Kim, L. E. Brus, *ACS Nano* **2011**, *5*, 4123.
[38] V. Geringer, M. Liebmann, T. Echtermeyer, S. Runte, M. Schmidt, R. Ruckamp, M. C. Lemme, M. Morgenstern, *Phys. Rev. Lett.* **2009**, *102*, 076102.
[39] A. Felten, C. Bittencourt, J.-J. Pireaux, G. Van Lier, J.-C. Charlier, *J. Appl. Phys.* **2005**, *98*, 074308.
[40] D. C. Kim, D.-Y. Jeon, H.-J Chung, Y. Woo, J. K. Shin, S. Seo, *Nanotechnology* **2009**, 375703.
[41] K. Kim, H. J. Park, B.-C. Woo, K. J. Kim, G. T. Kim, W. S. Yun, *Nano Lett.* **2008**, *8*, 3092.
[42] S. Kim, J. Nah, I. Jo, D. Shahrjerdi, L. Colombo, Z. Yao, E. Tutuc, S. K. Banerjee, *Appl. Phys. Lett.* **2009**, *94*, 062107.
[43] K. Yan, H. Peng, Y. Zhou, H. Li, Z. Liu, *Nano Lett.* **2011**, *11*, 1106.
[44] C. Gomez-Navarro, R. T. Weitz, A. M. Bittner, M. Scolari, A. Mews, M. Burghard, K. Kern, *Nano Lett.* **2009**, *9*, 2206.
[45] C. Su, Y. Xu, W. Zhang, J. Zhao, A. Liu, X. Tang, C.-H. Tsai, Y. Huang, L.-J. Li, *ACS Nano* **2010**, *9*, 5285.
[46] O. Leenaerts, B. Partoens, F. M. Peeters, *Phys. Rev. B* **2009**, *80*, 245422.
[47] L. Xie, X. Ling, Y. Fang, J. Zhang, Z. Liu, *J. Am. Chem. Soc.* **2009**, *131*, 9890.
[48] P.-J. J. Huang, J. Liu, *Small* **2012**, *8*, 977
[49] S. He, B. Song, D. Li, C. Zhu, W. Qi, Y. Wen, L. Wang, S. Song, H. Fang, C. A Fan, *Adv. Funct. Mater.* **2010**, *20*, 453.
[50] P.-J. J. Huang, J. Liu, *Anal. Chem.* **2012**, *84*, 4192.

Received: September 7, 2012

– This page intentionally left blank –

2.6 Additional Scientific Publications

2.6.11 *Increased Redox-Active Peptide Loading on Carbon Nanotube Electrodes*

K. E. Moore, **B. S. Flavel**, J. Yu, A. D. Abell, J. G. Shapter

Electrochimica Acta 89 (2013) 206–211

DOI: 10.1016/j.electacta.2012.10.108

Abstract

Carbon nanotube (CNT) electrodes for electrochemistry were fabricated from single- and double-walled carbon nanotubes. The electrodes were subsequently covalently loaded with a ferrocene modified α-aminoisobutyric acid peptide, and the electron transfer (ET) capabilities were probed with cyclic voltammetry. The CNT electrodes comprised of double walled CNTs (DWCNTs) demonstrated significantly higher peak current compared to their single walled counterparts (SWCNTs). This is attributed to a higher loading of the ferrocene modified peptide to the outer wall of the nanotube, through the presence of a larger number of defects sites within the sp^2 carbon lattice for the DWCNTs. This higher loading was achieved without compromising the ET rate, indicating that DWCNTs may offer a useful alternative to SWCNTs in future electrochemical sensors and biosensors.

Contribution

K.E.M, A.D.A and J.G.S conceived the idea for the project. K.E.M, B.S.F, J.Y performed the experiments. K.E.M wrote the paper and all authors contributed to the scientific evaluation of results.

– This page intentionally left blank –

Electrochimica Acta 89 (2013) 206–211

Contents lists available at SciVerse ScienceDirect

Electrochimica Acta

journal homepage: www.elsevier.com/locate/electacta

Increased redox-active peptide loading on carbon nanotube electrodes

Katherine E. Moore[a], Benjamin S. Flavel[b], Jingxian Yu[c,1], Andrew D. Abell[c], Joseph G. Shapter[a,*,1]

[a] *Flinders Centre for Nanoscale Science and Technology, Flinders University, Sturt Road, Bedford Park, Adelaide 5000, South Australia, Australia*
[b] *Institute of Nanotechnology, Karlsruhe Institute of Technology, D-76021 Karlsruhe, Germany*
[c] *School of Chemistry and Physics, The University of Adelaide, Adelaide 5000, South Australia, Australia*

ARTICLE INFO

Article history:
Received 20 July 2012
Received in revised form 17 October 2012
Accepted 19 October 2012
Available online 16 November 2012

Keywords:
Double walled carbon nanotubes
Ferrocene modified peptide
Redox probe loading

ABSTRACT

Carbon nanotube (CNT) electrodes for electrochemistry were fabricated from single- and double-walled carbon nanotubes. The electrodes were subsequently covalently loaded with a ferrocene modified α-aminoisobutyric acid peptide, and the electron transfer (ET) capabilities were probed with cyclic voltammetry. The CNT electrodes comprised of double walled CNTs (DWCNTs) demonstrated significantly higher peak current compared to their single walled counterparts (SWCNTs). This is attributed to a higher loading of the ferrocene modified peptide to the outer wall of the nanotube, through the presence of a larger number of defects sites within the *sp*^{2} carbon lattice for the DWCNTs. This higher loading was achieved without compromising the ET rate, indicating that DWCNTs may offer a useful alternative to SWCNTs in future electrochemical sensors and biosensors.

1. Introduction

Carbon nanotubes (CNTs) are a highly desirable material for incorporation into electrochemical [1,2] and biological sensing devices [3,4] owing to their fast heterogeneous electron transfer (ET), high surface area and electrochemical stability [5,6]. Furthermore the conductivity of CNTs has been shown to be remarkably sensitive to changes in surface adsorbates, making them ideal for highly sensitive nanoscale sensors [7]. To date many different carbon nanotube based electrochemical sensors and biosensors exist in the literature, consisting of either randomly dispersed [8,9] or well-ordered nanotube arrays [6,10,11]. However, in all cases the CNTs act as a molecular wire, allowing electrical communication between the underlying electrode and a redox species [7,12]. For well-ordered or vertically aligned CNT arrays, fast charge transfer has been demonstrated and is a significant advantage compared to randomly dispersed CNTs [5]. This has lead to the development of highly sensitive, reagentless sensing devices [7], where direct ET between the active redox-centre and an electrode surface occurs without the need for mediators. Due to the presence of a large working surface area and easy access of an analyte to the immobilized sensing probe [6], well-ordered or vertically aligned carbon nanotube electrodes have been loaded with molecular sensitive materials such as DNA [6,13], Cu nanoparticles [1] and anti-immunoglobulin G [11].

This has led to the detection of a wide range of analytes with improved sensitivity and selectivity [2]. For example, Guo et al. [13] recently reported a horizontally aligned CNT genosensor consisting of single-stranded DNA bridging a gap between SWCNTs, which was subsequently sensitive to complementary-stranded DNA. A well-matched DNA duplex was shown to exhibit resistance in the order of 1 MΩ, which in the presence of a GT or CA mis-match was increased ~300-fold. Somenath et al. also demonstrated a cholesterol sensor based upon modification of vertically aligned multi walled CNTs (MWCNTs) with the biocompatible polymer, polyvinyl alcohol, decorated with cholesterol oxidase (ChOx) [14]. In this sensor the use of carbon nanotubes was found to significantly increase sensor sensitivity through increases in the signal to noise ratio, and was directly attributed to an increase in surface area allowing a high loading of ChOx. An almost linear relationship between cholesterol concentration and the response current was observed in a clinical range up to 300 mg dL^{-1}. Flavel et al. [15] also demonstrated a copper ion sensor fabricated from CNT arrays decorated with the tripeptide Gly-Gly-His, capable of detecting concentrations at a micro molarity level. While this limit of detection is higher than previously reported gold-based sensors, where copper detection down to 3 nM was achieved [16], this novel silicon based sensor offers ease of integration into sophisticated electrical and electronic devices, and is of relevance under current water regulations within Australia. Additionally, Gooding et al. utilized vertically aligned glucose oxidase (GOx) modified SWCNTs on a cysteamine modified gold surface, demonstrating a GOx surface

---

* Corresponding author. Tel.: +61 8 8201 2005; fax: +61 8 8201 2905.
E-mail address: joe.shapter@flinders.edu.au (J.G. Shapter).

[1] ISE member.

0013-4686/$ – see front matter © 2012 Elsevier Ltd. All rights reserved.
http://dx.doi.org/10.1016/j.electacta.2012.10.108

concentration of 5.2×10^{-8} mol cm^{-2} with apparent ET rate of 9 s^{-1} [12].

As detailed in a recent review from Diao and Liu [17], several methods exist to chemically assemble CNTs on electrode surfaces. However, common to each method is chemical functionalization of the nanotubes, most commonly with carboxylic acid groups [18] and their subsequent covalent linking to a surface via an ester [19,20] or amide bond [12]. Unfortunately, such chemical functionalization introduces defects in the hexagonally bonded *sp*^{2} [21] lattice, which has the effect of disrupting many of the attractive properties of nanotubes, particularly charge transport [22]. We have recently shown that in order to avoid such disruption DWCNT are advantageous, whereby the outer tube can be selectively functionalized [23] with the inner tube retaining its undisrupted *sp*^{2} network and hence its intrinsic electronic properties. The ability to achieve this was then demonstrated in a comparison between carboxyl functionalized SWCNTs and DWCNTs immobilized on a self-assembled cysteamine layer on gold [24]. ET was then isolated to the CNTs by introduction of a polystyrene layer, filling the voids between CNT bundles, with DWCNTs showing a higher apparent ET rate constant for diffusion limited redox with $Ru(NH_3)_6{}^{3+/2+}$.

In this work the demonstrated benefits of utilizing DWNTs are capitalized upon by covalently linking an electro-active ferrocene terminated α-aminoisobutyric acid peptide (Aib_5-Fc), see Fig. 1(a), to vertically aligned arrays of DWCNTs on cysteamine modified gold substrates. As a further demonstration of the advantage of DWCNTs, an analogous system is also fabricated for SWCNTs. It is shown that not only do DWCNTs have an improved redox peptide loading, but also superior ET kinetics compared to SWCNTs.

2. Experimental

2.1. Synthesis of Aib_5-Fc

Fmoc-Aib-OH loaded 2-chlorotrityl chloride resin (GL Biochem Ltd.) was transferred into a sintered funnel. After the Fmoc group was removed by reaction with a solution of 25% piperidine (Merck) in N,N-dimethylformamide (DMF) (Merck) for 30 min, a solution of 0.05 M Fmoc-Aib-OH (GL Biochem Ltd.) in DMF containing 0.2 M 2-(1H-7-azabenzotriazol-1-yl)-1,1,3,3-tetramethyl uranium hexafluorophosphate methanaminium (HATU) (GL Biochem Ltd.) and 0.2 M diisopropylethyl amine (DIPEA) (Sigma–Aldrich) was added to the deprotected resin. The mixture was left for 2 h with occasional stirring, and then the resin was isolated by filtration. Successive additions of Fmoc-Aib-OH were carried out using this protocol to yield H_2N-Aib_4-OH loaded resin. In the last cycle, Boc-Aib-OH was capped onto the resin using the same protocol. The oligopeptide was cleaved with 2% trifluoroacetic acid (TFA) (Sigma–Aldrich)/DCM (v/v). After purification by high-performance liquid chromatography (HPLC), the resulting peptide Boc-Aib_5-OH was added to a solution of 0.05 M ferrocenylmethylamine [25,26] in DMF containing 0.2 M HATU and 0.2 M DIPEA. With stirring for 24 h at room temperature, the product Boc-Aib_5-Fc was purified by HPLC and further treated by a 4 M HCl/dioxane

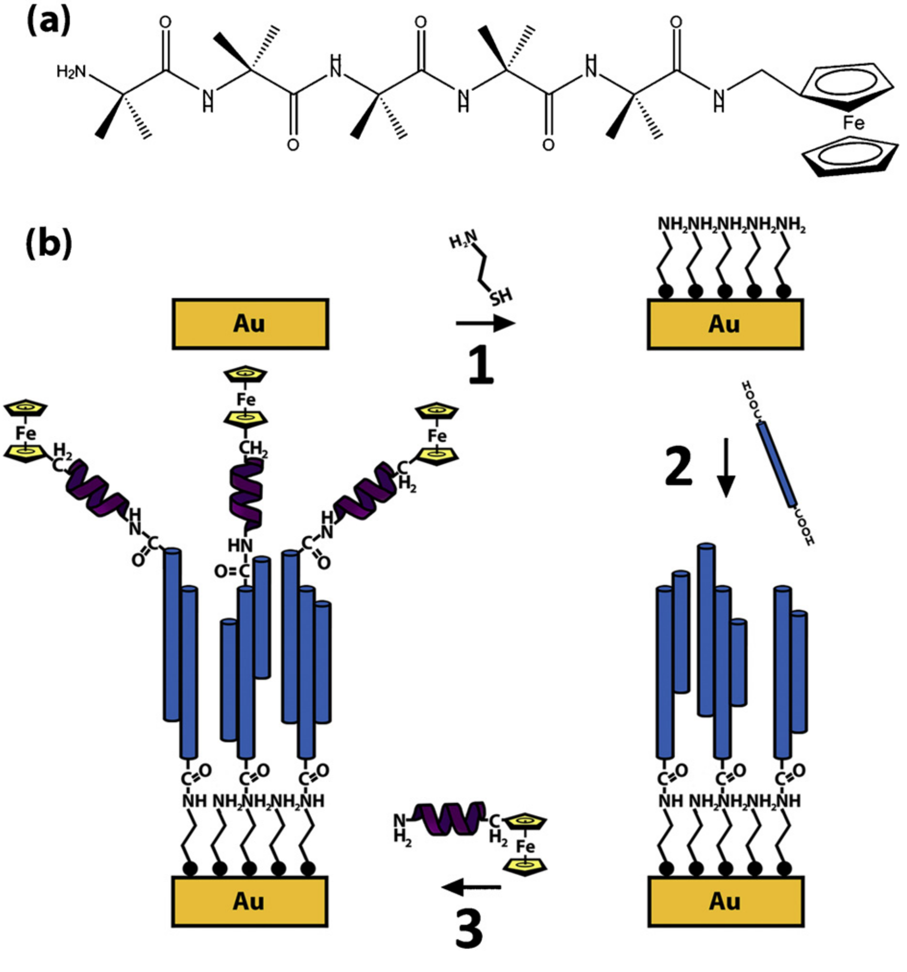

Fig. 1. (a) The redox peptide Aib_5-Fc and (b) fabrication of CNT electrodes decorated with covalently bound redox proteins.

solution (Sigma-Aldrich) for 15 min. After purification, the final H_2N-Aib$_5$-Fc was characterized by NMR and MS. ^1H NMR (300 MHz, DMSO) δ 8.44 (s, 1H, NH), 8.07 (s, 1H, NH), 7.91 (s, 1H, NH), 7.76 (s, 1H, NH), 7.24 (s, 1H, NH), 4.27 (m, 2H), 4.21 (m, 5H, Cp), 4.17 (m, 2H), 4.05 (d, 2H, CH_2), 1.52 (s, 6H, 2 βCH_3), 1.33 (s, 6H, 2 βCH_3), 1.32 (s, 6H, 2 βCH_3), 1.25 (s, 6H, 2 βCH_3), 1.23 (s, 6H, 2 βCH_3); MS: $[M+Na]^+_{calcd}$ = 663.6, $[M+Na]^+_{found}$ = 663.5.

2.2. Preparation of Au/cysteamine/CNT/Aib$_5$-Fc electrodes

DC arc discharge synthesized SWCNTs (Carbon Solutions Inc., P2-SWCNT, diameter 1.4–1.6 nm, length 0.5–1.5 μm) and CVD produced DWCNTs (Nanolab, diameter 3–5 nm, length 1–5 μm) were purchased and functionalized using previously reported methods [23]. CNTs were then suspended in a solution of dimethylsulfoxide (Sigma–Aldrich) containing 0.2 mg mL^{-1} CNTs, 0.25 mg mL^{-1} *N,N′*-dicyclohexylcarbodiimide (DCC) (Fluka) and 0.14 mg mL^{-1} dimethylaminopyridine (DMAP) (Sigma–Aldrich). Polished flat gold disc electrodes (2 mm diameter) were cleaned in 25% (v/v) H_2O_2/KOH (50 mM) for 20 min and then electrochemically cleaned by cycling between 0 and 1.5 V vs. Ag/AgCl in 50 mM KOH. This cleaning process yielded clean gold surfaces with peak separations of 59 mV for a (1 mM) $Ru(NH_3)_6{}^{3+/2+}$ containing solution. The clean, flat surfaces were then incubated in cysteamine (Sigma–Aldrich) for 24 h resulting in exposed amine groups (Fig. 1(b), step 1). These substrates were then exposed to SWCNT or DWCNT solution for 24 h, after which they were rinsed with propan-2-ol (Merck) and dried under nitrogen (Fig. 1(b), step 2). The surfaces were then exposed to 0.01 M H_2N-Aib$_5$-Fc in DMF solution containing 0.5 M HATU and 0.5 M DIPEA for 48 h before being further rinsed and dried (Fig. 1(b), step 3).

2.3. Electrochemistry

All electrochemistry measurements were taken with a CH Instruments Electrochemical Analyser (CH Instruments Inc.). The CNT modified gold surface formed the working electrode (geometric area of 0.33 cm^2), with platinum wire and Ag/AgCl used as the counter and reference electrodes, respectively. Cysteamine characterization was conducted in 1 mM pH 6.5 potassium phosphate buffer. The peak area of the cysteamine oxidation peak was calculated by subtracting the second scan from the first. Surface area calculation was conducted in 1 mM ruthenium hexamine trichloride in potassium phosphate buffer pH 7.5 by cycling between 0.2 V and −0.6 V vs. Ag/AgCl/KCl (3 M), in the negative direction initially. CNT electrodes were electrochemically characterized in 1 mM tetrabutylammoniumhexafluorophosphate (TBAPF6) (Sigma–Aldrich) in acetonitrile at scan rates of 25–1000 mV s^{-1}. Due to the low concentration of surface redox species, these cyclic voltammograms have been background subtracted using the fityk software v0.8.6 (http://www.unipress.waw.pl/fityk/).

3. Results and discussion

In order to determine the packing density of the cysteamine monolayer and thereby the availability of amine terminal groups for carbon nanotube attachment, the surface concentration of the cysteamine was calculated. Three self assembled monolayer (SAM) modified gold electrodes were cycled between 0 and 1.4 V by cyclic voltammetry in 1 mM pH 6.5 phosphate buffer against Ag/AgCl/KCl (3 M). Fig. 2 shows the first three cycles at a scan rate of 100 mV s^{-1}. In the first cycle a large oxidation peak centred at 0.997 V can be seen, and is absent from subsequent scans. Additionally, peaks centred at 0.930 V and 0.460 V can be seen and correspond to the oxidation and reduction of gold, and remain approximately equal for subsequent cycles. This indicates that the gold–sulphur bond of the cysteamine is irreversibly oxidized during the first scan, resulting in complete removal of the SAM from the gold surface. These observations are in excellent agreement with the literature [27–29] with the proposed mechanism for this reaction seen in Eq. (1) [27].

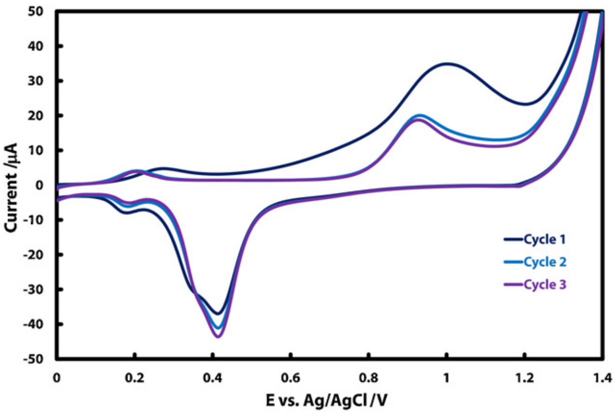

Fig. 2. Cyclic voltammetry cycle 1, 2 and 3 of a self assembled monolayer on polished gold in pH 6.5 potassium phosphate buffer, showing the irreversible oxidation of cysteamine at a scan rate of 100 mV s^{-1}.

$$AuS(CH_2)_2NH_2 + e^- \rightarrow Au(0) + {}^-S(CH_2)_2NH_2, \quad E = +1.00\,V\,vs.\,Ag/AgCl \qquad (1)$$

Using the oxidation peak area and Faraday's law below, the average surface concentration of cysteamine was determined [30].

$$\Gamma_{cyst} = \frac{Q_{cyst}}{nFA}$$

where Γ is the surface concentration (mol cm^{-2}), A is the electroactive area (cm^2), Q is the peak area of the voltammogram (C), I_p is the peak current (A) and n is the number of electrons involved.

The resultant surface concentration of cysteamine was found to be $5.6 \pm 0.69 \times 10^{-9}$ mol cm^{-2}, which is in agreement with Esplandiú et al. [28] who reported a surface coverage of 4.66×10^{-9} mol cm^2. This result suggests that a highly packed cysteamine layer was formed in this work and therefore a large number of surface amine sites for carbon nanotube attachment exist.

Fig. 3(a) shows diffusion limited cyclic voltammograms of gold surfaces before and after addition of the cysteamine SAM and subsequent attachment of CNTs with $Ru(NH_3)_6{}^{3+/2+}$ used as the redox probe. The reduction of ruthenium(III) to ruthenium(II) in aqueous solution involves the transfer of a single electron and exhibits close to ideal quasi-reversible outer sphere kinetic behaviour, making it a commonly used, fundamental redox reaction [8]. For a clean gold surface, the peak-to-peak potential (ΔE_p) was found to be 67 mV, and is comparable to the literature [31–33]. The electroactive area of the electrodes at each stage of fabrication was calculated with the use of the Randles–Sevcik equation.

$$i_p = \frac{0.447F^{3/2}An^{3/2}D^{1/2}Cv^{1/2}}{R^{1/2}T^{1/2}}$$

where i_p is the peak current, n is the number of electrons involved in oxidation or reduction, A is the area of the working electrode (cm^2), D is the diffusion coefficient of the electroactive probe (cm^2 s^{-1}), C is the concentration of electroactive probe in the solution (mol cm^{-3}), and v, F, R and T have their usual significance. Diffusion rates for the oxidized and reduced species (D_O and D_R) are 5.71×10^{-7} cm^2 s^{-1} and 8.8×10^{-7} cm^2 s^{-1}, respectively, as determined by Compton and co-workers [34]. From the slope in Fig. 3(b) and the Randles–Sevcik equation, the electroactive area of clean gold was calculated to be $5.7 \pm 0.17 \times 10^{-2}$ cm^2, which is slightly

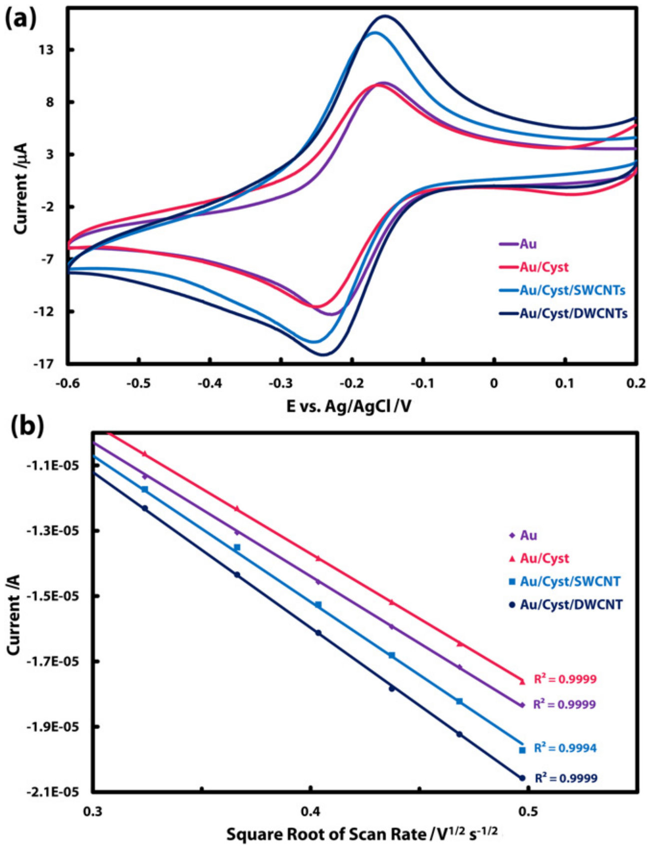

Fig. 3. (a) Cyclic voltammogram and (b) Randles–Sevcik plot of polished gold surfaces before and after addition of cysteamine and CNTs in 1 mM ruthenium hexaamine in potassium phosphate at a scan rate of 100 mV s^{-1}.

higher than the geometric area (3.14×10^{-2} cm^2) indicating the presence of surface roughness. After self-assembly of cysteamine a small decrease in current and an increase of ΔE_p to 87 mV is observed. The small reduction in current indicates that, despite the short chain length of the thiol, the cysteamine has increased resistance across the surface, slightly inhibiting ET to the underlying gold substrate. This has been shown in our previous work, where the addition of cysteamine resulted in a decrease of the apparent heterogeneous ET rate of approximately 25% [24]. After the addition of CNTs, the ΔE_p is 82 mV for both CNT types and a significant increase in current is observed, particularly for the oxidation reaction. It has been shown by Gooding et al. that by adding conductive nanoparticles to an insulating monolayer covered metal surface, the ET properties can be ‘switched on’ again by enabling electron tunnelling through the insulating barrier [35]. Since the current after nanotube addition is significantly higher than that of the original gold surface, we conclude that the increased current is not simply a ‘switching on’ effect but demonstrates an increase in surface area has occurred. This is in agreement with our previous work showing atomic force microscopy images before and after CNT addition [24] where high aspect ratio features are clearly visible on the surface. From the measured peak currents the calculated surface areas are $8.0 \pm 0.14 \times 10^{-2}$ cm^2 and $6.1 \pm 0.18 \times 10^{-2}$ cm^2 for SWCNTs and DWCNTs, respectively. Therefore, modification with a cysteamine tether layer and subsequent addition of vertically aligned CNTs has enhanced the electrochemical properties of the gold electrode, by increasing the electroactive surface area.

The electrochemical performance of both DWCNT and SWCNT electrodes before and after addition of Aib_5-Fc was then tested by cyclic voltammetry in TBAPF6/acetonitrile electrolyte solution. As can be seen in Fig. 4(a) prior to the addition of Aib_5-Fc no redox peaks can be seen, and as a result of a large active surface area, a prominent capacitive background is observed. This is expected as both DWCNTs and SWCNTs are electrochemically inactive within the potential window from 0.2 V to 0.6 V. However after the surfaces were left in Aib_5-Fc solution containing peptide coupling agents for 48 h, oxidation and reduction peaks centred at 0.43 V and 0.37 V can be seen. Fig. 4(b) shows background subtracted scans at 200 mV s^{-1} for both DWCNT and SWCNT electrodes, where the left y-axis corresponds to the DWCNT and the right corresponds to the SWCNT. Immediately it can be seen that the DWCNT electrodes have a much higher peak current compared to their single walled counterpart with oxidative currents of 350 nA and 40 nA, respectively. Since both electrode surfaces have very similar topographies [24] this almost tenfold increase in current is attributed to a higher number of Aib_5-Fc redox peptide bound to the nanotube walls. This is confirmed by calculation of the surface concentration of Aib_5-Fc molecules using Faraday’s law [30]. The surface concentration of Aib_5-Fc was determined to be $3.1 \pm 0.15 \times 10^{-11}$ mol cm^{-2} for the DWCNT electrode and $1.7 \pm 0.76 \times 10^{-11}$ mol cm^{-2} for the SWCNT electrode. The higher surface concentration for the DWCNT electrodes is expected due to the presence of significantly more carboxyl functionalities on the outer wall of a DWCNT compared to SWCNTs [23,36]. This allows for greater attachment of the redox peptide and a higher surface loading. Yu et al. [37] have calculated surface coverage of Aib_5-Fc on SWCNTs covalently bound to silicon in previous studies, with a coverage of 2.15×10^{-10} mol cm^{-2}. While this value is significantly higher than that reported here, one must consider that while Yu et al. have used same redox active peptide; the underlying CNT surface structure is vastly different.

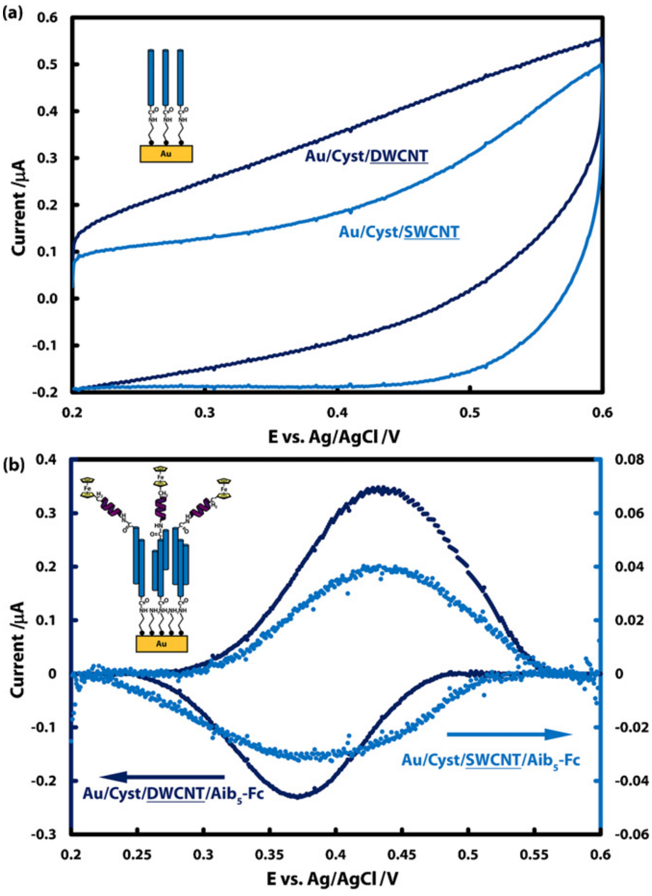

Fig. 4. Cyclic voltammograms of SWCNT and DWCNT electrode surfaces in 1 mM TBAPF6 in acetonitrile at a scan rate of 200 mV s^{-1} (a) before and (b) after functionalization with Aib_5-Fc, (b) has been background subtracted.

Yu et al. have directly attached SWCNTs to a hydroxylated silicon surface through an ester bond, allowing direct attachment to the surface. This procedure results in a very chemically homogeneous, atomically flat surface to which attachment can occur, resulting in high CNT density and good vertical alignment [19,37,38]. In contrast, the formation of a thiol monolayer on non-atomically flat gold leads to problems such as inhomogeneity in the SAM structure which will lead to some areas of bare substrate and potentially non availability for bonding of some of the amine terminal groups. These factors would lead to a more sparse CNT coverage and hence fewer CNT attachment sites available for Aib$_5$-Fc bonding. However the reported values can be compared to work by Okamoto et al. who achieved a surface concentration of 4.7×10^{-11} mol cm^{-2} for triferrocene functionalized double helix peptide chains covalently bound to a gold surface by two thiol bonds [39]. Since Okamoto et al. used a flat gold surface for attachment of their peptides, it is expected that the CNT surface would achieve a much higher loading. However one must consider that each peptide used by Okamoto et al. was bound with three ferrocene moieties, resulting in a higher surface concentration.

From Fig. 4(b), ΔE_p of the DWCNT and SWCNT electrodes is 65 mV and 37 mV, respectively. While the ideal ΔE_p should be zero for surface immobilized redox systems [40], these values still indicate very good ET between the underlying gold substrate and the surface adsorbed redox protein. The non zero ΔE_p values observed for both types of CNTs can be attributed to the presence of a potential difference between the electrode and the redox centre, possibly formed by the electric double layer in the vertically aligned CNT array [41].

The electrode kinetics for the Aib$_5$-Fc decorated CNT surfaces can be determined by plotting the oxidation and reduction peak currents against scan rate, as shown in Fig. 5. It can be seen that there is a clear linear relationship between the peak currents and the scan rate, which is indicative of surface bound electroactive species [42]. Furthermore, the slopes of the oxidation and reduction currents are symmetric around the origin, indicating that ΔE_p remains relatively constant with increasing scan rate.

The apparent ET rate constants of the Aib$_5$-Fc decorated DWCNT and SWCNT were also calculated using Laviron's method for the condition of $\Delta E_p < 200/\text{mV}$ [40]. By considering the value of the transfer coefficient, α, to be between 0.3 and 0.7, the average ET rates, k_{app}, were estimated according to the following equation.

$$k_{app} = \frac{mvnF}{RT}$$

where m is a dimensionless parameter related to the peak-to-peak separation. By using the slope from a plot of $v = f(m-1)$, mv could be determined and hence k_{app} found. The apparent ET rate for the DWCNT and SWCNT electrodes were 31 ± 6 s^{-1}, and 23 ± 2 s^{-1}, respectively. These values are comparable to ET rates reported for other redox bound vertically aligned CNT arrays on cysteamine modified gold. Gooding et al. [43] have reported the electrochemical properties of a glucose oxidase enzyme reconstituted around flavin adenine dinucleotide which was anchored to shortened SWCNT electrodes, with a rate of 9 s^{-1}. Similarly Gooding et al. [12] also reported the attachment of Microperoxidase MP-11, a small redox protein, to SWCNT arrays with a transfer rate of 3 s^{-1}. These rates are slower than that observed in this study due to the significantly larger distance electrons must travel from the redox centre of the protein to the CNT surface. Flavel et al. [44] reported a rate of 37 s^{-1} for ferrocene methanol functionalized SWCNTs on cysteamine modified electroless plated gold surfaces. This rate is very similar to that of the Aib$_5$-Fc modified SWCNT and DWCNT surfaces; however the slight difference can be attributed to the presence of the peptide chain used here to connect the redox active ferrocene to the CNTs. While the peptide chain is short and shows excellent ET properties, it does increase the distance electrons must travel by a further 10 Å [37] resulting in a lower transfer rate. The rates determined here can also be compared to work recently reported by Yu et al. [37] who determined a rate of 63 ± 4.3 s^{-1} for Aib$_5$-Fc decorated SWCNT arrays on silicon surfaces. As previously stated, Yu et al. have directly attached the CNTs to the underlying substrate resulting in very fast kinetic properties; while the cysteamine monolayer adds resistance to the surface, as seen by the increase in ΔE_p of 20 mV. Thus, it is reasonable that the system presented here demonstrates a slower ET rate than reported by Yu et al.

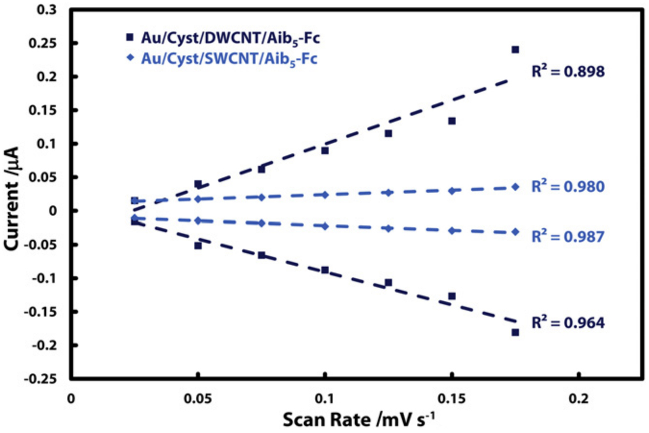

Fig. 5. Dependence of peak current on scan rate.

The slightly faster ET rate achieved for the DWCNTs suggests that the increased loading of redox peptide has not resulted in a loss of ET capabilities. This is as expected, as the higher functionality of the DWCNTs occurs on the outer wall only [23], maintaining the intrinsic electronic properties of the inner tube. This is in contrast to the SWCNTs, where functionalization of the carbon lattice directly affects the electronic properties, resulting in a lower ET rate [21,22]. This result also suggests that ET in the DWCNTs occurs largely through the inner tube, since modification results in less disruption of the electronic transport capabilities.

4. Conclusion

In this work, two types of electrochemical surfaces, consisting of DWCNTs and SWCNTs, with similar surface topographies were loaded with a ferrocene modified α-peptide. Due to the larger number of defects on the DWCNT outer walls, more of the peptide could be covalently bonded, resulting in a higher surface concentration and hence, a higher electrochemical current was observed. Determination of the apparent ET rate showed this was at no expense to the DWCNT's ET capabilities. This result suggests that DWCNT are advantageous to electrochemical surfaces, as they can be chemically modified for attachment without compromising the electronic properties.

Acknowledgements

KEM wishes to thank the Australian Government for an APA scholarship as well as the Playford Memorial Trust for a top up scholarship. This work is supported by the Australian Microscopy and Microanalysis Research Facility (AMMRF). BSF gratefully acknowledges the support of the Alexander von Humboldt Foundation. ADA and JY acknowledge financial support from the Australian Research Council.

References

[1] J. Yang, W.-D. Zhang, S. Gunasekaran, An amperometric non-enzymatic glucose sensor by electrodepositing copper nanocubes onto vertically well-aligned multi-walled carbon nanotube arrays, Biosensors and Bioelectronics 26 (2010) 279.

[2] S.K. Vashist, D. Zheng, K. Al-Rubeaan, J.H.T. Luong, F.-S. Sheu, Advances in carbon nanotube based electrochemical sensors for bioanalytical applications, Biotechnology Advances 29 (2011) 169.

[3] C.B. Jacobs, M.J. Peairs, B.J. Venton, Review: Carbon nanotube based electrochemical sensors for biomolecules, Analytica Chimica Acta 662 (2010) 105.

[4] M. Delvaux, S. Demoustier-Champagne, Immobilisation of glucose oxidase within metallic nanotubes arrays for application to enzyme biosensors, Biosensors and Bioelectronics 18 (2003) 943.

[5] J.J. Gooding, A. Chou, J. Liu, D. Losic, J.G. Shapter, D.B. Hibbert, The effects of the lengths and orientations of single-walled carbon nanotubes on the electrochemistry of nanotube-modified electrodes, Electrochemistry Communications 9 (2007) 1677.

[6] F. Berti, L. Lozzi, I. Palchetti, S. Santucci, G. Marrazza, Aligned carbon nanotube thin films for DNA electrochemical sensing, Electrochimica Acta 54 (2009) 5035.

[7] J. Wang, Carbon-nanotube based electrochemical biosensors: a review, Electroanalysis 17 (2005) 7.

[8] L.Y. Heng, A. Chou, J. Yu, Y. Chen, J.J. Gooding, Demonstration of the advantages of using bamboo-like nanotubes for electrochemical biosensor applications compared with single walled carbon nanotubes, Electrochemistry Communications 7 (2005) 1457.

[9] S.H. Lim, J. Wei, J. Lin, Q. Li, J. KuaYou, A glucose biosensor based on electrodeposition of palladium nanoparticles and glucose oxidase onto nafion-solubilized carbon nanotube electrode, Biosensors and Bioelectronics 20 (2005) 2341.

[10] X. Yu, B. Munge, V. Patel, G. Jensen, A. Bhirde, J.D. Gong, S.N. Kim, J. Gillespie, J.S. Gutkind, F. Papadimitrakopoulos, J.F. Rusling, Carbon nanotube amplification strategies for highly sensitive immunodetection of cancer biomarkers, Journal of the American Chemical Society 128 (2006) 11199.

[11] A. Venkatanarayanan, K. Crowley, E. Lestini, T.E. Keyes, J.F. Rusling, R.J. Forster, High sensitivity carbon nanotube based electrochemiluminescence sensor array, Biosensors and Bioelectronics 31 (2012) 233.

[12] J.J. Gooding, R. Wibowo, J. Liu, W. Yand, S. Orbons, F.J. Mearns, J.G. Shapter, D.B. Hibbert, Protein electrochemistry using aligned carbon naotube arrays, Journal of Ammerican Chemical Society 125 (2003) 9006.

[13] X. Guo, A.A. Gorodetsky, J. Hone, J.K. Barton, C. Nuckolls, Conductivity of a single DNA duplex bridging a carbon nanotube gap, Nat Nano 3 (2008) 163.

[14] R. Somenath, V. Harindra, C. Wonbong, Vertically aligned carbon nanotube probes for monitoring blood cholesterol, Nanotechnology 17 (2006) S14.

[15] B. Flavel, M. Nambiar, J. Shapter, Electrochemical detection of copper using a Gly-Gly-His modified carbon nanotube biosensor, Silicon 3 (2011) 163.

[16] W. Yang, J.J. Gooding, D.B. Hibbert, Redox voltammetry of sub-parts per billion levels of Cu at polyaspartate-modified gold electrodes, Analyst 126 (2001) 1573.

[17] P. Diao, Z. Liu, Vertically aligned single-walled carbon nanotubes by chemical assembly – methodology, properties, and applications, Advanced Materials 22 (2010) 1430.

[18] M.W. Marshall, S. Popa-Nita, J.G. Shapter, Measurement of functionalised carbon nanotube carboxylic acid groups using a simple chemical process, Carbon 44 (2006) 1137.

[19] J. Yu, J.G. Shapter, J.S. Quinton, M.R. Johnston, D.A. Beattie, Direct attachment of well-aligned single-walled carbon nanotube architectures to silicon (100) sufaces: a simple approach for device assembly, Physical Chemistry Chemical Physics 9 (2006) 510.

[20] S. Banerjee, T. Hemraj-Benny, S.S. Wong, Covalent surface chemistry of single-walled carbon nanotubes, Advanced Materials 17 (2005) 17.

[21] Q. Wang, W.H. Duan, N.L. Richards, K.M. Liew, Modeling of fracture of carbon nanotubes with vacancy defect, Physical Review B 75 (2007) 201405.

[22] H. Matsumura, T. Ando, Conductance of carbon nanotubes with a stone-wales defect, Journal of the Physical Society of Japan 70 (2001) 2657.

[23] K.E. Moore, B.S. Flavel, A.V. Ellis, J.G. Shapter, Comparison of double-walled with single-walled carbon nanotube electrodes by electrochemistry, Carbon 49 (2011) 2639.

[24] K.E. Moore, B.S. Flavel, C.J. Shearer, A.V. Ellis, J.G. Shapter, Electrochemistry of polystyrene intercalated vertically aligned single- and double-walled carbon nanotubes on gold electrodes, Electrochemistry Communications 13 (2011) 1190.

[25] F. Ossola, P. Tomasin, F. Benetollo, E. Foresti, P.A. Vigato, Synthesis, structure and properties of new ferrocene-containing compounds, Inorganica Chimica Acta 353 (2003) 292.

[26] P.D. Beer, D.K. Smith, Tunable bis(ferrocenyl) receptors for the solution-phase electrochemical sensing of transition-metal cations, Journal of the Chemical Society, Dalton Transactions (1998) 417.

[27] M.M. Walczak, D.D. Popenoe, R.S. Deinhammer, B.D. Lamp, C. Chung, M.D. Porter, Reductive desorption of alkanethiolate monolayers at gold: a measure of surface coverage, Langmuir 7 (1991) 2687.

[28] M.J. Esplandiú, H. Hagenström, D.M. Kolb, Functionalized self-assembled alkanethiol monolayers on Au(1 1 1) Electrodes: 1. Surface structure and electrochemistry, Langmuir 17 (2001) 828.

[29] M. Wirde, U. Gelius, L. Nyholm, Self-assembled monolayers of cystamine and cysteamine on gold studied by XPS and voltammetry, Langmuir 15 (1999) 6370.

[30] A.J. Bard, L.R. Faulkner, Introduction and Overview of Electrode Processes, in: Electrochemical Methods: Fundamentals and Applications, John Wiley and Sons, Inc., New York, 2001, pp. 1–43.

[31] H.O. Finklea, D.A. Snider, J. Fedyk, Passivation of pinholes in octadecanethiol monolayers on gold electrodes by electrochemical polymerization of phenol, Langmuir 6 (1990) 371.

[32] Q. Cheng, A. Brajter-Toth, Selectivity and sensitivity of self-assembled thioctic acid electrodes, Analytical Chemistry 64 (1992) 1998.

[33] S.E. Creager, D.M. Collard, M.A. Fox, Mediated electron transfer by a surfactant viologen bound to octadecanethiol on gold, Langmuir 6 (1990) 1617.

[34] Y. Wang, J.G. Limon-Petersen, R.G. Compton, Measurement of the diffusion coefficients of $[\mathrm{Ru(NH_3)_6}]^{3+}$ and $[\mathrm{Ru(NH_3)_6}]^{2+}$ in aqueous solution using microelectrode double potential step chronoamperometry, Journal of Electroanalytical Chemistry 652 (2011) 13.

[35] J.B. Shein, L.M.H. Lai, P.K. Eggers, M.N. Paddon-Row, J.J. Gooding, Formation of efficient electron transfer pathways by adsorbing gold nanoparticles to self-assembled monolayer modified electrodes, Langmuir 25 (2009) 11121.

[36] A.H. Barber, R. Andrews, L.S. Schadler, H.D. Wagner, On the tensile strength distribution of multiwalled carbon nanotubes, Applied Physics Letters 87 (2005) 203106.

[37] J. Yu, O. Zvarec, D.M. Huang, M.A. Bissett, D.B. Scanlon, J.G. Shapter, A.D. Abell, Electron transfer through α-peptides attached to vertically aligned carbon nanotube arrays: a mechanistic transition, Chemical Communications 48 (2012) 1132.

[38] J. Yu, S. Mathew, B.S. Flavel, M.R. Johnston, J.G. Shapter, Ruthenium porphyrin functionalized single-walled carbon nanotube arrays–a step toward light harvesting antenna and multibit information storage, Journal of the American Chemical Society 130 (2008) 8788.

[39] S. Okamoto, T. Morita, S. Kimura, Electron transfer through a self-assembled monolayer of a double-helix peptide with linking the terminals by ferrocene, Langmuir 25 (2009) 3297.

[40] E. Laviron, General expression of the linear potential sweep voltammogram in the case of diffusionless electrochemical systems, Journal of Electroanalytical Chemistry and Interfacial Electrochemistry 101 (1979) 19.

[41] I.M. Shiryaeva, J.P. Collman, R. Boulatov, C.J. Sunderland, Nonideal electrochemical behavior of biomimetic iron porphyrins: interfacial potential distribution across multilayer films, Analytical Chemistry 75 (2002) 494.

[42] M. Lyons, G. Keeley, The redox behaviour of randomly dispersed single walled carbon nanotubes both in the absence and in the presence of adsorbed glucose oxidase, Sensors 6 (2006) 1791.

[43] J. Liu, A. Chou, W. Rahmat, M.N. Paddon-Row, J.J. Gooding, Achieving direct electrical connection to glucose oxidase using aligned single walled carbon nanotube arrays, Electroanalysis 17 (2005) 38.

[44] B.S. Flavel, J. Yu, A.V. Ellis, J.G. Shapter, Electroless plated gold as a support for carbon nanotube electrodes, Electrochimica Acta 54 (2009) 3191.

2.6 Additional Scientific Publications

2.6.12 *Patterned Forests of Vertically-Aligned Multiwalled Carbon Nanotubes Using Metal Salt Catalyst Solutions*

D. J. Garrett, **B. S. Flavel**, K. H. R. Baronian, A. J. Downard

Journal of Nanotechnology & Nanoscience 13 (2013) 728–731

DOI: 10.1166/jnn.2013.7078

Abstract

A simple method for producing patterned forests of multiwalled carbon nanotubes (MWCNTs) is described. An aqueous metal salt solution is spin-coated onto a substrate patterned with photoresist by standard methods. The photoresist is removed by acetone washing leaving the acetone-insoluble catalyst pattern on the substrate. Dense forests of vertically aligned (VA) MWCNTs are grown on the patterned catalyst layers by chemical vapour deposition. The procedures have been demonstrated by growing MWCNT forests on two substrates: silicon and conducting graphitic carbon films. The forests adhere strongly to the substrates and when grown directly on carbon film, offer a simple method of preparing MWCNT electrodes.

Contribution

D.J.G, B.S.F and A.J.D conceived the idea for the project. D.J.G and B.S.F performed the experiments, D.J.G wrote the paper and all authors contributed to the scientific evaluation of the results.

– This page intentionally left blank –

Journal of
Nanoscience and Nanotechnology
Vol. 13, 728–731, 2013

Patterned Forests of Vertically-Aligned Multiwalled Carbon Nanotubes Using Metal Salt Catalyst Solutions

David J. Garrett[1,*,†], Benjamin S. Flavel[1,‡],
Keith H. R. Baronian[2], and Alison J. Downard[1,*]

[1] *MacDiarmid Institute for Advanced Materials and Nanotechnology, Department of Chemistry, University of Canterbury, Private Bag 4800, Christchurch, New Zealand*
[2] *School of Biological Sciences, University of Canterbury, Private Bag 4800, Christchurch, New Zealand*

A simple method for producing patterned forests of multiwalled carbon nanotubes (MWCNTs) is described. An aqueous metal salt solution is spin-coated onto a substrate patterned with photoresist by standard methods. The photoresist is removed by acetone washing leaving the acetone-insoluble catalyst pattern on the substrate. Dense forests of vertically aligned (VA) MWCNTs are grown on the patterned catalyst layers by chemical vapour deposition. The procedures have been demonstrated by growing MWCNT forests on two substrates: silicon and conducting graphitic carbon films. The forests adhere strongly to the substrates and when grown directly on carbon film, offer a simple method of preparing MWCNT electrodes.

Keywords: Vertically Aligned Carbon Nanotubes, Electrode, Voltammetry, Chemical Vapour Deposition, Photolithography.

Control of the position and alignment of CNTs on a substrate is important for potential applications in micro-, nano- and opto-electronics and sensing. Patterned growth of CNTs by chemical vapour deposition (CVD) usually relies on use of a substrate that is patterned with metal catalysts layers. Photolithography coupled with metal evaporation techniques is a standard route to such layers. However thin layers of metal salts and colloids can also generate active catalysts for CNT growth and this has led to the exploration of micro-and nanocontact printing as a method for catalyst patterning. Kind and co-workers printed solutions of Fe(III), Ni(II) and Co(II) salts on silicon substrates and demonstrated that use of high salt concentrations (≥ 120 mM) gives densely packed, vertically aligned VA-MWCNTs.[1] More recently, poly(styrene-block-acrylic acid) micellar 'ink' incorporating ferric chloride was printed onto silicon substrates and after removal of the organic polymer by oxygen plasma etching, the iron oxide patterns catalysed the growth of VA-MWCNTs by CVD.[2] Printed patterns of iron oxide[3] and cobalt[4] nanoparticles have also been used to grow single walled (SW) CNTs.

Photolithography is a convenient method for rapidly and accurately patterning large surface areas. There has been one report of the combination of photolithography with salt solutions for the patterned synthesis of sparse net-like SWCNTs.[5] In the present work we extend that approach to develop the procedures for preparation of patterned arrays of densely packed VA-MWCNTs on silicon and graphitic carbon film (pyrolysed photoresist film, PPF[6]) substrates. After conventional photolithographic patterning we use a simple and rapid catalyst spin-on and lift-off method based on an aqueous solution of $Fe(NO_3)_3$, $Al(NO_3)_3$ and, in some cases, poly(vinyl pyrrolidone) (PVP). The salts and the polymer are insoluble in acetone which can be used to wash off the photoresist, leaving a patterned catalyst layer on the silicon substrate. VA-MWCNTs were grown on the catalyst spots using conventional CVD. Figure 1 summarises the procedures.

Silicon wafers and PPF samples[6] (15 mm × 15 mm) were patterned with AZ1518 photoresist (Clariant). Solutions containing 1 M $Fe(NO_3)_3$, 1 M $Al(NO_3)_3$ and in some cases, PVP40 (average molecular weight 40,000 g mol^{-1})

---

[*] Authors to whom correspondence should be addressed.
[†] Present address: Melbourne Materials Institute, The University of Melbourne, The David Caro Building, Corner Swanston Street and Tin Alley, VIC 3010, Australia.
[‡] Present address: Institute of Nanotechnology, Karlsruhe Institute of Technology, D-76021, Karlsruhe, Germany.

1533-4880/2013/13/728/004 doi:10.1166/jnn.2013.7078

Fig. 1. Procedure for patterned growth of MWCNTs. (1) spin-coat 1 M $Fe(NO_3)_3$, 1 M $Al(NO_3)_3$, 0–5 mg/ml PVP40; (2) acetone wash with sample spinning at 4000 rpm; (3) 30 min, 750 °C, Ar/H_2; (4) 8 min, 750 °C, ethylene, Ar/H_2, water vapour.

in deionised water were spin coated (30 s, 3000–4000 rpm) onto patterned substrates. Samples were dried on a hot plate at 100 °C for 1 min. Photoresist, and its covering layer of metal salts, was then removed with a high flow of acetone (squirt bottle) while the sample was spinning at 4000 rpm. Metal salt layers deposited directly on the substrate surface are unaffected by this process.

Prior to MWCNT growth by CVD, patterned substrates were heated to 750 °C under 40% H_2 in Ar at a flow rate of 2000 sccm for 30 min in a tube furnace with a tube inner diameter of 40 mm. For growth of CNTs, the flow rates of Ar and H_2 were reduced to 1000 and 100 sccm, respectively, and a flow of Ar (50 sccm) passing through a water bubbler and ethylene (400 sccm) were added. The growth conditions were maintained for 8 min and then all gasses, except 1000 sccm of Ar, were removed while the furnace cooled.

Figure 2 shows transmission electron microscopy (TEM) images of MWCNTs grown on spin-coated catalyst layers and illustrates the wide range of tube sizes obtained. Figures 2(a) shows long tubes with a hollow core; (b) is a high magnification image of a section of (a) and clearly shows shells with 0.34 nm spacing consistent with the graphene layer spacing of MWCNTs.[7] The MWCNT has 32 walls and is 40 nm in diameter. Figure 2(c) shows a number of MWCNTs which are approximately 6–8 nm in diameter with between 4 and 5 walls. Such dimensions are typical of MWCNTs grown under similar CVD conditions but using the more conventional evaporated metal catalyst films[8,9] and hence we assume that there are similar CNT growth processes in both systems.

Growth of MWCNTs forests with uniform heights and no ‘cracks’ was dependent on preparing very thin and uniform catalyst layers. Hence method development focused on optimization of the spin-coated catalyst layers. Layers were more uniform on the more hydrophilic PPF surfaces than on silicon; a short oxygen plasma clean (2–3 min, 100 W) improved the wettability of silicon and the quality of the spin-coated catalyst layers. Solutions containing 1 M $Fe(NO_3)_3$ and 1 M $Al(NO_3)_3$ were viscous and could be readily spin-coated, however addition of a small amount of PVP40 (1–5 mg/ml) improved the quality of the catalyst layers, preventing cracking and peeling, presumably this was due to the polymer holding the catalyst pads intact during drying and growth. The optimum amount of PVP depended on the catalyst feature size: 5 mg/ml gave the most consistent results over the feature size range 50 to 100 μm whereas 0–1 mg/ml was suitable for smaller features. When larger amounts of PVP were used, catalyst layers on top of photoresist areas were not completely removed during the acetone wash. Figure 3 shows a catalyst spot, the resulting CNT forest and larger area CNT patterns. The CNTs forests replicate the patterned catalyst spots and have an overall vertical alignment, although high magnification scanning electron micrograph (SEM) images reveal significant kinking and curving of the tubes (Fig. 3(e)). Others have reported that highly intertwined CNT forests is an indicator or “tip growth” where the catalyst particle is pushed forward by the growing CNT.[10] Similarly to CNT forest grown by other methods adhesion to the substrate is low and CNTs could be easily removed.

Preliminary electrochemical measurements were made using MWCNT-epoxy composite electrodes fabricated from large area MWCNT forests grown directly on the conducting PPF substrates.[11] Figure 4 shows cyclic voltammograms (CVs) of 1 mM NADH in phosphate buffered saline, pH 7, obtained at polished[11] MWCNT-epoxy electrodes before and after activation of the surface by O_2 plasma. Figure 4(b) shows a high resolution SEM image of an electrode surface prepared in this way. The sigmoidal voltammogram recorded at the plasma-treated surface demonstrates that the surface functions as a microelectrode

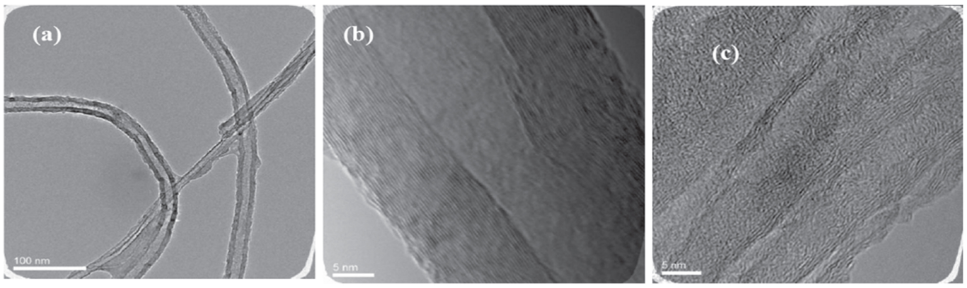

Fig. 2. TEM images of large (a) and (b), and small (c) MWCNTs grown by CVD from a layer of 1 M $Fe(NO_3)_3$ and 1 M $Al(NO_3)_3$ spin coated onto a silicon wafer at 3000 rpm.

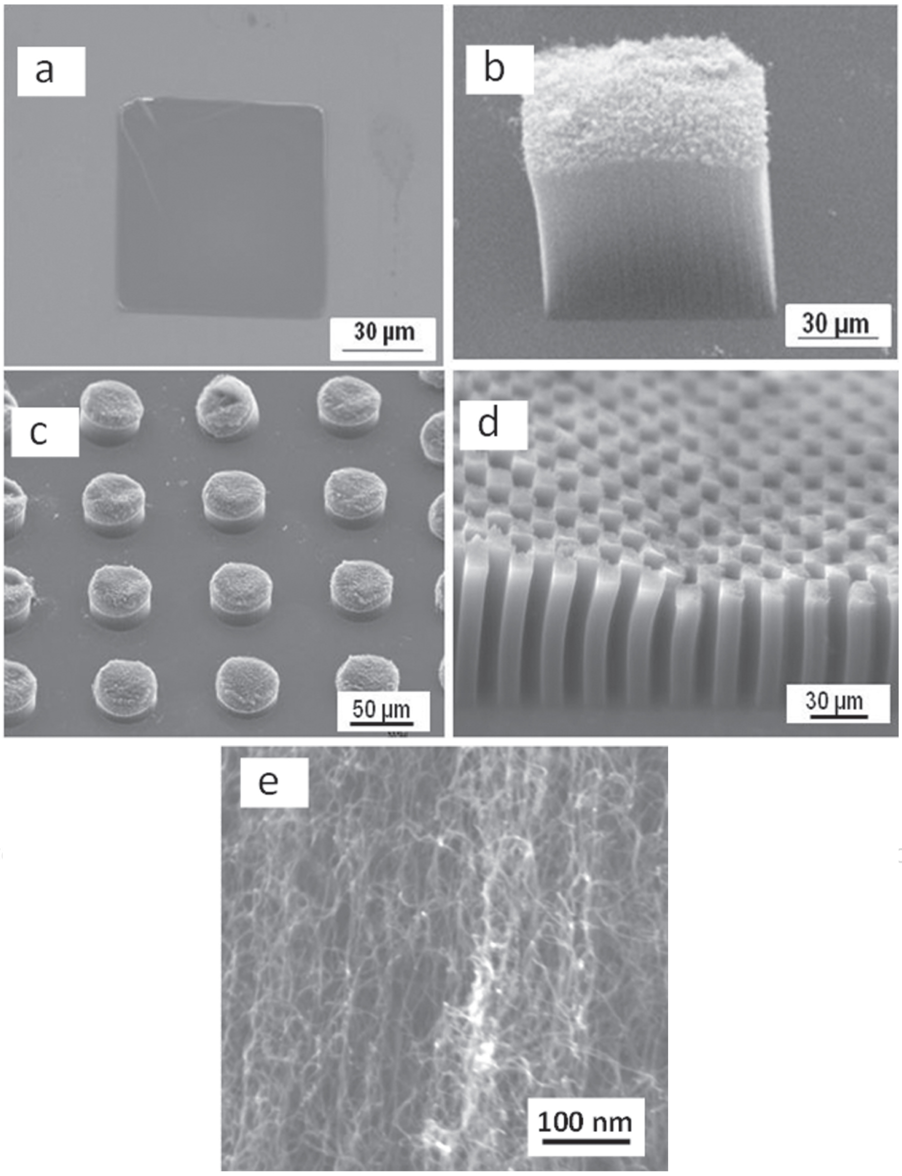

Fig. 3. SEM images of (a) a catalyst spot and (b)–(d), features grown from various catalyst patterns. All patterns were formed using catalyst solution that did not contain PVP. A high resolution SEM image of MWCNTs grown from a catalyst film of 1 M $Fe(NO_3)_3$ and $Al(NO_3)_3$ with 1 mg/ml of PVP40 is shown in (e).

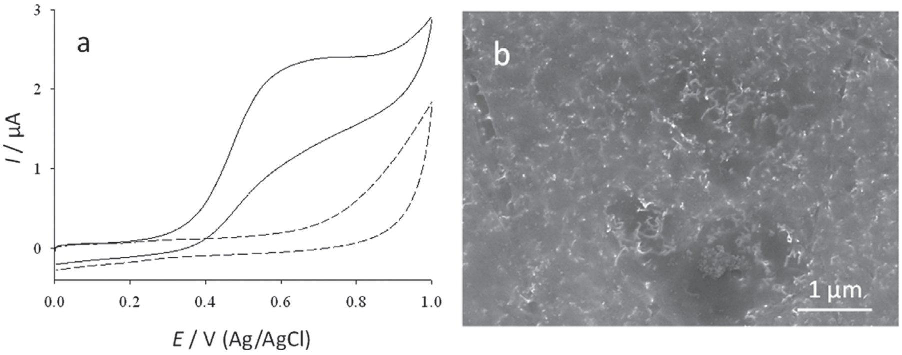

Fig. 4. (a) CVs obtained at a MWCNT-epoxy electrode (catalyst layer was 1 M $Fe(NO_3)_3$, 1 M $Al(NO_3)_3$ and 1 mg/ml PVP40) in 1 mM NADH, phosphate buffered saline, pH 7, before (dashed) and after (solid) O_2 plasma activation. Scan rate = 100 mV s^{-1}. (b) High resolution SEM image of MWCNT-epoxy composite electrode surface after polishing and oxygen plasma etching.

array, presumably because epoxy is etched from small, isolated regions of VA-MWCNT.[12] It is expected that more extended polishing and plasma treatment would yield a fully-activated electrode surface. Most importantly, it is clear that the electrode has good conductivity, indicating that MWCNTs are in electrical contact with the underlying substrate.

To conclude, combining photolithography and water soluble catalysts gives a simple method for patterning dense forests of VA-MWCNTs. Addition of PVP40 improves the stability and uniformity of the catalyst layers giving more uniform MWCNT forests. The optimum amount of PVP40 increases with feature size.

Acknowledgments: This work was funded by the MacDiarmid Institute for Advanced Materials and Nanotechnology. Benjamin S. Flavel thanks the Australian Government's Endeavour Research Fellowship program, AJG thanks the MacDiarmid Institute for a Doctoral Scholarship and David J. Garrett thanks the Tertiary Education Commission for a Bright Futures Top Achiever Doctoral Scholarship. We thank Helen Devereux for technical assistance.

References and Notes

1. H. Kind, J. M. Bonard, C. Emmenegger, L. O. Nilsson, K. Hernadi, E. Maillard-Schaller, L. Schlapbach, L. Forro, and K. Kern, *Adv. Mater.* 11, 1285 (**1999**).
2. R. D. Bennett, A. J. Hart, A. C. Miller, P. T. Hammond, D. J. Irvine, and R. E. Cohen, *Langmuir* 22, 8273 (**2006**).
3. L. Ding, W. W. Zhou, H. B. Chu, Z. Jin, Y. Zhang, and Y. Li, *Chem. Mater.* 18, 4109 (**2006**).
4. V. B. Golovko, M. Cantoro, S. Hofmann, B. Kleinsorge, J. Geng, D. Jefferson, A. C. Ferrari, J. Robertson, and B. F. G. Johnson, *Diamond Relat. Mater.* 15, 1023 (**2006**).
5. S. Y. Jeong, S. H. Jeon, G. H. Han, K. H. An, D. J. Bae, S. C. Lim, H. R. Hwang, C. S. Han, M. Yun, and Y. H. Lee, *J. Nanosci. Nanotechnol.* 8, 329 (**2008**).
6. P. A. Brooksby and A. J. Downard, *Langmuir* 20, 5038 (**2004**).
7. O. Zhou, R. M. Fleming, D. W. Murphy, C. H. Chen, R. C. Haddon, A. P. Ramirez, and S. H. Glarum, *Science* 263, 1744 (**1994**).
8. X. W. Cui, W. F. Wei, and W. X. Chen, *Carbon* 48, 2782 (**2010**).
9. X. M. Liu, K. H. R. Baronian, and A. J. Downard, *Carbon* 47, 500 (**2009**).
10. Y. Wei, G. Eres, V. I. Merkulov, and D. H. Lowndes, *Appl. Phys. Lett.* 78, 1394 (**2001**).
11. D. J. Garrett, P. A. Brooksby, F. J. Rawson, K. H. R. Baronian, and A. J. Downard, *Anal. Chem.* 83, 8347 (**2011**).
12. T. J. Davies, and R. G. Compton, *J. Electroanal. Chem.* 585, 63 (**2005**).

Received: 2 April 2012. Accepted: 6 November 2012.

2.6 Additional Scientific Publications

2.6.13 *Grafting of Poly(ethylene glycol) on Click Chemistry Modified Si(100) Surfaces*

B. S. Flavel, M. Jasieniak, L. Velleman, S. Ciampi, E. Luais, J. G. Shapter,
J. J. Gooding

Langmuir 29 (2013) 8355–8362

DOI: 10.1021/la400721c

Abstract

Poly(ethylene glycol) (PEG) is one of the most extensively studied antifouling coatings due to its ability to reduce protein adsorption and improve biocompatibility. Although the use of PEG for antifouling coatings is well established, the stability and density of PEG layers are often inadequate to provide optimum antifouling properties. To improve on these shortcomings, we employed the stepwise construction of PEG layers onto a silicon surface. Acetylene-terminated alkyl monolayers were attached to nonoxidized crystalline silicon surfaces via a one-step hydrosilylation procedure with 1,8-nonadiyne. The acetylene-terminated surfaces were functionalized via a copper-catalyzed azide–alkyne cycloaddition (CuAAC) reaction of the surface-bound alkynes with an azide to produce an amine terminated layer. The amine terminated layer was then further conjugated with PEG to produce an antifouling surface. The antifouling surface properties were investigated by testing adsorption of human serum albumin (HSA) and lysozyme (Lys) onto PEG layers from phosphate buffer solutions. Detailed characterization of protein fouling was carried out with X-ray photoelectron spectroscopy (XPS) and time-of-flight secondary ion mass spectrometry (ToF-SIMS) combined with principal component analysis (PCA). The results revealed no fouling of albumin onto PEG coatings whereas the smaller protein lysozyme adsorbed to a very low extent.

Contribution

B.S.F, J.G.S and J.J.G conceived the idea for the project. B.S.F, M.J, L.V, S.C, and E.L performed the experiments. B.S.F, M.J, and L.V wrote the paper and all authors contributed to the scientific evaluation of results.

– This page intentionally left blank –

Langmuir

Article

pubs.acs.org/Langmuir

Grafting of Poly(ethylene glycol) on Click Chemistry Modified Si(100) Surfaces

Benjamin S. Flavel,*[†] Marek Jasieniak,[‡] Leonora Velleman,[§] Simone Ciampi,[∥] Erwann Luais,[∥] Joshua R. Peterson, Hans J. Griesser,[‡] Joe G. Shapter,[§] and J. Justin Gooding*[∥]

[†]Institute of Nanotechnology, Karlsruhe Institute of Technology, 76021, Karlsruhe, Germany

[‡]Ian Wark Research Institute, University of South Australia, Mawson Lakes Campus, Adelaide, SA 5095, Australia

[§]School of Chemical and Physical Sciences, Flinders University, Bedford Park, Adelaide, SA 5042, Australia

[∥]School of Chemistry and Australian Centre for Nanomaterials, University of New South Wales, Sydney, NSW 2052, Australia

ABSTRACT: Poly(ethylene glycol) (PEG) is one of the most extensively studied antifouling coatings due to its ability to reduce protein adsorption and improve biocompatibility. Although the use of PEG for antifouling coatings is well established, the stability and density of PEG layers are often inadequate to provide optimum antifouling properties. To improve on these shortcomings, we employed the stepwise construction of PEG layers onto a silicon surface. Acetylene-terminated alkyl monolayers were attached to nonoxidized crystalline silicon surfaces via a one-step hydrosilylation procedure with 1,8-nonadiyne. The acetylene-terminated surfaces were functionalized via a copper-catalyzed azide−alkyne cycloaddition (CuAAC) reaction of the surface-bound alkynes with an azide to produce an amine terminated layer. The amine terminated layer was then further conjugated with PEG to produce an antifouling surface. The antifouling surface properties were investigated by testing adsorption of human serum albumin (HSA) and lysozyme (Lys) onto PEG layers from phosphate buffer solutions. Detailed characterization of protein fouling was carried out with X-ray photoelectron spectroscopy (XPS) and time-of-flight secondary ion mass spectrometry (ToF-SIMS) combined with principal component analysis (PCA). The results revealed no fouling of albumin onto PEG coatings whereas the smaller protein lysozyme adsorbed to a very low extent.

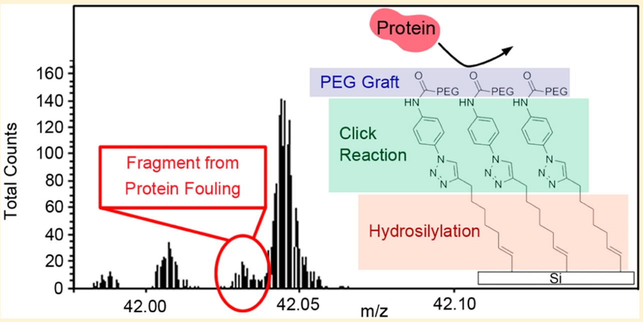

INTRODUCTION

Biofunctionalization of materials is an important aspect in the advancement of biosensors and biomedical devices. Functionalization of surfaces for biotechnological applications predominantly involves increasing the hydrophilicity of the surface to decrease fouling and improve biocompatibility.[1−3] Electrostatic repulsion and the hydrophilicity of the surface are the main factors that contribute to reducing the adsorption of biomolecules.[4] The modification of surfaces with antifouling layers to inhibit nonspecific biointeractions is important for the development of sensors,[5] tissue engineering,[6] implant materials,[7,8] microfluidics,[9,10] protein purification, and diagnostics.[11] Silicon surfaces are widely used in biosensors and biocompatible materials,[12−14] and therefore, it is particularly important to produce silicon surfaces resistant to nonspecific biomolecular and cellular adhesion.

Numerous surface modification methods have been implemented to attain antifouling surfaces including self-assembly,[15,16] polymer grafting,[17,18] and plasma modification.[19,20] Various types of polymers have been investigated for their antifouling properties including polyacrylates, oligosaccharides, and poly(ethylene glycol) (PEG). Much effort has been applied in the modification of surfaces with PEG to reduce protein adsorption and improve biocompatibility. PEG is one of the most extensively studied antifouling polymers due to its ability to resist protein adsorption.[21] Studies have determined that its hydrophilicity, entropy, large exclusion volume, and coordination with surrounding water molecules in an aqueous environment are main contributing factors in reducing bioadhesion.[22] Improved surface functionalization and coating technologies that impart enhanced antifouling performance in addition to high stability are greatly sought after.[23−25] Many of the surface modification techniques used to coat surfaces with PEG are simple but have long-term instability complications due to desorption.[26−28] In addition to improved stability, the PEG layer must be of high enough density and uniformity to provide an optimal barrier against bioadhesion. An integral factor in the development of antifouling surfaces with long-term stability is the formation of robust chemical bonds between the polymer and the surface.

Received: February 25, 2013
Revised: May 31, 2013
Published: June 7, 2013

dx.doi.org/10.1021/la400721c | *Langmuir* 2013, 29, 8355−8362

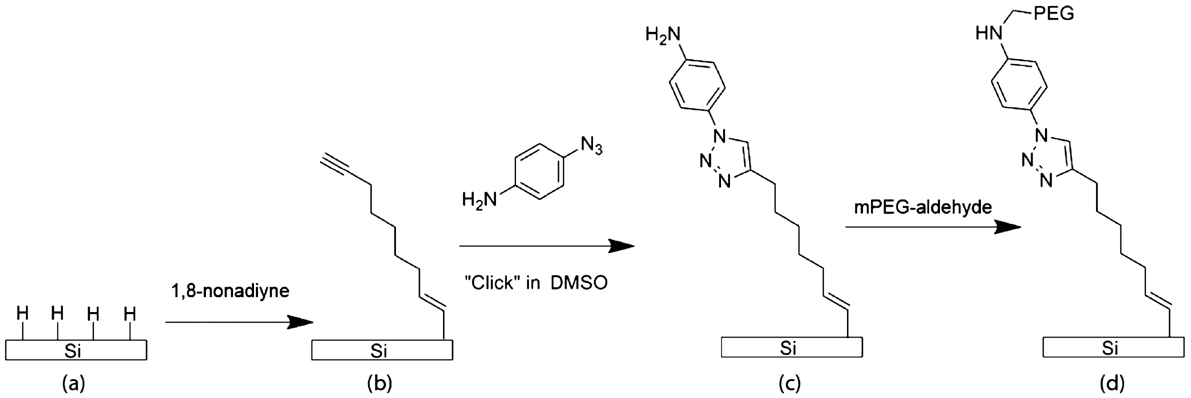

Figure 1. Hydride terminated Si(100) surface (a). Assembly of monolayers of 1,8-nonadiyne (b) and subsequent derivatization with an azide species (Cu(I) catalyzed Huisgen 1,3-dipolar cycloaddition reaction with 4-azidoaniline hydrochloride) (c). Immobilization of PEG via reductive amination (d)

Organic monolayers bound directly to nonoxidized crystalline silicon surfaces through a silicon−carbon bond produce highly stable monolayers in comparison to conventional silane films on oxidized silicon.[29−32] Such monolayers are easily used as platforms for further derivatization and have therefore become an advantageous approach in the fabrication of complex molecular architectures on surfaces. The stepwise construction of functional layers is also appealing due to the commercial availability of structural constituents and the synthetic versatility of established modular coupling techniques. Monolayers terminated with alkynyl groups have been shown to be easily conjugated via a copper-catalyzed azide−alkyne cycloaddition (CuAAC), a commonly used click reaction.[33] Consequently, click chemistry and in particular the CuAAC of alkynes and azides has generated considerable interest as a technique for the stepwise construction of highly organized functional layers on surfaces.[34,35] Several examples in the literature have already demonstrated the successful use of CuAAC grafting in the fabrication of polymer brushes on 2D solid surfaces. For example, Yameen et al.[36] utilized "click chemistry" in the attachment of polyelectrolyte brushes on planar silicon surfaces and nanochannels. Ostaci and coworkers[24,37] grafted poly(ethylene glycol) brushes to alkyne functionalized pseudobrushes and silicon substrates by "click chemistry", and Britcher et al.[38] demonstrated a two step PEGylation "click chemistry" process on porous silicon. Furthermore, these monolayers have been shown to provide unprecedented stabilization of the underlying silicon surface against oxidation which is important for electrically based biosensing devices.[39−41]

The purpose of this work is to investigate the scope and performance of stepwise derivatization of surfaces in the context of improving control on the density of tethered antifouling species. We report the direct attachment of acetylene-terminated monolayers to nonoxidized silicon surfaces and further derivatization by a CuAAC reaction to produce an amine terminated layer. The amine terminated layer was then further conjugated with PEG to produce an antifouling surface. Previous attempts to construct antifouling surfaces through direct CuAAC attachment of an antifouling azide (derived from tetra(ethylene oxide)) resulted in an insufficient reduction in fouling most likely due to a low density of tetra(ethylene oxide) attachment.[34] Consequently, for this study, we employed the CuAAC reaction to create a uniform platform to which the PEG could be later attached through simple coupling techniques in the hopes of achieving a higher density of PEG on the surface.

EXPERIMENTAL DETAILS

2.1. Materials. Hydrofluoric acid (48 wt % solid in water) was purchased from Riedel-de Haen. Dimethyl sulfoxide, dichloromethane, 1,8-nonadiyne, *N,N,N′,N′*-tetramethylethylenediamine (TMEDA), and 4-azidoaniline hydrochloride were of the highest purity grade and purchased from Sigma-Aldrich. Copper(I) bromide was purchased from Alfa Aesar (>99%). Albumin from human serum (>99% protein), lysozyme from chicken egg white (more than 90% protein), and phosphate buffer saline (PBS) were purchased from Sigma-Aldrich; mPEG-propionaldehyde, 5 kDa was supplied by Laysan Bio, Inc.; potassium sulfate (AR) and sodium cyanoborohydride (purum, >95%) were from Chem Supply Pty Ltd.

2.2. Assembly of Monolayers of 1,8-Nonadiyne. The preparation of 1,8-nonadiyne layers on silicon and subsequent chemical derivatizations are schematically represented in Figure 1. Silicon wafers were rinsed in dichloromethane and dried under argon. The wafers were immersed for 30 min in a piranha solution (2:1 H_2SO_4/H_2O_2) maintained at 100 °C. The silicon wafers were then immersed in an aqueous fluoride solution for 1.5 min (2.5% hydrofluoric acid). The samples were placed in a custom-made Schlenk flask containing a sample of 1,8-nonadiyne under an argon atmosphere (H_2O < 10 ppb, O_2 < 5 ppb). The 1,8-nonadiyne sample was degassed through a minimum of four freeze−pump−thaw cycles. The sample was kept under a stream of argon while the reaction vessel was immersed in an oil bath set to 165 °C for 3 h. The reaction vessel was allowed to cool to room temperature, and the flask was then opened to the atmosphere. The sample was rinsed thoroughly in dichloromethane and then stored in dichloromethane under argon before being either analyzed or further reacted with substituted azide species.

2.3. CuAAC Derivatization of Acetylene-Terminated Monolayers with an Azide Species. A 10 mM solution of 4-azidoaniline hydrochloride was prepared by dissolving 8.6 mg of 4-azidoaniline hydrochloride in 5 mL of DMSO. A solution consisting of 11.6 mg of TMEDA, 7.1 mg of CuBr, and 1.5 mL of DMSO was added to a reaction vial containing the alkyne functionalized silicon surfaces. Then 1 mL of the 4-azidoaniline hydrochloride solution and 2.5 mL of DMSO were added to the reaction vial, and the reaction was allowed to proceed for 1 h in the dark at room temperature, without excluding air from the reaction environment. The prepared samples were rinsed consecutively with copious amounts of DMSO and water, dried under air, and then stored under argon until analysis or further reaction.

2.4. PEG Attachment. PEG grafts were fabricated via reductive amination under marginal solvation conditions.[42] The amine functionalized samples of silicon were treated with a solution containing 2.5 mg/mL mPEG aldehyde, 3.0 mg/mL sodium cyanoborohydride, and

110 mg/mL potassium sulfate in 0.01 M PBS. The reaction was carried out at 60 °C (lower critical solution temperature of 5 kDa mPEG, LCST) for 18 h. Grafting PEG at the LCST has been shown previously to produce higher graft densities.[42] After the treatment, the samples were removed from the solution, washed sequentially 5× with water, and finally dried under a stream of nitrogen. A thorough washing aimed to remove trace elements from the modified surfaces, like sodium or potassium which, when present, would interfere with ToF-SIMS analysis and obscure the results.

2.5. Protein Fouling Protocol. For the laboratory protein fouling tests, human serum albumin (HSA) or lysozyme was dissolved in 0.01 M phosphate buffer saline (pH 7.4) to a concentration of 0.1 mg/mL. Tested samples were immersed in the protein solution at room temperature. The adsorption was allowed to progress for 3 h. Then samples were immersed in a 0.01 M PBS solution for 2h followed by a thorough washing in 0.01 M PBS solution to remove loosely bound protein. Finally, samples were rinsed with Milli-Q water and blown dry in a nitrogen stream. The fouling tendency of samples was determined by XPS, from the surface atomic concentration of nitrogen, and by ToF-SIMS with the aid of principle component analysis.

2.6. ToF-SIMS Analysis. ToF-SIMS measurements were performed with a PHI TRIFT V nanoTOF instrument (PHI Electronics Ltd.). A 30 keV, pulsed primary $^{197}Au^+$ ion beam was used to sputter and ionize species from each sample surface. PHI's patented dual beam charge neutralization system using a combination of low energy argon ions (up to 10 eV) and electrons (up to 25 eV) was employed to provide an excellent charge neutralization performance. Positive mass axis calibration was done with CH_3^+, $C_2H_5^+$, and $C_3H_7^+$. Spectra were acquired in the bunched mode for 60 s from an area of 100 μm × 100 μm. The corresponding total primary ion dose was less than 1×10^{12} ions cm^{-2} and thus met the static SIMS regime.[43] A mass resolution $m/\Delta m$ of >7000 at nominal m/z = 27 amu ($C_2H_3^+$) was typically achieved.

Each sample was characterized by 10 positive ion mass spectra, which were collected from sample areas that did not overlap. All recognizable, clear (i.e., unobscured by overlaps) immonium ions from the 2 up to 160 amu range were used in calculations. The peaks were normalized to the total intensity of all selected peaks. Multiple mass spectra were processed with the aid of principal component analysis, PCA.[44] PCA was performed using PLS_Toolbox version 3.0 (Eigenvector Research, Inc., Manson, WA) along with MATLAB software v. 6.5 (MathWorks Inc., Natick, MA).

2.7. XPS Analysis. X-ray photoelectron spectroscopy was performed with a Kratos AXIS Ultra DLD spectrometer, using monochromatic Al Kα radiation ($h\nu$ = 1486.7 eV). The system is equipped with a magnetically confined charge compensation system (low energy electrons are confined and transported to the sample surface by magnetic field). Spectra were recorded using an acceleration voltage of 15 keV at a power of 225 W. Survey spectra were collected with a pass energy of 160 eV and an analysis area of 300 × 700 μm^2. High-resolution spectra were obtained using a 20 eV pass energy and an analysis area of ~300 × 700 μm^2. Data analysis was performed with CasaXPS software (Casa Software Ltd.). All binding energies were referenced to the low energy C 1s peak at 285.0 eV. Core level envelopes were curve-fitted with the minimum number of mixed Gaussian−Lorentzian component profiles. The Gaussian−Lorentzian mixing ratio (typically 30% Lorentzian and 70% Gaussian functions), the full width at half-maximum, and the positions and intensities of peaks were left unconstrained to result in a best fit.

■ RESULTS

3.1. Preparation of Amine Functionalized Silicon Wafers via Hydrosilylation and Click Chemistry. A three-step process was used to construct a PEG surface of optimal surface coverage on silicon. The method of attachment involved the hydrosilylation of silicon surfaces with an acetylene terminated layer followed by a CuAAC click reaction to produce an amine terminated layer then subsequent attachment of aldehyde PEG via reductive amination. The attachment of 1,8-nonadyne to a silicon surface resulted in the surface shown in Figure 1b. Characterization of this surface has been previously reported.[34] Briefly, XPS revealed the presence of a densely packed monolayer of 1,8-nonadiyne. The Si 2p region was dominated by a doublet, with the Si $2p_{3/2}$ at BE of around 100.0 eV. A low intensity peak was also observed at 103.4 eV, indicating traces of silica contaminants. The survey spectrum for the amine-terminated surface formed upon "clicking" 4-azidoaniline to the alkyne-terminated substrate surface showed the presence of silicon, carbon, oxygen, and nitrogen, with atomic concentrations summarized in Table 1. The initial oxygen levels of the amine terminated substrate appear fairly high (13.4%) which may be attributed to surface bound water.[45] Figure 2a shows the C 1s core level spectra for the amine functionalized silicon surface where a peak centered around 285.0 eV can be seen, which is characteristic of carbon-bound carbons (C−C). Additionally, a contribution on the low binding energy (BE) side (BE of ~284.0 eV) can be seen, which could be attributed to carbon atoms in the C−Si environment. However, we did not try to fit this component as its low intensity would produce fits with poor S/N. As shown in Table 1, following PEG immobilization (aldehyde-terminated, 5 kDa) onto the amine terminated substrate, an increase in the atomic concentration of oxygen and carbon is observed accompanied by a decrease of the silicon exposure. However, as the silicon signal did not completely diminish after PEG grafting, this would suggest the PEG layer is thinner than the sampling depth of the XPS (5 nm) or the PEG layer is patchy. Given the use of a low molecular weight PEG, a thickness of less than 5 nm is probable. Atomic force microscopy can be used to analyze the integrity of the PEG layer but was not explored in this study. A decrease in the nitrogen exposure is also evident after grafting PEG. In the C 1s core level spectra of the PEG immobilized surface (Figure 2b), two distinct peaks can be seen at 285.0 and 286.5 eV, where the high BE component corresponds to the carbon atoms chemically associated with oxygen via a single bond (C−O) originating from the PEG and the low BE component corresponds once again to hydrocarbons (C−C/C−H). The PEG terminated surface exhibits an oxygen concentration of 23.87% (Table 1) which does not correspond to what is expected of a pure PEG layer (33% oxygen), but nevertheless indicates a high density of PEG grafts.[46] The PEG and grafting conditions used in our study were consistent with that used by Kingshott et al. which achieved PEG layers containing 19.6−21.3% oxygen when grafting onto heptylamine and allylamine polymer layers.[46] The improvement in the PEG grafting suggests a higher density of amine groups present on our click-generated amine layers in comparison with the heptylamine and allylamine layers. The high density of amine groups reinforces the application of click chemistry for the premodification of surfaces to improve the yield of subsequent grafting.

Table 1. Atomic Concentrations for Amine-Functionalized Surface and Its PEG Derivative by XPS

	concentration, atom %			
sample	O	N	C (%CC/CH; %C−O)[a]	Si
amine-terminated	13.43	0.92	36.88 (100; 0)	48.36
PEG-terminated	23.87	0.59	47.45 (39.5; 60.5)	28.09

[a]Composition of the C 1s envelope.

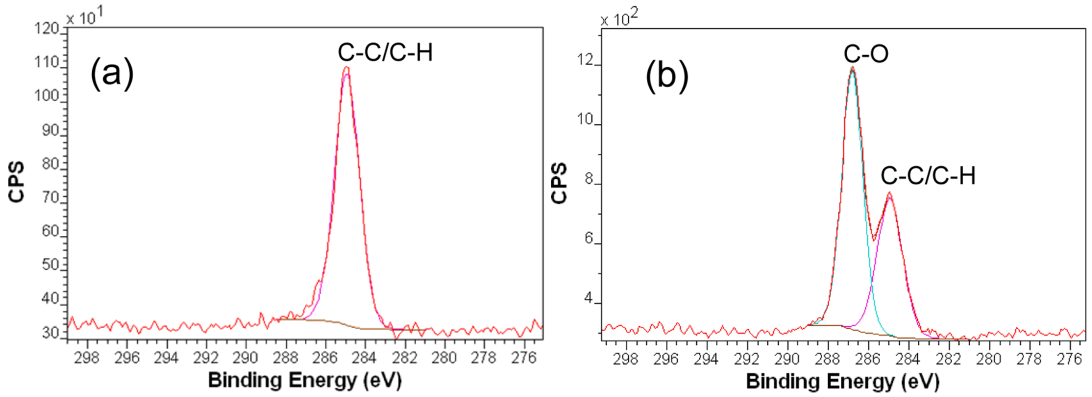

Figure 2. C 1s core level spectra of amine-functionalized surface (a) and its PEG modified derivative (b).

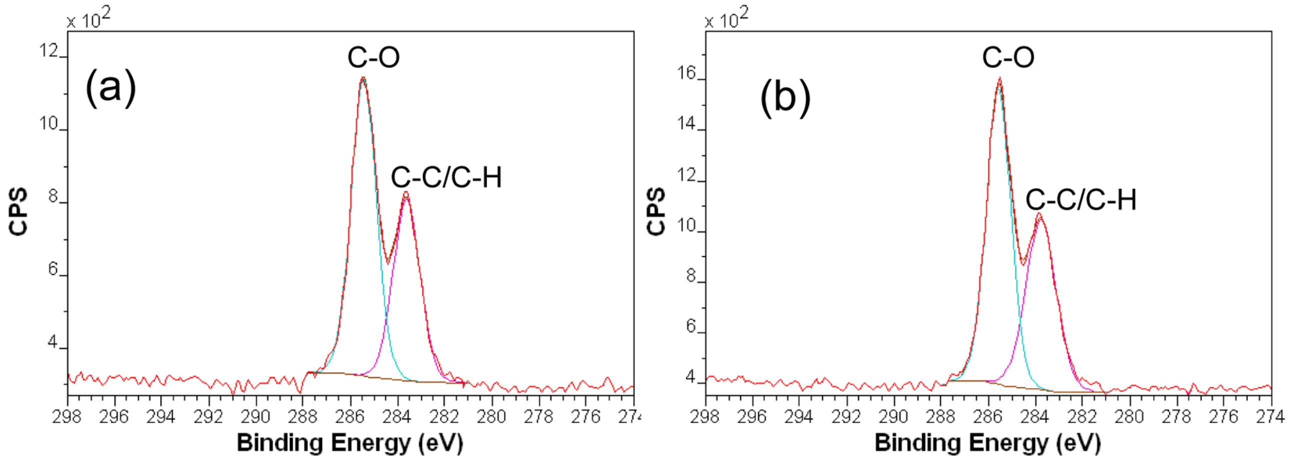

Figure 3. C 1s core level spectra of PEG modified surfaces after contact with lysozyme (a) and HSA (b).

To determine the potential for the PEG modified silicon surfaces in the prevention of nonspecific adsorption (biofouling), the surfaces were exposed to two test proteins HSA and lysozyme and their interaction measured by XPS and ToF-SIMS.

The high resolution C 1s XPS spectra of the PEG-modified surfaces after contact with the solutions of lysozyme and HSA are shown in Figure 3. It can be seen that following exposure to the two test proteins the C 1s core-level spectrum remains identical and indistinguishable from the control PEG graft in Figure 2b. Most importantly, no evidence of amide C (BE = 288.2 eV) can be seen which would be indicative of significant protein fouling.[46]

The quantitative data derived from the survey and C 1*s* spectra for the PEG modified surfaces after incubation in the protein solutions are listed in Table 2. Differences in the nitrogen concentration among the samples (0.59, 0.70, and 0.83 for [PEG], [PEG+lys], and [PEG+HSA], respectively) are too small to be used in the evaluation of fouling. The detection limit of XPS is 10^{-2} of a monolayer[47] which equates to the detection of a few ng/cm^2 adsorbed protein. However, this detection limit varies greatly depending on the substrate analyzed. Clearly, XPS does not indicate any detectable fouling of lysozyme and HSA onto the PEG grafted surfaces.

Table 2. Atomic Concentrations for PEG Modified Surfaces after Contact with Lysozyme and Human Serum Albumin

	concentration, atom %			
sample	O	N	C (%CC/CH; %C–O)[a]	Si
PEG + lys	22.71	0.70	48.05 (39.5; 60.5)	28.54
PEG + HSA	23.34	0.83	49.13 (41.3; 58.7)	26.70

[a] Composition of the C 1s envelope.

To provide greater information on the extent of the antifouling capabilities of these PEG coated samples, ToF-SIMS analysis was performed on the PEG surfaces after exposure to the protein solutions. The PEG surfaces were tested for the adsorption of HSA and lysozyme. ToF-SIMS is a highly specific analytical tool that has been shown to detect extremely low amounts of adsorbed proteins on PEG surfaces which were undetectable by XPS.[46] ToF-SIMs has been shown to achieve detection limits in the attomole range.[48−51] The sensitivity of ToF-SIMS for the detection of proteins arises from the identification of characteristic amino acid mass fragments (immonium ions) generated from the amino acids that are present in the backbone of the proteins.[52]

Figure 4 displays the positive survey ToF-SIMS spectra (m/z 0−200) for the amine terminated surface, PEG grafted surface, and PEG grafted surface after contact with lysozyme and HSA. For the amine terminated surface (Figure 4a), the intense ion signals at nominal m/z 28, 29, 43, 73, and 147 amu can be attributed mainly to Si^+, SiH^+, CH_3Si^+, $(CH_3)_3Si^+$, and $C_5H_{15}OSi_2^+$ fragments, which reflect covalently immobilized nonadiyne onto silicon. Most of the individual nominal masses contain multiple fragments (e.g., there are 5 components within the nominal mass of 42 amu as shown in Figure 4a), but in this

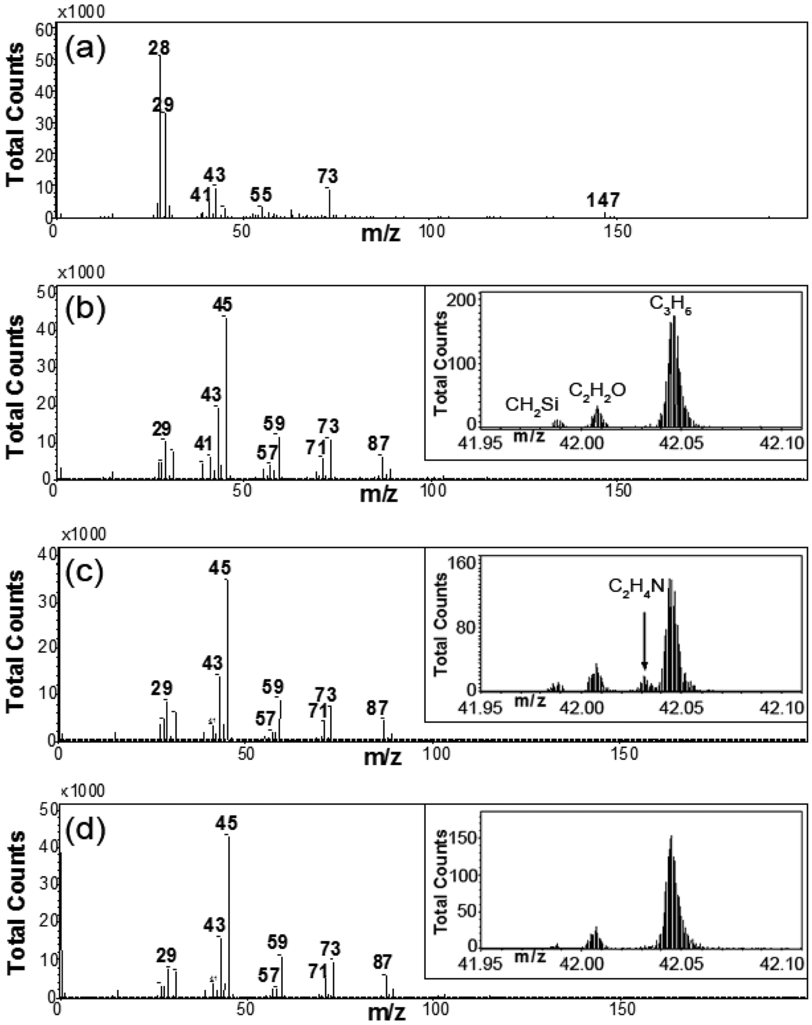

Figure 4. Positive survey mass spectra for (a) amine terminated Si surface; (b) PEG modified surface; (c) PEG modification after laboratory fouling test with lysozyme; (d) PEG modification after laboratory fouling test with human serum albumin. Insets: High mass resolution of static ToF-SIMs in the 42 amu region.

initial assignment we refer to the most prominent component within the group.

The ToF-SIMS positive mass spectrum of the PEG modified surface is shown in Figure 4b. The major peaks at nominal *m*/*z* 29, 31, 43, 45, 57, 59, 73, and 87 amu correspond to CHO^+, CH_3O^+, $C_2H_3O^+$, $C_2H_5O^+$, $C_3H_5O^+$, $C_3H_7O^+$, $C_4H_7O^+$, $C_3H_5O_2^+/C_4H_9O^+$, and $C_4H_7O_2^+$ respectively. These fragments are the PEG fingerprints, since they are present in the spectrum due to the fragmentation of the PEG backbone. The spectrum indicates high density of PEG on the surface, though low levels of the aminated substrate characteristics are still detectable in the high resolution mass spectra (numerous silicon containing positive fragment ions such as Si^+, SiH^+, CH_2Si^+, CH_3Si^+), consistent with the use of relatively low molecular weight PEG and hence a thickness of the vacuum-dried grafted layer not significantly exceeding the probing depth of ToF-SIMS.

Traces (c) and (d) in Figure 4 present the ToF-SIMS spectra for the PEG coated surface after exposure to lysozyme and HSA respectively. Both spectra appear very similar to the spectrum of the initial PEG surface (Figure 4b). Survey spectra show only intensities at nominal masses, which do not always provide sufficient discrimination between the examined samples. Differences, however, emerge upon close inspection of each nominal mass range utilizing high mass resolution of static ToF-SIMS. This is illustrated in the insets in Figure 4, which presents the magnified spectra in the mass region *m*/*z* 41.85–42.15 amu for the amine terminated surface, PEG coated surface and PEG coated surfaces after contact with HSA and lysozyme, a region that is hardly visible in the survey spectra in Figure 4. Interestingly, there appears to be a slight increase in the intensity of the $C_2H_4N^+$ fragment after exposure to lysozyme (Figure 4c inset) but not to HSA (Figure 4d inset). As the $C_2H_4N^+$ immonium ion reflects the alanine residue present in both proteins, it is likely that lysozyme has slightly adsorbed onto the PEG surface whereas HSA did not adsorb.

The differences between the samples shown by the positive mass spectra in Figure 4 are based only on a few peaks selected from a single positive mass spectrum. Although this univariate analysis is useful, it disregards information contained in the remaining peaks that can be important in proper evaluation of the antifouling potential of these surfaces. Therefore, in this study PCA, was also used to extract information from the complex ToF-SIMS data and to aid in the data interpretation. In our attempt to classify the spectra by PCA we used a set of positive fragment ions that are listed in Table 3.

Our focus was only on the nitrogen-containing peaks, which are characteristic of amino acid residues present in proteins so they could be used to indicate nonspecific protein adsorption.

Table 3. Positive Fragment Ions Used in PCA

no.	fragment	*m/z*	no.	fragment	*m/z*
1	H_3N^+	17.026	16	$C_3H_8NO^+$	74.056
2	H_4N^+	18.036	17	$C_5H_{10}N^+$	84.082
3	CH_2N^+	28.018	18	$C_4H_8NO^+$	86.070
4	CH_3N^+	29.026	19	$C_5H_{12}N^+$	86.096
5	CH_4N^+	30.034	20	$C_4H_4NO_2^+$	98.028
6	$C_2H_4N^+$	42.033	21	$C_4H_{10}N_3^+$	100.082
7	$C_2H_6N^+$	44.051	22	$C_4H_8NO_2^+$	102.059
8	$C_3H_4N^+$	54.033	23	$C_5H_8N_3^+$	110.055
9	$C_3H_6N^+$	56.049	24	$C_6H_{10}NO^+$	112.070
10	$C_3H_8N^+$	58.066	25	$C_8H_{10}N^+$	120.081
11	$C_3H_4NO^+$	70.038	26	$C_9H_8N^+$	130.069
12	$C_4H_8N^+$	70.067	27	$C_8H_{10}NO^+$	136.078
13	$C_4H_{10}N^+$	72.082	28	$C_{10}H_{11}N_2^+$	159.081

In the initial selection, which was based on the assignments taken from literature,[53−56] 39 were considered; however, some immonium ions had to be eliminated as other spectral lines interfered with them (e.g., $CH_3N_2^+$, which is related to arginine, overlaps with $C_2H_3O^+$, which originates from the PEG).

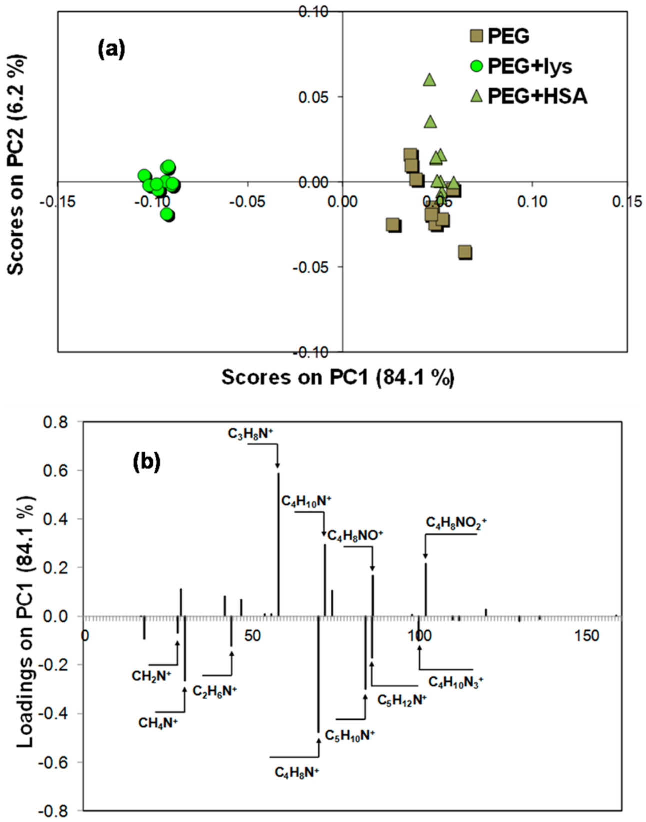

Figure 5. Scores on PC1 and PC2 (a) and loadings on PC1 (b) of immonium ions from static positive mass spectra of PEG modification and after its exposure to lysozyme and HSA.

Figure 5a shows the scores plot of immonium ions on PC1 and PC2 for the pristine PEG coated samples and for the PEG coated samples after contact with lysozyme (PEG+lysozyme) and HSA (PEG+HSA). Each sample was characterized by 10 groups of immonium ions derived from replicate positive static secondary ion mass spectra. PC1 and PC2 capture around 90% of the total variance, which indicates that most of the original information is retained in this two-PC model. The PEG and PEG+HSA groups overlap along both PCs, which reflects their similar surface chemistries in terms of nitrogen species. HSA appears not to foul onto the PEG modification upon contact. This cluster has positive scores on PC1. A high positive loading of $C_3H_8N^+$ on PC1 indicates its association with the PEG surface prior to contact with the proteins (Figure 5b). In contrast, the PEG+lysozyme cluster has negative scores on PC1 and it is well-separated from its PEG precursor signifying that the PEG surfaces before and after exposure to lysozyme are different. The loadings of immonium ions on PC1 point at the peaks that discriminate the groups. The spectra for PEG +lysozyme have more intense peaks at nominal *m/z* 28, 30, 44, 70, 84, 86, and 100 amu. The highest intensity at *m/z* 70 amu ($C_4H_8N^+$) reflects the proline residue, which is present in the lysozyme structure. In summary, PCA on the ToF-SIMS data reveals some fouling of lysozyme onto the PEG modified surface. These PCA results indicate that the PEG surface is fully antifouling to large proteins only. However, it should be noted that the amount of lysozyme adsorbed onto the surface is small. Lysozyme is a low-molecular weight protein (15 kDa) and is most likely too small to be completely repelled by the hydrated chains of the PEG layer and can therefore diffuse, to a limited extent, through the PEG layer and absorb onto the surface or become trapped in the PEG layer.[17,57,58] This molecular weight dependence is evident from the comparison of the adsorption of a comparatively large protein (HSA, 67 kDa) onto the PEG coated surface (Figure 4d), where ToF-SIMS was unable to detect any presence of HSA. These results therefore indicate that the surface is completely resistant to fouling by large proteins while smaller proteins may be able to adsorb to a small extent.

■ CONCLUSION

The stepwise construction of an antifouling layer was achieved through the conjugation of PEG to an amine terminated silicon surface which was prepared by covalent attachment of an acetylene terminated layer and subsequent CuAAC derivatization with an amine terminated azide. This method to attach PEG onto surfaces proved to be an excellent method for preparing antifouling surfaces. A high surface density of PEG was suggested by XPS results, where characteristic peaks from the acetylene/azide monolayer disappear after PEG grafting and a characteristic peak from PEG coupling (C−O) is observed. Characterization of the antifouling properties of the PEG layer was carried out with ToF-SIMS as XPS was not sensitive enough to suggest any fouling of lysozyme and HSA onto the PEG surfaces. The ToF-SIMs data after exposure of the PEG surfaces to two proteins; lysozyme (15 kDa) and HSA (67 kDa) revealed minute amounts of fouling by lysozyme and no fouling by HSA. PCA was used to further extract and clarify the information from the ToF-SIMS data and confirmed the adsorption of lysozyme onto the PEG modified surface due to discrepancies in the scores plot between the PEG surfaces before and after lysozyme exposure. In summary, although a high surface density of grafted PEG was achieved, the surface is completely antifouling to larger proteins while smaller biological species are significantly but not completely repelled. With the smaller biological species, it is hypothesized these may be able to penetrate into the PEG layer and adsorb and hence are less effectively repelled.

AUTHOR INFORMATION

Corresponding Author

*E-mail: benjamin.flavel@kit.edu (B.S.F.); justin.gooding@unsw.edu.au (J.G.).

Notes

The authors declare no competing financial interest.

REFERENCES

(1) Hester, J. F.; Banerjee, P.; Mayes, A. M. Preparation of protein-resistant surfaces on poly(vinylidene fluoride) membranes via surface segregation. *Macromolecules* **1999**, *32*, 1643−1650.

(2) Wang, Y. Q.; Wang, T.; Su, Y. L.; Peng, F. B.; Wu, H.; Jiang, Z. Y. Remarkable reduction of irreversible fouling and improvement of the permeation properties of poly(ether sulfone) ultrafiltration membranes by blending with pluronic F127. *Langmuir* **2005**, *21*, 11856−11862.

(3) Yu, Q. A.; Zhang, Y. X.; Wang, H. W.; Brash, J.; Chen, H. Anti-fouling bioactive surfaces. *Acta Biomater.* **2011**, *7*, 1550−1557.

(4) Holmlin, R. E.; Chen, X.; Chapman, R. G.; Takayama, S.; Whitesides, G. M. Zwitterionic SAMs that Resist Nonspecific Adsorption of Protein from Aqueous Buffer. *Langmuir* **2001**, *17*, 2841−2850.

(5) Wisniewski, N.; Reichert, M. Methods for reducing biosensor membrane biofouling. *Colloids Surf., B* **2000**, *18*, 197−219.

(6) Jordan, S. W.; Chaikof, E. L. Novel thromboresistant materials. *J. Vasc. Surg.* **2007**, *45*, 104A−115A.

(7) Ratner, B. D. The blood compatibility catastrophe. *J. Biomed. Mater. Res.* **1993**, *27*, 283−287.

(8) Pei, J.; Hall, H.; Spencer, N. D. The role of plasma proteins in cell adhesion to PEG surface-density-gradient-modified titanium oxide. *Biomaterials* **2011**, *32*, 8968−8978.

(9) Sebra, R. P.; Anseth, K. S.; Bowman, C. N. Integrated surface modification of fully polymeric microfluidic devices using living radical photopolymerization chemistry. *J. Polym. Sci., Polym. Chem.* **2006**, *44*, 1404−1413.

(10) Hawkins, K. R.; Steedman, M. R.; Baldwin, R. R.; Fu, E.; Ghosal, S.; Yager, P. A method for characterizing adsorption of flowing solutes to microfluidic device surfaces. *Lab Chip* **2007**, *7*, 281−285.

(11) Jain, P.; Baker, G. L.; Bruening, M. L. Applications of Polymer Brushes in Protein Analysis and Purification. *Annu. Rev. Anal. Chem.* **2009**, 387−408.

(12) Desai, T. A.; Hansford, D. J.; Leoni, L.; Essenpreis, M.; Ferrari, M. Nanoporous anti-fouling silicon membranes for biosensor applications. *Biosens. Bioelectron.* **2000**, *15*, 453−462.

(13) Kleps, I.; Miu, M.; Simion, M.; Ignat, T.; Bragaru, A.; Craciunoiu, F.; Danilia, M. Study of the Micro- and Nanostructured Silicon for Biosensing and Medical Applications. *J. Biomed. Nanotechnol.* **2009**, *5*, 300−309.

(14) Sun, W.; Puzas, J. E.; Sheu, T. J.; Liu, X.; Fauchet, P. M. Nano-to microscale porous silicon as a cell interface for bone-tissue engineering. *Adv. Mater.* **2007**, *19*, 921.

(15) Chan, Y. H. M.; Schweiss, R.; Werner, C.; Grunze, M. Electrokinetic characterization of oligo- and poly(ethylene glycol)-terminated self-assembled monolayers on gold and glass surfaces. *Langmuir* **2003**, *19*, 7380−7385.

(16) Lee, S. W.; Shang, H.; Haasch, R. T.; Petrova, V.; Lee, G. U. Transport and functional behaviour of poly(ethylene glycol)-modified nanoporous alumina membranes. *Nanotechnology* **2005**, *16*, 1335−1340.

(17) Kingshott, P.; Wei, J.; Bagge-Ravn, D.; Gadegaard, N.; Gram, L. Covalent attachment of poly(ethylene glycol) to surfaces, critical for reducing bacterial adhesion. *Langmuir* **2003**, *19*, 6912−6921.

(18) Chen, Y. M.; Liu, D. M.; Deng, Q. L.; He, X. H.; Wang, X. F. Atom transfer radical polymerization directly from poly(vinylidene fluoride): Surface and antifouling properties. *J. Polym. Sci., Polym. Chem.* **2006**, *44*, 3434−3443.

(19) Johnston, E. E.; Bayers, J. D.; Ratner, B. D. Plasma deposition and surface characterization of oligoglyme, dioxane, and crown ether nonfouling films. *Langmuir* **2005**, *21*, 870−881.

(20) Dong, B. Y.; Jiang, H. Q.; Manolache, S.; Wong, A. C. L.; Denes, F. S. Plasma-mediated grafting of poly(ethylene glycol) on polyamide and polyester surfaces and evaluation of antifouling ability of modified substrates. *Langmuir* **2007**, *23*, 7306−7313.

(21) Banerjee, I.; Pangule, R. C.; Kane, R. S. Antifouling Coatings: Recent Developments in the Design of Surfaces That Prevent Fouling by Proteins, Bacteria, and Marine Organisms. *Adv. Mater.* **2011**, *23*, 690−718.

(22) Harris, J. M., Ed. *Poly(ethylene glycol) chemistry: biotechnical and biomedical applications*; Plenum Press: New York, 1992.

(23) Dalsin, J. L.; Hu, B. H.; Lee, B. P.; Messersmith, P. B. Mussel adhesive protein mimetic polymers for the preparation of nonfouling surfaces. *J. Am. Chem. Soc.* **2003**, *125*, 4253−4258.

(24) Ostaci, R. V.; Damiron, D.; Al Akhrass, S.; Grohens, Y.; Drockenmuller, E. Poly(ethylene glycol) brushes grafted to silicon substrates by click chemistry: influence of PEG chain length, concentration in the grafting solution and reaction time. *Polym. Chem.* **2011**, *2*, 348−354.

(25) Zhao, C.; Zheng, J. Synthesis and Characterization of Poly(*N*-hydroxyethylacrylamide) for Long-Term Antifouling Ability. *Biomacromolecules* **2011**, *12*, 4071−4079.

(26) Nnebe, I. M.; Titon, R. D.; Scheider, J. W. Direct force measurement of the stability of poly(ethylene glycol)-polyethylenimine graft films. *J. Colloid Interface Sci.* **2004**, *276*, 306−316.

(27) Papra, A.; Gadegaard, N.; Larsen, N. B. Characterization of ultrathin poly(ethylene glycol) monolayers on silicon substrates. *Langmuir* **2001**, *17*, 1457−1460.

(28) Branch, D. W.; Wheeler, B. C.; Brewer, G. J.; Leckband, D. E. Long-term stability of grafted polyethylene glycol surfaces for use with microstamped substrates in neuronal cell culture. *Biomaterials* **2001**, *22*, 1035−1047.

(29) Sieval, A. B.; Opitz, R.; Maas, H. P. A.; Schoeman, M. G.; Meijer, G.; Vergeldt, F. J.; Zuilhof, H.; Sudholter, E. J. R. Monolayers of 1-alkynes on the H-terminated Si(100) surface. *Langmuir* **2000**, *16*, 10359−10368.

(30) Linford, M. R.; Fenter, P.; Eisenberger, P. M.; Chidsey, C. E. D. Alkyl monolayers on silicon prepared from 1-alkenes and hydrogen-terminated silicon. *J. Am. Chem. Soc.* **1995**, 3145−3155.

(31) Sung, M. M.; Kluth, G. J.; Yauw, O. W.; Maboudian, R. Thermal behavior of alkyl monolayers on silicon surfaces. *Langmuir* **1997**, *13*, 6164−6168.

(32) Ciampi, S.; Harper, J. B.; Gooding, J. J. Wet chemical routes to the assembly of organic monolayers on silicon surfaces via the formation of Si-C bonds: surface preparation, passivation and functionalization. *Chem. Soc. Rev.* **2010**, *39*, 2158−2183.

(33) Huisgen, R.; Szeimies, G.; Mobius, L. 1,3-dipolare cycloadditionen. 32. Kinetik der additionen organischer azide an cc-mehrfachbindungen. *Chem. Ber./Recl.* **1967**, *100*, 2494−2507.

(34) Ciampi, S.; Bocking, T.; Kilian, K. A.; James, M.; Harper, J. B.; Gooding, J. J. Functionalization of acetylene-terminated monolayers on Si(100) surfaces: A click chemistry approach. *Langmuir* **2007**, *23*, 9320−9329.

(35) Qin, G. T.; Santos, C.; Zhang, W.; Li, Y.; Kumar, A.; Erasquin, U. J.; Liu, K.; Muradov, P.; Trautner, B. W.; Cai, C. Z. Biofunctionalization on Alkylated Silicon Substrate Surfaces via "Click" Chemistry. *J. Am. Chem. Soc.* **2010**, *132*, 16432−16441.

(36) Yameen, B.; Ali, M.; Alvarez, M.; Neumann, R.; Ensinger, W.; Wolfgang, K.; Azzaroni, O. A facile route for the preparation of azide-terminated polymers. 'Clicking' polyelectrolyte brushes on planar surfaces and nanochannels. *Polym. Chem.* **2010**, *1*, 183−192.

(37) Ostaci, R. -V.; Damiron, D.; Grohens, Y.; Leger, L.; Drochenmuller, E. Click Chemistry Grafting of Poly(ethylene glycol) Brushes to Alkyne-Functionalised Pseudobrushes. *Langmuir* **2010**, *26*, 1304−1310.

(38) Britcher, L.; Barnes, T. J.; Griesser, H. J.; Prestige, C. A. PEGylation of Porous Silicon Using Click Chemistry. *Langmuir* **2008**, *24*, 7625−7627.

(39) Ciampi, S.; Eggers, P. K.; Le Saux, G.; James, M.; Harper, J. B.; Gooding, J. J. Silicon (100) Electrodes Resistant to Oxidation in Aqueous Solutions: An Unexpected Benefit of Surface Acetylene Moieties. *Langmuir* **2009**, *25*, 2530−2539.

(40) Ciampi, S.; James, M.; Le Saux, G.; Gaus, K.; Gooding, J. J. Electrochemical "Switching" of Si(100) Modular Assemblies. *J. Am. Chem. Soc.* **2011**, *134*, 844−847.

(41) Ng, C. C. A.; Magenau, A.; Ngalim, S. H.; Ciampi, S.; Chockalingham, M.; Harper, J. B.; Gaus, K.; Gooding, J. J. Using an Electrical Potential to Reversibly Switch Surfaces between Two States for Dynamically Controlling Cell Adhesion. *Angew. Chem.* **2012**, *51*, 7706−7710.

(42) Kingshott, P.; Thissen, H.; Griesser, H. J. Effects of cloud-point grafting, chain length, and density of PEG layers on competitive adsorption of ocular proteins. *Biomaterials* **2002**, *23*, 2043−2056.

(43) Briggs, D. *Surface Analysis of Polymers by XPS and Static SIMS*; Cambridge University Press: Cambridge, 1998.

(44) Jasieniak, M.; Graham, D.; Kingshott, P.; Gamble, L. J.; Griesser, H. J. Surfance Analysis of Biomaterials. In *Handbook of Surface and Interface Analysis*; Riviere, J. C., Myhra, S., Eds.; CRC Press: Boca Raton, FL, 2009; pp 529564

(45) Baio, J. E.; Weidner, T.; Brison, J.; Graham, D. J.; Gamble, L. J.; Castner, D. G. Amine terminated SAMs: Investigating why oxygen is present in these films. *J. Electon Spectrosc. Relat. Phenom.* **2009**, *172*, 2−8.

(46) Kingshott, P.; McArthur, S.; Thissen, H.; Castner, D. G.; Griesser, H. J. Ultrasensitive probing of the protein resistance of PEG surfaces by secondary ion mass spectrometry. *Biomaterials* **2002**, *23*, 4775−4785.

(47) Benninghoven, A. Chemical Analysis of Inorganic and Organic Surfaces and Thin Films by Static Time-of-Flight Secondary Ion Mass Spectrometry (TOF-SIMS). *Angew. Chem.* **1994**, *33*, 1023−1043.

(48) Braun, R. M.; Beyder, A.; Xu, J.; Wood, M. C.; Ewig, A. G.; Winograd, N. Spatially Resolved Detection of Attomole Quantities of Organic Molecules Localized in Picoliter Vials Using Time-of-Flight Secondary Ion Mass Spectrometry. *Anal. Chem.* **1999**, *71*, 3318−3324.

(49) Arlinghaus, H. F.; Schroeder, M.; Feldner, J. C.; Brandt, O.; Hoheisel, J. D.; Lipinsky, D. Development of PNA microarrays for gene diagnostics with TOF-SIMS. *Appl. Surf. Sci.* **2004**, *231−232*, 392−396.

(50) Sole-Domenech, S.; Johansson, B.; Schalling, M.; Malm, J.; Sjoevall, P. Analysis of Opioid and Amyloid Peptides Using Time-of-Flight Secondary Ion Mass Spectrometry. *Anal. Chem.* **2010**, *82*, 1964−1974.

(51) Wagner, M. S.; McArthur, S. L.; Shen, M.; Horbett, T. A.; Castner, D. G. Limits of detection for time of flight secondary ion mass spectrometry (ToF-SIMS) and X-ray photoelectron spectroscopy (XPS): detection of low amounts of adsorbed protein. *J. Biomater. Sci., Polym. Ed.* **2002**, *13*, 407−428.

(52) Mantus, D. S.; Ratner, B. D.; Carlson, B. A.; Moulder, J. F. Static secondary-ion mass-spectrometry of adsorbed proteins. *Anal. Chem.* **1993**, *65*, 1431−1438.

(53) Wagner, M. S.; Castner, D. G. Characterization of Adsorbed Protein Films by Time-of-Flight Secondary Ion Mass Spectrometry with Principal Component Analysis. *Langmuir* **2001**, *17*, 4649−4660.

(54) Henry, M.; Dupont-Gillian, C.; Bertrand, P. Conformation Change of Albumin Adsorbed on Polycarbonate Membranes as Revealed by ToF-SIMS. *Langmuir* **2003**, *19*, 6271−6276.

(55) Lhoest, J. B.; Detrait, E.; van den Bosch de Aguilar, P.; Bertrand, P. Fibronectin adsorption, conformation, and orientation on polystyrene substrates studied by radiolabeling, XPS, and ToF SIMS. *J. Biomed. Mater. Res.* **1998**, *41*, 95−103.

(56) Ratner, B. D.; Hoffman, A. S.; Schoen, F. J.; Lemons, J. E. *Biomaterials Science: An Introduction to Materials in Medicine*, 2nd ed.; Academic Press: New York, 2004.

(57) Daniels, C. R.; Reznik, C.; Kilmer, R.; Felipe, M. J.; Tria, M. C. R.; Kourentzi, K.; Chen, W. H.; Advincula, R. C.; Willson, R. C.; Landes, C. F. Permeability of anti-fouling PEGylated surfaces probed by fluorescence correlation spectroscopy. *Colloids Surf., B* **2011**, *88*, 31−38.

(58) Jeon, S. I.; Andrade, J. D. Protein—surface interactions in the presence of polyethylene oxide: II. Effect of protein size. *J. Colloid Interface Sci.* **1991**, *142*, 159−166.

2.6.14 *Waveguide-Integrated Electroluminescent Carbon Nanotubes*

S. Khasminskaya, F. Pyatkov, **B. S. Flavel**, W. H. Pernice, R. Krupke

Advanced Materials 26 (2014) 3465–3472

DOI: 10.1002/adma.201305634

Abstract

We demonstrate how light from an electrically driven carbon nanotube can be coupled directly into a photonic waveguide architecture. Waferscale, broadband sources are realized integrated with nanophotonic circuits allowing for propagation of light over centimeter distances. Moreover, we show that the spectral properties of the emitter can be controlled directly on chip with passive devices using Mach-Zehnder interfero-meters and grating structures.

Contribution

W.H.P and R.K conceived the idea for the project. S.K, F.P and B.S.F performed the experiments. S.K and F.P wrote the paper and all authors contributed to the scientific evaluation of results and the discussion.

– This page intentionally left blank –

Waveguide-Integrated Light-Emitting Carbon Nanotubes

Svetlana Khasminskaya, Feliks Pyatkov, Benjamin S. Flavel, Wolfram H. Pernice, and Ralph Krupke**

Photons propagating at the speed of light and outpacing electrons are the fastest carriers of information possible. For this reason a large proportion of mid- and long-distance electrical communication connections have been replaced by fiber optics in the last years.[1] The next evolutionary step will be the replacement of short-distance electrical connections by optical waveguides, which will thereby enhance on-chip data transfer rates, for example between processor and memory.[2] In order to achieve this goal the development of optical modules with large numbers of input and output channels will be required. Furthermore, on-chip generation of light will be needed to overcome foreseeable limitations in scalability and reproducibility. The then required level of integration will exceed the capacity of conventional integrated optical circuits[3] and will necessitate the use of waveguides with tight modal confinement, as well as the co-integration of active components. Recently, carbon based optoelectronic devices[4,5] have emerged as a promising platform to realize nanoscale light emitting diodes,[6] narrowband thermal emitters,[7] cavity controlled detectors[7,8] and wideband electro-optic modulators,[9] which can be used for chipscale information processing and for high bandwidth on-chip communication.[10,11]

Since the beginning of the field it has been a challenge to couple light into nanoscale photonic waveguides. The current state-of-the-art solution is to launch light from external sources, such as lateral microcavity lasers,[12] vertical cavity surface emitting lasers,[13] or microdisc lasers,[14] into the photonic waveguides using fiber-coupling techniques.[15,16] These hybrid solutions, however, require sophisticated multilevel nanofabrication processes for producing the lasers, which is in marked contrast to comparably simple photonic waveguide processing techniques. Furthermore, tight alignment tolerances for the orientation of the waveguide with respect to an optical fiber core make such an approach unfeasible for large numbers of input/output ports.

An alternative approach is the integration of monolithic nanoscale light emitters with photonic waveguide structures. A first proof-of-principle has been shown by Park et al., who placed a nanowire light source close to a photonic crystal waveguide.[17] More recently also carbon nanotubes (CNTs) have been combined with photonic waveguides and cavities.[18,19] In these experiments light emission from the nanotube has been stimulated optically by a free-space laser source and coupling of fluorescent light from nanotubes into photonic structures has been demonstrated. Carbon nanotubes, however, can also be stimulated electrically to emit light, which is the preferred method of excitation for chipscale solutions. Depending on the type of the nanotube, its diameter and the mode of operation the emission can be narrowband or broadband.[20–24] Moreover the emitted light is polarized along the nanotube axis and emitted preferentially perpendicular to the nanotube axis.[20] In this work we demonstrate efficient coupling of light emitted from an electrically-stimulated carbon nanotube into a photonic circuit by integrating a CNT with its long axis perpendicular to a photonic waveguide. We use electric-field assisted placement of solution-processed carbon nanotubes into pre-patterned structures containing the photonic waveguide, couplers, Mach-Zehnder structures and electrical wiring. Our approach allows for contacting multiple devices in parallel as a key step towards carbon based optical interconnects.

All the devices in this study consist of three basic components: carbon nanotubes, nanophotonic waveguides with coupler gratings, and metallic contacts. The device fabrication was performed in three steps. At first, 60 nm thick metal contacts with a gap of 1 µm were formed on a doped Si-wafer with SiO_2 (2 µm)/Si_3N_4 (0.2 µm) top layers, using electron-beam lithography and subsequent metal evaporation. Then, 500 nm wide waveguides terminated with focusing grating couplers were defined with electron beam lithography and formed by thinning 100 nm of the Si_3N_4 layer in between the metal contacts by reactive ion etching. Optimal etching parameters for obtaining the nominal etching depth in combination with minimal surface roughness were identified using reflectometry, scanning electron microscopy and atomic force microscopy. Finally, single-walled carbon nanotubes were deposited in between the metal contacts and onto the waveguide by dielectrophoresis from an aqueous dispersion.[25,26] Use of CNT based material enables us to employ nanotube solutions with high uniformity and sufficient CNT content for efficient contacting of many devices in one single deposition step, which is thus a procedure also suitable for waferscale fabrication. The dielectrophoretic force thereby ensures precise alignment of the nanotubes with the nanotube axis perpendicular to the direction of the waveguide, which guarantees optimal coupling of the emitted radiation into the underlying optical circuitry. The

---

S. Khasminskaya,[+] F. Pyatkov,[+] B. S. Flavel,
W. H. Pernice, R. Krupke
Institute of Nanotechnology
Karlsruhe Institute of Technology
76021, Karlsruhe, Germany
E-mail: wolfram.pernice@kit.edu; krupke@kit.edu

F. Pyatkov, W. H. Pernice, R. Krupke
DFG Center for Functional Nanostructures (CFN)
76031, Karlsruhe, Germany

F. Pyatkov, R. Krupke
Department of Materials and Earth Sciences
Technische Universität Darmstadt
64287, Darmstadt, Germany

[+]The authors contributed equally to this work.

DOI: 10.1002/adma.201305634

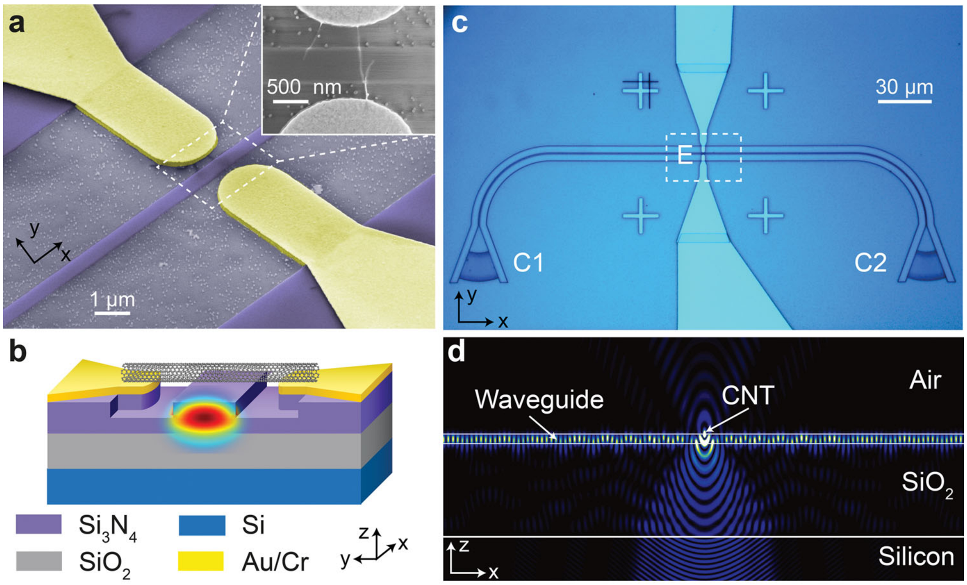

Figure 1. Waveguide-coupled carbon nanotube light emitter. (a) False-colored scanning electron micrograph showing two metal electrodes (yellow) and a photonic waveguide (purple), bridged by a single-walled carbon nanotube. Tilt angle 45°, scale bar 1 µm. The inset shows the indicated region at higher magnification. Carbon nanotubes appear as thin white lines. Tilt angle 0°, scale bar 500 nm. (b) Schematic cross-sectional view of the multi-layer device structure (not to scale). The central waveguide is etched into the Si$_3$N$_4$ layer and runs along the x-axis. The carbon nanotube is in contact with the Au/Cr metal and the waveguide, and aligned with the y-axis. (c) Low-magnification optical micrograph of a complete device comprising the indicated central emitter region, shown in (a), and the extended photonic waveguide with two terminating coupler gratings C1 and C2. Top view, scale bar 30 µm. (d) Cross-section through a 3D finite-difference time-domain simulation of the electric-field intensity $\vec{E}^2$. The carbon nanotube is simulated as an electrical dipole at the waveguide-air interface, oscillating perpendicular to the x-z-plane.

nanotube dispersion contained predominantly semiconducting nanotubes and residual metallic nanotubes. Even though the exact content of metallic nanotubes is currently not known, we verify by electrical measurements that some contacts are solely connected by semiconducting tubes. Variation of the dielectrophoresis parameters like exposure time, concentration of nanotubes as well as amplitude and frequency of the applied voltage was used to control the number of carbon nanotubes deposited in between the metal contacts. In our study we employ both devices with single CNT emitters as well as circuits that contain several CNTs in order to raise the emitted radiation signal to levels above the detector noise floor. Optical measurements on both types of devices show qualitatively similar spectral properties, where the devices with more CNT emitters provide stronger signal levels roughly proportional to the number of CNT devices. For further details on the device fabrication and materials we refer to the methods section.

Figure 1a shows the central device structure comprising of a nanotube which is positioned across the waveguide and is in contact with the metal electrodes. We will refer to this structure as the waveguide-coupled carbon nanotube emitter E in the following. A schematic cross-section of E is shown in Figure 1b. The chosen structure enables single-mode propagation of visible and near-infrared light within the waveguide, and ensures that light propagation is not perturbed by the 250 nm distant metal electrodes on either side of the waveguide. At the same time a direct contact between the nanotube sidewall and the waveguide top surface, and between the nanotube end and metal electrodes, respectively, is ensured. In all devices, the waveguides are terminated by two Bragg couplers C1 and C2, as shown in Figure 1c. This configuration allows the far-field coupling of light into and out of the waveguide for transmission experiments using an external light source as described in the methods section. The grating couplers provide typical insertion loss of 7 dB at 700–800 nm wavelength if the Si$_3$N$_4$ layer is thinned to half of its thickness, as shown in Figure 1b. The coupling bandwidth is roughly 30 nm, centered around a coupling wavelength that can be adjusted by varying the period of the grating (supplementary information). The couplers C1 and C2 also ensure that light which is generated by the carbon nanotube emitter E – coupled into the waveguide and propagating along the waveguide – will be coupled out for far-field detection. The expected near-field coupling of light from the nanotube into the waveguide has been simulated with 3D finite-difference time-domain calculations of the electric-field intensity $\vec{E}^2$, described in the methods section. The nanotube emitter is modeled as an elongated electrical dipole at the waveguide-air interface with the dipole moment oscillating perpendicular to the waveguide axis and hence parallel to the nanotube axis. Figure 1d shows, that near-field coupling of light from the nanotube emitter into the waveguide is expected, as well as the propagation of light within the waveguide. A cross-section through the waveguide mode at 750 nm is shown in Figure 1b as a color overlay on the waveguide facet. Figure 1d also shows that part of the emitted light will be far-field coupled into and out of the substrate along the surface normal. These light paths give rise to interference effects shaping the spectral profile of the emitter and allow for free-space spectral analysis of the emitted light.

Electrically induced light emission has been measured in the dark with a low-temperature CCD camera directly attached to

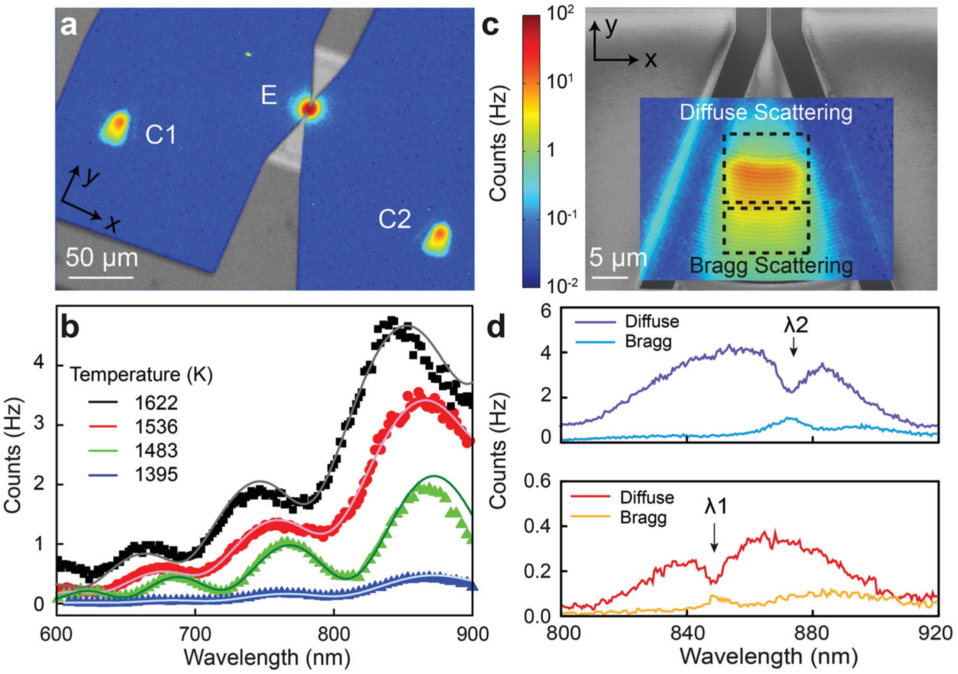

Figure 2. Light emission and propagation. (a) CCD-camera image of the device shown in Figure 1a-b under electrical bias. Light emission is observed from the carbon nanotube emitter (E) and from the terminating coupler gratings C1 and C2, both connected with (E) through the waveguide (not visible). Superimposed is a grayscale image of the sample under external illumination to reveal the position of the electrodes. Scale bar 50 µm. (b) Sequence of carbon nanotube emission spectra recorded at (E) with increasing electrical power dissipation. The data is fitted with a Planck spectrum modulated by substrate induced interference fringes. The fit-parameter temperature is given for every curve. (c) High-resolution CCD camera image of the coupler grating C2 (with 85% opacity). Indicated are regions of diffusive scattering and Bragg scattering, close and remote from the waveguide entrance, respectively. Superimposed is a scanning electron micrograph of C2 to reveal the position of the waveguide (entering from top). Scale bar 5 µm (d) Spectra from C1, recorded at regions of diffusive scattering and Bragg scattering, respectively. Spectra from diffusive scattering are similar to the spectra of (E) although with dips at λ_1 and λ_2. The missing intensity is recovered in the spectra from the Bragg scattering as explained in the text.

an optical microscope. The emission images were then compared with recordings under external illumination, enabling identification of light emission sources. Spectral information was obtained through a retractable grating in combination with a field aperture. The device was mounted on a motorized stage and electrically connected through probe needles. For details of the light-emission measurement setup we refer to the methods section. Upon electrical biasing of the nanotube in the range of typically 3–10 V (corresponding to an electrical power of 1–100 µW) we observe light emission from three spots as shown in **Figure 2**a. The central emission spot is correlated with the position of the waveguide-coupled carbon nanotube emitter E and hence due to the emission of photons along the surface normal within 60° acceptance angle of the microscope objective. The other two emission spots are located at the positions of the coupler gratings C1 and C2. Light is generated at E and the photons detected at C1 and C2 have propagated through the waveguide prior to being diffracted at the grating coupler. The image is thus direct evidence, that photons emitted from an electrically-driven carbon-nanotube, couple into the waveguide, propagate over 150 µm in both directions of the waveguide, and couple out into the far field. Comparing the signal intensities recorded at E, C1 and C2, we estimate a lower bound for the coupling efficiency into the waveguide on the order of 50%, in agreement with numerical simulations. Figure 2b shows a series of emission spectra recorded at E with increasing electrical power. Overall the signal intensity increases towards longer wavelength with a wavelength-dependent modulation. The spectra $I(\lambda)$, measured at the detector, show the typical profile of black-body radiation enveloped with the interference fringes due to back-reflection from the underlying silicon substrate. Photons emitted into air ($I_1(\lambda)$) are interfering with photons emitted towards the silicon substrate and reflected back at the SiO_2/Si interface ($I_2(\lambda)$), as described by $I(\lambda) = I_1(\lambda) + I_2(\lambda) + 2 \cdot \sqrt{I_1(\lambda) \cdot I_2(\lambda)} \cdot \mathrm{Re}\gamma_{12}(\tau)$.[27] $\gamma_{12}(\tau)$ is the complex degree of coherence function and τ is the delay time between the emitted and reflected photons. We have fitted the spectra to $f(\lambda) \propto \cdot f_{Planck}(\lambda, T) \cdot [1 + 2 \cdot \gamma_{12}(\tau) \cdot f_{\mathrm{int}}(\lambda)]$, with the electron temperature T dependent Planck curve $f_{\mathrm{Planck}}(\lambda, T)$ and a structure dependent interference term $f_{\mathrm{int}}(\lambda)$. The interference term has been calculated with a transfer matrix approach taking into account that the nanotube emitter is located at the Si_3N_4/air interface. For details on the fitting procedure we refer to the supplementary information.

In general the visibility of the interference fringes depends on the degree of temporal coherence and is determined by the magnitude of the coherence function $|\gamma_{12}(\tau)|$. A value of 1 is obtained for a fully coherent source and 0 for a completely incoherent source.[27] $\tau = \Delta z/c$ is defined by the optical path difference Δz. With $\gamma_{12}(\tau) = \int_0^\infty f_{Planck}(\nu) \cdot \exp(-2\pi i \nu \tau) d\nu$,[28] $\Delta z = 6.98$ µm,[29] and using the extracted nanotube emitter temperatures T = 1395–1622 K, we can calculate the theoretically expected value of $|\gamma_{12}(\tau)|$ for our thermal emitter and obtain $|\gamma_{12}(\tau)|$ = 0.0040–0.0026. Experimentally, however, we find a somewhat smaller value of $|\gamma_{12}(\tau)|$ = 0.025–0.016. This discrepancy could be related to the reduced dimension of the emitter – an argument that has been put forward to explain the enhanced coherence recently observed with metallic nanowires.[30] Use of CNTs as a thermal filament enables us to reach these significant temperatures without damage to the emitter. Because of the nanoscale diameter of the tube the driving current is sufficient to raise the CNT to temperature levels that lead to significant emission levels within the spectral bandwidth of the CCD camera. In our case we expect a long-wavelength cut-off because of the finite nanotube length, which would reduce the spectral width of the emitter and thus enhance the temporal coherence. However, studying these effects further is beyond the scope of this paper. That the emission spectrum does not reflect the narrow-band excitonic transitions of semiconducting nanotubes,[20,21] but rather broad-band thermal emission[22,24] can be attributed to residual metallic nanotubes present in our devices, which would also explain the small on-off ratios of the transfer characteristics (not shown). Fabricating similar devices from ultra-high purity semiconducting nanotube dispersions would alleviate this effect. On the other hand the appearance of electrically induced black-body radiation (incandescence) could also be a consequence of the limited sensitivity of our measurement setup, which requires operating the CNT emitter in a high current mode. In this regime the black-body radiation dominates weak S22 electroluminescent emission, which would be expected at 750 – 820 nm for our CNT solution (Figure S2). Unfortunately the fundamental transition S11 of the investigated nanotubes lies beyond the wavelength cutoff of the CCD camera (1100 nm) and can therefore not be observed.

We then study the spectral properties of the light that is coupled out by the coupler gratings C1 and C2. Figure 2c is a high-resolution image of C2, superimposed on a scanning electron micrograph. The waveguide is entering the coupler grating from the top of the image. One can observe that the coupling of light out of the surface into the far-field occurs over an extended region. The maximum signal intensity is recorded at the position of the first grating lines (compare with supplementary information Figure S1a) and is caused by diffusive scattering of photons with wavelengths outside the bandwidth of the grating coupler. Figure 2d shows incandescence spectra recorded at the diffusive scattering region of C2 for two gratings with different period and thus different central coupling wavelengths. The overall spectra from the diffusive scattering regions are qualitatively similar to the emission spectra recorded at E, and the intensity modulations due to interference effects at the emitter E are also reproduced. However the spectra reveal distinct dips at the wavelengths which correspond to the characteristic grating wavelengths λ_1 and λ_2 defined by the grating period, respectively. Those "missing" photons continue to propagate into the grating structure and are then coupled out closer to the bottom of the coupler. Hence the spectra recorded at the Bragg scattering regions are dominated by photons with wavelength λ_1 and λ_2, respectively. As a result, grating structures inscribed into the on-chip photonic waveguide architecture may be employed for spectral filtering.

For potential applications where electrical wiring is replaced by photonic leads it is important to demonstrate the coupling of light emited from an electrically driven carbon nanotube into extended waveguides and to determine propagation losses within the waveguide. Therefore, we have fabricated a series of nanophotonic circuits with asymmetric long waveguides between the waveguide-coupled nanotube emitter E and the couplers C1 and C2. The distance $d_{\text{E-C1}}$ between E and C1 is fixed to 25 µm, whereas the distance $d_{\text{E-C2}}$ between E and C2 is varied systematically from 1.6 mm to 10.1 mm for the devices shown in **Figure 3**a. Fabricating identical couplers within the field of view and keeping for all samples $d_{\text{E-C1}} \ll d_{\text{E-C2}}$, allows calculating the losses in the waveguide from the signal intensity at C1 and C2, even though the internal light source intensity varies from sample to sample. We first characterize the propagation loss in the photonic circuits by characterizing the transmission performance using a supercontinuum source and a spectrometer as shown in Figure 3b. The data reveals the Gaussian profile of the grating couplers, where the interference fringes result from Fabry-Perot-like reflections between the grating couplers. We note that the fine features are not fully resolved due to the limited resolution of the spectrometer. With increasing waveguide length higher absorption is present, leading to lower overall transmission within the spectrum. Then we characterize the on-chip losses using the emission from the CNT emitter. Figure 3b shows the CCD-camera image of the electrically biased device with a waveguide of length L = 6.5 mm. Similar to Figure 2a we observe light emission from E, C1 and C2. Also here, E is the only source of photons and hence the photons emitted at C2 are coupled out after propagation through the 6.5 mm long waveguide. The losses per unit length η are calculated via $\eta = \frac{d}{dL}\left(10\cdot Log\frac{IC1}{IC2(L)}\right)$. I_{C1} and I_{C2} are the signal intensities at C1 and C2 integrated within the indicated regions in Figure 3b. Figure 3d shows that the average loss per length is 9.1 ± 2.1 dB/cm, which is typical for the type of waveguide geometry used here.[31] The results are also confirmed by the independent loss measurements with the external light source (methods section). The transmission spectra shown in Figure 3c are dominated by the narrow-band couplers and therefore each spectrum has a maximum at 756 nm, corresponding to the characteristic wavelength of the used gratings. The overall signal intensity decreases with increasing waveguide length and is due to losses in the waveguide. Hence $\eta = \frac{d}{dL}\left(Log\left(\frac{I_0}{I_{C2,765nm(L)}}\right)\right)$, under the condition of identical fiber coupling for every sample. I_0 is the signal intensity of the external source determined with a reference detector. Figure 3d shows that the average loss per length is 12.7 ± 1.2 dB/cm, which was measured before the CNT-deposition, and compares reasonably well to the measurement with the internal nanotube light source. The absolute loss in dB in the CNT-based measurements is higher because of contamination of the waveguides after deposition, and accounts for the discrepancy in the fitted slope.

Finally, we realize Mach-Zender (MZ) interferometers co-integrated with a waveguide-coupled carbon nanotube emitter for the purpose of demonstrating electrically-driven interference of light on a chip. The MZ interferometer is located

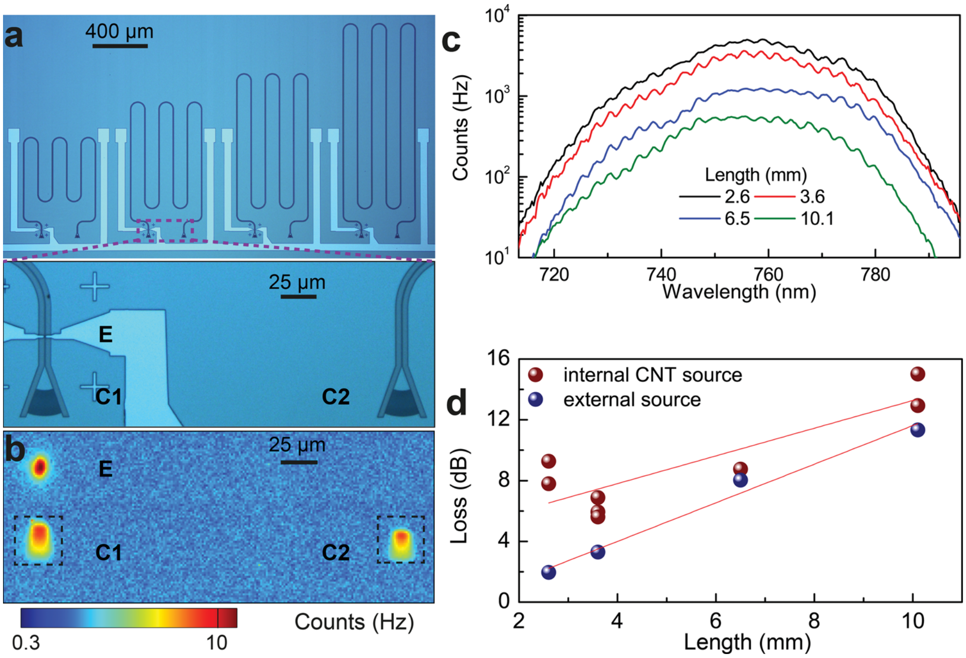

Figure 3. Propagation loss in extended waveguide structures. (a) Optical micrographs of 4 out of 7 devices with asymmetrically long waveguide segments between the nanotube emitter E and the coupler gratings C1 and C2. The segment between E and C1 is fixed to 25 µm. The total waveguide length L between C1 and C2 for the devices shown here is 3.6 mm, 5.3 mm, 6.5 mm and 7.3 mm. Scale bars indicated. (b) CCD-camera image of the device with L = 6.5 mm under electrical bias. Light emission is observed from the carbon nanotube emitter (E), the nearby coupler C1 and the remote coupler C2. Losses in the waveguides are calculated from the integrated scattering light intensities I(C1) and I(C2) at C1 und C2 within the dashed regions, respectively. Scale bar 25 µm. (c) Transmission spectra of complete devices (C1-waveguide-C2) measured with an external supercontinuum light source. Losses in the waveguide are calculated from the decreasing signal intensity at the peak wavelength 756 nm with increasing waveguide length L and are plotted in d). (d) Comparison between losses in the waveguide determined with the external supercontinuum light source (blue) and with the integrated waveguide-coupled carbon nanotube light emitter source (red).

between the emitter E and the coupler C2 and consists of a bifurcated waveguide, that splits into two arms with a path difference ΔL = 50 µm, before rejoining, as shown in **Figure** 4a. The total waveguide length between C1 and C2 is 640 µm when passing through the lower arm and 690 µm for the longer arm, respectively. Biasing the emitter E induces light emission from E, C1 and C2, as observed in the previous structures. We focus now on the emission at the coupler C2 at the output of the MZ structure. Figure 4b shows spatially resolved emission spectra of C2 along the y-axis. The dashed lines mark the location of C2 within the y-axis range. There are two types of wavelength-dependent intensity modulations: A long-wave modulation, with intensity minima at 800 nm and 900 nm, and a short-wave modulation with a period of a few nanometers. This can be better seen when integrating the spectra over the indicated y-axis range, including both Bragg and diffuse scattering. The resulting data is plotted Figure 4d together with a spectrum recorded at E. The long-wave intensity modulation reproduces the modulation directly measured at E, and hence is due to interference effects along the surface normal because of back-reflection from the silicon substrate. The short-wave intensity modulation, measured only at C2, is induced by the MZ structure and is hence due to the interference of light within the waveguide along the surface. The expected periodicity of the intensity modulation $\Delta\lambda$ (or free spectral range FSR), is given by $\Delta\lambda = \lambda^2/(n_g(\lambda)\cdot\Delta L)$,[32] where $n_g(\lambda)$ is the group refractive index of the waveguide according to the supplementary information. With n_g (850 nm) = 1.964 and ΔL = 50 µm we obtain $\Delta\lambda$ = 7.4 nm at 850 nm, which fits very well to the experimental value of ~ 7 nm. The data is confirmed by transmission measurements with an external light source, and similar short-wave intensity oscillation are observed, as shown in Figure 4c. The periodicity of ~5 nm, measured at 745 nm, fits well to $\Delta\lambda$ = 5.4 nm using n_g (750 nm) = 2.047. Figure 4e shows the excellent agreement between FSR measurements obtained with the on-chip waveguide-coupled carbon nanotube emitter and the external light source, along with a theoretical simulation with no fit parameter.

The direct, near-field coupling of light from an electrically-driven carbon nanotube into a waveguide, as opposed to the traditional far-field fiber coupling of an external light source, opens up new opportunities to produce compact optoelectronic systems. Considering the wide range of different, structure-dependent emission spectra of semiconducting and metallic carbon nanotubes and the continuing progress in the sorting of specific nanotubes, it seems possible to use nanotubes with specific emission lines in the near future. The use of electrically triggered on-chip nanotube emitters for signal transmission through extended waveguides and interferometers shown in this work provides the basis for next-generation nanoscale interconnects that can be seamlessly integrated with passive silicon photonic technology. While the emitters are operated at high currents in this work leading to incandescence, in contrast, tailored electroluminescent emission within the range

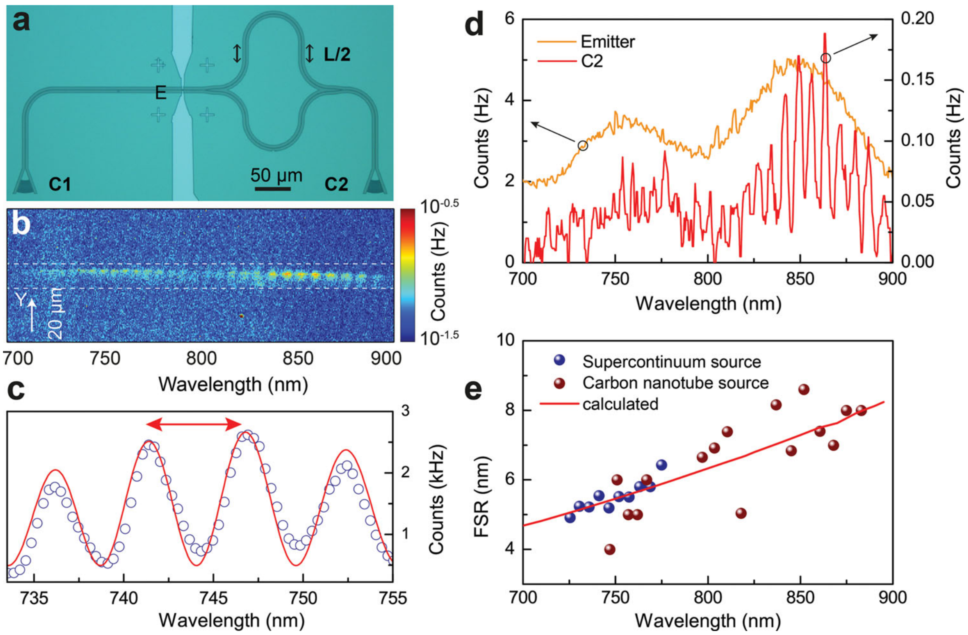

Figure 4. On-chip Mach-Zehnder optical interferometer. (a) Optical micrograph of a Mach-Zehnder (MZ) interferometer device. The waveguide in between the nanotube emitter E and the coupler grating C2 is split into two arms with a path difference of $\Delta L = 50$ µm. The total waveguide length between C1 and C2 is 640 µm and 640 µm + ΔL, respectively. Scale bar 50 µm. (b) CCD-camera image with combined spectral and spatial information of light emitted from the nanotube E, after passing through the MZ resonator and the coupler grating C2. The dashed lines mark the position of C2 in the y-direction and the MZ induced intensity oscillations. (c) Transmission spectra of a complete MZ resonator device measured with an external supercontinuum light source. The red line is a fit to the data (see text). An arrow indicates a free spectral range (FSR = $\Delta\lambda$). (d) Comparison of carbon nanotube emission spectra recorded at E (orange) with spectrum recorded at C2 after passing through the MZ resonator (red, integrated intensity from b)). (e) Free spectral range (FSR) versus wavelength extracted from the data shown in c) and d).

of the CCD detector will be possible by employing CNT material with an S11 peak at shorter wavelengths. Alternatively extending the detecting window of the camera into the technologically relevant NIR-range could reveal electroluminescence at low current levels where thermal radiation is expected to be absent. This mode of operation will then enable to use tailored spectral emission in nanophotonic circuits by using a suitable type of carbon nanotube.

Experimental Section

Device Fabrication and Materials: Rib waveguides were fabricated in close vicinity to electrical contacts using several steps of electron beam lithography with subsequent dry etching. The nanophotonic devices were prepared from high quality silicon carrier wafers, containing 200 nm of stoichiometric silicon nitride deposited by low pressure chemical vapor deposition (LPCVD) on top of 2000 nm buried oxide. Prior to lithography, all samples were cleaned via sonication in acetone for 10 min, rinsing in isopropanol followed by oxygen plasma etching (Diener Femto, 20 % power, 10 sccm, 0.4 mbar, 3 min) to remove organic residue. To drive off remaining water the samples were dried on a hot plate at 200 °C for 5 min. During the first lithography step the pattern for electrical contacts was written in 250 nm of PMMA on a Raith EBL system. After exposure the sample was developed in a solution of methylisobutylketon (MIBK): isopropanol (1:3). For manufacturing of metal contacts 50 nm gold was evaporated with a 5 nm adhesive layer of chromium and a 10 nm coating layer of chromium on top. The subsequent liftoff was performed by immersing the sample in acetone with subsequent weak sonication. In a second lithography step nanophotonic waveguides were defined in ZEP 520A positive resist with alignment accuracy better than 20 nm. After developing for 50 s in Xylene, reactive ion etching was used to transfer the pattern from resist into the silicon nitride on an Oxford 80 system. The etching recipe contained 50 sccm CHF_3 and 2 sccm O_2 at 175 W RF power and a base pressure of 55 mTorr. The sample was etched for roughly 90 s at a rate of 1.1 nm/s.

Carbon nanotube dispersions were prepared using the sorting method previously described by Flavel et al.[33] In brief 10 mg of raw single-walled carbon nanotube material (SWNT) from NanoIntegris was suspended in 15 mL of H_2O with 1 wt-% sodium dodecyl sulfate (SDS) using a tip sonicator (Bandelin, 200 W maximum power, 20 kHz, in pulsed mode with 100 ms pulses) applied for 2 h at ~20 % power. The resulting dispersion was then centrifuged at ~100,000 g for 1.5 h and carefully decanted from the pellet that was formed during centrifugation. The centrifuged SWNT material was then used for gel filtration fractionation. Gel filtration was performed as described previously by Moshammer et al.,[34] using a Sephacryl S-200 gel filtration medium in a glass column of 20 cm length and 2 cm diameter with a final bed height of ~14 cm. After separation of the metallic SWNTs from the semiconducting SWNTs (stuck on the gel) the pH of the 1 wt-% SDS in H_2O eluent was changed from 4 to 1 upon addition of the appropriate concentration of HCl. The pH was reduced in 12 steps with the (8,7) material collected as an early fraction. The collected fraction was then dialyzed for 24 h to readjust the pH to 7 in 1 mL Float-A-Lyzer G2 dialysis devices by using 500 mL of a 1 wt-% sodium cholate solution in H_2O. The absorption spectrum of the dispersion is shown in the supplementary information Figure S2.

Carbon nanotubes were deposited onto the electrodes by AC-dielectrophoresis. The CNT-suspension was diluted 1:100 in deionized water and a 20 µl droplet of the aqueous suspension was placed on the chip. The electric field (2 $V_{p\text{-}p}$ AC voltage at 10 MHz) was applied to the common electrode with a function generator SRS DS345.

After 5 min the sample was rinsed with water and methanol and the field was removed. Samples were annealed at 150 °C for 2 hours in oven to improve the contact adhesion. For further details we refer to.[25,26] Devices were measured at room temperature in air without further treatments.

Characterization of Waveguides and Couplers with an External Light Source: Light from a supercontinuum white light source (model number Leukos-SM-30-UV) was coupled into an optical fiber array (supplementary information Figure S3a-b). This array consists of eight fibers with a core size 8.5 µm and a distance between two adjacent fibers of 250 µm. The on-chip grating couplers were designed in accordance to this distance (250 µm separation for the long waveguides and 500 µm for the Mach-Zehnder interferometer devices). The end facet of the fibers are polished at an angle of 8° to reduce back reflections as commonly done in angle polished fiber connectors. Light from one fiber is coupled into the chip plane through Bragg diffraction on a grating coupler. After propagation through the device the transmitted signal is coupled out on a second grating coupler port and measured with a spectrometer (JAZ Spectrometer System, Ocean Optics) to acquire a spectrum in a range of 340–1014 nm with a spectral resolution of 0.3 nm. To minimize coupling losses the fiber array has to be in close proximity to the sample surface. Therefore the fiber array was mounted on a movable stage, which could be precisely controlled with a piezo actuator (Picomotor, New Focus). For coarse alignment of the sample to the fiber array an optical microscope with sufficient focal length was employed. For a fine alignment additional piezo stages were used to optimize the transmission signal, which was simultaneously recorded with a photoreceiver.

Finite-Difference Time-Domain Calculation of the Electric-Field Intensity: In order to analyze the near-field coupling of the CNT emitter to the waveguide structures FDTD simulations were performed using the commercial software package OmniSim distributed by Photon Design. The simulations were carried out full-vectorial in three dimensions using high grid resolution to ensure convergence within a 5% error margin. The CNT emitter was modeled as an elongated dipole source with dimensions corresponding to the real nanotube emitters, placed in direct contact with the top surface of the waveguide. Simulations were carried out both for continuous-wave excitation to obtain travelling wave modal distributions as shown in Figure 1d, as well as with pulsed excitation to obtain the broadband response of the waveguide structure.

Measurement Setup: Samples were mounted underneath a Zeiss AxioTech Vario microscope, directly attached to an Acton Research SpectraPro 2150i spectrometer and a Princeton Instruments PIXIS 256E Silicon CCD camera (1024 × 256 pixels, –60 °C), all within a light-tight box (supplementary information Figure S3d-e. The spectrometer can operate in the imaging mode, with a mirror to take real-space images, or in the spectroscopy mode, with a diffraction grating (300 grooves/mm, 750 nm blaze wavelength). The samples were mounted on a motorized stage, electrically contacted with probe needles and biased with a Keithley 6430 SourceMeter. Incandescence images and images under external illumination were recorded with Zeiss EC Epiplan-Neofluar 20×/0,50 and Motic Plan Apo 20×/0.42 objectives. Higher-resolution images were recorded with Zeiss LD EC Epiplan-Neofluar 100×/0,75 and Mitutoyo M Plan Apo 100×/0.70 objectives. The dark current of the CCD detector yields about 2 counts per pixel per hour, and allows integrating the signal over extended periods. We estimate the sensitivity of the setup on the basis of the quantum efficiency and amplifier gain of the CCD, the efficiency of the grating, the geometrical constraints of the microscope optics (optical path), and by assuming an isotropic emitter, to about 100 emitted photons per count, in reflection and diffraction mode, respectively, and the bandwidth per pixel $\Delta\lambda$ is 0.5 nm. The wavelength axis was calibrated with a mercury lamp, and the relative spectral response of the system has been measured with a calibrated halogen lamp. All recorded spectra were corrected accordingly. The spatial resolution is 0.26 µm and 1.34 µm for 100× and 20× objectives, and the spectral resolution is 1.5 nm.

Supporting Information

Supporting Information is available from the Wiley Online Library or from the author.

Acknowledgements

W. H. P. acknowledges support by DFG grant PE 1832/1–1 and PE 1832/1–2. B. S. F. acknowledges support by the Humboldt Foundation and support from the DFG under grant FL834/1-1. We also acknowledge support by the Deutsche Forschungsgemeinschaft (DFG) and the State of Baden-Württemberg through the DFG-Center for Functional Nanostructures (CFN) within subprojects A6.04 and B1.09. The authors thank Michael Engel, Martin Wegener and Ferdinand Evers for helpful discussions and Silvia Diewald for technical assistance.

Received: November 14, 2013
Revised: January 10, 2014
Published online: March 18, 2014

---

[1] M. J. O'Mahony, C. Politi, D. Klonidis, R. Nejabati, D. Simeonidou, *J. Lightwave Technol.* **2006**, *24*, 4684–4696.

[2] Y. Vlasov, W. M. J. Green, F. Xia, *Nature Photonics* **2008**, *2*, 242–246.

[3] M. Hochberg, T. Baehr-Jones, *Nature Photonics* **2010**, *4*, 492–494.

[4] P. Avouris, M. Freitag, V. Perebeinos, *Nature Photonics* **2008**, *2*, 341–350.

[5] F. Bonaccorso, Z. Sun, T. Hasan, C. Ferrari, *Nature Photonics* **2010**, *4*, 611–622.

[6] F. Xia, M. Steiner, Y.-M. Lin, P. Avouris, *Nat. Nanotechnol.* **2008**, *3*, 609–613.

[7] M. Engel, M. Steiner, A. Lombardo, A. C. Ferrari, H. v. Löhneysen, P. Avouris, R. Krupke, *Nature Communic.* **2012**, *3*, 906.

[8] M. Furchi, A. Urich, A. Pospischil, G. Lilley, K. Unterrainer, H. Detz, P. Klang, A. M. Andrews, W. Schrenk, G. Strasser, T. Mueller, *Nano Lett.* **2012**, *12*, 2773–2777.

[9] M. Liu, X. Yin, E. Ulin-Avila, B. Geng, T. Zentgraf, L. Ju, F. Wang, X. Zhang, *Nature* **2011**, *474*, 64–67.

[10] T. Mueller, F. Xia, P. Avouris, *Nature Photonics* **2010**, *4*, 297–301.

[11] K. Kim, J.-Y. Choi, T. Kim, S.-H. Cho, H.-J. Chung, *Nature* **2011**, *479*, 338–344.

[12] O. Painter, R. K. Lee, A. Scherer, A. Yariv, J. D. O'Brien, P. D. Dapkus, I. Kim, *Science* **1999**, *284*, 1819–1821.

[13] J. L. Jewell, J. P. Harbison, A. Scherer, Y. H. Lee, L. T. Florez, *IEEE Journal of Quantum Electronics* **1991**, *27*, 1332–1346.

[14] S. L. McCall, A. F. J. Levi, R. E. Slusher, S. J. Pearton, R. Logan, *Appl. Phys. Lett.* **1992**, *60*, 289.

[15] M. Lipson, *J. Lightwave Technol.* **2005**, *23*, 4222–4238.

[16] C. Kopp, S. Bernabe, B. B. Bakir, J.-M. Fedeli, R. Orobtchouk, F. Schrank, H. Porte, L. Zimmermann, T. Tekin, *IEEE Journal of Selected Topics in Quantum Electronics* **2011**, *17*, 498–509.

[17] H.-G. Park, C. J. Barrelet, Y. Wu, B. Tian, F. Qian, C. M. Lieber, *Nature Photonics* **2008**, *2*, 622–626.

[18] E. Gaufrès, N. Izard, A. Noury, X. Le Roux, G. Rasigade, A. Beck, L. Vivien, *ACS Nano* **2012**, *6*, 3813–3829.

[19] S. Imamura, R. Watahiki, R. Miura, T. Shimada, Y. K. Kato, *Appl. Phys. Lett.* **2013**, *102*, 161102.

[20] J. A. Misewich, R. Martel, Ph. Avouris, J. C. Tsang, S. Heinze, J. Tersoff, *Science*, **2003**, *300*, 783–786.

[21] M. H. P. Pfeiffer, N. Stürzl, C. W. Marquardt, M. Engel, S. Dehm, F. Hennrich, M. M. Kappes, U. Lemmer, R. Krupke, *Optics Express* **2011**, *19*, A1184.

[22] D. Mann, Y. K. Kato, A. Kinkhabwala, E. Pop, J. Cao, X. Wang, L. Zhang, Q. Wang, J. Guo, H. Dai, *Nat. Nanotechnol.* **2007**, *2*, 33–38.

[23] S. Essig, C. W. Marquardt, A. Vijayaraghavan, M. Ganzhorn, S. Dehm, F. Hennrich, F. Ou, A. A. Green, C. Sciascia, F. Bonaccorso, *Nano Lett.* **2010**, *10*, 1589–1594.

[24] Z. Liu, A. Bushmaker, M. Aykol, S. B. Cronin, *ACS Nano* **2011**, *5*, 4634–4640.

[25] R. Krupke, F. Hennrich, H. B. Weber, M. M. Kappes, H. V. Löhneysen, *Nano Lett.* **2003**, *3*, 1019–1023.

[26] A. Vijayaraghavan, S. Blatt, D. Weissenberger, M. Oron-Carl, F. Hennrich, D. Gerthsen, H. Hahn, R. Krupke, *Nano Lett.* **2007**, *7*, 1556–1560.

[27] M. Born, E. Wolf, *Principles of Optics*, Cambridge University Press, USA **2009**.

[28] C. L. Mehta, *Il Nuovo Cimento* **1963**, *28*, 401–408.

[29] $\Delta z = 2\cdot(n_{Si3N4}\cdot 0.2\ \mu m + n_{SiO2}\cdot 2\ \mu m)$, $n_{Si3N4} = 2.01$, $n_{SiO2} = 1.544$.

[30] L. J. Klein, H. F. Hamann, Y.-Y. Au, S. Ingvarsson, *Appl. Phys. Lett.* **2008**, *92*, 213102.

[31] M. Melchiorri, N. Daldosso, F. Sbrana, L. Pavesi, G. Pucker, C. Kompocholis, P. Bellutti, A. Lui, *Appl. Phys. Lett.* **2005**, *86*, 121111–3.

[32] F. Horst, W. M. J. Gree, S. Assefa, S. M. Shank, Y. A. Vlasov, B. J. Offrein, *Opt. Express* **2013**, *21*, 11652–8.

[33] B. S. Flavel, M. M. Kappes, R. Krupke, F. Hennrich, *ACS Nano* **2013**, *7*, 3557–3564.

[34] K. Moshammer, F. Hennrich, M. M. Kappes, *Nano Research* **2009**, *2*, 599–606.

2.6 Additional Scientific Publications

2.6.15 *Fabrication of Carbon Nanotube Nanogap Electrodes by Helium Ion Sputtering for Molecular Contacts*

C. Thiele, H. Vieker, A. Beyer, **B. S. Flavel**, F. Hennrich, D. Muñoz Torres, T. R. Eaton, M. Mayor, M. M. Kappes, A. Gölzhäuser, H. v. Löhneysen, R. Krupke

Appl. Phys. Lett. 104 (2014) 103102

DOI: 10.1063/1.4868097

Abstract

Carbon nanotube nanogaps have been used to contact individual organic molecules. However, the reliable fabrication of a truly nanometer-sized gap remains a challenge. We use helium ion beam lithography to sputter nanogaps of only (2.8 ± 0.6) nm size into single metallic carbon nanotubes embedded in a device geometry. The high reproducibility of the gap size formation provides a reliable nanogap electrode testbed for contacting small organic molecules. To demonstrate the functionality of these nanogap electrodes, we integrate oligo(phenylene ethynylene) molecular rods, and measure resistance before and after gap formation and with and without contacted molecules.

Contribution

R.K conceived the idea for the project. C.T, H.V, A.B, B.S.F, F.H, D.M.T, and T.R.E performed the experiments. C.T and R.K wrote the paper and all authors contributed scientifically to the interpretation of the results.

– This page intentionally left blank –

APPLIED PHYSICS LETTERS **104**, 103102 (2014)

Fabrication of carbon nanotube nanogap electrodes by helium ion sputtering for molecular contacts

Cornelius Thiele,[1,2,a)] Henning Vieker,[3] André Beyer,[3] Benjamin S. Flavel,[1]
Frank Hennrich,[1] David Muñoz Torres,[4] Thomas R. Eaton,[4] Marcel Mayor,[1,2,4]
Manfred M. Kappes,[1,2,5] Armin Gölzhäuser,[3] Hilbert v. Löhneysen,[1,2,6,7]
and Ralph Krupke[1,2,8,b)]
[1]*Institute of Nanotechnology, Karlsruhe Institute of Technology, 76021 Karlsruhe, Germany*
[2]*DFG Center for Functional Nanostructures (CFN), 76028 Karlsruhe, Germany*
[3]*Faculty of Physics, Bielefeld University, 33615 Bielefeld, Germany*
[4]*Department of Chemistry, University of Basel, 4056 Basel, Switzerland*
[5]*Institut für Physikalische Chemie, Karlsruhe Institute of Technology, 76131 Karlsruhe, Germany*
[6]*Physikalisches Institut, Karlsruhe Institute of Technology, 76128 Karlsruhe, Germany*
[7]*Institut für Festkörperphysik, Karlsruhe Institute of Technology, 76021 Karlsruhe, Germany*
[8]*Institut für Materialwissenschaft, Technische Universität Darmstadt, 64287 Darmstadt, Germany*

(Received 6 February 2014; accepted 24 February 2014; published online 10 March 2014)

Carbon nanotube nanogaps have been used to contact individual organic molecules. However, the reliable fabrication of a truly nanometer-sized gap remains a challenge. We use helium ion beam lithography to sputter nanogaps of only (2.8 ± 0.6) nm size into single metallic carbon nanotubes embedded in a device geometry. The high reproducibility of the gap size formation provides a reliable nanogap electrode testbed for contacting small organic molecules. To demonstrate the functionality of these nanogap electrodes, we integrate oligo(phenylene ethynylene) molecular rods, and measure resistance before and after gap formation and with and without contacted molecules. © *2014 AIP Publishing LLC*. [http://dx.doi.org/10.1063/1.4868097]

The use of individual metallic carbon nanotubes (CNTs) as electrodes is attractive for contacting nanocrystals,[1] single molecules,[2] and functional materials, such as phase-change materials,[3] due to the CNT's intrinsic one-dimensionality and electrical conductivity. The formation of CNT electrodes starts, typically, with a pristine CNT on a surface, where the nanotube is contacted by lithographically defined metallic electrodes. Subsequently, two opposing CNT electrodes are generated by forming a gap in the CNT near its center. The molecule or material of interest is assembled between or deposited onto the CNT electrodes.

Different methods for fabricating such nanogaps have been reported. For example, current-induced breakdown in high vacuum,[1] which has been shown to produce gaps down to 7 nm, however, the typical gap size is often much larger. Alternatively, plasma oxidation through a lithographic mask, a complicated technique, limited by reliability problems and highly variable gap sizes.[3] The use of electron-beam-induced oxidation has been shown to overcome variability in gap size,[4] but resulted in a typical gap of ≈20 nm, which is an order of magnitude too large for most organic molecules.

In this work, we report on the use of a helium ion microscope (HIM) to reliably fabricate nanogaps of (2.8 ± 0.6) nm in metallic single-walled carbon nanotubes (mSWNTs), see Fig. 1(a) for a scheme. The optimum helium ion sputtering condition for gap formation was determined by *in-situ* voltage-contrast microscopy analysis. The functionality of the nanogaps was demonstrated by contacting of oligo(phenylene ethynylene) (OPE) molecular rods and electrical characterization throughout the fabrication process.

Tungsten electrodes with a separation of 700 nm were fabricated on a silicon substrate with 800 nm of thermal oxide, using a two-layer photoresist system comprising 180 nm poly(methyl methacrylate) (PMMA) 600 K EL11 and 200 nm of PMMA 950 K A4.5. Standard electron-beam lithography was used to pattern the photoresist. To obtain a nearly flat sample surface, metallic electrodes were "buried" into the oxide by etching their pattern into the surface with a CHF_3 plasma. Sputter deposition was then used to fill these electrode trenches with tungsten. Finally, the photoresist and the undesired metal were lifted off in an acetone bath.

The mSWNTs were prepared by S-200 gel filtration and density-gradient ultracentrifugation (DGU). For an initial suspension, typically, 10 mg of raw CNT material from pulsed laser vaporization[5] was suspended in 15 ml H_2O with 1 wt. % of sodium dodecyl sulfate (SDS) using a tip sonicator (Bandelin, 200 W maximum power, 20 kHz, 100 ms pulses) for 2 h at ≈20% power. During sonication, the suspension was cooled by a 500 ml water bath. The resulting dispersion was then centrifuged with ≈100.000 *g* for 1.5 h and carefully decanted from the pellet, which was formed during centrifugation. The centrifuged CNT suspension was used as the starting suspension for gel filtration fractionation. Gel filtration was performed in a glass column of 20 cm length and 2 cm inner diameter. After filling the glass column with the filtration medium, the gel was slightly compressed to yield a final height of ≈14 cm. For the separation, ≈10 ml of initial suspension was applied to the top of the column and subsequently a solution of 1 wt. % SDS in H_2O as eluant was pushed through the column with compressed air by applying sufficient pressure to ensure a flow of ≈1 ml/min. After ≈10 ml of this eluant had been added most of the mSWNTs had moved through the column, whereas the semiconducting

---

[a)] Cornelius.Thiele@kit.edu
[b)] krupke@kit.edu

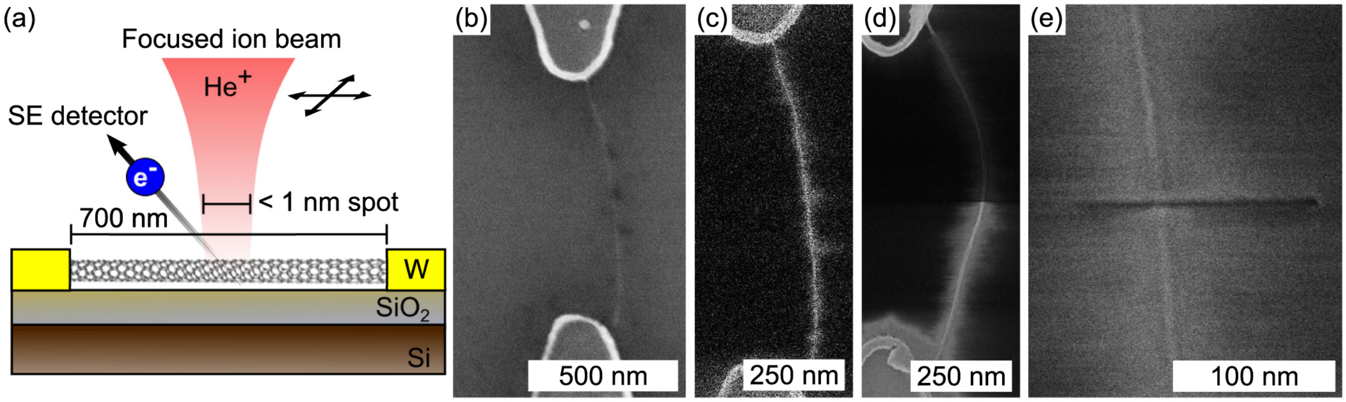

FIG. 1. (a) Scheme of helium ion sputtering of mSWNTs embedded in a device geometry. The nanotubes are deposited on tungsten electrodes and supported by SiO_2/Si substrates. (b) SEM image of a mSWNT device after dielectrophoretic deposition. (c) Fast alignment scan of the same device with the helium ion microscope. (d) Slow scan of a device after gap formation. One of the electrodes is now electrically floating and accumulates positive charges during scanning. (e) Slow scan of a device with both electrodes grounded after gap formation. A clear trench is visible, also in the silicon oxide substrate.

CNTs remained trapped in the upper part of the gel.[6] The mSWNTs were collected and used for DGU, to remove defected mSWNTs and any additional carbonaceous species present. Ultracentrifugation was performed in 20 wt. % iodixanol and 1 wt. % SDS in H_2O. mSWNTs with a diameter distribution of (1.2 ± 0.2) nm were used in this work.

mSWNTs were deposited between the tungsten electrodes using dielectrophoresis.[7] An alternating voltage with a frequency of 300 kHz and a peak-to-peak voltage between 1.0 and 1.3 V was applied between source and drain contacts, while a ≈50-μl drop of CNT dispersion with a concentration of ≈5 CNTs per μm^3 was placed on the device. After 5 min, the drop was first diluted with doubly distilled water, followed by methanol and finally allowed to dry.

Before the samples were transferred to the HIM, CNT deposition was assessed with a conventional scanning electron microscope (SEM), see Fig. 1(b). To eliminate any effects from electron-beam exposure, samples were annealed in a vacuum oven ($p = 10^{-6}$ millibars) at 600 °C for 30 min after imaging. Electrical characterization of pristine devices showed an Ohmic current-voltage behavior with a resistance of, typically, 500 kΩ.

The Zeiss Orion Plus HIM used in this work allows imaging similar to an SEM, except for a helium ion beam being scanned over the sample. The image is generated by the detection of secondary electrons from the sample. Due to the very small effective source size, favorable beam-sample interaction and a much smaller de Broglie wavelength of helium ions compared to electrons, the HIM offers an improved resolution compared to traditional SEMs.[8,9] The acceleration voltage of the HIM was always set to 35 kV. The 5-μm aperture was used, resulting in a spot size of below 1 nm and a beam current of ≈0.4 pA. The signal-to-noise ratio of an image and the implanted ion dose is depend on the beam current, the dwell time per pixel and the averaging settings. To minimize the ion dose, fast alignment images were recorded using the following settings: Pixel spacing 1 nm, dwell time 0.5 μs, no averaging. This led to a line dose of 0.2 nC/m per scan line. Later, slow scans for characterization were performed with fixed parameters: A pixel spacing of 5 Å, a dwell time of 0.5 μs, and 32× line averaging. This led to a line dose of 13 nC/m per scan line.

The focused helium ion beam can also be used to pattern samples by physical sputtering, similar to gallium ions in a focused ion beam instrument. This has been demonstrated, e.g., for graphene,[10–12] silicon nitride,[13] and recently gold nanorods.[14] Here, we employed helium ion beam lithography to pattern nanogaps into metallic carbon nanotubes, in a device geometry. These nanogaps were then used as contacts for a molecular wire, to demonstrate their practical usage. To reduce hydrocarbon deposition on the surface, all samples were stored in the helium ion microscope chamber under high vacuum for at least several hours. The chamber pressure, typically, reached 2.5×10^{-7} millibars before experiments were started.

In order to cut CNTs, a single pixel line with a pixel spacing of 2.5 Å and a dwell time in the millisecond range was scanned across a nanotube. To align this line perpendicularly to the nanotube, a fast scan was performed before the lithography was started, see Fig. 1(c).

To ascertain the critical dose for gap formation, we employed voltage-contrast microscopy (VCSEM), which is capable of locating defects and gaps within a nanotube and to reveal the nanotube's electronic type.[15] In our devices, this was realized by grounding one of the two metal electrodes. The other electrode remained floating, albeit connected to the grounded electrode by the mSWNT. After a single pixel line was scanned across the nanotube, a slow scan image of the device was acquired. Once an electrically insulating nanogap was formed in the metallic CNT, the floating electrode accumulated positive charges, thereby inhibiting secondary electrons from reaching the detector. Thus, the floating electrode appeared darker in the image, while the grounded electrode and the CNT segment connected to it appeared brighter, see Fig. 1(d) for an example. Using this experimental procedure, the critical dose for gap formation was determined to be ≈24 μC/m. Before proceeding to cut further nanogaps, the beam current was measured and the pixel dwell time adjusted accordingly to accommodate this value. We note that the line doses implanted by our fast- and slow-scan images are at least three orders of magnitude lower, and thus, have a negligible sputtering effect.

In order to precisely measure the size of the gap formed, the electrostatic charging of floating electrodes had to be avoided as charging always caused drifts. Also, the different secondary electron intensities on opposite sides of the gap would make an analysis difficult. To avoid charging, the samples were mounted in commercial 16-pin dual in-line package chip carriers, where the common drain electrode and source electrodes of devices were bonded to the chip carrier with Al wires. A customized sample holder in the HIM connected all pins to the stage/ground potential. In this way, detailed slow scans of the nanogaps after lithography were made possible, see Fig. 1(e).

Secondary electron intensity profiles were then recorded across 14 nanogaps in different carbon nanotube devices. The resulting curves were fitted with inverted Gaussians, see Fig. 2(a). A histogram of FWHM of the nanogaps is plotted in Fig. 2(b). With an average nanogap size of (2.8 ± 0.6) nm, direct helium ion sputtering is more precise by almost an order of magnitude than electron-beam-induced etching and a factor of 2–3 better than the smallest gaps achievable by current-induced breakdown. Most striking is the comparably narrow gap size distribution, which is an indication of the highly reproducible nature of this method. As we were targeting the smallest gap size possible for the subsequent insertion of molecules, we did not explore the formation of larger gaps.

Electrical measurements were performed on pristine mSWNTs and on mSWNTs after gap formation. The resistance of pristine mSWNTs yielded (479 ± 193) kΩ and is comparable to 1.2 nm diameter mSWNTs on Pd electrodes.[16] mSWNTs with nanogaps had a resistance of (643 ± 311) TΩ, which is nine orders of magnitude higher than in pristine devices. We attempted to measure tunneling or field-emission currents through the air gap and to correlate the current with the HIM derived gap size. However, despite the large electric fields of up to 5 V/nm in these nanogaps, we were not able to detect any sign of field emission.

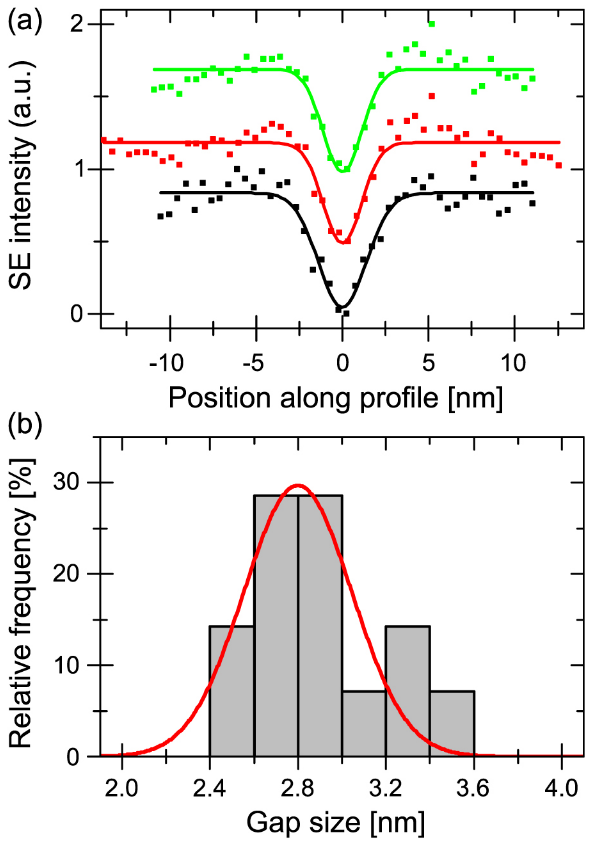

FIG. 2. (a) Secondary-electron intensity profiles from three different nanogaps. (b) Histogram of 14 nanogap sizes.

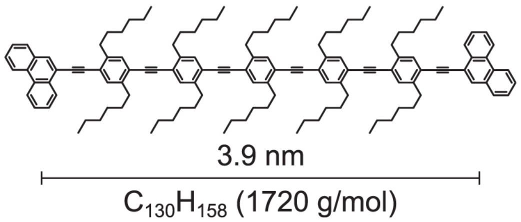

FIG. 3. Structure of **OPE Rod 1** which was contacted by the nanogaps. Phenanthrene anchor groups on each side couple to the sidewalls of a carbon nanotube.[17]

To demonstrate the utility of these nanogaps for contacting organic molecules, **OPE Rod 1**, a symmetric molecular wire of 3.9 nm length, with five subunits and phenanthrene anchor groups at each end was synthesized by performing a series of acetylene protection and deprotection steps,[18] similar to the molecule used by Grunder *et al.*,[19] see Fig. 3. A voltage of 1 V was applied across the nanogap device and the current monitored, and a drop of very dilute **OPE Rod 1** solution (less than 1 μg/ml in methylene chloride) was placed on the device and allowed to dry under ambient conditions. This process took, typically, no longer than 2 min, after which the devices exhibited a low-bias resistance of (90 ± 85) GΩ. See Fig. 4 for a resistance histogram over the lifetime of nanogap devices, including 50 devices with OPE molecules. For reference, experiments with clean solvent without the OPE molecule, the conductance of a nanogap was not changed. Interestingly, it was possible to wash off contacted molecules using clean solvent, thereby, restoring the conductance of a device to the level of an empty nanogap.

Scanning tunneling microscope break-junction measurements on an OPE of similar length revealed a resistance of ≈200 MΩ for a single molecule, albeit with the molecule covalently bonded to gold on both sides.[20] We observe an

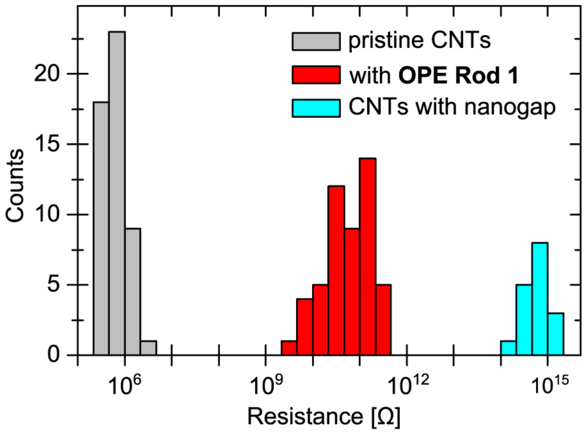

FIG. 4. Resistance histogram over the lifetime of nanogap electrode devices, including 50 CNT-OPE-CNT contacts. Pristine mSWNT devices: (479 ± 193) kΩ; CNTs with nanogap: (643 ± 311) TΩ; with OPE molecules: (90 ± 85) GΩ.

average resistance almost three orders of magnitude higher, with values spread over roughly two orders of magnitude. We ascribe this to a varying imperfect attachment of the molecules' anchor groups to the CNT electrodes and conformational freedom of molecules in the junction; both profoundly deteriorating the conductance.[21] Currently, STM investigations of the molecule and its electronic properties are underway to resolve these issues.

The reproducible engineering of nanogaps in carbon nanotubes that we have achieved will allow the study of many other organic or inorganic systems of nanoscale dimensions at the single-molecule or few-atom level, by providing a reliable way to fabricate nanoscale electrodes. Future work will have to address the issue of establishing reliable contacts between CNT electrodes and molecules.

[1] P. Qi, A. Javey, M. Rolandi, Q. Wang, E. Yenilmez, and H. Dai, J. Am. Chem. Soc. **126**, 11774 (2004).

[2] C. W. Marquardt, S. Grunder, A. Błaszczyk, S. Dehm, F. Hennrich, H. v. Löhneysen, M. Mayor, and R. Krupke, Nat. Nanotechnol. **5**, 863–867 (2010).

[3] F. Xiong, A. D. Liao, D. Estrada, and E. Pop, Science **332**, 568–570 (2011).

[4] C. Thiele, M. Engel, F. Hennrich, M. M. Kappes, K.-P. Johnsen, C. G. Frase, H. v. Löhneysen, and R. Krupke, Appl. Phys. Lett. **99**, 173105 (2011).

[5] S. Lebedkin, P. Schweiss, B. Renker, S. Malik, F. Hennrich, M. Neumaier, C. Stoermer, and M. M. Kappes, Carbon **40**, 417–423 (2002).

[6] K. Moshammer, F. Hennrich, and M. M. Kappes, Nano Res. **2**, 599–606 (2009).

[7] A. Vijayaraghavan, S. Blatt, D. Weissenberger, M. Oron-Carl, F. Hennrich, D. Gerthsen, H. Hahn, and R. Krupke, Nano Lett. **7**, 1556 (2007).

[8] D. C. Bell, Microsc. Microanal. **15**, 147 (2009).

[9] R. Hill, J. A. Notte, and L. Scipioni, in *Advances in Imaging and Electron Physics*, edited by P. W. Hawkes (Elsevier, 2012), Vol. 170, pp. 65–148.

[10] D. Bell, M. Lemme, L. Stern, J. Williams, and C. Marcus, Nanotechnology **20**, 455301 (2009).

[11] M. Lemme, D. Bell, J. Williams, L. Stern, B. Baugher, P. Jarillo-Herrero, and C. Marcus, ACS Nano **3**, 2674 (2009).

[12] D. Fox, Y. B. Zhou, A. O'Neill, S. Kumar, J. J. Wang, J. N. Coleman, G. S. Duesberg, J. F. Donegan, and H. Z. Zhang, Nanotechnology **24**, 335702 (2013).

[13] M. M. Marshall, J. Yang, and A. R. Hall, Scanning **34**, 101 (2012).

[14] O. Scholder, K. Jefimovs, I. Shorubalko, C. Hafner, U. Sennhauser, and G.-L. Bona, Nanotechnology **24**, 395301 (2013).

[15] A. Vijayaraghavan, S. Blatt, C. Marquardt, S. Dehm, R. Wahi, F. Hennrich, and R. Krupke, Nano Res. **1**, 321 (2008).

[16] W. Kim, A. Javey, R. Tu, J. Cao, Q. Wang, and H. Dai, Appl. Phys. Lett. **87**, 173101 (2005).

[17] S. Gotovac, Y. Hattori, D. Noguchi, J.-I. Miyamoto, M. Kanamaru, S. Utsumi, H. Kanoh, and K. Kaneko, J. Phys. Chem. B **110**, 16219 (2006).

[18] See supplementary material at http://dx.doi.org/10.1063/1.4868097 for full synthetic details.

[19] S. Grunder, D. Muñoz Torres, C. Marquardt, A. Blaszczyk, R. Krupke, and M. Mayor, Eur. J. Org. Chem. **2011**, 478 (2011).

[20] Q. Lu, K. Liu, H. Zhang, Z. Du, X. Wang, and F. Wang, ACS Nano **3**, 3861 (2009).

[21] L. Venkataraman, J. E. Klare, C. Nuckolls, M. S. Hybertsen, and M. L. Steigerwald, Nature **442**, 904 (2006).

2.6 Additional Scientific Publications

2.6.16 *Deposition of Semiconducting Single-Walled Carbon Nanotubes Using Light Assisted Dielectrophoresis*

W. Li, F. Pyatkov, S. Dehm, **B. S. Flavel**, R. Krupke

Physica Status Solidi B 251 (2014) 2475–2479

DOI: 10.1002/pssb.201451280

Abstract

Dielectrophoresis (DEP) is an established method for the integration of solution-processed single-walled carbon nano-tubes into nanoscale device structures. However, this method is less effective for small-diameter semiconducting nanotubes and leads to an enrichment of metallic tubes in multi-tube devices. In this work, we present the first results of a novel light-assisted DEP technique, which enhances the deposition of (6,5) semiconducting carbon nanotubes. Transistors fabricated with this technique show higher on/off ratios compared to transistors that were fabricated by conventional DEP. We explain this effect by an enhanced polarizability of the irradiated semiconducting nanotubes and discuss spontaneous and field-driven exciton dissociation as the underlying mechanism. Strategies to further improve the effect are also proposed.

Contribution

R.K conceived the idea for the project. W.L, F.P, S.D, B.S.F performed the experiments. W.L and R.K wrote the paper and all authors contributed to the scientific discussion of results.

– This page intentionally left blank –

Phys. Status Solidi B **251**, No. 12, 2475–2479 (2014) / **DOI** 10.1002/pssb.201451280

physica status solidi b
www.pss-b.com
basic solid state physics

Deposition of semiconducting single-walled carbon nanotubes using light-assisted dielectrophoresis

Wenshan Li[*,1,2], **Feliks Pyatkov**[1,2,3], **Simone Dehm**[1], **Benjamin S. Flavel**[1], **and Ralph Krupke**[**,1,2,3]

[1] Institute of Nanotechnology, Karlsruhe Institute of Technology, 76021 Karlsruhe, Germany
[2] Department of Materials and Earth Sciences, Technische Universität Darmstadt, 64287 Darmstadt, Germany
[3] DFG Center for Functional Nanostructures (CFN), 76031 Karlsruhe, Germany

Received 15 June 2014, revised 23 July 2014, accepted 6 August 2014

Keywords dielectrophoresis, exciton dissociation, nanotube, polarizability

---

[*] Corresponding author: e-mail wenshan.li@kit.edu, Phone: +49 721 608-28114
[**] e-mail e-mail krupke@kit.edu, Phone: +49 721 608-26417, Fax: +49 6151 16-6335

Dielectrophoresis (DEP) is an established method for the integration of solution-processed single-walled carbon nanotubes into nanoscale device structures. However, this method is less effective for small-diameter semiconducting nanotubes and leads to an enrichment of metallic tubes in multi-tube devices. In this work, we present the first results of a novel light-assisted DEP technique, which enhances the deposition of (6,5) semiconducting carbon nanotubes. Transistors fabricated with this technique show higher on/off ratios compared to transistors that were fabricated by conventional DEP. We explain this effect by an enhanced polarizability of the irradiated semiconducting nanotubes and discuss spontaneous and field-driven exciton dissociation as the underlying mechanism. Strategies to further improve the effect are also proposed.

1 Introduction Single-walled carbon nanotubes (SWNTs) hold great promise for a wide range of potential applications in electronics and optoelectronics [1–3]. However, the non-specific synthesis of SWNTs, yields mixtures of metallic (m-) and semiconducting (s-) species and poses a major problem to device integration. Recently, progress has been made toward the synthesis of s-SWNTs [4, 5]. Moreover advanced sorting methods that are capable of producing high-purity s-SWNTs semi-quantitatively have been developed [6–8]. Today, the challenge remains to reproducibly integrate these nanotubes from solution into either single-tube devices or dense and well-aligned thin film structures.

Dielectrophoresis (DEP) has been shown to be an efficient method for integrating m-SWNTs and s-SWNTs into nanoscale device structures and is used by an increasing number of research groups worldwide [9, 10]. On the other hand, DEP has also been shown to preferentially deposit m-SWNTs from dispersions containing mixtures of m-SWNTs and s-SWNT [11, 12], an effect which is directly related to the electric-field induced dipole moment of the SWNTs. Numerically, it has been shown that the dielectric permittivity of m-SWNTs is several orders of magnitude larger than the permittivity of s-SWNTs, and that the permittivity scales inversely with the square of the band gap [13, 14]. This dependence is the reason why the DEP force in electric field gradients is weak for s-SWNTs. Therefore, m-SWNTs are enriched during conventional dielectrophoretic deposition, an effect, which impedes s-SWNT based transistor fabrication from dispersions with residual m-SWNTs [15]. Also, the alignment of small diameter s-SWNTs along the electric field lines is weak as compared with m-SWNTs because of the weak torque. These effects make it difficult to reproducibly integrate especially small diameter s-SWNTs into single-tube or thin film devices. The demand for obtaining such devices, for fundamental and applied research studies has been the starting point to explore whether DEP of small-diameter s-SWNTs could be enhanced by simultaneous light exposure.

The approach we are seeking is different from optical trapping and tweezing [16–19] techniques that have been used for capturing and manipulating nano/micro-particles in suspensions. Optical trapping is DEP at optical frequencies where the light-induced dipole moment interacts in phase with the light-induced electric field gradient. Tan et al. [20] reported optical trapping of DNA-wrapped s-SWNTs in the focal point of a laser spot and achieved extraction of s-SWNTs out of a SWNT mixture. The result indicates a stronger response of s-SWNTs to the light field than m-SWNTs. The dielectric response of s-SWNTs has been studied in detail by Fagan et al. [21]. Indeed, the real part of the intrinsic permittivity of an s-SWNT diverges at each optical transition energy, as expected due to the Kramers–Kronig relation to the optical absorption peaks. On the other hand, the real part of the permittivity must change sign when tuning the laser energy from below to above the transition energy and hence the DEP force has to change from attractive to repulsive. Such behavior has not been reported. Moreover, the change of the real part of the permittivity close to the transition energy is well below a factor of ten and therefore rather weak compared to the permittivity of m-SWNTs. This phenomenon is known from molecular systems where the so-called excess polarizability is limited by the weak polarizability of excitons.

In this work, we intended to enhance the excess polarizability by irradiating the dispersed s-SWNTs in the presence of an AC electric field and thereby enhancing the DEP of s-SWNTs. We added a laser to our DEP system, and systematically studied the feasibility of preferential deposition of s-SWNT using this light assisted DEP (L-DEP). We characterized transistors fabricated from s-SWNT dispersions with electrical measurements and scanning electron microscopy to observe differences between the device fabrication with conventional DEP and L-DEP. The results indicate that L-DEP enhances the deposition of s-SWNTs, which could help to improve the fabrication of high-purity s-SWNTs single-tube or thin film devices.

2 Experimental A schematic of the L-DEP system is shown in Fig. 1. The setup comprises of a probe station, a microscope with video camera, an AC signal generator, and a laser light source to irradiate the central electrode structure as indicated. An array with 12 pairs of 50 nm thick electrodes (5 nm Cr/45 nm Pd) each having a gap size of 1 μm was patterned on a p-doped silicon wafer with an 800-nm-thick thermal oxide layer using standard electron beam lithography and sputtering. All electrodes share a common drain electrode and were biased during DEP with respect to the global back gate, to promote simultaneous SWNT deposition with the function principle explained elsewhere [9]. We have added to our DEP setup a fiber-coupled frequency-doubled Nd:YAG diode laser (532 nm, 30 mW) in order to irradiate the sample surface during DEP. A collimator in combination with a lens was used to focus the fiber-coupled laser into a spot with a diameter of ~200 μm, which is comparable to the area of electrode array. This yields an irradiation density on the order of 10^6 W m^{-2}.

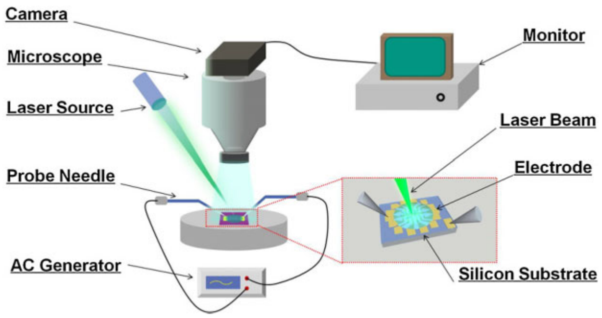

Figure 1 Schematic of the L-DEP experimental setup.

(6,5) SWNTs were chosen for the L-DEP experiment, since their E_{22} optical transition is close to the laser line. The aqueous dispersion with 3×10^{-5} wt.% (6,5) in 1 wt.% sodium dodecyl sulfate was prepared by size-exclusion chromatography as published elsewhere [8]. The concentration was estimated from the absorption spectrum taking into account the tube specific absorption cross-section [22]. The absorption spectrum of the (6,5) dispersion is shown in Fig. 2. The spectrum displays two dominant optical absorption peaks at 986 and 571 nm corresponding to the first and second optical transition of (6,5) SWNTs. The purity of the (6,5) dispersion has been estimated to 92% by a procedure described elsewhere [23]. Prior deposition the dispersion was diluted with double-distilled water by a factor of 1:300 in order to adjust the nanotube concentration to ~0.001 (6,5)-SWNTs/μm^3, based on the average length of the (6,5) SWNTs of ~0.6 μm.

AC electric fields were generated between multiple electrode pairs by use of a function generator with a peak-to-peak voltage set to 5 V, yielding a nominal electric field strength in the electrode gap on the order of 5×10^6 V m^{-1}. The AC frequency was set to 1 MHz. A drop of 10 μl diluted dispersion was applied to the electrode array and the function generator and laser were switched on. After 3 min, the deposition was terminated by rinsing the surface repeatedly with distilled water and methanol, and the generator and laser were switched off. The samples were subsequently annealed at 160 °C in air for 1.5 h. Electrical characterization

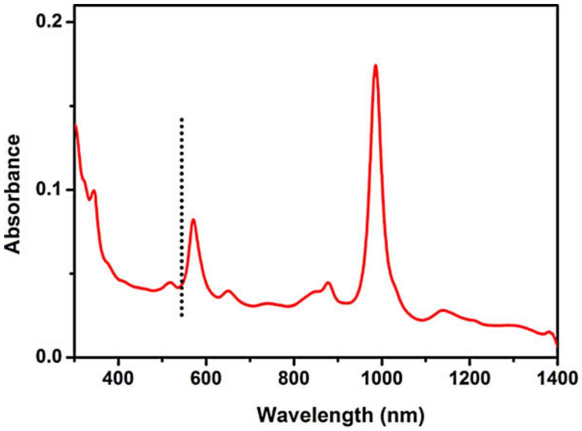

Figure 2 Optical absorption spectrum of the (6,5) SWNT dispersion used in this work. The dotted line marks the wavelength of the laser used in the L-DEP experiment.

was performed with an Agilent 4155C Semiconductor Parameter Analyzer system and a probe station with TRIAX probes. Trans-conductance curves were obtained by sweeping the back gate voltage from −80 to 80 V with step size 400 mV at source–drain voltages of 1, 2, and 3 V. After electrical characterization, the samples were characterized with a Zeiss Ultra Plus scanning electron microscope.

3 Results

Figure 3a and b shows representative scanning electron micrographs of devices prepared from (6,5) dispersions by normal DEP and L-DEP, respectively. The images indicate for both cases the deposition of individual SWNTs forming low-density thin films. Although the morphology does not seem to vary much, we recognize a slightly enhanced density and alignment for the samples prepared by L-DEP.

This observation coincides with significant differences in the electrical transport as shown in Fig. 3c and d. The devices prepared by L-DEP show a systematically higher on/off ratio as compared to devices prepared by normal DEP. For a statistical evaluation, we have measured the transfer characteristics of 32 devices fabricated by normal DEP and 24 devices prepared by L-DEP. Figure 4 is a statistical evaluation of the device characteristics by plotting the on-state current versus the on/off ratio.

The data show that L-DEP promotes the fabrication of devices with high on/off ratio. The improvement of the transistor characteristics indicates that DEP under illumination enhances the deposition of (6,5) SWNTs. This implies that the polarizability of (6,5) SWNT became larger due to the absorption of photons. A possible mechanism accounting for this effect could be attributed to a spontaneous or field-driven dissociation of excitons, as discussed in the following.

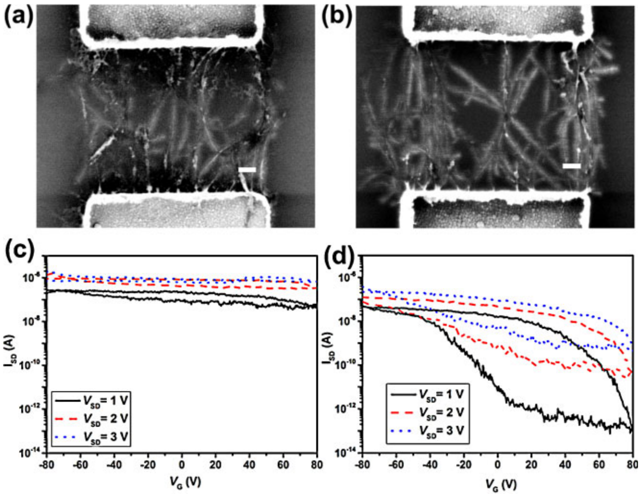

Figure 3 Scanning electron micrographs of devices prepared by normal DEP (a) and L-DEP (b). Scale bar equals 100 nm. Corresponding transfer characteristics, source–drain current I_{SD} versus gate voltage V_G, prepared by normal DEP (c) and L-DEP (d).

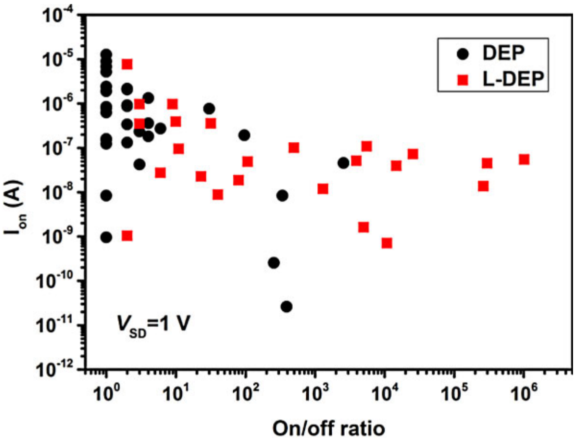

Figure 4 Statistical evaluation of devices prepared with illumination (L-DEP) and without illumination (DEP). Plotted is the on-state current I_{on} versus the on/off ratio at source–drain voltage of 1 V.

4 Discussion

Excitons in s-SWNTs are only weakly polarizable because photoexcited electrons and holes are spatially bound to each other on a length scale of a few nanometers. Unlike in bulk semiconductors, excitons in s-SWNTs should not spontaneously dissociate since the exciton binding energy is an order of magnitude higher than the thermal energy [24]. Recently, Kumamoto et al. [25] have discussed a spontaneous dissociation mechanism based on exciton–exciton annihilation (EEA) or Auger ionization (AI), in order to explain a high conversion efficiency of photoexcited excitons into free electrons and holes in their photocurrent experiment. Also Bindl et al. [26], have discussed spontaneous exciton dissociation in the context of free carrier generation in s-SWNT solar cells.

EEA/AI requires the co-existence of two excitons and the probability for bi-exciton generation is expected to increases with the photon flux. Bindl et al. [26] however observe a decrease of free carrier generation with the photon flux and hence concluded that the spontaneous exciton dissociation might rather occur at defects and/or traps. In Kumamoto et al.'s [25] experiment the importance of EEA/AI-induced spontaneous exciton dissociation is difficult to infer since the free carriers were extracted with an external electric field. Such a field can induce exciton dissociation by itself and generate free carriers as predicted theoretically [27] and confirmed experimentally [28, 29]. Thereby, the field-induced exciton dissociation rate depends on the exciton binding energy and on the field strength, and is predicted to be significant above 100 V μm^{-1} for a 1 nm diameter s-SWNT [27]. Furthermore, exciton dissociation can be induced by optical-phonon scattering at room temperature if the exciton binding energy is smaller than the relevant optical phonon energy (200 meV) [27].

In our L-DEP experiment, the polarizability of s-SWNTs is enhanced by the absorption of photons, which requires the dissociation of excitons. Although we cannot discriminate between the different mechanisms responsible for exciton dissociation, it is very likely that the AC electric field is of central importance. We can estimate the free carrier generation rate under illumination and in the presence of an electric field by comparing our experimental conditions to the quantitative photocurrent experiment of Kumamoto et al. [25]. For comparable laser power density ($10^6\,\mathrm{W\,m^{-2}}$) and electric field strength ($10^6\,\mathrm{V\,m^{-1}}$), and taking into account that the absorption cross-section for (6,5) SWNTs at 532 nm is 1/10 of its value at 986 nm, we can estimate a nominal current generation on the order 100 fA for s-SWNTs that are close to the electrode gap region. This current leads to an accumulation of electrons and holes at the ends of the s-SWNT and hence generates a dipole moment. A schematic of the mechanism is shown in Fig. 5a. The characteristic timescale τ for the dipole formation is expected to be on the order of $\tau = v \cdot l$, where v is the carrier saturation velocity v and l is the nanotube length. For $v \sim 10^5\,\mathrm{m\,s^{-1}}$ from transport measurements [30] and $l = 1\,\mu\mathrm{m}$, τ is $\sim$10 ps and therefore much smaller than the corresponding time scale of AC field frequency (1 μs). Of course the built-up of the dipole is a dynamical and self-limiting process since the accumulated charges are weakening the internal electric field that is required to separate the electrons and holes. At this point, a quantitative modeling is required, which will be addressed in the future. Nevertheless, we can safely conclude that under illumination and in the presence of an external field an induced dipole moment develops who oscillates in phase with the external AC field. Thereby, we have qualitatively explained why in our L-DEP experiments the polarizability of (6,5) SWNTs is enhanced by the absorption of photons.

Figure 5b indicates that L-DEP would be more effective if spontaneous EEA/AI is involved. Possibly this mechanism is already in operation. If not it could be induced by higher photon fluxes. Also adjusting the excitation wavelength to the wavelength of maximum light absorption should enhance the L-DEP. Both aspects have to be addressed to further optimize L-DEP.

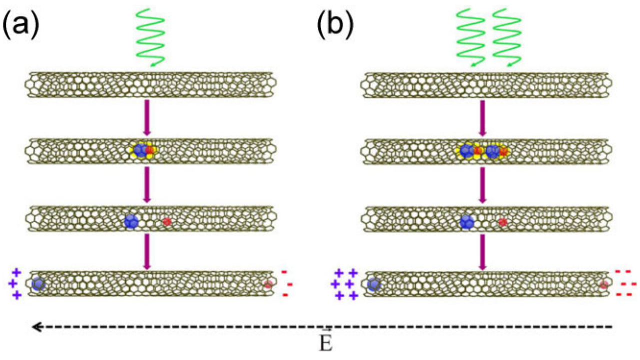

Figure 5 Schematics of the mechanism that enhances the polarizability of s-SWNTs during L-DEP: Electric-field induced exciton dissociation (a), and spontaneous dissociation by exciton–exciton annihilation (b). The external electric field E (- - -) and the built-up positive (+) and negative charges (−) are indicated.

In summary, we have developed a novel light-assisted dielectrophoresis technique (L-DEP), which promotes the deposition of (6,5) semiconducting carbon nanotubes. Transistors fabricated with L-DEP show systematically higher on/off ratios as compared to transistors that were fabricated by conventional DEP. We attribute the enhanced polarizability of s-SWNTs under illumination to spontaneous or field-induced exciton dissociation, which give rise to an induced dipole moment oscillating with the external AC field. The work demonstrates that L-DEP can be advantageous for the integration of s-SWNTs into electronic and optoelectronic devices.

Acknowledgements The authors acknowledge supports from the Helmholtz Research Program Science and Technology of Nanosystems (STN). B. S. Flavel acknowledges support from the Deutsche Forschungsgemeinschaft's Emmy Noether Program under grant number FL 834/1-1.

References

[1] J. Appenzeller, Proc. IEEE **96**, 201 (2008).
[2] P. Avouris, M. Freitag, and V. Perebeinos, Nature Photon. **2**, 341 (2008).
[3] D. Jariwala, V. K. Sangwan, L. J. Lauhon, T. J. Marks, and M. C. Hersam, Chem. Soc. Rev. **42**, 2824 (2013).
[4] W. S. Li, P. X. Hou, C. Liu, D. M. Sun, J. Yuan, S. Y. Zhao, L. C. Yin, H. Cong, and H. M. Cheng, ACS Nano **7**, 6831 (2013).
[5] H. Wang, L. Wei, F. Ren, Q. Wang, L. D. Pfefferle, G. L. Haller, and Y. Chen, ACS Nano **7**, 614 (2012).
[6] M. C. Hersam, Nature Nanotechnol. **3**, 387 (2008).
[7] H. Liu, D. Nishide, T. Tanaka, and H. Kataura, Nature Commun. **2**, 309 (2011).
[8] B. S. Flavel, K. E. Moore, M. Pfohl, M. M. Kappes, and F. Hennrich, ACS Nano **8**, 1817 (2014).
[9] A. Vijayaraghavan, S. Blatt, D. Weissenberger, M. Oron-Carl, F. Hennrich, D. Gerthsen, H. Hahn, and R. Krupke, Nano Lett. **7**, 1556 (2007).
[10] M. R. Islam and S. I. Khondaker, Mater. Express **4**, 263 (2014).
[11] R. Krupke, F. Hennrich, H. Löhneysen, and M. M. Kappes, Science **301**, 344 (2003).
[12] R. Krupke, F. Hennrich, M. M. Kappes, and H. v. Löhneysen, Nano Lett. **4**, 1395 (2004).
[13] L. X. Benedict, S. G. Louie, and M. L. Cohen, Phys. Rev. B **52**, 8541 (1995).
[14] B. Kozinsky and N. Marzari, Phys. Rev. Lett. **96**, 166801 (2006).
[15] M. Steiner, M. Engel, Y. M. Lin, Y. Wu, K. Jenkins, D. B. Farmer, J. J. Humes, N. L. Yoder, J. W. T. Seo, and A. A. Green, Appl. Phys. Lett. **101**, 053123 (2012).
[16] J. R. Moffitt, Y. R. Chemla, S. B. Smith, and C. Bustamante, Biochemistry **77**, 205 (2008).
[17] A. Ashkin, Proc. Natl. Acad. Sci. USA **94**, 4853 (1997).
[18] D. G. Grier, Nature **424**, 810 (2003).
[19] J. Plewa, E. Tanner, D. Mueth, and D. Grier, Opt. Express **12**, 1978 (2004).
[20] S. Tan, H. A. Lopez, C. W. Cai, and Y. Zhang, Nano Lett. **4**, 1415 (2004).
[21] J. Fagan, J. R. Simpson, B. Landi, L. Richter, I. Mandelbaum, V. Bajpai, D. Ho, R. Raffaelle, A. Walker, and B. Bauer, Phys. Rev. Lett. **98**, 147402 (2007).

[22] J. K. Streit, S. M. Bachilo, S. Ghosh, C. W. Lin, and R. B. Weisman, Nano Lett. **14**, 1530 (2014). The propagation path for the optical absorption measurement in this work is 1 cm in length, the mass density of water is 1 g cm^{-3}. The referential E_{11} cross section 2.54×10^{-17} cm^2 C^{-1} was account for the calculation of (6,5) tube-mass density in aqueous suspension.

[23] N. Nair, M. L. Usrey, W. J. Kim, R. D. Braatz, and M. S. Strano, Anal. Chem. **78**, 7689 (2006).

[24] R. B. Capaz, C. D. Spataru, S. I. Beigi, and S. G. Louie, Phys. Rev. B **74**, 121401 (2006).

[25] Y. Kumamoto, M. Yoshida, A. Ishii, A. Yokoyama, T. Shimada, and Y. K. Kato, Phys. Rev. Lett. **112**, 117401 (2014).

[26] D. J. Bindl, A. J. Ferguson, M. Y. Wu, N. Kopidakis, J. L. Blackburn, and M. S. Arnold, J. Phys. Chem. Lett. **4**, 3550 (2013).

[27] V. Perebeinos and P. Avouris, Nano Lett. **7**, 609 (2007).

[28] A. D. Mohite, P. Gopinath, H. M. Shah, and B. W. Alphenaar, Nano Lett. **8**, 142 (2008).

[29] A. Mohite, J. T. Lin, G. Sumanasekera, and B. W. Alphenaar, Nano Lett. **6**, 1369 (2006).

[30] Y. F. Chen and M. Fuhrer, Phys. Rev. Lett. **95**, 236803 (2005).

– This page intentionally left blank –

2.6 Additional Scientific Publications

2.6.17 *Light Emission, Light Detection and Strain Sensing with Nanocrystalline Graphene*

A. Riaz, F. Pyatkov, A. Alam, S. Dehm, A. Felten, V. S. K. Chakravadhanula,
B. S. Flavel, C. Kuebel, U. Lemmer, R. Krupke

Nanotechnology 26 (2015) 325202

DOI: 10.1088/0957-4484/26/32/325202

Abstract

Graphene is of increasing interest for optoelectronic applications exploiting light detection, light emission and light modulation. Intrinsically, the light–matter interaction in graphene is of a broadband type. However, by integrating graphene into optical micro-cavities narrow-band light emitters and detectors have also been demonstrated. These devices benefit from the transparency, conductivity and processability of the atomically thin material. To this end, we explore in this work the feasibility of replacing graphene with nanocrystalline graphene, a material which can be grown on dielectric surfaces without catalyst by graphitization of polymeric films. We have studied the formation of nanocrystalline graphene on various substrates and under different graphitization conditions. The samples were characterized by resistance, optical transmission, Raman and x-ray photoelectron spectroscopy, atomic force microscopy and electron microscopy measurements. The conducting and transparent wafer-scale material with nanometer grain size was also patterned and integrated into devices for studying light–matter interaction. The measurements show that nanocrystalline graphene can be exploited as an incandescent emitter and bolometric detector similar to crystalline graphene. Moreover the material exhibits piezoresistive behaviour which makes nanocrystalline graphene interesting for transparent strain sensors.

Contribution

R.K conceived the idea for the project. A.R, F.P, A.A, S.D, A.F, V.S.K.C and B.S.F performed the experiments. A.R and R.K wrote the paper and all authors contributed to the scientific interpretation of the results.

– This page intentionally left blank –

IOP Publishing Nanotechnology
Nanotechnology **26** (2015) 325202 (10pp) doi:10.1088/0957-4484/26/32/325202

Light emission, light detection and strain sensing with nanocrystalline graphene

Adnan Riaz[1,2], Feliks Pyatkov[1,3], Asiful Alam[1,3], Simone Dehm[1], Alexandre Felten[4], Venkata S K Chakravadhanula[1,6], Benjamin S Flavel[1], Christian Kübel[1,6,7], Uli Lemmer[2,5] and Ralph Krupke[1,3]

[1] Institute of Nanotechnology, Karlsruhe Institute of Technology, 76021 Karlsruhe, Germany
[2] Light Technology Institute, Karlsruhe Institute of Technology, 76021 Karlsruhe, Germany
[3] Department of Materials and Earth Sciences, Technische Universität Darmstadt, 64287 Darmstadt, Germany
[4] Research Center in Physics of Matter and Radiation, University of Namur, Namur, Belgium
[5] Institute of Microstructure Technology, Karlsruhe Institute of Technology, 76021 Karlsruhe, Germany
[6] Helmholtz Institute Ulm, 89081 Ulm, Germany
[7] Karlsruhe Nano Micro Facility, Karlsruhe Institute of Technology, 76021 Karlsruhe, Germany

E-mail: krupke@kit.edu

Received 11 March 2015, revised 19 May 2015
Accepted for publication 9 June 2015
Published 24 July 2015

Abstract

Graphene is of increasing interest for optoelectronic applications exploiting light detection, light emission and light modulation. Intrinsically, the light–matter interaction in graphene is of a broadband type. However, by integrating graphene into optical micro-cavities narrow-band light emitters and detectors have also been demonstrated. These devices benefit from the transparency, conductivity and processability of the atomically thin material. To this end, we explore in this work the feasibility of replacing graphene with nanocrystalline graphene, a material which can be grown on dielectric surfaces without catalyst by graphitization of polymeric films. We have studied the formation of nanocrystalline graphene on various substrates and under different graphitization conditions. The samples were characterized by resistance, optical transmission, Raman and x-ray photoelectron spectroscopy, atomic force microscopy and electron microscopy measurements. The conducting and transparent wafer-scale material with nanometer grain size was also patterned and integrated into devices for studying light–matter interaction. The measurements show that nanocrystalline graphene can be exploited as an incandescent emitter and bolometric detector similar to crystalline graphene. Moreover the material exhibits piezoresistive behavior which makes nanocrystalline graphene interesting for transparent strain sensors.

S Online supplementary data available from stacks.iop.org/NANO/26/325202/mmedia

Keywords: nanocrystalline graphene, light emission, light detection, strain sensing

(Some figures may appear in colour only in the online journal)

---

1. Introduction

Graphene has been extensively explored over the last decade and many aspects of its unique properties have been revealed and investigated [1]. Besides being a promising transparent, conductive and flexible coating material it is the material's potential for electronics and optoelectronics which has attracted a lot of attention [2]. In particular the light–matter interaction in graphene is of interest from a fundamental but also an applications perspective [3]. It has been shown that graphene can be operated as a broadband light detector or emitter and the mechanisms of photocurrent generation and light emission have been revealed as bolometric or electro-thermal and thermal, respectively [4–7]. More recently,

0957-4484/15/325202+10$33.00

narrow-band light emission and detection have been obtained by photonic engineering through integration into an optical microcavity [8, 9]. These devices were based on exfoliated or CVD-grown graphene with domain sizes on the order of micrometers. Thereby manual transfer processing was involved which still poses a challenge for reliable, wrinkle-free wafer-scale device fabrication [10]. Considering the light–matter interactions involved it is however not clear whether graphene with large crystalline domains would be required for operation. Recently the growth of thin carbon films on dielectric surfaces by graphitization of polymeric films has been demonstrated [11, 12]. The simple, metal catalyst-free process yields graphene with nanometer-scale domain size, often referred to as nanocrystalline graphene [13]. Although the low-bias electrical transport of nanocrystalline graphene is distinctly different from crystalline graphene, the material is still conducting and transparent and should be suitable for some of the potential optoelectronic applications [14]. Recently nanocrystalline graphene has been used as the transparent electrode in a silicon photodiode and an organic solar cell [12, 15]. In this work we synthesize, characterize and integrate nanocrystalline graphene into devices, and investigate its feasibility for nanoscale light emission, nanoscale light sensing, and strain sensing. We have studied first the formation of nanocrystalline graphene on various substrates and graphitization conditions, and characterized the material by resistance, optical transmission, atomic force microscopy (AFM), x-ray photoelectron spectroscopy (XPS), Raman and transmission electron microscopy (TEM) measurements. The conducting and transparent wafer-scale material with nanometer grain size was also patterned and integrated into several devices for studying light–matter interaction and strain sensing.

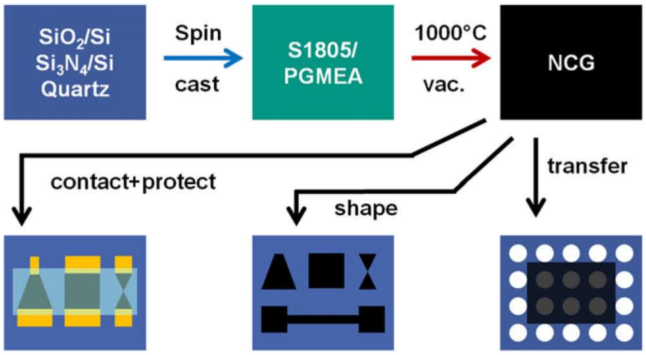

Figure 1. Schematic process flow. Substrates were spin-coated with a resist-solvent mixture and graphitized at high-temperature under high-vacuum. The wafer-scale nanocrystalline graphene (NCG) was characterized by Raman spectroscopy, x-ray photoelectron spectroscopy, sheet-resistance measurements and optical transmission spectroscopy. For transmission electron microscopy and diffraction the NCG was transferred onto a grid. Using lithography methods the NCG was patterned for atomic force microscopy and piezoresistivity measurements. Photocurrent and light emission measurements were performed on NCG with electric contacts and a dielectric coating.

2. Experimental details

Figure 1 shows the process flow schematically. For the synthesis of nanocrystalline graphene (NCG) we have modified the approach of Zhang and co-workers [11] by spin-coating photoresist onto various substrates and graphitizing the material under high vacuum at high temperatures. As substrates we have used p-doped-Si (⟨100⟩, boron, $\rho < 0.005\,\Omega$cm, thickness 0.381–0.525 mm) with 100 nm, 300 nm and 800 nm thermal oxide from Active Business Company GmbH; n-doped-Si (⟨100⟩, P, $\rho > 1000\,\Omega$cm, thickness 0.525 mm) with 500 nm Si$_3$N$_4$ on top of 800 nm thermal oxide from Active Business Company GmbH; quartz (⟨0001⟩, z-cut ±0.3°, thickness 0.5 mm) from Alineason Materials & Technology GmbH; and HOQ 310 Quartzglas (thickness 0.5 mm) from Aachener Quarz-Glas Technologie Heinrich GmbH. The lateral dimensions of the substrates were 1×1 cm^2. The substrates were cleaned for ∼10 s in a sonication bath with acetone, rinsed with Isopropanol (IPA) and dried in a nitrogen stream. Subsequently the substrates were exposed to an oxygen plasma (1 min, 0.2 mbar, 25 sccm O$_2$, 30% power) using an Atto LC PC from Diener electronic GmbH. The clean substrates were then pre-baked for 2 min on a hot plate at 110 °C. After cool-down, 30 μl of photoresist solution was spun onto the substrate under ambient conditions using 8000 rpm for 30 s. The substrates were then soft-baked for 1 min at 110 °C. The photoresist solution was prepared by diluting Microposit S1805 positive photoresist from Rohm&Haas with Propylene Glycol Monomethyl Ether Acetate (PGMEA) of 99% purity from Sigma Aldrich GmbH. PGMEA is the main component of S1805. We have used S1805: PGMEA dilution ratios of 1:14, 1:16, 1:18 and 1:21 to target NCG thicknesses of 6 nm, 4 nm, 2 nm and 1 nm, respectively. The polymer films were graphitized by loading them into a Gero Sr-A 70-500/11 high-temperature oven equipped with a quartz glass tube, a turbo-pump vacuum system and a temperature controller unit. After evacuation to $\leqslant 10^{-6}$ mbar the temperature was raised to 100 °C for ∼30 min to promote water desorption. The temperature was then raised to 1000 °C at a rate of 10 °C min^{-1} and stabilized for 10 h. The samples were cooled down by switching off the heater and were then released to the ambient at temperatures below 100 °C.

Before further processing, the NCG samples were characterized by measuring the sheet resistance with the van der Pauw method [16] in a Cascade probe station using gold-plated needles and an Agilent 4155C semiconductor parameter analyzer. Raman spectra were measured with a Witec CRM 200 confocal microsope under 1 mW laser excitation at 632.8 nm with a Nikon Plan 100x objective (NA = 0.9). X-ray photoelectron spectra (XPS) were measured with an Escalab 250Xi system from Thermo. XPS spectra of the NCG films were acquired with a monochromatic AlKα source (1486.6 eV), using a spot size of 400 μm and a pass energy of 20 eV. A flood gun was used to prevent charging of the dielectric substrates. Transmission spectra of NCG on quartz were measured in a Cary 500 UV–Vis–NIR spectrometer.

For further characterization the NCG samples had to be processed as indicated in figure 1. For transmission electron microscopy (TEM) characterization a 2 nm thin NCG layer synthesized on 800 nm-SiO_2/Si was transferred onto a Quantifoil holey carbon grid using a direct transfer process [17]. The TEM grid was placed on the sample and a few drops of IPA were added. Due to the hydrophobic nature of both the TEM carbon grid and the NCG, the grid adhered to the NCG layer. The thermal oxide layer was then etched by 2% hydrofluoric acid (HF) overnight. After etching, the TEM grid was rinsed with deionized water (DI) and with IPA. A Zeiss Ultra Plus scanning electron microscope (SEM) was used to confirm the transfer process and to image samples throughout subsequent processing steps. The images were recorded with the in-lens detector at 5 keV beam energy. The high-resolution transmission electron microscopy (HRTEM) images and selected area electron diffraction (SAED) patterns were acquired using an aberration (image) corrected FEI Titan 80–300 operated both at 80 kV and 300 kV acceleration voltage. The electron energy loss spectra (EELS) were recorded at 80 kV. The SAED patterns were processed using the Digital Micrograph (Gatan) script PASAD [18].

For characterizations that required laterally patterned NCG, the samples were locally etched by oxygen plasma. The areas of interest were defined by electron beam (ebeam) lithography and were protected by an aluminum layer. First, tungsten markers were defined by spin-coating 950 k PMMA ebeam resist from Allresist at 5000 rpm for 60 s and baking at 160 °C for 30 min, thus forming a 200 nm thin PMMA layer. The PMMA was exposed by 30 keV electrons using a Raith Elphy Plus pattern processor system attached to a LEO1530 SEM. The exposed PMMA was developed in methyl isobutyl ketone (MIBK) and IPA at a ratio of 1:3 for 35 s. The markers were then formed by sputtering 40 nm tungsten in a Bestec custom design sputtering system (400W DC, 1 min), subsequently lifted-off in acetone and rinsed with IPA. The NCG was then synthesized by the procedure outlined before. The NCG was then laterally structured with respect to the position of the tungsten markers in a second lithography step by forming, exposing and developing PMMA under conditions identical to the first lithography step. Then 15 nm Al was evaporated as an etch resist. After lift-off in acetone and IPA, the unprotected NCG was etched in an oxygen plasma (3.5 min, 60 mtorr, 20 sccm O_2, 30 W) using an Oxford Plasmalab 80 Plus reactive ion etching system (RIE). Subsequently the Al resist layer was etched in 3% metal ion-free tetramethylammonium hydroxide (MIF 726) for 30 s. The patterned NCG was then characterized with a Bruker dimension icon atomic force microscope (AFM) in tapping mode to determine the NCG thickness and surface roughness. Piezoresistance measurements of NCG on 800 nm-SiO_2/Si were taken in a custom designed three-point bending fixture with laser-assisted zero-point adjustment. The sample was electrically contacted by fixing flexible Au wires ($\phi = 0.2$ mm) using Indium disks ($\phi = 2$ mm). The strain induced by extending the central cylindrical post was calculated based on the distance of the cylindrical fixed posts (17.2 mm) and the substrate thickness (0.381 mm), translating into 0.1% strain per 200 μm vertical movement of the central post. Uniform curvature has been assumed.

For photocurrent and incandescence experiments the NCG was electrically contacted and subsequently coated by a dielectric using a third and a fourth lithography step, respectively, by forming, exposing and developing PMMA under conditions identical to the previous lithography steps. The electrical contacts to NCG were made by sputtering 70 nm tungsten and lifting-off in acetone and IPA. A protecting layer of 30 nm Al_2O_3 was formed in a Savannah 100 atomic layer deposition system (ALD) from Cambridge NanoTech, using 273 cycles of alternating 0.02s trimethyl aluminum (TMA) and 0.02s H_2O pulses at 200 °C. In a final lithography step using PMMA as etch resist the Al_2O_3 on top of the tungsten contact pads was etched within the RIE (6.5 min, 15 mtorr, 40 sccm Ar + 10 sccm CHF_3, 200 W) to ensure good electric contact between probe needles and the tungsten pads. Photocurrent maps have been measured using a NKT SuperK Extreme EXW-6 supercontinuum light source coupled through a NKT SuperK Select acousto-optic tunable filter, a NKT FD-9 fiber, and a reflective beam collimator to a Zeiss Axiotech Vario microscope, equipped with a beam-splitter to guide 90% of the light through a Mitutoyo Plan Apo NIR 100x/0.50 objective onto the sample. The remaining 10% intensity is used for in-situ monitoring of intensity fluctuations during measurement. Samples were mounted on a Standa 8MTF-102LS05 motorized stage (step size: 375 nm) and contacted with probe needles. The backreflected light was measured with a Silicon Sensor PC-50-6 silicon PIN photodiode, to correlate the photocurrent signal with the sample topography. The photocurrent signal was detected using a Sr 830 lock-in amplifier and a Sr 570 pre-amplifier. The AOTF was used to select the excitation wavelength and the chopping frequency to 1065 nm and 2.3 kHz at 600 μW irradiation power. For light emission measurements, a Zeiss AxioTech Vario microscope, directly attached to an Acton Research SpectraPro 2150i spectrometer and a Princeton Instruments PIXIS 256E Silicon CCD camera (1024 × 256 pixels, −60 °C) with in a light-tight box was used. The spectrometer can operate in the imaging mode, with a mirror to take real-space images, or in the spectroscopy mode, with a diffraction grating (300 grooves/mm, 750 nm blaze wavelength). The samples were mounted on a Standa 8MTF-102LS05 motorized stage, electrically contacted with probe needles and biased with a Keithley 6430 SourceMeter. Incandescence images and images under external illumination were recorded with a Mitutoyo Plan Apo 80×/0.50 objective.

3. Results and discussion

Figure 2(a) shows an AFM image across an edge of a structured 1 nm thin NCG layer on 800 nm-SiO_2/Si. The data shows that the surface roughness of NCG is similar to the roughness of the SiO_2 surface, indicating a conformal coating of the substrate. The edge appears straight and shows no sign of underetching. The NCG thickness was adjusted by diluting the resist to yield a targeted nominal thickness. The degree of control is shown in

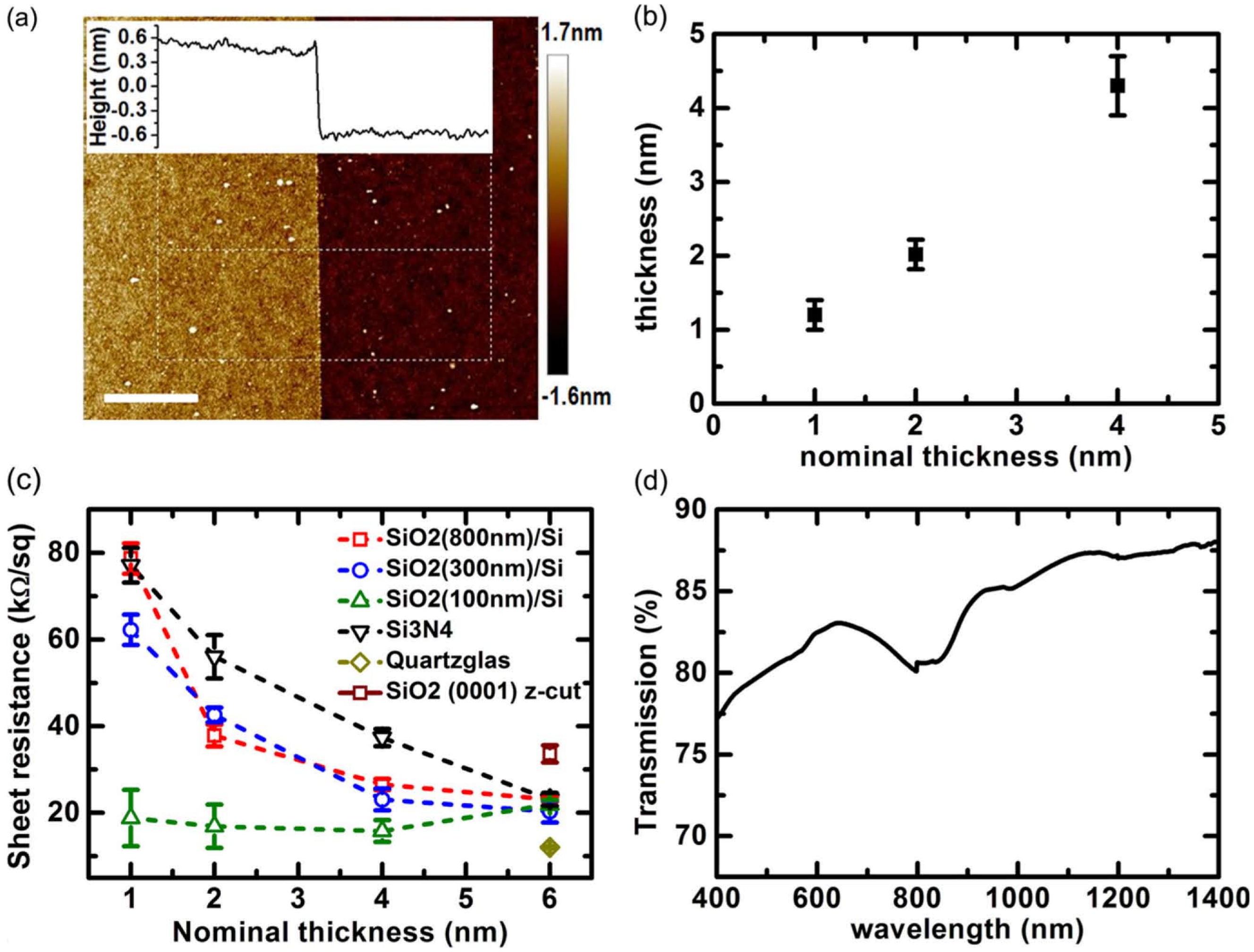

Figure 2. (a) Atomic force microscopy image of a patterned 1 nm thin NCG layer on 800 nm SiO_2/Si substrate. The inset shows an averaged cross-section of the indicated area. Scale bar = 1 μm. (b) Measured NCG thickness versus its nominal thickness. (c) Sheet resistance versus nominal thickness of NCG on various substrates as indicated. (d) Transmission spectrum of 6 nm thick NCG on ⟨0001⟩ z-cut quartz. All NCG samples have been synthesized at 1000 °C @ 10 h.

figure 2(b). The sheet resistance of the NCG is typically on the order of 20–80 kΩ/sq., depending on the NCG thickness and the type of substrate, as can be seen in figure 2(c).

The mean value and the error bars were obtained from measurements on 3–5 samples for each data point. Overall the data shows the expected dependence of the sheet resistance on the inverse layer thickness. The sheet resistance values are comparable to the 30 kΩ/sq. reported by Zhang *et al* [11] for 1 nm NCG, also formed at 1000 °C albeit under reducing atmosphere. Compared to CVD-graphene [19] and carbon nanosheets [14] the sheet resistance of our NCG is 2 orders of magnitude larger and 2 orders of magnitude smaller, respectively. Obviously the carrier transport across grain boundaries has a large influence on the overall resistance. We point out that the graphitization of the resist seems to depend on the surface structure of the SiO_2 as can be seen by the sensitivity of the sheet resistance to the substrate. Hence the catalytic activity appears to be slightly different for Quartzglass, ⟨0001⟩ z-cut quartz and 100 nm SiO_2 as compared to the thicker thermal oxides on Si. The optical transparency of a 6 nm thick NCG film on ⟨0001⟩ z-cut quartz is shown in figure 2(d). The transmission increases from 77% at 400 nm to 87% at 1400 nm and shows an enhanced absorption around 800 nm. Normalized by the thickness, the optical transmission of NCG is comparable to that of graphene. We speculate whether the enhanced absorption at 800 nm is correlated with the crystallite size and we will come back to this point later in the discussion. To determine the composition and the hybridization of the NCG material we have analyzed the C 1s peak of the XPS signal and compared the spectrum to data recorded on Bilayer graphene (mechanically exfoliated on 90 nm SiO_2/Si) and graphite. Figure 3(a) shows that the C 1s signal has a main peak at 284.4 eV similar to graphite, and hence assigned it to the sp^2 hybridized carbon atoms. Also the width of ∼1.2 eV fits very well to bilayer graphene which has a similar thickness as NCG.

Some peak broadening towards higher and lower binding energy is observed for NCG, which could have its origin in the nanocrystallinity of the material, similar to observations in low-crystalline carbon nanotubes and defective graphite [20, 21]. In

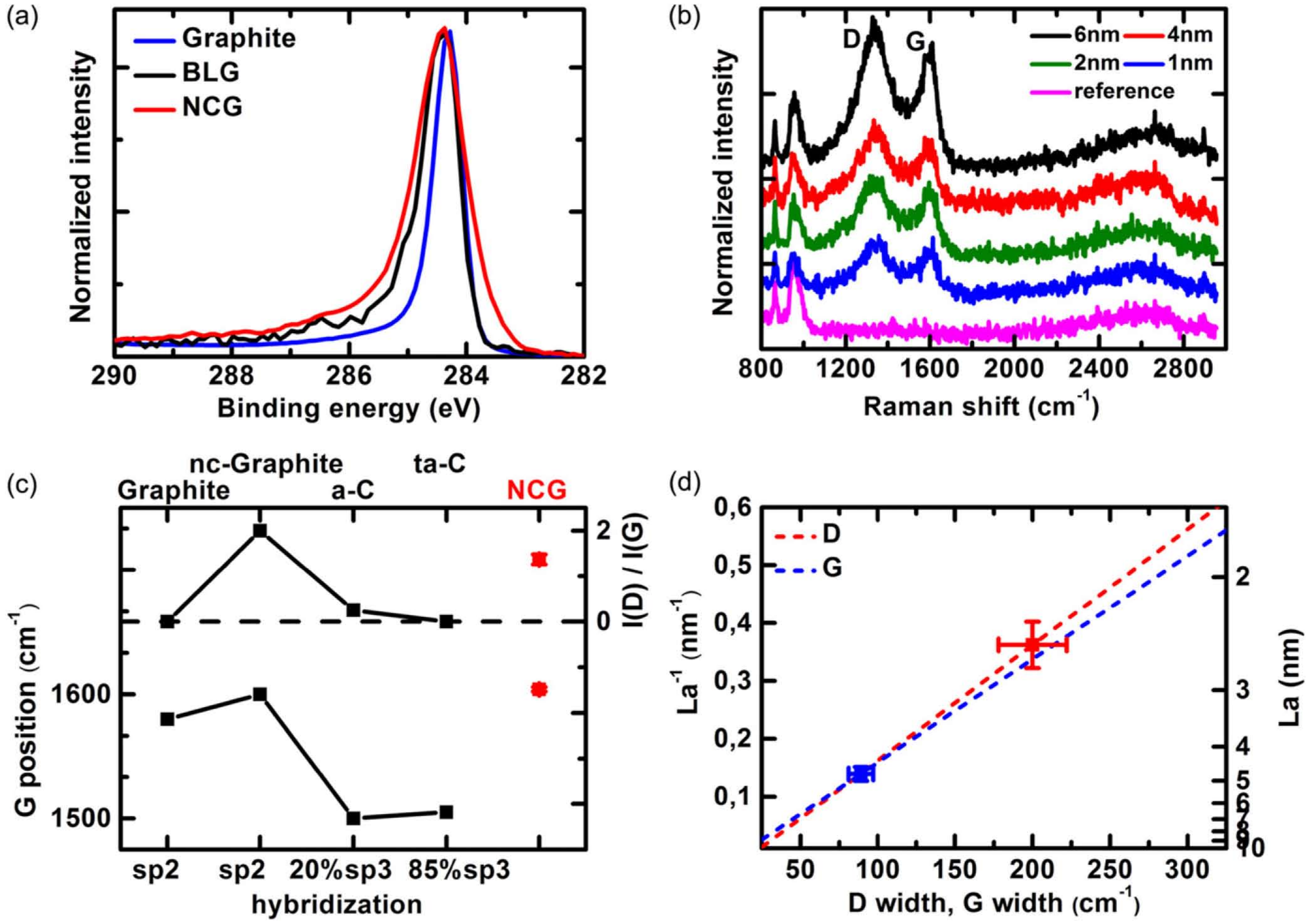

Figure 3. (a) XPS of 1 nm thick NCG layer on 800 nm SiO_2/Si, compared with bilayer graphene (BLG) and graphite. (b) Raman spectra of NCG with various thicknesses, grown on 800 nm SiO_2/Si. The spectra are normalized to the D-peak and vertically shifted for clarity. (c) Raman G-peak position and intensity ratio of D-peak and G-peak for NCG compared with data [23] for graphite, nanocrystalline graphite and two forms of DLC as explained in the text. The sp-hybridization is indicated. (d) Crystallite size La in NCG determined from the full-width-at-half-maximum of the D- and G-peaks. The dashed lines are extrapolated correlations based on [24]. The graphs (c) and (d) include a statistical evaluation of data from all samples synthesized at 1000 °C.

the survey spectrum (not shown), no additional elements besides Si and O from the substrate were detected. Hence we can safely conclude that our NCG is a graphitic material with a high degree of sp^2 hybridization. XPS also allows determining the thickness of the carbon layer from the attenuation of the photoelectrons emanating from the SiO_2 [22]. We have used the Si 2p with an attenuation length of 3.5 nm [14] and obtained 0.95 nm for a 1 nm thick layer. Hence the thickness determined by XPS is consistent with the AFM measurement. All samples were characterized by Raman spectroscopy to obtain an additional confirmation on the hybridization and to determine the crystallite size *L*a in the NCG layer. Figure 3(b) shows Raman spectra of NCG on 800 nm SiO_2/Si for different nominal layer thicknesses. For other process conditions we refer to figures S1–3. Characteristic to all samples are broad D and G modes, and the absence of a clear 2D peak, similar to [14] and [11]. We used the pioneering work of Ferrari and Robertson to determine the hybridization and crystallinity of our NCG [23]. In figure 3(c) we have compared the G-peak position and the intensity ratio *I*(D)/*I*(G) of the D-peak to the G-peak of NCG with the data measured on graphite, nanocrystalline graphite, diamond-like carbon (DLC) with 20% sp^3-content (a-C) and DLC with 85% sp^3 (ta-C). The NCG data fits well to the nanocrystalline graphite with 100% sp^2 content, and hence confirms nicely the XPS data. From the width of the D and G modes we estimated the size of *L*a by referring to the work of Cançado *et al* [24]. The D mode width corresponds accordingly to $La \approx 4$–5 nm, whereas the G mode width indicates $La \approx 2$-3 nm. To discern the difference we transferred a 2 nm thick NCG layer formed on 800 nm SiO_2/Si onto a TEM grid. The mean value and the spread of the ratio *I*(D)/*I*(G), the G-peak position and the width of the D and G modes have been evaluated from samples prepared on various substrates and of different NCG thicknesses (see table T1 in supporting information).

Figures 4(a)–(b) are low- and high-resolution TEM images which show that the NCG film is continuous. Since the morphology appears to be inconsistent with the AFM characterization we assume that the inhomogeneity, visible in figure 4(b), is due to residues from the HF etching of SiO_2. An SAED image was recorded on a flat region showing continuous diffraction rings (figure 4(c)). We were measuring

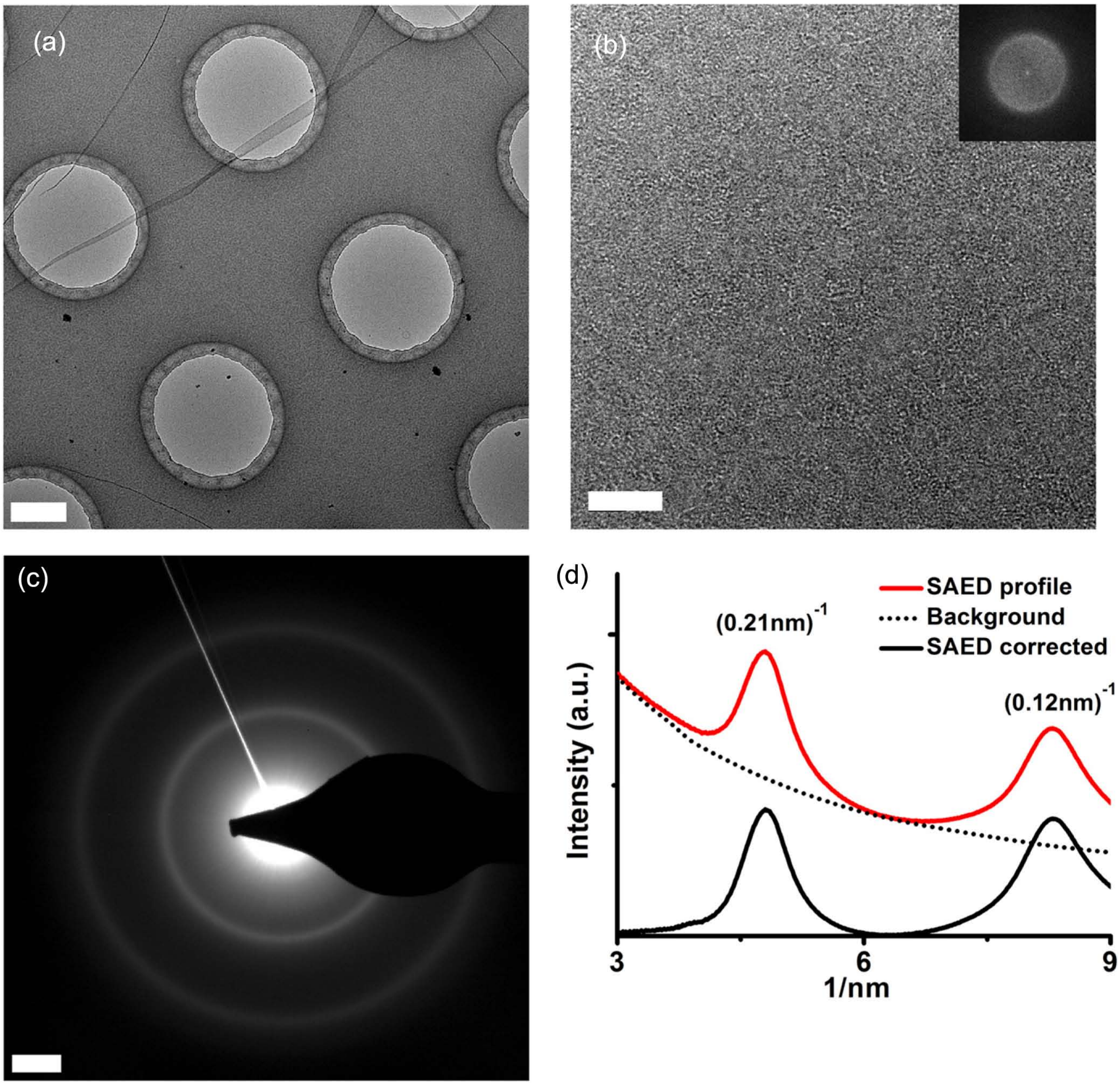

Figure 4. Transmission electron microscopy characterization of a 2 nm NCG layer synthesized on 800 nm SiO2/Si in 10 h @ 1000 °C. (a) Low-resolution TEM image of the NCG after transfer onto a holey carbon grid. A fault can be seen in the upper left. Scale bar = 0.4 μm. (b) High-resolution TEM image measured through a hole. Scale bar = 4 nm. (c) SAED image. Scale bar = 2 nm^{-1}. (d) Radially averaged line profile of the SAED image.

an SAED pattern of a polycrystalline material [25]. The position of the two rings at 0.12 nm^{-1} and 0.21 nm^{-1} match well to the (110) and (100) reflexes of in-plane oriented graphene, respectively. Although we do not see clear domains in the HRTEM image in figure 4(b), the FFT of the image shows nevertheless a lattice plane distance of 0.21 nm^{-1} (inset, figure 4(b)). A radially averaged line profile of the SAED image is shown in figure 4(d), which we have analyzed to determine the average domain size. After background correction we have applied the Scherrer equation to the peak of the (100) reflex with a FWHM of 0.656 nm^{-1} using a shape factor of 0.9 [26]. As a result we obtain an average domain size of 3 nm, which is closer to the 2.2 nm derived for this film from the width of the Raman D mode peak compared to the G mode width. It should be noted that similar domain sizes of 2–5 nm have been reported by Turchanin *et al* for organic monolayers graphitized on Au [13]. We have also measured EEELS spectra at the carbon edge of nanocrystalline graphene (figure S6) and observe transitions which fit to the π^* and σ^* states of a graphitic material [27, 28].

We will now describe the results of the first spatially resolved photocurrent measurements on NCG and discuss the mechanism of photocurrent generation. Figure 5(a) shows a typical photocurrent map of a 20 × 20 μm square-shaped NCG

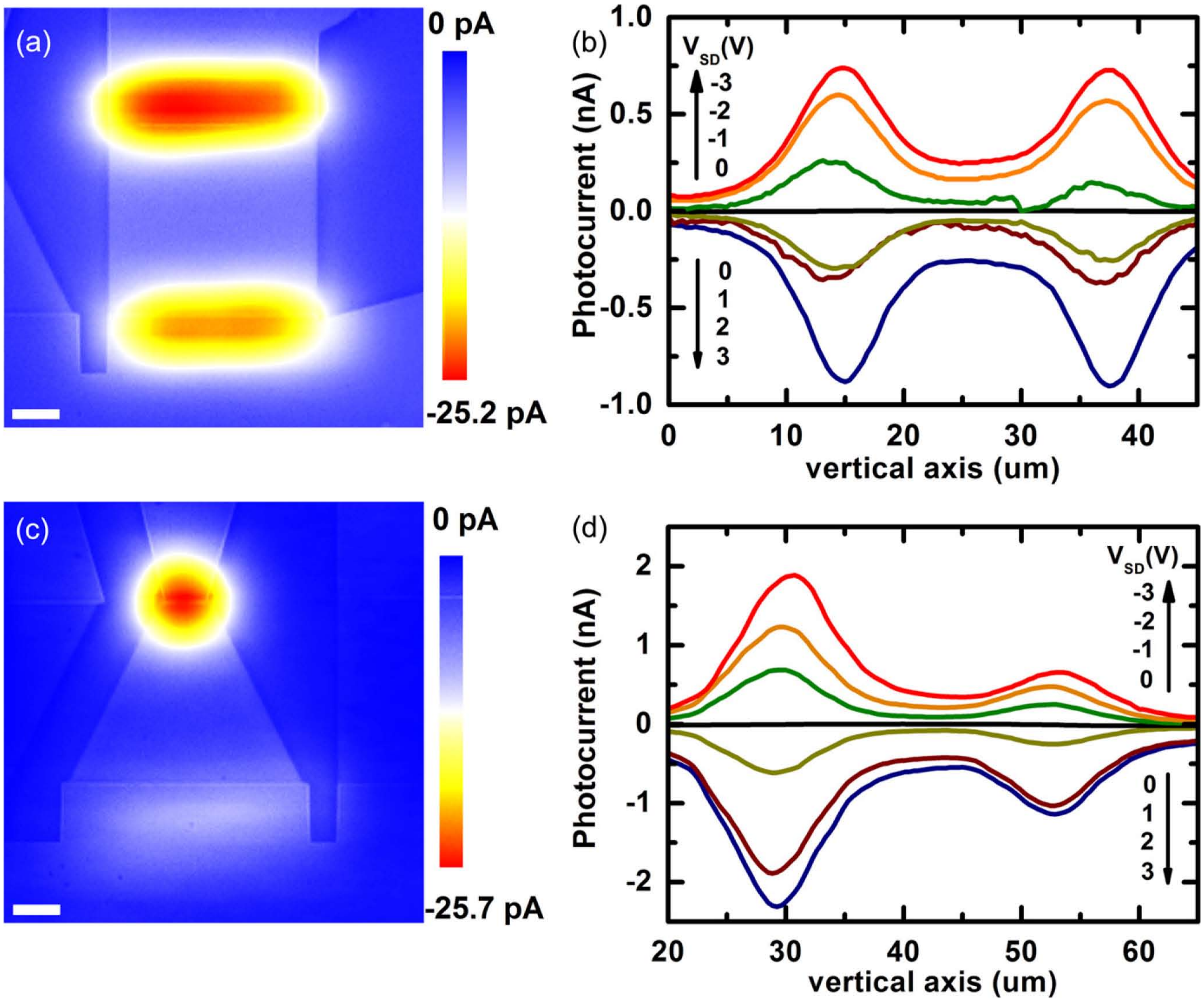

Figure 5. Photocurrent maps of square-shaped (a) and triangle-shaped (c) NCG devices. SEM images were superimposed as explained in the text. $V_{SD} = +1$ V. Scale bars equal 5 μm. (b), (d) Vertical cross-section through the corresponding photocurrent maps as a function of voltage bias. The devices were fabricated from 4 nm thin NCG layers synthesized on 800 nm- SiO_2/Si at 10 h @ 1000 °C.

in contact with tungsten electrodes (overlap 1 μm), recorded at +1 V source-drain voltage. We have measured simultaneously the local reflectivity (not shown) to correlate the photocurrent signal with the sample structure. Instead of superimposing the photocurrent map with the reflectivity map we have superimposed the corresponding SEM image for better visibility of the NCG and adjusted its relative position to the photocurrent map by matching it to the reflectance map (see also figure S4). From the data we can see that the photocurrent is generated at the two contacts between NCG and tungsten with similar magnitude. The sign of the photocurrent is phase-shifted by 180° and its magnitude increases with the applied bias. The behavior of the photocurrent is symmetric for both bias polarities as can be seen in the vertical cross-section shown in figure 5(b). Figure 5(c) shows a photocurrent map of a $20 \times 2\,\mu$m/20 μm triangular-shaped NCG in contact with W electrodes (overlap 1 μm), also recorded at +1 V source-drain bias. In this case the photocurrent is primarily generated at the contact with the smaller area, where the apex of the NCG triangle is in contact with tungsten. Again the photocurrent is phase-shifted by 180°, the magnitude increases with the applied bias and the photocurrent is symmetric with respect to the bias polarity (see figure 5(d)).

The discussion of the mechanism of photocurrent generation is rather straightforward. The fact that we do not observe a photocurrent signal at zero bias excludes a significant photovoltaic or electrothermal contribution and can only be explained with a bolometric effect [29]. The temperature dependence of the NCG resistance has then to be positive $dR/dT > 0$ since the photocurrent is phase-shifted by 180° with respect to the applied bias voltage; under illumination the resistance of the sample increases and hence the total current decreases. The photocurrent becomes negative since it is the difference between the total current and the dark current. A bolometric photocurrent must also be correlated with regions of high resistance. Apparently the contact

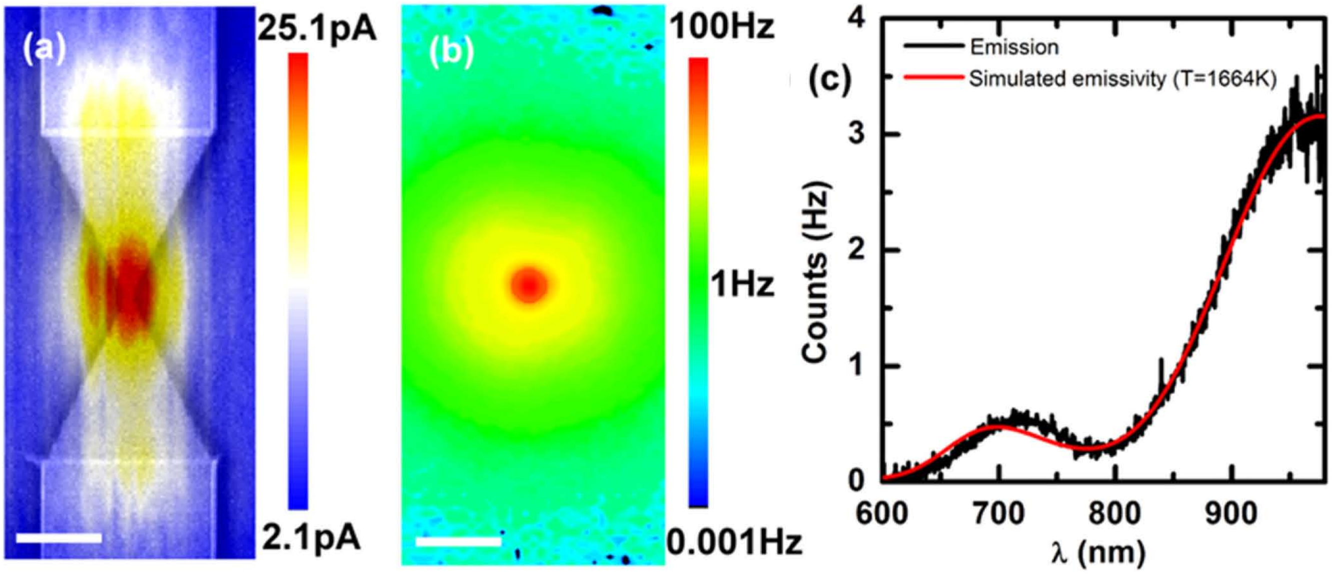

Figure 6. 1 nm thin NCG layer, patterned within two opposing NCG triangles connected by a 0.5 μm wide and 1 μm long NCG constriction. (a) Photocurrent map. $V_{SD} = -1$ V. Scale bar = 5 μm. (b) Light emission image from a contact at $V_{SD} = 33$ V and $I_{SD} = 150$ μA. Scale bar = 5 μm. (c) Emission spectrum recorded at the center of (b).

resistance between NCG and W in figure 5 is dominating the total device resistance and hence these regions show up in the photocurrent maps. For asymmetric contacts as in figure 5(c) it is only one contact that dominates the entire device resistance. Hence bolometric photocurrent mapping can be considered as a tool for mapping the internal device resistance. To test our hypothesis we have patterned within two opposing NCG triangles with 20×10 μm overall dimensions and a 0.5 μm wide and 1 μm long NCG constriction (see also figure S5). As in the previous devices NCG has been contacted with W (overlap 1 μm). Figure 6(a) shows that the photocurrent signal is now the highest at the position of the constriction and hence nicely confirms the bolometric picture. We refer also to the photocurrent study of Freitag *et al* who showed that the bolometric contribution is dominant for the photocurrent generation in doped graphene under bias [4]. The responsivity of our device is $1.7 \cdot 10^{-6}$ A W^{-1} at 1065 nm and hence two orders of magnitude lower than that of graphene [4]. Since the bolometric photocurrent is inversely proportional to the squared resistance[8], the lower responsivity is likely due to the one order of magnitude higher resistance of our device. We have demonstrated that nanocrystalline graphene can be used as a substitute to crystalline graphene for bolometric light detection.

We will now report the first study on light emission from nanocrystalline graphene and discuss the mechanism of light generation. Figure 6(b) shows a device with a NCG constriction under 33 V applied bias voltage and 150 μA current. The dimensions of the sample are identical to the one in figure 6(a). We observed a local light emission from the constriction, which we have identified previously as a region of high resistance (note that a logarithmic intensity scale has been used). As in the case of graphene we anticipate the source of light emission to be thermal radiation [5–7]. We have measured the spectrum of the emission which is shown in figure 6(c). The intensity overall increases towards higher wavelength however with obvious modulations. The data could be fitted nicely with a Planck curve and a structure dependent interference term (800 nm SiO_2/Si). Details can be found in the supporting information of [30]. We have extracted an electron temperature $T = 1664$ K. If we assume that the electrical power is mainly dissipated at the NCG constriction we can estimate a local power density p of 1000 kW cm^{-2}. These numbers are very similar to $T = 1600$ K at $p = 520$ kW cm^{-2} reported for graphene [5]. We have therefore demonstrated that nanocrystalline graphene can be used as a substitute to crystalline graphene for generating thermal light emission on the nanoscale with comparable efficiency. Related to our previous work on narrow-band thermal light emission from microcavity-integrated graphene [8], we are currently replacing graphene with NCG to make the entire manufacturing compatible to wafer-scale processing.

Finally we will discuss a piezoresistive effect that we have been able to measure on nanocrystalline graphene. Figure 7(a) shows a sample with a 1 nm thin double T-shaped NCG layer on 800 nm SiO_2/Si. The sample was loaded head up into a 3-point bending fixture after electrical wiring (figure 7(b)). The resistance had been measured continuously while increasing the strain by vertical displacement of the inner post of the fixture. Data was acquired under increasing strain until sample failure. Figure 7(c) shows the relative resistance change $\Delta R/R$ as a function of the strain ε for two samples. The samples show a linear increase of $\Delta R/R$ until the breaking of the substrate at $\varepsilon \approx 0.1\%$. The linear slope

---

[8] $\Delta I = -V \cdot R^{-2}(T_0) \cdot \partial R(T - T_0)/\partial T$; with the bolometric current ΔI, sample resistance R, temperature T and bias voltage V. T_0 is the temperature without illumination. The expression has been derived for $R(T_0)/[\partial R(T - T_0)/\partial T] \gg 1$.

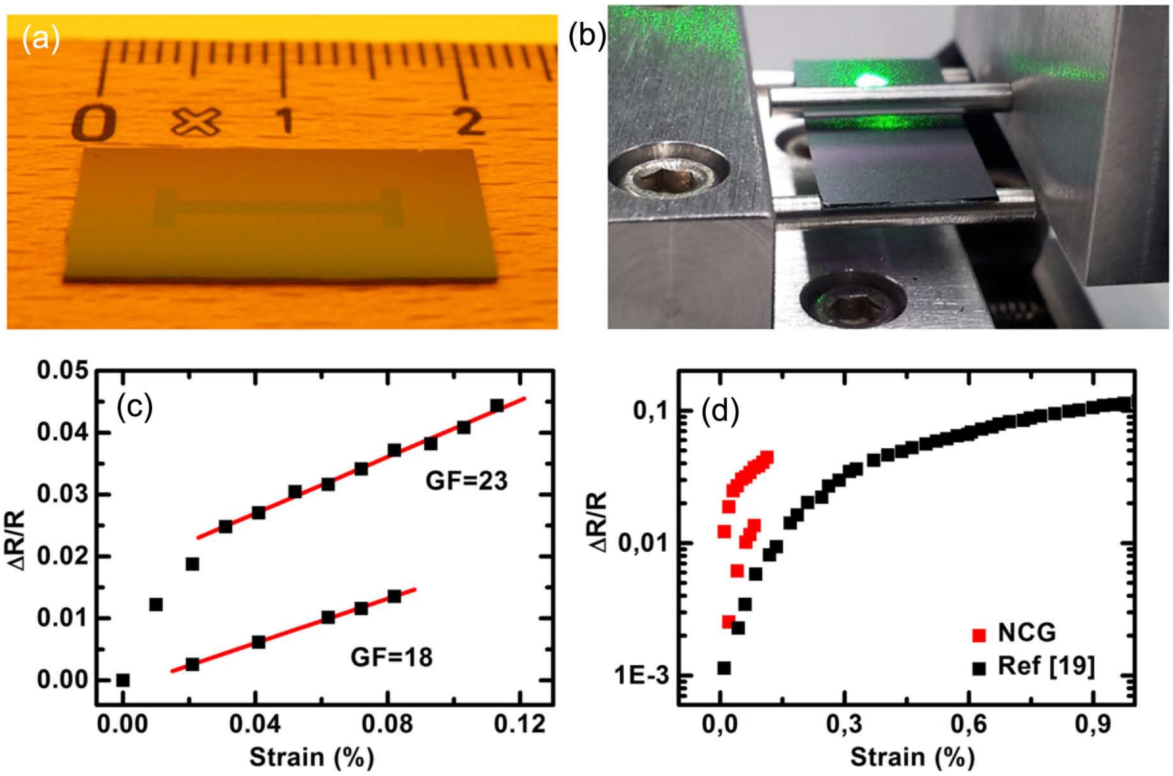

Figure 7. (a) Optical micrograph of a patterned 1 nm thin NCG layer on 800 nm SiO_2/Si suitable for piezoresistance measurements. (b) 3-point bending fixture with sample inserted head up. The movable piston and the adjustment laser spots are visible; the electrical contacts not. (c) Relative resistance change $\Delta R/R$ in NCG versus strain for two samples. The linear fits and corresponding gauge factors are indicated. (d) Comparison between $\Delta R/R$ of NCG with CVD-graphene from [19].

corresponds to the gauge factor and is on the order of 20 for both samples. Whether the linearity continues towards larger strain values is subject to a future study and requires the transfer of NCG onto a flexible substrate. Nevertheless we can compare the data of NCG with measurements on CVD graphene as shown in figure 7(d). We can see that the relative resistance change is larger in NCG than in graphene at a comparable strain. This obvious difference indicates that grain boundaries play an important role for the appearance of a piezoresistive effect in graphene. Indeed a recent calculation has shown that Klein tunneling should be absent for certain grain boundaries leading to strain-induced conductance modulation [31], which is piezoresistance. If the gauge values continue to be high also at high strain values, then the fabrication of transparent strain sensors based on NCG can be envisioned, which could offer new functionalities to the emerging field of transparent and flexible electronics.

4. Summary

We demonstrated the wafer-scale synthesis of nanocrystalline graphene on dielectric surfaces by graphitization of a photoresist under high vacuum annealing, where the thickness, the sheet resistance and the transparency of the layer was tailored by the process condition. The layer is entirely formed by sp^2-hybridized carbon as proven by XPS and Raman. The size of the graphitic domains is on the order of 2 nm, consistent with Raman and TEM measurements. Integrated into devices, the material showed photocurrent generation under illumination. The response to light could be traced to a bolometric origin, similar to experiments on doped crystalline graphene. Also light emission under electrical biasing was observed. The emission is due to heating of the layer, and the extracted electron temperature and power density is comparable to experiments reported from crystalline graphene. Furthermore a piezoresistive effect was observed that is significantly larger than in crystalline graphene and indicates the importance of grain boundaries for the appearance of piezoresistivity in graphene. Hence nanocrystalline graphene to appears to be an interesting material not only as an easy-to-fabricate alternative to crystalline graphene for nanoscale light detection and light generation but also towards the fabrication of transparent and flexible strain sensors.

Acknowledgments

RK acknowledges funding by the German Science Foundation (INST 163/354-1 FUGG), and RK and AR acknowledge funding by the VolkswagenStiftung. AF is supported by the Belgian fund for scientific research (FNRS).

Supporting information

Raman data of NCG layers synthesized at different temperatures (figure S1), for different graphitization times (figure S2), and on different quartz substrates (figure S3). NCG Raman D and G mode position, width and intensity ratio (table T1). Scanning electron micrograph of laterally patterned NCG (figures S4 and S5). EELS spectrum of NCG (figure S6).

References

[1] Geim A K 2009 Graphene: status and prospects *Science* **324** 1530–4

[2] Bonaccorso F, Sun Z, Hasan T and Ferrari A C 2010 Graphene photonics and optoelectronics *Nat. Photonics* **4** 611–22

[3] Liu M and Zhang X 2013 Silicon photonics: graphene benefits *Nat. Photonics* **7** 851–2

[4] Freitag M, Low T, Xia F and Avouris P 2012 Photoconductivity of biased graphene *Nat. Photonics* **7** 53–9

[5] Berciaud S, Han M Y, Mak K F, Brus L E, Kim P and Heinz T F 2010 Electron and optical phonon temperatures in electrically biased graphene *Phys. Rev. Lett.* **104** 227401

[6] Bae M H, Ong Z Y, Estrada D and Pop E 2010 Imaging, simulation, and electrostatic control of power dissipation in graphene devices *Nano Lett.* **10** 4787–93

[7] Freitag M, Chiu H-Y, Steiner M, Perebeinos V and Avouris P 2010 Thermal infrared emission from biased graphene *Nat. Nanotechnology* **5** 497–501

[8] Engel M, Steiner M, Lombardo A, Ferrari A C, Löhneysen H V, Avouris P and Krupke R 2012 light–matter interaction in a microcavity-controlled graphene transistor *Nat. Commun.* **3** 906

[9] Furchi M *et al* 2012 Microcavity-integrated graphene photodetector *Nano Lett.* **12** 2773–7

[10] Bonaccorso F, Lombardo A, Hasan T, Sun Z, Colombo L and Ferrari A C 2012 Production and processing of graphene and 2D crystals *Mater. Today* **15** 564–89

[11] Zhang Z, Ge B, Guo Y, Tang D, Wang X and Wang F 2013 Catalyst-free growth of nanocrystalline graphene/graphite patterns from photoresist *Chem. Commun.* **49** 2789–91

[12] Son S-Y, Noh Y-J, Bok C, Lee S, Kim B G, Na S-I and Joh H-I 2014 One-step synthesis of carbon nanosheets converted from a polycyclic compound and their direct use as transparent electrodes of ITO-free organic solar cells *Nanoscale* **6** 678–82

[13] Turchanin A, Weber D, Büenfeld M, Kisielowski C, Fistul M V, Efetov K B, Weimann T, Stosch R, Mayer J and Gölzhäuser A 2011 Conversion of self-assembled monolayers into nanocrystalline graphene: structure and electric transport *ACS Nano* **5** 3896–904

[14] Nottbohm C T, Turchanin A, Beyer A, Stosch R and Gölzhäuser A 2011 Mechanically stacked 1 nm-thick carbon nanosheets: ultrathin layered materials with tunable optical, chemical, and electrical properties *Small* **7** 874–83

[15] Zhang Z, Guo Y, Wang X, Li D, Wang F and Xie S 2014 Direct growth of nanocrystalline graphene/graphite transparent electrodes on Si/SiO 2 for metal-free Schottky junction photodetectors *Adv. Funct. Mater.* **24** 835–40

[16] van der Pauw L J 1958 A method of measuring specific resistivity and Hall effect of discs of arbitrary shape *Philips Res. Rep.* **13** 1–9

[17] Regan W, Alem N, Alemán B, Geng B, Girit C, Maserati L, Wang F, Crommie M and Zettl A 2010 A direct transfer of layer-area graphene *Appl. Phys. Lett.* **96** 113102

[18] Gammer C, Mangler C, Rentenberger C and Karnthaler H P 2010 Quantitative local profile analysis of nanomaterials by electron diffraction *Scr. Mater.* **63** 312–5

[19] Bae S *et al* 2010 Roll-to-roll production of 30-inch graphene films for transparent electrodes *Nat. Nanotechnology* **5** 1–5

[20] Yoon S W, Kim S Y, Park J, Park C J and Lee C J 2005 Electronic structure and field emission of multiwalled carbon nanotubes depending on growth temperature *J. Phys. Chem.* B **109** 20403–6

[21] Barinov A, Malcioğlu O B, Fabris S, Sun T, Gregoratti L, Dalmiglio M and Kiskinova M 2009 Initial stages of oxidation on graphitic surfaces: photoemission study and density functional theory calculations *J. Phys. Chem.* C **113** 9009–13

[22] Laibinis P E, Bain C D and Whitesides G M 1991 Attenuation of photoelectrons in monolayers of n-alkanethiols adsorbed on copper, silver, and gold *J. Phys. Chem.* **95** 7017–21

[23] Ferrari A C and Robertson J 2001 Resonant Raman spectroscopy of disordered, amorphous, and diamondlike carbon *Phys. Rev.* B **64** 1–13

[24] Cançado L, Jorio A and Pimenta M 2007 Measuring the absolute Raman cross section of nanographites as a function of laser energy and crystallite size *Phys. Rev.* B **76** 064304

[25] Hammond C 1997 *Basic Crystallography and Electron Diffraction from Crystals* (Oxford: Oxford University Press)

[26] Oprea C, Ciupina V and Prodan G 2008 Investigation of nanocrystals using tem micrographs and electron diffraction technique *Rom. J. Phys.* **53** 223–30

[27] Egerton R F 2011 *Electron Energy-Loss Spectroscopy in the Electron Microscope* (Boston, MA: Springer)

[28] Dasgupta S, Wang D, Kübel C, Hahn H, Baumann T F and Biener J 2014 Dynamic control over electronic transport in 3D bulk nanographene via interfacial charging *Adv. Funct. Mater.* **24** 3494–500

[29] Koppens F H L, Mueller T, Avouris P, Ferrari A C, Vitiello M S and Polini M 2014 Photodetectors based on graphene, other two-dimensional materials and hybrid systems *Nat. Nanotechnology* **9** 780–93

[30] Khasminskaya S, Pyatkov F, Flavel B S, Pernice W H and Krupke R 2014 Waveguide-integrated light-emitting carbon nanotubes *Adv. Mater.* **26** 3465–72

[31] Kumar S B and Guo J 2012 Strain-induced conductance modulation in graphene grain boundary *Nano Lett.* **12** 1362–6

3. Supporting Information

3.1.1 *Separation of Single-Walled Carbon Nanotubes by 1-Dodecanol-Mediated Size Exclusion Chromatography*

B. S. Flavel, M. Kappes, R. Krupke, F. Hennrich

ACS Nano 7 (2013) 3557–3564

DOI: 10.1021/nn4004956

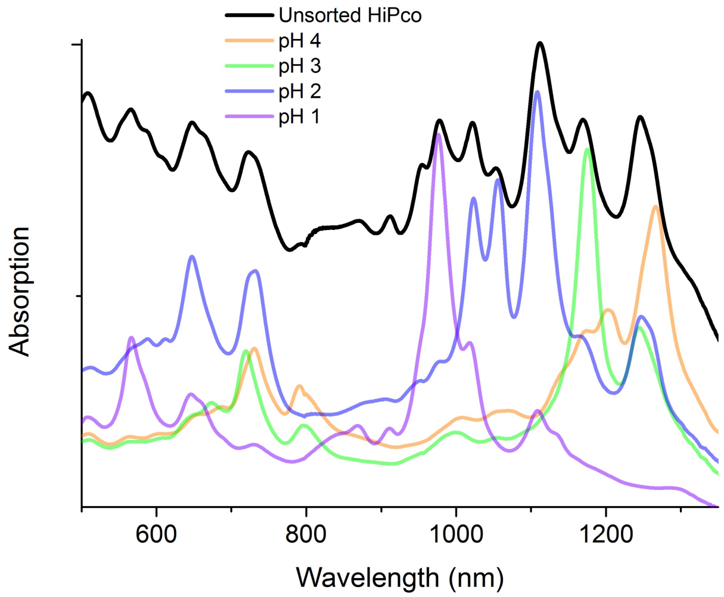

Figure S1 Absorption spectra of unsorted HiPco material and fractions obtained at pH 4 – 1 in 1 wt. % SDS.

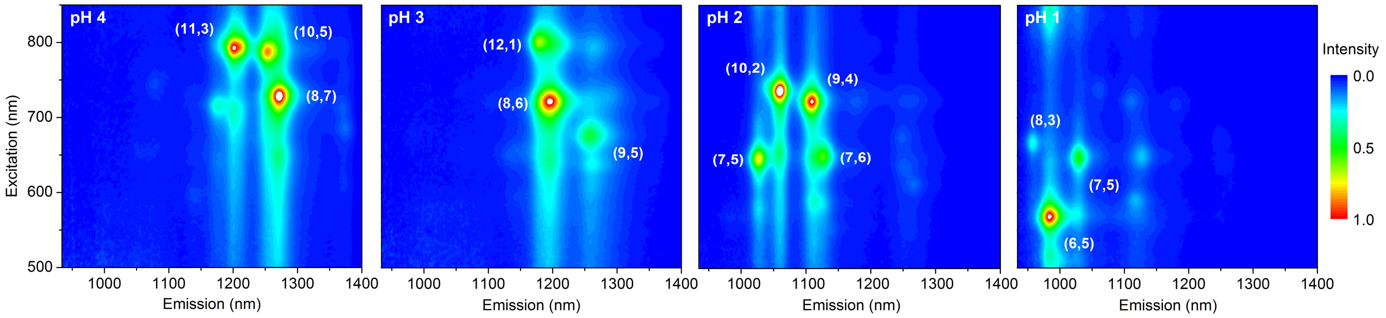

Figure S2 Photoluminescence spectra of fractions obtained at pH 4 – 1 in 1 wt. % SDS.

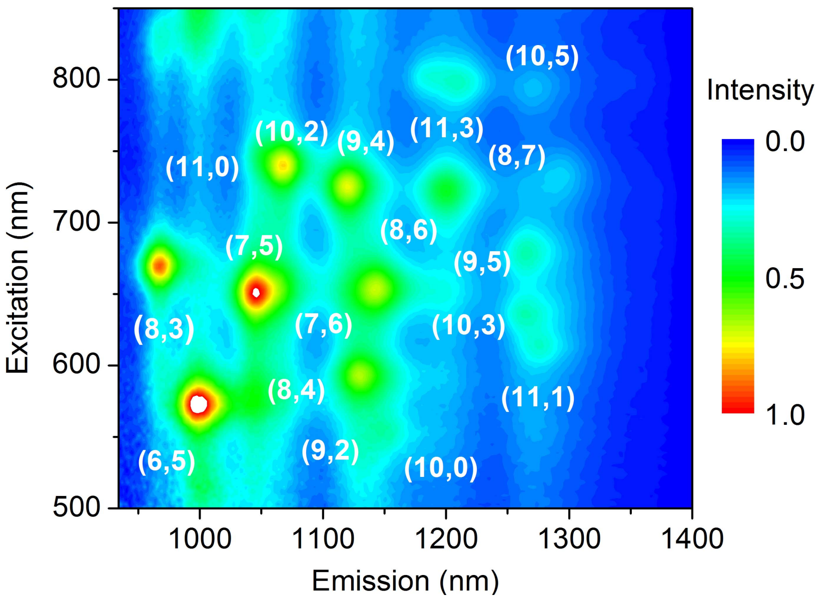

Figure S3 Photoluminescence spectra of unsorted HiPco SWCNT material suspended in 1 wt. % sodium cholate.

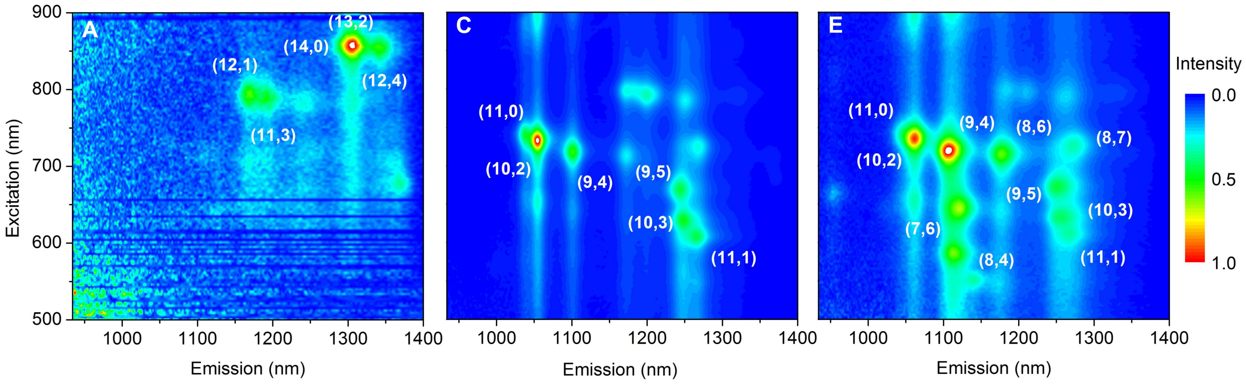

Figure S4 Additional photoluminescence spectra of fractions obtained upon addition of 1-dodecanol to the raw HiPco starting material.

3. Supporting Information

3.1.2 *Separation of Single-Walled Carbon Nanotubes with a Gel Permeation Chromatography System*

B. S. Flavel, K. E. Moore, M. Pfohl, M. M. Kappes, F. Hennrich

ACS Nano 8 (2014) 1817–1826

DOI: 10.1021/nn4062116

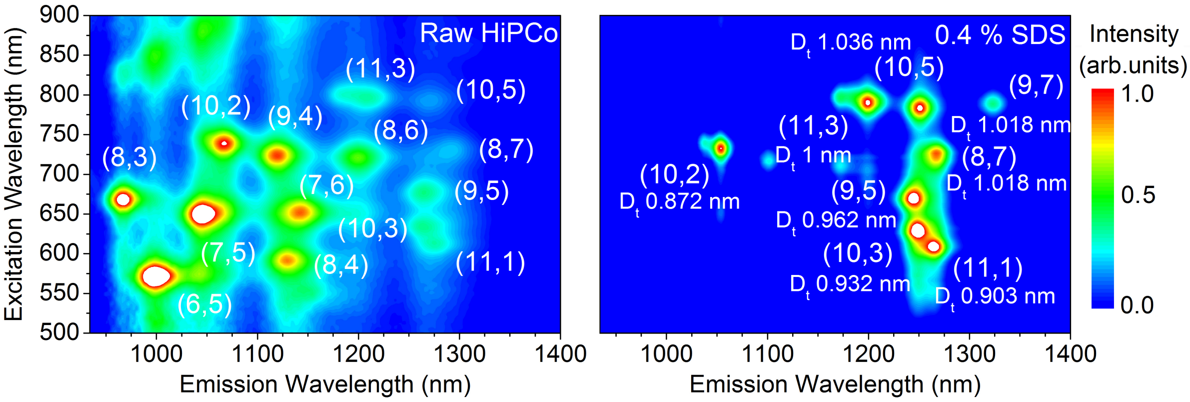

Figure S1 Photoluminescence contour map of raw HiPco SWCNT material (a) suspended in 1 wt % SDS and (b) absorbed to the Sephacryl gel at 0.4 wt % SDS.

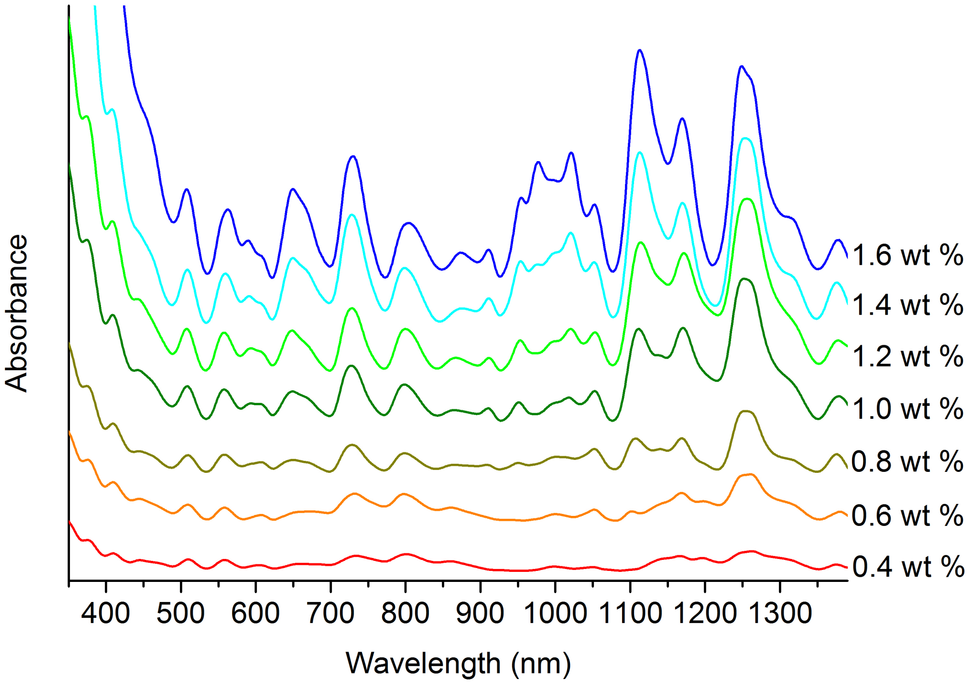

Figure S2 Absorption spectroscopy of raw the HiPco-SWCNT material. Following addition to the Sephacryl gel the ‘flow through’ material was sequentially reduced in concentration from 1.6 – 0.4 wt % SDS.

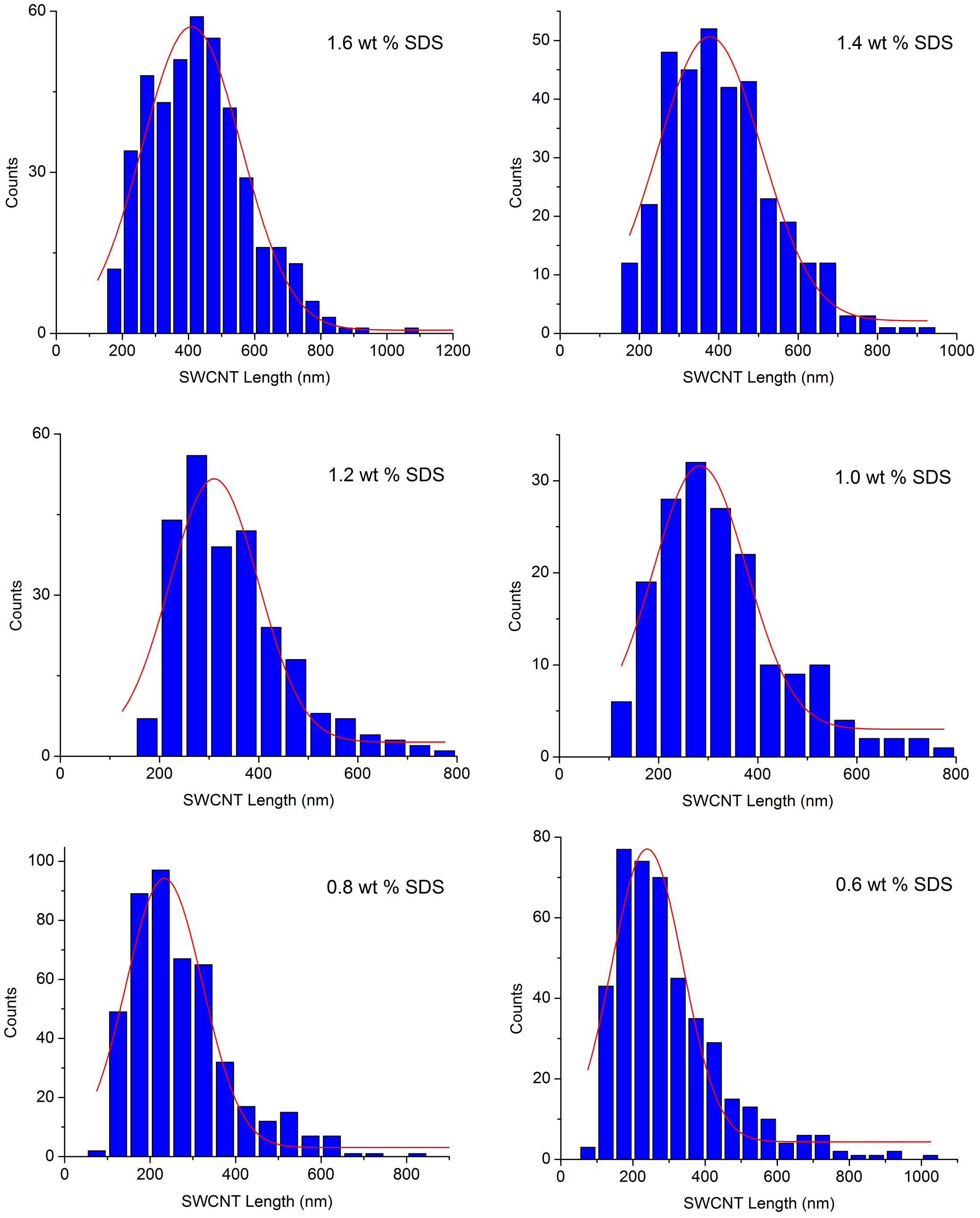

Figure S3 AFM measurement of the SWCNT length corresponding to the various 'start materials'.

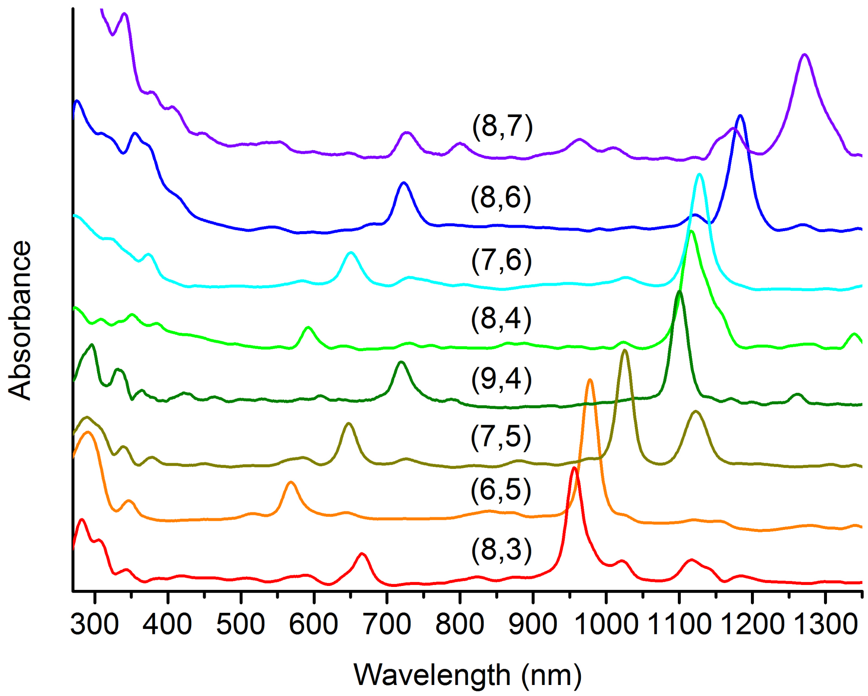

Figure S4 Normalized raw absorbance measurements corresponding to Figure 7.

– This page intentionally left blank –

3. Supporting Information

3.1.3 *Separation of Double-Walled Carbon Nanotubes by Size Exclusion Chromatography*

K. E. Moore, M. Pfohl, F. Hennrich, V. S. K. Chakradhanula, C. Kuebel, M. M. Kappes, J. G. Shapter, R. Krupke, **B. S. Flavel**

ACS Nano 8 (2014) 6756–6764

DOI: 10.1021/nn500756a

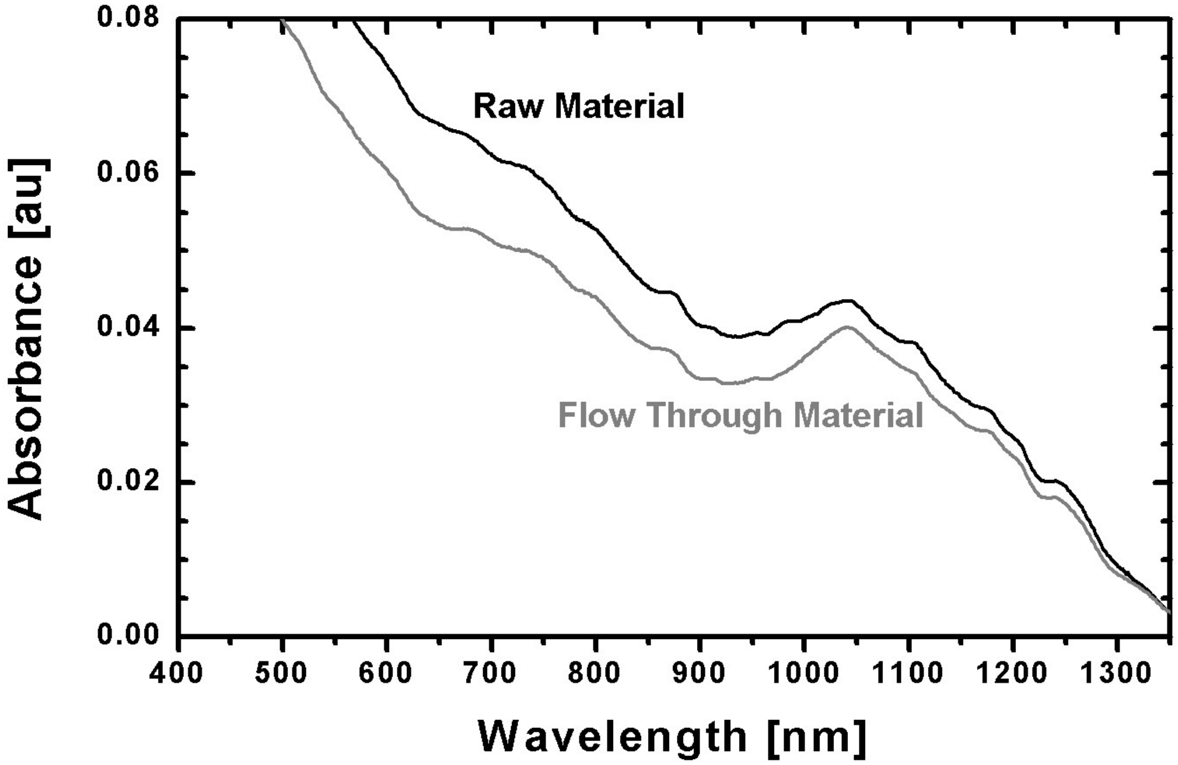

Figure S1 Absorption spectra of raw DWCNT material (2 wt % SDS) and 'flow through' solution. As expected for high SDS concentrations (1.6 – 2 wt % SDS) only a small amount of the overall nanotube population is adsorbed to the gel and hence the 'flow through' and raw material look similar.

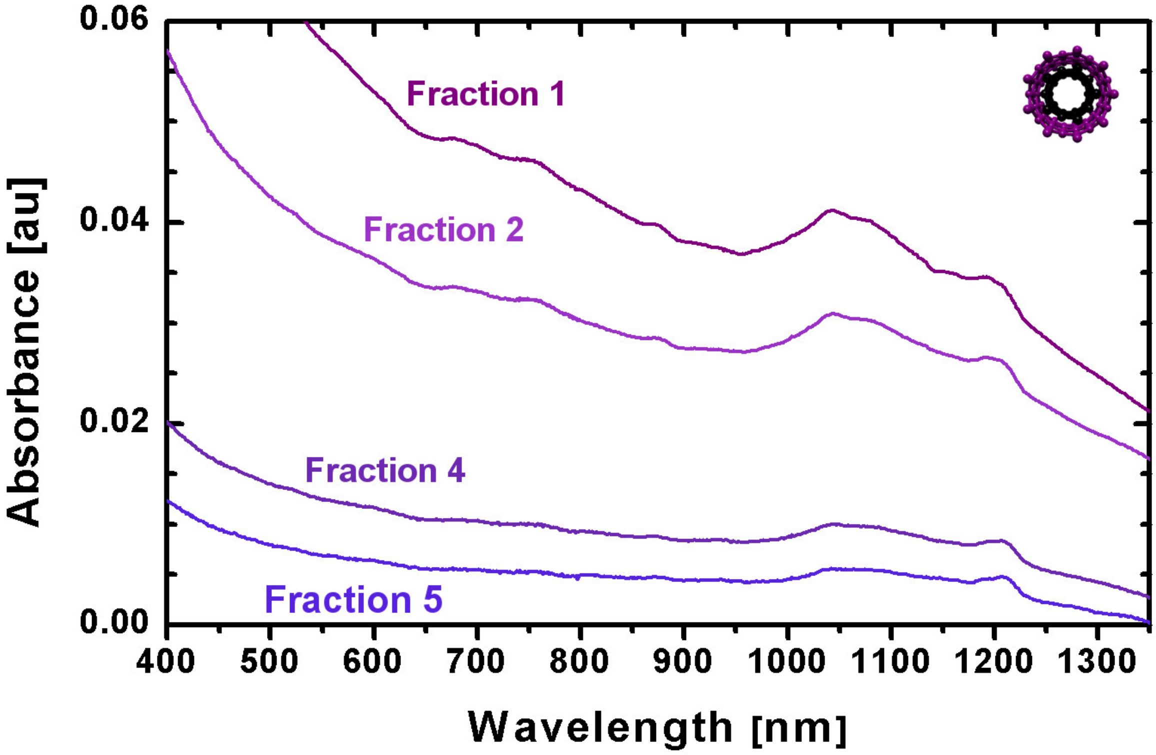

Figure S2 Absorption spectra of fractions 1, 2, 4 and 5 of the DWCNT band. A reduction of DWCNT concentration is seen for increasing fraction number.

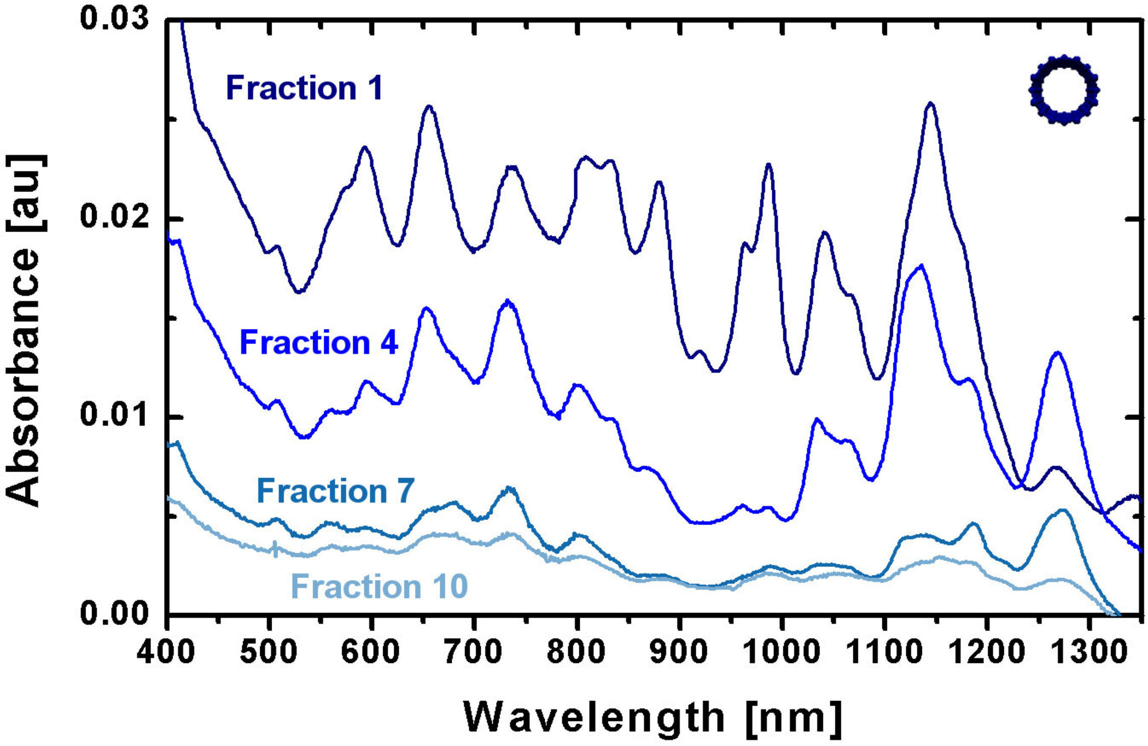

Figure S3 Absorption spectra of fractions 1, 4, 7 and 10 of the SWCNT band. A reduction of SWCNT concentration is seen for increasing fraction number.

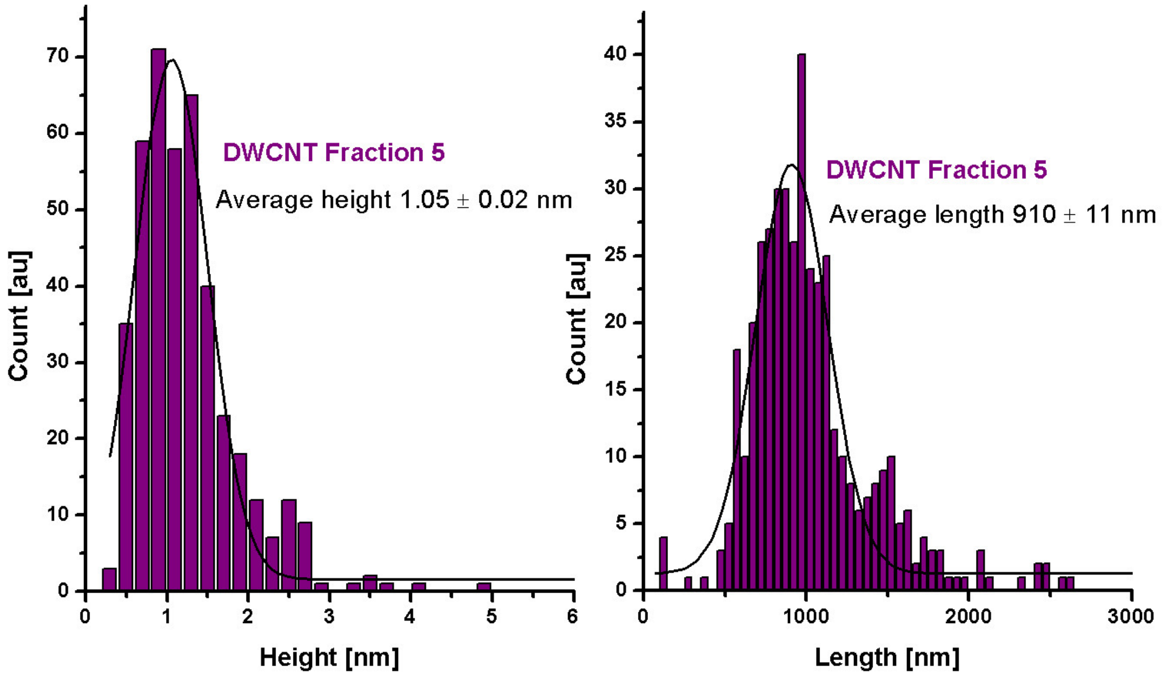

Figure S4 AFM analysis of DWCNT Fraction 5 showing comparable length distributions to band-edge DWCNTs. While in structure the material may be tube-like, the corresponding absorption data in Figure S2 shows poor optical properties; hence it is believed that the tubes are highly defected. Thus differing surface chemistry alters surfactant wrapping and hence adsorption to the gel. While similar in size, the defected material is separated from the pristine DWCNTs during elution.

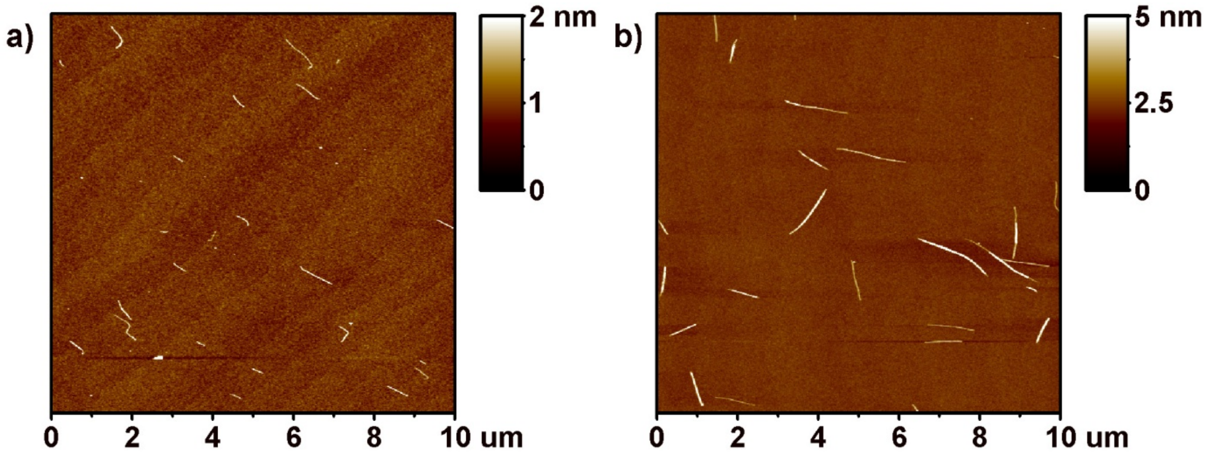

Figure S5 Representative AFM images of (a) SWCNTs and (b) DWCNTs on silicon.

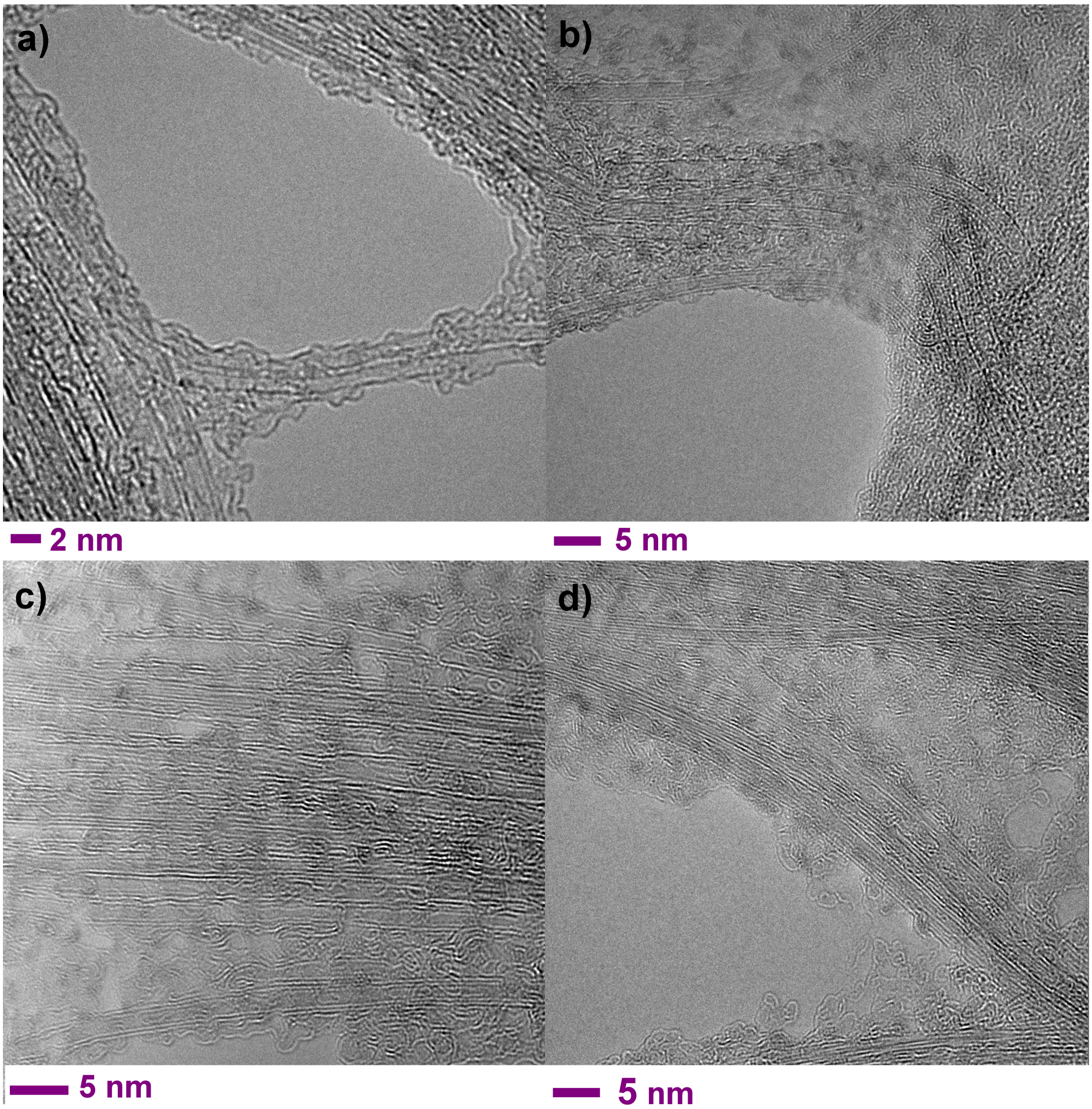

Figure S5 HRTEM micrographs of DWCNTs found in Fraction 1 of the DWCNT band.

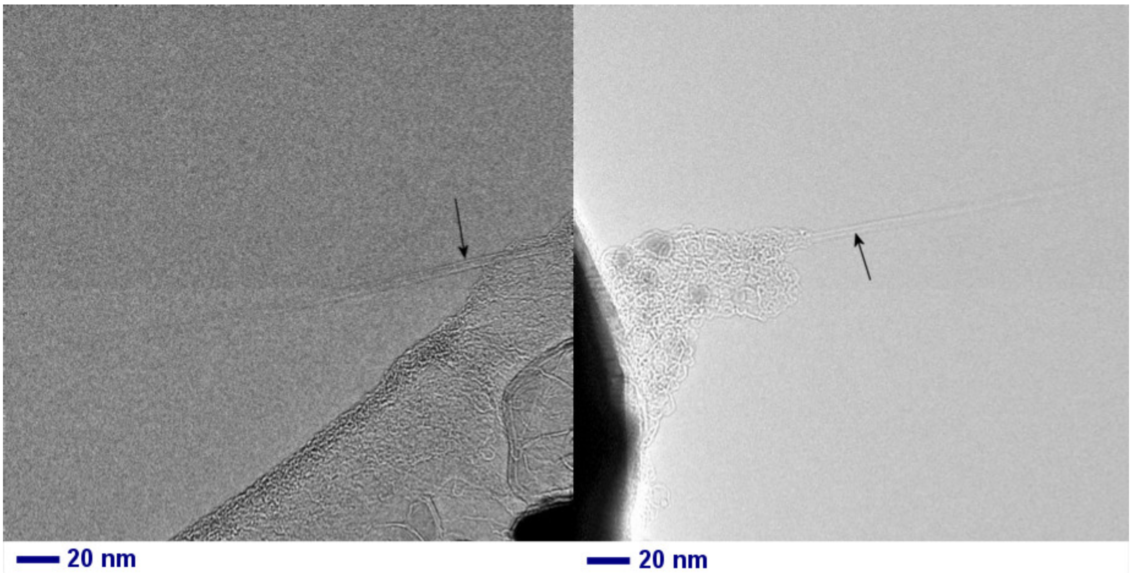

Figure S6 HRTEM micrograph of two SWCNTs from Fraction 1 of the SWCNT band with diameters of ~2 nm.

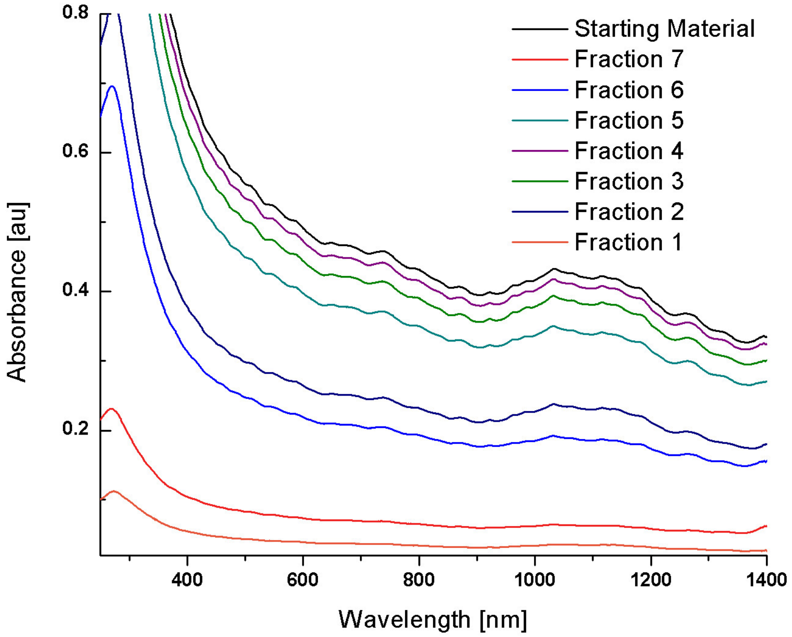

Figure S7 UV-Vis spectra of DWCNT raw material (1 wt % Sodium cholate) and CNT fractions that have passed through a gel column at 1 wt % SC.

To gain insight into the mechanism for DW and SW separation, the raw DWCNT material was prepared in 1 wt % SC and passed through a gel column at the same concentration. It was observed that there was no adsorption to the gel and the flow through material had the same CNT composition as the starting material.

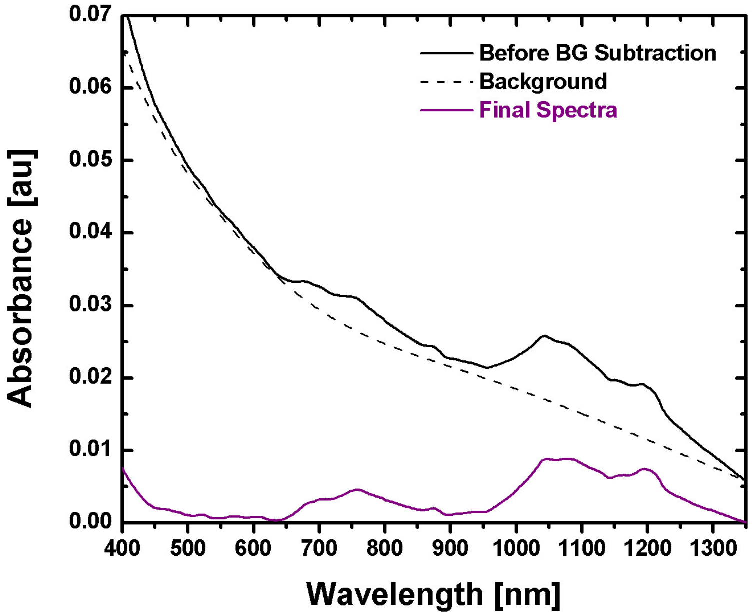

Figure S8 Method for background subtraction of DWCNT absorption spectra. The SWCNT spectrum was not background subtracted as it has minimal scattering and a flat baseline.

Raman analysis was used to analyse the DWCNT and SWCNT thin films. In this case Raman spectra were recorded for each film before and after treatment with sulphuric acid. The treatment of DWCNTs with sulphuric acid has been shown in our previous work[1] and in the work of Hersam and co-workers[2-3], to react with the exposed outer-wall nanotubes at a significantly faster rate than the inner-wall nanotubes, where the outer-wall acts as a protective shield for the inner-wall. Figure S9 shows Raman spectra for SWCNTs (left) and DWCNT (right) at the three different excitation wavelengths of 785, 638, and 532 nm. As peak position is inversely proportional to diameter, chiralities of the CNTs present in each sample were determine using the Kataura Plot[4-5] and Weisman data[6] can be seen in figures S10-S15.

Peaks in the shaded region of Figure S9, below 200 cm^{-1}, are a result of excitation of tubes with diameters greater than ~1.2 nm, which in the case of DWNTs correspond to outer-wall tubes. Inversely, the region above 200 cm^{-1} corresponds to tubes with diameters between 0.50 – 1.2 nm. After treatment there is a reduction in RBM peak intensity for both DWCNTs and SWCNTs owing to the structural degradation resultant from tube oxidation and cleavage. However, if one only considers the small tubes with RBM greater than 200 cm^{-1}, it can be observed that there is a greater degradation of the SWCNTs compared to the inner tubes of the DWCNTs. To quantify this, peak heights before and after treatment were determined and approximate percentage degradation could be calculated. The clearest example of this effect is seen at laser excitation of 785 nm. In the SWCNTs spectra there are four strong peaks present before acid treatment at ~ 209, 238, 271 and 375 cm^{-1}. The acid treatment results in significant degradation, with losses of intensity of 90, 85, 83 and 97 %, respectively. In the DWCNT sample there are two strong peaks at ~ 237 and 271 cm^{-1} which, after acid treatment, suffer comparatively smaller losses in intensity of 59 and 51 %, respectively. The fact that the smaller diameter DWCNT peaks retain more of their intensity after acid treatment indicates they are being shielded by an outer tube, hence providing further proof that the sorted DWCNTs retain their concentric structure. Comparatively the two strong peaks in the shaded region below 200 cm^{-1} centred at ~ 165 and 183 cm^{-1}, corresponding to the outer-wall nanotubes, suffer losses in intensity of 81 and 78 % respectively, as they are exposed to the acidic environment. Indeed by averaging the data over all excitation wavelengths, this trend is reflected with average degradations of ~ 68 and 40 % for SWCNTs and inner-tubes of the DWCNTs, respectively.

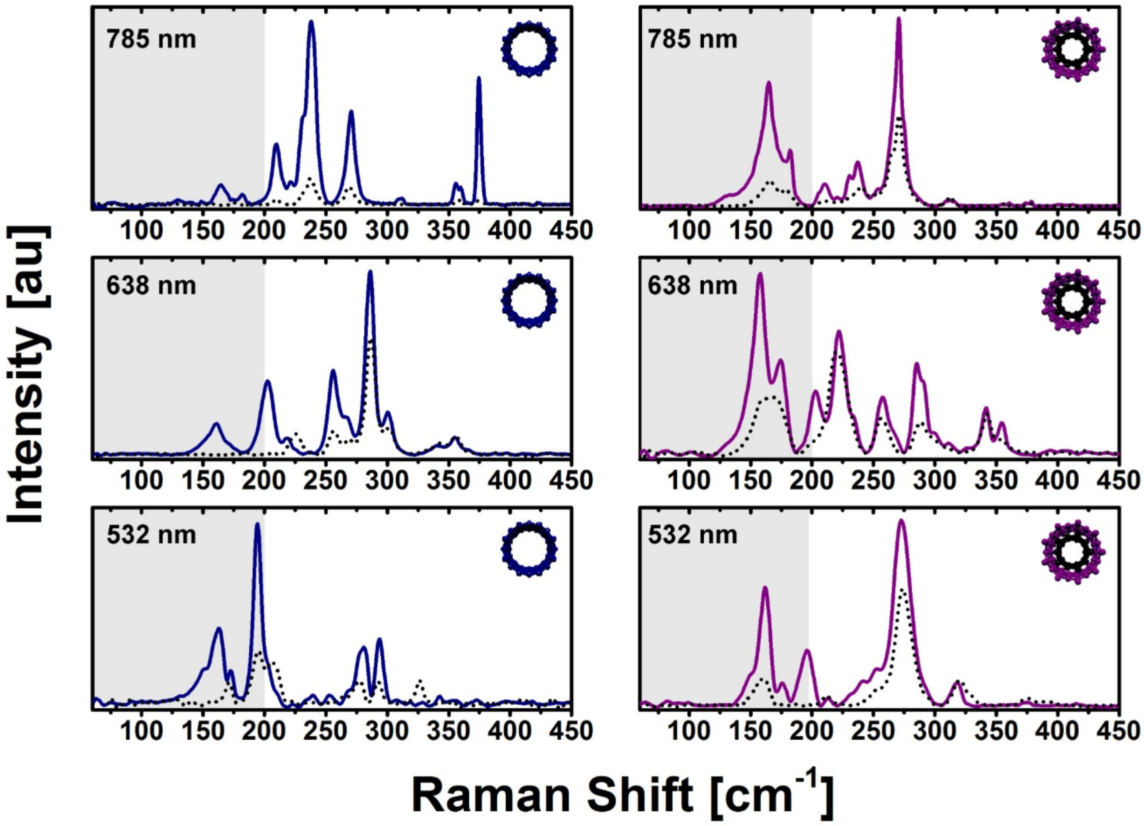

Figure S9 Raman spectra of the radial breathing modes of SWCNTs (left) and DWCNTs (right) with 785 nm, 638 nm and 532 nm laser excitation before and after treatment with sulphuric acid (solid and dashed lines, respectively).

Figures S10 – S15 show Raman spectra before and after thionyl choride doping and acid treatment. CNT chirality was assigned using the Kataura plot[4-5] and Weisman data[6] with ± 50 nm resonance.

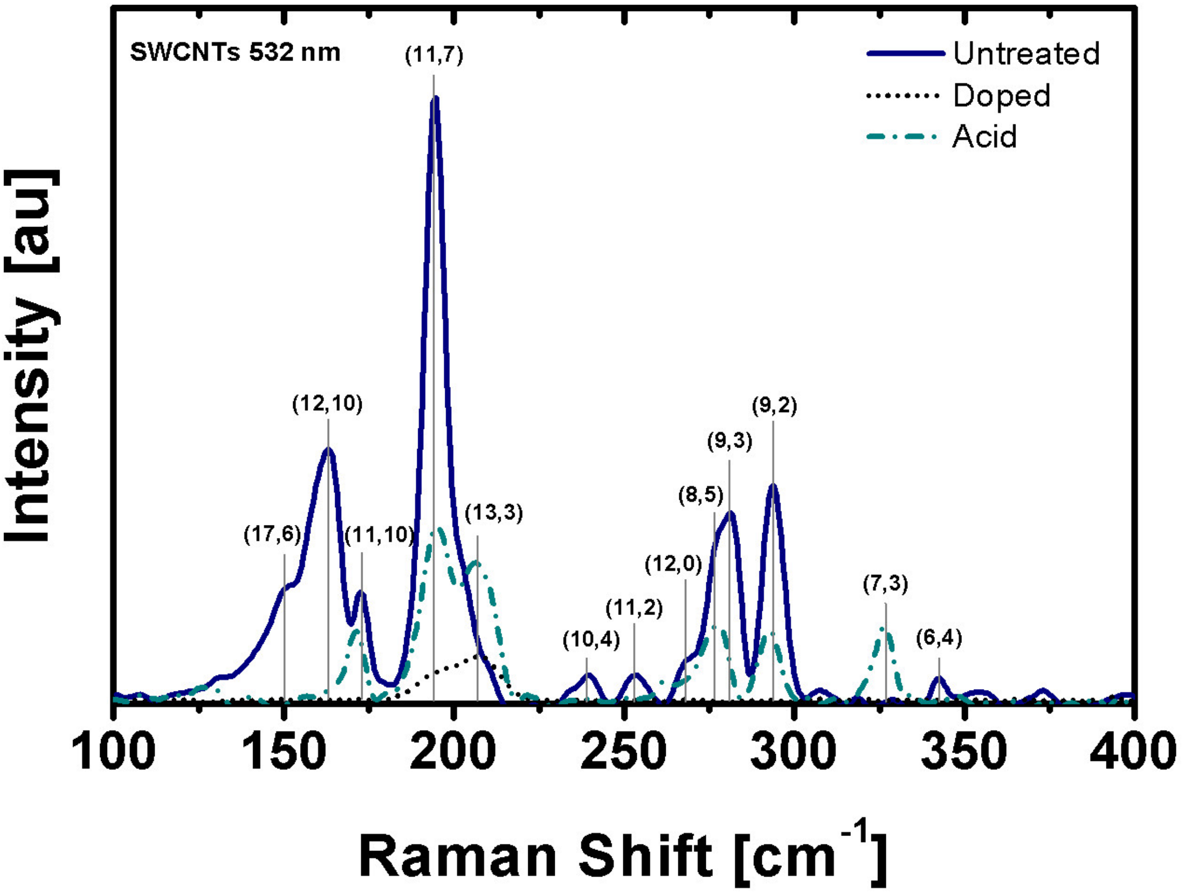

Figure S10 Raman spectra of untreated, thionyl chloride and acid treated SWCNTs at 532 nm laser excitation.

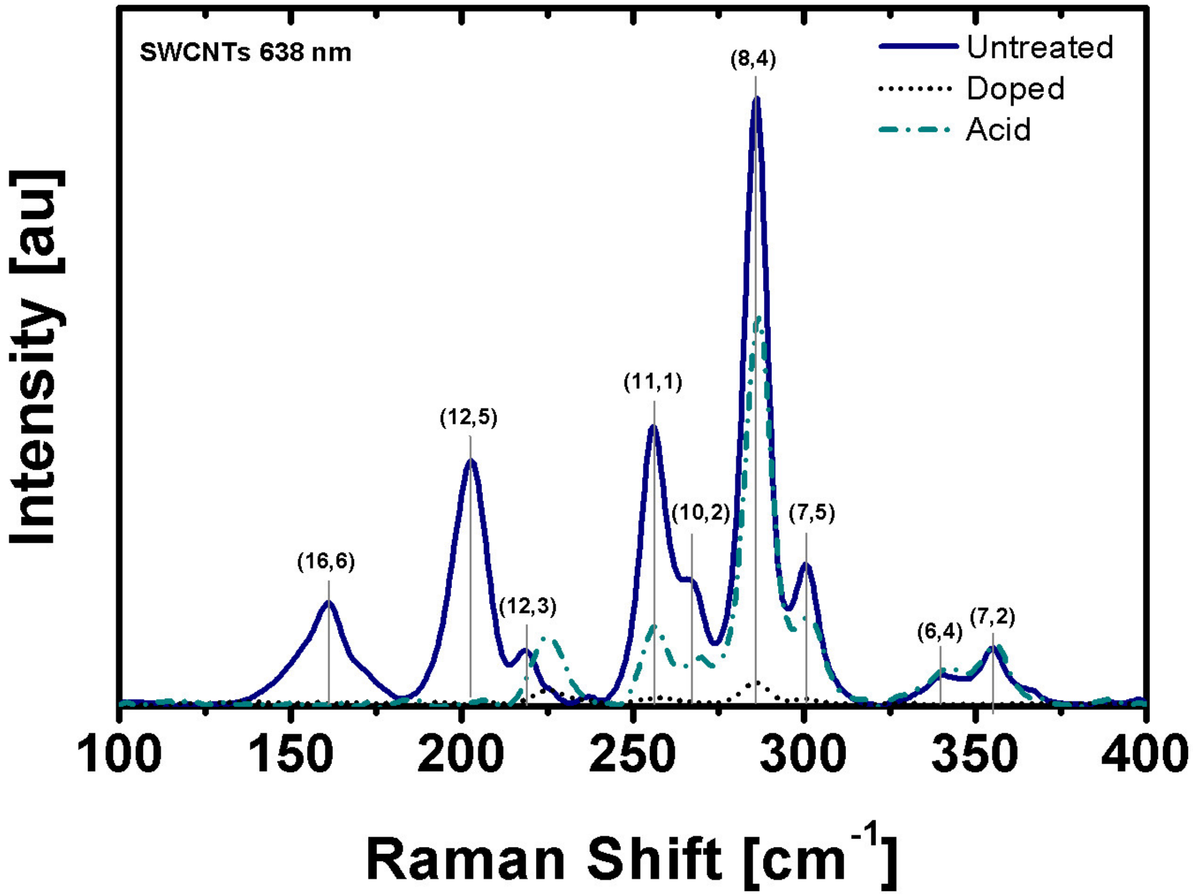

Figure S11 Raman spectra of untreated, thionyl chloride and acid treated SWCNTs at 638 nm laser excitation.

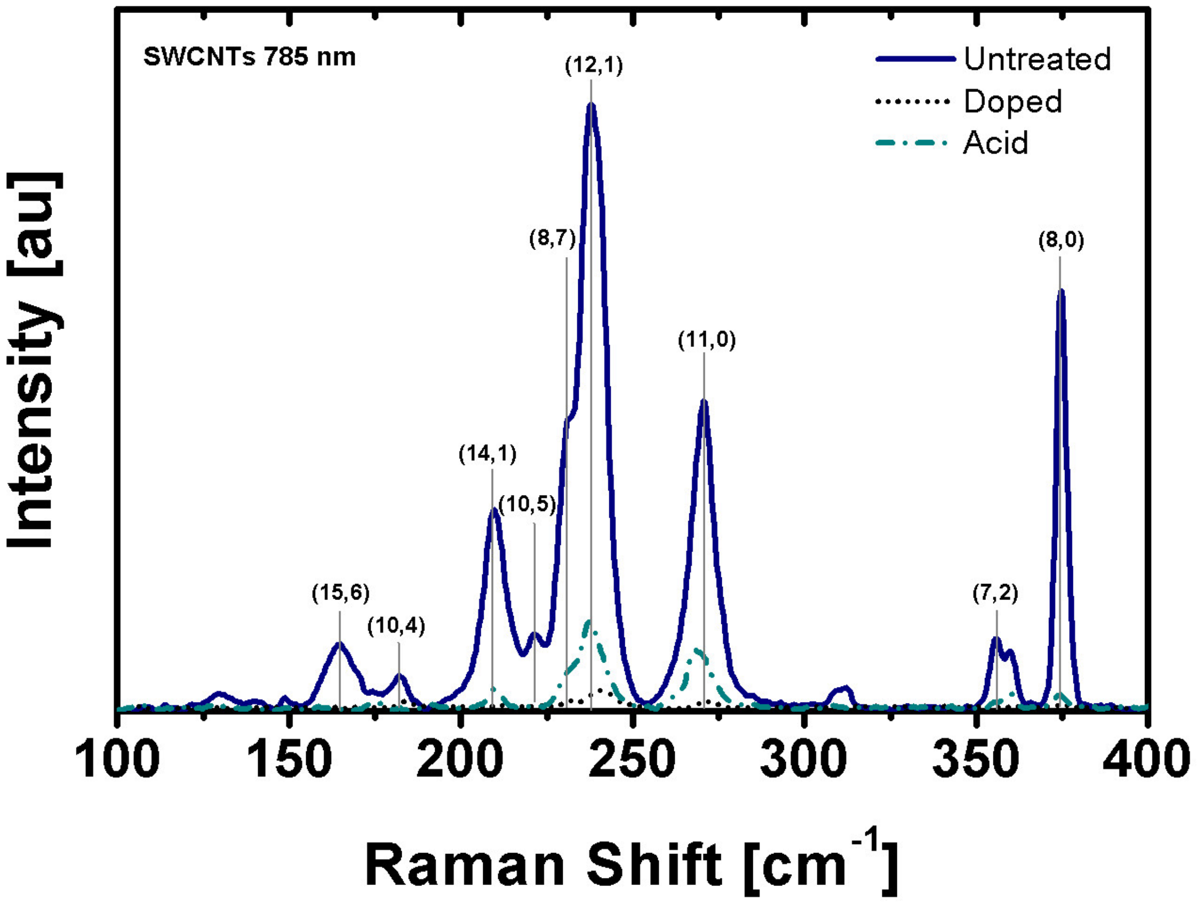

Figure S12 Raman spectra of untreated, thionyl chloride and acid treated SWCNTs at 785 nm laser excitation.

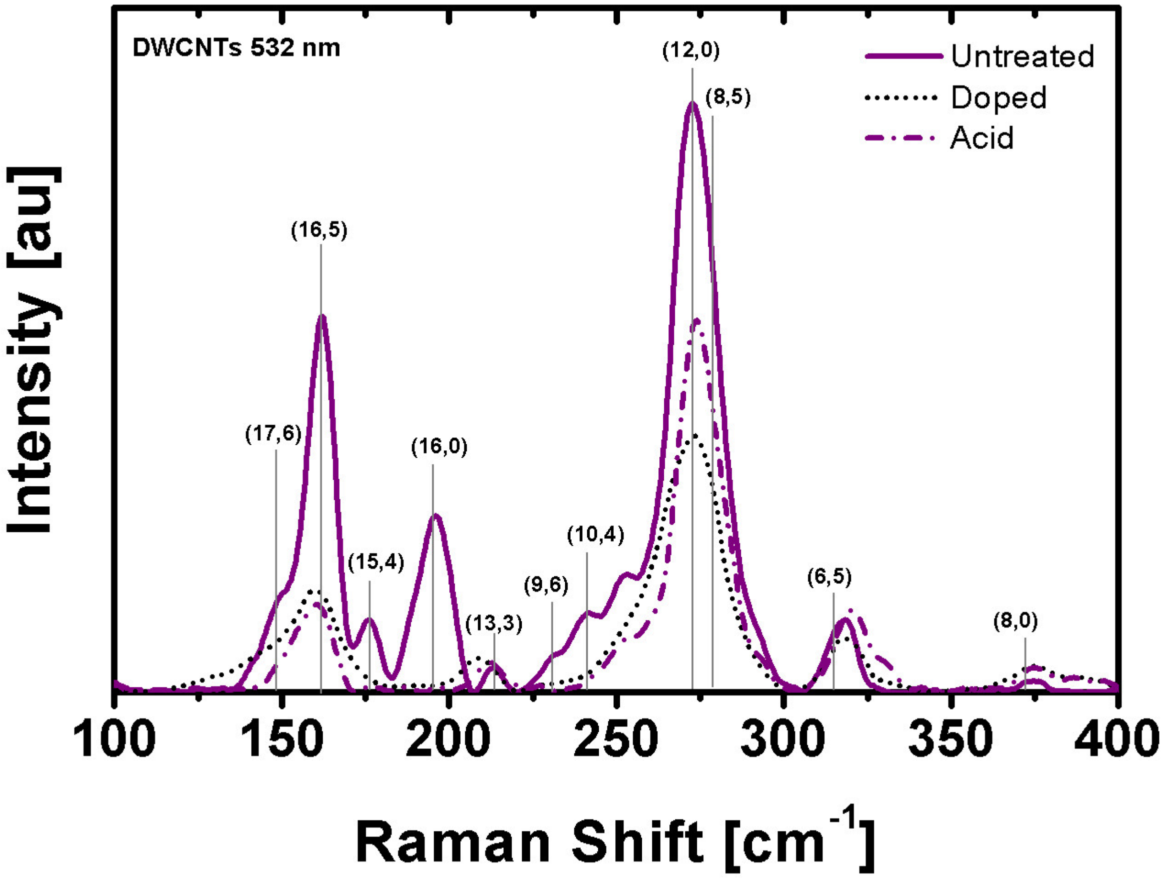

Figure S13 Raman spectra of untreated, thionyl chloride and acid treated DWCNTs at 532 nm laser excitation.

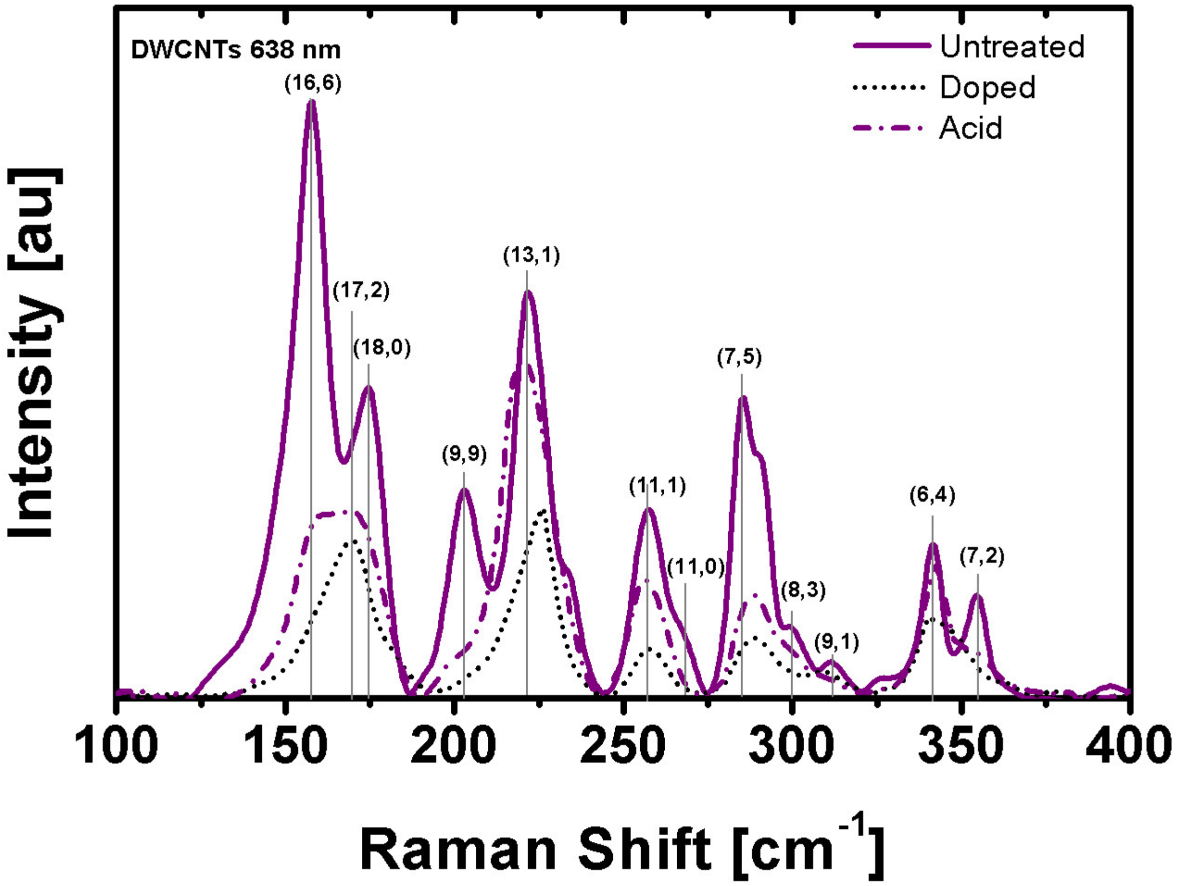

Figure S14 Raman spectra of untreated, thionyl chloride and acid treated DWCNTs at 638 nm laser excitation.

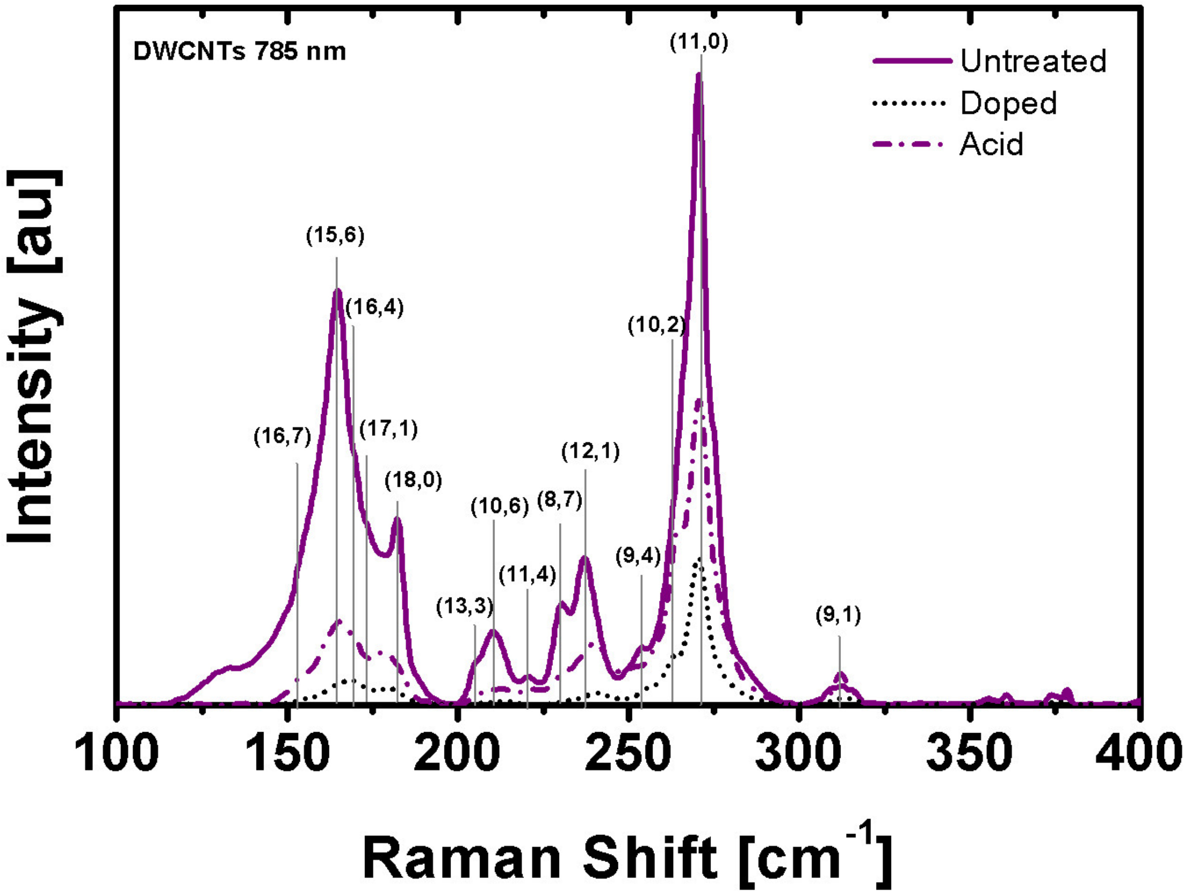

Figure S15. Raman spectra of untreated, thionyl chloride and acid treated DWCNTs at 785 nm laser excitation.

References

1. Moore, K. E.; Flavel, B. S.; Ellis, A. V.; Shapter, J. G., Comparison of Double-Walled with Single-Walled Carbon Nanotube Electrodes by Electrochemistry. Carbon 2011, 49, 2639-2647.
2. Green, A. A.; Hersam, M. C., Processing and Properties of Highly Enriched Double-Wall Carbon Nanotubes. Nat. Nanotechnol. 2009, 4, 64-70.
3. Green, A. A.; Hersam, M. C., Properties and Application of Double-Walled Carbon Nanotubes Sorted by Outer-Wall Electronic Type. ACS Nano 2011, 5, 1459-1467.
4. Maruyama, S. Kataura-Plot for Resonant Raman. http://www.photon.t.u-tokyo.ac.jp/~maruyama/kataura/kataura.html (accessed 07/02/2014).

5. Araujo, P. T.; Doorn, S. K.; Kilina, S.; Tretiak, S.; Einarsson, E.; Maruyama, S.; Chacham, H.; Pimenta, M. A.; Jorio, A., Third and Fourth Optical Transitions in Semiconducting Carbon Nanotubes. Phys. Rev. Lett. 2007, 98, 067401(1-4).
6. Bachilo, S. M.; Strano, M. S.; Kittrell, C.; Hauge, R. H.; Smalley, R. E.; Weisman, R. B., Structure-Assigned Optical Spectra of Single-Walled Carbon Nanotubes. Science 2002, 298 (5602), 2361-2366.

3. Supporting Information

3.1.4 *Sorting of Double-Walled Carbon Nanotubes According to Their Outer Wall Electronic Type via a Gel Permeation Method*

K. E. Moore, M. Pfohl, D. D. Tune, F. Hennrich, S. Dehm, V. S. K. Chakradhanula,
C. Kuebel, R. Krupke, **B. S. Flavel**

ACS Nano 9 (2015) 3849–3857

DOI: 10.1021/nn506869h

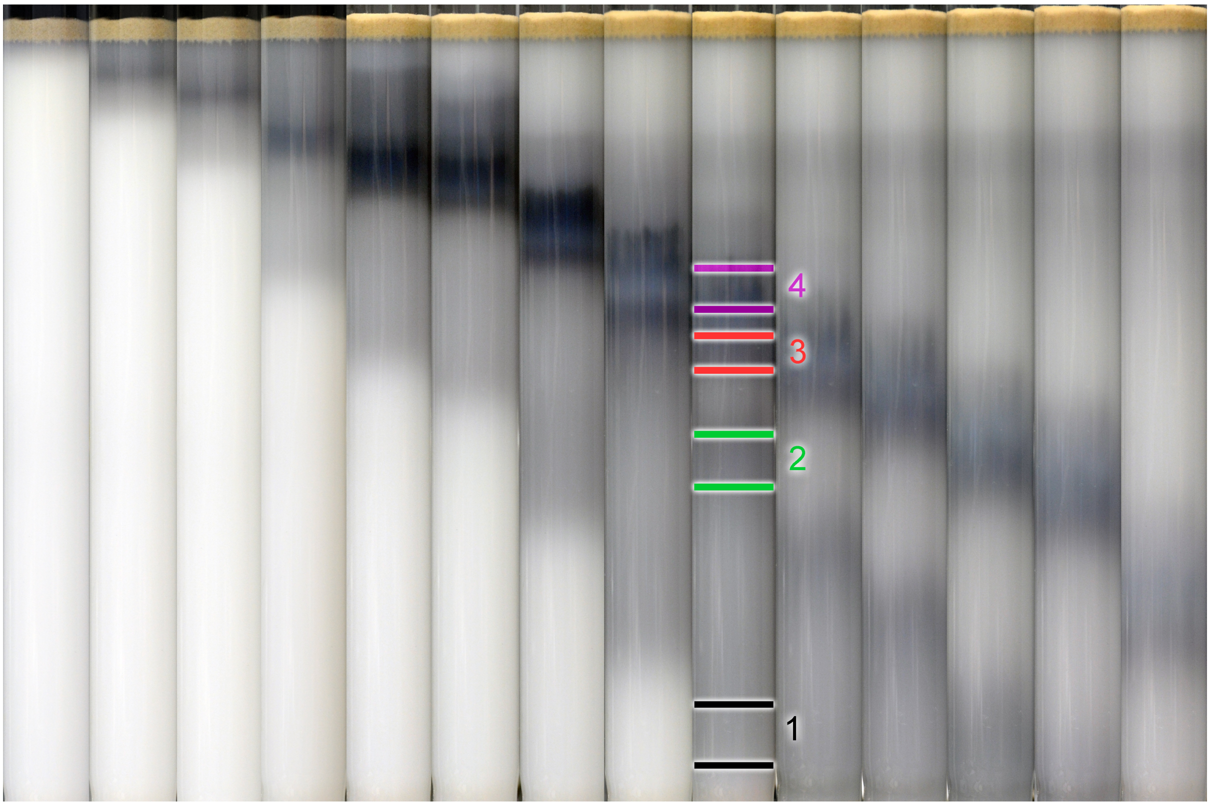

Figure S1 Time lapse photographs taken over a period of 20 min, showing addition of raw DWCNT in 1 wt % SC to an S-200 gel column at 1 wt % SDS. It can be seen that as the nanotubes flow through the gel matrix, separation occurs resulting in 'bands' of different nanotubes species. For ease of the viewer, the bands have been highlighted.

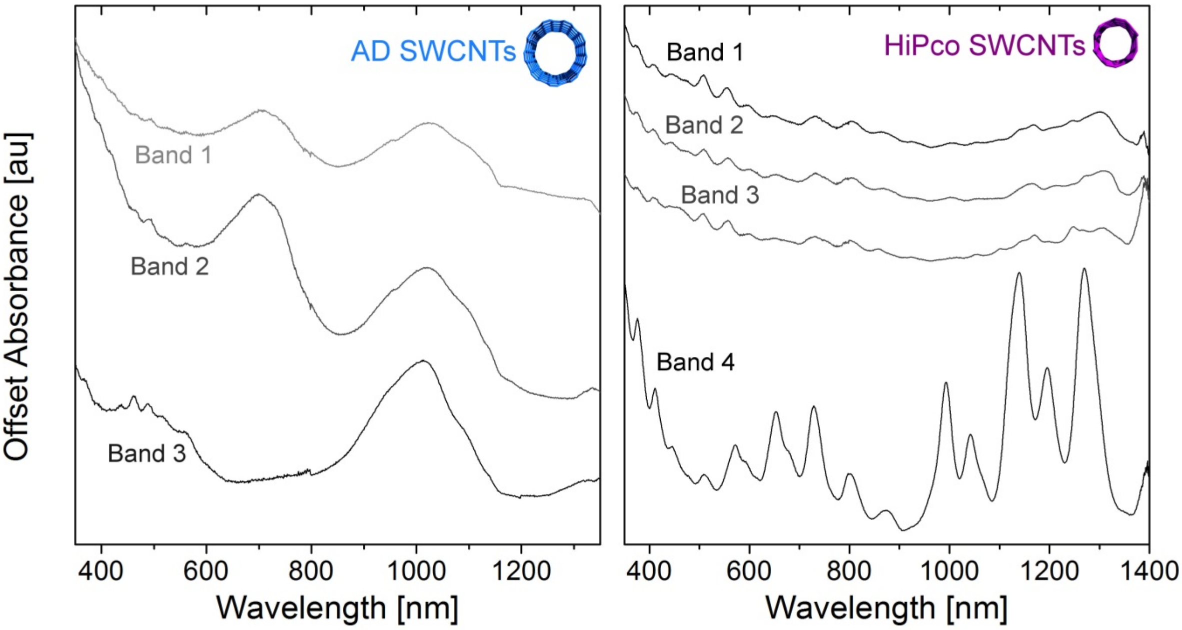

Figure S2 Absorbance spectra for Bands 1 – 3 of the AD SWCNT separation (left) and Bands 1 – 4 of the HiPco SWCNT separation (right).

For comparison the same separation procedure was performed on AD SWCNTs. These were chosen due to their average diameter (1.3 – 1.7 nm) being comparable to that of the DWCNTs and the large diameter SWCNTs found in the raw DWCNT material used. In the case of the AD SWCNTs, only three bands can be seen in the process Raman elution profile (Figure S2), occurring at 7, 10 and 16 min. The lack of a 4th band is to be expected because the AD SWCNT raw material should ideally consist of only ‘defected material’ and large m- and s-SWCNTs, whereas the DWCNT material consists of an additional small diameter SWCNT component. Interestingly, the three bands observed in the AD SWCNT separation occur at approximately the same time as the first three bands of the DWCNT material.

Comparison of the absorption measurements of the three bands with those of the DWCNT material reveals that the AD SWCNTs undergo the same, albeit less effective, separation process. Band 1 consisted of M_{11} (600 – 800 nm) and S_{22} (900 – 1100 nm) absorptions peaks from large diameter metallic and semiconducting nanotubes, respectively. As in the case of the DWCNTs, these peaks were of comparatively low intensity compared to Band 2 and we assume that these nanotubes had become defected during the sonication process. Similar to the DWCNTs, the AD SWCNT Band 2 was found to be enriched in large diameter m-SWCNTs, as evidenced by an enhancement of the M_{11} peak relative to the S_{22} from s-SWCNTs. For reference, an absorption measurement of the raw AD SWCNT material suspended in 1 wt % SC can be found in Figure S3. As seen in the DWCNT case, Band 3 of the AD SWCNT material consisted of large diameter semiconducting nanotubes without the presence of metallic species. This result is in good agreement with the work of Zhang et al.[S1] who used this method for the purification of s-SWCNTs from AD raw material. However, in that work they did not show a measurement for the m-SWCNTs, hence it remains unclear whether or not there was any separation for m-SWCNTs and, if they did, whether or not that separation was also not as specific as for large diameter s-SWCNTs.

A final control experiment was performed with the HiPco raw material and the corresponding absorption measurement can be found in Figure S3. HiPco SWCNTs were chosen due to their average diameter (0.8 – 1.2 nm) being similar to that of the small diameter SWCNTs present in the DWCNT raw material. Surprisingly, four bands were present; eluting at 8, 11, 14 and 20 min. Similar behavior to the AD SWCNTs was expected as it was supposed that the HiPco material only contained defected m- and s-SWCNTs, albeit with a smaller diameter. It is clear though that the bulk of the HiPco 'flow-through' material in Band 4 aligns well with the SWCNTs observed in the DWCNT separation at 20 min. This band was found to contain not only s-SWCNTs with S_{11} at 950 – 1300 nm and S_{22} at 600 – 800 nm, but also m-SWCNTs with M_{11} at 500 – 600 nm. Absorption measurements of Bands 1 – 3 revealed the presence of small and large diameter m-SWCNT (M_{11} 500 – 600 nm and 700 – 800 nm, respectively). Indeed, electronic character enrichment appears to occur via this method for small diameter SWCNTs; however the sorting efficiency is quite limited as evidenced by the remaining metallic species in Band 4. This is perhaps not unsurprising given the well established protocols for the trapping of small diameter SWCNTs on the gel under SDS followed by the subsequent washing with SC or 5 % SDS.[S2-S7] Methods that have been developed for the electronic separation of small diameter SWCNTs are not necessarily going to be applicable to large diameter SWCNTs and vice versa and the current control experiment certainly exemplifies that. Nevertheless, the two control experiments with AD and HiPco material allow for reasonable comments to be made regarding the types of impurities expected in the m- and s- DWCNT fractions, given the fact that all of the raw material flows through the gel.

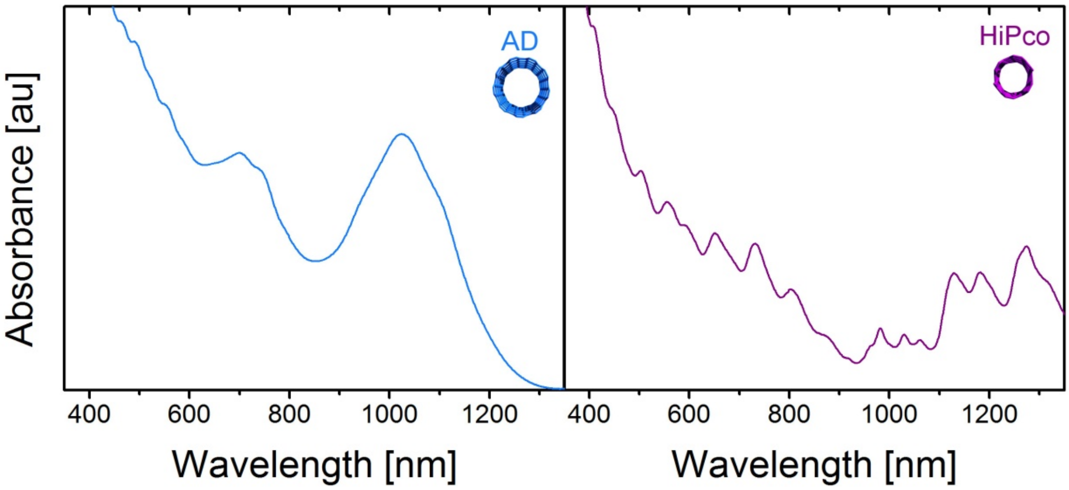

Figure S3 Normalised absorption spectra of raw AD (left) and HiPco (right) SWCNTs suspended in 1% SC.

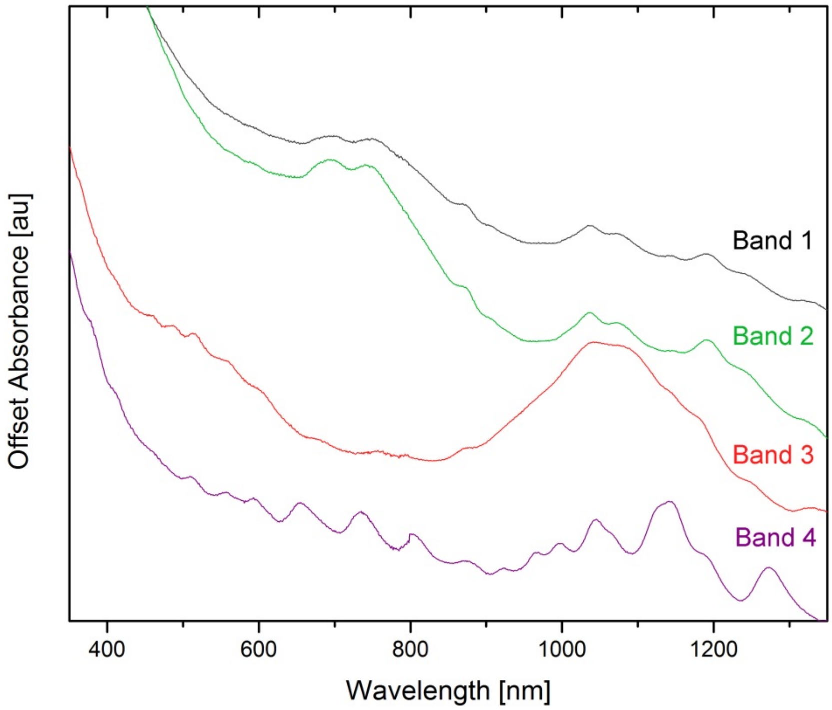

Figure S4 Absorbance spectra for Bands 1 – 4 of the DWCNT separation.

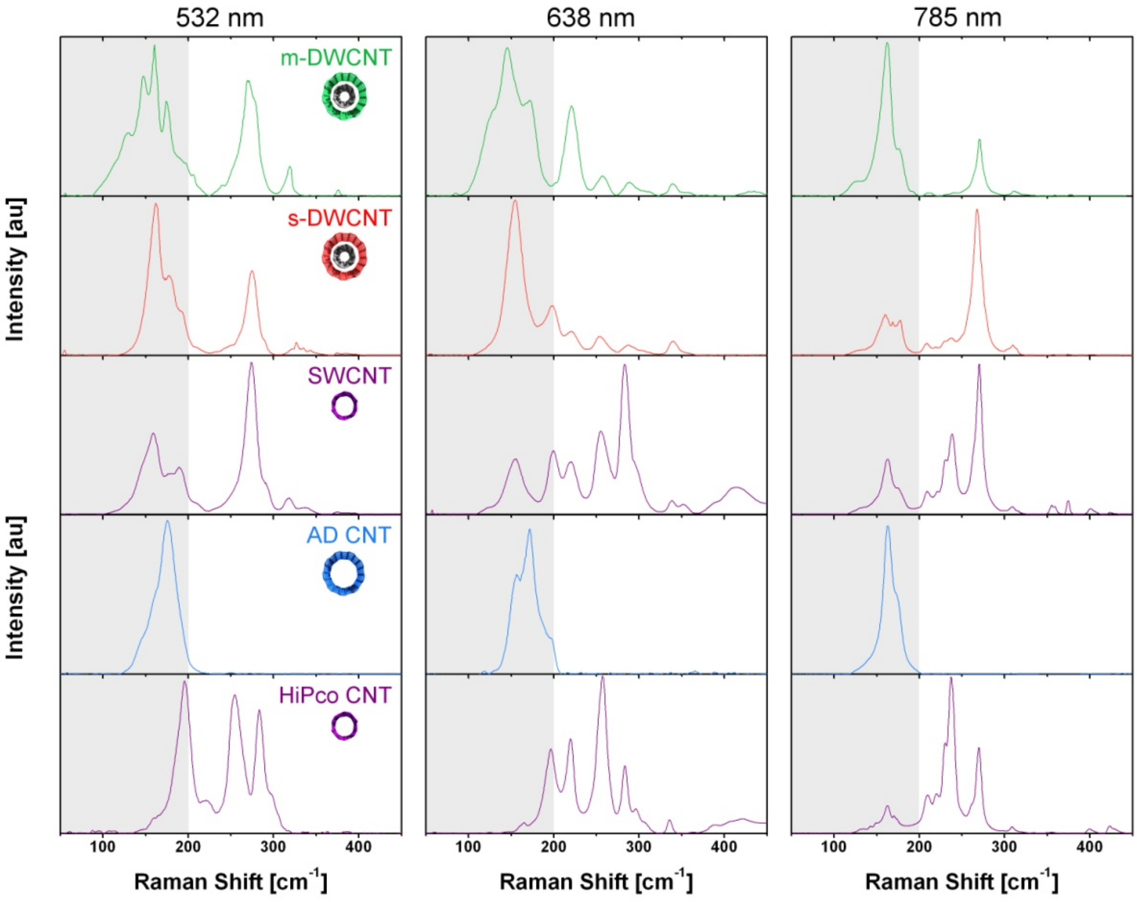

Figure S5 Raman spectra of separated DWCNT fractions as well as the AD and HiPco control samples at laser excitation of 532, 638 and 785 nm. Raman absorption spectra were taken with an XploRA confocal microscope (Horiba) with laser energies of 1.58 eV (785 nm), 1.94 eV (638 nm) and 2.33 eV (532 nm) under a x50 objective. Power and gratings were optimised appropriately for each wavelength.

Peaks in the shaded region, below 200 cm^{-1}, are a result of excitation of nanotubes with diameters greater than ~1.2 nm, which in the case of DWNTs correspond to outer wall nanotubes. Inversely, the region above 200 cm^{-1} corresponds to nanotubes with diameters between 0.50 – 1.2 nm. For both the m-DWCNT and s-DWCNT samples there are two distinct regions corresponding to the outer and inner walls, respectively, as is expected of DWCNTs.[S8] The outer wall peaks closely correlate with the large diameter AD SWCNTs, which further explains the strong correlation observed between the two species during separation. The clear difference between the AD and DWCNTs is the presence of small diameter inner walled nanotubes. The SWCNT sample resultant from the DWCNT separation (Band 4) can be compared to the small diameter HiPco SWCNTs with a multitude of nanotube species present, predominantly at Raman shifts above 200 cm^{-1}, indicative of small diameter nanotubes. However there are also some large diameter nanotubes present in the separated SWCNT fraction (peaks at ~ 170 cm^{-1} at laser excitations 532 and 638 nm), which from the TEM and AFM, can be attributed to the presence of DWCNTs.

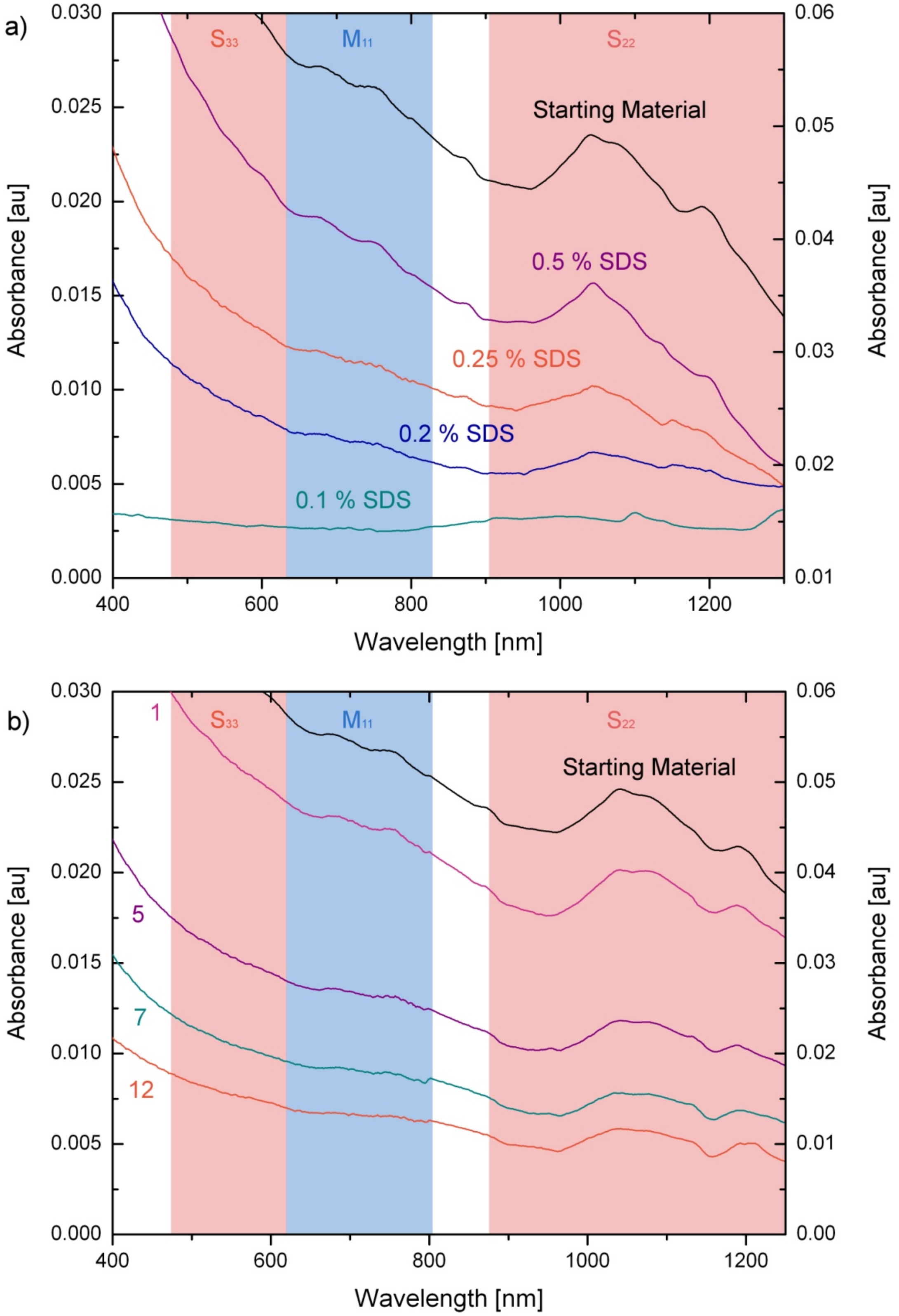

Figure S6 (a) Absorption spectra of starting and flow through material at decreasing SDS concentration. It can be seen that reduction in SDS concentration did not lead to an increase in the concentration of m-DWCNTs in the 'flow-through' material. For all concentrations above 0.15 wt % the 'flow-through' was found to contain both large diameter metallic (M_{11}: 640 – 800 nm) and semiconducting (S_{22}: 975 – 1175 nm) DWCNT and SWCNT species. We note that for concentrations below 0.2 wt %, complete adsorption to the gel occurred with no nanotubes visible via absorption spectroscopy in the flow-through material. Complete absorption at low SDS concentrations is also in agreement with the work of Blanch et al. who observed that at 0.2 wt %, a significant proportion of nanotubes are irreversibly adsorbed, while complete adsorption occurred at 0.1 wt %.[S2] (b) Absorption spectra of a two-step separation method, where material from our previously reported separation technique[S9] was used as the starting material for a second separation, in an attempt to sort by outer wall electronic character. Briefly, 10 mL of raw DWCNTs in 2 wt % SDS was applied to a 2 wt % SDS column. Adsorbed nanotube material was then eluted with 0.5 wt % SC. The fraction containing the highest concentration of sorted DWCNT material was adjusted to 1 wt % SC and applied to a second column at 1 wt % SDS. Fractional absorption spectra from the collected 'flow through', as well as the starting material can be seen. Fractions were collected in 2 mL aliquots and the fraction numbers can be seen on the left. As in the work of Zhang et al., it was expected that the m-DWCNTs would flow through the column leaving the s-DWCNT material adsorbed for subsequent elution.[S1] However all fractions were found to have the same nanotube composition, albeit with reduced concentration, and no material was found to adsorb to the gel. In both (a) and (b) starting material corresponds to the right axis while all other spectra correspond to the left axis. Red and blue shaded regions correspond to semiconducting and metallic absorption of large diameter nanotubes, respectively.

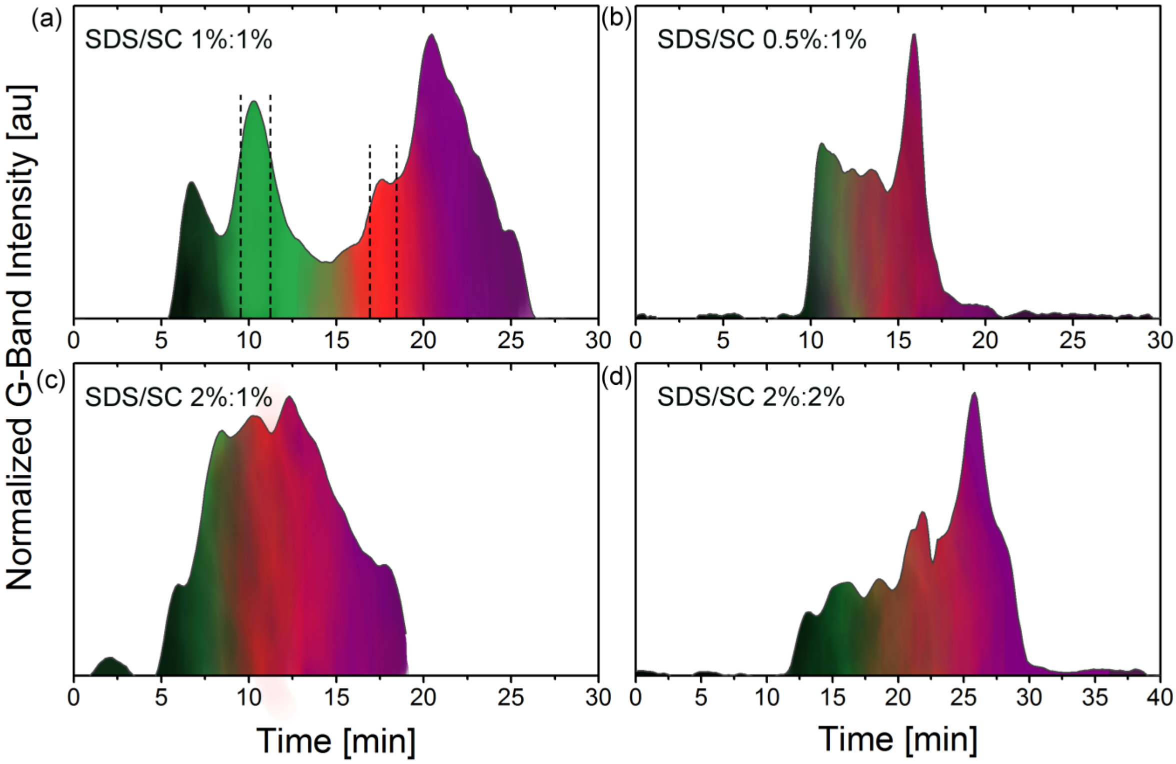

Figure S7 Elution profiles of DWCNT separations in varying SDS/SC ratios and concentration. (a) shows the optimized SDS/SC separation (1 %:1 %) used for the separation of m-DWCNTs and s-DWCNTs. (b) and (c) show the elution profiles for lower and higher SDS ratios of 0.5 % and 2 % respectively, with the SC concentration remaining constant. (d) shows the elution profile in the optimum ratio of 1:1, but with an increased concentration. In each case, the profile is colored in accordance with the nanotube species, where green corresponds to m-DWCNTs, red corresponds to s-DWCNTs and purple corresponds to SWCNTs.

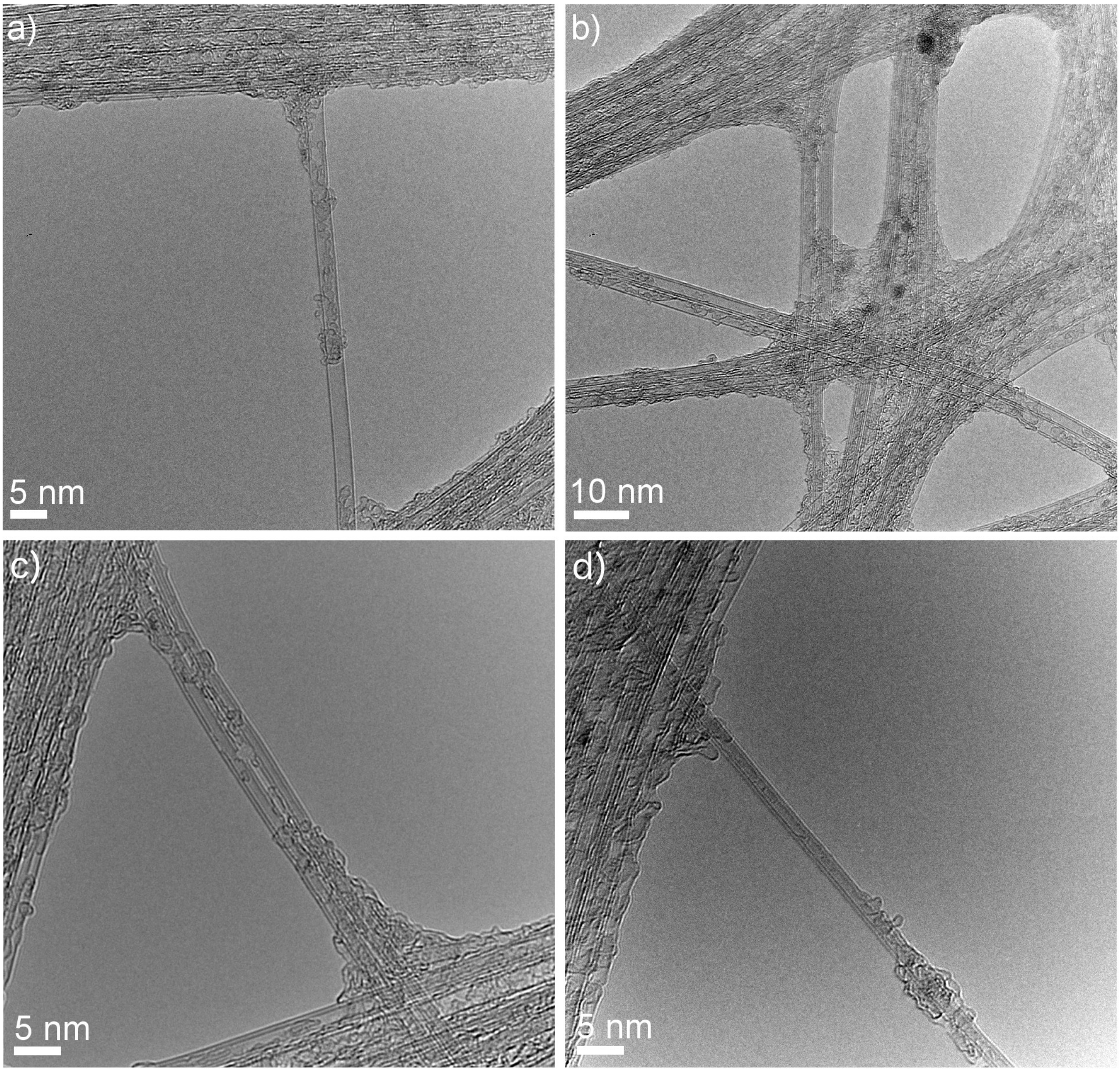

Figure S8 Representative HRTEM micrographs of Band 1 of sorted DWCNT material.

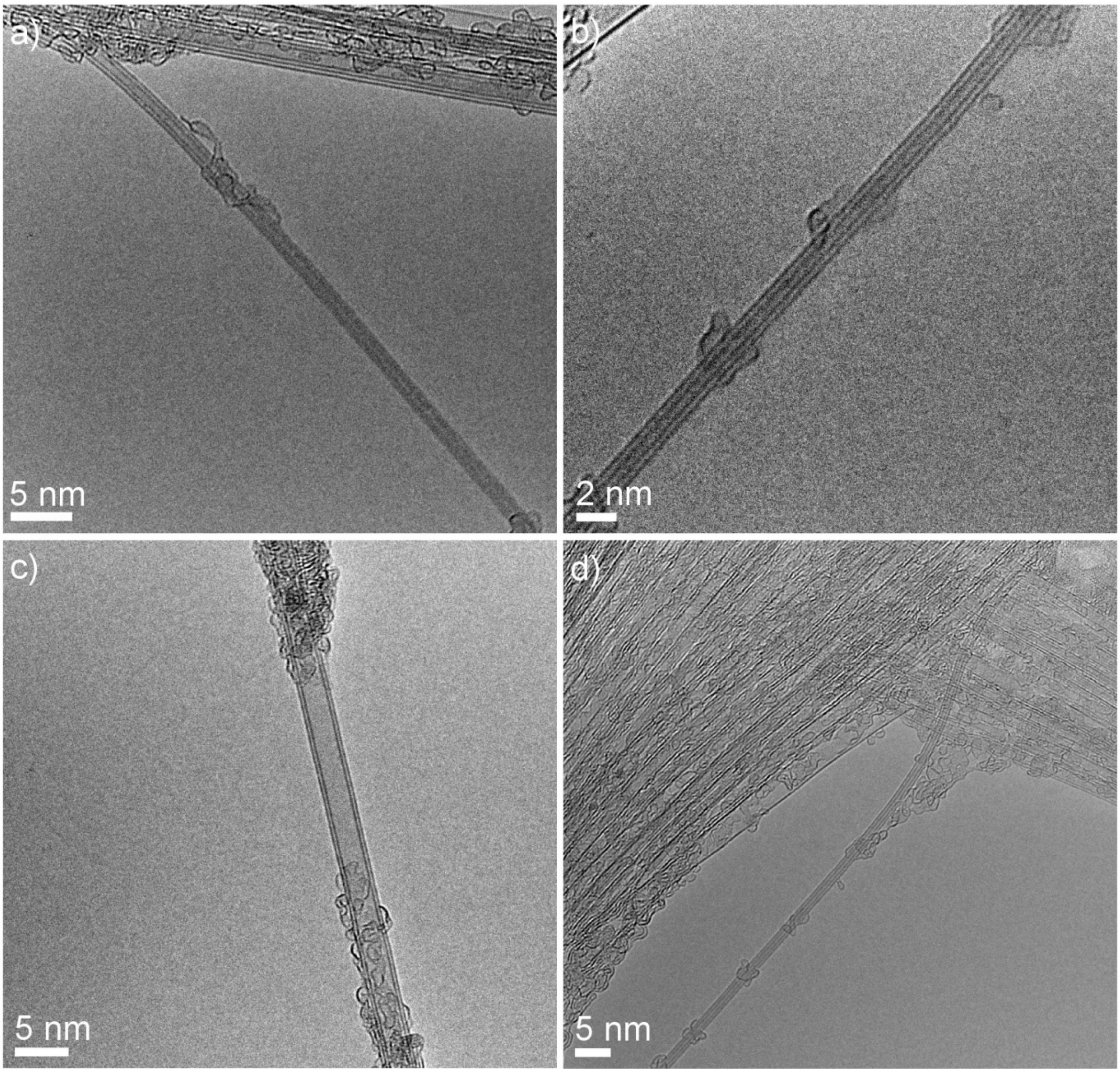

Figure S9 Representative HRTEM micrographs of Band 2 of the sorted DWCNT material.

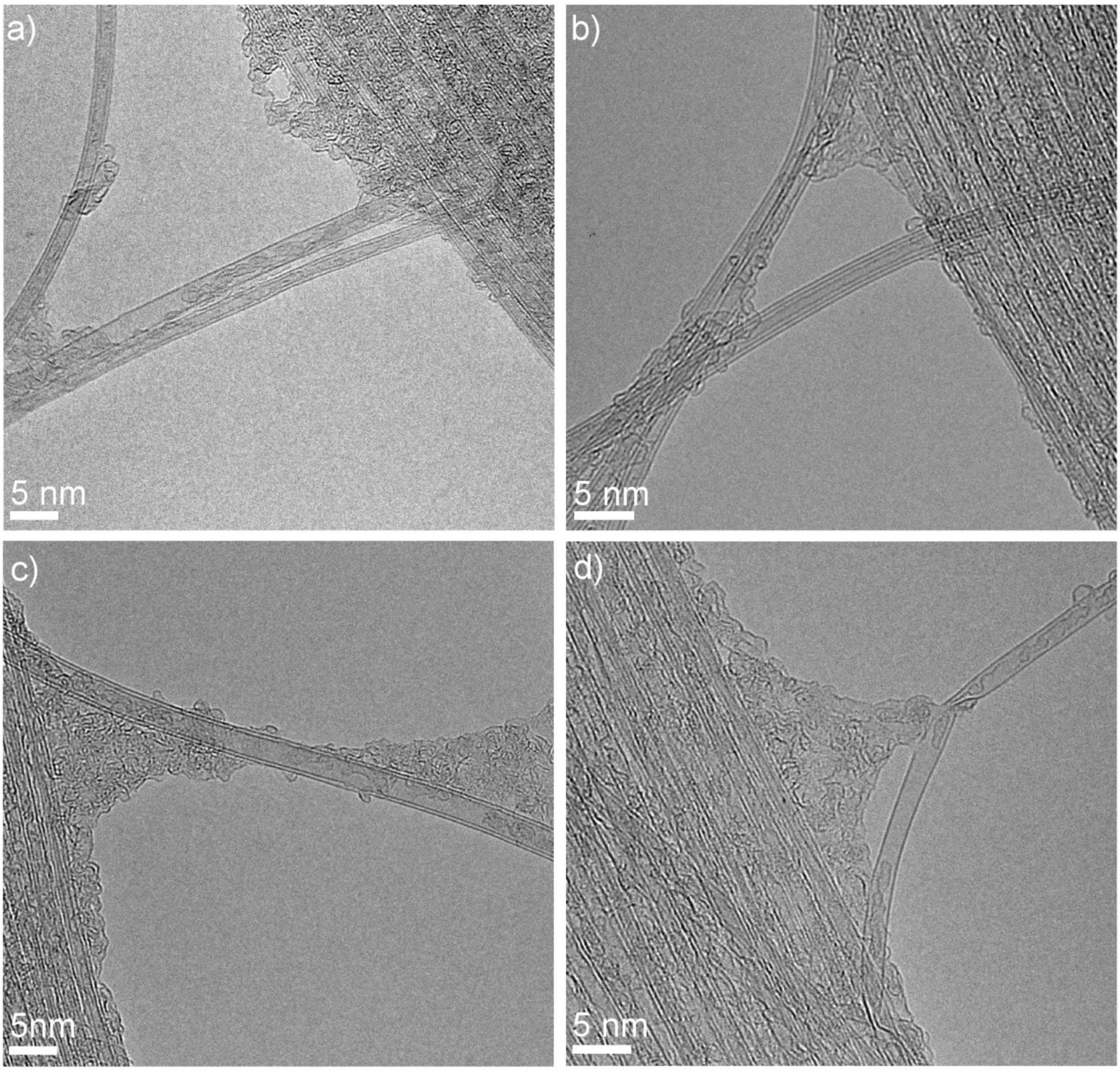

Figure S10 Representative HRTEM micrographs of Band 3 of the sorted DWCNT material.

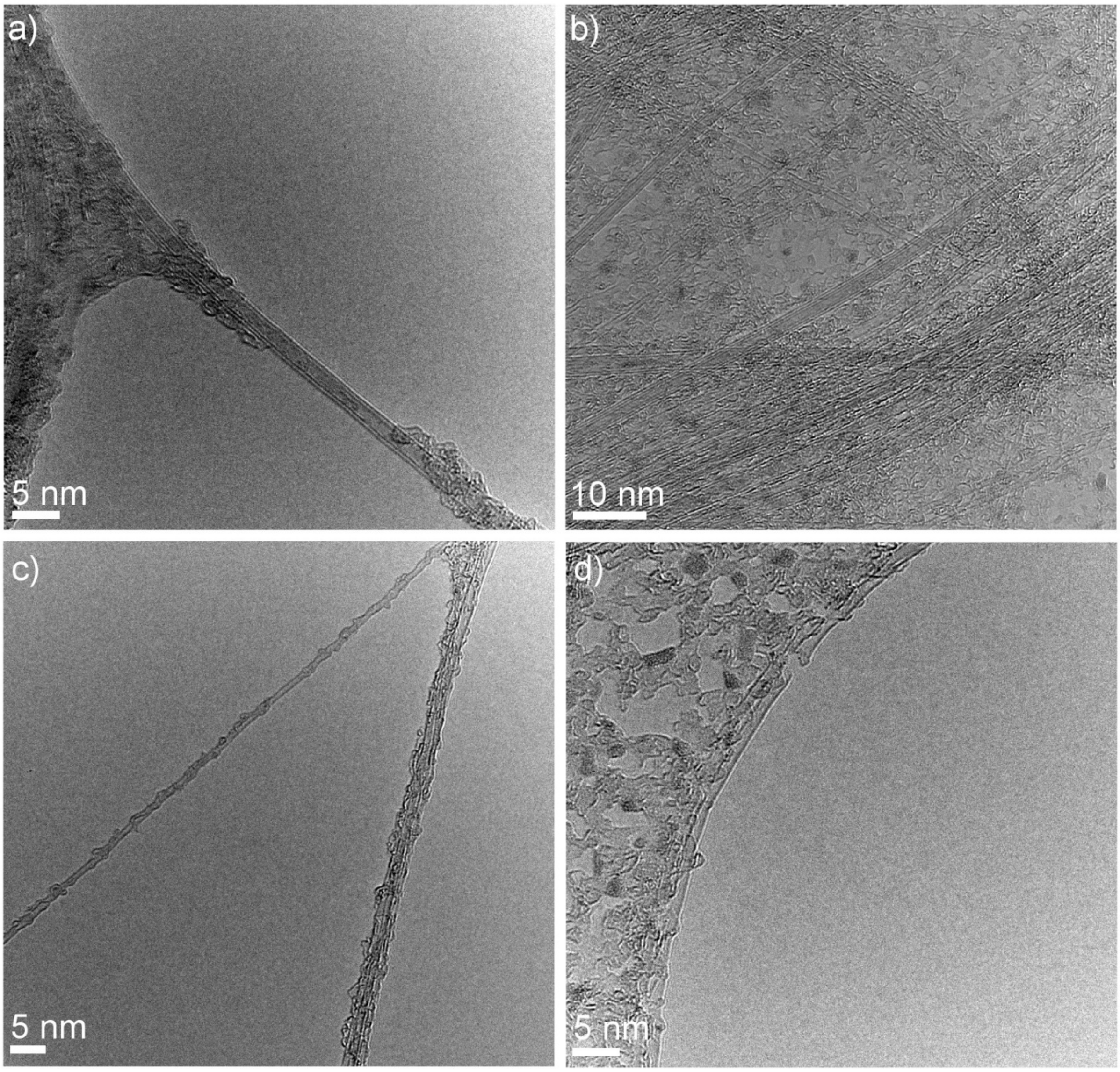

Figure S11 Representative HRTEM micrographs of Band 4 of the sorted DWCNT material.

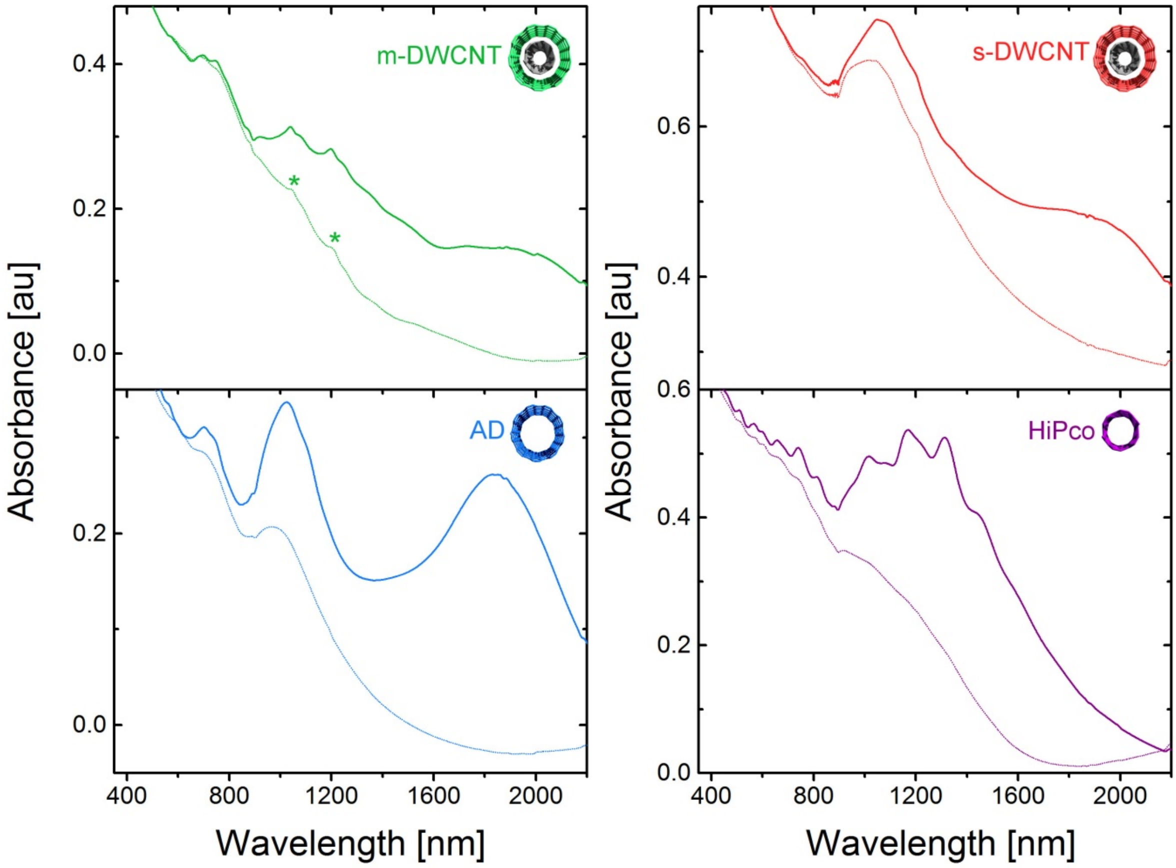

Figure S12 Absorption spectra of the nanotube films before (solid line) and after (dashed line) doping. Thin films of the sorted DW, AD SWCNT and HiPco SWCNTs were prepared by vacuum filtration[S10] and then transferred onto clean glass substrates. The presence of DWCNT and SWCNT fractions was verified via the method outlined by Green and Hersam,[S8,S11] which uses thionyl chloride doping of nanotube thin films. This strongly electron withdrawing treatment has been shown to suppress small band gap optical transitions by shifting the Fermi level of semiconducting nanotubes down into the highest occupied molecular orbital (HOMO) band. Thus, the S_{11} and even some S_{22} optical transitions (for large diameter nanotubes) are quenched in the case of DWCNTs where the outer wall provides some shielding (although not complete)[S9,S12] of the inner wall. Transitions that are strongly quenched are indicative of nanotubes exposed to the altered chemical environment i.e. the outer wall nanotubes. Figure S12 shows the absorption spectra of m- and s-DWCNTs as well as the AD and HiPco controls. As was also observed in the solution measurements, the m-DWCNT film is characterized by the M_{11} absorption of large diameter metallic nanotubes (600 – 800 nm) and the S_{11} absorption of small diameter nanotubes (1050 – 1250 nm). However, for the film measurements, underlying broad peaks at 900 – 1300 nm and 1500 - 2200 nm become apparent and are attributed to S_{22} and S_{11} of large diameter nanotubes, respectively. This further highlights the fact that the separation of m-DWCNT is not as complete as for the s-DWCNTs. In this regard, the purity presented by Green and Hersam[11] for m-DWCNTs using the DGU method remains superior. Upon chemical doping the peaks associated with the large diameter S_{11} and S_{22} transitions are suppressed while the M_{11} outer wall peaks remaining persistent. It is also interesting to note that the S_{11} of small diameter SWCNTs (assigned as inner wall nanotubes) are also persistent after doping, indicating a certain level of shielding by the outer wall, as demonstrated by Green and Hersam.[S8] For clarity, these peaks have been highlighted with stars. In comparison, it is noted that all S_{11} peaks (900 - 1300 nm) are suppressed after doping of the HiPco control.

The s-DWCNT film is characterized by S_{22} absorptions centered at 1050 nm and the corresponding S_{11} absorptions between 1600 and 2100 nm. As discussed previously in regards to the solution measurements, these peaks are indicative of large diameter semiconducting nanotubes and are consistent with the AD SWCNT control. Following doping, S_{11} transitions of the outer walls are completely suppressed with a slight suppression of S_{22}. Once again, structure can be seen in the region 900 – 1200 nm and this is associated with the S_{11} transitions of the inner walls. Optical absorption spectra of the sorted fractions were recorded on a Varian Cary 500 spectrophotometer. Films were doped with thionyl chloride (Sigma-Aldrich) by applying a few drops to the surface and then allowing it to dry in air for several minutes.

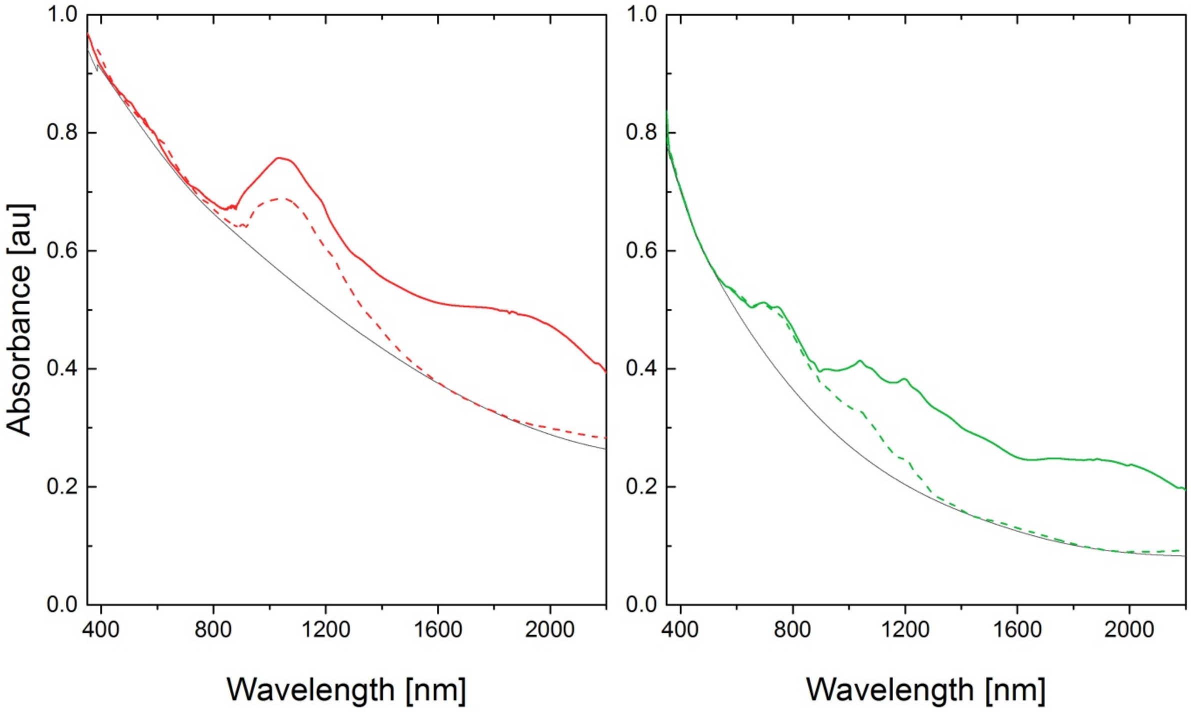

Figure S13 An example of the background subtraction conducted for s-DWCNT and m-DWCNT films to enable purity calculations. Background functions of the semiconducting and metallic spectra were fitted with a spline function using the software ‘fityk’[S13] according to the spectrum of the thionyl chloride treated film, which strongly dopes S_{11} transitions and thus, is expected to represent the true baseline. Following background subtraction, the thionyl chloride treated spectrum was subtracted to enable identification of S_{11} peaks and calculation of the S_{11} peak area. The M_{11} peak area was calculated using the background subtracted pristine spectrum. These peak areas were then compared to AD SWCNTs, which have a known composition of 1:2 M/S. Peak areas for AD SWCNTs were M_{11} 19.5 and S_{11} 234. By comparing m-DWCNT (M_{11} 27 S_{11} 73) and s-DWCNT (M_{11} 2.5 S_{11} 141) peak areas to that of the AD, purities of 70 % and 90 % are obtained.

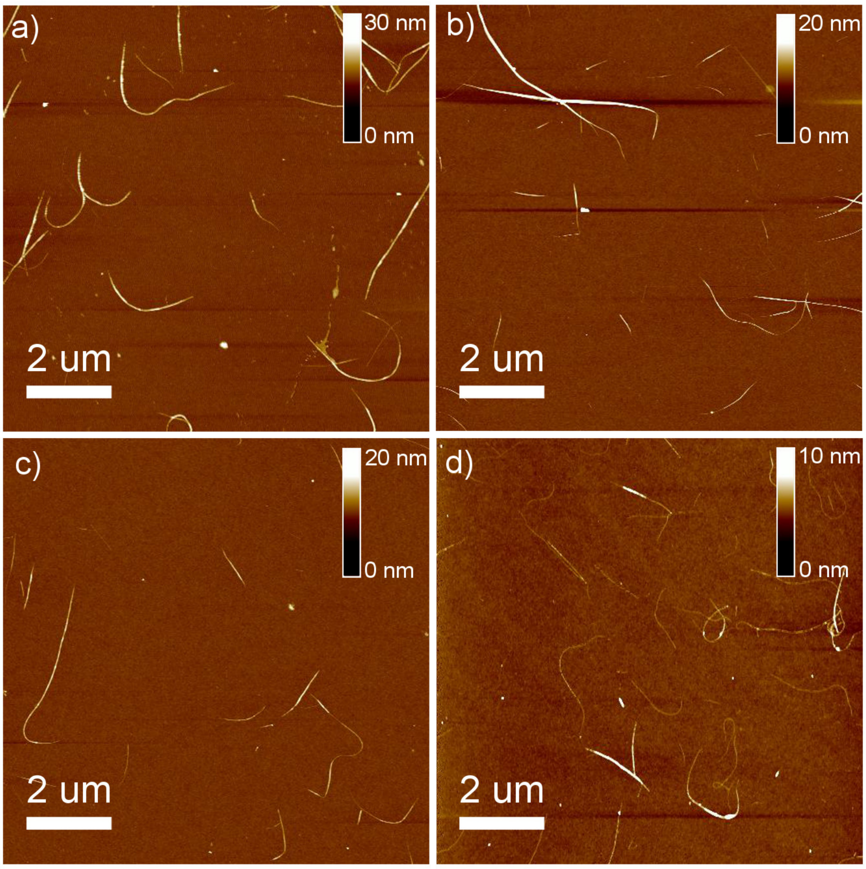

Figure S14 Representative AFM images of a) Band 1 b) Band 2 c) Band 3 and d) Band 4 of separated DWCNT fractions. Height and length scales are indicated for each topographical image.

Statistical height analysis of each band resultant from DWCNT separation is presented in Figure S15. Complete AFM analysis for DWCNT, AD and HiPco separated material can be found in Figure S15 to Figure S17. Immediately apparent from Figure S15 is the similarity between the m-DWCNT and the s-DWCNT height data (Bands 2 and 3), where a large amount of small diameter nanotubes can be seen. This is a surprising result as both TEM and absorption spectroscopy show very little contribution from small diameter nanotubes. Similarly the AD SWCNTs also contain an unusually high portion of small diameter nanotubes (25 % of the total population posses diameters of 1 nm or less) despite the fact that the accepted diameter range for AD produced SWCNTs is 1.3 – 1.7 nm. This large discrepancy may be due to difficulties in sample preparation, where bundling and adhesion may not be consistent across all nanotubes diameters. For instance, if large diameter nanotubes preferentially bundle, they will be excluded from the AFM analysis, leaving the results skewed towards individualized smaller diameter nanotubes. Similarly, if the surface adhesion forces are different for small and large diameter nanotubes, which may be the case as they experience different amounts of surfactant wrapping, this may skew the results also. Despite the conflict with absorption and TEM data, it can be seen that the large diameter species corresponding to m-DWCNTs and s-DWCNTs have average diameters of 1.61 ± 0.14 nm and 1.56 ± 0.04 nm, respectively, which is in agreement with the TEM analysis. In our previous work on the separation of SWCNTs from DWCNTs,[S9] a clear length difference between DWCNT and SWCNT fractions was demonstrated however, contrary to that work, no clear length difference can be observed between Bands 1, 2, and 3 (DWCNTs) and Band 4 (SWCNTs) for the DWCNT separation (Figure S15 (b)). This may be because our initial approach dealt with only a select portion of the overall nanotube population (i.e. those nanotubes which became stuck on the gel), compared to the current approach where no nanotube adsorption is apparent and the entire nanotube ensemble is represented.

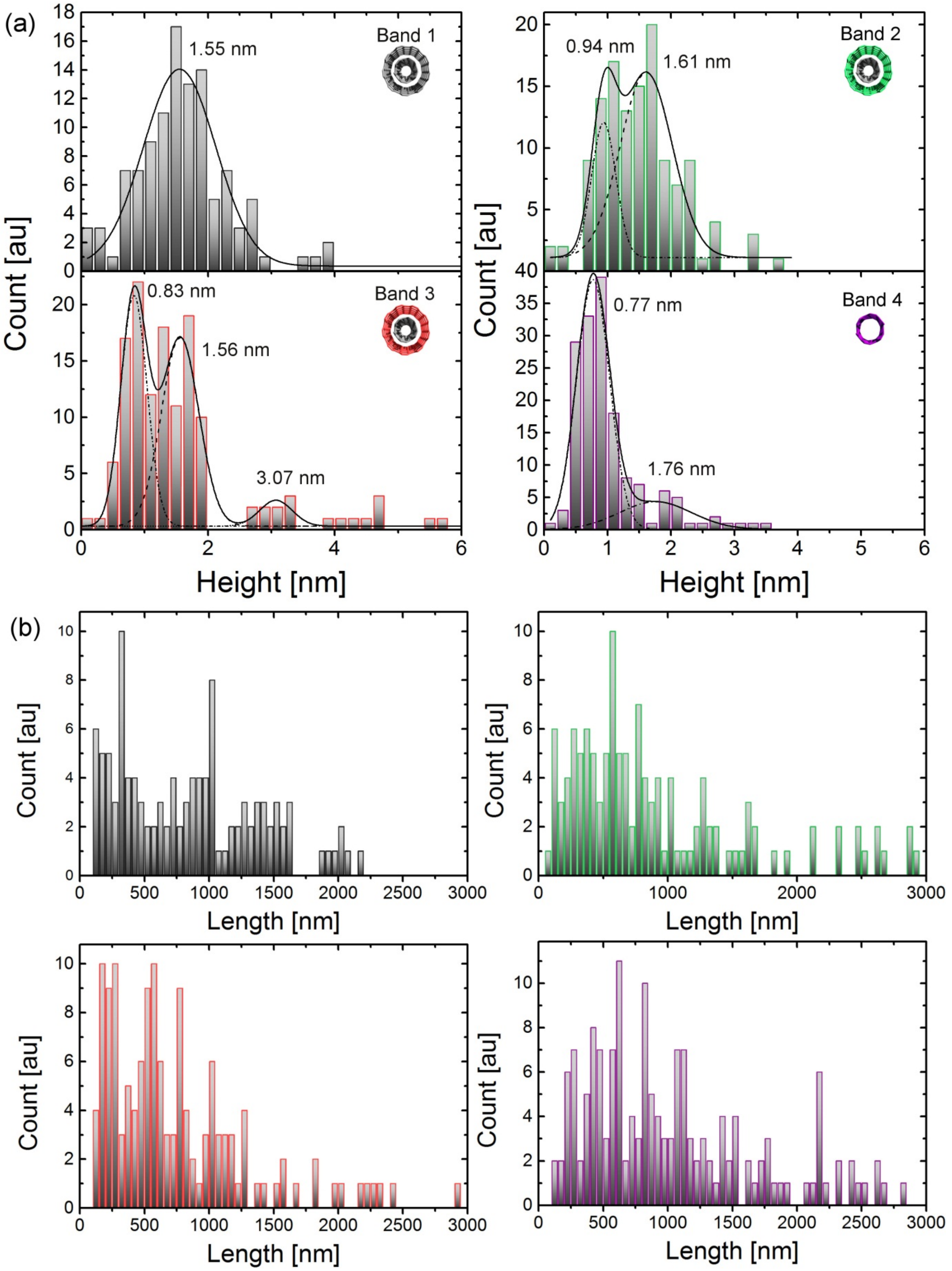

Figure S15 (a) Height and (b) length distributions of DWCNT sorted fractions, as determined from AFM.

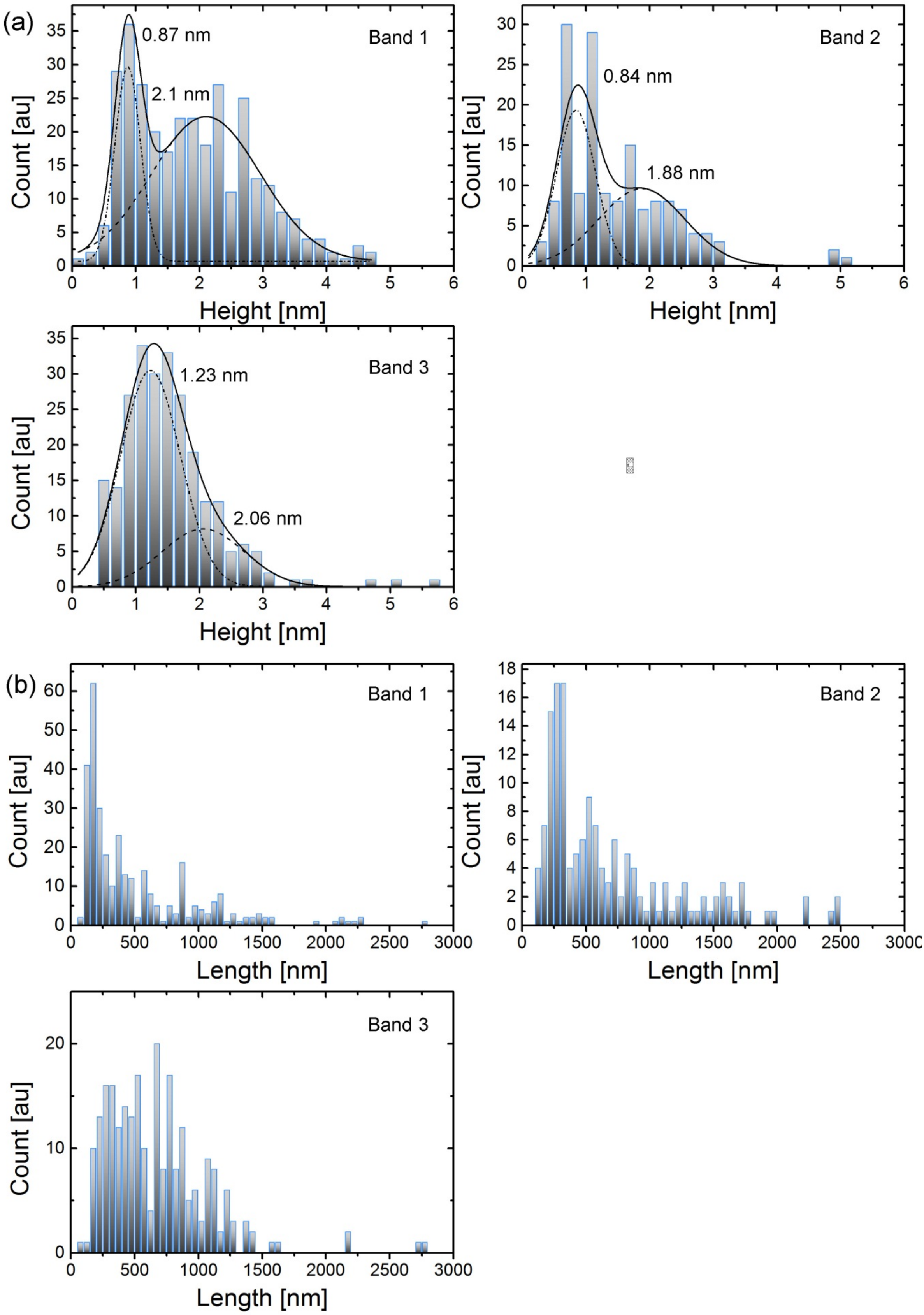

Figure S16 (a) Height and (b) length distributions of AD SWCNT sorted fractions, as determined from AFM.

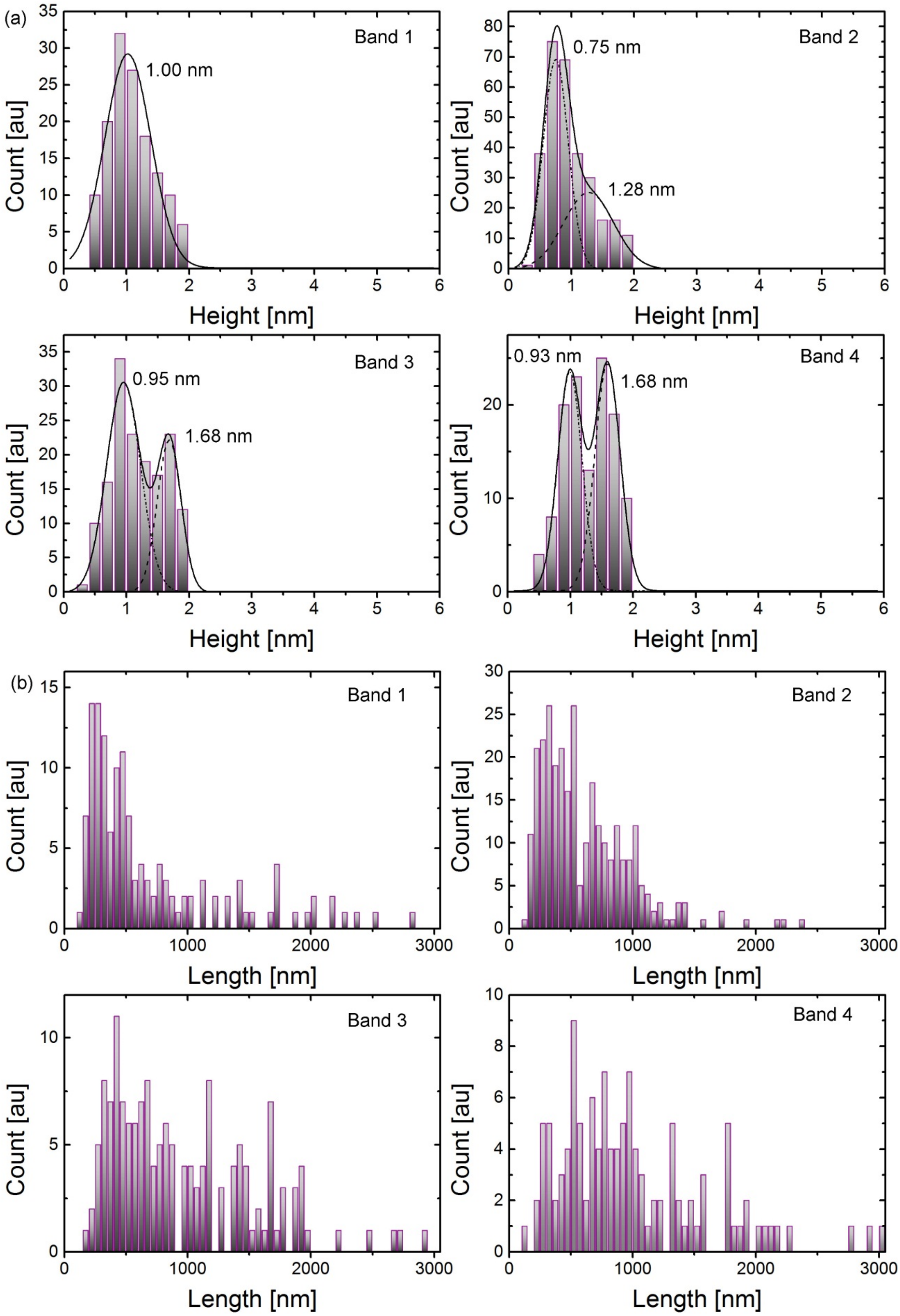

Figure S17 (a) Height and (b) length distributions of HiPco SWCNT sorted fractions, as determined from AFM.

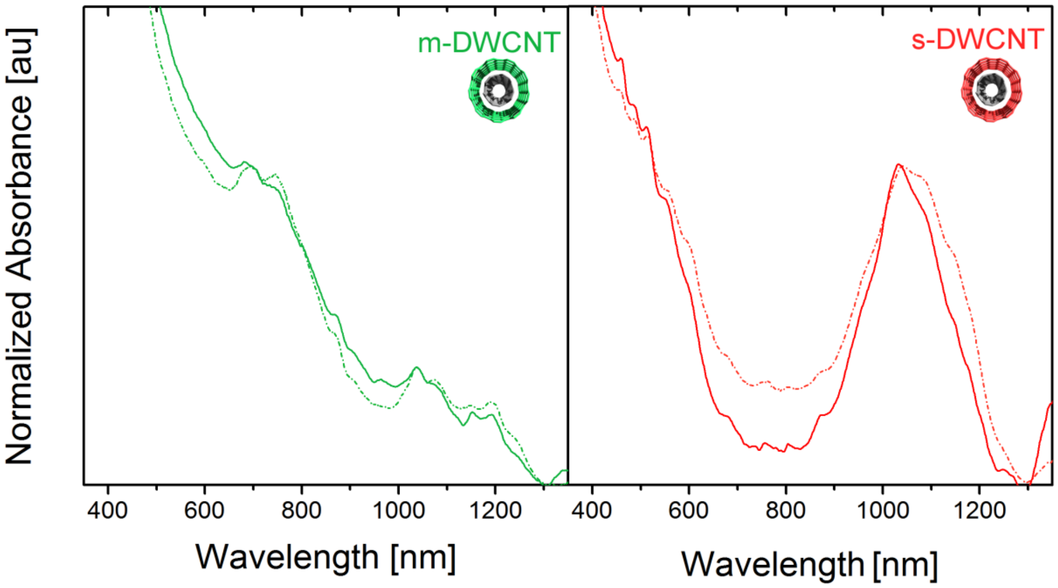

Figure S18 Absorbance spectra of the first (dashed line) and second (solid line) separation of m-DWCNT and s-DWCNT fractions.

In an attempt to improve the purity of the separated m- and s-DWCNT fractions, a subsequent separation step was conducted. The starting material for this step was prepared by taking ~6 mL of previously separated m- or s-DWCNT solution (eluted with 1 % SDS) and adding 3 mL of 2 wt % SC. This adjustment was necessary to bring the concentration to ~ 1 wt % SC which, when used with a 1 wt % SDS gel column, provides optimum separation, as seen in Figure S7.. This was then added to a gel column at 1 wt % SDS and washed through the column with 1 wt % SDS. Absorption measurements of the purest resultant m- and s-DWCNT samples along with the previously separated starting material are presented in Figure S18. For the m-DWCNTs, it can be seen that there is little difference between the output of the first separation (dashed line) and that of the second separation (solid line). In fact, the material resulting from just one separation step exhibits better M_{11} features. As it is highly unlikely that the solution has become less pure, the reduced M_{11} intensity may be a result of dilution, as indeed both the m-DWCNT and s-DWCNT solutions are also heavily diluted upon subsequent separation. This point is made clearer in Figure S19 where absolute concentration is shown. However, in the case of the s-DWCNT it can be seen that a secondary separation step results in increased purity, evidenced by a reduction in absorbance in the region of 600 – 900 nm. This is the region in which the M_{11} transitions of large diameter metallic nanotubes (DWCNT outer walls) are observed. There is also a depreciation of the large feature centered at ~ 1050 nm which is likely due to the removal of some small diameter SWCNTs. Thus, a second separation step can improve the purity of the s-DWCNT fraction but makes little difference to the m-DWCNT fraction. This is likely due to metallic nanotubes having a reduced interaction with the gel matrix compared to semiconducting nanotubes.[S2-S7]

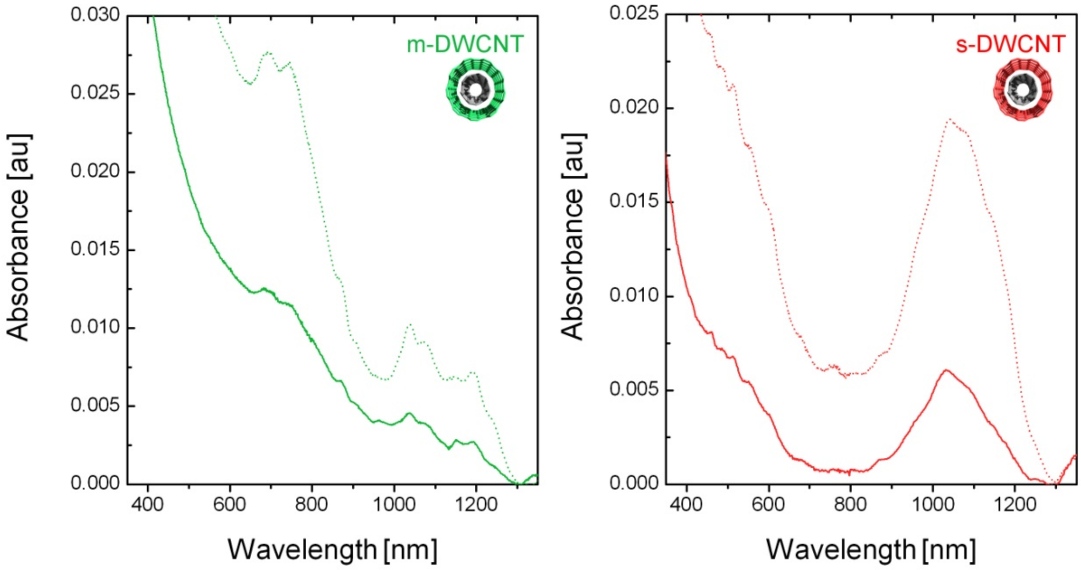

Figure S19 Absorbance spectra of original (dashed line) and second (solid line) separation of m-DWCNT and s-DWCNT fractions without scaling.

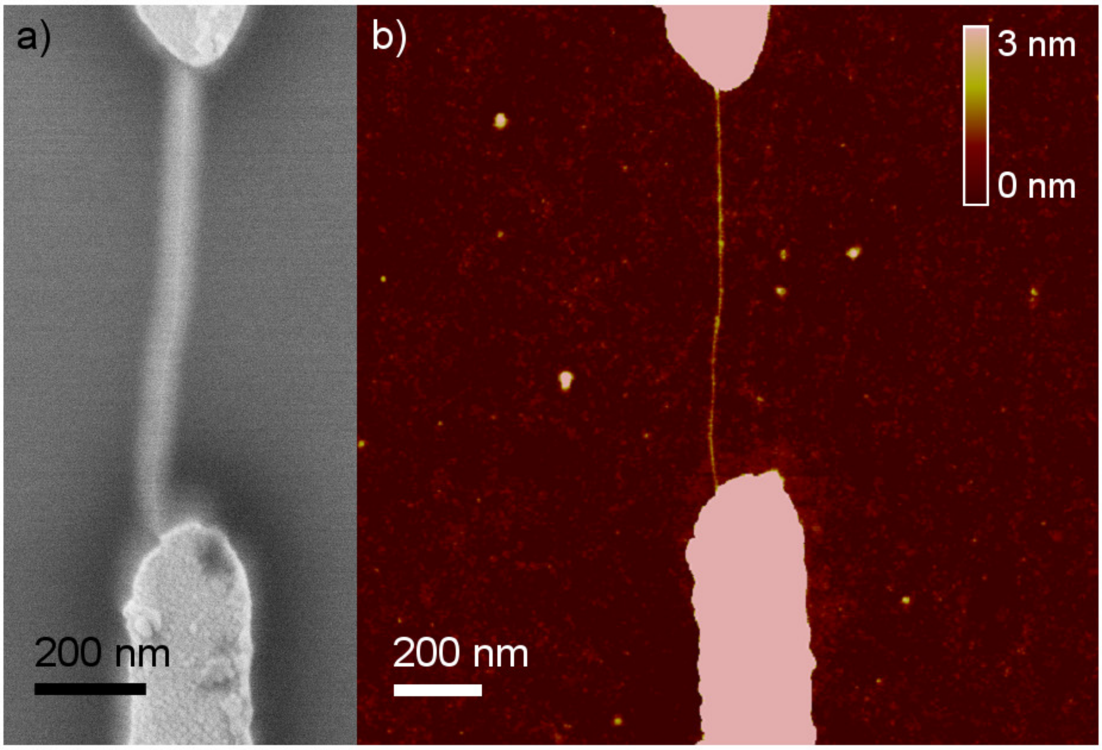

Figure S20 An SEM image of a nanotube electrode and its corresponding AFM image.

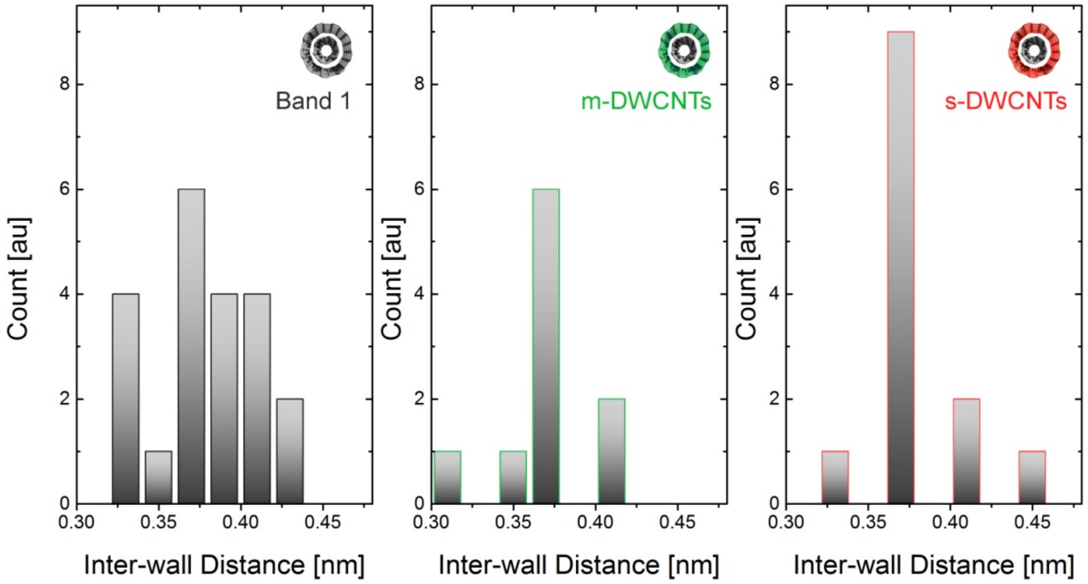

Figure S21 Frequency distributions of the inter-wall distance of Bands 1, 2 and 3, determined by HR TEM. It should be noted that single HRTEM images can be misleading and the focus of the TEM image is pivotal in the calculation of the inter-wall distance. Depending on the focus of the image, the walls appear dark or bright in the image. We have therefore only taken DWCNTs that were in focus and this afforded us an accuracy of ± 0.15 nm. For Band 1 (left), the mode is the range of 0.36 – 0.38 nm and the mean is 0.39 nm. Similarly, Bands 2 (m-DWCNTs) and 3 (s-DWCNTs) have modes in the range of 0.36 – 0.38 nm. The means are 0.37 nm and 0.38 nm, respectively. This is in agreement with previously reported inter-wall spacing.[S14] Interestingly, these values are slightly larger than the ideal inter-wall spacing determined by Okada and Oshiyama, which was found to be 0.352 nm,[S15] however it has been observed that experimental results exhibit substantial distribution around the optimum value. This is certainly the case in this work, with the experimentally determined inter-wall distance ranging between 0.30 and 0.46 nm. An interesting observation from Figure S21. is that Band 1 exhibits significantly more spread of inter-wall distance than the m- or s- DWCNT fractions, which show inter-wall distances within a tight range. This may be a result of the sorting process, which eliminates many (n,m)@(n,m) combinations, thus resulting in a tightening of the inter-wall distance distribution.

References

S1. Zhang, J.; Gui, H.; Liu, B.; Liu, J.; Zhou, C., Comparative Study of Gel-Based Separated Arcdischarge, Hipco, and Comocat Carbon Nanotubes for Macroelectronic Applications. Nano Res. 2013, 6, 906-920.
S2. Blanch, A. J.; Quinton, J. S.; Shapter, J. G., The Role of Sodium Dodecyl Sulfate Concentration in the Separation of Carbon Nanotubes Using Gel Chromatography. Carbon 2013, 60, 471-480.
S3. B. S. Flavel, M. M. Kappes, R. Krupke, F. Hennrich, ACS Nano 2013, 7, 3557.
S4. Flavel, B. S.; Moore, K. E.; Pfohl, M.; Kappes, M. M.; Hennrich, F., Separation of Single-Walled Carbon Nanotubes with a Gel Permeation Chromatography System. ACS Nano 2014, 8, 1817-1826.
S5. Moshammer, K.; Hennrich, F.; Kappes, M., Selective Suspension in Aqueous Sodium Dodecyl Sulfate According to Electronic Structure Type Allows Simple Separation of Metallic from Semiconducting Single-Walled Carbon Nanotubes. Nano Res. 2009, 2, 599-606.
S6. H. Liu, D. Nishide, T. Tanaka, H. Kataura, Nat. Comm. 2011, 2, 309.
S7. Tvrdy, K.; Jain, R. M.; Han, R.; Hilmer, A. J.; McNicholas, T. P.; Strano, M. S., A Kinetic Model for the Deterministic Prediction of Gel-Based Single-Chirality Single-Walled Carbon Nanotube Separation. ACS Nano 2013, 7, 1779-1789.

S8. Green, A. A.; Hersam, M. C., Properties and Application of Double-Walled Carbon Nanotubes Sorted by Outer-Wall Electronic Type. ACS Nano 2011, 5, 1459-1467.

S9. Moore, K. E.; Pfohl, M.; Hennrich, F.; Chakradhanula, V. S.; Kuebel, C.; Kappes, M. M.; Shapter, J. G.; Krupke, R.; Flavel, B. S., Separation of Double-Walled Carbon Nanotubes by Size Exclusion Column Chromatography. ACS Nano 2014, 8, 6756-64.

S10. Wu, Z.; Chen, Z.; Du, X.; Logan, J. M.; Sippel, J.; Nikolou, M.; Kamaras, K.; Reynolds, J. R.; Tanner, D. B.; Hebard, A. F., et al., Transparent, Conductive Carbon Nanotube Films. Science 2004, 305, 1273-1276.

S11. Green, A. A.; Hersam, M. C., Processing and Properties of Highly Enriched Double-Wall Carbon Nanotubes. Nat. Nanotechnol. 2009, 4, 64-70.

S12. Kalbac, M.; Green, A. A.; Hersam, M. C.; Kavan, L., Tuning of Sorted Double-Walled Carbon Nanotubes by Electrochemical Charging. ACS Nano 2010, 4, 459-469.

S13. Wojdyr, M., Fityk: a general-purpose peak fitting program. J. Appl. Cryst. 2010, 43, 1126.

S14. Moradian, R.; Azadi, S.; Refii-Tabar, H., When Double-Wall Carbon Nanotubes Can Become Metallic or Semiconducting. J. Phys. Condens. Matt. 2007, 19, 176209.

S15. Okada, S.; Oshiyama, A., Curvature-Induced Metallization of Double-Walled Semiconducting Zigzag Carbon Nanotubes. Phys. Rev. Lett. 2003, 91, 216801.

– This page intentionally left blank –

3. Supporting Information

3.3.1 *Aligned Carbon Nanotube Thin Films from Liquid Crystal Polyelectrolyte Inks*

D. D. Tune, A. J. Blanch, C. J. Shearer, K. E. Moore, M. Pfohl, J. G. Shapter,
B. S Flavel

Applied Materials & Interfaces (2015) 25857–25864

DOI: 10.1021/acsami.5b08212

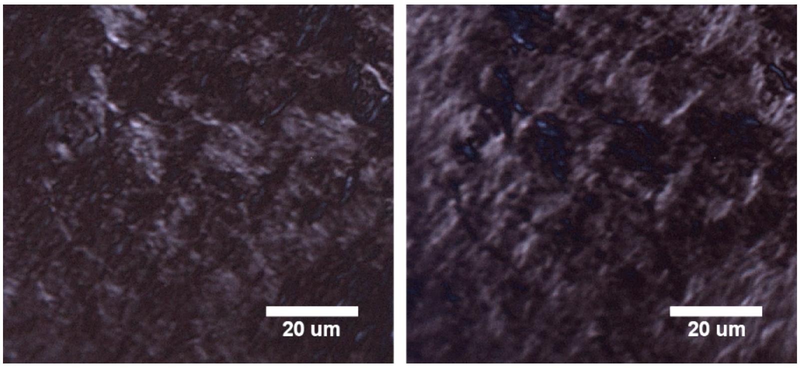

Figure S1 Cross polarized microscopy images of a carbon nanotube polyelectrolyte solution showing birefringence as evidenced by inversion of domain transmittance (brightness) as the polarization of the illumination is rotated between (a) and (b).

The images in Figure S1 were obtained by placing a small drop of nanotube solution between two microscope slides and compressing enough so that the liquid film is no longer opaque. As with the aligned film formation, this process was performed in a glove box under argon, with partial pressures of water and oxygen < 0.5 ppm. The slides with the liquid films were then sealed with parafilm before being removed from the glove box and measured immediately under the optical microscope. Images were taken from the middle of the film, far away from the edges of any bubbles or of the liquid film itself, where drying effects cause pronounced crystallinity which is not representative of the state of the solution. The inversion of the variation in brightness as the polarization is rotated between left and right images is indicative of the liquid crystal phase, with domain sizes of up to ~10 mm (grain boundary density of 0.1 mm^{-1}), though this varies considerably within and between samples. The solution is not biphasic, as evidenced by the lack of isotropic regions which would appear dark irrespective of the orientations of the polarizers.

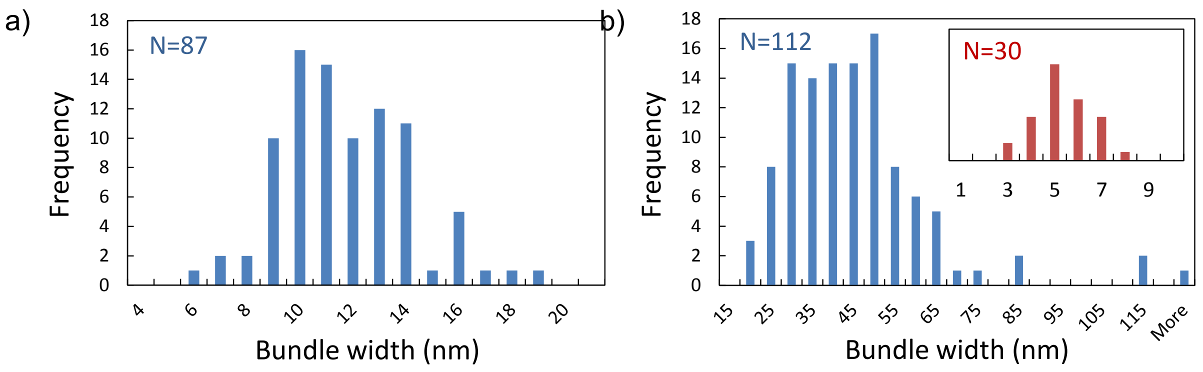

Figure S2 Distributions of bundle widths in (a) PE and (b) CSA films obtained from measurement of bundles observed in SEM images from Figure 2. Inset of (b) shows the width distribution of the smaller, randomly aligned bundles seen in Figure 2 (b).

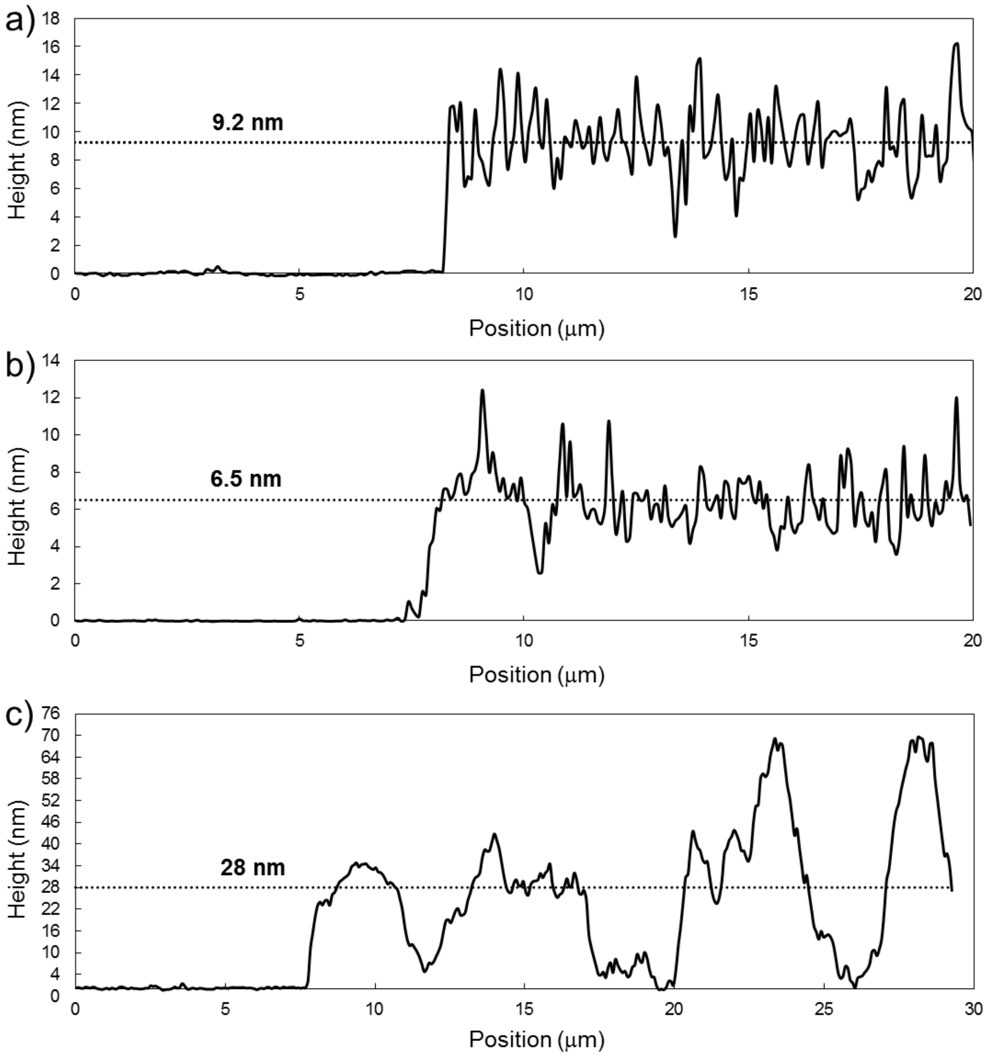

Figure S3 Estimation of film thickness from AFM height measurements of (a) CSA, (b) PE and (c) VF films. In the case of the highly nonhomogeneous VF films the concept of 'thickness' is difficult to justify, however the average height is given nonetheless as a guide to the eye and for a relative comparison with the CSA and PE films. The fact that both the PE and VF films are almost identical in terms of optical transmittance (T_{550} ~ 96 %) further highlights the differences in surface coverage.

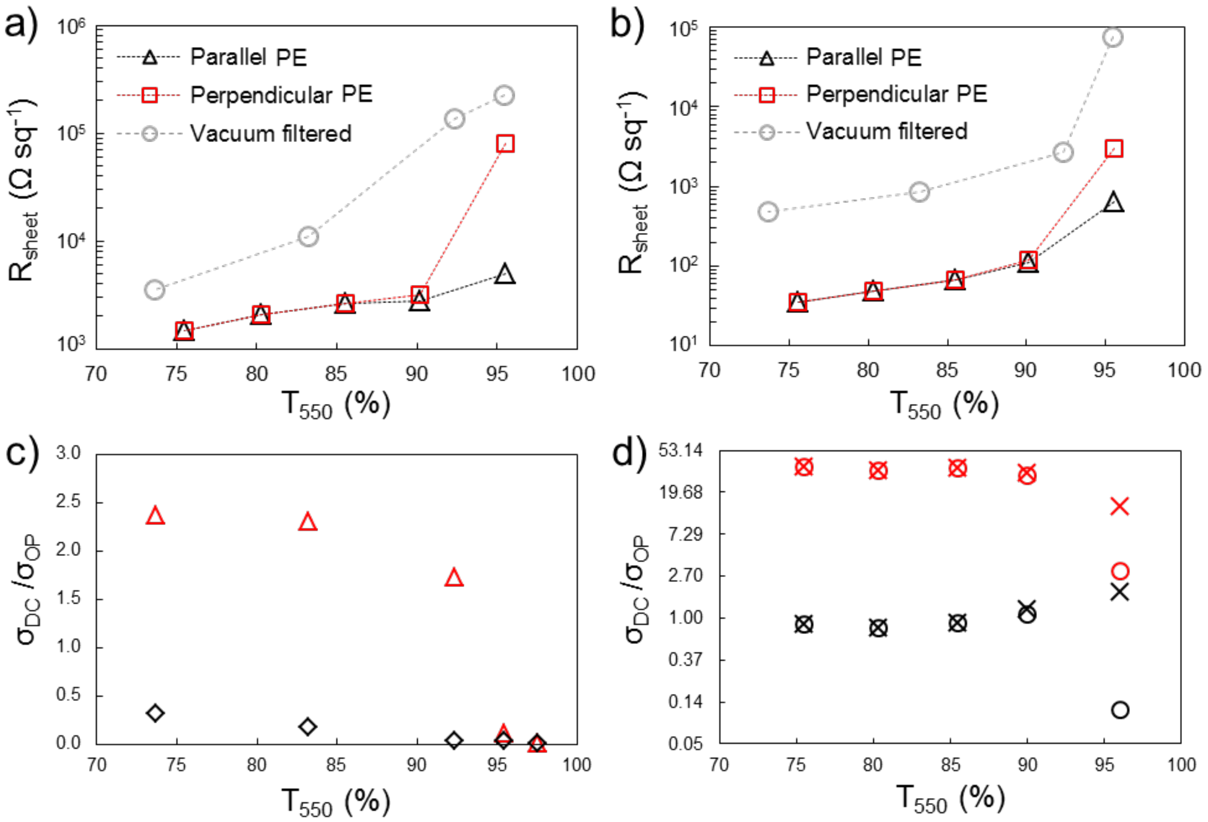

Figure S4 Comparison of the optical absorption of VF and PE films (a) before and (b) after doping with $SOCl_2$, (c) figure of merit of VF film before (black diamonds) and after (red triangles) doping, (d) figure of merit of PE films before (red) and after (black) doping, where crosses indicate measurements that were taken with the linear four-point probe parallel to the alignment director and circles indicate those taken perpendicularly.

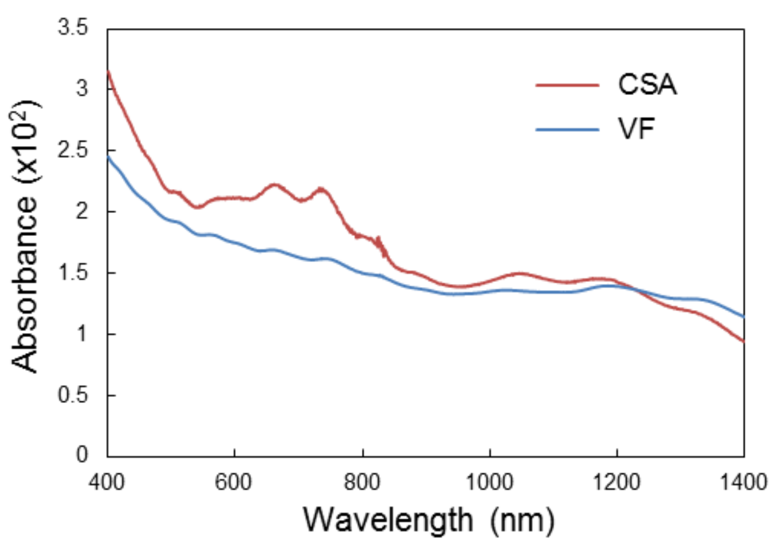

Figure S5 Optical spectra of CSA and VF films for comparison with the spectrum of the PE film shown in Figure 2e. As is usually observed, the characteristic absorbance features of the nanotubes are significantly suppressed in the VF films due to bundling, whilst the S_{11} absorbance features around 950 - 1400 nm in the spectrum of the CSA films are suppressed relative to the S_{22} around 500 – 850 nm due to the doping effect of residual acid.

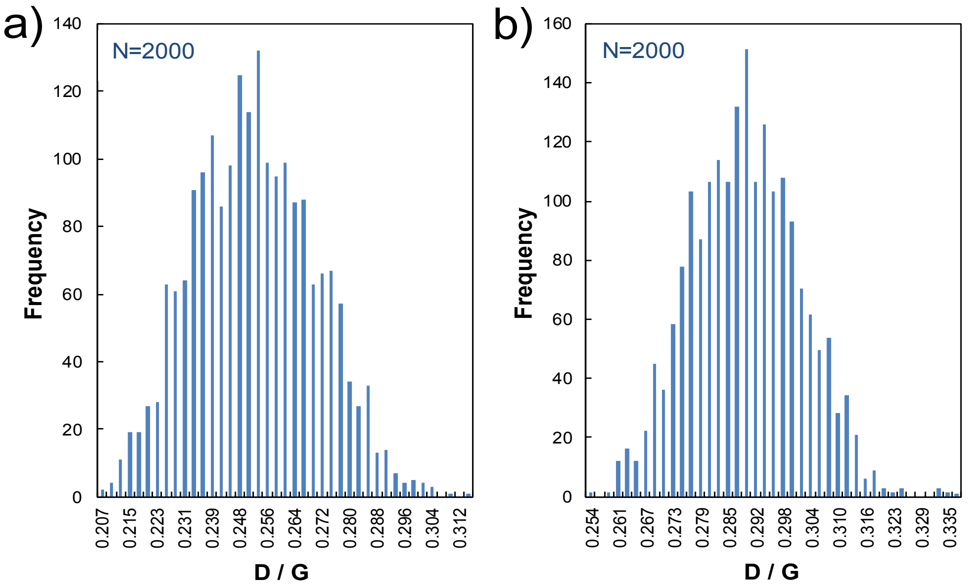

Figure S6 Histograms of the D- to G-band intensity ratio of (a) small diameter semiconducting starting material and, (b) the same material as a PE film. Statistics are extracted from 2000 µm^2 Raman maps of 2000 individual spectra taken with a 532 nm excitation wavelength.

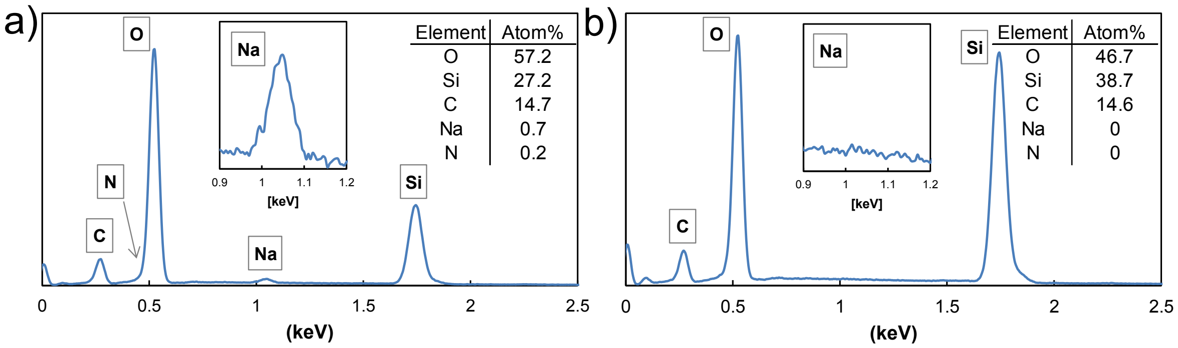

Element	Atom%
O	57.2
Si	27.2
C	14.7
Na	0.7
N	0.2

Element	Atom%
O	46.7
Si	38.7
C	14.6
Na	0
N	0

Figure S7 EDX spectra of PE films (a) as deposited (on silicon with a 300 nm oxide) and, (b) after water transfer to another substrate (silicon with a 100 nm oxide) and subsequent aqueous washing steps. Spectra were obtained over areas of approximately 100 x 100 mm^2.

3.2.2 *Dry Shear Aligning: A Simple and Versatile Method to Smooth and Align the Surfaces of Carbon Nanotubes*

D. D. Tune, B. W. Stolz, M. Pfohl, **B. S. Flavel**

Nanoscale 8 (2016) 3232–3236

DOI: 10.1039/C5NR08784H

Experimental Details

Various kinds of nanotubes were used in this study: commercially obtained small diameter single walled (Raw and SuperPure HiPco, NanoIntegris, USA) as well as material sorted in our labs by gel permeation chromatography from the raw HiPco source, large diameter single walled (P2-SWNT, Carbon Solution Inc, USA), double walled nanotubes (D4L1-5, NanoLab Inc, USA) and small diameter multiwalled nanotubes (NC3100, Nanocyl, Belgium). Further data is provided in Table S1 and the specific type used in each experiment is indicated along with the relevant data. The nanotube films shown in this report were produced by either vacuum filtration from aqueous suspension or by slide-casting from solutions of nanotubes dissolved in sodium polyelectrolyte (PE) inks or chlorosulphonic acid (CSA) (hazardous – read and understand MSDS and handle with care). In the case of vacuum filtration, nanotubes were added to 1 % aqueous TritonX-100 at 0.1 mg mL^{-1} then bath sonicated for 1 h. After centrifugation at 20 000 g for 20 mins, VF films were captured from the supernatant onto mixed cellulose ester (MCE) membranes (0.45 µm, HAWP, Merck Millipore) and rinsed thoroughly with copious DI water. Films were deposited by placing them nanotube side down on the desired substrate; they were then wet with a drop of water, compressed with Teflon and baked at 110 °C for 15 min. To remove the MCE from the films, the cooled substrates were placed in an acetone (EMSURE, Merck) bath for 30 min then transferred to two fresh acetone baths for a further 30 min each then baked for 10 min at 60 °C in air. Single and double walled nanotubes were dissolved in PE inks by adding freshly cleaved sodium (50 mmol) (ACS reagent, Sigma) to a solution of oven dried (150 °C, 3h) nanotubes in anhydrous DMA (3 mg mL^{-1}) (99.8 %, Alfa-Aesar) in an argon glovebox and stirring vigorously for three days, over which time the solutions evolved from discreet black particles in clear liquid to homogeneously dark bronze inks. Nanotubes were dissolved in CSA by simple addition of the oven-dried powder to the acid (97 %, Merck), followed by stirring for 3 days. It was not possible to dissolve the multiwalled nanotubes used in this study in either CSA or the PE solutions at the concentrations needed. Both CSA and PE films were produced in inert atmosphere by solution shearing a.k.a slide casting a.k.a shear casting. This involves placing a small drop (3-5 mL) in between two glass slides, applying a compressive force of between 40 - 80 N (corresponding to an applied pressure of 27 – 43 kPa on the 7.5 x 2.5 cm^2 glass slides used) and then rapidly drawing the slides apart at a shear velocity of ~0.01 m s^{-1}. After evaporation of the solvent, the films are exposed to atmosphere then redeposited onto fresh glass slides by aqueous transfer. This involves floating the films onto water by slowly immersing the glass slides at a near horizontal orientation, allowing the surface tension of the water to peel the film from the glass surface. The floating film can be exposed to various aqueous and water-miscible reagents or immediately transferred to a new substrate by simply lifting the target substrate up from underneath the floating film. Residual water remaining after this process is removed by heating to 110 °C in air for 15 min. For DSA on nanotube films attached to filtration membranes, a cylindrical 8 x 30 mm PTFE stirrer bar was used as the aligner. The membranes were placed on a flat glass surface, nanotube side up, and held in place while the stirrer bar was very firmly (~ 60 N) sheared across the film surface at around 2 - 3 mm s^{-1}. The nanotube films changed in appearance from matt grey/black to become visibly smoother and more reflective, with the direction of shear faintly discernible to the eye. For

DSA on bare nanotube films on glass, silicon, etc, latex (glove) was lightly (5 – 10 N) sheared across the film at around 5 mm s^{-1}. A similar change in appearance of the film occurred as for the films on the filtration membranes.

Table S1 Properties of the nanotubes used in this study

Type	Supplier	Product	Diameter (nm)	Length (μm)	Carbon purity (%)	Nanotube purity[#]
Single	NanoIntegris	Raw HiPco	0.8 - 1.2	0.1 - 1	> 65	high
Single	NanoIntegris	SuperPure HiPco	0.8 - 1.2	0.1 - 1	> 95	very high
Single	*gel sorted (6,5) from raw HiPco		0.75 - 0.85	0.1 - 1	> 95	very high
Single	Carbon Solutions	P2-SWNT	1.4	0.5 - 3	> 90	high
Double	NanoLab	D4L1-5	3 - 5	1 - 5	> 95	low
Multi	Nanocyl	NC3100	9.5	1.5	> 95	very high

[#] qualitative estimate from SEM images

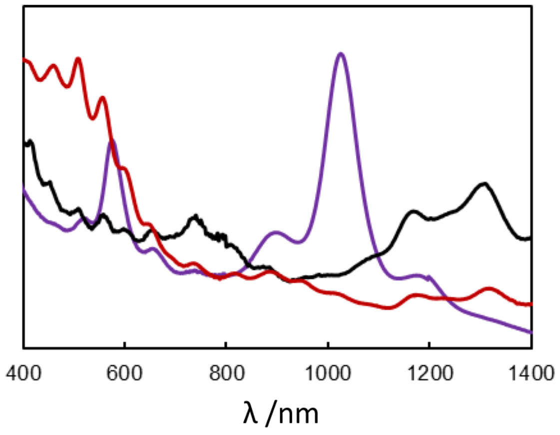

Figure S1 Absorption spectra of small diameter single walled nanotubes (Raw HiPco, NanoIntegris, USA) (black) as well as the 'metallic' fraction (red) and (6,5) chirality (purple) sorted from the raw material via gel chromatography.

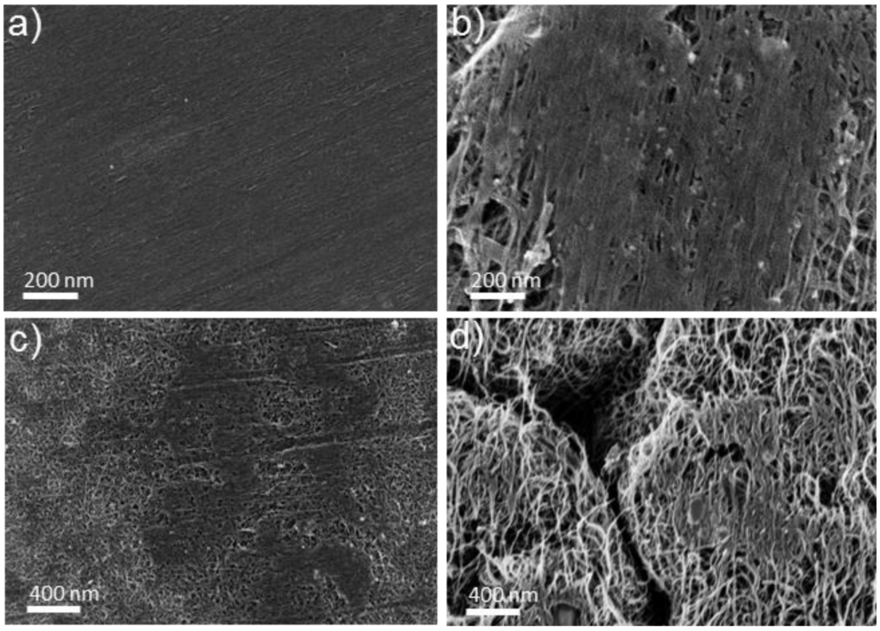

Figure S2 SEM images of films showing dependence of the extent of rearrangement of the films on the nanotube diameter where the images show nanotube films, vacuum filtered from surfactant solutions, where DSA has been applied directly on the membrane using a Teflon aligner, (a) small diameter single walled nanotubes flattened and highly aligned, (b) large diameter single walled nanotubes flattened and aligned in patches, (c) double walled nanotubes flattened and aligned in patches and (d) multiwalled nanotubes flattened and marginally aligned in patches. All films were identically prepared using the same surfactant and were of similar thickness. The images were obtained from the films whilst still bound to the filtration membrane.

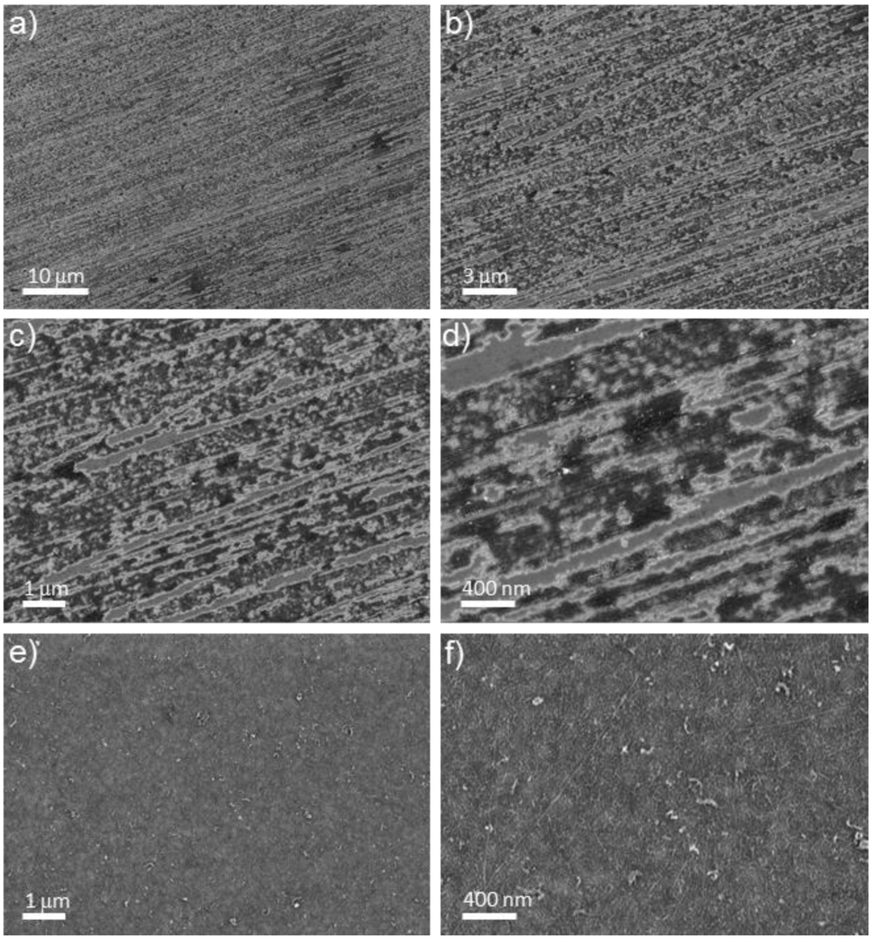

Figure S3 (a-d) SEM images at various magnifications showing tearing of films during DSA due to impurities and particulates leading to poor adhesion and uneven distribution of pressure. Films were formed from DW nanotubes (D4L1-5, NanoLab Inc, USA) slide cast from CSA then transferred to glass. The sheet resistance increased from ~70 kΩ for the freshly transferred films on glass, to >100 MΩ after DSA due to the severe disruption of the films by the tearing of the material from the substrate, (e-f) shows the same films before DSA.

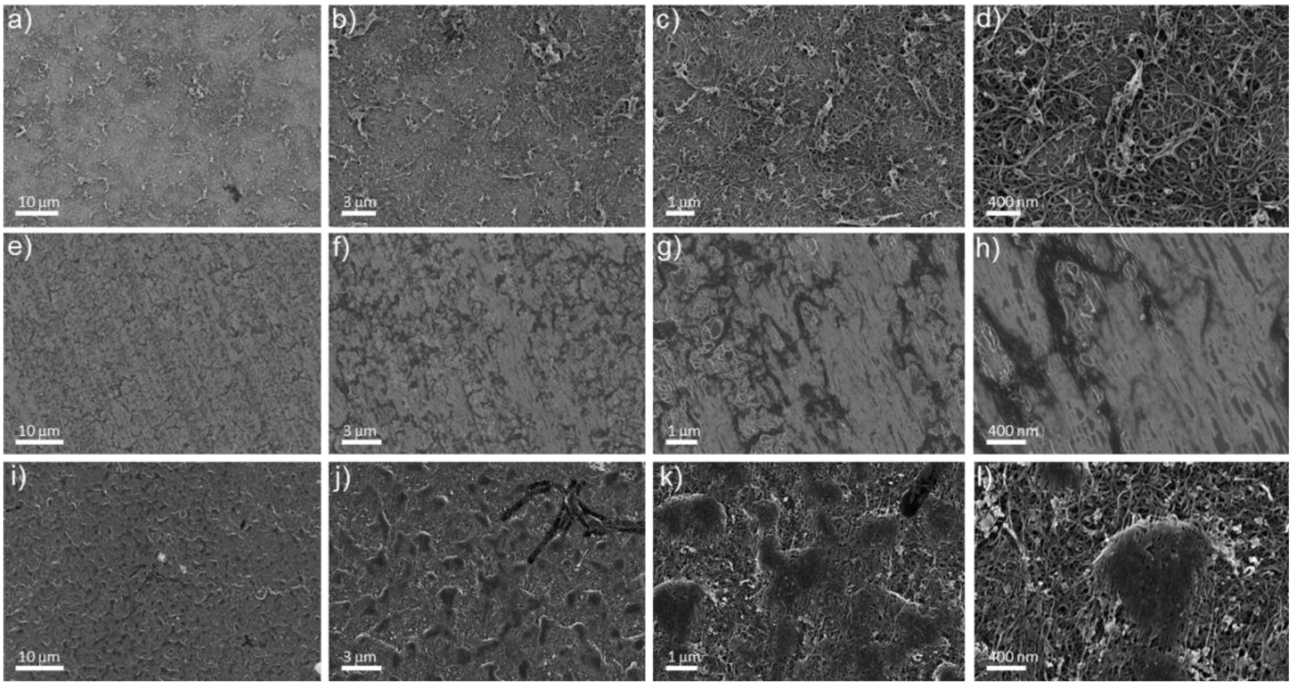

Figure S4 Large diameter single walled nanotube films, vacuum filtered from surfactant solutions, at different magnifications, (a-d) bare film, (e-h) DSA applied to film after transfer onto glass, (i-l) DSA applied directly on membrane. The nanotubes (P2-SWNT, Carbon Solutions Inc, USA) were filtered from 1 % aqueous TritonX-100 suspension formed by 1 h bath sonication onto 0.45 µm mixed cellulose ester membranes (Merck Millipore, Germany).

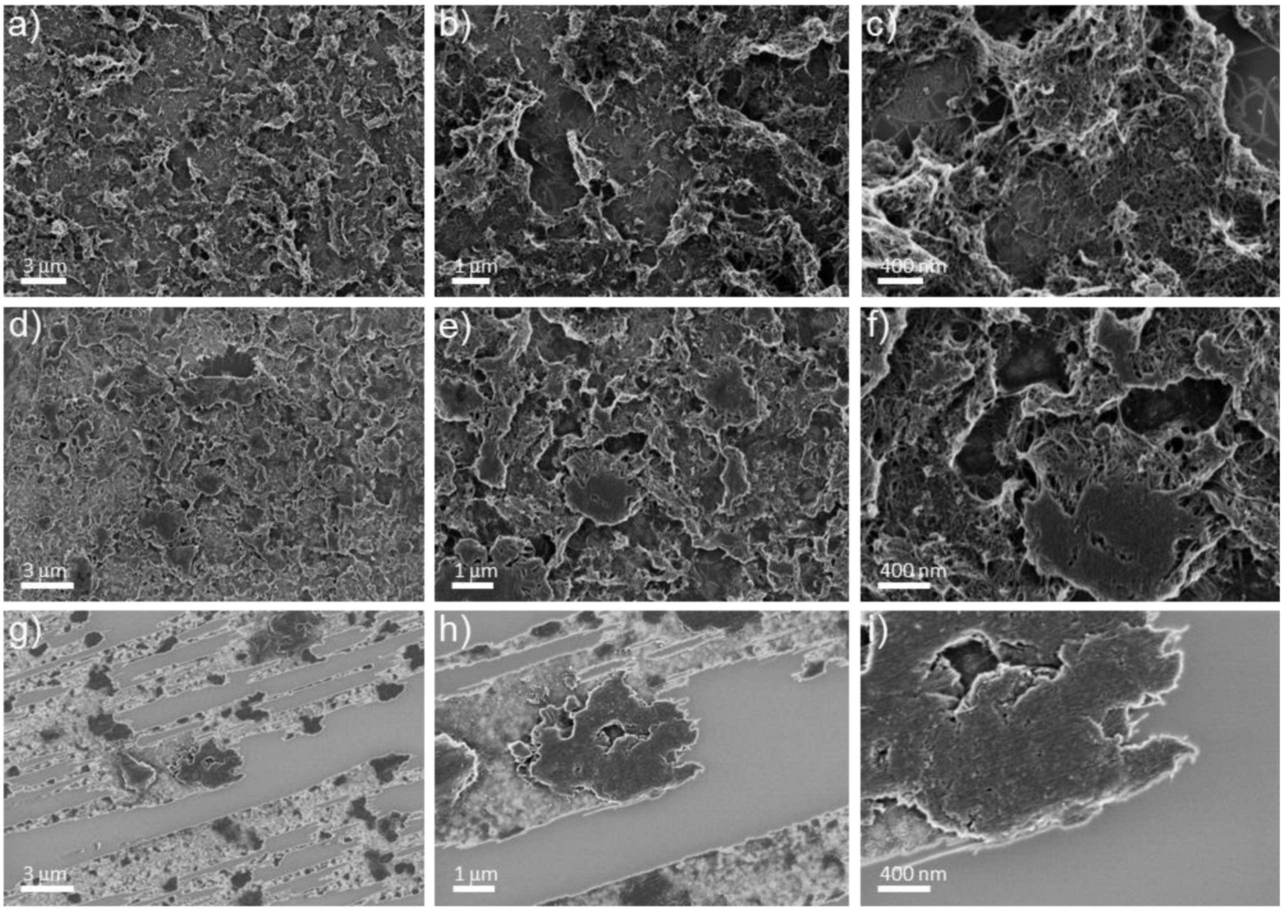

Figure S5 Double walled nanotube films, vacuum filtered from surfactant solutions, at different magnifications showing, (a-c) bare films and, (d-f) DSA applied directly on membrane. As shown in (g-i), it was not possible to perform DSA on films after transfer to glass due to tearing of the film caused by high level of impurities and particulates. The nanotubes (D4L1-5, NanoLab Inc, USA) were filtered from 1 % aqueous TritonX-100 suspension onto 0.45 mm mixed cellulose ester membranes (Merck Millipore, Germany).

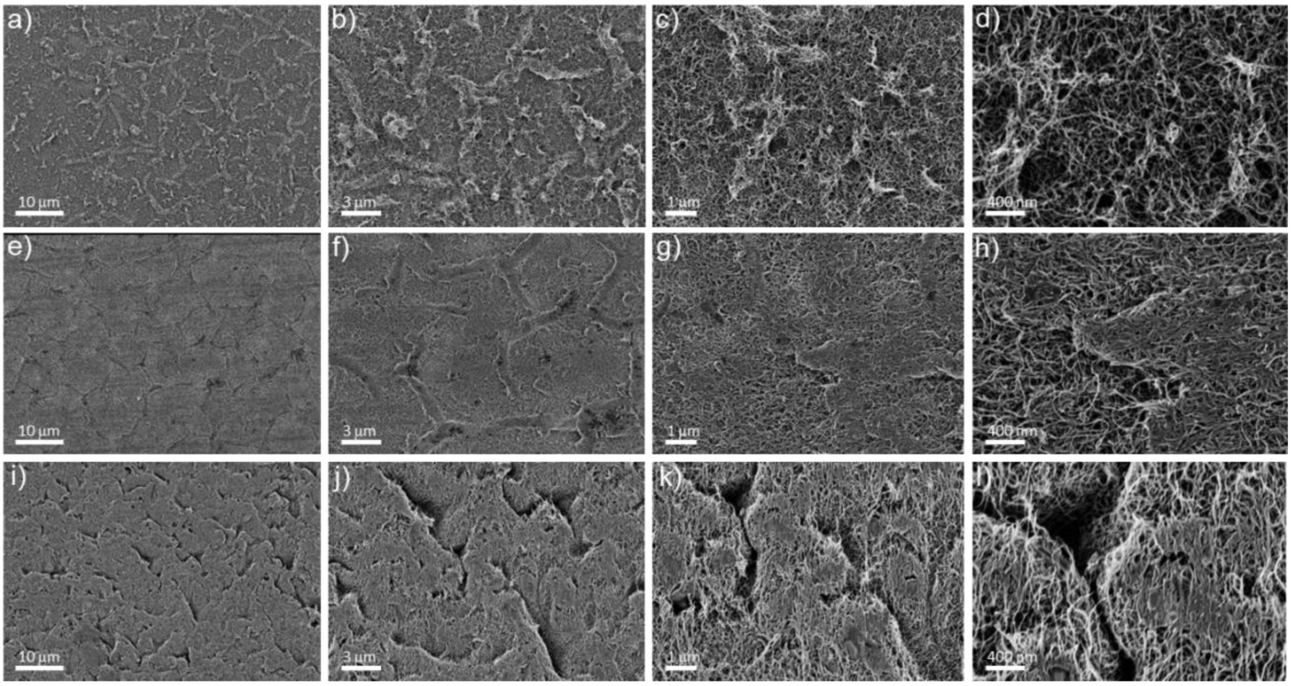

Figure S6 Multiwalled nanotube films, vacuum filtered from surfactant solutions, at different magnifications, (a-d) bare films, (e-h) DSA applied to film after transfer onto glass, (i-l) DSA applied directly on membrane. The nanotubes (NC3100, Nanocyl, Belgium) were filtered from 1 % aqueous TritonX-100 suspension onto 0.45 µm mixed cellulose ester membranes (Merck Millipore, Germany).

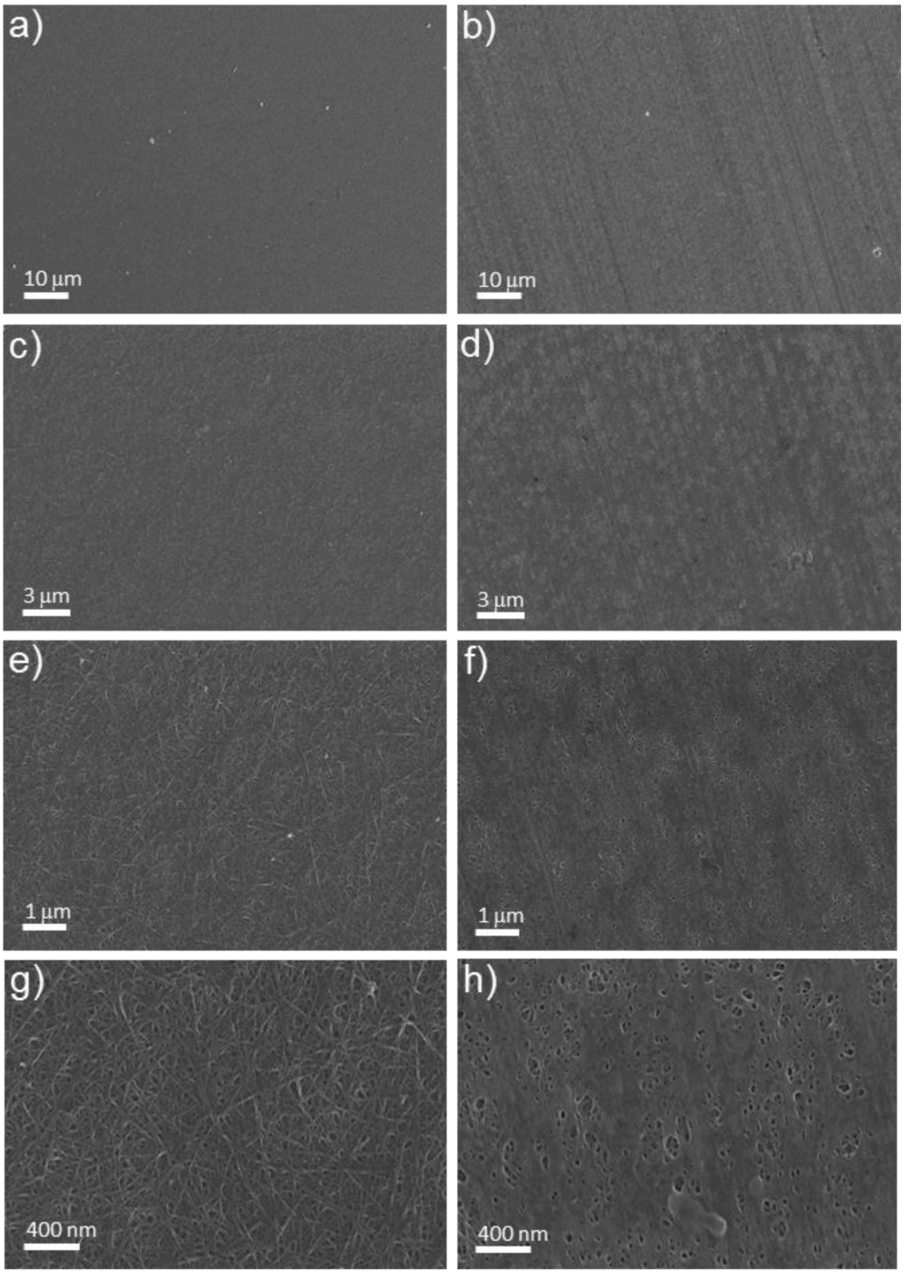

Figure S7 Gel-sorted (6,5) nanotube films formed by slide casting from CSA, (a, c, e, g) as deposited and (b, d, f, h) after transfer to glass and DSA. To prepare the ink for slide casting, the sorted fraction was diluted 1:1 with acetone to aggregate the nanotubes, which were then collected by filtration onto nylon membranes (0.5 µm, Phenomenex, UK) and rinsed with copious DI water and isopropanol. After drying at 130 °C for 4 h the filter cake was fully dissolved in CSA at 3 mg mL^{-1}.

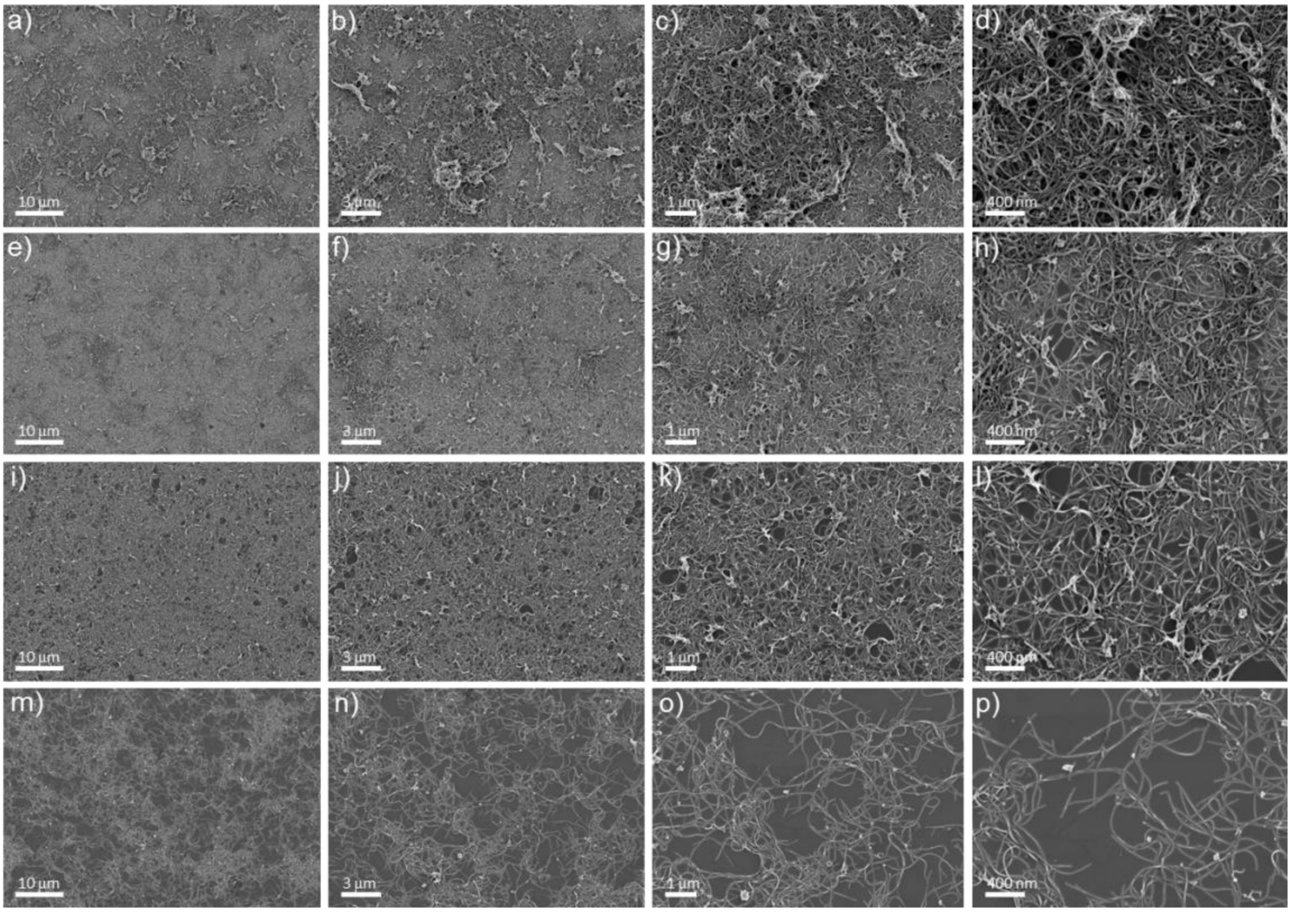

Figure S8 As deposited large diameter single walled nanotube films of varying thickness, vacuum filtered from surfactant solutions, at different magnifications; (a-d) T_{550} = 55 %, (e-h) T_{550} = 79 %, (i-l) T_{550} = 89 %, (m-p) T_{550} = 97 %.

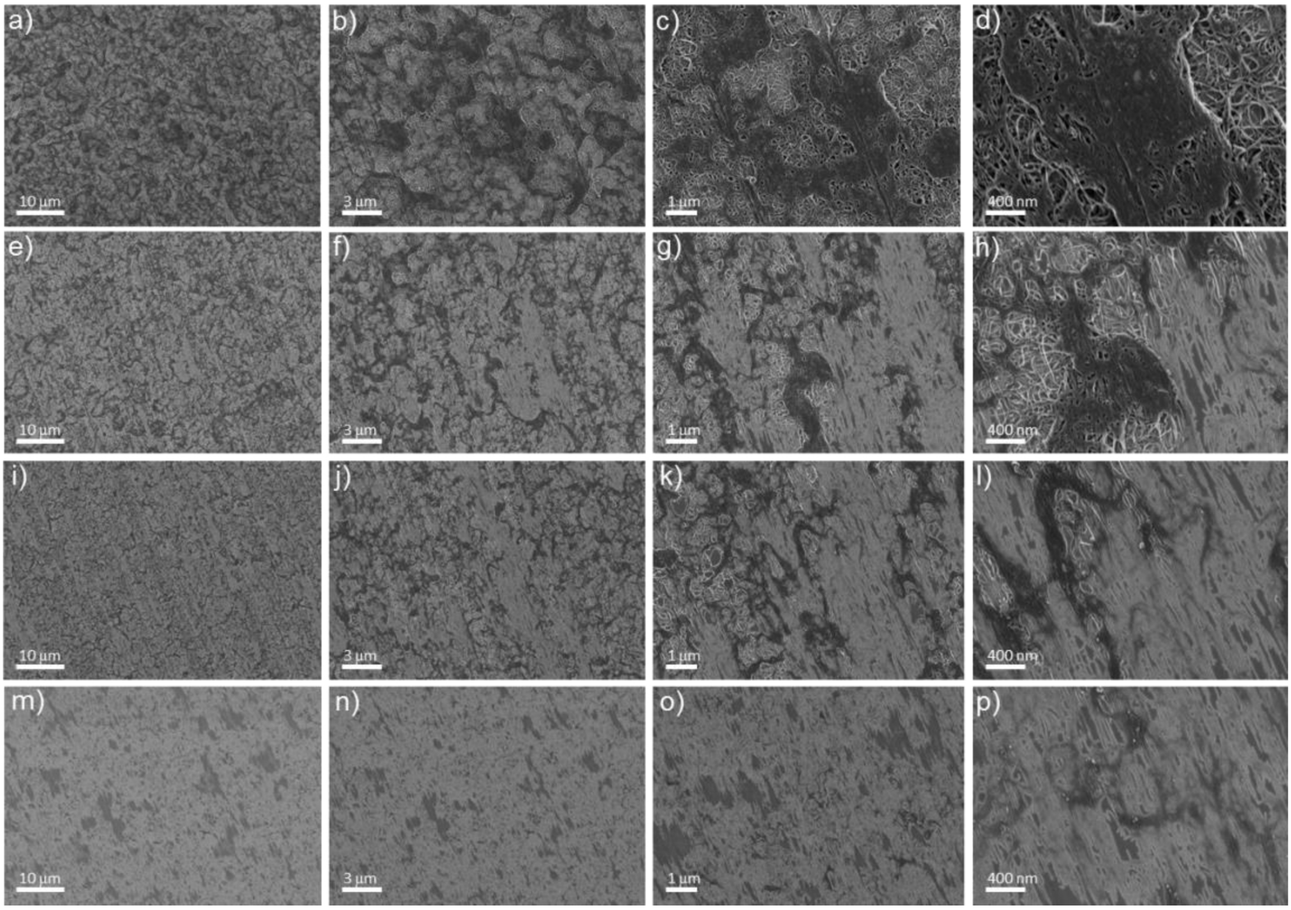

Figure S9 Aligned large diameter single walled nanotube films, vacuum filtered from surfactant solutions, at different magnifications after DSA was applied on top of the films shown in Figure S7; (a-d) T_{550} = 55 %, (e-h) T_{550} = 79 %, (i-l) T_{550} = 89 %, (m-p) T_{550} = 97 %. Note near-monolayer coverage by the thinnest film.

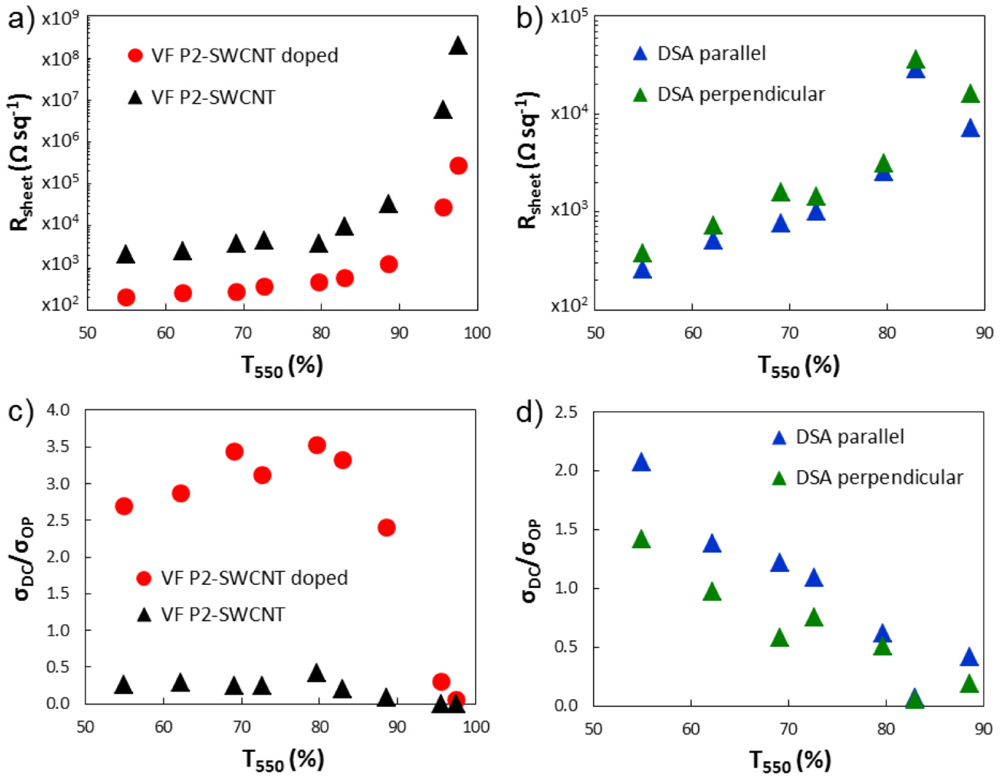

Figure S10 (a) variation in the sheet resistance with film thickness for vacuum filtered films of large diameter single walled nanotubes with and without $SOCl_2$ doping, (b) variation in the sheet resistance with film thickness for vacuum filtered films after DSA taken with the four point probe either parallel or perpendicular to the shear direction, (c) variation in the ratio of DC electrical to optical conductivity with film thickness with and without $SOCl_2$ doping, (d) variation in the ratio of DC electrical to optical conductivity with film thickness, calculated using either the parallel or perpendicular measurements.

The ratio of the electrical to optical conductivity, σ_{DC}/σ_{OP}, was calculated as per Hecht et al.[1] by substituting the measured R_{sheet} and T_{550} values into:

$$T(\lambda) = \left(1 + \frac{1}{2R_S} \cdot \sqrt{\frac{\mu_0}{\varepsilon_0}} \cdot \frac{\sigma_{OP}(\lambda)}{\sigma_{DC}}\right)^{-2}$$

where μ_0 and ε_0 are the free space permeability and permittivity, respectively.

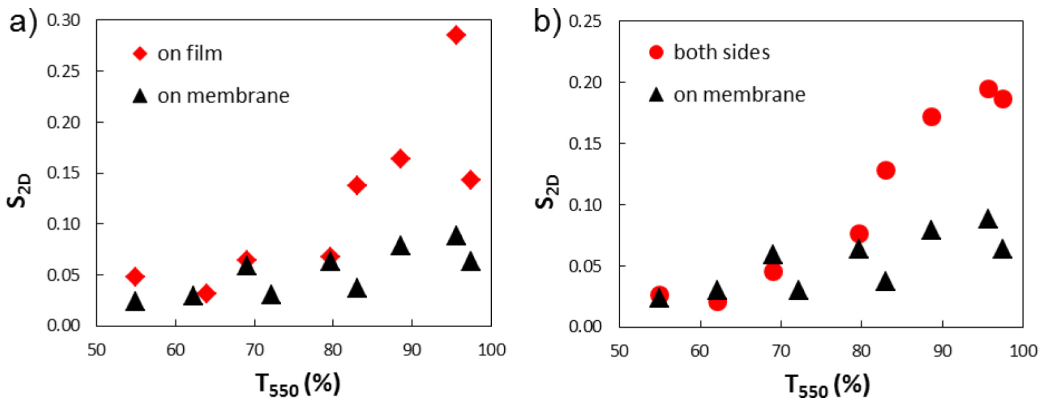

Figure S11 Variation in the 2D order parameter with film thickness where (a) compares DSA performed on the film whilst it is on the filtration membrane i.e., before transfer onto substrate, to DSA performed on the film after transfer onto glass substrate and, (b) compares DSA performed on the film whilst it is on the filtration membrane i.e., before transfer onto substrate, to DSA performed on the same films in the same direction after transfer onto substrate and removal of filtration medium. In both cases the effect of DSA on the film after transfer increases considerably for thinner films with T_{550} > 80 %, compared to the effect of performing DSA on films whilst still on the filtration membrane.

The 2D order parameter was calculated from the polarised optical data via;[2]

$$S_{2D} = (A_{\parallel} - A_{\perp})/(A_{\parallel} + 2A_{\perp})$$

It is possible to quantify surface-only alignment from direct measurement of SEM features using various graphics software packages, yielding much higher values of the order parameter than that stated in the text for the bulk of the film. However, this is a somewhat arbitrary process that depends on the choice of which surface features are considered in the statistics and so we have chosen to rely only on the superior method of polarised optical transmittance measurements, which cannot be affected by observer bias.

References

1. D. S. Hecht, A. M. Heintz, R. Lee, L. Hu, B. Moore, C. Cucksey and S. Risser, Nanotechnology, 2011, 22, 169501.
2. D. L. White and G. N. Taylor, J. Appl. Phys., 1974, 45, 4718-4723.

3. Supporting Information

3.3.1 *The Role of Nanotubes in Carbon Nanotube-Silicon Solar Cells*

D. D. Tune, F. Hennrich, S. Dehm, M. F. G. Klein, K. Glaser, A. Colsmann,
J. G. Shapter, U. Lemmer, M. M. Kappes, R. Krupke, **B. S. Flavel**

Advanced Energy Materials 3 (2013) 1091–1097

DOI: 10.1002/aenm.201200949

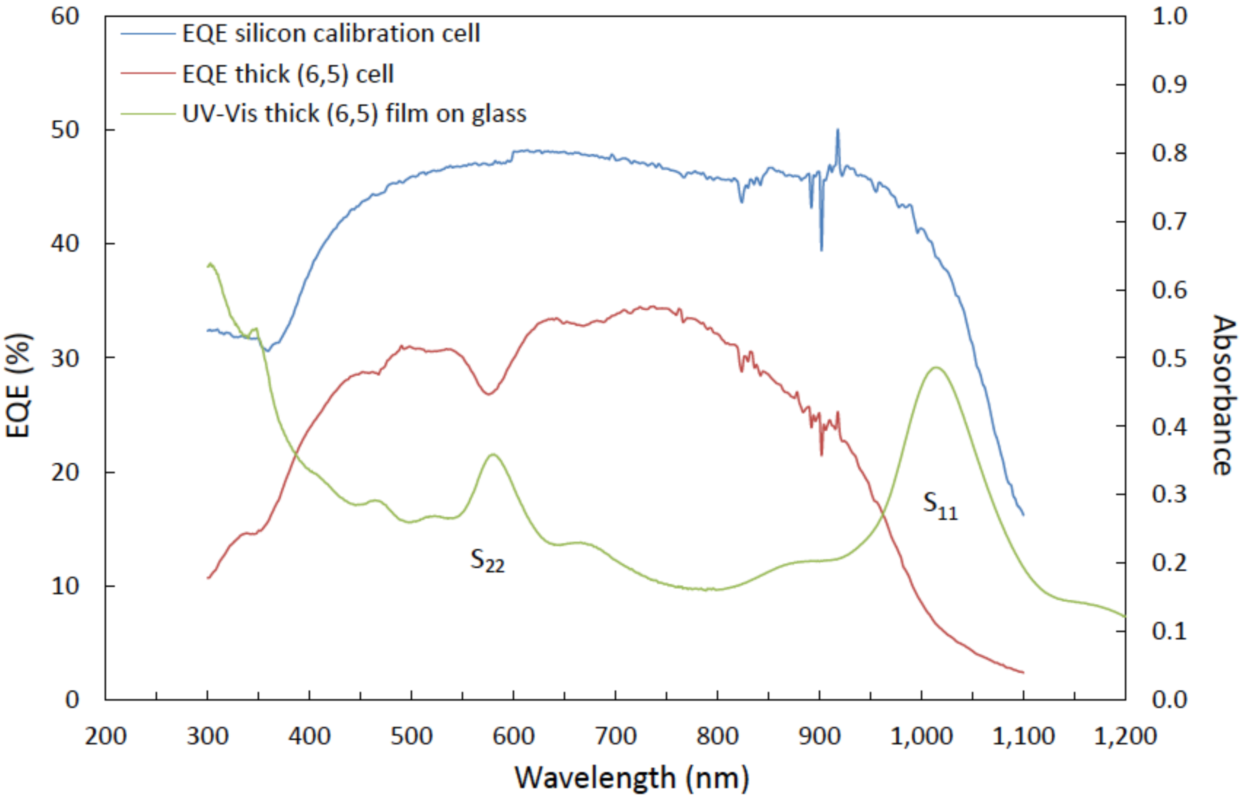

Figure S1 EQE (red) and UV-Vis (green) data corresponding to a device made with a very thick film of COM (6,5) nanotubes. The reduction in efficiency in the region of the nanotube S22 is quite clearly a result of light absorption by the nanotubes. The EQE of a silicon calibration cell (blue) displays no such features. Also apparent by comparison are the effects of the nanotube S11 in the 1050 nm region and p-p* absorption in the UV. The sharp features in the 800 – 1000 nm region are spectral artefacts from the instrument.

– This page intentionally left blank –

3.3.2 *Nanotube Film Metallicity and its Effect on the Performance of Carbon Nanotube-Silicon Solar Cells*

D. D. Tune, A. J. Blanch, R. Krupke, **B. S. Flavel**, J. G. Shapter

Phys. Status Solidi A (2014) 1479–1487

DOI: 10.1002/pssa.201431043

Optical spectroscopy of SWNT dispersions

UV-Vis-NIR spectra were recorded on a Cary 5G spectrophotometer (Varian, Melbourne, Australia) at 600 nm min^{-1} using 10 mm path length quartz cuvettes and a surfactant solution baseline correction and are shown in Figure S1.

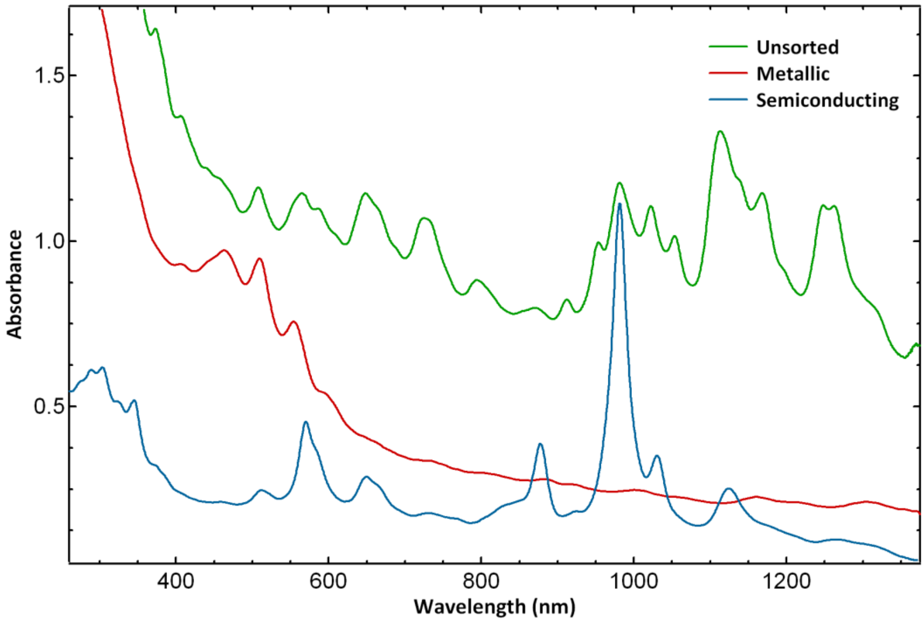

Figure S1 Optical absorbance spectra for the unsorted nanotube dispersion and separated SWNT fractions. Note that spectra were taken after 0.5 mM NaOH addition for the SWNTs in SDS surfactant (unsorted and metallic) to reverse the protonation effect.[1]

It is evident from these spectra that while the fractions are very different in terms of nanotube diameter populations, each still contains a mixture of nanotube species.[2, 3] The unsorted HiPCO dispersion contains upwards of 50 different species ranging in diameter from approximately 0.7 - 1.2 nm. The metallic fraction contains mostly pseudo-metallic species, (semiconductors with bandgap on the order of the thermal energy, k_BT) rather than the truly metallic 'armchair' nanotubes. There is also a very small proportion of semiconducting species remaining as impurities in the metallic fraction. These are generally mixed semiconducting/metallic bundles that passed through the gel without significant interaction during sorting. The semiconducting solution consists of predominantly small diameter semiconducting species, being dominated by the (6,5) SWNT, but also with significant amounts of (6,4), (7,5) and (7,6) nanotubes and traces of others.

Optical spectroscopy of SWNT films

To determine the optical density of the SWCNT films, the absorbance at two points on the spectra of each material was averaged as shown in Figure S2 and then converted to transmittance. UV-Vis-NIR spectra were taken from nanotube films on glass substrates and the contribution of the glass substrate was removed as background. The points were chosen to be at wavelengths least affected by the changes to the S_{11}, S_{22} or M_{11} optical transitions that are caused by chemical doping, as well as providing a meaningful comparison between the films within this work and with the T_{550} values given elsewhere. **Figure S3** shows the calibration data, where the slope gives a relative measure of the concentration of the SWCNT source suspension. As can be seen, the unsorted suspension (already diluted 1:5) is almost twice as concentrated as the metallic fraction and about 7x more concentrated than the semiconducting fraction. Figure S4 shows the variation in R_{sheet} of the SWCNT films with the volume of starting suspension, where the slope gives a relative measure of 'resistivity', here denoted r* and having the units of kW mL sq^{-1} but different to resistivity in its usual form, which has the units of W cm. The metallic material starts out with r* around 2 orders of magnitude lower than the unsorted material, itself about 20x lower than the semiconducting material but this changes with $SOCl_2$ doping. An anomaly exists in that the slopes of the m-SWCNTs before and after doping appear to show that the doping makes the m-SWCNT material more resistive. This is untrue, as shown in Table 1, and is most likely due to the highest R_{sheet} m-SWCNT data point being an outlier.

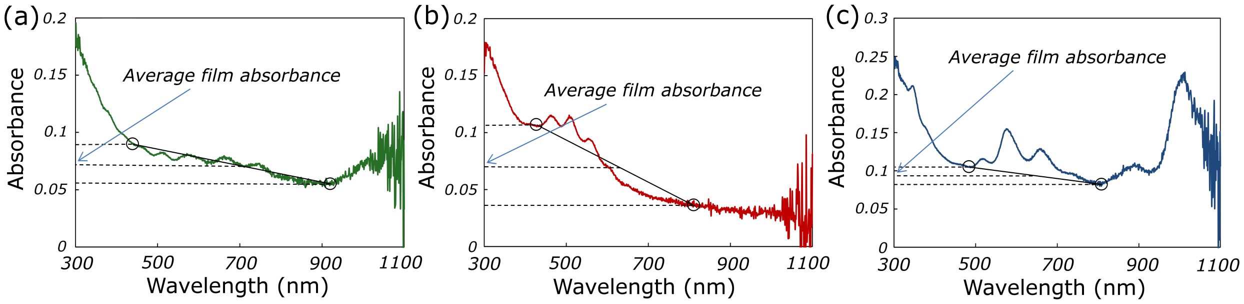

Figure S2 Method used to estimate average film absorbance for the three types of SWCNT material whilst avoiding any distortion due to the absorption peaks, (a) unsorted, 450 nm & 930 nm, (b) metallic, 440 nm & 800 nm, (c) semiconducting, 495 nm & 800 nm.

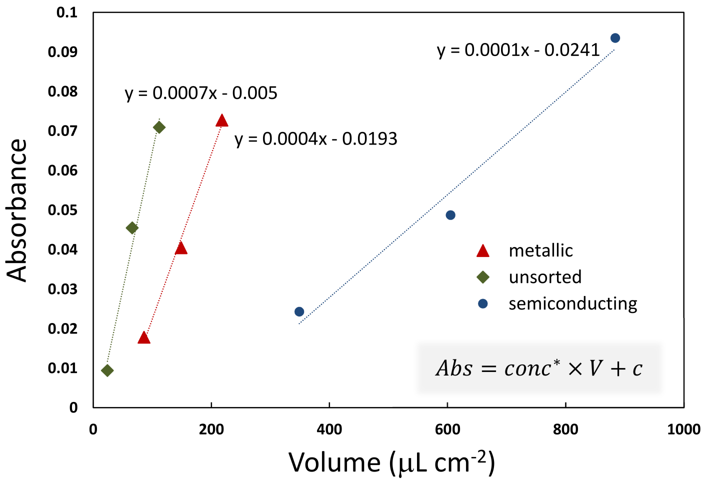

Figure S3 Calibration of SWCNT films showing the variation in optical density with the volume of SWCNT suspension used per area of filter membrane.

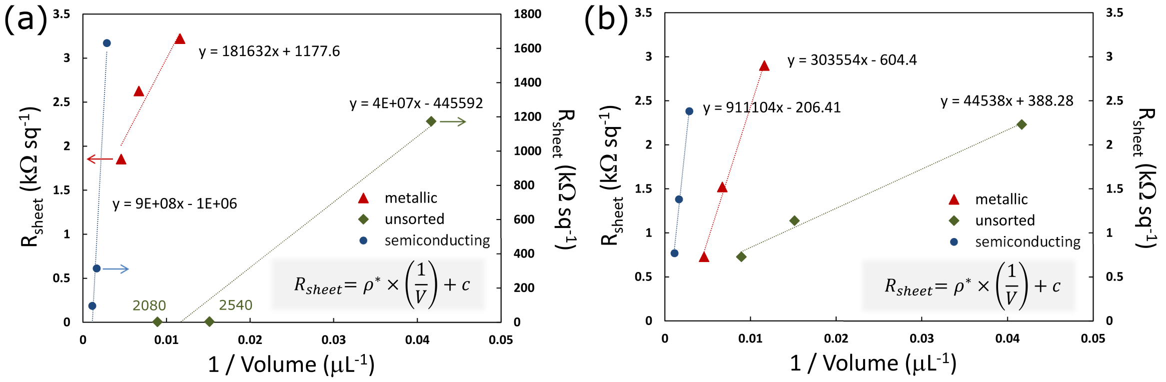

Figure S4 Variation in sheet resistance with the volume of SWCNT suspension used per area of filter membrane and corresponding to (a) as prepared devices and (b) $SOCl_2$ doped devices

Table 1 Detailed summary of measured and calculated photovoltaic performance and device parameters as well as optical transmittance and R_{sheet} of the SWCNT films used pre- and post-treatment with $SOCl_2$.

	U-96		U-90		U-84		M-96		M-90		M-84		S-96		S-90		S-84	
	pre-	post-	pre-	post-	pre-	post-	pre-	post-	pre-	post-	pre-	post-	pre-	post-	pre-	post-	pre-	post-
J_{sc} (mA cm^{-2})	0.08	1.06	1.46	18.48	3.12	21.68	5.05	13.93	11.51	17.89	18.03	19.71	0.02	1.63	0.39	5.98	1.17	11.00
V_{oc} (V)	0.14	0.46	0.14	0.53	0.18	0.54	0.27	0.48	0.41	0.50	0.44	0.50	0.18	0.44	0.32	0.49	0.33	0.50
FF	0.24	0.27	0.23	0.36	0.23	0.39	0.25	0.34	0.29	0.38	0.31	0.47	0.25	0.33	0.24	0.37	0.28	0.37
PCE (%)	0.00	0.13	0.05	3.58	0.13	4.51	0.34	2.28	1.36	3.39	2.45	4.51	0.00	0.26	0.03	1.08	0.11	2.01
R_{SH} (Ω)[a]	$2.3x10^4$	$1.2x10^4$	$1.1x10^3$	$8.3x10^2$	$6.5x10^2$	$1.5x10^3$	$7.9x10^2$	$9.1x10^2$	$7.1x10^2$	$3.9x10^3$	$6.6x10^2$	$1.3x10^4$	$1.1x10^5$	$1.0x10^4$	$1.2x10^4$	$2.3x10^3$	$6.1x10^3$	$1.2x10^3$
R_S (Ω)[a]	$2.7x10^4$	$7.1x10^3$	$1.3x10^3$	$1.8x10^2$	$7.7x10^2$	$1.5x10^2$	$7.4x10^2$	$2.5x10^2$	$4.1x10^2$	$2.0x10^2$	$2.5x10^2$	$1.5x10^2$	$1.1x10^5$	$3.5x10^3$	$1.4x10^4$	$5.0x10^2$	$4.5x10^3$	$2.7x10^2$
Ideality[b]	3.07	2.45	1.61	1.62	1.59	1.57	1.55	1.71	1.50	1.25	1.45	1.30	3.20	2.58	3.03	2.10	2.47	1.89
J_0 (mA cm^{-2})[b]	$2.0x10^{-3}$	$2.1x10^{-4}$	$2.3x10^{-3}$	$1.4x10^{-5}$	$1.2x10^{-3}$	$9.1x10^{-6}$	$2.8x10^{-4}$	$1.0x10^{-4}$	$6.0x10^{-5}$	$2.0x10^{-6}$	$7.8x10^{-5}$	$7.6x10^{-6}$	$5.7x10^{-3}$	$9.0x10^{-3}$	$5.5x10^{-3}$	$1.5x10^{-3}$	$7.6x10^{-3}$	$8.4x10^{-4}$
Φ_{SBH} (eV)[b]	0.70	0.76	0.71	0.71	0.72	0.84	0.75	0.78	0.81	0.88	0.81	0.86	0.76	0.76	0.74	0.77	0.73	0.79
Transmittance (%)	97.4	98.3	90.4	90.5	85.3	85.5	95.9	95.7	90.9	90.9	84.8	84.7	95.5	95.0	89.3	89.4	80.4	80.6
R_{sheet} (Ω sq^{-1})	$1.2x10^6$	$2.2x10^3$	$2.5x10^3$	$1.1x10^3$	$2.1x10^3$	$7.3x10^2$	$3.2x10^3$	$2.9x10^3$	$2.6x10^3$	$1.5x10^3$	$1.9x10^3$	$7.3x10^2$	$1.6x10^6$	$2.4x10^3$	$3.1x10^5$	$1.4x10^3$	$9.6x10^4$	$7.7x10^2$

AFM

Atomic force microscopy (AFM) measurements were performed on the same films as for Raman analysis, i.e. those in the 'as-prepared' state on bare Si substrates. Images were recorded on a Bruker Multimode 8 AFM with a Nanoscope V controller using NSC15 Si probes (MikroMasch). AFM images were acquired in either tapping or peak force tapping modes, with all parameters including set point, scan rate and feedback gains adjusted manually to optimize image quality and minimize imaging force. Figure S5 shows images of the metallic SWNT film at different length scales. All of the films have a similar topography with variations in height of over 1 mm common, most likely due to the film forming in the shape of the filter membrane which contains relatively deep pores. In this deposition method, the interface between the SWNT film and the filter membrane becomes the film surface, leading to the observed large variations in height. However, on a smaller scale the nanotubes within the films form smooth networks of bundles where large protrusions in the film are absent. These bundles range in diameter from approximately 5 - 15 nm (using height measurements) as shown in Figure S6.

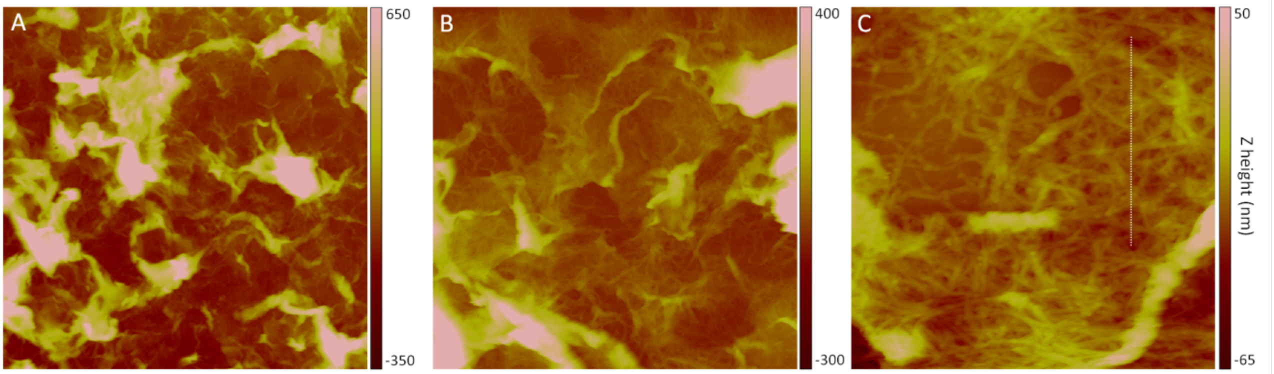

Figure S5 AFM images of the metallic SWNT film on Si at 15x15 (A), 5x5 (B) and 1x1 mm (C). Image A was acquired in tapping mode, while B and C were recorded in peak force tapping mode. The dotted line in C represents the cross-section presented in Figure S6.

Film thickness is difficult to define given the large variations in height. However there is a relatively constant baseline height of 40 - 60 nm beneath the larger protrusions. This is evident in the cross-sectional analysis of the unsorted film edge in Figure S7, which has an optical transparency of approximately 84 %. However, the films are not completely continuous towards the very edge, where small patches of the Si surface are visible, and it is plausible that the centre regions could be slightly thicker.

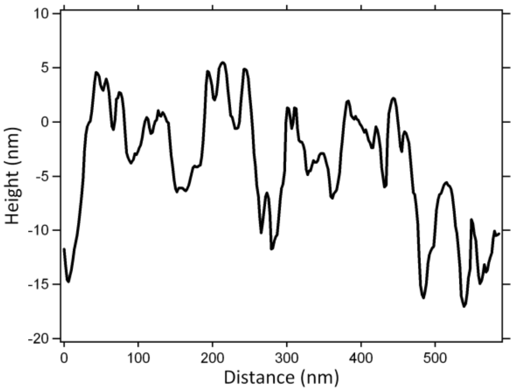

Figure S6 Cross-section of SWNT bundles from Figure S5 (C).

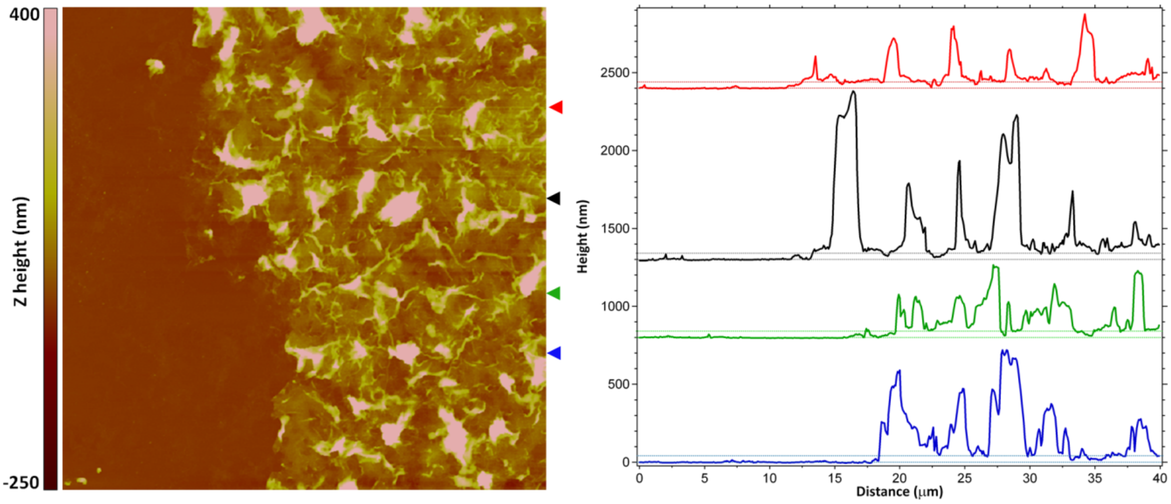

Figure S7 A 40x40 µm tapping mode AFM image of the unsorted nanotube film with 4 cross-sections. Coloured arrows indicate the positions of the corresponding scan lines plotted as cross-sections. Dashed lines are drawn at heights of 0 and 40 nm for each individual section.

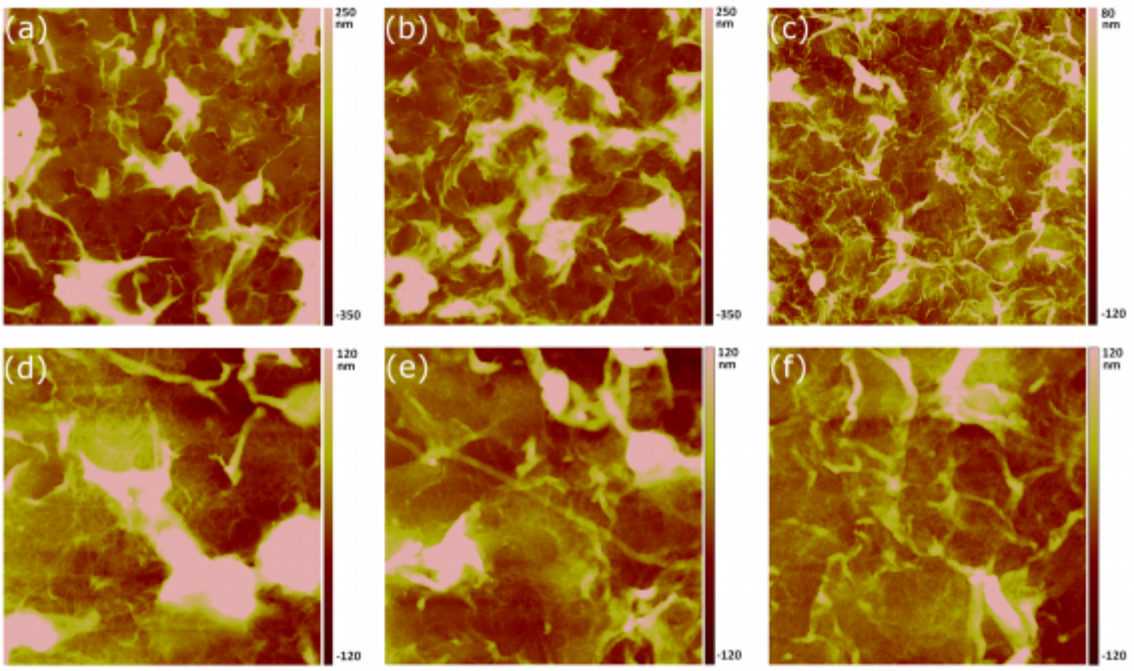

Figure S8 AFM images (15 x 15 µm) from films of (a) unsorted SWCNTs, (b) m-SWCNTs and (c) s-SWCNTs. (d-f) show the same films as (a-c) on a 5 x 5 µm scale.

Raman

Nanotube films prepared under identical conditions to those in the active devices (approx. 84% transmission) were deposited in the same manner onto clean n-type Si wafers with native surface oxides. Raman spectra of the films were collected using a Horiba XploRA confocal microscope under a 10x objective. Accumulations of 6 x 30 sec were averaged for each film using a 1800 line/mm grating and 50 % density filter at wavelengths of 2.33 eV (532 nm), 1.94 eV (638 nm) and 1.58 eV (785 nm). Spectra were recorded from 'as prepared' films as well as directly after treatment with $SOCl_2$ and HF. The Raman spectra in Figure S9 show the D, G and RBM features which are characteristic of SWNTs. The G bands of the separated metallic and semiconducting films are very different at both 2.33 and 1.96 eV excitation, where these two films have vastly different nanotube populations in resonance with the excitation energy. At 2.33 eV in particular, where mostly metallic species are resonant, the G^- band is broadened into a Breit-Wigner-Fano (BWF) line shape which is consistent with a large contribution from narrow gap semiconductors (or pseudo-metallic nanotubes).[4] The difference between these samples is less pronounced at 1.58 eV where large diameter semiconductors are present in both films. Larger diameter species are less well separated by the gel-chromatography technique and are therefore more likely to be present as impurities in the metallic fraction. Conversely, there is very little metallic SWNT material present in the semiconducting sample. It should be noted that the (6,5) nanotube RBM is not prominent in the 2.33 eV excitation spectrum due to the mismatch between the excitation wavelength and the second optical transition (S_{22}) of the (6,5) species. Only those CNTs with transitions resonant with the excitation energy will appear in the Raman spectrum, within a bandwidth window of approximately ±0.15 meV. The (6,5) tube is on the edge of this resonance window and is therefore only partially excited by 2.33 eV radiation

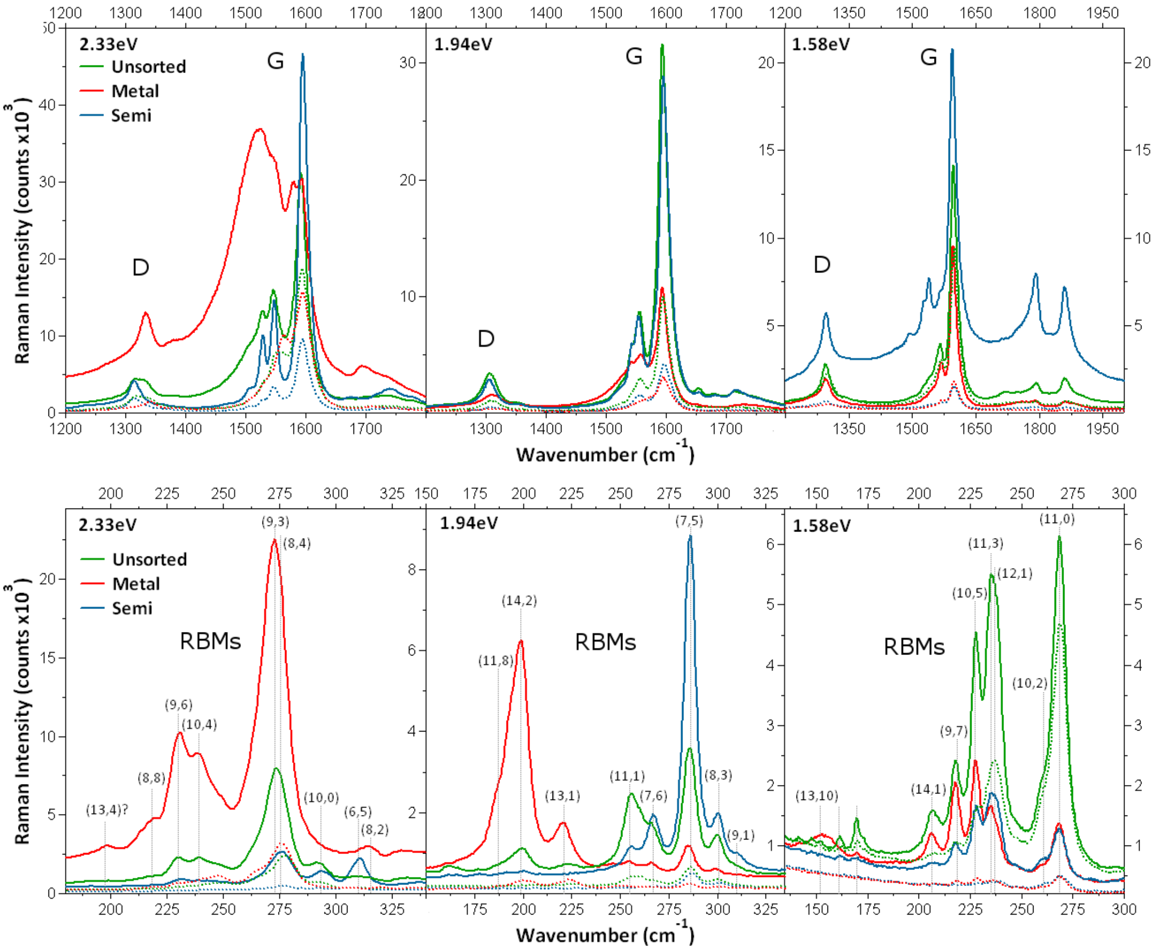

Figure S9 Raman spectra of the D and G (top) and RBM (bottom) mode regions for the different nanotube films. Species were assigned a likely nanotube candidate (n, m) species using known radial breathing mode (RBM) peak values providing that species possessed an optical transition within the resonance window.[2]

The films were also analysed by Raman spectroscopy after $SOCl_2$ treatment and after HF washing. Spectra for the semiconducting film after these treatments are shown in **Figure S10**, while similar results were observed for the other two films. The response of the Raman spectra to both treatments correlates well with the changes observed in the optical absorbance spectra. Directly after $SOCl_2$ treatment the Raman features lose at least 50 % of their intensity, with all SWNT species appearing to be equally affected. After HF treatment these features somewhat recover, but not to their original intensity.

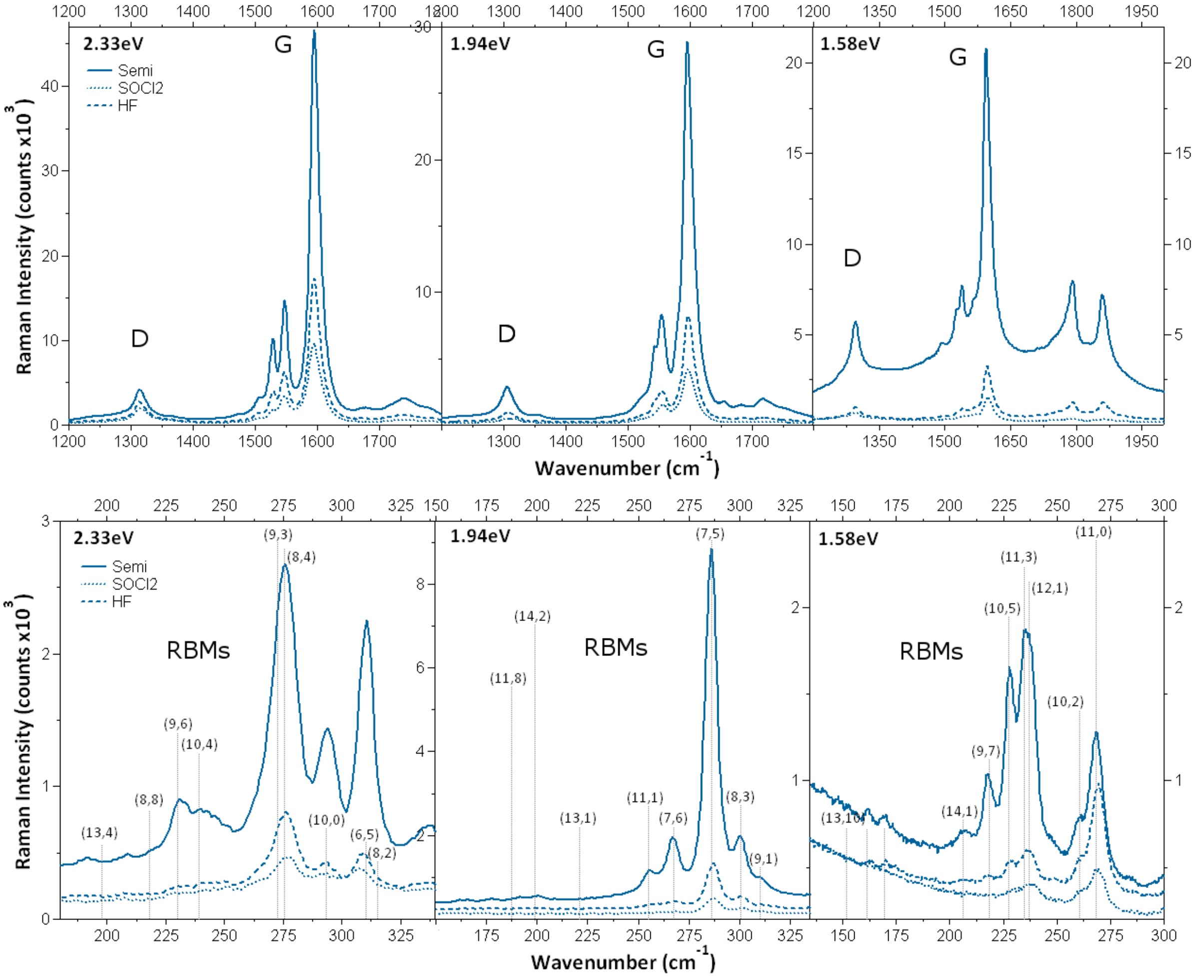

Figure S10 Raman spectra of the D and G mode (top) and RBM (bottom) regions for the semiconducting SWNT film in the ‘as-prepared state’, directly after thionyl chloride treatment, and also after final HF treatment.

References

1. M. S. Strano, C. B. Huffman, V. C. Moore, M. J. O'Connell, E. H. Haroz, J. Hubbard, M. Miller, K. Rialon, C. Kittrell, S. Ramesh, R. H. Hauge, R. E. Smalley, J. Phys. Chem. B 2003, 107, 6979.
2. E. H. Haroz, J. G. Duque, X. Tu, M. Zheng, A. R. Hight Walker, R. H. Hauge, S. K. Doorn, J. Kono, Nanoscale 2013, 5, 1411.
3. R. B. Weisman, S. M. Bachilo, Nano Lett. 2003, 3, 1235.
4. E. H. Hároz, J. G. Duque, W. D. Rice, C. G. Densmore, J. Kono, S. K. Doorn, Phys. Rev. B 2011, 84, 121403.

3.4.1 *Performance Enhancement of Polymer-Free Carbon Nanotube Solar Cells via Transfer Matrix Modeling*

M. Pfohl, K. Glaser, J. Ludwig, D. D. Tune, S. Dehm, C. Kayser, A. Colsmann,
R. Krupke, **B. S. Flavel**

Advanced Energy Materials 6 (2016) 1501345

DOI: 10.1002/aenm.20150134

Characterization of the (6,5) SWCNT suspension

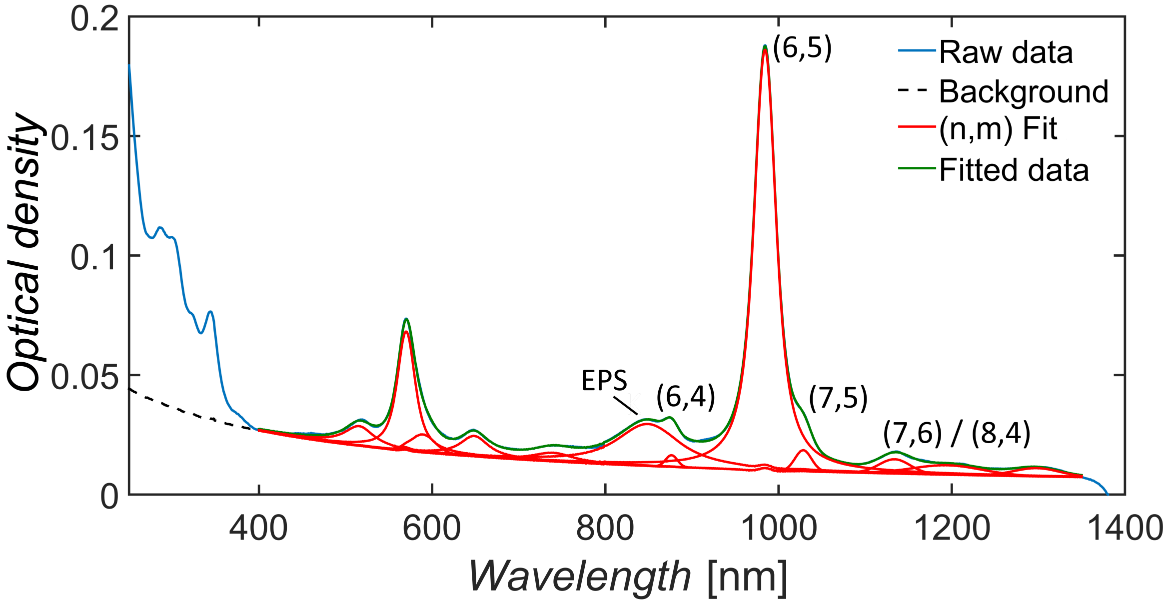

Figure S1 Absorption spectrum of the (6,5) SWCNT suspension in 1 wt % sodium cholate (SC) measured with a 2 mm path length, along with the background subtraction and peak fitting procedure used to determine purity. At 848 nm, the exciton-phonon sideband (EPS) is visible.

Using the procedure outline by Nair et al. the background was subtracted (black line) from the raw data (blue line).[1] Subsequently the software “Fityk” was used to fit Voigt functions to the (n,m) species in solution in the S_{11} (900 – 1300 nm) and S_{22} (550 – 900 nm) regions (red line) with peak positions provided in the literature so that the envelope of fitted peaks replicated the raw data with a mean χ^2 value of 3.95×10^{-5} (green line).[2] The peak at 848 nm is 0.2 eV shifted compared to the main S_{11} peak at 984 nm and therefore associated to a resonance effect emerging from absorption of light to a bound exciton-phonon state, as proposed by Perebeinos et al.[3] Using Equation S1 the purity of (6,5) was then calculated by taking only the S_{11} regime into account and assuming the absorbance cross section to be the same for all (n,m) species:

$$\text{Purity (\%)} = \frac{\text{Area}_{(6,5)}}{\sum_{\text{i}=1}^{\#(\text{n,m})} \text{Area}_\text{i}}. \qquad \text{(S1)}$$

Characterization of the (6,5) SWCNT film

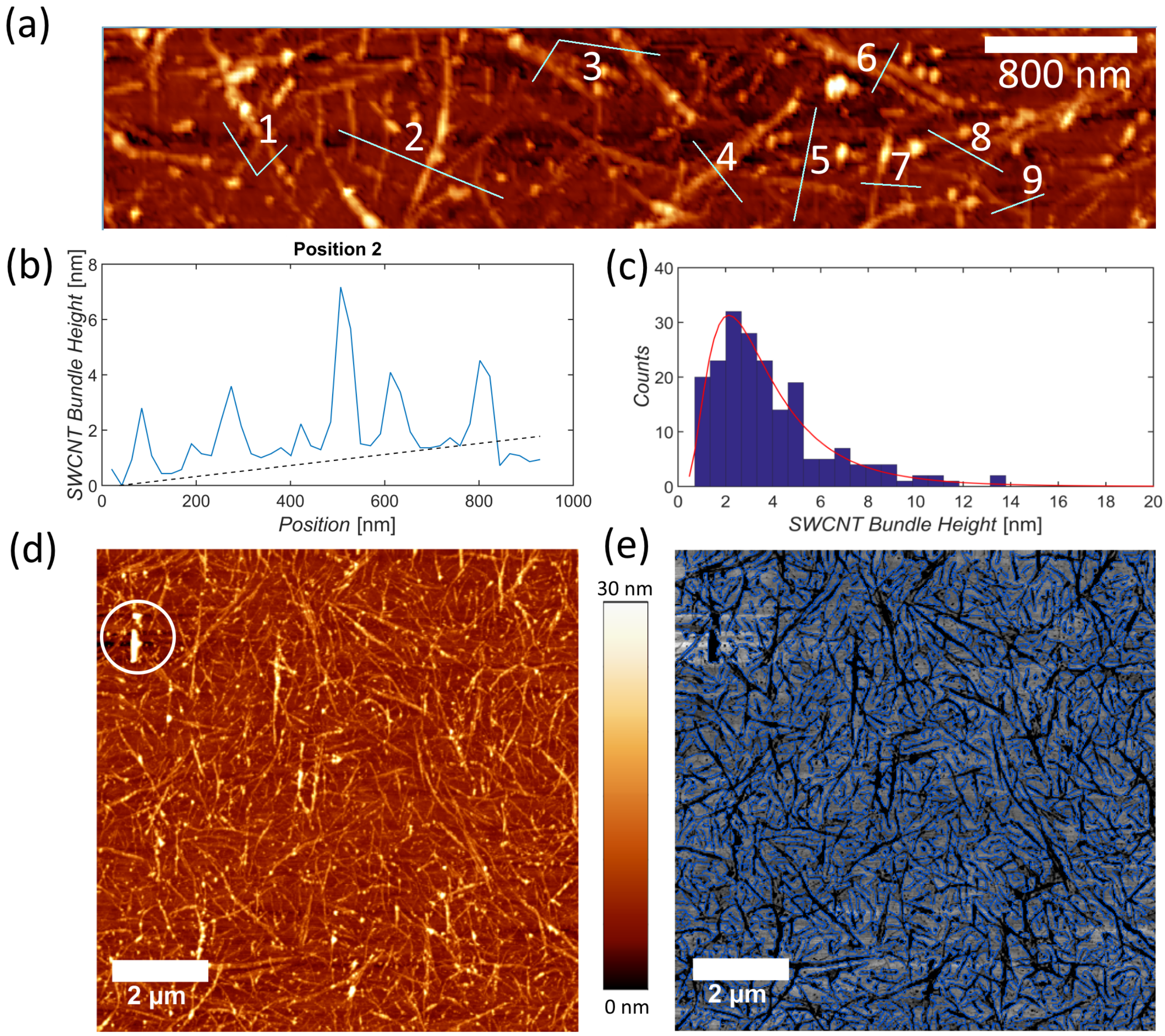

Figure S2 (a) The average bundle height was determined by cross-sectional analysis of 196 positions in the (6,5) SWCNT film. An example of the height analysis section and additional background subtraction (black dotted line) is shown in (b) and histogram in (c). SWCNT film coverage was calculated from 6 different AFM images taken from random spots across the film with a representative image shown in (d). Additionally highlighted in white circle is an object in the film with a height greater than 60 nm, as mentioned in the main text. Using the built in edge detection function “canny” in MATLAB® an overlay plot of the SWCNT edges and the original image was generated (e). This allowed the surface coverage to be calculated using the function “bwarea” to divide the number of SWCNT pixels by the total number in the image.

Photo-electron yield spectroscopy in air (PESA)

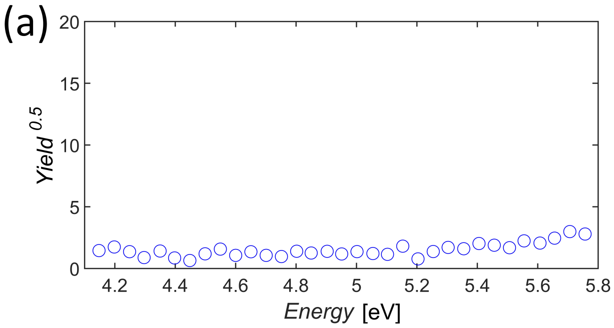

Figure S3 (a) Reference PESA measurement of ITO and (b) of a (6,5) SWCNT film on ITO. Both measurements were performed at 50 nW. The intersection of the background line and the photoemission curve provides a (6,5) SWCNT film HOMO energy of 5.1 eV.

Transfer Matrix Calculations

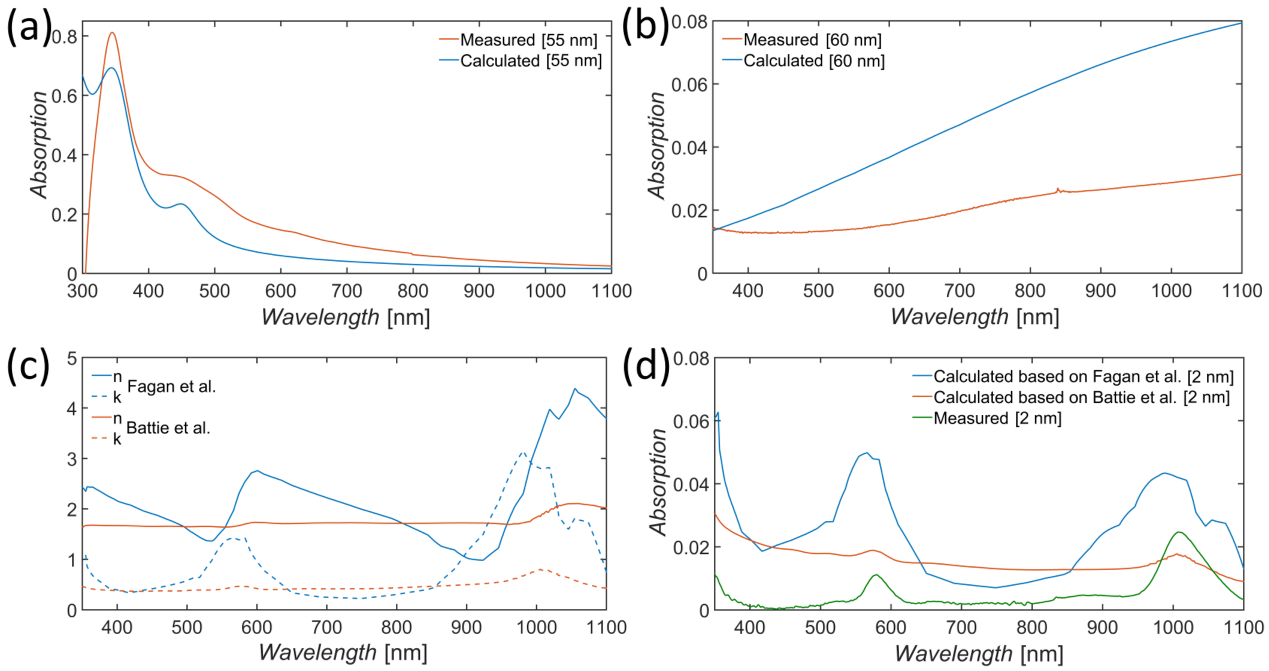

Figure S4 Comparison of calculated and measured absorption spectra for (a) C_{60} and (b) PEDOT:PSS on glass. The absorption of PEDOT:PSS is overestimated in the calculation but the overall curve shape matches the measurement. (c) Comparison of complex refractive indices for (6,5) SWCNTs (d) Comparison of the calculated and measured absorption of (6,5) SWCNTs on glass.

Transfer matrix calculations (TMCs) were performed with a modified version of the program provided by the McGehee Group at Stanford and outlined by Burkhard et al.[4] The complex refractive indices (n and k) for ITO were taken from the library provided along with the MATLAB® code. Optical data for PEDOT:PSS was provided by the producer H.C. Starck. The optical properties of the float glass were taken from the “Optical Glass – Data Sheets” provided by Schott AG and are available online at “refractiveindex.info”. The properties of C_{60} were calculated based on the formula by Ren et al. and the values for Ag were taken from Palik et al.[5]
For (6,5) SWCNTs the complex refractive index from Fagan et al. and the intrinsic relative permittivity from Battie et al. was compared to absorption measurements of our films.[6] For Fagan’s approach, the overall curve shape matches the one measured from the nanotube film fairly well. The problem is a broadening of S_{11}, an overestimate in intensity at S_{22} and the overall curve roughness. For Battie’s approach, the intensity values are a better match, but there is a broad absorption throughout the entire spectrum instead of distinct absorption peaks as our film measurements indicate in Figure S4 (d). As discussed in the main text the discrepancies in calculated and measured SWCNT absorption is caused by different preparation techniques of the nanotubes. Due to these discrepancies and the low absorbance of the nanotube films of ~ 2.5 %, nanotube contribution was neglected in the TMCs in this study.

Thin film absorption $\mathrm{I_{abs}}$ in Figure S4 (a), Figure S4 (b) and Figure S4 (d) was calculated based on the complex refractive index ($\tilde{\mathrm{n}} = \mathrm{n} + \mathrm{i} \cdot \mathrm{k}$) of the different materials and with Equation S2, Equation S3 and Equation S4.[7] The simulated layer stack consisted of glass, the appropriate layer thicknesses stated in Figure S4, and air. The absorption coefficient α is determined by the complex part of the material’s refractive index, k, and by the wavelength, λ:

$$\alpha(\mathrm{x},\lambda) = \frac{4\cdot\pi\cdot\mathrm{k}(\mathrm{x},\lambda)}{\lambda} \tag{S2}$$

The absorption of a specific material was then calculated based on the local absorption rate, β:

$$\beta(x, \lambda) = \alpha(x, \lambda) \cdot n(x, \lambda) \cdot |E|^2 \tag{S3}$$

$$I_{abs}(\lambda) = \int \beta(x, \lambda)\, dx \tag{S4}$$

The exciton generation rate, G, is calculated based on the local energy absorption, Q, at each position and wavelength, with the local energy absorption being:

$$Q(x, \lambda) = \beta(x, \lambda) \cdot AM1.5, \tag{S5}$$

and

$$AM1.5 = \frac{1}{2} c\varepsilon_0 |E_0^+(\lambda)|^2 \tag{S6}$$

with c the speed of light, ε_0 permittivity of free space and $|E_0^+(\lambda)|^2$ the incident electric field, G was determined by:

$$G = \iint \frac{Q(x,\lambda) \cdot \lambda}{h \cdot c} d\lambda dx, \tag{S7}$$

where h is Planck’s constant and c is the speed of light.[7]

Parametric Study

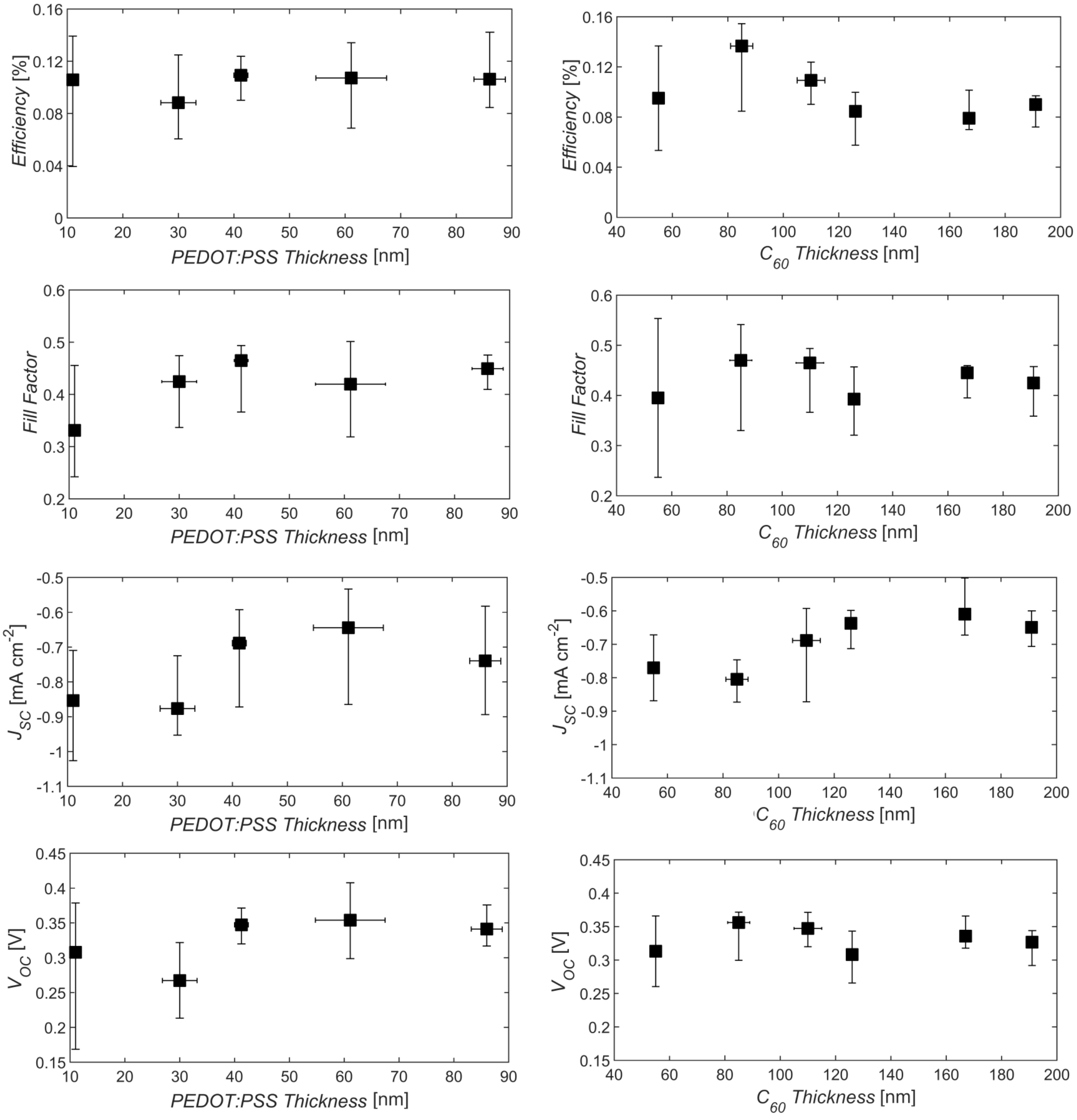

Figure S5 Part 1 of the detailed median results for the parametric study of PEDOT:PSS and C_{60} thicknesses shown in Figure 4 (a) and Figure 4 (b) of the main text.

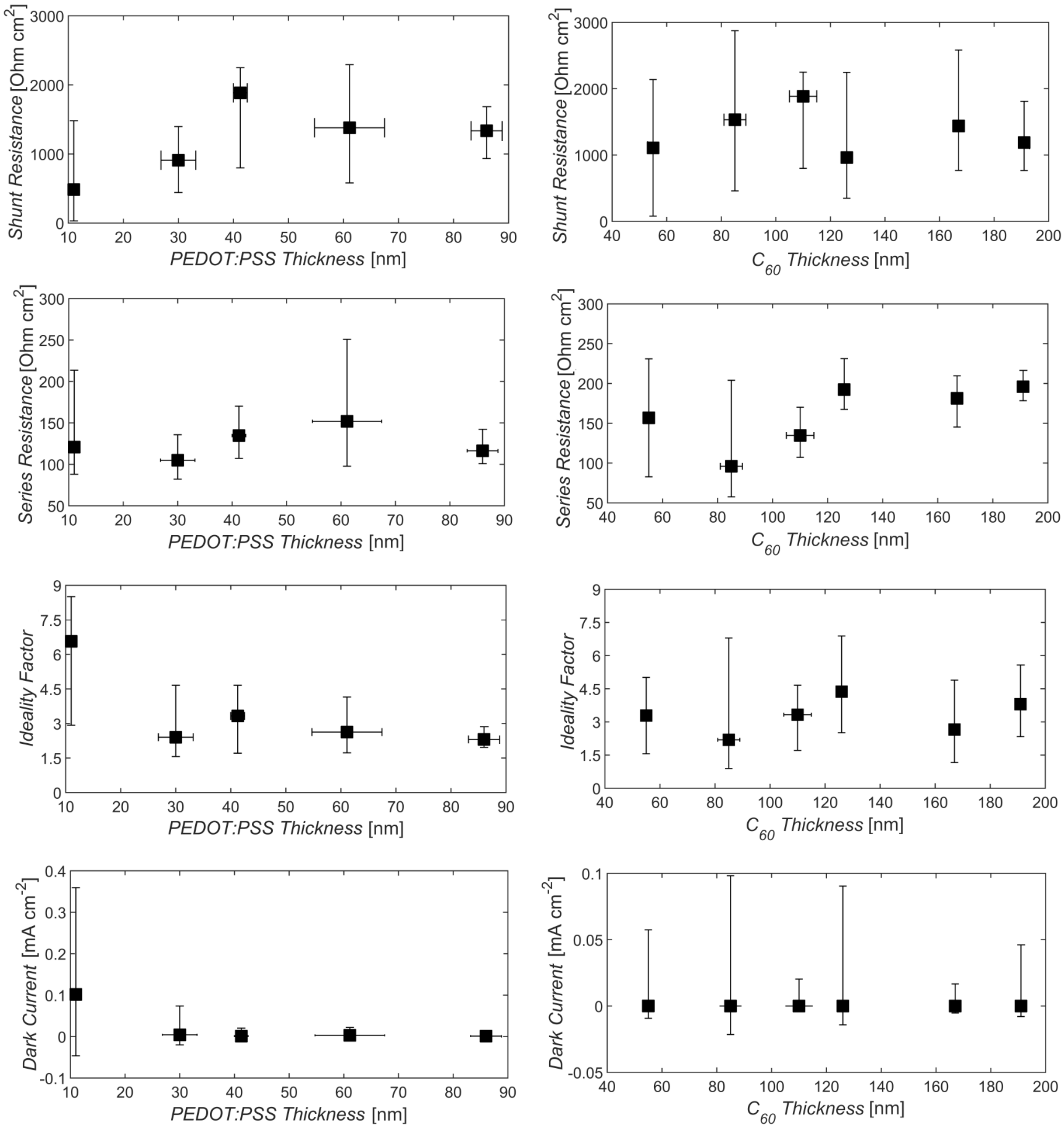

Figure S6 Part 2 of the detailed median results for the parametric study study of PEDOT:PSS and C_{60} thicknesses shown in Figure 4 (a) and Figure 4 (b) of the main text.

J-V curve for solar cell without PEDOT:PSS

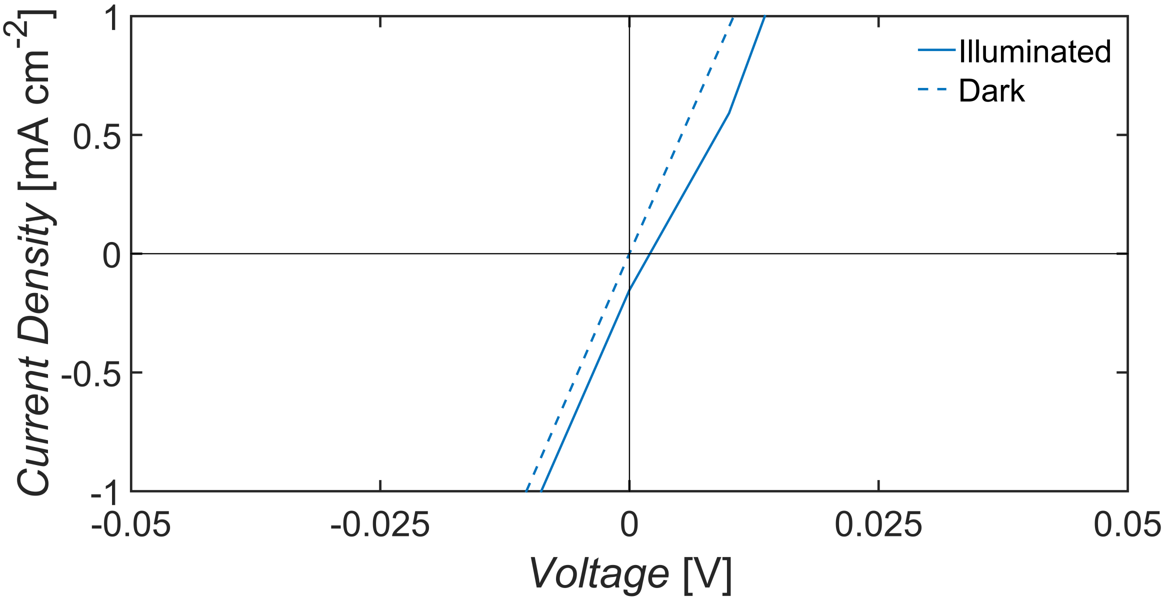

Figure S7 J-V curve of a solar cell without PEDOT:PSS (stack design: ITO/SWCNTs/C_{60}/Ag).

External quantum efficiency (EQE) analysis

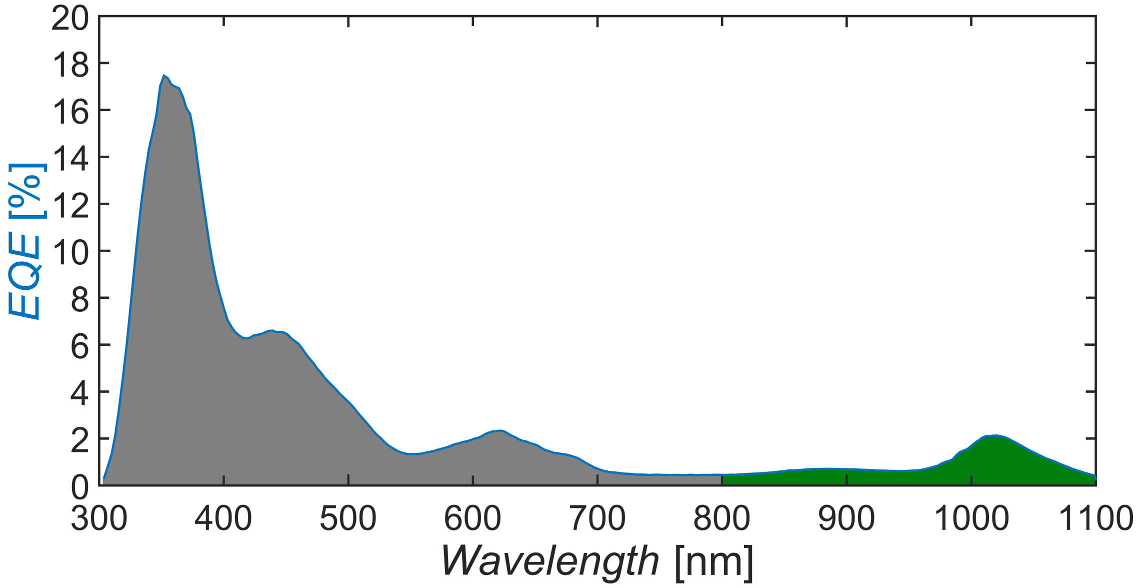

Figure S8 EQE spectrum of a solar cell with ~ 41 nm PEDOT:PSS and ~ 85 nm C_{60}. The photocurrent contribution from C_{60} is highlighted in grey, while the contribution from the S_{11} region of the SWCNTs is highlighted in green.

Optimization of $|E|^2$ at (6,5) absorption

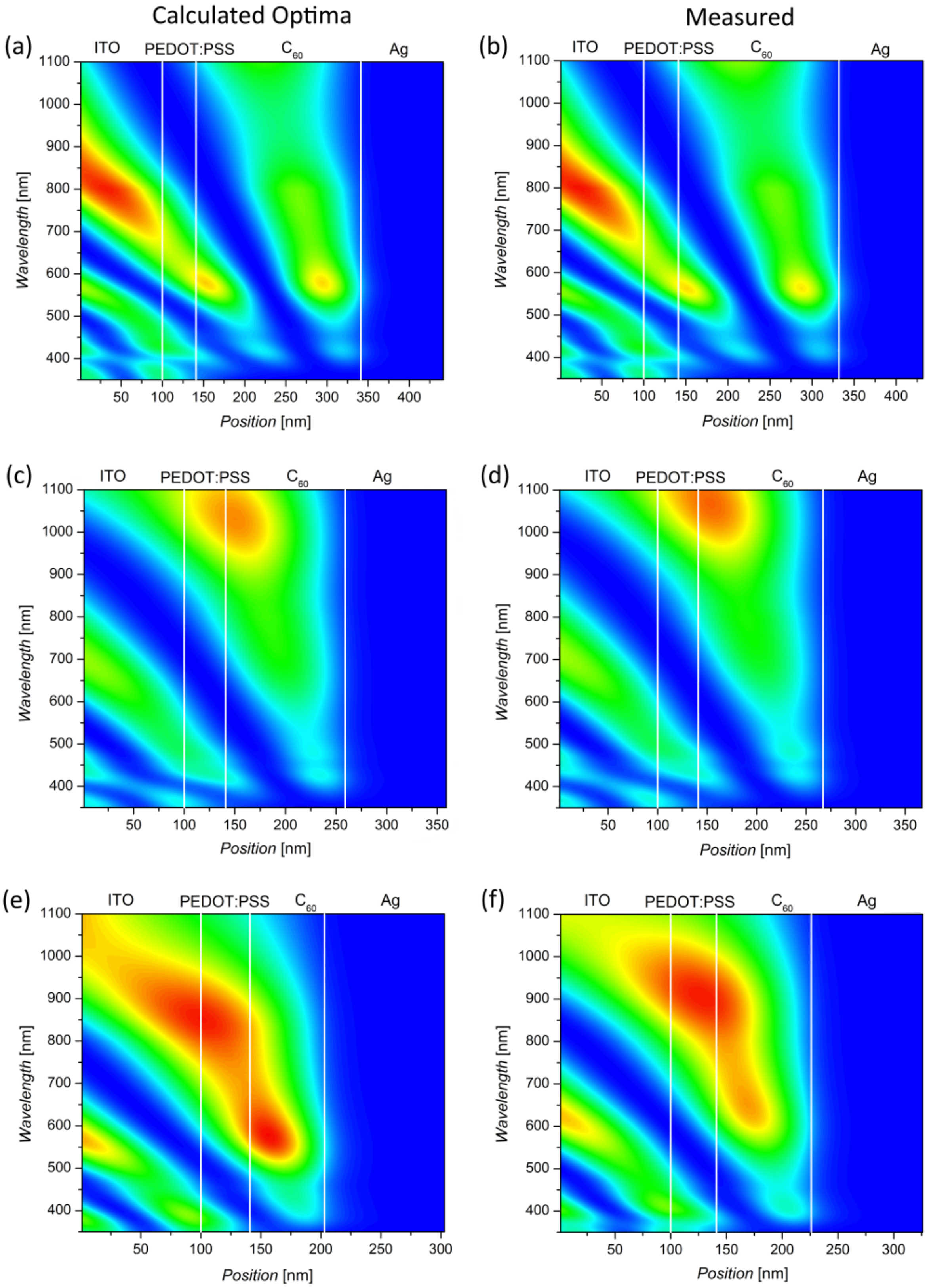

Figure S9 Comparison of $|E|^2$ for calculated optima and actual solar cells with varying thicknesses of C_{60} for a maximum $|E|^2$ at S_{22} (a) and (b), 200 and 191 nm C_{60}, respectively, S_{11} (c) and (d), 118 and 126 nm of C_{60}, respectively, and equal $|E|^2$ at both transitions (e) and (f), 62 and 85 nm of C_{60}, respectively, throughout the solar cell stack.

Exciton generation rate

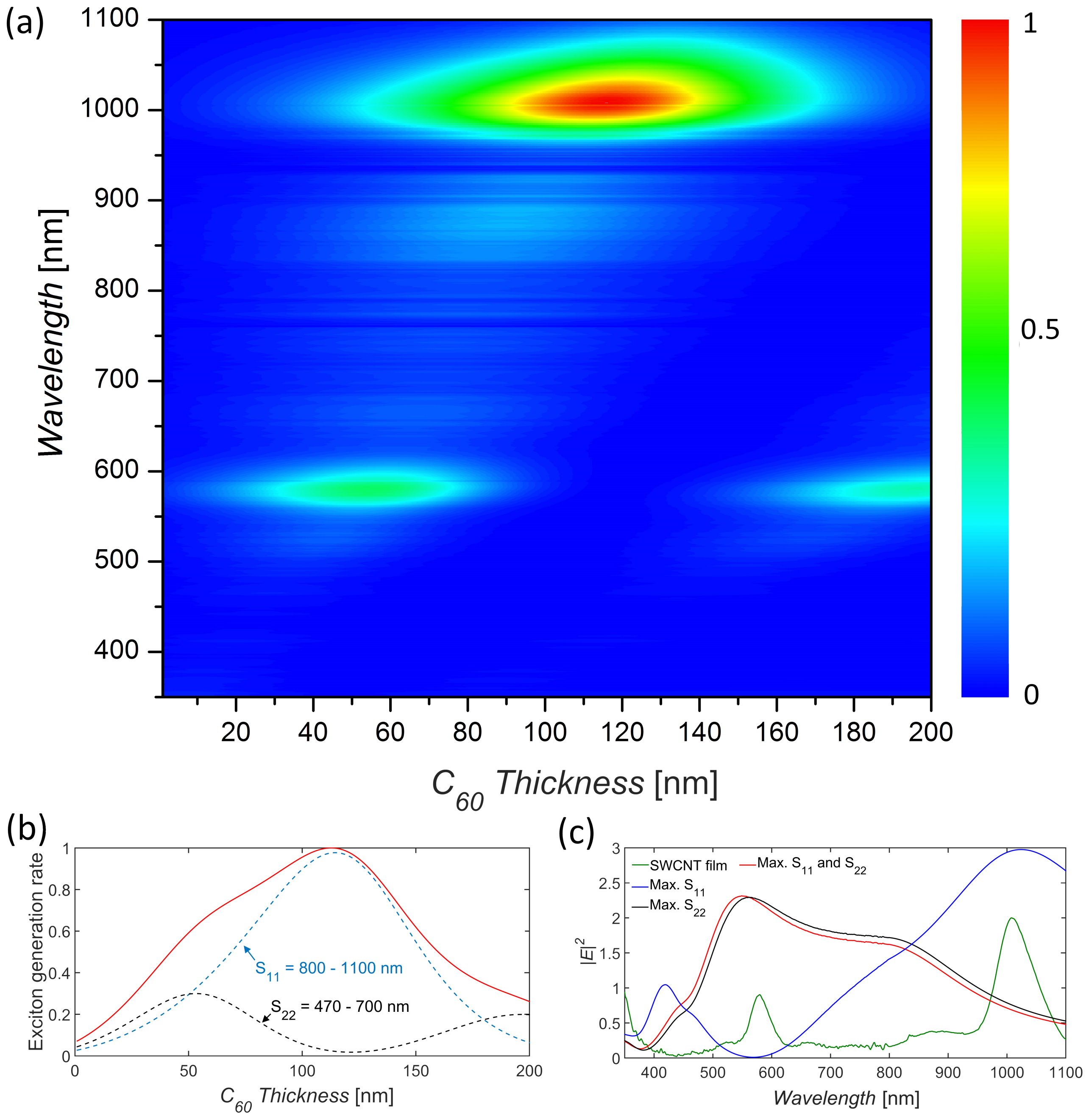

Figure S10 (a) Normalized exciton generation rate for 41 nm PEDOT:PSS and varying thicknesses of C_{60}. (b) In order to optimize light absorption at S_{11} and S_{22} of the (6,5) nanotube film, the exciton generation rate was integrated between 800 to 1100 nm (blue dashed curve) and 470 to 700 nm (black dashed curve), respectively. The intersection points in (b) resemble equal contribution from S_{11} and S_{22} to the exciton generation rate (50 nm and 180 nm). The maximum contribution from S_{22} and S_{11} was found to occur at 53 and 198 nm, and 114 nm of C_{60}, respectively. The corresponding electric fields are shown in (c) for the calculated optima at the intersection of PEDOT:PSS and C_{60}.

Determination of internal quantum efficiency (IQE)

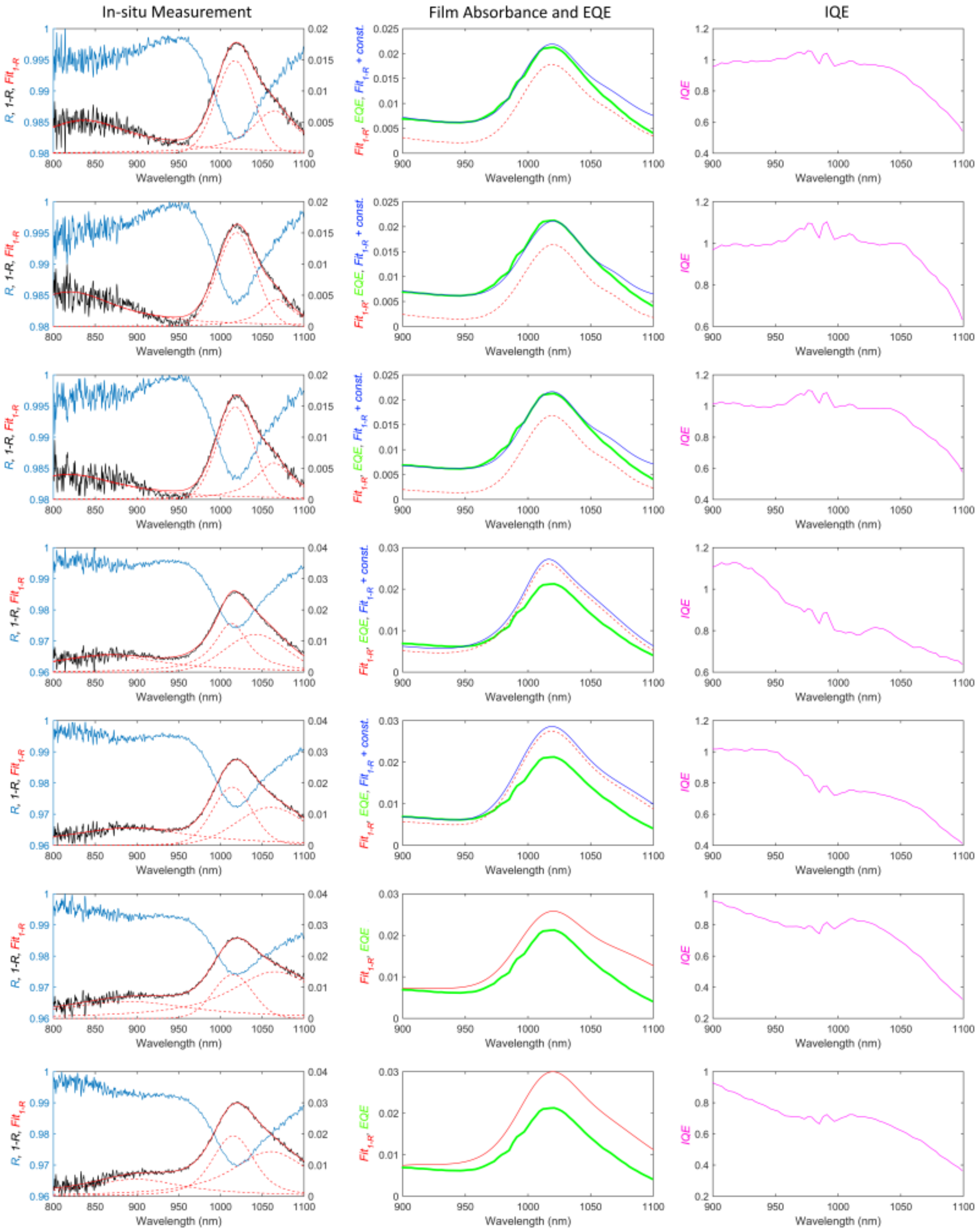

Figure S11 The internal quantum efficiency (IQE) was determined by measuring the absorbance of the nanotube film in situ in each final solar cell device. In order to measure absorbance only from the SWCNTs, the background was measured at the solar cell stack (Glass/ITO/PEDOT:PSS/C_{60}/Ag) without SWCNTs. Absorbance was obtained from reflectance (R) measurements in the active area (blue curve), where absorbance is 1-R (black curve). Due to the noisy signal the reflectance curve was manually shifted to have a maximum value of 1. The absorbance curve was then fitted with three Voigt profiles using the software “Fityk” (red curve). Underestimating the background correction necessitated addition of a constant value for some fitted curves (blue corrected curve in middle column) to guarantee a reliable IQE calculation without overestimating the true value. Due to the uncertainty caused by the noisy signal below 900 nm, EQE (green) and IQE (purple) curves are displayed in the range from 900 to 1100 nm.

The technique of measuring the SWCNT absorption in situ via reflectance measurements was adopted from Bindl et al.[8] It was outlined by Armin et al.[9] that a reliable IQE calculation should follow the subsequent routine: EQE measurement, reflectance measurement of whole cell and then transfer matrix calculation to determine absorption in each layer and overall parasitic absorption. Without considering the parasitic absorption the “IQE-like” curve is spectrally not flat and underestimates the true IQE. Having well defined refractive indices for all materials used, this is a promising approach to accurately calculate IQE.
Without the refractive index of (6,5) SWCNTs we were not able to perform a transfer matrix calculation to determine the parasitic absorption within the solar cell. Instead, we calculated IQE based on EQE and reflectance measurements with the likelihood of underestimating true IQE. For the first five measurements, a constant value was added to the absorbance curve (most likely due to an insufficient background correction) in order to yield a reliable IQE calculation and not overestimate it. IQE at the S_{11} transition of the (6,5) SWCNTs around 1021 nm was then determined to be 86 ± 12 % by dividing EQE and film absorbance. The measured and calculated J_{SC} (based on Equation 1) were within 6.7 %.

Enrichment of (6,5) SWCNTs

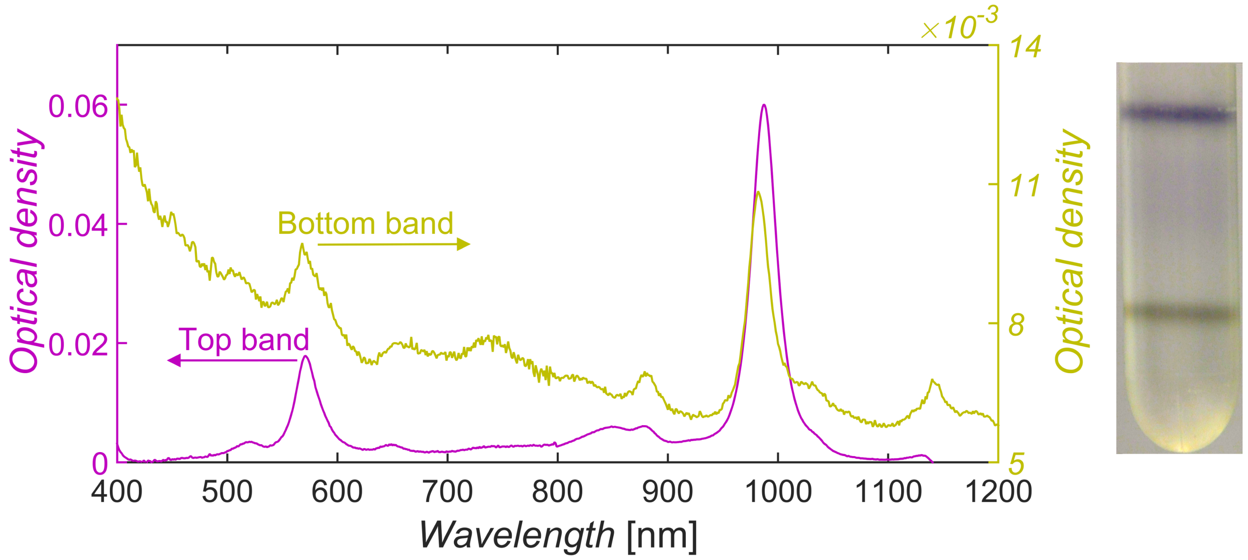

Figure S12 Absorption measurements of the two bands obtained from the as-prepared (6,5) suspension by density ultracentrifugation in 1 wt % SC using a 2 mm path length.

Determination of series resistance (R_S)

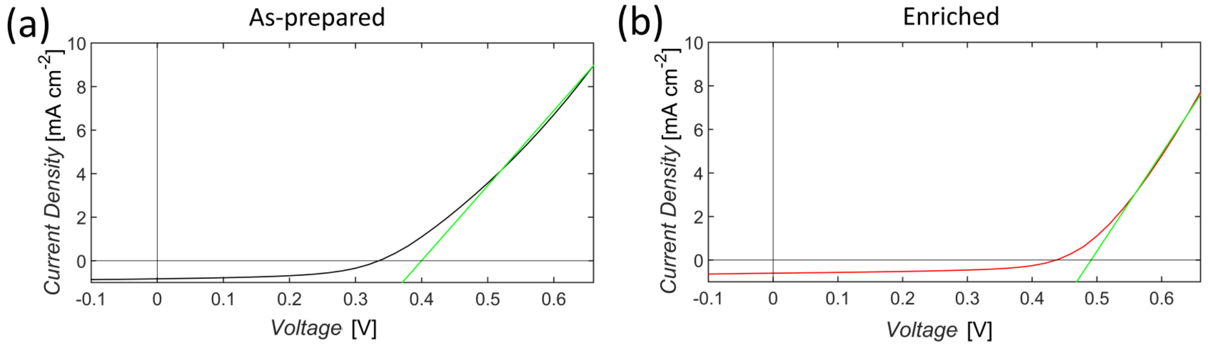

Figure S13 In order to calculate the series resistance a line was fitted to the linear regime of the J-V curves (green) of the as-prepared and enriched (6,5) material. The inverse of the slope of the green curve equals the series resistance.

Light Intensity Variation

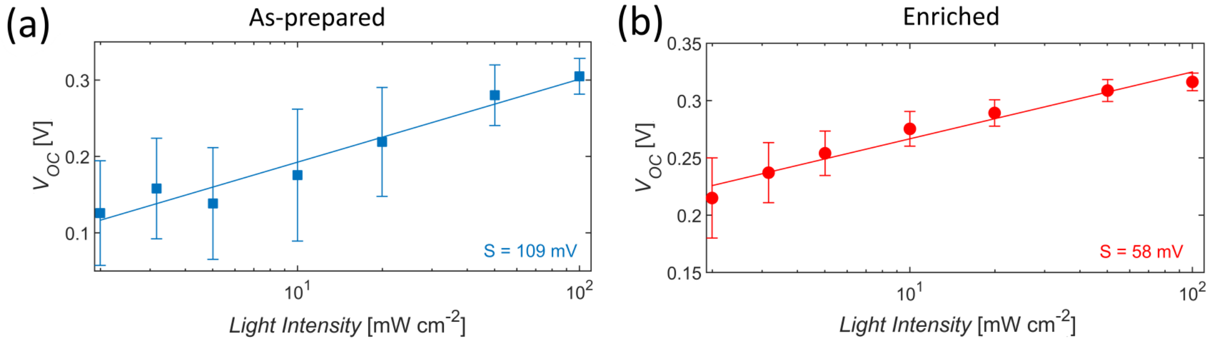

Figure S14 (a) and (b) V_{OC} values measured for varying light intensity from solar cells made from as-prepared and enriched (6,5) material. V_{OC} was set equal to $S \cdot \ln(I) + \text{constant}$, with S being the slope under investigation.

Comparison of a solar cell with and without SWCNTs

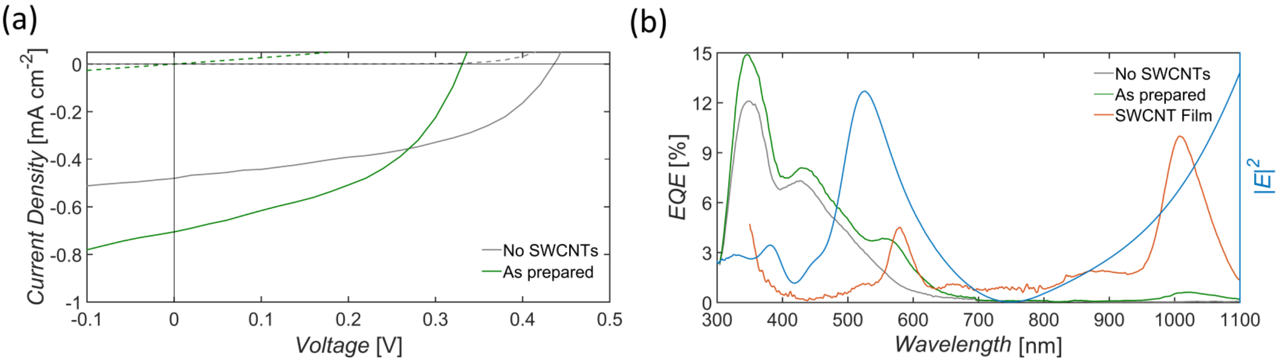

Figure S15 Comparison of J-V curves (a) and EQE measurements (b) for solar cells with 41 nm PEDOT:PSS and 167 nm C_{60} with (green) and without (grey) as prepared (6,5) SWCNTs. For the solar cell without SWCNTs the V_{OC} is comparable to (6,5) enriched devices which demonstrates the influence of metallic SWCNTs on the overall device performance as discussed in the main text. The "C_{60}-only" solar cell has a smaller current density than solar cells with as prepared SWCNTs. The increase in J_{SC} in (a) is also displayed in (b) by an increased EQE and resembles the influence of SWCNTs on the current generation. In addition to quantum efficiencies, $|E|^2$ and the SWCNT film absorbance were also plotted to demonstrate the effect of light absorption at S_{22} and S_{11} on the EQE spectrum of solar cells with nanotubes.

References

1. N. Nair, M. L. Usrey, W.-J. Kim, R. D. Braatz, M. S. Strano, Analytical Chemistry 2006, 78, 7689.
2. R. B. Weisman, S. M. Bachilo, Nano Letters 2003, 3, 1235.
3. V. Perebeinos, J. Tersoff, P. Avouris, Physical review letters 2005, 94, 027402.
4. G. F. Burkhard, E. T. Hoke, M. D. McGehee, Advanced Materials 2010, 22, 3293.
5. E. D. Palik, Handbook of optical constants of solids, Vol. 3, Academic press, Massachusetts, USA, 1998; S. L. Ren, Y. Wang, A. M. Rao, E. McRae, J. M. Holden, T. Hager, K. Wang, W. T. Lee, H. F. Ni, J. Selegue, P. C. Eklund, Applied Physics Letters 1991, 59, 2678.
6. J. A. Fagan, J. R. Simpson, B. J. Landi, L. J. Richter, I. Mandelbaum, V. Bajpai, D. L. Ho, R. Raffaelle, A. R. H. Walker, B. J. Bauer, E. K. Hobbie, Physical Review Letters 2007, 98, 147402; Y. Battie, D. Jamon, A. En Naciri, J.-S. Lauret, A. Loiseau, Applied Physics Letters 2013, 102, 091909.
7. Y. Li, Three Dimensional Solar Cells Based on Optical Confinement Geometries, Springer Science & Business Media, 2012.
8. D. J. Bindl, M. S. Arnold, The Journal of Physical Chemistry C 2013, 117, 2390.
9. A. Armin, M. Velusamy, P. Wolfer, Y. Zhang, P. L. Burn, P. Meredith, A. Pivrikas, ACS Photonics 2014, 1, 173.

3.5.1 *Photocurrent Spectroscopy of (n,m) Sorted Solution-Processed Single-Walled Carbon Nanotubes*

M. Engel, K. E. Moore, A. Alam, S. Dehm, R. Krupke, **B. S. Flavel**

ACS Nano 8 (2014) 9324–9331

DOI: 10.1021/nn503278d

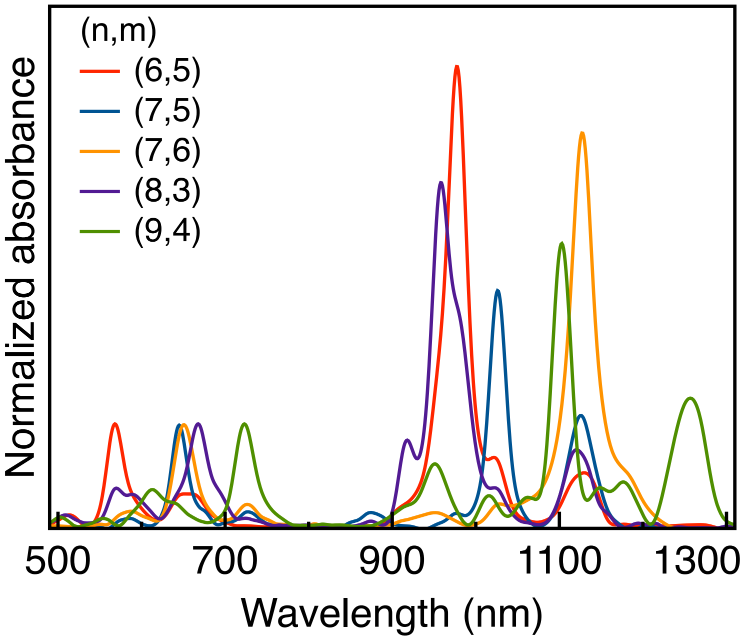

Figure S1 Absorption spectra of the chirality sorted SWCNT material used in this work. Spectra have been normalized to S_{22} via the following factors; (6, 5): 2.032×10^{-4}, (7, 5): 1.741×10^{-3}, (7, 6): 2.3×10^{-3}, (8, 3): 1.475×10^{-3}, (9, 4): 6.401×10^{-4}.

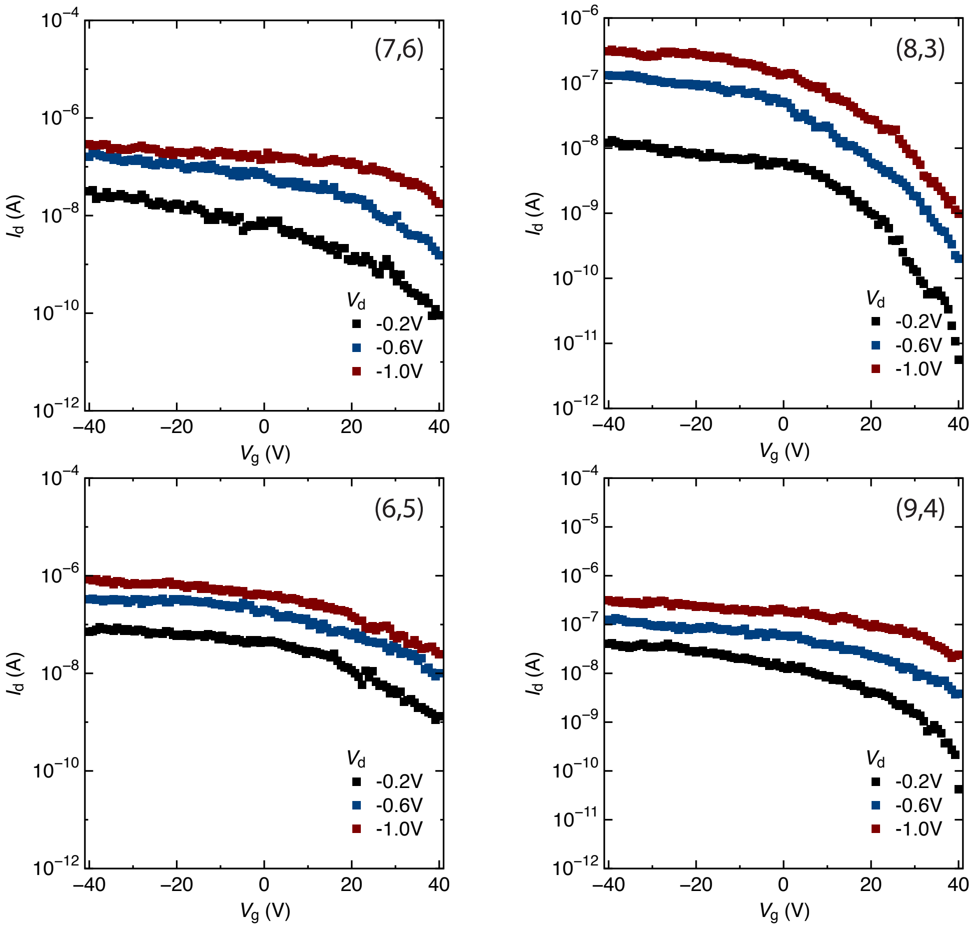

Figure S2 Representative transconductance curves for single chirality SWCNT devices used in photocurrent measurements.

3. Supporting Information

3.5.2 *Photocurrent Imaging of Semiconducting Carbon Nanotube Devices with Local Mirrors*

A. Alam, **B. S. Flavel**, S. Dehm, U. Lemmer, R. Krupke

Physica Status Solidi B 251 (2014) 2471–2474

DOI: 10.1002/pssb.201451272

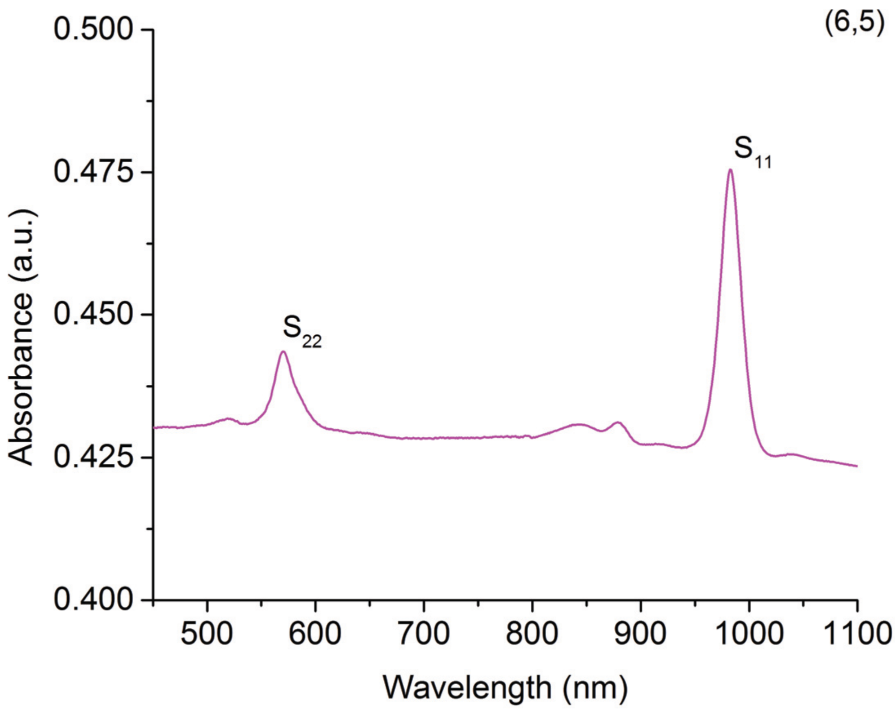

Figure S1 Absorption spectrum of the (6,5) CNT dispersion used in device fabrication. The first and second order interband transitions of (6,5) CNTs, denoted as S11 and S22, are shown at 570 nm and 982 nm, respectively.

– This page intentionally left blank –

4. References

1. Dresselhaus, M. S.; Dresselhaus, G.; Saito, R. Physics of carbon nanotubes. Carbon 1995, 33, 883-891.

2. Odom, T. W.; Huang, J.-L.; Kim, P.; Lieber, C. M. Atomic structure and electronic properties of single-walled carbon nanotubes. Nature 1998, 391, 62-64.

3. Odom, T. W.; Huang, J.-L.; Kim, P.; Lieber, C. M. Structure and Electronic Properties of Carbon Nanotubes. Journal of Physical Chemistry B 2000, 104, 2794-2809.

4. Dresselhaus, M. S.; Dresselhaus, G.; Jorio, A. Unusual properties and structure of carbon nanotubes. Annual Review Materials Research 2004, 34, 247-278.

5. Pfohl, M.; Tune, D. D.; Graf, A.; Zaumseil, J.; Krupke, R.; Flavel, B. S. Fitting single-walled carbon nanotube optical spectra. ACS Omega 2017, 2, 1163-1171.

6. Ebbesen, T. W.; Ajayan, P. M. Large-scale synthesis of carbon nanotubes. Nature 1992, 358, 220-222.

7. Spataru, C. D.; Ismail-Beigi, S.; Benedict, L. X.; Louie, S. G. Excitonic effects and optical spectra of single-walled carbon nanotubes. Phys. Rev. Lett. 2004, 92, 077402.

8. Bachilo, S. M.; Strano, M. S.; Kittrell, C.; Hauge, R. H.; Smalley, R. E.; Weisman, R. B. Structure-Assigned Optical Spectra of Single-Walled Carbon Nanotubes. Science 2002, 298, 2361-2366.

9. Pfeiffer, R.; Pichler, T.; Kim, Y. A.; Kuzmany, H. Double-wall carbon nanotubes. In Carbon Nanotubes, Springer: Berlin Heidelberg, 2008; pp 495-530.

10. Shen, C.; Brozena, A. H.; Wang, Y. Double-walled carbon nanotubes: Challenges and opportunities. Nanoscale 2011, 3, 503-518.

11. Kim, Y. A.; Yang, K.-S.; Muramatsu, H.; Hayashi, T.; Endo, M.; Terrones, M.; Dresselhaus, M. S. Double-walled carbon nanotubes: synthesis, structural characterization, and application. Carbon Lett 2014, 15, 77-88.

12. Shimada, T.; Sugai, T.; Ohno, Y.; Kishimoto, S.; Mizutani, T.; Yoshida, H.; Okazaki, T.; Shinohara, H. Double-wall carbon Nanotube Field-Effect Transistors: Ambipolar Transport Characteristics. Applied Physics Letters 2004, 84, 2412-2414.

13. Liu, K.; Wang, W.; Xu, Z.; Bai, X.; Wang, E.; Yao, Y.; Zhang, J.; Liu, Z. Chirality-Dependent Transport Properties of Double-Walled Nanotubes Measured in Situ on Their Field-Effect Transistors. Journal of the American Chemical Society 2008, 131, 62-63.

14. Kim, Y. A.; Muramatsu, H.; Hayashi, T.; Endo, M.; Terrones, M.; Dresselhaus, M. S. Thermal stability and structural changes of double-walled carbon nanotubes by heat treatment. Chemical Physics Letters 2004, 398, 87-92.

15. Li, Y. F.; Hatakeyama, R.; Kaneko, T.; Izumida, T.; Okada, T.; Kato, T. Electronic transport properties of Cs-encapsulated double-walled carbon nanotubes. Applied Physics Letters 2006, 89, 093110-3.

16. Kuwahara, S.; Akita, S.; Shirakihara, M.; Sugai, T.; Nakayama, Y.; Shinohara, H. Fabrication and Characterization of High-Resolution AFM Tips With High-Quality Double-Wall Carbon Nanotubes. Chemical Physics Letters 2006, 429, 581-585.

17. Saito, R.; Dresselhaus, G.; Dresselhaus, M. S. Physical properties of carbon nanotubes. Imperial College Press: London, 1998; Vol. 4.

18. Li, H.; Gordeev, G.; Wasserroth, S.; Chakravadhanula, V. S. K.; Neelakandhan, S. K. C.; Hennrich, F.; Jorio, A.; Reich, S.; Krupke, R.; Flavel, B. S. Inner- and outer-wall sorting of double-walled carbon nanotubes. Nature Nanotechnology 2017, 12, 1176.

19. Kociak, M.; Suenaga, K.; Hirahara, K.; Saito, Y.; Nakahira, T.; Iijima, S. Linking Chiral Indices and Transport Properties of Double-Walled Carbon Nanotubes. Physical Review Letters 2002, 89, 155501.

20. Liang, S. D. Intrinsic properties of electronic structure in commensurate double-wall carbon nanotubes. Physica B: Condensed Matter 2004, 352, 305-311.

21. Wang, S.; Grifoni, M. Helicity and electron-correlation effects on transport properties of double-walled carbon nanotubes. Physical Review Letters 2005, 95, 266802.

22. Okazaki, T.; Bandow, S.; Tamura, G.; Fujita, Y.; Iakoubovskii, K.; Kazaoui, S.; Minami, N.; Saito, T.; Suenaga, K.; Iijima, S. Photoluminescence quenching in peapod-derived double-walled carbon nanotubes. Physical Review B 2006, 74, 153404.

23. Moradian, R.; Azadi, S.; Refii-tabar, H. When double-wall carbon nanotubes can become metallic or semiconducting. Journal of Physics: Condensed Matter 2007, 19, 176209.

24. Villalpando-Paez, F.; Son, H.; Nezich, D.; Hsieh, Y. P.; Kong, J.; Kim, Y. A.; Shimamoto, D.; Muramatsu, H.; Hayashi, T.; Endo, M.; Terrones, M.; Dresselhaus, M. S. Raman Spectroscopy Study of Isolated Double-Walled Carbon Nanotubes with Different Metallic and Semiconducting Configurations. Nano Letters 2008, 8, 3879-3886.

25. Liu, K.; Jin, C.; Hong, X.; Kim, J.; Zettl, A.; Wang, E.; Wang, F. Van der Waals-coupled electronic states in incommensurate double-walled carbon nanotubes. Nat Phys 2014, 10, 737-742.

26. Uryu, S.; Ando, T. Electronic intertube transfer in double-wall carbon nanotubes. Physical Review B 2005, 72, 245403.

27. Pyatkov, F.; Fütterling, V.; Khasminskaya, S.; Flavel, B. S.; Hennrich, F.; Kappes, M. M.; Krupke, R.; Pernice, W. H. P. Cavity-enhanced light emission from electrically driven carbon nanotubes. Nature Photonics 2016, 10, 420.

28. Benjamin S. Flavel; Jingxian Yu; Joseph G. Shapter; Quinton, J. S. Patterned attachment of carbon nanotubes to silane modified silicon. Carbon 2007, 45, 2551-2558.

29. Khasminskaya, S.; Pyatkov, F.; Flavel, B. S.; Pernice, W. H. P.; Krupke, R. Waveguide-Integrated Light Emitting Carbon Nanotubes. Advanced Materials 2014, 26, 3465-3472.

30. Garrett, D. J.; Flavel, B. S.; Shapter, J. G.; Baronian, K. H. R.; Downard, A. J. Robust Forests of Vertically aligned carbon nanotubes chemically assembled on carbon surfaces. Langmuir 2009.

31. Tune, D. D.; Flavel, B. S.; Quiton, J. S.; Ellis, A. V.; Shapter, J. G. Single-walled carbon nanotube network electrodes for dye solar cells. Solar Energy Materials and Solar Cells 2010, 94, 1665-1672.

32. Thiele, C.; Vieker, H.; Beyer, A.; Flavel, B. S.; Hennrich, F.; Torres, D. M.; Eaton, T. R.; Mayor, M.; Kappes, M. M.; Gölzhäuser, A.; Löhneysen, H. v.; Krupke, R. Fabrication of carbon nanotube nanogap electrodes by helium ion sputtering for molecular contacts. Applied Physics Letters 2014, 104, 103102.

33. Flavel, B. S.; Garrett, D. J.; Lehr, J.; Shapter, J. G.; Downard, A. J. Chemically Immobilised Carbon Nanotubes on Silicon: Stable Surfaces for Aqueous Electrochemistry. Electrochimica Acta 2010, 55, 3995-4001.

34. Flavel, B. S.; Yu, J.; Shapter, J. G.; Quinton, J. S. Patterned Polyaniline & Carbon Nanotube/Polyaniline Composites on Silicon. Soft Matter 2008.

35. Flavel, B. S.; Yu, J.; Shapter, J. G.; Quinton, J. S. Electrochemical characterisation of patterned carbon nanotube electrodes on silane modified silicon. Electrochimica Acta 2008, 53, 5653-5659.

36. Poh, Z.; Flavel, B. S.; Shearer, C. J.; Shapter, J. G.; Ellis, A. V. Fabrication and Electrochemical Behavior of Vertically Aligned Carbon Nanotube Materials Covalently Attached to p-type Silicon via a Thioester Linkage. Materials Letters 2009, 63, 757-760.

37. Flavel, B. S.; Yu, J.; Ellis, A. V.; Shapter, J. G. Electroless plated gold as a support for carbon nanotube electrodes. Electrochimica Acta 2009, 54, 3191-3198.

38. Flavel, B. S.; Yu, J.; Ellis, A. V.; Quinton, J. S.; Shapter, J. G. Solution Chemistry Approach to Fabricate Vertically Aligned Carbon Nanotubes on Gold Wires: Towards Vertically Integrated Electronics. Nanotechnology 2008, 19, 445301.

39. Fechner, R. G.; Pyatkov, F.; Khasminskaya, S.; Flavel, B. S.; Krupke, R.; Pernice, W. H. P. Directional couplers with integrated carbon nanotube incandescent light emitters. Optics Express 2016, 24, 966-974.

40. Brozena, A. H.; Moskowitz, J.; Shao, B.; Deng, S.; Liao, H.; Gaskell, K. J.; Wang, Y. Outer Wall Selectively Oxidized, Water-Soluble Double-Walled Carbon Nanotubes. Journal of the American Chemical Society 2010, 132, 3932-3938.

41. Piao, Y.; Chen, C.-F.; Green, A. A.; Kwon, H.; Hersam, M. C.; Lee, C. S.; Schatz, G. C.; Wang, Y. Optical and Electrical Properties of Inner Tubes in Outer Wall-Selectively Functionalized Double-Wall Carbon Nanotubes. The Journal of Physical Chemistry Letters 2011, 2, 1577-1582.

42. Yu, J.; Mathew, S.; Flavel, B. S.; Johnston, M. R.; Shapter, J. G. Ruthenium Porphyrin Functionalized Single-Walled Carbon Nanotube Arrays - A Step Toward Light Harvesting Antenna and Multibit Information Storage. Journal of American Chemical Society 2008.

43. Felten, A.; Flavel, B. S.; Britnell, L.; Eckmann, A.; Louette, P.; Pireaux, J.-J.; Hirtz, M.; Krupke, R.; Casiraghi, C. Single- and Double-Sided Chemical Functionalization of Bilayer Graphene. Small 2013, 9, 631-639.

44. Moore, K. E.; Flavel, B. S.; Ellis, A. V.; Shapter, J. G. Comparison of double-walled with single-walled carbon nanotube electrodes by electrochemistry. Carbon 2011, 49, 2639-2647.

45. Flavel, B. S.; Yu, J.; Shapter J. G.; Quinton, J. S. Patterned ferrocenemethanol modifed carbon nanotube electrodes on silane modifed silicon. Journal of Materials Chemistry 2007, 17, 4757-4761.

46. Flavel, B. S.; Nambiar, M.; Shapter, J. G. Electrochemical Detection of Copper Using a Gly-Gly-His Modified Carbon Nanotube Biosensor. 2010.

47. Moore, K. E.; Flavel, B. S.; Yu, J.; Abell, A. D.; Shapter, J. G. Increased redox-active peptide loading on carbon nanotube electrodes Electrochimica Acta 2013, 89, 206-211.

48. Moore, K. E.; Flavel, B. S.; Shearer, C. J.; Ellis, A. V.; Shapter, J. G. Electrochemistry of polystyrene intercalated vertically aligned single and double walled carbon nanotubes on gold electrodes. Electrochemistry Communications 2011, 13, 1190-1193.

49. Mickelson, E. T.; Huffman, C. B.; Rinzler, A. G.; Smalley, R. E.; Hauge, R. H.; Margrave, J. L. Fluorination of single-wall carbon nanotubes. Chemical Physics Letters 1998, 296, 188-194.

50. Zhao, J.; Park, H.; Han, J.; Lu, J. P. Electronic Properties of Carbon Nanotubes with Covalent Sidewall Functionalization. The Journal of Physical Chemistry B 2004, 108, 4227-4230.

51. Zheng, M.; Jagota, A.; Semke, E. D.; Diner, B. A.; McLean, R. S.; Lustig, S. R.; Richardson, R. E.; Tassi, N. G. DNA-assisted dispersion and separation of carbon nanotubes. Nature Materials 2003, 2, 338-342.

52. Arnold, M. S.; Stupp, S. I.; Hersam, M. C. Enrichment of Single-Walled Carbon Nanotubes by Diameter in Density Gradients. Nano Lett. 2005, 5, 713-718.

53. Tvrdy, K.; Jain, R. M.; Han, R.; Hilmer, A. J.; McNicholas, T. P.; Strano, M. S. A Kinetic Model for the Deterministic Prediction of Gel-Based Single-Chirality Single-Walled Carbon Nanotube Separation. ACS Nano 2013, 7, 1779-1789.

54. Ghosh, S.; Bachilo, S. M.; Weisman, R. B. Advanced sorting of single-walled carbon nanotubes by nonlinear density-gradient ultracentrifugation. Nat Nano 2010, 5, 443-450.

55. Nish, A.; Hwang, J.-Y.; Doig, J.; Nicholas, R. J. Highly selective dispersion of single-walled carbon nanotubes using aromatic polymers. Nature Nanotechnology 2007, 2, 640-646.

56. Chen, F.; Wang, B.; Chen, Y.; Li, L.-J. Toward the Extraction of Single Species of Single-Walled Carbon Nanotubes Using Fluorene-Based Polymers. Nano letters 2007, 7, 3013-3017.

57. Hwang, J. Y.; Nish, A.; Doig, J.; Douven, S.; Chen, C. W.; Chen, L. C.; Nicholas, R. J. Polymer structure and solvent effects on the selective dispersion of single-walled carbon nanotubes. J Am Chem Soc 2008, 130, 3543-3553.

58. Gomulya, W.; Costanzo, G. D.; de Carvalho, E. J. F.; Bisri, S. Z.; Derenskyi, V.; Fritsch, M.; Fröhlich, N.; Allard, S.; Gordiichuk, P.; Herrmann, A.; Marrink, S. J.; dos Santos, M. C.; Scherf, U.; Loi, M. A. Semiconducting Single-Walled Carbon Nanotubes on Demand by Polymer Wrapping. Advanced Materials 2013, 25, 2948-2956.

59. Gerstel, P.; Klumpp, S.; Hennrich, F.; Poschlad, A.; Meded, V.; Blasco, E.; Wenzel, W.; Kappes, M. M.; Barner-Kowollik, C. Highly Selective Dispersion of Single-Walled Carbon Nanotubes via Polymer Wrapping: A Combinatorial Study via Modular Conjugation. ACS Macro Letters 2013, 3, 10-15.

60. Ding, J.; Li, Z.; Lefebvre, J.; Cheng, F.; Dubey, G.; Zou, S.; Finnie, P.; Hrdina, A.; Scoles, L.; Lopinski, G. P. Enrichment of large-diameter semiconducting SWCNTs by polyfluorene extraction for high network density thin film transistors. Nanoscale 2014, 6, 2328-2339.

61. Deng, S.; Brozena, A. H.; Zhang, Y.; Piao, Y.; Wang, Y. Diameter-dependent, progressive alkylcarboxylation of single-walled carbon nanotubes. Chemical Communications 2011, 47, 758-760.

62. Deng, S.; Zhang, Y.; Brozena, A. H.; Mayes, M. L.; Banerjee, P.; Chiou, W.-A.; Rubloff, G. W.; Schatz, G. C.; Wang, Y. Confined propagation of covalent chemical reactions on single-walled carbon nanotubes. Nature Communications 2011, 2, 382.

63. Bandyopadhyaya, R.; Nativ-Roth, E.; Regev, O.; Yerushalmi-Rozen, R. Stabilization of Individual Carbon Nanotubes in Aqueous Solutions. Nano Letters 2001, 2, 25-28.

64. Moore, V. C.; Strano, M. S.; Haroz, E. H.; Hauge, R. H.; Smalley, R. E.; Schmidt, J.; Talmon, Y. Individually Suspended Single-Walled Carbon Nanotubes in Various Surfactants. Nano Letters 2003, 3, 1379-1382.

65. Vaisman, L.; Wagner, H. D.; Marom, G. The role of surfactants in dispersion of carbon nanotubes. Advances in Colloid and Interface Science 2006, 128–130, 37-46.

66. Cooper, L.; Amano, H.; Hiraide, M.; Houkyou, S.; Jang, I. Y.; Kim, Y. J.; Muramatsu, H.; Kim, J. H.; Hayashi, T.; Kim, Y. A.; Endo, M.; Dresselhaus, M. S. Freestanding, bendable thin film for supercapacitors using DNA-dispersed double walled carbon nanotubes. Applied Physics Letters 2009, 95, 233104.

67. Blanch, A. J.; Lenehan, C. E.; Quinton, J. S. Optimizing Surfactant Concentrations for Dispersion of Single-Walled Carbon Nanotubes in Aqueous Solution. The Journal of Physical Chemistry B 2010, 114, 9805-9811.

68. Georgakilas, V.; Tagmatarchis, N.; Pantarotto, D.; Bianco, A.; Briand, J.-P.; Prato, M. Amino acid functionalisation of water soluble carbon nanotubes. Chemical Communications 2002, 3050-3051.

69. Hudson, J. L.; Casavant, M. J.; Tour, J. M. Water-Soluble, Exfoliated, Nonroping Single-Wall Carbon Nanotubes. Journal of the American Chemical Society 2004, 126, 11158-11159.

70. Ruther, M. G.; Frehill, F.; O'Brien, J. E.; Minett, A. I.; Blau, W. J.; Vos, J. G.; Panhuis, M. Characterization of covalent functionalized carbon nanotubes. Journal of Physical Chemistry B 2004, 108, 9665-9668.

71. Kim, W.-J.; Nair, N.; Lee, C. Y.; Strano, M. S. Covalent Functionalization of Single-Walled Carbon Nanotubes Alters Their Densities Allowing Electronic and Other Types of Separation. The Journal of Physical Chemistry C 2008, 112, 7326-7331.

72. Banerjee, S.; Wong, S. S. Demonstration of Diameter-Selective Reactivity in the Sidewall Ozonation of SWNTs by Resonance Raman Spectroscopy. Nano Lett. 2004, 4, 1445-1450.

73. An, K. H.; Park, J. S.; Yang, C.-M.; Jeong, S. Y.; Lim, S. C.; Kang, C.; Son, J.-H.; Jeong, M. S.; Lee, Y. H. A Diameter-Selective Attack of Metallic Carbon Nanotubes by Nitronium Ions. Journal of the American Chemical Society 2005, 127, 5196-5203.

74. Blanch, A. J.; Lenehan, C. E.; Quinton, J. S. Dispersant Effects in the Selective Reaction of Aryl Diazonium Salts with Single-Walled Carbon Nanotubes in Aqueous Solution. The Journal of Physical Chemistry C 2011, 116, 1709-1723.

75. Arnold, M. S.; Green, A. A.; Hulvat, J. F.; Stupp, S. I.; Hersam, M. C. Sorting carbon nanotubes by electronic structure using density differentiation. Nat Nano 2006, 1, 60-65.

76. Fagan, J. A.; Becker, M. L.; Chun, J.; Nie, P.; Bauer, B. J.; Simpson, J. R.; Hight-Walker, A.; Hobbie, E. K. Centrifugal Length Separation of Carbon Nanotubes. Langmuir 2008, 24, 13880-13889.

77. Bonaccorso, F.; Hasan, T.; Tan, P. H.; Sciascia, C.; Privitera, G.; Di Marco, G.; Gucciardi, P. G.; Ferrari, A. C. Density Gradient Ultracentrifugation of Nanotubes: Interplay of Bundling and Surfactants Encapsulation. The Journal of Physical Chemistry C 2010, 114, 17267-17285.

78. Green, A. A.; Hersam, M. C. Nearly Single-Chirality Single-Walled Carbon Nanotubes Produced via Orthogonal Iterative Density Gradient Ultracentrifugation. Advanced Materials 2011, 23, 2185-2190.

79. Liu, H.; Nishide, D.; Tanaka, T.; Kataura, H. Large-scale single-chirality separation of single-wall carbon nanotubes by simple gel chromatography. Nat Commun 2011, 2, 309.

80. Flavel, B. S.; Moore, K. E.; Pfohl, M.; Kappes, M. M.; Hennrich, F. Separation of Single-Walled Carbon Nanotubes with a Gel Permeation Chromatography System. ACS Nano 2014.

81. Wei, L.; Flavel, B. S.; Li, W.; Krupke, R.; Chen, Y. Exploring the upper limit of single-walled carbon nanotube purity by multiple-cycle aqueous two-phase separation. nanoscale 2017, 9, 11640-11646.

82. Zheng, M.; Jagota, A.; Strano, M. S.; Santos, A. P.; Barone, P.; Chou, S. G.; Diner, B. A.; Dresselhaus, M. S.; Mclean, R. S.; Onoa, G. B.; Samsonidze, G. G.; Semke, E. D.; Usrey, M.; Walls, D. J. Structure-Based Carbon Nanotube Sorting by Sequence-Dependent DNA Assembly. Science 2003, 302, 1545-1548.

83. Zheng, M.; Semke, E. D. Enrichment of Single Chirality Carbon Nanotubes. Journal of the American Chemical Society 2007, 129, 6084-6085.

84. Tu, X.; Manohar, S.; Jagota, A.; Zheng, M. DNA sequence motifs for structure-specific recognition and separation of carbon nanotubes. Nature 2009, 460, 250-253.

85. Nish, A.; Hwang, J. Y.; Doig, J.; Nicholas, R. J. Highly selective dispersion of single walled carbon nanotubes using aromatic polymers. Nat Nanotechnol 2007, 2, 640-646.

86. Chen, F. M.; Wang, B.; Chen, Y.; Li, L. J. Toward the extraction of single species of single-walled carbon nanotubes using fluorene-based polymers. Nano Lett 2007, 7, 3013-3017.

87. Islam, M. F.; Rojas, E.; Bergey, D. M.; Johnson, A. T.; Yodh, A. G. High Weight Fraction Surfactant Solubilization of Single-Wall Carbon Nanotubes in Water. Nano Letters 2003, 3, 269-273.

88. Duan, W. H.; Wang, Q.; Collins, F. Dispersion of carbon nanotubes with SDS surfactants: a study from a binding energy perspective. Chemical Science 2011, 2, 1407-1413.

89. Liu, H.; Tanaka, T.; Urabe, Y.; Kataura, H. High-Efficiency Single-Chirality Separation of Carbon Nanotubes Using Temperature-Controlled Gel Chromatography. Nano Lett. 2013, 13, 1996-2003.

90. Blanch, A. J.; Quinton, J. S.; Shapter, J. G. The role of sodium dodecyl sulfate concentration in the separation of carbon nanotubes using gel chromatography. Carbon 2013, 60, 471-480.

91. Flavel, B. S.; Kappes, M. M.; Krupke, R.; Hennrich, F. Separation of Single-Walled Carbon Nanotubes by 1-Dodecanol-Mediated Size-Exclusion Chromatography. ACS Nano 2013, 7, 3557-64.

92. Collins, P. G.; Arnold, M. S.; Avouris, P. Engineering Carbon Nanotubes and Nanotube Circuits Using Electrical Breakdown. Science 2001, 292, 706-709.

93. Xu, Z.; Yang, X.; Yang, Z. A Molecular Simulation Probing of Structure and Interaction for Supramolecular Sodium Dodecyl Sulfate/Single-Wall Carbon Nanotube Assemblies. Nano Letters 2010, 10, 985-991.

94. Tummala, N. R.; Striolo, A. SDS Surfactants on Carbon Nanotubes: Aggregate Morphology. ACS Nano 2009, 3, 595-602.

95. McDonald, T. J.; Engtrakul, C.; Jones, M.; Rumbles, G.; Heben, M. J. Kinetics of PL Quenching during Single-Walled Carbon Nanotube Rebundling and Diameter-Dependent Surfactant Interactions. The Journal of Physical Chemistry B 2006, 110, 25339-25346.

96. Hersam, M. C. Progress towards monodisperse single-walled carbon nanotubes. Nat Nano 2008, 3, 387-394.

97. Zheng, M.; Jagota, A.; Semke, E. D.; Diner, B. A.; McLean, R. S.; Lustig, S. R.; Richardson, R. E.; Tassi, N. G. DNA-assisted dispersion and separation of carbon nanotubes. Nat Mater 2003, 2, 338-342.

98. Kim, J. H.; Kataoka, M.; Kim, Y. A.; Shimamoto, D.; Muramatsu, H.; Hayashi, T.; Endo, M.; Terrones, M.; Dresselhaus, M. S. Diameter-selective separation of double-walled carbon nanotubes. Applied Physics Letters 2008, 93, 223107.

99. Kim, J. H.; Kataoka, M.; Shimamoto, D.; Muramatsu, H.; Jung, Y. C.; Hayashi, T.; Kim, Y. A.; Endo, M.; Park, J. S.; Saito, R.; Terrones, M.; Dresselhaus, M. S. Raman and Fluorescence Spectroscopic Studies of a DNA-Dispersed Double-Walled Carbon Nanotube Solution. ACS Nano 2010, 4, 1060-1066.

100. Nepal, D.; Geckeler, K. E. pH-Sensitive Dispersion and Debundling of Single-Walled Carbon Nanotubes: Lysozyme as a Tool. Small 2006, 2, 406-412.

101. Nepal, D.; Geckeler, K. E. Proteins and Carbon Nanotubes: Close Encounter in Water. Small 2007, 3, 1259-1265.

102. Mu, Q.; Liu, W.; Xing, Y.; Zhou, H.; Li, Z.; Zhang, Y.; Ji, L.; Wang, F.; Si, Z.; Zhang, B.; Yan, B. Protein Binding by Functionalized Multiwalled Carbon Nanotubes Is Governed by the Surface Chemistry of Both Parties and the Nanotube Diameter. The Journal of Physical Chemistry C 2008, 112, 3300-3307.

103. Raffaini, G.; Ganazzoli, F. Protein adsorption on biomaterial and nanomaterial surfaces: a molecular modeling approach to study non-covalent interactions. Journal of Applied Biomaterials & Biomechanics: JABB 2009, 8, 135-145.

104. Nie, H.; Wang, H.; Cao, A.; Shi, Z.; Yang, S.-T.; Yuan, Y.; Liu, Y. Diameter-selective dispersion of double-walled carbon nanotubes by lysozyme. Nanoscale 2011, 3, 970-973.

105. Horn, D. W.; Tracy, K.; Easley, C. J.; Davis, V. A. Lysozyme Dispersed Single-Walled Carbon Nanotubes: Interaction and Activity. The Journal of Physical Chemistry C 2012, 116, 10341-10348.

106. Calvaresi, M.; Hoefinger, S.; Zerbetto, F. Probing the Structure of Lysozyme–Carbon-Nanotube Hybrids with Molecular Dynamics. Chemistry – A European Journal 2012, 18, 4308-4313.

107. Mistry, K. S.; Larsen, B. A.; Blackburn, J. L. High-Yield Dispersions of Large-Diameter Semiconducting Single-Walled Carbon Nanotubes with Tunable Narrow Chirality Distributions. Acs Nano 2013, 7, 2231-2239.

108. Han, J.; Ji, Q.; Qiu, S.; Li, H.; Zhang, S.; Jin, H.; Li, Q. A versatile approach to obtain a high-purity semiconducting single-walled carbon nanotube dispersion with conjugated polymers. Chem Commun 2015.

109. Shea, M. J.; Mehlenbacher, R. D.; Zanni, M. T.; Arnold, M. S. Experimental Measurement of the Binding Configuration and Coverage of Chirality-Sorting Polyfluorenes on Carbon Nanotubes. J Phys Chem Lett 2014, 5, 3742-3749.

110. Liang, S.; Li, H.; Flavel, B. S.; Adronov, A. Effect of SWCNT composition on polyfluorene-based SWCNT dispersion selectivity. Chemistry A European Journal 2018.

111. Berton, N.; Lemasson, F.; Poschlad, A.; Meded, V.; Tristram, F.; Wenzel, W.; Hennrich, F.; Kappes, M. M.; Mayor, M. Selective Dispersion of Large-Diameter Semiconducting Single-Walled Carbon Nanotubes with Pyridine-Containing Copolymers. Small 2014, 10, 360-367.

112. Berton, N.; Lemasson, F.; Tittmann, J.; Sturzl, N.; Hennrich, F.; Kappes, M. M.; Mayor, M. Copolymer-Controlled Diameter-Selective Dispersion of Semiconducting Single-Walled Carbon Nanotubes. Chem Mater 2011, 23, 2237-2249.

113. Lemasson, F.; Berton, N.; Tittmann, J.; Hennrich, F.; Kappes, M. M.; Mayor, M. Polymer Library Comprising Fluorene and Carbazole Homo- and Copolymers for Selective Single-Walled Carbon Nanotubes Extraction. Macromolecules 2012, 45, 713-722.

114. Samanta, S. K.; Fritsch, M.; Scherf, U.; Gomulya, W.; Bisri, S. Z.; Loi, M. A. Conjugated Polymer-Assisted Dispersion of Single-Wall Carbon Nanotubes: The Power of Polymer Wrapping. Accounts Chem Res 2014, 47, 2446-2456.

115. Wang, H.; Li, Y.; Jiménez-Osés, G.; Liu, P.; Fang, Y.; Zhang, J.; Lai, Y.-C.; Park, S.; Chen, L.; Houk, K. N.; Bao, Z. N-type Conjugated Polymer-Enabled Selective Dispersion of Semiconducting Carbon Nanotubes for Flexible CMOS-Like Circuits. Advanced Functional Materials 2015.

116. Wang, H. L.; Koleilat, G. I.; Liu, P.; Jimenez-Oses, G.; Lai, Y. C.; Vosgueritchian, M.; Fang, Y.; Park, S.; Houk, K. N.; Bao, Z. N. High-Yield Sorting of Small-Diameter Carbon Nanotubes for Solar Cells and Transistors. Acs Nano 2014, 8, 2609-2617.

117. Mulla, K.; Liang, S.; Shaik, H.; Younes, E. A.; Adronov, A.; Zhao, Y. Dithiafulvenyl-grafted phenylene ethylene polymers as selective and reversible dispersants for single-walled carbon nanotubes. Chem Commun 2015, 51, 149-152.

118. Lemasson, F. A.; Strunk, T.; Gerstel, P.; Hennrich, F.; Lebedkin, S.; Barner-Kowollik, C.; Wenzel, W.; Kappes, M. M.; Mayor, M. Selective Dispersion of Single-Walled Carbon Nanotubes with Specific Chiral Indices by Poly(N-decyl-2,7-carbazole). J Am Chem Soc 2011, 133, 652-655.

119. Ozawa, H.; Fujigaya, T.; Niidome, Y.; Hotta, N.; Fujiki, M.; Nakashima, N. Rational Concept To Recognize/Extract Single-Walled Carbon Nanotubes with a Specific Chirality. J Am Chem Soc 2011, 133, 2651-2657.

120. Ozawa, H.; Fujigaya, T.; Song, S.; Suh, H.; Nakashima, N. Different Chiral Selective Recognition/Extraction of (n,m)Single-walled Carbon Nanotubes Using Copolymers Carrying a Carbazole or Fluorene Moiety. Chem Lett 2011, 40, 470-472.

121. Lee, H. W.; Yoon, Y.; Park, S.; Oh, J. H.; Hong, S.; Liyanage, L. S.; Wang, H. L.; Morishita, S.; Patil, N.; Park, Y. J.; Park, J. J.; Spakowitz, A.; Galli, G.; Gygi, F.; Wong, P. H. S.; Tok, J. B. H.; Kim, J. M.; Bao, Z. A. Selective dispersion of high purity semiconducting single-walled carbon nanotubes with regioregular poly(3-alkylthiophene)s. Nat Commun 2011, 2.

122. Gerstel, P.; Klumpp, S.; Hennrich, F.; Altintas, O.; Eaton, T. R.; Mayor, M.; Barner-Kowollik, C.; Kappes, M. M. Selective dispersion of single-walled carbon nanotubes via easily accessible conjugated click polymers. Polym Chem-Uk 2012, 3, 1966-1970.

123. Akazaki, K.; Toshimitsu, F.; Ozawa, H.; Fujigaya, T.; Nakashima, N. Recognition and One-Pot Extraction of Right- and Left-Handed Semiconducting Single-Walled Carbon Nanotube Enantiomers Using Fluorene-Binaphthol Chiral Copolymers. J Am Chem Soc 2012, 134, 12700-12707.

124. Sturzl, N.; Hennrich, F.; Lebedkin, S.; Kappes, M. M. Near Monochiral Single-Walled Carbon Nanotube Dispersions in Organic Solvents. J Phys Chem C 2009, 113, 14628-14632.

125. Wang, H. L.; Hsieh, B.; Jimenez-Oses, G.; Liu, P.; Tassone, C. J.; Diao, Y.; Lei, T.; Houk, K. N.; Bao, Z. N. Solvent Effects on Polymer Sorting of Carbon Nanotubes with Applications in Printed Electronics. Small 2015, 11, 126-133.

126. Gomulya, W.; Costanzo, G. D.; de Carvalho, E. J. F.; Bisri, S. Z.; Derenskyi, V.; Fritsch, M.; Frohlich, N.; Allard, S.; Gordiichuk, P.; Herrmann, A.; Marrink, S. J.; dos Santos, M. C.; Scherf, U.; Loi, M. A. Semiconducting Single-Walled Carbon Nanotubes on Demand by Polymer Wrapping. Adv Mater 2013, 25, 2948-2956.

127. Graf, A.; Zakharko, Y.; Schießl, S. P.; Backes, C.; Pfohl, M.; Flavel, B. S.; Zaumseil, J. Large scale, selective disperson of long single-walled carbon nanotubes with high photoluminescence quantum yield by shear force mixing. carbon 2016, 105, 593-599.

128. Moore, K. E.; Tune, D. D.; Flavel, B. S. Double Walled Carbon Nanotube Processing. Advanced Materials 2015, 27, 3105-3137.

129. Moshammer, K.; Hennrich, F.; Kappes, M. Selective Suspension in Aqueous Sodium Dodecyl Sulfate According to Electronic Structure Type Allows Simple Separation of Metallic from Semiconducting Single-Walled Carbon Nanotubes. Nano Res. 2009, 2, 599-606.

130. Liu, H.; Tanaka, T.; Kataura, H. Optical Isomer Separation of Single-Chirality Carbon Nanotubes Using Gel Column Chromatography. Nano Letters 2014, 14, 6237-6243.

131. Niyogi, S.; Densmore, C. G.; Doorn, S. K. Electrolyte Tuning of Surfactant Interfacial Behavior for Enhanced Density-Based Separations of Single-Walled Carbon Nanotubes. Journal of the American Chemical Society 2008, 131, 1144-1153.

132. Flavel, B. S.; Moore, K. E.; Pfohl, M.; Kappes, M. M.; Hennrich, F. Separation of Single-Walled Carbon Nanotubes with a Gel Permeation Chromatography System. ACS Nano 2014, 8, 1817-1826.

133. Duque, J. G.; Densmore, C. G.; Doorn, S. K. Saturation of Surfactant Structure at the Single-Walled Carbon Nanotube Surface. Journal of the American Chemical Society 2010, 132, 16165-16175.

134. Moore, K. E.; Pfohl, M.; Tune, D. D.; Hennrich, F.; Dehm, S.; Chakradhanula, V. S. K.; Kuebel, C.; Krupke, R.; Flavel, B. S. Sorting of double-walled carbon nanotubes according to their outer wall electronic type. ACS Nano 2015, 9, 3849-3857.

135. Miyata, Y.; Shiozawa, K.; Asada, Y.; Ohno, Y.; Kitaura, R.; Mizutani, T.; Shinohara, H. Length-sorted semiconducting carbon nanotubes for high-mobility thin film transistors. Nano Res. 2011, 4, 963-970.

136. Wu, J.; Xie, L.; Hong, G.; Lim, H.; Thendie, B.; Miyata, Y.; Shinohara, H.; Dai, H. Short channel field-effect transistors from highly enriched semiconducting carbon nanotubes. Nano Res. 2012, 5, 388-394.

137. Zhang, J.; Gui, H.; Liu, B.; Liu, J.; Zhou, C. Comparative study of gel-based separated arcdischarge, HiPCO, and CoMoCAT carbon nanotubes for macroelectronic applications. Nano Res. 2013, 6, 906-920.

138. Moore, K. E.; Pfohl, M.; Hennrich, F.; Chakradhanula, V. S. K.; Kübel, C.; Kappes, M. M.; Shapter, J. G.; Krupke, R.; Flavel, B. S. Separation of double-walled carbon nanotubes by size exclusion column chromatography. ACS Nano 2014, 8, 6756-6764.

139. Shimoda, H.; Oh, S. J.; Geng, H. Z.; Walker, R. J.; Zhang, X. B.; McNeil, L. E.; Zhou, O. Self-Assembly of Carbon Nanotubes. Adv. Mater. 2002, 14, 899-901.

140. Ko, H.; Tsukruk, V. V. Liquid-Crystalline Processing of Highly Oriented Carbon Nanotube Arrays for Thin-Film Transistors. Nano Lett. 2006, 6, 1443-1448.

141. Engel, M.; Small, J. P.; Steiner, M.; Freitag, M.; Green, A. A.; Hersam, M. C.; Avouris, P. Thin Film Nanotube Transistors Based on Self-Assembled, Aligned, Semiconducting Carbon Nanotube Arrays. ACS Nano 2008, 2, 2445-2452.

142. Li, X.; Jung, Y.; Sakimoto, K.; Goh, T.-H.; Reed, M. A.; Taylor, A. D. Improved efficiency of smooth and aligned single walled carbon nanotube/silicon hybrid solar cells. Energy Environ. Sc. 2013, 6, 879-887.

143. Saha, A.; Ghosh, S.; Weisman, R. B.; Martí, A. A. Films of Bare Single-Walled Carbon Nanotubes from Superacids with Tailored Electronic and Photoluminescence Properties. ACS Nano 2012, 6, 5727–5734.

144. Azoz, S.; Exarhos, A. L.; Marquez, A.; Gilbertson, L. M.; Nejati, S.; Cha, J. J.; Zimmerman, J. B.; Kikkawa, J. M.; Pfefferle, L. D. Highly conductive single-walled carbon nanotube thin film preparation by direct alignment on substrates from water dispersions. Langmuir 2015, 31, 1155-1163.

145. Giancane, G.; Ruland, A.; Sgobba, V.; Manno, D.; Serra, A.; Farinola, G. M.; Omar, O. H.; Guldi, D. M.; Valli, L. Aligning Single-Walled Carbon Nanotubes By Means Of Langmuir–Blodgett Film Deposition: Optical, Morphological, and Photo-electrochemical Studies. Adv. Funct. Mater. 2010, 20, 2481-2488.

146. Cao, Q.; Han, S.-j.; Tulevski, G. S.; Zhu, Y.; Lu, D. D.; Haensch, W. Arrays of single-walled carbon nanotubes with full surface coverage for high-performance electronics. Nat. Nano 2013, 8, 180-186.

147. Park, S.; Pitner, G.; Giri, G.; Koo, J. H.; Park, J.; Kim, K.; Wang, H.; Sinclair, R.; Wong, H. S.; Bao, Z. Large-area assembly of densely aligned single-walled carbon nanotubes using solution shearing and their application to field-effect transistors. Adv. Mater. 2015, 27, 2656-62.

148. Zamora-Ledezma, C.; Blanc, C.; Maugey, M.; Zakri, C.; Poulin, P.; Anglaret, E. Anisotropic Thin Films of Single-Wall Carbon Nanotubes from Aligned Lyotropic Nematic Suspensions. Nano Lett. 2008, 8, 4103-4107.

149. Lu, L.; Chen, W. Large-Scale Aligned Carbon Nanotubes from Their Purified, Highly Concentrated Suspension. ACS Nano 2010, 4, 1042-1048.

150. Ren, L.; Pint, C. L.; Booshehri, L. G.; Rice, W. D.; Wang, X.; Hilton, D. J.; Takeya, K.; Kawayama, I.; Tonouchi, M.; Hauge, R. H.; Kono, J. Carbon Nanotube Terahertz Polarizer. Nano Lett. 2009, 9, 2610-2613.

151. deHeer, W. A.; Bacsa, W. S.; Châtelain, A.; Gerfin, T.; Humphrey-Baker, R.; Forro, L.; Ugarte, D. Aligned Carbon Nanotube Films: Production and Optical and Electronic Properties. Science 1995, 268, 845-847.

152. Song, W.; Kinloch, I. A.; Windle, A. H. Nematic Liquid Crystallinity of Multiwall Carbon Nanotubes. Science 2003, 302, 1363.

153. Islam, M. F.; Alsayed, A. M.; Dogic, Z.; Zhang, J.; Lubensky, T. C.; Yodh, A. G. Nematic Nanotube Gels. Phys. Rev. Lett. 2004, 92, 088303.

154. Badaire, S.; Zakri, C.; Maugey, M.; Derré, A.; Barisci, J. N.; Wallace, G.; Poulin, P. Liquid Crystals of DNA-Stabilized Carbon Nanotubes. Adv. Mater. 2005, 17, 1673-1676.

155. Zakri, C.; Poulin, P. Phase behavior of nanotube suspensions: from attraction induced percolation to liquid crystalline phases. J. Mater. Chem. 2006, 16, 4095-4098.

156. Davis, V. A. Liquid crystalline assembly of nanocylinders. J. Mater. Res. 2011, 26, 140-153.

157. Ould-Moussa, N.; Blanc, C.; Zamora-Ledezma, C.; Lavrentovich, O. D.; Smalyukh, I. I.; Islam, M. F.; Yodh, A. G.; Maugey, M.; Poulin, P.; Anglaret, E.; Nobili, M. Dispersion and orientation of single-walled carbon nanotubes in a chromonic liquid crystal. Liq. Cryst. 2013, 40, 1628-1635.

158. Volpati, D.; Massey, M. K.; Johnson, D. W.; Kotsialos, A.; Qaiser, F.; Pearson, C.; Coleman, K. S.; Tiburzi, G.; Zeze, D. A.; Petty, M. C. Exploring the alignment of carbon nanotubes dispersed in a liquid crystal matrix using coplanar electrodes. J. Appl. Phys. 2015, 117, 125303.

159. Penicaud, A.; Poulin, P.; Derre, A.; Anglaret, E.; Petit, P. Spontaneous Dissolution of a Single-Wall Carbon Nanotube Salt. JACS 2004, 127, 8-9.

160. Liang, F.; Sadana, A. K.; Peera, A.; Chattopadhyay, J.; Gu, Z.; Hauge, R. H.; Billups, W. E. A Convenient Route to Functionalized Carbon Nanotubes. Nano Lett. 2004, 4, 1257-1260.

161. Chattopadhyay, J.; Sadana, A. K.; Liang, F.; Beach, J. M.; Xiao, Y.; Hauge, R. H.; Billups, W. E. Carbon Nanotube Salts. Arylation of Single-Wall Carbon Nanotubes. Org. Lett. 2005, 7, 4067-4069.

162. Liang, F.; Beach, J. M.; Kobashi, K.; Sadana, A. K.; Vega-Cantu, Y. I.; Tour, J. M.; Billups, W. E. In Situ Polymerization Initiated by Single-Walled Carbon Nanotube Salts. Chem. Mater. 2006, 18, 4764-4767.

163. Voiry, D.; Roubeau, O.; Penicaud, A. Stoichiometric control of single walled carbon nanotubes functionalization. J. Mater. Chem. 2010, 20, 4385-4391.

164. Hof, F.; Bosch, S.; Eigler, S.; Hauke, F.; Hirsch, A. New Basic Insight into Reductive Functionalization Sequences of Single Walled Carbon Nanotubes (SWCNTs). JACS 2013, 135, 18385-18395.

165. Tune, D. D.; Blanch, A. J.; Shearer, C. J.; Moore, K. E.; Pfohl, M.; Shapter, J. G.; Flavel, B. S. Aligned carbon nanotube thin films from liquid crystal polyelectrolyte inks. ACS Appl Mater Interfaces 2015, 7, 25857-25864.

166. Tune, D. D.; Stolz, B. W.; Pfohl, M.; Flavel, B. S. Dry shear aligning: a simple and versatile method to smooth and align the surfaces of carbon nanotube thin films. Nanoscale 2016, 8, 3232-3236.

167. Bindl, D. J.; Safron, N. S.; Arnold, M. S. Dissociating Excitons Photogenerated in Semiconducting Carbon Nanotubes at Polymeric Photovoltaic Heterojunction Interfaces. ACS Nano 2010, 4, 5657-5664.

168. Shea, M. J.; Arnold, M. S. 1% solar cells derived from ultrathin carbon nanotube photoabsorbing films. Applied Physics Letters 2013, 102, 243101-5.

169. Jain, R. M.; Howden, R.; Tvrdy, K.; Shimizu, S.; Hilmer, A. J.; McNicholas, T. P.; Gleason, K. K.; Strano, M. S. Polymer-free near-infrared photovoltaics with single chirality (6,5) semiconducting carbon nanotube active layers. Advanced materials 2012, 24, 4436-9.

170. Wang, H.; Koleilat, G. I.; Liu, P.; Jiménez-Osés, G.; Lai, Y.-C.; Vosgueritchian, M.; Fang, Y.; Park, S.; Houk, K. N.; Bao, Z. High-Yield Sorting of Small-Diameter Carbon Nanotubes for Solar Cells and Transistors. ACS Nano 2014.

171. Gong, M.; Shastry, T. A.; Xie, Y.; Bernardi, M.; Jasion, D.; Luck, K. A.; Marks, T. J.; Grossman, J. C.; Ren, S.; Hersam, M. C. Polychiral Semiconducting Carbon Nanotube–Fullerene Solar Cells. Nano letters 2014, 14, 5308-5314.

172. Guillot, S. L.; Mistry, K. S.; Avery, A. D.; Richard, J.; Dowgiallo, A.-M.; Ndione, P. F.; van de Lagemaat, J.; Reese, M. O.; Blackburn, J. L. Precision printing and optical modeling of ultrathin SWCNT/C 60 heterojunction solar cells. Nanoscale 2015.

173. Tune, D. D.; Shapter, J. G. The potential sunlight harvesting efficiency of carbon nanotube solar cells. Energy & Environmental Science 2013.

174. Bellisario, D. O.; Jain, R. M.; Ulissi, Z.; Strano, M. S. Deterministic modelling of carbon nanotube near-infrared solar cells. Energy & Environmental Science 2014, 7, 3769-3781.

175. Tune, D. D.; Hennrich, F.; Dehm, S.; Klein, M. F. G.; Glaser, K.; Colsmann, A.; Shapter, J. G.; Lemmer, U.; Kappes, M. M.; Krupke, R.; Flavel, B. S. The Role of Nanotubes in Carbon Nanotube–Silicon Solar Cells. Advanced Energy Materials 2013, 3, 1091-1097.

176. Engel, M.; Moore, K. E.; Alam, A.; Dehm, S.; Krupke, R.; Flavel, B. S. Photocurrent Spectroscopy of (n, m) Sorted Solution-Processed Single-Walled Carbon Nanotubes. ACS Nano 2014, 8, 9324-9331.

177. Yang, L.; Kim, P.; Meyer, H. M.; Agnihotri, S. Aging of nanocarbons in ambient conditions: Probable metastability of carbon nanotubes. Journal of Colloid and Interface Science 2009, 338, 128-134.

178. Chen, G.; Paronyan, T. M.; Pigos, E. M.; Harutyunyan, A. R. Enhanced gas sensing in pristine carbon nanotubes under continuous ultraviolet light illumination. Sci. Rep. 2012, 2.

179. Dürkop, T.; Getty, S. A.; Cobas, E.; Fuhrer, M. S. Extraordinary Mobility in Semiconducting Carbon Nanotubes. Nano letters 2003, 4, 35-39.

180. Tune, D. D.; Flavel, B. S.; Krupke, R.; Shapter, J. G. Carbon Nanotube-Silicon Solar Cells. Advanced Energy Materials 2012, 2, 1043-1055.

181. Tune, D. D.; Flavel, B. S. Advances in carbon nanotube-silicon heterojunction solar cells. Advanced Energy Materials 2018, 8, 1703241.

182. Tune, D. D.; Flavel, B. S.; Quinton, J. S.; Ellis, A. V.; Shapter, J. G. Single-walled carbon nanotube/polyaniline/n-silicon solar cells: fabrication, characterization, and performance measurements. ChemSusChem 2013, 6, 320-327.

183. Tune, D. D.; Blanch, A. J.; Krupke, R.; Flavel, B. S.; Shapter, J. G. Nanotube film metallicity and its effect on the performance of carbon nanotube-silicon solar cells. physica status solidi a 2014, 211, 1479-1487.

184. Kataura, H.; Kumazawa, Y.; Maniwa, Y.; Umezu, I.; Suzuki, S.; Ohtsuka, Y.; Achiba, Y. Optical properties of single-wall carbon nanotubes. Synthetic Metals 1999, 103, 2555-2558.

185. Weisman, R. B.; Bachilo, S. M. Dependence of Optical Transition Energies on Structure for Single-Walled Carbon Nanotubes in Aqueous Suspension: An Empirical Kataura Plot. Nano letters 2003, 3, 1235-1238.

186. Haroz, E. H.; Bachilo, S. M.; Weisman, R. B.; Doorn, S. K. Curvature effects on the E33 and E44 exciton transitions in semiconducting single-walled carbon nanotubes. Physical Review B 2008, 77, 125405.

187. Bindl, D. J.; Arnold, M. S. Efficient Exciton Relaxation and Charge Generation in Nearly Monochiral (7,5) Carbon Nanotube/C60 Thin-Film Photovoltaics. The Journal of Physical Chemistry C 2013, 117, 2390-2395.

188. Nish, A.; Hwang, J.-Y.; Doig, J.; Nicholas, R. J. Highly selective dispersion of single-walled carbon nanotubes using aromatic polymers. Nat Nano 2007, 2, 640-646.

189. Flavel, B. S.; Kappes, M. M.; Krupke, R.; Hennrich, F. Separation of Single-Walled Carbon Nanotubes by 1-Dodecanol-Mediated Size-Exclusion Chromatography. ACS Nano 2013, 7, 3557-3564.

190. Wu, M.-Y.; Jacobberger, R. M.; Arnold, M. S. Design length scales for carbon nanotube photoabsorber based photovoltaic materials and devices. Journal of Applied Physics 2013, 113, 204504.

191. Bindl, D. J.; Shea, M. J.; Arnold, M. S. Enhancing extraction of photogenerated excitons from semiconducting carbon nanotube films as photocurrent. Chemical Physics 2013, 413, 29-34.

192. Tulevski, G. S.; Franklin, A. D.; Afzali, A. High Purity Isolation and Quantification of Semiconducting Carbon Nanotubes via Column Chromatography. ACS Nano 2013, 7, 2971-2976.

193. Pfohl, M.; Glaser, K.; Graf, A.; Mertens, A.; Tune, D. D.; Puerckhauer, T.; Alam, A.; Wei, L.; Chen, Y.; Zaumseil, J.; Colsmann, A.; Krupke, R.; Flavel, B. S. Probing the diameter limit of single walled carbon nanotubes in SWCNT:fullerene solar cells. Advanced Energy Materials 2016, 6, 1600890.

194. Pfohl, M.; Glaser, K.; Ludwig, J.; Tune, D. D.; Dehm, S.; Kayser, C.; Colsmann, A.; Krupke, R.; Flavel, B. S. Performance enhancement of polymer free carbon nanotube solar cells via transfer matrix modeling. Advanced Energy Materials 2016, 6, 1501345.

195. Krupke, R.; Hennrich, F.; Weber, H. B.; Beckmann, D.; Hampe, O.; Malik, S.; Kappes, M. M.; Lohneysen, H. V. Contacting single bundles of carbon nanotubes with alternating electric fields. Appl Phys a-Mater 2003, 76, 397-400.

196. Vijayaraghavan, A.; Blatt, S.; Weissenberger, D.; Oron-Carl, M.; Hennrich, F.; Gerthsen, D.; Hahn, H.; Krupke, R. Ultra-large-scale directed assembly of single-walled carbon nanotube devices. Nano Lett 2007, 7, 1556-1560.

197. Li, W.; Pyatkov, F.; Dehm, S.; Flavel, B. S.; Krupke, R. Deposition of semiconducting single-walled carbon nanotubes using light-assisted dielectrophoresis. physica status solidi b 2014, 251, 2475-2479.

198. Avouris, P.; Freitag, M.; Perebeinos, V. Carbon-nanotube photonics and optoelectronics. Nat Photonics 2008, 2, 341-350.
199. Balasubramanian, K.; Burghard, M.; Kern, K.; Scolari, M.; Mews, A. Photocurrent imaging of charge transport barriers in carbon nanotube devices. Nano Lett 2005, 5, 507-510.

200. Chen, C. X.; Lu, Y.; Kong, E. S.; Zhang, Y. F.; Lee, S. T. Nanowelded carbon-nanotube-based solar microcells. Small 2008, 4, 1313-1318.

201. Engel, M.; Steiner, M.; Sundaram, R. S.; Krupke, R.; Green, A. A.; Hersam, M. C.; Avouris, P. Spatially Resolved Electrostatic Potential and Photocurrent Generation in Carbon Nanotube Array Devices. Acs Nano 2012, 6, 7303-7310.

202. Freitag, M.; Martin, Y.; Misewich, J. A.; Martel, R.; Avouris, P. H. Photoconductivity of single carbon nanotubes. Nano Lett 2003, 3, 1067-1071.

203. Gabor, N. M.; Zhong, Z. H.; Bosnick, K.; Park, J.; McEuen, P. L. Extremely Efficient Multiple Electron-Hole Pair Generation in Carbon Nanotube Photodiodes. Science 2009, 325, 1367-1371.

204. Lee, J. U.; Gipp, P. P.; Heller, C. M. Carbon nanotube p-n junction diodes. Appl Phys Lett 2004, 85, 145-147.

205. Barkelid, M.; Zwiller, V. Single carbon nanotube photovoltaic device. J Appl Phys 2013, 114.

206. Barkelid, M.; Zwiller, V. Photocurrent generation in semiconducting and metallic carbon nanotubes. Nat Photonics 2014, 8, 48-52.

207. Lee, J. U. Photovoltaic effect in ideal carbon nanotube diodes. Appl Phys Lett 2005, 87.

208. Alam, A.; Dehm, S.; Hennrich, F.; Zakharko, Y.; Graf, A.; Pfohl, M.; Hossain, I. M.; Kappes, M. M.; Zaumseil, J.; Krupke, R.; Flavel, B. S. Photocurrent spectroscopy of dye-sensitized carbon nanotubes. Nanoscale 2017, 9, 11205-11213.

209. Li, W.; Hennrich, F.; Flavel, B. S.; Kappes, M. M.; Krupke, R. Chiral-index resolved length mapping of carbon nanotubes in solution using electric-field induced differential absorption spectroscopy. Nanotechnology 2016, 27, 375706.

– This page intentionally left blank –